

Lawrence Berkeley National Laboratory

Recent Work

Title

NUCLEAR CHEMISTRY ANNUAL REPORT 1972

Permalink

<https://escholarship.org/uc/item/2qs14018>

Authors

Hendrie, D.L.

Tsang, C.F.

Zalkin, A.

Publication Date

1973-05-01

LBL-1666

(repl)^c 2

RECEIVED
LAWRENCE
RADIATION LABORATORY

OCT 9 1972

LIBRARY AND
DOCUMENTS SECTION

NUCLEAR CHEMISTRY

Annual Report

1972

Lawrence Berkeley Laboratory
University of California
Berkeley, California

LBL-1666 c.2

DISCLAIMER

This document was prepared as an account of work sponsored by the United States Government. While this document is believed to contain correct information, neither the United States Government nor any agency thereof, nor the Regents of the University of California, nor any of their employees, makes any warranty, express or implied, or assumes any legal responsibility for the accuracy, completeness, or usefulness of any information, apparatus, product, or process disclosed, or represents that its use would not infringe privately owned rights. Reference herein to any specific commercial product, process, or service by its trade name, trademark, manufacturer, or otherwise, does not necessarily constitute or imply its endorsement, recommendation, or favoring by the United States Government or any agency thereof, or the Regents of the University of California. The views and opinions of authors expressed herein do not necessarily state or reflect those of the United States Government or any agency thereof or the Regents of the University of California.

LBL-1666
UC - 4 Chemistry
TID - 4500 (59th Ed.)

NUCLEAR CHEMISTRY

Annual Report

1972

Editors

D.L. Hendrie

C.F. Tsang

A. Zalkin

Lawrence Berkeley Laboratory
University of California
Berkeley, California

Work done under
U.S. Atomic Energy Commission
Contract No. W-7405-eng-48

May 1973

Printed in the United States of America
Available from
National Technical Information Service
U.S. Department of Commerce
5285 Port Royal Road
Springfield, Virginia 22151
Price: Printed Copy \$10.60; Microfiche \$0.95

Contents

I. PHYSICS OF THE NUCLEUS

NUCLEAR SPECTROSCOPY, RADIOACTIVITY, AND FISSION

Table of Isotopes Project (C. M. Lederer, J. M. Hollander, E. Browne, J. M. Dairiki, R. E. Doebler, L. J. Jardine, A. A. Shihab-Eldin, and D. A. Shirley)	3
A = 225, A = 221, A = 217, and A = 213 Mass Chains (C. C. Maples)	3
Alpha Spectroscopy of Isotopes Produced by High-Energy Nuclear Reactions (J. D. Bowman, E. K. Hyde, and R. E. Eppley)	4
Absolute Energy Measurement of the Alpha Particles Emitted by ^{232}U and ^{240}Pu (D. J. Gorman, A. Rytz, and H. V. Michel)	6
^{148}Gd Production and Purification for Absolute Alpha Energy Measurements (H. V. Michel and F. Asaro)	8
Decay of ^{209}At to Levels in ^{209}Po (L. J. Jardine, S. G. Prussin, and J. M. Hollander)	9
The Electron-Capture Decay of ^{155}Tb (C. M. Lederer, R. A. Meyer, and R. Gunnink)	10
Energy-Level Systematics of Odd-Mass Lanthanum Isotopes; A New Coupling Scheme (J. R. Leigh, K. Nakai, K. H. Maier, F. Pühlhofer, F. S. Stephens, and R. M. Diamond)	12
Rotation of Moderately Deformed Odd-A Nuclei (F. S. Stephens, R. M. Diamond, D. Benson, Jr., and M. R. Maier)	15
A Coupling Scheme Relevant to High Angular Momenta and Intermediate Nuclear Deformations (F. S. Stephens, R. M. Diamond, and S. G. Nilsson)	17
Feeding Times Following (HI, xn) Reactions (J. O. Newton, F. S. Stephens, and R. M. Diamond)	19
Statistical Decay of Gamma Rays in (n_{th}, γ) Reactions (E. Nardi, L. G. Moretto, and S. G. Thompson)	22
Nuclear Level Density (J. Huizenga and L. G. Moretto)	25
Fission Fragment Angular Distributions in ^4He -Induced Fission of Nuclei in the ^{208}Pb Region (L. G. Moretto, R. C. Gatti, and S. G. Thompson)	25
The Evaporation of Complex Fragments: Kinetic Energy and Angular Distributions (L. G. Moretto)	28
Neutron Evaporation from ^{252}Cf Fission Fragments on the Basis of the Shell Model (E. Nardi, L. G. Moretto, and S. G. Thompson)	31

Simultaneous Emission of Two Light Charged Particles in the Spontaneous Fission of ^{252}Cf (S. K. Kataria, E. Nardi, and S. G. Thompson)	33
Search for Even-Odd Effects on the Kinetic Energies of Fission Fragments (H. Nifenecker)	35
Study of the Fragments Emitted in Heavy-Ion-Induced Reactions (L. G. Moretto, S. K. Kataria, D. Heunemann, R. C. Jared, and S. G. Thompson)	37
Fragment Production in ^{40}Ar -Induced Reactions on a Cu Target (S. G. Thompson, L. G. Moretto, R. C. Jared, D. Heunemann, and R. C. Gatti)	41
X-Ray-Gamma-Ray Analysis of Heavy-Ion Reaction Products (R. C. Jared, H. Nifenecker, L. G. Moretto, and S. G. Thompson)	43
Search for Superheavy Elements in Nature (R. C. Jared, E. Cheifetz, E. R. Giusti, S. G. Thompson, J. S. Drury, R. J. Silva, R. W. Stoughton, and J. Halperin).	44
Superheavy Elements (S. G. Thompson and C. F. Tsang)	46
NUCLEAR REACTIONS AND SCATTERING	
Observation of High-Lying Levels in ^8Be from Alpha-Alpha Elastic Scattering (A. D. Bacher, F. G. Resmini, H. E. Conzett, R. de Swiniarski, H. Meiner, and J. Ernst).	50
Further Evidence for the Dominance of Nucleon-Nucleon P-Wave Forces in Vector Polarizations in N-d Scattering Below 15 MeV (J. S. C. McKee, H. E. Conzett, R. M. Larimer, and Ch. Leemann)	52
The Vector Analyzing Power in $\vec{d} - ^4\text{He}$ Elastic Scattering Between 15 and 45 MeV (H. E. Conzett, W. Dahme, Ch. Leemann, J. A. Macdonald, and J. P. Meulders).	55
Deviations from the Barshay-Temmer Symmetry in the Reaction $^4\text{He}(\vec{d}, t)^3\text{He}$ (W. Dahme, J. Arvieux, J. Birchall, H. E. Conzett, and R. M. Larimer)	57
A Study of the $^4\text{He}(\vec{p}, d)^3\text{He}$ Reaction Between 32 and 53 MeV (A. Sagle, B. E. Bonner, W. E. Broste, H. E. Conzett, W. Dahme, N. S. P. King, and Ch. Leemann)	58
The Vector Analyzing Power in Elastic Deuteron-Deuteron Scattering Between 20 and 40 MeV (H. E. Conzett, W. Dahme, R. M. Larimer, Ch. Leemann, and J. S. C. McKee)	59
A Study of $(\vec{d}, ^3\text{He})$ and (\vec{d}, t) Reactions Induced by Polarized Deuterons (B. Mayer, H. E. Conzett, W. Dahme, D. G. Kovar, R. M. Larimer, and Ch. Leemann)	61
Excitation of the Ground State Rotational Band in ^{28}Si by Inelastic Scattering of 25.2-MeV Polarized Protons (R. de Swiniarski, H. E. Conzett, B. Frois, R. Lamontagne, and R. J. Slobodrian).	63
Analyzing Powers for (\vec{p}, t) and $(\vec{p}, ^3\text{He})$ Reactions on ^{13}C (J. A. Macdonald, H. L. Harney, J. Cerny, and A. D. Bacher)	67
The Solar-Neutrino Problem—A Search for a Narrow State Near 15.8-MeV Excitation in ^6Li Using the $\alpha(\tau, p)^6\text{Li}$ Reaction (N. A. Jelley, J. Arvieux, R. B. Weisenmiller, K. H. Wilcox, G. J. Wozniak, and J. Cerny)	70

A New Approach to the Neglected Alpha-Particle Pickup Reaction (α , ^8Be) (G. J. Wozniak, N. A. Jelley, H. L. Harney, R. B. Weisenmiller, and J. Cerny)	71
New Spectroscopic Measurements via Exotic Nuclear Rearrangement: The $^{26}\text{Mg}(^7\text{Li}, ^8\text{B})^{25}\text{Ne}$ Reaction (K. H. Wilcox, N. A. Jelley, G. J. Wozniak, R. B. Weisenmiller, H. L. Harney, and J. Cerny)	74
Mass and Energy Levels of ^{17}Ne from the $^{20}\text{Ne}(^2\text{He}, ^6\text{He})^{17}\text{Ne}$ Reaction (G. J. Wozniak, R. A. Mendelson, Jr., J. M. Loiseaux, and J. Cerny)	76
Concerning the Lowest $T = 3/2$ State in ^{41}Sc (R. A. Gough, R. G. Sextro, and J. Cerny)	77
The Beta-Delayed Proton Decay of ^{24}Mg (R. G. Sextro, R. A. Gough, and J. Cerny)	81
Heavy-Ion Direct Reactions at High Energies (F. Pühlhofer, F. Becchetti, B. G. Harvey, D. G. Kovar, J. Mahoney, B. Mayer, J. D. Sherman, and M. S. Zisman)	85
Inelastic Scattering of ^{16}O from ^{208}Pb (F. D. Becchetti, D. G. Kovar, B. G. Harvey, J. Mahoney, B. Mayer, and F. G. Pühlhofer)	87
j-Dependence of Heavy-Ion Induced Reactions (D. G. Kovar, F. D. Becchetti, B. G. Harvey, F. Pühlhofer, J. Mahoney, D. W. Miller, and M. S. Zisman)	87
Evidence of Recoil Effects in Heavy-Ion Transfer Reactions (D. G. Kovar, B. G. Harvey, F. D. Becchetti, J. Mahoney, and M. S. Nagarajan)	90
Nucleon Transfer Reactions Induced by ^{12}C on ^{208}Pb and ^{197}Au at Angles Much Smaller than the Grazing Angle (W. von Oertzen, F. D. Becchetti, D. G. Kovar, B. G. Harvey, D. L. Hendrie, H. Homeyer, and J. Mahoney)	93
Heavy-Ion Induced Single Nucleon Transfer Reactions in the Zr-Mo Region (M. S. Zisman, F. D. Becchetti, B. G. Harvey, D. Kovar, J. Mahoney, and J. D. Sherman)	93
Study of the Two-Proton Transfer Reactions: $^{208}\text{Pb}(^{12}\text{C}, ^{10}\text{Be})^{210}\text{Po}$ and $^{208}\text{Pb}(^{16}\text{O}, ^{14}\text{C})^{210}\text{Po}$ (F. D. Becchetti, D. G. Kovar, B. G. Harvey, D. L. Hendrie, H. Homeyer, J. Mahoney, and W. von Oertzen)	95
Systematics of the (α , 2α) Reaction (J. D. Sherman and D. L. Hendrie)	97
Test of the Independence Postulate in the Bohr Theory of Compound- Nucleus Decay: $^{50}\text{Cr}^*$ System (M. K. Go and S. S. Markowitz)	100
Study of Elementary Particle Effects in Simple High-Energy Nuclear Reactions (N. P. Jacob, Jr., and S. S. Markowitz)	106
New Isotopes Produced in the Reaction of High-Energy Protons on U (R. Klapisch, C. Thibault, A. M. Poskanzer, R. Prieels, C. Rigaud, and E. Roeckl)	108
On-Line Mass Spectrometric Measurement of the Masses of Neutron-Rich Sodium Isotopes (R. Klapisch, R. Prieels, C. Thibault, A. M. Poskanzer, C. Rigaud, and E. Roeckl)	109

Search for Superheavy Elements Produced by Secondary Reactions in Uranium (L. Westgaard, B. R. Erdal, P. G. Hansen, E. Kugler, G. Sletten, S. Sundell, J. Camplan, R. Klapisch, R. Meunier, A. M. Poskanzer, C. Stephan, and J. Tys).	112
NUCLEAR THEORY	
Concerning the Mechanism of Heavy-Ion Transfer Reactions (N. K. Glendenning and R. J. Ascutto).	113
On Sub-Coulomb Transfer Reactions (M. A. Nagarajan)	114
Recoil Effects in Single-Nucleon-Transfer Heavy-Ion Reactions (M. A. Nagarajan)	115
Particle-Wave Ambiguities in the Interpretation of Heavy-Ion Reactions (P. J. Siemens and F. D. Becchetti)	115
Neutron Transfer in Reactions Between Superconducting Nuclei (M. Kleber).	117
A Reaction Model for the $(\alpha, 2\alpha)$ Reaction (J. D. Sherman, D. L. Hendrie, and A. Giorni)	119
The $^{90}\text{Zr}(p, p')^{90}\text{Zr}^*$ Reaction at 40 MeV (F. Petrovich).	121
Core Polarization in Inelastic Proton Scattering from ^{209}Bi at 61 MeV (F. Petrovich)	122
Cross-Section Calculations for Heavy-Ion Reactions (J. Alonso).	124
Fission Half-Lives for Heavy Even-Even Nuclei (P. Möller and J. Randrup).	126
Geometric Properties of Leptodermous Distributions with Applications to Nuclei (W. D. Myers)	128
Fit of the Interaction Parameters of a Thomas-Fermi Model for Nuclei (H. von Groote).	131
Modified Definition of the Surface Energy in the Liquid-Drop Formula (H. J. Krappe and R. Nix).	132
Hydrodynamic Analysis of the Coalescence and Breakup of Viscous Nuclear Liquid Drops (C. T. Alonso)	134
Hartree-Fock Calculations of the Angular Shapes of Neutron and Proton Distributions in Deformed Nuclei (N. K. Glendenning, D. Vautherin, and M. Veneroni)	136
Radius Scaling for Deformed Nuclei (D. L. Hendrie)	136
The Nuclear Skin Thickness Treated as a Strutinsky Variable (H. H. von Groote, W. D. Myers, P. Möller, S. G. Nilsson, J. R. Nix, J. Randrup, W. J. Swiatecki, and C. F. Tsang).	140
A Consistent Test of the Strutinsky-Nilsson Method (W. H. Bassichis, C. F. Tsang, D. R. Tuerpe, and L. Wilets).	142
Effective Moment Operator for Magnetic Moments and M1 Transitions in the Pb Region (F. Petrovich).	144
Self-Consistent Quasiparticle-Phonon Coupling and Applications to the Rare Earth Nuclei (J. D. Immele and G. L. Struble).	146

On the Nature of 0^+ Excitations in the Even Actinide Nuclei (J. D. Immele and G. L. Struble)	147
Effect of Angular Momentum on the Shell Structure and Pairing Correlation of Excited Nuclei (L. G. Moretto and T. Clements)	149
Study of Excited Nuclei with δ -Force Residual Interaction Treated on the Basis of the Pairing Approximation (L. G. Moretto and S. K. Kataria).	153
Pairing Fluctuations in Excited Nuclei and the Absence of a Second-Order Phase Transition (L. G. Moretto)	155
Pairing Effects in Coriolis-Mixed Bands (C. T. Alonso and J. O. Rasmussen)	158
Nuclear Rotational Energies in Deformed Even-Even Nuclei (J. O. Rasmussen and C. W. Ma)	160
Nuclear Rotational Energy Expansions for Deformed Odd-Mass Nuclei (J. O. Rasmussen, J. Alonso, W. Ribbe, I. Rezanka and R. Needham)	163
Microscopic Calculations of the Variable Moment-of-Inertia Model (C. W. Ma and C. F. Tsang)	167

II. CHEMICAL AND ATOMIC PHYSICS

PHOTOELECTRON SPECTROSCOPY

X-Ray Photoelectron Spectroscopy of Fluorinated Benzenes (D. W. Davis, D. A. Shirley, and T. D. Thomas)	171
X-Ray Photoemission Spectra of Crystalline and Amorphous Si and Ge Valence Bands (L. Ley, S. P. Kowalczyk, R. A. Pollak, and D. A. Shirley)	177
High-Resolution XPS Spectra of Ir, Pt, and Au Valence Bands (S. P. Kowalczyk, L. Ley, R. A. Pollak, and D. A. Shirley)	180
X-Ray Photoemission Valence Band Spectra and Theoretical Valence Band Densities of States for Ge, GaAs, and ZnSe (R. A. Pollak, L. Ley, S. P. Kowalczyk, D. A. Shirley, J. D. Joannopoulos, D. J. Chadi, and M. L. Cohen)	181
X-Ray Photoemission Cross-Section Modulation in Diamond, Silicon, Germanium, Methane, Silane, and Germane (R. G. Cavell, S. P. Kowalczyk, L. Ley, R. A. Pollak, B. Mills, D. A. Shirley, and W. Perry)	184
New Multiplet Structure in Photoemission from MnF_2 (S. P. Kowalczyk, L. Ley, R. A. Pollak, F. R. McFeely, and D. A. Shirley)	187
Evidence for Covalent Bonding in Crystalline and Amorphous As, Sb, and Bi from Valence Band Photoelectron Spectra (L. Ley, R. A. Pollak, S. P. Kowalczyk, R. McFeely, and D. A. Shirley).	189
High-Resolution X-Ray Photoemission Spectra of PbS, PbSe, and PbTe Valence Bands (F. R. McFeely, S. P. Kowalczyk, L. Ley, R. A. Pollak, and D. A. Shirley).	192
Near-Equivalence of the Quantum Mechanical Potential Model and the Thermochemical Model of ESCA Shifts (D. A. Shirley)	195
A Relaxation Correction to Core-Level Binding-Energy Shifts in Small Molecules (D. W. Davis and D. A. Shirley)	197
The Evolution of Core States from Energy Bands in the 4d5s5p Region from Pd to Xe (R. A. Pollak, S. P. Kowalczyk, L. Ley, and D. A. Shirley)	202

The Effect of Atomic and Extra-Atomic Relaxation on Atomic Binding Energies (D. A. Shirley)	204
The Onset of Relativistic Effects in the Density of States of the 6s6p Elements Tl, Pb, and Bi (L. Ley, R. A. Pollak, S. P. Kowalczyk, and D. A. Shirley)	208
Relaxation Effects on Auger Energies (D. A. Shirley)	210
HYPERFINE INTERACTIONS	
Systematics of Isomer Shifts in Transition Metal Hosts (G. Kaindl and D. Salomon)	213
High-Resolution Study of Isomer Shifts of the 6.2-keV Gamma Rays of ^{181}Ta (G. Kaindl, D. Salomon, and G. Wortmann).	215
Temperature Shifts of the Energy of the 6.2-keV Gamma Rays of ^{181}Ta (G. Kaindl and D. Salomon)	220
Study of Electric-Quadrupole Hyperfine Interactions with the 6.2-keV Gamma Resonance of ^{181}Ta (G. Kaindl and D. Salomon)	223
Magnetic Hyperfine Interaction of ^{181}Ta in Nickel (G. Kaindl and D. Salomon)	225
Mössbauer Study of Pentavalent Gold Compounds (K. Leary, G. Kaindl, and N. Bartlett)	226
Isomer Shifts of the 84.3-keV Gamma Rays of ^{170}Yb (G. Kaindl and P. B. Russel)	228
Change of the Nuclear Charge Radius in Even-Even Ytterbium Isotopes (G. Kaindl, P. B. Russel, and S. S. Hanna).	232
Magnetic Moment of the 6.9-Hour Isomer of ^{93}Mo (G. Kaindl, F. Bacon, and D. A. Shirley).	234
Nuclear Quadrupole Alignment of $^{180\text{m}}\text{Hf}$ and ^{175}Hf in Hafnium Metal (G. Kaindl, F. Bacon, A. J. Soinski, and D. A. Shirley)	236
Nuclear Magnetic Resonance on Oriented $^{101\text{m}}\text{Rh}$ (G. Kaindl, F. Bacon, H. -E. Mahnke, and D. A. Shirley)	238
Magnetic Moments of the 12^- States in $^{196}, ^{198}, ^{200}\text{Au}$ (F. Bacon, G. Kaindl, H. -E. Mahnke, and D. A. Shirley)	241
Nuclear Quadrupole Interaction Studies by Perturbed Angular Corrections (H. Haas and D. A. Shirley)	242
ATOMIC AND MOLECULAR SPECTROSCOPY	
Properties of 2- and 3-Photon Decay (R. W. Schmieder)	246
Alignment of Some Triplet and Singlet D States of Helium (J. Yellin, T. Hadeishi, and M. C. Michel).	246
Time Resolved Hanle Effect in the $3^3\text{P}_{2,1,0}$ State of ^4He (J. Yellin, T. Hadeishi, and M. C. Michel).	248
Lifetime and Alignment of the 5^1D_2 State of ^4He by Beam-Foil Level Crossing (J. Yellin, T. Hadeishi, and M. C. Michel)	248
Energy Levels of Es I and II (J. G. Conway and E. F. Worden).	250

Spectrum and Energy Levels of Doubly Ionized Scandium (Sc III) (C. H. H. Van Deurzen, J. G. Conway, and S. P. Davis)	251
Spectrum of Thorium IV (J. G. Conway, G. V. Shalimoff, and C. H. H. Van Deurzen)	252
Zero-Field Splittings of Gd^{3+} and Cm^{3+} in CeO_2 and ThO_2 (W. Kolbe, N. Edelstein, C. B. Finch, M. M. Abraham)	253
Electronic Structure of Simple Inorganic Molecules (H. F. Schaefer III)	254
Electronic Structure of Simple Organic Molecules (H. F. Schaefer III)	258
Potential Energy Surfaces for Simple Chemical Reactions (C. F. Bender, D. H. Liskow, S. V. O'Neil, P. K. Pearson, H. F. Schaefer III, and D. R. Yarkony)	262

III. PHYSICAL, INORGANIC, AND ANALYTICAL CHEMISTRY

X-RAY CRYSTALLOGRAPHY

The Crystal Structure of $Xe_2F_{11}^+ AuF_6^-$ (K. Leary, A. Zalkin and N. Bartlett)	269
The Crystal Structures of $[XeF]^+[RuF_6]^-$ and $[XeF_5]^+[RuF_6]^-$ (N. Bartlett, M. Gennis, D. D. Gibler, B. K. Morrell and A. Zalkin)	270
The Crystal Structure of Rhodium Pentafluoride (B. K. Morrell, A. Zalkin, A. Tressaud, and N. Bartlett)	272
Structural Studies of Trifluorosulfur (IV)-yl, $[SF_3]^+$, Salts Including the Crystal Structure of $[SF_3]^+[BF_4]^-$ (D. D. Gibler, C. J. Adams, M. Fischer, A. Zalkin, and N. Bartlett)	274
A Dimeric π -Cyclooctatetraene Dianion Complex of Cerium(III). The Crystal and Molecular Structure of $[Ce(C_8H_8)Cl \cdot 20C_4H_8]_2$ (K. O. Hodgson and K. N. Raymond)	277
Rotameric Configurations of a Methyl-Substituted Cyclooctatetraene Dianion Complex of Uranium(IV). The Crystal and Molecular Structure of $U[C_8H_4(CH_3)_4]_2$ (K. O. Hodgson and K. N. Raymond)	279
An Ion Pair Complex Formed Between Bis(cyclooctatetraenyl) Cerium(III) Anion and an Ether-Coordinated Potassium Cation. The Crystal and Molecular Structure of $[K(CH_3OCH_2CH_2)_2O][Ce(C_8H_8)_2]$ (K. O. Hodgson and K. N. Raymond)	282
The Preparation and Structural Characterization of Tris(benzylcyclopentadienide) Chlorouranium(IV), $U(C_5H_4CH_2C_6H_5)_3Cl$ (J. Leong, K. O. Hodgson, and K. N. Raymond)	284
The Crystal Structure of l -Ferrous-Tris(1, 10-Phenanthroline) Bis(Antimonous d -Tartrate) Octahydrate (A. Zalkin, D. H. Templeton, and T. Ueki)	286
Investigations of Alkaline-Earth β -Diketone Complexes. I. The Crystal and Molecular Structure of Bis(Dimethylformamido)Bis(1,3-Diphenyl-1, 3-Propanedionato)Magnesium (F. J. Hollander, D. H. Templeton and A. Zalkin)	289
Investigations of Alkaline-Earth β -Diketone Complexes. II. The Crystal and Molecular Structure of Bis(1,3-Diphenyl-1,3-Propanedionato)Calcium Hemiethanolate (F. J. Hollander, D. H. Templeton, and A. Zalkin)	291

Investigations of Alkaline-Earth β -Diketone Complexes. III. The Crystal and Molecular Structure of Bis(1,3-Diphenyl-1,3-Propanedionato) Strontium Hemiacetonate (F. J. Hollander, D. H. Templeton, and A. Zalkin)	293
The Crystal and Molecular Structure of 1,3-Diphenyl-1,3-Propanedione Enol (F. J. Hollander, D. H. Templeton, and A. Zalkin)	295
The Crystal and Molecular Structure of 2-(N-Nitrosomethylamino) Acetamide (L. K. Templeton, D. H. Templeton, and A. Zalkin)	296
(\pm)4 α , 8 α , 14 β -Trimethyl-18-Nor-5 α , 13 β -Androst-9(11)-en-3, 17-Dione, A Synthetic Precursor to Fusidic Acid (D. L. Ward, D. H. Templeton, and A. Zalkin).	298
RADIATION CHEMISTRY	
Scavenger Effects in the Recoil Tritium Reactions of Cyclohexene (D. C. Fee and S. S. Markowitz).	300
Photolysis of Aqueous N-Acetylalanine at 2288 Å (M. E. Jayko, H. A. Sokol, and W. M. Garrison).	302
Radiation-Induced Reactions of Amino Acids and Peptides (W. M. Garrison).	303
Radiation Chemistry of Glycylglycine in Oxygen-Free Systems (W. M. Garrison, H. A. Sokol, and W. Bennett-Corniea).	304
Further Studies on the Metastable Dissociation of the CH ⁺ Ion Produced by Electron Impact (A. S. Newton and A. F. Sciamanna)	306
PHYSICAL AND INORGANIC CHEMISTRY	
Group Separations for Superheavy Elements (J. V. Kratz, J. O. Liljenzin, R. J. Silva, and G. T. Seaborg)	308
Anion Exchange Resin Selectivity as a Function of Resin Composition, Revisited (J. Bucher, R. M. Diamond, and B. Chu)	310
Anion Stabilization in the Extraction of H ₂ AuCl ₄ , H ₂ ReO ₄ , HClO ₄ , HI and HBr by Tributyl Phosphate in CCl ₄ and Benzene (J. J. Bucher and R. M. Diamond)	312
Multicolumn Radio-Gas-Chromatographic Analysis of Recoil Tritium Reaction Products (D. C. Fee and S. S. Markowitz)	314
Gas Chromatography in Environmental Studies (A. S. Newton, A. F. Sciamanna, and M. Evett)	317
Determination of Methyl Mercury with Anodic Stripping (R. G. Clem)	320
Computer Resolution of Polarographic Background Currents (R. G. Clem and G. Litton)	320
Some Preliminary Studies on the Chemistry of Dilute Solutions of Dimethyl Mercury (A. S. Newton and A. F. Sciamanna)	321
A Survey of Methyl Mercury in Food Fish of the San Francisco Bay Area (M. Evett, A. F. Sciamanna, and A. S. Newton).	322
Logical Approaches to the Selection of Separation Processes (R. W. Thompson and C. J. King)	325

Mass and Heat Transfer Between Phases; Influences of Interfacial Instability and High Rates of Mass Transfer (I. F. Davenport and C. J. King)	329
---	-----

APPLICATIONS OF ACTIVATION ANALYSIS METHODS

Quantitative Neutron Activation Analysis of Human Tissues (T. Budinger, B. Moyer, H. V. Michel, F. Asaro, and I. Perlman).	331
Archaeological Implications of Composition Variations in Obsidian Sources (H. R. Bowman, F. Asaro, and I. Perlman).	333
The Origin of the "Palestinian" Bichrome Ware (M. Artzy, F. Asaro, and I. Perlman).	336
Origin of the Colossi of Memnon (R. F. Heizer, F. S. Stross, R. F. Hester, A. D. Albee, H. R. Bowman, I. Perlman, and F. Asaro).	342
³ He Activation Analysis for S, Cl, K, and Ca (D. M. Lee and S. S. Markowitz).	346
Quantitative Analysis for the Major Elements in Rocks and Minerals by Nondispersive Soft X-Ray Fluorescence (A. J. Hebert and K. Street, Jr.)	350

IV. INSTRUMENTATION

Doppler-Tuned Beam-Foil X-Ray Spectrometer (R. W. Schmieder and R. Marrus)	355
Improved Resolution Methods for Beam-Foil Spectroscopy (T. Hadeishi, M. C. Michel, J. Yellin and E. Geneux).	355
Developments in Zeeman Atomic Absorption Spectroscopy (T. Hadeishi, R. D. McLaughlin, D. A. Church, B. Chang, and M. Nakamura).	358
Search for New Isotopes with the He-Jet Technique at the Bevatron (J. D. Bowman, A. M. Poskanzer, R. E. Eppley, and E. K. Hyde)	359
Design of, and Skimmer Tests with, A He-Jet Transport System (R. A. Gough, R. G. Sextro, and J. Cerny)	361
Efficiency of Detecting a ⁸ Be with a ΔE-E Counter Telescope (G. J. Wozniak and H. L. Harney)	364
A Proton Polarimeter of High Efficiency and Good Energy Resolution (J. Birchall, W. Dahme, J. Arvieux, R. M. Larimer and H. E. Conzett).	365
Particle-Identifying Focal Plane Detector (B. G. Harvey, H. Homeyer, J. Mahoney, and G. Gabor).	366
Heavy Ion Acceleration at the Berkeley 88-Inch Cyclotron (D. J. Clark, J. Steyaert, J. Bowen, A. Carneiro, D. Morris).	368
Cyclotron Injection Systems (D. J. Clark)	371
88-Inch Cyclotron Operation and Development (J. Bowen, D. J. Clark, P. Frazier, and D. Morris).	372
Accelerators for Nuclear Physics (D. J. Clark)	373
Design of a High-Temperature Neutron Irradiation Container (D. C. Fee and S. S. Markowitz)	376

A 100 psec Pulse-Width Discriminator (J. D. Bowman, A. M. Poskanzer, and D. Landis)	378
A Hilac Data Collection Program (J. B. Hunter, R. C. Jared and S. G. Thompson).	379
Real Time Fortran for a PDP-9 Computer (R. C. Jared, J. B. Hunter, and S. G. Thompson).	380
High Rate X-Ray Fluorescence Analysis by Pulsed Excitation (J. M. Jaklevic, F. S. Goulding and D. A. Landis).	380
Trace Element Analysis with Semiconductor Detector X-Ray Spectrometers (R. D. Giauque, F. S. Goulding, J. M. Jaklevic, and R. H. Pehl)	382
Instrumentation for Environmental Monitoring: Air (C. D. Hollowell, G. Y. Gee, R. D. McLaughlin)	385
A Two-Level Speed Controller for the Rotated Mercury Coulometer Cell (R. G. Clem and F. Vogelsberg)	386
Effect of Wax Crystallinity on the Performance of Anodic Stripping Electrodes (R. G. Clem)	388

V. THESIS ABSTRACTS

Nuclear Orientation Studies on Some High Spin Isomers in Ferromagnetic and Non-Ferromagnetic Lattices (Fredrick Bacon).	393
The Initiation of Natural Convection Caused by Time-Dependent Profiles (Ian Frank Davenport)	393
Glass Beads in African Archaeology: Results of Neutron Activation Analysis, Supplemented by Results of X-Ray Fluorescence Analysis (Claire C. Davison)	394
Some Properties of Protactinium Metal and its Compounds (Raymond Lloyd Dod).	395
Crystal Structures of Diketone Complexes of Alkaline Earth Metals and Other Compounds (Frederick John Hollander)	395
Beta Asymmetry from Oriented Manganese 52 (Sammy Tung-Chuen Hung)	396
A Self-Consistent Treatment of Phonons and Quasiparticles in Finite Fermi Systems and Applications to Rare Earth Nuclei (John David Immele)	397
The Application of ^3He -Induced Nuclear Reactions for Sensitive Chemical Analysis of Sulfur, Chlorine, Potassium, and Calcium (Diana M. Lee).	398
Production of L-Asparaginase by Cultures of <u>Erwinia Aroideae</u> (Thomas F. Murphy)	398
Electronic Densities of States of Solids from X-Ray Photoemission Spectroscopy (Roger Alan Pollak)	399
Large Separations via Cycling Zone Adsorption (Ross Dale Rieke)	400
Mössbauer Spectroscopy of the 6.2 keV γ Ray Transition of ^{181}Ta (Dan Ben Jacov Salomon)	401

	The Question of Equilibrium at a Phase Boundary During Crystal Growth (Tsung-Shen Thomas Shih)	401
	Synthesis of Separation Schemes (Roger W. Thompson).	402
	Mass Transfer to Newtonian and Non-Newtonian Systems in Stirred Tank Gas-Liquid Contactors (William C. Wernau).	402
	Transfer Reactions in the Zr-Mo Region Induced by α Particles and Heavy Ions (Michael Steven Zisman)	403
VI.	<u>1972 PUBLICATIONS</u>	407
VII.	<u>AUTHOR INDEX</u>	441

I. Physics of The Nucleus

Nuclear Spectroscopy, Radioactivity, and Fission

Nuclear Reactions and Scattering

Nuclear Theory

ALPHA SPECTROSCOPY OF ISOTOPES PRODUCED BY HIGH-ENERGY NUCLEAR REACTIONS

J. D. Bowman, E. K. Hyde, and R. E. Eppley

We have previously reported a program of the on-line study by the helium-jet recoil-transfer technique of the α -emitting products of the interaction of 5 GeV protons with heavy nuclei, and described the apparatus which was used.¹ Here we report a few additional experiments designed to improve the reliability and accuracy of our α spectroscopy and describe the procedures used to redetermine the energies of 40 α emitters with an accuracy substantially better than the literature values. A dramatic improvement was made for the rare earth α emitters where errors were reduced from about 20 keV to about 3 keV. A table of results is presented.

The complexity of the α spectra, which contained as many as 70 peaks, made the tasks of position determination, half-life analysis, and peak identification difficult, but conversely, since many peaks were present in each of our spectra, a precise determination of their relative energies was possible. Energy and time data were taken for a target of Ta, Au, Th, and U by using both the catcher plate and tape drive apparatuses described in Ref. 1. Collection periods of 10 min and 30 sec were to emphasize lines having different half-lives (as discussed in Ref. 1). Use of the tape drive collection apparatus ensured that source thickness effects were absent. The data were sorted into energy spectra and a time spectrum for each of the peaks. Peak positions were extracted by using the computer program SAMPO,² and half-lives were determined by nonlinear least-squares fits of the decay data to a super-position of exponentials. A comparison of the peak positions and half-lives was made between the various spectra to ensure that for each peak included in further energy analysis there was no position shift with target material, that energy absorption due to source thickness was negligible, and that the lines used in the energy analysis were essentially pure. Peaks were identified by searching a complete list of the α decay energies and half-lives reported in previous work.³ For each α decay given below there was quantitative agreement between our measurements and previously reported values for both the α energy and the half-life. Where

our detector-amplifier-ADC system, using appropriate, feeding and α multiplicity relations as well as yield systematics were considered. Of the 70 lines observed, 40 meet all of the above requirements.

Alpha energies were determined by a calibration of the nonlinear energy response of 20 selected peaks as internal standards. These standards are indicated in Table I. Short-lived α emitters in the rare earth region generally have poorly known energies. In order to obtain an internal standard in the rare earth region which occurred in our spectra as an isolated peak, we measured the energy of $^{150}\text{Dy } \alpha_0$ relative to $^{149}\text{Tb } \alpha_0$ in an off-line experiment where other activities produced had died away. Our result was $E = 4233(3)$ keV. Calibration fits were performed by assuming a polynomial relationship between peak position and energy. It was found that for polynomials of degree quadratic or higher the agreement was better than statistically expected, $(\chi^2/N-M)^{1/2} = 0.7$, and that no improvement in the fit was obtained as the degree was increased. The results reported below are based on a cubic fit. In a few cases the errors have been arbitrarily increased by 1 or 2 keV. It should be noted that the errors of the standards themselves have been reduced by the requirement of consistency among them.

The advantage of GeV proton irradiation of heavy targets in this connection is that a large number of α -lines appear in a single spectrum, which allows a simultaneous comparison of many peaks with standards previously measured by precise magnetic⁴ or semiconductor spectrometry. Previous measurements of short-lived rare earth activities have been restricted to samples made by heavy-ion reactions in which only a few α activities are made having energies in a region where few standards exist. We have now established a new set of α standards including many which will be useful for future work with rare earth α emitters. In addition, these accurate α energies will serve to test the predictions of mass formulas for short-lived nuclei far from stability.

Table I. Table of energies and identities of selected peaks. A literal reference by a nuclide indicates that its energy was used as an internal standard in the fitting procedure.

Nuclide	Energy, this work	Energy, previous work	Nuclide	Energy, this work	Energy, previous work
^{149}Tb	3972(5)	3967(3)	$^{198}\text{Po}^{\text{j}}$	6183(3)	6178(5)
$^{151}\text{Dy}^{\text{a, b}}$	4067(3)	4068(5)	$^{198}\text{Po}^{\text{j}}$	6339(3)	6338(3)
$^{154}\text{Er}^{\text{c}}$	4166(3)	4166(5)	$^{197\text{m}}\text{Po}^{\text{i}}$	6385(3)	6387(8)
$^{150}\text{Dy}^{\text{d, e, f}}$	4233(3)	4233(3)	$^{213}\text{Fr}^{\text{l}}$	6775(2)	6773(5)
^{152}Ho	4387(3)	4380(20)	$^{212}\text{Ra}^{\text{m}}$	6901(2)	6896(5)
$^{152\text{m}}\text{Ho}$	4453(3)	4450(20)	$^{204}\text{Ra}^{\text{m}}$	6970(3)	6973(5)
^{151}Ho	4517(3)	4510(20)	^{222}Ac	7013(2)	7010(10)
$^{151\text{m}}\text{Ho}$	4607(3)	4600(20)	$^{217}\text{At}^{\text{n, o}}$	7071(2)	7068(4)
^{153}Er	4671(3)	4670(20)	$^{218}\text{Rn}^{\text{p}}$	7133(2)	7127(10)
^{152}Er	4799(3)	4800(20)	^{219}Fr	7317(4)	7310(30)
^{154}Tm	4955(3)	4960(30)	$^{211}\text{Po}^{\text{c}}$	7448(2)	7450(3)
$^{154\text{m}}\text{Tm}$	5030(3)	5040(20)	^{214}Po	7692(5)	7687(1)
^{153}Tm	5103(3)	5110(20)	$^{217}\text{Rn}^{\text{q}}$	7739(2)	7742(4)
$^{179}\text{Pt}^{\text{g}}$	5156(3)	5150(10)	^{216}At	7800(3)	7810(10)
^{155}Yb	5191(5)	5210(20)	$^{218}\text{Fr}^{\text{r}}$	7867(2)	7870(10)
$^{178}\text{Pt}^{\text{g}}$	5440(3)	5440(20)	^{215}At	8026(4)	8010(10)
$^{177}\text{Pt}^{\text{g}}$	5510(3)	5510(10)	$^{213}\text{Po}^{\text{o}}$	8376(3)	8377(5)
$^{211}\text{At}^{\text{h}}$	5865(3)	5868(5)	$^{212}\text{Po}^{\text{s}}$	8785(1)	8785(1)
^{176}Pt	5743(4)	5740(10)	^{214}At	8819(4)	8810(10)
$^{199\text{m}}\text{Po}^{\text{i}}$	6060(3)	6064(4)	$^{211\text{m}}\text{Po}$	8885(5)	8880(20)

^aS. Mahunka, L. Fron, J. Fényes, and A. V. Khalkin, JINR-P-2553 (1966).

^bN. A. Golovkov, S. K. Khran, and V. G. Chumin, Proceedings of Int. Symp. Nucl. Structure, Dubna (1968).

^cN. A. Golovkov, Sh. Guetkh, B. S. Dzhelepov, Yu. V. Norseev, V. A. Khalkin, and V. G. Chvmin, Bull. Acad. Sci. USSR Phys. Ser. **33**, 1489 (1969).

^dThis work.

^eV. G. Chumin, K. Gromon, and B. Makhmudon, Zh. Zhelev, JINR-E-2721 (1966).

^fJ. Kormicki, H. Niewodniczanski, Z. Stachura, K. Zuber, and A. Budziak, Nucl. Phys. A100, 297 (1967).

^gA. Siivola, Nucl. Phys. **84**, 385 (1966).

^hR. W. Hoff, UCRL-2325 (1953).

continued

Table I (continued)

-
- ⁱE. Tielsch-Cassel, Nucl. Phys. A100, 425 (1967).
^jW. Treytl and K. Valli, Nucl. Phys. A97, 405 (1967).
^kK. Valli and E. K. Hyde, UCRL-16580 (1966).
^lK. Valli, E. K. Hyde, and W. Treytl, UCRL-17272 (1967).
^mK. Valli, W. Treytl, and E. K. Hyde, UCRL-17322 (1967).
ⁿR. J. Walen, Compt. Rend. 255, 1604 (1962).
^oK. Valli, Ann. Acad. Sci. Fennicae, Sev A, VI, No. 165, 1 (1964).
^pF. Asaro and I. Perlman, Phys. Rev. 104, 91 (1956).
^qC. P. Ruiz, UCRL-9511 (1961), adjusted according to the redetermination of $\text{Po}^{214} \alpha_0$ in s.
^rK. Escola, Phys. Rev. C 5, 942 (1972).
^sA. Rytz, Helva. Phys. Acta 34, 240 (1961).
-

References

- | | |
|--|--|
| <p>1. R. E. Eppley, J. D. Dowman, and E. K. Hyde, Nuclear Chemistry Annual Report LBL-666, (1971), pp. 18 and 325.</p> <p>2. J. T. Routti, SAMPO, UCRL-19452 (1969).</p> | <p>3. C. M. Lederer, J. M. Hollander, and I. Perlman, <u>Table of Isotopes</u> (Wiley, New York, 1967); K. Valli, in <u>Proceedings of the Third International Conference on Atomic Masses, Winnipeg</u> (1967), p. 296; P. Eskola, <u>Arkiv für Fysik</u> <u>36</u>, 477 (1967) and various original articles.</p> <p>4. A. H. Wapstra, Nucl. Phys. <u>57</u>, 48 (1964).</p> |
|--|--|

ABSOLUTE ENERGY MEASUREMENT OF THE ALPHA PARTICLES EMITTED BY ^{232}U AND $^{240}\text{Pu}^\dagger$

D. J. Gorman,* A. Rytz,* and H. V. Michel

As part of a continuing cooperative program with the Bureau International des Poids et Mesures, absolute alpha-particle energies of the α_0 and α_{58} groups of ^{232}U and the α_0 and α_{45} groups of ^{240}Pu have been measured. The absolute energy magnetic spectrograph of the B. I. P. M. which has been described previously,¹⁻³ was used in the determinations.

The ^{232}U was separated from the ^{228}Th and its daughters on a Dowex anion exchange column using HCl, and from Fe on an anion column using HNO_3 .

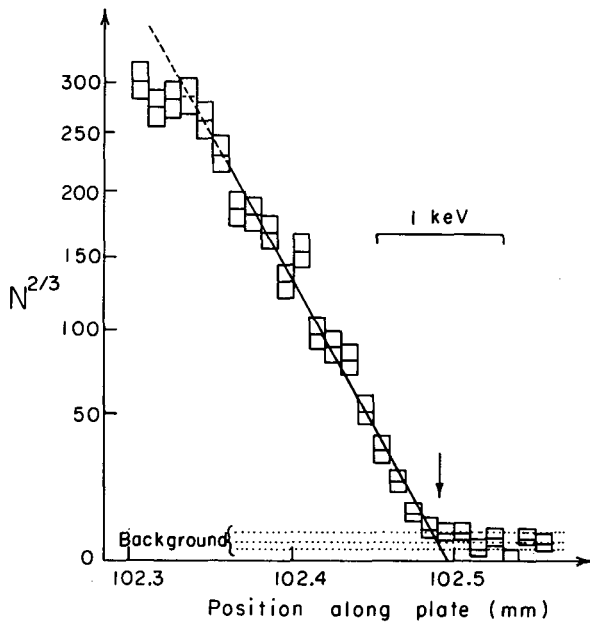
A mass analysis of the ^{232}U sample gave upper limits of 1% and 1.5% for the mass of ^{238}U and ^{233}U respectively and 0.3% for all other masses in this region. A mass analysis of the Pu shows the following composition: 11% ^{239}Pu , 88% ^{240}Pu , 0.6% ^{241}Pu , and 0.03% ^{242}Pu .

The sources of ^{232}U and of ^{240}Pu prepared by vacuum evaporation were used for several exposures. The low activity of the ^{240}Pu necessitated taking exposures for 6-14 days. Four exposures of the ^{232}U source were taken for 12 hours each at two different magnetic field values.

A window, accepting only a very limited energy region was placed in front of the photographic plate to reduce background on the plates.

The method employed in evaluating the data has been described in previous publications^{1,2} in which it is shown that the intensity of the alphas on the high-energy side of the peak is proportional to $X^{3/2}$, where X is the distance between the point under consideration and the point which corresponds to the maximum

energy. Figure 1 shows the ^{232}U α_0 group plotted as $N^{2/3}$ vs distance, where N is the number of α particles per unit distance. The best straight line has been calculated by using the least-squares method.



The small number of events collected on the plate exposed to ^{240}Pu suggested another method of extrapolation,⁴ based on the principle of maximum likelihood. Both methods gave the same result for ^{232}U ; however, for ^{240}Pu the extrapolated point was 90 eV lower than that calculated by the least-squares method. In both of these methods, an uncertainty exists due to the choice of points used in the extrapolation. We have taken the arithmetic mean of the two results.

Our final results, in the table, are the weighted means of the individual measurements with the weights equal to the reciprocals of the variances, i. e. $1/\sigma_i^2$.

Table I gives a comparison of our results with the relative measurements of Asaro,^{5,6} Baranov⁷ and Leang.⁸ The relative measurements have been normalized to the new absolute values of Grennberg and Rytz¹ and A. Rytz.⁹

Fig. 1. One section of the main ^{232}U α group. The ordinate is $N^{2/3}$ where N is the number of alpha particles counted in a band width of 10 microns; the abscissa is the position along the plate with increasing energy to the right. The extrapolated value is shown by the arrow. (XBL 732-2298)

Table I

Nuclide	Published values (normalized) ^a (keV)			Present work		
	Asaro ^(5,6)	Baranov ⁽⁷⁾	Leang ⁽⁸⁾	Average energy and estimated standard deviation ^b (keV)	Number of exposures	Number of sources
^{232}U (α_0)	5320±2	5320.8±1.0		5320.30±0.14	4	1
^{232}U (α_{58})	5263±2	5263.9±1.0		5263.54±0.09	4	1
Standard used by the authors	^{228}Th	^{240}Pu				
^{240}Pu (α_0)	5169±3		5168.0±0.7	5168.30±0.15	4	3
^{240}Pu (α_{45})	5125±3		5123.6±0.7	5123.43±0.23	2	2
Standard	^{210}Po		^{212}Bi			

^aThe published results of the authors have been normalized to the most recent value for the standard used.

^bTo the listed standard deviation a systematic error should be added whose upper limit is about 0.1 keV.

It is evident that our results are in good agreement with the previously published work after normalization and they are much more precise.

Footnotes and References

† Work condensed from LBL-622.

* Present address: Bureau International des Poids et Mesures, 92310 Sèvres, France.

1. B. Grennberg and A. Rytz, *Metrologia* **7**, 65 (1971).
2. B. Grennberg and A. Rytz, *Compt. Rend.* **269**, série B, 652 (1969).
3. B. Grennberg, A. Rytz, and F. Asaro, *Compt. Rend.* **272**, série B, 283 (1971).

4. D. J. Gorman and J. W. Müller, Maximum Likelihood Fit to Points Originating from Different Poisson Distributions, Report BIPM-72/6.

5. F. Asaro and I. Perlman, *Phys. Rev.* **99**, 37 (1955).

6. F. Asaro and I. Perlman, *Phys. Rev.* **88**, 828 (1952).

7. S. A. Baranov, V. M. Kulakov, and V. M. Shatinsky, *Yadernaya Fysica* **7**, 727 (1968).

8. C. F. Leang, *Compt. Rend.* **255**, 3155 (1962).

9. A. Rytz, *Helv. Phys. Acta* **34**, 240 (1961).

¹⁴⁸Gd PRODUCTION AND PURIFICATION FOR ABSOLUTE ALPHA ENERGY MEASUREMENTS

H. V. Michel and F. Asaro

¹⁴⁸Gd, a pure alpha emitter with a single 3.18-MeV alpha-particle group and an 84-year half-life, is nearly ideal as a low-energy alpha calibration standard. It can be prepared by the p, 4n reaction on ¹⁵¹Eu and purified by standard chemical techniques. The only major impurities after purification would be due to Gd isotopes. A substantial quantity of ¹⁴⁸Gd was prepared to make alpha and gamma spectroscopy measurements in our laboratory, a precise measurement of the absolute alpha particle energy in the magnetic spectrograph of the Bureau International des Poids et Mesures and to supply the National Bureau of Standards with material for calibration sources.

A target of 1.98 g of enriched (96.83%) ¹⁵¹Eu oxide was bombarded at the LBL 88-inch cyclotron with 42-MeV protons for 1570.5 μ Ahr. The enriched ¹⁵¹Eu enhanced the yield of ¹⁴⁸Gd, reduced the yield of the ¹⁵¹Gd and ¹⁵³Gd radioactive contaminants, and reduced the level of stable Gd isotopes in the Eu sufficiently that a chemical separation prior to irradiation was not necessary.

After waiting several months to allow the target to decay it was dissolved in HCl and passed thru a Jones reductor which changed the oxidation state of the Eu to +2 while the Gd remained in the +3 state. Immediately after the reduction column the eluant was

loaded onto a Dowex 50 \times 4% cation column where the +3 ions were held up and then eluted off in 6 M HCl. The solution was kept in a nitrogen atmosphere after reduction until all the Eu +2 had been washed off. It was necessary to add approximately 1 g of hydrazine hydrochloride to keep the Eu +2 reduced and prevent bubbling in the column.

Further purifications of the Gd were made with columns which contained Dowex 50 \times 12% cation exchange resin and were eluted with 0.4 M alpha-hydroxy isobutyrate with pH=4.2.

The alpha spectrum was measured with a solid state counter at a half width of 28 keV. No alpha particles other than the 3.18-MeV group of ¹⁴⁸Gd were detected except for small perturbations in the background spectrum at about 2.74 MeV with an abundance of less than 0.05%.

The gamma spectrum was measured on a Ge crystal with approximately .54 keV half width at 100 keV. No gamma rays other than the known radiations of ¹⁵⁴Gd and ¹⁵³Gd were seen.

About 5×10^8 alpha dis/min of ¹⁴⁸Gd were prepared of which one third was sent to the Bureau International des Poids et Mesures, Sevres, France where three sources of $10 \pm 5 \mu$ Ci each were prepared by vacuum vaporization. A comparable amount was sent

to the U. S. National Bureau of Standards for preparation of calibration sources.

The preliminary results¹ of the absolute alpha-particle energy measurements are shown in Table I. The best final value is 3182.787 ± 0.024 keV.

Table I

Source	Energy (keV)	No. of exposures
1	3182.78±0.03	10
2	3182.81±0.01	4
3	3182.62	5

Reference

1. D. J. Gorman, H. V. Michel, A. Rytz, and F. Asaro, to be published.

DECAY OF ²⁰⁹At TO LEVELS IN ²⁰⁹Po†

L. J. Jardine, S. G. Prussin, and J. M. Hollander

The electron-capture decay of ²⁰⁹At has been investigated with Ge(Li) γ-ray spectrometers and a Si(Li) electron spectrometer. The multipolarities of 31 transitions have been determined and combined with data from a recent ²¹⁰Po(p, d) reaction study¹ to assign spins and parities to levels. Figure 1 shows the decay scheme which was established.

Since ²⁰⁹Po is only two protons and one neutron hole away from doubly magic ²⁰⁸Pb, it is expected to be a relatively good shell-model nucleus. The low-lying level structure should be formed from protons in the h_{9/2} orbital and a neutron hole in the p_{1/2}, f_{5/2}, p_{3/2}, or i_{13/2} shell. Seniority 1 configurations of this type have been assigned to levels

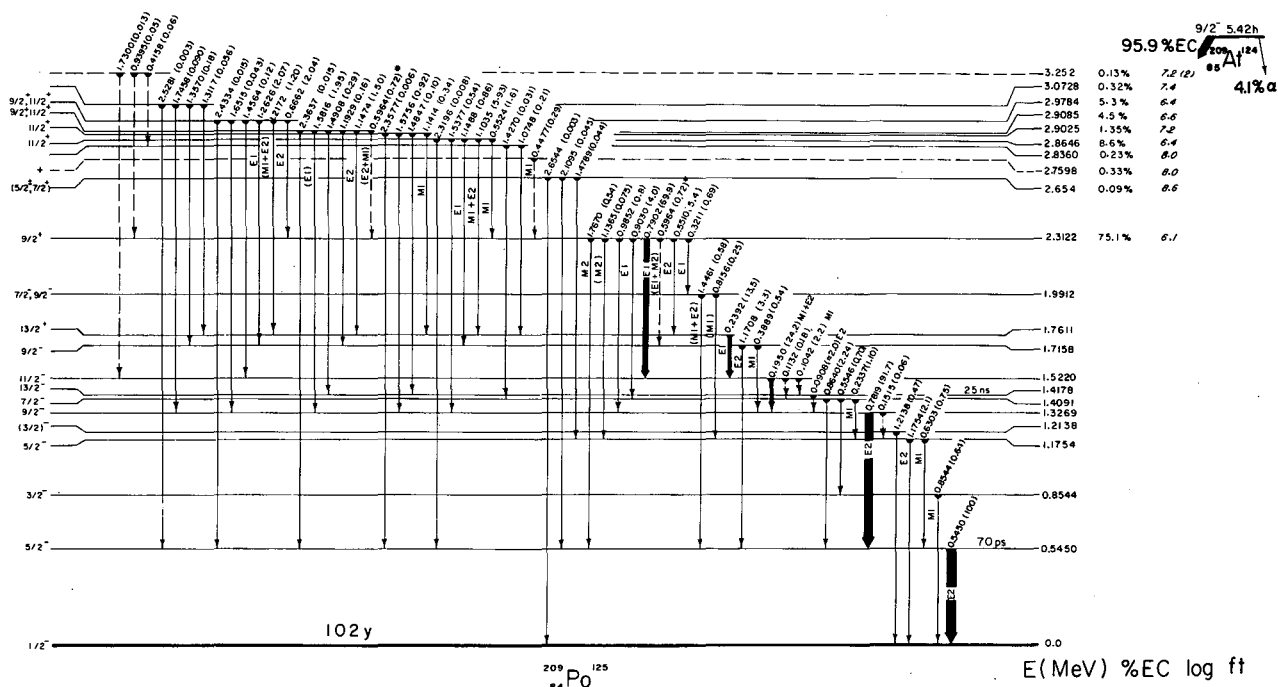


Fig. 1. Experimental decay scheme of ²⁰⁹At. Relative γ-ray intensities are shown on the level scheme. (XBL 731-2185)

at 0.0, 545.0, 854.4, and 1761.1 keV, respectively, observed in the $^{210}\text{Po}(p, d)$ pick-up reaction;¹ Our measurements confirm these assignments. The $f_{7/2}^{-1}$ neutron hole state appears to be fragmented over several states and has not been positively identified.

The $9/2^+$ state at 2312.2 keV receives about 75% of the total decay and was not populated in the (p, d) reaction. This state arises from excitation of the odd neutron across the $N = 126$ shell, and has the configuration $(\pi h_{9/2})_0^2 (\nu g_{9/2})$. Strong evidence for this assignment also derives from the $\log ft$ value (6.1) for the electron-capture transition to this state, which is very close to the values measured² for the same transition $(\pi h_{9/2} \xrightarrow{EC} \nu g_{9/2})$ in the decays of ^{210}At and ^{211}At .

States may be formed from seniority 3 configurations such as $(\pi h_{9/2})_0^2 (\nu p_{1/2})^{-1}$. In Fig. 2 we show the experimental level structure^{1, 3, 4} below 1.65 MeV together with a recent shell-model calculation⁵ based on a residual interaction generated by a non-local Tabakin potential with core polarization effects simulated by additional pairing-plus-quadrupole forces. A calculation based on effective two-particle interactions derived from experimental data on neighboring nuclei was also made. The details of this calculation and a complete discussion of the ^{209}Po level scheme are given in the full paper. A description of the measurements and the measured data are also presented.

Footnotes and References

[†] Condensed from LBL-245; to be submitted to Nucl. Phys. (1973).

1. T. R. Canada and T. S. Bhatia, private communication, Carnegie-Mellon University, Nov. 1971 and July 1972.

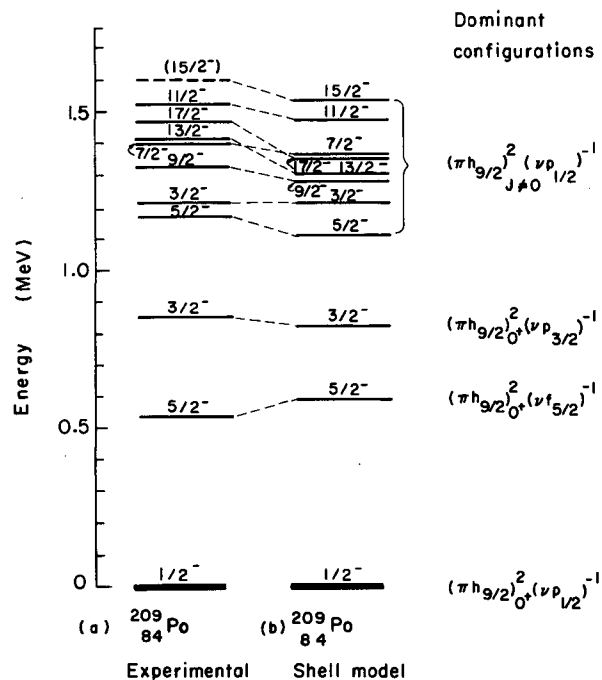


Fig. 2. Comparison of the experimental^{1, 3, 4} level scheme (a) of ^{209}Po with levels calculated from a recent⁵ shell-model calculation. (XBL 732-2277)

2. L. J. Jardine, S. G. Prussin, and J. M. Hollander, Nucl. Phys. **A190**, 261 (1972).
3. M. Alpsten, A. Appelqvist, and G. Astner, Physica Scripta **4**, 137 (1971).
4. K. Wikström, AFI 1971 Annual Report 3.1.43, p. 87.
5. W. Baldrige, N. Freed, and J. Gibbons, Phys. Letters **36B**, 179 (1971).

THE ELECTRON-CAPTURE DECAY OF $^{155}\text{Tb}^{\dagger}$

C. M. Lederer, R. A. Meyer,* and R. Gunnink*

The deformed nucleus ^{155}Gd has been of particular interest for several reasons: 1) A large number of intrinsic states occur at low energies; 2) the $N = 6$ (even-parity) states derived from the $i_{13/2}$ shell are strongly intermixed by the Coriolis force,¹ and the resulting band structure is very distorted, making identification of the states difficult; 3) the $N = 6$ states are also strongly

admixed with $N = 4$ states $1/2^+ [400]$ and $3/2^+ [402]$, due to level crossings that occur around 91 neutrons at deformations $\delta \approx 0.3$.²

Although the cross sections for (d, p) and (d, t) reactions have played a major role³⁻⁶ in the assignment of Nilsson states in ^{155}Gd , decay-scheme studies are involved in an important way, because many of the levels

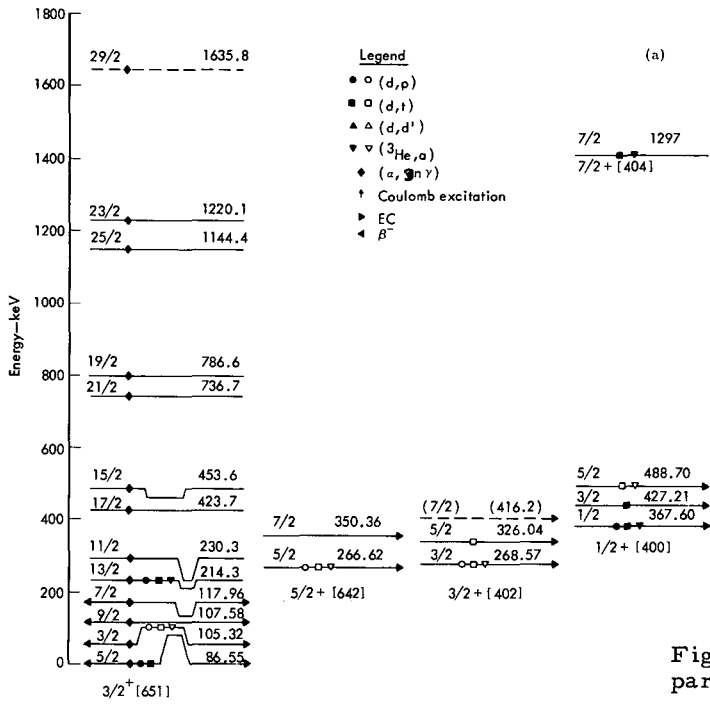


Fig. 1(a). Level scheme of ¹⁵⁵Gd: positive parity bands. (XBL 734-423)

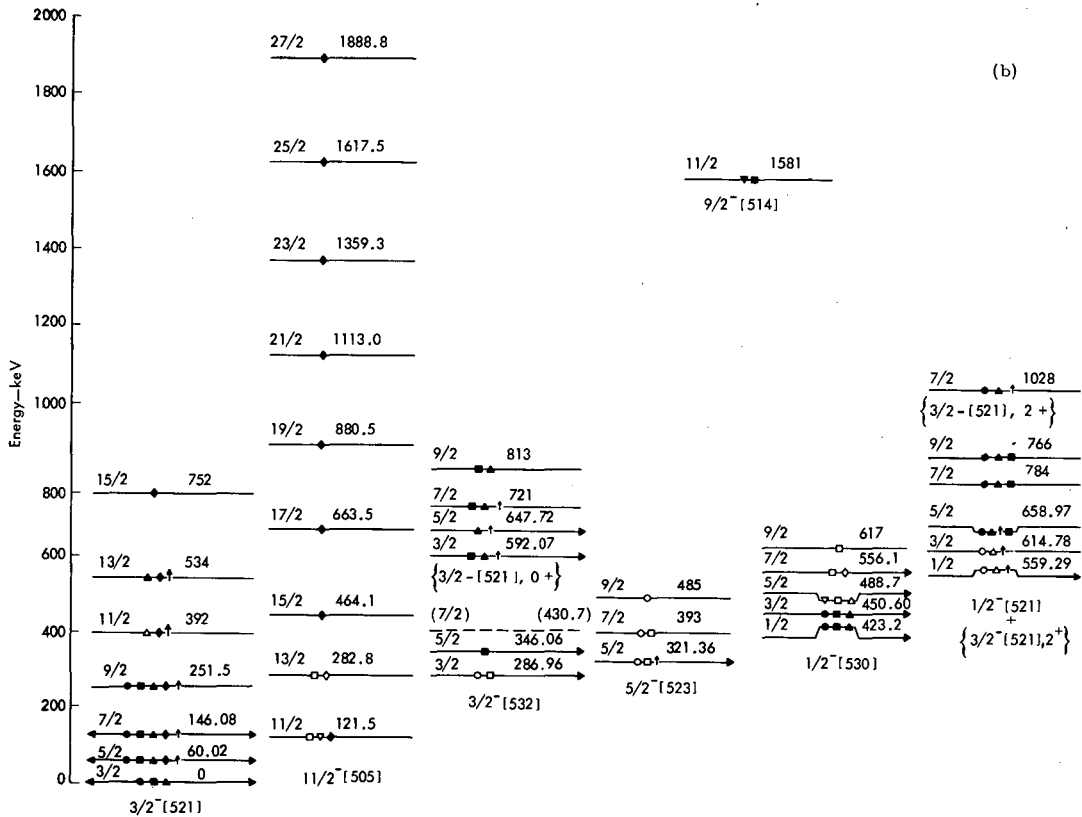


Fig. 1(b). Level scheme of ¹⁵⁵Gd: negative parity bands. [See Fig. 1(a) for legend.] (XBL 734-424)

observed in radioactive decay are too closely spaced to have been resolved in the reaction spectra. Recent studies of ^{155}Eu decay^{7, 8} have established the lowest-lying even-parity states as members of the badly distorted $3/2^+ [651]$ band, but the decay energy of ^{155}Eu is too low to populate higher-lying states.

In the present study we have remeasured the gamma-ray and conversion-electron spectra of ^{155}Tb . Gamma spectra were studied with singles and Compton suppression Ge(Li) spectrometers; electrons were measured with a Si(Li) spectrometer. Over 120 transitions were observed, and conversion coefficients were measured for many of them.

From the results, the level scheme shown in Fig. 1 was established. This scheme includes levels at 321.36, 346.06, 350.36, 423.2, 451.6, 488.7, 556.1, 658.97, and 721.06 keV that were not reported in previous studies of ^{155}Tb decay, although most of them are known or inferred from studies of stripping, pickup, or inelastic scattering reactions.

Our results provide more reliable spin and parity assignments for many of the levels: definite $5/2^+$ assignments for states at 266.62, 326.04, and 488.70 keV; $3/2^+$ for the 268.57-keV state and also (very probably) for the 427.21-keV state. Unambiguous assignments $3/2^-$ and $5/2^-$ for the states at 286.96 and 321.36 keV, respectively, remove the previous discrepancies³⁻⁶ in the characterization of low-lying odd-parity bands of ^{155}Gd . Our assignments for the higher-lying odd-parity states confirm previous characterization of these collective bands.

ENERGY-LEVEL SYSTEMATICS OF ODD-MASS LANTHANUM ISOTOPES; A NEW COUPLING SCHEME

J. R. Leigh,* K. Nakai,† K. H. Maier,‡ F. Pühlhofer,§ F. S. Stephens, and R. M. Diamond

The neutron-deficient nuclei with $Z > 54$, $N < 78$ have been extensively studied since this was first proposed as a new region of deformation.¹ The energy levels of the ground state rotational bands and the lifetimes of the first 2^+ levels of some of these doubly-even nuclei support the suggested deformation. Theoretical calculations of the shapes of nuclei in this region have indicated competition between oblate and prolate deformations.

The odd-A nuclei in this region have recently been studied by several authors in order to deduce the nuclear shape. For example

A fuller description of the experiments and the measured data, and a more extensive discussion of the results and of the level structure of ^{155}Gd are given in the full paper.

Footnotes and References

† Full paper to be submitted to Nuclear Physics.

* Lawrence Livermore Laboratory.

1. M. E. Bunker and C. W. Reich, Phys. Letters 25B, 396 (1967).
2. R. K. Sheline, M. J. Bennett, J. W. Dawson, and Y. Shida, Phys. Letters 26B, 14 (1967).
3. R. K. Sheline and Y. Shida, Phys. Letters 26B, 210 (1967).
4. P. O. Tjøm and B. Elbek, Kgl. Danske Videnskab. Selskab, Mat.-Fys. Medd. 36 No. 8 (1967).
5. M. Jaskola, P. O. Tjøm, and B. Elbek, Nucl. Phys. A133, 65 (1969).
6. I. Kanestrøm and P. O. Tjøm, Nucl. Phys. A145, 461 (1970).
7. R. A. Meyer and J. W. T. Meadows, Nucl. Phys. A132, 177 (1969).
8. A. J. Soinski, E. Karlsson, and D. A. Shirley, Phys. Letters 26B, 440 (1968).

the existence of low-lying $11/2^-$ levels, assigned as the [505] Nilsson state, in ^{129}La and ^{131}La has been used to support the proposed oblate deformation.^{2,3} But it should be noted that such results are not as definitive as might be hoped. The low-lying $11/2^-$ state might be the [505] Nilsson level, as has been suggested, and so indicate an oblate shape, or it might be the $11/2^-$ level of the band based on the [550] $\Omega = 1/2$ Nilsson state. The latter state has a large negative decoupling parameter and so results in a distorted band with the $11/2$ member lying low if on the prolate side. Thus, the mere occurrence of a low-

lying $11/2^-$ level really does not decide between oblate and prolate shapes.

The results of a study of the rotational band built on this level may allow a decision to be made. An oblate nucleus should show a normal rotational band with M1-E2 cascade and E2 cross-over transitions, while the $\Omega = 1/2$ band should show a simpler cascade made up only of E2 radiations. With this in mind, a sequence of odd-mass La isotopes from $A = 125$ to 137 was studied by in-beam spectroscopic techniques following (HI, xn) reactions.

In each of the nuclei studied, a band of levels based on a state with $I = 11/2$ has been found which has spin values increasing monotonically from the base level by $2\hbar$ per state, and energy-spacings very similar to the even-even Ba isotope with one less proton. The correspondence in energy is rather remarkable and is shown in Fig. 1. This spectrum might be explained by a particle-core weak-coupling model,⁴ but this model seems improbable for nuclei with core spacings as small as those in Fig. 1, and has not been notably successful even in more favorable cases. We believe that a new coupling scheme is involved (see following report) which arises as a general Coriolis effect without the weak-coupling assumption.

To demonstrate the physical effect involved, we consider qualitatively a particle coupled to

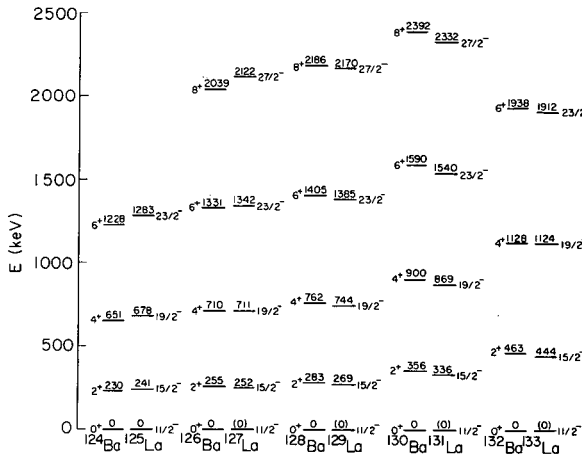


Fig. 1. A comparison of ground band levels in some Ba isotopes with the negative-parity bands in the neighboring La nuclei. In most cases (energy zero in parentheses) the La $11/2^-$ level is not the ground state, and its energy has been subtracted from all levels shown for that isotope. (XBL 724-2709)

a rotating core.⁵ The principal influence of the rotation on this coupling can be expressed by introducing the Coriolis effects, and these depend essentially on the Coriolis force, $\mathbf{R} \times \mathbf{j}$, where \mathbf{R} and \mathbf{j} are the core and particle angular momenta. But for those states where \mathbf{R} is coupled almost parallel to \mathbf{j} , achieving the maximum I , $\mathbf{R} \times \mathbf{j}$ is nearly zero. Thus the rotation has little effect on the coupling of the particle to the core for this orientation of the two, and the energy changes of the system just reflect the core energy changes. Such a band of levels has just the properties displayed in Fig. 1. To find under what conditions this "decoupled" band is likely to occur as a low-lying feature of the spectrum, we will examine a simple Hamiltonian that contains the essential features.

For a particle coupled to an axially-symmetric deformed core which can rotate, we can write the Hamiltonian as

$$H = H_{\text{intr}} + \frac{\hbar^2}{2\mathcal{I}} R^2 = H_{\text{intr}} + \frac{\hbar^2}{2\mathcal{I}} [I(I+1) - \Omega^2] + H_c + \frac{\hbar^2}{2\mathcal{I}} [\langle j^2 \rangle - \Omega^2], \quad (1)$$

with

$$H_c = -2 \frac{\hbar^2}{2\mathcal{I}} [\mathbf{I} \cdot \mathbf{j} - \Omega^2] = -\frac{\hbar^2}{2\mathcal{I}} [I_+ j_- + I_- j_+]. \quad (2)$$

The symbols have their usual meaning,⁶ and H_{intr} represents the Hamiltonian of the particle in the absence of any rotation of the core. Equation (1) is derived by using $\mathbf{R} = \mathbf{I} - \mathbf{j}$. In diagonalizing the right side of Eq. (1) we use a basis system where I and Ω are constants of the motion; this corresponds to the usual one for deformed nuclei. We can express H_{intr} by giving the energy of the system as a function of Ω , that is, as a function of the orientation of \mathbf{j} to the symmetry axis of the core. For a core with quadrupole deformation, the Nilsson calculations⁷ correspond to an evaluation of these energies, but if the deformation, β , is not too large, then we can use the limiting approximation:⁶

$$E(\Omega) = E_0(nl j) + \frac{206\beta}{A^{1/3}} \left[\frac{3\Omega^2 - j(j+1)}{4j(j+1)} \right] \text{ MeV}, \quad (3)$$

which gives reasonable agreement with the Nilsson solutions for the $h_{11/2}$ and $i_{13/2}$ orbitals up to around $\beta = 0.3$. We also include the effects of the pairing correlations, which are given by

$$H_{\text{intr}}(\Omega) = \sqrt{(E(\Omega) - \lambda)^2 + \Delta^2} - \Delta, \quad (4)$$

and the usual⁶ UV factor for H_c . Using Eq. (4), we can diagonalize the right side of Eq. (1) for any values of I , provided we have fixed $\hbar^2/2\mathfrak{J}$, β , λ , and Δ .

We can reduce these four parameters to two essential ones. There is a very general empirical relationship between $\hbar^2/2\mathfrak{J}$ and β (as defined from the E2-transition lifetime) that essentially all even-even nuclei follow.⁸ For the purpose of our survey we will use this relationship to eliminate one of these variables. This gives

$$6\left(\frac{\hbar^2}{\hbar\mathfrak{J}}\right) \equiv E_{2+} \approx \frac{1225}{A^{7/3} \beta^2} \text{ MeV.} \quad (5)$$

Of the remaining parameters, Δ is not very important and we take it always to be 0.8 MeV, so that the remainder of this note will consist of an attempt to understand Eq. (1) as a function of β and λ .

In Fig. 2 we have plotted the solutions to Eq. (1) for $j = 11/2$, $\lambda = E(1/2)$, and $\beta = 0 \rightarrow +0.35$. The outstanding feature is the coincidence of the energies of the "favored" high-spin states ($I = j, j+2, j+4, \dots$) with those of the core states for all β values. The effect of varying λ has been studied and indicates that the tendency to decouple is strongest when λ is low. It is apparent from simple geometrical considerations that the states with low Ω values are much more important in constructing a state with R parallel to j than are those with high Ω values. In prolate nuclei these essential states lie low in the spectrum when Ω is low. We found that at $\beta = +0.25$ (the largest value in the La nuclei) the decoupling of the favored states should occur provided λ is anywhere below $\sim E(5/2)$. In fact, λ is clearly far below this in the La region.

The previous argument can also be turned around, so that if one knows where the Fermi surface is and determines the nature of the band, i. e., whether normal rotational or decoupled, the shape of the nucleus is determined. With the odd-mass La nuclei ($Z=57$), the Fermi surface is below the $h_{11/2}$ proton shell and the bands built on the $11/2^-$ states are all decoupled. From Fig. 2 it can be seen that this requires that these nuclei be prolate with deformations in the range $0.15 \leq \beta \leq 0.25$. This is in contradiction to the conclusions of earlier workers, but we believe the evidence is very compelling.

In addition, we should point out that the type of behavior described above for the odd-mass La nuclei is certainly not restricted just to them. Any high- j shell should show this behavior under the proper conditions, and, in particular, the unique-parity levels in each

shell should be candidates, as they have the highest value of j in that shell and also are the purest states. Whenever the Fermi surface approaches such a shell from below on the prolate side or from above on the oblate side, the occurrence of a band $j, j+2, j+4, \dots$, with spacing similar to those of the ground band of the neighboring doubly-even core nuclei might be expected.

In conclusion, we believe the remarkable energy coincidences shown in Fig. 1 for some La isotopes can be understood as due to rotation-aligned decoupling of the observed

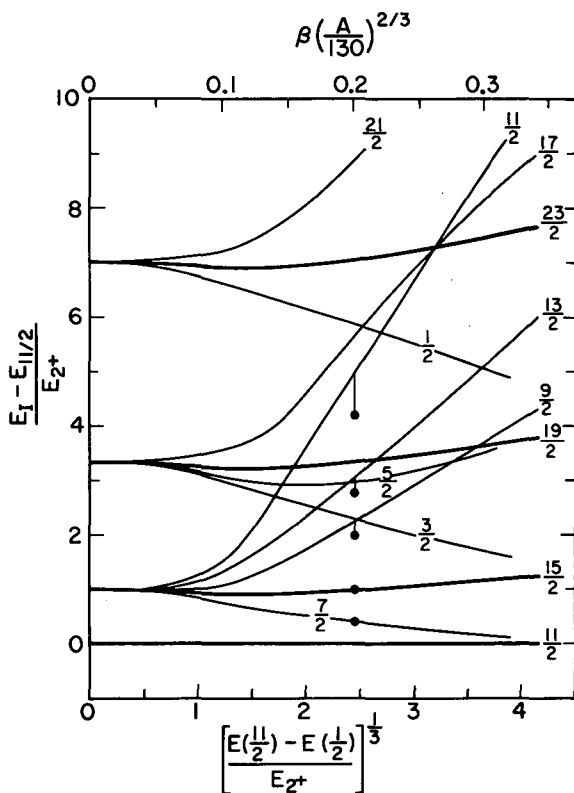


Fig. 2. The results of diagonalizing Eq. (1) for various β values are given for the lowest state of each spin up to $I = 21/2$ (the second $I = 11/2$ state is included). The ordinate is the eigenvalue less the lowest $I = 11/2$ eigenvalue, in units of E_{2+} . The abscissa is β (top) or the cube root of the total splitting of the $h_{11/2}$ orbital in units of E_{2+} (bottom). The Fermi surface, λ , is always located on the $\Omega = 1/2$ state, so that in the limit of very large β , the levels will become a pure $\Omega = 1/2$ band with a decoupling parameter of -6 . The dots show the effect of diagonalizing the Hamiltonian, $H = H_{intr} + \hbar^2/2\mathfrak{J} [R^2 - BR^4 + CR^6]$, instead of Eq. (1), where B and C were adjusted to fit the lowest few levels in ^{126}Ba .
(XBL 724-2608)

states. Indeed, this should be a general effect for the high- j unique-parity orbitals ($h_{11/2}$, $i_{13/2}$, etc.), occurring over a wide range of prolate deformations at the beginning of major shells (nearly empty orbitals) and oblate deformation at the end of major shells (nearly full orbitals).

Footnotes and References

* Present address: Research School of Physics, The Australian National University, Canberra, Australia.

† Present address: Department of Physics, University of Tokyo, Tokyo, Japan.

‡ Present address: Hahn-Meitner Institut, Berlin, Germany.

§ Present address: Universität Marburg, Marbury, Germany.

1. R. K. Sheline, T. Sikkeland, and R. N. Chanda, *Phys. Rev. Letters* **7**, 446 (1961).

2. K. F. Alexander, W. Neubert, H. Rotter S. Chojnacki, Ch. Droste, and T. Morek, *Nucl. Phys.* **A133**, 77 (1965).

3. T. W. Conlon and A. J. Elwyn, *Nucl. Phys.* **A142**, 359 (1970).

4. A. de-Shalit, *Phys. Rev.* **122**, 1530 (1961).

5. The case of two particles coupled to a rotating core has recently been studied by: F. S. Stephens and R. S. Simon, *Nucl. Phys.* **A183**, 257 (1971).

6. A. Bohr and B. R. Mottelson, *Nuclear Structure*, Vol. 1 (Benjamin, New York 1969); Vols. 2 and 3 to be published.

7. S. G. Nilsson, *Kgl. Danske Videnskab. Selskab, Mat.-Fys. Medd.* **29**, No. 16 (1955).

8. L. Grodzins, *Phys. Letters* **2**, 88 (1962).

ROTATION OF MODERATELY DEFORMED ODD-A NUCLEI

F. S. Stephens, R. M. Diamond, D. Benson, Jr., and M. R. Maier

The rotational model, proposed by Bohr¹ in 1952 and developed subsequently by Bohr and Mottelson² and others, requires that the spectrum of an odd-A rotational nucleus corresponds to that of a particle coupled to a non-spherical rotating core. This is well borne out in the regions of "deformed" nuclei, where the particle is strongly coupled to the deformed shape. This model has not really been studied in intermediate- or weak-coupling situations, although these were discussed in the early papers. An attempt to extend the model into these regions was made by Malik and Scholz³ in the mass region $A = 25 - 80$. The results were generally encouraging, although the data were nowhere sufficient to provide a very convincing picture. Recently the striking behavior of the high-spin states in the La nuclei⁴ gave the first strong indication that this model might apply outside the strong-coupling regions. In the present report we would like to discuss some results in the Au region, and then summarize the general features of the model.

The necessary equations are given in the preceding report; however, in the present case we eliminate all adjustable parameters. We fix $|\beta|$ by averaging the value obtained from $B(E2; 2 \rightarrow 0)$ measurements for the two adjacent even-even nuclei. For this $|\beta|$, the

Fermi surface, λ is fixed at the level corresponding to the correct number of particles according to the Nilsson diagram. Thus, for each odd-A case we calculate two spectra, corresponding to a prolate and an oblate shape for the nucleus.

A portion of the Nilsson diagram for protons is shown in Fig. 1, which contains particularly the $h_{9/2}$ and $h_{11/2}$ j -shells. The Tl and Au nuclei have λ values around 3 or 4 MeV on this chart, and this lies completely below the $h_{9/2}$ j -shell for $|\beta| \lesssim 0.2$. In such a case the results of solving the particle plus rotor model do not depend very much on λ and are shown as a function of β in Fig. 2a. For the Tl nuclei we use $|\beta| = 0.11$, which is taken from the even-even Hg nuclei. One set of dots in Fig. 2a shows the location of the observed negative-parity levels in ¹⁹⁹Tl, taken as representative of the lighter Tl isotopes⁵ and normalized to the lowest $I = j$ calculated level (in parentheses). The rotational-band-like character of these levels requires an oblate shape for these states according to Fig. 2a, which is consistent with the previous interpretation.⁵ We believe the explanation of: a) rotational bands in Tl nuclei; b) the approximate $\hbar^2/2\mathfrak{J}$ value of these bands; and c) the sign and rough magnitude of the deviations from a pure-rotor spectrum, are

rather convincing for a calculation with no adjustable parameters. To show that these calculations go over into the region of large deformation in reasonable fashion, we have indicated the predictions for ^{179}Re , where β is taken from ^{178}W and ^{180}Os , together with the observed states.⁶ Again the order of the observed levels is correct as is the approximate spacing of the levels. This interpretation of these levels in ^{179}Re is also consistent with that previously made.⁶

The situation for the $h_{11/2}$ j-shell is shown in Fig. 2b, and is quite similar to that of Fig. 2a, except that all spins are one higher and a given level pattern occurs for the opposite sign of β . This reversal is a result of the fact that λ is now above the j-shell rather than below it. The predicted position of ^{195}Au is indicated, with $|\beta|$ taken from ^{196}Hg and ^{194}Pt , and the experimental levels⁷ are again shown as dots. In this case, an oblate shape is clearly indicated by the decoupled-type Au spectrum and the order of levels and spacings are surprisingly well given. A lower λ value should be used for ^{179}Re in both the $h_{9/2}$ and $h_{11/2}$ j-shells; however, the differences are not very large so we have not made separate figures. The previously identified⁶ $\Omega = 9/2$ band in ^{179}Re is seen to be in rather good agreement with the calculations for a prolate shape.

Our recent results⁸ on the high-spin states in the odd-A Hg nuclei indicate that decoupled bands exist, similar to those in the La isotopes.⁴ A series of two or three stretched E2 transitions, whose energies approximate those of the adjacent even-even nuclei, were observed in $^{189}, ^{195}, ^{197}, ^{199}\text{Hg}$. In one of these cases the population of the known $i_{13/2}$ isomeric state was measured and shown to be large, suggesting that the E2 cascade populates this level. This is precisely what one would expect from the $i_{13/2}$ j-shell around $\beta = -0.1$ according to the present calculations. Thus in Tl, Hg, and Au, the levels from the high-j orbitals can be reasonably well accounted for by the particle-plus-rotor model, and consistently require oblate shapes.

The general features of the rotational model can be easily recognized in Fig. 2. At large deformation (of either sign) a good rotational region occurs. As the deformation decreases, there is a region where the Coriolis effects, coupling the particle to the rotation and mixing Ω values, can be treated as a perturbation. At the other limit of zero deformation, there is no coupling between the particle and the (non-existent) deformation, resulting in the degeneracy of all the states corresponding to different orientations of a given j and R. As the deformation increases from zero, there is

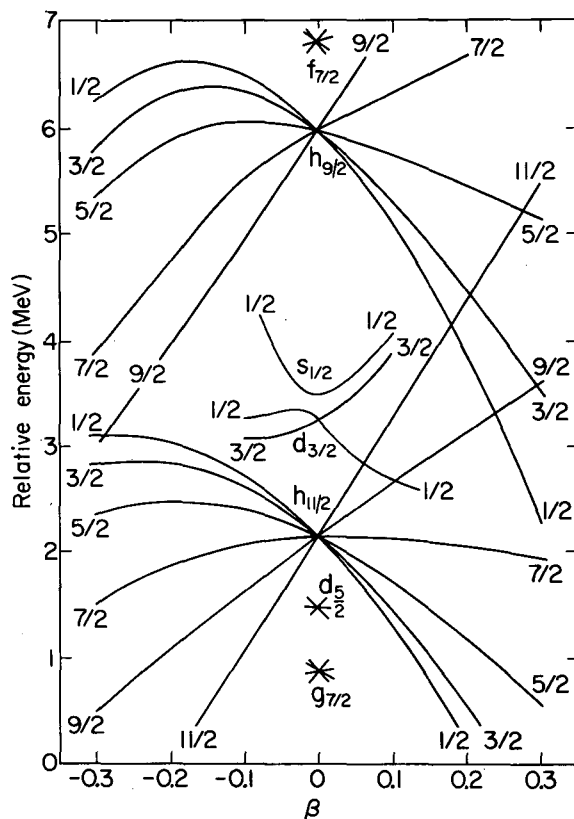


Fig. 1. A portion of the Nilsson diagram for protons, where only the $h_{9/2}$ and $h_{11/2}$ j-shells have been fully drawn. The ground states of the Tl and Au nuclei are in the $s_{1/2}$ and $d_{3/2}$ j-shells, which have been partially drawn. (XBL 725-2887)

a region where it can be treated as a perturbation in a particle-core weak-coupling model.⁹ If λ and the sign of β locate a nucleus near the high- Ω levels of a j-shell (in Fig. 1 for the Au region this would be prolate for $h_{11/2}$ and oblate for $h_{9/2}$) the above two perturbation regions merge into each other, and one shifts rather suddenly from the strong-coupling to the weak-coupling region around $|\beta| = 0.1$. For a nucleus situated near the low- Ω levels (opposite to the above shapes) there is a broad region between $\beta \sim 0.1$ and $\beta \sim 0.3$ where neither of these coupling schemes applies. In this region a new coupling scheme is approximated, in which α , the projection of j on the rotation axis, is a good quantum number. The most favorable states here are the ones where j is aligned with this axis as well as possible ($\alpha = j$), and the high-spin decoupled states discussed in the previous and following reports all have this configuration. For $|\beta| > 0.3$, the coupling scheme on this side again tends toward pure- Ω values.

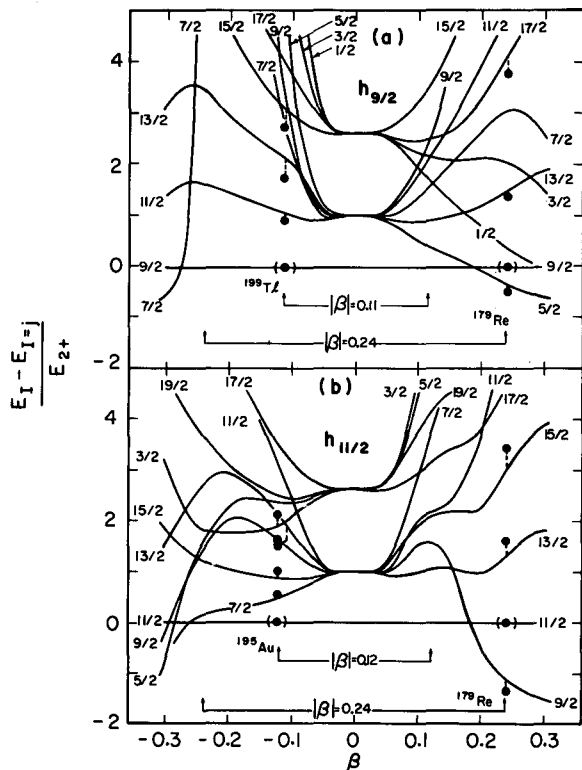


Fig. 2. Solutions to the rotational model, Eq. (1) of previous report, for the yrast states from the $h_{9/2}$ and $h_{11/2}$ j-shells, with $\lambda \approx 3.5$ MeV relative to Fig. 1. For H_{rot} , we used $H_{\text{rot}} = A\vec{R}^2 + B\vec{R}^4 + C\vec{R}^6$, with $B/A = (1.6 \times 10^{-2})(1 - 14\beta^2)$ and $C/A = (8.8 \times 10^{-5})(1 - 14\beta^2)$ and $B=C=0$ if $|\beta| > 0.267$. The measured negative-parity levels in ^{199}Tl , ^{195}Au , and ^{179}Re are shown as dots, with dashed lines connecting each dot to the calculated level having that spin value. (XBL 7210-4362)

A COUPLING SCHEME RELEVANT TO HIGH ANGULAR MOMENTA AND INTERMEDIATE NUCLEAR DEFORMATIONS

F. S. Stephens, R. M. Diamond*, and S. G. Nilsson*

Experimental studies, reported elsewhere,¹ have indicated that in a transitional region an entirely new coupling scheme develops.^{1,2} This new type of coupling becomes prevalent first for particular states of high spin. In the region of nuclear distortions and spin values in question, the odd single particle follows the rotating deformed core only partially, and orients its orbital plane in such a way as essentially to minimize the Coriolis energy. We consider the rotor-plus-particle Hamiltonian³

$$H = A[\vec{I}_+^2 + \vec{j}_-^2 - I_3^2 - j_3^2] + H'_C + H_{\text{sp}},$$

where (1)

$$H_{\text{sp}} = H_{\text{sph}} + k\beta Y_{20}(\hat{3})$$
(2)

and

$$H'_C = -A(I_+ j_- + I_- j_+).$$
(3)

References

1. A. Bohr, Kgl. Danske Videnskab. Selskab, Mat.-Fys. Medd. 26, No. 14 (1952).
2. A. Bohr and B. R. Mottelson, Kgl. Danske Videnskab. Selskab, Mat.-Fys. Medd. 27, No. 16 (1953).
3. F. B. Malik and W. Scholz, Phys. Rev. 150, 919 (1966); 176, 1355 (1968) and others.
4. F. S. Stephens, R. M. Diamond, J. R. Leigh, T. Kammuri, and K. Nakai, Phys. Rev. Letters 29, 438 (1972); also previous report.
5. J. O. Newton, S. D. Cirilov, F. S. Stephens, and R. M. Diamond, Nucl. Phys. A148, 593 (1970).
6. J. R. Leigh, J. O. Newton, L. A. Ellis, M. C. Evans, and M. J. Emmott, Nucl. Phys. A183, 177 (1972).
7. J. Frana, A. Spalek, M. Fiser, and A. Kokes, Nucl. Phys. A165, 625 (1972).
8. D. Benson, Jr., M. R. Maier, R. M. Diamond, and F. S. Stephens, to be published.
9. A de-Shalit, Phys. Rev. 122, 1530 (1961).

The single-particle Hamiltonian is thus associated with a quadrupole field oriented along the core symmetry axis 3. The term H'_C is conventionally called the Coriolis coupling term. In the representation of the normally employed adiabatic wave function basis, one has

$$\langle H \rangle = e'_j + A[I(I+1) + j(j+1)] + (K-2A)\Omega^2, \quad (4)$$

where the diagonal value of H_{sp} has been written as

$$\langle H_{sp} \rangle = e'_j + K\Omega^2. \quad (5)$$

The neglected term, H'_C , becomes very large for the small deformations and large rotational frequencies here considered.

It is apparent from Eq. (4) that a particularly favorable region of degeneracy occurs when $K = 2A$, in which case $\langle H \rangle$ is independent of Ω . This degeneracy can be exploited to diagonalize H'_C approximately. Let χ_α^j be an intrinsic wave function with the projection of j on the nuclear 1-axis equal to α . This can be decomposed in terms of states having $j_3 = \Omega$:

$$\chi_\alpha^j = \sum_{\Omega} d_{\alpha\Omega}^j \left(\frac{\pi}{2}\right) \chi_{\Omega}^j \quad (6)$$

From this a new wave function describing the entire system is constructed:

$$\psi_{M\alpha}^{Ij} = \sum_{\Omega} d_{\alpha\Omega}^j \left(\frac{\pi}{2}\right) \chi_{\Omega}^j D_{M\Omega}^I. \quad (7)$$

The restriction of reflection symmetry in the plane perpendicular to the 3-axis leads to the auxiliary condition that $I-\alpha$ must be even.

For the case $K = 2A$ in (4), one thus immediately obtains the following energy spectrum in terms of I, j, α :

$$E(I, j, \alpha) = e'_j + A[j(j+1) + I(I+1) - 2I\alpha]. \quad (8)$$

The lowest-lying high-spin states have $\alpha = j$ and the associated band has I -values compatible with $I-\alpha$ being even. The energy expression may be recast in the form

$$E = \text{const} + A \cdot (I-j)(I-j+1) = \text{const} + AR'(R'+1), \quad (9)$$

where $R' = 0, 2, 4, \dots$, reproducing an even-even rotational spectrum as found in recent experiments.¹

The above discussion has been restricted to $I > j$. For the case $I < j$ a completely analogous treatment can be carried out since

H'_C exhibits complete symmetry in I and j , leading to the expression

$$E(I, j, \kappa) = e'_j + A[j(j+1) + I(I+1) - 2j\kappa], \quad (10)$$

where κ is the projection of I along the rotation axis. The symmetry condition requires $j - \kappa$ to be even, restricting the permissible κ -values of (10).

To illustrate the region of validity of the present scheme, we have chosen to compare in Fig. 1 the diagonal energies of (1) for three coupling schemes, namely the "deformation-aligned" or "strong-coupling" scheme appropriate for $\beta \geq 0.25$, the "non-aligned" or "weak-coupling" scheme appropriate near $\beta = 0$, and the present "rotation-aligned" coupling scheme. In this figure the state

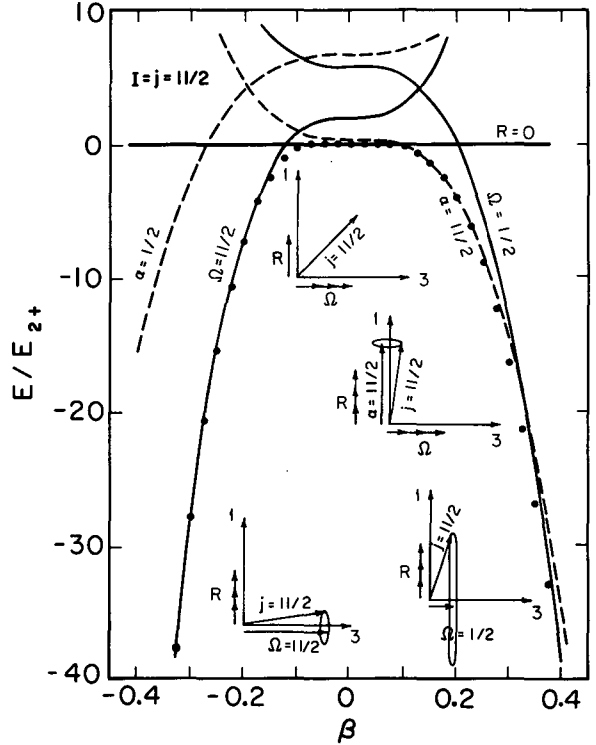


Fig. 1. The lines show the lowest-energy $I = j = 11/2$ states in each of three coupling schemes: the spherical ($R = 0$), the rotation-aligned ($\alpha = 1/2, 11/2$), and the deformation-aligned ($\Omega = 1/2, 11/2$). The inserts attempt to give a physical picture of the lowest of these configurations in each region, where multiple-headed arrows indicate mixture of states, and the 1-axis represents any direction perpendicular to the nuclear symmetry (3) axis. The dots show the result of exact diagonalization of the simple particle-plus-rotor model (Eq. 1). (XBL 7210-4361a)

Footnotes and References

$I = j = 11/2$ is shown for a case with one particle in the $h_{11/2}$ orbital. We have thus plotted the energy for pure configurations having $R = 0$, $\Omega = 1/2$ and $11/2$, and $\alpha = 1/2$ and $11/2$. For $|\beta| \lesssim 0.1$, the weak coupling $R = 0$ configuration lies lowest. On the oblate side the $\Omega = 11/2$ and $\alpha = 1/2$ states cross below the $R = 0$ state, but $\Omega = 11/2$ always lies well below $\alpha = 1/2$, resulting in nearly normal rotational bands for $\beta < -0.1$. On the prolate side $\Omega = 1/2$ and $\alpha = 11/2$ cross below $R = 0$, and $\alpha = 11/2$ is lowest for $0.1 \leq \beta \leq 0.3$, and thereafter $\Omega = 1/2$ becomes lowest. The exact energies of H are shown as dots in this figure. The close correspondence of these dots with the lowest lines in Fig. 1 indicates the adequacy with which the three coupling schemes represent the exact solution of H in Eq. (1). The rotation-aligned coupling scheme here proposed is seen to have a rather broad region of applicability connecting the weak-coupling region with that of the deformation-aligned coupling scheme on the side where low- Ω orbitals occur near the Fermi surface.

* On leave of absence from the Department of Mathematical Physics, Lund Institute of Technology, Lund, Sweden.

1. F. S. Stephens, R. M. Diamond, J. R. Leigh, T. Kammuri, and K. Nakai, Phys. Rev. Letters 29, 438 (1972); two previous reports.
2. A somewhat different approach to this problem is given in a report by J. O. Rasmussen, J. Alonso, W. Rille, I. Resantha, and R. Needham.
3. A. Bohr, Kgl. Danske Videnskab. Selskab, Mat.-Fys. Medd. 26, No. 14 (1952).

FEEDING TIMES FOLLOWING (HI, xn) REACTIONS

J. O. Newton, F. S. Stephens, and R. M. Diamond

Spectroscopy of the γ rays following heavy-ion (HI), xn reactions has been a prolific source of information on high-spin states in nuclei. The way in which these states are populated following formation of the highly excited product nucleus, and the nature of the states through which the γ -ray population passes is a topic of considerable current interest. A simple model¹ has been proposed to explain the experimental data for doubly-even nuclei. The highly excited states formed after neutron emission first decay by fast E1 transitions down to the region of the yrast line, after which decay must occur along the yrast region. If, as proposed in Ref. 1, the states involved in this region consist for the most part of rotational states (based mainly on two quasi-particle states) decay should be mainly by E2 transitions. There should be few, if any, traps giving rise to isomeric states in the yrast region; thus, decay should be fast (\sim few psec). When the population reaches the point where the ground-state band (gsb) intersects the yrast region, it then flows into the gsb; the transition time from the yrast region to the gsb must also be of the order of psec. In a previous paper² we found that the mean feeding times, T_f , for the nuclei ^{160}Er , ^{158}Er , and ^{156}Er , made by (^{40}Ar , 4n) reactions, were (6 ± 3) psec, (11 ± 3) psec, and (16 ± 3) psec, respectively. These nuclei range from being rotational (^{160}Er) to near

vibrational (^{156}Er), and the tendency for the feeding times to become longer as the nuclei become more vibrational is interesting. In all cases the fraction of slow feeding, f_l , was found not to exceed a few percent of the fast (~ 10 psec) feeding. It is very desirable to see whether these results are of general validity, and for this reason the present experiments were undertaken.

The recoil-distance Doppler shift method was used to determine the lifetimes. In this method² the excited nuclei recoiling from the target are stopped in a moveable plunger placed near it. For lifetimes longer than a few psec, as is the case here, the nuclei which decay in the plunger yield an unshifted γ -ray line, while those that decay in flight yield a line, observed in a detector placed at 0° to the beam direction, which is Doppler shifted and slightly broadened. If the distance between the target and plunger is varied, the fraction, f , of the γ -ray profile which is unshifted changes, and from this information and knowledge of the velocity the lifetime can be deduced.

The reactions were initiated by beams of ^{20}Ne and ^{28}Si ions from the Berkeley Hilac incident on self-supporting metal targets stretched tightly over a holder assembly. The recoiling nuclei from the (HI, 4n) reactions

were stopped in a lead-covered plunger whose position could be adjusted to an accuracy of ± 0.003 mm by means of a precision micrometer. "Unshifted" spectra were obtained by bombarding similar targets evaporated onto 0.0025-cm-thick lead foil. The mean velocities of the recoiling nuclei were determined from the fractional energy shifts of the completely shifted peaks, obtained by moving the plunger sufficiently far back so that a negligible number of nuclei decayed in it. The velocities so obtained, after correction for the finite angular spread of the detector, were approximately 0.9% of the velocity of light for the ^{20}Ne -induced reactions and 1.4% for the ^{28}Si -induced reaction.

In order to measure the feeding times, it is also necessary to determine the zero point of the apparatus, that is, that position of the plunger when it exactly touches the target and produces only an unshifted peak. Actually, a purely unshifted peak cannot be realized in practice because of mechanical imperfections in the target and in the plunger assembly. We determined the zero point in this case by measurements on the strong γ rays arising from Coulomb (and/or nuclear) excitation of rotational states of the target nuclei. In contrast to the states populated in (HI, xn) reactions, these states are populated essentially instantaneously (not quite true since there is a small amount of feeding from the next higher state). Hence if one extrapolates the curves of $\log f$ vs distance back to unity for these Coulomb-excited lines one should obtain the zero point. Care has to be taken in the extrapolation, because the recoiling Coulomb-excited nuclei are not tightly collimated in direction nor do they have constant energy as in (HI, xn) reactions.

In Fig. 1 we show examples of the γ -ray spectra from the $^{152}\text{Sm}(^{20}\text{Ne}, 4n)^{168}\text{Hf}$ reaction for various plunger settings. For each transition of interest the intensities of the shifted and unshifted peaks were determined. The most important source of error in this procedure is the estimation of the background under each peak since, apart from the main γ -ray lines, numerous weak ones also occur in the spectra from (HI, xn) reactions. These lines are likely to be associated with different lifetimes than those of the lines of interest and hence can cause uncertainties when they are close together. In some cases account had to be taken of such close-lying lines. After such corrections had been made, the unshifted fraction, f , was calculated. In the ^{20}Ne -induced reactions with the 1 mg/cm^2 targets, f would tend to a finite constant value for large plunger distances even if there were no slow-feeding component, because some ions are completely stopped in the target. In the examples of plots

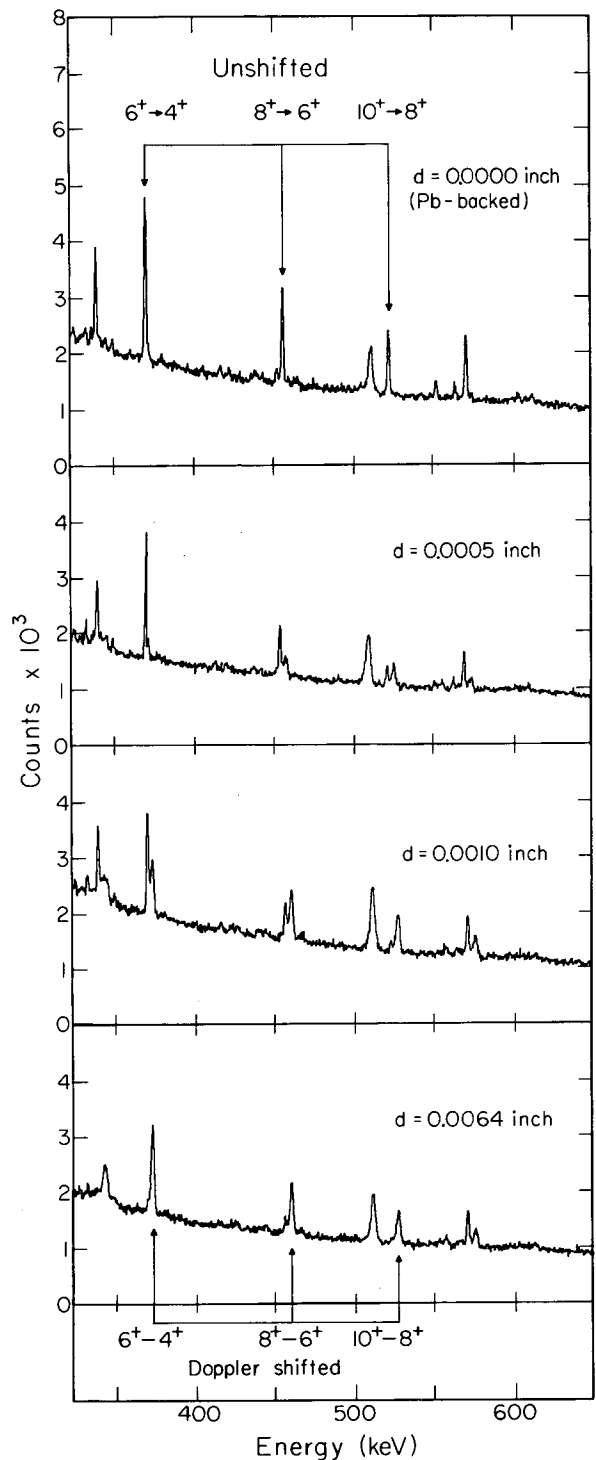


Fig. 1. Pulse-height spectra for the γ rays from the $^{152}\text{Sm}(^{20}\text{Ne}, 4n)^{168}\text{Hf}$ reaction for various plunger settings. (XBL 731-2046)

of $\log f$ vs target-plunger separation shown in Fig. 2, the effect of this constant background, which could also arise from a slow-feeding component, has been removed. The zero-point micrometer setting, as determined from the Coulomb excitation peaks, is also indicated in the figure.

A number of other corrections have also to be considered. The results of these measurements are summarized in Table I. As before,² the mean feeding time, T_f , was taken to be the time required for the unshifted fraction of the fastest observed transition to decrease by $1/e$. Clearly this procedure gives

Table I. Summary of data.

Nucleus	Velocity (%)	T_f (psec)	I	$E_\gamma(I)$	$E_\gamma(I)/E_\gamma(4)$	f_ℓ (%)	Intensity	
^{166}Hf	0.96 ± 0.002		4	311.8	1.000		1.41	
			6	426.5	1.368	3 ± 3	1.00	
			8	~ 511	~ 1.64			
			10	565.0	1.812	10 ± 3	0.55	
			11 ± 3	12	593.9	1.905	5 ± 4	0.41
^{168}Hf	0.91 ± 0.02		4	261.5	1.000		1.22	
			6	371.1	1.419	13 ± 1	1.00	
			8	456.5	1.746	5 ± 3	0.88	
			5 ± 2.5	10	522.0	1.996	1.5 ± 1.6	0.72
				12	~ 569	~ 2.18		0.54
^{170}Hf	0.89 ± 0.02		4	221.0	1.000		1.35	
			6	320.9	1.452		1.00	
			8	400.5	1.812	2 ± 2	0.78	
			10	462.3	2.092	7 ± 4	0.65	
				12	~ 511	~ 2.31		
	3 ± 3	14	550.8	2.492	8 ± 5	0.32		
^{178}Os	1.39 ± 0.02		4	266.8	1.000		1.16	
			6	363.0	1.361		1.00	
			8	432.6	1.621	1 ± 2	0.86	
			10	488.3	1.830	6 ± 3	0.56	
			$12 \pm \frac{2.5}{4}$	12	538.0	2.016	6 ± 4	0.47

an upper limit to T_f , but since the mean lives of the fastest transitions are in all cases estimated to be less than ~ 2 psec, the correction is in fact much less than experimental error. The fraction of the γ -ray intensity with an (apparent), slow feeding time is given in percent in the column headed by f_f . We did not attempt to obtain lifetimes for the quasi-rotational states populated in these reactions because, as the intensities in Table I show, there is a significant amount of side feeding of the states. This is in contrast to the ($^{40}\text{Ar}, 4n$) reactions where feeding occurs mainly near the top of the observed band.

The results in Table I show the same general features as the earlier measurements,² i. e., feeding times of the order of 10 psec or less, a tendency for the feeding times to increase as the nuclei become more vibrational, and a small upper limit ($\leq 5\%$) on long-lived components from isomeric states. In addition, Kutschera et al.³ have recently reported similar conclusions in measurements on the nuclei $^{120,122}\text{Xe}$ formed in the $^{108,110}\text{Pd}(^{16}\text{O}, 4n)^{120,122}\text{Xe}$ reactions. The fact that there are now nine cases showing these features considerably strengthens the suggestion that this may be a general phenomenon, at least in rotational and vibrational nuclei. Any detailed model for the (HI, xny) reactions must explain these fast transitions in the yrast cascade and also the fast transfer from the yrast region to the gsb.

References

1. J. O. Newton, F. S. Stephens, R. M. Diamond, W. H. Kelley, and D. Ward, Nucl. Phys. A141, 631 (1970).
2. R. M. Diamond, F. S. Stephens, W. H. Kelley, and D. Ward, Phys. Rev. Letters 22, 546 (1969).
3. W. Kutschera, D. Dehnhardt, O. C. Kistner, P. Kump, B. Povh, and H. J. Shann, Phys. Rev. C 5, 1658 (1972).

STATISTICAL DECAY OF GAMMA RAYS IN (n_{th}, γ) REACTIONS

E. Nardi, L. G. Moretto, and S. G. Thompson

The relative population of the ground states and spin isomers occurring after gamma decay in neutron capture reactions has been studied on the basis of the statistical model by various authors.¹⁻³ The main result of this kind of investigation has been some information concerning the spin cutoff parameter. The previous investigations employed level

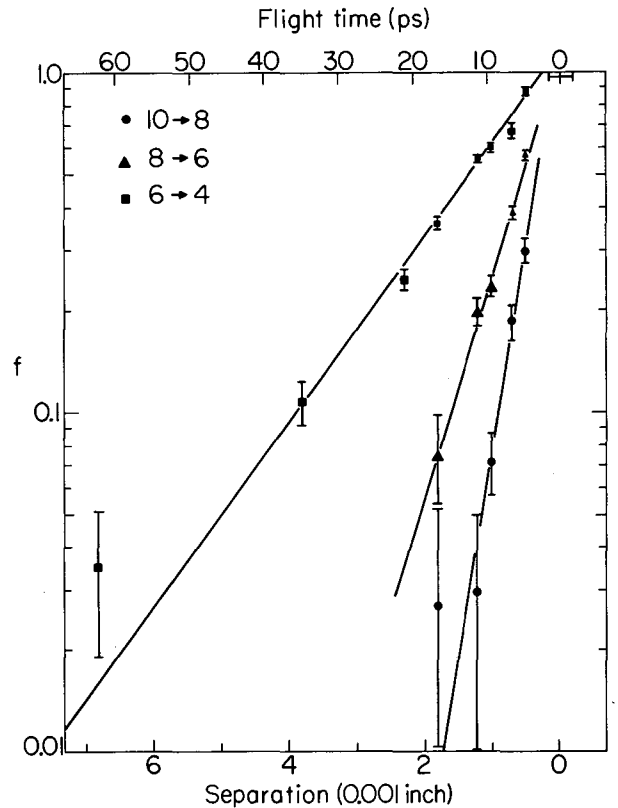


Fig. 2. The unshifted fraction f as a function of target-plunger separation and flight time for transitions following the $^{152}\text{Sm}(^{20}\text{Ne}, 4n)^{168}\text{Hf}$ reaction with a 1-mg/cm^2 target. The approximately constant value of f for large separations has been subtracted. The horizontal error bar indicates the experimental error in the zero of the time scale. (XBL 731-2044)

densities based upon the uniform model. It is of some interest to see whether an improved description of the statistical emission of γ rays can be obtained by means of level densities based upon the shell model and the pairing Hamiltonian.^{4,5} The probability of emitting a γ ray of energy ϵ and multipolarity ℓ is given by:

$$P \propto |M(\epsilon, l, I_i, I_f)|^2 \rho(E-\epsilon, 0) \exp - \frac{(I+1/2)^2}{2\sigma^2},$$

where E is the initial excitation energy, I_i and I_f are the initial and final angular momentum respectively, $\rho(x, 0)$ is the density of levels of zero angular momentum, and σ^2 is the spin cutoff parameter.

The form of the matrix element M is very uncertain. For a dipole transition, the following forms have been used:

1) $M^2 \propto \epsilon^3$; 2) $M^2 \propto \epsilon^3 S(I_i, I_f)$, where S is the geometrical factor which can be calculated in the case of a single-particle transition;

$$3) M^2 \propto \epsilon^2 \left[\frac{(\epsilon^2 - \epsilon_0^2)^2}{\epsilon_0^2 \Gamma^2} + 1 \right]^{-1} = \epsilon^2 \sigma(\epsilon).$$

this last form is based upon the use of the inverse cross section, given by the E1 giant resonance. Two different level densities were employed: in one case pairing was included, in the second case pairing was left out. In both cases the Nilsson diagram was employed with the parameters recommended for the various mass regions. In order to illustrate the difference between the two level density calculations, the spin cutoff parameters for selected nuclei are shown in Fig. 1 for paired and unpaired systems.

The evaporation cascade was followed by means of a Monte Carlo method. The direct feeding of the ground state and of the isomer state at every stage of the evaporation makes the calculation sensitive to the absolute values of the level density. The cascade was stopped when the residual nucleus had an excitation energy between 0.5 and 1.0 MeV. The next transition was required to feed either the ground state or the isomeric level.

The calculated isomer ratios, obtained with the expressions for the matrix elements illustrated above and with both kinds of level densities are shown in Table I.³ In the same table the available experimental values are also shown. The most obvious conclusion is that the use of pairing in the level density leads to isomer ratios which are too small. This seems to be due to the very low values of the level densities which allow a substantial direct decay to the ground and isomer levels and prevent a spreading of the spin population to larger angular momentum values. The reason for the disagreement either rests on the inability of the level density formalism to predict the absolute level density values or in the inadequacy of the matrix elements.

The introduction of the unpaired level density in the calculation leads to a better agreement with the experimental data. The use of the form $|M|^2 \propto \epsilon^3$ seems to be the most successful. In Fig. 2 the experimental γ -ray spectrum for Cd is shown together with the theoretical predictions obtained with the unpaired level density and two forms for $|M|^2$. Again it seems that the expression $|M|^2 \propto \epsilon^3$ reproduces best the experimental data.

In conclusion, it is possible, with a suitable choice of the level density and of the square of the matrix elements, to reproduce the experimental data approximately. However, it is not clear if and why the paired level density does not give satisfactory results although it has a better theoretical foundation. Also, the

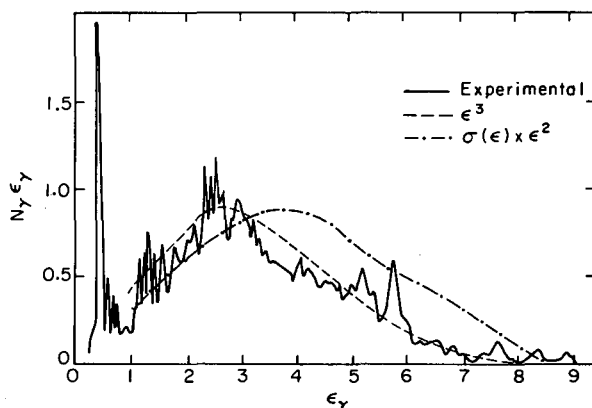


Fig. 1. Ratios between spin cutoff parameters calculated from the shell model and from the uniform model. On the right pairing is included, on the left it is excluded.

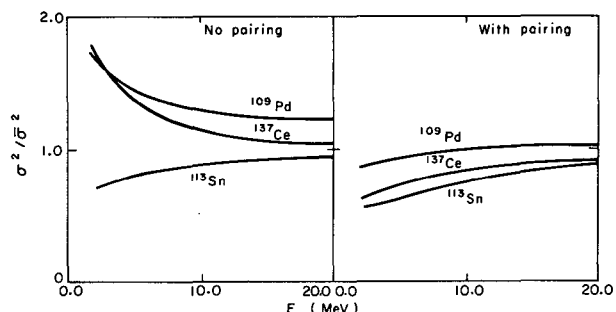


Fig. 2. Total gamma-ray spectrum from neutron capture in Cd. The spectrum N_γ is multiplied by the gamma-ray energy ϵ_γ . The experimental spectrum is shown together with the theoretical calculations.

success of the form $|M|^2 \propto \epsilon^3$, is not understood, because such a form refers to a single nucleon transition, which is hardly the case at high excitation energies. Therefore great

caution should be used in drawing conclusions concerning any physical quantities obtained from this kind of analysis.

Table I.

Nuclide formed in nth capture	Experimental isomer ratio (%)	Calculated isomer ratios, non-paired nucleon system $ \langle M \rangle ^2 =$			Calculated isomer ratio, paired nucleon system $ \langle M \rangle ^2 = \epsilon^3$
		ϵ^3	$\sigma(\epsilon)\epsilon^2$	$\epsilon^3 S$	
^{69}Zn	8.0, 9.0±2, 7.0, 7.0	6.6	3.7	14	1.1
^{71}Zn	17.0±2, 8.0±2	6.0	2.4	12	0.5
^{75}Ge	19±2	16.0	11.0	29	0.7
^{77}Ge	47±12	22.0	15	37	0.8
^{77}Se	6±3	29.0	18	49	1.2
^{81}Se	12±1, 17.0±2, 12±3	30.0	20	48	0.9
^{83}Se	8	14.0	7.3	24	1.4
^{85}Kr	40.0±20, 0.44	20.0	12.4	35	1.9
^{85}Sr	40	39.0	25.4	57	3.0
^{109}Pd	2.2±0.4, 1.8±0.4	2.0	0.5	8.4	0
^{111}Pd	4.3, 1.1±0.1	1.5	0.3	6.8	0
^{115}Cd	12.0	13.2	7.1	30	0.3
^{113}Sn	40.0±10	18.2	10	27	3.0
^{121}Sn	0.7±0.7	7.9	3.7	20	0
^{123}Sn	0.6±0.6	6.8	3.1	17	0
^{125}Sn	3.2, 2.0±1.3	5.1	1.7	14	0
^{121}Te	14±4	10.5	6.5	26	0.4
^{127}Te	13±2, 8±3	7.1	3.9	16	0
^{129}Te	7.4±1.5, 10±3	6.0	3.0	15	0
^{131}Te	5	4.4	1.9	12	0
^{133}Ba	8	10.5	5.6	22	0.3
^{137}Ce	13.1±1, 9±4	10.5	6.7	25	0.3
^{191}Os	31.0±1	14.0	6.8	27	0.5
^{197}Pt	6.5±1.3	1.0	0.3	4.5	0
^{197}Hg	4.4±0.8, 4.2±0.8	1.0	0.2	6	0

References

1. J. R. Huizenga and R. Vandenbosch, Phys. Rev. 120, 1305 (1960).
2. R. Vandenbosch and J. R. Huizenga, Phys. Rev. 120, 1313 (1960).
3. C. T. Bishop, H. K. Vonath, and J. R. Huizenga, Nucl. Phys. 60, 241 (1964).
4. L. G. Moretto, Energia Nucleare 17, 36 (1970).
5. L. G. Moretto, Nucl. Phys. A182, 641 (1972) and A185, 145 (1972).
6. L. V. Groshev, A. M. Demipov, V. M. Lutsenko, and V. I. Pelekhov, Atlas of Gamma Ray Spectra from Radiative Capture of Thermal Neutrons (Pergammon Press, New York).

NUCLEAR LEVEL DENSITY*

J. Huizenga and L. G. Moretto

This is an abstract of a review article which summarizes the theoretical and experimental knowledge on the level densities and other statistical properties of nuclei.

In the first part the methods and models used in the theoretical evaluation of the nuclear level density are discussed. The methods which have been presented are, in order of generality, the combinatorial method, the recursion method, and the saddle point method. The last is given particular attention as the most powerful tool yet devised in statistical mechanics.

The historical evolution of the models ranges from the initial equidistant model, where the single particle levels are equally spaced and which can be treated analytically, to the more realistic shell model. In the latter model the shell effects, very large in the ground state, are progressively washed out as the excitation energy increases. The residual interaction is treated in the pairing approximation and permits a most general description of the statistical nuclear properties. The deformation can also be included in the statistical calculation which yields the deformation probability at each excitation energy.

The second part of the article deals with the sources of experimental information on the level densities and with the problems

associated with the analysis of experimental data. The neutron resonances still provide the most abundant and most direct information on the level densities. The shortcoming of the method is related to the approximately constant excitation energy (the neutron binding energy) at which the level densities can be measured. Similarly the charged particle resonances also provide information about the level density, though the analysis of the data is more involved and uncertain. Inelastic scattering and nuclear reactions which lead to resolved levels as well as energy spectra of evaporated particles provide further information over a larger energy range. The excitation functions of isolated levels also are connected with the level density of the compound nucleus. The study of Ericson fluctuations provides information on the level density at rather high excitation energy (10-20 MeV). Recently the channeling and blocking technique in single crystals has offered the possibility of calculating the compound nuclear lifetime which is directly expressible in terms of the compound nucleus level density.

Footnote

* Annual Review of Nuclear Physics, (in press).

FISSION FRAGMENT ANGULAR DISTRIBUTIONS IN ^4He -INDUCED FISSION OF NUCLEI IN THE ^{208}Pb REGION

L. G. Moretto, R. C. Gatti, and S. G. Thompson

In a previous study of the angular distributions in ^4He -induced fission of ^{206}Pb and

^{207}Pb , a remarkable anomaly was observed in the anisotropies very close to the fission

barrier.¹ The rapid increase of the anisotropies with decreasing excitation energy led to the hypothesis that a substantial freezing of the intrinsic degrees of freedom, possibly due to pairing, was taking place.

In order to obtain further information regarding such an effect, angular distributions have been measured for the ^4He -induced fission of ^{204}Pb , ^{208}Pb , ^{209}Bi , and ^{197}Au . The beams of ^4He ions were provided by the 88-inch cyclotron. The angular distributions were measured by means of strips of mica covering the angular range $\sim 80^\circ$ to 175° . The use of mica as a detector was necessary due to the very small fission cross sections involved when close to the barrier.

The mica strips, after etching with a concentrated solution of hydrofluoric acid were scanned continuously from $\sim 90^\circ$ to 175° by means of an optical microscope.

The experimental angular distributions, after transformation to the center-of-mass system, were analyzed by means of the standard expression:

$$W(\theta) \propto \sum_{I=0}^{\infty} (2I+1)^2 T_I \left[\text{erf} \frac{I+1/2}{(2K_0^2)^{1/2}} \right]^{-1} \\ \times \exp \left[-\frac{(I+1/2)^2 \sin^2 \theta}{4K_0^2} \right] I_0 \left[\frac{(I+1/2)^2 \sin^2 \theta}{4K_0^2} \right],$$

where I is the orbital angular momentum assumed to be equal to the total angular momentum, T_I are optical model transmission coefficients, I_0 is the modified Bessel function of order zero, and K_0^2 is the second moment of the distribution of angular momentum projection K on the fission axis. This quantity can be expressed as

$$K_0^2 = \frac{\mathcal{J}_{\text{eff}}}{\hbar^2} T,$$

where

$$\frac{1}{\mathcal{J}_{\text{eff}}} = \frac{1}{\mathcal{J}_{\parallel}} - \frac{1}{\mathcal{J}_{\perp}},$$

\mathcal{J}_{\parallel} and \mathcal{J}_{\perp} are the principal moments of inertia of the nucleus at the saddle point and T is the saddle-point temperature.

Since in the nuclei considered here it is expected that $\mathcal{J}_{\perp} \gg \mathcal{J}_{\parallel}$, the contribution to K_0^2 comes principally from \mathcal{J}_{\parallel} . Furthermore

$$K_0^2 \approx \frac{\mathcal{J}_{\parallel}}{\hbar^2} T = \bar{n} k^2$$

where \bar{n} is the average number of excitations (quasiparticles) at the saddle point and k^2 is the average square projection of the single-particle angular momenta on the fission axis. Therefore a measurement of K_0^2 as a function of excitation energy above the barrier gives information concerning the number of intrinsic excitations of the nucleus at the saddle point.

The experimental values of K_0^2 as a function of excitation energy are shown in Figs. 1-6. In these figures the position of the fission barriers obtained from the most recent analysis of fission cross sections² is indicated. Also an example of the angular distribution is shown in Fig. 7.

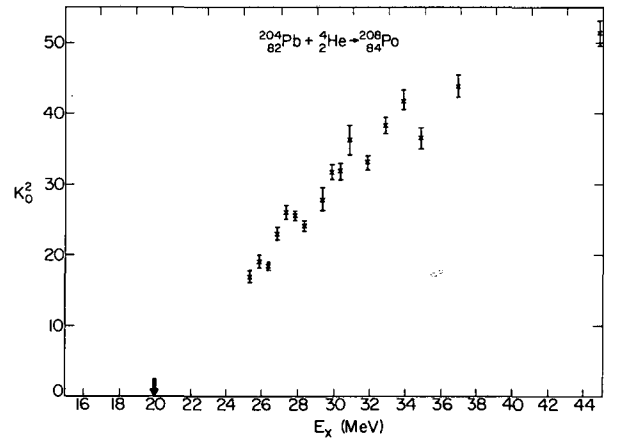


Fig. 1. Experimental values of K_0^2 as a function of the compound nucleus excitation energy in ^4He -induced fission of ^{204}Pb .

(XBL 732-2270)

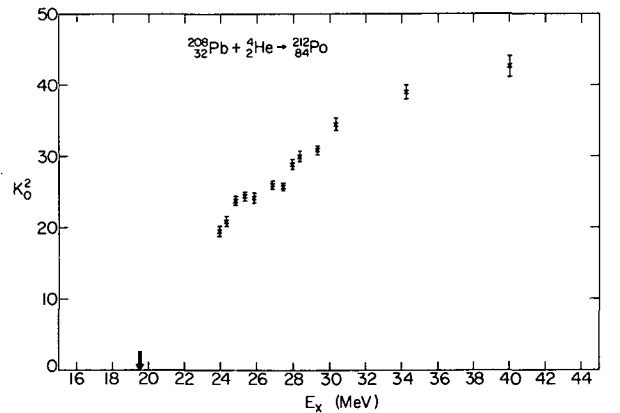


Fig. 2. Experimental values of K_0^2 as a function of the compound nucleus excitation energy in ^4He -induced fission of ^{208}Pb .

(XBL 732-2271)

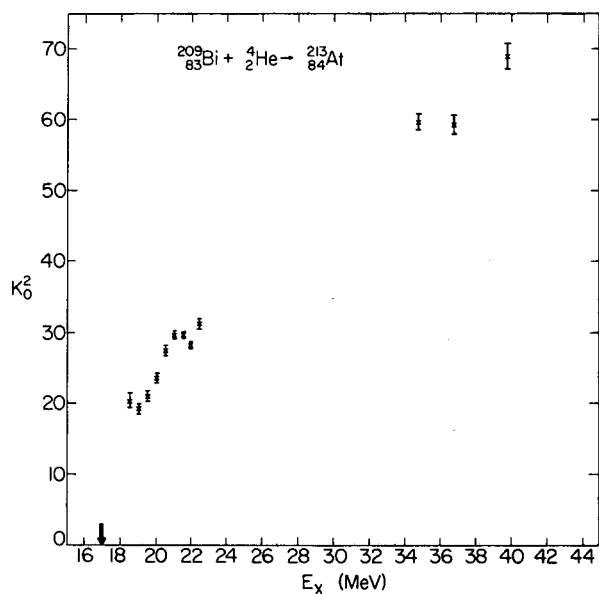


Fig. 3. Experimental values of K_0^2 as a function of the compound nucleus excitation energy in ^4He -induced fission of ^{209}Bi .
(XBL 732-2272)

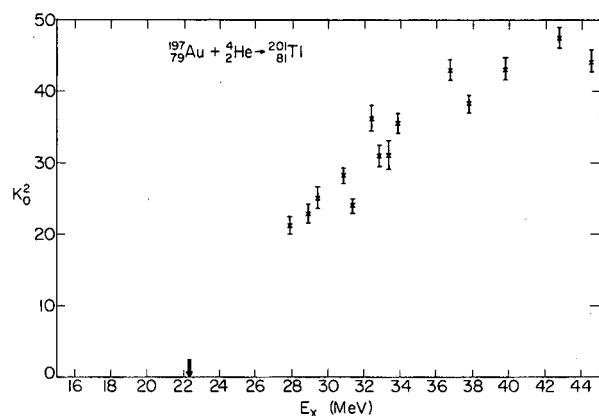


Fig. 4. Experimental values of K_0^2 as a function of the compound nucleus excitation energy in ^4He -induced fission of ^{197}Au .
(XBL 732-2273)

The overall behavior of the K_0^2 quantity as a function of excitation energy is very similar for all the nuclei studied. It appears that the odd-A nuclei tend to have a larger value of K_0^2 at the same excitation energy above the barrier than the even-even nuclei. There is a tendency in even-even nuclei, especially

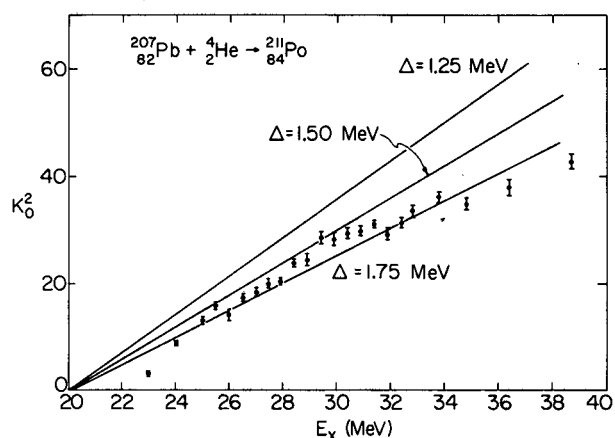


Fig. 5. Experimental values of K_0^2 as a function of the compound nucleus excitation energy in ^4He -induced fission of ^{207}Pb . The three lines correspond to B. C. S. calculations with different values of the gap parameter.
(XBL 732-2274)

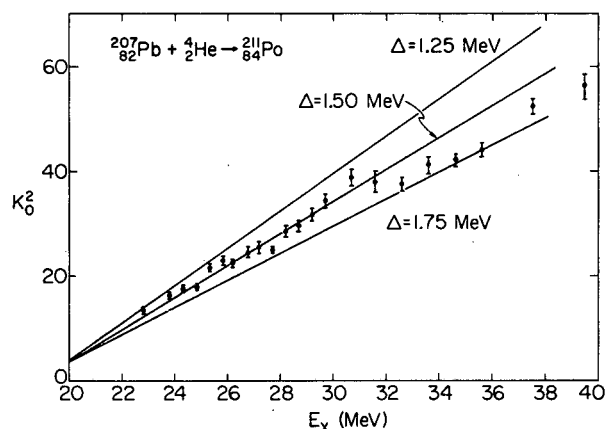


Fig. 6. Experimental values of K_0^2 as a function of the compound nucleus excitation energy in ^4He -induced fission of ^{207}Pb . The three lines correspond to B. C. S. calculations with different values of the gap parameter.
(XBL 732-2275)

visible in the ^{210}Po case, to reach very low values of K_0^2 when close to the fission barrier. In order to illustrate the apparent freezing of the intrinsic degrees of freedom, calculations by means of the B. C. S. Hamiltonian have been performed. The necessary quantity k^2 has been obtained from shell-model calculations

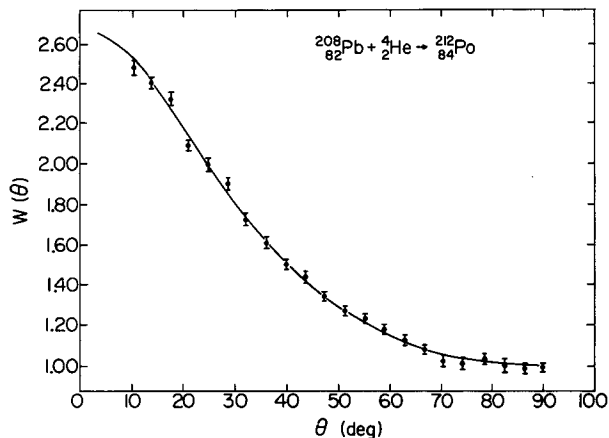


Fig. 7. Experimental angular distribution of fission fragments in the 50-MeV ^4He -induced fission of ^{208}Pb . (XBL 732-2276)

at the ^{210}Po fission barrier by R. Nix. In Fig. 5 the experimental values of K_0^2 are shown for ^{210}Po together with the theoretical predictions. Three values of the gap parameter Δ have been used. In Fig. 6 the same

data and theoretical predictions are reported for ^{211}Po . Notice that the theoretical predictions are larger than in the ^{210}Po case due to the presence of an extra quasi-particle. In both cases it appears that a rather large value of Δ fits the experimental data best.

In fact a value of Δ between 1.5 and 1.75 MeV agrees well with the pairing gap $2\Delta > 3$ MeV deduced from the K_0^2 value at the energy closest to the fission barrier of ^{210}Po .

A more accurate analysis of the experimental angular distribution and a more complete theoretical calculation on the basis of the shell model and pairing Hamiltonian is under way.

References

1. L. G. Moretto, R. C. Gatti, S. G. Thompson, J. R. Huizenga, and J. O. Rasmussen, *Phys. Rev.* **178**, 1845 (1969).
2. L. G. Moretto, S. G. Thompson, J. Routti, and R. C. Gatti, *Phys. Letters* **38B**, 471 (1972).

THE EVAPORATION OF COMPLEX FRAGMENTS: KINETIC ENERGY AND ANGULAR DISTRIBUTIONS

L. G. Moretto

In a previous paper¹ it was shown that the statistical emission of complex particles from highly excited compound nuclei can be handled effectively by means of the transition state method. The transition state can be located in the potential energy surface as a function of a fission-like coordinate, a mass asymmetry coordinate, and other deformation coordinates. At constant mass asymmetry, the potential energy as a function of the fission-like coordinate has a maximum (Fig. 1a). If the potential energy is minimized with respect to all the other degrees of freedom, such a point is a saddle-point in the $(n-1)$ dimensional deformation space which excludes the mass asymmetry coordinate. For this reason "ridge point" seems a suitable name for this configuration. If the mass asymmetry is large, the resulting configuration is strongly necked in. We can take advantage of this fact in two ways. On one hand it provides an easy physical definition of the mass asymmetry coordinate. On the other hand the narrowness of the neck makes the inertia associated with the mass asymmetry degree of freedom very large. This effectively

freezes the motion of the system along such a coordinate, of which we need to consider the potential energy only. Therefore one may be justified in considering the ridge points as saddle points where the transition states can be located. A further advantage of the ridge point is that of being, in general, very close to the scission point where the two fragments separate. Therefore, if the distributions of the various dynamical quantities can be determined at the ridge point, they can be easily transformed into the distributions at infinity. For the sake of discussion let us describe the ridge point shape as prolate spheroid with a small sphere touching it at one of its poles. Two important effects can be observed. First, the equilibrium deformation of the spheroid is always prolate; therefore, the Coulomb interaction energy and thus the kinetic energy of the system at infinity is always smaller than the nominal Coulomb barrier corresponding to two touching spheres. The second effect consists of an amplification of energy fluctuations at the ridge point. Let us consider Fig. 1b. The total potential energy, plotted

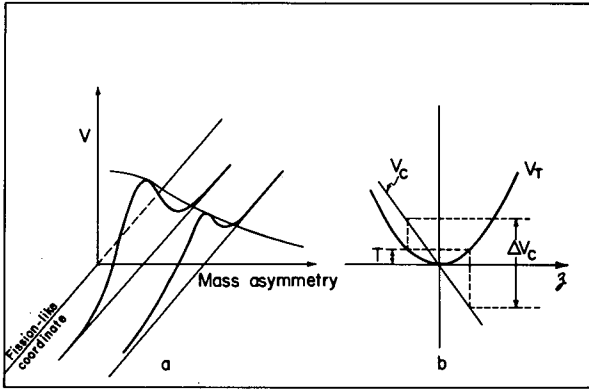


Fig. 1. (a) Schematic illustration of the ridge points in the nuclear potential energy surface versus a fission-like coordinate and a mass asymmetry coordinate. (b) Description of the amplifying effect associated with the deformation coordinate, z . The total potential energy and the Coulomb interaction energies are plotted versus z . An input fluctuation of the order of T is amplified to a value, $\Delta V_c \propto \sqrt{pT}$. (XBL 721-2027)

against the deformation of the spheroid, has a minimum at the ridge point while the Coulomb interaction energy decreases monotonically with increasing deformation. The thermal fluctuation in deformation involves an energy of the order of the nuclear temperature at the ridge point while the resulting fluctuation in Coulomb interaction energy and thus in the final kinetic energy is of the order of \sqrt{pT} , where $p = C^2/K$, C is the first derivative of the Coulomb interaction energy with respect to deformation, K is the second derivative of the total potential energy with respect to deformation, both evaluated at the ridge point. The parameter p can be called amplification parameter.

The normal modes at the ridge point can be amplifying like the one just discussed and non-amplifying, like, for instance, the oscillations of the small sphere about the tip of the spheroid. In the latter case, the restoring force is completely Coulombian and the full energy of this degree of freedom can be expected to appear in the form of kinetic energy. Let us consider now the case of a single amplifying mode accompanied by zero, one, and two non-amplifying modes. It is possible to derive the corresponding kinetic energy distributions in analytical form:

$$P(x)dx \propto \operatorname{erfc}\left(\frac{p-2x}{2\sqrt{pT}}\right) \exp(-x/T)dx, \quad (1)$$

$$P(x)dx \propto \left[(2x-p)\exp(-x/T)\operatorname{erfc}\left(\frac{p-2x}{2\sqrt{pT}}\right) + 2\sqrt{pT/\pi} \exp\left(\frac{p^2+4x^2}{4pT}\right) \right]^2 dx, \quad (2)$$

$$P(x)dx \propto \left[\left(\frac{p^2}{4} + \frac{pT}{2} + x^2 - px \right) \exp(-x/T)\operatorname{erfc}\left(\frac{p-2x}{2\sqrt{pT}}\right) + \frac{1}{2\sqrt{\pi}} (pT)^{1/2} (2x-p) \exp\left(\frac{p^2+4x^2}{4pT}\right) \right] dx. \quad (3)$$

In these expressions p is the amplification parameter and $x = E_k - E_0$, where E_k is the kinetic energy at infinity and E_0 is the Coulomb interaction energy at the ridge point. In Figs. 2 and 3 the kinetic energy distributions calculated with Eq. (2) are shown for different temperatures and different amplification parameters. It can be observed that at small values of p the distributions are Maxwellian-like, while at large values of p the distributions are nearly Gaussian. At zero amplification the three formulae reduce to

$$P(E_k)dE_k \propto \begin{cases} \exp(-E_k/T) \\ -E_k \exp(-E_k/T) \\ E_k^2 \exp(-E_k/T) \end{cases} dE_k$$

The second equation, which contains the relevant degrees of freedom to describe the emission of a neutron reduces to a Maxwellian, as expected. In Fig. 4 the kinetic energy distributions calculated on the basis of Eqs. (1), (2), and (3) for a low value of p and for a large value of p are shown. For a small value of p the shape depends very much on the number of non-amplifying degrees of freedom. At large values of p the distributions are Gaussian and they differ in their widths and in the location of the maximum. This is to be expected because, at large p , the non-amplifying degrees of freedom become rather unimportant, so that one may account for them by incorporating their average contribution to the mean and the width of the distribution. This observation is of help when large amplifications are expected from more than one degree of freedom. In Fig. 5 the potential energy at the ridge point is shown for the system. The ridge point shapes are represented by two spheroids touching by their poles. The potential energy is plotted as a function of the deformation of the two spheroids. It is possible to identify two normal modes which are amplifying, as can be seen by comparing Fig. 5 with Fig. 6, where the Coulomb interaction energy is plotted

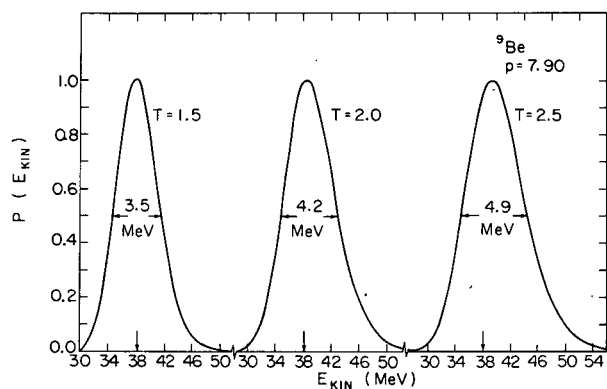


Fig 2. Kinetic energy distributions for ${}^9\text{Be}$ emitted from ${}^{236}\text{U}$ at different temperatures. (XBL 721-2028)

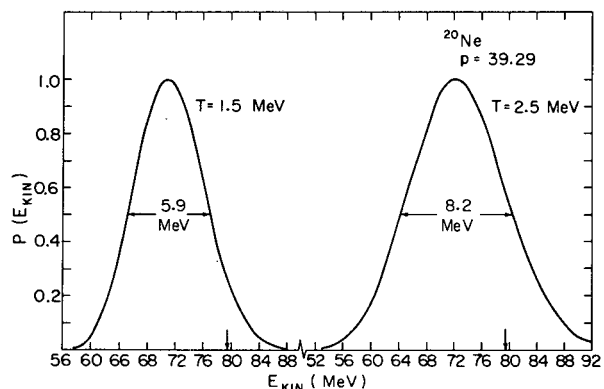


Fig. 3. Same as in Fig. 2; the emitted particle is ${}^{20}\text{Ne}$. (XBL 721-2030)

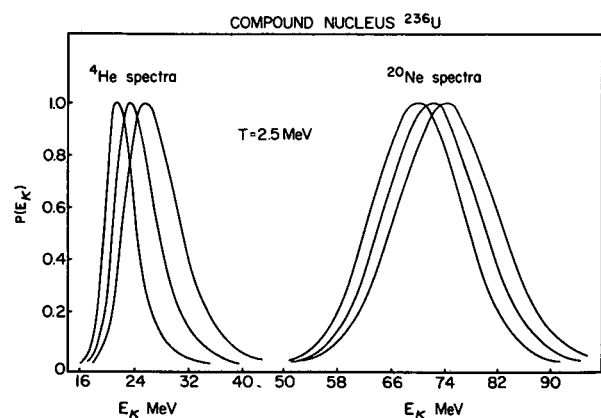


Fig. 4. Kinetic energy distributions on the basis of Eqs. (1), (2), and (3) for widely different values of the amplification parameter p . (XBL7210-5771)

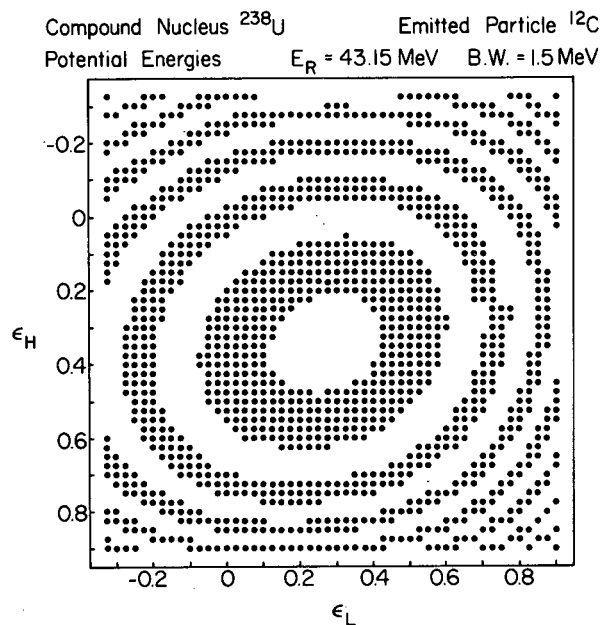


Fig. 5. Potential energy in a region close to the ridge point as a function of the deformation of both the light and the heavy fragment. (XBL7210-5772)

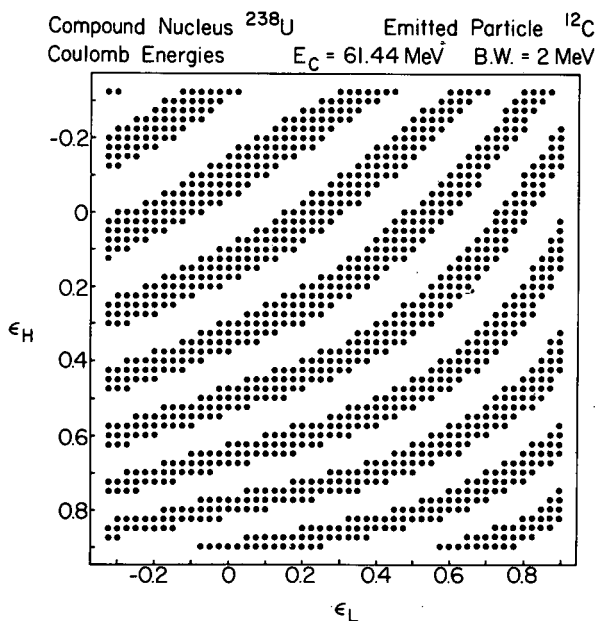


Fig. 6. Coulomb interaction energy as a function of the deformation of the light and heavy fragment. (XBL7210-5773)

also as a function of the deformations of the two spheroids. In the limit of large amplifications, like in this case, the kinetic energy distribution can be written down very simply

$$P(x)dx \propto \exp \left[\frac{x^2}{(p_1 + p_2)T + 2nT^2} \right] dx,$$

where p_1 and p_2 are the amplification parameters of the two amplifying modes, $x = E_k - E_0 - nT$, and n is the total number of collective degrees of freedom at the ridge point.

The present approach also permits us to calculate the angular distributions. If one assumes the classical distribution of angular momenta in a particle-induced reaction, the angular distribution is:

$$K_0^2 = \frac{\mathcal{J}_{\text{eff}}}{\hbar^2} T, \quad \beta = \frac{\hbar^2}{2\mathcal{J}_n T_n} - \frac{\hbar^2}{2\mathcal{J}_\perp T}$$

$$\frac{1}{\mathcal{J}_{\text{eff}}} = \frac{1}{\mathcal{J}_\parallel} - \frac{1}{\mathcal{J}_\perp}, \quad \mathcal{J}_\parallel \text{ and } \mathcal{J}_\perp \text{ are the principal}$$

moments of inertia at the ridge point, \mathcal{J}_n is the moment of inertia of the residual nucleus after neutron emission, T and T_n are the ridge

point temperature and the temperature of the nucleus after neutron emission. This expression reduces to the following limits:

$$W(\theta) \propto \exp(-Z) \left[I_0(Z) + I_1(Z) \right] + \frac{1}{2} \beta I_m^2 \exp(-Z) \left[I_0(Z) + \frac{2}{3} I_1(Z) - \frac{1}{3} I_2(Z) \right],$$

where $Z = I_m^2 \sin^2 \theta / 4K_0^2$, I_m is the classical maximum angular momentum, and I_0 , I_1 , and I_2 are the modified Bessel functions of order zero, one, and two. Also:

$$W(\theta) = \text{constant} \quad \text{for } Z \rightarrow 0,$$

$$W(\theta) = \frac{1}{\sin \theta} \quad \text{for } Z \rightarrow \infty.$$

Furthermore it can be observed that the larger the emitted particle, the more deformed is the ridge point configuration and the larger is the value of Z . Therefore, everything being equal, the emission of the large fragments is predicted to occur more anisotropically than the emission of small fragments.

Reference

1. L. G. Moretto, Phys. Letters **40B**, 185 (1972).

NEUTRON EVAPORATION FROM ^{252}Cf FISSION FRAGMENTS ON THE BASIS OF THE SHELL MODEL

E. Nardi, L. G. Moretto, and S. G. Thompson

A large amount of experimental information is available on the neutron emission of ^{252}Cf .¹ In particular the average number of neutrons $\bar{\nu}(A)$ and their average kinetic energy $\bar{\eta}(A)$ have been measured as a function of the fragment mass A . It is surprising to notice that, while the function $\bar{\nu}(A)$ has the well-known saw-tooth behavior with a sharp discontinuity at $A \approx 126$, the kinetic energy $\bar{\eta}(A)$ is peaked and nearly symmetric with respect to the same mass.

It has been shown that the fission neutrons are statistically emitted by the excited fragments.² However, in order to account for the quantitative features of the experimental data it is necessary to assume the presence of large shell effects. It is now possible to evaluate the statistical nuclear properties on the basis of the shell model and the pairing Hamiltonian.^{3,4} Therefore it is interesting to ascertain whether the experimental data

on fission neutrons can be explained on the basis of such a knowledge.

The neutron evaporation spectra have been calculated by means of a Monte Carlo method. The probability of emitting a neutron of kinetic energy ϵ from a nucleus of excitation energy E is given by:

$$P(\epsilon)d\epsilon \propto \sigma_{\text{inv}}(\epsilon)\rho(x,0)d\epsilon.$$

In this expression $x = E - B_N - \epsilon$, B_N is the neutron binding energy, $\rho(x,0)$ is the density of zero angular momentum states of the residual nucleus, and $\sigma_{\text{inv}}(\epsilon)$ is the inverse cross section.

The inverse cross section was calculated by means of an optical model potential. The level density ρ was calculated by using the Nilsson model for the various fragments at

their equilibrium deformation. The calculations were carried out both with and without the pairing interaction. In the case in which pairing was not introduced, the necessary even-odd effects were obtained by means of an empirical energy shift Δ which reproduces the even-odd mass differences.

The calculations of the average kinetic energy $\bar{\eta}(A)$ were performed for selected fission fragment masses whose charges Z were equal to the most probable values.

The average excitation energy of each fragment was evaluated in such a way that the calculated and experimental values of $\bar{\nu}(A)$ coincided. The initial distribution of excitation energies was assumed to be a Gaussian whose width was deduced from the experimental second moment of the number of neutrons.⁵

The experimental and theoretical average kinetic energies $\bar{\eta}(A)$ are plotted in figs. 1 and 2. The calculations have been performed without and with pairing respectively. Both calculations show reasonably good agreement with the data; in particular, the calculation performed without pairing seems to reproduce the minimum close to $A = 145$ quite well. The residual excitation energy that cannot be carried away by neutrons is emitted in the form

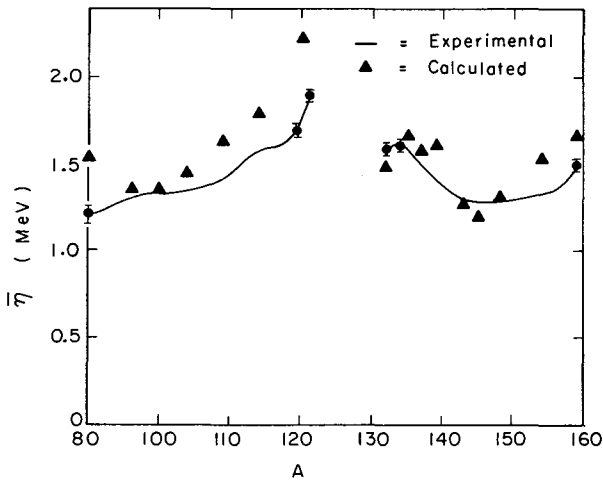


Fig. 1. Experimental and calculated values of the average center-of-mass kinetic energy of the neutrons $\bar{\eta}$. The experimental results are represented by a solid line. Typical experimental errors are shown by full dots with error bars. The theoretical values are presented by means of triangles. The calculated values are obtained by using level densities without pairing. (XBL 7210-4128)

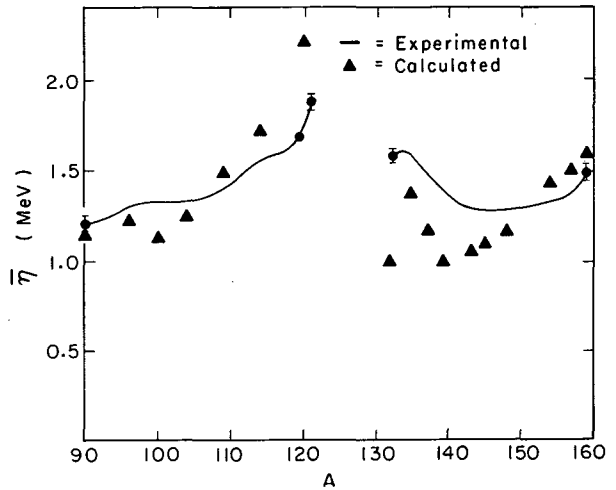


Fig. 2. Same as in Fig. 1. The theoretical values are obtained by including pairing in the level density calculations. (XBL 7210-4127)

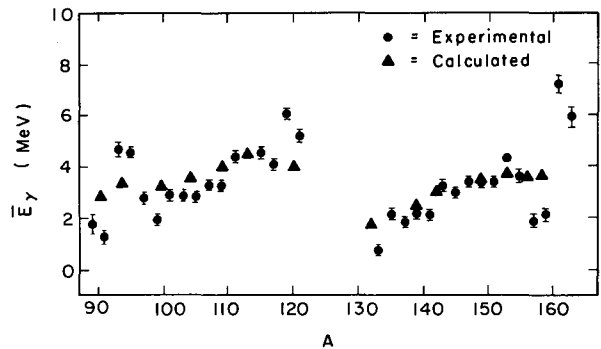


Fig. 3. Experimental and calculated values of the average energy emitted in the form of gamma rays, $\bar{E}_\gamma(A)$, as a function of A . The results are obtained by using level densities without pairing. (XBL 7210-4129)

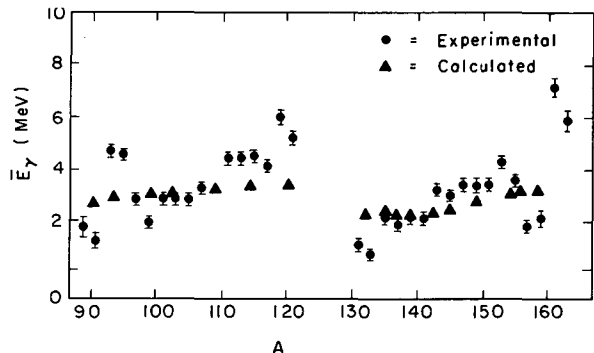


Fig. 4. Same as in Fig. 3. The results are obtained by including pairing in the level density calculations. (XBL 7210-4130)

of gamma rays and can be obtained immediately from the calculations illustrated above. The calculated average energy emitted in the form of gamma rays is shown in Figs. 3 and 4 together with the experimental data.⁶ Again the calculations were performed without and with pairing respectively. A good agreement between calculation and experiment is observed in both cases although the calculations performed with pairing seem slightly worse. The overall agreement between experimental and calculated results shows that it is possible to describe quantitatively the statistical decay of fission fragments on the basis of our knowledge of nuclear structure without the introduction of empirical parameters.

References

1. H. R. Bowman, J. C. D. Milton, S. G. Thompson, and W. J. Swiatecki, *Phys. Rev.* 126, 2133 (1963).
2. D. W. Lang, *Nucl. Phys.* 53, 113 (1964).
3. L. G. Moretto, *Energia Nucleare* 17, 36 (1970).
4. L. G. Moretto, *Nucl. Phys.* A182, 641 (1972) and A185, 145 (1972).
5. A. Gavron and Z. Fraenkel, *Phys. Rev. Letters* 27, 1148 (1971).
6. E. Nardi, A. Gavron, and Z. Fraenkel, to be published.

SIMULTANEOUS EMISSION OF TWO LIGHT CHARGED PARTICLES IN THE SPONTANEOUS FISSION OF ^{252}Cf

S. K. Kataria, E. Nardi, and S. G. Thompson

The process of nuclear fission accompanied by a third light charged particle has been the subject of many investigations.¹ The main motivation for these studies is that this process is thought to yield information on the conditions of the fissioning nucleus at the scission point. Recently Kapoor et al.² found evidence for the simultaneous emission of two light charged particles in coincidence with fission fragments in the thermal fission of ^{235}U . These authors, however, did not identify the particles and were able to measure only the gross features of the energy distribution. Further data on this process should shed light on the mechanism of light-particle emission in fission.

In the present work we describe a four-dimensional experiment in which two coincident light particles emitted in the spontaneous fission of ^{252}Cf were simultaneously identified and their energies recorded. Two semiconductor particle telescopes, each consisting of a 50- μ ΔE counter and a 1-mm E counter were placed on the opposite sides of a strong ^{252}Cf source. Each telescope was placed at a distance of 1.2 cm from the source, and the distance between the ΔE and E counters was about 2 mm. The source strength was 0.6×10^7 fissions per minute. The source was covered on both sides by absorber foils of 12 mg/cm² of Pt and 3.6 mg/cm² of Al. The thickness of the foils was selected in order to stop the fission fragments and 6.18-MeV alpha particles from reaching the particle telescopes.

A four-dimensional analyzer was triggered by the coincidence events between the two ΔE counters. Hence all the twofold, threefold, and fourfold coincidences among the four counters were recorded. The coincidences were made using the zero cross-over technique with a resolution time of 40 nsec. The energy calibrations for all the detectors were done twice a week for the entire run. The timing between $\Delta E1$ and $\Delta E2$ counters was monitored by using a ^{228}Th (8.78-MeV alphas) source. Essentially no timing or pulse-height drift was observed during the course of the experiment, which lasted for a period of 25 days.

Particle identification was carried out offline, using the power law method.³ The particles identified in the fourfold events were ^4He , ^3H , and ^1H . No event involving heavier particles was observed. A significant part of the ^1H events are probably due to (n, p) reactions⁴ in coincidence with long-range alphas. The yields of alpha particles and tritons from the reactions induced by fission neutrons in the surrounding material are very low in the energy region of interest and can be neglected. We therefore limit our discussion to the emission of ^4He and ^3H .

In Table I the type and number of detected fourfold events are given, i. e., the events in which signals were registered simultaneously in detectors $\Delta E1$, $\Delta E2$, E1 and E2. The ratio of number of tritons to the number of total

Table I. Number of various quaternary coincidence events observed.

Telescope 1	Telescope 2	No. of events
${}^4\text{He}$	${}^4\text{He}$	371
${}^3\text{H}$	${}^3\text{H}$	51
${}^4\text{He}$	${}^3\text{H}$	56
${}^3\text{H}$	${}^3\text{H}$	0

*

$$\frac{({}^3\text{H}-{}^4\text{He})}{({}^4\text{He}-{}^4\text{He})+({}^4\text{He}-{}^3\text{H})} = 11.9 \pm 2\% ;$$

$$\frac{({}^4\text{He}-{}^3\text{H})}{({}^4\text{He}-{}^4\text{He})+({}^3\text{H}-{}^4\text{He})} = 13 \pm 2\%$$

*Relative yields of tritons to alpha particles in the two telescopes in quaternary fission.

alphas detected in each counter is also given for these events in Table I. The observed, uncorrected ratios of triton yield to alpha-particle yield for the normal ternary fission for the two telescopes are $11 \pm 0.5\%$ and $10 \pm 0.5\%$ respectively. The results in Table I indicate that the relative yield of tritons to alpha particles in the quaternary fission events is essentially the same as that in normal ternary fission.

The kinetic energy spectrum of the alpha particles in quaternary fission observed in one of the telescopes is plotted in Fig. 1 together with the kinetic energy spectrum observed in the same telescope in the case of ternary fission. The quaternary alpha-energy spectrum is seen to be shifted towards lower energies by about 2.0 MeV. The energy spectrum of alphas in coincidence with tritons is similar to the one shown in Fig. 1. The combined energy spectrum of tritons observed in both the telescopes is also seen to be shifted by about 1.5 MeV in the direction of lower energy as compared to the ternary fission triton spectrum (Fig. 2). The mean energies of alpha particles as a function of the energy of the other alpha particle is given in Fig. 3. It

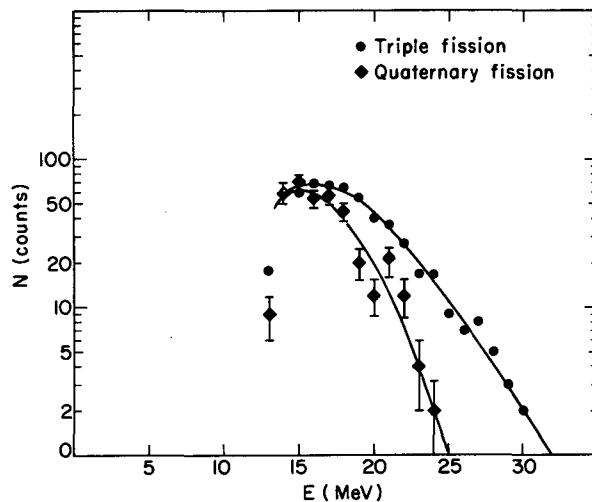


Fig. 1. Kinetic energy spectrum of alpha particles observed in telescope 1 in coincidence with alpha particles detected in telescope 2. The kinetic energy spectrum of alpha particles in ternary fission is also shown. (XBL 7210-4216)

can be concluded that there is no correlation between the energies of the two alpha particles in the quaternary fission.

The probability of quaternary fission events, under the assumption that there is no angular correlation between the two light particles, is about one per million binary fission events. If one assumes that the two light particles are emitted at the scission point independently of each other, and that the probability of emission of each particle is the same as in ternary fission, the probability for such events is ten per million binary events, in qualitative agreement. The above hypothesis is also consistent with the observed ratio of tritons to alpha particles in quaternary fission, and with the fact that there is no correlation between the energies of the two alpha particles.

The study of the angular correlation will permit one to obtain the total probability of the quaternary events and will provide further data to test the hypothesis of independent emission of these light particles. Preliminary results show that there is no angular correlation between the two particles. Trajectory calculations are being performed in order to obtain the initial conditions at scission which satisfy both the kinetic energy spectra and the angular correlation.

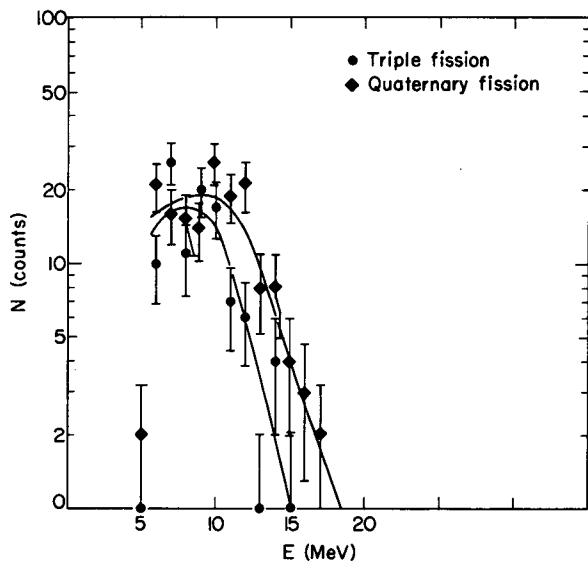


Fig. 2. Kinetic energy spectrum of tritons in coincidence with alpha particles. The triton energy spectrum for the normal ternary fission is also shown. (XBL 7210-4217)

References

1. I. Halpern, *Ann. Rev. Nucl. Sci.* **21**, 245 (1971).
2. S. S. Kapoor, R. K. Chaudhary, S. K. Kataria, S. R. S. Murthy, V. S. Ramamurthy, presented at the Nuclear Physics and Solid State Physics Symposium, Chandigarh, India, December 28-31, 1972 (proceedings to be published).

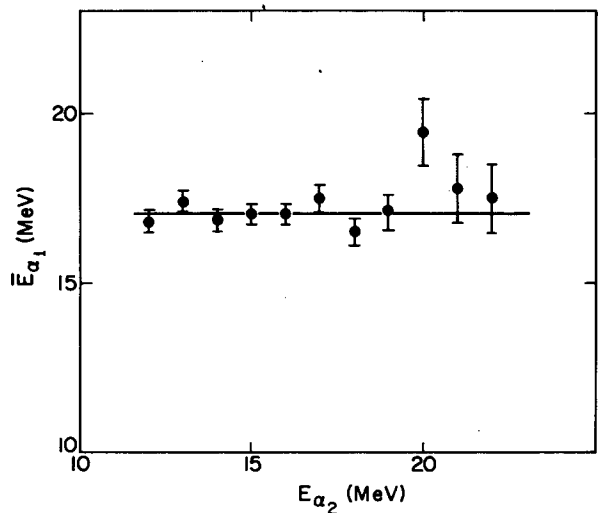


Fig. 3. Mean kinetic energy of alpha particles detected in telescope 1 plotted as a function of the kinetic energy of the coincident alpha particle detected in telescope 2. (XBL 7210-4219)

3. F. S. Goulding, D. A. Landis, J. Cerny, and R. H. Pehl, *IEEE Trans. Nucl. Sci.* **NS-13**, 514 (1966).
4. S. W. Casper, J. Cerny, and R. C. Gatti, *Phys. Rev.* **154**, 1193 (1967).

SEARCH FOR EVEN-ODD EFFECTS ON THE KINETIC ENERGIES OF FISSION FRAGMENTS

H. Nifenecker

When an even-even nucleus undergoes fission, the two fragments both have an even or an odd number of protons and neutrons. On the average, about 2.5 MeV more energy is released when even fragments are produced than when fragments with odd charges are obtained. It is of interest for understanding both the fission reaction itself and the de-excitation mechanism of the fragments to investigate what fraction of this energy difference appears in neutron or gamma emission or in kinetic energy of the fragments. It has recently been shown that the total gamma energy emitted when both fragments have even charges is about 0.7 MeV higher than when they have

odd charges.^{1,2} On the other hand, no evidence for even-odd effects on the total number of neutrons emitted by the fragments was found. Consequently it is anticipated that an even-odd effect should appear in the fragment kinetic energies or in the neutron kinetic energies to account for the 1.8 MeV which do not appear in neutron number and gamma energy measurements.

As an auxiliary measurement of the fission gamma ray experiment carried on in this laboratory and described several times,³ a three-dimensional recording of the two fission fragments' kinetic energies and coin-

cident K x-ray energies as obtained from a Si(Li) detector was carried out.

We are using these data to look for possible even-odd effects on the total kinetic energy of the fission fragments. In the following we discuss briefly the method of analysis used to obtain relevant information such as the variations of the average value of the total kinetic energy of fragments as a function of the charge of one of them, $\bar{E}_k(Z)$. In principle, the experiment can provide a two-dimensional array $N(E_k, i)$ giving the number of events observed with the total kinetic energy $E_k (\pm 2 \text{ MeV})$ with an x-ray detector output falling in channel i . Assuming that a K shell vacancy in an element of charge Z gives rise to a typical response of the x-ray detector, $R(Z, i)$, the channel yields can be transformed into charge yields, minimizing the sum of squares:

$$X^2 = \sum_i W_i \left[N(E_k, i) - \sum_Z R(Z, i) Y(E_k, Z) \right]^2,$$

where W_i is the weight given to each experimental point. The least-squares analysis expresses the charge yields $Y(Z, E_k)$ as linear functions of the channel yields:

$$Y(E_k, Z) = \sum_i A(Z, i) N(E_k, i).$$

From the array $Y(E_k, Z)$ it is possible to obtain the interesting quantities $E_k(Z)$ and, more generally, all moments of the E_k distribution for a fixed charge.

This method, however, suffers some important drawbacks: it requires a high statistical accuracy; asks for a least-squares analysis of many spectra, one for each sample value of E_k ; and finally gives much more information than needed. It is known that if one chooses the weights W_i to be independent of E_k , the matrix $A(Z, i)$ will itself be independent of E_k , so that any linear function of the channel yields will be transformed in the same manner as the yields themselves. For instance if $Y_T(Z) = \sum_{E_k} Y(E_k, Z)$ and

$$N_T(i) = \sum_{E_k} N(E_k, i), \text{ the relation}$$

$$Y_T(Z) = \sum_i A(Z, i) N_T(i) \text{ is evidently true.}$$

Similarly one can write that

$$\sum_{E_k} E_k Y(E_k, Z) = \sum_i A(Z, i) \sum_{E_k} E_k N(E_k, i). \quad (1)$$

Since for instance,

$$\bar{E}_k(Z) = \sum_{E_k} E_k Y(E_k, Z) / \sum_{E_k} Y(E_k, Z), \text{ Eq. (1) is}$$

$$\text{equivalent to } \bar{E}_k(Z) Y_T(Z) = \sum_i A(Z, i) E_k(i) N_T(i).$$

The analysis then can proceed as follows:

- 1) obtain the channel yields $N_T(i)$ and average kinetic energies per channel, $E_k(i)$;
- 2) obtain the yields $Y_T(Z)$ from a least-squares analysis;
- 3) replace the second members of the least-squares equations $N_T(i)$ by the quantities $E_k(i) N_T(i)$ and obtain the quantities $E_k(Z) Y_T(Z)$. By a simple division the quantities $E_k(Z)$ are obtained.

This method is being applied to histograms of $E_k(i)$ and $N_T(i)$ similar to those shown in Figs. 1 and 2.

Since the experiment allowed the measurement of both the masses and the kinetic energies of the fragments, it provided a two-dimensional array $P(m, E_k)$ for each channel in the x-ray dimension. Any moments of this two-dimensional distribution can then, using

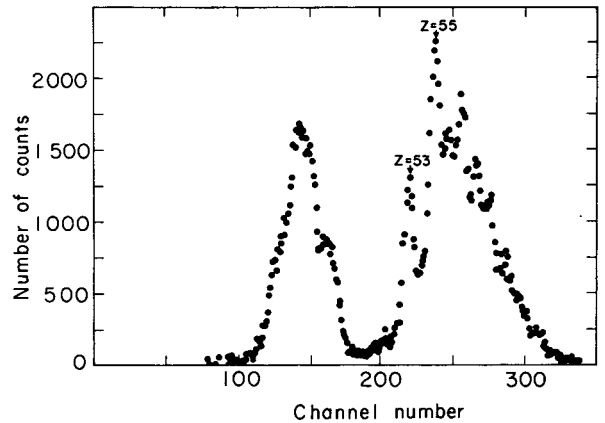


Fig. 1. Fission x-ray spectrum, corrected for background. (XBL 732-2268)

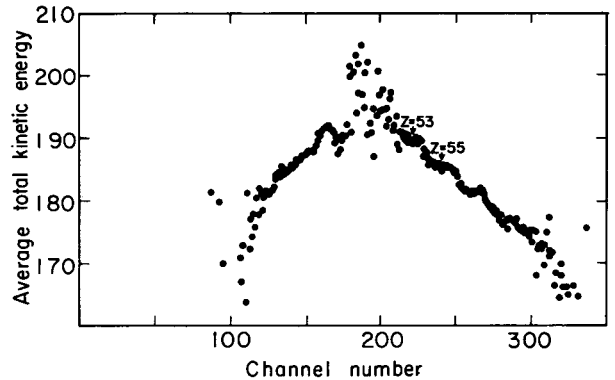


Fig. 2. Average total kinetic energy of the fission fragments as a function of x-ray pulse height. (XBL 732-2269)

the same method as above, be expressed as a function of the charge of the fragments. It is possible, in particular, to study the variation of the average kinetic energy $E_k(m, Z)$ as a function of m for a given charge. In this case the variations in the average total kinetic energy would only be related to the geometrical configuration of the fragments at scission.

References

1. H. Nifenecker, J. Girard, J. Matuszek, and M. Ribrag, Even-Odd Effects in the Prompt Deexcitation Process of the Fission Fragments of ^{252}Cf , Europhysics Conference, Aix en Provence, France, July 1972.

2. H. Nifenecker, J. Poitou, R. Babinet, J. Girard, J. Matuszek, and M. Ribrag, Gamma and Neutron Emission by Fragments of Known Charges in the Binary and Long Range Particle Accompanied Fission of ^{252}Cf , submitted to Nuclear Physics.

3. E. Cheifetz, R. C. Jared, S. G. Thompson, and J. B. Wilhelmy, Phys. Rev. Letters 25, 38 (1970).

STUDY OF THE FRAGMENTS EMITTED IN HEAVY-ION-INDUCED REACTIONS

L. G. Moretto, S. K. Kataria, D. Heunemann, R. C. Jared, and S. G. Thompson

The emission of large fragments in heavy-ion-induced reactions is a very puzzling phenomenon which, at one extreme, shows a compound-nucleus-like behavior, at the other resembles some well known direct reactions with lighter projectiles. In order to learn about the various features of such a process, a project has been started with the aim of studying the particles emitted in the reaction of ^{14}N with various targets. The ^{14}N beams of 160 MeV and 250 MeV are being provided by the 88-inch cyclotron. In order to detect and identify the various particles a semiconductor counter telescope is used. The telescope is mounted on a movable arm in the reaction chamber which allows the collection of data from $\sim 10^\circ$ to $\sim 170^\circ$. The telescope is composed of four counters with the following thicknesses: 16μ , 32μ , 400μ , 600μ . The electronics associated with the system is shown in Fig. 1.

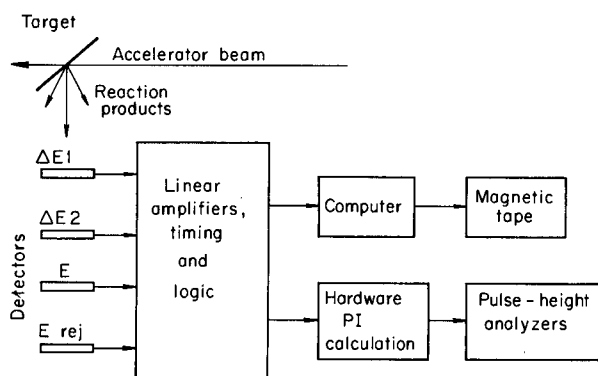


Fig. 1. Schematic diagram of the experimental equipment. (XBL 731-2062)

The experiment is monitored on-line by displaying a particle identification spectrum obtained from the second and third counter, and by observing the kinetic energy distribution of two isotopes selected by means of two single-channel analyzers whose windows are set on two peaks of the particle identification spectrum. The data are also recorded on magnetic tape, event by event, by means of a PDP5 computer. In the runs at backward angles, the ^4He particles are so overwhelming in number that it is necessary to gate them out by means of a single-channel analyzer set on the ^4He particle peak in the particle identification spectrum. The data recorded on the magnetic tape are analyzed both on a PDP9 computer and on a CDC 7600 computer. Two identifications are performed, whenever possible, by means of the $\Delta E2$ and $(\Delta E2+E)$ signals and by means of the $\Delta E1$ and E_{total} signals. Consistency is required between the two identifications: otherwise the event is rejected. The kinetic energy spectra associated with each isotope (or element) is then displayed.

The data presented here refer to an indium target bombarded with 160-MeV ^{14}N . When the telescope is set at the critical angle, corresponding to a trajectory in which the projectile grazes the target nucleus, a tremendous variety of reactions takes place. In fact, all of the elements with $Z \leq Z_{\text{projectile}} + 1$ are observed. This can be seen in Fig. 2 where the identification spectrum is presented. The separation of the various isotopes has only been achieved partially in this run. However, it is possible to notice that all the elements from oxygen on down have been produced. The nitrogen peak is very large because of the closeness to the critical angle.

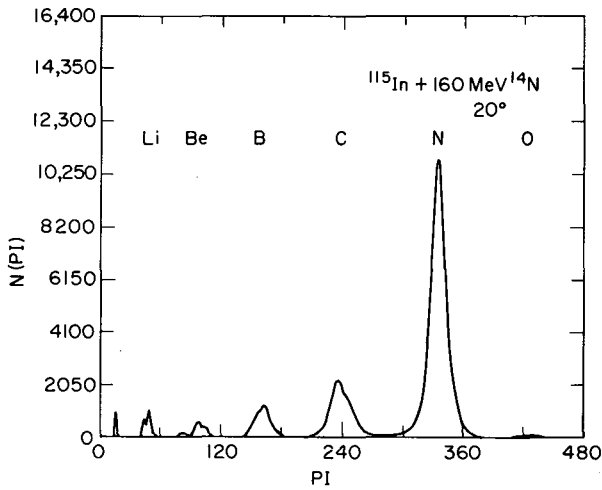


Fig. 2. Particle identification spectrum at 20° for the reaction $\text{In} + ^{14}\text{N}$ at 160 MeV. (XBL 731-2061)

As the telescope is moved backwards (Figs. 3-5) the strong nitrogen peak decreases in intensity; furthermore, the intensities of all the heavier fragment peaks are decreasing with respect to those of the lighter fragment peaks. These experimental features can possibly be accounted for as follows. Let us consider the potential energy of two spherical liquid-drop nuclei in contact as a function of the mass asymmetry of the system. For small values of the fissionability parameter x , the potential energy has a maximum at symmetry and decreases as the asymmetry increases. For large values of the fissionability parameter x , the potential energy

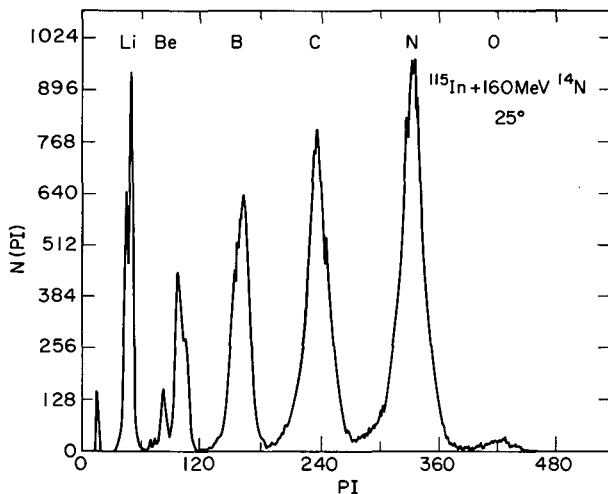


Fig. 3. Particle identification spectrum at 25° for the reaction $\text{In} + ^{14}\text{N}$ at 160 MeV. (XBL 731-2060)

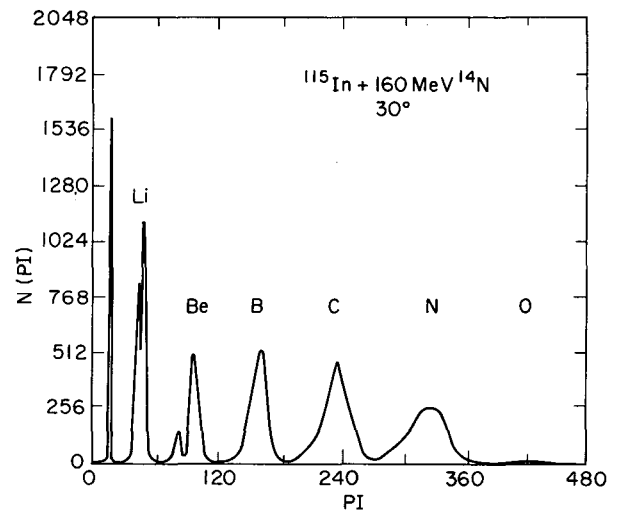


Fig. 4. Particle identification spectrum at 30° for the reaction $\text{In} + ^{14}\text{N}$ at 160 MeV. (XBL 731-2059)

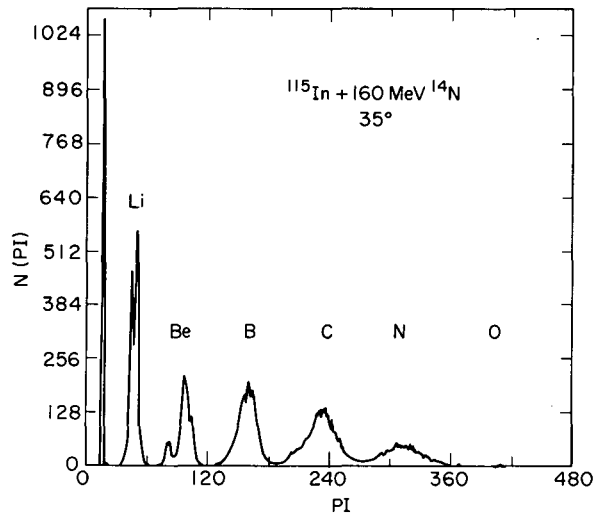


Fig. 5. Particle identification spectrum at 35° for the reaction $\text{In} + ^{14}\text{N}$ at 160 MeV. (XBL 731-2058)

presents a minimum at symmetry, a maximum at some intermediate asymmetry, and a decreasing trend for larger asymmetries. Therefore, for small values of x , the tendency is always that of making the light nucleus lighter and the heavy nucleus heavier. At larger values of x , if the two touching nuclei are widely different in mass, such a difference will tend to increase; on the other hand, if the two nuclei are nearly equal in mass, they will tend to equalize their mass. The present experiment shows that the indium target tends to grow at the expense of the ^{14}N projectile as expected.

The decrease in abundance of the heavy fragments with respect to the light fragments at more backward angles could be due to a decrease of the impact parameter of the projectile and thus in the centrifugal barrier. The fusion of the two nuclei tends to go more towards completion.

The presence of small kinetic energies at more backward angles indicates that indeed a strong relaxation is taking place.

As the telescope is moved in the backward hemisphere, the dominant isotope produced is ^4He with some trace of ^6He . ^6Li and ^7Li are produced in measureable amount as well as ^7Be and ^9Be (Fig. 6). Only a few events of Be isotopes can be detected. The kinetic energy spectra indicate an almost complete thermalization. The kinetic energy spectra at various angles have also been measured for the various elements and are displayed in Figs. 7-11.

The heavier fragments seem to show two components in their kinetic energy spectra: a hard component with energies close to that of the incoming projectile and a soft component at energies closer to the Coulomb barrier. As the telescope is moved to larger angles the hard component disappears while the soft component persists.

The lighter fragments show mainly the soft component, which is persistent at all angles.

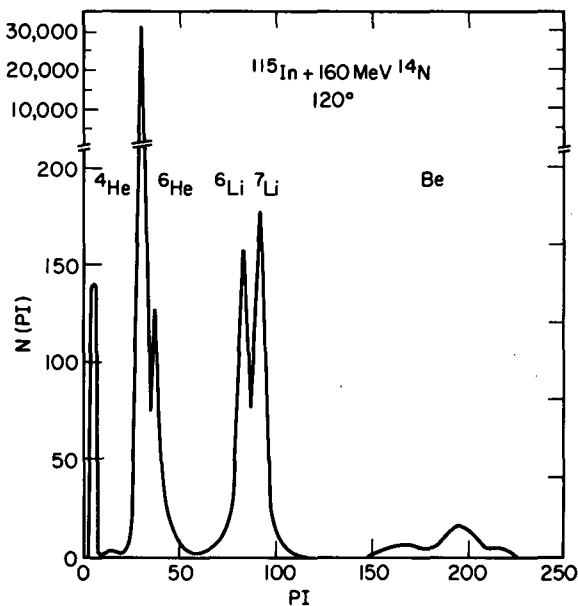


Fig. 6. Particle identification spectrum at 120° for the reaction $\text{In} + ^{14}\text{N}$ at 160 MeV. (XBL 731-2057)

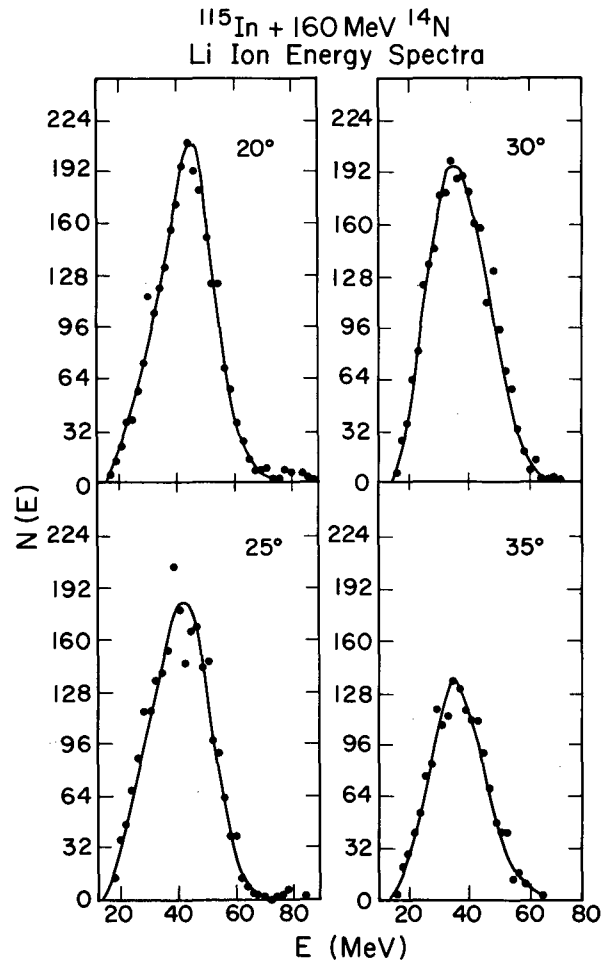


Fig. 7. Li kinetic energy distributions. (XBL 731-2069)

The hard component may be due to quasi-elastic processes, while the soft component suggests that a very strong thermalization or relaxation is taking place. In the backward hemisphere the spectra of the lighter fragments, especially those of ^4He and Li, seem almost completely statistical. Therefore it is possible that some fraction of the observed particles is evaporated by the compound nucleus. This view is also supported by the fact that the angular distributions are less forward peaked for lighter fragments, and by the fact that Li and Be fragments with similar kinetic energies have also been observed in the backward direction when bombarding the same target with 160-MeV ^3He .

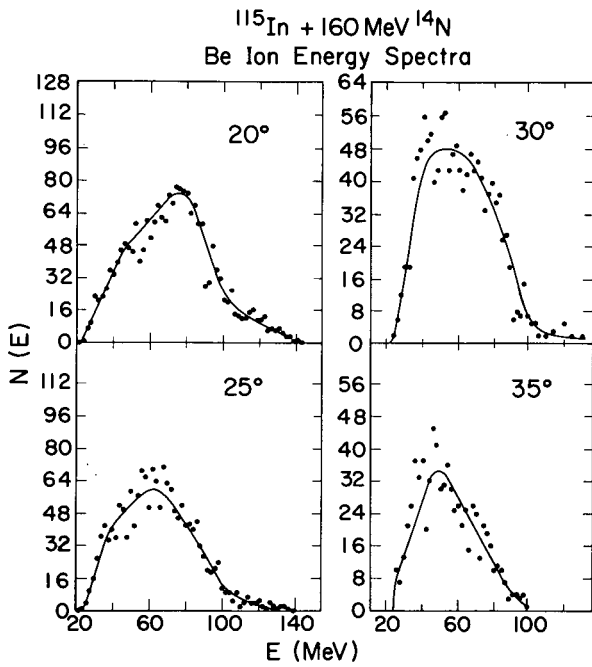


Fig. 8. Be kinetic energy distributions.
(XBL 731-2070)

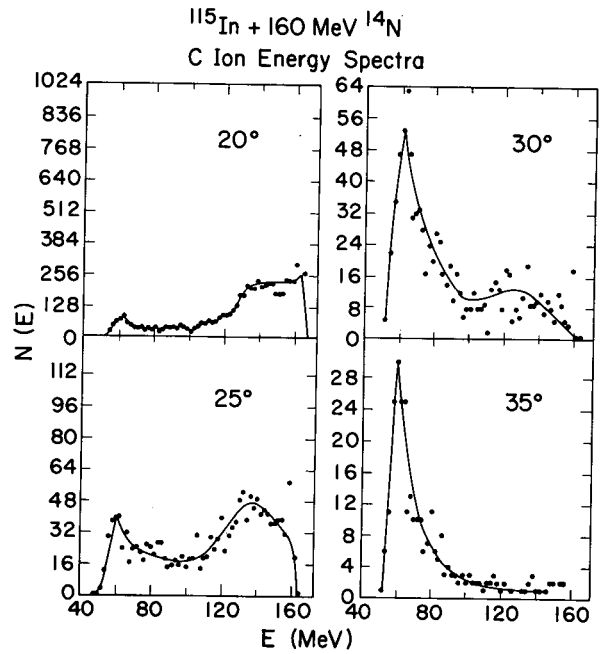


Fig. 10. C kinetic energy distributions.
Notice the instrumental cutoff at low energies.
(XBL 731-2072)

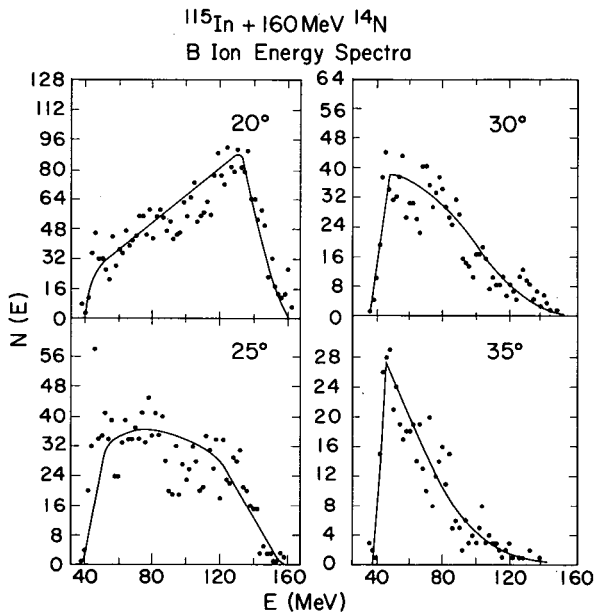


Fig. 9. B kinetic energy distributions.
Notice the instrumental cutoff at low energies.
(XBL 731-2071)

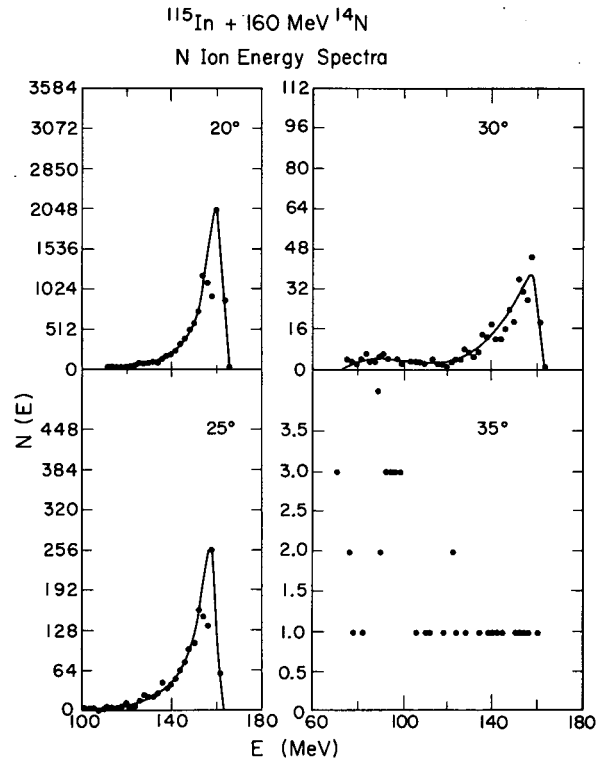


Fig. 11. N kinetic energy distributions.
Notice the instrumental cutoff at low energies.
(XBL 731-2073)

FRAGMENT PRODUCTION IN ^{40}Ar -INDUCED REACTIONS ON A Cu TARGET

S. G. Thompson, L. G. Moretto, R. C. Jared, D. Heunemann, and R. C. Gatti

The interaction between a heavy ion and a moderately heavy target nucleus is expected to present macroscopic features which are not observed in reactions with lighter particles. We are interested in studying the relevance of collective coordinates, as it may appear in the transfer of mass and charge between the two nuclei. Furthermore we would like to determine the presence, or absence, of dissipative forces which transfer the collective kinetic energy to the internal degrees of freedom.

In order to explore the general features of these reactions, a preliminary investigation has been undertaken about the nature and the kinetic energy of the fragments produced in the interaction of 288-MeV ^{40}Ar ions with Cu nuclei.

The experiments have been performed with the 288-MeV full energy ^{40}Ar beam provided by the new SuperHILAC. The ^{40}Ar beam, after suitable collimation, is directed on a natural Cu target $\sim 1 \text{ mg/cm}^2$ oriented at 45° with respect to the beam direction. The beam is then collected in a Faraday cup and monitored. The fragments produced in the targets are detected by means of a four-counter telescope mounted on a movable arm which can explore all the angles between $\sim 15^\circ$ and 175° . The entrance of the telescope is protected by a strong magnetic field produced by two pills of a rare earth magnetic alloy. The four silicon counters have the following thicknesses: 16μ , 26μ , 400μ , 400μ . The signals from the four counters, after suitable amplification and discrimination, are digitalized and stored, event by event, on a magnetic tape. At the same time, for monitoring purposes, an identification signal is generated by means of a Landis-Goulding particle identifier, on the basis of the second and third counter signals. The particle identification spectrum is then generated by means of a pulse-height analyzer and displayed.

The data collected on the magnetic tape are analyzed in a CDC 7600 computer. A suitable version of a particle identification formula, based upon an approximation to the energy range relations, is employed to generate particle identification spectra. The choice of the parameters contained in the formula is made by checking the independence of the particle identification on kinetic energy. The particles which do not go beyond the second

counter are identified by means of a single-particle identification process. The particles which stop in the third counter undergo two identifications, the first by means of the signals from the second and the third counters, and a second one by means of the signal from the first counter and a combination of the signals from the second and the third counters. A match is required between the two identifications in order to accept the event as valid. The particles which reach the fourth counter are rejected. After having obtained a satisfactory particle identification spectrum, windows are set on the peaks corresponding to the various elements or isotopes and the kinetic energy distributions are obtained. The particles emitted in the reaction have been detected at four angles: 20° , 30° , 40° , 50° . The first angle is very close to the expected critical angle. The four particle identification spectra corresponding to the four angles are shown in Figs. 1-4. A most striking feature of these spectra is the appearance of fifteen peaks corresponding to all the elements from boron to argon. Also He and Li have been detected but are not shown here. No elements of Z larger than 18 seem to be formed, in agreement with the liquid-drop prediction that, for such a system, the potential energy favors the increase of the larger nucleus at the expense of the smaller. Another interesting feature is the variation of the relative abundances of the detected elements with angle. Close to the critical angle, the elements with higher Z are the most abundant. As the angle increases, the abundance of the elements of higher Z decreases while the abundance of the lighter elements remains higher. This seems to indicate that smaller impact parameters lead to the absorption of a larger fraction of the projectile by the target. Somehow, the reaction mechanism seems to favor the production of even- Z products, as can be seen in the even-odd alternation in Fig. 1. The kinetic energy distributions appear as broad peaks whose most probable values increase rather smoothly with Z . In Fig. 5 the kinetic energy distributions of three typical elements are shown at the four angles. In Fig. 6 the most probable values of the kinetic energy are plotted as a function of Z and angle. The analysis of the angular distributions and kinetic energy distributions will allow one to determine the degree of inelasticity of these reactions and to obtain information on the relaxation mechanisms involved.

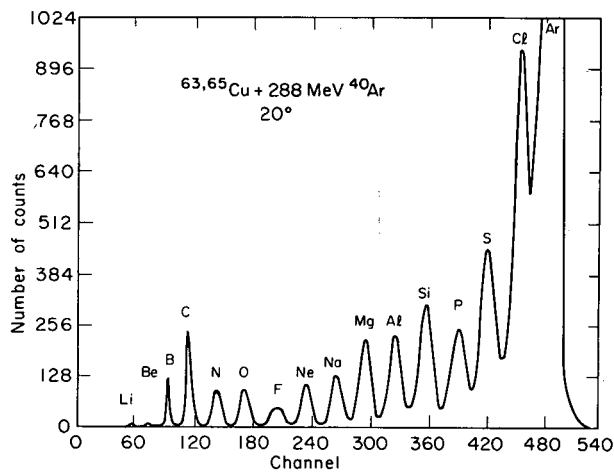


Fig. 1. Particle identification spectrum for Cu reacting with 288-MeV ^{40}Ar . The laboratory angle is 20° . (XBL 731-2105)

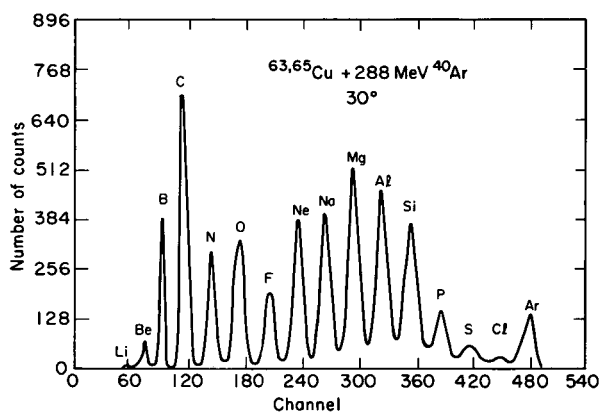


Fig. 2. Particle identification spectrum for Cu reacting with 288-MeV ^{40}Ar . The laboratory angle is 30° . (XBL 731-2106)

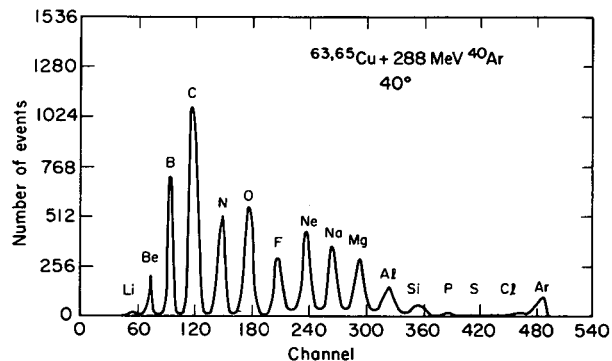


Fig. 3. Particle identification spectrum for Cu reacting with 288-MeV ^{40}Ar . The laboratory angle is 40° . (XBL 731-2107)

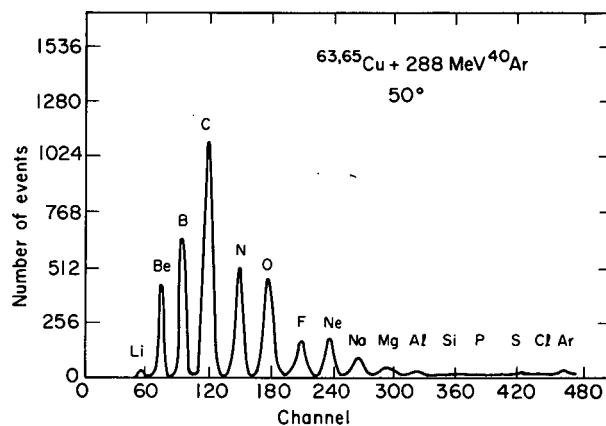


Fig. 4. Particle identification spectrum for Cu reacting with 288-MeV ^{40}Ar . The laboratory angle is 50° . (XBL 731-2108)

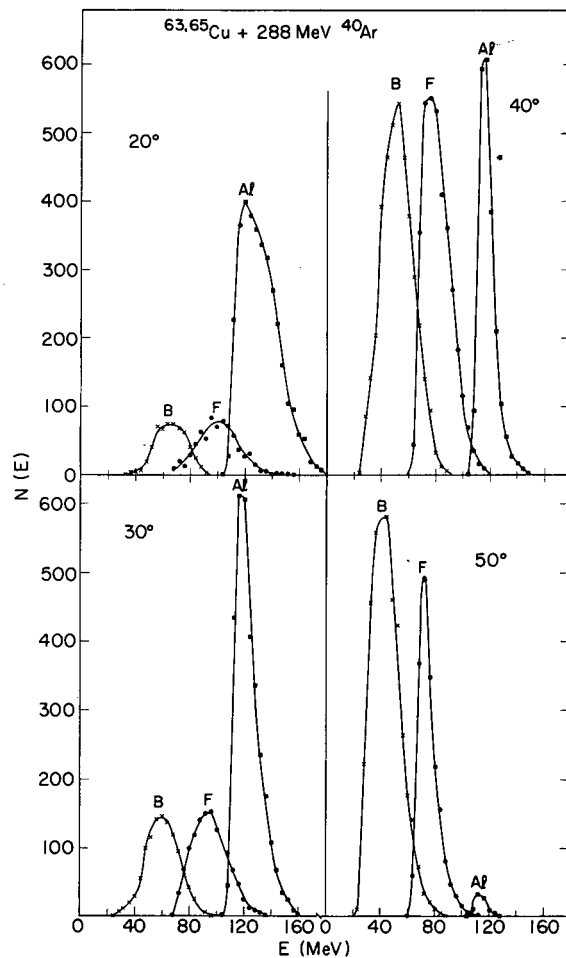


Fig. 5. Kinetic energies of B, F, and Al at the various angles. The low-energy side of the Al KE distribution is partially affected by the energy cutoff. (XBL 731-2102)

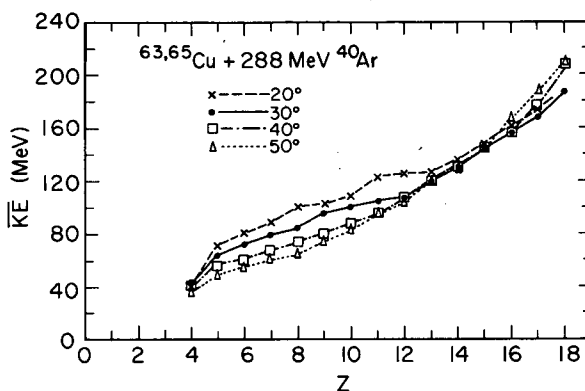


Fig. 6. Most probable kinetic energies as a function of atomic number. (XBL 731-2104)

X-RAY-GAMMA-RAY ANALYSIS OF HEAVY-ION REACTION PRODUCTS

R. C. Jared, H. Nifenecker, L. G. Moretto, and S. G. Thompson

The identification and yield of the high-mass products in heavy-ion reactions is usually made by on-line mass spectrometry or by radiochemical methods. However, a comparatively simple broad survey of reaction products can be performed using K x-rays as a method of identification. The method has been shown to be quite useful in the identification of fission fragments in the recent past.¹

We have undertaken a preliminary investigation of heavy-ion reaction products, using off-line x-ray analysis. The interpretation based on x-ray spectra alone may be ambiguous because of uncertainties about the mass chains that produce the x-rays. This ambiguity can be minimized if one measures gamma-rays in coincidence with x-rays to determine the isotopes that are decaying in the mass chains.

The experimental setup consisted of two solid state detectors sandwiching the irradiated sample. The x-ray detector had a volume of 1 cm³ and the γ detector volume was 6 cm³. We have obtained preliminary results using both the x-ray singles spectra and the x-ray- γ -ray coincidence spectra.

In Fig. 1 the x-ray spectra observed after the irradiation of thick W, Au, and Th targets with a 288-MeV Ar beam are shown. The spectra obtained with the W and Au targets present approximately the same features with a broad distribution of nuclear charges centered slightly above the original target atomic number, Z. In these two cases the pick-up of nucleons by the target seems to be the dominant reaction. However, in the case of

thorium the distribution is centered around Hg, much like the results from the Au irradiation. This shift in the charge distribution of the products with respect to the target charge could be the result of a high fission probability of the elements heavier than Th associated with the predominant alpha decay of the elements between Bi and Th. Still, the relative high yields observed for elements around Hg seem to require some type of many nucleon transfer process.

In Fig. 2 we show the x-ray spectra obtained after irradiation of two copper targets, a thin one of 1.5 mg/cm² thickness and a thick one. The very strong peaks corresponding to nickel and nearby elements appear in both spectra. Their presence can be explained in terms of quasi-elastic processes where a small number of nucleons are exchanged between the two nuclei, leaving the products moderately excited. In such a case the heavy product gains a very small kinetic energy and does not escape from the thin target. On the other hand, the silver compound nucleus is produced with a kinetic energy of about 110 MeV in the forward direction and can only stick to the thin target if it undergoes large-angle collisions. The same might be said of the reaction products which are only slightly lighter than the compound nucleus. The thin-target irradiation shows comparable intensities for the elements ranging from a few charges above copper to the compound nucleus, pointing to the existence of processes in which many nucleons are picked up by the target. These products should also have high kinetic energy at the expense of the projectile. This result is com-

patible with those of the $(\Delta E, E)$ counter experiments² described elsewhere in this report. The strong enhancement of the Rh and Ru K x-rays (which are most probably produced in the decay of the silver compound nucleus) in the thick-target spectrum is due to the complete stopping of the recoils and also probably related to an increase in the probability of forming a compound nucleus when the incident beam energy decreases.

A preliminary experiment was performed by using the gamma-x-ray coincidence system. A thick W target, irradiated by the 288-MeV Ar beam was used. The sample was counted from 7 to 10 hours after the irradiation.

In this preliminary experiment the following isotopes were identified: ^{182}Re , ^{183}Os , ^{184}Ir , and ^{186}Ir . Cumulative mass yields for these isotopes should therefore be possible to obtain.

The isotope ^{123}I has also been identified as a product of the irradiation and is most probably a fragment produced in the fission of a very neutron-deficient heavy nucleus.

In summary it can be said that the analysis of the products obtained in heavy-ion irradiation, using x-ray and/or gamma-ray detectors, will be a useful method at least for cases where the products decay mainly by electron capture.

References

1. R. L. Watson, J. B. Wilhelmy, R. C. Jared, C. Ruge, H. R. Bowman, S. G. Thompson, and J. O. Rasmussen, Nucl. Phys. A141, 449 (1970).
2. S. G. Thompson, L. G. Moretto, R. C. Jared, D. Heunemann, and R. C. Gatti, "Fragment Production in ^{40}Ar Induced Reactions on a Cu Target," elsewhere in this report.

SEARCH FOR SUPERHEAVY ELEMENTS IN NATURE

R. C. Jared, E. Cheifetz, E. R. Giusti, S. G. Thompson,
J. S. Drury,* R. J. Silva,* R. W. Stoughton,* and J. Halperin*

Previous work by our group in searching for superheavy elements in nature was reported in reference 1. Some subsequent results obtained in a collaborative effort with a group at Oak Ridge National Laboratory are reported here. The method of detection, as in the previous work (Ref. 1), made use of a

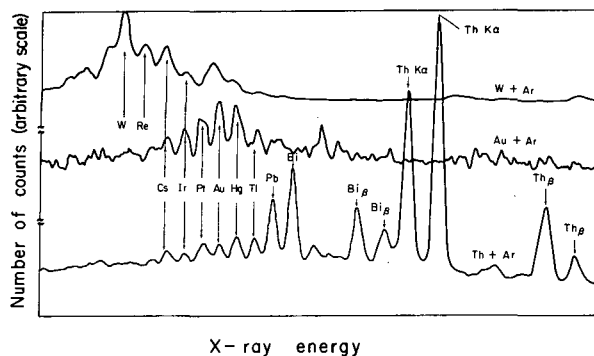


Fig. 1. The x-ray spectrum obtained after irradiation of different targets with 288-MeV Ar. The arrows show the $K\alpha_1$ peak position for several elements except where stated otherwise. (XBL 732-2278)

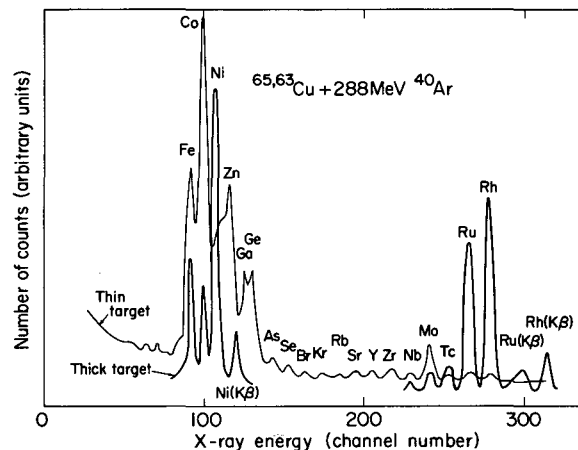


Fig. 2. The x-ray spectra obtained after irradiation by a 288-MeV Ar beam of a thin and a thick Cu target respectively. The labels show the positions of the $K\alpha_1$ lines of several isotopes. The heavy line drawn through the experimental points corresponds to the thick target spectrum. (XBL 731-2103)

large liquid scintillator to detect spontaneous fission events in which unusually large numbers of neutrons are emitted. The apparatus was located in a tunnel under about 250 m of earth shielding in order to reduce the interfering effects of cosmic rays.

The additional samples tested using our counter system are listed below. The negative results on these samples are consistent with a lower limit of spontaneous fission half-life of about 10^{23} years (3 kg) to 10^{24} years (20 kg) for the principal component(s). (Alternatively, if the half-life of the superheavy element is 10^9 years, an upper limit of about 10^{-14} g of superheavy element per gram of sample is indicated.) A more complete description of some of the samples counted is available in the Oak Ridge Annual Report.² A report is in preparation by R. W. Stoughton which is expected to give complete information on all the samples discussed here and in addition on many that have been counted using the ORNL ^3He high neutron multiplicity counting system.

The ores and ore products obtained from the Sudbury region are:

<u>Wt. (kg)</u>	<u>Description</u>
3	Composite sample, precious metals
4	Ni concentrate
3	Blast furnace dust
3	Flue dust, Intern. Nickel
4	CuS, mill concentrate, Intern. Nickel
3	Blast furnace dust
3	Smelter flue dust

The ores and ore products from Colorado are:

<u>Wt. (kg)</u>	<u>Description</u>
4	Ag, Cu, Pb conc. from Creede
10	PbS concentrate, Silverton
4	Pb, Ag, Zn sulfide, Creede
4	Cu, Ag, Pb, Au, Zn concentrate, Telluride
4	Pb, Ag, Au, Zn sulfide concentrate, Telluride
10	Pb, Zn sulfide ore, Creede
3	Zn, Pb, Cu, Ag, Au sulfide ore, Silverton
4	Cu, Pb, Zn sulfide ore, Silverton
4	Pb, Ag, Fe, Zn sulfide ore, Creede
4	Pb, Ag, Zn sulfide ore, Creede

<u>Wt. (kg)</u>	<u>Description (cont.)</u>
4	PbS ore cont. Ag, Au, Zn, Telluride
4	PbS ore, Telluride

Other miscellaneous ores are:

<u>Wt. (kg)</u>	<u>Description</u>
3	Pt, Pd bearing rock, Transvaal
3	Composite chromite, S. Rhodesia
3	Composite strontium ore, Hamm, Westphalia
3	Quartz concentrate containing Au, S. Dakota
20	Galena, Ivigtut, Greenland
4	Cinnabar, Arizona
10	Galena, Cour D'Alone Region, Idaho
3	Chromite + Zn concentrate, S. Rhodesia
12	Cerussite (PbCO_3), New Mexico
3	Unburned bag house fume dust, Tooele, Utah
7	Barite, Sweetwater, Tennessee
3	Serpentinite from mid-Atlantic ridge at equator
20	Bastnasite (CeFCO_3), Mt. Pass, California
3	KCl ore, Hobbs, New Mexico
20	Fe meteorites, Canyon Diablo
10	Kimberlite, North Lake Region, Tennessee

References

*Present address: Oak Ridge National Laboratory, Oak Ridge, Tenn.

1. E. Cheifetz, R. C. Jared, E. R. Giusti, and S. G. Thompson, Phys. Rev. C 6, 1348 (1972).

2. R. C. Jared, E. Cheifetz, E. R. Giusti, S. G. Thompson, J. S. Drury, R. J. Silva, R. W. Stoughton, and J. Halperin, ORNL Annual Report 4791, period ending May 20, 1972.

SUPERHEAVY ELEMENTS

S. G. Thompson and C. F. Tsang

Since 1965 there has been considerable interest among nuclear physicists and chemists in the possibility of discovering superheavy elements. In this review article, we summarize the recent research in this field and indicate some efforts that are planned for the near future.

Superheavy elements are those elements that lie somewhat beyond the end of the present periodic table (Fig. 1). Interest at present is focused on a region of isotopes—centered at proton number $Z = 114$ and neutron number $N = 184$ —expected to have special stability, due to the closing of both a proton shell and a neutron shell expected to occur at this location. These expectations depend essentially on our ability to calculate nuclear masses accurately.

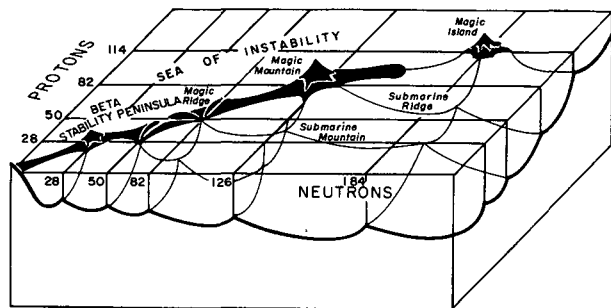


Fig. 1. Nuclear stability is illustrated in a scheme that shows a peninsula of known elements and an island of predicted stability (nuclei around $Z = 114$ and $N = 184$) in a "sea of instability." Grid lines show magic numbers of protons and neutrons giving rise to exceptional stability. Magic regions on the mainland peninsula are represented by mountains or ridges. (CBB 725-2592)

Recent significant advances in the calculation of masses occurred with the merger of the shell model and the liquid-drop model. The shell effects or local fluctuations [of the order of a few MeV] are extracted from the results of shell-model calculations and combined with the liquid-drop binding energies (about 2000 MeV for a heavy nucleus). Through the studies of Swiatecki, Myers, Strutinsky, Nilsson, Nix, Tsang, Pauli, and others,¹ the method (known as the Strutinsky method) has been employed to calculate the stability of superheavy elements.

These calculations indicate that the region centered around $Z = 114$ and $N = 184$ should be very stable. These nuclei form an island somewhat beyond the tip of the peninsula of known elements in a plane of proton and neutron numbers as shown in Fig. 1. Contours of total half-lives involving all major modes of decay, namely, spontaneous fission, alpha decay, and beta decay, have been calculated. It turns out that the island centers around $Z = 110$ (instead of $Z = 114$) and $N = 184$. The shift from $Z = 114$ to $Z = 110$ is mainly due to the competition between spontaneous fission (where $Z = 114$ is the most stable) and alpha decay (where nuclei with lower Z are more stable). This longest-lived nucleus, ${}_{110}^{294}184$ (or it could be an adjacent odd A or odd Z nucleus), has a half-life as long as 10^9 years. Such a half-life is nearly as long as the age of the solar system. If one considers only nuclei with half-lives of 1 minute or longer, one is confined to an island with Z between 106 and 116 and N between 174 and 192. These are the nuclei experimentalists are attempting to produce. The calculations involve great uncertainties. Thus the prediction of a half-life of 10^9 years may be uncertain by a factor of 10^6 either way; that is, the half-life may well be anything between 10^3 and 10^{15} years.

Detailed predictions concerning the chemical properties of superheavy elements are not easy to make. Nevertheless, some progress in this direction has been made by the use of the Mendeleev method, and the relativistic Hartree-Fock-Slater calculations. Such calculations have been carried out by several groups² at Los Alamos Scientific Laboratory, Oak Ridge National Laboratory, Northwestern University, the University of Frankfurt, and elsewhere. The predicted properties of some of the superheavy elements are shown in Table I.

It should be pointed out that the study of these chemical properties may be important to the identification of the atomic numbers of these superheavy elements if they are discovered.

The theoretical prediction that the half-life of the nucleus ${}_{110}^{294}184$ (eka-platinum) should be in the neighborhood of 10^8 years suggested that small amounts of superheavy elements might be present in nature. The presence of these elements on the earth could have resulted from their formation along with the other elements at the time the earth was formed. If some of the nuclei have half-lives

Table I. Some physical and chemical properties of elements 110 through 115, according to Fricke and Waber.²

Element	Electronic ground-state configuration	Chemical group	Most favorable oxidation state	First ionization potential (eV)	Metallic radius (Å)	Ionic radius (Å)	Density (g/cm ³)	Melting point (°C)	Boiling point (°C)	K α_1 x-ray energy ^a (keV)
110	6d ⁸ 7s ²	VIII	+6	9.4	1.4		27.4			157
111	6d ⁹ 7s ²	IB	+1, +3	10.3	1.5		24.4			161
112	6d ¹⁰ 7s ²	IIB	+1, +2	11.2	1.6		16.8			165
113	7p ¹ 7s ²	IIIA	+1	7.4	1.7	1.5	16	430	1130	169
114	7p ² 7s ²	IVA	+2	8.5	1.8	1.3	14	67	147	173
115	7p ³ 7s ²	VA	+1, +3	5.9	1.9		13.5			177

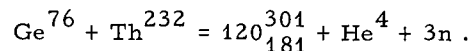
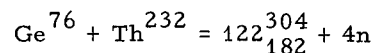
^aFrom Ref. 3.

near 2×10^8 years, small fractions could have survived the period ($\sim 4.5 \times 10^9$ years) since the earth was formed.

Comprehensive searches for these elements in nature have been made by many groups both in the USSR and in the USA, including Flerov and his collaborators; Price, Fowler, and their co-workers; Herrmann and his co-worker; as well as Thompson's group at LBL. The details of the search are described⁴ elsewhere in this Annual Report. However, none of these searcher has given conclusive evidence of their presence. Although the results up to now do not definitely rule out the presence of these elements in nature, the weight of evidence is such as to suggest strongly that they do not exist on the earth. Thus if the half-lives are much less than 2×10^8 years, they would have disappeared by radioactive decay during the 4.5×10^9 years since the earth was formed. On the other hand, if the half-lives are long enough, the conclusion would be that they probably were not formed during nucleogenesis in which the other elements were formed.

Probably the most promising approach to the production of superheavy nuclei involves the use of heavy ions. In this process the heavy ions are accelerated to a high energy and used to bombard a target nucleus such as Th²³² or U²³⁸. Hopefully, the projectile and target will fuse together, forming compound nuclei within the island of stability.

One of the most favorable target-projectile combinations, advocated by Swiatecki,⁵ after consideration of various effects that enter into heavy-ion reactions, is



Both final nuclei indicated would (hopefully) decay by successive alpha emission or electron capture toward the center of the island. Even with these reactions, certain difficulties are likely to be encountered, which are summarized as follows.

High excitation energies. Calculations by Moretto⁶ show that the very shell effects responsible for the stability of the superheavy nuclei will be destroyed as the excitation energy is increased. The survival at such high excitation energies becomes a question of the competition between fission and neutron or charged-particle emission. The optimum combination, Ge⁷⁶ + Th²³², that Swiatecki proposed is estimated to have a survival probability of approximately 1 : 10,000.

Angular momentum effects. When a heavy ion collides with a target nucleus, rotational angular momentum is necessarily introduced. The centrifugal forces which arise make the system less stable. Some estimates of the result of this effect have been made which indicate that the expected yields of superheavy products should be further reduced by factors ranging from 10 to 10³.

Fusion probability. The largest uncertainty of all has to do with the probabilities for the projectiles and targets to fuse together.⁵ It is not sufficient for the projectile and the target nuclei to merely come in contact with each

Table II. Previous attempts to make superheavy elements by heavy-ion reactions (σ , cross section; τ , half-life).

Investigators	Reference	Reaction	Results
Sikkeland	(10)	$^{18}\text{Ar}^{40} + ^{92}\text{U}^{238} \rightarrow \text{fission fragments}$	Fission fragment from $^{110}\text{Zr}^{278} (?)$
Thompson; Nurmia et al.	(11)	$^{18}\text{Ar}^{40} + ^{96}\text{Cm}^{248} \rightarrow ^{114}\text{Zr}^{288-x} + xn$	$\sigma < 5 \times 10^{-32} \text{ cm}^2$ for $\tau > 10^{-9}$ second
Oganesyan et al.	(8)	$^{54}\text{Xe}^{136} + ^{92}\text{U}^{238} \rightarrow \text{fission fragments}$	Fission fragments from $^{146}\text{Ba}^{374} (?)$
Flerov et al.	(9)	$^{30}\text{Zn}^{66} + ^{93}\text{U}^{238} \rightarrow ^{122}\text{Zn}^{304-x} + xn$	$\sigma < 5 \times 10^{-30} \text{ cm}^2$ for $\tau > 10^{-8}$ second
Bimbot et al.	(7)	$^{36}\text{Kr}^{84} + ^{90}\text{Th}^{222} \rightarrow ^{126}\text{Kr}^{316-x} + xn$	High-energy α from $^{126}\text{Kr}^{316-x} (?)$

other: an extra push is necessary to force them to fuse together. The probability that they can be made to fuse together into a final spherical compound nucleus involves not only the nuclear inertia, which acts against the push, but also the viscosity of the flow of nuclear matter, which is a dissipative effect converting the pushing energy into useless excitation energy. Good estimates of nuclear inertias and viscosities have not been made so far; these are important gaps in our knowledge of nuclear properties.

Small beams of energetic krypton ions have been available at Orsay, and zinc and xenon projectiles have been available at Dubna. To date, attempts by both the French⁷ and the Soviet^{8,9} groups (summarized in Table II together with previous efforts) to produce observable amounts of superheavy nuclei have not been successful. However, a new SuperHILAC in Berkeley and the improved accelerating facilities at Dubna will make possible a major assault on the production of superheavy elements. It is a completely open question whether it will indeed be possible to synthesize these elements by heavy-ion reactions. On the other hand there is still a possibility that superheavy elements might be found in cosmic radiation. The results of recent searches in cosmic rays have not been conclusive.

References

1. S. G. Nilsson, C. F. Tsang, A. Sobiczewski, Z. Szymański, S. Wycech, C. Gustafson, I. L. Lamm, P. Möller, and B. Nilsson, Nucl. Phys. A131, 1 (1969); M. Brack, J. Damgaard, A. Stenholm-Jensen, H. C. Pauli, V. M. Strutinsky, and C. Y. Wong, Rev. Mod. Phys. 44, 320 (1972); J. Grumann, U. Mosel, B. Fink, and W. Greiner, Z. Physik 228, 371 (1969); M. Bolsterli, E. O. Fiset, J. R. Nix, and J. L. Norton, Phys. Rev. Letters 27, 681 (1971); Phys. Rev. C 5, 1050 (1972);
2. W. D. Myers and W. J. Swiatecki, Nucl. Phys. 81, 1 (1966); V. M. Strutinsky, Yad. Fiz. 3, 614 (1966); Sov. J. Nucl. Phys. 3, 449 (1966); Nucl. Phys. A95, 420 (1967); A122, 1 (1968).
3. B. Fricke and J. T. Waber, Actinides Rev. 1, 433 (1971), and references therein.
4. S. G. Thompson, talk given at APS meeting, Miami, Nov. 25-27, 1968.
5. S. G. Thompson, R. C. Gatti, L. G. Moretto, H. R. Bowman, and M. C. Michel, Nuclear Chemistry Division Annual Report for 1968, UCRL-18667, p. 277; S. G. Nilsson, S. G. Thompson, C. F. Tsang, Phys. Letters B28, 458 (1969).
6. E. Cheifetz, R. C. Jared, E. R. Giusti, and S. G. Thompson, Search for Superheavy Elements in Nature, Phys. Rev. C 6, 1348 (1972). See also: R. C. Jared, E. Cheifetz, E. R. Giusti, et al., Search for Superheavy Elements in Nature, elsewhere in this Annual Report.
7. W. J. Swiatecki, talk given at Ebeltoft Conference, Ebeltoft, Denmark, May 1971 (LBL-549 (December 1971)).
8. L. G. Moretto, Nucl. Phys. A182, 641 (1972); ibid. 180, 337 (1972).
9. R. Bimbot, C. Deprun, D. Gardès, H. Gauvin, Y. LeBeyec, M. Lefort, and J. Pèter, Nature 234, 215 (1971).
10. Yu. Ts. Oganesyan, O. A. Orlova, Yu. E. Penionshkevich, K. A. Gavrilov, and K. De En, Joint Inst. Nucl. Res. (Dubna, USSR), Report P7-6300 (1972).
11. G. N. Flerov, S. A. Karamian, Yu. E. Penionshkevich, S. P. Tretiakova, and I. A. Shelaev, Joint Inst. Nucl. Res. (Dubna, USSR), Report P7-6262 (1972).

10. T. Sikkeland, Phys. Letters 27B, 277 (1968).

11. H. R. Bowman, R. C. Gatti, R. C. Jared, L. G. Moretto, W. J. Swiatecki, and S. G. Thompson, Nuclear Chemistry Division Annual Report for 1967, UCRL-17989; M. Nurmia, T. Sikkeland, R. Silva, and A. Giorso, Phys. Letters 26B, 78 (1967).

OBSERVATION OF HIGH-LYING LEVELS IN ^8Be FROM
ALPHA-ALPHA ELASTIC SCATTERING*

A. D. Bacher,[†] F. G. Resmini,[‡] H. E. Conzett,
R. de Swiniarski,[§] H. Meiner,^{||} and J. Ernst[¶]

Below an excitation energy of 16 MeV, the level structure of ^8Be is well understood^{1,2} in terms of states predominantly of a two-alpha-particle configuration. Above 16 MeV the level structure rapidly becomes more complex as other configurations for these states (e.g., $p + ^7\text{Li}$, $n + ^7\text{Be}$, and $d + ^6\text{Li}$) become important. Those states of ^8Be which have both even spin and parity can decay into the 2α channel, and this selectivity is extremely useful in identifying levels of ^8Be that lie above the $^7\text{Li} + p$ threshold. Although multi-level R- and S-matrix analyses of $^7\text{Li}(p,\alpha)^4\text{He}$ (Ref. 3) and $^6\text{Li}(d,\alpha)^4\text{He}$ (Ref. 4) data have provided some level assignments between excitation energies of 19 and 26 MeV in ^8Be , these assignments are not unique. However, any state with a significant alpha-particle width will appear as a resonance in α - α elastic scattering, which permits immediate assignment of spin and parity from a determination of the resonant partial wave. Earlier studies of the elastic scattering provided some information on ^8Be states above 16 MeV;⁵ however, it was clear that more detailed measurements were required in order to remove ambiguities in the phase-shift analysis.

The present measurements were performed with alpha-particle beams from the Berkeley 88-inch cyclotron using a beam analysis system⁶ which provided a high-resolution beam ($\Delta E/E \approx 0.02\%$) of accurately known⁷ energy ($\pm 0.03\%$). Measurements were taken at about 100 energies between 30 and 70 MeV (spanning a region of excitation in ^8Be between 15 and 35 MeV). An array of seven detectors was used to obtain cross sections at 21 center-of-mass angles between 16° and 96° . The relative errors are typically less than $\pm 2\%$, while the absolute normalization of the cross section is accurate to better than 4%.

A standard χ^2 minimization search routine was employed to determine phase shifts including $l = 8$ at the higher energies. A small $l = 6$ phase shift ($\approx 2^\circ$) was required at the lowest energies. Continuity of the phase shifts as a function of energy was required for an acceptable solution. This criterion was particularly useful in regions where the level structure was most complex, e.g., near $E_\alpha = 40$ MeV, where three resonances overlap. Phase shifts corresponding to the only acceptable solution are presented in Fig. 1 as functions of the alpha-particle laboratory energy, E_α .

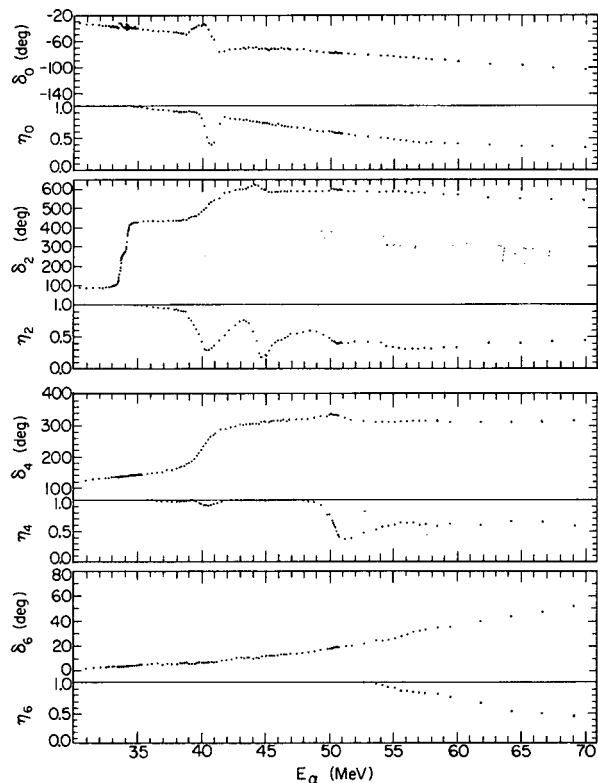


Fig. 1. Nuclear phase shifts, δ_l , and inelastic parameters, η_l , derived from α - α elastic scattering, for the $l = 0, 2, 4,$ and 6 partial waves. The S-matrix element is $S_l = \eta_l \exp(2i\delta_l)$. The excitation energy in ^8Be is $E_\alpha/2 - 0.091$ MeV.

(XBL 728-3956)

The $l = 0$ phase shift decreases monotonically between 30 and 38 MeV in a manner similar to Darriulat's previous work,⁵ but the present values are 5-10° more positive. The resonant behavior centered around $E_\alpha = 40.7$ MeV corresponds to a new 0^+ level in ^8Be near 20.3 MeV with a level width of less than 1 MeV. Since the resonant part of δ_0 passes through 0° at the resonance energy, the elasticity, $|\eta_0|$, is less than 1/2 (Ref. 9). The existence of a 0^+ level in this region of excitation has been predicted by intermediate-coupling shell-model calculations.^{10,11} Although the most recent multi-level analysis³ of the $^7\text{Li}(p,\alpha)^4\text{He}$ reaction requires 0^+ levels at 19.7 and 21.8 MeV,

the alpha-particle reduced widths obtained are so small that the calculated α - α , $\ell = 0$ phase shift does not show any trace of resonant behavior. This is in contradiction with our present result.

Five 2^+ levels are apparent in the $\ell = 2$ phase shifts shown in Fig. 1. The elastic resonances ($\Gamma_\alpha = \Gamma$) near 16.6 and 16.9 MeV excitation correspond to the isospin-mixed² doublet previously identified by Shield et al.⁵ The position of the next 2^+ level at 20.2 MeV excitation is also consistent with previous work.³⁻⁵ The two remaining 2^+ levels near 22.2 and 25.2 MeV excitation have been located previously by the multi-level analyses. Additional evidence for the 2^+ spin assignments has come from studies of the ${}^6\text{Li}(d, \alpha){}^4\text{He}$ reaction with polarized deuterons.¹² The phase shift behavior for the 25.2-MeV level shows it to have a small partial width for α -particles.

Two levels are prominent in an examination of the $\ell = 4$ phase shifts. The rapid rise of δ_4 at $E_\alpha = 40$ MeV corresponds to a 4^+ level near 19.8 MeV excitation in ${}^8\text{Be}$. Since the resonant part of δ_4 goes through $\pi/2$ and $\eta_4 \approx 0.92$ at the position of the resonance, $\Gamma_\alpha/\Gamma \approx 0.96$. The total width Γ , and hence Γ_α , is less than 1 MeV, which is at least a factor of 20 smaller than that corresponding to an α -particle reduced width equal to the Wigner limit. Hence, unless some other parentages (e.g., ${}^6\text{Li} + d$) are unexpectedly large,¹⁰ the f-wave nucleon reduced widths for this state are not as small as suggested,³ but the nucleon partial widths are small because of the small f-wave penetration factors. The broad 4^+ resonance near $E_\alpha = 51.3$ MeV corresponds to a new level in ${}^8\text{Be}$ near 25.6 MeV excitation. We find no evidence for an additional 4^+ state at 27.5 MeV with a width of approximately 1 MeV as was previously assigned by Clark et al.¹³ on the basis of the behavior of the coefficients of Legendre polynomial fits to ${}^6\text{Li}(d, \alpha){}^4\text{He}$ cross-section angular distributions.

The behavior of the $\ell = 6$ phase shift is also shown in Fig. 1. The gradual increase in δ_6 from about 2° at 30 MeV to about 30° at 70 MeV is in reasonable agreement with previous work.⁸

In order to compare our results with those of previous studies, Fig. 2 contrasts our level scheme derived from the α - α phase shifts with schemes based on analyses of the ${}^7\text{Li}(p, \alpha){}^4\text{He}$ reaction³ and the ${}^6\text{Li}(d, \alpha){}^4\text{He}$ reaction.⁴ For the level scheme based on the ${}^6\text{Li}(d, \alpha){}^4\text{He}$ reaction, three combinations (each consisting of three levels) which produce acceptable results have been joined by a vertical dashed line.¹⁴ In addition we include some predictions based on intermediate-coupling shell-model calculations. The new 0^+ state near 20.3 MeV may be

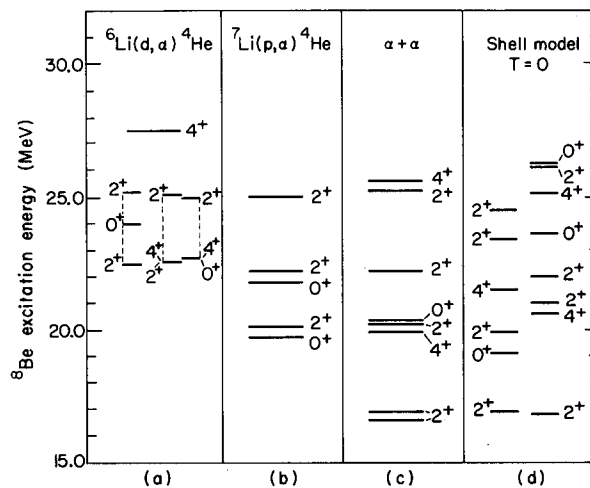


Fig. 2. Comparison of level positions for the even-spin positive parity states in ${}^8\text{Be}$ between 15 and 30 MeV excitation. (a) ${}^6\text{Li}(d, \alpha){}^4\text{He}$, Refs. 4 and 13. The $(2, 0, 2)$ sequence is from Tsan et al., and the 4^+ level at 27.5 is from Clark et al. (b) ${}^7\text{Li}(p, \alpha){}^4\text{He}$, Ref. 3. (c) Present work, α - α elastic scattering. (d) $T = 0$ levels from shell-model calculations by Barker¹⁰ (left) and Kumar¹¹ (right).

(XBL 728-3955)

identified with the lowest 0^+ state predicted to lie at 19.8 MeV¹⁰ or at 23.6 MeV.¹¹ Other levels can be matched to the three observed 2^+ levels and to the 4^+ levels observed at 19.8 and 25.6 MeV, but more detailed comparisons must await a more formal extraction of level parameters.

The comparison with the results of multi-level fits to the ${}^7\text{Li}(p, \alpha){}^4\text{He}$ and ${}^6\text{Li}(d, \alpha){}^4\text{He}$ reactions is less satisfactory. It seems clear that, due to the nonzero spin in the entrance channel and the resulting large number of parameters which can be varied, the multi-level analyses of these reaction data are at present unable to produce reliable level assignments. It is of particular interest now to investigate whether the present assignments based on elastic scattering measurements will be able to explain adequately the reaction data.

Footnotes and References

* Condensed from Phys. Rev. Letters **29**, 1331 (1972), LBL-1228.

† Present address: Physics Department, Indiana University, Bloomington, Indiana 47401.

‡ Present address: University of Milan, Italy.

§ Present address: Institut des Sciences Nucleaires, Grenoble, France.

¶ Present address: Schweizerische Bundesbahnen, Bern, Switzerland.

¶ Present address: Institut für Strahlen und Kernphysik der Universität, Bonn, Germany.

1. T. Lauritsen and F. Ajzenberg-Selove, Nucl. Phys. 78, 1 (1966).

2. F. C. Barker, H. J. Hay, and P. B. Treacy, Aust. J. Phys. 21, 239 (1968); F. C. Barker, Aust. J. Phys. 22, 293 (1969).

3. N. Kumar and F. C. Barker, Nucl. Phys. A167, 434 (1971).

4. R. M. Freeman and G. S. Mani, Proc. Phys. Soc. 85, 267 (1965); Tsan Ung Chan, J. P. Longequeue, and H. Beaumeville, Nucl. Phys. A124, 449 (1969).

5. H. E. Conzett, R. J. Slobodrian, S. Yamabe, and E. Shield, Proceedings of the International Congress on Nuclear Physics, Paris, 1964, edited by P. Gugenberger (CNRS, Paris, 1964), Vol. II, p. 228; E. Shield, H. E. Conzett, P. Darriulat, H. Pugh, and R. J. Slobodrian, Bull. Am. Phys. Soc. 9, 703 (1964); P. Darriulat, thesis, University of Paris (1965); M. W. Kermod, Phys. Letters 25B, 183 (1967); H. E. Conzett and R. J. Slobodrian, Bull. Am. Phys. Soc. 13, 1388 (1968).

6. R. E. Hintz, F. B. Selph, W. S. Flood, B. G. Harvey, F. G. Resmini, and E. A. McClatchie, Nucl. Instr. Methods 72, 61 (1969).

7. A. D. Bacher, E. A. McClatchie, M. S. Zisman, T. A. Weaver, and T. A. Tombrello, Nucl. Phys. A181, 453 (1972).

8. P. Darriulat, G. Igo, H. Pugh, and H. D. Holmgren, Phys. Rev. 137B, 315 (1965).

9. R. H. Dalitz, Ann. Rev. Nucl. Sci. 13, 339 (1963).

10. F. C. Barker, Nucl. Phys. 83, 418 (1966).

11. N. Kumar, as quoted in Ref. 3.

12. H. Bürgisser, E. Baumgartner, R. E. Benenson, G. Michel, F. Seiler, and H. R. Streibel, Helv. Phys. Acta. 40, 185 (1967); G. R. Plattner, E. Baumgartner, S. E. Darden, H. Meiner, and F. Seiler, Helv. Phys. Acta, 40, 465 (1967).

13. G. J. Clark, D. J. Sullivan, and P. B. Treacy, Nucl. Phys. A98, 473 (1967).

14. More recently Tsan Ung Chan, J. Phys. (Paris), Suppl. 31, C2-219 (1970), has attempted to fit Darriulat's α - α excitation functions,⁵ starting with his alternative level sequences from the ${}^6\text{Li}(d,\alpha){}^4\text{He}$ analysis. By introducing an additional 2^+ level at 22.1 MeV he concludes that the quartet of levels (2, 0, 4, 2) is preferred. We see no evidence for these 0^+ and 4^+ levels at 22.7 MeV in our phase-shift analysis.

FURTHER EVIDENCE FOR THE DOMINANCE OF NUCLEON-NUCLEON P-WAVE FORCES IN VECTOR POLARIZATIONS IN N-d SCATTERING BELOW 15 MeV*

J. S. C. McKee,[†] H. E. Conzett, R. M. Larimer, and Ch. Leemann

During the past eight years the experimental determination of polarization effects in nucleon-deuteron scattering below 50 MeV has shown that measurable polarizations occur at energies as low as 2 MeV and that these rapidly reach substantial values with increasing energy.¹ Theoretical progress in fitting these polarization results has proved to be difficult. The earlier exact three-body calculations,^{2,3} which used the Faddeev-Lovelace⁴ equations with simple S-wave separable nucleon-nucleon potentials, had given fair quantitative agreement with the experimental elastic N-d differential cross section data at energies up to about 50 MeV. However, because of the simple S-wave forces used, those calculations could

not provide the observed polarizations. It was clear that more realistic, i. e., more complicated, nucleon-nucleon potentials would be required and that the polarization data would provide the important and essential tests of any more refined theory. Later calculations⁵⁻⁷ with more complicated two-body forces produced polarizations of the required magnitude, but they did not succeed in obtaining quantitative agreement with experiment. These calculations, however, did result in the clear and important conclusion that in any three-body calculation of N-d scattering the P-wave nucleon-nucleon interaction is the dominant cause of the nucleon and deuteron vector polarization. Finally, very recent calculations^{8,9}

that include P-wave nucleon-nucleon forces have provided quantitative fits to the nucleon polarizations in N-d elastic scattering at energies up to 40 MeV. The agreement with the deuteron vector polarizations is not as good, although the data are less accurate and less extensive, reaching only to 10.8 MeV.¹⁰

The purpose of the present work, therefore, was to obtain accurate angular distributions of the vector analyzing power, iT_{11} , in \bar{d} -p scattering with polarized deuterons at 20 and 30 MeV, corresponding to proton energies of 10 and 15 MeV. This would provide more accurate data at 10 MeV and extend the measurements to higher energies, thus providing further tests for the calculations. For time-reversal-invariant interactions, the vector analyzing power, iT_{11} , in \bar{d} -p scattering is equal to the deuteron vector polarization, it_{11} , produced in p-d scattering,¹¹ so the calculated polarizations and measured analyzing powers can be compared directly.

The experiment was performed in a 36-inch diameter scattering chamber, using the axially injected polarized deuteron beam from the Berkeley 88-inch cyclotron. The beam had a vector polarization of 82% of the maximum possible value $p_V = 2/\sqrt{3}$ $it_{11} = 2/3$, and the tensor components were zero. A 7.5 cm diameter gas target with a 5 μ m Havar foil window was used at H₂ gas pressures ranging from 0.25 to 0.75 atm. Left-right asymmetry data were taken simultaneously at two angles separated by 20°, using pairs of ΔE -E silicon detector telescopes. In order to eliminate instrumental asymmetries, alternate runs were taken with the spin vector of the beam oriented up and down with respect to the scattering plane. The angular resolution, defined by tantalum collimators, was 0.85° and 1.5° (FWHM) for the forward and backward telescopes, respectively. Two monitor counters were placed left and right of the beam axis at a scattering angle of $\theta \approx 23^\circ$ and azimuthal angles $\phi \approx 70^\circ$ and 110° . A polarimeter, consisting of a smaller scattering chamber containing a gas target and a pair of ΔE -E counter telescopes at equal left and right scattering angles, was placed downstream of the main scattering chamber and provided continuous monitoring of the beam polarization. The analyzer used was ⁴He, whose analyzing power in \bar{d} -⁴He elastic scattering had been measured in detail previously.¹² Particle identification was used with all detector systems except the monitors. This allowed simultaneous detection of forward scattered deuterons and recoil protons from backward scattered deuterons.

Our 20-MeV data are shown in Fig. 1, where the relative errors include the statistical error and a contribution of ± 0.004 determined from

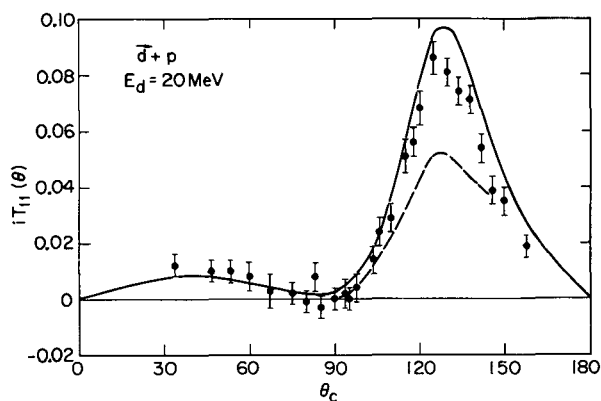


Fig. 1. The angular distribution of the vector analyzing power $iT_{11}(\theta)$ in \bar{d} -p scattering at 20 MeV. The solid curve is the theoretical result from Ref. 9. The dashed curve represents the back-angle data from Ref. 10 at 21.7 MeV. (XBL 7210-4160)

measured asymmetries with the beam polarization set to zero. In addition, there is an overall normalization uncertainty of $\pm 5\%$. The Saclay back-angle data¹⁰ at 21.7 MeV are also indicated in Fig. 1. The shapes of the angular distributions are similar, and the discrepancy of a factor of about 1.7 in overall normalization is most likely due to an uncertainty in the Saclay beam polarization.¹³ Also shown in Fig. 1 is the result from Pieper's⁹ recent calculation. The agreement is excellent, particularly in view of the fact that there has been no adjustment of the two-body input parameters in order to improve the fit to these data.

Figure 2 shows our 30-MeV data along with the predictions from the calculations of both Doleschall⁸ and Pieper⁹ at 28.2 MeV deuteron energy. They both fit the backward peak very well, but Pieper also succeeds in providing the negative maximum at $\theta = 95^\circ$. Clearly it would be of interest to identify the feature of the Pieper calculation that produces this result, which is not predicted by Doleschall. Of course, the calculations are not directly comparable. The Doleschall calculation is an exact one using the Faddeev-Lovelace⁴ equations with a complete set of P-wave interactions, and it also provides good fits to the differential cross section and nucleon polarization data at the same energy.⁸ The Pieper calculation is based on a perturbative treatment of three-particle scattering¹⁴ in which the nucleon-nucleon T-matrix is taken as the sum of two parts: $t = t^{(s)} + t^{(w)}$. The strong part $t^{(s)}$ is derived from potentials of the Yamaguchi type¹⁵ in the ¹S₀ and ³S₁ partial waves, and it is treated exactly in the Faddeev equations. The weak part $t^{(w)}$ contains all the additional

nucleon-nucleon input information and is treated in first-order perturbation theory. Sets of both P and D partial waves are included, so it is possible that the D-wave contributions account for the major differences seen in the curves in Fig. 2.

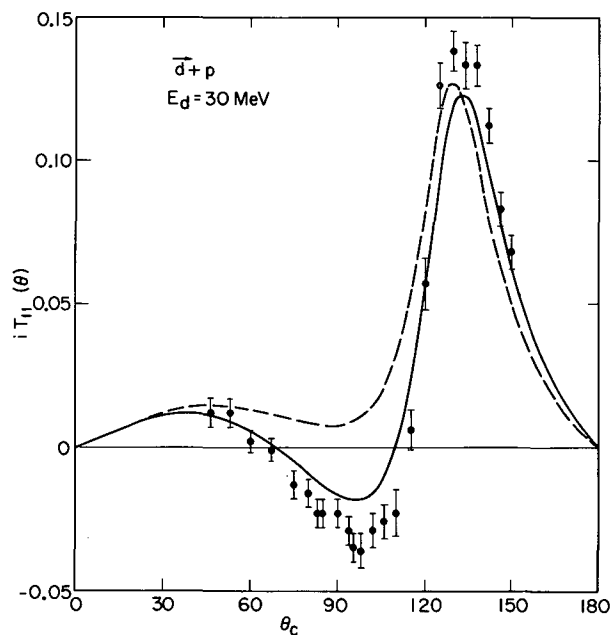


Fig. 2. Angular distribution of the vector analyzing power $iT_{11}(\theta)$ in d - p scattering at 30 MeV. The dashed curve is from Ref. 8, the solid curve from Ref. 9, both calculated for $E_d = 28.2$ MeV. (XBL 7210-4159)

Although the older work showed that the cross sections in N - d scattering could be quite well reproduced in three-body calculations using just the S -wave two-nucleon forces, it is now very clear that accurate and extensive polarization data have provided the tests that prove the necessity for the inclusion of higher partial waves in the calculations.

Footnotes and References

* Condensed from Phys. Rev. Letters 29, 1613 (1972), LBL 1270.

† Summer 1972 visitor. Permanent address: Department of Physics, University of Birmingham, England.

1. W. Haeblerli, *The Three-Body Problem in Nuclear and Particle Physics*, edited by J. S. C. McKee and P. M. Rolph (North-Holland, Amsterdam, 1970), p. 188 and references therein.
2. R. Aaron, R. D. Amado, and Y. Y. Yam, Phys. Rev. 140, B1291 (1965).
3. I. H. Sloan, Phys. Rev. 185, 1361 (1969); Nucl. Phys. A168, 211 (1971).
4. L. D. Faddeev, ZhETF 39, 1459 (1960) [trans: Sov. Phys. JETP 12, 1014 (1961)]; C. Lovelace, Phys. Rev. 135, B1225 (1964).
5. S. C. Pieper and K. L. Kowalski, Phys. Rev. C 5, 306 (1972).
6. J. C. Aarons and I. H. Sloan, Nucl. Phys. A182, 369 (1972).
7. P. Doleschall, Phys. Letters 38B, 298 (1972).
8. P. Doleschall, Phys. Letters 40B, 443 (1972).
9. S. C. Pieper, Nucl. Phys. A193, 529 (1972); Proceedings of the International Conference on Few Particle Problems in the Nuclear Interaction, Los Angeles, August 1972 (North-Holland, Amsterdam, to be published); and private communication.
10. J. Arvieux, R. Beurtey, J. Goudergues, B. Mayers, A. Papineau, and J. Thirion, Nucl. Phys. A102, 503 (1967).
11. G. R. Satchler, Nucl. Phys. 8, 65 (1958).
12. Ch. Leeman, H. E. Conzett, W. Dahme, J. MacDonald, and J. P. Meulders, Bull. Am. Phys. Soc. 17, 562 (1972), and to be published.
13. In a paper contributed to the International Conference on Few Particle Problems in the Nuclear Interaction, Los Angeles, August 1972, A. Fiore, J. Arvieux, Nguyen Van Sen, G. Perrin, F. Merchez, J. C. Gondrand, C. Perrin, J. L. Durand, and R. Darves-Blanc report measurements of vector analyzing powers in d - p scattering at 20 and 30 MeV which are in good agreement with our results.
14. K. L. Kowalski and S. C. Pieper, Phys. Rev. C 5, 324 (1972).
15. Y. Yamaguchi and Y. Yamaguchi, Phys. Rev. 95, 1635 (1954); Y. Yamaguchi, Phys. Rev. 95, 1628 (1954).

THE VECTOR ANALYZING POWER IN $\vec{d} - {}^4\text{He}$ ELASTIC
SCATTERING BETWEEN 15 AND 45 MeV

H. E. Conzett, W. Dahme,* Ch. Leemann, J. A. Macdonald, and J. P. Meulders†

Extensive measurements have been made of the differential cross-sections¹ and the vector and tensor analyzing powers² in $d - {}^4\text{He}$ elastic scattering at energies below 12 MeV. Phase-shift analyses^{1,3} of these data have led progressively to improved agreement with the data and to the determination of level parameters for those states of ${}^6\text{Li}$ that appear as resonances in the $d + {}^4\text{He}$ channel. As usual, the accuracy in the absolute values of the analyzing power measurements depends directly on the accuracy with which the beam polarization is known. Thus, the selection and calibration of a suitable analyzer for the monitoring of the beam polarization is always an important first task.

Since the energies of the polarized deuteron beam of the Berkeley 88-inch cyclotron extend to 60 MeV, a suitable polarization analyzer over a wide portion of that energy range is needed. Because of the large analyzing powers measured in the experiments cited above, we selected ${}^4\text{He}$ as a potentially good analyzer for polarized deuteron beams at energies beyond 12 MeV. Also, two independent determinations of the absolute vector analyzing power at $E_d = 11.5$ MeV, $\theta_c = 118^\circ$ had been made, giving the values $A_y = -0.418 \pm 0.010$ (Ref. 4) and $A_y = -0.411 \pm 0.014$ (Ref. 5), which are in very good agreement. Therefore, this served as the calibration reference point in the subsequent absolute normalization of our results. Although earlier measurements near 20 MeV (Ref. 6) indicated a substantial reduction of the vector analyzing power as compared with lower energies, this could be only a tentative conclusion because of the uncertainty in the value of the beam polarization. Our early measurements showed, however, that large values of the analyzing power persisted up to 20 MeV, so we extended our investigation to $E_d = 45$ MeV.

For the scattering of a purely vector-polarized deuteron beam the differential cross section is

$$\sigma(\theta, \phi) = \sigma_0(\theta) \left[1 + \frac{3}{2} p_y A_y(\theta) \cos \phi \right], \quad (1)$$

where $\sigma_0(\theta)$ is the unpolarized differential cross section, θ and ϕ are the polar and azimuthal scattering angles respectively, p_y is

the incident beam polarization, and $A_y(\theta)$ is the vector analyzing power. In the coordinate system with the z -axis along the incident deuteron direction, the y -axis is taken parallel to the beam polarization. From (1) it follows that a measured left ($\phi = 0$) - right ($\phi = \pi$) asymmetry is proportional to the product $p_y A_y$:

$$\begin{aligned} \epsilon(\theta) &= [\sigma(\theta, 0) - \sigma(\theta, \pi)] / [\sigma(\theta, 0) + \sigma(\theta, \pi)] \\ &= \frac{3}{2} p_y A_y(\theta). \end{aligned} \quad (2)$$

Asymmetry data were taken at 5-MeV intervals from 15 to 45 MeV at center-of-mass angles from 30° to 165° . At all angles the elastically scattered deuterons were detected with ΔE - E counter telescopes placed at equal angles to the left and right of the beam axis. Particle identification served to separate deuterons from protons which came from the deuteron breakup reaction. A gas target of ${}^4\text{He}$ at ~ 1 atm pressure was used with beams typically of 50 nA. A polarimeter, consisting similarly of a gas target and a left-right pair of counter telescopes, was placed downstream of the main scattering chamber, and it provided continuous monitoring of the beam polarization during the course of the experiment.

Absolute normalization of our data to the calibration point $A_y(E, \theta_c)$ at $E = 11.5$ MeV, $\theta_c = 118^\circ$ was achieved in the following manner. The beam of energy E_1 (e.g., 15 or 20 MeV) incident in the first target was degraded in aluminum to an energy $E_2 = 11.5$ at the polarimeter where the asymmetry $\epsilon_2(11.5, 118^\circ)$ was measured. At the same time, $\epsilon_1(E_1, \theta)$ was measured in the main scattering chamber, so from (2),

$$A_y(E_1, \theta) = A_y(11.5, 118^\circ) \epsilon_1 / \epsilon_2, \quad (3)$$

which gives $A_y(E_1, \theta)$ in terms of the measured asymmetries and the A_y calibration value. At higher energies for E_1 , a previously determined value for $A_y(E_2, \theta)$ served as a reference polarimeter analyzing power.

Our results are shown in Figures 1 and 2. It is clear that $\vec{d} - {}^4\text{He}$ elastic scattering serves as a very good vector polarization analyzer over a wide range of deuteron energies.

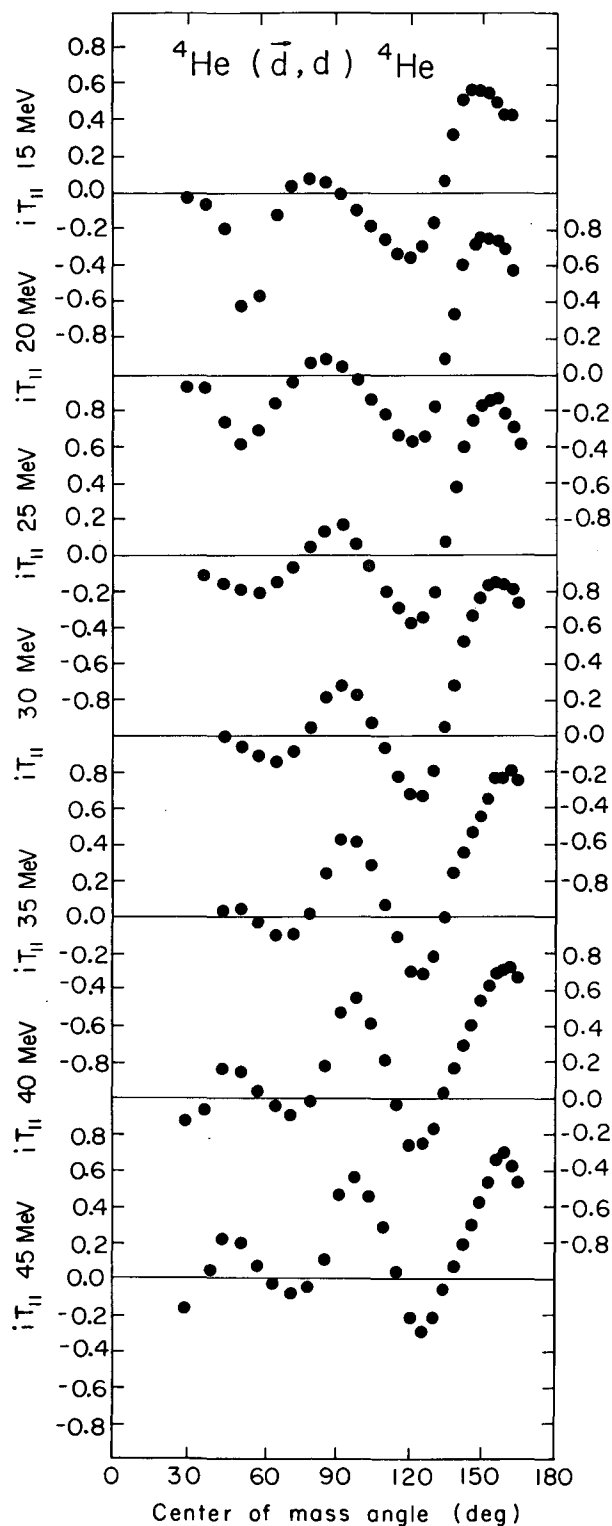


Fig. 1. Angular distributions of the vector analyzing powers, $iT_{11}(\theta) = (\sqrt{3}/2) A_{11}(\theta)$, in $d-{}^4\text{He}$ elastic scattering from 15 to 45 MeV. (XBL 731-2007)

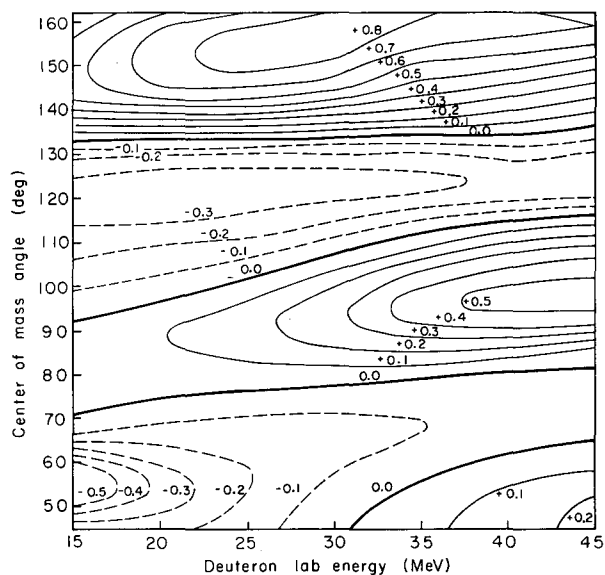


Fig. 2. Contour plot of the vector analyzing powers, $iT_{11}(\theta) = (\sqrt{3}/2) A_{11}(\theta)$, in $d-{}^4\text{He}$ elastic scattering from 15 to 45 MeV. (XBL 731-2008)

Footnotes and References

*DAAD exchange student from the University of Munich, West Germany.

†Present address: Centre de Physique Nucléaire, Université de Louvain, Belgium.

1. L. S. Senhouse, Jr. and T. A. Tombrello, Nucl. Phys. 57, 624 (1964).
2. W. Gruebler, V. König, P. A. Schmelzbach, and P. Marmier, Nucl. Phys. A148, 391 (1970).
3. L. G. Keller and W. Haerberli, Nucl. Phys. A156, 465 (1970); P. A. Schmelzbach, W. Gruebler, V. König, and P. Marmier, Nucl. Phys. A184, 193 (1972).
4. W. Gruebler, V. König, P. A. Schmelzbach, and P. Marmier, Nucl. Phys. A134, 686 (1969); V. König, W. Gruebler, A. Ruh, R. E. White, P. A. Schmelzbach, R. Risler, and P. Marmier, Nucl. Phys. A166, 393 (1971).
5. V. S. Starkovich and G. G. Ohlsen, LA-4465-MS (1970).
6. J. Arvieux, P. Darriulat, D. Garreta, A. Papineau, A. Tarrats, and J. Testoni, Nucl. Phys. A94, 663 (1967).

DEVIATIONS FROM THE BARSHAY-TEMMER SYMMETRY
IN THE REACTION ${}^4\text{He}(\vec{d}, t){}^3\text{He}$

W. Dahme,* J. Arvieux,† J. Birchall, H. E. Conzett, and R. M. Larimer

The nuclear reaction ${}^4\text{He}(\vec{d}, t){}^3\text{He}$ has drawn attention of several investigators¹⁻³ since Barshay and Temmer⁴ pointed out its elegance for testing the validity of the concept of isospin conservation in reactions which lead to final nuclei which are members of the same isospin multiplet (isobaric analogs). For isospin-conserving forces, they predicted the angular distribution of each of the reaction products ${}^3\text{H}$ and ${}^3\text{He}$ to be symmetric with respect to 90° c.m. angle. Because of the equal masses this leads to the equality of the respective yields at the same laboratory angle. Thus, by detecting both reaction products ${}^3\text{H}$ and ${}^3\text{He}$ with the same detector the determination of the ratio of yields

$$R = \frac{d\sigma}{d\Omega}({}^3\text{H}) / \frac{d\sigma}{d\Omega}({}^3\text{He})$$

is limited in accuracy, in principle, only by counting statistics.

Gross et al.¹ first reported deviations of R from unity for the reaction ${}^2\text{H}(\alpha, t){}^3\text{He}$ at an incident energy of 82 MeV. In an extended measurement³ to lower energies of the α -particle beam they found deviations up to 20% at an incident energy $E_\alpha = 64.3$ MeV ($E_{\text{c.m.}} = 21.4$ MeV). A DWBA analysis of their data produced the right pattern of the deviation but only about half the measured magnitude, and this calculated forward-backward asymmetry was seen to be due to the difference in the bound-state form factors for the proton and neutron separation energies in ${}^4\text{He}$. Since the calculated asymmetries were consistently smaller than those observed, it was suggested that some isospin impurity could be responsible for the larger asymmetry observed. They obtained their potential parameters by searching for optical-model potential parameters that gave good overall fits to elastic cross-section data of the entrance channel, $d + {}^4\text{He}$, and the exit channel, ${}^3\text{H} + {}^3\text{He}$, respectively. Since polarization data were not available for the analysis, the spin-orbit term of the optical potentials could not be well determined.

In order to provide data for a more complete and perhaps more sensitive testing of the DWBA calculations, we have measured the vector analyzing powers of the reactions ${}^4\text{He}(\vec{d}, t){}^3\text{He}$ and ${}^4\text{He}(\vec{d}, {}^3\text{He}){}^3\text{H}$ at an incident energy $E_d = 32.1$ MeV ($E_{\text{c.m.}} = 21.4$ MeV).

The purely vector-polarized deuteron beam available from the Berkeley 88-inch cyclotron was scattered from a ${}^4\text{He}$ -gas target at ~ 1 atm pressure. The beam current was typically ~ 40 nA. The outgoing triton and ${}^3\text{He}$ were detected by using ΔE - E counter telescopes placed symmetrically to the left and the right of the beam axis ($\phi = 0, \pi$) and particle identification. Data were taken at two angles simultaneously covering an angular range from $\theta_{\text{lab}} = 10^\circ$ to $\theta_{\text{lab}} = 35^\circ$ in 2° steps corresponding to center-of-mass angles from 22.5° to 80° . The angular resolution was 0.7 and 0.9° (FWHM) for the forward and backward detector systems respectively.

The beam polarization was monitored continuously using ${}^4\text{He}$ as an analyzer in a polarimeter placed downstream from the scattering chamber. The vector analyzing power of elastic \vec{d} - ${}^4\text{He}$ scattering had been measured over an energy range from 15 to 45 MeV at this laboratory recently.⁵

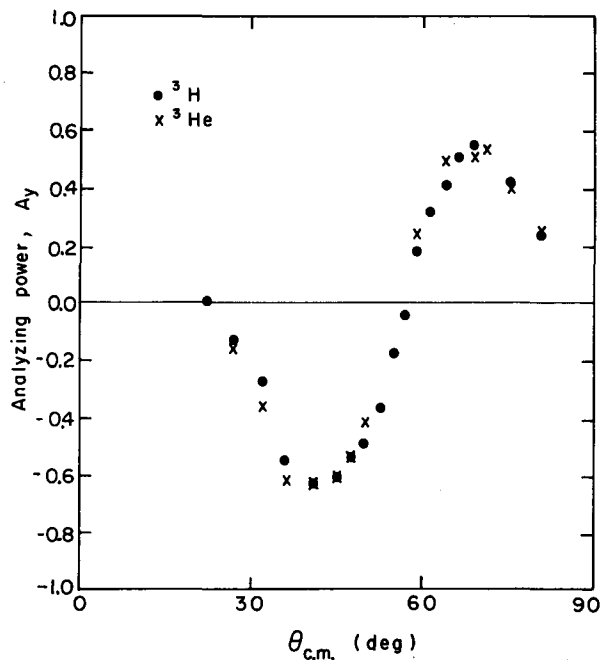


Fig. 1. Vector analyzing powers, $A_y({}^3\text{H})$ and $A_y({}^3\text{He})$, of the reactions ${}^4\text{He}(\vec{d}, t){}^3\text{He}$ and ${}^4\text{He}(\vec{d}, {}^3\text{He}){}^3\text{H}$, respectively, at $E_d = 32.1$ MeV. (XBL 732-2279)

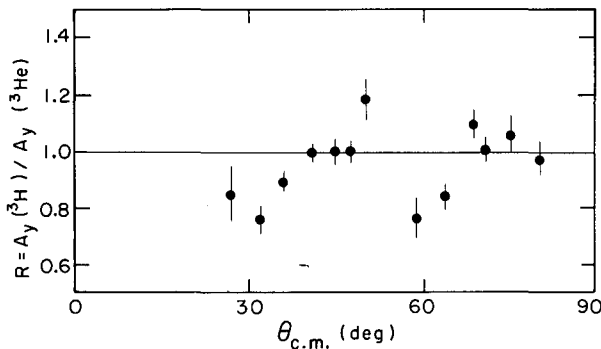


Fig. 2. Angular distribution of the ratio $R = A_y(^3\text{H})/A_y(^3\text{He})$ for the reactions $^4\text{He}(d,t)^3\text{He}$ and $^4\text{He}(d,^3\text{He})^3\text{H}$.
(XBL 732-2280)

The analyzing powers of the reactions $^4\text{He}(d,t)^3\text{He}$ and $^4\text{He}(d,^3\text{He})^3\text{H}$ measured at a deuteron beam energy $E_d = 32.1$ MeV are shown in Fig. 1. The quoted errors are the statistical errors combined with an instrumental uncertainty of ± 0.004 .

The data have not yet been corrected for small detector geometry effects. Figure 2 shows the angular distribution of the ratio of the two analyzing powers, $R = A_y(^3\text{H})/A_y(^3\text{He})$. We observe deviations from unity as large as 20%. It is intended to extend the measurement to other deuteron energies.

An analysis of our recent elastic $d\text{-}^4\text{He}$ analyzing power data in terms of an optical model using the computer code MAGALI⁶ is under way. This analysis is expected to reduce further the

ambiguities in the potential parameters of the entrance channel $d+^4\text{He}$. Thus, one may be able, in a DWBA analysis, to examine in more detail the relative differences in the neutron and proton pick-up processes which participate in the reaction.

Footnotes and References

- * DAAD exchange student from University of Munich, West Germany.
- † Permanent address: Institut des Sciences Nucleaires, Grenoble, France.
1. E. E. Gross, E. Newman, W. J. Roberts, R. W. Rutkowski, and A. Zucker, Phys. Rev. Letters 24, 473 (1970), and references therein.
 2. G. J. Wagner, C. C. Foster, and B. Greenebaum, Nucl. Phys. A174, 123 (1971), and references therein.
 3. E. E. Gross, E. Newman, M. B. Greenfield, R. W. Rutkowski, W. J. Roberts, and A. Zucker, Phys. Rev. C 5, 602 (1972).
 4. S. Barshay and G. M. Temmer, Phys. Rev. Letters 12, 728 (1964).
 5. Ch. Leemann, H. E. Conzett, W. Dahme, J. Macdonald, and J. P. Meulders, Bull. Amer. Phys. Soc. 17, 562 (1972), and to be published.
 6. J. Raynal, CEN Saclay Report DPhT/69-42 (1969).

A STUDY OF THE $^4\text{He}(p,d)^3\text{He}$ REACTION BETWEEN 32 AND 53 MeV

A. Sagle,* B. E. Bonner,[†] W. E. Broste,* H. E. Conzett,
W. Dahme,[‡] N. S. P. King,* and Ch. Leemann

A considerable number of differential cross-section measurements have been reported on the $^4\text{He}(p,d)^3\text{He}$ reaction up to 93 MeV¹ as well as the inverse stripping reaction $^3\text{He}(d,p)^4\text{He}$ over a wide range of deuteron energies.² Almost no experiments measuring deuteron asymmetries have been done with polarized protons above 32 MeV.³ For energies below 32 MeV the deuteron asymmetries can be determined from the inverse stripping reaction results for proton polarizations² and the "polarization-asymmetry theorem".⁴ Hopefully, a clearer theoretical understanding of the $^4\text{He}(p,d)^3\text{He}$ reaction can be obtained by studying the energy dependence of the cross sections and polarizations obtained in this experiment.

The results of this experiment will also aid in optimizing the design for a polarized neutron beam from the $T(d,n)^4\text{He}$ reaction.⁵ By using a polarized proton beam, the energy and angular dependence of P^2I can be found for the $^3\text{He}(d,p)^4\text{He}$ reaction from reciprocity arguments. These results should be similar to those expected from the charge-symmetric $T(d,n)^4\text{He}$ reaction.

The polarized proton beam from the 88-inch cyclotron was used to measure analyzing powers and cross sections for the $^4\text{He}(p,d)^3\text{He}$ reaction at bombarding energies of 32.0, 40.0, 50.0, and 52.5 MeV. (The analyzing power is equal to the measured asymmetry divided by the beam polarization.) Proton beams of from

50 to 150 nA with ~ 0.75 polarization were used on a ^4He target at 1 atm pressure. The beam polarization was obtained from a ^4He polarimeter and the $p\text{-}^4\text{He}$ analyzing powers were recently published by Bacher et al.⁶

The measured relative cross sections are in agreement with previous data for either the $^4\text{He}(p,d)^3\text{He}$ reaction or the inverse reaction. Analyzing powers for angles greater than 80° were obtained from recoil ^3He rather than deuteron mass-gated spectra. The analyzing powers observed at 32 and 50 MeV are given in

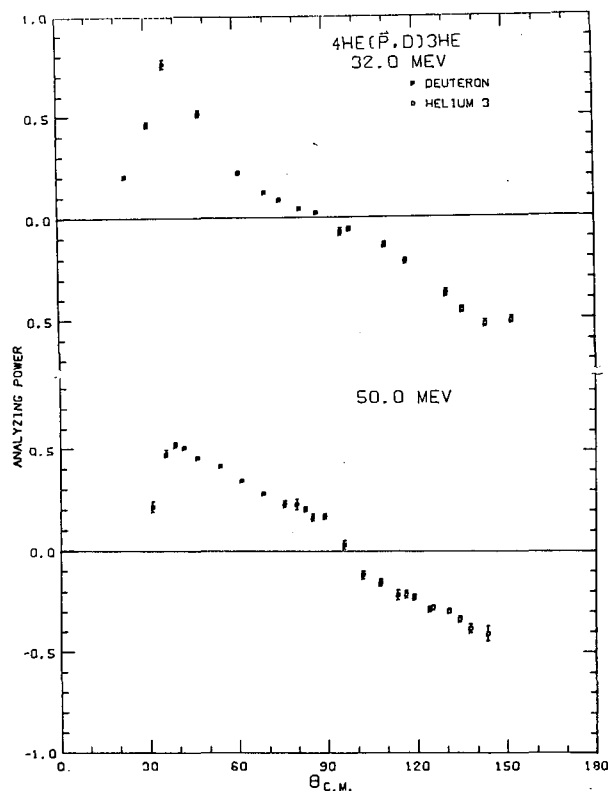


Fig. 1. Angular distribution of the analyzing power for the $^4\text{He}(p,d)^3\text{He}$ reaction at 32 and 50 MeV. (XBL 731-20)

Fig. 1. The 32-MeV data are in good agreement with Brown and Haeberli⁷ at forward angles; however, disagreements up to 30% are found for large backward angles.

An interesting energy-dependent effect is the appearance and disappearance from 32 to 52 MeV of a pronounced oscillation in the analyzing power at $\theta_{c.m.} \approx 90^\circ$. Some evidence for this can be seen in the 50-MeV results. This oscillation does not appear to have a counterpart in the observed cross sections.

Data reduction is essentially complete and attempts are presently being made to obtain theoretical fits to the analyzing powers and cross sections from DWBA calculations.

Footnotes and References

* Crocker Nuclear Laboratory, University of California, Davis, California 95616.

† Los Alamos Scientific Lab, Los Alamos, New Mexico.

‡ DAAD Exchange student from University of Munich, West Germany.

1. S. A. Harbison et al., Nucl. Phys. **A152**, 503 (1970) and S. Hayakawa et al., J. Phys. Soc. Japan **19**, 2004 (1964) and references therein.
2. W. G. Weitkamp and W. Haeberli, Nucl. Phys. **83**, 46 (1966) and references therein.
3. E. T. Boschitz et al., UCRL-16218 (1965).
4. G. R. Satchler, Nucl. Phys. **8**, 65 (1958) and L. C. Biedenharn, Nucl. Phys. **10**, 620 (1959).
5. Crocker Nuclear Laboratory Progress Report, University of California, Davis, California, 1971, page N-25.
6. A. D. Bacher et al., Phys. Rev. **5**, 1147 (1972).
7. R. I. Brown and W. Haeberli, Phys. Rev. **130**, 1163 (1963).

THE VECTOR ANALYZING POWER IN ELASTIC DEUTERON-DEUTERON SCATTERING BETWEEN 20 AND 40 MeV

H. E. Conzett, W. Dahme,* R. M. Larimer, Ch. Leemann, and J. S. C. McKee†

The subject of d-d elastic scattering has not received very much attention in the past. The cross sections are quite smooth functions of energy in the region up to 20 MeV where

there are the most data available. However, the complexity of the spin structure and the low threshold for inelastic processes has made any meaningful phase-shift analysis impossible

because of the large number of parameters involved and the resulting multiplicity of solutions.¹ A recent resonating-group calculation² has obtained good agreement with the cross-section data between 5 and 20 MeV, but the use of a purely central nucleon-nucleon potential precludes the prediction of any spin polarization observables.

From an experimental point of view, recent polarization experiments in elastic d-d scattering have raised a qualitative question. Determinations have been made of the vector-analyzing power, iT_{11} , in d-d scattering with polarized deuterons at several energies below 12 MeV,^{1,3} and at 21.4 MeV.⁴ Non-zero but very small values of iT_{11} were obtained, reaching a maximum value of about 0.04 at 21.4 MeV. These values are almost an order of magnitude smaller than the nucleon and deuteron vector polarizations found in other elastic processes involving few nucleon systems, e.g., $N + {}^2\text{H}$, ${}^3\text{He}$, ${}^4\text{He}$ and $d + {}^3\text{He}$, ${}^4\text{He}$. Since sizable contributions of S, P, and D waves were required to fit the cross sections,^{1,2} the lack of substantial polarizations could not be explained as resulting from the unimportance of partial waves with $l > 0$. Thus, its reason remained unexplained.

We have extended the measurements of vector analyzing powers in d-d scattering to 40 MeV to examine whether or not its anomalously small value persists at these higher energies. Also, another determination near 20 MeV was desired, since the older measurement at 21.4 MeV was rather uncertain because of lack of knowledge of the beam polarization. We used the axially injected vector-polarized deuteron beam from the Berkeley 88-inch cyclotron. Left-right asymmetry data were taken simultaneously at two angles separated by 20° , using pairs of ΔE -E silicon detector telescopes. A polarimeter, consisting of a gas target and a pair of ΔE -E counter telescopes, was placed downstream of the main scattering chamber and provided continuous monitoring of the beam polarization. The analyzer used was ${}^4\text{He}$, whose analyzing power in d- ${}^4\text{He}$ elastic scattering had been measured in detail previously.⁵ For a deuteron beam with its purely vector polarization, iT_{11} , along the normal to the scattering plane, $\underline{n} = (\underline{k}_i \times \underline{k}_f) / |\underline{k}_i \times \underline{k}_f|$, the differential cross section is given by $\sigma(\theta, \phi) = \sigma_0(\theta) [1 + 2(it_{11})iT_{11}(\theta)\cos\phi]$, where $\sigma_0(\theta)$ is the differential cross section for scattering of an unpolarized beam and ϕ , the azimuthal scattering angle, is equal to 0 and π for left and right scattering, respectively. Thus a left-right asymmetry measurement, $\epsilon = [\sigma(\theta, 0) - \sigma(\theta, \pi)] / [\sigma(\theta, 0) + \sigma(\theta, \pi)] = 2(it_{11})(iT_{11})$, combined with the simultaneous determination of the beam polarization, yields the vector analyzing powers, $iT_{11}(\theta)$. Figure 1 shows our data at $E_d = 20, 30,$ and 40 MeV. Our 20-MeV

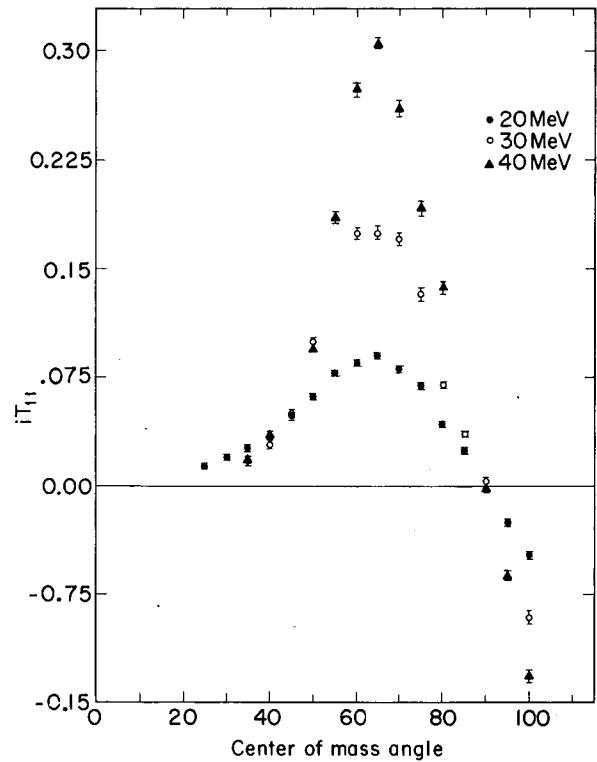


Fig. 1. Angular distributions of the vector analyzing power $iT_{11}(\theta)$ in d-d scattering at 20, 30, and 40 MeV. (XBL 728-3846)

values are a factor of 2 larger than the previous results at 21.4 MeV, and clearly the vector-analyzing powers increase rapidly with increasing energy. These values, when compared with the analyzing powers in d-p elastic scattering measured recently at comparable center-of-mass energies,⁶ can no longer be considered anomalously small.

Footnotes and References

* DAAD Exchange student from University of Munich, West Germany.

† Summer 1972 visitor. Permanent address: Department of Physics, University of Birmingham, England.

1. G. R. Plattner and L. G. Keller, Phys. Letters **30B**, 327 (1969).
2. F. S. Chwieroth, Y. C. Tang, and D. R. Thompson, Nucl. Phys. **A189**, 1 (1972).
3. W. Gruebler, V. König, R. Risler, P. A. Schmelzbach, R. E. White, and P. Marmier. Nucl. Phys. **A193**, 149 (1972).

4. J. Arvieux, J. Goudergues, B. Mayer, and A. Papineau, Phys. Letters 22, 610 (1966).

5. Ch. Leemann, H. E. Conzett, W. Dahme, J. Macdonald, and J. P. Meulders, Bull. Amer. Phys. Soc. 17, 562 (1972), to be published.

6. J.S.C. McKee, H. E. Conzett, R. M. Larimer, and Ch. Leeman, Phys. Rev. Letters 29, 1613 (1972).

A STUDY OF $(\vec{d}, {}^3\text{He})$ AND (\vec{d}, t) REACTIONS INDUCED BY POLARIZED DEUTERONS

B. Mayer,* H. E. Conzett, W. Dahme,† D. G. Kovar, R. M. Larimer, and Ch. Leemann

A number of experiments have shown that the vector-analyzing powers for (\vec{d}, p) and (p, \vec{d}) reactions depend strongly on the j -values of the transferred neutron for a given orbital angular momentum transfer.^{1,2} This property can be very useful in providing spin assignments to states which can be populated by such reactions. It has been found, also, that the (\vec{d}, t) reaction shows a similar effect.³ In order to investigate an expected similar j -dependence of the analyzing power in reactions involving a proton transfer, we have studied the ${}^{208}\text{Pb}(\vec{d}, {}^3\text{He})$ and ${}^{12}\text{C}(\vec{d}, {}^3\text{He})$ and ${}^{12}\text{C}(\vec{d}, t)$ are mirror reactions leading to isobaric analog final states, it is of interest to examine deviations from the equality of the differential cross sections and analyzing powers that is expected because of the charge-symmetry of nuclear forces. Angular distributions were measured at laboratory angles from 25° to 60° .

The ${}^{208}\text{Pb}(\vec{d}, {}^3\text{He})$ and ${}^{208}\text{Pb}(\vec{d}, t)$ Reactions

The experiment was performed with a 30-MeV vector-polarized deuteron beam from the Berkeley 88-inch cyclotron. The target was a 0.85-mg/cm^2 ${}^{208}\text{Pb}$ foil. Left-right asymmetry data were taken simultaneously at two angles separated by 20° , using pairs of ΔE - E silicon detector telescopes. In order to eliminate instrumental asymmetries, alternate runs were taken with the spin vector of the beam oriented up and down with respect to the reaction plane. Particle identification was used to gate the ${}^3\text{He}$ and tritons into separate spectra. The beam polarization was monitored continuously with a polarimeter placed downstream of the main scattering chamber. The analyzer used was ${}^4\text{He}$, whose analyzing power in d - ${}^4\text{He}$ elastic scattering had been measured previously.⁴ The vector polarization of the beam was typically $p_y \approx 0.52$.

The $(\vec{d}, {}^3\text{He})$ and (\vec{d}, t) reactions populate essentially the $3s_{1/2}$, $2d_{3/2}$, $1h_{11/2}$, and $2d_{5/2}$ proton hole states and the $3p_{1/2}$, $2f_{5/2}$, $3p_{3/2}$, $4i_{13/2}$, and $2f_{7/2}$ neutron hole states in ${}^{207}\text{Pb}$, respectively. As shown in Fig. 1, the angular distributions of the vector-analyzing power, $A_y(\theta)$, exhibit a strong j -dependence for the $2d$ states populated by the $(\vec{d}, {}^3\text{He})$ reaction and for the $3p$ and $2f$ states from the (\vec{d}, t) reaction. The sign of $A_y(\theta)$ for $j = \ell + 1/2$ is almost always opposite that for $j = \ell - 1/2$, so the ease and unambiguity of j -assignment from measurements of the vector-analyzing powers is clearly demonstrated.

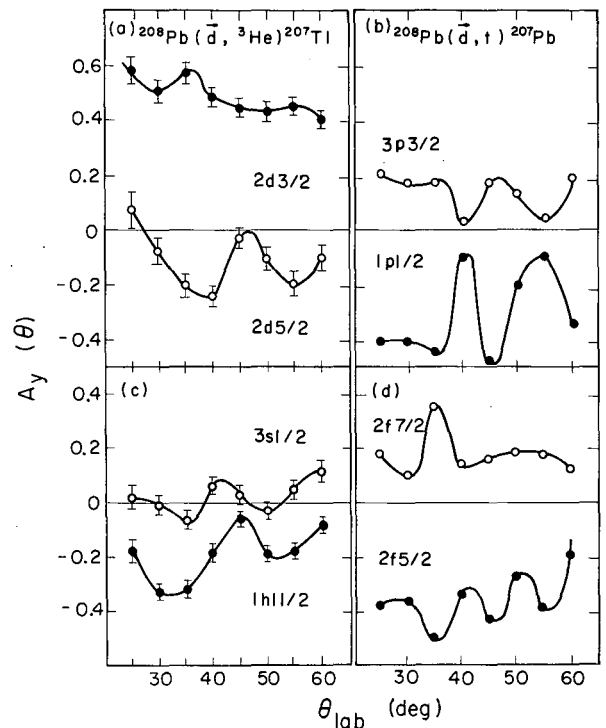


Fig. 1. Angular distributions of the vector-analyzing power $A_y(\theta)$ of the (a) ${}^{208}\text{Pb}(\vec{d}, {}^3\text{He})$ ${}^{207}\text{Tl}$ and (b) ${}^{208}\text{Pb}(\vec{d}, t)$ ${}^{207}\text{Pb}$ reactions at $E_d = 30$ MeV. (XBL 732-2281)

The $^{12}\text{C}(\vec{d}, ^3\text{He})$ and $^{12}\text{C}(\vec{d}, t)$ Reactions

The experiment was done at an incident deuteron energy of 45 MeV with a 1.0-mg/cm^2 carbon target. The large negative reaction Q-value increases the difference in the deuteron and ^3He energy loss in the target as compared with the case for ^{208}Pb . In order to reduce this effect for better energy resolution, the target was rotated so that its normal was near the detector angle. This required all telescopes to be on the same side of the beam, so spin up-down asymmetries were measured for equal integrated beam flux.

Figure 2 shows the angular distributions $A_y(\theta)$ for the $(\vec{d}, ^3\text{He})$ reaction. A j-dependence is obvious, although it is not as striking as it was for the $^{208}\text{Pb}(\vec{d}, ^3\text{He})$ reaction. Also, there is a definite difference between the analyzing powers leading to the $3/2^-$ ground state and the $3/2^-(4.8\text{-MeV})$ state. This could be due to a difference in the Q-values, but that possibility must await a DWBA analysis for substantiation.

The cross sections and vector-analyzing powers in the $^{12}\text{C}(\vec{d}, t)^{11}\text{C}$ reaction are, as suggested, very close to those found for the mirror states in the $^{12}\text{C}(\vec{d}, ^3\text{He})^{11}\text{B}$ reaction. As an

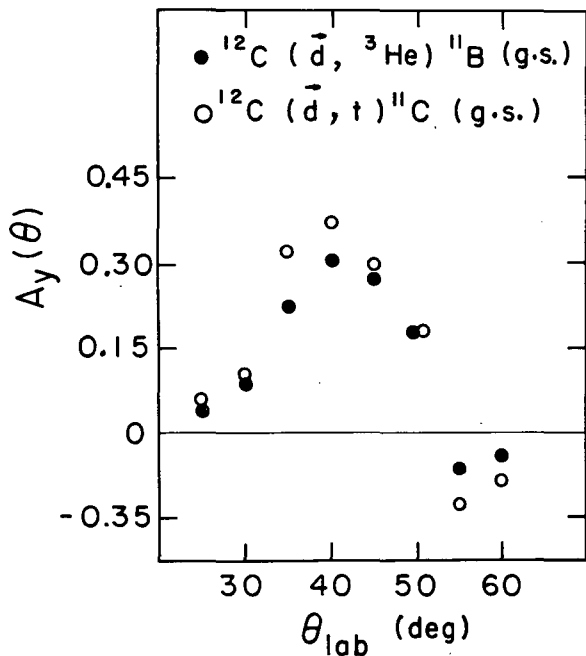


Fig. 2. Angular distributions of the vector-analyzing power $A_y(\theta)$ of the $^{12}\text{C}(\vec{d}, ^3\text{He})^{11}\text{B}$ reaction at $E_d = 45$ MeV. (XBL 732-2282)

example, Fig. 3 shows the analyzing powers for the $3/2^-(\text{g. s.})$ levels in ^{11}C and ^{11}B . The distributions are very similar, and the suggested differences cannot yet be considered significant because these preliminary results have not had final background subtractions made.

In summary, a strong j-dependence of the vector analyzing power in $(\vec{d}, ^3\text{He})$ reactions has been experimentally established for $\ell = 2$ transitions in ^{208}Pb and for $\ell = 1, 3$ transitions in ^{12}C . Thus $(\vec{d}, ^3\text{He})$ reactions with polarized deuteron beams can be very useful in providing spin assignments.

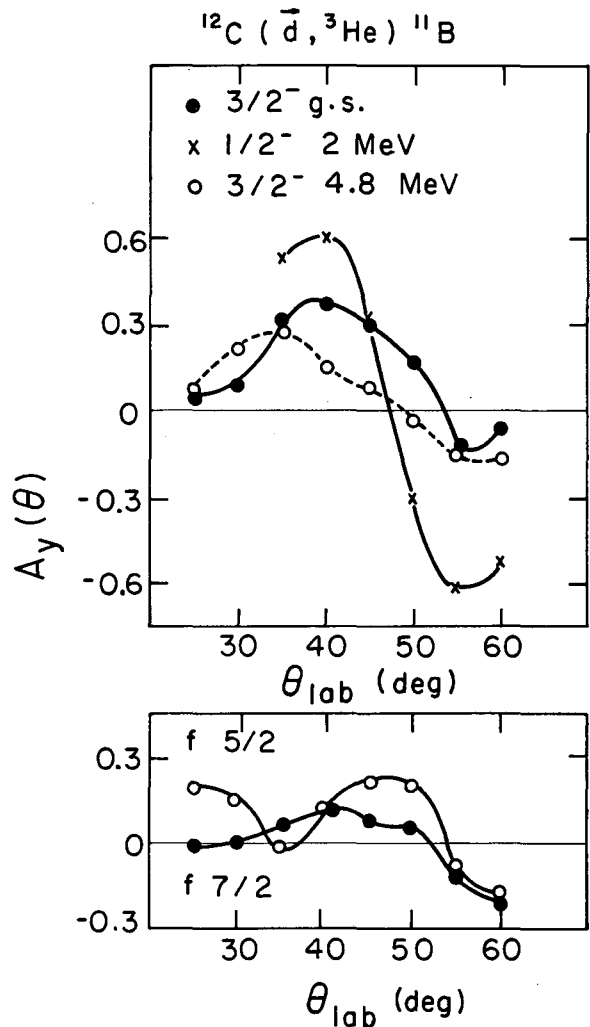


Fig. 3. Angular distributions of the vector-analyzing power $A_y(\theta)$ of the $^{12}\text{C}(\vec{d}, ^3\text{He})^{11}\text{B}$ (g. s.) and $^{12}\text{C}(\vec{d}, t)^{11}\text{C}$ (g. s.) transitions at $E_d = 45$ MeV. (XBL 732-2283)

Footnotes and References

* Present address: CEN Saclay, France.

† DAAD exchange student from University of Munich, West Germany.

1. T. J. Yule and W. Haeberli, Nucl. Phys. A117, 1 (1968).

2. B. Mayer, J. Gosset, J. L. Escudié, and H. Kamitsubo, Nucl. Phys. A177, 205 (1971).

3. H. S. Liers, R. D. Rathmell, S. E. Vigdor, and W. Haeberli, Phys. Rev. Letters 26, 261 (1971).

4. Ch. Leemann, H. E. Conzett, W. Dahme, J. Macdonald, and J. P. Meulders, Bull. Amer. Phys. Soc. 17, 562 (1972), and to be published.

EXCITATION OF THE GROUND STATE ROTATIONAL BAND IN ^{28}Si BY INELASTIC SCATTERING OF 25.2-MeV POLARIZED PROTONS*

R. de Swinarski,[†] H. E. Conzett, B. Frois,[‡] R. Lamontagne,[‡] and R. J. Slobodrian[‡]

In recent years, extensive polarization data have become available due to the increase in the number of polarized ion sources in operation. Measurements of the analyzing power in inelastic proton scattering have been made at different energies and for many targets for which cross-section data had been available. Analyses of the data (cross sections and analyzing power) have been reasonably successful for collective 2^+ or 3^- states for several nuclei in the $f_{7/2}$ shell, the $g_{9/2}$ shell, or for the s - d shell.^{1,6} In the framework of the distorted-wave Born approximation (DWBA) with macroscopic-model form factors, good fits to the data were obtained only by including real, imaginary, and spin-orbit terms of the deformed optical potential. For simplicity, the spin-orbit deformation used was essentially a phenomenological one.^{5,7} After Sherif and Blair had introduced the concept of the "full Thomas term" of the spin-orbit potential in the DWBA macroscopic collective-model formalism,⁸ considerable improvements to the fits for the polarization data, mainly at forward angles, were observed.⁹ Such a deformed spin-orbit term was then introduced by Raynal into a coupled-channels program (ECIS 1971). The calculations to be presented here have been carried out with this program in an analysis of our measurements of both cross sections and analyzing powers for the inelastic scattering of 25.2-MeV polarized protons by ^{28}Si . One of the goals of this experiment was to test the sensitivity of the data to higher-order deformation in this strongly deformed nucleus. Recent coupled-channels calculations fitting only cross section data have suggested the possible existence of a large hexadecapole deformation (Y_4) in ^{28}Si and an oblate shape for this nucleus.¹¹ The experiment which is reported here was designed to provide a more precise determination of the deformations,

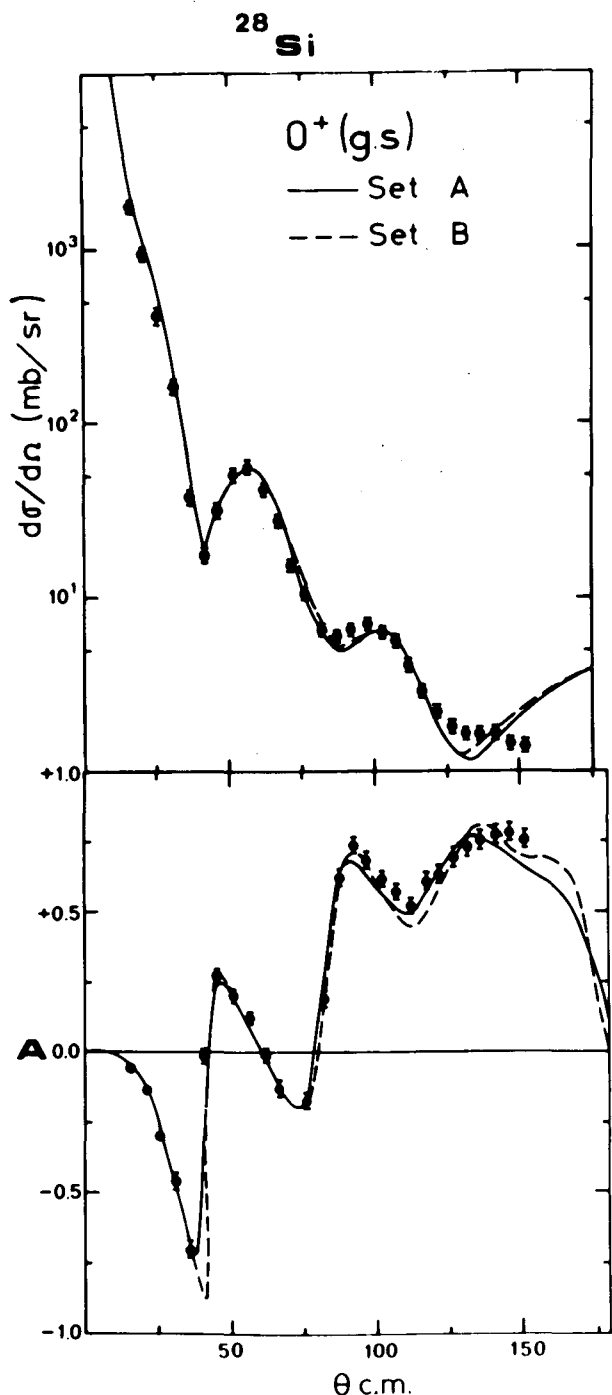
since for the first time accurate cross sections and analyzing powers for the low-lying 0^+ , 2^+ , and 4^+ states were measured simultaneously.

The experiment was performed with a beam of 25.2-MeV protons, using the polarized ion source of the Berkeley 88-inch cyclotron. Scattered particles were detected by four pairs of cooled (-30°C), 5-mm-thick, Li-drifted silicon detectors. The two detectors in each pair were placed at equal angles on opposite sides of the beam. Up to 50 nA of polarized protons were delivered on target with a polarization of about 78%. The beam polarization was monitored continuously during the experiment with a ^4He polarimeter which had been accurately calibrated.¹² Two monitor detector, placed left and right of the beam axis at a fixed scattering angle, served to monitor the incident particle flux for relative differential cross-section measurements. The polarization was calculated from the ratios of left and right detector yields. The absolute normalization of the cross sections was made from comparison with results taken from the literature at about the same energy.

Optical-model parameters were obtained by simultaneously fitting both the elastic cross sections and polarizations, using the search code MAGALI.¹³ The definition of the optical potential and search procedures employed are conventional.¹ Very good fits for both the elastic cross section and polarizations were obtained with a purely surface absorption W_D . Several sets of parameters usually used in this mass region,^{7,14} were used as starting parameters and gave very similar results. It was also possible to get very good fits to the data with some combination of volume absorption W_V and surface absorption W_D , with only minor changes in the other parameters. The

Table I

	V_o (MeV)	r_o (F)	a_o (F)	W_V (MeV)	W_D (MeV)	r_I (F)	a_I (F)	V_{LS} (MeV)	r_{LS} (F)	a_{LS} (F)	χ_σ^2	χ_p^2	$\sigma_R^{theor.}$
Set A	48.20	1.15	0.65	0.00	5.14	1.33	0.67	6.55	0.92	0.52	138	87	823
Set B	48.95	1.15	0.65	2.01	4.33	1.33	0.60	6.97	0.94	0.57	88	134	757



results of the best optical-model calculations are presented in Table I, while Fig. 1 shows the corresponding fits to the elastic data.

It is generally accepted that nuclei in the first half of the 2s-1d shell exhibit a rotational character.¹⁵ Furthermore, the large static quadrupole moments for the first excited states and the results of Hartree-Fock type calculations^{16,17} characterize the s-d shell as a region of permanent ground state deformation. Some of these calculations suggest also that several nuclei in this region should have a ground state hexadecapole as well as a quadrupole deformation.^{18,19} Recent measurements of the inelastic scattering protons¹¹ and alpha particles²⁰ from ^{20}Ne have shown without doubt that a large hexadecapole (Y_4) deformation was needed to reproduce the experimental cross sections for the low-lying excited states of the $K=0^+$ band. Recent measurements with polarized protons have confirmed that the analyzing powers for the 0^+ , 2^+ , and 4^+ states in ^{20}Ne require the same hexadecapole deformation that was previously determined from the cross section data alone.²¹

The ^{28}Si data were analyzed in the coupled-channels (c. c.) formalism because of the strong coupling between the ground and excited states of the rotational band. In this formalism the nuclear radius is defined by

$$R = R_i(1 + \beta_2 Y_{20} + \beta_4 Y_{40} \dots),$$

where the β 's are the deformation parameters determined by fitting the experimental data, the Y 's are spherical harmonics, and R_i corresponds to the various optical potential radii.

Partly on experimental and partly on the theoretical grounds, the so-called "full Thomas form" of the deformed spin-orbit potential is to be preferred over the simplified form^{5,7} used earlier. Furthermore there are indications

Fig. 1. Optical-model prediction for the elastic cross section and polarization. The two sets of parameters of Table I were used.

(XBL 732-129)

that the spin-orbit part should have a greater deformation than the central part.²² The coupled-channels program for the present calculations contains the "full Thomas form" of the deformed spin-orbit term, and allows one to keep the deformation length constant ($\delta_{\text{real}} = \beta_{\text{real}} R_{\text{real}} = \delta_{\text{Imag}} = \delta_{\text{LS}}$); to keep the deformation parameter constant ($\beta_{\text{real}} = \beta_{\text{Imag}} = \beta_{\text{LS}}$), or to make the deformation parameter β_{SO} of the spin-orbit deformed potential larger than that of the central potential, β_{cent} . Recent analyses by Sherif and Blair^{8,9,23} have shown that the fitting of inelastic proton scattering data for the first excited 2^+ state of ^{28}Si requires a spin-orbit deformation somewhat larger than that of the central potential.

Coupled-channels calculations are shown in Figs. 2, 3, and 4 together with the experimental data for the 2^+ and 4^+ states. Figure 2 presents the c. c. calculations using a rotational model or a vibrational model with set A parameters of Table I. This figure shows clearly the poor fit obtained when a positive quadrupole deformation ($\beta_2 = +0.40$) is used together with a negative hexadecapole deformation, and the agreement with the data is even worse when β_4 is set equal to zero. On the other hand the vibrational model gives a good account of the 2^+ data but here, also, the agreement with the 4^+ data is rather poor. These calculations were done by using the same deformation length for the various deformed terms of the optical potential ($\delta_0 = \beta R_0 = \beta_{\text{I}} R_{\text{I}} = \beta_{\text{LS}} R_{\text{LS}}$). On the other hand Fig. 3 shows the very good fits to the cross sections and polarization obtained by using set A parameters with a negative quadrupole deformation $\beta_2 = -0.40$ (oblate) and a positive hexadecapole deformation $\beta_4 = +0.15$ (curve 1). Curve 2 shows the extreme sensitivity of the calculations to the β_4 deformation. Although the magnitude of the analyzing power for the 4^+ is not reproduced, the calculation gives the right phases while the overall agreement for all the data is very good.

Equivalent fits can also be obtained when the spin-orbit deformation is made greater than the central deformation. Figure 4 presents the c. c. calculations using set A parameters, $\beta_2 = -0.40$, $\beta_4 = +0.15$ and various values of the ratio $\beta_{\text{LS}}/\beta_{\text{cent}}$ of the spin-orbit deformation to the central deformation. Best agreement with the data is obtained when this ratio is equal to 1.5 (curve 1 of Fig. 4). This figure shows also that a good fit to the 4^+ analyzing power can be obtained by increasing this ratio to 2.0 and decreasing β_4 slightly, from 0.15 to 0.10. However, the calculation then underestimates the 4^+ cross section.

Finally the use of set B optical-model parameters gives equivalent fits to those reported here and therefore they are not presented.

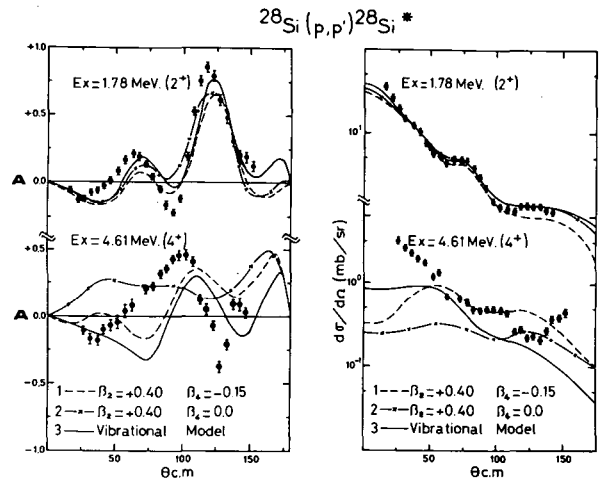


Fig. 2. Coupled-channels calculations for the experimental cross section and analyzing power of the 2^+ and 4^+ states in ^{28}Si . (1) c. c. rotational-model prediction with $\beta_2 = +0.40$, $\beta_4 = -0.15$; (2) c. c. rotational model with $\beta_2 = +0.40$, $\beta_4 = 0.00$; (3) c. c. vibrational model $\beta(2^+) = 0.40$, $\beta(4^+) = 0.15$. Set A optical-model parameters were used.

(XBL 732-130)

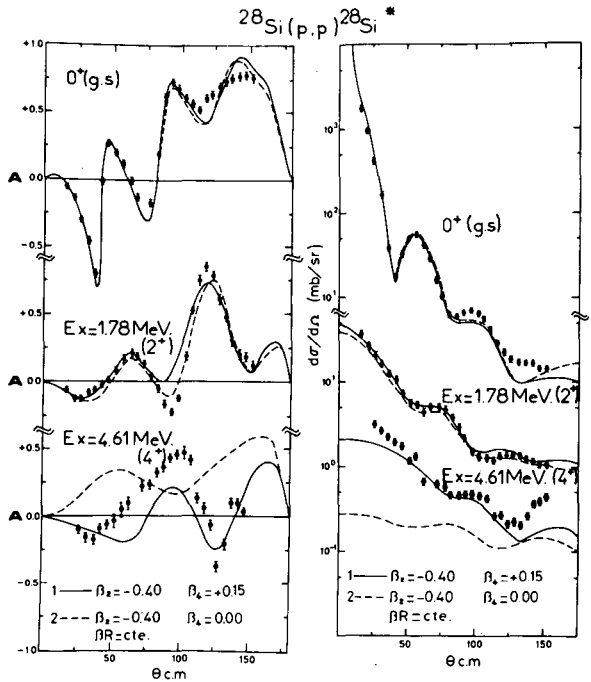


Fig. 3. The c. c. rotational-model predictions for the 0^+ , 2^+ , and 4^+ cross sections and analyzing power; (1) $\beta_2 = -0.40$, $\beta_4 = +0.15$; (2) $\beta_2 = -0.40$, $\beta_4 = 0.00$. Calculations were done using set A (Table I) optical-model parameters and keeping the same deformation length for the different terms of the deformed optical potential. ($\beta R = \text{cte.}$)

(XBL 732-131)

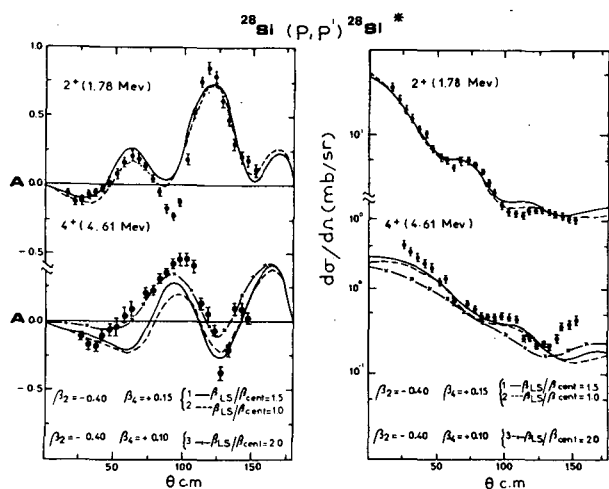


Fig. 4. The c. c. rotational-model predictions for the 2^+ and 4^+ states in ^{28}Si , using parameters set A (Table I) and increasing the spin-orbit deformation parameter relative to the central deformation from 1.0 to 2.0.

- (1) $\beta_2 = -0.40$, $\beta_4 = +0.15$, $\beta_{\text{LS}} = 1.5 \beta_{\text{cent}}$
 (2) $\beta_2 = -0.40$, $\beta_4 = +0.15$, $\beta_{\text{LS}} = \beta_0 = \beta_1$
 (3) $\beta_2 = -0.40$, $\beta_4 = +0.15$, $\beta_{\text{LS}} = 2 \beta_{\text{cent}}$
 (XBL 732-132)

Table II gives the final deformation parameters obtained from this study together with some recently reported values.

Table II. Deformation parameters of ^{28}Si .

β_2	β_4	Ref.	Method
-0.40	+0.15	This work	(p, p') c. c.
-0.32	+0.08±0.01	20	(α, α') c. c.
-0.34	+0.25	11	(p, p') c. c.
-0.39	+0.10	25	(e, e')
-0.55	+0.33	7	(p, p') c. c.
0.36	---	26	(p, p') c. c.

In summary, coupled-channels calculations are in reasonably good agreement with our measurements of inelastic scattering of polarized protons exciting the $K=0^+$ ground state rotational band in ^{28}Si . The best agreement is obtained using negative quadrupole deformation $\beta_2 = -0.40$ (oblate) and a positive hexadecapole deformation, $\beta_4 = +0.15$. Therefore the oblate shape of this nucleus is confirmed, and it is found that the β_4 deformation is considerably

smaller than previously determined from cross-section data alone.¹¹ However, the inelastic scattering data might be equally well described by a vibrational model alone, with some modification of the values of β_2 and β_4 . Thus the interpretation of β_2 and β_4 as describing the static Y_2 and Y_4 deformations of the ground state band relies upon measurement of a non-zero quadrupole moment. Such a measurement has been made recently,²⁴ and it has confirmed the oblate shape of ^{28}Si . Finally the good fits to the polarization data obtained with the full Thomas term provide additional evidence for the required use of this term instead of the phenomenological form used previously.

Footnotes and References

* Condensed from LBL-1620, submitted for publication in Canadian Journal of Physics.

† Present address: Institut des Sciences Nucléaires, Grenoble, France.

‡ Present address: Département de Physique, Université Laval, Quebec, Canada.

1. C. Glashausser, R. De Swiniarski, J. Thirion, and A. D. Hill, Phys. Rev. **164**, 1437 (1967).

2. C. Glashausser and J. Thirion, in *Advances in Nuclear Physics*, Vol. 2 (Plenum Press, New York, 1968), p. 79.

3. C. Glashausser, R. De Swiniarski, J. Goudergues, R. M. Lombard, B. Mayer, and J. Thirion, Phys. Rev. **184**, 1217 (1969).

4. D. J. Baugh, M. J. Kenny, J. Lowe, D. L. Watson, and H. Wojciechowski, Nucl. Phys. **A99**, 203 (1967).

5. M. P. Fricke, E. E. Gross, and A. Zucker, Phys. Rev. **163**, 1113 (1967).

6. V. E. Lewis, E. J. Burge, A. A. Rush, and D. A. Smith, Nucl. Phys. **A101**, 589 (1967).

7. A. G. Blair, C. Glashausser, R. De Swiniarski, J. Goudergues, R. Lombard, B. Mayer, J. Thirion, and P. Vaganov, Phys. Rev. **C1**, 444 (1970).

8. H. Sherif and J. S. Blair, Phys. Letters **26B**, 489 (1968).

9. H. Sherif, Nucl. Phys. **A131**, 532 (1969).

10. J. Raynal, in *Proceedings of the Symposium on Nuclear Reactions Mechanisms and Polarizations Phenomena* (Laval University, Quebec, 1969, p. 75).

11. R. De Swiniarski, C. Glashausser, D. I. Hendrie, J. Sherman, A. D. Bacher, and E. A. McClatchie, *Phys. Rev. Letters* 23, 317 (1969).
12. A. D. Bacher, G. R. Plattner, H. E. Conzett, D. J. Clark, H. Grunder, and W. F. Tivol, *Phys. Rev. C* 5, 1147 (1972).
13. J. Raynal, MAGALI, CEN Saclay Report D. Ph. -T/69.42 (1969).
14. S. A. Fulling and G. R. Satchler, *Nucl. Phys.* A111, 81 (1968).
15. H. E. Gove, in Proceedings of the International Conference on Nuclear Structure (Toronto University Press, 1960), p. 436, and University of Rochester Report UR. NSRL-7 (1968).
16. S. Das Gupta and M. Harvey, *Nucl. Phys.* A94, 602 (1967).
17. G. Ripka, in Advances in Nuclear Physics, Vol. 1, edited by M. Baranger and E. Vogt (Plenum Press, New York, 1968).
18. C. Brihaye and G. Reidemeister, *Nucl. Phys.* A100, 65 (1967).
19. A. L. Goodman, G. L. Struble, J. Bar-Touv, and A. Goswami, *Phys. Rev. C* 2, 380 (1970).
20. H. Rebel et al., *Nucl. Phys.* A182, 145 (1972).
21. R. De Swiniarski, A. D. Bacher, F. G. Resmini, G. R. Plattner, and D. L. Hendrie, *Phys. Rev. Letters* 28, 1139 (1972).
22. G. R. Satchler, in Proceedings of the Polarization Phenomena in Nuclear Reactions, edited by H. H. Barschall and W. Haeberli (The University of Wisconsin Press, Madison, 1971), p. 155.
23. H. Sherif and J. S. Blair, in Proceedings of the Polarization Phenomena in Nuclear Reactions, edited by H. H. Barschall and W. Haeberli (The University of Wisconsin Press, Madison, 1971), p. 693.
24. K. Nakai, J. L. Quebert, F. S. Stephens, and R. M. Diamond, *Phys. Rev. Letters* 24, 903 (1970).
25. Y. Horikawa, Y. Torizuka, A. Nakada, S. Mitsunobo, Y. Kojima, and M. Kimura, *Phys. Letters* 36B, 9 (1971).
26. R. M. Craig, J. C. Dore, G. W. Greenless, and D. L. Watson, *Nucl. Phys.* 86, 493 (1966).

ANALYZING POWERS FOR (\vec{p}, t) AND $(\vec{p}, {}^3\text{He})$ REACTIONS ON ${}^{13}\text{C}$

J. A. Macdonald, H. L. Harney,* J. Cerny, and A. D. Bacher[†]

Comparative studies of (p, t) and $(p, {}^3\text{He})$ transitions to mirror final states from odd-mass $T = 1/2$ targets have been used to test the assumptions made in current theories of direct two-nucleon transfer reactions.¹ Experiments involving polarized proton beams on p-shell targets have been carried out in the hope that the enhanced sensitivity to transferred spin, that reaction analyzing powers ought to show, would provide a powerful aid in the understanding of such reactions in general, as well as mirror cross-section ratios in particular. Earlier experiments on ${}^{16}\text{O}$ and ${}^{15}\text{N}$ targets showed that, while DWBA calculations provided good agreement with measured analyzing powers for many cases, some striking anomalies at variance with the theory were found in $L=2$ (p, t) transfers.² Two distinct types of $L=2$ transitions were evident; one agreed rather well with the theory, while the other showed analyzing powers which were virtually completely out of phase with the theory.

In order to further pursue this study, as well as to establish broader experience with empirical systematics, (p, t) and $(p, {}^3\text{He})$ reactions have been carried out on ${}^{13}\text{C}$.

Proton beams from the 88-inch cyclotron, using the polarized ion axial injection source, of 49.5 MeV and about 75% polarization with an intensity of ~ 10 -50 nA on target were used. Two pairs of counter telescopes were utilized, each pair being situated symmetrically on either side of the beam and feeding standard particle-identifier systems. Two angles could thus be observed simultaneously; angular distributions were obtained ranging from $\sim 15^\circ$ to $\sim 70^\circ$ in the center of mass. The target was a gas cell containing methane enriched to 93% ${}^{13}\text{CH}_4$, at about 200 Torr.

In the ${}^{13}\text{C}(\vec{p}, t){}^{11}\text{C}$ reaction, three examples of pure $L=2$ transfer were observed; these were to the $(3/2^-)$ ground state, the $(5/2^-)$ 4.32-

MeV, and the $(3/2^-)$ 4.80-MeV states. All three transitions showed similar gross features, characterized primarily by a broad negative maximum analyzing power at $\sim 35^\circ$. Figure 1 shows that the ground state transition was fit quite well by DWBA (solid curve). The potentials³ used included a spin-orbit term of 5.75 MeV in the proton channel, but none in the triton channel. When these same parameters were applied to the excited states, agreement with the data was less satisfactory, although prediction of the qualitative trends remained good.

It is reasonable to suppose that in fact there is also a spin-orbit interaction in the triton channel, although Hardy et al.² and Nelson et al.⁴ have reported moderate insensitivity of an-

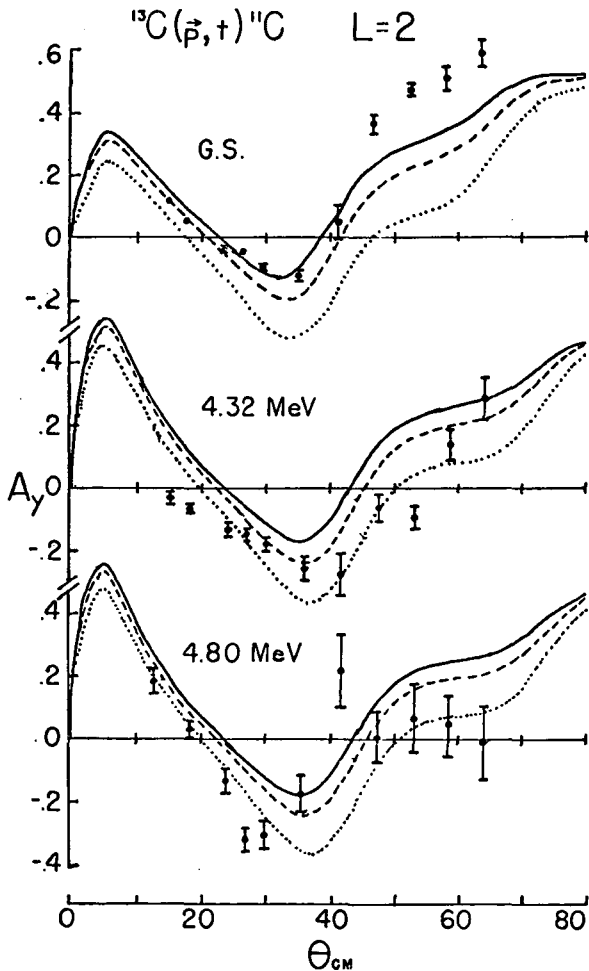


Fig. 1. Analyzing powers for $L=2$ transfers on ^{13}C . The curves are DWBA fits: the solid curve includes no spin-orbit potential in the triton channel; the dashed and dotted curves include $V_t(\text{s.o.})=2$ and 6 MeV, respectively. (XBL 732-182)

alyzing power calculations to a trinucleon spin-orbit potential. Their experience along with some polarization measurements of ^3He scattering,⁵ would indicate the strength of such a potential to be about 4-5 MeV. If one naively assumes that the two neutrons coupled to zero spin in ^3H are "spectators" to the proton, one might expect a triton spin orbit potential of about one-third of the proton spin-orbit potential (since, in the triton, the proton carries one-third of the orbital angular momentum).

Calculations were performed including a triton spin-orbit potential, $V_t(\text{s.o.})$ (a) equal to one-third that of the proton and (b) equal to the proton spin-orbit potential. The results are shown in Fig. 1 where it can be seen that for both the 4.32- and 4.80-MeV states the fit was considerably improved, although less dramatically in the latter case. Unfortunately, inclusion of the spin-orbit term in both channels substantially worsened the fit to the ground state, so that it appears difficult to fit simultaneously all three $L=2$ transitions with the same optical potential.

The (\vec{p}, t) reaction yielding the $1/2^-$ state at 2.00 MeV in ^{11}C required $L=0$ transfer and its differential cross section was in good agreement with theory. However, the analyzing power shown in Fig. 2(a), though exhibiting the rather typical (for $L=0$) positive maximum at about 60° predicted by the theory, shows very small values at angles forward of 40° , in sharp contrast to the DWBA. There is some similarity with the $^{12}\text{C}(\vec{p}, t)^{10}\text{C}$ ground state transition reported by Nelson et al.⁴ but the discrepancy with the theoretical calculations is, as yet, unaccounted for. Inclusion of a spin-orbit potential in the exit channel produced no significant improvement.

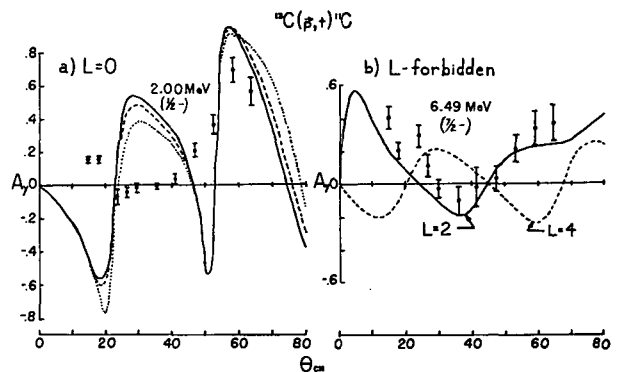


Fig. 2. (a) Analyzing power for $L=0$ transfer on ^{13}C . The curves are DWBA fits as described in the caption to Fig. 1.

(b) Analyzing power for L -forbidden transition on ^{13}C described in text. The curves are DWBA calculations. (XBL 732-178)

Figure 2(b) shows the analyzing power for the "L-forbidden" (\vec{p}, t) transition to the $7/2^-$ state at 6.49 MeV in ^{11}C . The mechanism for this reaction has been discussed in terms of a possible two-step process and also in terms of a $(1p\ 1f)$ neutron pair pickup to provide the necessary $L=4$, without satisfactory resolution of the problem.¹ The analyzing power of this transition shows qualitative similarity to $L=2$ cases and is, in fact, fit rather well by the DWBA using $L=2$. Since an $L=4$ calculation failed completely to account for the data, these results suggest a multistep process for this transition involving $L=2$ transfer which evidently dominates the analyzing power.

Using the (p, t) and $(p, ^3\text{He})$ reactions, pairs of states with $T = [T(\text{target}) + 1]$ can be populated, and theory predicts the identical shapes of the differential cross sections which have been well established experimentally.⁶ Reactions on ^{16}O leading to O^+ , $T=1$ analogs in $^{14}\text{O}(\text{g. s.})$ and $^{14}\text{N}(2.31\ \text{MeV})$ have also shown identical analyzing powers as predicted.⁷

In this work, two more pairs of analog final states have been measured: The ^{16}O target data have been further analyzed to extract analyzing powers for the 2^+ , $T=1$ states in ^{14}O (6.59 MeV) and ^{14}N (9.17 MeV); and the $1/2^-$, $T=3/2$

states at 12.48 MeV in ^{11}C and 12.94 MeV in ^{11}B have been measured from the ^{13}C target. In Fig. 3 one can see that the experimental analyzing powers are clearly similar. Of special interest was the mass-14 case where the $^{14}\text{O}(6.59\ \text{MeV})$ state analyzing power was shown² to be in disagreement with DWBA and therefore "anomalous" in shape for an $L=2$ transition. Nevertheless there is a clear similarity with its analog, particularly forward of 60° c.m. Furthermore, the mass-11 data in Fig. 3 do not conform to the typical $L=0$ transition analyzing power shape. The differential cross sections for both the $L=0$ and the $L=2$ analog transition pairs do agree with calculations, in spite of the curious analyzing power results. These anomalies stand unresolved at the present time.

DWBA theory predicts analyzing powers for two-nucleon transfer reactions which, in many cases, are in quite satisfactory agreement with experiment. Notwithstanding this success, a number of transitions have been observed which present considerable difficulties, and there is need for more theoretical effort to account for the results. The present paucity of analyzing power data for two-nucleon transfer reactions precludes establishing reliable empirical systematics which might be of value in either spectroscopic or reaction mechanism studies.

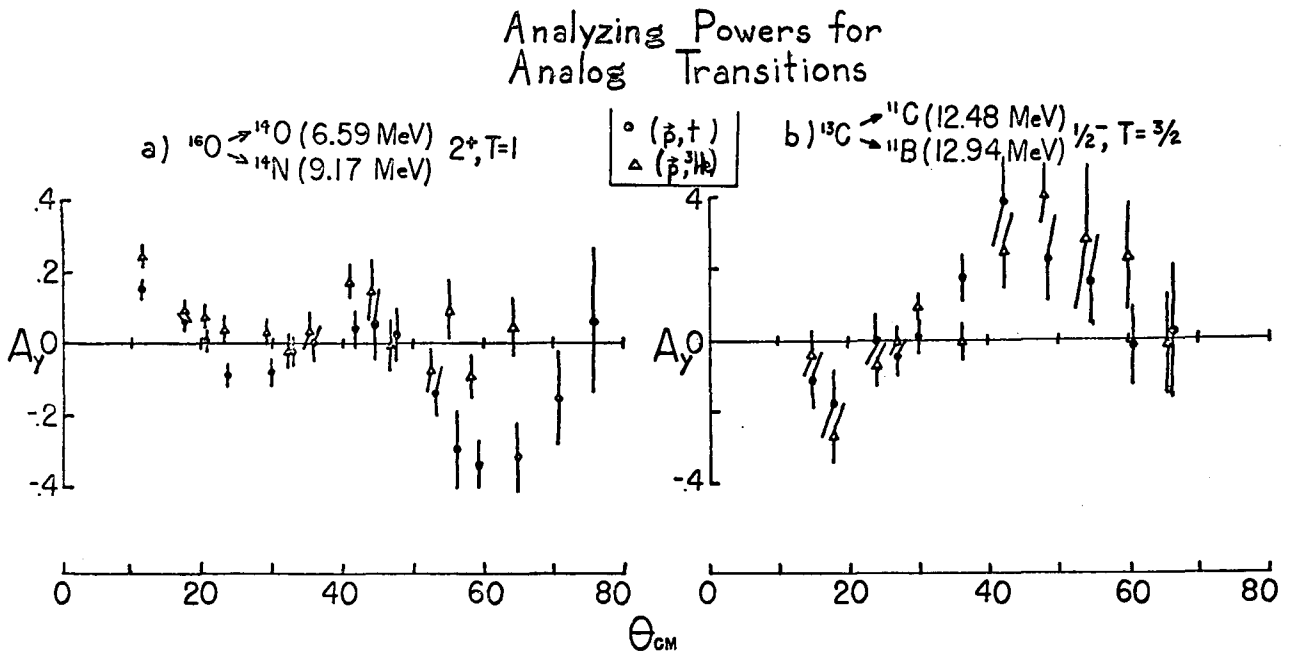


Fig. 3. Analyzing powers for (\vec{p}, t) and $(\vec{p}, ^3\text{He})$ analog transitions from (a) ^{16}O and (b) ^{13}C .
(XBL 732-177)

Footnotes and References

*Present address: Max Planck Institut für Kernphysik, Heidelberg, West Germany.

†Present address: Physics Department, Indiana University, Bloomington, Indiana 47401.

1. D. G. Fleming, J. Cerny, and N. K. Glendenning, Phys. Rev. 165, 1153 (1968).

2. J. C. Hardy, A. D. Bacher, G. R. Plattner, J. A. Macdonald, and R. G. Sextro, Phys. Rev. Letters 25, 298 (1970).

3. The optical potentials were the first proton and the second triton potentials from Table III in D. G. Fleming, J. C. Hardy, and J. Cerny, Nucl. Phys. A162, 225 (1971).

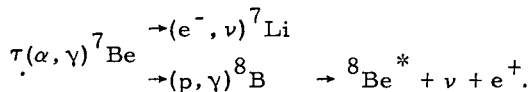
4. J. M. Nelson, N. S. Chant, and P. S. Fisher, Nucl. Phys. A156, 406 (1970).

5. W. S. McEver, T. B. Clegg, J. M. Joyce, and E. J. Ludwig, Phys. Rev. Letters 24, 1123 (1970).

THE SOLAR-NEUTRINO PROBLEM—A SEARCH FOR A NARROW STATE NEAR 15.8-MeV EXCITATION IN ${}^6\text{Li}$ USING THE $\alpha(\tau, p){}^6\text{Li}$ REACTION

N. A. Jelley, J. Arvieux, R. B. Weisenmiller, K. H. Wilcox, G. J. Wozniak, and J. Cerny

It has recently been pointed out^{1,2} that a possible explanation for the surprisingly low solar-neutrino flux detected by Davis³ would be the existence of a low-energy resonance ($J^\pi = 0^+$) in the ${}^3\text{He}+{}^3\text{He}$ system. In the sun this would lead to a considerable increase in the predicted cross section for the reaction $\tau(\tau, 2p)\alpha$ and, as a consequence, a decrease in the calculated neutrino flux from the competing reaction chains:



Such a resonance could lead² to a cross section for $\tau(\tau, 2p)\alpha$ some 10^4 times larger than that extrapolated from low-energy measurements,⁴ whereas with only a 10^2 increase in the $\tau(\tau, 2p)\alpha$ reaction rate the predicted neutrino flux would be below the experimental value found by Davis.

Fetisov and Kopysov,¹ from a consideration of the experimental data on the levels of ${}^6\text{Li}$ and ${}^4\text{He}$, predict a $0^+, T=1$ state in ${}^6\text{Be}$ near the threshold for formation of two ${}^3\text{He}$ clusters. This state is expected to be based upon a monopole excitation of an alpha-cluster with a large reduced width in the ${}^3\text{He}+{}^3\text{He}$ channel. If this state occurred just above the threshold for breakup of ${}^6\text{Be}$ into ${}^3\text{He}+{}^3\text{He}$ then a significant low-energy resonance in the reaction $\tau(\tau, 2p){}^4\text{He}$ could appear.

It has been suggested by Fetisov and Kopysov that such a level could be seen in ${}^6\text{Be}$ by using the reaction $\alpha(\tau, n){}^6\text{Be}$. However, owing to the difficulties in detecting neutrons, we have tried to find the analog state in ${}^6\text{Li}$, which would lie near 15.8 MeV excitation, using the $\alpha(\tau, p){}^6\text{Li}$ reaction.

Two counter telescopes were used to identify the protons from the $\alpha(\tau, p){}^6\text{Li}$ reaction, and proton spectra were collected at a ${}^3\text{He}$ bombarding energy of 49.4 MeV from the 88-inch cyclotron. A totally depleted 250- μm ΔE detector with a 3-mm E detector (rotated to 45°) and backed by a reject detector covered the excitation range 10-23 MeV for small angles, while a 3-mm ΔE with a 5-mm E (also rotated to 45°) and a reject detector covered 0-12 MeV excitation in ${}^6\text{Li}$. In the latter case the totally depleted sides of the lithium-drifted silicon detectors faced each other to ensure good particle identification spectra. A cylindrical gas-cell was used as the target with ${}^4\text{He}$ contained at $\sim 1/4$ atm pressure by 0.1-mil Havar⁵ foil.

A complete proton spectrum, combining data from the two counter telescopes, is shown in Fig. 1. ($\theta_{c.m.} = 23^\circ$ at 15.8 MeV excitation). The region about 15.8 MeV excitation is indicated and as is evident no peak can be seen above the continuum. From the 250-keV resolution (principally determined by the kinematics) and the statistical uncertainty, an upper limit of 40 $\mu\text{b}/\text{sr}$ can be placed on the c.m. cross section for forming a narrow state near 15.8 MeV in ${}^6\text{Li}$ via the $\alpha(\tau, p){}^6\text{Li}$ reaction. Similar spectra at $\theta_{c.m.} = 29^\circ$ and $\theta_{c.m.} = 36^\circ$ establish limits of $< 80 \mu\text{b}/\text{sr}$ $< 50 \mu\text{b}/\text{sr}$ respectively. The energy calibration in the region corresponding to 15.8 MeV excitation was established from spectra obtained at more backward angles.

Estimating the cross section with which this reaction would be expected to populate a state based upon a monopole excitation of an α -cluster is difficult. During the course of this experiment Parker et al.⁶ reported a limit on the spectroscopic factor $S({}^6\text{Be}^* \rightarrow {}^3\text{He}+{}^3\text{He})$ of less than 6×10^{-3} for any narrow state near the ${}^3\text{He}+{}^3\text{He}$ threshold in ${}^6\text{Be}$ from a study of the

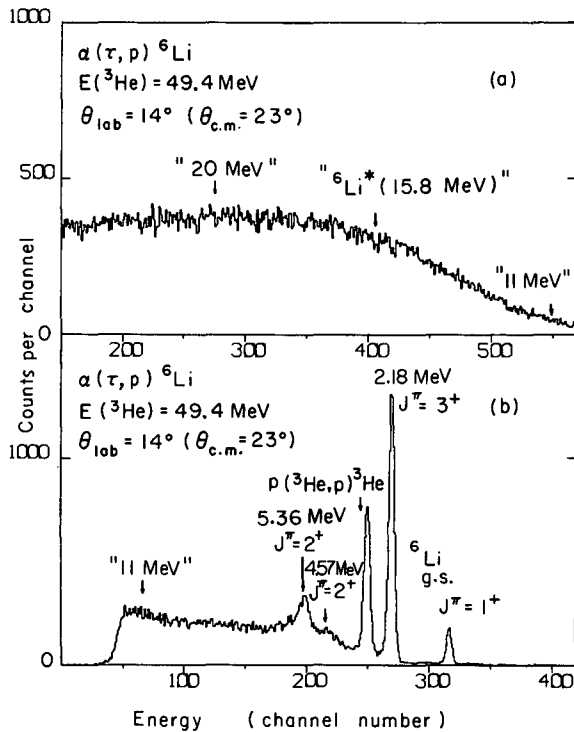


Fig. 1(a) Portion of proton spectrum taken at $\theta_{\text{lab}} = 14^\circ$ with a "thin" counter telescope ($\Delta E = 250 \mu\text{m}$, $E = 3 \text{ mm}$ at 45°), showing expected location of proton peak corresponding to a state at 15.8-MeV excitation in ${}^6\text{Li}$.

(b) Proton spectrum taken with a "thick" counter telescope ($\Delta E = 3 \text{ mm}$, $E = 5 \text{ mm}$ at 45°) at $\theta_{\text{lab}} = 14^\circ$ at the same time as spectrum (a) was collected, showing protons corresponding to low-lying states in ${}^6\text{Li}$ and knock-on protons from trace hydrogen impurity in the gas cell. (XBL 732-2284)

References

1. V. N. Fetisov and Yu. S. Kopysov, Phys. Letters **40B**, 602 (1972).
2. W. A. Fowler, Nature **238**, 24 (1972).
3. R. Davis, Jr., B. A. P. S. **17**, 527 (1972).
4. M. R. Dwarakaneth and H. Winkler, Phys. Rev. C **4**, 1532 (1971).
5. Hamilton Watch Co., Metals Division, Lancaster, Pennsylvania.
6. P. D. Parker, D. J. Pisano, M. E. Cobern, and G. H. Marks, Yale preprint 3074-3283.

${}^6\text{Li}({}^3\text{He}, t){}^6\text{Be}$ reaction. While we are unable to set a comparable limit for this spectroscopic factor, we have shown that even using a quite different reaction mechanism (stripping rather than charge exchange) no narrow state in ${}^6\text{Li}$ near the ${}^3\text{He}+{}^3\text{H}$ threshold has been seen, providing further evidence that such a state is unlikely to exist as required for a possible solution^{1,2} to the solar neutrino problem.

A NEW APPROACH TO THE NEGLECTED ALPHA-PARTICLE PICKUP REACTION ($\alpha, {}^8\text{Be}$)

G. J. Wozniak, N. A. Jelley, H. L. Harney,* R. B. Weisenmiller, and J. Cerny

The transfer of an alpha-cluster from a target to a projectile yields information about the alpha-cluster wave functions of the target nucleus. Thus the ($d, {}^6\text{Li}$) and (${}^3\text{He}, {}^7\text{Be}$) reactions have been studied by several groups^{1,2} on many targets over a large energy range and have been used to infer the extent of alpha-clustering in nuclei. It has been pointed out by Holmgren³ that the alpha-cluster used to describe the ground state of the target may not have the same structure as the alpha-cluster in ${}^6\text{Li}$ or ${}^7\text{Be}$, and furthermore all of these structures may differ from that of the free

alpha-particle. Therefore it is important to be able to compare data from several alpha-cluster pickup reactions.

An alpha-cluster pickup reaction in which the outgoing particle has a large alpha-structure amplitude is ($\alpha, {}^8\text{Be}$). The spectroscopic factor for this reaction calculated by Kurath⁴ is 1.50. The ${}^8\text{Be}$ ground state is unbound to decay into two alpha-particles by 92 keV, while the Q-values for ${}^6\text{Li} \rightarrow \alpha + d$ and ${}^7\text{Be} \rightarrow \alpha + {}^3\text{He}$ are -1.47 and -1.59 MeV, respectively. Since ${}^8\text{Be}$ has no excited states other than those of al-

most pure $\alpha + \alpha$ parentage below an excitation energy of 16 MeV, the alpha-clustering in ${}^8\text{Be}$ should be very similar to that of a free alpha-particle. Thus $(\alpha, {}^8\text{Be})$ should be a "good" alpha-particle pickup reaction. Because the alpha-particle will be transferred in an s-wave relative to the core as opposed to the p-wave transfer involved in $({}^3\text{He}, {}^7\text{Be})$, the theoretical interpretation will be simpler. Moreover, experimentally, events arising from the detection of ${}^8\text{Be}$ in its 2.90-MeV first excited state will be hindered by approximately a factor of 30 relative⁵ to the ground state, thus largely eliminating the problem of "shadow peaks" as experienced with ${}^7\text{Be}$. Studies of the $(\alpha, {}^8\text{Be})$ reaction at beam energies of 11.8 to 19.4 MeV (Ref. 6) and 35.5 to 41.9 MeV (Ref. 7) demonstrated that at these beam energies the main reaction strengths were in non-direct processes. However, at higher energies a more direct mechanism might be expected to dominate. Since ${}^8\text{Be}$ is particle unstable, the two breakup alpha-particles must be detected in coincidence. Thus use of this reaction for nuclear structure studies at higher energies has lagged far behind corresponding studies utilizing the $(d, {}^6\text{Li})$ and $({}^3\text{He}, {}^7\text{Be})$ reactions.

Recently, it has been demonstrated with the $({}^{12}\text{C}, {}^8\text{Be})$ reaction⁸ that the ${}^8\text{Be}$ decay products detected in a counter telescope (employing two ΔE 's and one E detector) will identify as a ${}^7\text{Li}$ in "particle identification" space. For light $A = 4N$ nuclei the Q-value of the $(\alpha, {}^8\text{Be})$ reaction is more positive than that of the $(\alpha, {}^7\text{Li})$ reaction, and the energy spectra from the $(\alpha, {}^8\text{Be})$ reaction can be observed for at least 14 MeV of excitation uncontaminated by states populated by the $(\alpha, {}^7\text{Li})$ reaction.

A setup similar to that described previously⁹ was used in preliminary experiments to study reaction products from the irradiation of a $150\text{-}\mu\text{g}/\text{cm}^2$ carbon target with 70-MeV alphas from the 88-inch cyclotron. The "observed cross section" of the four-particle transfer reaction ${}^{12}\text{C}(\alpha, {}^8\text{Be}){}^8\text{Be}$ is approximately two orders of magnitude less than that of the three-particle pickup reaction ${}^{12}\text{C}(\alpha, {}^7\text{Li}){}^9\text{B}$. In fact $(\alpha, {}^7\text{Li})$ peaks from the isotopic impurity ${}^{13}\text{C}$ are substantially larger than the $(\alpha, {}^8\text{Be})$ g.s. transitions (see Fig. 1) and obscure any evidence of the broad 11.4-MeV 4^+ state. Background seen above the ${}^8\text{Be}$ ground state results from α - α chance coincidence pileup and limits the counting rate to approximately 10 000 crossovers per sec in the first detector. Since the "absolute" cross section of ${}^{12}\text{C}(\alpha, {}^8\text{Be}){}^8\text{Be}$ is only $\sim 30\ \mu\text{b}/\text{sr}$ and the even smaller "observed cross section" is due to the 1% efficiency⁵ of detecting ${}^8\text{Be}$ events, one must substantially improve this detection efficiency before the $(\alpha, {}^8\text{Be})$ reaction can be fruitfully used to obtain spectroscopic information.

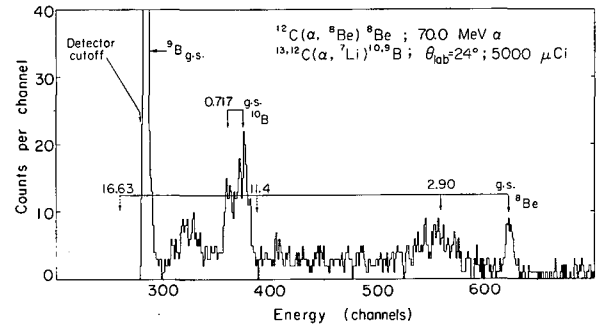


Fig. 1. Energy spectrum produced by bombarding a carbon target with 70.0-MeV alphas with a gate around the ${}^7\text{Li}$ region of the PI spectrum. ${}^{10}\text{B}$ states are produced by the $(\alpha, {}^7\text{Li})$ reaction on the ${}^{13}\text{C}$ isotopic impurity in the target. Most of the large peak due to the ${}^{12}\text{C}(\alpha, {}^7\text{Li}){}^9\text{B}$ reaction has been eliminated by an electronic energy threshold.

(XBL 732-2327)

From detailed calculations of the detection efficiency,⁵ it is possible to optimize the parameters of the detector configuration for measuring ${}^8\text{Be}$ events. While one wants to use large-area detectors to encompass as much of the ${}^8\text{Be}$ breakup cone as possible, this must be counterbalanced by the need to maintain adequate resolution (limited by kinematics) and by counting rate limitations. A way of overcoming this problem is to use a position sensitive detector (PSD) as the E-detector in a ΔE -E(PSD) counter telescope; this enables one to increase the solid angle while maintaining acceptable energy resolution. Noting Fig. 2, the approach then is as follows.

In a PSD a signal proportional to the distance of the detected particle from the grounded end times the energy of the particle (denoted XE) is generated. (This simply follows from the charge division on a resistive layer on the back of the surface barrier detector.¹⁰) There is also a signal proportional to the energy (E) generated at the front surface. Since the center-of-mass breakup energy of the two alpha-particles is so small (92 keV), the two alphas have essentially the same energy ($E/2$). One alpha particle therefore gives a signal $X_1E/2$, the other $X_2E/2$. Since both alphas arrive within a few picoseconds of each other the resultant position signal obtained by dividing out the energy dependence is

$$X = \frac{X_1 + X_2}{2}$$

Since this is the position at which the ${}^8\text{Be}$ would have been detected had it not decayed, the position signal can be used to identify those ${}^8\text{Be}$'s

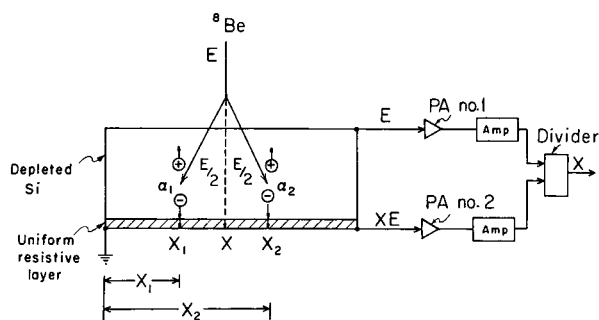


Fig. 2. Schematic diagram for the detection of the decay alphas from a ^8Be event in a position-sensitive surface barrier detector. See discussion in text. (XBL 732-2328)

emitted at the same angle, hence maintaining good energy resolution.

To test out this technique, a thin carbon target was bombarded with 65-MeV alphas. A counter telescope consisting of a wide-area (9.1×10.0 mm) rectangular transmission detector and a portion of a position-sensitive detector (10×50 mm) having depletion depths of 150 μm and 300 μm respectively was used to feed a particle identifier. Figure 3 shows a particle identification spectrum from this system. A gate was set around the $^6, ^7\text{Li}$ region and appropriate total-energy (E_T) signals were sent to a pulse-height analyzer. In "position" space four adjacent angular windows 1.2° wide were set and were used to route the E_T spectra in the analyzer.

An energy spectrum from one of these angular windows at $\theta_{\text{lab}} = 19^\circ$ (which was acquired in one hour) is shown in Fig. 4. Theoretically, one would expect a ^8Be detection efficiency of $\sim 20\%$. Very little background appears above the ^8Be ground state. Both the ^8Be 0^+ ground state and the 2.90-MeV 2^+ first excited state are made strongly with any evidence of the broad 11.4-MeV 4^+ state obscured by peaks from the $(\alpha, ^6\text{Li})$ reaction on ^{16}O and ^{13}C impurities (as noted above, ^6Li groups were also taken in this case). States above 16 MeV excitation in ^8Be can not be seen due to peaks arising from strongly populated ^9B and ^{10}B states made by the $(\alpha, ^6\text{Li})$ and $(\alpha, ^7\text{Li})$ reactions on ^{12}C .

These results demonstrate that a detailed systematic study of the $(\alpha, ^8\text{Be})$ reaction on light 4N nuclei is quite experimentally feasible if one employs a wide-area ΔE -E(PSD) counter telescope. At bombarding energies substantially greater than 50 MeV, where the reaction may be expected to be direct, this alpha-particle pickup reaction may prove to be a very powerful tool for studying alpha-particle clustering in nuclei.

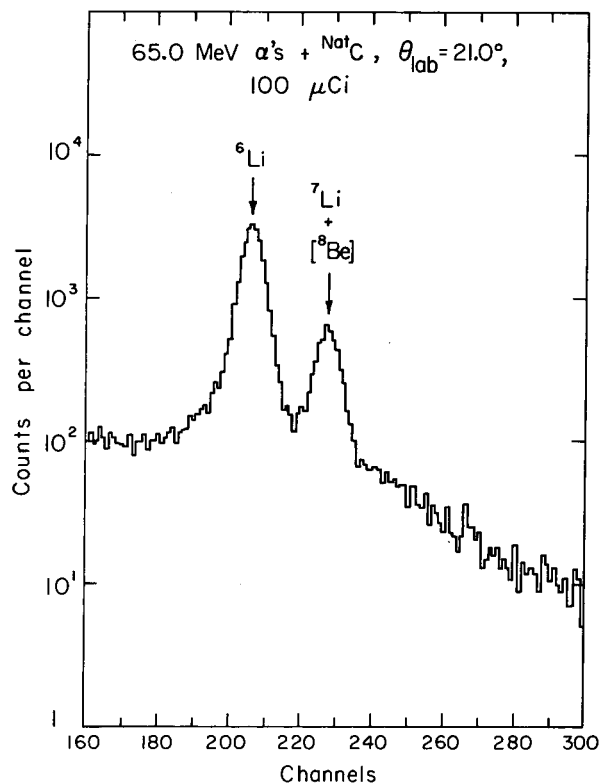


Fig. 3. A particle identification spectrum generated by a ΔE -E(PSD) system observing the reaction products from the irradiation of a carbon target by a 65.0-MeV alpha beam at $\theta_{\text{lab}} = 21^\circ$ over range of 4.8° . (XBL 732-2329)

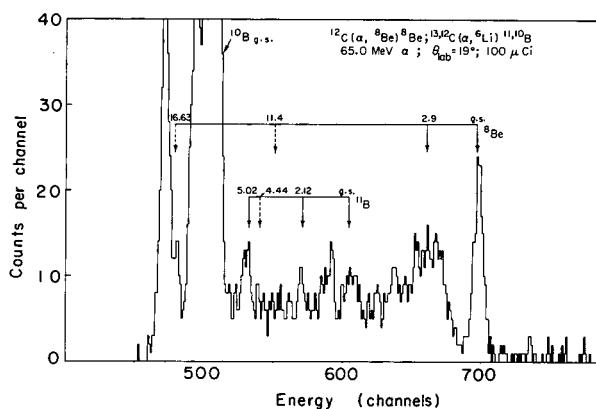


Fig. 4. The energy spectrum corresponding both to those events in the $^6, ^7\text{Li}$ peak region of the PI spectrum shown in Fig. 3 and to those events which were detected in one of four position gates. Most of the small peaks seen above the ^8Be 2.90-MeV peak can be accounted for by states arising from the $^{13}\text{C}(\alpha, ^6\text{Li})^{11}\text{B}$ reaction on ^{13}C isotopic impurities in the target. These could be easily eliminated by resetting the PI gate to observe only ^7Li and ^8Be events. (XBL 732-2330)

Footnote and References

* Present address: Max Planck Institut für Kernphysik, Heidelberg, West Germany.

1. K. Bethge, *Ann. Rev. Nucl. Sci.* 20, 255 (1970) and references therein.

2. C. Détraz, C. D. Zafiratos, C. E. Moss, and C. S. Zaidins, *Nucl. Phys.* **A177**, 258 (1971) and reference therein.

3. H. D. Holmgren, *International Conference on Clustering Phenomena of Nuclei*, Vol. 17, IAEA, Vienna, (1969).

4. D. Kurath, preprint.

5. H. L. Harney and G. J. Wozniak, LBL-1214.

6. P. Chevallier, F. Scheibling, G. Goldring, I. Plessner, and M. W. Sachs, *Phys. Rev.* **160**, 827 (1967).

7. R. E. Brown, J. S. Blair, D. Bodansky, N. Cue, and C. D. Kavaloski, *Phys. Rev.* **138**, B1394 (1965).

8. G. J. Wozniak, H. L. Harney, K. H. Wilcox, and Joseph Cerny, *Phys. Rev. Letters* **28**, 1278 (1972).

9. G. Butler, J. Cerny, S. W. Cospers, and R. L. McGrath, *Phys. Rev.* **166**, 1096 (1968).

10. *Guide to the Selection and Use of Position Sensitive Detectors, Nuclear Diodes*, edited by W. W. Daehnick (1969).

NEW SPECTROSCOPIC MEASUREMENTS VIA EXOTIC NUCLEAR REARRANGEMENT: THE $^{26}\text{Mg}(^7\text{Li},^8\text{B})^{25}\text{Ne}$ REACTION

K. H. Wilcox, N. A. Jelley, G. J. Wozniak, R. B. Weisenmiller, H. L. Harney, and J. Cerny

Although all of the $T_z = (N - Z)/2 = 5/2$ nuclei from ^{11}Li to ^{35}P (except ^{13}Be) are known to be particle stable, relatively few of their masses are accurately known and no data on the position of their excited states are available. Knowledge of their masses and energy levels is important, because it permits the testing of systematic mass relations and the comparison of experimental with theoretical level schemes for nuclei in a region far from stability. Good spectroscopic information on such neutron-excess nuclei has been difficult to obtain via "in-beam" reactions, since a large isospin transfer is required in the production process. Unusual heavy-ion rearrangement reactions may then be an excellent means of overcoming this restriction. In this spirit, we have investigated the feasibility of using the $(^7\text{Li},^8\text{B})$ reaction ($|\Delta T_z| = 3/2$) as a prototype for such studies.

By bombarding ^{26}Mg with an ~ 80 -MeV ^7Li beam from the 88-inch cyclotron, we have successfully detected ^8B nuclei from the $^{26}\text{Mg}(^7\text{Li},^8\text{B})^{25}\text{Ne}$ reaction ($Q \sim -22$ MeV), determining the mass of ^{25}Ne and, for the first time, the level structure of a $T_z = 5/2$ nucleus in the very light elements. Reactions yielding ^8B nuclei are particularly suitable for the study of neutron-excess isotopes for several reasons. Proton-rich ^8B is the lightest particle-stable $T_z = -1$ nuclide, and the fact that both ^7B and ^9B are proton-unbound simplifies its identification. Further, since ^8B possess no bound excited states, any possible "shadow peak" problems are eliminated.

This reaction was studied by utilizing a lithium beam produced with a PIG-type internal ion source.¹ Cathode buttons were employed which consisted of a mixture of 20% LiF and 80% tungsten pressed into a tantalum shell under very high pressure. Heating of the buttons by the arc maintained a partial pressure of lithium in the source. Additional lithium was supplied by a perforated cylindrical tantalum sleeve loaded with fused LiF which was inserted in the anode. Maximum long-term beam intensities of approximately 200 nA (3^+) on target were obtained with a low arc power which slowly vaporized the LiF over a period of ~ 4 hours. The maximum energy ^7Li beam (78.9 MeV) was used to bombard a 99.4% isotopically enriched self-supporting ^{26}Mg target of thickness $150 \mu\text{g}/\text{cm}^2$. The energy of the beam was determined using a high-precision analyzing magnet.² Outgoing ^8B particles were detected in two counter telescopes, each subtending a solid angle of 0.43 msr, located on opposite sides of the beam. These telescopes consisted of two ΔE detectors (15μ and 11μ thick), a $200\text{-}\mu\text{E}$ detector and a $500\text{-}\mu$ reject detector. After a fast coincidence among the first three detectors restricted the origin of all allowed events to a single beam burst, two particle identifications were performed and compared using the signals from the successive ΔE detectors and the E detector.³ Figure 1 presents a particle identification spectrum showing good separation in the region of the boron isotopes.

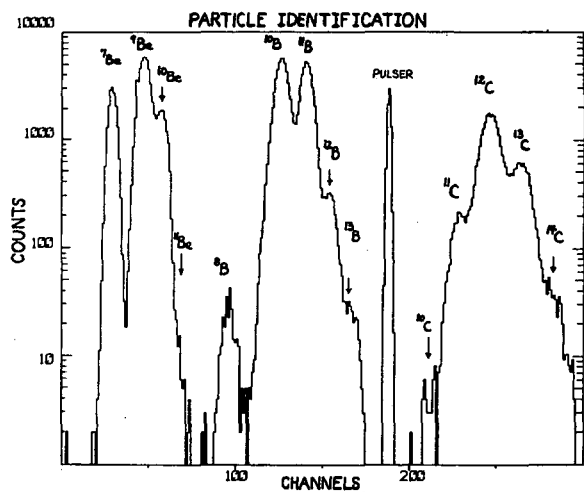


Fig. 1. A particle identification spectrum from 78.9-MeV ${}^7\text{Li}$ on ${}^{26}\text{Mg}$ at $\theta_{\text{lab}} = 10^\circ$. (XBL 732-183)

An energy calibration of the ${}^8\text{B}$ data shown in Fig. 2 was obtained by concurrently observing ${}^{10}\text{B}$ particles at $\theta_{\text{lab}} = 10^\circ, 15^\circ$, and 20° from the ${}^{26}\text{Mg}({}^7\text{Li}, {}^{10}\text{B}){}^{25}\text{Ne}$ reaction. Linearity and stability of the electronics were established by a high-precision pulser calibrated with alphas from a ${}^{212}\text{Pb}$ source. Reactions yielding ${}^8\text{B}$ nuclei from possible ${}^{12}\text{C}$ and ${}^{16}\text{O}$ contaminants were not observed. The ${}^{12}\text{C}({}^7\text{Li}, {}^8\text{B}){}^{11}\text{Be}$ reaction lies well outside the energy region of interest and the kinematic shifts (10° to 15°) of all the observed states (in ${}^{25}\text{Ne}$) were only consistent with the ${}^7\text{Li} + {}^{26}\text{Mg}$ reaction. The ${}^8\text{B}$ data collected at $\theta_{\text{lab}} = 15^\circ$ have been kinematically corrected and added to that obtained at $\theta_{\text{lab}} = 10^\circ$. In addition to the ground state, five excited states of ${}^{25}\text{Ne}$ can be seen in Fig. 2 lying at excitation energies of $1.65 \pm 0.05, 2.03 \pm 0.05, 3.25 \pm 0.08, 4.05 \pm 0.08$, and 4.7 ± 0.1 MeV. (The 3.25 MeV, and possibly the 4.05 MeV, state may be doublets). The cross section for population of the ground state at 10° and 15° was similar and was ~ 350 nb/sr.

From the energy of the ${}^8\text{B}$ ground state peak the Q-value for the ${}^{26}\text{Mg}({}^7\text{Li}, {}^8\text{B}){}^{25}\text{Ne}$ reaction is found to be -22.05 ± 0.10 MeV, corresponding to a mass excess for ${}^{25}\text{Ne}$ of -2.18 ± 0.10 MeV. This is in good agreement with the two previous experimental results of -1.96 ± 0.30 MeV by Goosman et al.⁴ and -2.2 ± 0.3 MeV by Kabachenko et al.⁵ (see discussion in Ref. 4), both from β -end point measurements arising in the decay of ${}^{25}\text{Ne}$. Our measurement is in some disagreement with the prediction of Thibault and Klapisch⁶ of -1.28 MeV obtained using the approach of Garvey et al.⁷ but employing results of more recent mass measurements.

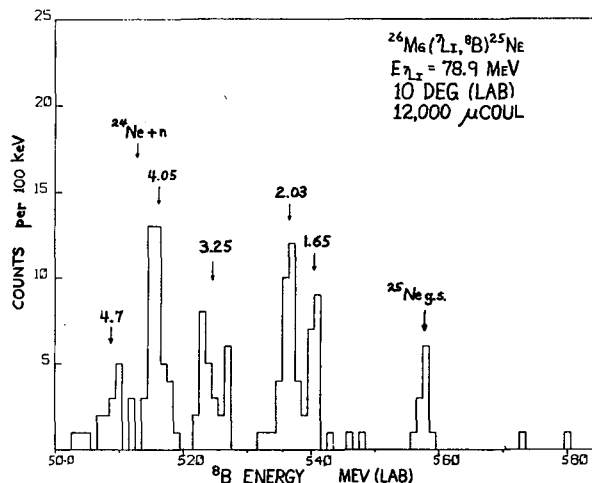


Fig. 2. A composite ${}^8\text{B}$ spectrum at $\theta_{\text{lab}} = 10^\circ$ including $\theta_{\text{lab}} = 15^\circ$ data kinematically corrected to 10° . Peaks corresponding to the ground state and five excited states of ${}^{25}\text{Ne}$ are indicated. (XBL 732-179)

Unfortunately no theoretical calculations are available on the level scheme of ${}^{25}\text{Ne}$. Assuming that the lowest states in ${}^{25}\text{Ne}$ arise from a $(\pi d_{5/2})^2 (vs_{1/2})^1$ configuration, simple particle-hole theorems lead one to expect it to possess a low-lying level structure similar to that of ${}^{27}\text{Mg}$. Since the first two excited states of ${}^{27}\text{Mg}$ lie at 0.98 and 1.69 MeV the ground state of ${}^{25}\text{Ne}$, as observed, is likely to be well separated from excited states. However, we see no evidence for a state near 1 MeV. Further observations must await detailed nuclear-model calculations of nuclei far from stability like ${}^{25}\text{Ne}$.

References

1. D. J. Clark, J. Steyaert, J. Bowen, A. Carneiro, and D. Morris, Sixth International Cyclotron Conference, U. of B. C., July 1972 and LBL-644 preprint.
2. A. D. Bacher, E. A. McClatchie, M. S. Zisman, T. A. Weaver, and T. A. Tombrello, Nucl. Phys. **A181**, 453 (1972).
3. G. W. Butler, J. Cerny, S. W. Cosper, and R. L. McGrath, Phys. Rev. **166**, 1096 (1968).
4. D. R. Goosman, D. E. Alburger, and J. C. Hardy, submitted to Phys. Rev. C, Nov. 1972.
5. A. P. Kabachenko, I. B. Kyznetsov, K. Sivek-Vilchinka, E. A. Skakun, and N. I. Tarantin, Joint Institute for Nuclear Science, Dubna Report: D7-5769, 204 (1971).

6. C. Thibault and R. Klapisch, Phys. Rev. C 6, 1509 (1972).

7. G. T. Garvey, W. J. Gerace, R. L. Jaffe, I. Talmi, and I. Kelson, Rev. Mod. Phys. Suppl., 41, S1 (1969).

MASS AND ENERGY LEVELS OF ^{17}Ne FROM THE $^{20}\text{Ne}(^2\text{He}, ^6\text{He})^{17}\text{Ne}$ REACTION

G. J. Wozniak, R. A. Mendelson, Jr.,* J. M. Loiseaux,† and J. Cerny

The ($^3\text{He}, ^6\text{He}$) reaction has been extensively used to determine the ground state masses of proton-rich ($T_Z = -3/2$) nuclei.¹ Less information is generally known about excited states of $T_Z = -3/2$ nuclei, except for ^{25}Si , which has been extensively investigated.² This present report deals with an investigation of the mass and energy level scheme of ^{17}Ne .

The experiment was performed with 62.6-MeV ^3He and 71.6-MeV ^4He beams from the 88-inch cyclotron. Semiconductor telescopes were used to observe the reaction $^{20}\text{Ne}(^3\text{He}, ^6\text{He})^{17}\text{Ne}$ and the calibration reactions $^{12}\text{C}(^3\text{He}, ^6\text{He})^9\text{C}$, $^{16}\text{O}(^3\text{He}, ^6\text{He})^{13}\text{O}$, and $^{12}\text{C}(\alpha, ^6\text{He})^{10}\text{C}$. Two similar four-counter telescopes (consisting of 130-, 110-, 300-, and 150- μm counters) were simultaneously employed at equal angles on opposite sides of the beam axis. The electronic system has been described previously³ and utilized a triple particle identifier, time-of-flight information, and subnanosecond pileup rejection to identify ^6He 's and to suppress spurious events.

^3He ions, bombarding a gas target consisting of a mixture of 80% separated isotope ^{20}Ne (99%) and 20% CO_2 , produced ^6He nuclei corresponding to ^{17}Ne states and to the ^9C and ^{13}O ground states (see Fig. 1 bottom). As shown in Fig. 1 (top), a background run on pure CO_2 gave no evidence of any contaminating states above the ^{13}O ground state. The well-known ground state masses of ^9C and ^{13}O were used as calibrants, and the slope of the ^6He energy scale was determined by observing the ground and first excited state in ^{10}C produced by alpha-particle bombardment of ethane.

From the present work the mass excess of ^{17}Ne is determined to be 16.48 ± 0.05 MeV, which is in good agreement with a previous value⁴ of 16.4 ± 0.25 MeV. The ^{17}Ne mass was obtained by averaging the Q-values measured with two detector systems at $\theta_{\text{lab}} = 11.6^\circ$ on opposite sides of the beam. ^{17}Ne completes an isobaric quartet and thus provides an opportunity to check the validity of the isobaric multiplet mass equation (IMME), $M = a + bT_Z + cT_Z^2$. Its predicted mass of 16.514 ± 0.021 MeV (IMME) agrees with our experimental number, thus indicating the validity of the IMME. The Kelson-Garvey nuclidic mass relationship⁵ predicts a mass of

16.63 MeV for the ^{17}Ne ground state which is also in reasonable agreement with experiment.

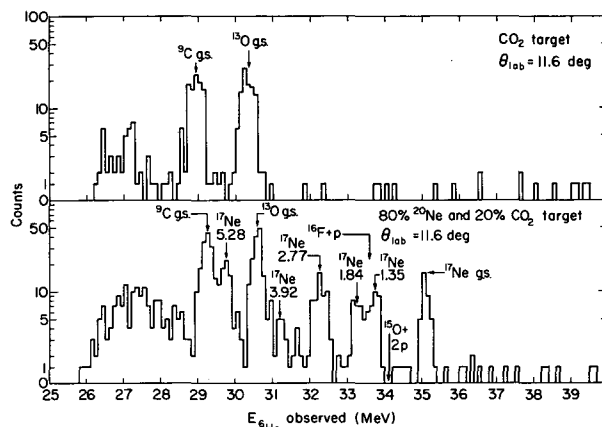


Fig. 1. The upper half shows the energy spectrum of the ($^3\text{He}, ^6\text{He}$) reaction on a CO_2 target with a 62.6-MeV ^3He beam. The lower half is the spectrum of the same reaction on a mixed ^{20}Ne and CO_2 target. (XBL 7012-4225)

Over an excitation range of 5 MeV, five excited states of ^{17}Ne were observed (see Fig. 1). The experimental energy resolution for the ^{17}Ne states is 250 keV. Except for the strongly populated 5.28-MeV level, possible levels above 3.92 MeV excitation are obscured by the calibrant ^9C and ^{13}O ground state peaks. Excitation energies determined at $\theta_{\text{lab}} = 11.6^\circ$ from the two detection systems are given in Table I.

Table I. $T = 3/2$ energy levels observed in ^{17}Ne .

J^π	$E_x(^{17}\text{Ne})$ MeV \pm keV	Coefficients of IMME for A=17		
		b	c	d
		keV (\pm keV)		
$1/2^-$	(M-A)=16.48 \pm 50	-2878(5.4)	238(8.1)	4.8(9.1)
$3/2^-$	1.350 \pm 70	-2845(5.6)	216(8.1)	-8.7(11.5)
	1.840 \pm 70			
	2.770 \pm 70			
	3.920 \pm 90			
	5.280 \pm 70			

Differential c.m. cross sections for transitions to the ground state and first four excited states were determined to be about 100 nb/sr, with the 5.28-MeV level being populated a factor 2 stronger.

Other known $T=3/2$, $A=17$ levels⁶ are compared with levels found in the present experiment in Fig. 2. It is clear that the 1.35-MeV level of ^{17}Ne corresponds to the first excited state of its mirror ^{17}N and the second analog levels in ^{17}O and ^{17}F . However, with our experimental resolution, it is impossible to tell whether the peak populated at 1.84 MeV excitation in ^{17}Ne consists of one or two states corresponding to analogs of the 1.861-MeV state or the 1.908-MeV state in ^{17}N , or both. The 2.77-MeV peak in the ^{17}Ne spectrum was consistently broader than the experimental resolution in both systems and probably corresponds to an unresolved doublet.

Since the first excited $J^\pi=3/2^+$, $T=3/2$ states are known for all four member nuclei of the $A=17$ isobaric quartet, the coefficients of the

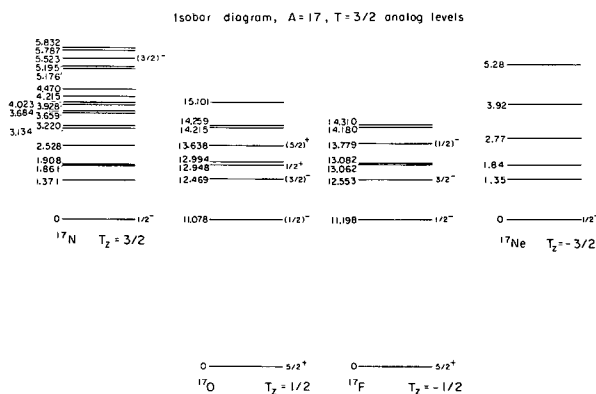


Fig. 2. Energy level diagrams of the members of the mass-17 isospin quartet showing the positions of the $T=3/2$ levels in each nucleus.

(XBL 7012-4292)

CONCERNING THE LOWEST $T=3/2$ STATE IN $^{41}\text{Sc}^\dagger$

R. A. Gough, R. G. Sextro, and J. Cerny

Precise energies have been reported for the lowest $T=3/2$ states in all mass $4n+1$, $T_z=1/2(N-Z)=-1/2$ nuclei with $9 \leq A \leq 41$.¹⁻¹⁰ Such measurements provide one component in testing the model-independent isobaric multiplet mass equation (IMME).¹ Using a techni-

que which provides a simple method of cross checking one such measurement against another, we have observed the β^\dagger -delayed proton decay of ^{24}Mg , ^{25}Si , ^{29}S , ^{37}Ca , and ^{41}Ti . These results lead to a value of 5.935 ± 0.008 MeV for the excitation energy of the lowest

mass equation can be calculated and compared to values determined from the four members of the ground state ($J^\pi=1/2^+$, $T=3/2$) quartet. See Table I. As in all previously studied multiplets with the exception of $A=9$, the d coefficient of T_z^3 arising in the second-order treatment of the IMME for the $A=17$ ground state multiplet is consistent with zero. The d coefficient of the first excited state multiplet is also of this order, and the b and c coefficients show at most only a slight dependence on excitation energy and spin.

Thus the present experiment does not indicate any strong energy dependence of the b, c, and d terms of the IMME for the $A=17$ system.

Footnotes and References

* Present address: University of California, San Francisco Medical Center.

† Permanent address: University of Grenoble, Grenoble, France.

1. J. Cerny, *Ann. Rev. Nucl. Sci.* **18**, 27 (1968).
2. W. Benenson, J. Driesbach, I. D. Proctor, G. F. Trentelman, and B. M. Freedom, *Phys. Rev. C* **5**, 1426 (1972).
3. Joseph Cerny, R. A. Mendelson, Jr., G. J. Wozniak, John E. Esterl, and J. C. Hardy, *Phys. Rev. Letters* **22**, 612 (1969).
4. R. A. Esterlund, R. McPherson, A. M. Poskanzer, and P. L. Reeder, *Phys. Rev.* **156**, 1094 (1967); A. M. Poskanzer, private communication.
5. I. Kelson and G. T. Garvey, *Phys. Letters* **23**, 689 (1966).
6. F. Ajzenberg-Selove, *Nucl. Phys.* **A166**, 1 (1971).

$T=3/2$ in ^{41}Sc , which disagrees with the previously accepted value of 5.863 ± 0.006 MeV (Refs. 2 and 6)* from $^{40}\text{Ca}(p,p)$ resonance measurements.

Experimental masses for only three members of the $A=41$, $T=3/2$ multiplet are known: the ^{41}K ground state,¹¹ its analog in ^{41}Ca (Ref. 12) and this new result for ^{41}Sc . The IMME can now be used to predict a value of -15.78 ± 0.03 MeV for the ground state mass excess of ^{41}Ti . This agrees favorably with a value of -15.72 MeV predicted by Kelson and Garyey.¹³ Although the lowest $T=3/2$ level in ^{41}Sc has been previously studied in lower-resolution, β^+ -delayed proton work,¹⁴ a precise measurement of its excitation energy was not reported.¹⁵

In the present experiment, a He-jet transport system¹⁶ and standard particle-identification techniques were used to detect β^+ -delayed protons emitted from the lowest $T=3/2$ level in each of the following $T_z=-1/2$ nuclei: ^{21}Na , ^{25}Al , ^{29}P , ^{37}K , and ^{41}Sc . Their precursors, with half-lives ranging from 88 to 220 msec^{14, 17-19}, were produced by ($^3\text{He}, 2n$) reactions on target nuclei of ^{20}Ne , ^{24}Mg , ^{28}Si , ^{36}Ar , and ^{40}Ca using ~ 3.5 μA of beam on target. A beam energy of 29.5 MeV was used for all but the ^{36}Ar ($^3\text{He}, 2n$) reaction for which the energy was increased to 40 MeV to improve the yield. The counter-telescope employed consisted of a 48- μm ΔE followed by a 500- μm E detector with an additional reject detector to aid in background reduction. An experimental energy resolution of 30 keV (FWHM) was achieved, permitting centroid determinations reproducible to within one or two keV.

Typical background-free identified-proton energy spectra resulting from the decay of ^{25}Si and ^{41}Ti are shown in Fig. 1. The low log ft values [typically ~ 3.3 (Ref. 20)] associated with superallowed β^+ transitions provide an unambiguous identification of the observed $T=3/2$ decays. In Fig. 1(a) the $T=3/2$ level in ^{25}Al is seen to decay both to the ground state of ^{24}Mg (peak 1) and to its first excited state (peak 2). In Fig. 1(b), peak 3 represents proton decays from the lowest $T=3/2$ level in ^{41}Sc to the ground state of ^{40}Ca . As discussed in the following paragraph, this ground state branch accounts for $\geq 86\%$ of all the proton decays from the analog state.

Using thinner ΔE counters, a search was made for decays from the lowest $T=3/2$ level in ^{41}Sc to the first three excited states in ^{40}Ca . A $4 \pm 2\%$ branch to the 3.35-MeV level was observed, while no decays corresponding to the transition to the 3.90-MeV level in ^{40}Ca were detected. A limit of $\leq 10\%$ was set for branching to the second excited state in ^{40}Ca at 3.73 MeV. An improved measurement of this branch

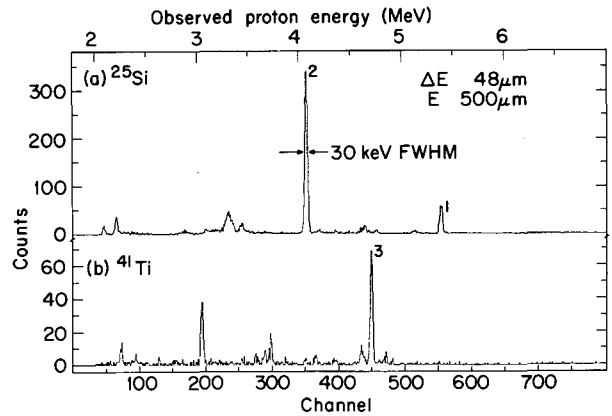
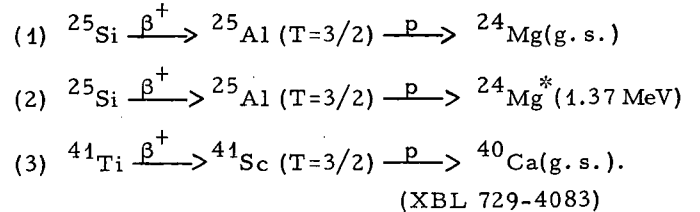


Fig. 1. Beta-delayed proton spectra of (a) ^{25}Si and (b) ^{41}Ti . The numbered peaks correspond to proton emission from the lowest $T=3/2$ analog states in ^{25}Al and ^{41}Sc via the decays:



could not be made owing to low-energy proton background from ^{40}Sc (Ref. 21) [produced via $^{40}\text{Ca}(^3\text{He}, p2n)$] and to the presence of an observed level at 6.105 MeV in ^{41}Sc which possibly decays, with the same energy, to the third excited state in ^{40}Ca .

The results of our energy measurements, corrected for detector dead layers and very slight gain drifts, appear in Table I, where center-of-mass (c.m.) proton decay energies are shown for the lowest $T=3/2$ level in each of the $T_z=-1/2$ nuclides investigated. Each entry in the first column is a weighted average of values deduced from previous experimental measurements. Since the decay energies for ^{37}K and ^{25}Al are the most precisely known, they were used as calibrants. Our results are presented in the second column of the table. Excepting the 72-keV discrepancy in the ^{41}Sc result, the present values agree very well with the results of earlier experiments.

Information on the locations, widths and (isospin-forbidden) decay modes of high-isospin states is important to an understanding of the charge independence of nuclear forces. The lowest $T=3/2$ level in ^{41}Sc at 5.935 ± 0.008 MeV proton decays primarily to the ^{40}Ca ground state with a c.m. decay energy of 4.851 ± 0.006 MeV. Our IMME prediction of -15.78 ± 0.03 MeV for the ground state mass excess of ^{41}Ti is of interest because no simple technique exists for its precise experimental measurement.

Table I. Center-of-mass proton decay energies of the lowest $T=3/2$ analog states.

Precursor $T=3/2$ $T_z = -3/2$	β^+	Emitter $T=3/2$ $T_z = -1/2$	p	Residual nucleus $T_z = 0$	Proton decay energies (c. m.)		
					Deduced from previous work (MeV \pm keV)	Present results (MeV \pm keV)	Best value (MeV \pm keV)
^{37}Ca	β^+	^{37}K	p	$^{36}\text{Ar}(\text{g. s.})$	3.1898 ± 2.4^a	Calibrant	
^{25}Si		^{25}Al		$^{24}\text{Mg}(1.37)$	$4.2623 \pm 2.8^{b, c, d}$	Calibrant	
^{41}Ti		^{41}Sc		$^{40}\text{Ca}(\text{g. s.})$	4.779 ± 4^d	4.851 ± 6	4.851 ± 6
^{21}Mg		^{21}Na		$^{20}\text{Ne}(1.63)$	$4.908 \pm 5^{e, f}$	4.898 ± 6	4.904 ± 4
^{25}Si		^{25}Al		$^{24}\text{Mg}(\text{g. s.})$	$5.6309 \pm 2.8^{b, c}$	Calibrant	
^{29}S		^{29}P		$^{28}\text{Si}(\text{g. s.})$	$5.633 \pm 4^{c, g}$	5.633 ± 6^h	5.633 ± 3
^{21}Mg		^{21}Na		$^{20}\text{Ne}(\text{g. s.})$	6.542 ± 5^e	6.533 ± 6	6.538 ± 4

^aReferences 4 and 10.

^bReferences 5, 7 and 10.

^cProton resonance energies in Ref. 7 were measured with probable errors of 6 keV (Ref. 22).

^dReference 2.

^eReference 8.

^fReference 23.

^gReferences 3, 5, 7, and 9.

^hBy combining this result with the resonance energy measurements from Refs. 3, 7, and 9, and with the direct excitation energy measurements from Refs. 5 and 9, an improved value for the ^{29}P ground state mass excess of -16.949 ± 0.004 MeV can be calculated.

Table II. Branching ratios and log ft values for the positron decay of ^{24}Mg .

Energy level in ^{24}Na	Branching ratio (%)	Log ft
g. s.	15.80±4.0	5.25±0.10
0.338	40.70±5.0	4.79±0.05
1.723	10.90±2.0	5.10±0.07
3.551	0.45±0.07	6.09±0.06
4.293	5.36±0.31	4.82±0.02
4.468	10.45±0.46	4.48±0.02
5.022	2.53±0.25	4.94±0.04
5.751	0.34±0.03	5.59±0.03
5.855	0.62±0.04	5.30±0.03
5.971	0.47±0.06	5.38±0.05
6.085	0.14±0.01	5.87±0.03
6.20	0.14±0.02	5.84±0.06
6.346	0.86 ^{+0.07} -0.42	4.99 ^{0.03} -0.17
6.488	1.07±0.06	4.84±0.02
6.775	0.30 ^{+0.21} -0.11	5.29 ^{+0.23} -0.13
8.004	2.43 ^{+0.57} -0.21	3.85 ^{+0.09} -0.03
8.296	0.31±0.03	4.60±0.03
6.411	0.18 ^{+0.02} -0.10	4.77 ^{+0.05} -0.19
8.812	1.19±0.13	3.72±0.04
8.969	2.79±0.16	3.26

Footnotes and References

* Throughout this report, the 1971 Atomic Mass Table¹¹ is used in all calculations requiring masses for which explicit references are not cited.

† Condensed from Physics Letters 43B, 33 (1973).

1. J. Cerny, Ann. Rev. Nucl. Sci. 18, 27 (1968).

2. P. M. Endt and C. Van der Leun, Nucl. Phys. A105, 1 (1967) and references therein.

3. D. H. Youngblood, G. C. Morrison, and R. E. Segel, Phys. Letters 22, 625 (1966).

4. D. R. Goosman and R. W. Kavanagh, Phys. Rev. 161, 1156 (1967).

5. G. C. Morrison, D. H. Youngblood, R. C.

Bearse, and R. E. Segel, Phys. Rev. 174, 1366 (1968).

6. L. R. Greenwood, T. R. Canada, and C. M. Class, Bull. Am. Phys. Soc. 13, 1382 (1968); see also D. H. Youngblood, B. H. Wildenthal, and C. M. Class, Phys. Rev. 169, 859 (1968).

7. B. Teitelman and G. M. Temmer, Phys. Rev. 177, 1656 (1969).

8. A. B. McDonald, J. R. Patterson, and H. Winkler, Nucl. Phys. A137, 545 (1969).

9. T. T. Bardin, J. A. Becker, and T. R. Fisher, Phys. Rev. C 5, 1351 (1972).

10. W. Benenson, E. Kashy, and I. D. Proctor, Bull. Am. Phys. Soc. 17, 891 (1972) and private communication.

11. A. H. Wapstra and N. B. Gove, Nucl. Data Tables 9, 265 (1971).

12. T. A. Belote, F. T. Dao, W. E. Dorenbusch, J. Kuperus, J. Rapaport, and S. M. Smith, Nucl. Phys. A102, 462 (1967) and references therein; U. Lynen, R. Bock, R. Santo, and R. Stock, Phys. Letters 25B, 9 (1967).

13. I. Kelson and G. T. Garvey, Phys. Letters 23, 689 (1966).

14. A. M. Poskanzer, R. McPherson, R. A. Esterlund, and P. L. Reeder, Phys. Rev. 152, 995 (1966).

15. A complete report of these studies on the β^+ -delayed proton emission of ^{41}Ti will be published.

16. R. D. Macfarlane, R. A. Gough, N. S. Oakey, and D. F. Torgerson, Nucl. Instr. Methods 73, 285 (1969); R. G. Sextro, R. A. Gough, and J. Cerny, to be published.

17. J. C. Hardy and R. E. Bell, Can. J. Phys. 43, 1671 (1965).

18. P. L. Reeder, A. M. Poskanzer, R. A. Esterlund, and R. McPherson, Phys. Rev. 147, 781 (1966).

19. J. C. Hardy and R. I. Verrall, Phys. Letters 13, 148 (1964).

20. J. C. Hardy and B. Margolis, Phys. Letters 15, 276 (1965).

21. R. I. Verrall and R. E. Bell, Nucl. Phys. A127, 635 (1969).

22. G. M. Temmer, private communication.

23. F. Ajzenberg-Selove, Nucl. Phys. A190, 1 (1972).

THE BETA-DELAYED PROTON DECAY OF $^{21}\text{Mg}^\dagger$

R. G. Sextro, R. A. Gough, and J. Cerny

The nuclide ^{21}Mg is one of the series of $T_z = -3/2$, $A = 4n + 1$ β^- -delayed proton precursors. These nuclei have substantial position decay branches to particle-unbound levels in their daughters. The energies and intensities of the particle spectra resulting from breakup of the unbound levels can be used to determine excitation energies of states in the β^- -decay daughter nucleus, and the transition strength feeding these levels. If these relative transition rates can be related to absolute decay rates to the daughter, measurement of the particle decays will yield absolute ft values for the preceding β^- decay. This method permits the accurate determination of β^- -decay rates spanning several orders of magnitude.

The external beam of the 88-inch cyclotron was used to initiate the $^{20}\text{Ne}(^3\text{He}, 2n)^{21}\text{Mg}$ reaction. The chosen bombarding energy of 29.5 MeV was also sufficient to produce ^{20}Na [via $^{20}\text{Ne}(^3\text{He}, p2n)$]; however, ^{20}Na is a β^+ -delayed alpha precursor and has no known β^+ -decay branch to proton unbound levels. In order to minimize the background and obtain high-resolution particle spectra, a helium-jet system was developed which allowed the transport of the activity away from the target area and beam to a position in front of a counter telescope. (A description of this system is in another section of this Report.)

Several different ΔE - E detector combinations were used in the course of these experiments in order to span a broad energy range. All detectors were cooled to -25°C , except the very thin ΔE detectors. The electronic energy resolution was dependent upon the exact combination of detectors, but ranged from 25 keV to 45 keV FWHM.

Combining half-life data from four independent experiments, our determination of the ^{21}Mg half-life is 123.1 ± 3.3 msec. This compares well with the previous measurement of 121 ± 5 msec.¹ The resultant weighted average of 122.5 ± 2.8 msec is used for all subsequent calculations and results quoted in this paper.

The lowest $T = 3/2$ states in ^{21}Na and ^{25}Al are accurately known^{2,3} and exhibit significant proton decay branches to both the ground and first-excited states in their respective decay daughters, ^{20}Ne and ^{24}Mg . The energies of their prominent proton decays -- $E_{\text{lab}} \approx 4.09$ and 5.40 MeV for ^{25}Al , and ≈ 4.67 and 6.23 MeV for ^{21}Na -- can therefore be used as calibration points for the high-energy portion of the ^{21}Na proton spectrum ($E_{\text{lab}} \approx 2$ to 7 MeV). As part

of this calibration, the delayed-proton precursor ^{25}Si was produced by the $^{24}\text{Mg}(^3\text{He}, 2n)^{25}\text{Si}$ reaction at 29.5 MeV. The low-energy proton spectra ($E_{\text{lab}} \approx 700$ keV to 2 MeV) were calibrated by using the well-known states⁴ at $E_x \approx 4.29$ and 4.47 MeV in ^{21}Na .

An identified proton spectrum obtained with an $11\text{-}\mu\text{m}$ ΔE and $265\text{-}\mu\text{m}$ E detector telescope is shown in Fig. 1. The energy region between 2.4 and 7.5 MeV, taken with $50\text{-}\mu\text{m}$ ΔE and $500\text{-}\mu\text{m}$ E counters, is shown in Fig. 2. The numbers above the peaks correspond to the peak numbers and decay assignments in Table I. Additional data, not shown here, were acquired with a $6\text{-}\mu\text{m}$ ΔE and $50\text{-}\mu\text{m}$ E telescope, spanning the energy range from ~ 0.7 to 2.2 MeV.

Three peaks arise from the decay of the $T = 3/2$ state (these are denoted by vertical arrows in Figs. 1 and 2) corresponding to decays to the ground state and first- and third-excited states. The proton decay to the second-excited state was not observed, although it would appear in the region of peak 8. This peak consistently exhibits a width three times larger than is observed for the other isospin-forbidden decays.

As can be noted from the ^{21}Mg decay scheme shown in Fig. 3, states in ^{21}Na with $E_x \geq 6.56$ MeV are unbound to alpha decay to ^{17}F . In particular, the lowest $T = 3/2$ state is unbound by 2.4 MeV.⁵ An experimental search for this possible decay mode used a counter telescope

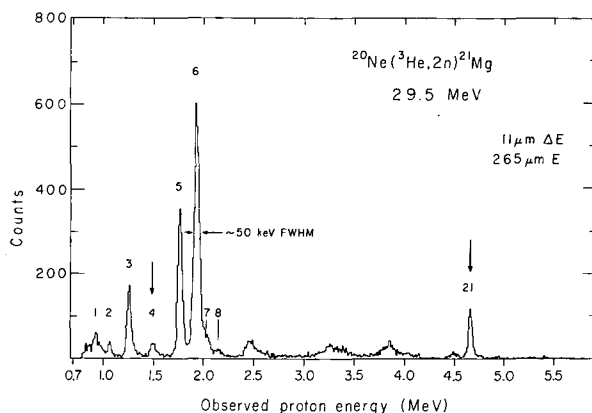


Fig. 1. Identified protons following the decay of ^{21}Mg . The energies corresponding to the peak numbers are shown in Table I. Vertical arrows denote decays of the analog state.

(XBL 72 10-5776)

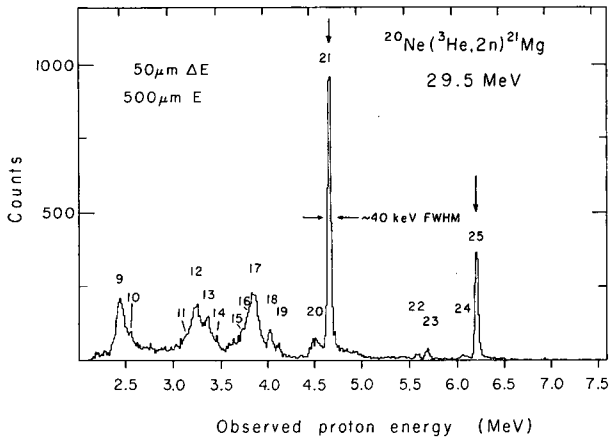


Fig. 2. Delayed protons from ^{21}Mg with energies greater than 2.5 MeV. The numbers correspond to energies listed in Table I. Vertical arrows point to decays from the $T=3/2$ state.

(XBL-7210-5777)

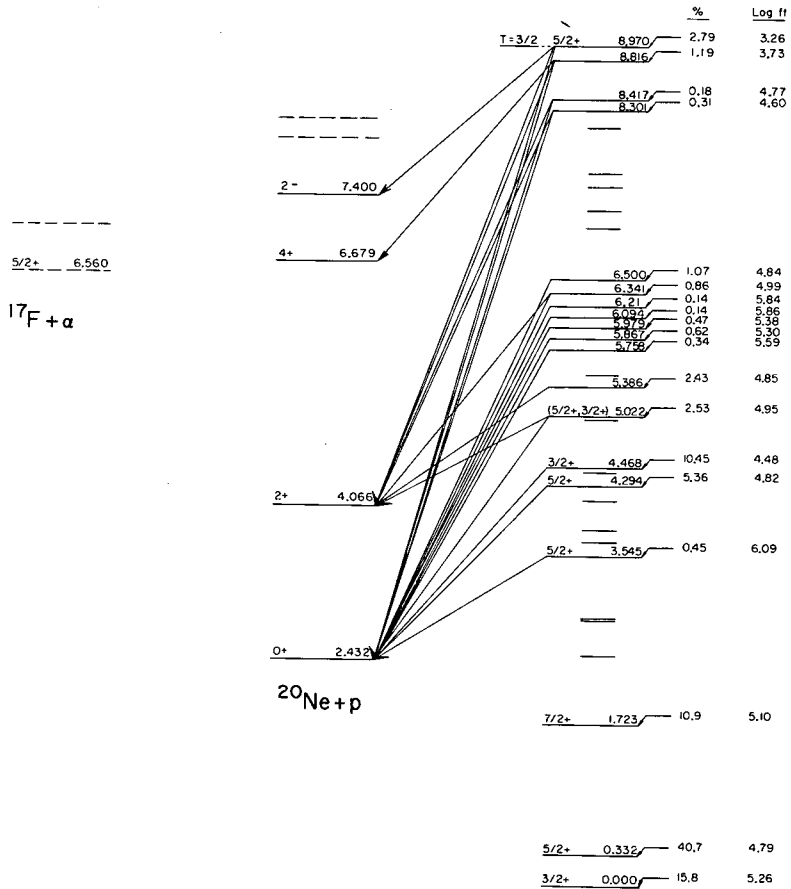
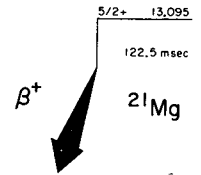


Fig. 3. Proposed decay scheme. The level energies in ^{21}Na listed above 5 MeV are from this work only (except for the $T=3/2$ state). Branching ratios and log ft values are also listed.

(XBL 731-2055)

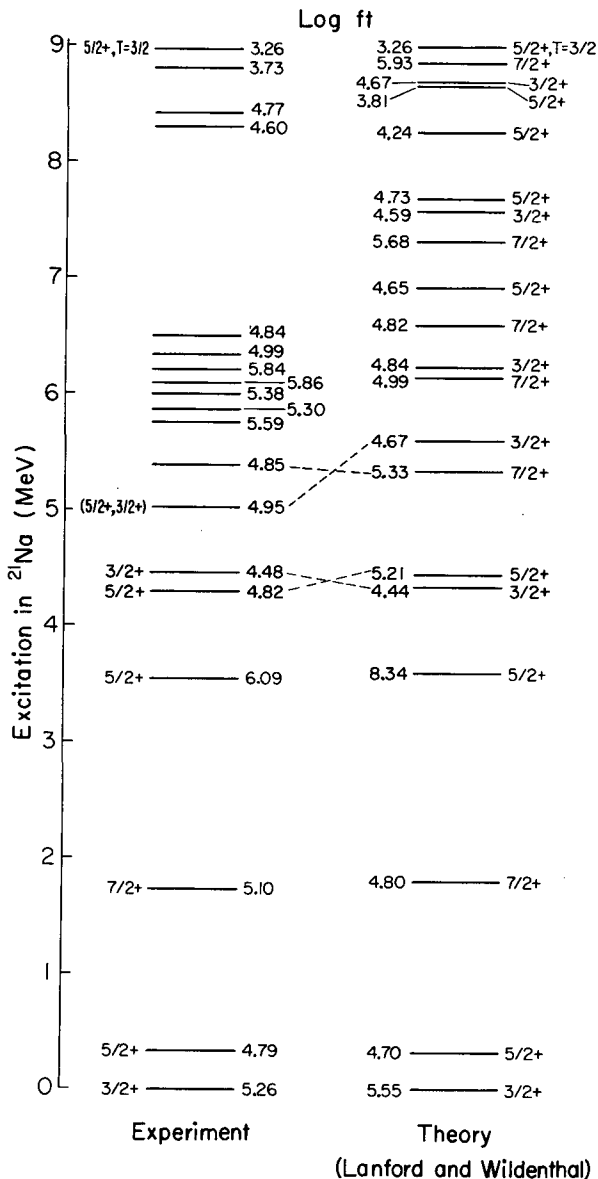


Fig. 4. Comparison of experimental and theoretical excitation energies and $\log ft$ values. The experimental energies below 2 MeV are from Ref. 4. (XBL 733-2473)

consisting of a 4- μm ΔE detector, a 48- μm E detector, and a 100- μm anti-coincidence detector to reject long-range particles. Alpha particles with energies as low as 1.4 MeV could be reliably identified. The resulting spectrum is dominated by the delayed-alpha decay of ^{20}Na . Since proton data were collected simultaneously,

direct comparison of the intensities could be made. This establishes a limit for this possible branch of < 1.6% of the total particle decay.

The center of mass (c.m.) proton energy and the parent state in ^{21}Na for each of 25 analyzed peaks are shown in Table I. The observed proton energies are averages over several different experiments and ΔE -E detector combinations.

Absolute branching ratios for β^+ -decay to these unbound levels can be obtained by utilizing the calculated β -transition strength to the analog state. Assuming complete isospin purity for the $J^\pi, T=5/2^+, 3/2^+$ level in ^{21}Na , the ft value for this transition is calculated to be 3.26⁶. Based on this, absolute branching ratios and partial half-lives can be derived for β^+ -decays to proton-emitting states.

Intensity ratios for bound levels are taken from the mirror $^{21}\text{F} \beta^- \rightarrow ^{21}\text{Ne}$ decay, and are renormalized to the total decay strength to these levels as deduced from the proton intensity. The resulting branching ratios and $\log ft$ values for all β^+ -decay transitions to ^{21}Na are shown in the decay scheme for ^{21}Mg in Fig. 3. These $\log ft$ values compare well with those calculated⁶ from the shell model up to 5.6 MeV, as is shown in Fig. 4.

Footnote and References

[†] Condensed from LBL-1600. Submitted to Phys. Rev. C.

1. J. C. Hardy and R. E. Bell, Can. J. Phys. **43**, 1671 (1965).
2. A. B. McDonald, J. R. Patterson, and H. Winkler, Nucl. Phys. **A137**, 545 (1969); R. A. Gough, R. G. Sextro, and J. Cerny, Phys. Lett. **43B**, 33 (1973).
3. W. Benenson, E. Kashy, and I. D. Proctor, BAPS **17**, 891 (1972); Michigan State University Report MSUCL-69 (Oct. 1972) and references therein.
4. F. X. Haas, C. H. Johnson, and J. K. Bair, Nucl. Phys. **A193**, 65 (1972) and references therein.
5. A. H. Wapstra and N. B. Gove, Nuc. Data Tables **9**, 265 (1971).
6. W. A. Lanford and B. H. Wildenthal, Phys. Rev. C **7**, 668 (1973), and private communication.

Table I. Proton energies following decay of ^{21}Mg and energy levels in ^{21}Na . Underlined numbers preceding each entry correspond to peak numbers in Figs. 1 and 2.

Proton energies (c.m.) corresponding to decays to the following levels in ^{20}Ne :		(MeV \pm keV)			Deduced ^a energies in ^{21}Na
g. s.		1.634 MeV	4.247 MeV	4.968 MeV	
<u>2</u>	1.113 \pm 0.4 ^b				3.545 \pm 2
<u>5</u>	1.862 \pm 2 ^b	-- ^c			4.294 \pm 3
<u>6</u>	2.036 \pm 5 ^b	--			4.468 \pm 5
<u>9</u>	2.598 \pm 20	<u>1</u> 0.947 \pm 20			5.022 \pm 15
	X	<u>3</u> 1.320 \pm 10			5.386 \pm 10
<u>11</u>	3.326 \pm 35	X ^c			5.758 \pm 35
<u>12</u>	3.435 \pm 25	X			5.867 \pm 25
<u>13</u>	3.547 \pm 15	X			5.979 \pm 15
<u>14</u>	3.662 \pm 35	X			6.094 \pm 35
<u>15</u>	3.78 \pm 50	X			6.21 \pm 50
<u>16</u>	3.930 \pm 35	<u>8</u> 2.265 \pm 25			6.341 \pm 20
<u>17</u>	4.068 \pm 20	X			6.500 \pm 20
<u>22</u>	5.865 \pm 15	<u>18</u> 4.246 \pm 25	X	X	8.301 \pm 15
<u>23</u>	5.986 \pm 15	<u>19</u> 4.350 \pm 20	X	X	8.417 \pm 15
<u>24</u>	6.387 \pm 25	<u>20</u> 4.741 \pm 15	<u>7</u> 2.145 \pm 15	X	8.816 \pm 10
<u>25</u>	6.538 \pm 4 ^b	<u>21</u> 4.904 \pm 4 ^b	X	<u>4</u> 1.573 \pm 1	8.970 \pm 4

Unassigned proton peak: 10 2.718 \pm 30

^aThe energies are calculated using a proton separation energy of 2.432 ± 0.002 MeV, which represents an average of values determined in Refs. 4 and 5.

^bThese proton energies were used, in part, to determine the energy calibration (see discussion in text).

^cUnobserved, but energetically-allowed, proton decays within our experimental range are marked by X, while those outside our range (≤ 700 keV) are shown by --.

HEAVY-ION DIRECT REACTIONS AT HIGH ENERGIES

F. Pühlhofer,* F. Becchetti, B. G. Harvey, D. G. Kovar, J. Mahoney,
B. Mayer, J. D. Sherman, and M. S. Zisman

In a recent HILAC experiment, the yields of in-beam γ 's from the direct reactions from $^{20}\text{Ne} + ^{27}\text{Al}$ as a function of bombarding energy were found to increase rapidly above $E_L \approx 130$ MeV.¹ This increase could be associated with an angular momentum limitation $l_{cr} \approx 35 \hbar$ on the formation of the compound nucleus.²

In order to elucidate the processes involved, we have studied reactions induced by $^{20}\text{Ne} + ^{27}\text{Al}$, using the 88-inch cyclotron, magnetic spectrometer and focal-plane detector system (see Section IV). The ^{20}Ne beam energies were 99 and 150 MeV. These energies correspond to incident angular momenta below and above l_{cr} ($\approx 35 \hbar$). Reaction products having $\pm 10\%$ of the incident ^{20}Ne momentum were detected. These can be considered quasi-elastic reaction products. Spectra for the $(^{20}\text{Ne}, ^{19}\text{F})$ reaction are shown in Fig. 1. We have labeled a number of states seen at both energies. One observes that: a) the same groups ($E_x < 10$ MeV) are observed in both reactions, b) the states observed are known single-particle levels in either ^{19}F or ^{28}Si , and c) there is an energy-dependent Q-window. A number of other reactions such as $(^{20}\text{Ne}, ^{19}\text{Ne})$, $(^{20}\text{Ne}, ^{20}\text{Ne}^*)$, and $(^{20}\text{Ne}, ^{16}\text{O})$ were also observed and exhibited similar characteristics.

We have also measured the elastic scattering and find that the data can be fit by using the optical model with energy-independent parameters. The results are shown in Fig. 2. Using the optical-model parameters deduced, we have calculated angular distributions for transfer reactions by using DWBA³ (Buttle-Goldfarb method). We find that DWBA correctly fits the shape and magnitude (to within factor 2) of the 150-MeV data without parameter changes. A typical calculation is compared with data in Fig. 3.

In Fig. 4 we summarize the results for $^{20}\text{Ne} + ^{27}\text{Al}$. The top part of the figure compares the reaction cross section (σ_R) calculated (parabolic model, top solid line) and "measured" (optical model, open circles). When the measured⁴ (Kowalski et al.) complete-fusion cross sections are subtracted one obtains the direct + fission + ? cross section ($\sigma_R - \sigma_{Xn}$) shown at the bottom of Fig. 4. Vertical bars indicate integrated "direct" reaction yields determined from γ -yields and direct measurement (present experiment). The remaining cross section ($< 1b$) is not yet accounted for and may include

fission and/or very inelastic reactions ($\Delta p/p \gg \pm 10\%$).

Our analysis indicates that quasi-elastic reactions ($\Delta p/p \lesssim \pm 10\%$) exhibit similar characteristics above and below l_{cr} and no new mechanisms need be invoked to explain the results.

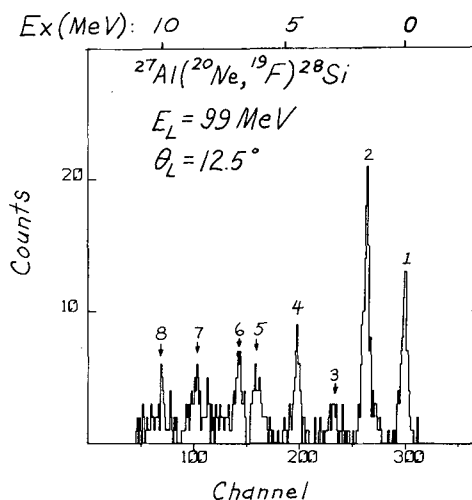
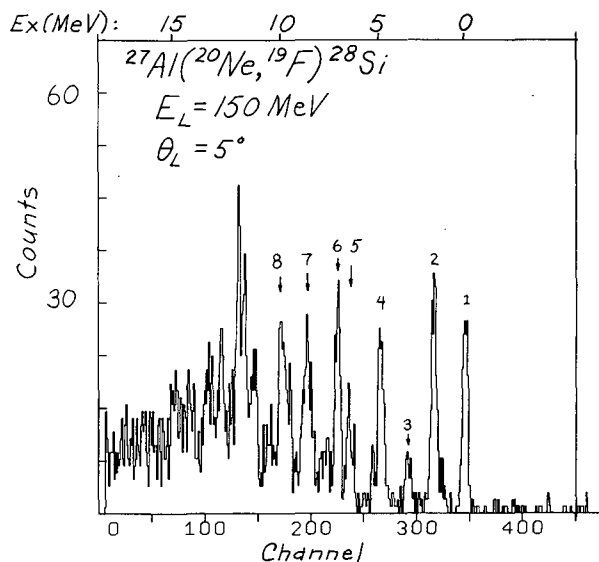


Fig. 1. Spectra for proton stripping on ^{27}Al . Groups labeled are at same excitation energy. (XBL 729-1958)

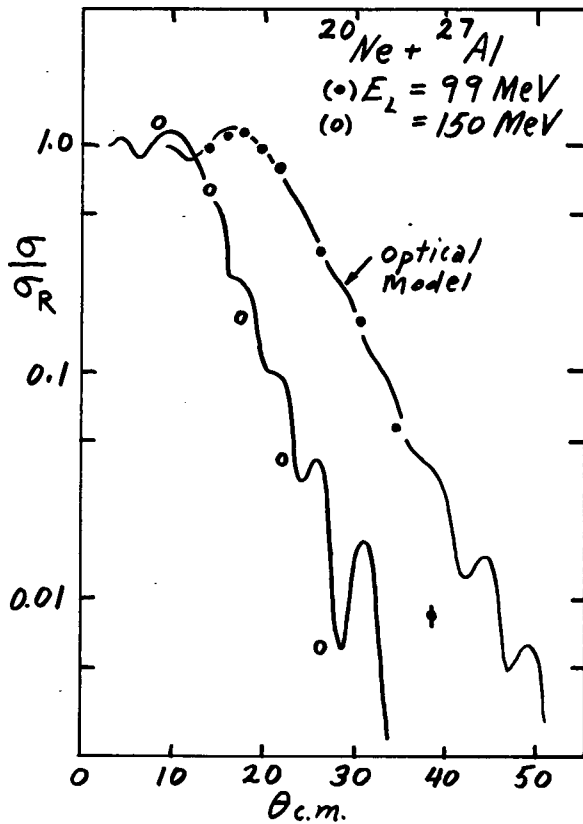


Fig. 2. $^{20}\text{Ne} + ^{27}\text{Al}$ elastic scattering data compared with optical-model calculations. The parameters were deduced from the fit to the 99-MeV data ($l < l_{cr}$). (XBL 7210-1964)

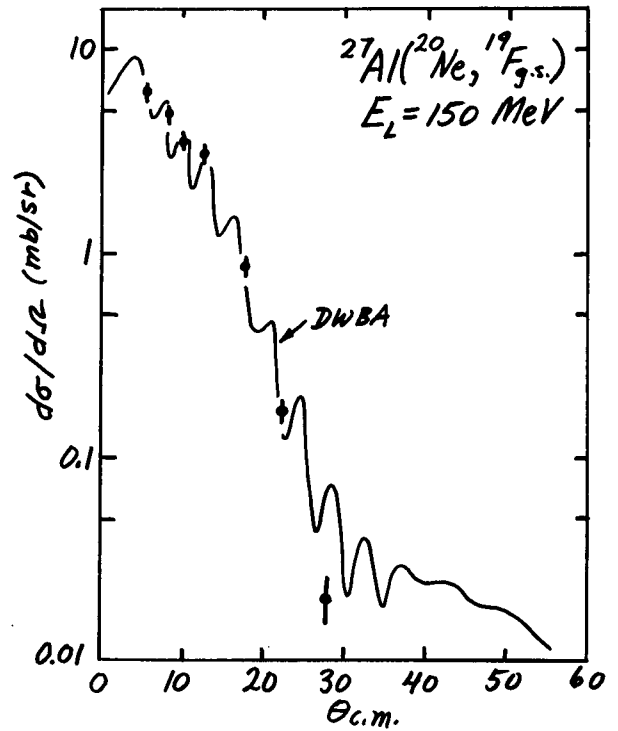
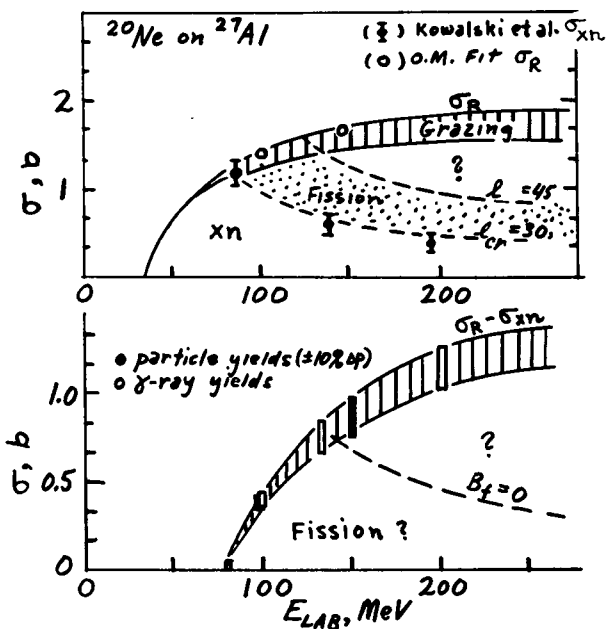


Fig. 3. A comparison of transfer data obtained at 150 MeV ($l > l_{cr}$) with a DWBA calculation for a one-step direct transfer. (XBL 7210-1960)

Footnote and References

* Present address: Universität Marburg, Marburg, Germany.

1. F. Pühlhofer and R. Diamond, Nucl. Phys. A191, 561 (1972).
2. S. Cohen, F. Plasil, and W. J. Swiatecki, in Proc. of Third Conf. on Reactions between Complex Nuclei, edited A Ghiorso et al. (Univ. of Letters 29, 303 (1972)).
3. DWUCK, P. D. Kunz (unpublished).
4. L. Kowalski, J. C. Jodogne, and J. M. Miller, Phys. Rev. 169, 894 (1968).

Fig. 4. Top: A summary of measured and calculated (Refs. 1 and 2) total and partial reaction cross sections. Bottom: Residual cross section ($\sigma_R - \sigma_{xn}$) compared with integrated "direct" cross sections obtained from γ -yields (Ref. 1) and present experiment. The widths of the bars are proportional to the experimental values. $B_f = 0$ is the calculated l -value where the fission barrier is zero (Ref. 2).

(XBL 732-181)

INELASTIC SCATTERING OF ^{16}O FROM ^{208}Pb F. D. Becchetti, D. G. Kovar, B. G. Harvey, J. Mahoney,
B. Mayer,* and F. G. Pühlhofer†

The inelastic scattering of ^{16}O from ^{208}Pb has been studied at an incident ^{16}O energy of 104 MeV at the 88-inch cyclotron. The angular distributions to the 3^- , 5^- , and 2^+ levels at 2.62-, 3.30-, and 4.10-MeV excitation in ^{208}Pb show interference patterns characteristic of those expected from the destructive interference of Coulomb and nuclear excitation.¹ The results have been analyzed using DWBA. The phase, α , of the nuclear excitation form factor, is determined (Fig. 1) to be $\alpha = 30 \pm 15^\circ$, in good agreement with the collective model ($\alpha \approx 20^\circ$). Values of the transition probabilities deduced from the potential deformation parameters are found to be smaller by a factor of ~ 2 than the electromagnetic transition probabilities measured in (e, e') or Coulomb excitation. This can be attributed to projectile size effects.

The results of this experiment have been accepted for publication in Phys. Rev. C (December 1972).

Footnotes and Reference

* Present address: CEN Saclay, France.

† Present address: Universität Marburg, Marburg, Germany.

1. G. R. Satchler, Phys. Letters **33B**, 385 (1970); Particles and Nuclei **2**, 265 (1971).

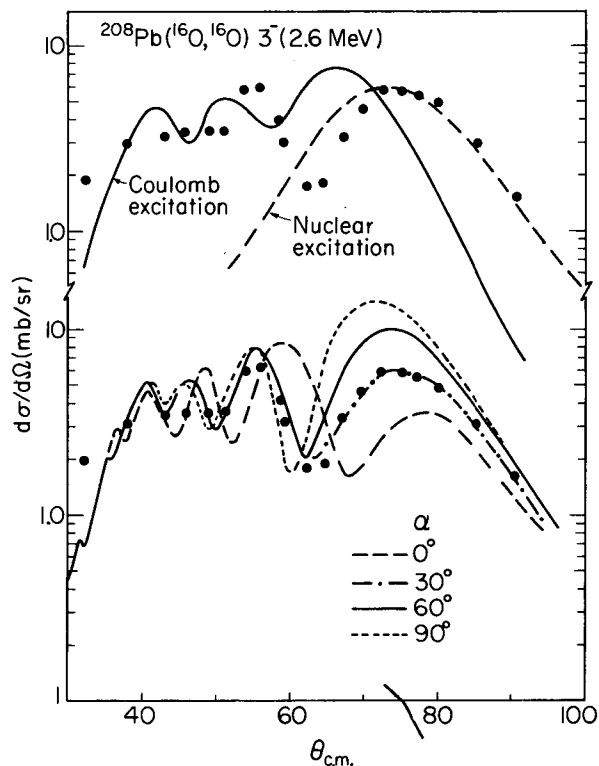


Fig. 1. Top: DWBA calculations for excitation due to Coulomb forces [$F_L(r) = F_L^C(r)$] or nuclear forces [$F_L(r) = F_L^N(r)$]. Bottom: DWBA calculations for combined Coulomb and nuclear excitation as a function of the phase factor $\alpha[F_L(r) = F_L^C(r) + e^{i\alpha} F_L^N(r)]$.

(XBL 726-3222)

j-DEPENDENCE OF HEAVY-ION INDUCED REACTIONS

D. G. Kovar, F. D. Becchetti, B. G. Harvey, F. Pühlhofer,*
J. Mahoney, D. W. Miller,† and M. S. Zisman

A study has been made of heavy-ion induced single-proton stripping reactions using different targets and projectiles to examine the reaction mechanism. The experiment were performed with 78-MeV ^{12}C and 104-MeV ^{16}O ion beams on the magnetic spectrometer system at the 88-inch cyclotron. Isotopically enriched targets ($\geq 99\%$) of ^{54}Fe , ^{62}Ni , and ^{208}Pb were

used. The reaction products were detected by a multiwire proportional counter and plastic scintillator system¹ which provided information on position ($B\rho$), dE/dx , and time of flight (tof), sufficient for unambiguous identification.

The spectra obtained for the reactions (^{12}C , ^{11}B) and (^{16}O , ^{15}N) on ^{62}Ni and ^{208}Pb are

compared in Figs. 1 and 2. The measured angular distributions peak at angles corresponding to a grazing collision at a radius $\sim 1.7(A_1^{1/3} + A_2^{1/3})$ fm but are otherwise featureless and nearly independent of the final state populated. Several features can be noted, however, from a comparison of the relative cross sections of the final states populated in the two reactions. First, in all cases the cross sections to the states with $j = l + 1/2 (=j_>)$ in the final nucleus are larger than those to states with $j = l - 1/2 (=j_<)$. This is shown graphically in Fig. 3 where the peak cross-section ratio $\sigma_{j_>}/\sigma_{j_<}$ for both reactions are plotted. The $j_>$ states are populated 2-4 times more strongly than the $j_<$ states in both reactions. Second, the same final states are found to be populated by different relative intensities in the two reactions, depending on the j of the final state. This is shown in Fig. 4 where the peak cross-section ratio $\sigma(^{16}\text{O}, ^{15}\text{N})/\sigma(^{12}\text{C}, ^{11}\text{B})$ for the same final state is plotted versus l for the six single-particle states in ^{209}Bi . One observes that the $j_>$ states are populated 1.5 to 3.0 times more strongly in the $(^{16}\text{O}, ^{15}\text{N})$ reaction compared to the $(^{12}\text{C}, ^{11}\text{B})$ reaction than are the $j_<$

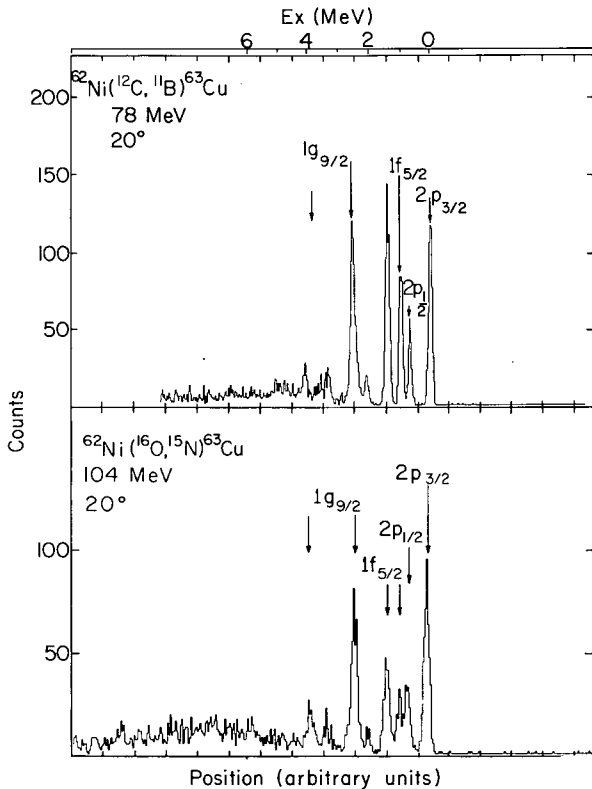


Fig. 1. Spectra for the $(^{12}\text{C}, ^{11}\text{B})$ and $(^{16}\text{O}, ^{15}\text{N})$ reactions on ^{62}Ni . The states with the major fragments of the proton single-particle strength are labeled according to their shell-model orbitals. (XBL 726-3229)

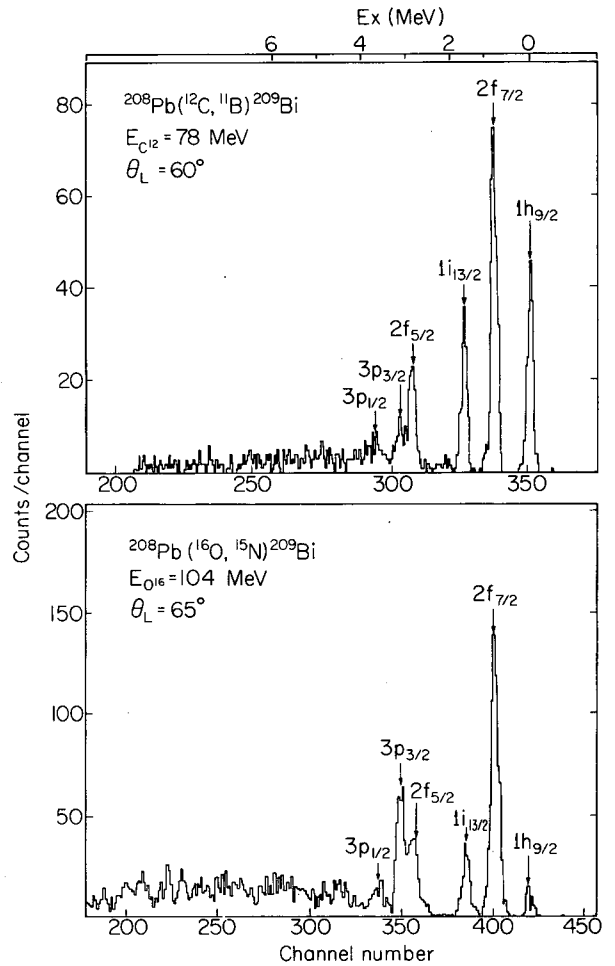


Fig. 2. Spectra for the $(^{12}\text{C}, ^{11}\text{B})$ and $(^{16}\text{O}, ^{15}\text{N})$ reaction on ^{208}Pb . The six known proton single-particle states are labeled according to their shell-model orbitals. (XBL 726-3221)

states. Similar results are found in the reactions on the other targets. DWBA calculations indicate that the results cannot be explained by Q -effects, which are known to be important in heavy-ion reactions. However, the results can be understood, at least qualitatively, by examining the selection rules.

In the DWBA theory which has been extended to include heavy-ion transfer²⁻⁴ reactions, several rules which follow from this theory are as follows:

$$\begin{aligned}
 |l_1 - l_2| &\leq L \leq l_1 + l_2 \\
 |j_1 - j_2| &\leq L \leq j_1 + j_2 \\
 l_1 + l_2 + L &= \text{even},
 \end{aligned}
 \tag{1}$$

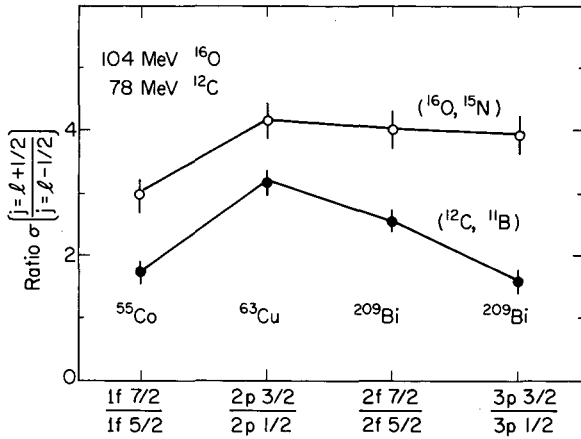


Fig. 3. Peak cross-section ratios for $j=l+1/2$ and $j=l-1/2$ proton single-particle states in the residual nuclei indicated. (XBL 726-3225)

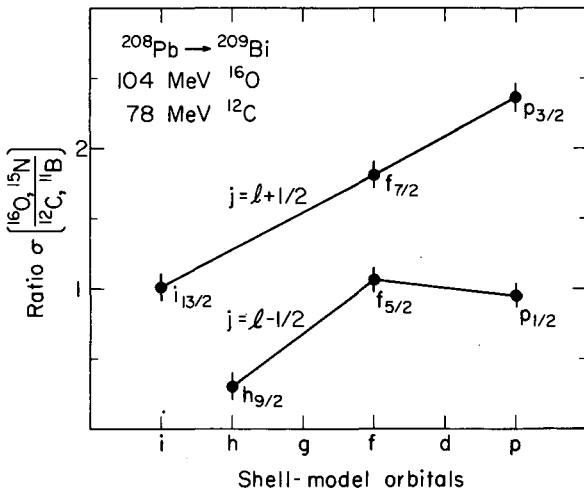


Fig. 4. Peak cross-section ratios for the ($^{16}\text{O}, ^{15}\text{N}$) and ($^{12}\text{C}, ^{11}\text{B}$) reactions to the same final state in ^{209}Bi . (XBL 726-3224)

where $l_1 j_1$ and $l_2 j_2$ are the orbital and total angular momentum of the transferred nucleon in the projectile and residual nucleus, respectively. One finds that for the ($^{16}\text{O}, ^{15}\text{N}$) reaction, where a $p_{1/2}$ proton is transferred from the projectile, only one L value is allowed with $L=l_2 \pm 1$ for $j_2=l_2 \pm 1/2$. In contrast, the ($^{12}\text{C}, ^{11}\text{B}$) reaction, which involves a $p_{3/2}$ proton transfer from ^{12}C , usually proceeds by two L values: $L=l_2+1$ and $L=l_2-1$ for either $L=l_2 \pm 1/2$. In a light-ion reaction $l_1=0, j_1=1/2$ so that only $L=l_2$ is allowed. Thus, nucleon transfer between heavy ions contains an inherent dependence on the value of j_2 , which appears explicitly in the selection

rules. This is in contrast to the j -dependence observed in light-ion reactions which arises from the spin orbit part of the projectile-nucleus potential and is a small effect except for polarization phenomena.

These selection rules are important because of the strong L dependence of the cross section. In the reactions considered here, DWBA predicts $\sigma_{L+2} \approx 10\sigma_L$ for a given $n_1 l_1 j_1$ and $n_2 l_2 j_2$. This strong L dependence then leads to a marked j -dependence in the magnitude of the transfer cross section because of the selection rules. To isolate this effect, we have compared cross-section ratios (Figs. 3 and 4). The cross-section ratio $\sigma(^{16}\text{O}, ^{15}\text{N})/\sigma(^{12}\text{C}, ^{11}\text{B})$, for example, is expected to be proportional to the ratio of DWBA σ_L 's; i.e.,

$$\frac{\sigma(^{16}\text{O}, ^{15}\text{N})}{\sigma(^{12}\text{C}, ^{11}\text{B})} \propto \frac{\sigma_{l_2 \pm 1}}{(A\sigma_{l_2+1} + B\sigma_{l_2-1})} \quad \text{for } j_2 = l_2 \pm \frac{1}{2}, \quad (2)$$

where A and B are statistical and coupling coefficients ($A, B \approx 1$). The j -dependence of the cross-section ratios exhibited in Figs. 3 and 4 can be explained, at least qualitatively, by the fact that $\sigma_{L+2} > \sigma_L$. The quantitative agreement is not so good, however, since the DWBA⁵ predicts that the cross sections to the $j_>$ and $j_<$ states should differ by factors of 10, whereas experimentally we observe factors of 2-4. Expressed in terms of relative spectroscopic factors ($S_j = S_2$), we find for the $^{208}\text{Pb}(^{16}\text{O}, ^{15}\text{N})^{209}\text{Bi}$ reaction that the spectroscopic factors, which should fall close to unity, fall into two distinct groups with $S_{j_<} \approx 3S_{j_>}$, whereas for the ($^{12}\text{C}, ^{11}\text{B}$) reaction, $S_{j_<} \approx 1/2 S_{j_>}$. Similar results were found for the reactions on ^{54}Fe and ^{62}Ni . These discrepancies are believed to arise from the neglect of recoil effects which are discussed in more detail in another report. In any event it is apparent that a better understanding of the reaction mechanism is needed before one can use DWBA reliably to extract spectroscopic factors from heavy-ion induced reactions. Despite the uncertainties in DWBA, however, the j -dependence observed in the present experiments indicates that nucleon transfers between heavy ions can provide spectroscopic information complementary to that obtain using light ions.

Footnotes and References

*The results of this work have been published in Phys. Rev. Letters 29, 1023 (1972).

†Present address: Universität Marburg, Marburg, Germany.

‡Present address: Indiana University, Bloomington, Indiana 47401.

1. B. G. Harvey, J. Mahoney, F. G. Pühlhofer, F. S. Golding, D. A. Landis, J-C Faivre, D. G. Kovar, M. S. Zisman, J. R. Meriwether, S. W. Cosper, and D. L. Hendrie, Nucl. Instr. Methods 104, 21 (1972).
2. P. J. A. Buttle and L. J. B. Goldfarb, Nucl. Phys. A176, 299 (1971), and references cited therein.
3. D. Trautman and K. Alder, Helv. Phys. Acta 43, 363 (1970).
4. F. Schmittroth, W. Tobocman, and A. Golestaneh, Phys. Rev. C 1, 377 (1970).
5. The DWBA form factors were calculated by using the program RDRC (W. Tobocman, unpublished). The DWBA cross sections were calculated by using the program DWUCK (P. D. Kunz, unpublished).

EVIDENCE OF RECOIL EFFECTS IN HEAVY-ION TRANSFER REACTIONS

D. G. Kovar, B. G. Harvey, F. D. Becchetti, J. Mahoney,
and M. S. Nagarajan

Extraction of nuclear structure information from heavy-ion transfer reactions has been limited by uncertainties in the applicability of DWBA.¹ In particular, most DWBA codes use the no-recoil approximation,² whose validity in many reactions is questionable.^{1,3} We present data here on ¹⁶O- and ¹²C-induced reactions on ²⁰⁸Pb at high bombarding energies. Analysis of the data shows that no-recoil DWBA is inadequate for these reactions. Evidence is presented that demonstrates that one must include recoil effects and that their importance can be predicted in the framework of a simple first-order recoil treatment.

The single-proton stripping reactions (¹²C, ¹¹B) at 78 MeV and (¹⁶O, ¹⁵N) at 104 MeV and 140 MeV were studied by using the magnetic spectrometer system at the 88-inch cyclotron. Typical spectra for the (¹⁶O, ¹⁵N) reactions are shown in Fig. 1, where the well-known proton single particle states in ²⁰⁹Bi are seen to dominate the excitation spectrum. The cross-section j-dependence noted previously⁴ (see preceding paper), favoring the $j=l+1/2$ states in the final nucleus, becomes less pronounced as the bombarding energy is increased. The angular distributions for the transitions to the six single-particle states in ²⁰⁹Bi for the three reactions are shown in Figs. 2 and 3.

The angular distributions were fit by using the no-recoil DWBA theory.² Calculations were performed using finite-range form factors⁵ and the distorted-wave code DWUCK⁶ with 140 partial waves. Optical-model parameters from elastic scattering and bound state parameters from the literature were used in the calculations. The fits to the angular distributions are shown in Figs. 2 and 3. The DWBA cross sections have the correct shape, but are shifted back in angle for states at higher excitation,

whereas the data are not. The spectroscopic factors obtained are listed in Table I together with the results of light-ion reactions. The spectroscopic factors obtained in the (¹⁶O, ¹⁵N) reactions for the $j=l-1/2 (=j_<)$ states in ²⁰⁹Bi are found to uniformly exceed those obtained for the $j=l+1/2 (=j_>)$ states (by a factor of 4 at 104 MeV and a factor of 8 at 140 MeV). In contrast, the spectroscopic factors obtained from the (¹²C, ¹¹B) reaction for the $j_<$ states are smaller than those deduced for the $j_>$ states by almost a factor of 2. The results of analysis with no-recoil DWBA are: 1) it is not possible to obtain consistent spectroscopic factors simultaneously for both the $j_<$ and $j_>$ states for either reaction, 2) the spectroscopic factors for $j_<$ and $j_>$ states from the ¹⁶O- and ¹²C-induced reactions show opposite systematics, and 3) the discrepancies in the spectroscopic factors in the ¹⁶O reactions show an energy dependence, becoming greater with increasing bombarding energy.

To determine whether these discrepancies are the result of recoil effects, we fit the angular distributions by using DWBA cross sections calculated in a formalism in which recoil is taken into account in first order.⁷ Additional terms result which are added to the normal no-recoil cross section. Hence the transfer cross section with first-order recoil effects included has the form:

$$\frac{d\sigma}{d\Omega} = \frac{d\sigma}{d\Omega}(\text{no recoil}) + K \frac{d\sigma}{d\Omega}(\text{interference}) + K^2 \frac{d\sigma}{d\Omega}(\text{recoil}), \quad (1)$$

where the recoil and interference terms are cross sections calculated in a standard no-recoil DWBA code, but with L transfers which are determined from the recoil formalism. These are usually adjacent to the L transfer normally allowed (see Table I). The coefficient K can be shown to have the form

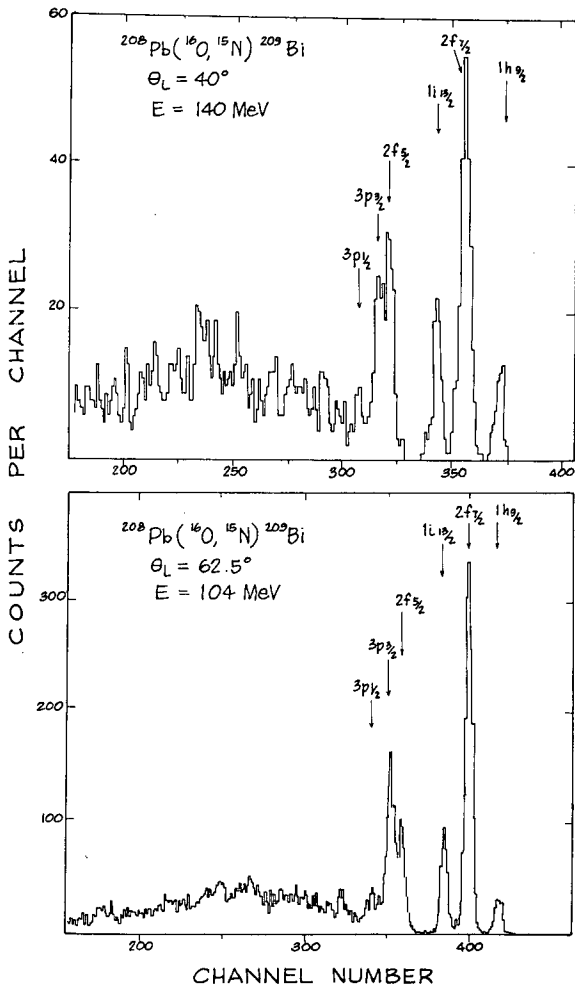


Fig. 1. Spectra obtained for the $^{208}\text{Pb}(^{16}\text{O}, ^{15}\text{N})^{209}\text{Bi}$ reaction at ^{16}O energies of 104 and 140 MeV. The proton single-particle states are labeled by their shell-model orbitals.

(XBL 7240-5829)

$$K = \left[\frac{M_p}{M_{c1}} \right] \left[\frac{k_i}{\chi_2} \right], \quad (2)$$

where M_p , M_{c1} are the masses of the transferred proton and the projectile, k_i is the wave number in the incident channel at the interaction distance, and χ_2 is the bound state decay parameter in the final nucleus [i. e., $\chi_2 = (2m E_B / \hbar^2)^{1/2}$], which contains a dependence on the binding energy E_B .

Cross sections were calculated as outlined above. The shapes of the predicted angular distributions were found to be very nearly the same as those obtained in the no-recoil calculations using the same optical model and bound state parameters. The spectroscopic factors are

listed in Table I and are found to be in much better agreement with those from light-ion reactions. That the agreement is not better is not surprising since an approximation (which greatly simplified the recoil correction terms) was made which is only valid for weakly bound states and is not exact for the states considered here. Nevertheless, the results we obtained indicate that the

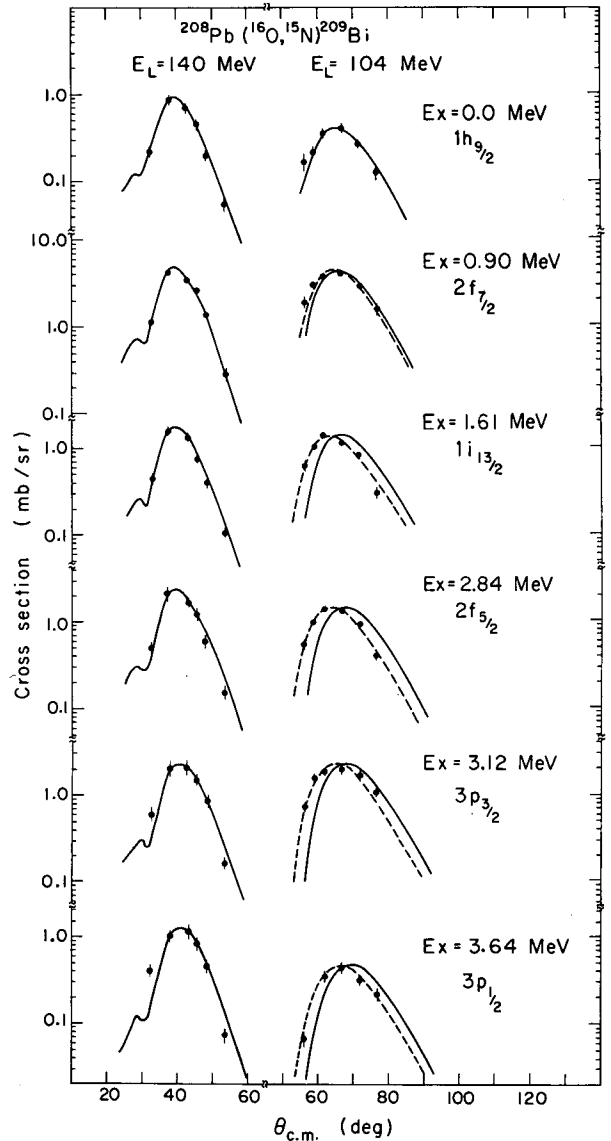


Fig. 2. Angular distributions obtained in the $(^{16}\text{O}, ^{15}\text{N})$ reaction for the transitions leading to the six single states in ^{209}Bi . The solid curves are the predicted DWBA cross sections. The dashed curves are the DWBA cross sections shifted to fit the data points.

(XBL 731-2091)

Table I.

E_x (MeV)	nlj	No-recoil spectroscopic factor						Recoil spectroscopic factors				$(^3\text{He}, d)^a$
		$(^{16}\text{O}, ^{15}\text{N})$			$(^{12}\text{C}, ^{11}\text{B})$			$(^{16}\text{O}, ^{15})$		$(^{12}\text{C}, ^{11}\text{B})$		
		L	104 MeV	140 MeV	L	78 MeV	L	104 MeV	140 MeV	L	78 MeV	
0.00	1h9/2	4	4.14	8.53	4, 6	0.64	4, (5) ^c	1.45	2.29	4, (5), 6	0.77	1.00
0.90	2f7/2	4	1.00 ^b	1.00 ^b	2, 4	1.00 ^b	(3), 4	1.00 ^b	1.00 ^b	2, (3), 4	1.00 ^b	1.12
1.61	1i13/2	7	0.88	0.84	5, 7	0.83	(6), 7	0.85	0.80	5, (6), 7	0.84	0.94
2.84	2f5/2	2	4.96	7.06	2, 4	0.53	2, (3)	1.33	1.72	2, (3), 4	0.70	1.14
3.12	3p3/2	2	1.05	0.70	0, 2	1.76	(1), 2	1.08	0.80	0, (1), 2	2.05	1.08
3.64	3p1/2	0	4.32	8.07	2	0.64	0, (1)	0.82	1.40	(1), 2	0.94	0.7-0.9

^aWildenthal et al., Phys. Rev. Letters 19, 960 (1967).

^bNormalized to unity.

^cL-values in parenthesis are used in evaluating the recoil correction.

largest part of the discrepancies in the spectroscopic factors can be removed by inclusion of first-order recoil effects.

The analysis of the single-proton stripping reactions induced by ^{12}C and ^{16}O ions on ^{208}Pb indicates the inadequacy of the no-recoil approximation used in DWBA for reactions at energies far above the Coulomb barrier. The j -dependence of the spectroscopic factors as well as the energy dependence of the cross sections are as predicted by DWBA theory which includes recoil effects in first order. The importance of recoil effects are determined by the factor $(M_p/M_c)(k_i/\chi_2)$ which suggests that recoil effects are most important for high bombarding energies and weakly bound states. The first-order treatment used here approximates the gradient of the distorted wave and the nuclear overlap integral by the use of the Buttler-Goldfarb approximation. To obtain more reliable spectroscopic factors we believe one must evaluate the recoil terms more exactly. The results we have obtained here, however, suggest that for a large number of single-nucleon transfer reactions it may be sufficient to consider recoil as a first-order effect and thus avoid the lengthy calculations involved in a full finite-range treatment.³

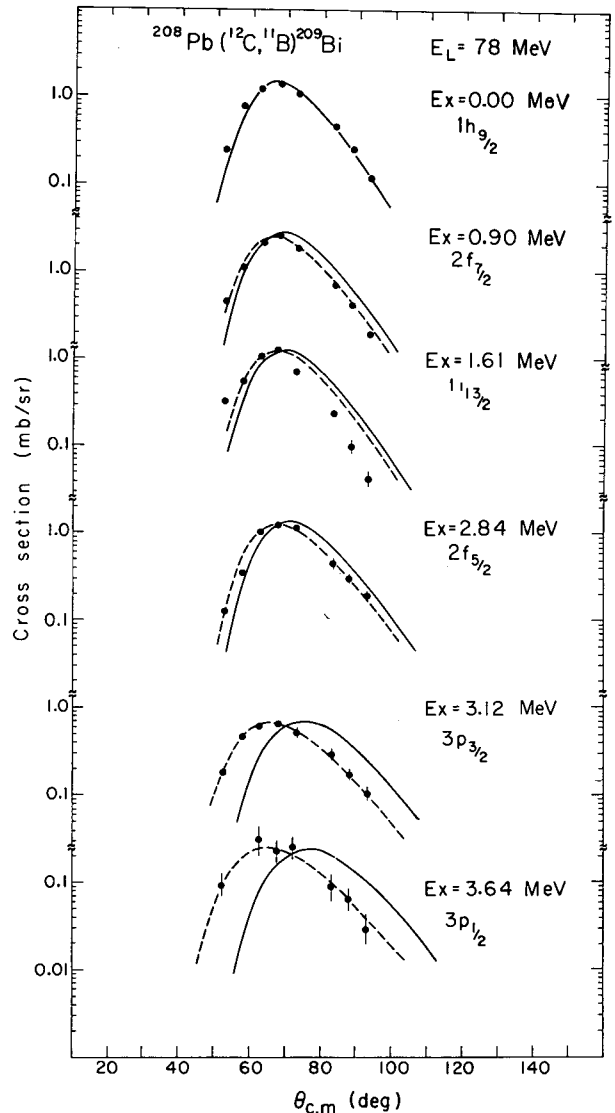


Fig. 3. Angular distributions obtained in the $(^{12}\text{C}, ^{11}\text{B})$ reaction leading to the six single-particle states in ^{209}Bi . The solid curves are the predicted DWBA cross sections. The dashed curves are the same DWBA cross sections but shifted in angle to fit the data points. (XBL 731-2090)

References

1. K. R. Grieder, Nuclear Reactions Induced by Heavy Ions, edited by R. Bock and W. Hering (North-Holland, Amsterdam, 1970).
2. P. J. A. Buttle and L. J. B. Goldfarb, Nucl. Phys. A176, 299 (1971).
3. R. M. DeVries and K. I. Kubo, to be published in Phys. Rev. Letters.
4. D. G. Kovar, F. D. Becchetti, B. G. Harvey, F. G. Pühlhofer, J. Mahoney, D. W. Miller, and M. S. Zisman, Phys. Rev. Letters 29, 1023 (1972).
5. Using code of W. Tobocman, unpublished.
6. P. D. Kunz, unpublished.
7. M. S. Nagarajan, Nucl. Phys. A196, 34 (1972).

NUCLEON TRANSFER REACTIONS INDUCED BY ^{12}C ON ^{208}Pb AND ^{197}Au AT ANGLES MUCH SMALLER THAN THE GRAZING ANGLE

W. von Oertzen, F. D. Becchetti, D. G. Kovar, B. G. Harvey,
D. L. Hendrie, H. Homeyer, and J. Mahoney

In studies of nucleon transfer reactions by Kaufmann and Wolfgang (1961)¹ and in more recent experiments performed at Orsay,² a rise in the intensity of reaction products attributed to few-nucleon transfer has been observed at very small angles. Simultaneously, the usual maximum of the cross section at the grazing angle was always observed. The Orsay group, who used solid state detectors interpreted the rise at small angles as being due to transitions with rather negative Q-values, whereas the intensity at the grazing angle was found mainly to be due to the transitions leading to the low-lying states.

Using the magnetic spectrometer at the 88-inch cyclotron, we have measured the yields of the products ^{11}B , ^{10}B , ^{11}C , ^{13}C at 10° lab in reactions induced by 78-MeV ^{12}C on ^{208}Pb and ^{197}Au . For each setting of the magnetic field, background measurements using a ^{12}C target were performed since the ^{208}Pb had a carbon backing and the Au target had ^{12}C contamination from ^{12}C buildup. The spectra were taken over a range of 0-30 MeV excitation and the background from ^{12}C contamination was then subtracted.

The main yield observed at magnetic field settings corresponding to 10-30 MeV excitation in the heavy residual nuclei was found to be due to the ^{12}C contaminant. After subtraction of the background, typical cross sections for the reactions (^{12}C , ^{11}C) and (^{12}C , ^{10}B), (^{12}C , ^{11}B) and (^{12}C , ^{13}C) on Pb and Au of 0.02 mb/sr·MeV \pm 50% were obtained at 10° lab. These cross sections are at least a factor of 10 smaller than those reported in Ref. 2 and for similar reactions induced by ^{12}C and ^{14}N on Ag.

References

1. R. Kaufmann and R. Wolfgang, Phys. Rev. 121, 192 (1961).
2. J. Galin, D. Guerreau, M. Lefort, J. Peter, X. Tarrago, and R. Basile, Nucl. Phys. A159, 461 (1970).

HEAVY-ION INDUCED SINGLE NUCLEON TRANSFER REACTIONS IN THE Zr-Mo REGION

M. S. Zisman,* F. D. Becchetti, B. G. Harvey, D. Kovar, J. Mahoney, and J. D. Sherman

The (^{16}O , ^{15}N) and (^{16}O , ^{15}O) reactions on targets of $^{90,91,94}\text{Zr}$, ^{92}Mo , and ^{93}Nb have been investigated with a 104-MeV $^{16}\text{O}(4+)$ beam from the Berkeley 88-inch cyclotron. The (^{16}O , ^{17}O) reaction (leading to the ground state of the final nucleus) was also observed. Spec-

tra for the (^{12}C , ^{11}B) reaction on ^{90}Zr and ^{92}Mo were also obtained. Outgoing heavy ions were detected in the focal plane of a magnetic spectrometer with a Borkowski-Kopp type position-sensitive proportional counter backed by a plastic scintillation (see Section IV). The

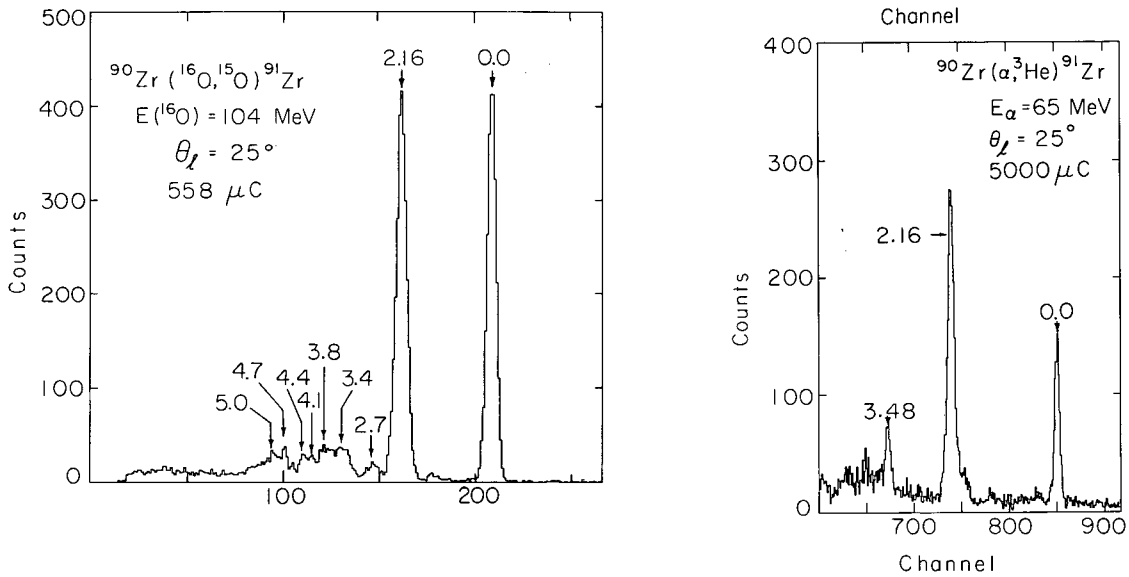
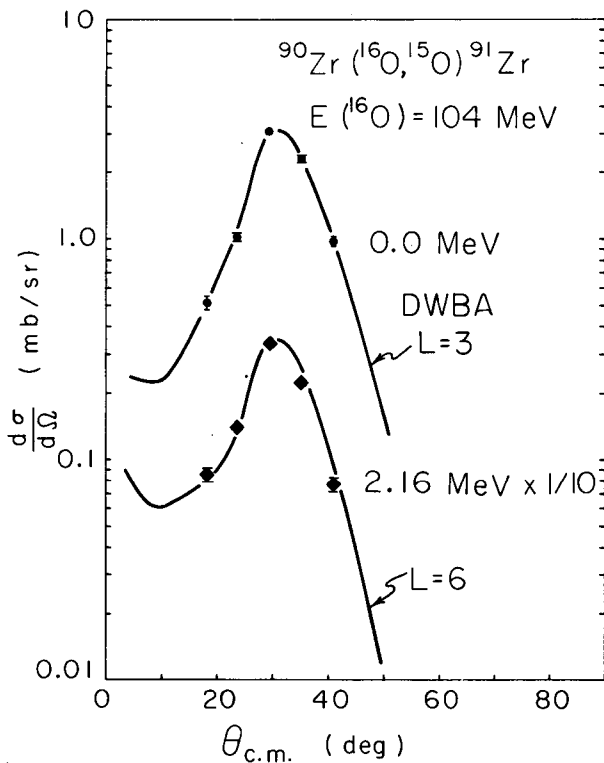


Fig. 1. An ^{15}O position spectrum from the $^{90}\text{Zr}(^{16}\text{O}, ^{15}\text{O})^{91}\text{Zr}$ reaction at $\theta_L = 25^\circ$. A $^{90}\text{Zr}(\alpha, ^3\text{He})^{91}\text{Zr}$ spectrum is shown for comparison. The ^{91}Zr ground state and 2.16-MeV levels are $5/2^+$ and $11/2^-$, respectively. (XBL 727-3410)



$(^{16}\text{O}, ^{15}\text{N})$ and $(^{16}\text{O}, ^{15}\text{O})$ data indicate a preference for high angular momentum transfer similar to (but less pronounced than) that shown by the (α, t) and $(\alpha, ^3\text{He})$ reactions on the same targets (see Figs. 1 and 2). Contrary to a suggestion by Nickles et al., no strong evidence for a multi-step excitation of core-excited states is apparent from the present data.

Footnote

* Present address: Tandem Laboratory, University of Washington, Seattle, Washington.

Fig. 2. Angular distributions of ^{15}O from the $^{90}\text{Zr}(^{16}\text{O}, ^{15}\text{O})^{91}\text{Zr}$ reaction. The L values are those for $d_{5/2}$ and $h_{11/2}$ states in ^{91}Zr (see Fig. 1) used in no-recoil DWBA calculations (solid curves). (XBL 731-2001)

STUDY OF THE TWO-PROTON TRANSFER REACTIONS:
 $^{208}\text{Pb}(^{12}\text{C}, ^{10}\text{Be})^{210}\text{Po}$ AND $^{208}\text{Pb}(^{16}\text{O}, ^{14}\text{C})^{210}\text{Po}$

F. D. Becchetti, D. G. Kovar, B. G. Harvey, D. L. Hendrie, H. Homeyer,
 J. Mahoney, and W. von Oertzen

We have studied the reactions: $^{208}\text{Pb}(^{12}\text{C}, ^{10}\text{Be})^{210}\text{Po}$, $E_L = 78$ MeV, and $^{208}\text{Pb}(^{16}\text{O}, ^{14}\text{C})^{210}\text{Po}$, $E_L = 104$ and 140 MeV at the 88-inch cyclotron, using the magnetic spectrometer and focal plane counter (see Section IV). The energy resolution was 120-200 keV FWHM.

The low-lying levels in ^{210}Po of the form $[\pi h_9/2 \otimes \pi l j]_J$ have been studied previously via single-proton transfers on ^{209}Bi .^{1,2} Other levels have been studied from the decay of near-by nuclei.³ Most of the expected two-proton configuration levels have not been observed, however.

In Fig. 1 we compare ($^{16}\text{O}, ^{14}\text{C}$) and ($^{12}\text{C}, ^{10}\text{Be}$) spectra (taken near the grazing angle) with the position of known $[\pi h_9/2 \otimes \pi l j]_J$ levels. The following features are observed: a) many levels in addition to known levels are populated and are the strongest in the spectra, b) the ($^{12}\text{C}, ^{10}\text{Be}$) and ($^{16}\text{O}, ^{14}\text{C}$) reactions populate the same levels but with different intensities in some cases. c) The 0^+ ground state of ^{210}Po is populated more strongly than the 2^+ , 4^+ , 6^+ , or 8^+ members of the $(h_9/2)^2$ multiplet.

Angular distributions are shown in Fig. 2. Transitions to known states sometimes show a slight L-dependence, the high spin states having a less pronounced peaking.

The data are being analyzed with DWBA theory. The form factor is calculated by using the Moshinsky-Talmi expansion of the motion of the two nucleons into relative and center-of-mass (c.m.) coordinates about the projectile and target. The form factor has the form⁴

$$F_L(R) = \sum \Omega_{12} G_1 G_2 U_{12}(R), \quad (1)$$

where G_1 and G_2 are projectile and target structure factors, Ω_{12} is a spatial overlap, and $U_{12}(R)$ describes the c.m. motion of the transferred nucleon pair. The form factor (1) resembles that used in light-ion reactions⁵ such as (t,p) etc., except projectile structure factors are included explicitly. The coherent sum indicated in (1) is over all the intermediate configurations of the two nucleons which connect the initial and final states. Collectivity in the target, projectile, or both can greatly enhance cross sections since the terms in (1) can add constructively.

If we assume ($^{12}\text{C}, ^{10}\text{Be}$) and ($^{16}\text{O}, ^{14}\text{C}$) are $(p_{3/2})^2$ and $(p_{1/2})^2$ transfers, respectively, then

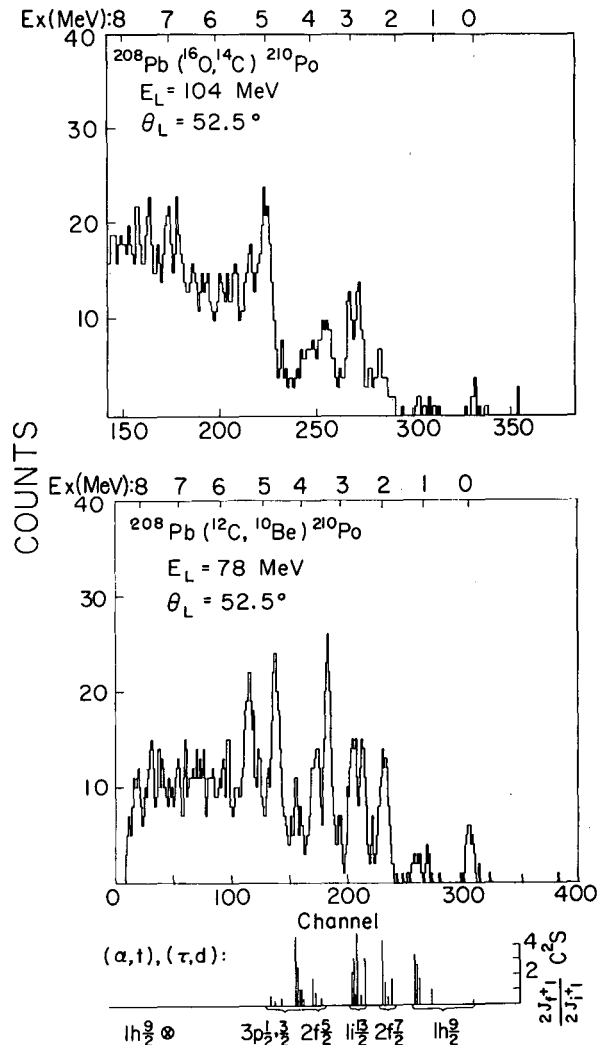


Fig. 1. Top: Spectra obtained for two-proton transfer reactions near the grazing angle. Bottom: States in ^{210}Po observed (Ref. 2) in $^{209}\text{Bi}(\alpha, t)$ and $^{209}\text{Bi}(\tau, d)$ and assumed to be of the form $[\pi h_9/2 \otimes \pi l j]_J$. (XBL 731-2013)

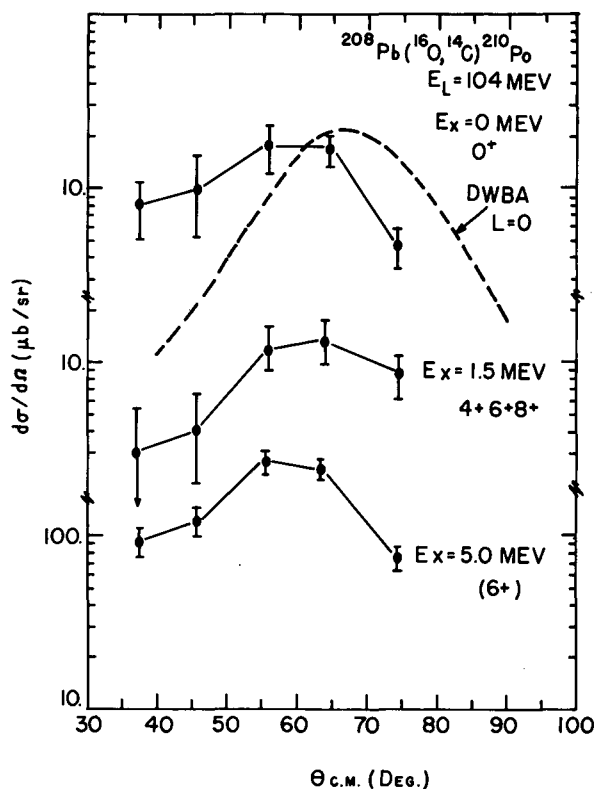


Fig. 2. Angular distributions for $^{208}\text{Pb}(^{16}\text{O}, ^{14}\text{C})^{210}\text{Po}$. A typical DWBA calculation is shown. The other calculations are similar, in shape, to that shown. (XBL 732-184)

one finds from (1); d) the two protons are transferred in relative $1S$ and $2S$ states, e) the structure factors for $(^{12}\text{C}, ^{10}\text{Be})$ and $(^{16}\text{O}, ^{14}\text{C})$ are very similar, and f) aligned configurations are favored, i.e., $[\ell_1 j_1 \otimes \ell_2 j_2]_J$ with $J=0$ or j_1+j_2 .

DWBA calculations⁶ have been performed (without recoil), assuming various configurations for levels in ^{210}Po . A typical calculation is compared with experimental data in Fig. 2. The calculations miss the peak in $\sigma(\theta)$ by about 20° , an effect similar to that seen in $(^{16}\text{O}, ^{15}\text{N})$. In Fig. 3 we compare peak cross sections for $(^{12}\text{C}, ^{10}\text{Be})$ populating the lowest 0^+ (g.s.), 2^+ , and unresolved $4+6+8^+$ levels in ^{210}Po (see Fig. 1) with DWBA calculations, assuming both pure $(h_9/2)^2$ configurations and various shell-model wave functions.^{7,8} The enhancement of 0^+ (g.s.) and 2^+ states is due to the $(f_{7/2})^2$, $(p_{3/2})^2$, and $(f_{5/2})^2$ admixtures in the ^{210}Po wave functions.

Among the possible two-proton configurations, the $(f_{7/2})^2$ 6^+ and $(f_{7/2}f_{5/2})^2$ 6^+ levels are calculated to be populated strongest (by a factor ~ 2) in the $(^{12}\text{C}, ^{10}\text{Be})$ and $(^{16}\text{O}, ^{14}\text{C})$ reactions studied here. The best candidates for

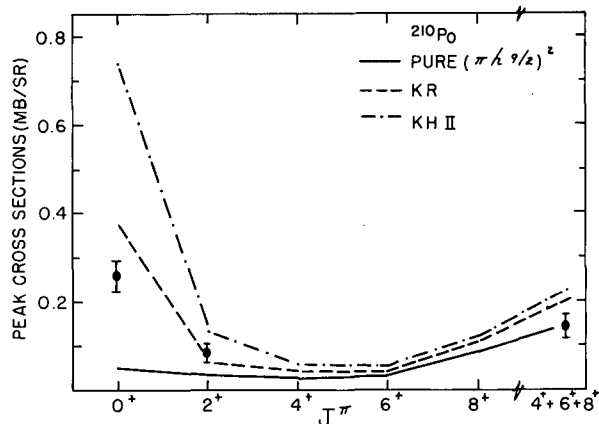


Fig. 3. Calculated and experimental peak cross sections for $^{208}\text{Pb}(^{12}\text{C}, ^{10}\text{Be})^{210}\text{Po}$, $E_L=78$ MeV. The curves are calculated by assuming pure or mixed configurations. The latter are taken from Ref. 7 (KR) and Ref. 8 (KH-II). The calculations are normalized to the $4+6+8^+$ summed cross section as indicated. (XBL 732-180)

these levels are those observed at 3.7 and 5.0 MeV, respectively (see Fig. 1). These levels are close in energy (± 300 keV) to those predicted in the shell-model calculations.^{7,8} The high selectivity of the $(^{12}\text{C}, ^{10}\text{Be})$ and $(^{16}\text{O}, ^{14}\text{C})$ reactions (which is due to the large S-state components in the di-nucleon wave functions) suggests that these reactions will be very useful probes of two-proton wave functions.

References

1. R. Tickle and J. Bardwick, Phys. Letters **36B**, 32 (1971).
2. W. A. Lanford, W. P. Alford, and H. W. Fulbright, submitted for publication.
3. L. J. Jardine, S. G. Prussin, and J. M. Hollander, Nucl. Phys. **A190**, 261 (1972).
4. R. Broglia et al., J. Physique, suppl. 11-12, **32**, C6-151 (1971).
5. N. K. Glendenning, Phys. Rev. **137**, B102 (1965).
6. Program DWUCK, P. D. Kunz (unpublished).
7. Y. E. Kim and J. O. Rasmussen, Nucl. Phys. **47**, 184 (1963).
8. T. S. Kuo and G. H. Herling, NRL Memorandum Report 2258 (1971).

SYSTEMATICS OF THE $(\alpha, 2\alpha)$ REACTION

J. D. Sherman and D. L. Hendrie

The first $(\alpha, 2\alpha)$ results on the ^{40}Ca and ^{44}Ca targets have been reported.¹ The primary purpose of that work was to investigate the concept of enhanced alpha-clustering in ^{40}Ca compared to ^{44}Ca .² Since this early work, the $(\alpha, 2\alpha)$ experiment at $E_\alpha = 90$ MeV has been improved and expanded. The purpose has been to study a range of nuclei from ^{12}C to ^{66}Zn in order to investigate systematics of cluster or four-particle correlations³ in these nuclei. Further, it is possible to compare $(\alpha, 2\alpha)$ results with the $(^3\text{He}, ^7\text{Be})$ " α " pickup reaction, which has recently been reviewed.⁴

Most measurements have been made in a symmetric coplanar geometry, and Table I summarizes the targets and angles studied. Sufficient data were accumulated to construct partial angular correlations; note that the "quasi-elastic angle" is always included. Energy and momentum correlations have also been extracted for all ground state transitions and some excited states. Asymmetric angle data on the ^{12}C and ^{16}O nuclei have also been obtained, with the intent of using this data on studying an impulse approximation reaction model.

Table I

Target	Angle θ	=	$(\theta_1 = -\theta_2)$
^{12}C	28°, 35°, 41°, 42°, 47°		
^{16}O	28°, 35°, 41°, 42°, 47°		
^{24}Mg	28°, 35°, 41°, 47°		
^{26}Mg	28°, 35°, 41°, 47°		
^{28}Si	28°, 35°, 41°, 47°		
^{30}Si	28°, 35°, 41°, 47°		
^{40}Ca	28°, 32°, 42°, 47°		
^{44}Ca	28°, 42° 47°		
^{66}Zn	28°, 35° 43°		

The experiments used a 90-MeV momentum-analyzed beam from the 88-inch cyclotron. The ΔE - E particle telescopes acted as particle discriminators; i. e., $Z \neq 2$ particles are rejected. The $(\alpha, \alpha, ^3\text{He})$ Q-values are quite negative compared to the $(\alpha, 2\alpha)$ Q-values; hence, the ^3He particles are not a problem in the coincidence

data. Three parameter data—two summed energy signals and a timing signal—are stored event-by-event in a PDP-5 computer and periodically dumped onto magnetic tape. Energy resolutions as measured by the summed energies of both alphas when the residual nucleus is left in a known sharp state are typically 250-300 keV (FWHM). Projections of kinematic bands onto the summed energy axis for selected spectra are given in Figs. 1-4. In order to get best energy resolutions in these spectra, we have applied a kinematic correction to the band lying in the T3+T4 vs T3 plane.

Figure 1 is the $^{16}\text{O}(\alpha, 2\alpha)^{12}\text{C}$ reaction. The transition to the $^{12}\text{C}(4.43)$ MeV level is markedly weaker than to the $^{12}\text{C}(0.00)$ state. The strength ratio of the 4.44-MeV state to the ground state increases as θ ($=\theta_1 = -\theta_2$) moves forward, but the ratio is < 1 for all observed angle pairs (cf. Table I). This is in apparent disagreement with two-body reactions, since the $(d, ^6\text{Li})$ ⁵ and the $(^3\text{He}, ^7\text{Be})$ ⁶ results as well as shell-model calculations⁷ indicate that the parentage of ^{16}O is largely $^{12}\text{C}(4.44) + \alpha$.

Figure 2 illustrates the $^{26}\text{Mg}(\alpha, 2\alpha)^{22}\text{Ne}$ T3+T4 (total energy) projection. The ground state is most strongly populated. This feature is characteristic of all the targets studied. A comparatively large population of levels in the 5- to 7-MeV region of ^{22}Ne is seen to occur. Levels in this excitation region were also observed in the $^{18}\text{O}(^7\text{Li}, t)^{22}\text{Ne}$ reaction.⁸ All targets heavier than ^{12}C and ^{16}O were bothered by carbon and oxygen contamination; the resulting ^8Be and ^{12}C levels in the ^{22}Ne spectrum are so labeled.

Figure 3 and 4 show the T3+T4 projections for the ^{40}Ca and ^{44}Ca target nuclei. The ^{40}Ca target is exceptional among the heavier targets ($> ^{16}\text{O}$) because of the large population of excited ^{36}Ar states, comparable to the ground state transition at some angles. The $^{44}\text{Ca}(\alpha, 2\alpha)^{40}\text{Ar}$ spectrum is dominated by the ground state transition, which approximately equals the $^{40}\text{Ca}(\alpha, 2\alpha)^{36}\text{Ar}(0.0)$ in excitation strength. However, transitions to excited states in ^{36}Ar are far stronger than similar transitions in ^{40}Ar . The tentative earlier $(\alpha, 2\alpha)$ results¹ in these nuclei are substantiated with the improved data.

Figure 5 shows the momentum correlations for the ground state transitions presented for all targets. The quoted symmetric angle is the quasi-elastic angle. The broad distribution of points with peaking at recoil momentum (q) equal to zero is characteristic of an $L=0$ quasi-elastic

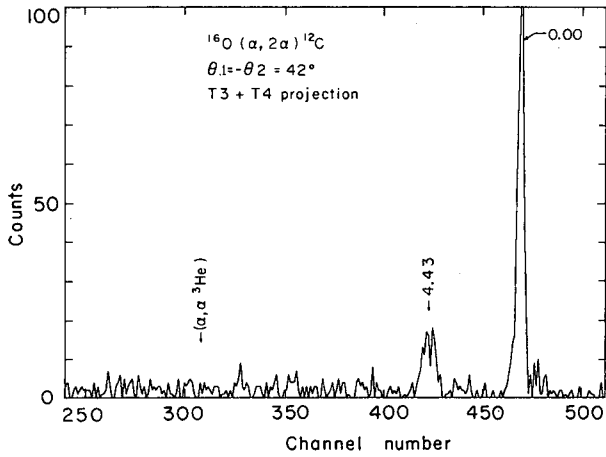


Fig. 1. Summed energy projection of the $^{16}\text{O}(\alpha, 2\alpha)^{12}\text{C}$ reaction. (XBL 729-4023)

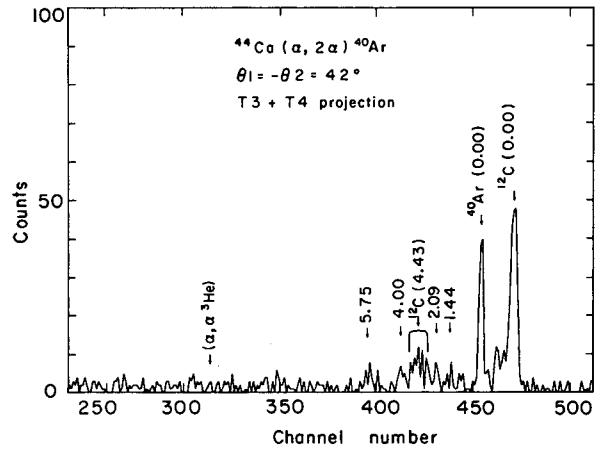


Fig. 4. Summed energy projection of $^{44}\text{Ca}(\alpha, 2\alpha)^{40}\text{Ar}$ reaction. (XBL 729-4029)

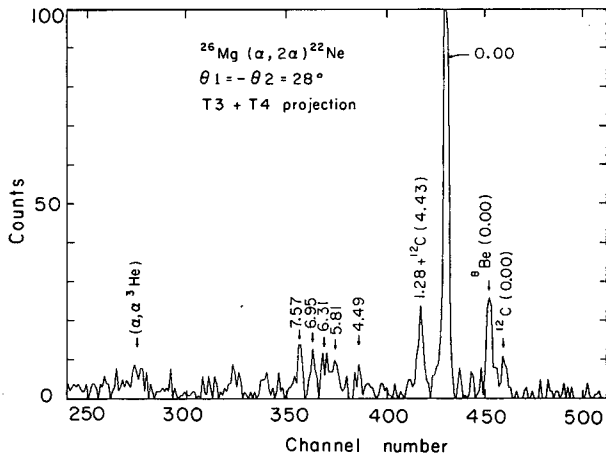


Fig. 2. Summed energy projection of $^{26}\text{Mg}(\alpha, 2\alpha)^{22}\text{Ne}$ reaction.

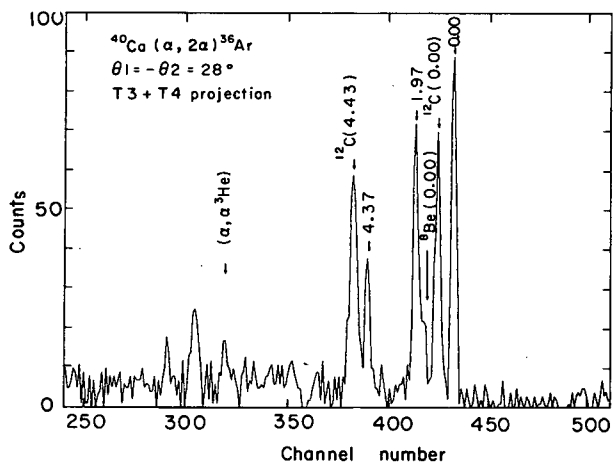


Fig. 3. Summed energy projection of $^{40}\text{Ca}(\alpha, 2\alpha)^{36}\text{Ar}$ reaction. (XBL 729-4028)

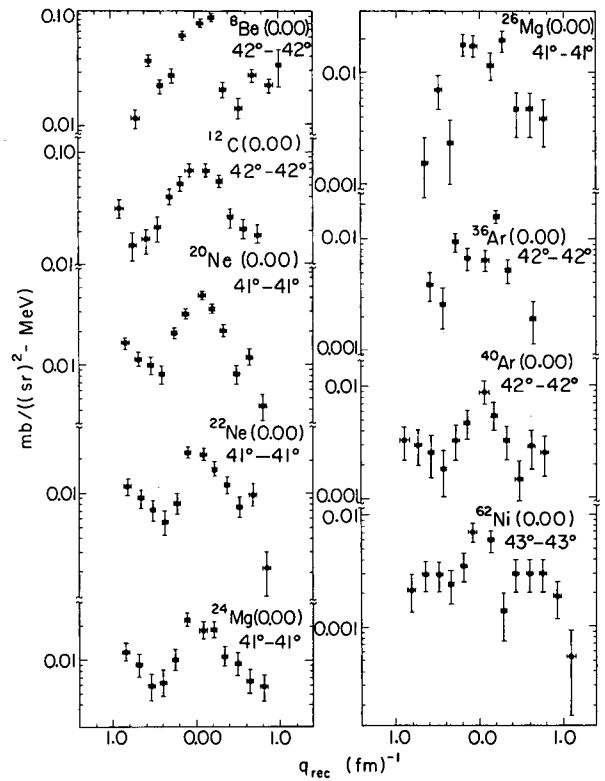


Fig. 5. Momentum correlations for ground state transitions taken at the quasi-elastic angle. (XBL 731-2094)

mechanism. Note that this behavior is present even for the heaviest nucleus, ^{66}Zn .

Figure 6 displays the symmetric angular correlations for the ground state transitions over the range given in Table I. The angular

correlations are similar, with a maximum at $\theta_1 = -\theta_2 = 35^\circ$. The main features seem to be explained within an impulse approximation model in which free α - α scattering data are used. In particular the fall of $\sigma^3(\theta)$ at large and small angle pairs (at least for the ^{16}O target) follows the free α - α scattering $[\sigma_{\alpha\alpha}(E, \theta)]$ when $\sigma_{\alpha\alpha}(E, \theta)$ is interpolated by the relative α - α energy in the final state.⁹ The impulse approximation calculation for the $(\alpha, 2\alpha)$ reaction is described in another article.

Figure 7 is a plot of the triple differential cross section taken at the angular correlation maximum (35°). The abscissa is a quantity proportional to the area of a ring where the ring width is parametrized as

$$\Delta r = r_2 - r_1 = r_0 A^{1/3} - r_0 (A-4)^{1/3}.$$

It is assumed that the cross section is proportional to the area, and Fig. 7 indicates a linear

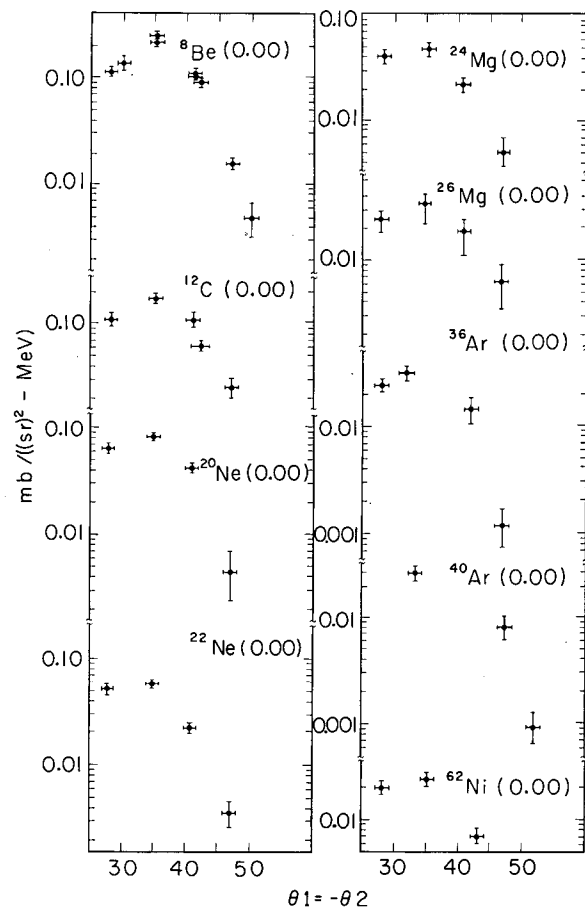


Fig. 6. Ground state angular correlations taken with the condition $\theta_1 = -\theta_2$ and $T_3 = T_4$. (XBL 731-2095)

relation from ^{12}C to ^{30}Si . The leading term in a binomial expansion of $A^{2/3} - (A-4)^{2/3}$ goes as $A^{-1/3}$, as does the surface-to-volume ratio. The $(\alpha, 2\alpha)$ cross sections seem to decrease linearly with $A^{-1/3}$ up to ^{30}Si where a leveling off in the data from ^{30}Si to ^{66}Zn is observed. These results might be interpreted as showing that, as (S/V) decreases or equivalently as the mass increases, the absorption processes are assuming a more dominant role, and thereby decreases the $(\alpha, 2\alpha)$ cross section. Further analysis of the data will include impulse approximation calculations described elsewhere in this report.

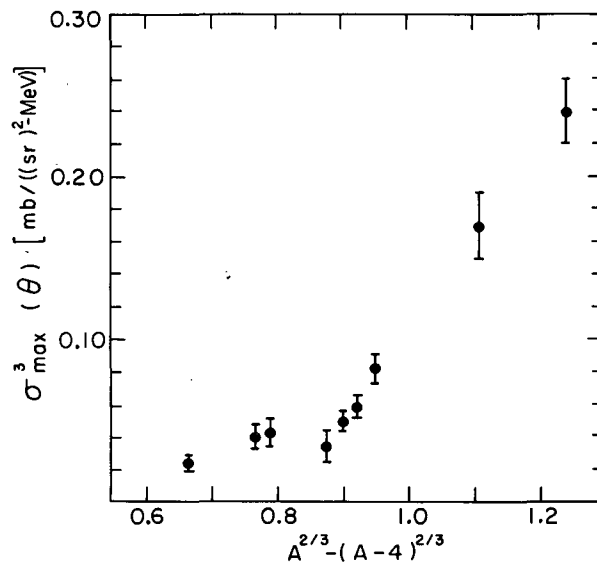


Fig. 7. Plot of maximum in the angular correlations for all targets studied vs a quantity proportional to ring area $[A^{2/3} - (A-4)^{2/3}]$. (XBL 731-2092)

References

1. J. D. Sherman and D. L. Hendrie, Nuclear Chemistry Division Annual Report for 1971, LBL-666, p. 84.
2. R. Stock et al., Phys. Rev. C 6, 1226 (1972).
3. D. Brink, Int. School of Physics, Enrico Fermi, XXXVI, 247 (1966).
4. C. D. Zafiratos, Scientific American 227, 100 (1972).
5. R. L. McGrath et al., Phys. Letters 34B, 289 (1971).

6. C. Détraz, H. H. Duhm, and H. Hafner, *Nucl. Phys. A* **147**, 488 (1970).

7. H. H. Gutbrod, H. Yoshida, and R. Bock, *Nuclear Reactions Induced by Heavy Ions*, edited by R. Bock and W. R. Herring (1970), p. 311.

8. W. Scholz, P. Neoge, K. Bethge, and R. Middleton, *Phys. Rev. C* **6**, 893 (1972).

9. H. G. Pugh et al., *Phys. Rev. Letters* **22**, 408 (1969); P. Gaillard et al., *Phys. Rev. Letters* **25**, 593 (1970).

TEST OF THE INDEPENDENCE POSTULATE IN THE BOHR THEORY OF COMPOUND-NUCLEUS DECAY: $^{50}\text{Cr}^*$ SYSTEM*

M. K. Go[†] and S. S. Markowitz

Excitation functions for the production of ^{48}V and ^{48}Cr from incident ions ^3He , α , ^{16}O , ^{18}O , and ^{22}Ne involving the compound system $^{50}\text{Cr}^*$ have been measured. Test of the independence postulate was performed in a Ghoshal type of experiment. Effects of the nuclear Coulomb barrier and high reaction Q value upon the two-nucleon evaporation excitation functions were noted.

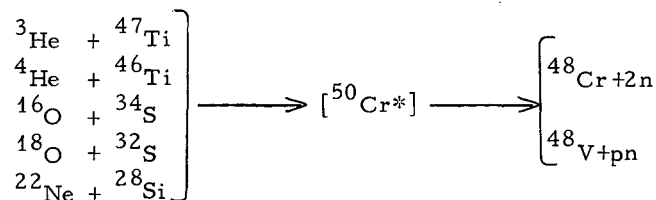
For all the reaction pairs, the ^{48}V production is more than a factor of 10 bigger than the corresponding ^{48}Cr cross section. This phenomenon can be explained by the effect of odd-even nucleon number of the product nucleus.

Simple calculations of the angular momentum and rotational energy of the compound nucleus were performed. The energy shift of the excitation function can be explained by the effect of angular momentum. The reactions involved were found to be generally consistent with the compound-nucleus model.

I. Introduction

One of the important theories concerning nuclear reactions in the intermediate energy region (<10 MeV per incident nucleon) is the compound-nucleus model.¹ In this model, the decay of the compound nucleus is independent of its mode of formation. Since the work by Ghoshal² in which the decay of the $^{64}\text{Zn}^*$ compound nucleus formed with protons was compared with that formed with α particles, many investigations³⁻⁷ have been performed along the same line. In most cases, the independence postulate is upheld roughly. More recently, when comparing the reaction excitation functions, care has been taken to match not only the excitation energy of the compound nucleus, but also its angular momentum.^{8,9} However, very few investigations have compared heavy-ion-induced reactions with those induced by light projectiles (such as p, n, ^3He , α). It is felt that the independence postulate can be subjected to a more severe test when comparing reactions involving vastly different reactants.

In this work, the compound nucleus $^{50}\text{Cr}^*$ is formed by different entrance channels, and the decay of this compound nucleus is observed through products from pn and 2n emissions. The reactions are given below.



In all the reactions studied, the excitation energy of the compound nucleus is less than 60 MeV.

II. Experimental Procedures

A stacked-foil method was used. Target foils and aluminum degrader foils were interspaced in a target holder and bombarded with appropriate ion beam from particle accelerators. For He and alpha bombardments, the Berkeley 88-inch cyclotron was used, whereas the Berkeley Heavy Ion Linear Accelerator was used for the source of heavy ions. The beam intensity was measured to within $\pm 1\%$ with a Faraday cup connected to an integrating electrometer. The ^3He or ^4He beam was magnetically analyzed, so that the incident energy is known accurately. For the heavy-ion beams, the full energy (10.4 ± 0.2 MeV/nucleon) was used. The energy at various positions in the stack was determined with conventional range-energy curves. For ^3He and ^4He , the tables of Williamson et al.¹⁰ were used, while for the heavy ions the range-energy curves were calculated with a computer code by Steward.¹¹

The targets used were prepared by vacuum evaporation of natural materials or enriched isotopes obtained from Oak Ridge National Laboratory. The backing and recoil catcher for the targets is thin Al foil (1.6 mg/cm^2). To prevent sublimation or loss of sulfur material during

bombardment, a thin ($\sim 100 \mu\text{g}/\text{cm}^2$) aluminum layer was evaporated on top of the sulfur deposit to serve as a protective shield and heat conductor.

Gamma spectroscopy was used to identify and measure the radioactivity produced. Two Ge(Li) semiconductor γ -ray detectors were employed. The active volumes are 7 and 14 cm^3 with resolutions respectively of 2.5 and 1.4 keV (full width at half maximum) for the 122-keV ^{57}Co γ ray. The γ -ray spectra from the 1024-channel analyzer were recorded in 7-in. -reel magnetic tapes. Gamma spectra photopeak analyses were handled by the CDC 6600 computer with the code SAMPO.¹² Energy and efficiency calibration of the γ -ray detection systems were facilitated with a set of eight absolute γ -ray standards.¹³

The radioactivities of ^{48}Cr and ^{48}V were determined with the 116-keV (98%) and the 938-keV (100%) gamma rays, respectively. Graphical analysis of the decay curves is adequate to obtain the decay rates at the end of bombardment. The decay rates were converted to absolute cross sections by making appropriate corrections for beam intensities, saturation effects during bombardment, and detector efficiencies.

III. Experimental Results

Excitation functions for the various reactions are given in Fig. 1. The contributions to the cross sections from other isotopes in the target are very small by isotopic abundance arguments and experiments involving targets enriched in the suspected isotopes. Contribution of the ^{48}V activity from the decay of the ^{48}Cr has been subtracted.

In all the five cases, the cross sections (x, pn) are about 13 times that of (x, 2n); here x stands for any of the five projectiles. The same enhancement of proton emission cross section has been observed by several authors.^{2, 14, 15} The greater emission probability can be explained by the difference in the level density of the product nuclei. The nucleus ^{48}V is odd-odd, and is expected¹⁶ to have many more levels available, at equal excitation energies, than the ^{48}Cr , an even-even nucleus. Since there are more channels available for the compound nucleus to decay to ^{48}V , enhancement of proton evaporation results.

The excitation functions for the ^4He reactions agree reasonably with those obtained by Raleigh.¹⁷

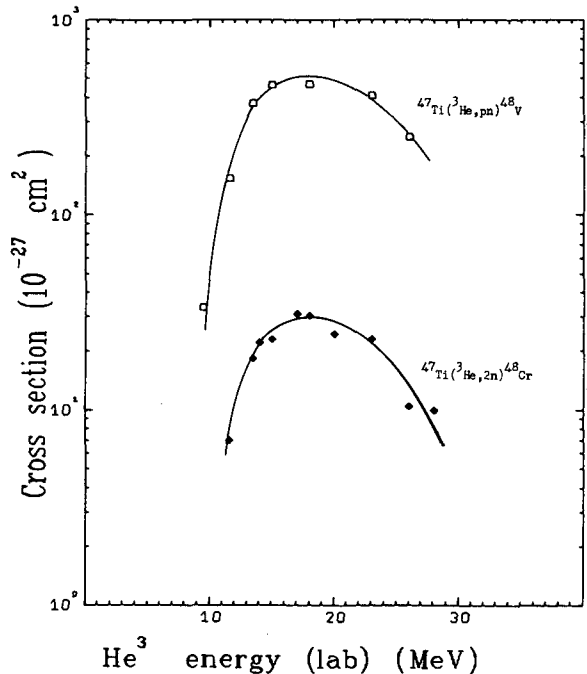


Fig. 1(a) Experimental excitation functions for the production of ^{48}V and ^{48}Cr from various charged particles involving the compound nucleus $^{50}\text{Cr}^*$. The solid lines are drawn only to aid the eyes and have no theoretical significance. (XBL 7012-7468)

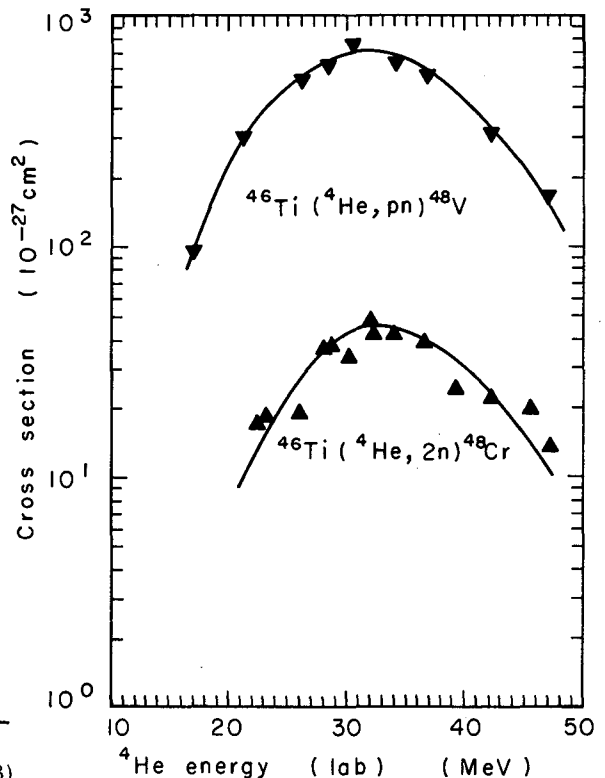


Fig. 1(b) See caption for Fig. 1(a). (XBL 728-3943)

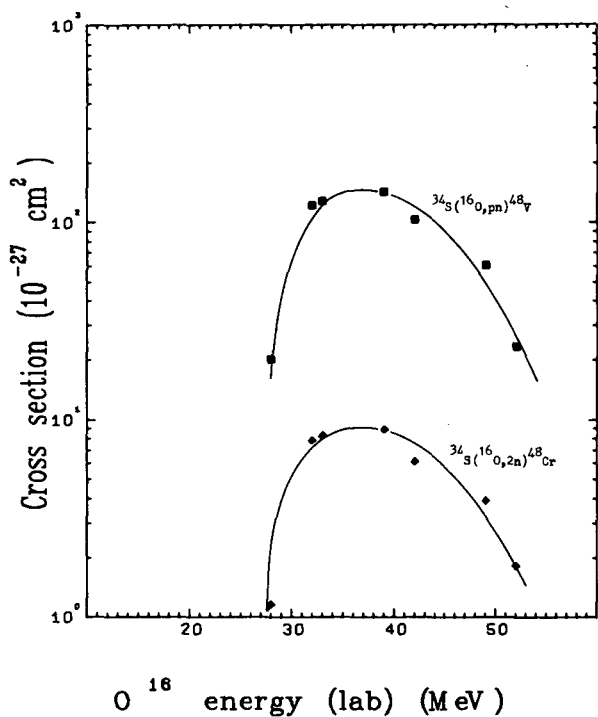


Fig. 1(c) See caption for Fig. 1(a).
(XBL 7010-6859)

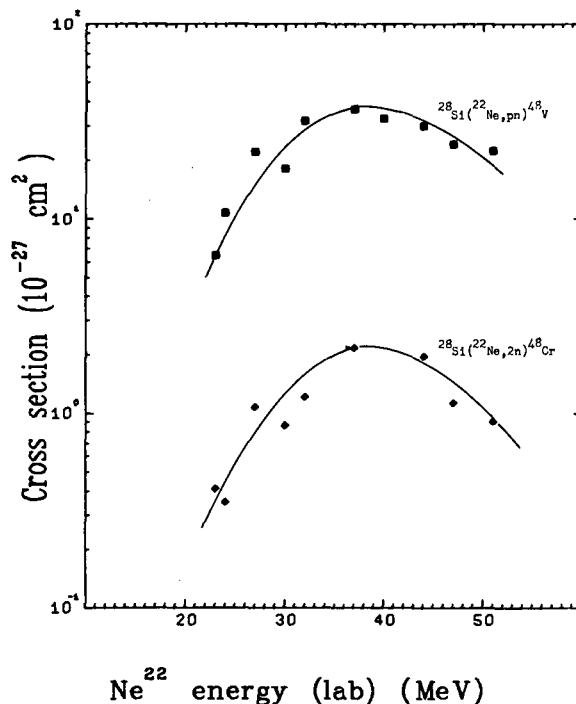


Fig. 1(e) See caption for Fig. 1(a).
(XBL 7010-6849)

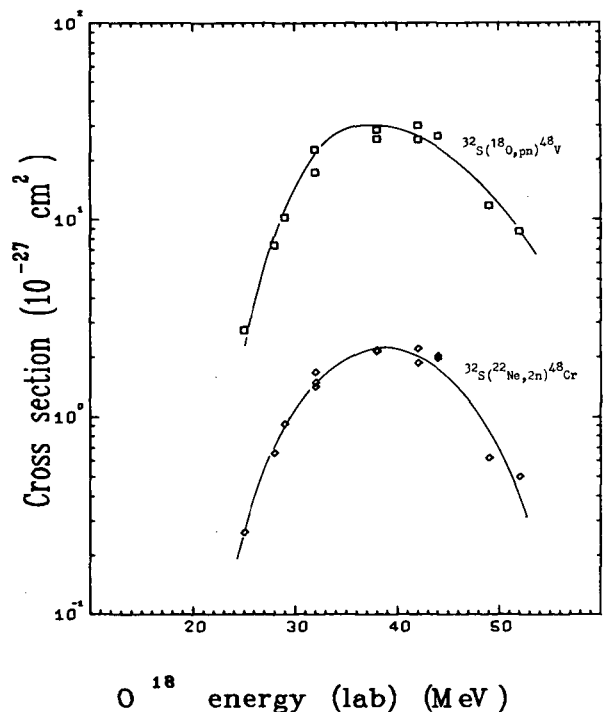


Fig. 1(d) See caption for Fig. 1(a).
(XBL 7010-6860)

IV. Calculations and Discussion

A. Comparison of Excitation Functions

In the classical test of the independence postulate, the excitation functions from different reactions involving the same compound nucleus forming the same product are compared in a plot where the excitation energy is one of the axes.

Before performing such a comparison, we wish to point out that some nuclear reactions are strongly suppressed by the Coulomb barrier and should not be compared with others not so suppressed. The excitation energy of the $^{50}\text{Cr}^*$ compound nucleus from the $^{18}\text{O}+^{32}\text{S}$ reaction near the Coulomb barrier is about 45 MeV. The excitation function for two-nucleon evaporation is expected to have peaked and become small. The shape of the excitation function observed is possibly due to the increasing penetration of the Coulomb barrier and the decreasing probability for two-nucleon evaporation as excitation energy is increased. Figure 2 shows a comparison of the excitation functions for 2n and pn evaporation from $^{16}\text{O}+^{34}\text{S}$ and $^{18}\text{O}+^{32}\text{S}$ reactions.

The corresponding cross sections for the ^{18}O -induced reactions is a factor of 10 less

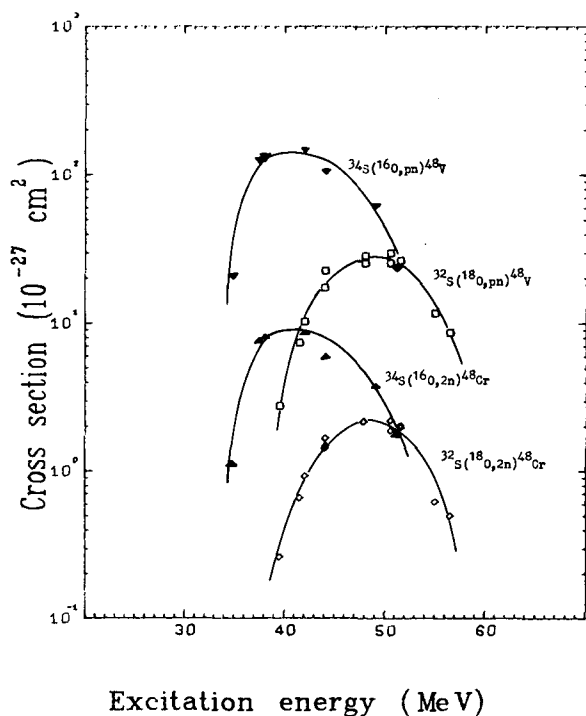


Fig. 2. Comparison of the excitation functions from ^{18}O - and ^{16}O -induced reactions. The difference in magnitude of these cross sections can be attributed to Coulomb barrier effect. (XBL 7010-6868)

than the ^{16}O -induced reactions, and the peaks of the ^{18}O excitation functions are displaced about 9 MeV toward higher excitation energies. The discrepancy should not be taken as evidence against the independence postulate, because this effect is mainly due to the Coulomb barrier.

Because the ^{22}Ne excitation functions studied are also strongly suppressed by the Coulomb barrier, we wish to compare the cross sections of the other three reacting pairs. Figure 3 shows the comparison of the ^3He , α , and ^{16}O -induced two-nucleon emission excitation functions.

In the classical test of the independence postulate, the comparison must be made after the cross sections have been normalized with respect to the total reaction cross sections. However, the ^3He and ^{16}O excitation functions are near the Coulomb barrier, and the calculation of total reaction cross section in this region by the optical model¹⁸ is very sensitive to the parameters used. Furthermore, as of now, there are no experimentally determined optical parameters available for the reaction studied. The following procedure is used to facilitate the

comparison. The magnitude of the cross sections for the $(^3\text{He}, \text{pn})$ and $(^{16}\text{O}, \text{pn})$ reactions were arbitrarily increased so that they are about equal to the (α, pn) excitation function at the peak position. The $(^3\text{He}, 2\text{n})$ and $(^{16}\text{O}, 2\text{n})$ cross sections were also increased the same percentage as the respective pn excitation functions. The result is shown in Fig. 4.

It is interesting to compare the excitation functions from ^{22}Ne and ^{18}O reactions. All these cross sections are severely suppressed by the Coulomb barrier, and presumably arise from the evaporation of high-energy neutrons and protons. Figure 5 shows such a comparison.

The $(^{18}\text{O}, 2\text{n})$ and $(^{18}\text{O}, \text{pn})$ excitation functions have the same shape and the same magnitude as the corresponding excitation functions from $^{22}\text{Ne} + ^{28}\text{Si}$. However, the ^{18}O cross sections are shifted about 5.5 MeV toward higher excitation energy. This shift in energy can be explained by angular momentum effects, discussed in detail in LBL-1230.

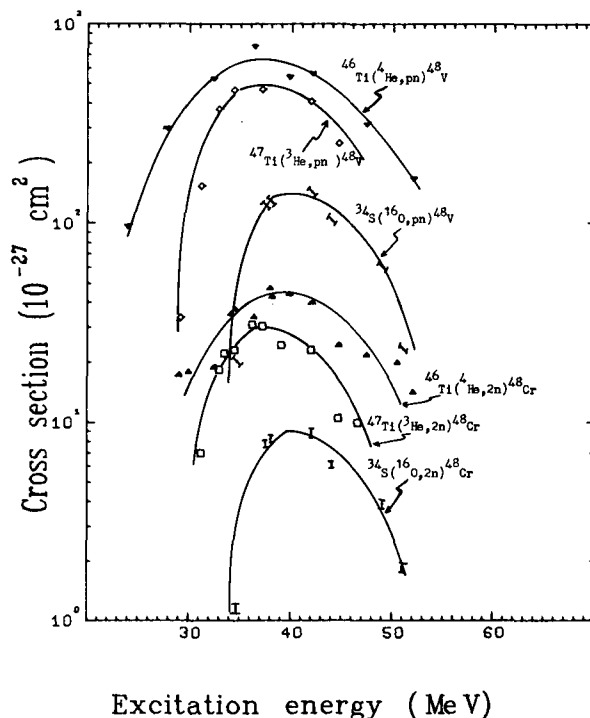


Fig. 3. Three-way comparison of the 2n and pn evaporation excitation functions from $^3\text{He} + ^{47}\text{Ti}$, $^4\text{He} + ^{46}\text{Ti}$, and $^{16}\text{O} + ^{34}\text{S}$ reactions. (XBL 7012-7474)

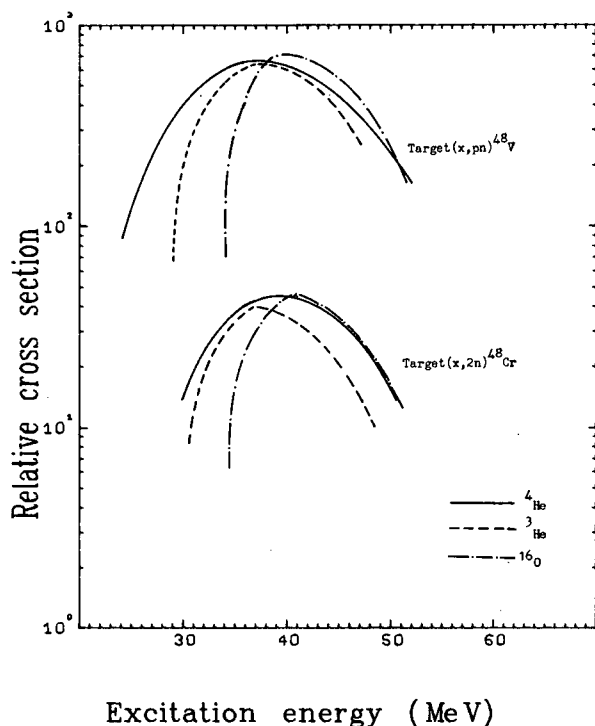


Fig. 4. Three-way comparison of the 2n and pn evaporation excitation functions after arbitrarily shifting the magnitude of the ^{16}O and ^3He cross sections (see text).

(XBL 7012-7470)

The calculated angular momentum for the various reactant pairs is presented in Fig. 6. At the peak position of the (α, pn) and $\alpha, 2n$ excitation functions the bombarding energy is about 31 MeV. The $\langle J(J+1) \rangle$ value is 130 and the rotational energy is 6.4 MeV. For the $(^{16}\text{O}, 2n)$ and $(^{16}\text{O}, pn)$ excitation functions, the rotational energy at the peak is 7.4 MeV. The expected energy shift between the ^{16}O - and α -induced reactions will therefore be 1 MeV. The observed shift is about 2 MeV. This discrepancy may be caused by the Coulomb barrier acting on the low-energy edge of the ^{16}O excitation functions.

For the ^{22}Ne -induced reactions, the rotational energy at the peak of the two-nucleon evaporation excitation functions is about 2.0 MeV, and the ^{18}O -induced reactions' E_R is 5.9 MeV. The expected displacement is about 3.9 MeV. The observed shift is 5.5 MeV.

Although the calculated energy shifts do not agree perfectly with the observed ones, these approximate calculations do allow qualitative understanding of the effect of angular momentum upon the de-excitation of the compound nucleus. Better agreement can be achieved if the moment of inertia of the rotating compound

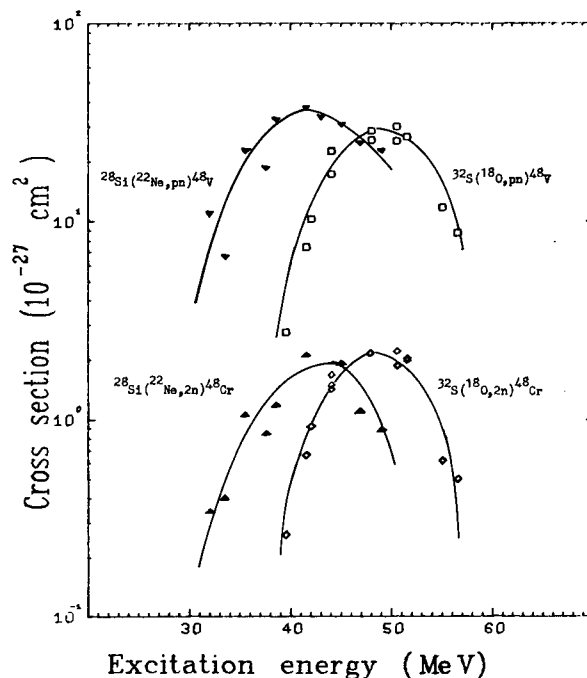


Fig. 5. Comparison of the 2n and pn emission excitation functions from the $^{18}\text{O}+^{32}\text{S}$ and $^{22}\text{Ne}+^{28}\text{Si}$ reactions. All these cross sections are suppressed severely by the Coulomb barrier (XBL 7010-6865)

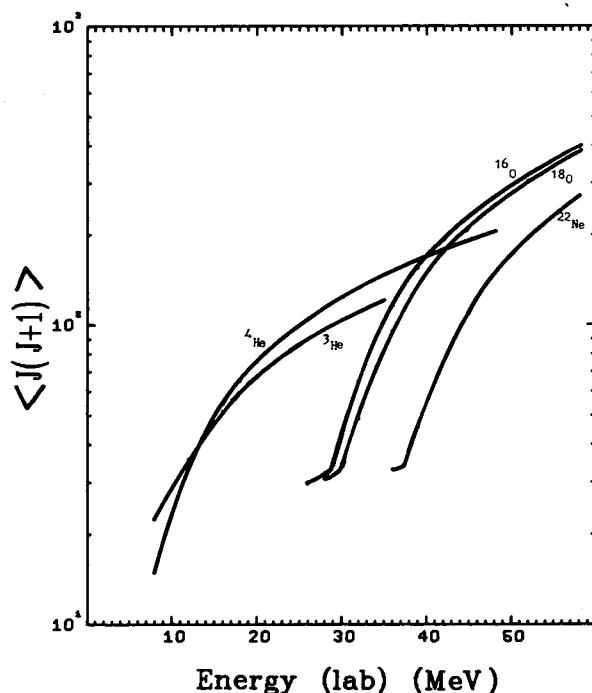


Fig. 6. Calculated average angular momentum quantum number for the $^{50}\text{Cr}^*$ compound nucleus as a function of bombarding energy for various reactant pairs. (XBL 7012-7479)

nucleus is taken to be $7 k I_r$, where k is a parameter, and I_r is the moment of inertia of a rigid sphere. For more accurate and realistic calculations, the treatment involves the detailed calculation of the γ -ray de-excitation and spin distribution¹⁹ of the decaying compound nucleus.

For the compound-nucleus reaction $a+A \rightarrow C^* \rightarrow b+B$, according to the independence postulate, the cross section can be formulated as

$$\sigma(a, b) = \sigma_C(a) P(C, b) \quad (1)$$

where $\sigma_C(a)$ is the cross section for the formation of the compound nucleus C^* from the entrance channel $a+A$; $P(C, b)$ is the probability that the compound nucleus decays through the exit channel $b+B$. $P(C, b)$ depends only on the exit channel and the compound nucleus.

Furthermore, for reactions involving different exit channels, we have

$$\frac{\sigma(a, b)}{\sigma(a, d)} = \frac{\sigma_C(a) P(C, b)}{\sigma_C(a) P(C, d)} = \frac{P(C, b)}{P(C, d)}, \quad (2)$$

where $\sigma(a, d)$ designates the reaction cross section for the reaction $a+A \rightarrow C^* \rightarrow d+D$. Because $P(C, b)$ and $P(C, d)$ do not depend on the entrance channel, the ratio of cross sections from different entrance channels should be equal,²⁰ or,

$$\frac{\sigma(a, b)}{\sigma(a, d)} = \frac{P(C, b)}{P(C, d)} = \frac{\sigma(a', b)}{\sigma(a', d)}, \quad (3)$$

where $\sigma(a' b)$ is the cross section for the reaction $a'+A' \rightarrow C^* \rightarrow b+B$; similarly for $\sigma(a', d)$.

Figure 7 shows the ratios of pn cross sections to the 2n cross sections for all the reactant pairs studied. Although the ratios lie mainly between 12 and 18, it is obvious that Eq. (3) is not strictly upheld. For a more quantitative comparison, effects of isospin,²¹ Coulomb barrier, and γ -ray competition²² on the decay of the compound nucleus must be taken into account.

Footnotes and References

* Condensed from LBL 1230; Phys. Rev. C, in press.

† Submitted in partial fulfillment of the Ph.D. requirements at the Department of Chemistry, University of California, Berkeley, Thesis of M. K. Go, UCRL-20483, May 1971. Present address: Western Regional Laboratory, USDA, Albany, California.

1. N. Bohr, Nature 137, 344 (1936).

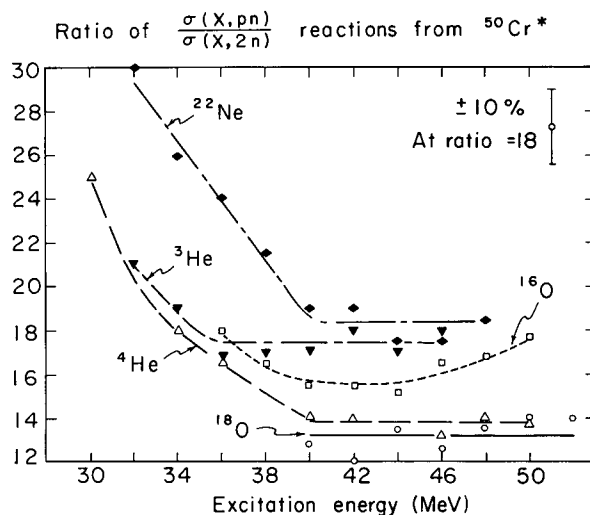


Fig. 7. Ratio of $\sigma(x, pn)$ to $\sigma(x, 2n)$ reaction from $^{50}\text{Cr}^*$. The lines are to guide the eye. A 10% error bar is shown. (XBL 728-3942)

2. S. N. Ghoshal, Phys. Rev. 80, 939 (1950).
3. W. John, Jr., Phys. Rev. 103, 704 (1956).
4. C. M. Stearns, Ph.D. thesis, NYO-10387 (1962).
5. S. Tanaka, M. Furukawa, S. Iwata, M. Yagi, H. Amano, and T. Mikumo, J. Phys. Soc. Japan 15, 2125 (1960).
6. K. C. Chen and J. M. Miller, Phys. Rev. 134, B1269 (1964).
7. C. F. Smith, Jr., Lawrence Radiation Laboratory Report UCRL-11862, 1965 (unpublished).
8. J. M. D'Auria, M. J. Fluss, G. Herzog, L. Kowalski, J. M. Miller, and R. C. Reedy, Phys. Rev. 174, 1409 (1968).
9. M. J. Fluss, J. M. Miller, J. M. D'Auria, N. Dudev, B. M. Foreman, Jr., L. Kowalski, and R. C. Reedy, Phys. Rev. 187, 1449 (1969).
10. C. F. Williamson, J. P. Boujot, and J. Picard, Commissariat a l'Energie Atomique Report CEA-R3042 (1966).
11. P. G. Steward, Lawrence Radiation Laboratory Report UCRL-18127, 1968 (unpublished).
12. J. T. Routti and S. Prussin, Nucl. Instr. Methods 72, 125 (1969).
13. Obtained from International Atomic Energy Agency, Vienna, Austria.

14. S. S. Markowitz, J. M. Miller, and G. Friedlander, *Phys. Rev.* 98, 1197 (1955).
15. N. T. Porile, *Phys. Rev.* 315, 939 (1959).
16. H. Hurwitz and H. A. Bethe, *Phys. Rev.* 81, 898 (1951).
17. D. O. Raleigh, Ph.D. thesis, Columbia University, 1960 (unpublished).
18. For example, E. H. Auerbach, Brookhaven National Laboratory Report BNL-6562, 1964 (unpublished).
19. J. R. Grover and J. Gilat, *Phys. Rev.* 157, 802 (1967).
20. G. Friedlander, J. W. Kennedy, and J. M. Miller, *Nuclear and Radiochemistry*, 2nd ed. (Wiley, New York, 1966), p. 342.
21. C. C. Lu, J. R. Huizenga, C. J. Stephan, and A. J. Gorski, *Nucl. Phys.* A164, 225 (1971).
22. S. M. Ferguson, H. Ejiri, and I. Halpern, *Nucl. Phys.* A188, 1 (1972).

STUDY OF ELEMENTARY PARTICLE EFFECTS IN SIMPLE HIGH-ENERGY NUCLEAR REACTIONS

N. P. Jacob, Jr., and S. S. Markowitz

The study of simple nuclear reactions induced by high-energy projectile (≥ 0.1 GeV), such as protons and in particular π mesons, is a feasible approach for investigating how collisions between particles in nuclear matter can be correlated to collisions between the same particles in free space.¹ Because the predominant mechanism for high-energy reactions of the form (p, 2p), (p, pn), and (π , π n) involves a single collision between the projectile and a surface nucleon in the target, followed by the unhindered escape of both collision partners, one would anticipate that changes observed in the experimental excitation functions for this particular class of reactions would reflect similar changes in the well-known elementary particle scattering cross sections.

Because the p-p free-particle excitation function exhibits a marked increase in cross section, from about 25 mb at 0.3 GeV to 50 mb at 0.9 GeV, and then a gradual decrease at higher energies, as illustrated in Fig. 1, we have concentrated the initial stage of this research on measuring the cross sections for the $^{48}\text{Ti}(p, 2p)^{47}\text{Sc}$ reaction from 0.3 to 6 GeV to see if a similar change occurs. Thin targets of $^{48}\text{TiO}_2$, which have been carefully prepared by vacuum evaporation of target material onto thin aluminum, are activated in either the LBL 184-inch synchrocyclotron or the Bevatron, and the desired product is assayed by monitoring the gamma-ray spectrum with a high-resolution Ge(Li) detector. A significant rise of about 20%, from 23.0 ± 0.2 mb at 0.3 GeV to 28.4 ± 1.1 mb at 0.8 GeV does indeed occur for the above-mentioned reaction. Due to the proton momentum in the nucleus, this rise is not as pronounced as the rise in the free-particle cross sections between the same energies.

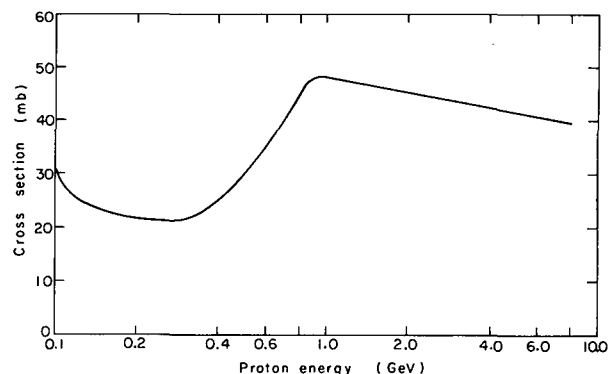


Fig. 1. The total p-p free-particle cross section versus incident proton energy, taken from Ref. 10. (XBL 732-2285)

In addition, we have formulated a simple classical "knock-on" theory similar to that of Das et al.² that has predicted the magnitude of cross sections to within 10%, as well as the shape of the excitation functions for (p, 2p) reactions that have been the subject of previous investigations.³⁻⁵ In this treatment, we have assumed the average effective momentum transfer in the initial collision to be equal to twice the Fermi momentum p_F and have used the theory of Clements and Winsberg⁶ to calculate the values of collision cross sections in nuclear matter. The only parameter r_0 , then, is adjusted to give the best possible agreement with experiment. The results for (p, 2p) reactions above 0.2 GeV on ^{25}Mg , ^{57}Fe , ^{68}Zn , and ^{142}Ce are shown in Figs. 2 to 5. Although the calculation predicts a maximum cross section

shifted to lower energies in comparison to the experimental curves, the results constitute better agreement with experiment than has been achieved by the more sophisticated Monte Carlo treatments for simple nuclear reactions.^{7,8} Results on ^{48}Ti are forthcoming.

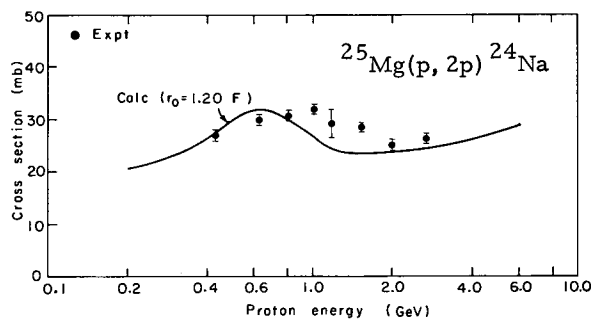


Fig. 2. The calculated and experimental cross sections for the $^{25}\text{Mg}(p, 2p)^{24}\text{Na}$ reaction ($r_0 = 1.20 F$). (XBL 732-2286)

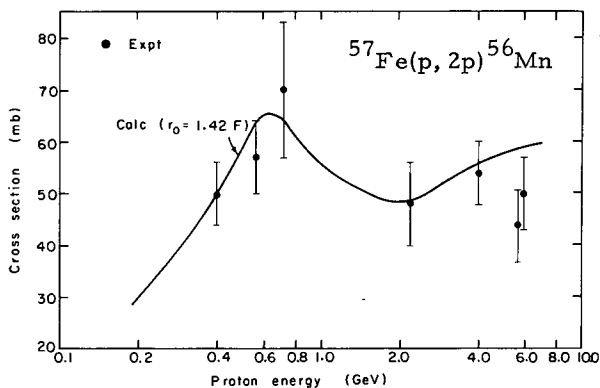


Fig. 3. The calculated and experimental cross sections for the $^{57}\text{Fe}(p, 2p)^{56}\text{Mn}$ reaction ($r_0 = 1.42 F$). (XBL 732-2287)

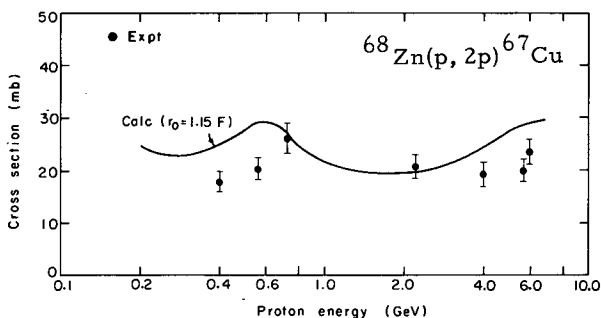


Fig. 4. The calculated and experimental cross sections for the $^{68}\text{Zn}(p, 2p)^{67}\text{Cu}$ reaction ($r_0 = 1.15 F$). (XBL 732-2288)

A project on simple pion-induced nuclear reactions that will use the intense pion beams at LAMPF (Los Alamos Meson Physics Facility) has been accepted. This research will investigate the relationship between pion-nucleon free-particle cross sections and similar cross sections within nuclear matter that was introduced previously.⁹

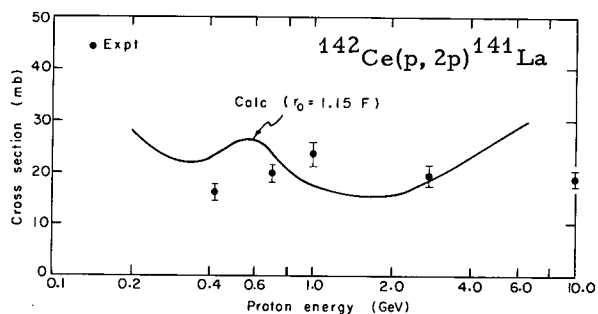


Fig. 5. The calculated and experimental cross sections for the $^{142}\text{Ce}(p, 2p)^{141}\text{La}$ reaction ($r_0 = 1.15 F$). (XBL 732-2289)

References

1. J. R. Grover and A. A. Caretto, Jr., *Ann. Rev. Nucl. Sci.* **14**, 51 (1964).
2. S. Das, B. K. Gupta, P. C. Bhattacharya, and M. M. Biswas, *Nucl. Phys.* **A190**, 501 (1972).
3. P. L. Reeder, UCRL-10531 (1962).
4. S. Meloni and J. B. Cumming, *Phys. Rev.* **136**, B1359 (1964).
5. P. L. Reeder, *Phys. Rev.* **178**, 1795 (1969).
6. T. Clements and L. Winsberg, *Phys. Rev.* **122**, 1623 (1961). Tabulated results used in the calculation are found in Clements and Winsberg, UCRL-8982 (1960).
7. K. Chen, Z. Fraenkel, G. Friedlander, J. R. Grover, J. M. Miller, and Y. Shimamoto, *Phys. Rev.* **166**, 949 (1968).
8. K. Chen, G. Friedlander, and J. M. Miller, *Phys. Rev.* **176**, 1208 (1968).
9. P. L. Reeder and S. S. Markowitz, *Phys. Rev.* **133**, B639 (1964).
10. V. S. Barashenkov and V. M. Maltsev, *Fortschr. Physik* **9**, 549 (1961).

NEW ISOTOPES PRODUCED IN THE REACTION OF HIGH-ENERGY PROTONS ON U[†]

R. Klapisch, C. Thibault, A. M. Poskanzer,
R. Prieels, C. Rigaud, and E. Roeckl

With an on-line mass spectrometer we have discovered, by means of the reaction of 24-GeV protons on uranium, the very neutron-rich isotope ^{32}Na and measured its half-life. We have also produced in the same reaction the new isotopes ^{33}Na , $^{48-50}\text{K}$, and $^{227, 228}\text{Fr}$ and found evidence for shell effects in the cross sections of the new sodium isotopes.

Light nuclei with a large excess of neutrons can be produced in the reaction of high-energy protons on heavy targets,^{1, 2} or in complex transfer from heavy-ion induced reactions.³ In the case of high-energy reactions it was shown that the on-line mass spectrometric technique¹ can sort out selectively the isotopes of alkali elements and supply information on their half-lives. This work has been further extended with the construction of an improved instrument, and this report contains the first results obtained.

The technique has been described in detail elsewhere.⁴ In brief, the energetic recoils from the reaction are caught in heated graphite foils from which they diffuse out very quickly. The alkali ions (Li^+ , Na^+ , K^+) produced by surface ionization are then mass analyzed in a Nier-type mass spectrometer. The detection of ions is achieved by an electron multiplier capable of counting single ions.

To increase the production of rare nuclei, the effective target thickness was increased to 2 g/cm^2 of U. The mass spectrometer is a magnetic sector (90° , $r = 35 \text{ cm}$). It has a wide gap to accept ions from the long target (50 mm) and is slightly inhomogeneous ($n = 0.23$) to ensure high transmission by means of z focusing.

The experiment was performed with 24-GeV protons in the "neutrino" fast-ejected beam of the CERN proton synchrotron. Short ($2.1 \mu\text{sec}$) and intense (1.5×10^{12} protons) bursts were directed on our 6-mm-diam target every 10 sec. The detector was installed in a shielded enclosure lined with a thin sheet (0.7 mm) of cadmium. A combination of electrostatic quadrupole lenses was used to refocus the ions after the exit slit of the spectrometer through a beam pipe traversing the shielding wall (40 cm iron, 80 cm concrete) onto the detector. This was extremely effective in reducing the magnitude of the background and shortening its decay time.

The sensitivity is increased further by modulating the ion beam of the mass spectrometer and detecting the resulting peaks in the ion-counting rate. The peak counting rates decrease after each beam burst both because of radioactive decay and because of diffusion out of the target. The diffusion rate is calibrated with long-lived isotopes, and the resulting half-lives are given in Table I for the new isotope ^{32}Na and other short-lived Na isotopes.

Table I. Half-life measurements (msec).

^{26}Na	1070 ± 30
^{27}Na	295 ± 10
^{28}Na	35.7 ± 1
^{29}Na	48.6 ± 2
^{30}Na	55 ± 3
^{31}Na	17.7 ± 1
^{32}Na	14.5 ± 3
^{33}Na	20 ± 15

A search was made for ^{33}Na using the same procedure during a 3-hr experiment with a total of 7×10^{15} protons. Two peaks of ^{33}Na were found with 86 ± 15 and 61 ± 15 counts, respectively, after a background of 76 ± 9 had been subtracted. This thus establishes the particle stability of ^{33}Na even though the data are not adequate to deduce the half-life. The stability of ^{33}Na was indeed expected because of the existence of ^{32}Na and the extra stability due to the neutron pairing energy.

Following the same procedure as for ^{32}Na , the isotopes ^{48}K , ^{49}K , and ^{50}K were found. However, their half-lives were not short compared with the diffusion time, and hence could not be determined. We also observed the new neutron-rich isotopes ^{227}Fr and ^{228}Fr produced in the spallation of the uranium target.

The cross sections for formation of all the sodium and potassium isotopes in this high-energy reaction are shown in Fig. 1. The error bars on ^{33}Na represent the two extreme values for the half-life of ^{33}Na (5 and 35 msec) that could be compatible with the least-squares fit to our data. It can be seen that the cross sections show a more or less regular decrease of a constant factor until ^{31}Na , closing the

$N=20$ neutron shell, and ^{47}K , closing the $N=28$ neutron shell.

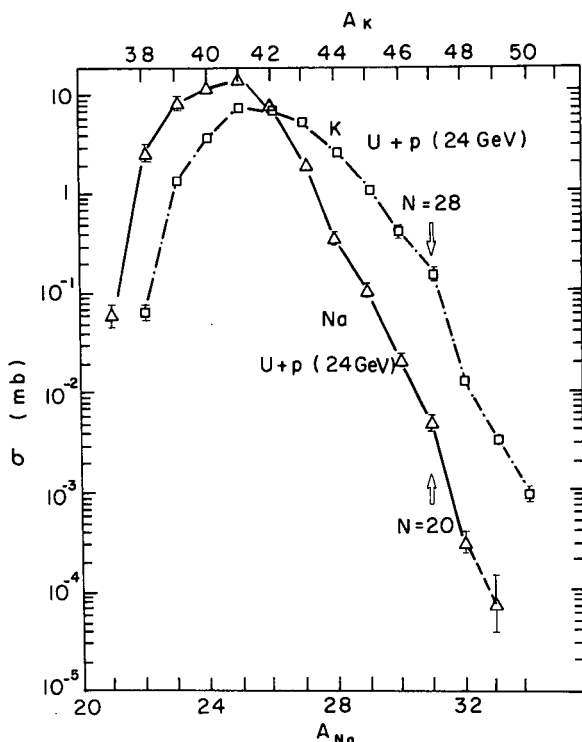


Fig. 1. Cross section for production of isotopes of sodium and potassium in the reaction of 24-GeV protons on uranium. Notice the abrupt decreases between ^{31}Na and ^{32}Na , and ^{47}K and ^{48}K , after the closure of the $N=20$ and 28 shells, respectively. (XBL 732-2290)

The decreases at ^{31}Na - ^{32}Na and ^{47}K - ^{48}K are, respectively, factors of 3.5 and 5 greater than the average decreases. These dramatic breaks seem to be associated with shell effects, and one can expect that the continued decrease in cross sections for other isotopes in the same shells will be moderate. This conclusion is not substantially affected by the uncertainties in the half-life of ^{33}Na and gives strong support to the experimental possibility of detecting by the same technique nuclei that are still richer in neutrons.

Footnotes and References

†Work performed at the Centre de Spectrométrie Nucléaire et de Spectrométrie de Masse, 91 Orsay, France, where one of the authors (AMP) was a Guggenheim Fellow for 1970-71. Condensed from *Phys. Rev. Letters* **29**, 1254 (1972).

1a. R. Klapisch, C. Thibault-Philippe, C. Detraz, J. Chaumont, R. Bernas, and E. Beck, *Phys. Rev. Lett.* **23**, 652 (1969).

1b. C. Thibault-Philippe, thesis, Orsay, 1971 (unpublished).

2. A. M. Poskanzer, G. W. Butler, and E. K. Hyde, *Phys. Rev. C* **3**, 882 (1971).

3. A. G. Artukh, V. V. Avdeichikov, G. F. Gridnev, V. L. Mikheev, V. V. Volkov, and J. Wilczynski, *Nucl. Phys.* **A176**, 284 (1971).

4. R. Klapisch, J. Chaumont, C. Philippe, I. Amarel, R. Ferreau, M. Salomé, and R. Bernas, *Nucl. Instr. Methods* **53**, 216 (1967). See also Ref. 1b.

ON-LINE MASS SPECTROMETRIC MEASUREMENT OF THE MASSES OF NEUTRON-RICH SODIUM ISOTOPES*

R. Klapisch, R. Prieels, C. Thibault, A. M. Poskanzer, C. Rigaud, and E. Roeckl

Using an on-line mass spectrometer, we have measured directly, to an accuracy of 150 to 500 keV, the masses of $^{27-30}\text{Na}$ produced in the reaction of 24-GeV protons on uranium.

In most of the experiments¹⁻³ where light nuclei with a large excess of neutrons have been produced only the existence (i.e., particle stability) of the more exotic nuclei is known. This information is of particular value if the calculated limits of nuclear stability can be tested this way. A few experiments also give other ground state characteristics such as half-lives⁴ or masses.⁵

Mass calculations are the basis on which the stability of very-neutron-rich nuclei are predicted. Since all these calculations derive their parameters from a region of nuclei with measured masses near the valley of beta stability, it can be expected that very distant extrapolations can lead to sizable errors. That this is the case is seen by comparing among themselves the prediction of different mass formulas.^{2,6} One is led to observe that for $T_Z \geq 3$ the predictions can differ by several MeV. Hence, the measurement of masses of nuclei far from stability can lead to a very severe test of the validity of mass formulas even when the

measurements have an accuracy of only 200-500 keV. Measurements to this accuracy for sodium isotopes (about 10^{-5}) can be obtained with a spectrometer with a resolving power of only 500 (FWHM) by measuring the centroid of the peaks to an accuracy of 1/2% of their widths. The purpose of this paper is to report the first on-line mass spectrometric mass measurements by demonstrating the technique for the isotopes of sodium produced in the reaction of 24-GeV protons on uranium at the CERN proton synchrotron.

On-line mass spectrometry had already been used to identify new isotopes and measure their half-lives,⁴ and an extensive description is available elsewhere.² For this discussion it is appropriate to think of the instrument as an ordinary mass spectrometer with a special surface ionization ion source that is loaded with short-lived nuclei ($T_{1/2} \ll 1$ sec) at regular time intervals by the interaction of intense proton bursts with a target of uranium.

The measurement of masses rests on the same theorem that is used in high-resolution mass measurements:⁷ Two ions A^+ and B^+ of masses M_A and M_B follow the same trajectory in the spectrometer if the magnetic field configuration remains constant and all electrostatic potentials are changed to satisfy the ratio

$$\frac{M_A}{M_B} = \frac{V_B}{V_A} \quad (1)$$

To measure the ratio of two masses with our instrument it is thus necessary to keep the field fixed and measure the accelerating potentials V_A and V_B corresponding to ions that follow the same trajectories to the exit slit of the spectrometer. To meet this condition, a calibrated triangular modulation is applied to the dc accelerating potential U in order to sweep the ions past the slit. From the peak in counting rate and the known modulation, an increment v is determined, so that one has

$$V_A = U_A + v_A \quad \text{and} \quad V_B = U_B + v_B$$

During alternate pulses of the synchrotron (i. e., every 10 seconds) data are recorded on masses A and B. U_A and U_B come from two physically distinct, highly regulated ($2 \cdot 10^{-5}$) power supplies and are switched by a system of relays. The dc potentials (6 to 10 kV) are measured each beam burst through a dividing bridge with a digital voltmeter accurate to 10^{-6} . To determine the increments v , the centroids of the peaks (both means and medians) are calculated during the experiment with a PDP-15 computer.

In order to account for systematic errors Eq. (1) was modified by introducing the parameter δ such that $M_A/M_B = (V_B + \delta)/(V_A + \delta)$. The parameter δ probably accounts for many causes of systematic errors. Some of these are obvious, like the constant 3-volt dc heating of the surface ionization source, which is not changed when jumping from mass A to mass B. There are, of course, other causes of systematic errors that still remain unknown to us because the method is so new. It was thus felt indispensable to calibrate the instrument by measuring δ on pairs of known masses in actual experimental conditions. A systematic study of Na isotopes with known masses⁸ showed δ values of the order of 8 V. While this value in itself is not unreasonable, its long-term variation during the time of the experiment was relatively large [$\sigma(\delta) = 2.4$ V] and thus it was decided to measure δ at least twice just before and just after each unknown mass measurement with two known masses differing by the same mass number jump. For example, a measurement of $M(^{25}\text{Na})/M(^{27}\text{Na})$ would be calibrated before and after by $M(^{24}\text{Na})/M(^{26}\text{Na})$.

The results of the mass determinations are presented in Table I⁹ with their errors determined from the errors in the voltage measurements and the uncertainty in the quantity delta. The errors in the voltage measurements come primarily from the counting statistics that determine the centroids of the peaks. For the delta measurements, which had good counting statistics, it appeared that the major error came from the error in the digital voltmeter measurements. However, this error was overestimated because of the effect of the voltage modulation. Thus the delta errors only were determined from the agreement of replicates and came to about one volt. A chi-square value was calculated for the deviations of the 36 independent mass measurements represented in Table I from the four means, and came to 26 for 32 degrees of freedom. The reproducibility of the mass measurements therefore agrees with what one would expect from our calculated errors. It is also worth pointing out that our accuracy seems at present limited by counting statistics, rather than by systematic errors.

We can deduce neutron separation energies from our measurements and compare them with the calculated values. It is apparent from Table II for ^{29}Na and ^{30}Na that the calculated odd-even effect is significantly greater than the experimental one. It would be of obvious interest to improve these mass measurements and to extend them to ^{31}Na , ^{11}Li , and other isotopes.

Table I. Atomic mass excesses (M-A) in keV. The numbers in parentheses are the number of measurements.

Reference mass	New mass	New mass			
		27	28	29	30
^{25}Na	-9356	-5775±635 (2)	-1014±200 (9)	3105±495 (4)	
^{26}Na	-6854±30 ^a	-5881±145 (4)	-1619±475 (1)	2665±260 (6)	8195±685 (3)
^{27}Na	-5880±140		-2249±460 (2)		7686±1360 (1)
^{28}Na	-1260±170			2576±480 (2)	
^{29}Na	2730±210				8712±690 (2)
Best value		-5880±140	-1260±170	2730±210	8370±460

^aSee Ref. 9

Table II. Comparison with calculations.

Isotope	T_z	(M-A), MeV			E_n (MeV)	
		Experimental	G. et al. revised	G. et al. 1969	Experimental	G. et al. revised
^{27}Na	5/2	-5.88±0.14	-5.98	-6.65	7.10±0.14	7.10
^{28}Na	3	-1.26±0.17	-1.55	-3.38	3.45±0.22	3.64
^{29}Na	7/2	2.73±0.21	0.86	-2.14	4.08±0.27	5.66
^{30}Na	4	8.37±0.46	6.89	2.72	2.43±0.51	2.04

Footnote and References

* Work performed at the Centre de Spectrométrie Nucléaire et de Spectrométrie de Masse, 91 Orsay, France, where one of the authors (AMP) was a Guggenheim Fellow for 1970-71.

1. A. M. Poskanzer, G. W. Butler, and E. K. Hyde, Phys. Rev. C **3**, 882 (1971) and references therein.

2. C. Thibault-Philippe, thesis, Orsay (1971) and references therein.

3. A. G. Artukh, V. V. Avdeichikov, G. F. Gridnev, V. L. Mikheev, V. V. Volkov, and J. Wilizynski, Nucl. Phys. **A176**, 284 (1971).

4. R. Klapisch, C. Thibault, A. M. Poskanzer, R. Prieels, C. Rigaud, and E. Roeckl, Phys. Rev. Letters **29**, 1254 (1972).

5. A. G. Artukh, G. F. Gridnev, V. L. Mikheev, V. V. Volkov, and J. Wilizynski, Nucl. Phys. **A192**, 170 (1972).

6. R. Klapisch and C. Thibault, in Proceedings of the 4th International Conference on Atomic Masses and Related Constants, Teddington, 1971 (to be published).

7. See for example the discussion by W. H. Johnson, Jr. in Proceedings of the International Conference on the Properties of Nuclei Far from the Region of Beta-stability, CERN 70-30 (1970), p. 307.

8. When not otherwise indicated, masses are taken from A. H. Wapstra and N. B. Gove, *Nuclear Data Tables* 9, 267 (1971).

9. G. C. Ball, W. G. Davies, J. S. Forster, and J. C. Hardy, *Phys. Rev. Letters* 28, 1069 and 1497 (1972).

10. G. T. Garvey, W. J. Gerace, R. L. Jaffe, I. Talmi, I. Kelson, *Rev. Mod. Phys.* 41, 51 (1969).

11. C. Thibault and R. Klapisch, *Phys. Rev. C* 6, 1509 (1972).

SEARCH FOR SUPERHEAVY ELEMENTS PRODUCED BY SECONDARY REACTIONS IN URANIUM*

L. Westgaard, B. R. Erdal, P. G. Hansen, E. Kugler, G. Sletten, S. Sundell, J. Camplan,
R. Klapisch, R. Meunier, A. M. Poskanzer, C. Stephan, and J. Tys

It was pointed out by Hyde¹ that when uranium is bombarded with GeV-energy protons, the flux of energetic neutron-rich fragments might give rise to observable yields of superheavy elements through build-up reactions in the target.

The main features of the experiment can be summarized as follows: (a) natural uranium was chosen as the target material in order to maximize the yield of neutron-rich fragments and to have a target for the secondary reaction as heavy as possible; (b) the volatile fraction of the reaction products was separated from the molten target matrix by vacuum distillation and collected in a cold trap, since according to theoretical predictions eka-Hg ($Z=112$) and eka-Pb ($Z=114$), if present, were expected to be contained in the volatile fraction; (c) the contents of the cold trap were introduced into an electromagnetic isotope separator tuned to the mass region of interest; and (d) the collectors from the isotope separation were viewed by charged-particle track detectors to search for spontaneous fission activity.

The irradiations with 24-GeV protons were performed at the CERN proton synchrotron: an internal irradiation of a few hours with a multiple-traversal target to search for short-lived products, and a long irradiation in an external beam line. The internal target was made up of two U foils, sandwiched between Al monitor foils. The target for the external beam consisted of a U-rod of about one proton interaction length canned in stainless steel under a He atmosphere. This target was bombarded intermittently over a period of 23 days.

The only track that was observed in the quartz was not accompanied by a track at 180° in the matching plate. The event is therefore not likely to have been a binary fission decay. Thus, the experiment gives no evidence for production of superheavy elements. As a way of summarizing this result the upper limit of the overall cross section for the production of

a superheavy element decaying only by spontaneous fission was calculated to $2 \times 10^{-40} \text{ cm}^2$, assuming a half-life of one month. The limit was not quite as low for longer or shorter half-lives.

To interpret this result one must consider separately the primary and secondary sections that contribute to the process. By extrapolation of experimental data one can arrive at a value for the flux of heavy fragments with enough energy to induce the secondary reaction. This procedure contains large uncertainties, however, because even though the energy spectra for the Ar fragments exhibit high-energy tails,¹ this does not seem to be the case for Cu fragments.² There is additional experimental evidence^{3, 4} that heavy fragments with sufficiently high energy do not exist. Nevertheless, an attempt has been made for the secondary reaction $^{238}\text{U}(^{56}\text{Ca}, 4n)^{290}112_{178}$. This represents one of several possible reactions leading to products in the superheavy-element region. With the upper limit for a one-month half-life, one gets an upper limit of 5 mb for the cross section of the heavy-ion secondary reaction. One is led to conclude that the type of secondary reaction considered is not promising for the production of superheavy elements.

Footnote and References

*Work performed at Orsay and CERN. One of the authors (AMP) was a Guggenheim Fellow for 1970-71. Condensed from *Nucl. Phys. A192*, 517 (1972).

1. A. M. Poskanzer, G. W. Butler, and E. K. Hyde, *Phys. Rev. C* 3, 882 (1971).

2. K. Bachmann and J. B. Cumming, *Phys. Rev. C* 5, 210 (1972).

3. S. Katcoff and M. L. Perlman, *Nature* 231, 522 (1971).

4. G. N. Flerov, Yu. P. Gangrsky, and O. A. Orlova, JINR preprint E7-5887, Dubna (1971).

CONCERNING THE MECHANISM OF HEAVY-ION TRANSFER REACTIONS

N. K. Glendenning and R. J. Ascutto*

Although by now many experiments involving the transfer of one or several nucleons between heavy ions have been carried out, there remain unsettled questions concerned with the mechanism of these reactions. Do second-order processes involving the inelastic excitation of the target or residual nucleus play an important role in the reaction? To date such theoretical analyses as have been carried out assume that they do not. The distorted wave Born approximation (DWBA) has been used to compute the direct transfer contribution, and there is no strong disagreement with experiment to suggest that this approach is inadequate. However, from our earlier work on reactions induced by light nuclides, such as (p, t) and (d, p), we do know that the higher-order processes mentioned above are sometimes very important.¹ The fact that in Coulomb excitation experiments, collective states are produced with probability approaching unity suggests to us that they ought to be important in heavy-ion reactions also.

Here we report a schematic calculation of the reaction $^{120}\text{Sn}(^{18}\text{O}, ^{16}\text{O})^{122}\text{Sn}$ at 100 MeV, designed to estimate the role of higher-order processes, comprising all the transitions shown in Fig. 1. In the usual DWBA treatment only a single transition is computed, namely that from the target ground state to the residual state of the product nucleus. Our method of doing this type of calculation is the so-called source term method which we have developed in earlier publications.²

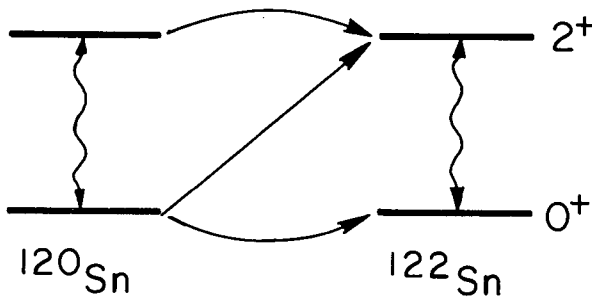


Fig. 1. Various routes that can excite the 0^+ and 2^+ state in ^{122}Sn in the reaction $^{120}\text{Sn}(^{18}\text{O}, ^{16}\text{O})^{122}\text{Sn}$ which are included in the calculation. The usual DWBA treats only the direct transition from the ground state to each product state. (XBL 733-2453)

We describe briefly the nature of the structure of the nuclei which is relevant to this reaction. The ground state of ^{18}O is treated as an inert core of ^{16}O plus two neutrons which may occupy the $s_{1/2}$, $d_{3/2}$ and $d_{5/2}$ orbitals in a Woods-Saxon potential which binds them at approximately the energies observed in ^{17}O . The interaction matrix elements between pairs of neutrons in each of these configurations is assumed to be of the pairing force type of such a strength that the binding energy of the last two neutrons is correct. We assume that the ^{18}O projectile does not itself become excited in the reaction. Two states of each tin nucleus are included, the ground and the collective 2^+ state. The former is described as a BCS vacuum state, and the latter as a collective two-quasiparticle state. The form factor for the transfer of two nucleons based on these nuclear descriptions is computed using the finite

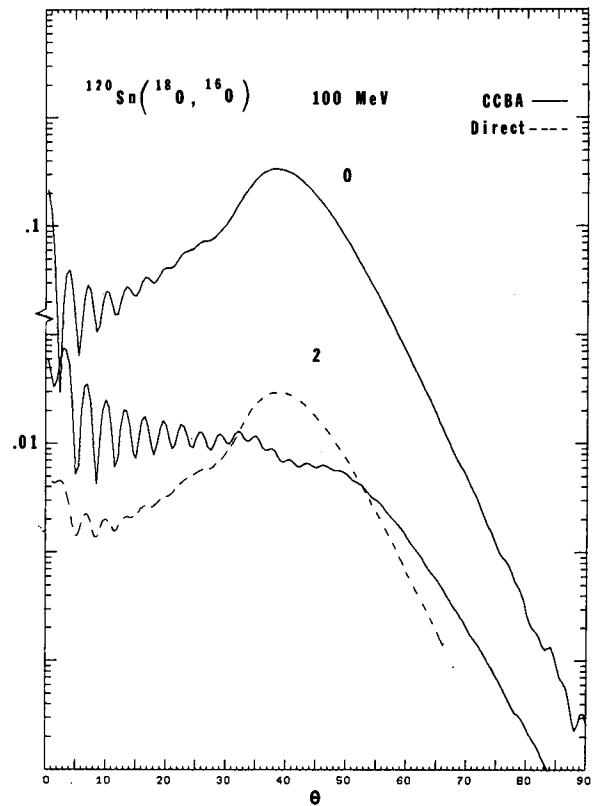


Fig. 2. Differential cross sections are shown by dashed line corresponding to direct transitions and by solid line corresponding to all processes illustrated in Fig. 1. (XBL 733-249)

Woods-Saxon potential that binds the two neutrons in ^{18}O . However, recoil effects are neglected. We do not believe that this neglect can effect our estimate of the importance of higher-order processes compared to the direct transition, although in a detailed comparison with experiment it may well be important to include recoil effects.

In Fig. 2 the results of the calculations can be seen. The dashed lines correspond to the direct transition from the ground state of the target to the 0^+ and 2^+ states of the final nucleus, respectively, and corresponds to the usual DWBA aside from the effect of virtual inelastic excitations. These distributions have the characteristic maximum at an angle corresponding to a grazing collision in a classical picture (about 25°) and fall off at forward angle due to the small overlap of bound states for ions which do not approach each other closely while they fall off at large angle due to absorption of the projectile into more complicated reactions in intimate collisions. The solid lines include all the higher-order processes illustrated in Fig. 1 and produce two marked results for the excited state. First the magnitude of the cross section is decreased at the grazing angle, and the fall-off at small angle characteristic of the direct process is filled in. The ground state

transition in contrast receives a much smaller contribution from the higher-order processes.

There remains much to be done in clarifying the details of the reaction mechanism. We can conclude from this work, so far, that the usual first-order treatment of heavy-ion transfer reactions is often inadequate and that the higher-order processes involving the excitation of the target or residual nucleus are for some states more important than the direct transition.

Footnote and References

* Physics Department, Yale University, New Haven, Connecticut 06520.

1. R. J. Ascutto and N. K. Glendenning, *Phys. Rev. C* **2**, 1260 (1970); R. J. Ascutto, N. K. Glendenning, and B. Sorensen, *Phys. Rev. Letters*, **34B**, 17 (1971) and *Nucl. Phys.* **A183**, 60 (1972); N. K. Glendenning and R. S. Macintosh, *Nucl. Phys.* **A168**, 575 (1971).
2. R. J. Ascutto and N. K. Glendenning, *Phys. Rev.* **181**, 1396 (1969) and *Nucl. Phys.* **A188**, 185 (1972).

ON SUB-COULOMB TRANSFER REACTIONS

M. A. Nagarajan

The motivation for the study of transfer reactions at energies well below the Coulomb barrier was provided by Breit, Hull, and Gluckstern¹ who pointed out that one could use a classical description of the relative motion of the particles. The calculations of Breit and Ebel² have been very successful in explaining the results of the experiments of McIntyre et al.³ Buttle and Goldfarb⁴ had proposed a DWBA theory of transfer reactions, where one could approximate the distorted wave by a Coulomb wave function. They, however, found a number of cases where there existed large discrepancies between the post and prior versions of the theory. They suggested that the discrepancy was due to a neglect of recoil, and included recoil effects approximately by modifying the initial and final momenta. This approximate method of including recoil is equivalent to assuming that the transfer of the nucleon takes place along the vector joining the two nuclei at their distance of closest approach, and also partly ignores the effect of Coulomb distortion.

An improved treatment of recoil has been attempted by the author by calculating the gradi-

ent of the Coulomb wave functions exactly and approximating the Coulomb integrals in the transition amplitude in a manner that has been illustrated by Goldfarb and Buttle.⁵ Calculations are being done to compare our results with those of other authors who have utilized Goldfarb's approximation.

References

1. G. Breit, M. H. Hull, and R. L. Gluckstern, *Phys. Rev.* **87**, 74 (1952).
2. G. Breit and M. E. Ebel, *Phys. Rev.* **103**, 679 (1956).
3. L. C. Becker and J. A. McIntyre, *Phys. Rev.* **138**, B339 (1965).
4. L. J. B. Goldfarb and P. J. A. Buttle, *Nucl. Phys.* **78**, 409 (1966).
5. P. J. A. Buttle and L. J. B. Goldfarb, *Nucl. Phys.* **A176**, 299 (1971).

RECOIL EFFECTS IN SINGLE-NUCLEON-TRANSFER HEAVY-ION REACTIONS

M. A. Nagarajan

During recent years, there have been a large number of experiments which have studied single and multinucleon transfer between a heavy ion and a target-nucleus. Attempts have been made to extract spectroscopic factors from the experimental cross section by using the distorted wave Born approximation theories proposed by Buttle and Goldfarb¹ and Tobocman et al.³ The results indicate that the existing DWBA theories are incapable of explaining the magnitudes of the cross section.

The above theories make an approximation of neglecting the mass of the transferred nucleon, m , in comparison with the mass of the cores, M , involved in the reaction. The neglect of these terms of the order of m/M in the radius vectors allows for a considerable simplification in the evaluation of the distorted wave amplitude. The above approximation, often referred to as a no-recoil approximation, predicts a parity selection rule on the angular momentum of the form factor thereby reducing the multiplicity of angular momenta which could otherwise have been transferred between the initial and final distorted waves.

It was suggested by the author³ that the discrepancy between the experiment and theory could be due to the neglect of terms of the order m/M in the DWBA theories. Even though the ratio m/M is small compared with unity, the fact that the reaction is confined to a region around the surface of the target nucleus implies that an angular momentum of the order of $(m/M)\kappa R$, where κ is a local momentum at the distance of closest approach and R is a nuclear radius, is being neglected. At projectile energies well above the Coulomb barrier, the single nucleon being transferred could carry orbital angular momenta of the order of one or two units. The transfer amplitude is known to be a very sensitive function of the angular momentum transfer, and a recoil correction of one or two units of angular momentum would thus cause a drastic

change in its magnitude. The recoil correction was calculated by the author in collaboration with Kovar, Becchetti, and Harvey⁴ for the proton transfer on ^{208}Pb by ^{16}O and ^{12}C ions, and it was found that the recoil effects do reproduce the j -dependence observed in these reactions⁵ as well as the energy dependence of the cross section. Recent calculations of Devries⁶ tend to further emphasize the importance of including recoil effects in high-energy heavy-ion reactions.

Due to the fact that the spectroscopic factors are very sensitive to the magnitude and phase of the recoil amplitude, an exact expression for the first-order recoil amplitude has been obtained by the author. The expectations are that, due to the properties of the nuclear overlap integrals, a first-order recoil correction would be adequate for most of the single-nucleon transfer reactions. Attempts are being made to incorporate these into the existing DWBA program.

References

1. P. J. A. Buttle, L. J. B. Goldfarb, Nucl. Phys. 78, 409 (1966).
2. F. Schmittroth, W. Tobocman, and A. A. Golestaneh, Phys. Rev. C 1, 377 (1970).
3. M. A. Nagarajan, Nucl. Phys. A196, 34 (1972).
4. F. Becchetti, D. G. Kovar, B. G. Harvey, and M. A. Nagarajan, in preparation.
5. D. G. Kovar, F. D. Becchetti, B. G. Harvey, F. Pühlhofer, J. Mahoney, D. W. Miller, and M. S. Zisman, Phys. Rev. Letters 29, 1023 (1972).
6. R. M. Devries and K. I. Kubo (preprint), to be published in Phys. Letters.

PARTICLE-WAVE AMBIGUITIES IN THE INTERPRETATION OF HEAVY-ION REACTIONS

P. J. Siemens* and F. D. Becchetti

Most direct heavy-ion reactions are characterized by a simple angular distribution which is peaked about an angle θ_{gr} .¹ The observed dependence of θ_{gr} on the energy and charge of

the incident ion leads to the interpretation of these reactions as "grazing reactions," in which the projectile and target move on classical trajectories such that the ions' surfaces

just touch.² The reaction is limited to such trajectories by two effects: if the ions pass farther from each other, the interactions between them are weaker and less likely to induce the reaction, while if the ions approach each other too closely, competition from other processes, such as compound-nucleus formation, reduces the direct cross section. Alternatively, the "grazing reactions" may be thought of as being limited to a narrow range of angular momentum of the projectile and target.³

One finds, however, that the parameters obtained by using various models often differ substantially and cannot be simply related. This means the physical meaning of such parameters is very uncertain. In this work we present an explanation for some of these apparent ambiguities and give an illustration using DWBA.

Limits of the classical (particle) and diffractive (wave) theories are derived and found to predict angular distributions whose widths (in angle e.g.) vary directly and inversely with the width of the interaction region in r-space, respectively. Thus, many ambiguities arise in the interpretation of angular distributions.

We illustrate the ambiguities noted above in Figs. 1 and 2.

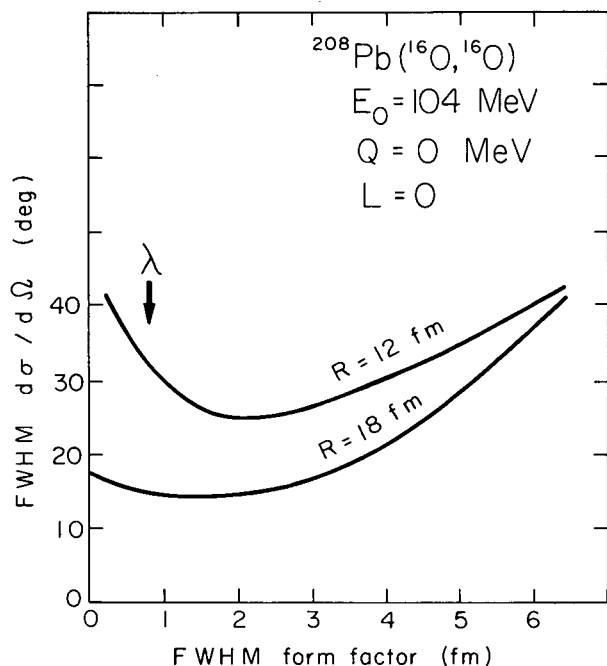


Fig. 1. The variation of the width (FWHM) of the DWBA angular distribution vs the width (FWHM) and peak ($r = R$) of the form factor (see Fig. 2). λ is the projectile wavelength ($r = \infty$). (XBL 729-4033)

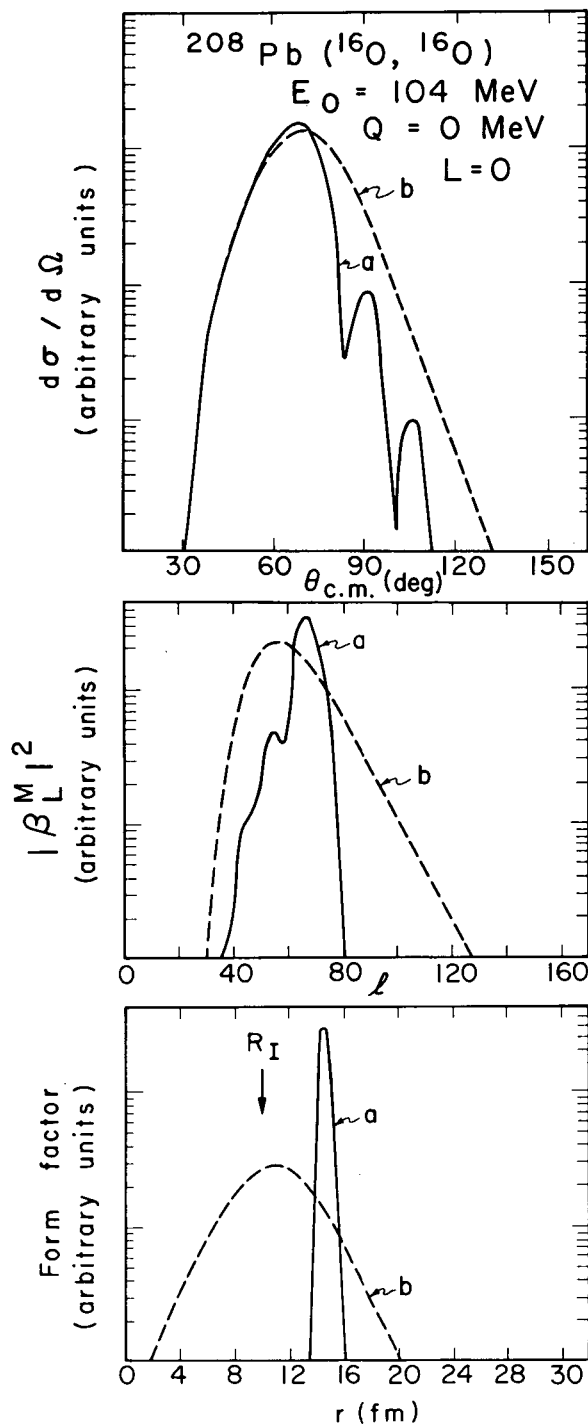


Fig. 2. DWBA calculations for a "quasi-elastic" reaction for two different form factors (a, b). A Woods-Saxon optical potential was used with $V = 0$, $W = -15$ MeV, $R_I = 11$ fm, and $a_I = 0.5$ fm. The quantity $|\beta_L^M|^2$ is proportional to the square of the DWBA transition amplitude. (XBL 729-4034)

In Fig. 1 we show the results of DWBA calculations for $^{208}\text{Pb}(^{16}\text{O}, ^{16}\text{O})$. We have used a purely absorptive optical potential of Woods-Saxon shape with $W = -15$ MeV, $R_I = 11$ fm, and $a_I = 0.5$ fm. The absence of a real potential allows one to use the classical relations between l, θ, r for Coulomb trajectories, but otherwise does not alter the qualitative results deduced from calculations. The form factor was taken to be a derivative of a Woods-Saxon shape (see Figure 2) with a variable width and peak radius ($=R$). Plotted in Fig. 1 is the FWHM of the calculated $\sigma(\theta)$ vs the FWHM of the form factor for two values of R . One finds two solutions which give the same width for $\sigma(\theta)$: $\text{FWHM}(r) \geq \lambda$ (classical limit), and $\text{FWHM}(r) \ll \lambda$ (diffraction limit), where λ is the wavelength of the projectile.

In Fig. 2 we show DWBA calculations obtained with two very different form factors which, however, give similar shapes for $\sigma(\theta)$. Also shown is the quantity $|\beta_L^M|^2 \propto T_\ell^* T_\ell$ vs l , where L is the angular momentum transfer ($L = M = 0$). The decrease in $|\beta_L^M|^2$ for small l values is due to the decrease of $|\beta_L^M|^2$ arising from the absorptive potential, $W(r), r \sim R_I$ ($l_{r=R_I} = 30$). Similarly, the shape of $\sigma(\theta)$ at large angles is sensitive to the optical potential (which was not adjusted). At forward angles the calculations are nearly identical, even though the asymptotic parts of the form factors are quite different.

Results similar to those shown in Figs. 1 and 2 were obtained for angular momentum (L), energy (Q), and mass transfers typical of many heavy-ion reactions.

We conclude from this study that:

(a) Classical and diffraction models can give similar shapes for heavy-ion reaction angular distributions, but often this will require very different parameters.

(b) DWBA calculations exhibit similar ambiguities in that the shape of $\sigma(\theta)$ does not uniquely determine the shape of the form factor even in the asymptotic region $r \rightarrow \infty$.

Of course, if one calculates the form factor from some nuclear model and obtains the distorting potentials from other sources (e.g., an optical-model analysis of elastic scattering) then one a priori determines which behavior, classical or diffractive (particle or wave), will dominate (if either). Lacking such a prescription, however, can result in an ambiguous and unphysical determination of parameters.

Footnote and References

* Present address: Niels Bohr Institute, Copenhagen, Denmark.

1. R. Kaufman and R. Wolfgang, Phys. Rev. Letters 3, 232 (1959).
2. M. L. Halbert and A. Zucker, Phys. Rev. 108, 336 (1957).
3. W. E. Frahn and R. H. Ventner, Nucl. Phys. 59, 651 (1964).

NEUTRON TRANSFER IN REACTIONS BETWEEN SUPERCONDUCTING NUCLEI

M. Kleber*

The scattering of two heavy ions is characterized by the strong Coulomb interaction between target and projectile. This fact is reflected in the Sommerfeld number (Coulomb parameter) η being large compared to unity:

$$\eta = Z_1 Z_2 e^2 / \hbar v = ka \gg 1. \quad (1)$$

Z_1 and Z_2 stand for the charges of the two ions, v is the initial velocity of their relative motion, and k denotes the corresponding wave number. The distance $2a$ is the classical distance of closest approach in a head-on collision. Whenever $\eta \gg 1$ then the relative motion of the two heavy ions can be described in terms of classical ($\hbar \rightarrow 0$) orbits. For bombarding energies below the Coulomb barrier the relative motion is to a good approximation a Rutherford trajec-

tory. If the bombarding energy is larger than the Coulomb barrier, one has to take into account the strong nuclear absorption in the overlap region between projectile and target. Treating the nuclear core as an "opaque" sphere, one finds² for energies above the Coulomb barrier that the differential cross section for elastic scattering shows a diffraction pattern of Fresnel type.

Transfer reactions take place mainly at bombarding energies near the Coulomb barrier, or more precisely they are confined to the region where projectile and target touch each other. For distances larger than the touching distance the tunneling matrix elements become very small, whereas for distances smaller than the touching distance the transfer is reduced be-

cause of the many open channels in the overlap region. A very useful classical model has been developed by Brink.³ The model treats the coupling between the kinematics of the transfer and the nuclear degrees of freedom. Of particular interest are theoretical predictions for optimum Q values, for the transfer of angular momentum, and for the effect of recoil.⁴ Another important problem is the investigation⁵ of Coulomb excitation during the transfer of particles.

The coupling of two superconducting nuclei just below the Coulomb barrier is weak. The situation is similar to the coupling of two superconducting metals separated by a thin oxide layer. This device is known as a Josephson junction. The scattering of two superconducting nuclei differs in two ways:

1. the coupling of the two nuclei occurs only during a short period;
2. the two nuclei are finite systems.

One can show⁶ that there is an oscillatory transfer of nucleon pairs if its oscillation period is smaller than the reaction time t_r and if the chemical potentials of the two nuclei are not very different. The last condition is not a severe limitation. The reaction time for the scattering is approximately

$$t_r \approx a/v. \quad (2)$$

The corresponding energy $E_r = \hbar/t_r$ lies in most cases between 2 and 4 MeV. It is approximately equal to the energy E_t of the oscillatory transfer which is essentially the derivative of the chemical potential μ with respect to the neutron number N:

$$E_t \approx \frac{\partial \mu}{\partial N}. \quad (3)$$

This means that about one oscillation could be detected assuming that Coulomb excitation does not destroy the effect. It seems to be that in direct nuclear reactions an oscillatory transfer⁷ is confined to a very small number of oscillations whereas, for example, the differential cross section for resonant electron capture in proton-hydrogen collisions⁸ shows a large number of oscillations for fixed energy and variable angle or variable energy and fixed angle.

A calculation of the transfer of neutrons in reactions between superconducting nuclei has been performed⁹ in the framework of perturbation theory assuming Rutherford trajectories for the relative motion between the two nuclei. The BCS Hamiltonian of the coupled system is constructed in terms of commuting field operators. We use this Hamiltonian and calculate

the transition probabilities P_T for the transfer. Within the semiclassical approximation the differential transfer cross section is given by

$$\left(\frac{d\sigma}{d\Omega}\right)_T = P_T \left(\frac{d\sigma}{d\Omega}\right)_{el}. \quad (4)$$

We confine ourselves to bombarding energies below the Coulomb barrier and replace $\left(\frac{d\sigma}{d\Omega}\right)_{el}$ by the Rutherford cross section. Our calculation does not consider interference between Coulomb excitation and transfer. In Fig. 1 we show the differential cross sections for the total one-neutron transfer in the reaction $^{200}\text{Hg}(^{196}\text{Hg}, ^{195}\text{Hg})^{201}\text{Hg}$ and for the transfer of two neutrons into the ground states of ^{194}Hg and ^{202}Hg at $E_{c.m.} = 560$ MeV. The Coulomb barrier is about $E_{cb} = 562$ MeV. The quantity F is the sum of the probabilities for all processes which are allowed within perturbation theory. F depends on $\theta_{c.m.}$, and its deviation from unity indicates the limitation of perturbation theory. In Fig. 2 the energy dependence of

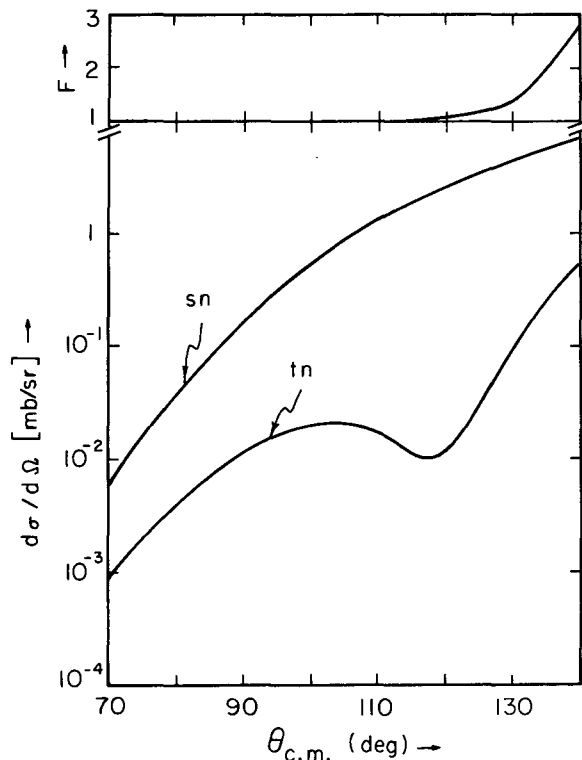


Fig. 1. Differential cross sections, for the total single-neutron (sn) transfer $^{200}\text{Hg}(^{196}\text{Hg}, ^{195}\text{Hg})^{201}\text{Hg}$ and for the ground state two-neutron (tn) transfer $^{200}\text{Hg}(^{196}\text{Hg}, ^{194}\text{Hg})^{202}\text{Hg}$ at $E_{c.m.} = 560$ MeV. The deviation of F from unity is a measure for the failure of perturbation theory. (XBL 7211-4403)

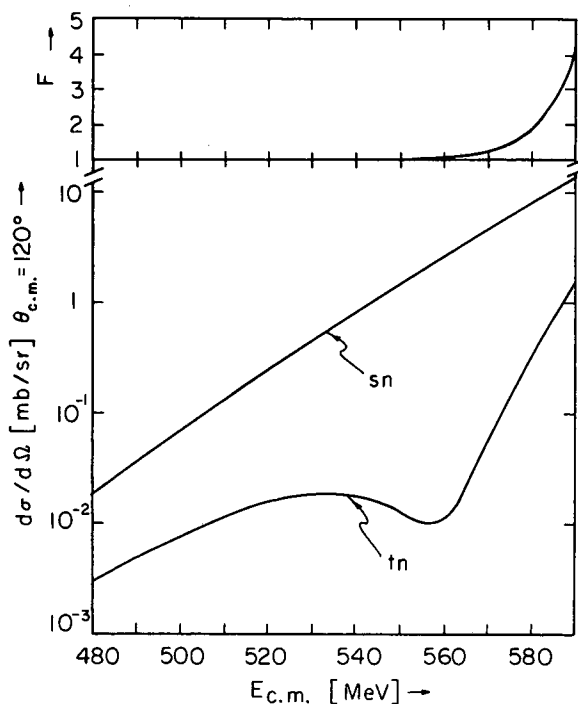


Fig. 2. Differential cross section at $\theta_{c.m.} = 120^\circ$ as a function of the bombarding energy $E_{c.m.}$. The symbols sn and tn are defined as in Fig. 1. (XBL 7211-4404)

the differential cross sections is plotted for $\theta_{c.m.} = 120^\circ$. Again perturbation theory is limited to $F \approx 1$.

The two-neutron transfer shows an interesting interference pattern because of the fact that the imaginary parts of the amplitudes for double

single-neutron transfer and for pair transfer are opposite in sign. The shallow minimum belongs to the node of the imaginary part. Perturbation theory fails to describe the details of the second rise. This could be an indication for the existence of a non-perturbative effect as discussed above.

Footnote and References

* On leave from the Physik Department der Technischen Universität München, Munich, West Germany.

1. R. A. Broglia and A. Winther, Phys. Reports **4C**, 153 (1972).
2. W. E. Frahn, Ann. Phys. (N.Y.) **72**, 524 (1972).
3. D. M. Brink, Phys. Letters **40B**, 37 (1972).
4. P. J. A. Buttle and L. J. B. Goldfarb, Nucl. Phys. **A176**, 299 (1971); M. A. Nagarajan, Nucl. Phys. **A196**, 34 (1972).
5. R. J. Ascuitto and N. K. Glendenning, Nucl. Phys. **A188**, 185 (1972).
6. K. Dietrich, Phys. Letters **32B**, 428 (1970); K. Hara, Phys. Letters **35B**, 198 (1971); M. Kleber and H. Schmidt, Z. Physik **245**, 68 (1971).
7. W. von Oertzen, Nucl. Phys. **A148**, 529 (1970).
8. G. Lockwood and J. Everhart, Phys. Rev. **125**, 567 (1962).
9. M. Kleber and G. Holzwarth, LBL-1293 (1972).

A REACTION MODEL FOR THE $(\alpha, 2\alpha)$ REACTION

J. D. Sherman, D. L. Hendrie, and A. Giorni

The systematics of the $(\alpha, 2\alpha)$ reaction has recently been investigated.¹ Theories relating to knock-out reaction mechanisms and nuclear structure information derived from such reactions has been reviewed.² The purpose of this article is to briefly describe a reaction calculation which provides more realistic treatment of the scattered particles than does the plane wave impulse approximation (PWIA).²

The transition amplitude for a quasi-elastic knock-out reaction factorizes^{2,3} into the product of two integrals in the PWIA:

$$T = \int d\vec{r} e^{i\vec{s}\cdot\vec{r}} V(|\vec{r}|) \int d\vec{\rho} e^{i\vec{q}\cdot\vec{\rho}} \psi_{\text{NLM}}(\vec{\rho}), \quad (1)$$

where

- \vec{q} = recoil momentum of the residual nucleus,
- $\vec{\rho}$ = relative coordinate of the bound alpha and the binding core,
- \vec{s} = momentum transferred by the projectile to the bound alpha,
- \vec{r} = relative coordinate between the two alpha particles.

The interaction potential $V(|\vec{r}|)$ is closely related to free α - α scattering, and in the impulse approximation the first integral of (1) is replaced by the free (α - α) scattering cross section, including the appropriate kinematical quantities. In the PWIA the second integral is seen to be the Fourier transform of the coordinate space wave function, $\psi_{\text{NLM}}(\vec{\rho})$.

The distorted wave impulse approximation replaces the quantity $e^{i\vec{q}\cdot\vec{\rho}}$ by the product of three distorted waves.⁴ A somewhat simpler version of the model which has had utility in describing the (p, 2p) reaction⁵ is to use parametrized distorted waves⁶ in place of the partial wave expansions extracted from optical-model calculations. The Fourier transform integral given in (1) has the form in DWIA:

$$\begin{aligned} \phi_{\text{NLM}}(\vec{q}) = & \int \psi_4^{*(-)}(\vec{k}_4, \vec{\rho}) \psi_3^{*(-)}(\vec{k}_3, \vec{\rho}) \\ & \times \psi_{\text{NLM}}(\vec{\rho}) \psi_1^{+}(\vec{k}_1, \vec{\rho}) d\vec{\rho}, \end{aligned} \quad (2)$$

where the notation $1+2 \rightarrow 3+4+5$ is used in the reaction description. Particle 1 is the incident α , and 3 and 4 represent the outgoing α 's. The incident distorted wave is

$$\psi_1^{+}(\vec{k}_1, \vec{\rho}) = N_1 e^{i(\beta_1 + i\gamma_1)\vec{k}_1 \cdot \vec{\rho}} \quad (3)$$

The parameters β_1 and γ_1 can, in principle, be derived⁷ from the real and imaginary parts of the relevant optical-model potentials, but in practice they are empirically determined. When $\beta_1 = \beta_3 = \beta_4 = 1$ and $\gamma_1 = \gamma_3 = \gamma_4 = 0$, the plane wave theory is recovered. The focus term⁶ required in nucleon scattering is not included in the present calculation, as focus effects were negligible in (α , α') scattering. The wave function $\psi_{\text{NLM}}(\vec{\rho})$ is calculated in a finite well,⁸ assuming an $S=0$, $T=0$ particle bound to the core with $N=2$ and $L=0$.

Figure 1 shows the fit to the $^{16}\text{O}(\alpha, 2\alpha)^{12}\text{C}$ (g. s.) angular correlation, where θ is the scattering angle common to both outgoing alphas. A family of β and γ values have been found which give equally good fits. One set is shown by the solid line in the figure. The dashed lines indicate results for $\pm 1^\circ$ changes in θ , corresponding to experimental angular resolution. The calculations are arbitrarily normalized to the 35° data point. The dropping cross section at forward and backward angles is largely due to the interpolated free (α - α) scattering cross section. The correspondence between the calculation and the data provides partial evidence for the validity of the quasi-elastic model. The calculation is now being extended to include $0^+ \rightarrow 2^+$ transitions; preliminary indications are

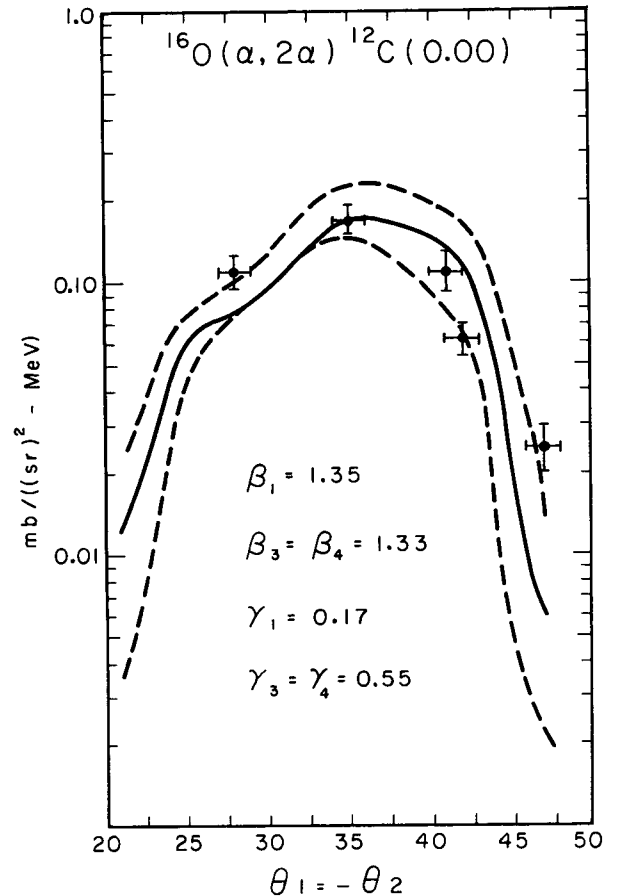


Fig. 1. Comparison of experimental angular correlation extracted from the $^{16}\text{O}(\alpha, 2\alpha)^{12}\text{C}$ (0.0) reaction with theoretical result. (XBL 731-2093)

that fitting this additional data may help eliminate the present ambiguity in the β , γ parameters. There are some hopes that this will then remove the present arbitrariness in the normalization.

References

1. J. D. Sherman and D. L. Hendrie, Nuclear Chemistry Division Annual Report, 1972.
2. D. F. Jackson, Adv. in Nucl. Phys. **4**, 1 (1971).
3. Y. Kudo, Prog. Theor. Phys. **34**, 942 (1965).
4. D. F. Jackson and T. Berggren, Nucl. Phys. **62**, 353 (1965).
5. P. A. Deutchman and I. E. McCarthy, Nucl. Phys. **A112**, 399 (1968).
6. I. E. McCarthy and D. L. Pursey, Phys. Rev. **122**, 578 (1961).

7. E. I. McCarthy, Introduction to Nuclear Theory (Wiley, New York, 1968), p. 422.

8. P. D. Kunz, code DWUCK, private communication.

THE $^{90}\text{Zr}(p, p')^{90}\text{Zr}^*$ REACTION AT 40 MeV \dagger

F. Petrovich

Differential cross sections for the excitation of the 2^+ (2.18 MeV), 5^- (2.32 MeV), 4^+ (3.08 MeV), 6^+ (3.45 MeV), and 8^+ (3.60 MeV) levels in ^{90}Zr have been measured using 40-MeV protons from the Michigan State University sector-focused cyclotron. These excitations are of considerable interest to physicists working to understand inelastic proton scattering in a microscopic model. The primary factor here is the wide range of multipolarity covered by these transitions. The data also contains interesting information on the behavior of core polarization as a function of multipole.

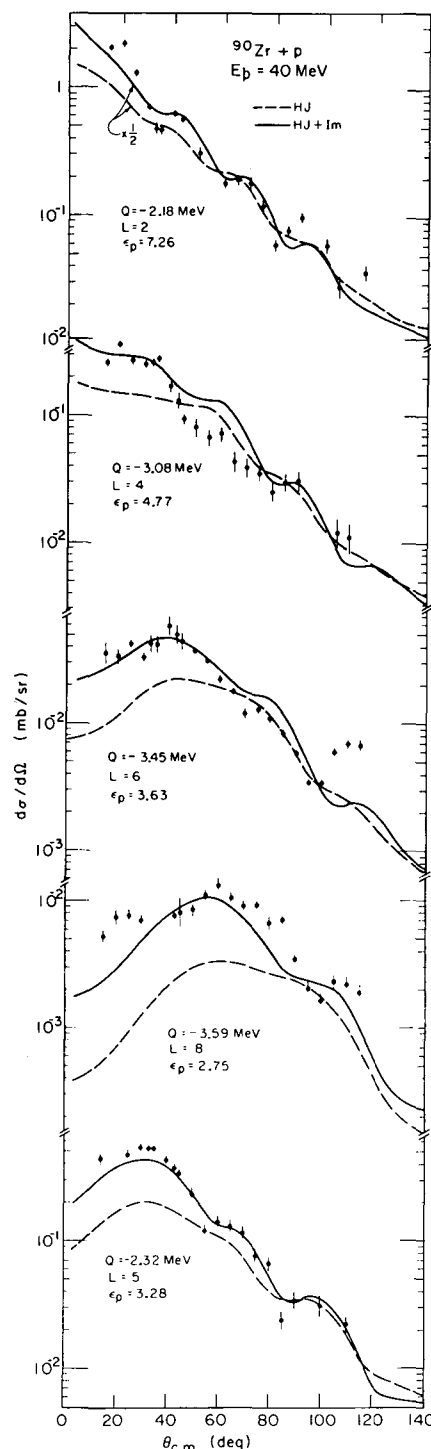
Theoretical calculations have been made for comparison with the experimental data. It has been assumed that the ground state of ^{90}Zr is given by

$$|0^+(\text{g. s.})\rangle = 0.8|(2p_{1/2})^2 0^+\rangle + 0.6|(1g_{9/2})^2 0^+\rangle,$$

that the 2^+ , 4^+ , 6^+ , and 8^+ states are due to the $g_{9/2}^2$ configuration, and that the 5^- state has the structure $|(g_{9/2} p_{1/2}) 5^- \rangle$. Three particle-one hole admixtures have been included in these wave functions, using first-order perturbation theory. Two coupling interactions have been considered. The first was a "realistic" central G-matrix interaction.¹ The second was a central interaction which gives a reasonable reproduction of the low-lying spectrum of ^{90}Zr in a simple shell-model calculation using a $g_{9/2} - p_{1/2}$ model space. Harvey² has suggested that this might be a reasonable means of estimating higher-order core polarization effects. The real part of the interaction between the incident proton and the ^{90}Zr target was also taken to be a "realistic" central G-matrix interaction.³ The imaginary component of this interaction was obtained by using a prescription due to Satchler.⁴ The main features of these calculations are that they contain no free parameters and that the bound-state coupling interaction is consistent with the real part of the projectile-target interaction.

Fig. 1. Results of microscopic calculations for lowest 2^+ , 4^+ , 6^+ , 8^+ , and 5^- states in ^{90}Zr for $E_p = 40$ MeV. The dashed curves are results including only real component in projected-target interaction. The solid curves are results with both real and imaginary components.

(XBL 729-4075)



The theoretical calculations are compared with the data in Fig. 1. The agreement between the theoretical results and the experimental data is quite good. The contributions from the imaginary part of the interaction are seen to be important. These have been omitted in most microscopic model calculations. The factor ϵ_p gives a measure of the importance of core polarization. It is analogous to the effective charge employed in discussions of γ -transitions. Contributions from core polarization decrease smoothly with increasing multipolarity, but they are not negligible, even for the excitation of the 8^+ state.

The theoretical wave functions indicate that polarization of core neutrons and core proton was of comparable importance for the excitation of the 2^+ state. As the multipolarity of the transitions increased, however, the polarization of core neutrons becomes dominant. The spin-orbit component of the projectile-target interaction provides a test of this result. The spin-orbit force acts primarily in triplet-odd states, so it is quite important in the excitation of target protons and fairly weak in exciting target neutrons in inelastic proton scattering.⁵ In addition it gives rise to cross sections which peak at larger angles than do the cross sections arising from the central parts of the interaction.⁵ Thus, in (p, p) tran-

sitions of high multipolarity where the spin-orbit force is important, proton and neutron excitations are characterized by different shape contributions to the cross section. Calculations with the two-body spin-orbit force included, supported the result that neutron polarization was dominant in the excitation of the high-spin states.

Footnote and References

[†]R. A. Hinrichs, D. Larsen, B. M. Freedom, W. G. Love, and F. Petrovich (LBL-1649), submitted to Phys. Rev.

1. G. E. Brown, Unified Theory of Nuclear Models and Nucleon-Nucleon Forces (North-Holland, Amsterdam, 1967, 2nd ed.
2. M. Harvey, Chalk River report (unpublished).
3. G. R. Satchler, *Comm. Nucl. Particle Phys.* **5**, 39 (1972).
4. G. R. Satchler, *Phys. Letters* **35B**, 279 (1971).
5. W. G. Love, *Phys. Letters* **35B**, 371 (1971), and *Nucl. Phys.* **A192**, 651 (1972).

CORE POLARIZATION IN INELASTIC PROTON SCATTERING FROM ^{209}Bi AT 61 MeV*

F. Petrovich

Differential cross sections for the excitation of the 0.90- and 1.61-MeV levels and the group of states at 2.62 MeV in ^{209}Bi have been measured using 61.2-MeV protons from the Oak Ridge Isochronous Cyclotron. The ground, 0.90-MeV, and 1.61-MeV levels are the $1h_{9/2}$, $2f_{7/2}$, and $1i_{13/2}$ single-particle proton states,¹ respectively, while the multiplet of states at 2.62 MeV is obtained by coupling the $1h_{9/2}$ proton to the lowest 3^- state of ^{208}Pb core.² The main purpose of the experiment was to study core polarization effects in the excitation of the single-particle states. Admixtures built on positive parity states of the ^{208}Pb core are expected to be important in the $1h_{9/2} \rightarrow 2f_{7/2}$ transition. The negative parity states of ^{208}Pb enter in the case of the $1h_{9/2} \rightarrow 1i_{13/2}$ transition. Admixture of the $|1h_{9/2} \times 3^-; 13/2\rangle$ state into the $1i_{13/2}$ single-particle state is of particular importance in this transition.³⁻⁷

The cross section for the 2.62-MeV multiplet was found to be essentially identical with the

cross section for exciting the 3^- (2.62-MeV) level in ^{208}Pb by 61.2-MeV protons⁸—in agreement with the expectation that the multiplet has the structure $|1h_{9/2} \times 3^-; J\rangle$. The angular distribution for the 1.61-MeV level was observed to have an $L=3$ shape nearly the same as that for the 2.62-MeV multiplet, but the cross section was 19 times smaller. The $L=3$ shape is consistent with the fact that the $1i_{13/2}$ state contains an appreciable admixture of $|1h_{9/2} \times 3^-; 13/2\rangle$. The shape of the cross section for the 0.90-MeV level indicates that $L=4$ and $L=6$ transfers are important in this transition. This is interesting because this transition is known to go by $L=2$ in Coulomb excitation.^{4, 5}

The data for the two single-particle excitations has been analyzed using a microscopic model for the (p, p') reaction.⁹ Several descriptions of core polarization were considered. In the case of the $1h_{9/2} \rightarrow 2f_{7/2}$ transition it was found that the importance of core polarization decreased only slowly as the positive parity mul-

tipoles increased from $L=2$ through 8. An appreciable fraction of the core strength was found to be concentrated in the states formed by coupling the $1 h_{9/2}$ and $2 f_{7/2}$ levels to the first 2^+ , 4^+ , 6^+ , and 8^+ states in ^{208}Pb . The theoretical cross section is compared with the data in Fig. 1. The importance of the $L=4, 6$, and multipoles in the cross section is evident.

Calculations for the $1 h_{9/2} \rightarrow 1 i_{13/2}$ transition indicate that there is an 8% admixture of the $13/2$ member of the 2.62-MeV multiplet in the $1 i_{13/2}$ state. In arriving at this value we have included the effect of mixing between the $1 h_{9/2}$ and $|1 i_{13/2} \times 3^-; 9/2\rangle$ states and contribution from high-lying $L=3$ core excitation. These three effects contribute to the transition amplitude in the ratio 10.6: 2.3: 3.0, respectively. The theoretical cross section is compared with the data in Fig. 2.

The 8% admixture is in accord with the results of one-nucleon transfer studies.¹ The present experimental data is also in agreement with the Coulomb excitation data of Hertel et al.,⁴ but does not agree with the Coulomb excitation results of Broglia et al.⁵ which indicate a much smaller admixture. The (d, d') experiment of Ungrin et al.⁷ suggests an admixture intermediate to those implied by the two Coulomb excitation experiments.

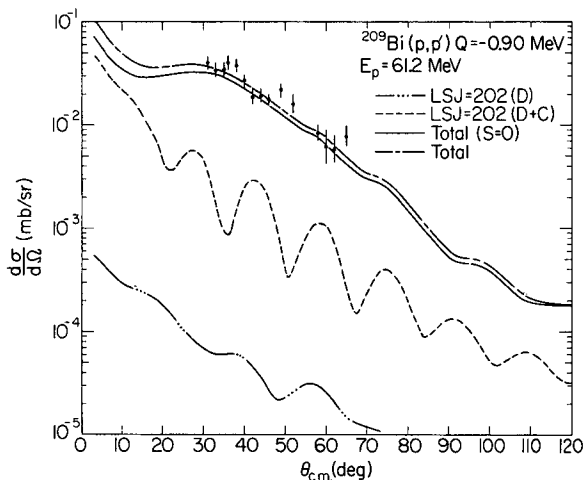


Fig. 1. Microscopic model result for 0.90-MeV excitation at 61.2 MeV. The LSJ=202 valence (D) and valence-plus-core (D+C) contributions are shown, as well as the complete $S=0$ cross section which includes LSJ = 202, 404, 606, and 808 contributions. The total result includes the effect of "spin-flip" multipoles. (XBL 724-2813)

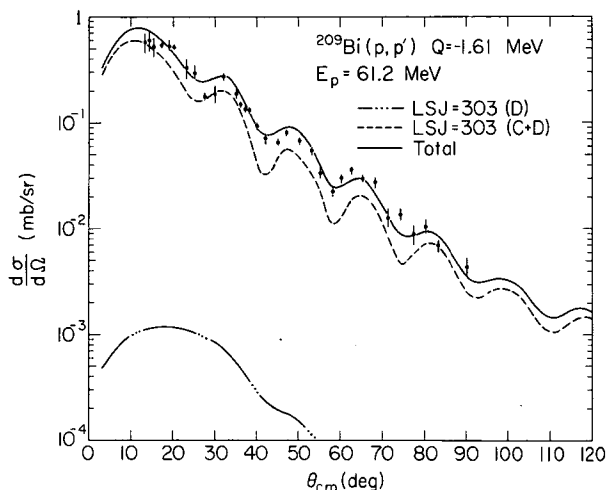


Fig. 2. Microscopic model result for 1.61-MeV excitation at 61.2 MeV. The curves show the LSJ=303 valence (D) and valence-plus-core (D+C) contributions and the total result includes contributions from all allowed multipoles. (XBL 724-2815)

Footnote and References

- * A. Scott, M. Owais, and F. Petrovich (LBL-672), submitted to Nucl. Phys.
1. R. Woods, P. D. Barnes, E. R. Flynn, and G. J. Igo, Phys. Rev. Letters **19**, 453 (1967).
 2. J. C. Hafele and R. Woods, Phys. Letters **23**, 519 (1966).
 3. B. N. Mottleson, J. Phys. Soc. Japan, **24** Suppl. 96 (1968).
 4. J. W. Hertel, D. G. Fleming, J. P. Schiffer, and H. E. Gove, Phys. Rev. Letters **23**, 448 (1969).
 5. R. A. Broglia, J. S. Lilley, R. Perazzo, and W. R. Phillips, Phys. Rev. C **1**, 1508 (1970).
 6. W. Benenson, S. M. Austin, P. J. Locard, F. Petrovich, J. Borysowicz, and H. McManus, Phys. Rev. Letters **24**, 907 (1970).
 7. J. Ungrin, R. M. Diamond, P. O. Tjøm, and B. Elbek, Kgl. Danske Videnskab. Selskab, Mat.-Fys. Medd. **38**, 8 (1971).
 8. A. Scott, N. P. Mathur, and G. R. Satchler, Bull. Am. Phys. Soc. **13**, 1368 (1968).
 9. G. R. Satchler, Comm. Nucl. Part. Phys. **5**, 39 (1972).

CROSS-SECTION CALCULATIONS FOR HEAVY-ION REACTIONS

J. Alonso

This work consists of an extension of the program written by Sikkeland et al.^{1, 2} for cross-section calculations for the production of transuranic elements. Many ideas incorporated into this extension were worked on by the author and John Rasmussen^{3, 4} both here and at Yale University over the last two years.

The original version of the program first calculates the total reaction cross section, making use of the Hill-Wheeler parabolic approximation⁵ for penetration of the potential barrier by the projectile. Assuming that all of the reaction strength goes into compound nucleus formation, the nuclear excitation energy is then dissipated by neutron boil-off, calculated by the Jackson statistical model,⁶ with the probability of fission of the compound system being estimated after each successive boil-off.

The program was remarkably successful for predicting cross sections in the transuranic region,^{1, 2} and has been utilized extensively in the heavy-element research program at the HILAC for many years.

Although successful in the transuranium region, the results obtained for calculations outside this region are not realistic. Thus one is forced to examine the model employed, and attempt to make it conform more to physical reality. Several aspects of the original program are ready targets for upgrading. 1) Nuclear deformations are not taken into account. It is expected that the shape of the total reaction cross section will depend fairly sensitively on nuclear shapes, especially near the Coulomb barrier.³ 2) Other possible reactions can rob strength from the compound nucleus channel, and 3) only neutron evaporations are included, whereas it is known that for many reactions, products including an alpha boil-off have higher yields than pure xn products.

Deformation has been introduced by a shape parametrization of the Wood-Saxon potential,^{3, 4} and thus absorption coefficients are calculated over a whole range of angles.

The inclusion of other reaction channels can be summarized by reference to Fig. 1. As the two particles come within the range of nuclear forces, first the probability of a transfer reaction occurring is calculated (based on the Breit-Ebel semiclassical tunneling formalism,⁷ with several parameters adjusted to match experimental data). If fission occurs during this process (Coulomb fission is included here), the result goes into the fission channel. If no fission

occurs, the probability of barrier penetration is calculated, for both transfer and non-transfer cases. If the classical turning radius of the projectile is within the nucleus, (Fig. 2a) the probability of forming a compound nucleus is estimated by the density of states available in the well. This is a relaxation of the usual assumption of a black sticky nucleus. The compound nuclei which survive prompt fission are then allowed to de-excite by particle boil-off, with fission competition calculated at each stage.

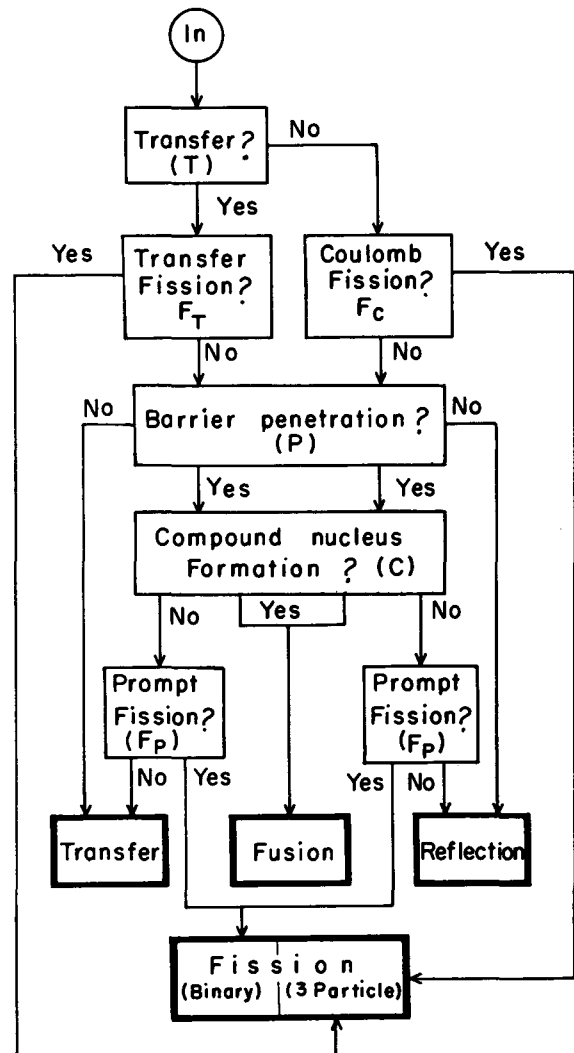


Fig. 1. Flow chart of nuclear reaction possibilities. (XBL 733-2246)

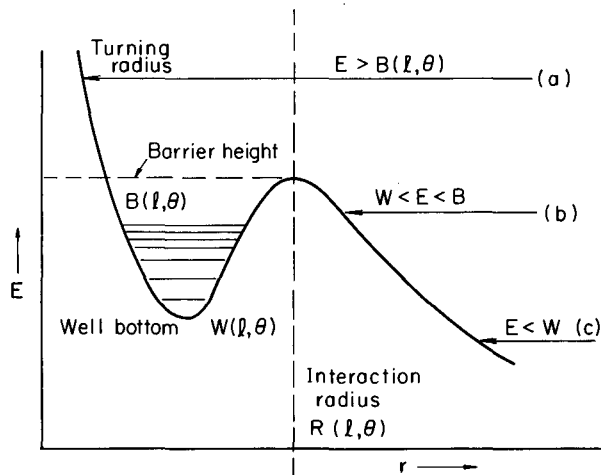


Fig. 2. Representation of effective potential for particular l, θ value, including Coulomb and centrifugal terms.

(a) Available energy is greater than barrier top, penetration occurs, but capture is dependent on level density in well.

(b) Energy is below barrier height, tunneling is possible.

(c) No absorption is possible; no states are available to tunnel into. (XBL 733-2456)

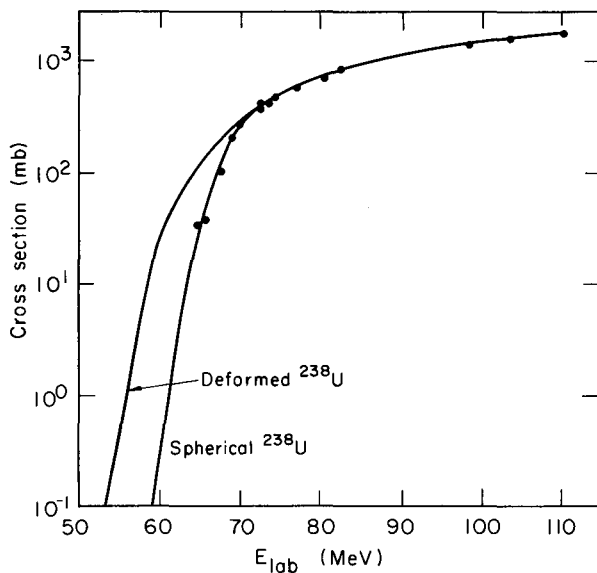


Fig. 3. Calculated total reaction cross sections for spherical and deformed $^{238}\text{U} + ^{12}\text{C}$ ions.

Data points are fission cross sections measured by Viola and Sikkeland (Ref. 10). Parameters used in calculations are:

$$r_0 = 1.25,$$

$$d = 0.50,$$

$$V_0 = 70 \text{ (not sensitive)}. \quad (\text{XBL 733-2457})$$

To date, particles other than neutrons are not considered, but in the near future we expect to include the code of Winn, Gutbrod, and Blann⁸ which considers all modes of evaporation.

Our formalism is thus capable of predicting gross cross sections for many classes of events. To date, most of the testing and parameter evaluation have been carried out for fusion reactions. For these cases, we have found that transfer and prompt fission are relatively minor contributions.

We are then left with the basic result that the main influence on the fusion cross section is the barrier penetration factor. In the usual parabolic approximation, the cross section is calculated by carrying out a sum over many partial waves, each one an average over all orientations of the nuclear deformation axis. Wong⁹ at Oak Ridge has recently shown that by making several realistic approximations a closed-form expression can be obtained for the cross section, involving no sum over l partial waves. His formulas have been checked against rigorous calculations, and have proved quite accurate, with a saving of a factor of over 100 in computation time.

A detailed comparison is in progress between calculated total reaction cross sections and experimental results of Viola and Sikkeland¹⁰ of fission cross sections of ^{238}U with heavy ions. The most interesting effect to date is shown in Fig. 3, demonstrating that although we know ^{238}U is deformed, calculations assuming ^{238}U to be spherical yield a closer agreement with experiment. This effect is puzzling, indicating that somehow the heavy ion is not feeling the nuclear deformation. Further experiments to test whether or not the Coulomb barrier is sensitive to nuclear deformations are clearly in order.

References

1. T. Sikkeland, A. Ghiorso, M. Nurmia, Phys. Rev. **172**, 1232 (1968).
2. T. Sikkeland, J. Maly, D. Lebeck, Phys. Rev. **169**, 1000 (1968).
3. J. O. Rasmussen, K. Sugawara-Tanabe, Nucl. Phys. **A171**, 497 (1971).
4. J. Alonso and J. O. Rasmussen, Bull. Am. Phys. Soc. II, **17**, 78 (1972).
5. D. L. Hill and J. A. Wheeler, Phys. Rev. **89**, 1102 (1953).
6. J. D. Jackson, Can. J. Phys. **34**, 767 (1956).

7. G. Breit and M. E. Ebel, Phys. Rev. 103, 679 (1956) and 104, 1030 (1956).

8. W. G. Winn, H. H. Gutbrod, and M. Blann, Nucl. Phys. A188, 423 (1972).

9. C. Y. Wong, private communication.

10. V. Viola and T. Sikkeland, Phys. Rev. 128, 767 (1962).

FISSION HALF-LIVES FOR HEAVY EVEN-EVEN NUCLEI

P. Möller and J. Randrup

The calculation of fission half-lives is essential for the understanding of the synthesis of heavy nuclei. However, previous calculations have not been able to reproduce the known half-lives better than to within a factor of typically 10^6 . In recent years more refined calculations have been made of the fission potential barriers, and, as will be shown, it is possible to determine the liquid-drop parameters so that the second barrier heights agree with experiment. This second barrier has a dominating influence on the fission half-lives. With such potential barriers available, it seems worthwhile to utilize the by now rather rich experimental half-life data to obtain some semi-empirical information on the fission inertias. We hope by this approach to develop a more reliable prescription for predicting the fission half-lives and, further, to gain insight into the dynamical nature of the heavy nuclei.

The theoretical fission-barrier extrema used for this purpose below are basically those obtained in Ref. 1, but two corrections have been made. First, we have corrected the first barrier peak for the effect of the γ degree of freedom, according to the results obtained by Larsson.² Second, we have modified the liquid-drop parameters relative to those suggested by Myers and Swiatecki³ (used in Ref. 1).

Pauli and Lederberger⁴ have suggested that the increase of the theoretical second barrier peak as a function of N (for fixed Z) found by them and also by Möller,¹ and which is in contrast to the experimentally encountered behavior, might be due to a too-small value for the surface energy symmetry constant κ_s suggested by Myers and Swiatecki. This⁵ suggested value of κ_s is rather uncertain as it has not been independently fitted to data but was assumed *a priori* equal to the volume energy symmetry constant. Pauli and Lederberger⁴ have suggested a method for determining the surface symmetry constant κ_s and the ratio $2a_2/c_3$ by fitting theoretical barriers to experimental values at the second barrier peak. Using their notation we write

$$E_{LD} = a_2 (1 - \kappa_s I^2) A^{2/3} B_S(\text{def}) + \frac{3}{5} \frac{Z^2 e^2}{R_0} B_C(\text{def}) \\ = c_3 \frac{Z^2}{A^{1/3}} \left\{ \zeta \frac{A}{2Z^2} [B_S(\text{def}) - 1] + B_C(\text{def}) - 1 \right\},$$

where

$$I = \frac{N-Z}{A}, \quad \zeta = \frac{2a_2}{c_3} (1 - \kappa_s I^2), \quad \text{and } c_3 = 0.720 \text{ MeV.}$$

Figure 1 shows the ζ 's that will bring the theoretical barriers into agreement with the experimental values given by Bjornholm and Lynn,⁵ for 11 even-even actinide nuclei, and in case the pairing strength G is independent of distortion. A zero-point energy of 0.5 MeV was added at the potential-energy minimum while no correction was added for the second saddle point. The error bars correspond to an uncertainty of ± 0.5 MeV in the barrier heights. The straight line represents a least-squares fit of $2a_2/c_3 (1 - \kappa_s I^2)$ to the experimental ζ 's, giving the result

$$\kappa_s = 4.17, \quad 2a_2/c_3 = 56.66.$$

In the alternative case of a pairing strength proportional to the nuclear surface, one obtains instead

$$\kappa_s = 4.02, \quad 2a_2/c_3 = 57.99.$$

Although the resulting barriers fit experiments well, one should point out that the above values for κ_s and $2a_2/c_3$ yield erroneous ground state masses. To determine a consistent set of liquid-drop parameters a renewed simultaneous fit to barriers and masses must be made. An alternative, a little further ahead, is the use of the more refined droplet model developed by Myers and Swiatecki.⁶ The above fit of second barrier heights seems to indicate strongly a larger value than previously assumed for the surface-symmetry term. One should note the importance of this fact for the problem of the possible synthesis of heavy elements along the r -process path.

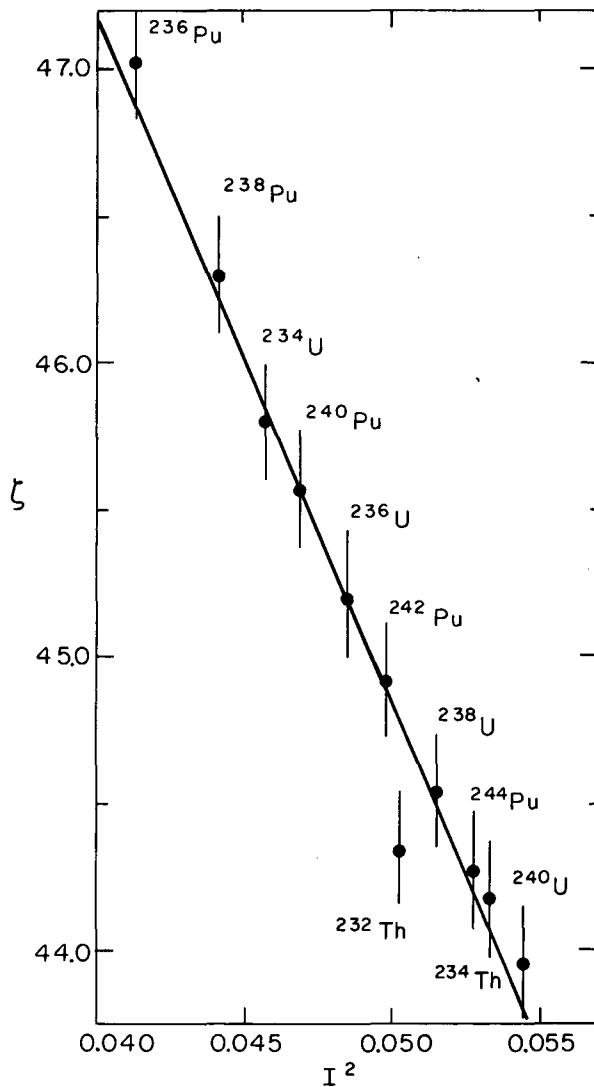


Fig. 1. "Experimental" ζ determined for $G = \text{const}$ from eleven experimental values of the second barrier height. The full line is a least-squares fit of the expression $2a_2/c_3 (1 - \kappa_s I^2)$ to these data. (XBL 733-2428)

As stated in the introduction, with the improved knowledge of the potential-energy surface we now proceed to study the problem of the observed spontaneous-fission half-lives. The potential-energy surface is a multidimensional surface, but we have chosen to collect all variables into one coordinate s , denoting a fission-path coordinate in terms of a path passing through the minima and saddle points of the energy surface.

Provided one knows the potential energy $V(s)$ along this fission path, as well as the

inertia $B(s)$, associated with motion along this path, the fission half-lives may be obtained by ordinary WKB theory:

$$t_{1/2} = 10^{-28.04} (1 + e^K) \text{ years,}$$

where K is the action along the path

$$K = \frac{2}{\hbar} \int_{s_{\min}}^{s_{\max}} ds \sqrt{2B(s)[V(s) - E_{\text{vib}}]} .$$

In this first, simple-minded approach, the fission coordinate s is simply taken to correspond to the projection of the path onto the axis of spheroidal deformation. Furthermore, the wiggly potential felt by the fissioning system is assumed to be a smooth function passing through the four stationary points (I, A, II, and B) and a fifth point beyond the second saddle. Appropriate polynomials are thus splined through these points. For the first part of the path this is probably a fairly safe approach; however, the dynamical path is rather uncertain beyond the second saddle. The fifth point chosen here ($\epsilon_2 = 1.0$, $\epsilon_4 = 0.14$) lies approximately on the liquid-drop fission path, and appears to account pretty well for certain systematic trends in the half-lives. Hopefully, systematic errors inherent in the present approach may to some extent be compensated for by a renormalization of the associated effective inertia $B(s)$.

Because of the singular character of ϵ_2 for large distortions, this coordinate is probably not the best for studying the fission process. A more suitable fission coordinate, having appealing asymptotic properties, is the center-of-mass distance between the two "fragments." Assuming equal fragments (and purely ellipsoidal shapes) the corresponding transformation of the potentials is simple. In terms of this coordinate the effective inertia should not have a too drastic variation. Hence it seems worthwhile, for a first orientation, to use simply a constant as the trial form of the inertia. Figure 2 shows the results of such an approach. Twenty-five even-even actinide nuclei have been used as a test sample, and that (constant) inertia which minimizes the average order-of-magnitude deviation has been determined. It is seen that with a constant inertia of around $3AM/4$ one is able to reproduce the experimental ground state half-lives to within one order of magnitude on the average, which is surprisingly good. Furthermore, the main trends of the half-lives for the heavier nuclei are correct. Thus this method seems the most promising one available for predicting the half-lives of

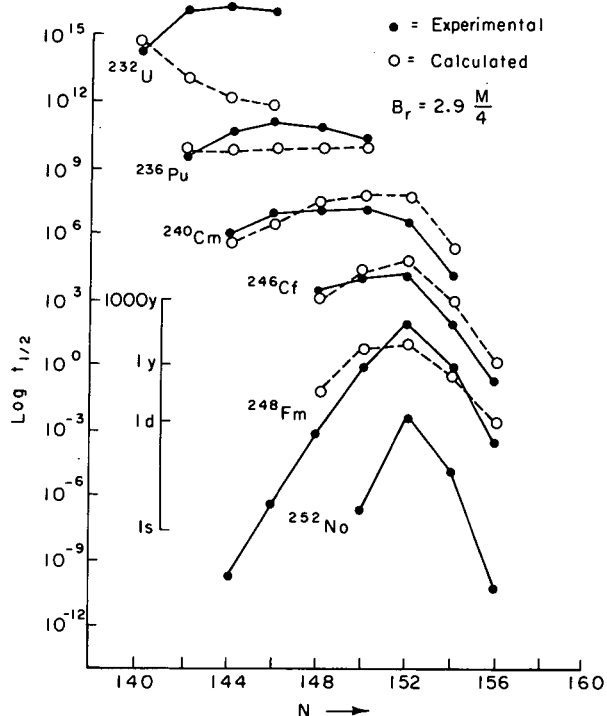


Fig. 2. Experimental ground state half-lives for the chosen test sample of nuclei. Broken line: The corresponding theoretical half-lives, calculated with the assumption of a constant inertia $B_r = 2.9 AM/4$. (XBL 733-2535)

unobserved nuclei in this region, and in particular we focus our attention to certain isotopes of the element 106.

GEOMETRIC PROPERTIES OF LEPTODERMOUS* DISTRIBUTIONS WITH APPLICATIONS TO NUCLEI†

W. D. Myers

A scheme for characterizing the geometric properties of nuclear density distributions and potential wells originated by the author (a suggestion of a similar sort is also to be found in Ref. 1) and substantially elaborated by Süssmann² has been employed in an analysis of various experimental results.

The study concerns the geometrical quantities:

- C, the "central radius,"
 R, the "equivalent sharp radius,"
 Q, the "equivalent r. m. s. radius,"
 b, the "surface width,"
- (1)

Finally, it should be mentioned that one can not immediately from this material extract the structure of the true fission inertia. The inertia derived from the fit to the ground state half-lives does not fit the relatively short isomer half-lives; instead they require a considerably smaller inertia to be used throughout the second barrier. Furthermore, calculations seem to bear out that these lighter nuclei make large excursions into other dimensions of the distortion space when passing through the first barrier. Hence the effective inertia should be correspondingly larger when projection is made onto one degree of freedom. This multidimensionality of the fission path probably explains the large deviations for the lighter nuclei (especially U), and we shall attempt to include this problem in the forthcoming more detailed treatment.

References

1. P. Möller, Nucl. Phys. A192, 529 (1972).
2. S. E. Larsson, preprint, Lund, 1972.
3. W. D. Myers and W. F. Swiatecki, Ark. Fys. 36, 343 (1967).
4. H. C. Pauli and T. Ledergerber, Nucl. Phys. A175, 545 (1971).
5. S. Björnholm and E. Lynn, private communication (1971).
6. W. D. Myers and W. F. Swiatecki, Ann. Phys. (N. Y.) 55, 395 (1969).

whose detailed definitions are to be found in Ref. 3. Figure 1 serves to illustrate these quantities. They are related to each other by the expressions

$$\begin{aligned} C &= R[1 - \beta^2 + \dots], \\ Q &= R[1 + \frac{5}{2}\beta^2 + \dots], \end{aligned} \quad (2)$$

where

$$\beta = b/R$$

is the expansion parameter. For nuclei $b \approx 1$ fm, consequently $\beta \ll 1$ for most nuclei and the simple expressions given in Eqs. (2) are expected to be quite accurate.

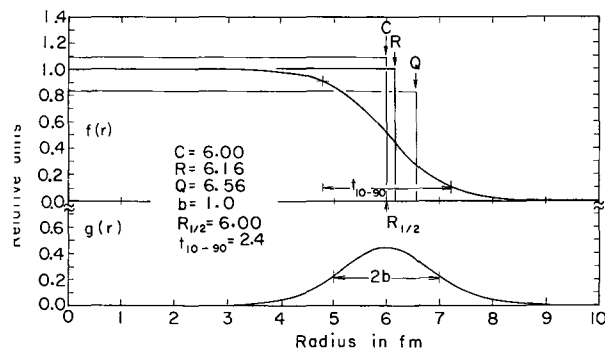


Fig. 1. The normalized, spherically symmetric, leptodermous distribution $f(r)$ and the corresponding surface distribution function $g(r)$ are plotted against the radial distance r . The values of $R_{1/2}$ and t_{10-90} are given for this distribution in addition to the values of C , R , Q , and b whose use is advocated here. Sharp density distributions having the same volume integrals as $f(r)$ and radii equal to C , R , and Q have also been drawn in for the purpose of demonstrating the geometrical importance of R . (XBL 7210-4123)

If nuclei are considered to be incompressible, only the quantity R is expected to be proportional to $A^{1/3}$. Attempts to describe Q or C values in terms of a constant times $A^{1/3}$ tend to create confusion. Figure 2 shows the result when the ratios of Q values (from μ -mesic atoms) and C values (from electron scattering) to $A^{1/3}$ are plotted against $A^{-2/3}$ for nuclei throughout the periodic table. Neither of these ratios is a constant, but they both lie on the dot-dashed lines corresponding to the predictions of Eqs. (2) with

$$\begin{aligned} R &= 1.128 A^{1/3} \text{ fm}, \\ b &= 1 \text{ fm}. \end{aligned} \quad (3)$$

The values of the ratio of R (calculated from the Q and C values) to $A^{1/3}$ are plotted as squares in Fig. 2; they scatter about the constant value 1.128 fm. This constant, which provides a proportionality between $A^{1/3}$ and the equivalent sharp radius of the proton distribution, is not equal to r_0 , the radius constant of symmetric uniform infinite nuclear matter. These numbers differ because nuclei are not strictly incompressible and because there is a neutron skin on neutron-rich nuclei. The connection between them is provided by the droplet model which is discussed in some detail in Ref. 3.

Relationships like those in Eqs. (2) can be obtained to show the connection between the geometric properties of one leptodermous distribution and another which is obtained from it by folding in a short-range function. The following relationships:

$$\begin{aligned} C_2 &= C_1(1 - \beta_c^2 + \dots), \\ R_2 &= R_1, \\ Q_2 &= Q_1(1 + \frac{5}{2}\beta_c^2 + \dots), \end{aligned} \quad (4)$$

hold when β_1 and β_2 are small, where the quantity β_c is defined by

$$\beta_c = \frac{1}{3} \langle r^2 \rangle_{\text{folding}} / R_1 \cdot \text{function}$$

These relationships were employed in a study of nuclear density distributions and optical model potential wells. One of the conclusions of this work was that the optical model wells cannot be obtained by folding a simple Gaussian interaction into the density distribution. The experimental values of R_0 and R_V differ, and in Eqs. (4) above we see that they must be the same if the two distributions are to be related by a folding.

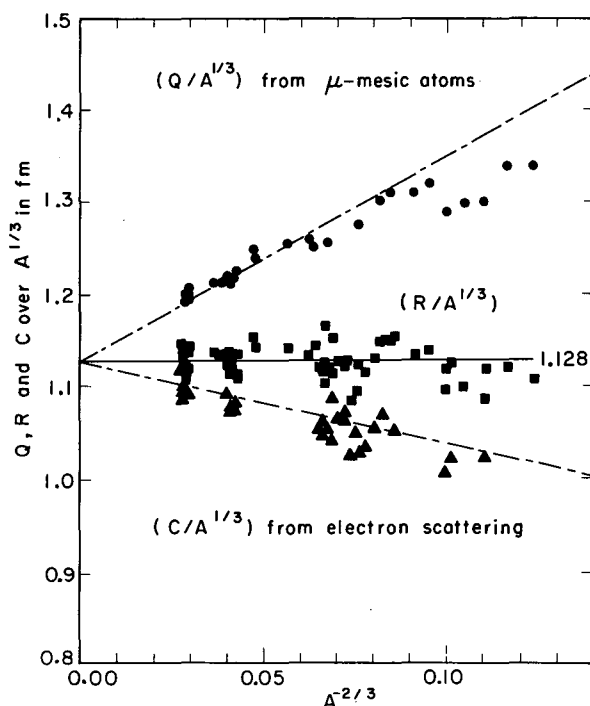


Fig. 2. Experimental values from Ref. 4 of $Q/A^{1/3}$ (from μ -mesic atoms) and $C/A^{1/3}$ (from electron scattering) are plotted against $A^{-2/3}$. The values of $R/A^{1/3}$ for these experimental points are also plotted and are seen to scatter about the constant value at 1.128 fm. The corresponding predictions for $Q/A^{1/3}$ and $C/A^{1/3}$ are given as dot-dashed lines.

(XBL 7210-4120)

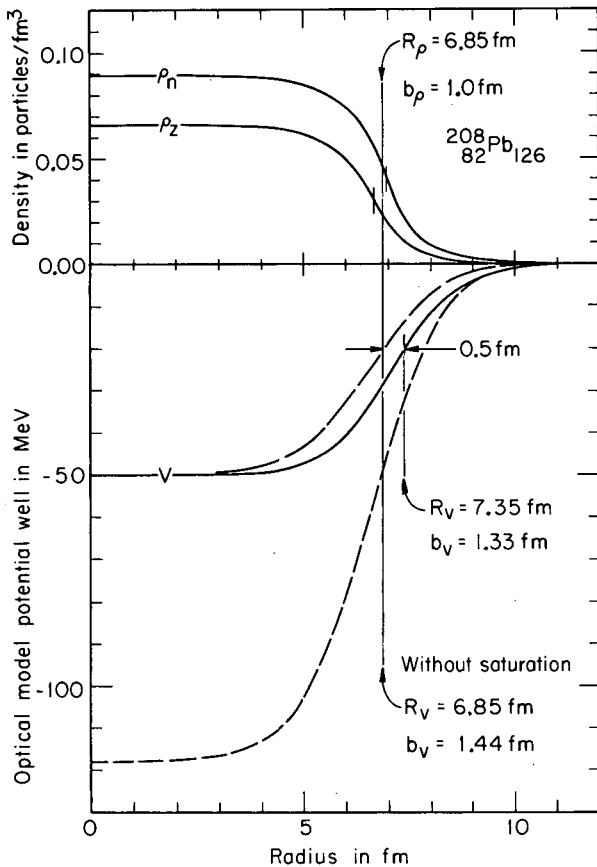


Fig. 3. Droplet model density distributions for $^{208}_{82}\text{Pb}_{126}$ are plotted against radial distance in the upper part of the figure. Short vertical bars on ρ_n and ρ_z indicate the location of the equivalent sharp radii R_n and R_z . The long vertical line indicates the location of the equivalent sharp radius of the total density R_ρ . This same line indicates the location of the equivalent sharp radius of the potential (obtained by folding a non-saturating force into the density) plotted in the lower part of the figure as a dashed line. The lower dashed line is the potential itself and the upper dashed line is the same curve normalized to the solid line which represents the potential obtained when saturating interaction is used. A shorter vertical line indicates the location of the equivalent sharp radius of this latter potential and shows that it lies substantially outside that of the non-saturating potential.

(XBL 7210-4156)

Of course there is no physical reason to expect that the densities and potentials should be related in such a simple way. This is especially true since the almost incompressible nature of nuclear matter depends on the saturation of the nuclear force. When a more reasonable force of this kind (one which includes saturation) is employed, there is no longer any difficulty in relating the nuclear density distributions and potential wells. Figure 3 shows how a potential well generated by folding a saturating interaction into the density (solid line) lies outside a similar well (dashed line) generated without saturation.

This work has shown that if the geometrical relationships between various nuclear properties are treated correctly a number of problems arising in nuclear physics can be easily resolved.

Footnotes and References

* Lep.to.der.mous--having a thin skin. This term has been employed by Swiatecki and co-workers for the depiction of distributions that are essentially homogeneous except at the surface. Its application implies that all deviations from bulk behavior are confined to a relatively thin surface region.

† Condensed from Ref. 3.

1. Hahn, Ravenhall, and Hofstadter, Phys. Rev. 101, 1131 (1956).
2. Georg Stussmann, Lawrence Berkeley Laboratory Report LBL-1615.
3. William D. Myers, Lawrence Berkeley Laboratory Report LBL-1259.
4. H. R. Collard, L. R. B. Elton, and R. Hofstadter, in Nuclear Radii, Vol. 2, Group I, Landolt-Börnstein, Numerical Data and Functional Relationships in Science and Technology (Springer-Verlag, Berlin, 1967).

FIT OF THE INTERACTION PARAMETERS OF A
THOMAS-FERMI MODEL FOR NUCLEI

H. von Groote*

The two-particle interaction used in the Thomas-Fermi (TF) model described by Myers and Swiatecki¹

$$V(r, p) = C_{\ell, u} \frac{\exp(-r/a)}{r/a} [1 - (p/b)^2],$$

where

$$r = |\bar{r}_1 - \bar{r}_2|, \quad p = |\bar{p}_1 - \bar{p}_2|,$$

contains the four parameters C_{ℓ} , C_u (interaction strengths for like and unlike particles), a (Yukawa range), and b (critical momentum) or T (equal to $b^2/2M$, the critical energy), which are closely related to the four liquid-drop parameters a_1 (volume energy), a_2 (surface energy), J (symmetry energy), and r_0 (radius constant). These force parameters were determined by a least-squares fit to the experimentally known masses of nine odd-mass nuclei scattered over the periodic table (denoted by circles in Fig. 1). These masses were corrected for shell effects as calculated by Seeger² and a Wigner term $30 \text{ MeV} \cdot [(N-Z)/A]$ (Ref. 3). For convenience the related parameters a_2 , J , r_0 , and a were the ones actually fitted. The fit gave the following results: $C_{\ell} = 353.686 \text{ MeV}$, $C_u = 516.526 \text{ MeV}$, $T = 89.210 \text{ MeV}$, and $a = 0.55724 \text{ fm}$ and an r. m. s. deviation of 0.834 MeV . As a test the masses of 69 additional nuclei ($A = 35, 45, \dots$, 255 with three isobars for each A) were then calculated with these parameters and compared with the corrected experimental masses. The deviations are shown in Fig. 1 and display a good agreement between the theoretical and ex-

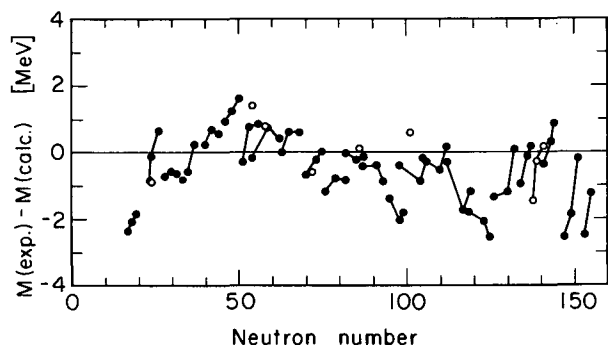


Fig. 1. Deviations of the calculated masses from the corrected experimental ones plotted versus the neutron number. Isobars are connected. Circles denote the nuclei used in the fit. (XBL 733-2458)

perimental masses, the rms deviation for all 78 masses being 1.09 MeV . However, there still remain some shell effects and for $A > 200$ the calculated valley of β -stability bends away from the $N=Z$ line more strongly than the experimental one.

The droplet-model coefficients¹ resulting from these TF-parameters are:

$$r_0 = 1.1594 \text{ fm}, \quad a_1 = 16.103 \text{ MeV}, \quad a_2 = 18.01 \text{ MeV}, \\ a_3 = 7.8 \text{ MeV},$$

$$J = 33.99 \text{ MeV}, \quad Q = 28.5 \text{ MeV}, \quad K = 306 \text{ MeV}, \\ L = 107 \text{ MeV}, \quad M = 4 \text{ MeV},$$

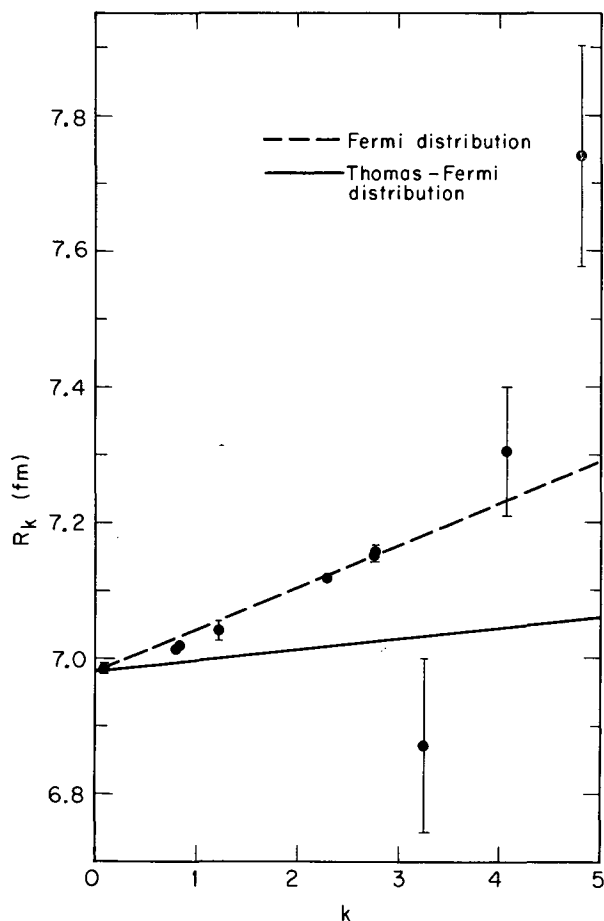


Fig. 2. Moments R_k plotted versus k for the Fermi distribution of Ref. 6 and the TF distribution calculated with the parameter set which reproduces the masses best. (XBL 733-2459)

all of which lie within the expected ranges.⁴ The radius constant r_0 agrees especially well with the value 1.16 fm derived from electron scattering and transition energies of muonic atoms.⁵

This 4-parameter TF-model is capable of reproducing the nuclear masses throughout the periodic table as well as the radius constant r_0 . A further investigation of the charge distribution, however, shows deficiencies of the TF model which seem to be due to the fact that the calculated density distributions lack an outward tail. Figure 2 shows the moments

$$R_k = \left[\frac{k+3}{3} \langle r^k \rangle \right]^{1/k}, \quad 0 \leq k,$$

of the TF-charge distribution for ^{208}Pb compared with the moments Ford and Wills⁶ obtained by fitting a Fermi distribution to the transition energies. While both lines have the same intercept R_0 , their slopes differ considerably, and furthermore, the 10-90 surface thickness t is 2.24 fm with the Fermi distribution and $t = 1.56$ fm in the TF case. It can be shown that there is no parameter set which simultaneously reproduces the three quantities R_0 , slope,

and t , even if one is willing to tolerate a poor fit to the masses.

Footnote and References

* Visitor from Physikalisches Institut der Univ. Würzburg, 87 Würzburg, Germany. Present address: Institut für Theoretische Kernphysik der T.H. Darmstadt, 61 Darmstadt, Germany.

1. W. D. Myers and W. J. Swiatecki, *Ann. Phys.* **55**, 395 (1969).
2. P. A. Seeger, private communication.
3. W. D. Myers, private communication.
4. S. Ludwig, H. von Groote, and E. Hilf, to be published in *Nucl. Phys.*
5. W. D. Myers, *Nucl. Phys.* **A145**, 387 (1970).
6. K. W. Ford and J. G. Wills, *Phys. Rev.* **185**, 1429 (1969).

MODIFIED DEFINITION OF THE SURFACE ENERGY IN THE LIQUID-DROP FORMULA

H. J. Krappe* and R. Nix†

The usual liquid-drop expression for nuclear deformation energies has the undesirable feature that:

- 1) for strongly necked-in configurations the energy is very sensitive to the unphysical fine details of the parametrization of the shape in the neck region,
- 2) the contour lines of the energy surface have discontinuous derivatives at the scission line whereas in reality the transition should be smooth; that affects especially the predicted Coulomb barrier heights in heavy-ion reactions.

The common reason for these shortcomings is the assumption of an infinitely sharp nuclear surface in the idealized liquid-drop model. In order to allow for a diffuseness of the surface of range a , we propose to substitute the surface energy term in the Bethe-Weizsäcker formula by the integral

$$E = - \frac{V}{4\pi a^3} \int d^3r \int d^3r' \frac{\exp\left(-\frac{|r-r'|}{a}\right)}{|r-r'|} \quad (1)$$

to be taken over the volume of the nucleus. The range a and strength V of the Yukawa force are free parameters, which have to be fitted to reproduce empirical fission barrier heights and Coulomb barriers in heavy-ion reactions. As the range a is supposed to be small compared with the nuclear radius, formula (1) allows a leptodermous type of expansion which yields a volume, a surface, and higher-order terms. In our studies of deformation effects the nuclear volume is kept constant. By suitably fitting the parameters V and a , the surface and higher contributions are supposed to describe closely the corresponding terms in a self-consistent Thomas-Fermi treatment of the smooth part of the deformation energy surface.

For a sphere of radius R_0 formula (1) yields

$$E = -V \left(\frac{4\pi}{3} R_0^3 - 2\pi R_0^2 a + 2\pi a^3 - 2\pi a (R_0 + a)^2 e^{-2R_0/a} \right), \quad (2)$$

where the exponential term is negligible for heavy nuclei and $a < 1$ fm. There is no curvature term in (2). If the surface term in the Bethe-Weizsäcker formula is defined as $c_s A^{2/3}$,

then comparison with the second term in (2) gives the relation

$$c_s = 2\pi V a r_0^2$$

with $R_0 = r_0 A^{1/3}$. One can show that there is also no curvature term for almost spherical configurations: If the shape is given by

$$R = R_0 \left[1 + \sum_{\mu \geq 2} \beta_{\mu\nu} Y_{\mu\nu}(\Omega) - \frac{1}{4\pi} \sum_{\mu \geq 2} |\beta_{\mu\nu}|^2 \right]$$

to second order in β the nuclear part of deformation energy is given by

$$E(\beta_{\mu\nu}) - E(0) = \frac{E_s}{4\pi} \sum_{\mu \geq 2} |\beta_{\mu\nu}|^2 C_\mu, \quad (3)$$

where E_s is the surface energy of the sphere and the restoring force C_μ is

$$C_\mu = - \left(\frac{R_0}{a} \right)^4 \int_{-1}^1 dx P_\mu(x) \exp \left\{ - \frac{2R_0^2}{a^2} (1-x) \right\}^{\frac{1}{2}} \cdot \left[\frac{2R_0^2}{a^2} (1-x) \right]^{-\frac{1}{2}} + \left[1 + \frac{R_0}{a} \right] \left[\frac{R_0}{a} - 1 + \left(\frac{R_0}{a} + 1 \right) e^{-2R_0/a} \right]. \quad (4)$$

An expansion in powers of $A^{1/3}$ yields

$$\frac{E_s}{4\pi} C_\mu = \frac{c_s}{8\pi} \left\{ \left[\mu(\mu+1) - 2 \right] A^{2/3} - \frac{3}{4} (\mu-1)\mu(\mu+1)(\mu+2) \left(\frac{a}{r_0} \right)^2 + 0 \left(\frac{a^4}{r_0^4} A^{-2/3} \right) + 0 \left(e^{-2R_0/a} A^{2/3} \right) \right\},$$

which has the well known limit $(E_s/8\pi)[\mu(\mu+1)-2]$ for $a \rightarrow 0$, i. e., the usual definition of the surface energy term. For large multipole order μ , C_μ becomes independent of μ because the first term in (4) vanishes.

Of special interest is the case $\mu=2, \nu=0$. If one adds the Coulomb energy to (3), the total quadrupole deformation energy δE is

$$\delta E = \frac{E_s}{4\pi} \beta_{20}^2 \left[2 - 2x - 9 \frac{a^2}{R_0^2} + 0 \left(e^{-2R_0/a} \right) \right]$$

with $x = E_{\text{Coul}}/2E_s$. The critical value of x for which the nucleus in this model loses stability against fission is

$$x_{\text{cr}} \approx 1 - \frac{9}{2} \frac{a^2}{R_0^2}$$

instead of the usual value 1.

As an interesting application of (1) we can write down the nuclear part of the interaction energy of two spherical nuclei of radii R_1 and R_2 and center-of-mass distance $D \geq R_1 + R_2$:

$$E_{\text{int}} = -4 \left(\frac{a}{r_0} \right)^2 C_s \left[\frac{R_1}{a} \cosh \left(\frac{R_1}{a} \right) - \sinh \frac{R_1}{a} \right] \times \left[\frac{R_2}{a} \cosh \left(\frac{R_2}{a} \right) - \sinh \left(\frac{R_2}{a} \right) \right] \frac{e^{-D/a}}{D/a}.$$

Another configuration for which (1) can be integrated analytically is the spherical bubble nucleus with inner radius R_1 and outer radius R_2 :

$$E = - \left(\frac{a}{r_0} \right)^2 c_s \left[\frac{2}{3} \left(\frac{R_2}{a} \right)^3 - \frac{2}{3} \left(\frac{R_1}{a} \right)^3 - \left(\frac{R_2}{a} \right)^2 - \left(\frac{R_1}{a} \right)^2 + 2 + 2 \left(\frac{R_1}{a} - 1 \right) \left(\frac{R_2}{a} + 1 \right) e^{(R_1 - R_2)/a} + 2 \left(\frac{R_1}{a} + 1 \right) \left(\frac{R_2}{a} + 1 \right) e^{-(R_1 + R_2)/a} - \left(\frac{R_2}{a} + 1 \right)^2 e^{-2R_2/a} - \left(\frac{R_1}{a} + 1 \right)^2 e^{-2R_1/a} \right].$$

To make use of formula (1) for more general deformations it is essential to reduce the six-dimensional integral to a numerically tractable size. It is in fact possible to reduce it to a double surface integral which further reduces to a three-dimensional integral (with a non-singular integrand) for axially symmetric shapes. The computation time for the new surface energy is therefore comparable with the time necessary to evaluate the Coulomb energy. As a result of a numerical calculation we show in Figs. 1 and 2 the fission barrier height (in units of E_s) and the deformation of the saddle point, respectively, as a function of a/r_0 and the fissility x (nuclei along the valley of β -stability, Myers-Swiatecki liquid-drop parameters). For a diffuseness range larger than 0.5 fm the barrier heights are drastically reduced and the saddle-point shapes look more compact compared with the usual zero-range case. These figures are only meant to show general trends. The liquid-drop parameters including V and a have still to be refitted carefully.

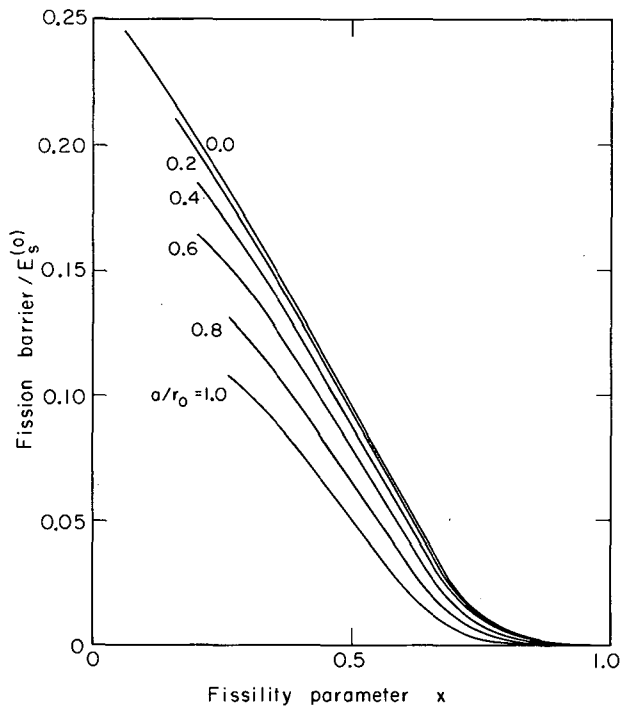


Fig. 1.

(XBL 733-2460)

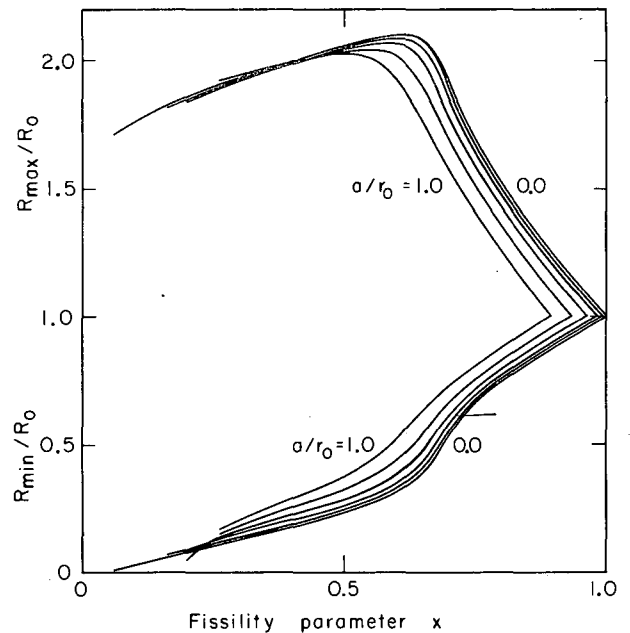


Fig. 2.

(XBL 733-2461)

Footnotes

* On leave from Hahn-Meitner Institut, Berlin, Germany.

† Los Alamos Scientific Laboratory.

HYDRODYNAMIC ANALYSIS OF THE COALESCENCE AND BREAKUP OF VISCOUS NUCLEAR LIQUID DROPS

C. T. Alonso

For several decades a great deal of attention has been directed to such static properties of the nuclear liquid-drop model as the potential barriers for fusion and fission. While an enormous amount of information has been gathered from these studies, a complete picture is lacking owing to an almost total neglect of the dynamics of the problem.

Recent developments in computer methods for programming complex fluid dynamics have now made such dynamic studies feasible.¹ We are currently creating computer simulations of the collision, fusion, and subsequent fission of charged incompressible liquid drops with surface tension and other classical liquid parameters scaled to typical nuclear values. A nuclear viscosity coefficient is included as one of these parameters.

During the past year the question of nuclear viscosity has begun to attract increasing attention, especially with respect to its possible role in the interaction of heavy nuclei. On the one hand, if a nuclear core is a pure superfluid (as in liquid ${}^4\text{He}$) its viscosity is zero, but on the other hand if the nuclear core more closely resembles liquid ${}^3\text{He}$, its viscosity at low temperatures can be very large. Since the pairing interaction in nuclei is relatively weak, it is expected that the superfluid component in a real nucleus might be quite small and that viscosity, which heretofore has not been included in any model calculations, might be more important than was previously thought.

Our model uses the marker-and-cell method developed by Harlow and Amsden at Los Alamos for a solution of the Navier-Stokes equation de-

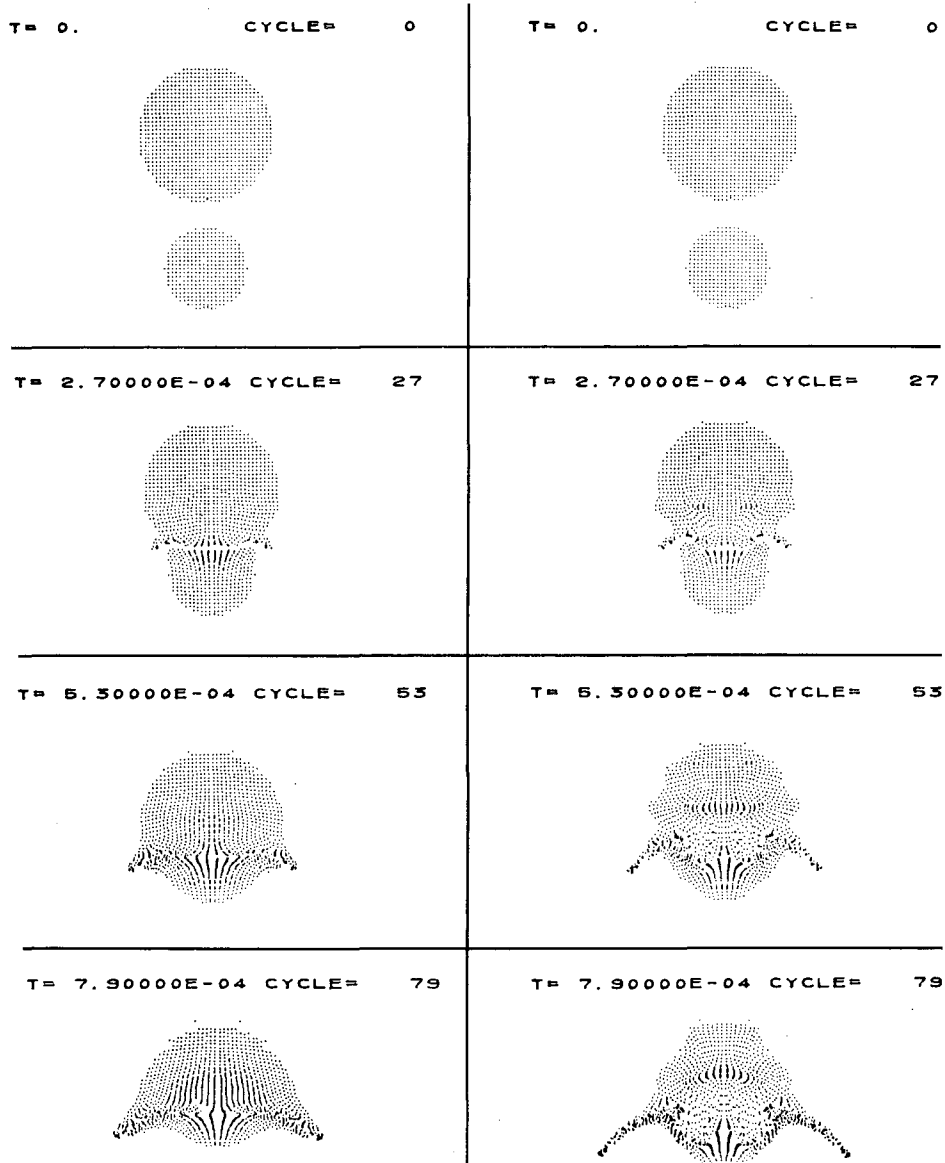


Fig. 1. Collision of two droplets. The vertical sequence to the right has a viscosity of 0.2 in relative units, while that to the left has a viscosity of 1.0. (XBL 733-2462)

describing the hydrodynamics of a fluid moving with a low Mach number.¹ Using this method, we are able to trace the trajectory of a fluid element during the collision process. The computer program generates a film strip of the interaction as well as a printout of the various dynamic parameters such as shape, velocity, and pressure as a function of time. Figure 1 shows, more for illustration than for its applicability to nuclei, a preliminary set of frames describing the collision of two spherical droplets with a low coefficient of surface tension and a low charge density. In the frames at the left the viscosity was 1.0 (in relative units), while in the frames at the right the viscosity was 0.2. Differences in the rate of shape formation for the two viscosities are apparent.

Comprehensive studies of the effect of viscosity are in progress but are not yet completed. At present our model utilizes a purely classical liquid, but we are currently developing ways of inserting quantum-mechanical properties as well as compressible surface properties.

Reference

1. F. H. Harlow and A. A. Amsden, J. Comp. Physics 6, 322 (1970).

HARTREE-FOCK CALCULATIONS OF THE ANGULAR SHAPES OF NEUTRON AND PROTON DISTRIBUTIONS IN DEFORMED NUCLEI

N. K. Glendenning, D. Vautherin,* and M. Veneroni*

The first determination of details of the shape of nuclei beyond the quadrupole component were made by an analysis of alpha scattering on selected rare earth nuclei.¹ These analyses yielded values of β_λ in the parametrization of the shape according to

$$R = R_0 \left[1 + \sum_{\lambda} \beta_{\lambda} Y_{\lambda 0}(\theta) \right].$$

More recently Coulomb excitation experiments have yielded measurements of the 4-pole electric moment for several of the same nuclei.² Unfortunately, among the groups reporting such measurements there are disagreements. Several groups report Coulomb excitation measurements in agreement with the alpha scattering experiments, while several others report significantly larger values.

The two types of experiments do not in fact measure quite the same quantity. The alpha particles feel the nuclear field of both protons and neutrons, while the Coulomb excitation measurements concern the charge distribution. Moreover, the finite size of the alpha particle was not unfolded from the alpha measurements, and there is no known prescription having a sound basis, for unfolding the alpha size. Notwithstanding these reservations, there is a suggestion that the angular shape of neutron and proton distributions in deformed nuclei may be different. The difference could arise because of the Coulomb repulsion amongst protons, not experienced by neutrons, and because neutrons and protons fill quite different shells. On the other hand the neutron-proton interaction will tend to encourage equal distributions.

We have begun some Hartree-Fock calculations in order to get an indication of how the various effects balance out with respect to neutron and proton angular shapes. The contour corresponding to half the value of the av-

erage central density of neutrons and protons was adopted as a definition of the angular shape. For the two nuclei investigated so far, we find that the distributions of neutrons and protons have significantly different values of β_4 , as listed in Table I. This result has not been anticipated to our knowledge, and should encourage a resolution of the disagreements among the experimental groups.

Table I. Deformation parameters of neutron and proton distributions as calculated for ^{166}Er and ^{176}Yb .

		β_2	β_4
^{176}Yb	n	0.283	0.013
	p	0.288	0.009

^{166}Er	n	0.298	0.046
	p	0.301	0.034

Footnotes and References

* Summer visitors during 1972. Permanent address: Laboratoire de Physique Theorique, Saclay, France.

1. N. K. Glendenning, D. L. Hendrie, and D. H. Jarvis, *Phys. Letters* **26B**, 131 (1968); D. L. Hendrie et al., *Phys. Letters* **26B**, 127 (1968).

2. F. S. Stephens, private communication, F. S. Stephens, R. M. Diamond, N. K. Glendenning, and J. deBoer, *Phys. Rev. Letters* **24**, 1137 (1970); F. S. Stephens, R. M. Diamond, and J. deBoer, *Phys. Rev. Letters* **27**, 1151 (1971).

RADIUS SCALING FOR DEFORMED NUCLEI

D. L. Hendrie

It has been well established that permanently deformed nuclei often have shapes that are more complicated than simple spheroidal deformation. These shapes were first accurately measured in the nuclear potential by scattering

of alpha particles with energies well above the Coulomb barrier and for the rare earth nuclei.¹ A systematic trend of hexadecapole deformation was discovered. Since then these basic results have been confirmed by a num-

ber of other experiments using other projectiles and energies,²⁻⁸ have been extended to other regions of the periodic table,^{9,10} and have been described theoretically.¹¹ The experiments can be classified into two major categories, those that measure the shape of the nuclear potential^{1-3,8,9} and those that measure the charge deformation.^{4-8,10}

A simple and usual way of characterizing these deformations is to describe an appropriate nuclear radius in a multipole expansion

$$R = R_0 (1 + \beta_2 Y_{20} + \beta_4 Y_{40} + \beta_6 Y_{60} + \dots) \quad (1)$$

where the Y_{L0} 's are spherical harmonics and the β_L 's are the experimentally determined deformation parameters.

A puzzling aspect has appeared in what seems to be a systematic discrepancy between the nuclear and Coulomb experiments, in that the Coulomb work shows a trend to larger values of the β_4 deformation parameter. This would, of course, be of basic importance, if verified. A long-standing problem in the comparison has been due to the different radii that characterize the two type of experiments. The Coulomb radius has been accurately measured by electron scattering to be about $1.1A^{1/3}$ fm for a suitably diffuse radial charge distribution, where the optical potential of Ref. 1, for example, was $1.44A^{1/3}$ fm, where A is the atomic mass of the target nucleus. Since the transition amplitudes depend sensitively on the radius, scaling of the measured β 's with their corresponding radii must be done with care. Traditionally, this scaling has been accomplished by using a suggestion of Blair that the product $B_L R_0$ is a constant. This note will show, using a very simple model for the nuclear interaction, the origin of the simple scaling law, and also that significant higher-order effects occur which serve to reduce the discrepancy between the nuclear and Coulomb results for β_4 . A sharp-edged spherical alpha particle is assumed to interact with a sharp-edged deformed nucleus only at the edges. However, from this picture we can extract purely geometric terms that would be common to any more realistic calculation.

From Fig. 1, let $R(\theta)$ describe the edge of a deformed target nucleus, Δ be the radius and $r(\theta)$ describe the locus of the center of an alpha particle which just touches the nuclear surface. We define

$$r(\theta) = r_0 [1 + \beta_2 Y_{20}(\theta) + \beta_4 Y_{40}(\theta) + \beta_6 Y_{60}(\theta) + \dots] \quad (2)$$

and

$$R(\theta) = R_0 [1 + \epsilon(\theta)], \quad (3)$$

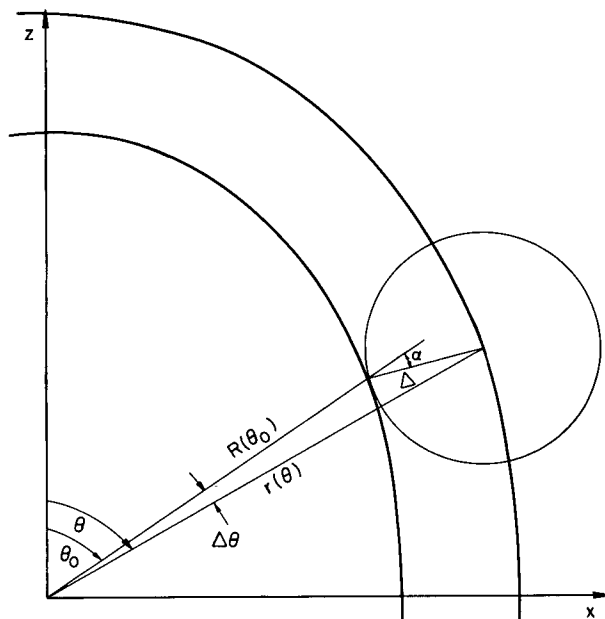


Fig. 1. Construction of new surface $r(\theta)$, from an original surface $R(\theta)$ just touched by an alpha particle of radius Δ . (XBL 733-2463)

where

$$\epsilon(\theta) = \beta_{20} Y_{20}(\theta) + \beta_{40} Y_{40}(\theta) + \beta_{60} Y_{60}(\theta). \quad (4)$$

We wish to compare the values of $r_0, \beta_2, \beta_4, \beta_6$ etc. with the values of $R_0, \beta_{20}, \beta_{40}, \beta_{60}$.

From the construction of Fig. 1, we have the angle α defined as the angular difference between the direction of $R(\theta_0)$ and the normal to the surface at θ_0 . From the differential geometry we obtain

$$\begin{aligned} \tan \alpha &= - \frac{R'(\theta_0)}{R(\theta_0)} \\ &= - \frac{\epsilon'(\theta_0)}{1 + \epsilon(\theta_0)}. \end{aligned} \quad (5)$$

We expand $R(\theta) = R(\theta_0) + \left. \frac{dR}{d\theta} \right|_{\theta_0} \Delta\theta + \dots$

so that

$$\epsilon(\theta_0) = \epsilon(\theta) - \epsilon'(\theta) (\Delta\theta) + \dots, \quad (6a)$$

$$\epsilon'(\theta_0) = \epsilon'(\theta) - \epsilon''(\theta) (\Delta\theta) + \dots \quad (6b)$$

From the trigonometric relationships, we obtain

$$r^2(\theta) = R^2(\theta_0) + \Delta^2 + 2\Delta R(\theta_0) \cos \alpha \quad (7)$$

and

$$\sin(\Delta\theta)/\Delta = \sin \alpha/r(\theta). \quad (8)$$

For convenience we define

$$\rho(\theta) = r(\theta)/R_0 \quad \text{and} \quad \delta = \Delta/R_0 \quad (9)$$

so that Eq. 7 is rewritten

$$\rho^2 = [1 + \epsilon(\theta_0)]^2 + \delta^2 + 2\delta[1 + \epsilon_0(\theta_0)] \cos \alpha. \quad (10)$$

We also define the small dimensionless parameter η by

$$\rho = 1 + \epsilon(\theta) + \delta + \eta(\theta). \quad (11)$$

Now from Eqs. 5 and 6 we obtain, to second order in the small parameters ϵ and ϵ' ,

$$\alpha \approx \tan \alpha \approx \sin \alpha = -\epsilon'(\theta) \quad (12)$$

From Eqs. 8 and 12 we obtain

$$\Delta\theta \approx \sin(\Delta\theta) \approx -\frac{\delta}{1+\delta} \epsilon'(\theta). \quad (13)$$

Table II. List of deformation parameters.

		^{152}Sm	^{154}Sm	^{158}Gd	^{166}Er	^{174}Yb	^{176}Yb	^{178}Hf	^{182}W
$R_0 = 1.44 A^{1/3} \text{Fm}$	β_{20}	0.205	0.225	0.235	0.230	0.230	0.230	0.205	0.190
	β_{40}	0.040	0.045	0.030	0	-0.040	-0.045	0.060	-0.060
	β_{60}	-0.010	-0.015	-0.015	-0.015	0	-0.005	0	0
1st Order $r_0 = 1.1 A^{1/3} \text{Fm}$	β_2	0.268	0.295	0.308	0.301	0.301	0.301	0.268	0.249
	β_4	0.052	0.059	0.040	0	-0.052	-0.059	-0.079	-0.079
	β_6	-0.013	-0.020	-0.020	-0.020	0	-0.006	0	0
2nd Order $r_0 = 1.11 A^{1/3} \text{Fm}$	β_2	0.255	0.279	0.294	0.294	0.302	0.302	0.273	0.253
	β_4	0.061	0.070	0.053	0.014	-0.041	-0.046	-0.069	-0.070
	β_6	-0.006	-0.010	-0.013	0.018	-0.007	-0.014	-0.009	-0.009
Ref. 6 $r_0 = 1.1 A^{1/3} \text{Fm}$	β_2	0.286	0.315	0.330	0.350				
	β_4	0.068	0.066	0.030	-0.048				
Ref. 11 $r_0 = 1.1 A^{1/3} \text{fm}$	B_4	0.076	0.083	0.063	0.024	-0.021	-0.032	-0.033	-0.047

Now using Eqs. 6, 10, 11, 12, and 13, to lowest order we have

$$\eta(\theta) = \frac{1}{2} \frac{\delta}{1+\delta} \epsilon'(\theta)^2. \quad (14)$$

Substituting Eq. 14 into Eq. 11, we have

$$\rho(\theta) = 1 + \delta(\theta) + \frac{1}{2} \frac{\delta}{1+\delta} \epsilon'(\theta)^2. \quad (15)$$

Finally, to obtain the values of β_L , we multiply both sides by Y_{L0} and integrate over the sphere

$$r_0 = R_0 \left[1 + \delta + \frac{1}{2} \frac{\delta}{1+\delta} \frac{1}{\sqrt{4\pi}} \int Y_{00} \epsilon'(\theta)^2 dr \right], \quad (16a)$$

$$\beta_L = R_0/r_0 \left[\beta_{L0} + \frac{1}{2} \frac{\delta}{1+\delta} \int Y_{L0} \epsilon'(\theta)^2 dr \right]. \quad (16b)$$

We define the constants C_{ij}^L to yield the following:

$$r_0 = R_0 \left[1 + \delta + \frac{\delta}{1+\delta} \sum_{ij} C_{ij}^0 \beta_{i0} \beta_{j0} \right], \quad (17a)$$

$$\beta_L = R_0/r_0 \left[\beta_{L0} + \frac{\delta}{1+\delta} \sum_{ij} C_{ij}^L \beta_{i0} \beta_{j0} \right]. \quad (17b)$$

A tabulation of the C_{ij}^L 's is given in Table I. By neglecting the second-order terms, we have immediately the scaling law proposed by Blair. These corrections only include effects of the angular integrations; they are independent of and in addition to diffuseness etc. included in the radial integrals.

We use these results to scale the results of Ref. 1 ($R_0 = 1.44A^{1/3}$ fm) to an appropriate Coulomb radius ($r_0 = 1.1A^{1/3}$ fm). Table II shows the original measurements and the results after both first- and second-order scaling. Also shown for comparison are the corresponding results of Ref. 6. The agreement between the β_4 's is improved by the inclusion of the second-order term, but the β_2 's agree less well. It is still probably premature to draw inferences from comparisons such as this however, since the spreads in published Coulomb excitation values are far greater than the apparent discrepancies with the particle results. The comparison of the particle results for β_4 and β_6 with the theoretical predictions of Ref. 11, however, is significantly improved. The extreme sensitivity of β_6 to the second-order terms suggests that even better treatment may be necessary.

Table I. C_{ij}^L .

L \ ij	22	24	26	44	46	66
0	0.067	0	0	0.275	0	0.471
2	0.270	2.418	0	1.393	6.680	3.131
4	-0.484	0.492	3.340	0.685	0.747	2.028
6	0	-1.908	0.963	-0.071	1.267	1.202

References

1. D. L. Hendrie et al., Phys. Letters 26B, 127 (1968).
2. M. -P. Barbier, R. Lombard, J. M. Moss, and Y. Terrien, Phys. Letters 34B, 386 (1971).
3. A. A. Aponick, C. M. Chesterfield, D. A. Bromley, and N. K. Glendenning, Nucl. Phys. A159, 367 (1970).
4. F. S. Stephens, R. M. Diamond, and J. de Boer, Phys. Rev. Letters 27, 1151 (1971).
5. W. Bertozzi et al., Phys. Rev. Letters 28, 1711 (1972).
6. K. A. Erb et al., Phys. Rev. Letters 29, 1010 (1972).
7. J. S. Greenberg and A. H. Shaw, in Proceedings of the Osaka Conference on Nuclear Moments (1972), p. 113.
8. W. Bruckner et al., Phys. Rev. Letters 30, 57 (1973).
9. J. M. Moss et al., Phys. Rev. Letters 26, 1488 (1971).
10. F. K. McGowan et al., Phys. Rev. Letters 27, 1741 (1971).
11. S. G. Nilsson et al., Nucl. Phys. A131, 1 (1969); P. Möller et al. Physics Letters 26B, 418 (1968).

THE NUCLEAR SKIN THICKNESS TREATED AS A STRUTINSKY VARIABLE

 H. H. von Groote,* W. D. Myers, P. Möller, S. G. Nilsson,† J. R. Nix,‡
 J. Randrup, W. J. Swiatecki, and C. F. Tsang

The Strutinsky shell correction method has been widely used in the calculations of potential energy surfaces.^{1,2} In these calculations the nuclear angular shape parameters have been considered basic variables spanning the energy surface. One may generalize this method also to allow for the fact that the nucleus may adjust also its radial shape as a function of nucleon numbers.

As a basic radial shape parameter one may consider the surface diffuseness t_n and t_p defined as the radial distance between 90% and 10% density for neutrons and protons respectively. This diffuseness parameter t relates to the parameter a for a Fermi density distribution as

$$t = (4 \ln 3) a \approx 4.40 a \quad (1)$$

The shell correction energies are calculated as usual² as

$$E_{sh} = \sum_{\nu} e_{\nu}(t_n, t_p) - \langle \sum_{\nu} e_{\nu}(t_n, t_p) \rangle \quad (2)$$

employing the Strutinsky shell averaging function in the evaluation of the second term.

In different regions of neutron and proton numbers, the shell correction term may favor large or small diffuseness, providing a driving force toward increasing or decreasing diffuseness parameters. The total energy of the nucleus is the summation of the shell correction energy and a smooth "liquid-drop" background of averaged nuclear behavior. This smooth liquid-drop energy has a minimum of energy at t_p and t_n of about 2.6 fm and provides a restoring force against deviations from these values. In our calculations this background energy has been derived from a Thomas-Fermi calculation described in some detail elsewhere in this Annual Report.³

The shell energies of Eq. (2) have been calculated as functions of the skin diffuseness parameter employing two nuclear single-particle potentials. The first of these is the "folded Yukawa potential" constructed by Nix.⁴ This potential comes very close to a Wood-Saxon potential in its radial-shape dependence. The second single-particle potential used is the modified-oscillator potential as developed by the Lund-Berkeley-Warsaw group.⁵ Recently we are also studying for comparison the more conventional Wood-Saxon potential, using the distortion expansion developed by Glendenning.⁶

Tables I and II are based on the "folded-Yukawa" potential. We give in these tables the derivative of the shell plus pairing energies at $t_n = t_p = 2.6$ fm. These derivative indicate by their signs whether the shell correction term for these particular neutron and proton numbers prefers a larger (oscillator-like) or smaller (square-well-like) skin diffuseness. Figure 1 is based on the modified oscillator potential. In this figure the spherical single-neutron energy levels are plotted as a function of the diffuseness parameter μ of the modified-oscillator model. This parameter reflects essentially the inverse value of t . The diagram assumes a spin-orbit strength valid in the mass $A \approx 16 - 100$ region.

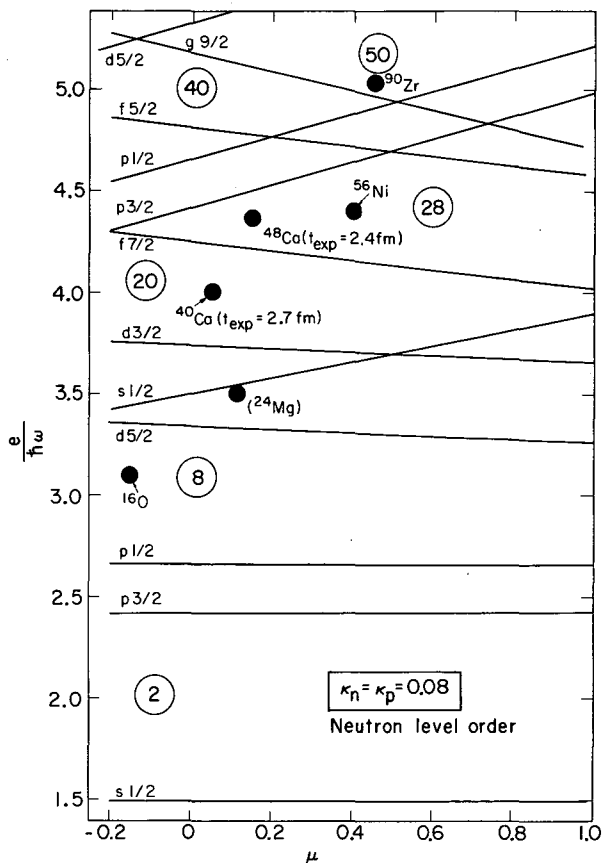


Fig. 1. Spherical single-neutron energy levels for the modified harmonic oscillator model as functions of the l^2 strength parameter μ . (XBL 7210-4231)

The elements ^{16}O , ^{24}Mg , ^{40}Ca , ^{48}Ca , ^{56}Ni , and ^{90}Zr are represented by solid dots whose position in terms of μ has been determined from an optimal fit in μ of observed single-particle levels in neighboring odd-A nuclei. In addition, in parenthesis, t values are given as obtained from electron-scattering experiments.⁷ The trend brought out in Tables I and II is verified in this diagram. Thus if we draw a smooth line through the dots to represent the "average empirical" values of μ as a function of N , then ^{40}Ca should deviate from this line in the "oscillator-like" direction and similarly ^{56}Ni , in the "square-well" direction.

Table I. The derivative of the proton shell plus pairing energy.

Z	$a \frac{dE}{da}$	$a \frac{dE}{da} A^{-2/3}$	Trend towards
20	-2.11	-0.18	Osc.
28	+6.08	+0.41	Sq.
40	-2.58	-0.13	Osc.
50	+6.49	+0.32	Sq.
82	-5.90	-0.17	Osc.
106	+7.24	+0.17	Sq.
114	+8.82	+0.20	Sq.
124	-15.1	-0.33	Osc.

Table II. The derivative of the neutron shell plus pairing energy.

N	$a \frac{dE}{da}$	$a \frac{dE}{da} A^{-2/3}$	Trend towards
20	-0.85	-0.07	Osc.
28	+4.57	+0.34	Sq.
40	-3.15	-0.16	Osc.
50	+7.06	+0.35	Sq.
82	--	--	--
126	-1.84	-0.05	Osc.
164	15.2	+0.36	Sq.
184	-17.3	-0.39	Osc.

The quantitative results of the calculations where both the shell correction and the background energies are included is given from Table III.

It is found that the restoring force provided by the background energy has the effect of coupling the neutron and proton diffuseness coefficients so that they largely follow each other (a symmetry energy effect). Also, the stabilizing effect of the restoring force on the distortion is strong so that very small changes in the final diffuseness are obtained theoretically; in fact, the changes never exceed 5%. The associated energy gains are also very small and rarely in excess of 0.5 MeV for the few selected cases studied.

Table III.

Nuclide	$\frac{\Delta a}{(a^2)}$	$\frac{\Delta a}{(a^2)}$	Energy gain $\frac{\Delta E}{\Delta E}$ (MeV)
$^{40}_{20}\text{Ca}$	1.9	1.5	-0.03
$^{48}_{20}\text{Ca}$	-0.4	-2.7	-0.06
$^{56}_{28}\text{Ni}$	-3.5	-4.2	-0.20
$^{90}_{40}\text{Zr}$	-3.6	-2.7	-0.16
$^{90}_{50}\text{Sn}$	-0.4	-2.3	-0.07
$^{204}_{82}\text{Pb}$	1.1	0.2	-0.03
$^{206}_{82}\text{Pb}$	1.2	0.4	-0.03
$^{208}_{82}\text{Pb}$	1.4	0.9	-0.05
$^{270}_{106}$	-3.9	-4.7	-0.50
$^{298}_{114}$	-0.2	2.0	-0.18
$^{308}_{124}$	3.8	3.7	-0.61

Footnotes and References

* On leave from Physikalisches Institut der Univ. Würzburg, Würzburg, Germany.

† On leave from Department of Mathematical Physics, University of Lund, Sweden.

‡ Los Alamos Scientific Laboratory, New Mexico.

1. W. D. Myers and W. J. Swiatecki, Arkiv Fysik 36, 343 (1967).

2. V. M. Strutinsky, *Yad. Fiz.* 3, 614 (1966).
3. H. H. von Groote, Nuclear Chemistry Division Annual Report for 1972, LBL-4666.
4. J. R. Nix, *Ann. Rev. Nucl. Sci.* 22, 65 (1972); M. Bolsterli, E. O. Fiset, J. R. Nix, and J. L. Norton, *Phys. Rev. C* 5, 1050 (1972).
5. S. G. Nilsson, C. F. Tsang, A. Sobiczewski, Z. Szymanski, S. Wycech, C. Gustafson, I. L. Lamm, P. Möller, and B. Nilsson, *Nucl. Phys.* A131, 1 (1969).
6. N. K. Glendenning, private communication.
7. Landolt-Börnstein, Group I, Vol. 2, edited by H. Schopper (Springer, Berlin, 1967), p. 34.

A CONSISTENT TEST OF THE STRUTINSKY-NILSSON METHOD

W. H. Bassichis,* C. F. Tsang, D. R. Tuerpe,† and L. Wilets‡

The Strutinsky-Nilsson¹ procedure for obtaining energy-deformation surfaces for nuclei consists of the following steps:

A. Nature supplies single-particle energies, e_n , at the ground state deformation and the total binding energy.

B. The parameters of the Nilsson potential are adjusted to optimally reproduce these e_n , and the potential thus obtained generates single-particle energies, $e_n(Q)$, as a function of deformation, Q .

C. The smoothly varying part of the sum of the $e_n(Q)$ up to the Fermi level, as a function of deformation, is extracted using the Strutinsky averaging procedure and the remainder is interpreted as the shell correction.

D. The smoothly varying part of the energy is obtained from a liquid-drop model (LDM) which is fit to total binding energies of all nuclei.

E. The energy deformation surface, obtained by adding the shell corrections to the LDM energy as a function of deformation, is compared to the "experimental" energy deformation surface by considering fission half-lives, etc.

A simple consistent global test, the results of which are reported here, involves the replacement of nature by the constrained Hartree-Fock (CHF) results both for the energy deformation surface and the single-particle energies to be fit, on the average, by "Nilsson" e_n . Thus the extent to which the CHF results correspond to experimental data is irrelevant, because the entire procedure, steps A-E, is carried out within the model. This comparison closely approximates what Strutinsky practitioners in fact do.

The nucleus chosen for consideration was ^{108}Ru , which contains few enough particles so that CHF calculations may be carried out in a sufficiently large space in a reasonable amount of computer time and yet is heavy

enough to exhibit the complexities of the fissionable nuclei of interest. (The details of these calculations are given in Ref. 2.) Although it is possible to impose constraints on higher-moment operators and thus obtain multidimensional energy surfaces, only the quadrupole was constrained. Thus it is assumed that the energy is minimized, at each quadrupole deformation, with respect to all other moments. The parameters of a Nilsson potential were then adjusted so as to fit, on the average, the CHF e_n at zero (quadrupole) deformation. The potential was then deformed in the usual manner so as to obtain $e_n(Q)$. This Nilsson potential contained the usual two deformation parameters, ϵ_2 and ϵ_4 . For each ϵ_2 (or quadrupole moment) the following procedure was used to determine the appropriate value of ϵ_4 . There are two deformation-dependent energy terms in the LDM: the surface and the Coulomb terms. The Coulomb parameter was determined from the CHF r. m. s. proton radius and the surface parameter was adjusted to fit the CHF total energy, on the average, as a function of deformation. The total energy was then calculated by adding to the LDM energy the shell corrections determined by the Strutinsky method. The value of ϵ_4 was then chosen, at each quadrupole deformation, so as to minimize the total energy.

The average fit of single-particle orbitals at zero (quadrupole) deformation as well as a comparison of the orbitals at the CHF ground state deformation is given in Fig. 1. In order to eliminate size-difference effects the results of the two calculations were always compared at the same β , the ratio of the quadrupole moment to the r. m. s. radius. (This is roughly equivalent to using an effective mass to re-scale the nuclear size.) It is seen from Fig. 1 that the Nilsson e 's fit the CHF e 's at the ground state about as well as at zero deformation. Thus the results to follow would

be essentially unchanged if the Nilsson parameters were adjusted for an optimal fit at the ground state. In fact the $e(Q)$ generated followed the CHF e 's remarkably well over the entire range of deformation considered. At each CHF local minimum, except for the ones at -2.0 and $+2.5$ barns, the configuration as given by the Nilsson calculation was the same as that of CHF. Between minima the level crossings occurred at different deformations, but in general the two configurations differed by only one orbital.

The smoothly varying part of the sum of the Nilsson $e(Q)$ is obtained by the Strutinsky averaging procedure and the remainder is

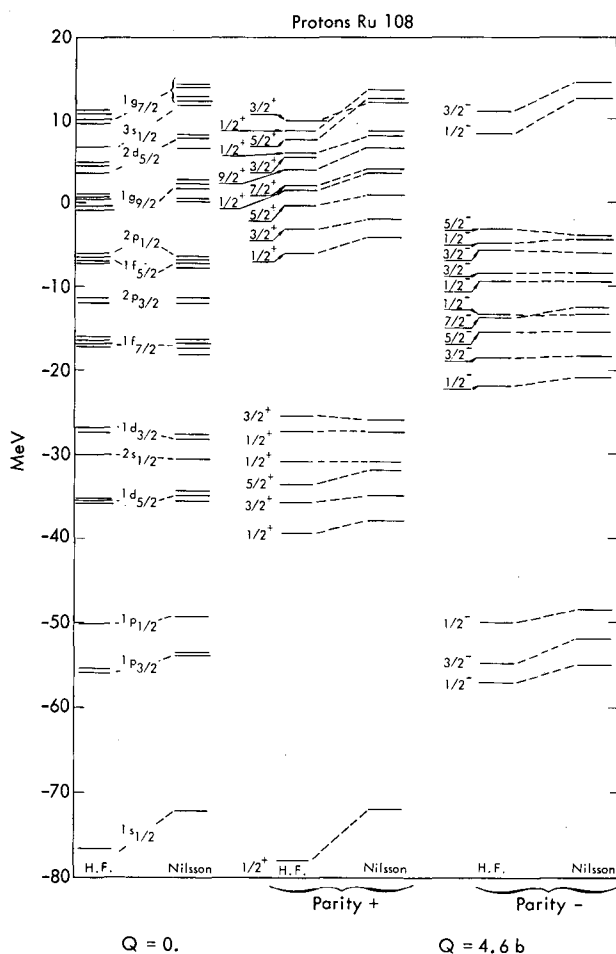


Fig. 1. Nilsson levels fit to CHF e 's at zero deformation. The parameters of the Nilsson potential were adjusted to give the average fit to the CHF e 's at zero deformation. The fit to the CHF e 's at the CHF ground state is seen to be of the same caliber. The levels shown are for protons. The neutron fit is similar at both deformations.

(XBL 733-302)

identified with the shell correction. This is added to the energy of the LDM, the parameters of which are chosen according to the procedure defined above, to yield the total Strutinsky-Nilsson energy, shown as the middle curve (labeled $E_{\text{Nil-Str}}$) in Fig. 2, as a function of deformation. The broken line indicates the LDM energy. It is not smooth as

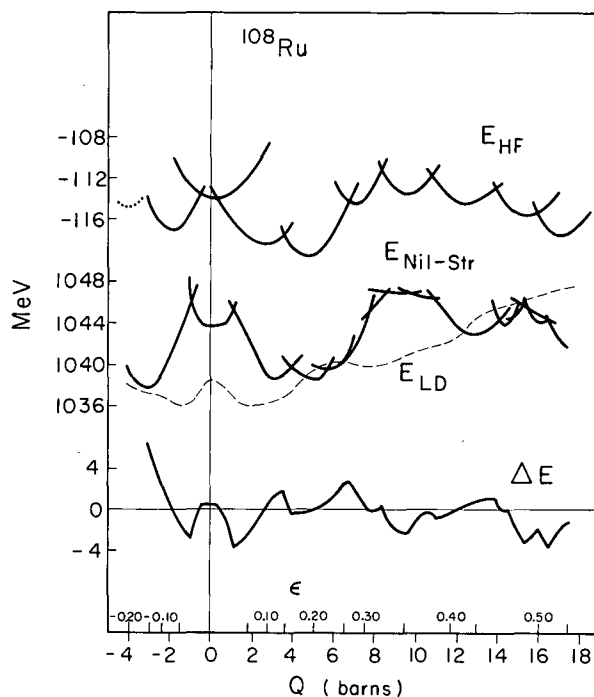


Fig. 2. Top curve: The CHF $E(Q)$. At each deformation the configuration which leads to the lowest energy is, of course, retained. The cusps correspond to the intersections of the energies of two configurations and would be smoothed by the inclusion of pairing. The scallop on the left end is dotted to indicate that the most optimal deformation basis has not been used in this case and the energy may be slightly overestimated (by less than 0.5 MeV).

Middle curve: The total Strutinsky-Nilsson energy. The shell corrections were extracted from the Nilsson $e(Q)$ and added to a LDM energy (broken line). The parameters of the LDM were fit to the CHF results.

Lowest curve: The difference between the CHF and the Strutinsky-Nilsson energy, apart from a constant 1158.7 MeV. If the Strutinsky hypothesis were entirely valid this difference would be zero (or a smoothly varying function of deformation if our LDM parameters are poorly determined). The deviations, of the order of 30%, indicate the degree to which the method is unreliable.

(XBL 728-3951)

a function of ϵ_2 , because even though its value in the two-dimensional ϵ_2 - ϵ_4 space is smooth, the projection of a path in this space onto the ϵ_2 axis need not be smooth. The CHF energy, as a function of deformation, is shown as the top curve (labeled E_{HF}). According to the Strutinsky hypothesis all of the fluctuating part of the energy is contained in the sum of the Nilsson $e(Q)$. Thus the test of the method consists of examining the difference between the two total energies. This should, if the hypothesis were correct, be a smooth curve representing the difference between the LDM energy and the smoothly varying part of the CHF energy. This difference is shown in the lowest curve in Fig. 2. The deviations from a smooth curve represent the degree to which the hypothesis is violated. It should be noted that the fitting procedure for the LDM will minimize the magnitude of the overall deviations. Even with such a bias, however, the shell corrections are seen to be unreliable by ~ 2 MeV, or about 30% on the average.

Thus the result of this preliminary test indicates a strong warning (caveat emptor!) to those who might take the calculations based on the Strutinsky-Nilsson procedure on their face value. We have applied the procedure in a consistent way to a fairly heavy nucleus, ^{108}Ru . Although the Nilsson model does rather well in tracking the single-particle energies as a function of deformation, when fit at one deformation, the assumption that the sum of these eigen-energies contains all of the fluctuating part of $E(Q)$ seems to be unjustified. An uncertainty of at least 30% would have to be borne in mind in any application of the procedure. For example, in the

prediction of the fission barrier of a super-heavy nucleus (which is due almost completely to shell effects), an uncertainty of 2 or 3 MeV out of the predicted ~ 10 MeV implies an uncertainty of the fission half-life of a factor 10^{10} .

Finally it should be noted that pairing effects have been consistently ignored here. Inclusion of a pairing force would just smooth out the cusps in $E(Q)$ which occur when the configuration changes. These effects will be included in the fundamental test of the method, now in progress.

Footnotes and References

* Texas A&M University, College Station, Texas 77840 and Lawrence Livermore Laboratory, Livermore, California 94550.

† Lawrence Livermore Laboratory, Livermore, California 94550.

‡ University of Washington, Seattle, Washington 98105

1. V. M. Strutinsky, Nucl. Phys. A95, 420 (1967); S. G. Nilsson, C. F. Tsang, A. Sobiczewski, Z. Szymanski, S. Wycech, C. Gustafson, I. L. Lamm, P. Möller, and B. Nilsson, Nucl. Phys. A131, 1 (1969).

2. W. H. Bassichis, A. K. Kerman, C. F. Tsang, D. R. Tuerpe, and L. Wilets, The Wheeler Festschrift: Magic Without Magic, edited by J. R. Klander, (W. H. Freeman San Francisco, 1972), p. 15.

EFFECTIVE MOMENT OPERATOR FOR MAGNETIC MOMENTS AND M1 TRANSITIONS IN THE Pb REGION*

F. Petrovich

It is well known that experimental magnetic moments and M1 transition rates exhibit deviations from the theoretical single-particle values. Several effects are responsible for these deviations. Most important is the effect of configuration admixtures resulting from the interaction of the shell-model valence nucleons with the core nucleons, i. e., core polarization.^{1,2} Other contributions can come from mesonic currents³ and Brueckner correlations.⁴

As a result of recent experimental activity, there is presently a substantial amount of data available on magnetic moments and M1 transitions in the Pb region.⁵ This has prompted several recent theoretical studies,⁶⁻⁹ all of

which succeed in providing a qualitative account of the experimental data, but fail to account completely for the observed deviations. In addition, an attempt to parametrize the data in terms of an effective moment operator proved to be only partially successful.¹⁰

The magnetic moment operator is given by

$$\bar{\mu}(q) = g_\ell(q)\bar{l} + g_s(q)\bar{s}, \quad (1)$$

where $g_\ell(p) = 1$, $g_s(p) = 5.58$, $g_\ell(n) = 0$, and $g_s(n) = -3.82$, all in nuclear magnetons. The effective operator has the form

$$\bar{\mu}_{\text{eff}}(q) = \bar{\mu}(q) + \delta\bar{\mu}(q) \quad (2a)$$

$$\delta\bar{\mu}(q) = \delta g_\ell(q)\bar{\ell} + G_0(q)\bar{s} + G_2(q)\bar{p}, \quad (2b)$$

where \bar{p} is a vector with z-component

$$p_z = [i^2 Y_2 \times \bar{s}]_0^1. \quad (3)$$

In the simplest of models δg_ℓ is associated with mesonic currents and Brueckner correlations while G_0 and G_2 are associated with core polarization. There are six parameters in Eq. (2). In Ref. 10, two were eliminated with the aid of the iso-vector assumption, i. e., $G_i(p) = -G_i(n)$, and the other four were adjusted to fit the data. A reasonable fit to the magnetic moments was achieved, but the retardation of the M1 transition rates was severely overestimated. It is significant that magnetic moments are sensitive to G_0 - G_2 while M1 transitions are sensitive to G_0 & G_2 .

By introducing an explicit model for the core and treating core polarization in first order with a zero-range coupling interaction, it is possible to obtain closed expressions for G_0 and G_2 . Schematically the result is

$$G_i \approx \frac{A}{E} I, \quad (4)$$

where A is a measure of the strength of the coupling interaction, E is a measure of the energy of the core admixtures, and I is a factor which expresses the quality of the overlap between the radial wave functions of the valence nucleons and core nucleons. The variation in I is roughly 1-2 in arbitrary units. The essential point is that the effective-moment operator should be state dependent.

Table I. Summary of magnetic moments and M1 transition rates obtained in calculations with zero-range interaction. Approximation 1 and 2 refer to calculations made with uncorrelated and correlated intermediate states, respectively.

Magnetic moments							
State	μ_{exp}	Approximation 1 ^a		Approximation 2 ^b		Maier et al. ¹⁰	
		G_0	μ	G_0	G_2	μ	μ
$^{209}\text{Bi}(1h_{9/2})$	4.08	-3.82	4.06	-3.78	-4.26	4.10	3.98
$^{209}\text{Bi}(2f_{7/2})$	4.41(65)	-2.08	5.16	-2.07	-2.33	5.15	4.65
$^{209}\text{Bi}(1i_{13/2})$	7.9	-3.42	7.90	-3.41	-3.84	7.87	7.98
$^{207}\text{Tl}(3s_{1/2})$	1.63	-2.12	1.73	-2.12	-2.38	1.73	1.08
$^{207}\text{Pb}(3p_{1/2})$	0.59	1.64	0.60	1.61	1.74	0.56	0.63
$^{207}\text{Pb}(2f_{5/2})$	0.65(5)	1.95	0.78	1.91	2.06	0.74	0.49
$^{207}\text{Pb}(3p_{3/2})$	-1.09	1.64	-1.23	1.61	1.74	-1.23	-0.44
$^{207}\text{Pb}(1i_{13/2})$	-0.98	3.22	-0.98	3.16	3.40	-0.96	-0.91
M1 Transitions							
Transition	$B(M1)_{\text{exp}}$	G_0	$B(M1)$	G_0	G_2	$B(M1)$	$B(M1)$
$^{207}\text{Pb}(p_{3/2} \rightarrow p_{1/2})$	0.32±0.08	1.68	0.24	1.63	1.75	0.26	0.001
$^{207}\text{Pb}(f_{7/2} \rightarrow f_{5/2})$	0.25±0.06	2.15	0.12	2.01	2.15	0.16	0.001

^aThese results are obtained with $A_{pp}^1 = 221 \text{ MeV} \cdot \text{fm}^3$, $A_{pn}^1 = -49 \text{ MeV} \cdot \text{fm}^3$, $\delta g_\ell(p) = 0.08 \text{ nm}$, and $\delta g_\ell(n) = -0.06 \text{ nm}$.

^bThese results are obtained with $A_p^1 = 255 \text{ MeV} \cdot \text{fm}^3$, $A_{pn}^1 = -94 \text{ MeV} \cdot \text{fm}^3$, $\delta g_\ell(p) = 0.08 \text{ nm}$, and $\delta g_\ell(n) = -0.06 \text{ nm}$.

With this approach there are still four parameters: the two δg_l and the proton-proton (A_{pp}) and proton-neutron (A_{pn}) coupling interactions. Results obtained by using two different models for the core are compared with the data and the results of Ref. 10 in Table I. The fit is quite good and the importance of the state dependence is evident. The values of δg_l required to fit the data were in reasonable agreement with previous theoretical estimates, but the required strength of the coupling interaction was found to be 1.4 - 2.3 times the strength of current realistic interactions.⁶⁻⁹

Footnotes and References

*Condensed from LBL-649; to be published in Nucl. Phys.

1. A. Arima and H. Horie, Prog. Theor. Phys. 11, 509 (1954).
2. R. J. Blin-Stoyle and M. A. Perks, Proc. Phys. Soc. A67, 885 (1954).
3. S. Wahlborn and J. Blomqvist, Nucl. Phys. A133, 50 (1969).
4. G. F. Bertsch, Phys. Letters 28B, 302 (1968).
5. See summary in Ref. 10.
6. K. Harada and S. Pittel, Nucl. Phys. A159, 209 (1970).
7. J. D. Vergados, Phys. Letters 36B, 12 (1971).
8. A. Arima and L. J. Huang-Lin, Phys. Letters 41B, 429 (1972).
9. A. Arima and L. J. Huang-Lin, Phys. Letters 41B, 435 (1972).
10. K. H. Maier, K. Nakai, J. R. Leigh, R. M. Diamond, and I. S. Stephens, Nucl. Phys. A183, 289 (1972).

SELF-CONSISTENT QUASIPARTICLE-PHONON COUPLING AND APPLICATIONS TO THE RARE EARTH NUCLEI

J. D. Immele and G. L. Struble*

Using a Green's function formalism, the quasiparticle self-energy in a finite Fermi system has been described¹ in terms of the coupling of even- and odd-mass nuclear eigenmodes. The self-energy includes the usual QPC core polarization diagram (Fig. 1a), a "backwards" exchange diagram with ground state correlations (Fig. 1b), a diagram which corrects for exclusion principle violations in the propagation of the quasiparticle and the microscopic phonon (Fig. 1c), and also certain two-phonon diagrams (Fig. 1d). Intermediate lines in the self-energy are described self-consistently, thereby including multiple phonon core excitations (Fig. 1e). It is shown that the dynamical equation for the self-energy may be solved by matrix diagonalization rather than the usual dispersion relation. Renormalized phonons are calculated by taking into account the splitting of the quasiparticle strength by QPC in the solution of the Bethe-Salpater equation. The quasiparticle self-energy and the phonon are calculated self-consistently.

The theory has been used to calculate energy levels, transition probabilities, and one-nucleon transfer cross sections for even- and odd-mass nuclei in the rare earth region. Our calculations have verified the prominent

role of the Pauli principle in nuclear structure schematics, as well as the importance of other higher-order contributions to the self-energy. The significant results for the even nuclei were that the higher-order contributions to the self-energy (exclusion principle diagram Fig. 1c and two-phonon diagrams Fig. 1d, e) did not renormalize the phonon. This was expected from the theory. Also the backwards correlations (Fig. 1b) made a substantial contribution around ¹⁶⁶Er, both reducing the pairing field and bringing the trend of 2+ energies into better agreement with experiment. In the odd-mass rare earth isotopes, we found exclusion principle violations to have substantial effects on the energy level spectra—in all cases pushing the energies of the eigenstates upward. This phenomenon naturally explains the absence of certain phonon states from experimental spectra. The two-phonon contributions implicit in the self-consistency and higher-order coupling terms (Fig. 1e, d) were also responsible for major energy level shifts, e. g., the consistent pushing down of the 1/2 [510] and 3/2 [512] levels in odd-neutron isotopes. For the same reasons, an intruder 1/2 [550] was computed at low excitation energy in the Eu and Tb isotopes. It was also found that the diagram of

Fig. 1c was responsible (at least in part) for the $K_0 \neq 2$ splittings experimentally observed in ^{165}Ho and ^{167}Er .

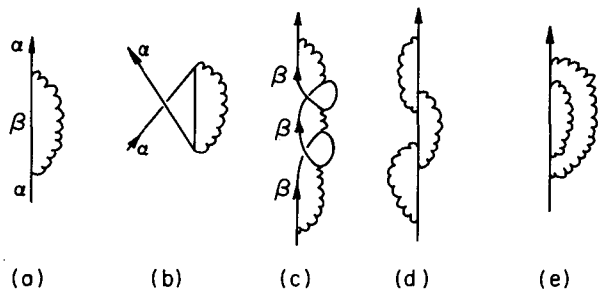


Fig. 1. Examples of diagrams included in self-energy. (XBL 733-2464)

The consequences of QPC for transition probabilities were also explored. Typically, for low-energy states, the single-particle $B(E2)$ strength and the collective $B(E2)$ are in phase. Nevertheless, the incoherent states can be observed experimentally, and the single-particle and collective contributions should interfere destructively, thereby substantially reducing the expected $B(E2)$. It was also found that Pauli principle corrections can reduce the transition probabilities of a phonon state by as much as 40%.

Footnote and Reference

*Lawrence Livermore Laboratory, Livermore, California.

1. J. D. Immele, Ph. D. Thesis, LBL-676 (1972).

ON THE NATURE OF 0_1^+ EXCITATIONS IN THE EVEN ACTINIDE NUCLEI

J. D. Immele and G. L. Struble*

The second 0_1^+ states (denoted 0_1^+) in the even actinide nuclei have usually been described as beta vibrations. However, this description has proved to be inadequate since Maher et al.¹ studied the (p, t) reaction on a series of even actinide targets and found that all the 0_1^+ states were populated with between 10 and 24% of the transition strength to the ground state. Since the beta-band is incoherent with respect to two-nucleon transfer, and since the intensity with which the pairing vibration is populated depends on the details of the single-particle structure near the Fermi surface, Maher et al. suggested these states exhibited a new type of collectivity. Later a survey of (t, p) reactions on these same isotopes² failed to excite the states with more than 2 or 3% of the transition strength to the ground state. The authors of Refs. 3 and 4 use schematic models and offer three different mechanisms for producing the required collectivity. In order to clarify the situation we are reporting calculations based on the theory of finite Fermi systems which includes in a natural fashion both non-constant pairing forces and spin dependence in the (ph) channel. Although the 0_1^+ energies which we calculate agree relatively well with experiment, the two-neutron transfer data is reproduced only for ^{228}Th . In addition, the calculations predict a pair vibration with large pickup and stripping ratios for $N = 142$ nuclei. For most of the nuclei, however, the (p, t) ratios are much lower than experiment, contrary to the predictions of Refs. 3 and 4.

Our result for ^{228}Th is similar to that of Ref. 3. The effect of non-constant pairing matrix elements on the correlation functions Δ for ^{228}Th is strikingly seen in Table I. The prolate and oblate orbitals become largely uncoupled because pairing matrix elements between oblate and prolate orbitals are reduced on the average by more than a factor of 4. Further, because the oblate orbitals are beneath the Fermi surface, there is little pairing among them. Thus their correlation functions are small. This also has a pronounced effect on the nature of the 0_1^+ state in ^{228}Th , for which the dominant amplitudes, Z^+ , are also displayed in Table I. This 0_1^+ state is formed predominantly from oblate pairs beneath the Fermi surface, because they are uncoupled from the prolate superfluid pairs due to the small magnitude of oblate-prolate matrix elements in both the (pp) and (ph) channels. It is seen that this state is correlated rather than being merely two-holes as suggested in Ref. 3. It has a high (p, t) cross section because the oblate pairs have large spectroscopic amplitudes, as evidenced by the values of S given in Table I. The state is not populated in the (t, p) reaction because the oblate orbitals are occupied in the ground state of ^{226}Th . The (ph) interaction, which has not been included in most calculations, is also important in ^{228}Th . Its inclusion mixes proton components into the wave function which enhance the $B(E2)$ value from 0.073 s. p. u. to 1.15 s. p. u. However, this 0_1^+ state is predominantly a second fluid pairing vibration,

Table I. ²²⁸Th pairing matrix elements, pair correlation functions (Δ), RPA amplitudes (X), and two-neutron pair spectroscopic amplitudes (S).

	1/2[501]	3/2[501]	5/2[503]	13/2[606]	1/2[770]	1/2[640]	3/2[642]	3/2[761]	3/2[631]	5/2[752]	5/2[633]
Δ	0.466	0.465	0.502	0.466	0.828	0.867	0.857	0.848	0.756	0.840	0.775
$Z_{\beta\beta}^+$	-0.706	-0.177	-0.335	-0.226	0.172	0.14	0.119	0.222	0.021	0.240	0.05
$S_{\beta\beta}$	0.21	0.208	0.162	0.058	0.049	0.092	0.096	0.047	0.098	0.044	0.079

that is, a pairing vibration in the oblate orbitals and a pairing rotation in the prolate orbitals. Unfortunately, RPA is unable to account for the pairing rotation. As a result, the average number of particles in this 0_1^+ state is 226. The main shortcoming of the non-constant pairing model is its failure to explain the two-nucleon transfer cross sections in nuclei with $A > 228$ in a natural fashion. The oblate orbitals are sufficiently far from the Fermi surface that they do not influence the character of any 0_1^+ state.

We see no evidence for the type of enhancements calculated by Abdulvagabova et al.⁴ The coherent strength involving quasiparticle pairs in Nilsson orbitals with quadrupole moments of the same sign is concentrated on our spurious state. Thus, while our calculations for the heavier actinides have the proper downsloping orbitals close to the Fermi surface, little (p,t) or (t,p) strength was observed to any 0_1^+ state. Our $B(E2)$'s are also an order of magnitude less than those given in Ref. 4.

We feel that the nature of the collectivity in the 0_1^+ states in the actinides cannot be understood in terms of correlated (pp) and/or (ph) excitations built on the ground state. The actual explanation must account not only for the large $E0$ and $E2$ transition probabilities, and the striking dependence of the systematics on the proton number, but also for the differing (p,t) and (t,p) strengths. This latter asymmetry between holes and particles suggests that the explanation is rooted in the description of the self-consistent fields. In this context it is interesting to note that in both the rare earth and actinide isotopes, regions of large $R(p,t)$ and small $R(t,p)$ coincide with rapid changes in deformation.⁵ These changes in deformation occur because the Nilsson orbitals above the Fermi surface are on the average more downsloping than those below, so that the addition of two particles causes an increase in deformation. These same level systematics suggest that (ph)-excited states will have a slightly greater ϵ_2 and ϵ_4 deformation than the ground state. This means that the ground state of an N and an excited state of an $N-2$ nucleus will be more strongly connected by a (p,t) reaction relative to

two-nucleon pick-up ground state transitions, because the latter will be somewhat inhibited by the change in deformation, while the transition to the $N-2^*$ state is enhanced by a non-negligible admixture of the unexcited BCS configuration with deformation corresponding to that of the N nucleus. A similar argument explains why the (t,p) reactions to the 0_1^+ states are very weak. These arguments are graphically presented in Fig. 1. There is quantitative support for this explanation in the recent work of Takemasa et al.⁶ who show that just such deformation changes in the rare earth region reduce the (p,t) ground state to ground state transitions in ¹⁵²Sm, ¹⁵⁶Gd, ¹⁶²Dy, ¹⁶⁶Er by 29, 13.7, 7.7, and 0.16%. These percentages should be compared with the $R(p,t)$'s of 25, 12, 13, and 2% observed experimentally for these same nuclei. Such deformation changes become negligible as one approaches the Cf isotopes in the actinide region and the Er rare earth isotopes. This is consistent with recent experimental data which show the $R(p,t)$ is large below ¹⁶⁶Er.

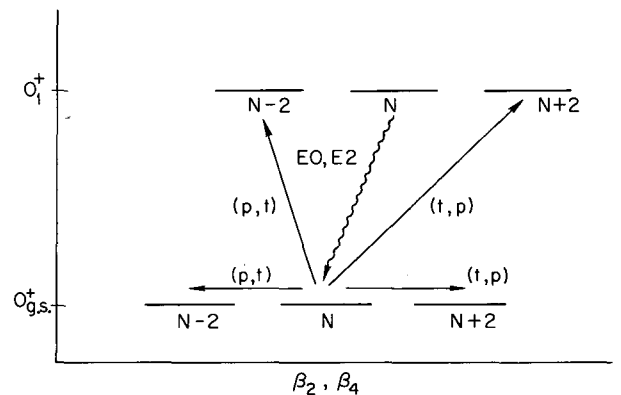


Fig. 1. Relative two-nucleon transfer cross section due to changing deformation. The (p,t) reactions to 0_1^+ states are enhanced, while the (t,p) are retarded relative to the ground-state-to-ground-state transitions.

(XBL 733-2465)

Footnote and References

* Lawrence Livermore Laboratory,
Livermore, California.

1. J. V. Maher, J. R. Erskine, A. M. Friedman, R. H. Siemssen, and J. P. Schiffer, Phys. Rev. C 5, 1380 (1972).

2. Ole Hansen, R. F. Casten, E. R. Flynn, and J. D. Garrett, Bull. Am. Phys. Soc. 17, 30 (1972).

3. W. I. van Rij and S. H. Kahana, Phys. Rev. Letters 28, 50 (1972).

4. S. K. Abdulvagabova, S. P. Ivanova, and N. I. Pyatov, Phys. Letters 38B, 215 (1972).

5. S. G. Nilsson, C. F. Tsang, A. Sobieszewski, Z. Szymanski, S. Wyceck, C. Gustafson, J. Lamm, P. Möller, and B. Nilsson, Nucl. Phys. A131, 1 (1969).

6. T. Takemasa, M. Sakagami, and M. Sano, Phys. Rev. Letters 29, 133 (1972).

EFFECT OF ANGULAR MOMENTUM ON THE SHELL STRUCTURE AND PAIRING CORRELATION OF EXCITED NUCLEI

L. G. Moretto and T. Clements

In a previous paper¹ the complete formalism describing the statistical properties of a shell-model nucleus with pairing residual interaction and angular momentum has been derived. In the same paper, an application of this formalism was made to the uniform model, where a nucleus is described by means of a single-particle spectrum uniform both in level spacing and spins.

In the present paper calculations based upon the general formalism will be presented for actual shell-model nuclei, and the interaction between angular momentum, pairing correlation, excitation energy, and shell structure will be discussed.

First, the statistical expressions will be reported. The logarithm of the grand partition function is:

$$\Omega = -\beta \Sigma (\epsilon_k - \lambda - E_k) + \Sigma \ln \left\{ 1 + \exp[-\beta(E_k - \gamma m_k)] \right\} \\ + \Sigma \ln \left\{ 1 + \exp[-\beta(E_k + \gamma m_k)] \right\} = \frac{\beta \Delta^2}{G} .$$

In this expression ϵ_k and m_k are the single-particle energies and spin projections; β , $\alpha = \beta\lambda$, and $\mu = \beta\gamma$ are the Lagrange multipliers used to fix the energy, particle number, and angular momentum projection respectively; G is the pairing strength; Δ is the gap parameter; the quasiparticle energy E_k is given by $E_k = [(\epsilon_k - \lambda)^2 + \Delta^2]^{1/2}$. The quantities β , λ , γ , and Δ are defined by the following equations:

$$\text{The gap equation: } \Sigma \frac{1}{2E_k} \left[\tanh \frac{1}{2} \beta(E_k - \gamma m_k) \right.$$

$$\left. + \tanh \frac{1}{2} \beta(E_k + \gamma m_k) \right] = \frac{2}{G} ;$$

The particle equation:

$$N = \Sigma \left\{ 1 - \frac{\epsilon_k - \lambda}{2E_k} \left[\tanh \frac{1}{2} \beta(E_k - \gamma m_k) \right. \right. \\ \left. \left. + \tanh \frac{1}{2} \beta(E_k + \gamma m_k) \right] \right\} ;$$

The angular momentum equation:

$$M = \Sigma m_k \left[\frac{1}{1 + \exp\beta(E_k - \gamma m_k)} - \frac{1}{1 + \exp\beta(E_k + \gamma m_k)} \right] ;$$

The energy equation:

$$E = \Sigma \epsilon_k \left\{ 1 - \frac{\epsilon_k - \lambda}{2E_k} \left[\tanh \frac{1}{2} \beta(E_k - \gamma m_k) \right. \right. \\ \left. \left. + \tanh \frac{1}{2} \beta(E_k + \gamma m_k) \right] \right\} - \frac{\Delta^2}{G} .$$

The entropy is given by:

$$S = \Sigma \ln \left\{ 1 + \exp[-\beta(E_k - \gamma m_k)] \right\} \\ + \Sigma \ln \left\{ 1 + \exp[-\beta(E_k + \gamma m_k)] \right\} \\ + \beta \Sigma \frac{E_k - \gamma m_k}{1 + \exp\beta(E_k - \gamma m_k)} \\ + \beta \Sigma \frac{E_k + \gamma m_k}{1 + \exp\beta(E_k + \gamma m_k)} .$$

The level density is given by:

$$\rho(E, N_i, M) = \frac{\exp S}{(2\pi)^{n/2} D^{1/2}},$$

where N_i is the number of particles of each component, n is equal to the number of Lagrange multipliers and $D = \det |\partial^2 \Omega / \partial \alpha_i \partial \alpha_j|$, where α_i and α_j stand for the Lagrange multipliers. The various thermodynamical quantities can now be evaluated for actual nuclei. Initially only one component at the time will be considered.

At $T = 0$ the dependence of the gap parameter Δ upon angular momentum in the case of the uniform model is given by $\Delta = \Delta_0 [1 - I/I_{cr}]^{1/2}$, where $I_{cr} = mg\Delta_0$, m is the average single-particle spin projection, and g is the density of the double-degenerate single-particle levels.

In Fig. 1 the neutron and proton gap parameters for the nucleus $^{194}_{78}\text{Pt}$ are presented as a function of angular momentum (notice that the angular momentum is that of each component separately). The calculations have been performed on the basis of the Nilsson model. It can be observed that qualitatively the gap parameters do decrease as the angular momentum increases. However, the detailed behavior shows strong single-particle effects, visible especially in the proton component. As the temperature increases, the pairing correlation decreases and eventually vanishes. In Fig. 2 the critical temperature as a function of angular momentum is shown for the neutron and proton components of the same nucleus. The anomalous behavior of the critical temperature near the critical angular momentum, consisting in the double valuedness of the function, is due to the thermally assisted pairing correlation. Such an effect, explained in a previous paper,¹ consists of a decreased blocking effect of the quasi-particles associated with an increase in temperature. The overall dependence of the gap parameter Δ upon temperature and angular momentum can be seen in Figs. 3 and 4. In these isometric projections the gap parameter Δ is presented as a surface: the intersection of such a surface with the Δ, I plane gives the $T = 0$ dependence of Δ on I ; the intersection of the same surface with the Δ, T plane gives the $I = 0$ dependence of Δ on T and the intersection with the I, T plane gives the dependence of the critical temperature T on I . This representation then summarizes all of the pairing relationships discussed above.

The entropies of the neutron and proton components calculated for various temperatures are shown as a function of angular momentum in Figs. 5 and 6. As a general guide,

to understand such pictures one should recall that, for the uniform model without pairing interaction, the entropy does not depend upon angular momentum but only upon temperature.

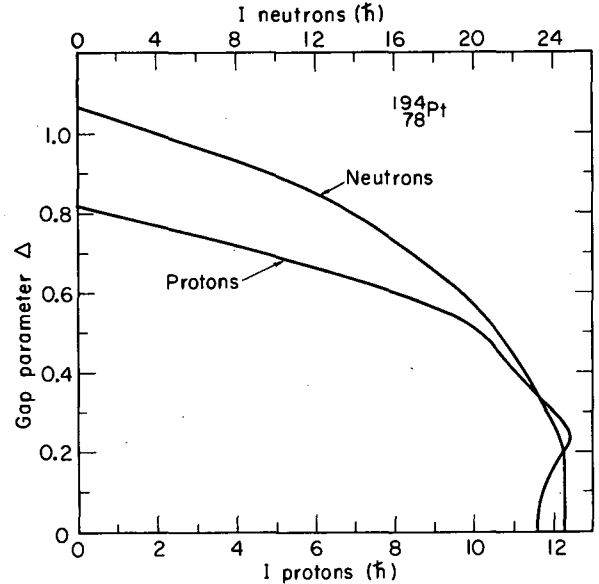


Fig. 1. Neutron and proton gap parameters as a function of the angular momentum. The double-valuedness which appears in the proton component is associated with configurations with different pairing correlation but with the same energy. (XBL 731-2066)

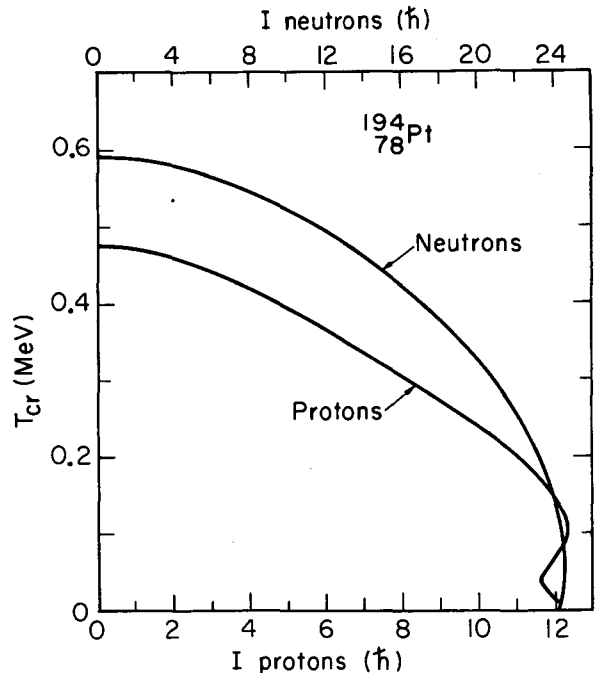


Fig. 2. Dependence of the neutron and proton critical temperatures upon angular momentum. (XBL 731-2067)

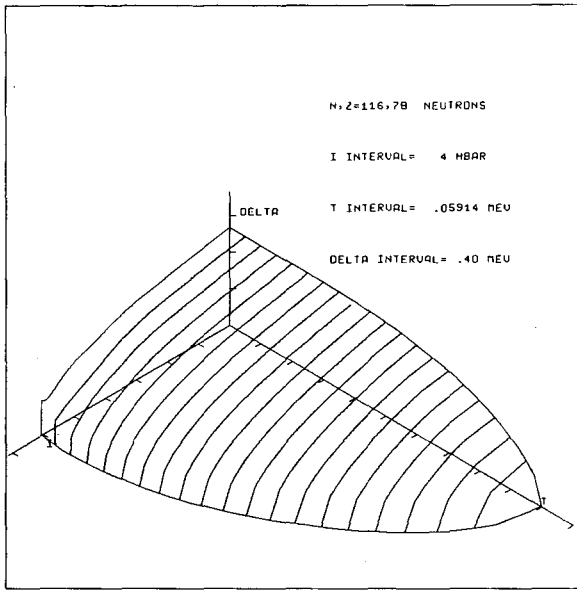


Fig. 3. Neutron gap parameter as a function of temperature and angular momentum. (XBL 731-31)

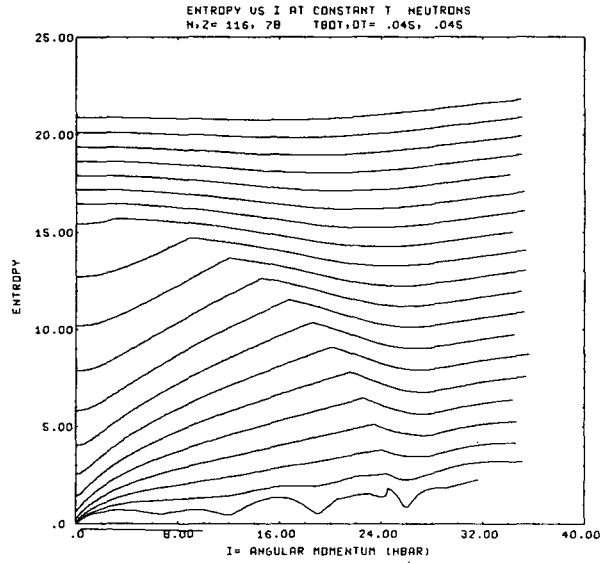


Fig. 5. Entropy of the neutron component as a function of angular momentum for various temperatures. (XBL 731-29)

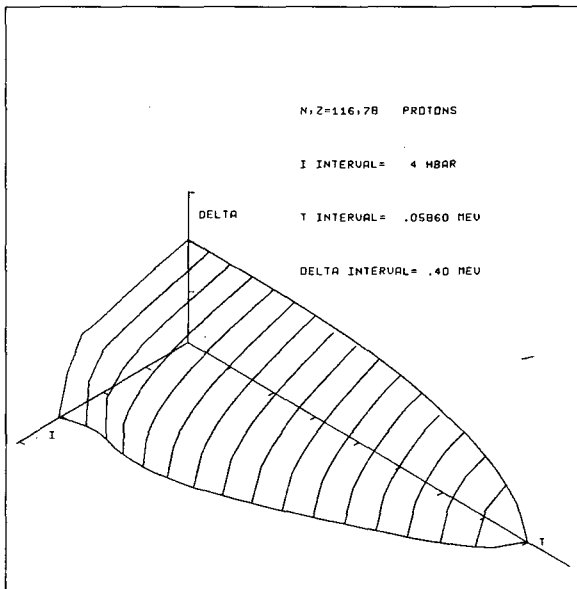


Fig. 4. Proton gap parameter as a function of temperature and angular momentum. (XBL 731-30)

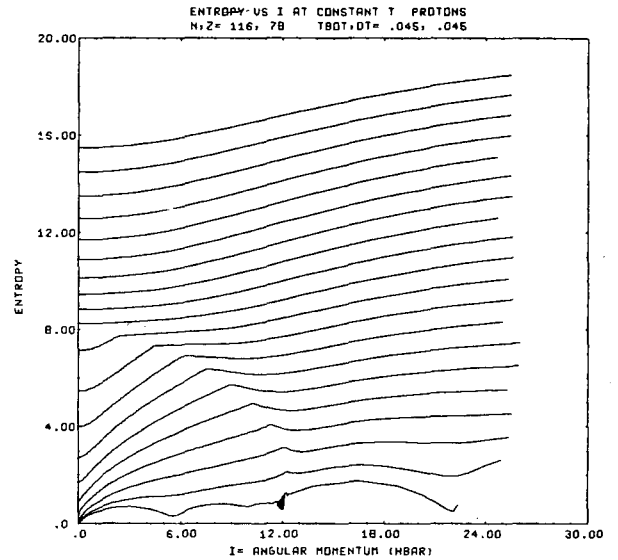


Fig. 6. Entropy of the proton component as a function of angular momentum for various temperatures. (XBL 731-28)

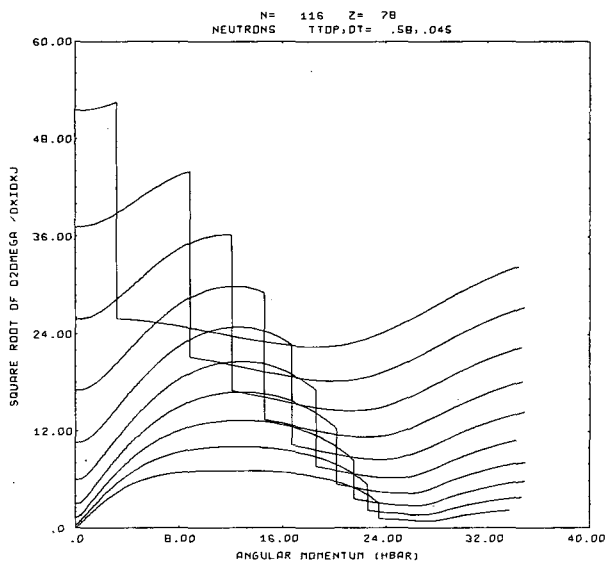


Fig. 7. Level density denominator for the neutron component as a function of angular momentum for different temperatures. (XBL 731-34)

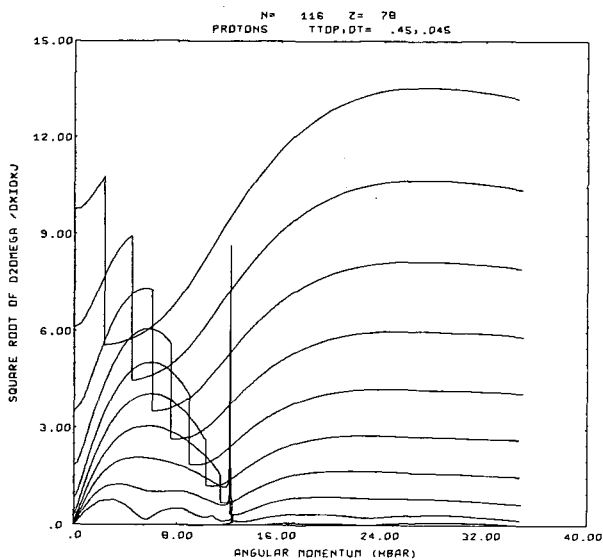


Fig. 8. Level density denominator for the proton component as a function of angular momentum for different temperatures. (XBL 731-35)

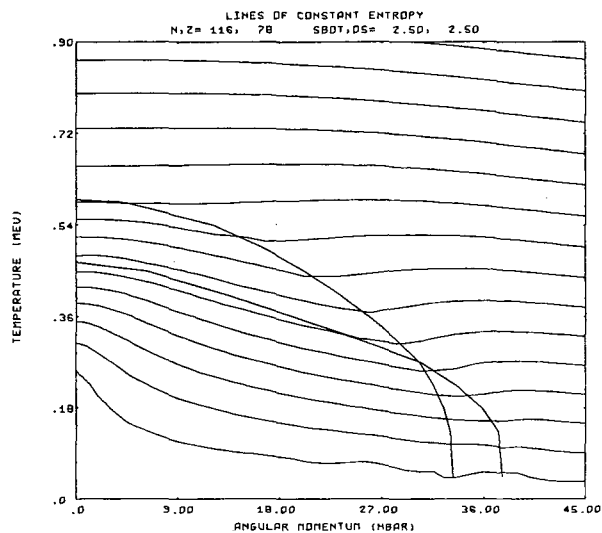


Fig. 9. Entropy of the entire nucleus $^{194}_{78}\text{Pt}$ as a function of angular momentum and temperature. In the figure the neutron and proton critical temperatures are also shown as a function of angular momentum. (XBL 731-32)

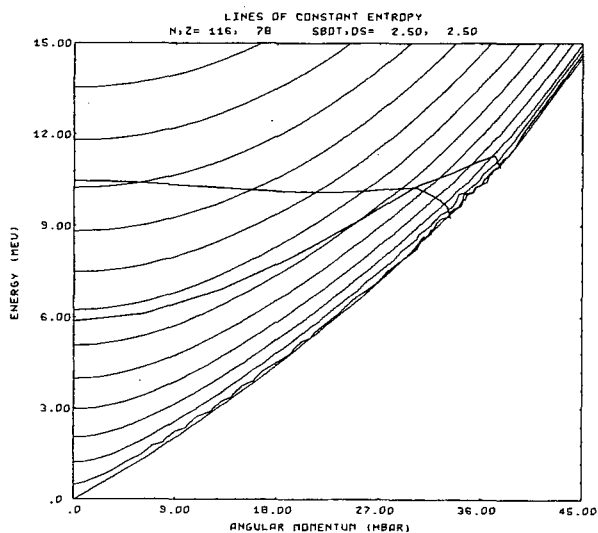


Fig. 10. Entropy of the entire nucleus $^{194}_{78}\text{Pt}$ as a function of angular momentum and energy. The line corresponding to zero entropy corresponds to the yrast line. The critical energy curves for neutrons and protons are also shown. (XBL 731-33)

The discontinuities associated with the disappearance of the pairing correlation are best seen in the level density denominator, which is a monotonic function of the specific heat. In Figs. 7 and 8 the square root of the determinant in the level density denominator is plotted versus angular momentum for various temperatures. The discontinuities are seen as sharp drops in the function which occur at progressively lower angular momenta as the temperature increases.

The combination of the two components of the nucleus, neutrons and protons, can be performed by summing the state functions at the same value of β and γ . In Fig. 9 the entropy of the nucleus $^{194}_{78}\text{Pt}$ is plotted versus temperature and angular momentum. In the same picture, the critical temperatures versus total angular momentum for neutrons and pro-

tons are plotted. It is interesting to notice that, while at low angular momentum the critical temperature is larger for neutrons than for protons, at larger angular momentum the opposite is true. In Fig. 10 the entropy versus angular momentum and excitation energy is presented. The zero entropy line, which also corresponds to the zero temperature line, represents the yrast function, namely the locus of the lowest energy states at fixed angular momentum. In the same picture the critical energy curves are presented both for neutrons and protons.

References

1. L. G. Moretto, Nucl. Phys. A185, 145 (1972).

STUDY OF EXCITED NUCLEI WITH δ -FORCE RESIDUAL INTERACTION TREATED ON THE BASIS OF THE PAIRING APPROXIMATION

L. G. Moretto and S. K. Kataria

The short-range residual interaction in nuclei is usually accounted for by means of the pairing Hamiltonian

$$H = \sum_k \epsilon_k a_k^+ a_k - \sum_{kk'} G_{kk'} a_{k'}^+ a_{\bar{k}'}^+ a_{\bar{k}} a_k \quad (1)$$

where ϵ_k are the single particle energies, a_k^+ and a_k are the creation and annihilation operators, and $G_{kk'}$ are the residual interaction matrix elements. A commonly used approximation consists of assuming that all the pairing matrix elements are constant and equal to a quantity G called the pairing strength. In order to avoid divergences and to obtain reasonable results, the approximation requires a truncated shell-model space and a renormalization of the pairing strength G which now depends upon the dimensionality of the problem. This approximation has been previously used in the evaluation of the thermodynamical functions of excited nuclei.¹⁻³

In order to avoid the shortcoming illustrated above, the Hamiltonian (Eq. 1) without any further approximation has been used to generate a complete statistical description of an excited nucleus. The single-particle energy eigenvalues and eigenfunctions have been obtained from the Nilsson shell model, and the matrix elements $G_{kk'}$ have been obtained by means of a volume δ -force residual interaction

$$G_{kk'} = G_0 \iint \psi_k^+ \psi_{\bar{k}}^+ \delta(r-r') \psi_{\bar{k}'} \psi_{k'} d\bar{r} d\bar{r}' \quad (2)$$

The strength G_0 of the residual interaction has been adjusted to reproduce the experimental even-odd mass differences.

The logarithm of the grand partition function can be derived from the Hamiltonian (Eq. 1):¹

$$\Omega = -\beta \sum_k (\epsilon_k - \lambda - E_k) + 2 \sum \ln [1 + \exp(-\beta E_k)] - \beta \sum_{kk'} G_{kk'} \chi_k \chi_{k'} \quad (3)$$

where β is the inverse of the temperature, λ is the chemical potential,

$E_k = [(\epsilon_k - \lambda)^2 + \Delta_k^2]^{1/2}$, and Δ_k is related to the χ_k 's by the relation $\Delta_k = \sum_{k'} G_{kk'} \chi_{k'}$.

The quantities Δ_k are related to the other physical parameters of the problem by the relation

$$\Delta_k = \frac{1}{2} \sum_{k'} G_{kk'} \Delta_{k'} \frac{\tanh \frac{1}{2} \beta E_{k'}}{E_{k'}} \quad (4)$$

which is called the gap equation.

By means of (3) in the saddle point approximation it is possible to calculate the constants of motion, like the particle number,

$$N = \sum_k \left(1 - \frac{\epsilon_k - \lambda}{E_k} \tanh \frac{1}{2} \beta E_k\right) \quad (5)$$

and the total energy:

$$E = \sum_k \epsilon_k \left(1 - \frac{\epsilon_k - \lambda}{E_k} \tanh \frac{1}{2} \beta E_k\right) - \sum_{kk'} G_{kk'} \chi_k \chi_{k'} \quad (6)$$

The entropy is given by

$$S = 2 \sum \ln [1 + \exp(-\beta E_k)] + 2\beta \sum \frac{E_k}{1 + \exp \beta E_k} \quad (7)$$

The level density is

$$\rho(E, N) = \frac{\exp S}{(2\pi)^{n/2} D^{1/2}}, \quad (8)$$

where $D = \det |\partial^2 \Omega / \partial \alpha_i \partial \alpha_j|$, α_i being the Lagrange multipliers introduced into the problem.

In order to obtain the strength of the δ -force residual interaction and to check at the same time whether the dependence of the even-odd mass differences is reproduced, the zero temperature form of the gap equation (Eq. 4) and of the particle equation (Eq. 5) have been solved for Δ_k and λ by means of an iteration method, for various nuclei throughout the periodic table. Convergence in the values of Δ_k was achieved when the number of levels used in the computation was about 100. In Fig. 1 the gap parameter Δ_k corresponding to the level closest to the Fermi surface is plotted as a function of Z . It can be observed that while strong shell effects are present, the overall Δ dependence reflects, at least qualitatively, the experimental dependence $\Delta = 12 A^{-1/2}$.

The dependence of the gap parameters on temperature is shown for selected levels in Fig. 2. It is interesting to notice that, while the various Δ_k have different values at or close to zero temperature, they all vanish at the same temperature T_c , which is called the critical temperature of the system. At this temperature the system undergoes a second-order phase transition which appears in the specific heat of the nucleus in the form of a discontinuity.

In Fig. 3 the entropy of the system is plotted versus the excitation energy. Such a function shows a substantially different energy dependence below and above the critical

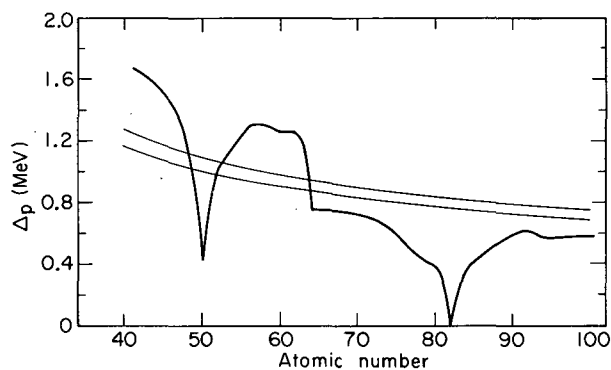


Fig. 1. Proton gap parameter Δ_p at the Fermi surface as a function of atomic number. The calculation has been performed along the line of β -stability. The smooth dependence $\Delta = kA^{-1/2}$ with $k = 11$ and $k = 12$ is also shown. (XBL 731-2068)

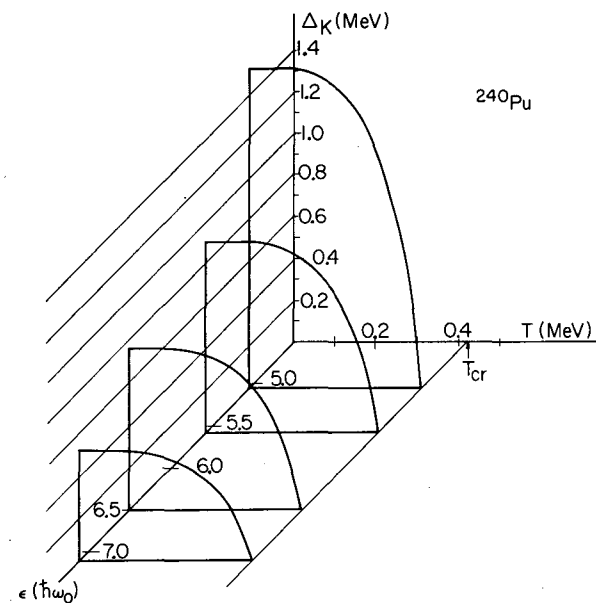


Fig. 2. Proton gap parameters for various levels as a function of temperature. Each function is displayed at a value ϵ corresponding to the energy of the level in units of $\hbar\omega_0$. (XBL 731-2064)

temperature. Below the critical temperature the dependence is nearly linear, while above the critical temperature the parabolic dependence typical of the unpaired nucleus is observed.

All the calculations performed so far refer to a single component (protons) of a spherical

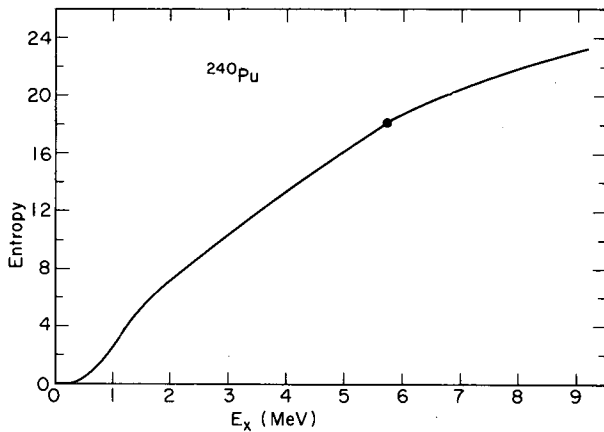


Fig. 3. Entropy of the proton component as a function of excitation energy.

(XBL 731-2063)

nucleus. The generalization to two components is immediate and the possibility of extending the calculation to deformed nuclei is being considered. It is hoped that the introduction of the residual interaction in the level density calculation in the form of the reasonable realistic δ -force will provide a reliable method of studying the moderately excited nuclei.

References

1. M. Sano and S. Yamasaki, *Prog. Theor. Phys.* **29**, 397 (1963).
2. P. Decowski, W. Grochulski, A. Marcinkowski, R. Siwek, and Z. Wilhelmi, *Nucl. Phys.* **A110**, 129 (1968).
3. L. G. Moretto, *Nucl. Phys.* **A182**, 641 (1972).

PAIRING FLUCTUATIONS IN EXCITED NUCLEI AND THE ABSENCE OF A SECOND-ORDER PHASE TRANSITION

L. G. Moretto

The statistical fluctuations in the nuclear gap parameter are studied. The difference between the average and most probable gap parameter is discussed and the absence of a sharp second order phase transition is shown.

The standard theory of pairing as applied to excited systems is based on the grand partition function $\exp \Omega$ obtained from the BCS Hamiltonian.¹⁻⁵ The function Ω is given by the expression

$$\Omega = -\beta \sum (\epsilon_k - \lambda - E_k) + 2 \sum \ln [1 + \exp(-\beta E_k)] - \beta \Delta^2 / G,$$

where $E_k = [(\epsilon_k - \lambda)^2 + \Delta^2]^{1/2}$, $\beta = 1/T$ is the inverse of the statistical temperature, λ is the chemical potential, and G is the pairing strength. The gap parameter Δ , which is a measure of the pairing correlation, is defined by the gap equation:

$$\sum \frac{1}{E_k} \tanh \frac{1}{2} \beta E_k = \frac{2}{G}.$$

Such an equation predicts the existence of a critical temperature T_c at which Δ vanishes. Following this formalism at the critical temperature the system undergoes a second-order phase transition reverting back to a system of uncorrelated fermions. In the microcanonical ensemble, the gap equation is obtained by minimizing the energy at fixed quasi-particle occupation numbers. Similarly, in the canonical ensemble, the gap parameter

can be determined by minimizing the free energy at fixed temperature. In fact, the gap equation can be also written as

$$\left. \frac{\partial \Omega}{\partial \Delta} \right|_T = 0.$$

Thus, the gap parameter values obtained from the gap equation are to be understood as most probable values. In the case of a system with a large number of particles, the use of the most probable value of Δ is completely justified. In this case, the fluctuations are very small, the probability distribution in the gap parameter approaches a delta function, and the most probable value coincides with the average values. However, nuclei are composed of a small number of particles, and the fluctuations are expected to be very large indeed. The presence of fluctuations in the gap parameter is responsible for a difference between the most probable and the average value due to high-order moments in the probability distribution. It will be shown that because of the presence of such fluctuations, it is not quite proper in the case of a nucleus to employ the most probable value of Δ . In fact, the second-order phase transition and the associated discontinuity in the specific heat, which are present when the most probable value is used, disappear altogether when the average value is used.

The isothermal probability distribution⁶ for the quantity Δ is given by

$$P(\Delta) \propto \exp \left\{ \Omega(\beta, \Delta) \right\}.$$

This expression assumes strong coupling between the Δ degree of freedom and all the intrinsic degrees of freedom, and disregards quantal effects. In Fig. 1 a set of probability functions corresponding to different temperatures is plotted. The calculations have been performed for a uniform model. The density of the doubly degenerate single-particle levels g is equal to 7 MeV^{-1} and the zero temperature gap parameter is equal to 1 MeV .

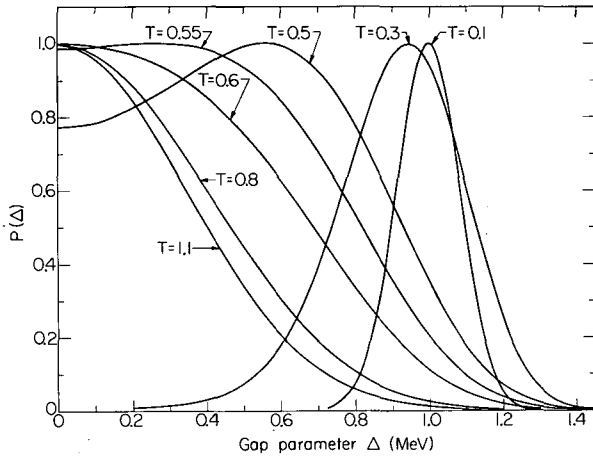


Fig. 1. Probability distributions for the gap parameter Δ at different temperatures. The value of Δ at the maximum corresponds to the solution of the gap equation. The critical temperature is $T = 0.57$. (XBL 724-2698)

At very low temperatures, the probability curve is symmetrical and Gaussian-like. The maximum of the distribution occurs at a value of Δ corresponding to the solution of the gap equation. Because of the symmetry of the distribution, the average value and the most probable value coincide. As the temperature increases, the distribution curves become broader and tend to become asymmetrical. While the maximum of the distribution still corresponds to the solution of the gap equation, the average value becomes distinctly different from the most probable value. At the critical temperature, the distribution has a maximum at $\Delta = 0$. Thus, the standard theory predicts the disappearance of the pairing correlations. A discontinuity in the specific heat of the system indicates a second-order phase transition:

$$C = \frac{dE}{dT} = \frac{1}{2} \sum \text{sech}^2 \left(\frac{1}{2} \beta E_k \right) \left[\beta^2 E_k^2 - \beta \Delta \frac{d\Delta}{dT} \right].$$

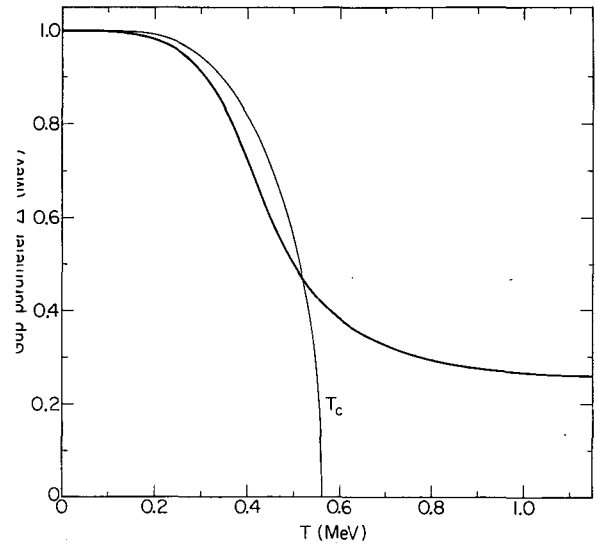


Fig. 2. The average gap parameter (thick line) and the most probable gap parameter as a function of temperature. (XBL 724-2697)

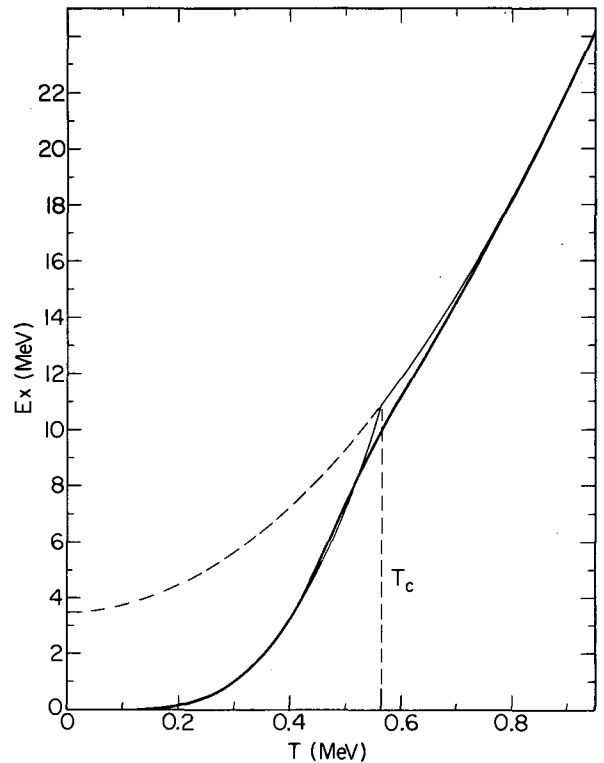


Fig. 3. The excitation energy as a function of temperature. The thick and thin line correspond to the use of the average and the most probable gap parameter respectively. The dashed line corresponds to the unpaired system. (XBL 724-2696)

However, at the critical temperature, the average gap parameter is larger than zero, indicating that for small systems there is no discontinuity and phase transition. Only in the limit of an infinitely sharp distribution, typical of a macroscopic system, the average and most probable values do coincide and the discontinuity is present. For temperatures above the critical temperature, the most probable value of Δ remains zero, while the average value remains rather large and decreases slowly with increasing temperature. This can be seen in Fig. 2, where the most probable and the average gap parameter are plotted as a function of temperature.

It may be interesting to evaluate the thermodynamical quantities on the basis of the average instead of the most probable gap parameter. The total energy of the system is given by:

$$E = \sum \epsilon_k \left[1 - (\epsilon_k - \lambda) \tanh\left(\frac{1}{2} \beta E_k\right) / E_k \right] - \Delta^2 G$$

$$- (\Delta^2 + \beta \Delta \partial \Delta / \partial \beta) \sum \tanh\left(\frac{1}{2} \beta E_k\right) / (E_k - 2/G).$$

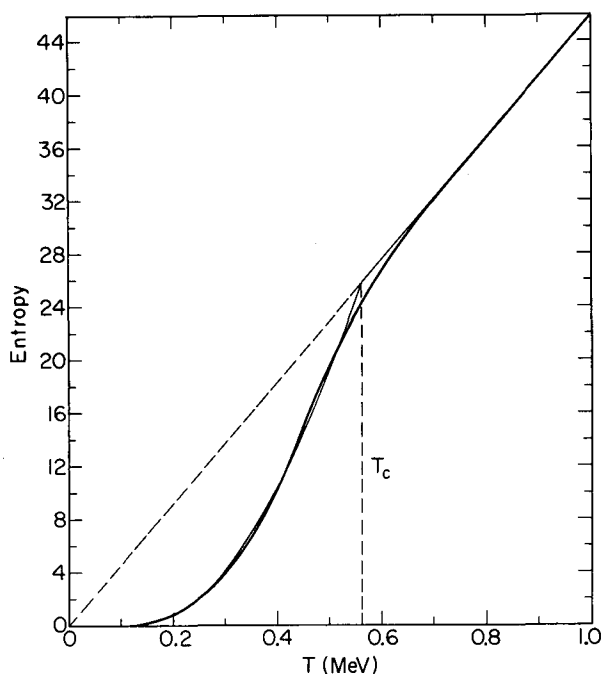


Fig. 4. The entropy as a function of temperature. The thick and thin line correspond to the use of the average and the most probable gap parameter respectively. The dashed line corresponds to the unpaired system.

(XBL 724-2700)

In the standard theory the last term is absent⁵. In fact, because of the gap equation, this term is zero for the most probable gap parameter and non-zero for the average gap parameter. The temperature dependence of the excitation energy is shown in Fig. 3. The thick line corresponds to the use of the average value of Δ ; the thin line corresponds to the use of the most probable value of Δ ; the dashed parabola corresponds to the behavior of the system in absence of pairing. At very low temperature, the two curves are very close. At the critical temperature, the standard theory predicts a kink which is nicely avoided by the present theory. The entropy of the system can be calculated from the expression

$$S = \Omega - \beta E + \beta \lambda N.$$

In Fig. 4 the entropy is presented as a function of temperature. As in the previous figure, the thick line corresponds to the present theory, the thin line corresponds to the standard theory, and the dashed line corresponds to the unpaired system. Again, the present theory avoids the critical temperature kink, typical of the standard theory. The most

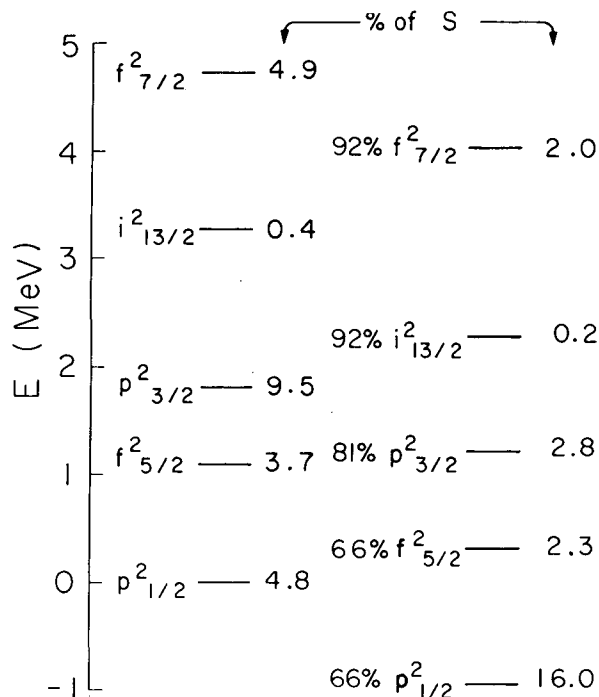


Fig. 5. The specific heat as a function of temperature. The thick and thin line correspond to the use of the average and the most probable gap parameter respectively.

(XBL 724-2699)

dramatic changes are seen in the behavior of the specific heat as a function of temperature. In the case of the average gap parameter, the specific heat has been calculated by numerical differentiation of the energy as a function of temperature. This quantity is presented in Fig. 5. The discontinuity seen in the standard theory prediction at the critical temperature is characteristic of the second-order phase transitions. The present theory does not show any discontinuity. However, it is quite remarkable to notice that the specific heat does go through a maximum and a minimum. The lambdoid appearance of this curve tells that, close to the critical temperature, the nucleus undergoes a qualitative change, although this change is not so sharp as in the case of a second-order phase transition.

References

1. M. Sano and S. Yamasaki, *Prog. Theor. Phys.* 29, 397 (1963).
2. D. W. Lang, *Nucl. Phys.* 42, 353 (1963).
3. H. K. Vonak, R. Vandenbosch, and J. R. Huizenga, *Nucl. Phys.* 60, 70 (1964).
4. P. Decowski, W. Grochulski, A. Marcinkowski, K. Siwek, and Z. Wilhelmi, *Nucl. Phys.* A110, 129 (1968).
5. L. G. Moretto, *Nucl. Phys.* A182, 641 (1972); *Phys. Letters* 35B, 379 (1971); Lawrence Berkeley Laboratory Report LBL-219, August 1971, to be published in *Nucl. Phys.*
6. L. D. Landau and E. M. Lifshitz, *Statistical Physics* (Addison and Wesley, 1966), p. 348.

PAIRING EFFECTS IN CORIOLIS-MIXED BANDS

C. T. Alonso and J. O. Rasmussen

The continuing explosion in experimental information about energy levels in odd-mass nuclei has provided a much more rigorous test of nuclear Coriolis theory, with the result that some discrepancies have arisen between theory and experiment. The major difficulties are an unexpected attenuation factor on the off-diagonal matrix elements (which may have been explained by Pyatov¹) and a tendency for the BCS pairing theory to overstate itself, often by bunching levels too closely together. This trouble with pairing is connected with further discrepancies in levels near the Fermi surface, which often require an attenuation of the matrix elements crossing the Fermi surface.²

The problems near the Fermi surface suggested to us that the traditional pairing constants λ (chemical potential) and Δ (gap parameter) should in fact have some functional dependence on Ω (z -projection of particle angular momentum), especially in the vicinity of the Fermi surface.

Closely associated with λ is the number of particles comprising the Fermi gas, since λ is essentially a Lagrange multiplier that ensures that the average number of particles is N . Statistical deviations in N , which have heretofore been largely ignored, are rather important in nuclear ensembles, where N is typically of the order of 100 or less.

We treat these fluctuations in N by partitioning the nucleons between the high- j and all other orbitals, considering the nucleus as a mixture of two Fermi gases. We can then consider fluctuations in the high- j N by taking into account scattering of nucleons from the high- j orbital gas into or out of the other gas. We describe this scattering by expanding the ordinary Coriolis matrix into the "supermatrix" illustrated in Fig. 1. Each diagonal block of the supermatrix is an ordinary Coriolis matrix corresponding to the present number of nucleons in the high- j gas. The chemical potential is adjusted according to the change in nucleon number N . These blocks are then connected by matrix elements of the order of the pairing force G . The supermatrix shown in Fig. 1 considers two possible N -state: the usual N -matrix at the lower right and the scattered $N \pm 2$ matrix at the upper left.

In Fig. 2 we show the Nilsson levels for the $i 13/2^+$ bands in ^{173}Hf . These positive-parity orbitals comprise the high- j gas, and the remaining opposite-parity orbitals make up the other gas. The odd nucleon lies along a parabolic potential as shown. Possible pair scattering events into or out of the high- j gas are indicated by arrows. Notice the difference between particle states (odd particle in $\Omega = 9/2$ to $13/2$) and hole states ($1/2$ to $7/2$) in terms of the pair scattering probability. Because pairs in the particle states can scatter

more easily than in the hole states, we expect a basic difference in Δ between particle states and hole states since Δ is connected with pair mobility. In our supermatrix this results in the scattered hole states having less energy than the normal hole states, while the scattered particle states gain energy (see lower diagram in Fig. 1). Thus the particle states and hole states are now connected only in second order by G, and the attenuation of matrix elements over the Fermi surface observed by Stephens² occurs naturally.

Note also in Fig. 2 that at the Fermi surface ($\Omega = 7/2$) the odd nucleon blocks the scattering of the last pair so that we expect blocking to diminish Δ in the vicinity of the Fermi surface.

We applied this expanded supermatrix to all of the known $i 13/2^+$ bands in the odd Hf isotopes (171 to 179).⁴ Standard Coriolis fits of these bands yield an accuracy of about 10 keV. Our supermatrix fits improved the average accuracy to 1 to 2 keV for all bands. Even in the case of ^{177}Hf , where two bands are known, we were able to get a good fit of all the levels by using purely theoretical band head energies from Nilsson and Chin Fu

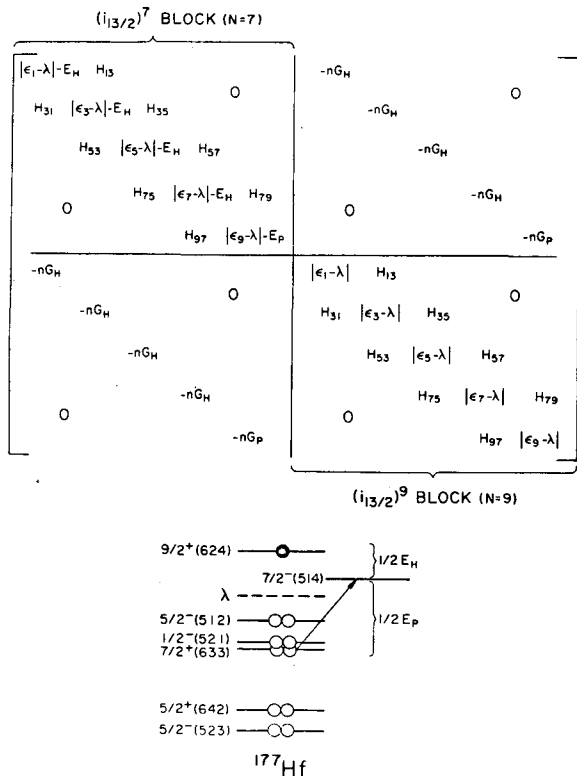


Fig. 1. Illustration of a "supermatrix" describing the scattering of one pair out of the high-j orbital gas. (XBL 733-301)

Tsang.³ However we should qualify our success by noting that in all such many-parameter fits there remains a question of uniqueness.

The output parameters of our fits indicated the expected difference in Δ between particle and hole states, as well as the drop in Δ particle.

We are currently using these semiempirical results to derive expressions for the pairing matrix elements as a function of Ω by including blocking and pair-scattering in the BCS equations. We will also include a variation of the pair breakup and recombination proposed by Pyatov¹ in an effort to eliminate the need for an off-diagonal matrix element attenuation.

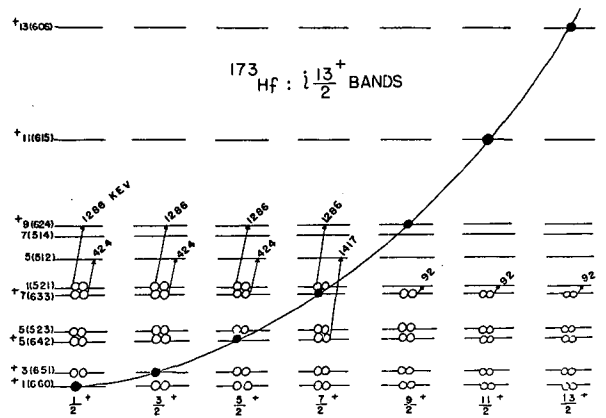


Fig. 2. Nilsson levels in the region of the $i 13/2^+$ orbitals in ^{173}Hf . (XBL 733-300)

References

1. N. I. Pyatov, M. I. Chernej, and M. I. Boxnat, Dubna E4-5468, 1970.
2. F. S. Stephens, LBL-1251, September 1972.
3. S. G. Nilsson et al., Nucl. Phys. A131, 1 (1969).
4. I. Rezanka, J. O. Rasmussen, F. M. Bernthal, C. T. Alonso, J. R. Alonso, S. Hultberg, and H. Ryde, LBL-1223, August 1972; submitted to Nucl. Phys.

NUCLEAR ROTATIONAL ENERGIES IN DEFORMED EVEN-EVEN NUCLEI

J. O. Rasmussen* and C. W. Ma†

In extending our earlier work¹ on the generalized multidimensional stretch model, we have adapted the semiclassical stretching-molecule model of Diamond, Stephens, and Swiatecki² to allow for stretch in pairing dimensions as well as in the quadrupole distortion dimension. We shall not here report on our model studies in their most general form, including stretch in three dimensions with fourth-order cranking corrections in the kinetic energy term. Instead, we restrict ourselves to the simplified treatment of the well-deformed ($N \geq 96$) rare earth nuclei, for which it is experimentally known that quadrupole deformation stretching is negligible. Thus, Coriolis Anti Pairing (CAP) should be primarily responsible for the increasing moment-of-inertia.

In order to treat Coriolis Anti Pairing as a classical stretch we introduce (see Ref. 1) pairing coordinates ν_p and ν_n which generate a wave function of BCS form. The ratio (ν/G) is essentially the number of Nilsson orbitals participating in the pairing correlation, with G the usual pairing-force matrix element. If $\nu = 0$, we have a sharp Fermi surface with no pairing correlation, and if $\nu = \Delta$, we have the BCS ground state.

We have carried out cranking model moment-of-inertia calculations for a range of ν values for several deformed nuclei, using the sophisticated wave functions including hexadecapole deformation and mixing among many oscillator shells in the manner of the 1969 work of Nilsson and collaborators.³ A striking result of our calculations is the near exponential dependence of the moments-of-inertia on parameters ν_p and ν_n . There are large deviations of moments-of-inertia from the rigid body values [$= (2/5)MR^2(1 + \delta)$] for

no pairing correlation $\nu_p = \nu_n = 0$, as shown in Table I. It has been proved that the rigid-body value should be obtained at equilibrium deformation with no spin-orbit potential and a pure anisotropic harmonic oscillator potential. Evidently, the spin-orbit potential and anharmonicity of the well cause large deviations, positive at the beginning of the deformed region and going negative with increasing mass, corresponding to the filling of the highest- j orbitals.

We proceed with the two-dimensional pairing modification of the Diamond-Stephens-Swiatecki stretch mode.² Whereas their energy expression was

$$E = \frac{\hbar^2}{6B\beta^2} I(I+1) + \frac{1}{2} C(\beta - \beta_0)^2, \quad (2)$$

we write an analogous equation in the two pairing coordinates ν_p and ν_n :

$$E = \frac{\hbar^2}{2J(\nu_p, \nu_n)} I(I+1) + V_{\text{PBCS}}(\nu_p) + V_{\text{PBCS}}(\nu_n). \quad (3)$$

The kinetic energy term makes use of the exponential form found by cranking as follows: The experimental moment-of-inertia at ground ($E_{2+}/3\hbar^2$) and the zero-pairing cranking moments of Table I fix the moment-of-inertia function

$$J(\nu_p, \nu_n) = J_p^{(0)} \exp(-\gamma_p \nu_p) + J_n^{(0)} \exp(-\gamma_n \nu_n) \quad (4a)$$

with

Table I. Cranking moments of inertia with no pairing.

Z	N	A	$2J_p^{(0)}/\hbar^2$ (MeV ⁻¹)	$2J_n^{(0)}/\hbar^2$	$2J_{\text{total}}^{(0)}/\hbar^2$	$2J_{\text{rigid}}/\hbar^2$
66	96	162	60.22	102.68	162.90	145
68	100	168	40.98	76.39	117.37	155
70	102	172	40.65	82.38	123.03	160
72	106	178	38.05	76.30	114.35	170
74	108	182	22.03	55.73	77.76	175

Table II. Ground band transition energies $E_I - E_{I-2}$ (keV).

Nucleus	I	This calculation		Extended VMI 3-parameter χ^2	Experimental
		1-parameter	2-parameter		
$^{162}_{66}\text{Dy}$	2	80.73	80.70	80.660	80.660
	4	181.41	185.16	185.005	185.005
	6	268.59	282.72	282.865	282.864
	8	339.71	370.96	372.9	372.6
	10	395.56	448.78	455.4	453.7
	12	438.24	516.09	530.9	526.2
	14	470.03	573.44	600.5	
			621.67		
$^{168}_{68}\text{Er}$	2	79.81	79.80	79.7994	79.7998
	4	180.59	184.50	184.283	184.281
	6	269.70	285.27	284.634	284.646
	8	344.30	380.40	379.545	379.536
	10	404.14	468.67	468.5	
	12	450.38	549.37	551.7	
	14	484.58	622.20		
	16	508.16	687.10		
18	522.01	744.15			
$^{172}_{70}\text{Yb}$	2	78.74	78.73	78.74	78.74
	4	177.89	181.57	181.52	181.52
	6	264.97	279.57	279.74	279.74
	8	337.25	370.72	372.2	371.9
	10	394.61	453.74	458.9	444.9
	12	438.37	528.00	540.2	498.0
	14	470.18	593.38	616.9	
	16	491.49	650.01	689.9	
	18	503.23	698.12		
$^{178}_{72}\text{Hf}$	2	93.21	93.20	93.118	93.181
	4	208.02	213.63	213.503	213.444
	6	304.06	325.62	325.533	325.562
	8	378.37	426.12	426.377	426.371
	10	432.16	513.60	515.2	
	12	468.31	587.69	592.7	
	14	489.74	648.69		
	16	498.64	697.04		
	18	496.23	732.70		
$^{182}_{74}\text{W}$	2	100.09	100.09	100.104	100.102
	4	225.61	229.34	229.323	229.317
	6	334.84	349.29	350.69	351.02
	8	424.19	456.65	464.1	464.0
	10	493.60	549.80	571.5	567.6
	12	544.73	628.41	676.4	

$$\frac{E_{2+}}{3\hbar^2} = J_p^{(0)} \exp(-\gamma_p \Delta_p) + J_n^{(0)} \exp(-\gamma_n \Delta_n) \quad (4b)$$

fixing the arbitrary factor η adjusting the cranking model calculations $\gamma_p^{(c)}$ and $\gamma_n^{(c)}$ to the values fitting Eq. (4b). That is, $\gamma_p = \eta \gamma_p^{(c)}$ and $\gamma_n = \eta \gamma_n^{(c)}$. The quantities Δ_p and Δ_n are the experimental odd-even mass differences. We have used the tabulated values of Nemirovsky and Adamchuk.⁴ The number-projected BCS energy that plays the role of potential energy is calculated in the continuous model [cf. Eq. (4.20) of Ref. 1]. The Berkeley minimum search routine MINSER was used to find the minimum of the energy function (3) for successive even values of spin.

The values of pairing force strength were taken from Nilsson et al.,³ and our cutoff μ was chosen as $0.8 \hbar\omega_0$ to correspond approximately to theirs.

The effective orbital densities ρ_p and ρ_n were then determined by demanding that Belyaev's continuous model⁵ limit of the gap equation be satisfied for experimental odd-even mass differences Δ :

$$1 = G\rho \sinh^{-1} \frac{\mu}{\Delta}. \quad (5)$$

These calculations were carried out for five well-deformed nuclei: $^{162}_{66}\text{Dy}$, $^{168}_{68}\text{Er}$, $^{172}_{70}\text{Yb}$, $^{178}_{72}\text{Hf}$, and $^{182}_{74}\text{W}$. The one adjustable parameter for fitting the bands essentially forces agreement of the $2+$ energy. Table II lists theoretical and experimental transition energies. Compare this calculation, headed "one-parameter", and the experimental values in the last column. It is evident that in all cases the one-parameter calculation gives too soft rotors. We are forced to conclude that the cranking-model zero-pairing moments-of-inertia are too large for some reason. If we had used the ordinary BCS energy without the number-projection correction, the discrepancy would be worse. Likewise, inclusion of fourth-order cranking corrections would make agreement worse.

Let us introduce a second fitting parameter, a factor reducing the zero-pairing moments-of-inertia. By adjustment of this parameter we force the fit of the $4 \rightarrow 2$ transition energy. The column headed "two-parameter" gives these results. Indeed, our two-parameter model calculations are generally (except for ^{182}W) in better agreement with experiment at higher spins than are the three-parameter extended VMI (variable moment-of-inertia) model χ^2 fits of Jägar et al.⁶

Table III. Pairing parameters for increasing spin.

Nucleus	Spin I	Gap parameters (MeV)	
		$\Delta_p(I)$	$\Delta_n(I)$
$^{162}_{66}\text{Dy}$	0	0.879	0.989
	6	0.826	0.917
	12	0.815	0.760
	18	0.596	0.564
$^{168}_{68}\text{Er}$	0	0.933	0.774
	6	0.902	0.715
	12	0.832	0.576
	18	0.751	0.385
$^{172}_{70}\text{Yb}$	0	0.785	0.800
	6	0.750	0.736
	12	0.676	0.587
	18	0.597	0.386
$^{178}_{72}\text{Hf}$	0	0.969	0.753
	6	0.932	0.666
	12	0.864	0.474
	18	0.812	0.220
$^{182}_{74}\text{W}$	0	0.585	0.734
	6	0.543	0.645
	12	0.467	0.448
	18	0.410	0.183

The factors reducing the zero-pairing moments-of-inertia for the five nuclei are, respectively, 0.61, 0.60, 0.62, 0.625, and 0.76. Now these moments-of-inertia at zero pairing should be the effective values for quite high angular momentum ($I \approx 20$). Thus, the lowest-order cranking formula may not be adequate, but we may hope that the cranking problem without pairing might be more tractable at high angular momentum than the problem with pairing.

Table III lists pairing gap values for our two-parameter calculations.

We note that in no case has there been a pairing collapse. In the case of the one-

parameter calculation for ^{178}Hf , a back-bending reversal occurs for the highest-spin transitions. Here, though, pairing collapse has not yet occurred, though the Δ_n value has dropped to 0.107 MeV at spin 18.

Our finding that the straightforward cranking calculations give too soft rotors represents the same difficulty earlier encountered by Marshalek⁷ and by us¹ in different approaches. It is important to understand better why the moment-of-inertia depends less strongly on the pairing correlation than the cranking model predicts. In part it may be due to systematically larger diagonal than off-diagonal pairing matrix elements (cf. Ref. 8).

The quality of our two-parameter fits and those of Draper's EXP model⁸ are strong indications that the moment-of-inertia dependence on pairing is essentially exponential.

We plan to extend the model to the shape-stretching nuclei at the edges of the deformed region.

Footnotes and References

*Nuclear Chemistry Division, Lawrence Berkeley Laboratory, on leave from Yale University.

†Department of Physics, Indiana University, Bloomington, Indiana.

1. C. W. Ma and J. O. Rasmussen, Phys. Rev. C 2, 798 (1970).
2. R. M. Diamond, F. S. Stephens, and W. J. Swiatecki, Phys. Letters 11, 315 (1964).
3. S. G. Nilsson, C. F. Tsang, A. Sobiczewski, Z. Szymanski, S. Wycech, C. Gustafson, I. Lamm, P. Möller, and B. Nilsson, Nucl. Phys. A131, 1 (1969).
4. P. E. Nemirowsky and Yu. V. Adamchuk, Nucl. Phys. 39, 551 (1962).
5. S. T. Belyaev, Kgl. Danske Videnskab Selskab, Mat.-Fys. Medd. 31, No. 11 (1959).
6. S. Jägare, A. Johnson, S. A. Hjorth, H. Ryde, Z. Szymanski, and O. Saethre, preprint (1972).
7. E. R. Marshalek, Phys. Rev. 139, B770 (1965); 158, 993 (1967).
8. J. E. Draper, Phys. Letters, 41B, 105 (1972).

NUCLEAR ROTATIONAL ENERGY EXPANSIONS FOR DEFORMED ODD-MASS NUCLEI

J. O. Rasmussen,* J. Alonso, W. Ribbe,† I. Rezanka‡ and R. Needham‡

As the accuracy and extent of gamma energy measurements on rotational bands have improved, more detailed tests of rotational energies have become possible. The leading order $I(I+1)$ dependence must be corrected by terms of higher power in the angular momentum. Perturbation theory on the Coriolis band mixing problem suggests the following general expansion:

$$\begin{aligned}
 E(I, K) = & E_0 + AI(I+1) + BI^2(I+1)^2 \\
 & + CI^3(I+1)^3 + \dots \\
 & + (-)^{I+K} \frac{(I+K)!}{(I-K)!} [A_{2K} + B_{2K} I(I+1) + \dots].
 \end{aligned}
 \tag{1}$$

Note that this expansion applies also to $K = 1/2$, but the usual decoupling parameter a equals A_{2K}/A . Dzhelepov et al.¹ have made a comprehensive survey and analysis of properties of $K = 1/2$ bands including extensive 4-parameter energy fits.

In the course of analysis of ^{165}Tm level studies made at the Yale Heavy Ion Accelerator we have applied expansion (1) to fit bands of $K = 1/2$ and $7/2$ in this nucleus and neighboring odd-proton nuclei. We developed a least-squares computer program that could be used in an interactive manner with the BRFF system of the LBL computer center. Level weighting was assigned on the basis of energy uncertainty of the level. Special difficulties with the signature-dependent terms (those with alternating sign -1^{I+K}) arise at high spin, and these difficulties call for special care in comparing and interpreting band fits. Reasonable least-squares fits for lower levels can be obtained, but often the divergence rapidly sets in for higher spins than those fitted. If the higher levels are included in the fit, the fit becomes poor for the lower levels. The constants of Eq. (1) thus depend both on how many terms were used in the expansion and on how many levels were included in the fit.

Figures 1 and 2 illustrate these difficulties with four and five parameter fits through

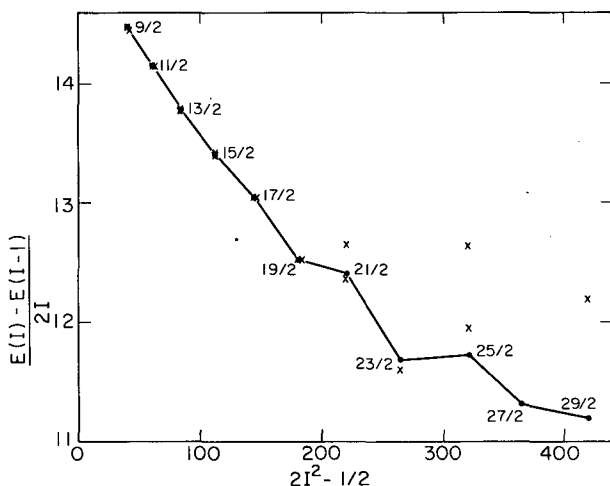


Fig. 1. Rotational band energy difference plot for $7/2^+[404]$ band in ^{165}Tm . The solid line connects experimental points and the crosses and circles represent Eq. (1) weighted least-squares fits through the $I = 19/2$ level with 5 and 4 parameters, respectively (see Table I). Experimental energies are mainly from work of Gizon et al.⁵ (XBL 733-2466)

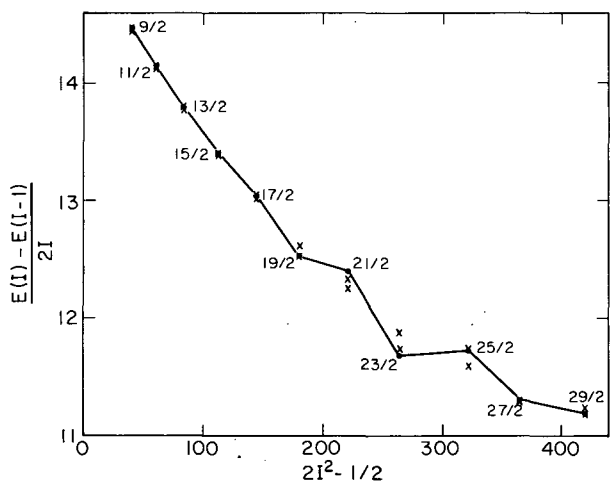


Fig. 2. Same as Fig. 1 except fits are carried through $I = 29/2$ level. (XBL 733-2467)

$19/2$ and $29/2$ levels of ^{165}Tm , respectively. Table I shows the change in the constants for these cases.

While the coefficients of the leading terms A and B are relatively constant in the fits of Table I, the coefficient A_{2K} is very unstable, with even the sign uncertain. Clearly if one is to cross-compare constants for various nuclei, the fits must be made with the same number of coefficients and levels.

In Table II we give the coefficients determined in 7-level, 4-parameter (A, B, C, A_7) fits for $7/2^+[404]$ bands and 9-level, 5-parameter (A, B, C, A_7, B_7) fits for $7/2^-[523]$ bands in several nuclei.

We note that B and C are of opposite sign for the two bands. In an earlier paper on ^{161}Ho , Alonso et al.¹ discussed the B and A_7 parameters in terms of perturbation theory of the Coriolis interaction. The positive B in the $7/2^-$ band was attributed to the dominance of fourth-order Coriolis interaction among the high- j $h_{11/2}$ Nilsson states. The negative sign of B , characteristic of the even-even core, is exhibited in the $7/2^+[404]$ bands, where the specific Coriolis band mixing effects are smaller. See also discussion by Hamamoto and Udagawa² and by Hjorth, Ryde, and Skånberg.³

Similarly, the large positive values of A_7 for the $7/2^-$ band arise in seventh order of the Coriolis interaction among the $h_{11/2}$ orbitals. The small A_7 values of varying sign in the $7/2^+$ bands probably reflect the smaller Coriolis matrix elements and a cancellation of effects within the $g_{7/2}$ and $d_{5/2}$ orbital family.

The fact that A is always smaller for the $7/2^-$ bands than for $7/2^+$ bands is a consequence of the large second-order Coriolis interaction among $h_{11/2}$ orbitals, which renormalizes the moment-of-inertia.

Finally, we would make some remarks on the difficulties with the power series expansion (1). The form of the power series can be derived from perturbation treatment of the Coriolis interaction. That is, it is most valid for spins sufficiently low that all Coriolis band-mixing matrix elements are smaller than the energy separation of the bands.

$$\frac{\hbar^2}{2J} \langle I, K+1 | j_+ | I, K \rangle \ll |E_{J,K} - E_{I,K+1}|. \quad (2)$$

This inequality fails first at modest spin values for the $h_{11/2}$ $7/2^-$ case either for the $1/2^-$ and $3/2^-$ bands or for the $7/2^-$ band and its nearest neighbor $5/2^-$ or $9/2^-$ band, and the expansion breaks down.

To get simple analytic expressions for the energy we need to have the strong inequality (2) in one or the other direction.

When inequality (2) is not satisfied, the best alternative is the numerical matrix diagonalization of the Coriolis interaction. Unfortunately, there are so many parameters, such as band-head energies and attenuation factors for Coriolis matrix elements, that unless

data on higher band positions and spectroscopic factors are known (see work of Kleinheinz et al.⁴) the parameter sets from one-band energy fits are far from unique.

One simple limiting case with Coriolis matrix elements larger than band separation does occur experimentally for $i_{13/2}$ orbitals in odd-neutron rare earths. These cases are most readily recognized in a plot of $\Delta I = 2$

transition energies vs I as Fig. 3. The intercepts of normal bands are at $I_i = 1/2$. The intercepts of the special cases with inequality (2) reversed have larger intercepts.

We take in zero order two bands K and $K + 1$ completely degenerate, with $K > 1/2$. With the Coriolis interaction included, there are simple 2×2 matrices with equal diagonal elements to be diagonalized for each I value.

Table I. Expansion coefficients for $7/2^+[404]$ band in ^{165}Tm .

Coefficient (keV) power	Levels fitted \rightarrow	7	7	12	12	9
	Parameter \rightarrow	4	5	4	5	3
A		15.13±0.02	15.17±0.00	15.09±0.07	15.16±0.03	14.73±0.05
B $\times 10^2$		-1.74±0.041	-1.85±0.01	-1.70±0.07	-1.79±0.04	-1.13±0.03
C $\times 10^5$		2.52±0.24	3.31±0.05	2.44±0.21	2.76±0.11	—
$A_{2K} \times 10^7$		1.16±0.14	-3.01±0.20	5.59±8.95	2.06±0.36	0.331±0.447
$B_{2K} \times 10^9$		—	5.09±0.24	—	-1.02±0.18	—

Table II

Nucleus	A (keV)	B (keV $\times 10^2$)	C (keV $\times 10^5$)	A_7 (keV $\times 10^7$)	B_7 (keV $\times 10^9$)
$7/2^+[404]$ bands					
^{161}Ho	13.73±0.02	-1.64±0.04	3.26±0.22	0.76±0.13	—
^{165}Tm	15.13±0.02	-1.74±0.04	2.52±0.24	1.16±0.14	—
^{167}Tm	13.48±0.02	-1.31±0.03	0.93±0.20	-0.96±0.12	—
^{171}Lu	13.98±0.00	-1.07±.01	1.60±.05	0.21±.03	—
^{177}Lu	13.79±0.00	-0.683±0.002	0.19±0.01	-0.029±0.006	—
^{177}Ta	15.10±0.03	-1.34±0.06	0.85±0.39	-0.58±0.22	—
$7/2^-[523]$ bands					
^{161}Ho	10.95±0.02	0.45±0.04	-2.86±0.18	8.79±0.69	-5.37±0.56
^{165}Tm	9.80±0.09	1.66±0.14	-6.83±0.63	11.3±2.4	-7.96±1.96
^{167}Tm	9.95±0.06	0.71±0.09	-3.51±0.43	4.18±1.63	-2.91±1.32

The energies are given by

$$E_I = E_0 + \frac{\hbar^2}{2J} I(I+1) \pm \frac{\hbar^2}{J} \langle K+1 | j_+ | K \rangle \times \sqrt{I(I+1) - K(K+1)}. \quad (3)$$

For $I \gg K$ we see that a term linear in I has been introduced, and we can write approximately

$$E_I \approx E'_0 + \frac{\hbar^2}{2J} I^*(I^* + 1), \quad (4a)$$

where

$$I^* = I \pm \langle K+1 | j_+ | K \rangle \quad (4b)$$

The minus sign applies to the lower branch. For the high- j orbitals, where j is approximately a good quantum number, the intrinsic matrix element should be

$$\langle K+1 | j_+ | K \rangle \approx \sqrt{j(j+1) - K(K+1)}.$$

The geometrical significance of this value is as j_{\perp} , the fluctuating component of the odd-particle angular momentum perpendicular to the nuclear symmetry axis. The energy expression (4) bears close analogy to those from aligned coupling schemes where the core angular momentum adds in stretched coupling to the odd-particle j vector. Here the perpendicular component j_{\perp} is involved, not j .

For degenerate $K = 1/2$ and $K = 3/2$ orbitals with j a good quantum number, the decoupling term for $K = 1/2$ somewhat complicates the solutions. The energies are

$$E = \frac{\hbar^2}{2J} \left[I(I+1) + \frac{-(-)^{I-j} \hat{j} \cdot \hat{I} \pm \sqrt{17 \hat{j}^2 \hat{I}^2 - 16(\hat{I}^2 + \hat{j}^2) + 16}}{2} \right] \quad (5)$$

with $\hat{I} = I + 1/2$ and $\hat{j} = j + 1/2$. In the large- I , large- j limit this becomes

$$E = \frac{\hbar^2}{2J} \left\{ I(I+1) + \frac{1}{2} \hat{j} \hat{I} [-(-)^{I-j} \pm \sqrt{17}] \right\}. \quad (6)$$

Equation (6) can be recast in the form of Eq. (4a) but now Eq. (4b) is modified, depending on the signature $(-)^{I-j}$. For the lower branch

$$I^* = \begin{cases} I - \frac{\sqrt{17} + 1}{4} (j + 1/2), & I - j, \text{ even} \\ I - \frac{\sqrt{17} - 1}{4} (j + 1/2), & I - j, \text{ odd.} \end{cases} \quad (7)$$

The ratio of intercepts in plots of the type of Fig. 3 should thus be 3.13:5.13, and this is only somewhat larger than what is observed for 91-neutron ^{155}Gd . The ratio is somewhat smaller in 93-neutron ^{161}Er , where the assumptions of degenerate $K = 1/2$ and $3/2^+$ bands with all other $i_{13/2}$ bands neglected would be less valid.

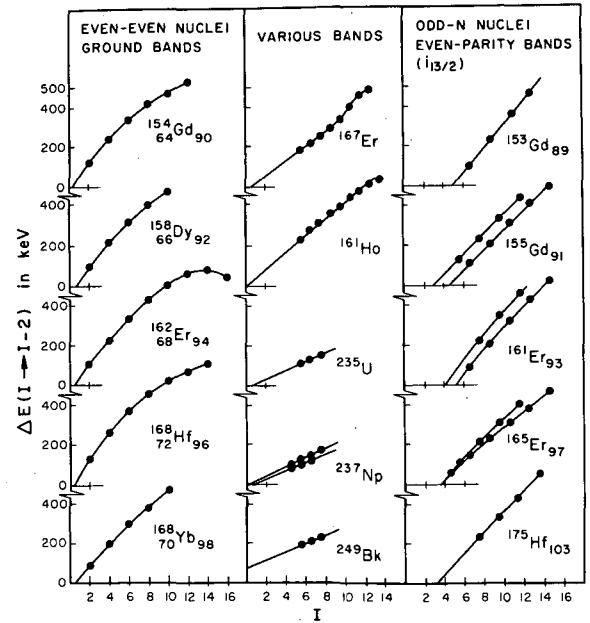


Fig. 3. Plots of cross-over ($\Delta I = -2$) transition energies vs initial state spin for various rotational bands. Note the small ($I_1 = 1/2$) intercepts for most bands and the larger intercepts for the odd-n $i_{13/2}$ bands on the right. (XBL 731-15)

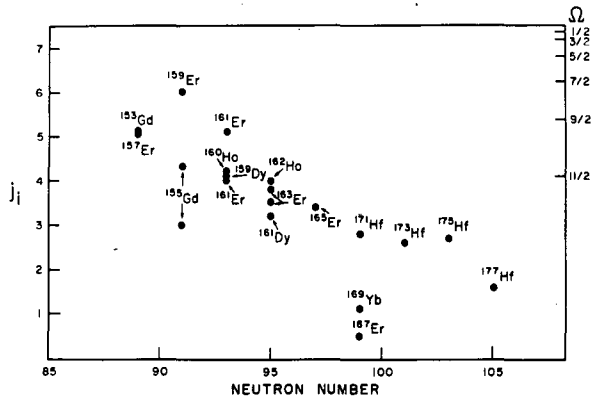


Fig. 4. A plot of the systematics of intercept values for odd-n even parity bands of the deformed rare earths. Note the two values of intercepts plotted for ^{155}Gd and ^{161}Er , with the significance of two intercepts discussed in text. (XBL 731-16)

In Fig. 4 we plot the intercept values for the odd- n $i_{13/2}$ cases. According to Eq. (4b) the intercept equals the intrinsic Coriolis matrix element between the two low-lying mixed bands. The usual special attenuation factor of about one half, only part of which is accounted for by the pairing factor, is evidently operative. The low points ^{167}Er and ^{169}Yb are for cases where the even-parity band is at ground and the two-band degeneracy condition is not fulfilled.

Finally, we easily generalize the two-band mixing expression (3) to the case of two-band ($K \neq 1/2$) mixing with zero-order separation of bands by energy $E_K - E_{K+1}$ (where the E_K may be quasi-particle energies). The resulting 2×2 matrices are easily diagonalized to give

$$E_I = E_a + \frac{\hbar^2}{2J} I(I+1) \pm \left\{ \frac{(E_K - E_{K+1})^2}{4} + 4 \left(\frac{\hbar^2}{2J} \right)^2 \langle K+1 | j_+ | K \rangle^2 \right\}^{1/2} \times [I(I+1) - K(K+1)]^{1/2}. \quad (8)$$

When $E_K = E_{K+1}$, Eq. (8) reduces to Eq. (3). When the band energy difference term is large compared to the Coriolis, Eq. (8) reduces to the perturbation theory expansion. Hopefully, such intermediate cases as ^{167}Er and ^{169}Yb may be fitted by the above 3-parameter expression (parameters $\hbar^2/2J$, $E_K - E_{K+1}$, and $\langle K+1 | j_+ | K \rangle^2$). The influence of higher bands might be treated in perturbation theory.

MICROSCOPIC CALCULATIONS OF THE VARIABLE MOMENT-OF-INERTIA MODEL

C. W. Ma and C. F. Tsang

The variable-moment-of-inertia model,¹ which has been very successful in describing the low-spin as well as the high-spin nuclear rotational energies E , can be expressed as follows:

$$E = \frac{1}{2} C (J - J_0)^2 + \frac{I(I+1)}{2J}, \quad (1)$$

$$\frac{\partial E}{\partial J} = 0,$$

where J_0 is the moment-of-inertia of the nucleus and C is called the force constant; both of them can be determined experimentally by fitting to the energy levels.

Inclusion of the $K = 1/2$ band will complicate the expressions, but they will still be expressible as roots of a quadratic equation. The expansion of Eq. (8) in powers of $(\hbar^2/2J)^2/(E_K - E_{K+1})^2$ shows the origin of the positive $I^2(I+1)^2$ term often appearing when the odd-particle is in a high- j orbital.

Footnotes and References

* On leave from Yale University, New Haven, Connecticut.

† September 1972 visitor at LBL, on leave from Hahn-Meitner Institute, W. Berlin, Germany; presently at Heavy Ion Accelerator Laboratory, Yale University, New Haven, Connecticut.

‡ Heavy Ion Accelerator Laboratory, Yale University, New Haven, Connecticut.

1. J. Alonso, H. Bakhru, F. M. Bernthal, J. Boutel, B. Olsen, I. Rezanka, and J. O. Rasmussen, Nucl. Phys. A160, 193 (1970).

2. I. Hamamoto and T. Udagawa, Nucl. Phys. A126, 241 (1969).

3. S. A. Hjorth, H. Ryde, and B. Skånberg, J. de Physique 33, 23 (1972).

4. P. Kleinheinz, R. F. Casten, and B. Nilsson, Nucl. Phys., in press.

5. J. Gizon, A. Gizon, S. A. Hjorth, D. Barneoud, S. Andre, and J. Treheone, Nucl. Phys. A456, 654 (1972).

We report here a calculation which tried to calculate microscopically the parameter J and C . First, the nucleons are considered to move in a deformed potential with pairing interaction acting between them. The pairing strength and the detailed shape of the deformed potential are taken to be similar to those in the work of Nilsson et al.,² except that we have now readjusted several neutron levels around neutron number $N = 104$ and 108 in order to reproduce better the experimental levels. Next, based on the cranking model of Inglis,³ the moment-of-inertia J_0 can be evaluated by the Belyaev formula.⁴ The results are plotted in Fig. 1.

The force constant C can also be expressed microscopically as

$$C^{-1} = \sum_i \frac{1}{C_i} \left(\frac{\partial J_0}{\partial X_i} \right)^2, \quad (2)$$

where X_i ($i = 1 - 5$) are variables associated respectively with the P_2 deformation, the P_4 deformation, the proton pairing, the neutron pairing, and the fourth-order cranking; and C_i are the corresponding force constants. In the present calculations, the fixed-particle-number corrections have been included in evaluating the pairing force constant. We have also applied the Strutinsky^{6,2} method to take into account the shell-correction effect in evaluating the P_2 and P_4 shape force constant. The final results of C are given in Fig. 2.

In general, the microscopic calculation is able to reproduce very well the general trends of J_0 and C versus the mass number A . The values of J_0 and C are generally reproduced with 70% to 80% accuracy. We consider this to be satisfactory. The biggest discrepancy of the values of C occurs at neutron number $N = 90$, which deserves more careful attention. Our calculations also show that the contributions of the P_2 and P_4 deformation to the force constant C are in general negligible.

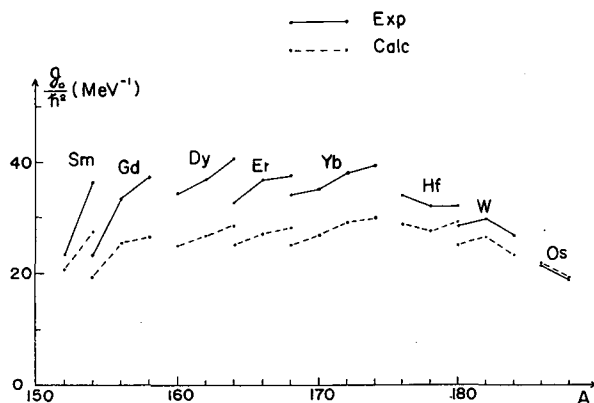


Fig. 1. Calculated values of the moment-of-inertia parameter, J_0 for the rare earth nuclei compared with experimental results.

(XBL 733-299)

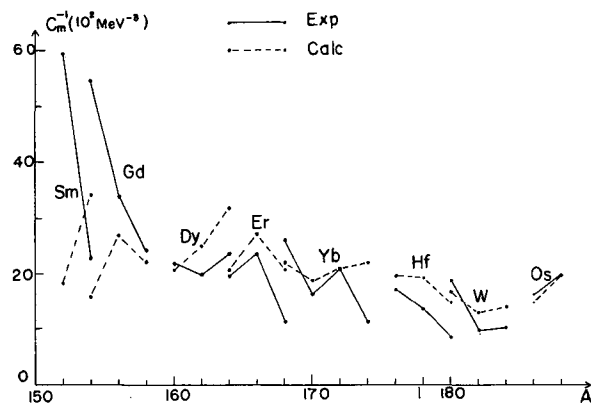


Fig. 2. Calculated values of the force constant for the rare earth nuclei compared with experimental results. (XBL 733-298)

References

1. M. A. J. Mariscotti, G. Scharff-Goldhaber, and B. Buck, *Phys. Rev.* **178**, 1864 (1969).
2. S. G. Nilsson, C. F. Tsang, A. Sobiczewski, Z. Szymanski, S. Wycech, C. Gustafson, I. L. Lamm, P. Möller, and B. Nilsson, *Nucl. Phys.* **A131**, 1 (1969).
3. D. R. Inglis, *Phys. Rev.* **96**, 1059 (1954).
4. S. T. Belyaev, *Kgl. Danske Videnskab. Selskab, Mat.-Fys. Medd.* **31**, No. 11 (1959).
5. C. W. Ma and J. O. Rasmussen, *Phys. Rev. C* **2**, 798 (1970).
6. V. M. Strutinsky, *Nucl. Phys.* **A95**, 420 (1967).

II. Chemical and Atomic Physics

Photoelectron Spectroscopy

Hyperfine Interactions

Atomic and Molecular Spectroscopy

X-RAY PHOTOELECTRON SPECTROSCOPY OF FLUORINATED BENZENES*

D. W. Davis, D. A. Shirley, and T. D. Thomas

In this paper we report the results of an experimental study of the chemically induced shifts in the binding energies of carbon and fluorine 1s electrons in fluorine-substituted benzenes. The 1s binding energy of each atom is rather directly sensitive to the local electrostatic potential. An electrostatic potential model is used, together with CNDO wave functions, to predict shifts. We describe also a "point charge" model that allows the interpretation of chemical shifts in binding energy in terms of an experimental population analysis for each molecule. This model is used to estimate atomic charges for the fluorine-substituted benzenes. Trends are discussed and compared with expectations based on chemical properties.

Experimental Section

Binding energies were measured by x-ray

photoemission, using Mg $K\alpha_{1,2}$ radiation (1253.6 eV) and electrons were analyzed in the Berkeley iron-free spectrometer.¹ The samples were all studied as gases at pressure in the 10^{-2} Torr range. Pressures were monitored by a MacLeod gauge. The pressure sensitivity of peak positions was found to be negligible, in contrast to the results reported by Siegbahn, et al.² Our experimental pressures were much lower than theirs (which ranged up to 1 Torr), while our counting rates were typically somewhat higher. The peak-to-back ground ratios in the spectra ranged from as high as 15/1 in the best cases down to less than 1/1 for the worst cases (weaker peak of a

Table I. C(1s) and F(1s) Binding Energy Shifts

Compound X	$\Delta E_B(\text{C } 1s)^b$		$\Delta E_B(\text{F } 1s)^c$, eV
	Lower E_B peak, eV	Higher E_B peak, eV	
C_6H_6	(0.00)		
$\text{C}_6\text{H}_5\text{F}$	0.39 (3) ^a	2.43 (4)	-1.38 (5)
1,4- $\text{C}_6\text{H}_4\text{F}_2$	0.76 (4)	2.74 (6)	-1.08 (5)
1,3- $\text{C}_6\text{H}_4\text{F}_2$	0.70 (5)	2.92 (6)	-1.08 (5)
1,2- $\text{C}_6\text{H}_4\text{F}_2$	0.72 (4)	2.87 (6)	-1.01 (5)
1,3,5- $\text{C}_6\text{H}_3\text{F}_3$	0.56 (13)	3.02 (9)	-0.87 (8)
1,2,3,4- $\text{C}_6\text{H}_2\text{F}_4$	0.96 (10)	3.20 (10)	-0.68 (10)
1,2,3,5- $\text{C}_6\text{H}_2\text{F}_4$	0.86 (12)	3.05 (12)	-0.45 (6)
1,2,4,5- $\text{C}_6\text{F}_2\text{H}_4$	1.12 (10)	3.20 (10)	-0.48 (10)
C_6HF_5	1.32 (17)	3.38 (14)	-0.31 (15)
C_6F_6		3.57 (9)	(0.00)

^a Error in last place given parenthetically. ^b $\Delta E_B(\text{C } 1s, X) \equiv E_B(\text{C } 1s, X) - E_B(\text{C } 1s, \text{C}_6\text{H}_6)$. ^c $\Delta E_B(\text{F } 1s, X) \equiv E_B(\text{F } 1s, X) - E_B(\text{F } 1s, \text{C}_6\text{F}_6)$.

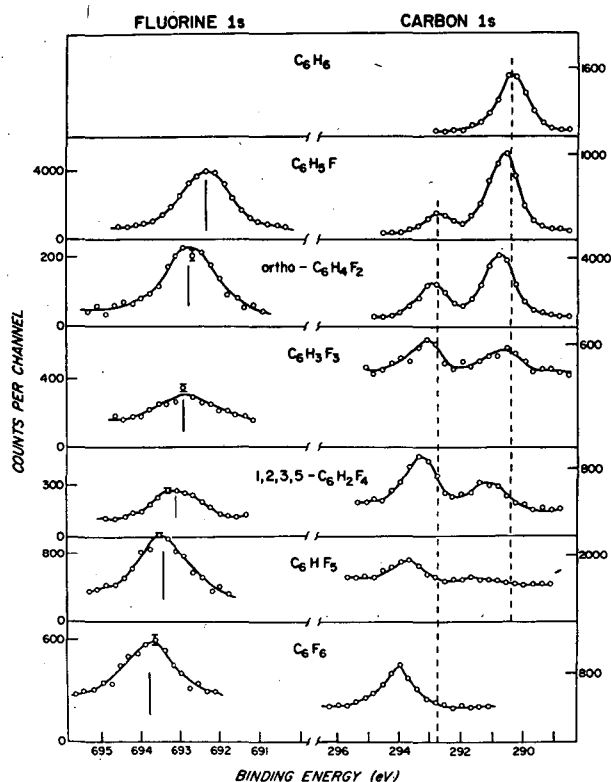


Fig. 1. X-ray photoelectron spectra of fluoro-benzenes, obtained with Mg $K\alpha$ radiation.

(XBL 733-309)

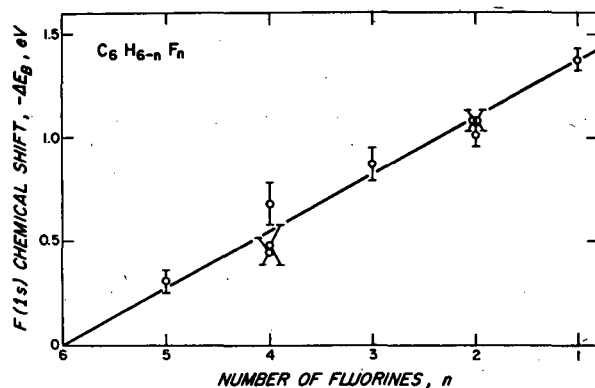


Fig. 2. Fluorine 1s binding-energy shifts of fluorobenzenes relative to C_6F_6 , plotted against number of fluorines.

(XBL 733-310)

doublet, in the presence of a reference gas); for most cases the ratio was 5/1 or greater.

Considerable care was taken to measure binding energy shifts with the highest accuracy feasible within the constraints of this study. In order to achieve this goal it was necessary to monitor all measurements with a standard reference gas. Both fluoroform and fluorobenzene were used as references.

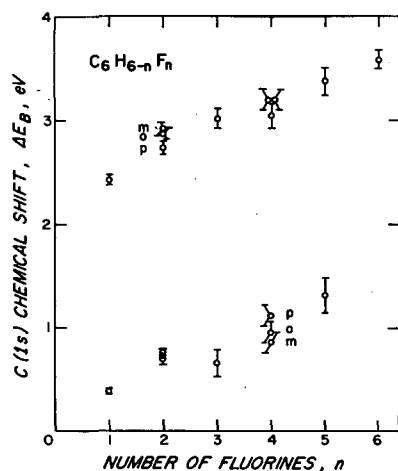


Fig. 3. Carbon 1s binding energies of fluoro-benzenes relative to that of benzene, plotted against number of fluorines. The upper points refer to carbons to which fluorines are bonded; the lower points refer to carbons to which hydrogens are bonded. (XBL 733-311)

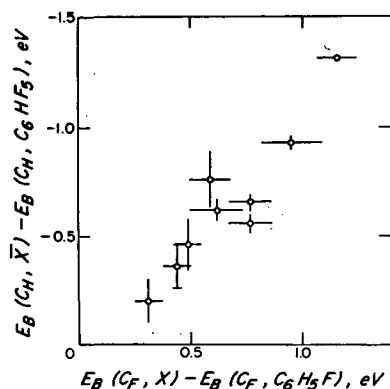


Fig. 4. Shift of C_H 1s binding energies (relative to that of C_6HF_5) for the complementary compounds $C_6H_{6-n}F_n$. (XBL 733-313)

A CNDO Potential Model

An electrostatic potential model based on SCF wave functions and Koopmans' theorem has been found to predict quantitatively chemical shifts in some small molecules.^{3,4} It would be desirable to apply this model to larger molecules if one could avoid the expense of calculating *ab initio* wave functions, and the CNDO/2 approximation was explored to this end. While requiring little computer time, CNDO/2 has been successful in predicting the properties of molecules composed of first-row elements.⁵

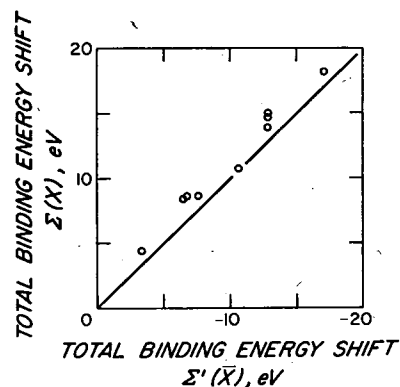


Fig. 5. The ordinate is the shift in total binding energy of carbon 1s electrons relative to those in benzene for the compound $C_6H_nF_{6-n}$. The abscissa is the shift in total binding energy of carbon 1s electrons relative to those in C_6F_6 for the complementary compound $C_6H_{6-n}F_n$. (XBL 733-312)

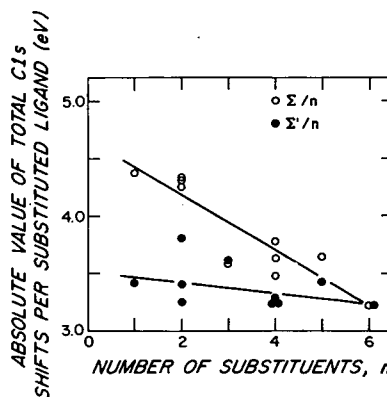
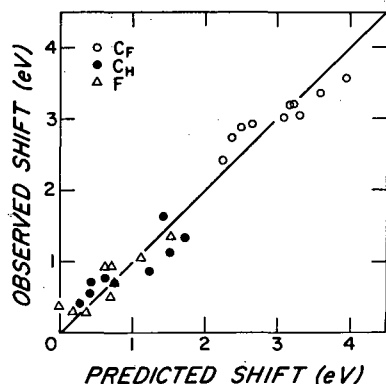


Fig. 6. Shift in the total binding energy of carbon 1s electrons per substituted ligand, plotted vs number of ligands. The open circles refer to substitution of fluorines for hydrogens on benzene; the closed circles refer to substitution of hydrogens for fluorines on C_6F_6 .

Theory and experiment are compared in Table IV. The numerical results of both of the approaches are quite close, and agreement with experiment is comparable to that obtained from ground state ab initio calculations.^{1,4,7} This agreement is further illustrated in Fig. 7, where we have plotted the experimental shifts vs. those predicted by the first of the two CNDO/2 methods.



(XBL 733-314)

Fig. 7. Experimental shifts for binding energies of 1s electrons plotted against the shifts calculated by the first of the two CNDO/2 methods described in the text. (XBL 733-315)

An Atomic Charge Analysis

In this section we discuss the derivation of an "atomic charge" analysis and its application to the fluorine-substituted benzenes. We seek both to test the model and (if possible) to derive information about charge distributions in these molecules.

Let us consider a molecule with n inequivalent atoms. If all n 1s electron-binding energies are known, they may be referred to suitable standard binding energies to yield a set of binding-energy shifts δE_i ($i = 1, 2, \dots, n$). These shifts carry information about the electronic charge distribution.

Assigning charge q_j to atom j , and denoting by R_{ij} the internuclear distance between atoms i and j , we may write

$$\delta E_i = \sum_j (\partial E_i / \partial q_j) \delta q_j = (\partial E_i / \partial q_i) \delta q_i + \sum_{j \neq i} (e^2 / R_{ij}) \delta q_j \quad (3)$$

as the incremental change in the binding energy of a core electron in atom i accompanying a redistribution of charge in the molecule described by the set of numbers $\{\delta q_j\}$. Note that q_j is thus the charge on atom j in units of $|e|$. If we choose the binding-energy reference state as $q_j = 0$ for all j (i.e., hypothetical neutral atoms within the molecule) and invoke the essential constancy of $(\partial E_i / \partial q_i)$ as q_i is varied, Eq. 3 becomes

$$\delta E_i = k_i q_i + \sum_{j \neq i} (e^2 / R_{ij}) q_j \quad (4)$$

Equations similar to this are well known in x-ray photoelectron spectroscopy.⁸

Equation 4 is a linear equation in n unknowns $\{q_j\}$. There are n such equations, one for the shift δE_i on each atom i . It is convenient to write these equations in matrix form

$$\vec{\delta} = A\vec{q} \quad (5)$$

Here $\vec{\delta}$ and \vec{q} are n -dimensional vectors whose components are the ordered sets $\{\delta E_i\}$ and $\{q_i\}$, respectively. The $n \times n$ matrix A has elements

$$A_{ii} = k_i = (\partial E_i / \partial q_i),$$

$$A_{ij} = \sum_{j \neq i} e^2 / R_{ij} \text{ for } i \neq j. \quad (6)$$

The off-diagonal elements A_{ij} are easily worked out from a knowledge of the molecular geometry. Diagonal elements can be evaluated as discussed below. The important point here is that the entire matrix A can be obtained from Coulomb's law plus free-atom wave functions, with no reference whatever to molecular orbital models. Thus we may combine the matrix A , calculated essentially from first principles, with a complete set of n experimentally determined shifts $\vec{\delta}$ to solve for the n charges \vec{q} , thereby obtaining an empirical population following the evaluation of $A_{ii} = k_i$ for the elements carbon and fluorine. If the electron population of the valence δq , corresponding to an increase of charge in the valence shell by the fraction δq of one charge unit $|e|$, then the binding energy of a 1s electron would be changed by an amount

$$\delta E \approx \delta V = e^2 \langle r^{-1} \rangle \delta q, \quad (7)$$

where $\langle r^{-1} \rangle$ is the expectation value of r^{-1} for the valence electron.⁹ Comparison with the "diagonal" terms in Eq. 3 and 4 yields

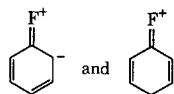
$$k_i = e^2 \langle r_i^{-1} \rangle. \quad (8)$$

In this analysis we use a single value of k_i for each element. The s and p valence orbitals on the same atom have slightly different values of $\langle r^{-1} \rangle$. However, we prefer to avoid any arbitrariness that might result from the introduction of additional parameters (e.g., to describe hybridization). This is certainly justified, because the derived charges are actually not very sensitive to the exact value of k used. The linear equations were solved for the nine molecules studied containing C, F, and H, using a program named ACHARGE. This program also inverts the coefficient matrix, to test the sensitivity of derived charges to errors in the shifts. This sensitivity was surprisingly small, typically $0.1 |e|/eV$. Thus errors of ~ 0.1 eV in shifts lead to uncertainties of only ~ 0.01 in q_i . Results are given in Table VII, together with atomic charges obtained from the CNDO/2 calculations described previously.

Discussion of the Atomic Charge Values

The agreement displayed in Table VII between the charges obtained from ACHARGE and those calculated by CNDO/2 is extremely good for most cases. Not only are the numerical values very close, but several trends are revealed by both sets of charges. The good agreement arises largely from similarities between the two approaches.

The dipole moment of fluorobenzene is normally attributed to polarization of the C-F bond, while its tendency to accept electrophilic substituents in the ortho and para positions is attributed to resonance tautomers such as



Polarizations of the C-F bond are clearly evident in the charge values in Table VII. The difference $q(C_F) - q(F)$ ranges from about 0.3 to

0.45. There is a clear trend in the (average) fluorine charge, from about -0.20 in fluorobenzene to about -0.15 in C_6F_6 .

No such trend is evident in the carbon charges, because of the dominant effects associated with the ortho, meta, and para positions. These effects are indicated in Table VIII. The ortho, meta, and para charges for the C_H carbons in fluorobenzene give this effect directly. It may be found also in the C_F carbon in fluorobenzene. The effect is evident in both bases (and the CNDO/2 charges also show it). The photoelectron data with the ACHARGE analysis appear to show a negative charge of about -0.04 on the ortho carbon, and, with less certainty, a very small positive charge on the meta carbon. The para carbon appears to be essentially neutral.

Table III. The Ortho, Meta, and Para Shifts

Molecule	$E(C_F 1s) - E(C_F 1s, C_6H_5F)$, eV	Molecule	$E(C_H 1s) - E(C_H 1s, C_6H_5F)$, eV
<i>o</i> - $C_6H_4F_2$	0.44 (6)	<i>o</i> - $C_6H_2F_4^a$	-0.36 (10) ^b
<i>m</i> - $C_6H_4F_2$	0.49 (6)	<i>m</i> - $C_6H_2F_4$	-0.46 (12)
<i>p</i> - $C_6H_4F_2$	0.31 (6)	<i>p</i> - $C_6H_2F_4$	-0.20 (10)

^a Here ortho, meta, and para refer to the hydrogen positions.

^b The error in the C_6H_5F energy is not included, since we wish to compare these three shifts.

The ortho, meta, and para effects are present in the multiply substituted fluorobenzenes. This is most readily apparent in 1,3-difluorobenzene and 1,3,5-trifluorobenzene, for which the additional tautomeric forms reinforce one another. In 1,3-difluorobenzene, for example, the carbon in position 2 is ortho to both fluorines and should therefore carry a large negative charge. It does; for this case $q(C) = -0.09$. This effect should be even larger in 1,3,5-trifluorobenzene, because carbons in the 2, 4, and 6 positions are each ortho to two fluorines and para to another. The ACHARGE result, $q(C_H) = -0.13$, confirms this expectation. Furthermore, for this molecule the C_F carbons have the largest positive charge observed in this study. This is also expected because each is meta to two fluorines.

Table II. Splitting of the C(1s) Peaks in Fluorobenzene

Run no.	Splitting, eV
10 B	2.036 (76)
15 B	2.013 (57)
17 D	2.122 (79)
19 D	1.994 (71)
21 D	1.966 (107)
23 D	2.112 (68)
25 D	2.017 (69)
Weighted av	2.040 (30)

A number of other systematic trends can be observed among the charges in Table VII. They all appear to be in accord with what is expected on chemical grounds. We conclude that the ACHARGE analysis yields charges that are useful in understanding chemical properties. With further refinement, and especially in combination with higher resolution spectra, the ACHARGE analysis of photoelectron data may permit prediction of the reactivities of new compounds.

Table IV. Carbon and Fluorine 1s Electron Binding Energy Shifts in eV^a

Compound	Nucleus	Calcd (point charge)	Calcd, diagonal plus p-p' elements	Expt ^b
	C ₁	2.25	2.79	2.43 (4)
	C _{2,6}	0.17	0.16	
	C _{3,5}	0.42	0.52	0.39 (3)
	C ₄	0.10	0.11	
	F			
	C _{1,2}	2.48	2.98	2.87 (6)
	C _{3,6}	0.76	0.84	
	C _{4,5}	0.67	0.78	0.72 (4)
	F	-0.03	-0.08	0.37 (10)
	C _{1,3}	2.66	3.30	2.92 (6)
	C ₂	0.33	0.29	
	C _{4,6}	0.27	0.26	0.70 (5)
	C ₅	0.84	1.04	
	F	0.36	0.37	0.30 (10)
	C _{1,4}	2.36	2.91	2.74 (6)
	C _{2,3,5,6}	0.61	0.68	0.76 (4)
	F	0.16	0.18	0.30 (10)
	C _{1,3,5}	3.08	3.82	3.02 (9)
	C _{2,4,6}	0.42	0.40	0.56 (13)
	F	0.71	0.74	0.51 (13)
	C _{1,4}	3.15	3.77	3.20 (10)
	C _{2,3}	3.25	3.84	3.81
	C _{5,6}	1.43	1.63	0.96 (10)
	F _{1,4}	0.63	0.62	0.70 (15)
	F _{2,3}	0.86	0.78	
	C _{1,3}	3.40	4.09	3.05 (12)
	C ₂	2.96	3.48	3.92
	C ₅	3.31	4.02	
	C _{4,6}	1.23	1.32	0.86 (12)
	F _{1,3}	0.80	0.77	
	F ₂	0.66	0.61	0.69
	F ₄	0.58	0.61	
	C _{1,2}	3.15	3.77	3.20 (10)
	C _{3,6}	1.51	1.66	1.12 (10)
	F	0.62	0.61	0.90 (15)
	C _{1,5}	3.62	4.34	3.38 (14)
	C _{2,4}	3.44	4.06	4.24
	C ₃	3.71	4.39	
	C ₆	1.71	1.90	1.32 (17)
	F _{1,5}	1.09	1.04	
	F _{2,4}	1.05	1.04	1.07 (10)
	F ₃	1.28	1.21	
	C	3.94	4.64	3.57 (9)
	F	1.52	1.48	1.38 (5)

^a Carbon shifts relative to benzene; fluorine shifts relative to fluorobenzene. ^b Error in last place given parenthetically.

Table V. Dipole Moments

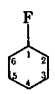
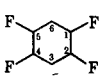
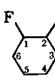
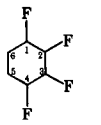
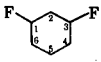
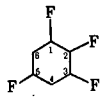
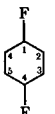
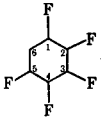
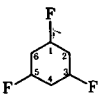
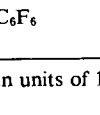
	Exptl	CNDO/2
Fluorobenzene	1.57 ^a	1.52
1,2-Difluorobenzene	2.40 ^b	3.07
1,3-Difluorobenzene	1.58 ^c	1.50

^a Reference 10 ^b Reference 11 ^c Reference 12

Table VI. Fluorine Shifts Relative to a Hypothetical Neutral Standard State

Compound	$\delta E(\text{F } 1s)$, eV	Compound	$\delta E(\text{F } 1s)$, eV
$\text{C}_6\text{H}_5\text{F}$	-3.81	1,2,3,4- $\text{C}_6\text{H}_2\text{F}_4$	-3.11
<i>p</i> - $\text{C}_6\text{H}_4\text{F}_2$	-3.51	1,2,3,5- $\text{C}_6\text{H}_2\text{F}_4$	-2.88
<i>m</i> - $\text{C}_6\text{H}_4\text{F}_2$	-3.51	1,2,4,5- $\text{C}_6\text{H}_2\text{F}_4$	-2.91
<i>o</i> - $\text{C}_6\text{H}_4\text{F}_2$	-3.44	C_6HF_5	-2.74
1,3,5- $\text{C}_6\text{H}_3\text{F}_3$	-3.30	C_6H_6	-2.43

Table VII. Derived Atomic Charges

Compound	Atom ^a	q (ACHARGE)	q (CNDO/2)	Compound	Atom	q (ACHARGE)	q (CNDO/2)	
	C ₁	23 ^b	24		C _{1,2,4,5}	18	19	
	C _{2,6}	-4	-5		C _{3,6}	-7	-8	
	C _{3,5}	1	3		F	-15	-18	
	C ₄	0	-1		H	2	5	
	F	-19	-20		C _{1,4}	19	19	
	H	0	0		C _{2,3}	14	15	
	C _{1,2}	19	19		C _{5,6}	-6	-3	
	C _{3,6}	-3	-3		F _{1,4}	-17	-18	
	C _{4,5}	1	1		F _{2,3}	-16	-16	
	F	-17	-18.5		H	+4.5	-3	
	H	0	1		C _{1,3}	19	23	
	C _{1,3}	25	26		C ₂	12	11	
	C ₂	-9	-12		C _{4,6}	-10	-12	
	C _{4,6}	-4.5	-7		C ₅	25	27	
	C ₅	2	5		F _{1,3}	-12	-17	
	F	-18	-20		F ₂	-15	-17	
	H	0.5	2		F ₅	-16	-19	
	C _{1,4}	23	22		H	1	5	
	C _{2,3,5,6}	-3	-3		C _{1,5}	19	21	
	F	-18	-20		C _{2,4}	14	13	
	H	1	2		C ₃	14	17	
	C _{1,3,5}	27	28.5		C ₆	-9	-10	
	C _{2,4,6}	-13	-14		F _{1,5}	-15	-17	
	F	-18	-19		F _{2,4}	-15	-16	
	H	4	4		F ₃	-15	-16	
	C _{1,2,4,6}	-13	-14		H	4.5	6	
	F	-18	-19		C	14	15.5	
	H	4	4		F	-14	-15.5	
	C _{6\text{F}_6}							

^a Here \bar{H} denotes average of all hydrogen charges. ^b Charges are given in units of $10^{-2}|e|$.

Table VIII. Ortho, Meta, and Para Alternation in Atomic Charges

Position	C _H carbons in fluorobenzene		(Charge on C _F carbon in difluorobenzenes) minus (charge on C _F carbon in fluorobenzene)		
	From ACHARGE	From CNDO/2	Molecule	Δq from ACHARGE	Δq from CNDO/2
Ortho	-0.05	-0.05	<i>o</i> -Difluorobenzene	-0.04	-0.05
Meta	+0.02	+0.02	<i>m</i> -Difluorobenzene	+0.01	+0.03
Para	0.00	-0.02	<i>p</i> -Difluorobenzene	0.00	-0.01

Footnote and References

* Condensed from LBL-270, Published in J. Am. Chem. Soc. 94, 6565 (1972).

1. C. S. Fadley, S. B. M. Hagstrom, M. P. Klein, and D. A. Shirley, J. Chem. Phys. 48, 3779 (1968).
2. K. Siegbahn, C. Nordling, G. Johannsson, J. Hedman, P. F. Hedén, K. Hamrin, U. Gelius, T. Bergmark, L. O. Werme, R. Manne, and Y. Baer, ESCA Applied to Free Molecules (North-Holland, Amsterdam, 1969), pp.18-21.
3. H. Basch, Chem. Phys. Letters 5, 337 (1970).
4. M. E. Schwartz, Chem. Phys. Letters 6, 631 (1970).
5. J. A. Pople and D. L. Beveridge, Approximate Molecular Orbital Theories (McGraw-Hill, 1970), Chapter 4.
6. D. W. Davis, J. M. Hollander, D. A. Shirley, and T. D. Thomas, J. Chem. Phys. 52, 3295 (1970).
7. H. Basch and L. C. Snyder, Chem. Phys. Letters 3, 333 (1969).
8. U. Gelius, B. Roos, and P. Siegbahn, Chem. Phys. Letters 4, 471 (1970).
9. T. K. Ha and C. T. O'Konski, Chem. Phys. Letters 3, 603 (1969).
10. E. C. Hardis and C. P. Smyth, J. Am. Chem. Soc. 64, 2212 (1942).
11. E. Bergmann, L. Engel, and H. A. Wolff, Z. Physik. Chem. B10, 106 (1930).
12. E. M. Moore and M. E. Hobbs, J. Am. Chem. Soc. 71, 411 (1949).

X-RAY PHOTOEMISSION SPECTRA OF CRYSTALLINE AND
AMORPHOUS Si AND Ge VALENCE BANDS*

L. Ley,[†] S. P. Kowalczyk, R. A. Pollak, and D. A. Shirley

The valence-band densities of states $\rho(E)$ of the crystalline modifications of Si and Ge are of current and continuing interest because relatively little experimental information is as yet available concerning the more tightly bound valence electrons. In addition, a considerable amount of recent activity has been directed toward elucidating the electronic structure in the amorphous forms.³ Thorpe and Weaire⁴ have discussed three alternative models for the densities of states of amorphous Si and Ge, and Joannopoulos and Cohen⁵ have recently given quantitative predictions for $\rho(E)$. In this report the first high-resolution x-ray photoelectron (XPS) spectra for the densities of states of crystalline and amorphous Si and Ge are obtained and compared with theory.

The crystalline samples were cleaved in a dry inert atmosphere from 20- Ω cm n-type silicon and intrinsic Ge single crystals immediately before introduction into a Hewlett Packard HP5950A photoelectron spectrometer with monochromatic Al K α x rays.

To prepare amorphous specimens, Si and Ge films were evaporated onto clean gold surfaces at room temperature in the spectrometer sample preparation chamber. Surface contaminations

by oxygen or carbon were negligible in all cases.

The valence band spectra $I'(E)$, corrected for inelastically scattered electrons are shown in Fig. 1.

Several band-structure calculations have predicted $\rho(E)$ for crystalline Si and Ge. These calculations show very good agreement among themselves. They yield three characteristic peaks in $\rho(E)$. We shall label these peaks according to the symmetry points X_4 , L_1 , and L_2' , in order of increasing binding energy. Of course the peaks do not arise entirely from bands at these symmetry points. This notation is used only for identification. To facilitate comparison with experiment we have plotted (Fig. 1) for Si and Ge both $\rho(E)$ as calculated^{1c, 2b} and a broadened version that is consistent with the experimental resolution.

The agreement between theoretical and experimental peak positions and shapes is striking for crystalline Si and Ge. Table I lists the energies of the characteristic features, the theoretical densities of states $\rho(E)$, and the corrected XPS spectra, which we denote as $I'(E)$. The marginal ability to locate the feature W_2 gives an indication of the resolving power of our spectrometer. As Table I shows, $I'(E)$ provides

very strong confirmation of all three theoretical methods for calculating $\rho(E)$. The relative intensities of the p-like X_4 and the s-like $L_1 + L_2$ peaks in $I'(E)$ vary markedly between Si and Ge and in neither case agree with $\rho(E)$. This is not unexpected, since $I'(E)$ resembles $\rho(E)$ weighted with the photoemission cross section σ .

The results for amorphous Si and Ge are significantly different from the respective crystalline modifications. From the $I'(E)$ spectra (Fig. 1) we note the following observations: (1) The gross variation of intensity with respect to energy is similar for the amorphous and crystalline materials in both elements. (2) The " X_4 " peak remains essentially intact from crystalline to amorphous material. (3) The L_1 and L_2' peaks merge into a single broad peak of intermediate energy. (4) $I'(E)$ shows a distinct minimum between the " X_4 " peak and the broad peak in the amorphous materials. (5) The

centroid of the " X_4 " peak shifts toward E_F in each case, by 0.4 eV in Si and 0.5 eV in Ge. (6) The amorphous Ge spectra were in good agreement for samples prepared by evaporation and by Ar^+ ion bombardment (1000 eV, 10 μA for 1 hr).

Observations (1)-(3) are in agreement with the Si $L_{2,3}$ (SXS) results of Wiech and Zöpf.⁶ Observation (2) is expected because X_4 arises from localized p-like bonding orbitals, which are relatively insensitive to long-range order. Observation (5) is in qualitative agreement with earlier uv-photoemission work.^{3a} Pierce and Spicer^{3c} have recently emphasized the sensitivity of uv photoemission spectra to the method of sample preparation, but observation (6) indicates that $I'(E)$ for amorphous Ge was reproducible even though the method of sample preparation was varied.

Observations (3)-(5) are the ones that allow a distinction to be made among different theoretical models for amorphous semiconductors.

Thorpe and Weaire⁴ have recently discussed three theoretical models for amorphous Si and Ge. The Brust model⁷ yields a $\rho(E)$ spectrum which is a broadened version of the densities of states for the crystalline case. Thorpe and Weaire indicated that the Penn model might apply to amorphous semiconductors. The $\rho(E)$ curve for the Penn model shows no minimum, but rather a (broadened) logarithmic divergence near E_F and a free-electron $\rho(E)$ below. Our data exclude both of these shapes for $\rho(E)$, thereby ruling out these two models as being applicable to amorphous Si and Ge. Our spectra definitely require a model that predicts large changes in the s-like L_1 and L_2' peaks but not in the p-like X_4 peak on going from the crystalline to the amorphous state. Thorpe and Weaire described a model that distinguished between the effects of local and long-range interactions. They sketched a curve for $\rho(E)$ that is in good agreement with our amorphous Si and Ge spectra, especially observations (2)-(4).

A more quantitative comparison with theory is provided by the recent empirical-pseudopotential calculations of Joannopoulos and Cohen⁵ on several forms of Ge. Their $\rho(E)$ results for Ge (ST-12), after smoothing to eliminate sharp features associated with long-range order, show very good agreement with our $I'(E)$ curve. Their $\rho(E)$ curves are shown in Fig. 1. As they pointed out, Ge (ST-12) shows short-range disorder, but the peak near E_F still arises from p-like bonding orbitals. Their model predicts the shift of this peak toward E_F [observation (5)]. The crucial feature of the ST-12 structure is the presence of five- and seven-membered rings. This feature causes the two lower-energy peaks in $I'(E)$ to merge.

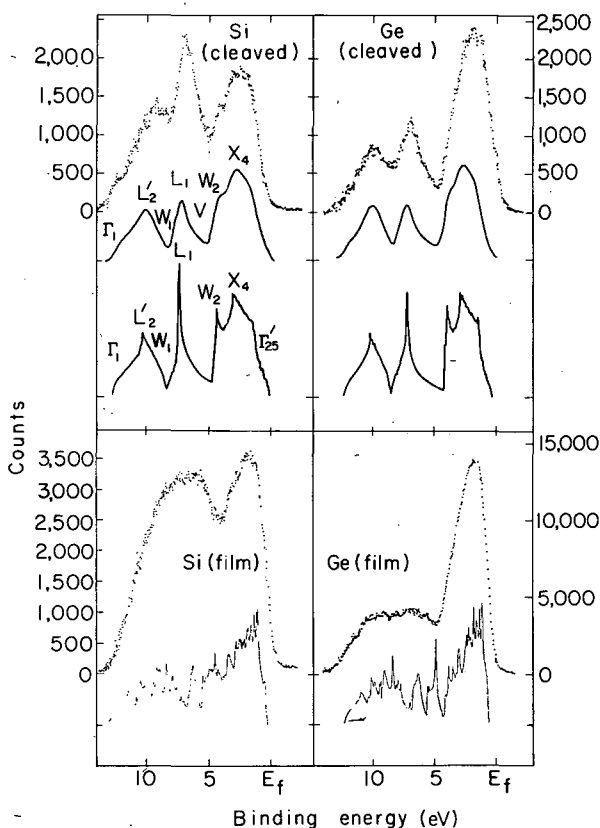


Fig. 1. Point plots, corrected spectra $I'(E)$; lower curves, calculated (Refs. 1c, 2b, and 5) densities of states $\rho(E)$ for the valence bands of crystalline and amorphous (ST-12) Si and Ge; middle curves, broadened $\rho(E)$ spectra for crystalline Si and Ge. (XBL 727-3392a)

TABLE I. Energies of characteristic features in the valence-band spectra of Si and Ge. The theoretical entries are taken from density of states calculations after appropriate broadening.

Crystalline silicon				
	Experiment ^a	Theory ^b		
	Γ (E) (eV)	EPM (Cohen ^c) (eV)	SCOPW (Stukel ^d) (eV)	
X ₄	2.2	2.6		2.5
W ₂	3.6	4.0		3.1
V ^e	4.4	5.1		4.5
L ₁	6.6	7.1		6.9
W ₁	7.8	8.2		8.2
L ₂ ¹	9.2	10.0		9.6
Γ_1	14.7	13.0		11.8

Crystalline germanium				
	Experiment ^a	Theory ^b		
	Γ (E) (eV)	EPM (Cohen ^f) (eV)	OPW (Herman ^g) (eV)	SCOPW (Stukel ^d) (eV)
X ₄	2.4	2.3	2.7	2.6
W ₂	3.6	3.4	3.8	3.6
V ^e	4.9	4.4	4.9	4.9
L ₁	7.2	6.9	7.3	6.8
W ₁	8.6	8.5	8.6	7.8
L ₂ ¹	10.3	9.7	10.2	9.4
Γ_1	13.0	12.4	12.7	11.7

^a Positions relative to gold Fermi level.

^b Positions relative to the top of the valence bands.

^c See Ref. 1c.

^d See Ref. 1b.

^e The valley between W₂ and L₁ is arbitrarily called V.

^f See Ref. 2b.

^g See Ref. 2a.

It is a pleasure to acknowledge the generous contributions of Professor Marvin Cohen and Mr. John Joannopoulos to this research. One of us (L. L.) greatly appreciates a grant from the Max-Kade Foundation.

Footnotes and References

* Condensed from LBL-688. Published in Phys. Rev. Letters **29**, 1088 (1972).

† On leave from University of Bonn, Bonn, Germany.

1a. See, for example, E. O. Kane, Phys. Rev. **146**, 558 (1966).

1b. D. J. Stukel, T. C. Collins, and R. N. Euwema, in Electronic Density of States. Proceedings of the Third International Materials Research Symposium, Gaithersburg, Maryland, 1969, edited by L. H. Bennett, National Bureau of Standards Special Publication No. 323 (U.S. GPO, Washington, D.C., 1971).

1c. M. L. Cohen and J. D. Joannopoulos, private communication.

2a. See, for example, F. Herman, R. L. Kortum, C. D. Kuglin, and J. L. Shay, in Proceedings of the International Conference on II-VI Semiconducting Compounds, Brown University, 1967 (Benjamin, New York, 1967).

2b. M. L. Cohen and J. D. Joannopoulos, private communication.

2c. M. Cardona and F. H. Pollak, *Phys. Rev.* **142**, 530 (1966).

3a. See, for example, T. M. Donovan and W. E. Spicer, *Phys. Rev. Letters* **21**, 1572 (1968).

3b. D. T. Pierce and W. E. Spicer, *Phys. Rev. B* **5**, 3017 (1972); T. E. Fischer and N. Erbudak, *Phys. Rev. Letters* **27**, 1220 (1971).

3c. D. T. Pierce and W. E. Spicer, *Phys. Rev. Letters* **27**, 1217 (1971).

4. M. F. Thorpe and D. Weaire, *Phys. Rev. Letters* **27**, 1581 (1971).

5. J. D. Joannopoulos and M. L. Cohen, to be published.

6. G. Wiech and E. Zöpf, in Proceedings of the International Conference on Band-Structure Spectroscopy of Metals and Alloys, Glasgow, Scotland, September 1971 (to be published).

7. D. Brust, *Phys. Rev. Letters* **23**, 1232 (1969).

8. D. Penn, *Phys. Rev.* **128**, 2093 (1962).

HIGH-RESOLUTION XPS SPECTRA OF Ir, Pt, AND Au VALENCE BANDS*

S. P. Kowalczyk, L. Ley,[†] R. A. Pollak,[‡] and D. A. Shirley

X-ray photoelectron spectroscopy (XPS) spectra [hereafter denoted by $I(E)$] of the valence bands of several sixth-row elements have been reported earlier.^{1,2} Those spectra were obtained from heated metal foils at resolutions of ~ 1 eV, in the presence of hydrogen gas. Although trends in $I(E)$ for the fcc metals Ir, Pt, and Au were suggestive of band filling, detailed interpretation was precluded both by experimental limitations and by a lack of appropriate theoretical densities of states, $\rho(E)$, with which to compare $I(E)$. Several relativistic $\rho(E)$ calculations on Au have recently become available. Two of them^{3,4} compare very well with the high-resolution (~ 0.6 eV) XPS spectrum of Au⁵. The results of a high-resolution and high-vacuum study of $I(E)$ for argon ion scrubbed Ir, Pt, and Au single crystals that confirms the band-filling model for these elements are reported.

The raw spectra $I(E)$ are shown in Fig. 1, together with $I'(E)$, the spectra after correction for inelastic scattering. The similarity of $I'(E)$ for these three elements is striking, and its variation from Ir to Pt to Au confirms band-structure expectations. To permit discussion of these $I'(E)$ within the framework of theoretical $\rho(E)$ predictions, we have truncated the $\rho(E)$ for Au, as calculated by Connolly and Johnson², to correspond to occupancies of 9 and 10 electrons in the 5d bands, thus simulating Ir and Pt, respectively. The results

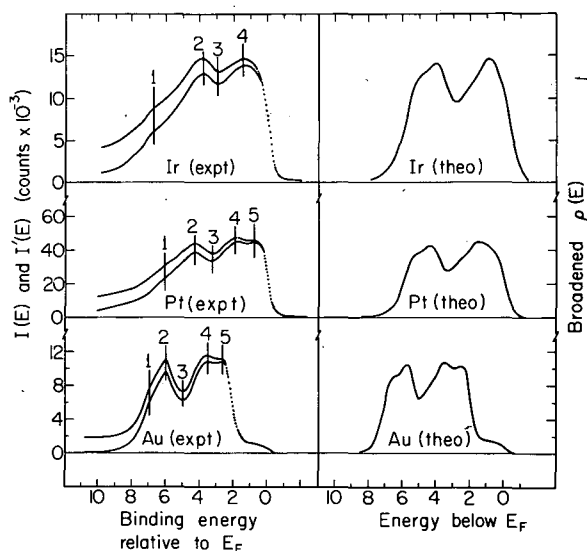


Fig. 1. Left panels and left ordinate: experimental XPS spectra of 5d bands of Ir, Pt, and Au. Upper curve in each case shows raw spectrum $I(E)$; lower curve is the corrected spectrum $I'(E)$. Data were all taken digitally. They are shown as points only for the leading edges of the 5d bands, where data density permits. Right panels and right ordinate: theoretical densities of states obtained by broadening Connolly and Johnson's $\rho(E)$ results. For Ir and Pt this $\rho(E)$ was truncated and the energy scale expanded. (XBL 727-3550)

were broadened to simulate the experimental resolution^{1,5}, and the energy scales were expanded by 1.35 for Ir and 1.20 for Pt, to roughly match the experimental bandwidths. The resulting very approximate $\rho(E)$'s are also shown in Fig. 1.

Proceeding from Ir to Pt to Au, the band-filling phenomenon is quite evident. Four features, numbered in Fig. 1, are present in all three cases. These are: (1) A shoulder at 6.8 eV in Ir, 6.1 eV in Pt, and 7.0 eV in Au. (2) A peak at 3.8₅ eV in Ir, 4.3₅ eV in Pt, and 6.1 eV in Au. (3) A minimum at 3.0 eV in Ir, 3.3 eV in Pt, and 5.0 eV in Au. This feature is present in the calculated $\rho(E)$ for Au only if spin-orbit interaction is included. It may be less pronounced in Ir and Pt because for these lighter elements the ratio of lattice interactions to spin-orbit interactions is larger. (4) Another peak component at 1.4₅ eV in Ir, 1.7₅ eV in Pt, and 3.5₅ eV in Au. The quoted energies are known to ± 0.1 eV.

A fifth feature — a second component of the second peak — appears at 0.8 eV in Pt and at 2.65 eV in Au. This part of $\rho(E)$ is at least partially unoccupied in Ir. The dip between feature 4 and 5 is very shallow, especially in Au. In Au the 5d bands have become filled and dropped below E_F , as expected. The width of the occupied 5d bands as measured between the outermost inversion points of $I'(E)$ decreases systematically from 7.4 eV (Ir) to 7.1 eV (Pt) to 5.4 eV (Au). This is also expected. In auxiliary studies on liquid Hg ($Z = 80$) we found that the 5d states have assumed the character of a spin-orbit split core doublet, at 7.7 and 9.5 eV.

In summary, these high-resolution XPS spectra support the band-filling concept in considerable detail. It would be of interest to compare these $I'(E)$ spectra with $\rho(E)$ results from a systematic theoretical study of these three adjacent isostructural elements.

One of us (L. L.) greatly appreciates a grant from the Max Kade Foundation. We thank Professor G. A. Somorjai for providing us with single crystals of Ir, Pt, and Au.

Footnotes and References

*Condensed from LBL-691. Published in Phys. Letters 41A, 455 (1972).

†On leave from University of Bonn, Germany.

‡Present address: IBM, Thomas J. Watson Research Center, Yorktown Heights, N. Y.

1. C. S. Fadley and D. A. Shirley, J. Res. Nat. Bur. Standards 74A, 543 (1970).

2. Y. Baer, P. F. Hedén, J. Helman, M. Klasson, C. Nordling, and K. Siegbahn, Physica Scripta 1, 55 (1970).

3. J. W. D. Connolly and K. H. Johnson, MIT Solid State and Molecular Theory Group Report No 72, p. 19, 1970 (unpublished); and private communication.

4. N. E. Christensen and B. O. Seraphin, Phys. Rev. B4, 3321 (1972).

5. D. A. Shirley, Phys. Rev. B5, 4709 (1972).

X-RAY PHOTOEMISSION VALENCE BAND SPECTRA AND THEORETICAL VALENCE BAND DENSITIES OF STATES FOR Ge, GaAs, AND ZnSe

R. A. Pollak, L. Ley,* S. P. Kowalczyk, D. A. Shirley,
J. D. Joannopoulos,† D. J. Chadi,‡ and M. L. Cohen†

Much theoretical and experimental effort has been devoted to the study of the band structures of tetrahedrally coordinated semiconductors because of their numerous applications. Most earlier measurements (optical spectroscopy, transport properties, etc.) have been useful in yielding information concerning electronic properties near the Fermi energy. Only recently have there been any experimental data (e.g., soft x-ray spectroscopy) which yield information about the density of states in regions near the bottom of

the valence band.

We report here the first high-resolution XPS (X-ray Photoemission Spectroscopy) spectra for all valence bands in the isoelectronic series Ge, GaAs, and ZnSe. These experimental results are compared with theoretical valence band density-of-states calculations using the EPM¹ (Empirical Pseudopotential Method). Since the lattice constants and ion cores are essentially constant for the series, the band spacings are

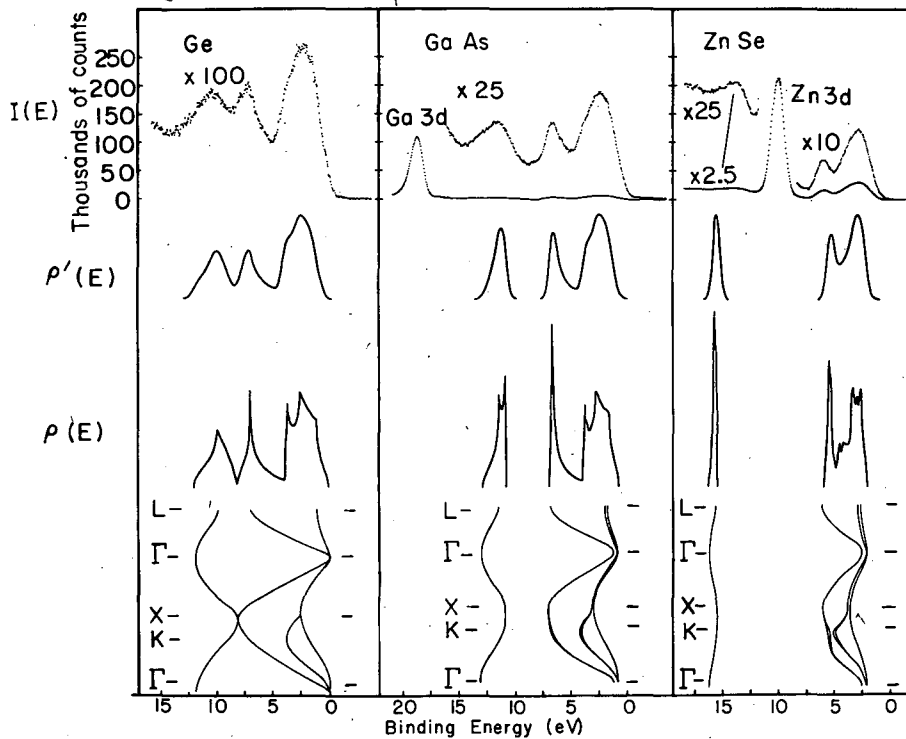


Fig. 1. XPS-spectra, band structures, and densities of states for Ge, GaAs, and ZnSe. The top row $I(E)$ shows the uncorrected experimental spectra. At the bottom are shown the corresponding band structures $E(k)$ and densities of states $\rho(E)$ as derived from EPM calculations. The broadened theoretical densities of states $\rho'(E)$ in the second row facilitate comparison with experiment. (XBL 727-3597)

used to obtain information about the increasing ionicity from purely covalent Ge to the more ionic ZnSe. The experimental results also yield information about the asymmetric part of the pseudopotential.

In Fig. 1 are shown the experimental and theoretical densities of states for Ge, GaAs, and ZnSe, and the corresponding theoretical band structures. The theoretical valence-band densities of states were obtained from band-structure calculations for Ge,³ GaAs,⁴ ZnSe⁵ using the EPM. A broadened theoretical density of states is also provided to facilitate comparison with experiment. The experimental curves have not been corrected for energy losses. This tends to exaggerate the intensities of the peaks at the bottom of the valence-band. In Table I we list the energies of the various peaks from the theoretical density of states and from the XPS spectra.

For Ge there is good agreement between theory and experiment in regard to the energy positioning and the widths of the peaks, as was reported earlier.² In the XPS spectrum the 3d states of Ge fall at 29.0 eV, which is 18.7 eV

lower than the first peak shown in Fig. 1. In GaAs we again find good agreement between theory and experiment. The first peak on the left in the XPS spectrum (Fig. 1) comes from the 3d states of Ga. The lowest s-like valence band has shifted to a lower energy and has become dissociated from the next peak. This shift to a lower energy occurs because of the localization of electrons in the first band around the strong As potential, and can be related to the antisymmetric form factors. The "antisymmetric gap" (between the lowest s-like valence band and the second valence band) may provide some measure of the ionicities of these compounds. It is surprising that the EPM agrees so well with experiment for this lowest valence band. This band does not make any contribution to optical transitions in the 2.8- to 6-eV range, which were used to determine⁴ the pseudopotential form factors. Furthermore these states are far from E_F and the energy dependence of the pseudopotential has not been taken explicitly into account.

The largest differences between the experimental and theoretical spectra are found in ZnSe. Here the XPS spectrum shows that the

Table I. Energies of characteristic features in the valence band spectra of Ge, GaAs, and ZnSe. The theoretical entries are taken from the density of states calculations after appropriate broadening.

	Ge		GaAs		ZnSe	
	Expt. ^a (eV)	Theory ^b (eV)	Expt. ^a (eV)	Theory ^b (eV)	Expt. ^a (eV)	Theory ^b (eV)
X ₄	2.4	2.4	2.4	2.4	3.0	3.0
W ₂	3.6	3.5	3.9	3.4	--	--
V ^c	4.9	4.5	5.1	4.6	5.2	4.6
L ₁	7.2	7.0	6.8	6.5	6.3	5.3
W ₁	8.6	8.6	8.9	--	--	--
L ₂ ¹	10.3	9.8	11.5	11.2	13.8	15.6
Γ ₁	13.0	12.5	13.8	12.9	14.5	16.4

^aPositions relative to gold Fermi level.

^bThe positions are normalized to the experimental values of X₄.

^cThe valley between W₂ and L₁ is arbitrarily called V.

Zn 3d-states lie higher in energy than the s-like states at the bottom of the valence band, and the "antisymmetric gap" has become larger. The agreement between theory and experiment is less satisfying than for Ge and GaAs. The widths of the theoretical peaks are smaller than the corresponding experimental widths and the theoretical energy gap between the first two valence bands is larger than the experimental energy gap. It appears that the explicit energy dependence of the pseudopotential form factors cannot be neglected for ZnSe. It is interesting to note that the introduction of an explicit energy dependence⁶ to lowest order, by using an effective mass, gives better agreement with experiment for the two peaks at the top of the valence band but leaves the antisymmetric gap almost unchanged. OPW calculations⁷ for several II-VI compounds give band structures and density of states curves very similar to EPM results.

Footnotes and References

† Condensed from LBL-1204. Published in *Phys. Rev. Letters* **29**, 1103 (1972).

* On leave from University of Bonn, Germany.

‡ Inorganic Materials Research Division; Supported in part by the National Science Foundation Grant GP 13632.

1. M. L. Cohen and V. Heine, *Solid State Phys.* **24**, 37 (1970).
2. L. Ley, S. P. Kowalczyk, R. A. Pollak, and D. A. Shirley, to be published.
3. M. L. Cohen and T. K. Bergstresser, *Phys. Rev.* **141**, 789 (1966).
4. R. L. Zucca, J. P. Walter, Y. R. Shen, and M. L. Cohen, *Solid State Comm.* **8**, 627 (1970).
5. J. P. Walter and M. L. Cohen, *Phys. Rev. B* **1**, 2661 (1970).
6. J. Chelikowsky, private communication.
7. F. Herman et al., in *Proceedings of the 1967 Int. Conf. on II-IV Semiconducting Compounds*, edited by D. G. Thomas (Benjamin, New York, 1967), p. 503.

X-RAY PHOTOEMISSION CROSS-SECTION MODULATION IN DIAMOND, SILICON, GERMANIUM, METHANE, SILANE, AND GERMANE*

R. G. Cavell,[†] S. P. Kowalczyk, L. Ley,[‡] R. A. Pollak,
B. Mills, D. A. Shirley, and W. Perry

The allotropic form of carbon, diamond, is the prototype for Group IV crystals of the diamond structure. Many calculations of the energy-band structure have been carried out,¹ yielding results that vary more widely than is the case for its congeners, silicon and germanium. Thus, it is especially desirable to determine the positions of the diamond energy bands experimentally. We report here the total valence band density-of-states spectrum of a cleaved single crystal of diamond. The spectrum was obtained by using x-ray photoemission spectroscopy (XPS) which has recently been employed to yield total valence-band spectra for silicon and germanium.² The diamond spectrum is compared with theory and with the XPS molecular orbital spectra of CH₄, SiH₄, and GeH₄.

The valence-band spectrum I'(E) after correction for inelastic losses is shown in Fig. 1. There are three peaks in I'(E) as was the case for Si and Ge,² which are also

shown in Fig. 1 for comparison. The wider spacing of I'(E) for diamond is consistent with theoretical expectations¹ and is due to the smaller lattice constant in diamond. With two atoms per unit cell and four electrons per atom, diamond has four doubly occupied valence bands, as indicated in Fig. 2. These bands produce three peaks in the density of states, $\rho(E)$, with the top two bands forming a single peak. Labeling the I'(E) peaks as I, II, and III (Fig. 2), we identify most of peak I with band 1, peak II with band 2, and peak III with bands 3 and 4.

Comparison of Figs. 1 and 2 reveals that cross-section modulation is very important in diamond, Si, and Ge. The valence-electron wave functions are of course eigenfunctions of linear momentum rather than angular momentum because of the lattice periodicity. Expansion into atomic orbitals therefore extends over the whole Hilbert space that is orthogonal to the ion cores. However —

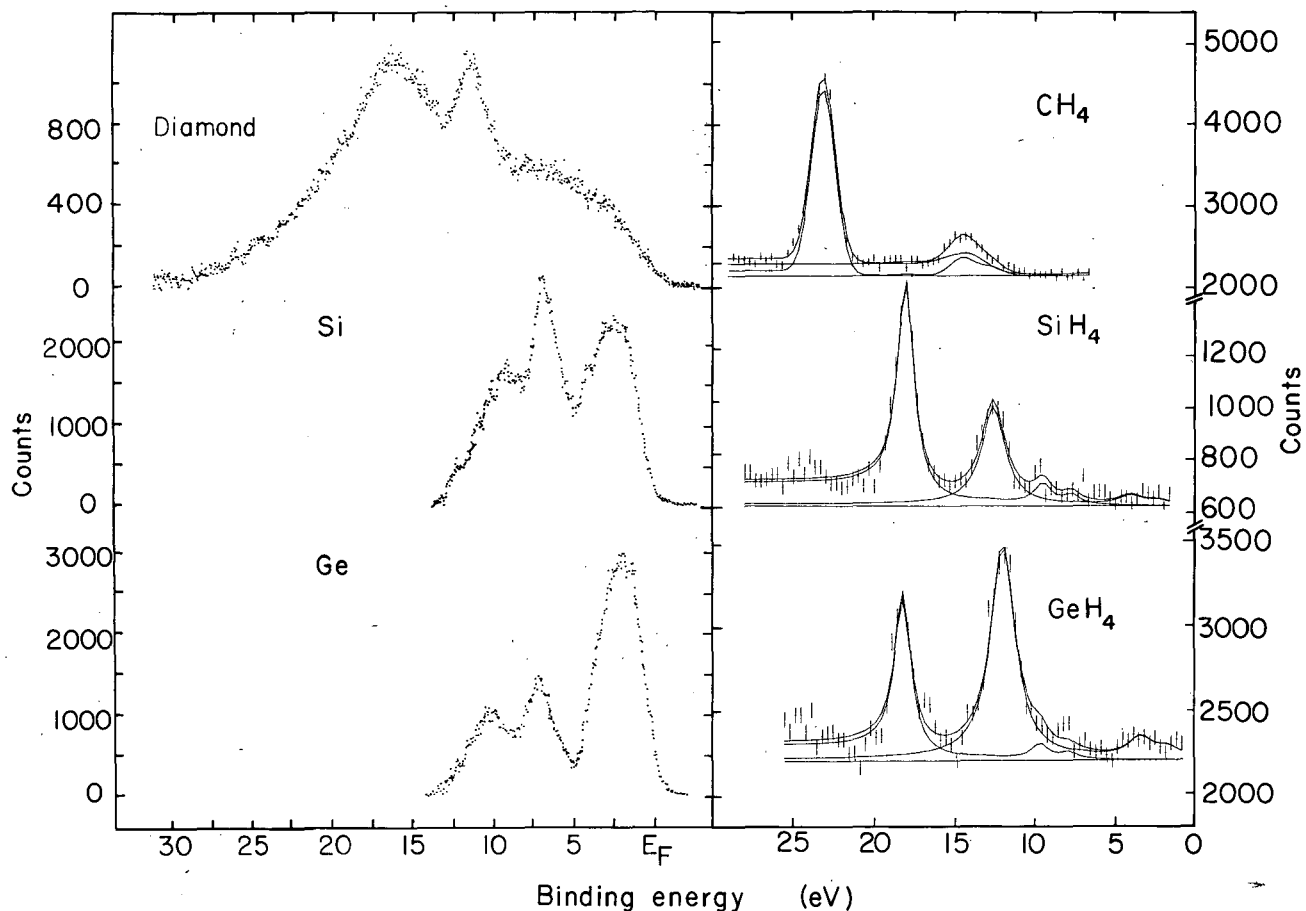


Fig. 1. (a) Corrected valence band spectra $I'(E)$ for diamond, Si, and Ge. (b) Molecular orbitals for CH_4 , SiH_4 , and GeH_4 . The $K\alpha_{3,4}$ satellites in these spectra are accounted for in the least-squares computer fit. (XBL 7211-4391)

especially near the nucleus — the largest contributions to this expansion come from the ns and np orbitals, where n is the principal quantum number of the valence electrons in C, Si, and Ge respectively. In this sense band 1 is mostly s -like and bands 3 and 4 are mostly p -like. Band 2 is a mixture of s - and p -like functions. The variation in the peak area ratio $(I + II)/III$ should therefore correspond to a similar variation in the atomic-orbital cross-section ratio $\sigma(s)/\sigma(p)$, as noted earlier for Si and Ge.

To investigate this point more quantitatively we obtained XPS spectra of the valence regions of the gaseous compounds methane (CH_4), silane (SiH_4), and germane (GeH_4) in the Berkeley iron-free spectrometer, using a $\text{Mg } K\alpha_{1,2}$ x-ray source. In all three cases the spectra (Fig. 1) exhibit two peaks which correspond to the (s -like) A_1 level and the (p -like) T_2 level.

An LCAO calculation for the three molecules yields the parentages of the two levels in terms of the atomic s and p orbitals. From these parentages and the measured peak intensities we deduced the ratios $\sigma(ns)/\sigma(np)$. These ratios show a dramatic change from C to Ge, thus accounting for the intensity variation of peaks I, II, and III in the valence band spectra of the elements. In fact the atomic ratios show more variation because the valence bands in the solids do not have pure s or p character. Even in the tight binding approach the states which make up $\rho(E)$ are mixtures of the s and p basis functions for every value of E . This mixture alone tends to equalize the cross section over the valence region. Thus cross-section modulation can slightly shift the apparent positions of characteristic features from $\rho(E)$ to $I'(E)$.

At Γ , the center of the Brillouin zone, bands 2-4 all have p character. Since they all

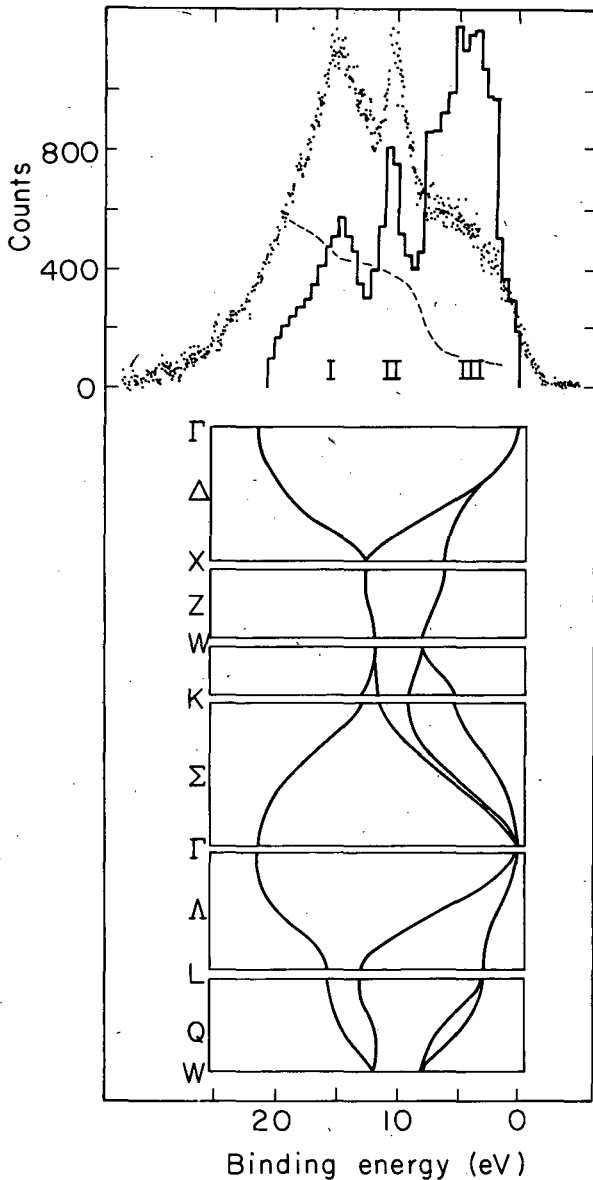


Fig. 2. Comparison of the calculated density of states (Ref. 3) with $I'(E)$ for diamond. The broken line gives the cross-section modulation as obtained by dividing $I'(E)$ into $\rho(E)$.

(XBL 7211-4364)

approach Γ_{25}' with zero slope, the density-of-states falls rather sharply at this energy — the top of the valence bands. Thus, in principle, $E(\Gamma_{25}')$ could be determined rather accurately, without ambiguity due to s, p mixing or unfavorable structure in $\rho(E)$. By extrapolating down from the steepest part of the Peak III, we obtained $E(\Gamma_{25}') = 1.8 \pm 0.3$ eV relative to $E_F(\text{Au})$, the Fermi energy of an

evaporated layer of gold.

The peaks in $I'(E)$ should fall at maxima in $\rho(E)$ with small shifts between the two sets of maxima arising from instrumental broadening of unsymmetrical peaks and from s/p mixing. The overall increase of s character with energy below E_F tends to bias $I'(E)$ downward in energy relative to $\rho(E)$. With these factors considered, we assign the positions of peak I and II as 17.9 ± 0.2 eV and 13.2 ± 0.1 eV below $E_F(\text{Au})$ respectively.

The upper portion of Fig. 2 compares the calculated $\rho(E)$ of Painter, Ellis, and Lubinsky³ with our $I'(E)$. Their band structure is shown in the lower portion of Fig. 2. Since $\rho(E)$ and $I'(E)$ show excellent agreement in the positions of all characteristic features, it is valid to deduce the variation of $\sigma(E)$ over the valence region, as indicated by the broken line in Fig. 2. This line exhibits the smooth decrease from the bottom of the valence band to its top, as expected from the discussion given above. Thus the relative intensities in photoelectron spectra can provide a valuable tool in exploring the atomic origin of different regions in the valence bands of solids.

Footnotes and References

*Condensed from LBL-1213.

† On leave from University of Alberta (1971-1972).

‡ On leave from University of Bonn, Germany.

1. Detailed references to the early literature appear in Refs. 4 and 5 below.

2. L. Ley, S. P. Kowalczyk, R. A. Pollak, and D. A. Shirley, *Phys. Rev. Letters* **29**, 1088 (1972).

3. G. S. Painter, D. E. Ellis, and A. R. Lubinsky, *Phys. Rev. B* **4**, 3610 (1971).

4. J. M. Thomas, E. L. Evans, M. Barber, and P. Swift, *Trans. Faraday Soc.* **67**, 1875 (1972).

5. T. Gora, R. Stanley, J. D. Rimstidt, and J. Sharma, *Phys. Rev. B* **5**, 2309 (1972).

NEW MULTIPLY STRUCTURE IN PHOTOEMISSION FROM MnF_2^\dagger S. P. Kowalczyk, L. Ley,* R. A. Pollak,‡
F. R. McFeely, and D. A. Shirley

Early XPS studies^{1,2} of multiplet splitting in transition metal ions established the effect but left some basic questions unanswered. In particular, for the 3s doublet in the XPS spectra of Mn^{2+} and Fe^{3+} compounds, neither the intensity ratio (2:1 rather than the multiplet ratio 7:5) nor the magnitude of the splitting was completely understood. Recent studies in which multiplet splitting has been correlated with the initial-state spin, S,^{3,4} or used to derive information about covalency,^{5,6} have emphasized the urgency of acquiring a truly quantitative understanding of the essential phenomenon.

The simplest description of the 2s and 3s XPS spectra from Mn^{2+} ($1s^2 2s^2 2p^6 3s^2 3p^3 3d^5; ^6S$) is obtained by coupling each s hole state to the valence shell. Two final states may be reached by one-electron photoemission from either the 2s or the 3s shell. These final states have 7S and 5S symmetry in each case. In the 7S states the remaining 2s or 3s electron is coupled parallel to the d-shell spin $S = 5/2$, while in the 5S states the two spins are anti-parallel. For either the 2s or the 3s case the photoemission spectral line intensities should be the multiplet ratio $^7S: ^5S = 7:5$ in this approximation, while the two components should be split by $(6/5)G^2(sd)$, according to Van Vleck's theorem.⁸ Here $G^2(sd)$ is the appropriate sd Slater exchange integral.

More careful consideration leads to several modifications of the above model. These have been covered in detail recently by Freeman, Bagus, and Mallow.⁹ First, estimates of the 5S - 7S splitting based on ground-state UHF calculations may give fortuitously good agreement with experiment because two effects of opposite sign have been omitted. A more realistic hole-state calculation increases the splitting, both because it properly couples final-state spins and because it properly couples final-state spins and because it allows the orbitals to relax properly in the hole state.⁹ Electron correlation, however, tends to reduce the splitting because the 5S state's energy is lowered more than that of the 7S state. This is true because s and 3d electrons of like spin (in the 7S state) are already relatively well correlated owing to the use of antisymmetrized wave functions in HF or UHF theory to satisfy the Pauli principle. Correlation of the motion of the antiparallel s and 3d pairs in the 5S states thus improves these states' energies more. Pressing this line of reasoning further, one might

intuitively expect better agreement between the Hartree-Fock splittings and experiment when the one-electron hole states and the magnetic shell have different principal quantum numbers. This follows because an increase in radial separation of the s and d or s and f pairs would diminish the importance of correlation between anti-parallel electrons on the multiplet splitting. Thus in rare earths the Hartree-Fock estimates of splitting should be more accurate for the 5s than the 4s shell (as observed⁴) while the 2s splitting would be predicted more accurately than the 3s splitting in the 3d ions (see below). Freeman et al.⁹ have reached the same conclusion, using configuration-interaction arguments.

Going beyond Hartree-Fock estimates, Sasaki and Bagus⁷ made configuration-interaction calculations on the Mn^{3+} ($3s^1 3p^6 (3d^5; ^6S)$) states. They found that 5S states formed from the configuration $3s^2 3p^4 3d^6$ were very important. They were able to make three predictions that could be experimentally tested. First, the 7S - 5S splitting was reduced to 4.7 eV (or to 7.8 eV if semi-internal correlations were also considered), in reasonable agreement with the experimental value of 6.62 eV (see Table I). Second, the intensity ratio of these two peaks is correctly predicted as 2.2:1, thereby clearing up a vexing anomaly.

The third prediction, which is tested for the first time is that 5S satellite peaks should appear in the spectrum. These satellites may be understood by writing the seven (or more if semi-internal correlations are considered) eigenstates of 5S symmetry as

$$|\psi_i\rangle = C_{i1} |3s^1 3p^6 3d^5\rangle + \sum_{j=2}^7 C_{ij} |\phi_j\rangle,$$

where $i=1, 2, \dots, 7$, and $|\phi_j\rangle$ represents the j th admixed configuration. Since the intensity of a 3s-photoemission line from the $(3s^2 3p^6 3d^5; ^6S)$ ground state is proportional, for one-electron transition, to $|C_{i1}|^2$ (neglecting small deviations from unity of the overlap between the initial and final state passive electron), it follows that the intensity lost from the main 5S line, viz. $1 - |C_{i1}|^2$, must appear at eigenenergies E_j of the states $|\psi_i\rangle$. In this way Sasaki and Bagus predicted peaks at ~ 25 eV and ~ 43 eV relative to the 7S peak position, with the first,

more intense, peak arising from two neighboring eigenstates. Our spectra (Fig. 1) confirm this prediction very nicely. We identify these satellites with the observed peaks at 20.7 and 37.8 eV below the 7S peak. Furthermore, the ratio of the intensity of the septet peak to the sum of the intensities of the quintet peaks, 1.3 ± 0.2 , compares well with the value 1.4 expected from multiplicity considerations. A detailed comparison is made in Table I.

The 2s line (Fig. 2) shows doublet structure, as expected. Both the splitting and the relative intensity are in very good agreement with the predictions of multiplet hole theory (Table I): thus the 2s hole state 7S - 5S splitting is not strongly reduced by correlation and the 7S : 5S ratio is very nearly the multiplicity ratio.

The hole structure for Mn^{3+} ($\overline{2s}$ or $\overline{3s}$) final states is now quantitatively understood; theory and experiment show good agreement in splitting, relative intensity, and satellite structure. The complexity of the 3s spectrum precludes the quantitative validity of simplistic correlations of 3s splitting with total spin or covalent character (at least without further analysis), although qualitative trends of this nature have already been observed.

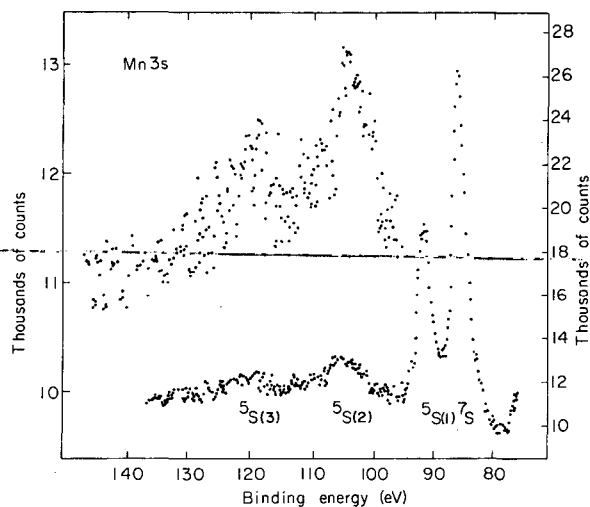


Fig. 1. The manganese 3s spectrum with the energy scale referenced to the Au $4f_{7/2}$ (84.00 ± 0.01 eV) peak. The right ordinate refers to the complete spectrum and the left ordinate refers to the expanded portion of the spectrum. (XBL 7210-4224)

Table I. Summary of the Mn 3s and 2s photoelectron results and comparison with theoretical predictions.

Manganese 3s final state	Binding Energies (eV)*					Intensity Ratios†				
	7S	${}^5S(1)$	${}^5S(2)$	${}^5S(3)$	${}^7S/{}^5S(1)$	${}^5S(1)/{}^5S(2)^\ddagger$	${}^5S(2)/{}^5S(3)^\ddagger$	${}^5S(1)/{}^5S(2')^\ddagger$	${}^5S(2')/{}^5S(2'')^\ddagger$	
Experiment	0.00	6.62 ± 0.01	20.7 ± 0.1	37.8 ± 0.7	2.3 ± 0.1	2.1 ± 0.1	2.5 ± 0.1	--	--	
Theory ‡										
1. Freeman, Bagus, and Mallow (MHT) ⁹	0.00	14.3	--	--	1.4	--	--	--	--	
2. Sasaki and Bagus (CI) ⁷	0.00	4.71	$\left. \begin{matrix} 22.53 \\ 23.75 \end{matrix} \right\}$	43.06	--	2.87	1.58	3.58	4.00	
3. Sasaki and Bagus (CI) ⁷	0.00	7.83	$\left. \begin{matrix} 25.19 \\ 27.58 \end{matrix} \right\}$	--	2.2	4.1	--	4.48	4.47	
Manganese 2s final state			7S		5S		${}^7S/{}^5S$			
Experiment			0.00		5.85 ± 0.05		1.4 ± 0.1			
Theory Freeman, Bagus, and Mallow (MHT) ⁹			0.00		6.10		1.4			

*The binding energies are given relative to the 7S peak and are the result of analytically least squares fitting the experimental spectrum with Lorentzian lineshapes. The Mn 3s results are the average of two runs on different single crystals.

†The intensity ratios for the Mn 3s peaks were arrived at by measuring the areas of the peaks with a planimeter. The Mn 2s ratios were result of areas derived from a least squares fit to Lorentzian peak shape.

‡ ${}^5S(2)$ refers to the total intensity due to two neighboring theoretical eigenstates (which could not be experimentally resolved), while ${}^5S(2')$ and ${}^5S(2'')$ refer to respectively the intensity due to the first and the second of the two neighboring eigenstates.

§Theory 1 is a multiplet hole theory - optimized orbital calculation. Theories 2 and 3 are configuration-interaction calculations. Theory 2 takes only internal correlations into account, while theory 3 also includes semi-internal correlations.

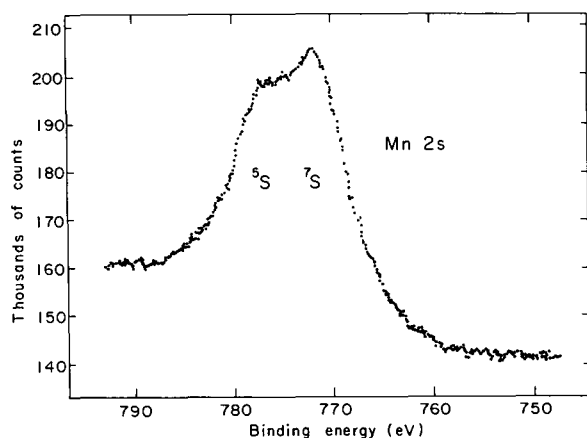


Fig. 2. The manganese 2s spectrum with the energy scale referenced to the Au $4f_{7/2}$ (84.00 ± 0.01 eV) peak. (XBL 7210-4221)

One of us (L. L.) would like to thank the Max-Kade Foundation for a grant. We greatly appreciate gifts of MnF_2 single crystals from Dr. Robert Feigelson and from Dr. Herbert Rinneberg.

Footnotes and References

† Condensed from LBL-1275.

* On leave from University of Bonn, Germany.

‡ Present address: IBM, Thomas J. Watson Research Center, Yorktown Heights, N. Y.

1. C. S. Fadley, D. A. Shirley, A. J. Freeman, P. S. Bagus, and V. J. Mallow, *Phys. Rev. Letters* **23**, 1397 (1969).
2. C. S. Fadley and D. A. Shirley, *Phys. Rev. A* **2**, 1109 (1970).
3. The correlation of observed 3s peak splitting with S was first made by T. Novakov in the Uppsala EUCHEN Conference, September 1970.
4. R. L. Cohen, G. K. Wertheim, A. Rosencwaig, and H. J. Guggenheim, *Phys. Rev. B* **5**, 1037 (1972).
5. D. T. Clark and D. B. Adams, *Chem. Phys. Letters* **10**, 121 (1971).
6. J. C. Carver, G. K. Schweitzer, and T. A. Carlson, *J. Chem. Phys.* **57**, 973 (1972).
7. F. Sasaki and P. S. Bagus, submitted to *Physical Review*.
8. J. W. Van Vleck, *Phys. Rev.* **45**, 405 (1934).
9. A. J. Freeman, P. S. Bagus, and J. V. Mallow, *Multiplet Hole Theory of Core Electron Binding Energies in Transition Metal Ions*, to be published).

EVIDENCE FOR COVALENT BONDING IN CRYSTALLINE AND AMORPHOUS As, Sb, AND Bi FROM VALENCE BAND PHOTOELECTRON SPECTRA

L. Ley,* R. A. Pollak, S. P. Kowalczyk, R. McFeely, and D. A. Shirley

Weaire and Thorpe have used the concept of topological disorder in attempting to understand the properties of amorphous semiconductors.¹ They used model Hamiltonians of the tight binding type to calculate the density of states in crystals of the diamond structure, and obtained the characteristic splitting in the lowest, "s-like" peaks in the valence bands by using these Hamiltonians. They emphasized the importance of six-membered rings in the diamond structure, and suggested that a random-network amorphous structure, with both fivefold and sixfold rings, would not exhibit well-resolved splitting in the s-like peak.

The form of Weaire and Thorpe's one-band Hamiltonian may be interpreted as implying

splitting in the s-like peak in a broader context than the diamond lattice, and loss of this splitting in the amorphous state. XPS spectra on crystalline and amorphous As, Sb, and Bi show exactly this behavior.

Monocrystalline samples of As, Sb, and Bi were cleaved in a dry N_2 atmosphere immediately prior to insertion into the Hewlett-Packard 5950A ESCA spectrometer. Small amounts of oxygen on the Sb and Bi samples were easily removed by gentle (200 eV, 10 μ amp) argon-ion bombardment.

The uncorrected photoelectron spectra $I(E)$ of the valence-band regions of crystalline As, Sb, and Bi are shown on the left side of Fig. 1

Table I. Energies of characteristic features in the XPS spectra of crystalline As, Sb, and Bi.

	As		Sb		Bi
Bottom of VB	16.1 ± 0.3 eV	Bottom of VB	11.7 ± 0.3 eV	Bottom of VB	13.4 ± 0.2 eV
1	13.26 ± 0.10	1	10.45 ± 0.08	1	11.54 ± 0.10
2	10.64 ± 0.08	2	8.78 ± 0.06	2	10.36 ± 0.08
3	3.53 ± 0.06	3'	3.68 ± 0.20	3	3.45 ± 0.05
3'	2.51 ± 0.13	3	2.63 ± 0.09	4	1.30 ± 0.06
E_F	0.0	4	1.87 ± 0.08	E_F	0.0
		4'	0.82 ± 0.06		
		E_F	0.0		

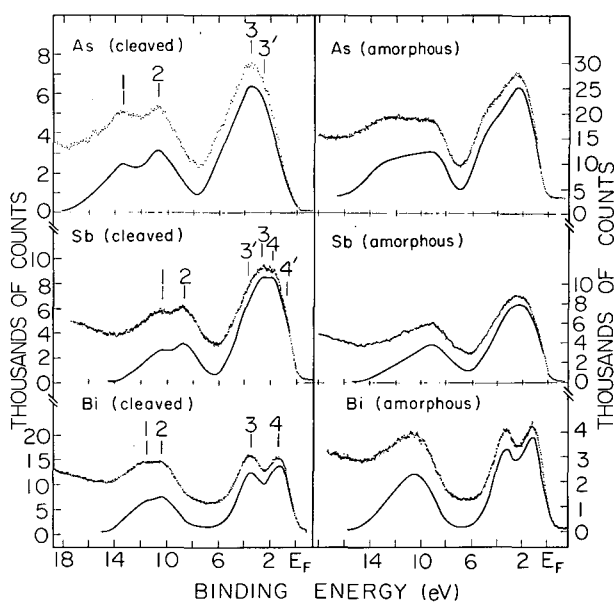


Fig. 1. Uncorrected (dots) and corrected (line) photoelectron spectra of the crystalline and amorphous semimetals. (XBL 729-4052)

together with spectra I' (E), which are corrected for inelastic secondary processes in the electron spectrum.

Also shown in Fig. 1 are the measured $I(E)$ and $I'(E)$ for amorphous samples of As, Sb, and Bi. Amorphous As was prepared in the spectrometer by flash evaporation of a thin film onto a gold substrate at room temperature. The amorphous Sb and Bi samples were prepared

by argon-bombarding single crystal surfaces for about 30 minutes with $10 \mu\text{amp}$ of 900 eV Ar^+ ions. Earlier experience² with Si and Ge yielded essentially identical "amorphous" spectra for evaporated films and argon-bombarded crystals.

The overall similarity of the XPS spectra in Fig. 1 reflects the similarities of electronic configuration ($s^2 p^3$) and, for the crystalline samples of crystal structure (A7 in each case) in these Group V elements. There are two atoms per unit cell in the A7 structure, with ten electrons filling five valence bands. Theoretical band-structure calculations show two reasonably well-separated s-like bands several eV below the Fermi level E_F , and three p-like bands near E_F . We assign the lower peak (labeled 1-2 in Fig. 1) to the former and the upper peak (3-4 in Fig. 1) to the latter.

Moving down from As to Bi, changes in the structure of the p-like peak arise dominantly from relativistic effects rather than from crystal-field in Sb. The splitting increases to 2.2 eV in Bi. It has been shown for ^{14}Bi that this splitting can be identified with the effect of spin-orbit interaction on the p-like bands near the center of the Brillouin zone (Γ). The relativistic Hartree-Fock-Slater free-atom value⁴ of 2.16 eV for the 6p spin-orbit splitting in Bi corresponds closely to the observed splitting in the p-like band. The measured value for Sb of 0.76(8) eV compares equally well with the calculated 5p free-atom value of 0.71 eV.

Turning now to the s-like bands, we observe for the first time a pronounced splitting of the s-peak (1-2 in Fig. 1) in the densities of states of all three Group V semimetals As, Sb, and Bi.

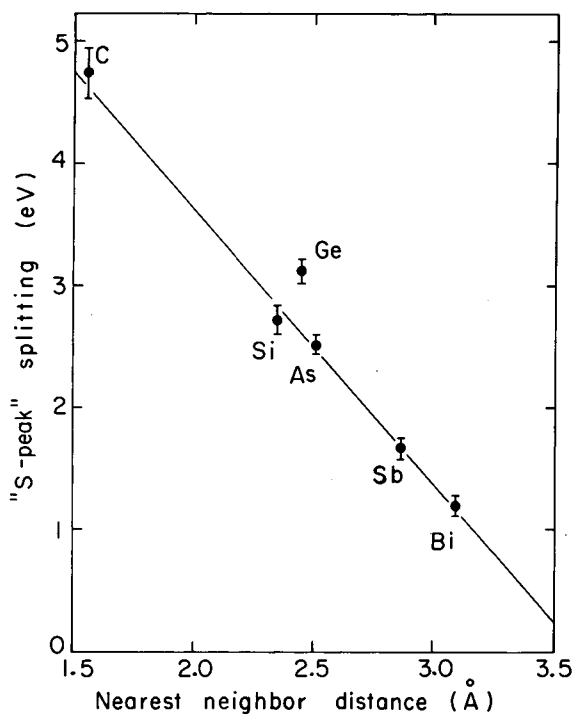


Fig. 2. Plot of the s-band splitting versus the nearest-neighbor distance for covalently bonded elements. (XBL 7210-4340)

Table II. Comparison of the observed s-band splitting with the calculated separation of these bands at Points T_1 and T_2 in the Brillouin zone.

As			
Exp.	TB	EPM	SCF OPW
2.62 ± 0.08 eV	2.90 eV	2.83 eV	3.27 eV
Sb			
Exp.		EPM	
1.67 ± 0.06 eV		1.71	
Bi			
Exp.	EPM	APW	
1.18 ± 0.08 eV	1.78	1.29 eV	

This splitting decreases from 2.62(8) eV in As to 1.67(6) eV in Sb to 1.18(8) eV in Bi (see Table II). A parallel decrease in width (FWHM) of this peak from 5.2(2) to 4.6(2) to 4.0(1) eV is also evident.

The density-of-states results for amorphous As, Sb, and Bi are significantly different from those of the respective crystalline modifications. The s-bands do not exhibit double-peaked structure and there is much less structure in the p-like bands in As and Sb, while the spin-orbit splitting in Bi is essentially the same. In all three cases the maximum in the density of states is shifted toward the Fermi energy by a few tenths of an electron volt. This shift gives for the amorphous state under study a direct measure of the deviation of the sample from its ground equilibrium state. The replacement of peaks 1 and 2 in the crystalline samples by a single peak in the amorphous spectra is caused by a redistribution in the density of states rather than simply by broadening of the two peaks. This is especially true in Sb and Bi. As evidence for this we note that the total widths of the s-band peaks as well as the valley between the s- and p-bands remain essentially the same in going from the crystalline to the amorphous material.

The startling agreement between these observations and those made earlier² for the prototypical covalent crystals Si and Ge suggests an interpretation of the semimetal spectra along similar lines. The distortions which lead from the diamond fcc lattice to the A7 lattice of As, Sb, and Bi obviously do not destroy the main features in the density of states. It has been pointed out that the existence of sixfold rings in the diamond structure is crucial for the preservation of well-separated s-bands (peaks 1 and 2) in the density of valence band states which correspond to the bonding and anti-bonding s-levels of covalently bonded atoms.^{1,5} In As, Sb, and Bi the lattice is composed of layers normal to the trigonal axis. There are three weak bonds per atom between layers, and within a layer there are three stronger bonds which produce a two-dimensional array of distorted hexagonal rings.⁶ We therefore interpret the XPS spectra of As, Sb, and Bi as extending the generality of the "odd-even" ring effect on the valence bands. Apparently s-peak splitting is present in these covalently-bonded A7-lattice crystals because of the even-numbered rings, while the odd-numbered rings that presumably are present in the amorphous materials preclude resolution of these peaks into two simple components.

Finally, the observed splitting in the valence band s peaks of the covalent Groups IV and V elements C(diamond), Si, Ge, As, Sb, and Bi are related in a very simple way. When plotted

against nearest-neighbor distance d , these splittings follow a universal curve given by

$$\Delta E(\text{eV}) = 8.0 - 2.2 \times d(\text{\AA}),$$

as shown in Fig. 2. That ΔE should follow such a simple equation is somewhat surprising, because differences in coordination and hybridization might be expected to play a larger role. Apparently the effect of overlap, which of course decreases strongly with distance, is dominant. With further study it may be feasible to give a detailed explanation for the variation of ΔE . Meanwhile the observed ΔE versus d relation can serve as a covalent reference point in establishing an experimental ionicity scale based on valence-band spectra.

Footnote and References

*Max-Kade Foundation fellow on leave from University of Bonn, Germany.

1. D. Weaire and M. F. Thorpe, in Computational Methods for Large Molecules and Localized States in Solids, edited by F. Hermann, A. D. McLean, and R. K. Nesbet (Plenum Press, New York, 1972).
2. L. Ley, S. P. Kowalczyk, R. A. Pollak, and D. A. Shirley, *Phys. Rev. Letters* **29**, 1088 (1972).
3. L. Ley, R. A. Pollak, S. P. Kowalczyk, and D. A. Shirley, *Phys. Letters* **41A**, 429 (1972).
4. C. C. Lu, T. A. Carlson, F. B. Malik, T. C. Tucker, and C. W. Nestor, Jr., *Atomic Data* **3**, 1 (1971).
5. J. D. Joannopoulos and M. L. Cohen, *Phys. Rev.*, in press.
6. J. L. Yarnell, J. L. Warren, R. G. Wenzel, and S. H. Koenig, *IBM J. Res. Develop.* **8**, 234 (1964).

HIGH-RESOLUTION X-RAY PHOTOEMISSION SPECTRA OF PbS, PbSe, AND PbTe VALENCE BANDS

F. R. McFeely, S. P. Kowalczyk, L. Ley, *R. A. Pollak, and D. A. Shirley

The "lead salts," PbS, PbSe, and PbTe, have in recent years been the object of considerable experimental and theoretical study. In this work, x-ray photoemission spectroscopy (XPS) has been used to determine the valence-band density of states for each of the lead salts. Derived quantities are compared with several theoretical band structure calculations, which are critically examined in light of these results.

The sample used for these experiments were high-purity single crystals. In order to minimize contamination of the samples by adsorption of hydrocarbons and/or oxygen, the crystals were cleaved under dry nitrogen in a glove bag and placed in a Hewlett-Packard 5950A electron spectrometer at 5×10^{-9} Torr without exposure to the atmosphere. In-situ monitoring of the carbon and oxygen 1s levels indicated that the samples were not significantly contaminated.

The spectra $I(E)$ for each of the three lead salts are shown in Fig. 1. There is striking similarity in the valence-band spectra of the three salts. The positions of the core-like Pb 5d_{5/2} peaks for these salts vary within a

range of 0.2 eV and the values of the spin-orbit splitting in the Pb 5d peaks are identical to within experimental error (0.02 eV). The spectra show in each case a strong broad peak, which we call peak 1, centered at about 2-2.5 eV below E_F , and exhibiting quite prominent structure on the low-binding-energy side. This structure is evident only as a shoulder in PbTe, but in progressing through PbSe to PbS it becomes a well-defined extra peak which we label 1'. Between the (1-1') peak and the Pb 5d lines there are two less intense peaks labeled 2 and 3 in Fig. 1. The absolute binding energies of these peaks show no monotonic trend with the atomic number of the Group VI element. Peaks 2 and 3 have the highest binding energies in PbSe. However, the energy difference between peaks 2 and 3 increases monotonically in going from the telluride to the sulfide. The 3-2 splitting is 3.5 eV in the telluride, 4.3 eV in the selenide, and 4.4 in the sulfide.

These IV-VI compounds have a total of ten valence electrons per Pb atom, which must occupy five valence bands. In light of many recent band structure calculations, the (1-1') peak structure of the photoelectron spectra in

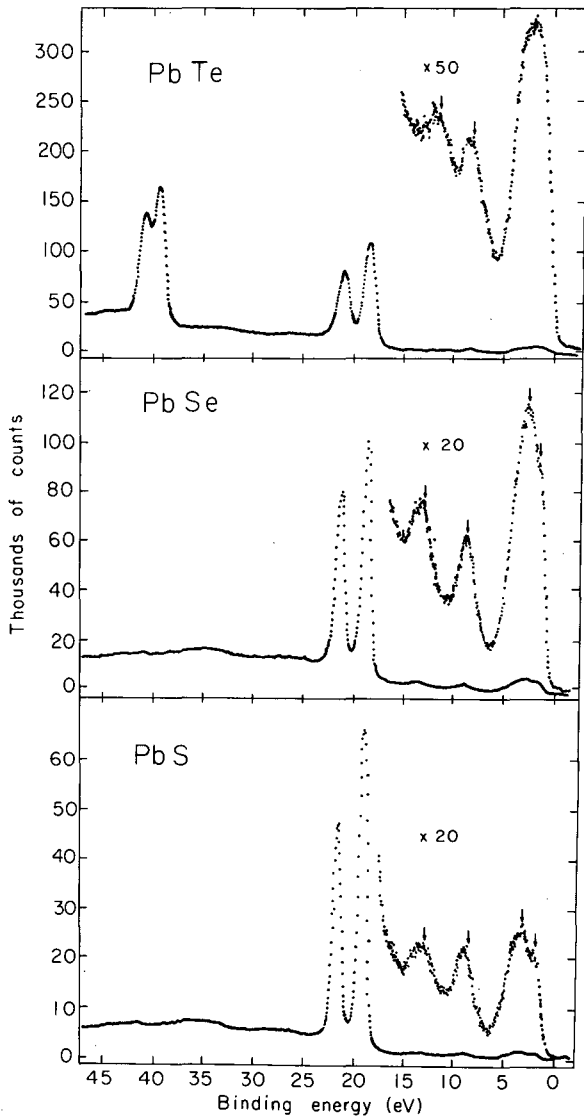


Fig. 1. Raw valence band spectra of the lead salts; the strong double peaks at ~ 20 eV are the lead $5d_{3/2}$ and $5d_{5/2}$ levels; the tellurium $4d$ are at about 40 eV binding energy. (XBL 7210-4157)

all three lead salts may be unequivocally identified with three p-like bands. At the Γ point, two of these bands are degenerate and have Γ_8^- symmetry, while the third band has Γ_6^- symmetry. Calculations of the band structure by the EPM,^{1,2,3} OPW,⁴ and relativistic APW^{5,6} methods give qualitative agreement on this point.

While there is reasonable agreement on the positions of the three p-like bands and the corresponding maxima in the densities of states,

agreement among theoretical predictions of the two lower-lying peaks (2 and 3) is much poorer. Clearly these peaks can only represent the two s-like (Γ_6^+) bands arising from the $6s$ level of Pb and the highest s-level of the Group VI atom. The assignment of the spectra therefore appears to be completely straightforward. The 1-1' complex arises from the top three "p-like" bands and peaks 2 and 3 each arise from an "s-like" band.

In comparing the spectra with theoretical calculations, the one-electron transition model⁷ and Koopmans' theorem⁸ were used. It must be emphasized that disagreement between theory and experiment could result from the inapplicability of either of these assumptions.

In light of our spectra it appears that only the relativistic KKR band structure of Overhof and Rössler⁹ is qualitatively wrong. Relativistic APW calculations put all the bands in about the right places but exhibit some disagreement in the positions of the s-like bands.

Tung and Cohen² and Tsang and Cohen³ have calculated the band structures for PbTe and for PbSe and PbS respectively, using the Empirical Pseudopotential Method (EPM). In these calculations spin-orbit interaction was included but other relativistic effects were not. In addition to band structures, the resulting densities-of-states curves were calculated.

The results of these calculations, shown in Fig. 2, match the experimental results for the p-like peak(s). Particularly striking is the way in which the calculation shows the

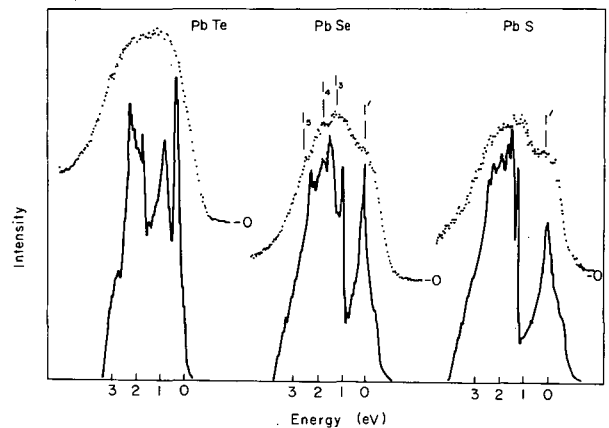


Fig. 2. EPM densities of states^{5,6} compared with the shape of the (1-1') peaks in the valence bands of the lead salts (relative energy scale). (XBL 7210-4158)

Table I. Calculations of Herman et al.⁴ compared with experiment.

	PbS		PbSe		PbTe	
	OPW	Expt.	OPW	Expt.	OPW	Expt.
Peak 1	2.6	2.5	~2.6	2.2	~2.0	2.3
Peak 2	6.6	8.4	7.4	8.6	7.4	8.4
Peak 3	14.0	12.8	14.0	12.9	11.5	11.7

origin of the 1' peak out of the 1 peak in progressing from PbTe to PbS. The position indicated for the highest s-band (not shown) is also reasonable though not exactly correct.

The major disagreement of this calculation with experiment lies in the predicted energy of the lowest s-peak (not shown in the density of states curve). This level is predicted to lie at 17 eV in PbTe, 24.5 in PbSe, and 27.5 in PbS. This discrepancy is not unexpected, because a local pseudopotential was used. In the case of ZnSe,¹⁰ a local pseudopotential was shown to be inadequate for the lowest bands. Thus the nonlocal nature of the pseudopotential should be considered when calculating these bands.

The most successful band structure calculation was undertaken by Herman et al.⁴ In this calculation the OPW method, with relativistic effects included directly in the Hamiltonian, was used to calculate the energy levels at certain symmetry points in the Brillouin zone. A pseudopotential technique was then used to connect the regions between the symmetry points. The resulting band structures were not fitted to any experimental data. The results for PbTe, PbSe, and PbS are shown in Table I. While the predicted binding energy for Peak 2 in PbS and PbSe is lower than observed (as in the case in all the band structures), the results for PbTe agrees very well with experiment.

It is evident from the agreement shown in Fig. 2 and Table I that the EPM and OPW band structures are of high quality. We therefore attempted to correlate the features in our spectra with the energies of various symmetry points in the band structures. The agreement even at this level was encouraging, the most striking correlation being the evolution of the 1' peak in PbSe and PbS owing to the lowering

in energy of the high density of states region near L, as shown in both the EPM and OPW band structures.

Footnotes and References

* Max-Kade Foundation fellow on leave from University of Bonn, Germany.

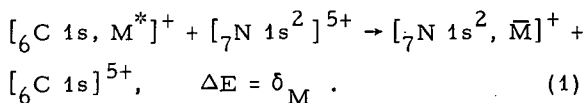
1. P. J. Lin and L. Kleinman, *Phys. Rev.* **142**, 478 (1966).
2. Y. W. Tung and M. L. Cohen, *Phys. Rev.* **180**, 823 (1969).
3. Y. W. Tsang and M. L. Cohen, to be published.
4. F. Herman, R. L. Kortum, I. B. Outenburger, and J. P. Van Dyke, *J. de Physique* **29**, C4-62 (1968).
5. J. B. Conklin, Jr., L. E. Johnson, and G. W. Pratt, Jr., *Phys. Rev.* **137**, 478 (1966).
6. S. Rabii, *Phys. Rev.* **167**, 801 (1968); **173**, 918 (1968).
7. C. S. Fadley and D. A. Shirley, in *Electronic Density of States*, National Bureau of Standards special publication No. 323, 163 (1971).
8. F. Herman, I. B. Outenburger, and J. P. Van Dyke, *Intern. J. Quantum Chem.* **III S**, 82 (1963).
9. H. Overhof and U. Rössler, *Phys. Stat. Solidi* **37**, 691 (1970).
10. R. A. Pollak, L. Ley, S. P. Kowalczyk, D. A. Shirley, J. D. Joannopoulos, D. Chadi, and M. L. Cohen, *Phys. Rev. Letters* **29**, 1103 (1972).

NEAR-EQUIVALENCE OF THE QUANTUM MECHANICAL POTENTIAL
MODEL AND THE THERMOCHEMICAL MODEL OF ESCA SHIFTS

D. A. Shirley

Shifts in core-electron binding energies (ESCA shifts) are closely connected to charge distributions in molecules, and are therefore of considerable value in elucidating chemical structures. Because of this fundamental connection, ESCA shifts can be correlated with almost any chemical parameter that varies systematically through a series of molecules. It is sometimes useful to compare two or more types of correlation in detail. In this work we demonstrate the near-equivalence of the potential model and the thermochemical model, both of which have been eminently successful in predicting ESCA shifts.

Variations in the electrostatic potential experienced by core electrons play a major role in ESCA shifts. The potential model has been early and extensive application in explaining these shifts. Basch¹ and Schwartz² independently discussed the basic of the model. Jolly and co-workers³⁻⁶ introduced a "thermochemical model" which allows the prediction of ESCA shifts from thermodynamic data on molecules and ions in their ground states. The model was derived by combining a series of reactions for each compound. All the reactions except one were empirical; therefore their energies could be added rigorously. This one reaction was a hypothetical "core-exchange" reaction, which was necessary to get rid of the core electron hole in each compound. It would have the form



Here a charge 5+ core, consisting of a carbon nucleus plus a single 1s electron in the excited 1s hole state M^* produced by photoemission of a C 1s electron from the molecule M is replaced by another core of the same charge, i. e., a N^{5+} ion in its ground state. This exchange of equivalent cores yields a hydrogenic C^{5+} core plus the molecule-ion \bar{M} in its ground state. If M^* is the hole state of CH_4^+ formed by ejection of a C 1s electron from methane, for example, then \bar{M} would be the NH_4^+ ion in its ground state.

We can calculate the energy δ_M of the core-exchange reactions from the total energies of each of the four species involved: $E(\bar{M})$, $E(M^*)$, $E(\text{C } 1s, 5+)$, and $E(\text{N } 1s^2, 5+)$. Let us consider $E(\bar{M})$ first. It is convenient to express this energy in terms of Hartree-Fock integrals. Interactions between any two particles in orbitals outside the $N 1s^2$ core will be negligibly affected by core exchange. Because they will ultimately cancel out in evaluating δ_M , these integrals will be noted collectively as "(other integrals)" rather than being displayed explicitly. We can write, in standard Hartree-Fock notation,

$$\begin{aligned} E(\bar{M}) = & 2\epsilon_0(N 1s, \bar{M}) + J(N 1s, N 1s)\bar{M} \\ & + 2 \sum_{i \neq 1s}^n \left[2J(N 1s, i) - K(N 1s, i) \right] \\ & - 2 \sum_{m \neq N} Z_m \langle N 1s(1) | r_{1m}^{-1} | N 1s(1) \rangle \\ & - 2 \sum_{i \neq 1s}^n Z_N \langle \phi_i(1) | r_{1N}^{-1} | \phi_i(1) \rangle \\ & + \sum_{m \neq N} \frac{Z_m Z_N}{R_{mN}} + (\text{other integrals}). \quad (2) \end{aligned}$$

Writing similar expressions for the other three species in Eq. (2), are combining, we obtain

$$\left. \begin{aligned} \Delta E = & 2\epsilon_0(N 1s, \bar{M}) - 2\epsilon_0(N 1s) \\ & + \epsilon_0(\text{C } 1s) - \epsilon_0(\text{C } 1s, M^*) \\ & + J(N 1s, N 1s)\bar{M} - J(N 1s, N 1s) \end{aligned} \right\} I$$

$$\begin{aligned}
& + \left. \begin{aligned} & \sum_{\substack{i \neq N \text{ 1s} \\ \text{(or C 1s)}}} \left\{ \begin{aligned} & 2[2J(N \text{ 1s}, i) - K(N \text{ 1s}, i)] \\ & - [2J(C \text{ 1s}, i) - K(C \text{ 1s}, i)] \\ & + 2Z_C \langle \phi_i(1) | r_{1C}^{-1} | \phi_i(1) \rangle \\ & - 2Z_N \langle \phi_i(1) | r_{1N}^{-1} | \phi_i(1) \rangle \end{aligned} \right\} \\ & \end{aligned} \right\} \text{II} \\
& + \left. \begin{aligned} & \sum_{\substack{m \neq N \\ \text{(or C)}}} Z_m \left[\begin{aligned} & \frac{Z_N}{R_{mN}} - \frac{Z_C}{R_{mC}} \\ & - 2 \langle N \text{ 1s} | r_{1m}^{-1} | N \text{ 1s} \rangle \\ & + \langle C \text{ 1s} | r_{1m}^{-1} | C \text{ 1s} \rangle \end{aligned} \right] \\ & \end{aligned} \right\} \text{III} \\
& \quad \quad \quad (3)
\end{aligned}$$

Here we have used the fact that the "other integrals" cancel between \bar{M} and M^* . By straightforward arguments terms I and III can be shown to be negligible. Using the good approximations

$$\begin{aligned}
\langle \phi_i(1) | r_{iN}^{-1} | \phi_i(1) \rangle & \approx \langle \phi_i(1) | r_{iC}^{-1} | \phi_i(1) \rangle, \\
J(N \text{ 1s}, i) & \approx J(C \text{ 1s}, i), \\
K(N \text{ 1s}, i) & \approx K(C \text{ 1s}, i),
\end{aligned}$$

term II reduces to a residue

$$\begin{aligned}
R = & \sum_{\substack{\text{local} \\ i \neq N \text{ 1s} \\ \text{(or C 1s)}}} \left[\begin{aligned} & 2J(N \text{ 1s}, i) - K(N \text{ 1s}, i) \\ & - 2 \langle \phi_i(1) | r_{1N}^{-1} | \phi_i(1) \rangle \end{aligned} \right]. \quad (4)
\end{aligned}$$

This expression for R is equivalent to the difference between two sums considered by Schwartz. In demonstrating the near-equivalence of these two sums, and especially of their variation from one compound to another, Schwartz performed the crucial step in establishing the validity of the potential model of core-level binding-energy shifts. By showing that R is the most important contributor to δ_M , we have now derived the result that

the thermochemical model and the potential model represent the same level of approximation, with the validity of both hinging on the near-constancy of a residue of the form given by Eq. (4) from one compound to another.

We can use Schwartz's numerical results to estimate the approximate size of δ for a typical core-exchange reaction. Using his integrals for methane, we find

$$\begin{aligned}
& \sum_{i=\text{loc}} \left[(2J_{1si} - K_{1si}) \right. \\
& \left. - 2 \langle L_i(1) | 1/r_{1n} | L_i(1) \rangle \right] = 0.2228 \text{ a. u.} \\
& \quad \quad \quad = 6.0 \text{ eV}.
\end{aligned}$$

This should be a reasonable estimate of R , and thus of δ , for the corresponding core-exchange reaction. Thus δ is too large to be neglected. However, the same combination of integrals for CH_3F gives an estimate of $\delta \approx 5.9 \text{ eV}$ for this molecule, indicating the constancy of δ from one molecule to another. Thus the thermochemical model is valid in its "weak" form $\delta \approx \text{constant}$, but not in the "strong" form $\delta \approx 0$.

The following conclusions follow from this discussion:

1. Given identical geometries in the initial molecules M and the comparison ion \bar{M} , the thermochemical model has essentially the same validity as the potential model, with each depending on the invariance of a residue R of the form given in Eq. (4).

2. The thermochemical model has the conceptual advantage of dealing with final states, wherein the passive orbitals are relaxed. The potential model as originally conceived deals with initial states only, although it can be extended to account for relaxation.

3. The thermochemical model can be generalized. For cases in which thermochemical data are unreliable or unavailable, or in which the molecular geometries of the ground-state molecule M and the comparison ion \bar{M} differ, total internal energies from Hartree-Fock calculations on \bar{M} (with bond distances and angles constrained to be those on M) can be used in place of thermochemical data. It might also be desirable to use the equivalent-cores concept, together with Hartree-Fock ground-state energies of equivalent ions \bar{M} in their ground states to calculate core-level binding-energy shifts for cases in which hole-state calculations were in doubt because hole

states are not protected by the Variation Principle.

Footnote and References

* Condensed from LBL-653. Published in Chem. Phys. Letters 15, 325 (1972).

1. H. Basch, Chem. Phys. Letters 5, 337 (1970).
2. M. E. Schwartz, Chem. Phys. Letters 6, 631 (1970).

3. W. L. Jolly and D. N. Hendrickson, J. Am. Chem. Soc. 1863 (1970).

4. J. M. Hollander and W. L. Jolly, Accounts Chem. Research 3, 193 (1970).

5. P. Finn, R. K. Pearson, J. M. Hollander, and W. L. Jolly, Inorg. Chem. 10, 378 (1971).

6. W. L. Jolly, in Electron Spectroscopy, edited by D. A. Shirley (North-Holland, Amsterdam, 1972), p. 629.

A RELAXATION CORRECTION TO CORE-LEVEL BINDING-ENERGY SHIFTS IN SMALL MOLECULES*

D. W. Davis and D. A. Shirley

Core level binding-energy shifts in molecules are given by energy differences between initial and final states in photoemission processes, although they are usually interpreted in terms of initial-state properties alone. This approach would yield correct shifts if the passive molecular orbitals remained "frozen" during photoemission, or if they relaxed by the same amount (in total energy) for all molecules. Differential relaxation from one molecule to the next will alter the shifts. It is therefore useful to correct for this effect. It has been shown that *ab initio* 1s hole-state calculations can be done directly on molecules,⁸ and explicit relations describing relaxation in the final state have also been given.⁹ Hedin and Johansson⁹ derived an expression for the binding energy of a core orbital. In our notation their result is

$$-E_B(1s) \approx \epsilon(1s) + \frac{1}{2} \langle 1s | V_R | 1s \rangle. \quad (1)$$

Here V_R is a relaxation potential energy arising from the difference between the Hartree-Fock potential V_k of the passive orbitals in the final (1s-hole) state and the initial state. Specifically,

$$V_R = \sum_{k \neq 1s} (V_k^{(f)} - V_k^{(i)}). \quad (2)$$

Hedin and Johansson rearranged Eq. (1) to prove a result that Liberman¹⁰ had discovered earlier,

$$-E_B(1s) = \frac{1}{2} [\epsilon(1s) + \epsilon(1s)^*], \quad (3)$$

where $\epsilon(1s)^*$ is the orbital energy of a 1s electron in the hole state. Let us write each orbital energy as the sum of the interaction energy of the 1s electron with its own nucleus, plus a "potential-energy" term that includes interactions of the 1s electron with other electrons and other nuclei:

$$\epsilon(1s) = \langle 1s | h | 1s \rangle + \langle 1s | V | 1s \rangle. \quad (4)$$

Combining Eqs. (3) and (4), taking differences (as between two compounds), and noting that the differences in the first terms of Eq. (4) are negligibly small,² we have

$$\Delta E_B(1s) \approx -\frac{1}{2} \Delta \langle 1s | (V + V^*) | 1s \rangle. \quad (5)$$

From the work of Basch¹ and Schwartz² it is clear that it is sufficient to evaluate the electrostatic potential ϕ at the host nucleus. Thus for shifts in carbon 1s binding energies,

$$\Delta E_B(C1s) = (e/2) \Delta [\phi(C) + \phi(C^*)], \quad (6)$$

where the relation $e\phi = -V$, appropriate for an electron, has been used, and the asterisk denotes a hole in the carbon 1s shell. The relaxation correction is of course contained in the second potential term, $\phi(C^*)$.

In CNDO theory there is no way to calculate

$\phi(C^*)$ directly, because this theory does not include 1s orbitals in second-row elements, let alone provide for calculations on states in which these orbitals are only singly occupied. It is possible, using CNDO theory, to estimate shifts in $\phi(C^*)$, however. We may invoke the idea of "equivalent cores".¹¹ Since 1s electrons shield out essentially one complete nuclear charge, the attraction exerted on valence orbitals by the "core" consisting of a nitrogen nucleus plus a doubly-occupied 1s shell is essentially equal to that exerted by a carbon nucleus plus a singly-occupied 1s shell. For purposes of estimating shifts in the potential at the nucleus arising from "relaxed" valence orbitals we may therefore simply substitute $\phi(N)$ for $\phi(C^*)$ in Eq. (6), obtaining

$$\Delta E_B(C1s) = (e/2) \Delta [\phi(C) + \phi(N)] \quad (7)$$

Since photoemission is a very fast process, the same initial-state molecular geometry is used to calculate $\phi(N)$ and $\phi(C)$, i. e., valence electrons have time to relax, but nuclei do not. We may therefore obtain an estimate of $\Delta E_B(C1s)$ by carrying out two CNDO calculations for each molecule, one on the ground state and one on an isoelectronic state with the same molecular geometry but with nitrogen substituted for carbon.

By using this approach we have estimated 35 carbon 1s, 9 nitrogen 1s, and 10 oxygen 1s shifts in a number of small molecules containing up to 12 atoms. The results are compared with experiment in Figs. 1-3. Experimental values were taken from several sources.^{3-5, 6, 7, 12, 13} Only gas-phase shifts were used.

The relaxation correction given here appears to give improvement over the already reasonably good agreement between theoretical and experimental shifts that can be obtained with the CNDO potential model.

To be theoretically acceptable, this method for correcting binding energies must not only give improved values of binding-energy shifts, but the relaxation correction to E_B itself should also be approximately of the right magnitude. By arguments similar to those yielding Eq. (7), we have derived from Eq. (1) the relation

$$-E_B(C1s) \approx \epsilon(C1s) + (e/2) [\phi(C) - \phi(N)] \quad (8)$$

for carbon 1s shifts, and similar relations for shifts in other elements. The second term on the right is the relaxation energy, V_R . In Table II values of V_R obtained from the model presented here are compared with differences between *ab initio* hole-state and orbital-energy results for several molecules. The good agreement both supports the validity of this approach and indicates its possible usefulness in estimating binding energies from orbital energies.

Finally, some physical insight into the origins of differential molecular relaxation can be obtained by studying the charges assigned the host atom in the CNDO scheme before and after photoemission. Table III gives the initial charge q and the changes Δq for selected carbon cases from Fig. 1 plus all the nitrogen and oxygen shifts shown in Figs. 2 and 3; let us consider the carbon charges. When a C 1s electron is ejected, the remaining electronic charge in the molecule collapses

Table I
Quality of theoretical fits to 1s binding energies

Case	Intercept (eV) ^{a)}		Standard deviation (eV)	
	CNDO potential model only	relaxation correction added	CNDO potential model only	relaxation correction added
thirty-five C 1s shifts	0.22	-0.18	1.06	0.84
fifteen C 1s shifts in fluoroalkanes	0.59	0.19	0.35	0.41
nine N 1s shifts	1.16	1.18	2.35	1.30
ten O 1s shifts	2.12	0.70	0.84	1.15

a) All shifts are referred to the hydrides CH_4 , NH_3 , and H_2O . A straight line of unit slope was fitted to the data, as in figs. 1-3. This intercept is the theoretical value of the line at an experimental shift of zero.

Table II
Comparison of V_R with ab initio results (energies in eV)

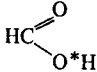
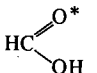
Molecule	$-\epsilon(1s)$	$E_B^a)$	$-\epsilon_B - E_B$	V_R (this work)
CH ₄	305.2 b,c)	291.0 d)	14.2 14.4 e)	15.9
CO(C1s)	310.7 b)		12.3 e)	11.9
CO(O1s)	563.5 b)		21.4 e)	21.5
NH ₃	423.5 c)	405.7 d)	17.8	19.0
H ₂ O	560.1 c)	539.4 d)	20.7 20.2 e)	20.6

a) From hole-state calculations.

b) Ref. [14]; c) ref. [15]; d) ref. [8].

e) Obtained from a configuration interaction calculation by Hillier et al. [14].

Table III

Molecule	q	Δq	V_R	$\Delta E_b^a)$	$\Delta E_B(R)^a)$	$\Delta E_B(\text{expt})^a)$	Ref.
Carbon 1s shifts							
CH ₄	-0.05	-0.04	15.89	-	-	-	-
CH ₃ F	0.18	-0.08	15.92	2.99	2.96	2.80	[4]
CH ₂ F ₂	0.40	-0.10	15.73	5.82	5.98	5.55	[8]
CHF ₃	0.61	-0.10	15.38	8.54	9.05	8.30	[4]
CF ₄	0.81	-0.08	14.91	11.13	12.11	11.00	[4]
HCN	0.03	0.18	14.40	0.31	1.80	2.60	[4]
CO	0.04	0.54	12.41	0.67	4.65	5.40	[4]
CO ₂	0.54	0.16	12.86	6.57	9.60	6.84	[4]
Nitrogen 1s shifts							
N ₂	0.0	0.38	16.67	2.32	4.66	4.35	[4]
NO	0.0	0.0	15.73	3.11	6.39	5.15	b)
NO ₂	0.39	-0.08	20.39	9.96	8.58	7.35	b)
CH ₃ NO ₂	0.50	-0.02	20.00	11.32	10.33	6.58	[15]
HCN	-0.10	0.41	18.50	1.07	1.59	1.25	[4]
NH ₂ NH ₂	-0.13	0.10	19.98	1.08	0.12	0.50	[14]
CH ₃ NH ₂	-0.19	0.14	19.75	0.37	- 0.38	- 0.45	[14]
NF ₃	0.36	0.08	19.32	10.20	9.89	8.85	[14]
ONF ₃	0.70	-0.12	20.63	16.08	14.47	11.45	[14]
Oxygen 1s shifts							
CO	-0.04	0.29	21.46	4.83	4.00	2.94	[4]
NO	0.0	0.38	20.35	6.28	6.56	4.14	b)
CO ₂	-0.27	0.38	22.01	2.96	1.58	1.44	[4]
NO ₂	-0.20	0.45	20.35	3.93	4.21	2.41	b)
CH ₃ NO ₂	-0.33	0.36	23.14	0.89	- 1.62	- 0.51	[15]
	-0.24	0.31	22.36	4.06	2.33	0.67	[4]
	-0.30	0.30	23.30	0.84	- 1.83	- 0.95	[4]
NNO	-0.28	0.43	22.02	2.53	1.09	1.54	[4]
CH ₃ OH	-0.25	0.30	22.18	2.25	0.70	- 0.80	[4]
C ₂ H ₄ O	-0.21	0.32	22.82	2.43	- 0.24	- 1.05	[4]

a) All shifts referred to the hydrides CH₄, NH₃, and H₂O.

b) Ref. [5], except that binding energies were taken as weighted averages over the multiple peaks in paramagnetic molecules.

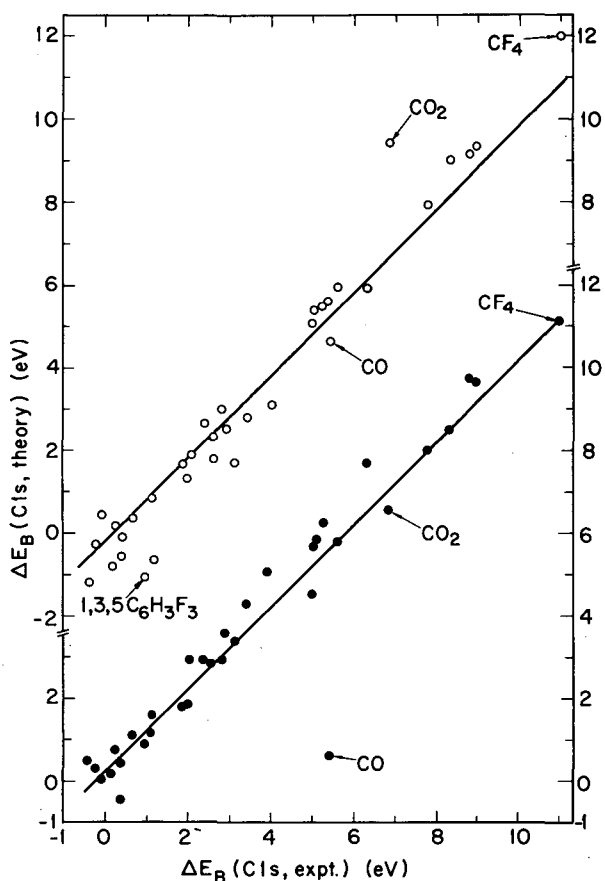


Fig. 1. Carbon 1s binding-energy shifts, theoretical versus experimental for a series of gaseous molecules. Filled circles, which go with lower ordinate scale, represent initial-state CNDO potential-model calculations. Open circles, and upper ordinate scale, include relaxation correction. Scales refer to a methane standard. Lines represent best least-squares fits under the constraint of unit slope. Selected molecules are labeled.
(XBL 723-2627)

toward the positive hole to minimize the total energy [only very fast ($< 10^{-5}$ sec) adiabatic processes are of interest here, because these processes alone shift the full-energy photoelectron lines]. In methane and the fluoromethanes this leads to essentially complete charge compensation; in fact, the valence electron "population" assigned to the carbon atom in the hole-state ion is actually slightly larger than in the molecular initial state. That a large fraction of this compensation should occur in these molecules is not surprising, because there are four single bonds

from which the positive hole can draw electrons without creating strong centers of positive charge elsewhere. By contrast, a very different situation obtains in the multiple-bonded small molecules CO, HCN, and CO₂.

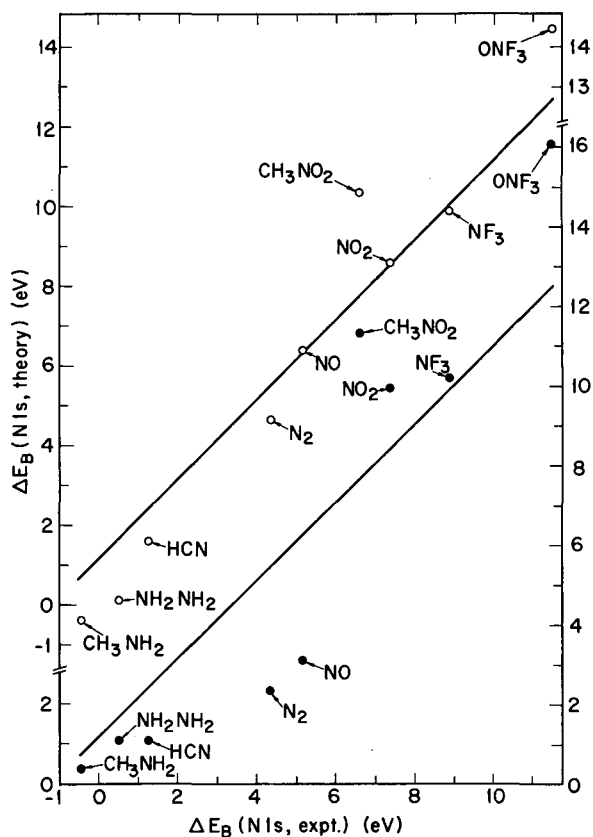


Fig. 2. Nitrogen 1s binding-energy shifts for a series of gaseous molecules, using NH₃ as reference. Format is the same as in Fig. 1.
(XBL 723-2628)

In the extreme case of CO, for example, the valence shell population assigned to carbon in the hole state is only about 0.5 larger than in the initial state. Further electronic charge could only come from the single oxygen atom, and this would require too much charge separation. Thus the relaxation energy of CO is expected to be smaller than that of methane.

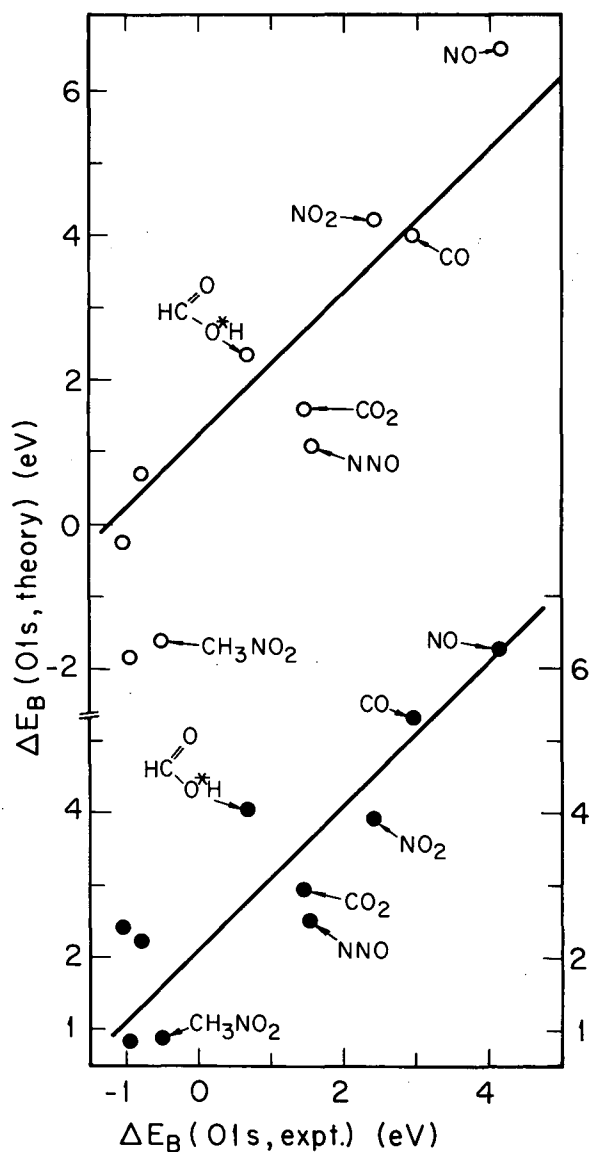


Fig. 3. Oxygen binding-energy shifts for a series of gaseous molecules, using H_2O as reference. Format is the same as in Fig. 1. (XBL 723-2629)

Footnote and References

*Condensed from LBL-633. Published in *Chem. Phys. Letters* **15** (2), 185 (1972).

1. H. Basch, *Chem. Phys. Letters* **5**, 337 (1970).
2. M. E. Schwartz, *Chem. Phys. Letters* **6**, 631 (1970).
3. D. W. Davis, J. M. Hollander, D. A. Shirley, and T. D. Thomas, *J. Chem. Phys.* **52**, 3295 (1970).
4. V. Gelius, P. F. Hedén, J. Hedman, B. J. Lindberg, R. Manne, R. Nordberg, C. Nordling, and K. Siegbahn, *Physica Scripta* **2**, 70 (1970).
5. K. Siegbahn, C. Nordling, G. Johansson, J. Hedman, P. F. Hedén, K. Hamrin, V. Gelius, T. Bergmark, L. O. Werme, R. Manne, and Y. Baer, *ESCA Applied to Free Molecules* (North-Holland, Amsterdam, 1969).
6. D. W. Davis, D. A. Shirley, and T. D. Thomas, *J. Chem. Phys.* **56**, 671 (1972).
7. D. W. Davis, D. A. Shirley, and T. D. Thomas, in *Electron Spectroscopy*, edited by D. A. Shirley (North-Holland, Amsterdam, 1972) p. 707.
8. M. E. Schwartz, *Chem. Phys. Letters* **5**, 50 (1970).
9. L. Hedin and A. Johansson, *J. Phys. B, Ser. 2*, **2**, 1336 (1969).
10. D. Liberman, *Bull. Am. Phys. Soc.* **9**, 731 (1964).
11. W. L. Jolly and D. N. Hendrickson, *J. Am. Chem. Soc.* **92**, 1863 (1970).
12. P. Finn, R. K. Pearson, J. M. Hollander, and W. L. Jolly, *Inorg. Chem.* **10**, 378 (1971).
13. D. W. Davis and D. A. Shirley, unpublished.
14. I. H. Hillier, V. R. Saunders, and M. H. Wood, *Chem. Phys. Letters* **7**, 323 (1971).
15. F. A. Gianturco and C. Guidotti, *Chem. Phys. Letters* **9**, 539 (1971).

THE EVOLUTION OF CORE STATES FROM ENERGY BANDS IN THE
4d5s5p REGION FROM Pd TO Xe[†]

R. A. Pollak, S. P. Kowalczyk, L. Ley,* and D. A. Shirley

Most discussions of band structure in metals are predicted on the assumption that the tightly bound electrons can be regarded as belonging to separate ion cores, while those that are more loosely bound occupy valence bands. In passing beyond the end of a transition series one would expect the d bands to become narrower, fall below the Fermi energy E_F , and evolve into core levels. It is not always clear, however, just which atomic levels can be safely treated as core states and which ones must be explicitly included as part of the band structure. In this

letter we report x-ray photoelectron spectroscopy (XPS)¹ experiments addressed to this question for the 4d5s5p elements Pd ($Z=46$) through I ($Z=53$). By following the $4d_{3/2} - 4d_{5/2}$ spin-orbit splitting from I down through Cd to Ag one can unambiguously trace the onset of band-structure broadening. We also report the first observation by XPS of structure in the sp bands. This structure exhibits systematic changes between Cd and Te.

Doublet structure in the 4d shell is evident from Ag through I. The energy splitting ΔE between the two components of the doublet is plotted in Fig. 2a. Also plotted is a theoretical splitting which was estimated by normalizing orbital energy differences taken from free-atom relativistic Hartree-Fock-Slater calculations² to $\Delta E(\text{Sb})$. That the free-atom values of spin-orbit splitting are appropriate in metals is confirmed by the good agreement of this normalized curve with the experimental splitting in gaseous xenon,³ also shown in Fig. 2a. The free-atom values are lowered 0.1 eV by this normalization. The trend from Sn to I is in excellent agreement with the theoretical curve. The intensity ratio of the two components is in each case close to 1.3, in only fair agreement with the value 1.5 expected for a $d_{3/2}, d_{5/2}$ doublet on the basis of multiplicity alone. For the heavier elements Sn to I the 4d electrons can be assigned to the ion cores with confidence. The splitting in indium may be just slightly larger than the free-atom spin-orbit splitting. For Cd the experimental splitting $\Delta E = 0.99$ eV greatly exceeds the predicted spin-orbit splitting of 0.73 eV, and is in fact even larger than the observed splitting in indium. We conclude that band structure affects the 4d shell in Cd, at 11 eV below E_F , and is perhaps perceptible even for the 4d shell of In at $E_F - 17$ eV.

The spin-orbit splitting energy ΔE is a uniquely reliable parameter for detecting the onset of lattice effects because it is independent of component linewidth, which can be affected by lifetime broadening. Nevertheless, the total "4d bandwidth" can also be used to study broadening by the lattice. In Fig. 2b the 4d bandwidth (FWHM) is plotted against Z . The bandwidth drops monotonically with increasing Z across the 4d transition series from 6 eV in Mo (not shown) to 3.4 eV in Ag, going through a minimum at In and increasing thereafter because of spin-orbit splitting. The width in Cd is greater than in In, showing again that band

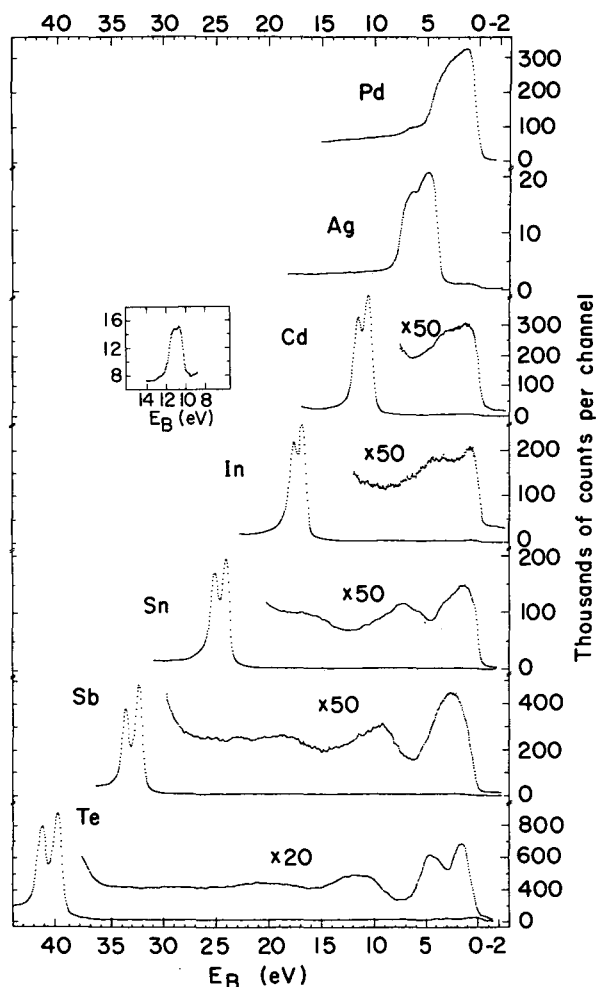


Fig. 1. X-ray photoelectron spectra of the valence band region for Pd through Te.
(XBL 725-3060)

Table I. Summary of experimental data.

	Ag	Cd	In	Sn	Sb	Te	I	Xe
Binding energy $4d_{3/2}$ (eV)	--	11.46(9) ^a	17.64(9)	24.76(9)	33.44(9)	41.80(9)	--	--
Binding energy $4d_{5/2}$ (eV)	--	10.47(9)	16.74(9)	23.68(9)	32.14(9)	40.31(9)	--	--
FWHM $4d_{3/2}$ = FWHM $4d_{5/2}$	--	0.81(18)	0.78(15)	0.83(8)	0.76(18)	0.94(2)	--	--
$4d$ Splitting (eV)	1.6(1)	0.990(46)	0.899(10)	1.075(34)	1.254(42)	1.51(1)	1.76(16)	1.97 ^b
HFS free atom $4d$ splittings normalized to Sb	0.59	0.73	0.88	1.06	1.25	1.48	1.72	1.98
Binding energy 5s (eV)	--	2.2(5)	4.1(4)	7.0(5)	9.1(2)	11.5(2)	--	--
FWHM 5s (eV)	--	5.0(7)	4.0(5)	5.8(5)	4.0(5)	5.3(5)	--	--
Binding energy 5p (eV)	--	--	0.75(13)	1.25(27)	2.35(25)	$\begin{cases} 4.0(2) \\ 1.13(5) \end{cases}$	--	--
FWHM 5p (eV)	--	--	2.0(2)	3.5(5)	3.9(2)	$\begin{cases} 2.3(2) \\ 2.1(2) \end{cases}$	--	--
$4s/4p$ rel. areas	--	--	1.85	0.7	0.63	0.5	--	--
n/m	--	--	2.00	1	0.66	0.5	--	--

^aErrors in last place given in parenthesis.

^bRef. 3.

structure effects are present in Cd metal.

In the past, XPS studies of valence bands in transition-series metals have yielded little information about s and p bands.^{1,4,5,6} This was a consequence of their small cross section for photoemission, the presence of $K\alpha_{1,2}$ lines, and bremsstrahlung in the exciting radiation. With these unwanted components removed by monochromatization it was possible to observe for the first time a considerable amount of structure in the 5s5p bands of Cd, In, Sn, Sb, and Te. A detailed analysis of the spectra must await more intensive measurements and further density of states calculations, but the systematic variation of the 5s5p spectra from Cd to Te (Fig. 1) suggests a preliminary interpretation in terms of a transition from band structure to atomic core-level character for the 5s band with a simultaneous filling of the 5p band. Three systematic effects occur between Cd and Te. First, the s-p valence band which shows structure even in Cd resolves into two peaks in Sn and Sb and three in Te. Second, the higher binding-energy peak which we designate as 5s, falls monotonically below E_F as Z increases.

We designate the lower binding-energy bands in In, Sn, Sb, and Te as 5p. Finally, the experimental area ratio (5s/5p) in In to Te agrees well with the occupation number ratio (n/m) for the respective free-atom ground state configurations $5s^n 5p^m$ (Table I).

We interpret this behavior in terms of the evolution of core-like 5s and 5p shells. Figure 2c illustrates the approach of the 5s and 5p bands toward the core s and p levels of Xe. The bars in Fig. 2c represent the widths (FWHM) of the 5s and 5p bands. In Cd through Te all bands are considerably broader than the corresponding levels in Xe. It should also be noted that the 5p splitting in Te is dominated by band structure effects, yielding a splitting much larger (2.9 eV) than the spin-orbit splitting in Xe (1.3 eV). Thus the systematic trend toward core-like levels aids assignment of the peaks, although solid-state interactions are clearly present in Cd to Te.

One of us (L. L.) greatly appreciates a grant from the Max-Kade Foundation. We thank Professor G. Somorjai for giving us single crystal Ag, In, and Sn.

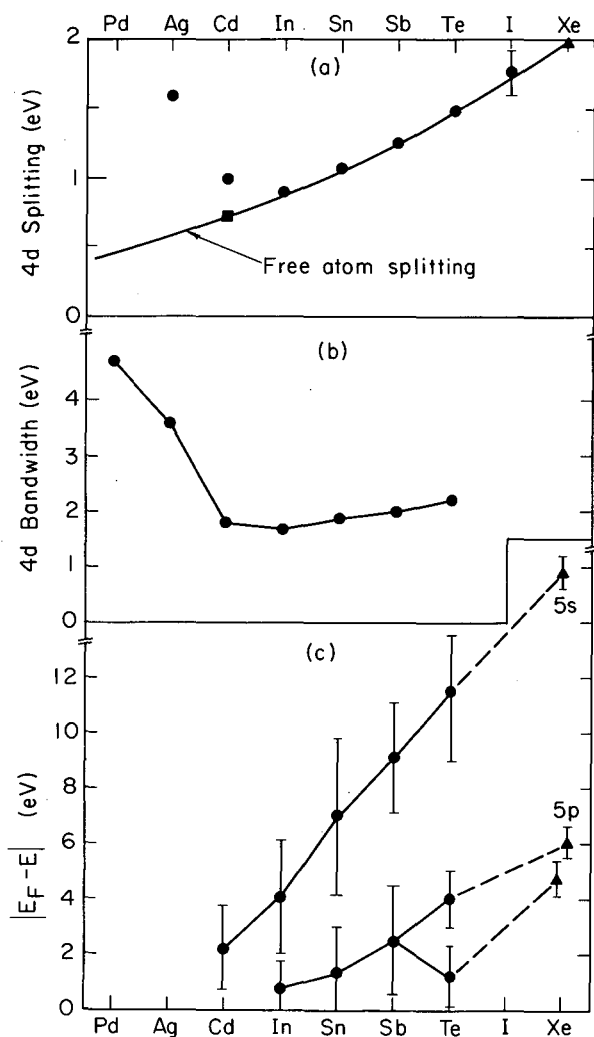


Fig. 2. a) Comparison of the experimental 4d level splitting with free-atom HFS calculations; the Cd-point \square refers to the experimental value for Cd atoms sputtered onto a Au(111) surface. b) The experimental 4d-bandwidths. c) Positions of the 5s- and 5p-bands relative to the Fermi level; the vertical bars represent the bandwidths at half maximum. The Xe-values in a) and c) are taken from Ref. 3.

(XBL 725-3059)

Footnotes and References

[†] Condensed version of paper in Phys. Rev. Letters 29, 274 (1972).

* On leave from University of Bonn, Germany.

1. C. S. Fadley and D. A. Shirley, Phys. Rev. Letters 21, 980 (1968).

2. T. A. Carlson, C. C. Lu, T. C. Tucker, C. W. Nestor, and F. B. Malik, Oak Ridge National Laboratory Report ORNL-4614 (1970).

3. K. Siegbahn, C. Nordling, G. Johansson, J. Hedman, P. F. Heden, K. Hamrin, U. Gelius, T. Bergmark, L. O. Werme, R. Manne, and Y. Baer, ESCA Applied to Free Molecules (North-Holland, Amsterdam, 1969).

4. G. Broden, S. B. M. Hagström, and C. Norris, Phys. Rev. Letters 24, 1173 (1971).

5. C. S. Fadley and D. A. Shirley, J. Res. Nat. Bur. Standards 74A, 543 (1970).

6. Y. Baer, P. F. Hedén, J. Hedman, M. Klasson, C. Nordling, and K. Siegbahn, Physica Scripta 1, 55 (1970).

THE EFFECT OF ATOMIC AND EXTRA-ATOMIC RELAXATION ON ATOMIC BINDING ENERGIES*

D. A. Shirley

Siegbahn et al.^{1, 2} have given a rather complete of experimental electron binding energies for the chemical elements, to a precision of 1 eV or better. There exist as yet relatively few theoretical values with which these results may be compared. This V report describes a method for estimating atomic core-electron binding energies from Hartree-Fock orbital energies plus a relaxation-energy correction that employs integrals calculated from atomic ground state properties. The results appear to be as accurate as those obtained from hole-state calculations, especially for heavy

atoms. Comparison of experimental core-level binding energies of elements with various theoretical estimates leads to the conclusion that extra-atomic relaxation amounts to several electron volts when measurements are made on molecules or condensed phases. Thus, except for the noble gases, any comparisons of available experimental binding energies of core electrons with atomic calculations should include corrections for extra-atomic relaxation.

The binding energy $E_B(i)$ of the i th orbital may be related to its orbital energy $\epsilon(i)$ by

$$E_B(i) = -\epsilon(i) - E_R(i),$$

where the relaxation energy $E_R(i)$ has been given by Hedin and Johansson³ as

$$E_R(i) = \frac{1}{2} \langle i | V_R | i \rangle,$$

with V_R representing a "polarization potential." This potential requires certain difficult-to-obtain hole-state Coulomb and exchange integrals for its evaluation. By recognizing that inner orbitals shield outer orbitals almost completely, we have been able to approximate the necessary integrals by corresponding integrals in the next higher element, i. e.,

$$F_k(nl, n'l'; Z(\overline{nl})^*) \approx F_k(nl, n'l'; Z+1),$$

$$G_k(nl, n'l'; Z(\overline{nl})^*) \approx G_k(nl, n'l'; Z+1).$$

Here $Z(\overline{nl})^*$ denotes the nl hole state in element

Z. Using this approximation, one can show that

$$\langle nl | V_R | nl \rangle = \sum_{\substack{l' \\ n' > n}} \frac{N(n'l')}{(4l'+2)} \left\{ f(ll') \Delta[F_0(nl, n'l')] \right. \\ \left. - \Delta \sum_k [g_k(ll') G_k(nl, n'l')] \right\},$$

where

$$\Delta F_0(nl, n'l') \equiv F_0(nl, n'l'; Z+1) - F_0(nl, n'l'; Z)$$

and

$$\Delta G_k(nl, n'l') \equiv G_k(nl, n'l'; Z+1) - G_k(nl, n'l'; Z).$$

Here $N(n'l')$ is the occupation number of the $n'l'$ subshell in the parent atom. The factors $g(ll')$ and $f(ll')$ are given in Table I.

Table I. The f and g Coefficients in Eq. (9).

l	l'	$f(ll')$	$g_0(ll')$	$g_1(ll')$	$g_2(ll')$	$g_3(ll')$	$g_4(ll')$	$g_5(ll')$	$g_6(ll')$
0	0	2	1						
0	1	6		1					
0	2	10			1				
0	3	14				1			
1	0	2		1/3					
1	1	6	1		2/5				
1	2	10		2/3		3/7			
1	3	14			3/5		4/9		
2	0	2			1/5				
2	1	6		2/5		9/35			
2	2	10	1		2/7		2/7		
2	3	14		3/5		4/15		10/33	
3	0	2				1/7			
3	1	6			9/35		4/21		
3	2	10		3/7		4/21		25/77	
3	3	14	1		4/15		2/11		100/429

The above approach was used to estimate relaxation energies for the noble gases Ne, Ar, Kr, and Xe, for which both usable orbital energies and experimental binding energies are available. Slater integrals were taken from the tables given by Mann.⁴ Table II gives the relaxation energies (E_R), the binding energies estimated on the theory given above (E_B^H), the experimental binding energies (E_B),^{1,2} and, where available, the binding energies obtained

from hole-state calculations (E_B^H).⁵ The agreement of both E_B^R and E_B^H with one another and with experiment is excellent in most cases. The agreement of E_B^H with E_B shows that the "equivalent-core" potential model given here yields an excellent estimate of the relaxation energy. Of the 27 measured binding energies in Table II, 16 are within 2 eV of the E_B^R predictions, and 21 are within 4 eV.

Table II. Noble Gas Core-Electron Binding Energies (eV).

Orbital	$E_R^{(a)}$	$E_B^H(b)$	$E_B^R(c)$	$E_B^{(d)}$
Ne 1s	25.6	870	868.4	870.2
Ar 1s	37	3209	3203	3205.9
Ar 2s	10.5	327	325.5	326.3
Ar 2p _{1/2}	11	250	251	250.6
Ar 2p _{3/2}	11	248	248	248.5
Kr 1s	59	14358	14351	14326
Kr 2s	32	1933	1926	1924.6
Kr 2p _{1/2}	32	1735	1730	1730.9
Kr 2p _{3/2}	32	1681	1676	1678.4
Kr 3s	7	296	297	292.8
Kr 3p _{1/2}	7	225	226	222.2
Kr 3p _{3/2}	7	217	218	214.4
Kr 3d _{3/2}	7	93	94	94.9
Kr 3d _{5/2}	7	92	93	93.7
Xe 1s	72	34689	34684	34561
Xe 2s	44	5472	5462	5453.2
Xe 2p _{1/2}	44		5115	5107.2
Xe 2p _{3/2}	44		4789	4787.4
Xe 3s	18		1150	1148.7
Xe 3p _{1/2}	18		1005	1002.1
Xe 3p _{3/2}	18		941	940.6
Xe 3d _{3/2}	19		687	689.0
Xe 3d _{5/2}	19		674	676.4
Xe 4s	4.8		224	213.2
Xe 4p _{1/2}	4.8		170	--
Xe 4p _{3/2}	4.8		157	145.5
Xe 4d _{3/2}	4.8		68.3	69.5
Xe 4d _{5/2}	4.8		66.2	67.5

Turning now to binding energies in solid elements, let us consider carbon specifically. The C 1s binding energy in atomic carbon can be estimated in three ways. All give values in the range 297-300 eV. The measured binding C(1s) energy in graphite is 284 eV. After correction for the work function, this becomes $E_B(\text{C } 1s, \text{ graphite}) = 288 \text{ eV}$ relative to the vacuum level. A discrepancy of about 10 eV thus clearly exists for carbon. Similar considerations lead to discrepancies of about this size for the other second-row elements, as Fig. 1 indicates. We attribute this discrepancy to extra-atomic relaxation accompanying photoemission in the solid state.

Relaxation during photoemission may be understood as the natural consequence of minimizing the emitting system's Coulombic energy. In a free atom, the passive orbitals relax adiabatically, and the relaxation energy can be estimated as discussed above. If the atom were a classical system, and charge were continuous, it would be natural to describe this relaxation in terms of the outward diffusion of

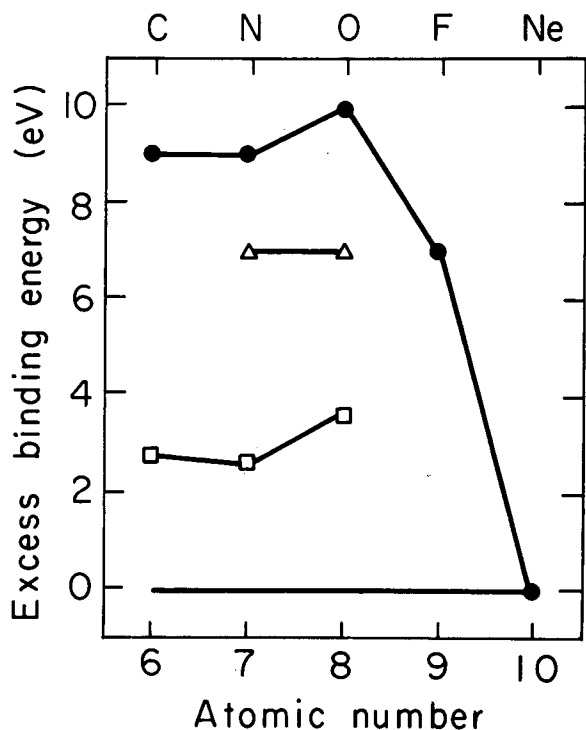


Fig. 1. The binding-energy discrepancy for 1s orbitals of second-row elements in solids. Filled circles represent $E_B^H(\text{atomic}) - E_B(\text{expt.})$. Only the neon point is a gas-phase result. Triangles and squares show excess binding energies (over the experimental values in solids) for gaseous diatomics and hydrides, respectively. (XLB 726-3129)

a quantity of charge of value $+e$, suddenly introduced near the center of the atom, in order to reduce the Coulombic repulsion energy. This picture facilitates an understanding of extranuclear relaxation molecules and solids. In a solid sample the positive charge can migrate farther than the nearest ligand during photoemission, thereby further reducing the core-electron binding energy. This effect accounts for the reduction of $E_B(\text{C } 1s, \text{ graphite})$ below $E_B(\text{C } 1s, \text{ CH}_4)$, for example. Similar results should obtain for other solids.

Having once established the importance of extra-atomic relaxation in relation to core-level binding-energy measurements on condensed phases, we note that this phenomenon may be the key factor in understanding several previously unexplained observations. For example, core electron binding energies of noble gases embedded in metallic foils¹ were in most cases 2-5 eV higher than those of the same orbitals studies with gas-phase samples.² Shifts of about 3 eV have also been observed in molecules between the gas and solid phase. Thus Siegbahn et al.² found that the N 1s binding energies of aminobenzene and nitrobenzene are, respectively, 3.1 eV and 2.4 eV higher in the solid phase. This shift can be tentatively attributed to "extramolecular relaxation" due to polarization of neighboring molecules in the solid.

Extra-atomic relaxation has broad implications for all atomic binding energies obtained from data taken on solids. Because the relaxation is a property of the hole state rather than of the photoelectric process per se, it affects binding energies obtained from x-ray data, such as those tabulated by Bearden and Burr.⁶ It will be of interest both to estimate the corrections that must be applied to calculated free-atom binding energies before they can be compared to experiment and to measure binding energies in free atoms of more elements.

Footnote and References

* Condensed from LBL-678. Published in Chem. Phys. Letters, 1972.

1. K. Siegbahn, C. Nordling, A. Fahlman, R. Nordberg, K. Hamrin, J. Hedman, G. Johansson, T. Bergmark, S.-E. Karlsson, I. Lindgren, and B. J. Lindberg, *ESCA - Atomic, Molecular and Solid State Structure by Means of Electron Spectroscopy*, Nova Acta Regiae Soc. Sci. Upsaliensis Ser. IV, Vol. 20 (1967).
2. K. Siegbahn, C. Nordling, G. Johansson, J. Hedman, P. F. Hedén, K. Hamrin, U. Gelius, T. Bergmark, L. O. Werme, R. Manne, and Y. Baer, *ESCA Applied to Free Molecules* (North-Holland, Amsterdam, 1969).

3. L. Hedin and G. Johansson, *J. Phys.* **B2**, 1336 (1969).

4. J. B. Mann, "Atomic Structure Calculations I. Hartree-Fock Energy Results for the Elements Hydrogen to Lawrencium," Los Alamos Scientific Laboratory Report LASL-

3690 (1967).

5. A. Rosen and I. Lindgren, *Phys. Rev.* **176**, 114 (1968).

6. J. A. Bearden and A. F. Burr, *Rev. Mod. Phys.* **39**, 125 (1967).

THE ONSET OF RELATIVISTIC EFFECTS IN THE DENSITY OF STATES OF THE 6s6p ELEMENTS Tl, Pb, AND Bi†

L. Ley, R. A. Pollak, S. P. Kowalczyk, and D. A. Shirley

Relativistic effects, e.g. spin-orbit splitting, have to be taken into account in electronic level calculations for even the lightest atoms. For the valence and conduction electrons, however, crystal-field interactions are usually stronger by several orders of magnitude. Therefore spin-orbit splitting may well be treated as a small perturbation in band structure calculations.

This is certainly not the case for the elements Tl, Pb, and Bi, with atomic numbers 81, 82, and 83. Relativistic band structure calculations¹⁻³ show that spin orbit interactions result in band splittings that are comparable to crystal-field splittings. Experiments show that spin-orbit splitting in the valence-p-electrons of Pb and Bi prevails in the presence of crystal-field splitting.

Figure 1 shows the XPS-spectra of the valence region of Tl, Pb, and Bi obtained with monochromatic Al K α x-rays in a Hewlett-Packard HP 5950A spectrometer. The valence bands extend to 7 eV below E_F in Tl, to about 12 eV in Pb, and to 13.5 eV in Bi. Included in these spectra are the high-intensity 5d peaks at energies which are listed in Table I.

The single broad peak at the bottom of the valence band represents electrons with mainly 6s-like character. The shift of this peak to higher binding energy as one goes from Tl to Bi can be explained by the increasing depth of the atomic potential with increasing atomic number. In Bi the 6s state is already very nearly a core level.

In Tl the p-like electrons are concentrated in one narrow peak near E_F . By contrast, Pb and Bi show two peaks at the top of the valence band which are split apart by 1.8 eV in Pb and 2.2 eV in Bi. The calculated spin-orbit splittings obtained at certain symmetry points in the Brillouin zone are 0.3 eV for Tl

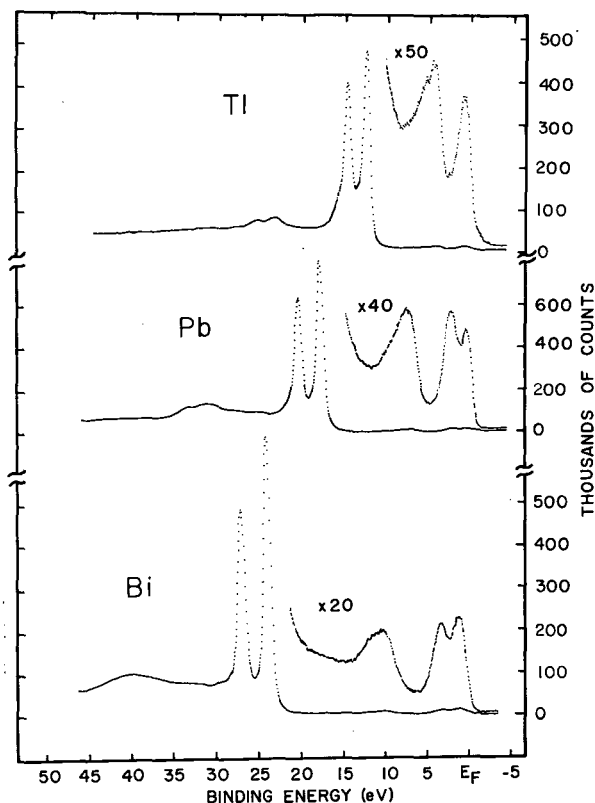


Fig. 1. High-resolution XPS spectra of thallium, lead, and bismuth. The $5d_{3/2}$ - $5d_{5/2}$ doublet is the strongest feature in each spectrum. Characteristic energy-loss maxima appear to the left in each case, with the losses in thallium showing up as two well-resolved peaks. The broad peak to the right of the 5d doublet is the 6s band, and the narrower, spin-orbit split 6p bands fall near the Fermi energy.

(XBL 726-985A)

Table I. Valence-band binding energies.

	Tl	Pb	Bi
Bind. Energ. $5d_{3/2}$	14.53(5) eV	20.32(5) eV	26.94(7) eV
Bind. Energ. $5d_{5/2}$	12.30(5)	17.70(5)	23.90(7)
d-splitting	2.23(2)	2.62(2)	3.04(2)
Free atom d-splitting (HFS theory, Ref. 5)	2.44	2.83	3.26
6s-band	4.90(25)	7.68(20)	9.95(18)
6p-band	0.80(12)	{ 2.33(8) 0.53(5)	{ 3.34(12) 1.18(12)
6p-splitting	--	1.80(5)	2.16(8)
Free atom 6p splitting (HFS theory) Ref. (5)	--	--	2.16

(Ref. 1), 1.4 eV for Pb (Ref. 2), and 2 eV for Bi (Ref. 3). The excellent agreement between these figures and the experimental values strongly supports our interpretation of these bands as being split by spin-orbit interactions rather than by the crystal field. In this connection it is of interest to note (Table I) that even free-atom HFS-calculations⁴ reproduce the 6p-band splitting quite well.

In this discussion we have neglected the differences in crystal structure among these three elements. This is somewhat justified by the fact that the rhombohedral Bi lattice can be regarded as a slightly distorted cubic lattice, as compared with the cubic lattice of Pb. Of course the lattice symmetries were taken into account in the band-structure calculations.¹⁻³

Two other relativistic effects—the Darwin and mass-velocity terms—should also be considered. These terms should have the effect of lowering the energies of the s bands. Comparison of the positions of the s-bands in Tl, Pb, and Bi with those of In, Sn, and Sb⁵ shows a relative depression of the s-band energies in the heavier elements. We interpret this as a probable indication of these other relativistic effects. Loucks' relativistic APW calculation on Pb (Ref. 2) located the 6s band

lower relative to the 6p band than did an interpolated OPW calculation of Anderson and Gold.⁶ Since the former used a relativistic Hamiltonian, it is probable that part of the difference is a consequence of the 6s bands being lowered somewhat by the Darwin and mass-velocity terms.

Footnote and References

† Condensed from LBL-1203.

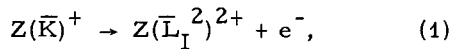
1. P. Soven, Phys. Rev. A 6, 1706 (1972).
2. T. L. Loucks, Phys. Rev. Letters 14, 1072 (1965).
3. L. G. Ferreira, J. Phys. Chem. Sol. 28, 1891 (1967).
4. C. C. Lu, T. A. Carlson, F. B. Malik, T. C. Tucker, and C. W. Nestor, Jr., Atomic Data 3, 1 (1971).
5. R. A. Pollak, S. P. Kowalczyk, L. Ley, and D. A. Shirley, Phys. Rev. Letters 29, 274 (1972).
6. J. R. Anderson and A. V. Gold, Phys. Rev. 139, A1459 (1965).

RELAXATION EFFECTS ON AUGER ENERGIES*

D. A. Shirley

In the course of a systematic study of the theory of Auger electron energies, it has become clear that an important effect—outer-shell relaxation in the final state—has been generally neglected until now. The use of three- or four-parameter semiempirical theories to fit existing data has obscured the significance of outer-shell relaxation, because these theories were flexible enough to give good fits. However, the agreement deteriorates drastically if one attempts to use calculated, rather than empirically adjusted, Slater integrals. In this report a new theoretical approach that includes relaxation is derived. It relates Auger energies to measured one-electron binding energies plus to-electron integrals from Hartree-Fock calculations in the ground states of neutral atoms. One adjustable parameter is required if the integrals employed are based on nonrelativistic wave functions; none is required if the wave functions are relativistic. Comparison of the predictions of this theory with experimental $KL_I L_I$ Auger energies of the elements shows generally excellent agreement with experiment.

For brevity let us consider the $KL_I L_I$ Auger transition explicitly. In an element of atomic number Z this process may be denoted by



where the atom is assumed to have its full complement of electrons excepting those denoted by the "hole-state" notation \bar{K} , \bar{L}_I , etc. An approximate estimate of the kinetic energy of the outgoing electron is given by

$$E(KL_I L_I) \approx E_B(K) - 2E_B(L_I), \quad (2)$$

i. e., by a combination of one-electron binding energies. In deriving Eq. (2) one implicitly considers Eq. (1) to be obtained as a combination of the processes

$$Z \rightarrow Z(\bar{K})^+ + e^-, \quad (3a)$$

$$Z \rightarrow Z(\bar{L}_I)^+ + e^-, \quad (3b)$$

$$Z(\bar{L}_I)^+ \rightarrow Z(\bar{L}_I^2)^{2+} + e^-, \quad (3c)$$

and the energy of step (3c) is assumed to be identical to that of (3b) in the derivation of Eq. (2), a very poor assumption.

To improve on Eq. (2), Asaad and Burhop¹

noted that step (3c) differs from step (3b) in one important way: when the second electron is ejected from the L_I shell, there is no electron remaining in this shell. The binding energy will therefore be increased by the two-electron interaction energy. Thus Eq. (2) becomes, according to Asaad and Burhop,

$$E(KL_I L_I) = E_B(K) - 2E_B(L_I) - F^0(2s, 2s). \quad (4)$$

By adjusting the value of F^0 , which was described by four adjustable parameters; theory could be made to fit experiment. More recently, accurate values of F^0 have become available.² If these are used, the calculated $KL_I L_I$ energies disagree seriously with experiment, showing that Eq. (4) is not really viable.

The reason for this is rather simple. Equation (4) does not properly take into account the effect of relaxation in the passive outer orbitals. Dynamic relaxation effects (i. e., the binding-energy contribution arising from acceleration of the outgoing electron by adiabatic collapse of occupied outer orbitals toward the hole during the emission process) are automatically accounted for by the use of empirical binding energies in Eq. (4). However, there is also a static effect. The dynamic relaxation of the outer orbitals during ejection of the first electron from the L_I subshell creates a more repulsive environment for the second L_I electron, raising its orbital energy by an amount R . Thus the binding energy of step (3c) is lowered by R , and Eq. (4) is replaced by

$$E(KL_I L_I) = E_B(K) - 2E_B(L_I) + R - F^0(2s, 2s). \quad (5)$$

The energy R may be estimated by using an "equivalent cores" approach that has proved successful recently in calculating the effects of relaxation on atomic binding energies. The essence of this approach is that a one-electron outer orbital of an atom of element Z which has a hole in an inner orbital may be rather accurately represented by the corresponding outer orbital of a neutral atom of element $Z+1$. It follows that

$$\left. \begin{aligned} F^0[2s, nl; Z(\bar{2s})] &\approx F^0(2s, nl; Z+1) \\ G^l[2s, nl; Z(\bar{2s})] &\approx G^l(2s, nl; Z+1) \end{aligned} \right\} \quad (6)$$

Table I. Predicted and Experimental $E(KL_I L_I)$ Energies of the Elements (in eV).

Z	R	$E(KL_I L_I)$ This Work	$E(KL_I L_I)$ Experiment ^a	Z	R	$E(KL_I L_I)$ This Work	$E(KL_I L_I)$ Experiment ^a
10	6	751	748.0(4)	56	92	25320	25251(6)
11	8	922	922.8(4)	57	93	26239	
12	10	1101	1101.3(4)	58	95	27190	
13	12	1296		59	96	28161	
14	14	1511		60	98	29153	
15	16	1739		61	99	30160	
16	18	1980		62	101	31188	31175(20) ^b
17	20	2247		63	103	32238	32224(20) ^b
18	22	2524		64	104	33305	
19	25	2814	2809	65	105	34393	34430(50)
20	28	3121		66	107	35502	35496(6) ^b
21	31	3451		67	109	36632	
22	33	3793		68	110	37781	
23	36	4163	4159(6)	69	112	38953	38958(25)
24	39	4552		70	113	40146	40149(4)
25	42	4953	4962(2) ^b	71	115	41359	41351(10) ^b
26	45	5373	5376 ^b	72	117	42588	
27	48	5806		73	118	43832	
28	51	6265		74	120	45097	45080(40)
29	54	6734	6735(6) ^b	75	121	46387	46400(25)
30	57	7216	7220(4)	76	122	47694	
31	58	7713		77	123	49026	
32	60	8218	8212(6)	78	124	50382	50370(100) ^b
33	61	8749	8742(10)	79	126	51761	51780(20) ^b
34	62	9283		80	127	53160	53141(25) ^b
35	63	9839	9860(10)	81	129	54567	54510(100)
36	65	10411		82	130	56007	
37	67	10994		83	132	57468	57467(30) ^b
38	68	11593	11584.4(16)	84	133	58939	58920(50)
39	70	12211		85	135	60450	
40	72	12849	12851.8(15)	86	136	62006	
41	73	13501		87	137	63552	
42	75	14176	14176.1(13)	88	138	65134	
43	76	14862		89	139	66754	
44	78	15570		90	140	68379	
45	80	16294		91	141	70056	
46	81	17034		92	142	71748	71738(20) ^b
47	83	17793	17740(60)	93	143	73486	73555(150) ^b
48	85	18563		94	144	75257	75180(15)
49	85	19347	19352(1)	95	145	77116	
50	86	20149		96	146	78928	
51	87	20968		97	147	80660	
52	88	21806	21787(10)	98	148	83352	
53	88	22659	22652(10)	99	149	85294	
54	89	23516		100	150	87286	
55	90	24415	24395(14) ^b				

^aFrom Ref. 3. Errors in last place appear parenthetically.^bIn cases for which two or more experimental values are available. Either an average was taken or a single value chosen.

Predicted KL_1L_1 Auger energies of the elements are set out in Table I, together with experimental values, where available. The agreement between predicted and experimental³ values of $E(KL_1L_1)$ is generally excellent. It is even slightly better than that of the published semiempirical values. Thus the necessity for considering the static relaxation energy R has been demonstrated, and a recipe has been given for calculating R with reasonable accuracy.

Footnote and References

* Condensed from LBL-1207. Published in Chem. Phys. Letters (1972).

1. W. N. Asaad and E. H. S. Burhop, Proc. Phys. Soc. 71, 369 (1958).
2. J. B. Mann, "Atomic Structure Calculations I. Hartree-Fock Energy Results for the Elements Hydrogen to Lawrencium," Los Alamos Scientific Laboratory Report LASL-3690 (1967).
3. Kenneth D. Sevier, Low Energy Electron Spectroscopy (John Wiley, New York, 1972).

SYSTEMATICS OF ISOMER SHIFTS IN TRANSITION METAL HOSTS

G. Kaindl* and D. Salomon

Recently, large isomer shifts of the 6.2-keV gamma rays of ^{181}Ta in transition metal hosts have been observed,¹⁻³ revealing systematic features when plotted versus the number of valence electrons (N) of the host metals. Similar systematics had previously been reported for isomer shifts of the 14.4-keV gamma rays of ^{57}Fe .⁴ In the present paper a corresponding study for dilute impurities of ^{197}Au and ^{99}Ru is presented, employing the well-known Mössbauer resonances at 77 and 90 keV.

The experiments reported here were performed with sources of ^{197}Pt and $^{99}\text{Rh}(\text{Ru})$, respectively, melted as dilute impurities into the various host metals with the help of an

argon-arc furnace. With this technique the impurity concentration could be kept smaller than 0.2 at.% in the ^{99}Ru case. The Mössbauer transmission experiments were performed with both sources and absorbers at 4.2 K, using single-line absorbers of gold metal (50 mg/cm²) and ^{99}Ru metal (26 mg/cm²), respectively.

Some typical single-line spectra obtained with the 77-keV gamma rays of ^{197}Au are presented in Fig. 1, while Fig. 2 shows absorption spectra of the 90-keV gamma rays of ^{99}Ru . In the two cases the total ranges of observed isomer shifts exceed the experimental line widths by factors of ~ 4 (for ^{197}Au) and ~ 3 (for ^{99}Ru), respectively.

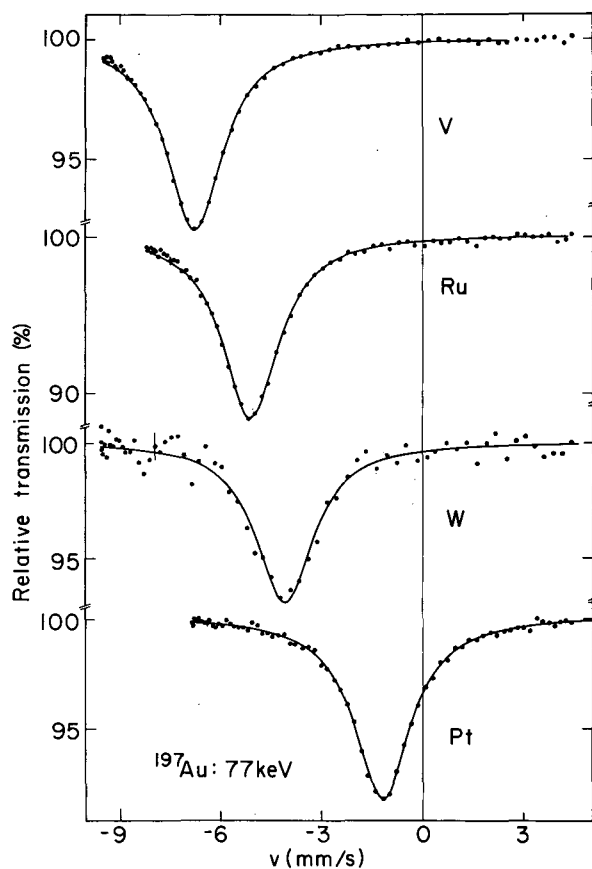


Fig. 1. Mössbauer absorption spectra of the 77-keV gamma rays of ^{197}Au , measured at 4.2 K with sources of dilute impurities of ^{197}Pt in V, Ru, W, and Pt, using a single-line gold metal absorber. (XBL 727-3566)

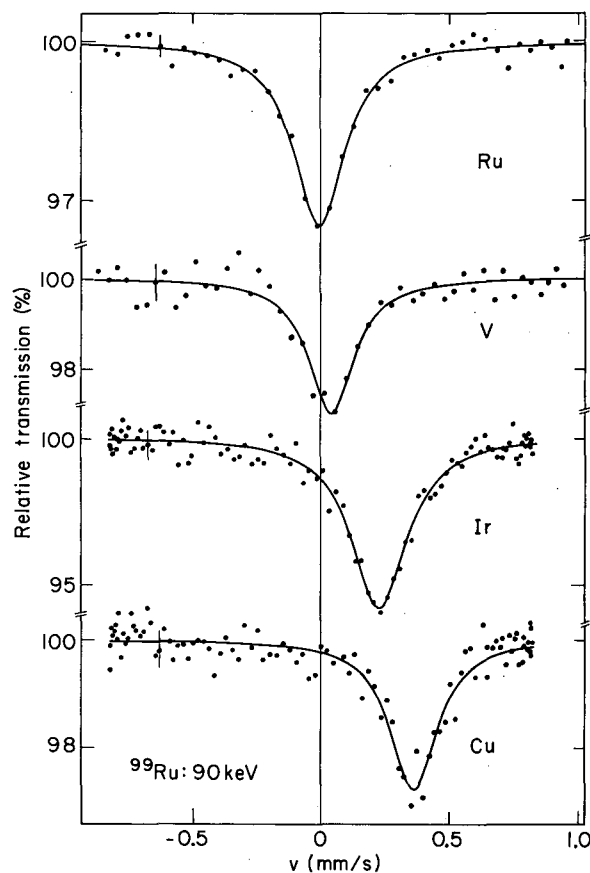


Fig. 2. Mössbauer absorption spectra of the 90-keV gamma rays of ^{99}Ru , obtained with a single-line ruthenium metal absorber, and sources of dilute impurities of ^{99}Rh in Ru, V, Ir, and Cu, both at 4.2 K. (XBL 727-3569)

The present isomer shift results, together with previously published data on ^{57}Fe (Ref. 4) are plotted in Fig. 3 versus the number of valence electrons of the host metals. With the used sign convention a more positive isomer shift corresponds to a larger transition energy. For all three gamma resonances, values for the changes of the mean-squared nuclear charge radii are well established.⁵⁻⁷ From the signs for $\Delta \langle r^2 \rangle$ it follows that in

the ^{57}Fe case the total electron density at the nucleus ($|\psi_0|^2$) decreases with increasing isomer shift, while it increases in the ^{197}Au and ^{99}Ru cases. From the results presented in Fig. 3 we may then conclude that $|\psi_0|^2$ generally increases from 5d via 4d to 3d host metals in a vertical column of the periodic table. Exceptions from this rule are observed only for the homologues of Fe, where drastic structure changes occur. This increase in $|\psi_0|^2$ from 5d to homologous 4d and 3d hosts corresponds to an effective $d \rightarrow s$ electron transfer in the electronic charge on the impurity atom. Such effects have been discussed theoretically by da Silva et al., using a pseudopotential approach.⁸

The variation of $|\psi_0|^2$ within a d-series of transition metal hosts, on the other hand, exhibits certain differences between impurities of ^{57}Fe , ^{197}Au , and ^{99}Ru . This behaviour of $|\psi_0|^2$ should reflect changes in the band structure as well as differences in the atomic volumes of the host metals. While band structure effects should cause a decrease in $|\psi_0|^2$ with increasing N, atomic volume effects are expected to lead to a maximum in $|\psi_0|^2$ at $N \approx 7$, since the atomic volumes reach a minimum there. The differences of the variation of $|\psi_0|^2$ with N suggest that the relative weight of both effects is strongly dependent on the impurity atoms.

The authors would like to thank Prof. D. A. Shirley for support of this work and for valuable discussions.

Footnote and References

* Present address: Physik-Department E15, Technische Universität München, D-8046 Garching, Germany.

1. D. Salomon, G. Kaindl, and D. A. Shirley, *Phys. Letters* **36A**, 457 (1971).
2. G. Kaindl and D. Salomon, in *Perspectives in Mössbauer Effect Spectroscopy*, edited by S. G. Cohen and M. Pasternak (Plenum Press, New York, 1973).
3. G. Kaindl, D. Salomon, and G. Wortmann, following contribution.
4. S. M. Quaim, *Proc. Phys. Soc. (London)* **90**, 1065 (1967). B. Window, G. Longworth, and C. E. Johnson, *J. Phys. C, Solid State Physics* **3**, 2156 (1970). A. H. Muir, Jr., K. J. Ando, and H. M. Coogan, *Mössbauer Effect Data Index 1958-1965* (Interscience Publishers, New York 1966).
5. W. Potzel, F. E. Wagner, R. L. Mössbauer, G. Kaindl, and H. E. Seltzer, *Z. Physik* **241**, 179 (1971).

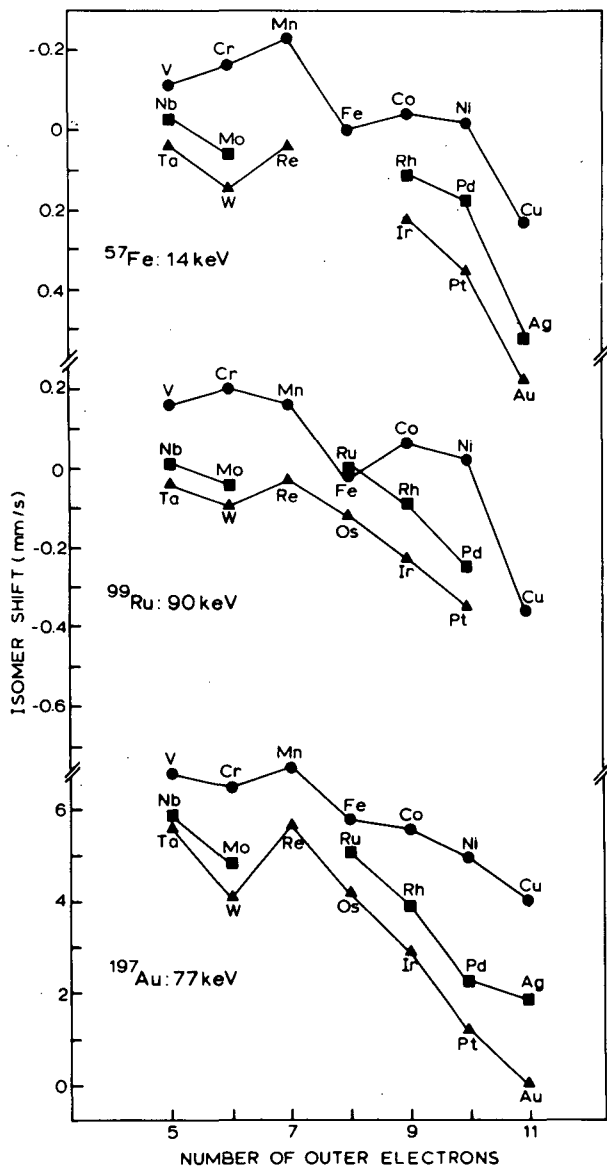


Fig. 3. Systematics of isomer shifts of Mössbauer gamma rays of ^{57}Fe (14.4 keV), ^{197}Au (77 keV), and ^{99}Ru (90 keV) for dilute impurities of the Mössbauer elements in transition metal hosts. (XBL 733-330)

6. G. K. Shenoy and G. M. Kalvius, in *Hyperfine Interactions in Excited Nuclei*, edited by G. Goldring and R. Kalish (Gordon and Breach, 1971), p. 1201.

7. H. Micklitz and P. H. Barrett, *Phys. Rev. Letters* **28**, 1547 (1972).

8. X. A. da Silva, A. A. Gomes, and J. Danon, *Phys. Rev.* **4B**, 1161 (1971).

HIGH-RESOLUTION STUDY OF ISOMER SHIFTS OF THE 6.2-keV GAMMA RAYS OF ^{181}Ta

G. Kaindl,* D. Salomon, and G. Wortmann†

This paper reports on the study of isomer shifts of the 6.2-keV gamma rays of ^{181}Ta for dilute impurities of tantalum in 3d, 4d, and 5d transition metal hosts and for several tantalum compounds. The observed isomer shifts cover a total range of 110 mm/sec, corresponding to 17 000 times twice the natural line width of the 6.2-keV gamma resonance, or 1600 times the minimum experimental line width obtained up to now.

The experiments divide into source and absorber experiments. In the former ones the hyperfine splitting of the Mössbauer gamma rays emitted from dilute impurities of ^{181}Ta in transition metal hosts was investigated by using a single-line tantalum metal absorber. In the latter cases Mössbauer spectra were measured for absorbers of tantalum compounds by using a single-line source of ^{181}W diffused into tungsten metal. More details of the experimental technique have been presented elsewhere.¹

Some representative single-line spectra for metallic sources are shown in Fig. 1. The pronounced asymmetry of the line shapes results from an interference between photoelectric absorption and Mössbauer absorption followed by internal conversion.²⁻⁴ Accordingly, the absorption spectra were least-squares fitted with dispersion-modified Lorentzian lines, using a value of $2\xi = -0.30$ (in the definition of Ref. 3) for the amplitude of the dispersion term.⁵⁻⁷

The isomer shift results for dilute impurities of ^{181}Ta in transition metal hosts, with both sources and absorbers at room temperature, are summarized in Table I. The isomer shifts are defined in such a way that a more positive value corresponds to a larger transition energy.

Mössbauer spectra have also been measured at room temperature for the alkali tantalates LiTaO_3 (Ref. 9), NaTaO_3 (Ref. 9), and KTaO_3 (Refs. 10 and 11), and for TaC (Ref. 11).

The single-line spectra obtained for TaC and KTaO_3 , with both compounds having cubic structure, are presented in Fig. 2. Table II summarizes all of the isomer shift results obtained up to now for compounds of tantalum.

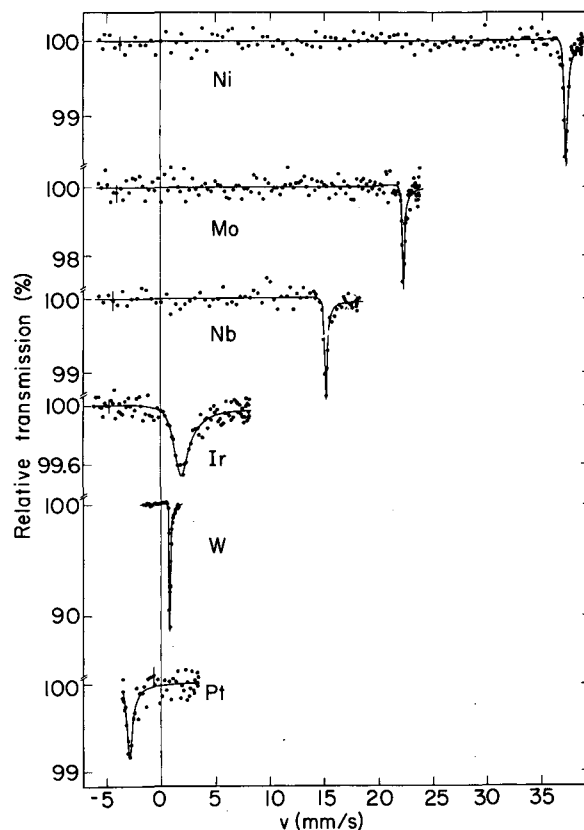


Fig. 1. Single-line absorption spectra of the 6.2-keV gamma rays, obtained with a tantalum metal absorber and sources of ^{181}W diffused into various cubic transition metal hosts. The solid lines represent the results of least-squares fits of dispersion modified Lorentzian lines to the data. (XBL 727-3567)

Table I. Summary of isomer shift results for sources of ^{181}W diffused into various transition metal hosts, relative to a tantalum metal absorber, with both sources and absorbers at room temperature.

Source lattice	IS (mm/s)	W(FWHM) (mm/s)	Effect (%)
V	-33.2 ±0.5	5.0 ±1.0	0.1
Ni	-39.5 ±0.2 ^a	0.50 ±0.08	1.6
Nb	-15.26 ±0.10	0.19 ±0.06	1.5
Mo	-22.60 ±0.10	0.13 ±0.04	3.0
Ru	-27.50 ±0.30	1.3 ±0.2	0.7
Rh	-28.80 ±0.25	3.4 ±0.5	0.3
Pd	-27.80 ±0.25	1.3 ±0.3	0.3
Hf	- 0.60 ±0.30	1.6 ±0.4	0.2
Ta	- 0.075±0.004	0.184±0.006	2.4
W	- 0.860±0.008	0.069±0.001	2.0
Re	-14.00 ±0.10	0.60 ±0.04	1.3
Os	- 2.35 ±0.04	1.8 ±0.2	0.8
Ir	- 1.84 ±0.04	1.60 ±0.14	0.5
Pt	+ 2.66 ±0.04	0.30 ±0.08	1.5

^aExtrapolated to room temperature from the temperature dependence of the line position, measured for the $^{181}\text{W}(\text{Ni})$ -source in the temperature range 685 to 1003 K.⁸

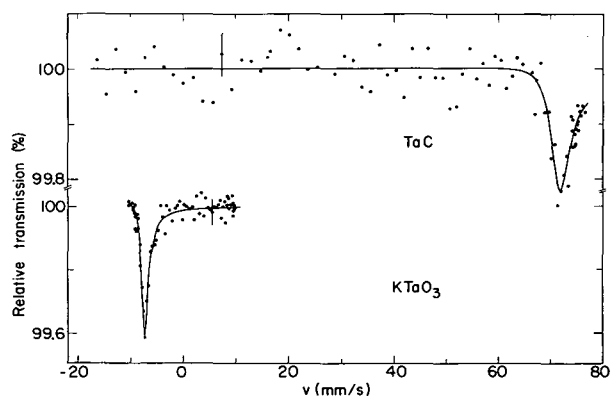


Fig. 2. Mössbauer absorption spectra for TaC and KTaO₃, recorded with a source of $^{181}\text{W}(\text{W})$. (XBL 727-3563)

Table II. Compilation of isomer shift results for several tantalum compounds, relative to a tantalum metal absorber at room temperature.⁹⁻¹¹

Compound	IS (mm/s)	W(FWHM) (mm/s)	Effect (%)
LiTaO ₃	-24.04±0.30	1.6±0.2	0.9
NaTaO ₃	-13.26±0.30	1.0±0.2	0.9
KTaO ₃	- 8.11±0.15	1.5±0.2	0.3
TaC	+70.8 ±0.5	2.4±0.4	0.2

The isomer shifts for dilute impurities of ^{181}Ta in transition metal hosts exhibit systematic features when plotted versus the number of electrons in the valence shell of the elements, as shown in Fig. 3. The data can be arranged in three groups corresponding to 3d, 4d, and 5d host metals. Without exception, the transition energy decreases when

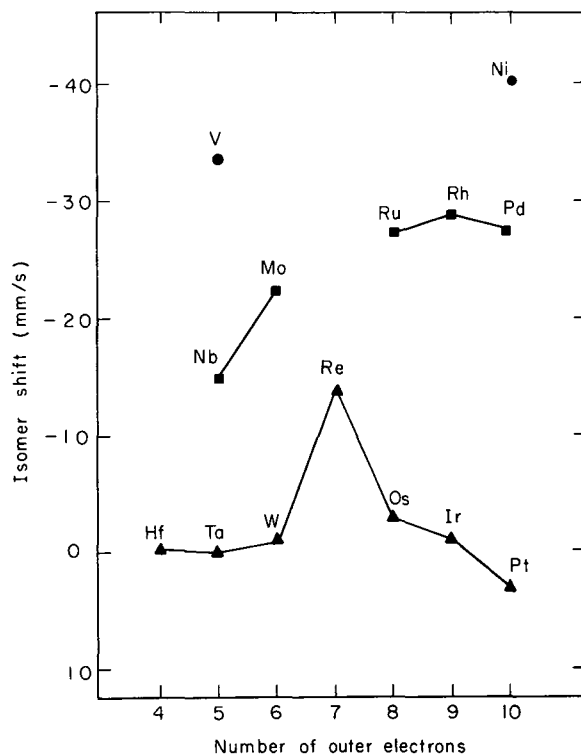


Fig. 3. Systematics of isomer shifts of the 6.2-keV gamma rays for dilute impurities of ^{181}Ta in transition metal hosts. (XBL 725-2957)

Table III. (a) Isomer shift differences between homologous 4d and 5d transition metal hosts, measured with gamma resonances of impurities of ^{181}Ta (6.2 keV), ^{197}Au (77 keV), ^{193}Ir (73 keV), ^{99}Ru (90 keV), and ^{57}Fe (14.4 keV). (b) Ratios of $\Delta\text{IS}(^{181}\text{Ta})$ to those of the other gamma resonances (X), measured for the same pair of most metals.

		4d - 5d host metal pairs					
		Nb - Ta	Mo - W	Ru - Os	Rh - Ir	Pd - Pt	References
(a)	^{181}Ta	-15.18 ±0.11	-21.64 ±0.11	-25.15 ±0.35	-26.96 ±0.30	-30.46 ±0.30	This work
	^{197}Au	0.28 ±0.03	0.75 ±0.05	0.91 ±0.05	1.00 ±0.07	1.04 ±0.04	13, 14, 15
ΔIS	^{193}Ir	0.27 ±0.04	0.37 ±0.08	0.43 ±0.02	0.62 ±0.02	0.65 ±0.03	14, 15
(mm/s)	^{99}Ru	0.055±0.011	0.092±0.010	0.109±0.005	0.121±0.009	0.123±0.014	13, 14, 15
	^{57}Fe	- 0.25 ±0.05	- 0.23 ±0.05	- 0.08 ±0.05	- 0.14 ±0.02	- 0.18 ±0.02	12
(b)	X= ^{197}Au	- 54±6	- 29± 2	- 28± 2	- 27± 2	- 29± 2	
	X= ^{193}Ir	- 57±10	- 59±14	- 58± 3	- 44± 2	- 47± 3	
$\frac{\Delta\text{IS}(^{181}\text{Ta})}{\Delta\text{IS}(X)}$	X= ^{99}Ru	-276±57	-235±27	-231± 14	-223±19	-248±31	
	X= ^{57}Fe	61±13	96±22	314±200	197±32	174±20	

proceeding from a 5d to a 4d and further to a 3d host metal in the same column of the periodic table.

A similar systematic behavior has been observed for isomer shifts of Mössbauer gamma rays of ^{57}Fe (14.4 keV), $^{12}\text{ }^{99}\text{Ru}$ (90 keV), ^{197}Au (77 keV), and ^{193}Ir (73 keV).¹³⁻¹⁵ In all of these cases estimates for the changes of the mean-squared nuclear charge radii $\Delta \langle r^2 \rangle$ are well established,¹⁶ so that information on the systematic behavior of electronic densities at impurity nuclei may be derived. This in turn can be used to estimate $\Delta \langle r^2 \rangle$ for the present gamma resonance.

As we have seen in the preceding contribution¹³ the electron density at the nucleus of the impurity atom as a rule increases when going from a 5d via a 4d to a 3d host metal in a vertical column of the periodic table.

Table III summarizes the experimental isomer shift differences between homologous 4d and 5d transition metal hosts (ΔIS) for gamma resonances of ^{197}Au , ^{193}Ir , ^{99}Ru , ^{57}Fe , and ^{181}Ta . We will compare only isomer shift differences between those transition metal hosts, since for them effects of differences in the atomic volumes of the host metals are expected to be small. The reason is that

the atomic volumes of homologous 4d and 5d host metals are almost equal. In the lower part of the table, the ratios of ΔIS for ^{181}Ta to those measured for other gamma resonances (X) between the same pair of host metals are listed. With a few exceptions these ratios are remarkably constant within the limits of error for a given pair of gamma resonances. This means that the differences of electron densities measured for two transition metal impurities for various homologous 4d-5d host metal pairs are approximately proportional to each other. If the proportionality factors can be estimated, the ratios of isomer shift differences listed in Table IV may be used to obtain ratios of $\Delta \langle r^2 \rangle$ for the pertinent gamma resonances, using the following relation

$$\frac{\Delta \langle r^2 \rangle_1}{\Delta \langle r^2 \rangle_2} = \frac{\Delta IS_1}{\Delta IS_2} \frac{E_1 Z_2}{E_2 Z_1} \frac{1}{C_{1,2}}$$

Here the indices 1 and 2 refer to two separate gamma resonances with energies E_1 and E_2 in elements with atomic numbers Z_1 and Z_2 , respectively. The proportionality factor $C_{1,2}$ describes the ratio of electron density differences at impurity element 1 to those at impurity element 2 for homologous 4d-5d host metal pairs.

Table IV. Derivation of $\Delta \langle r^2 \rangle$ for the 6.2-keV gamma resonance from systematics of isomer shifts in transition metal hosts. For explanations see text.

Gamma resonance X	$\frac{\Delta IS(^{181}\text{Ta})}{\Delta IS(X)}$	$C_{^{181}\text{Ta}, X}$	$\frac{\Delta \langle r^2 \rangle_{\text{Ta}}}{\Delta \langle r^2 \rangle_X}$	$\Delta \langle r^2 \rangle_X$ (10^{-3} fm^2)	$\Delta \langle r^2 \rangle_{\text{Ta}}$ (10^{-3} fm^2)
^{197}Au , 77 keV	- 30	0.45	-5.81	9 ^a	-52.3
^{193}Ir , 73 keV	- 49	0.44	-9.98	4.6 ^b	-45.9
^{99}Ru , 90 keV	-236	4.5	-2.18	25 ^c	-54.5
^{57}Fe , 14.4 keV	154	11.5	2.05	-25 ^d	-51.2
				Average:	-51

^aRef. 21.

^bRef. 16.

^cRef. 22.

^dRef. 23.

Under the assumption that the effective $d \rightarrow s$ electron transfer, which obviously takes place in the electronic charge on the impurity atom when placing it from a 5d transition metal host into its 4d homologue, is of the same magnitude for different transition metal impurities, values for $C_{1,2}$ have been estimated by using the results of relativistic free-ion Dirac-Fock calculation for Ru, Ta, and Au (Ref. 18), and those of non-relativistic Hartree-Fock calculations for Fe (Ref. 19) and Ir (Ref. 20).

Table IV summarizes the data employed for deriving estimates for $\Delta \langle r^2 \rangle$. In column 2 the weighted mean of the individual ratios $\Delta IS(^{181}\text{Ta})/\Delta IS(X)$, given in Table III, are listed for the four gamma resonances relative to the ^{181}Ta resonance. From them the values for $\Delta \langle r^2 \rangle_{\text{Ta}}$, listed in column 6, were obtained, using the $C_{181\text{Ta},X}$ factors of column 3 and the values for $\Delta \langle r^2 \rangle_X$ given in column 5. As a final result for $\Delta \langle r^2 \rangle_{\text{Ta}}$ we take the mean value of the four estimates:

$$\Delta \langle r^2 \rangle = -5.1 \times 10^{-2} \text{ fm}^2.$$

The error in $\Delta \langle r^2 \rangle$ can only be estimated, especially since it is directly correlated with the uncertainties of the $\Delta \langle r^2 \rangle_X$ values from which it was derived. We think, however, that an upper limit of 30% is appropriate.

This is one of the largest changes of the nuclear charge radius found for Mössbauer transitions. In combination with the small natural width of the 6.2-keV gamma rays, the large magnitude of $\Delta \langle r^2 \rangle$ forms the basis for the extreme resolving power of this Mössbauer resonance.

The authors would like to thank Profs. D. A. Shirley, G. M. Kalvius, and R. L. Mössbauer for valuable discussions as well as continuous support of this work. We are also indebted to Drs. N. K. Krakorian, J. J. Nickel, and V. Gotthard for supplying high-purity TaC samples, as well as to Dr. J. B. Mann for communication of theoretical results prior to publication.

Footnotes and References

* Present address: Physik-Department E15, Technische Universität München, D-8046 Garching, Germany.

† Present address: Physik-Department E15 Technische Universität München, Germany.

1. D. Salomon (thesis), LBL-1276 (1972).
2. C. Sauer, E. Matthias, and R. L. Mössbauer, Phys. Rev. Letters 21, 961 (1968).
3. G. T. Trammel and J. P. Hannon, Phys. Rev. 180, 337 (1969).
4. Yu. M. Kagan, A. M. Afanasev, and V. K. Vojtovetskii, Sov. Phys. - JETP Letters 9, 91 (1969).
5. G. Kaindl and D. Salomon, Phys. Letters 32B, 364 (1970).
6. G. Kaindl and D. Salomon, in Perspectives in Mössbauer Effect Spectroscopy, edited by C. G. Cohen and M. Pasternak, (Plenum Press, New York, 1973).
7. G. Kaindl and D. Salomon, Nuclear Chemistry Division Annual Report for 1970, UCRL-20426, p. 215.
8. G. Kaindl and D. Salomon, submitted to Phys. Rev. Letters, and following contribution.
9. G. Kaindl and D. Salomon, Bull. Am. Phys. Soc. 17, 681 (1972) and following contributions.
10. D. Salomon, G. Kaindl, D. A. Shirley Phys. Letters 36A, 457 (1971).
11. G. Kaindl and D. Salomon, Nuclear Chemistry Division Annual Report for 1971, LBL-666, p. 196.
12. S. M. Quaim, Proc. Phys. Soc. (London) 90, 1065 (1967).
13. G. Kaindl and D. Salomon, Proc. of the International Conference on Applications of the Mössbauer Effect, Israel (1972), and preceding contribution.
14. G. Wortmann, F. E. Wagner, and G. M. Kalvius, in Proceedings of the International Conference on Applications of the Mössbauer Effect, Israel, 1972.
15. G. Wortmann, F. E. Wagner, and G. M. Kalvius, preprint (1972).
16. C. K. Shenoy and G. M. Kalvius, in Hyperfine Interactions in Excited Nuclei, edited by G. Goldring and R. Kalish (Gordon and Breach, New York, 1971), p. 1201.
17. X. A. da Silva, A. A. Gomes, and J. Danon, Phys. Rev. B 4, 1161 (1971).
18. J. B. Mann, Los Alamos Scientific Laboratory, University of California, private communication (1972).
19. J. Blomquist, B. Roos, and M. Sundbom, J. Chem. Phys. 55, 141 (1971).

22. W. Potzel, F. E. Wagner, R. L. Mössbauer, G. Kaindl, and H. E. Seltzer, *Z. Physik* **241**, 179 (1971).

23. H. Micklitz and P. H. Barrett, *Phys. Rev. Letters* **28**, 1547 (1972).

20. L. W. Panek and G. J. Perlow, Argonne National Laboratory Report ANL-7631 (1969), unpublished.

21. L. D. Roberts, D. O. Patterson, J. O. Thomson, and R. P. Levey, *Phys. Rev.* **179**, 656 (1969).

TEMPERATURE SHIFTS OF THE ENERGY OF THE 6.2-keV GAMMA RAYS OF ^{181}Ta

G. Kaindl* and D. Salomon

The effects of temperature on the energy of Mössbauer gamma rays have been studied up to now in detail only for ^{57}Fe (Refs. 1-4) and ^{119}Sn .⁵ For both these Mössbauer resonances the observed variations with temperature were found to be mainly caused by the second-order Doppler (SOD) effect (thermal redshift).⁶ Accordingly, information on the variation of the total electron density at the nucleus with temperature could be derived only after dominant corrections for the thermal redshift had been made;^{5,7} therefore, this procedure may have introduced large systematic errors, limiting the accuracy of the derived results.

The case of the 6.2-keV gamma resonance of ^{181}Ta is quite different, as will be reported in this paper. Recently this Mössbauer resonance has been applied extensively to high-resolution studies of hyperfine interactions,⁸ and its especially high resolving power in the field of isomer shifts has been recognized.^{8,9} We have now found that the energy of the 6.2-keV gamma rays, emitted from ^{181}Ta as a dilute impurity in transition metals, exhibits a strong temperature dependence far beyond the expected SOD shift. The results underline the exceptional sensitivity of the 6.2-keV gamma resonance and open new possibilities in solid state applications of isomer shift studies.

The host metals investigated in this study are Ta, W, Ir, Pt, Nb, Mo, Pd, and Ni. Sources of ^{181}W diffused into these metals were studied at temperatures up to 1000°K, using a single-line Ta metal absorber at room temperature ($\approx 4 \text{ mg/cm}^2$ thick). Details of the experimental technique have been presented elsewhere.¹⁰

Figure 1 shows the experimental variations with temperature of the line positions for five of the sources. It is striking that in the case of the nickel host the transition energy increases with temperature with a slope which is 32 times larger, and of opposite sign, than

the one expected from the SOD shift alone. While the slopes of the temperature shifts for W, Ta, and Pt hosts are of the same sign as the SOD shift, they are up to 8 times larger. Within the accuracy of the present experiments the data can be described by a linear relationship between the lineshift S and the source temperature T . The solid lines are the results of a least-squares fit of straight lines to the data.

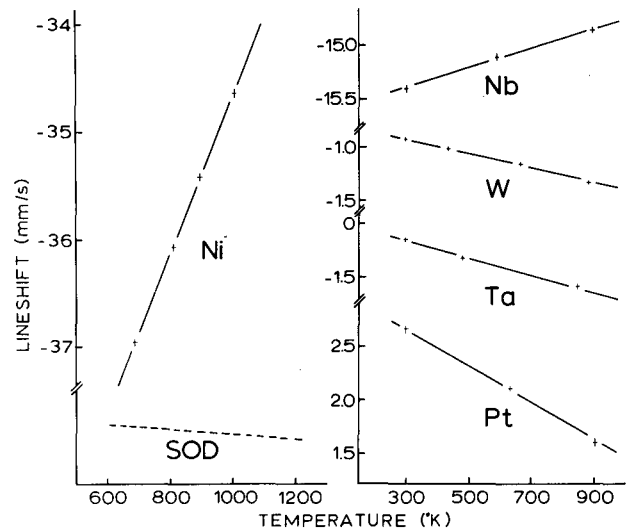


Fig. 1. Temperature dependence of line positions for sources of ^{181}W diffused into Ni, Nb, W, Ta, and Pt. For comparison, the SOD shift, expected for a Debye solid in the limit of high temperatures, is also shown. All curves are plotted on the same scale.

(XBL 733-331)

We may write for the experimentally observed temperature variation of the line position S

$$\left(\frac{\partial S}{\partial T}\right)_P = \left(\frac{\partial S_{\text{SOD}}}{\partial T}\right)_P + \left(\frac{\partial S_{\text{IS}}}{\partial T}\right)_V + \left(\frac{\partial S_{\text{IS}}}{\partial \ln V}\right)_T \left(\frac{\partial \ln V}{\partial T}\right)_P \quad (1)$$

The first term accounts for the temperature variation of the SOD shift which is given for a Debye solid in the limit of high temperatures by $-2k/2Mc$ in cm/s, amounting to $-2.30 \cdot 10^{-4}$ mm/s per degree for the present gamma transition. The second term represents the explicit temperature dependence of the isomer shift at constant volume due to temperature-induced changes of the total electron density at the nucleus. The third term describes the volume dependence of the isomer shift caused by thermal expansion of the lattice.

Table I summarizes the experimental data, with the lineshifts S for both source and absorber at room temperature listed in column 2, and the experimental results for the isobaric temperature variation of the transition energy, $(\partial S/\partial T)_P$, presented in column 3. The values for the isobaric temperature dependence of the isomer shift, $(\partial S_{\text{IS}}/\partial T)_P$. In view of the fact that these corrections are small compared to the total temperature shifts, and that the measurements were carried out in

the temperature range 300 to 1000°K, where the high-temperature Debye model should approximately hold, this procedure should be satisfactory within the present accuracy. Also presented are representative values for the thermal expansion coefficients, $(\partial \ln V/\partial T)_P$ (column 5).

Until now temperature shifts of the 6.2-keV gamma rays have been reported only for a W host by Taylor et al.,¹¹ and their results agree well with the present measurements. In the case of ^{57}Fe , temperature shifts of the energy of the 14.4-keV gamma rays have been measured for dilute impurities of ^{57}Fe in 3d, 4d, and 5d transition metals.^{3,4} Even though these shifts arise mainly from the SOD effect, the derived values for $(\partial S_{\text{IS}}/\partial T)_P$ exhibit characteristics similar to the present case.⁷

A separation of $(\partial S_{\text{IS}}/\partial T)_P$ into the explicitly temperature-dependent part and the volume-dependent part of Eq. (1) cannot be carried out quantitatively with the present results alone. The necessary additional information could be obtained from high-pressure isomer-shift studies, which would directly provide values for $(\partial S_{\text{IS}}/\partial \ln V)_T$.

For a qualitative discussion we use a value of $\Delta \langle r^2 \rangle \approx -5 \times 10^{-2} \text{ fm}^2$ for the change of the mean-squared nuclear charge radius, as recently derived from isomer shift studies in transition metal hosts.⁹ Since the electron

Table I. Summary of experimental results and derived quantities for dilute impurities of ^{181}Ta in transition metal hosts.

Host metal	S (mm/s)	$(\partial S/\partial T)_P$ (10^{-4} mm/s $^{-1}$ · deg $^{-1}$)	$(\partial S_{\text{IS}}/\partial T)_P$ (10^{-4} mm/s $^{-1}$ · deg $^{-1}$)	$(\partial \ln V/\partial T)_P$ (10^{-5} deg $^{-1}$)
Ni	-39.5 ± 0.2 ^a	73.2 ± 3.5	75.5 ± 3.5	5.2
Nb	-15.3 ± 0.1	9.2 ± 1.0	11.5 ± 1.0	2.5
Mo	-22.5 ± 0.1	3.6 ± 0.6	5.9 ± 0.5	1.7
Pd	-27.6 ± 0.3	-16.7 ± 7.0	-16.7 ± 7.0	3.5
Ta	- 0.075 ± 0.004	- 8.0 ± 0.5	- 5.7 ± 0.5	2.0
W	- 0.86 ± 0.01	- 7.1 ± 0.2	- 4.8 ± 0.2	1.4
Ir	- 1.84 ± 0.04	-10.7 ± 3.3	- 8.4 ± 3.3	2.0
Pt	+ 2.66 ± 0.04	-17.6 ± 0.9	-15.3 ± 0.9	2.9

^aExtrapolated to room temperature from the temperature dependence of the line position, measured in the range 685 to 1003 K

density at the nucleus, $|\psi_0|^2$, should decrease with increasing volume, we expect positive values for $(\partial S_{IS}/\partial \ln V)_T$ in all cases, even though their magnitudes might exhibit large variations, as observed in the case of ^{57}Fe . There, isomer shifts have been measured as a function of pressure for impurities of ^{57}Fe in a series of 3d, 4d, and 5d transition metal hosts,¹² and $(\partial S_{IS}/\partial \ln V)_T$ was found to increase with decreasing isomer shift (or increasing $|\psi_0|^2$), as expected from a scaling of $|\psi_0|^2$, as expected from a scaling of $|\psi_0|^2$ with volume. We may expect a similar behavior of $(\partial S_{IS}/\partial \ln V)_T$ in the ^{181}Ta case. This means that the negative values of $(\partial S_{IS}/\partial T)_P$, observed for the Pd, Ta, W, Ir, and Pt hosts, originate from an overcompensation of the positive volume shifts by negative contributions due to an explicit temperature dependence of the isomer shift.

Since $|\psi_0|^2$ is found to increase from 5d to 4d and to 3d hosts in a vertical column of the periodic system,⁹ it is expected that $(\partial S_{IS}/\partial \ln V)_T$ is larger for 3d than for 5d hosts. The large positive value of $(\partial S_{IS}/\partial T)_P$ observed for the nickel host may then be explained by a dominant contribution due to thermal expansion, especially since the thermal expansion coefficient is so large for this metal. For an order-of-magnitude estimate of $(\partial S_{IS}/\partial T)_V$ we take for the conduction electron contribution to $|\psi_0|^2 \approx 3.0 \times 10^{26} \text{ cm}^{-3}$, as estimated from the⁰ results of Dirac-Fock calculations for free-ion configurations of Ta (Ref. 13) and from band structure calculations for tantalum metal.¹⁴ With the simple volume scaling assumption

$$\Delta |\psi_0|^2 \approx - \frac{\Delta V}{V} |\psi_0|^2_{c.e.} \quad (2)$$

we then estimate for $(\partial S_{IS}/\partial \ln V)_T (\partial \ln V/\partial T)_P$ a value of $\sim 32 \times 10^{-4} \text{ mm/sec per degree}$, resulting in $(\partial S_{IS}/\partial T)_V \approx - 27 \times 10^{-4} \text{ mm/sec per degree}$ for tantalum metal.

We may conclude from this estimate that $|\psi_0|^2$ increases in tantalum metal explicitly with temperature by $\sim 5 \times 10^{21} \text{ cm}^{-3}$ per degree, which corresponds to a $d \rightarrow s$ electron transfer with increasing temperature of approximately 10^{-5} electrons per degree. Such effects have been discussed theoretically in connection with the temperature dependence of the Knight shift, and have been interpreted as arising from an effective decrease in the strength of the lattice potential caused by lattice vibrations.¹⁵ In this way, the energy bands become more free-electron like, leading to an increase in the s character of the wave functions. This effect should exhibit a strong dependence on the electronic structure of the metals. It is to be expected that, as soon as

pressure data will be available for the ^{181}Ta gamma resonance, the present results will provide a very detailed insight into these subtle effects.

The authors would like to thank Prof. D. A. Shirley for his constant interest in this work. They are also indebted to Prof. L. M. Falicov for valuable discussions.

Footnote and References

*Present address: Physik-Department, Technische Universität München, D-8046 Garching, Germany.

1. R. V. Pound and G. A. Rebka, Jr., Phys. Rev. Letters **4**, 274 (1960).
2. R. V. Pound, G. B. Benedek, and R. Drever, Phys. Rev. Letters **7**, 405 (1961).
3. R. S. Preston, S. S. Hanna, and J. Heberle, Phys. Rev. **128**, 2207 (1962).
4. W. A. Steyert and R. D. Taylor, Phys. Rev. **134**, A716 (1964).
5. G. M. Rothberg, S. Guimard, and N. Benczer-Killer, Phys. Rev. B **1**, 136 (1970).
6. B. D. Josephson, Phys. Rev. Letters **4**, 341 (1960).
7. R. M. Housley and F. Hess, Phys. Rev. **164**, 340 (1967).
8. G. Kaindl and D. Salomon, in Perspectives in Mössbauer Effect Spectroscopy, edited by S. G. Cohen and M. Pasternak (Plenum Press, New York, 1973).
9. G. Kaindl, D. Salomon, and G. Wortmann, submitted to Phys. Rev. B, and preceding contribution.
10. D. Salomon (thesis), LBL-1276 (1972).
11. R. D. Taylor and E. K. Storms, Bull. Am. Phys. Soc. **14**, 836 (1969).
12. R. Ingalls, H. G. Drickhamer, and G. de Pasquali, Phys. Rev. **155**, 165 (1967).
13. J. B. Mann, Los Alamos Scientific Laboratory, University of California, private communication (1972).
14. L. F. Mattheiss, Phys. Rev. B **1**, 373 (1970).
15. R. V. Kasovski and L. M. Falicov, Phys. Rev. Letters **22**, 1001 (1969).

STUDY OF ELECTRIC-QUADRUPOLE HYPERFINE INTERACTIONS
WITH THE 6.2-keV GAMMA RESONANCE OF ^{181}Ta

G. Kaindl* and D. Salomon

Recently, the electric quadrupole hyperfine splitting of the 6.2-keV gamma rays of ^{181}Ta has been observed for the first time, using a source of ^{181}W diffused into single-crystal rhenium metal.¹ From the completely resolved spectra the ratio of the electric quadrupole moments, the electric quadrupole interaction of ^{181}Ta in rhenium metal, and the isomer shift relative to Ta metal were derived. As a consequence of the small natural width of the 6.2-keV gamma rays and the large electric quadrupole moments of the ^{181}Ta nucleus in both nuclear states, this Mössbauer resonance offers unusual resolution for the study of electric quadrupole interactions.

In this paper we report on an extension of

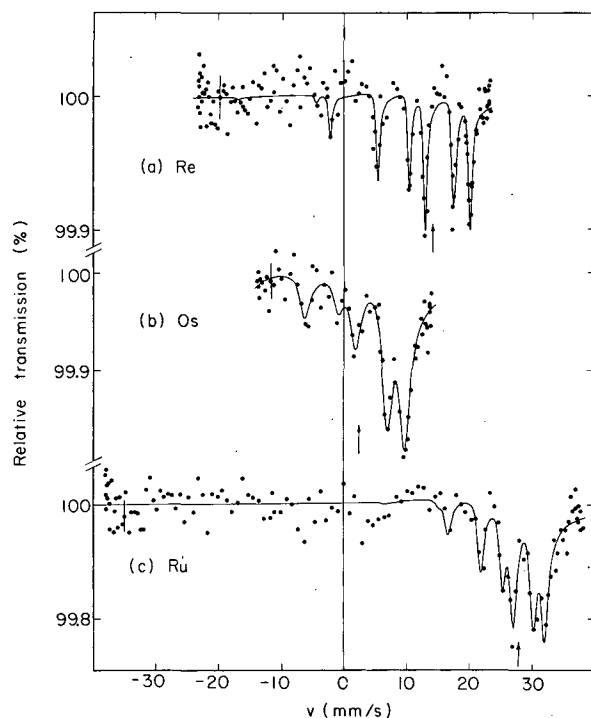


Fig. 1. Mössbauer absorption spectra for sources of $^{181}\text{W}(\text{Re})$ (single-crystal, observed perpendicular to the $[0001]$ axis) (a), $^{181}\text{W}(\text{Os})$ (polycrystalline) (b), and $^{181}\text{W}(\text{Ru})$ (single-crystal, observed perpendicular to the $[0001]$ -axis) (c), all three analyzed with a single-line tantalum metal absorber.

(XBL 725-2960)

this work: we have studied the electric quadrupole interaction of ^{181}Ta as an impurity atom in Re, Os, Hf, and Ru metal, and in LiTaO_3 and NaTaO_3 . All experiments were performed with both sources and absorbers at room temperature in the same way as described previously.¹

Some typical velocity spectra are presented in Fig. 1: in (a) for a single-crystal $^{181}\text{W}(\text{Re})$ source; in (c) for a single-crystal $^{181}\text{W}(\text{Ru})$ source, in both cases with direction of observation perpendicular to the $[0001]$ direction;¹ and in (b) for a polycrystalline $^{181}\text{W}(\text{Os})$ source. For the assignment of individual transitions to the observed lines we refer to Ref. 1.

The absorption spectra obtained for absorbers of LiTaO_3 and NaTaO_3 are presented in Fig. 2. In both cases the absorber preparation technique was found to result in a highly preferred orientation of the axis of the

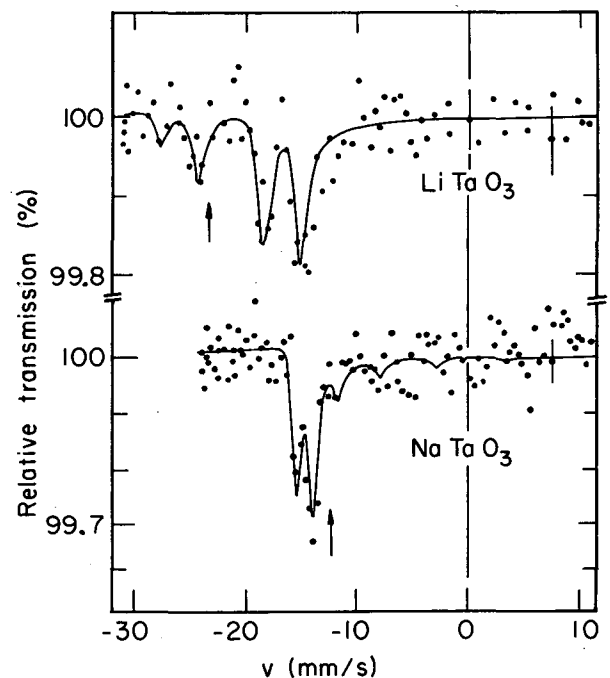


Fig. 2. Hyperfine splitting of the 6.2-keV gamma rays in LiTaO_3 and NaTaO_3 at room temperature. The centers of the spectra are indicated by arrows.

(XBL 733-2561)

electric field gradient (EFG) perpendicular to the absorber planes. Therefore the spectra of Fig. 2 were measured with the absorber planes tilted by 45° relative to the gamma-ray direction, in order to get an appreciable intensity in the $\pm 1/2 \rightarrow \pm 1/2$ component, which is necessary for a determination of the sign of the EFG.

From least-squares fits of a superposition of dispersion-modified Lorentzian lines² to the data, values for the electric quadrupole interaction of the ^{181}Ta ground state, $e^2qQ(7/2)$ and for the isomer shift of the 6.2-keV gamma rays were obtained. In all cases, the EFG was assumed to be axially symmetric. The amplitude of the dispersion term, $2\xi = -0.30 \pm 0.01$ (Ref. 2), and — for all spectra besides the one for the rhenium host — the ratio of electric quadrupole moments $Q(9/2)/Q(7/2) = 1.133 \pm 0.010$ (Ref. 1), were kept constant during the fit procedure.

The experimental results are summarized in Table I. The values for eq , given in column 3, were obtained with $Q(7/2) = +3.9 \pm 0.4$ barns (Ref. 3) for the electric quadrupole moment of the ground state of ^{181}Ta , and the errors of eq are mainly due to the $\sim 10\%$ uncertainty in $Q(7/2)$. For all the studied cases the sign of eq was also determined.

Presently, no satisfactory theory exists for electric field gradients in hexagonal transition metals. Our result shows that a simple "point-ion and uniform background model"⁴ alone is not sufficient, since the electric field gradients calculated with its help are positive for all the studied metals, while the experimental values are negative for Re, Os, and Ru. Such a model

considers only the lattice contribution q_{latt} to the electric field gradient. Obviously, the local contributions, caused by a non-cubic arrangement to localized charge around the central atom, as well as by a non-uniform distribution of conduction electrons within the central cell, play an essential role. The latter effect has been discussed by Watson et al.,⁵ who predicted an "overshielding effect", caused by the conduction electrons, especially in cases with a high density of states at the Fermi energy. According to them this local conduction electron contribution should be linearly related to the lattice field gradient, $q_{\text{loc}} = r \cdot q_{\text{latt}}$, so that we may write for the total electric field gradient $q = q_{\text{latt}} [(1 - \gamma_\infty) + r(1 - R_Q)]$, where γ_∞ and R_Q are the lattice and atomic Sternheimer factors, respectively. With $\gamma_\infty \approx -60$ (Ref. 6) and $R_Q \approx -0.2$ (Ref. 7) for Ta, and using q_{latt} values calculated with Ref. 4, we may derive overshielding factors r of -160 , -85 , and -75 for Ta in Re, Os, and Ru, respectively. These values are not too different from those predicted for the pure metals: $r \approx -100$ for Re and $r \approx -55$ for Os.⁵

On the other hand, the electric field gradient for $^{181}\text{Ta}(\text{Hf})$ is positive and even bigger than $q_{\text{latt}}(1 - \gamma_\infty)$, and its temperature dependence measured by TDPAC of the $5/2^+$ state at 482 keV of ^{181}Ta (Ref. 8), is well described by the anisotropic variation of the lattice parameters with temperature. This means that in this case the lattice contribution may play an essential role. In order to clarify the situation further, a study of the temperature dependence of the EFG for these host metals is under way.

The authors would like to thank Professor D. A. Shirley for his constant interest.

Table I. Summary of experimental results, obtained for the electric quadrupole interaction of the ground state of ^{181}Ta , $e^2qQ(7/2)$, the electric field gradient eq at the Ta nucleus, the isomer shift (IS) relative to Ta metal, and the total experimental line width W .

Host metal:	$e^2qQ(7/2)$ (10^{-6} eV)	eq (10^{17} V/cm ²)	IS (mm/s)	W (mm/s)
Re	-2.15 ± 0.02	-5.5 ± 0.5	-14.0 ± 0.1	0.60 ± 0.04
Os	-2.35 ± 0.04	-6.0 ± 0.7	-2.9 ± 0.2	1.8 ± 0.2
Hf	$+1.83 \pm 0.10$	$+4.7 \pm 0.7$	-0.6 ± 0.3	1.6 ± 0.4
Ru	-1.56 ± 0.04	-4.0 ± 0.5	-27.6 ± 0.3	1.3 ± 0.2
Compound:				
LiTaO_3	$+2.75 \pm 0.06$	$+7.05 \pm 0.80$	-24.0 ± 0.3	1.6 ± 0.2
NaTaO_3	-1.02 ± 0.07	-2.61 ± 0.45	-13.3 ± 0.3	1.0 ± 0.2

Footnotes and References

* Present address: Physik-Department E15, Technische Universität München, D-8046 Garching, Germany.

1. G. Kaindl, D. Saloman and G. Wortmann, Phys. Rev. Letters **28**, 952 (1972), and G. Kaindl and D. Salomon, Nuclear Chemistry Division Annual Report for 1971, LBL-666, p. 199.

2. C. Sauer, E. Matthias, and R. L. Mössbauer, Phys. Rev. Letters **21**, 961 (1968). G. Kaindl and D. Salomon, Phys. Letters **32B**, 364 (1970).

3. L. Lindgren, Arkiv Fysik **29**, 553 (1965).

4. F. W. De Wette, Phys. Rev. **123**, 103 (1961).

5. R. E. Watson, A. C. Gossard, and Y. Yafet, Phys. Rev. **140**, A375 (1965).

6. F. D. Feiock and W. R. Johnson, Phys. Rev. **187**, 39 (1969).

7. R. Sternheimer, private communication, (1972).

8. R. M. Lieder, N. Buttler, K. Killing, K. Beck, and E. Bodenstedt, in Hyperfine Interactions in Excited Nuclei, edited by G. Goldring and R. Kalish (Gordon and Breach, New York, 1971), p. 449.

MAGNETIC HYPERFINE INTERACTION OF ^{181}Ta IN NICKEL

G. Kaindl* and D. Salomon

As we have seen in the preceding contributions, the 6.2-keV gamma resonance of ^{181}Ta has been used successfully for studying electric quadrupole hyperfine interactions¹ and isomer shifts.² Up to now, however, the magnetic splitting of the 6.2 keV gamma rays has only been observed in externally applied magnetic fields.³ This paper reports on the first application of this gamma resonance to the study of magnetic hyperfine interactions.

Using a single-line Ta metal absorber (4 mg/cm² thick) and a $^{181}\text{W}(\text{Ni})$ source, Mössbauer spectra were measured with both the source heated above the Curie point of nickel and at room temperature. The source was prepared by diffusing the ^{181}W activity for a period of 20 hours at $\sim 10^{-8}$ Torr and a temperature of $\sim 1350^\circ\text{C}$ into a single-crystal disk of nickel metal, cut perpendicular to the [111] direction. For the room-temperature measurement, the sinusoidally moved source was magnetized in longitudinal direction by an external polarizing field of 1.7 kOe produced by a small permanent magnet. The stray field at the absorber, which was kept at room temperature for both measurements, was negligibly small (< 1 Oe).

The results of the measurements are presented in Fig. 1. With the source heated above the Curie point, a single-line spectrum is observed (Fig. 1a), while at room temperature the emission line is widely split by magnetic hyperfine interaction (Fig. 1b). In longitudinal direction, the total spectrum resulting from the $9/2 \rightarrow 7/2$ E_i transition consists of 16 com-

ponents with $\Delta m = \pm 1$. Due to the small size of the resonance effect in the split spectrum, however, the velocity range had to be chosen so small that only the three outermost absorption lines were observed.

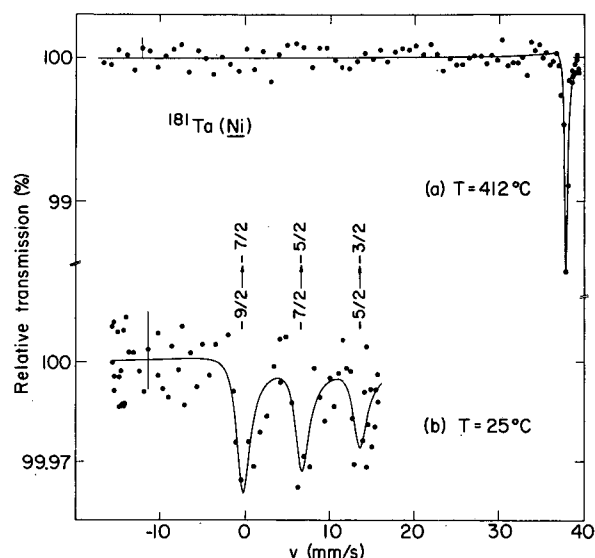


Fig. 1. Absorption spectra obtained with a Ta metal absorber at room temperature and a $^{181}\text{W}(\text{Ni})$ source at 412°C (a) and at 25°C (b), respectively. At the top of Fig. 1b individual transitions are assigned to the observed hyperfine components.

(XBL 726-3385)

Table I. Summary of experimental results.

	T (°C)	W/2 (mm/s)	IS (mm/s)	$g(7/2)\mu_N H_{\text{eff}}$ (mm/s)	Total effect (%)
Single-line	412(5)	0.20(1)	-36.96(5)		1.6(3)
Magn. split	25(1)	1.2(3)	--	8.93(5)	0.25(5)

The results of the least-squares fit analysis of both spectra are given in Table I. A dispersion term (with $2\xi = -0.30$)³ was fitted to spectrum (a). The split spectrum was analyzed with a superposition of dispersion-modified Lorentzians using $g(7/2)\mu_N H_{\text{eff}}$ as the only parameter to determine the line positions. To this end, the g-factor ratio $g(9/2)/g(7/2) = 1.78 \pm 0.02$ (Ref. 3) and the isomer shift at room temperature, $IS = -39.8 \pm 0.2$ mm/sec, were kept constant during the fit. The latter value was linearly extrapolated from a measurement of the temperature dependence of the isomer shift for ¹⁸¹Ta(Ni) in the temperature range from 412 to 730 °C.⁴

From the size of the magnetic splitting in the ground state, given in Table I, and taking into account the external polarizing field, a value of $H = (-)89.6 \pm 1$ kOe can be derived for the induced hyperfine field at room temperature. Previously a value of $H = -98 \pm 2$ kOe has been measured by spin-echo NMR at 4.2° K.⁵ We may therefore derive for the reduced hyperfine field at room temperature a value of $H(298)/H(4.2) = 0.91 \pm 0.02$, which is in good agreement with the results of a recent TDPAC study of the temperature dependence of H for ¹⁸¹Ta(Ni).⁶

The authors would like to thank Prof. D. A. Shirley for his constant interest and support of this work.

MÖSSBAUER STUDY OF PENTAVALENT GOLD COMPOUNDS*

K. Leary, G. Kaindl,[†] and N. Bartlett

Aurous and auric compounds have been the subject of extensive investigations by nuclear gamma-resonance spectroscopy.¹⁻³ The 77-keV M1 transition from the first excited state of ¹⁹⁷Au with spin $I = 1/2$ to the $I = 3/2$ ground state is very well suited for this type of investigation.

Recently pentavalent gold compounds have been prepared for the first time in the form

Footnote and References

*Present address: Physik-Department der Technischen Universität München, D-8046 Garching, Germany.

1. G. Kaindl, D. Salomon, and G. Wortmann, Phys. Rev. Letters **28**, 952 (1972); G. Kaindl and D. Salomon, Phys. Letters **40A**, 179 (1972); preceding contribution.
2. G. Wortmann, Phys. Letters **35A**, 391 (1971); D. Salomon, G. Kaindl, and D. A. Shirley, Phys. Letters **36A**, 457 (1971), and preceding contribution.
3. C. Sauer, E. Matthias, and R. L. Mössbauer, Phys. Rev. Letters **21**, 961 (1968); G. Kaindl and D. Salomon, Phys. Letters **32B**, 364 (1970).
4. G. Kaindl and D. Salomon, Phys. Rev. Letters **30**, 579 (1973). Also, preceding contribution.
5. M. Kontani and J. Itoh, J. Phys. Soc. Japan **22**, 345 (1967).
6. J. S. Barrett, J. A. Cameron, and Z. Zamori, Can. J. Phys. **50**, 619 (1972).

of $[\text{AuF}_6]^-$ salts.⁴ This paper reports on a Mössbauer study of these compounds: the obtained results for isomer shift and electric quadrupole interaction confirm the pentavalent state of gold as well as the proposed molecular structure.

$[\text{Xe}_2\text{F}_{11}]^+[\text{AuF}_6]^-$ was prepared from stoichiometric amounts of XeF_2 and AuF_3 at 400 °C and ~ 1000-psi F_2 pressure in a Monel

bomb. $[\text{XeF}_5]^+[\text{AuF}_6]^-$ was obtained from $[\text{Xe}_2\text{F}_{11}]^+[\text{AuF}_6]^-$ by heating it to 110°C under vacuum, followed by a sublimation purification process. CsAuF_6 finally was prepared by heating an equimolar mixture of CsF and $[\text{Xe}_2\text{F}_{11}]^+[\text{AuF}_6]^-$ under dry nitrogen to 110°C in a Monel crucible. All compounds were characterized by their mutual x-ray powder patterns, their Raman spectra, and by analysis for Xe. More details of the preparation technique are given in Ref. 4.

The standard Mössbauer transmission experiments were performed with both source and absorber cooled to 4.2°K , using a sinusoidal velocity spectrometer and a $\text{Ge}(\text{Li})$ -diode for recording the 77-keV gamma rays. The ^{197}Pt source was prepared by irradiating ~ 3 mg platinum metal enriched to 65% in an integrated thermal neutron flux of $\sim 3 \times 10^{19}$ n/cm 2 .

Figure 1 shows as an example the Mössbauer absorption spectrum of $[\text{Xe}_2\text{F}_{11}]^+[\text{AuF}_6]^-$. The solid line is the result of a least-squares fit of a Lorentzian line to the data. Almost identical spectra were obtained for $[\text{XeF}_5]^+[\text{AuF}_6]^-$ and CsAuF_6 . For completeness the Mössbauer spectrum was also measured for AuF_3 . Since this compound was prepared in pure form as a starting material for the synthesis of the pentavalent compounds. Due to quadrupole interaction its spectrum consists of two Lorentzian lines, separated by $\text{QS} = 2.71 \pm 0.02$ mm/sec, in agreement with the result of Ref. 1.

The results are summarized in Table I. In all cases the absorbers had a thickness of ~ 50 mg/cm 2 of gold. The experimental line widths, when compared with twice the natural width of the Mössbauer gamma rays, $W_0 = 2\hbar/\tau = 1.88 \pm 0.02$ mm/sec, 5 demonstrate

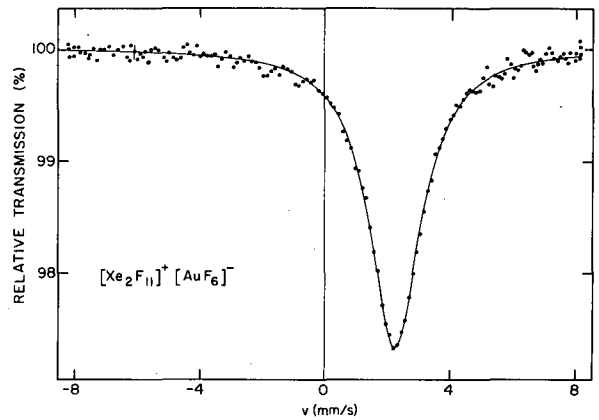


Fig. 1. Mössbauer absorption spectrum of $[\text{Xe}_2\text{F}_{11}]^+[\text{AuF}_6]^-$ recorded with a metallic ^{197}Pt source, both at 4.2°K .

(XBL 726-6405)

the absence of electric quadrupole interaction at the gold site in the pentavalent compounds. This is in agreement with the proposed octahedral structure of the $[\text{AuF}_6]^-$ complex. 4

The isomer shifts of the pentavalent compounds, listed in column 4 of Table I, are almost identical with each other, supporting the existence of identical $[\text{AuF}_6]^-$ complexes in all of the studied pentavalent compounds. A graphical representation of the present isomer shift results together with those of auric and aurous compounds with halogen ligands, taken from Ref. 1-3, is given in Fig. 2. With the only exception of AuF_3 the isomer shifts arrange themselves into three separate groups corresponding to monovalent, trivalent, and pentavalent gold compounds, with approximately identical distances between neighbouring

Table I. Compilation of experimental results: ϵ =resonance effect, W = total experimental line width (FWHM); IS = isomer shift relative to the platinum metal source; $\text{QS} = e^2qQ(3/2)/2(1 + \eta^2/3)^{1/2}$ = electric quadrupole splitting of the ground state.

Compound	ϵ (%)	W (mm/s)	IS (mm/s)	QS (mm/s)
$\text{Xe}_2\text{F}_{11}\text{AuF}_6$	2.9	1.98 ± 0.02	2.28 ± 0.01	
XeF_5AuF_6	4.0	2.10 ± 0.06	2.31 ± 0.02	
CsAuF_6	2.8	2.02 ± 0.06	2.39 ± 0.02	
AuF_3	4.6	2.00 ± 0.02	-1.06 ± 0.02	2.71 ± 0.02

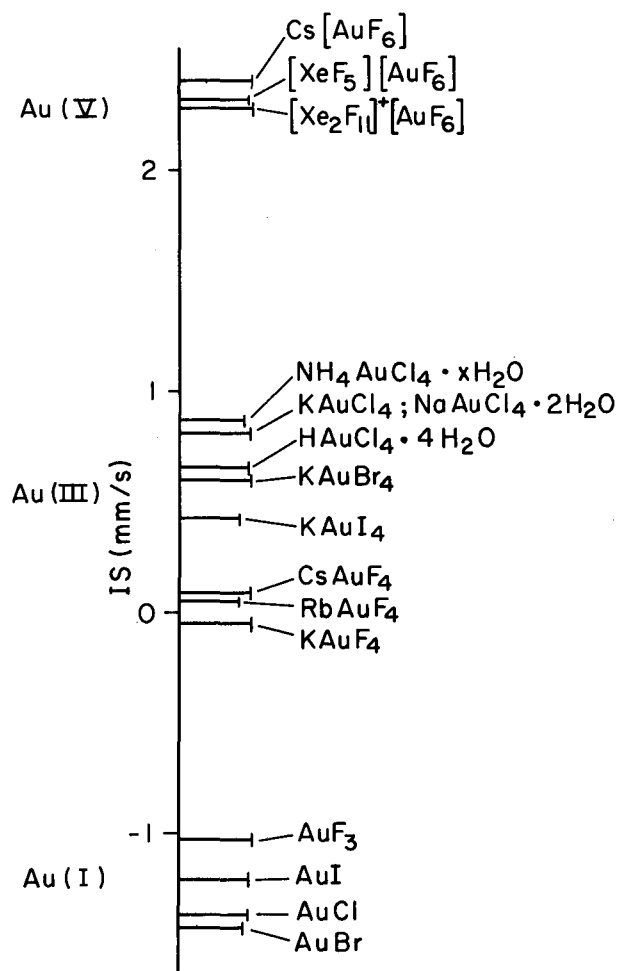


Fig. 2. Graphical representation of isomer shifts for aurous, auric, and pentavalent gold compounds with halogen ligands.

(XBL 733-2562)

groups. This is remarkable in view of the different molecular structures of these compounds.

The increase in isomer shift with increasing formal oxidation state is in agreement with a positive value for $\Delta \langle r^2 \rangle$ (Ref. 6) and an increase of the total electron density at the nucleus, expected on the basis of d-electron shielding arguments.² The present isomer shift results thus confirm the pentavalency of gold in the studied compounds.

The authors would like to thank Prof. D. A. Shirley for helpful discussions and support of this work.

Footnotes and References

* To be submitted to Journal of Chemical Physics.

† Present address: Physik-Department E15, Technische Universität München, D-8046 Garching, Germany.

1. M. O. Faltens and D. A. Shirley, *J. Chem. Phys.* **53**, 4249 (1970).
2. H. D. Bartunik, W. Potzel, R. L. Mössbauer, and G. Kaindl, *Z. Physik* **240**, 1 (1970).
3. J. S. Charlton and D. I. Nichols, *J. Chem. Soc. (A)*, 1484 (1970).
4. K. Leary and N. Bartlett, *Chem. Comm.* 903 (1972).
5. P. Steiner, E. Gerdau, W. Hantsch, and D. Steenken, *Z. Physik* **221**, 281 (1969).
6. L. D. Roberts, D. O. Patterson, J. O. Thomson, and R. P. Levey, *Phys. Rev.* **179**, 656 (1969).

ISOMER SHIFTS OF THE 84.3-keV GAMMA RAYS OF ^{170}Yb

G. Kaindl* and P. B. Russel†

This paper reports on Mössbauer isomer shifts of the 84.3-keV gamma rays of ^{170}Yb in various ytterbium compounds. Since the total range of observed isomer shifts amounts to not more than $\sim 13\%$ of the experimental line width, single-line absorbers, preferably with cubic structure, were exclusively investigated in order to prevent systematic errors. The isomer shifts were found to arrange themselves in three separate groups corresponding to divalent, trivalent, and metallic

compounds. In addition, the small dispersion terms in the shape of Mössbauer absorption lines, recently also observed for E2 gamma transitions,¹ were investigated.

The Mössbauer absorption experiments were performed in transmission geometry with a sinusoidal velocity drive and both source and absorber cooled to liquid helium temperature. ^{170}Tm ($T_{1/2} = 170$ d) in TmAl_2 , activated by thermal neutron irradiation, was used

as a single-line source. Several cubic divalent ytterbium compounds were prepared in sealed molybdenum crucibles in a way as described by Catalano.²

Figure 1 shows a few typical Mössbauer spectra. The isomer shift between divalent compounds YbF_2 and YbTe and the trivalent compound Yb_2S_3 is clearly exhibited. The data were least-squares fitted both with a symmetrical and a dispersion-modified Lorentzian line; in the latter case the amplitude of the dispersion term, 2ξ ,³ was used as an adjustable parameter.

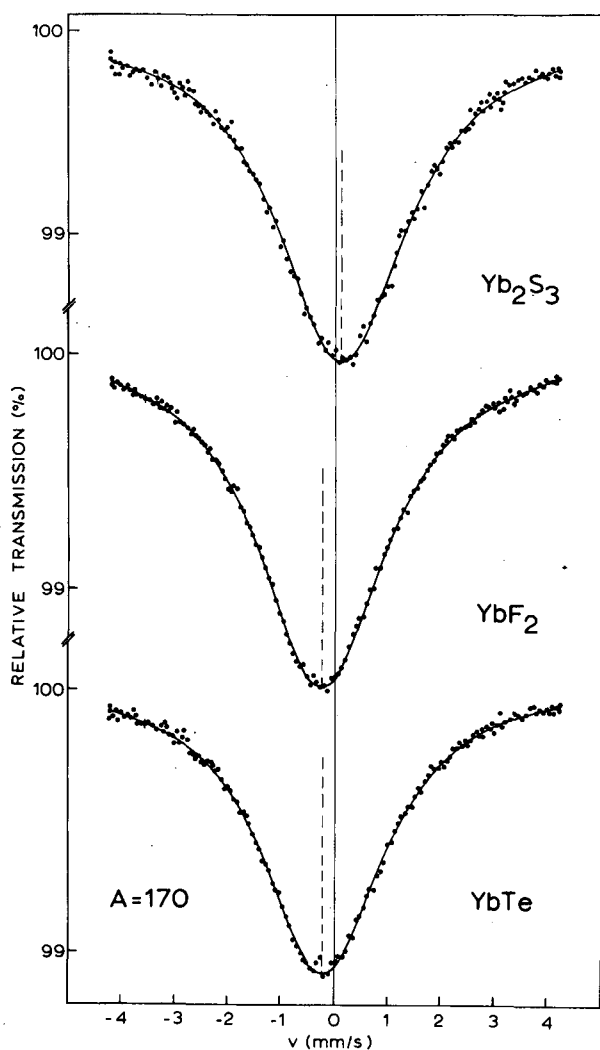


Fig. 1. Mössbauer absorption spectra of the 84-keV gamma rays of ^{170}Yb for various ytterbium compounds. The solid lines are the results of a least-squares fit of a symmetrical Lorentzian line to the data. (XBL 733-332)

A summary of the experimental results is presented in Table I. In column 4 the fit results for 2ξ are listed; they agree with each other within the limits of error. Their weighted mean, $2\xi = -0.030 \pm 0.004$, is in good agreement with the value reported in Ref. 1, $2\xi = -0.0340 \pm 0.0076$.

The isomer shifts obtained for $2\xi = 0$ are listed in column 2, while those resulting from fits with constant $2\xi = -0.030$ are presented in column 3. The neglect of the dispersion effect in the data analysis obviously changes the isomer shifts by approximately $\xi \cdot W$, where W represents the experimental line width.¹ This means that even though a neglect of the dispersion term leads to apparent shifts, relative isomer shift differences between different absorbers will not be affected within the present accuracy. This rule, however, may not hold if drastic differences in the thickness of the absorbers should occur.⁴ In column 7 previously published isomer shift values for the studied compounds are listed; they should be compared with our results obtained for $2\xi = 0$ (column 2).

Figure 2 presents a graphical representation of the present isomer shift results. Since the total electron density at the nucleus ($|\psi_0|^2$) is expected to be smaller for divalent than for trivalent ytterbium compounds due to the shielding effect of the additional 4f electron, the change of the mean-squared nuclear charge radius, $\Delta \langle r^2 \rangle$, is found to be positive for the 84.3-keV gamma transition. The isomer shifts obtained for Yb_2S_3 and YbCl_3 agree with each other, and also with those published for the same and for other trivalent ytterbium compounds, especially $\text{YbCl}_3 \cdot 6\text{H}_2\text{O}$, $\text{Yb}_2(\text{SO}_4)_3 \cdot 8\text{H}_2\text{O}$, and YbOOH .⁵⁻⁸

The smallest $|\psi_0|^2$ is found for YbF_2 , while the divalent mono-chalcogenides YbS , YbSe , and YbTe exhibit somewhat larger $|\psi_0|^2$. This is very similar to the results of isomer shift studies with the 22.5-keV gamma rays of ^{149}Sm in compounds of samarium.⁹ In addition $|\psi_0|^2$ is found to increase from YbTe to YbSe and YbS , in qualitative agreement with the situation found for the equivalent europium compounds.¹⁰

Even though the ytterbium ion is divalent in the metal, the isomer shift found for it falls between the divalent and trivalent regions. This is a consequence of the direct contribution of the conduction electrons to $|\psi_0|^2$. From the present results we derive for the ratio,

$$\frac{|\psi_0|^2(\text{c. e.})}{(|\psi_0|^2(\text{Yb}^{3+}) - |\psi_0|^2(\text{Yb}^{2+}))} = 0.64 \pm 0.15,$$

Table I. Summary of results for the 84.3-keV gamma resonance of ^{170}Yb , obtained with a source of $^{170}\text{TmAl}_2$.

Absorber	IS ^a (mm/s)	IS ^b (mm/s)	2ξ ^c	W/2 ^d (mm/s)	IS ^e (mm/s)
YbF ₂	-0.251(6)	-0.296(6)	-0.033(5)	1.40(3)	
Yb ₂ S ₃	0.111(13)	0.067(13)	-0.024(7)	1.45(3)	0.10(4) ^f
YbCl ₃	0.091(21)	0.047(21)	-0.032(14)	1.61(5)	0.09(4) ^g
YbS	-0.181(8)	-0.227(8)	-0.035(10)	1.45(2)	
YbSe	-0.178(10)	-0.223(10)	-0.028(11)	1.39(2)	
YbTe	-0.203(7)	-0.247(7)	-0.031(10)	1.47(3)	
YbB ₆	-0.220(9)	-0.266(9)	-0.029(14)	1.42(2)	
YbAl ₂	-0.028(10)	-0.075(10)	-0.024(8)	1.47(4)	$\left\{ \begin{array}{l} -0.08(2)^g \\ 0.00(7)^h \end{array} \right.$
Yb metal	-0.021(38)	-0.065(38)	-0.033(10)	1.60(2)	
YbC ₂	-0.030(7)	-0.076(7)	-0.029(12)		

^aFrom a least-squares fit with a symmetrical Lorentzian line (2ξ = 0).

^bFrom a least-squares fit with a dispersion-modified Lorentzian line with constant amplitude of the dispersion term (2ξ = - 0.03).

^cFrom a fit with 2ξ as a free parameter.

^dLine widths are uncorrected for finite absorber thickness.

^ePublished isomer shift values for 2ξ = 0.

^fRef. 5.

^gRef. 6.

^hValue has been adapted from published value, which was referred against YbAl₂.⁷

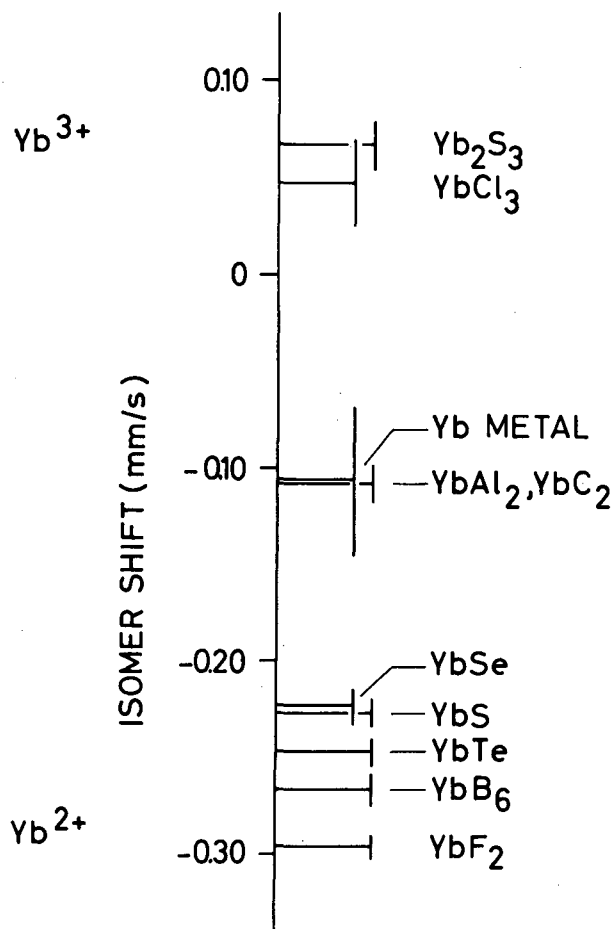


Fig. 2. Graphical representation of present isomer shift results with the 84.3-keV gamma rays of ^{170}Yb for various absorber materials relative to a $^{170}\text{TmAl}_2$ source, with $2\xi = -0.03$. (XBL 733-333)

which is in good agreement with a previously published value of 0.75 ± 0.12 .¹¹

The authors would like to thank Prof. D. A. Shirley for support of this work and for his constant interest. They are also indebted to the late Prof. B. B. Cunningham for his teachings in the chemistry of the lanthanides.

Footnotes and References

* Miller Fellow 1969-1971.

Present address: Physik-Department E15, Technische Universität München, D-8046 Garching, Germany.

† Department of Physics, Stanford University.

1. F. E. Wagner, B. D. Dunlap, G. M. Kalvius, H. Schaller, R. Felscher, and H. Spieler, *Phys. Rev. Letters* **28**, 530 (1972).
2. E. Catalano, R. G. Bedford, U. G. Silveira, and H. H. Wickman, *J. Phys. Chem. Solids* **30**, 1613 (1969).
3. G. T. Trammel and J. P. Hannon, *Phys. Rev.* **180**, 337 (1969).
4. W. Henning, G. Baehre, and P. Kienle, *Phys. Letters* **31B**, 203 (1970).
5. W. Henning, G. Baehre, and P. Kienle, *Z. Physik* **241**, 138 (1971).
6. W. Henning, *Z. Physik* **217**, 438 (1968).
7. U. Atzmony, E. R. Bauminger, J. Hess, A. Mustachi, and S. Ofer, *Phys. Rev. Letters* **18**, 1061 (1967).
8. U. Atzmony, E. R. Bauminger, J. Hess, and S. Ofer, in *Hyperfine Structure and Nuclear Radiations*, edited by E. Matthias and D. A. Shirley (North-Holland, Amsterdam, 1968), p. 71.
9. M. Eibschütz, R. L. Cohen, and J. H. Wernick, in *Hyperfine Interaction in Excited Nuclei* edited by G. Goldring and R. Kalish (Gordon and Breach, New York (1971), p. 720.
10. G. Gerth, P. Kienle, and K. Luchner, *Phys. Letters* **27A**, 557 (1968).
11. W. Henning, G. Baehre, and P. Kienle, in *Hyperfine Interactions in Excited Nuclei*, edited by G. Goldring and R. Kalish (Gordon and Breach, New York, 1971), p. 795.

CHANGE OF THE NUCLEAR CHARGE RADIUS IN EVEN-EVEN YTTERBIUM ISOTOPES

G. Kaindl,* P. B. Russel,[†] and S. S. Hanna[†]

Mössbauer isomer shifts of $2^+ \rightarrow 0^+$ ground state rotational transitions in even-even ytterbium isotopes ^{170}Yb , ^{172}Yb , ^{174}Yb , and ^{176}Yb were investigated. From the experimental results absolute values for the changes of the mean-squared nuclear charge radii, $\Delta\langle r^2 \rangle$, as well as ratios of them, could be derived. Although these ytterbium isotopes are among the best examples of rotational nuclei with virtually constant deformation over the series, the present results reveal drastic differences in $\Delta\langle r^2 \rangle$. For ^{170}Yb and ^{172}Yb the nuclear charge distribution is found to expand upon rotation excitation while it is found to shrink for ^{174}Yb and ^{176}Yb . This fine structure of $\Delta\langle r^2 \rangle$ is explained by a recent microscopic theory of Meyer and Speth.¹

For the experiments described here, two methods of populating the Mössbauer levels of interest were employed. While the 84.3-keV gamma level of ^{170}Yb was populated by β -decay from ^{170}Tm ($T_{1/2} = 130$ d), using a source of ^{170}Tm in TmAl_2 (see preceding contribution), the Mössbauer sources for the other gamma resonances (^{172}Yb : 78.7 keV; ^{174}Yb : 76.5 keV;

^{176}Yb : 82.1 keV) were produced by Coulomb excitation in conjunction with recoil implantation through vacuum.² A detailed schematic of the arrangement of targets, catchers, and Mössbauer absorbers is presented in Fig. 1. A beam of 65-MeV ^{35}Cl ions from the Stanford FN tandem Van de Graaf accelerator was focused on a thin metallic Yb target (~ 2.5 mg/cm² thick), highly enriched in the isotope of interest. The Coulomb-excited recoil nuclei were implanted through vacuum into an aluminum catcher at a temperature of $\sim 13^\circ\text{K}$, which served as a source for the conventional Mössbauer transmission experiments. For improved counting rates a series arrangement of two targets and two catchers was used. In addition the system allowed the use of two separate Mössbauer absorbers,

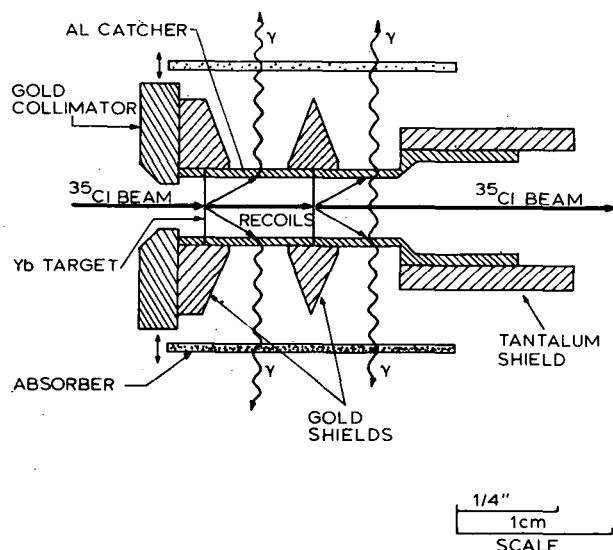


Fig. 1. Detailed schematic of the series arrangement of two targets and two catchers used to increase the gamma-ray yield in Mössbauer effect experiments using the method of Coulomb excitation and recoil implantation through vacuum. (XBL 733-334)

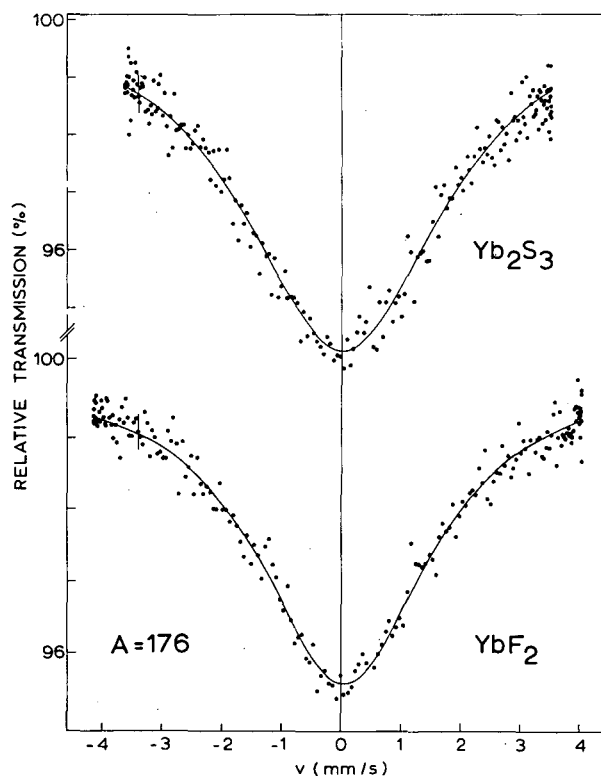


Fig. 2. Mössbauer absorption spectra of the 82.1-keV gamma rays of ^{176}Yb for YbF_2 and Yb_2S_3 . The solid lines are the results of a least-squares fit of a dispersion-modified Lorentzian line ($2\xi = -0.03$) to the data. (XBL 733-335)

Table I. Derivation of experimental values for $\Delta \langle r^2 \rangle$ and ratios of $\Delta \langle r^2 \rangle$ of even-even ytterbium isotopes. The isomer shifts ΔIS_A and ΔIS_{170} are those obtained from least-squares fits with $2\xi = -0.03$.

Isotope A	^a ΔIS_A	^b ΔIS_{170}	^c $\Delta \langle r^2 \rangle_A / \Delta \langle r^2 \rangle_{170}$	$\Delta \langle r^2 \rangle_A$ (10^{-3} fm^2)
	(mm/s)	(mm/s)		
170	0.362(14)	0.362(14)	(1.0)	1.20(40)
172	0.114(23)	0.312(12)	0.341(82)	0.41(20)
174	-0.135(17)	0.334(29)	-0.366(71)	-0.44(19)
176	-0.052(14)	0.358(14)	-0.141(43)	-0.17(10)

^aIsomer shift between Yb_2S_3 and YbF_2 measured with the Mössbauer resonance of isotope A.

^bIsomer shift measured with the 84.3-keV gamma rays of ^{170}Yb between the identical absorber pair as in (a).

^cDerived from the isomer shifts given in columns 2 and 3.

moved simultaneously with a common drive system, which were positioned at 180° to each other and cooled to $\sim 10\text{-}12^\circ\text{K}$. The experimental technique has been described in more detail elsewhere.³

Isomer shifts were measured between single-line absorbers of YbF_2 and Yb_2S_3 . The absorbers used for the accelerator experiments were highly enriched ($\sim 70\text{-}90\%$) in the isotopes of interest, and additionally contained 3-5% ^{170}Yb to allow a measurement of the isomer shift of the 84.3-keV gamma rays for test purposes. Some typical Mössbauer spectra are shown in Fig. 2 for ^{176}Yb .

The experimental results are summarized in Table I. While the isomer shifts of the 84.3-keV gamma rays of ^{170}Yb found for different YbF_2 absorbers always agreed with each other within statistics, those determined for the various Yb_2S_3 compounds exhibited variations slightly outside of statistics. Therefore in all cases the differences in isomer shift between Yb_2S_3 and YbF_2 were also measured with the ^{176}Yb gamma resonance (column 3 of Table I), and these results of ΔIS_{170} were used to derive the ratios of $\Delta \langle r^2 \rangle_A / \Delta \langle r^2 \rangle_{170}$ listed in column 4. In the last column, absolute values for $\Delta \langle r^2 \rangle_A$ are presented. They were obtained by using an electron density difference between Yb^{3+} and Yb^{2+} (represented by Yb_2S_3 and YbF_2 , respectively) of $\Delta |\psi_0|^2 = + (4.0 \pm 1.2) \times 10^{26} \text{ cm}^{-3}$.⁴

Figure 3 presents a comparison of the present results with previous experimental data;⁵⁻⁷

absolute values of $\Delta \langle r^2 \rangle$ have been recalculated by using the same $\Delta |\psi_0|^2$ as in the present work. While there is good agreement for ^{170}Yb and ^{172}Yb , a discrepancy exists in the case of ^{174}Yb .

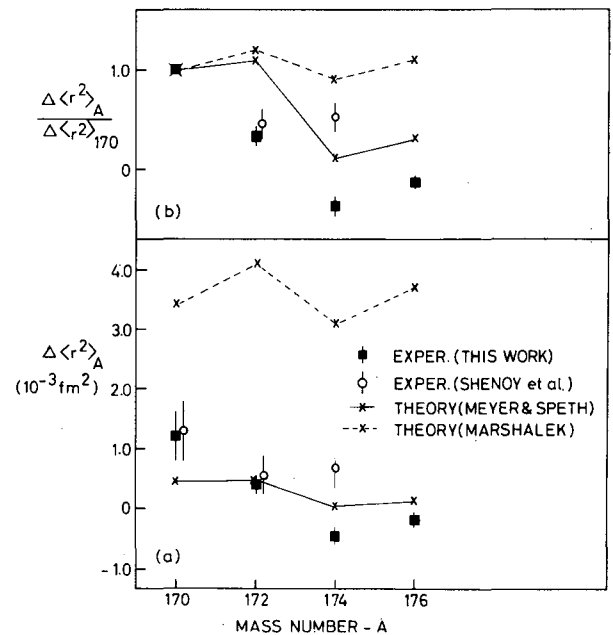


Fig. 3. Comparison of experimental and theoretical values for $\Delta \langle r^2 \rangle$ (b) and ratios of $\Delta \langle r^2 \rangle$ (a) in the even-even ytterbium isotopes. (XBL 733-336)

The observation of changes of the mean-squared nuclear charge radius upon rotational excitation demonstrates the existence of non-adiabatic effects on the intrinsic nuclear structure caused by nuclear rotation. The centrifugal stretching model, in a semiclassical way, predicts values for $\Delta \langle r^2 \rangle$ which are positive and too large by approximately one order of magnitude.^{3, 7}

Two microscopic theories exist, however, which predict $\Delta \langle r^2 \rangle$ for rotational transitions.^{1, 8} Their predictions, based on calculations within the self-consistent cranking model, are also plotted in Fig. 3. Marshalek's theory⁸ results in $\Delta \langle r^2 \rangle$ values which are all positive for the even-even Yb isotopes and too large by factors of 3 to 20. This probably is a consequence of an overestimation of the centrifugal stretching effect. On the other hand, the theory of Meyer and Speth¹ predicts the right order of magnitude for $\Delta \langle r^2 \rangle$, and even accounts for the minimum in $\Delta \langle r^2 \rangle$ observed at $A = 174$. According to this theory, changes of $\langle r^2 \rangle$ in $2^+ \rightarrow 0^+$ rotational transitions of well-deformed nuclei are mainly determined by the redistribution of only a few nucleons near the diffuse Fermi edge. Upon rotational excitation the decrease in pairing force tends to depopulate levels just above the diffuse Fermi energy in favor or levels below. The change in nuclear radius is then mainly determined by the fact that near the proton Fermi edge of rare earth nuclei, $N = 4$ levels are mixed with $N = 5$ levels which have comparatively larger radii. Depending on the detailed balance of the redistribution process, positive as well as negative values of $\Delta \langle r^2 \rangle$ are therefore possible.

The authors would like to thank Prof. D. A. Shirley for valuable discussions and support of this work.

Footnotes and References

* Miller-Fellow, 1969-1971. Present address: Physik-Department E15, Technische Universität München, D-8046 Garching, Germany.

† Department of Physics, Stanford University.

1. J. Meyer and J. Speth, preprint (1972).
2. G. D. Sprouse, G. M. Kalvius, and S. S. Hanna, Phys. Rev. Letters 18, 1041 (1967).
3. P. B. Russel (thesis), Department of Physics, Stanford University (1971).
4. P. B. Russel, S. S. Hanna, and G. Kaindl, to be published in Phys. Rev. C.
5. W. Henning, G. Baehre, and P. Kienle, Z. Physik 241, 138 (1971).
6. G. K. Shenoy, G. M. Kalvius, W. Henning, G. Baehre, and P. Kienle, in Hyperfine Interactions in Excited Nuclei, edited by G. Goldring and R. Kalish (Gordon and Breach, New York, 1971 p. 699).
7. W. Henning, Z. Physik 217, 438 (1968).
8. E. R. Marshalek, Phys. Rev. Letters 20, 214 (1968).

MAGNETIC MOMENT OF THE 6.9-HOUR ISOMER OF ⁹³Mo

G. Kaindl,* F. Bacon,[†] and D. A. Shirley

The 6.9-hour isomer of ⁹³Mo decays via a cascade of 263-, 685-, and 1477-keV gamma rays to the ground state of ⁹³Mo. A spin sequence of $21/2^+ \rightarrow 13/2^+ \rightarrow 9/2^+ \rightarrow 5/2^+$ has been postulated.¹ This paper reports on a measurement of the magnetic moment of the isomeric state by thermal equilibrium nuclear orientation technique (NO) and nuclear magnetic resonance on oriented nuclei (NMR-ON). In addition the spin of the isomeric state was confirmed, as well as spins and gamma multiplicities of the gamma cascade.¹

^{93m}Mo was produced in practically pure radioactive form via the ⁹³Nb(d, 2n)^{93m}Mo reaction, using natural niobium targets

(~15 mg/cm² thick) and 13-MeV deuterons. Samples containing 0.6 at.% ⁹³Mo(Nb) in an iron matrix were prepared by repeatedly melting a small chip of the radioactive Nb metal with 99.999% pure iron; for the NO experiments a matched amount of ⁶⁰Co activity, to be used for thermometry, was added. Thin foils (~10 000 Å thick), produced by cold rolling and annealing, were attached to the Cu fin of an adiabatic demagnetization apparatus. Gamma-ray spectra were taken at 0° and 90° relative to the external polarizing field with high-resolution coaxial Ge(Li)-diodes for the NO experiments, and with NaI(Tl) detectors for the NMR-ON experiments. For the NMR-ON experiments an rf field was applied

perpendicular to the polarizing field.

Figure 1 shows the results of a single demagnetization run for the anisotropy of the 263-, 1477-, and 685-keV gamma rays of $^{93m}\text{Mo}(\text{Fe})$. During the warming up of the sample over a time of 7 hours, spectra were taken continuously for periods of 15 minutes. The temperature of the sample was determined from the anisotropy of ^{60}Co gamma lines.

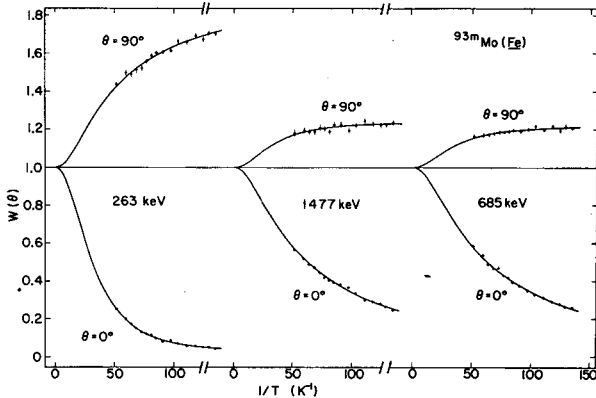


Fig. 1. Temperature dependence of the anisotropies $W(\theta)$ of the 263-, 1477-, and 685-keV gamma rays emitted from a source of $^{93m}\text{Mo}(\text{Fe})$ parallel ($\theta = 0^\circ$) and perpendicular ($\theta = 90^\circ$) to the external polarizing field $H_{\text{ext}} = 4$ kOe. (XBL 726-3387)

For each of the three gamma rays the 0° and 90° anisotropy curves were simultaneously least-squares fitted with

$$W(\theta) = 1 + \sum_{k=2,4} B_k U_k F_k Q_k P_k(\cos \theta),$$

using suitable solid-angle correction factors Q_k for each case.³ The hyperfine interaction of the isomeric state, μH_{eff} , and an amplitude factor were used as free parameters. The individual results for μH_{eff} , presented in Table I, agree very well with each other within the limits of error; their mean value is

$$\mu H_{\text{eff}} = (12.08 \pm 0.20) \times 10^{-18} \text{ erg.}$$

In a separate experiment nuclear magnetic resonance of ^{93m}Mo in iron was observed by the effects of an external rf field on the anisotropy of nuclear gamma rays emitted from oriented nuclei.⁴ The rf frequency was modulated with 100 Hz over a bandwidth of ~ 2 MHz, and the rf amplitude was kept constant at ~ 0.5 mOe. Figure 2 shows the results of this experiment. The observed effect is rather

Table I. Results of a simultaneous fit of the 0° and 90° anisotropy curves.

Gamma line (keV)	μH_{eff} (10^{-18} erg)
263	12.24 ± 0.19
1477	12.11 ± 0.39
685	11.89 ± 0.36
Average:	12.08 ± 0.20

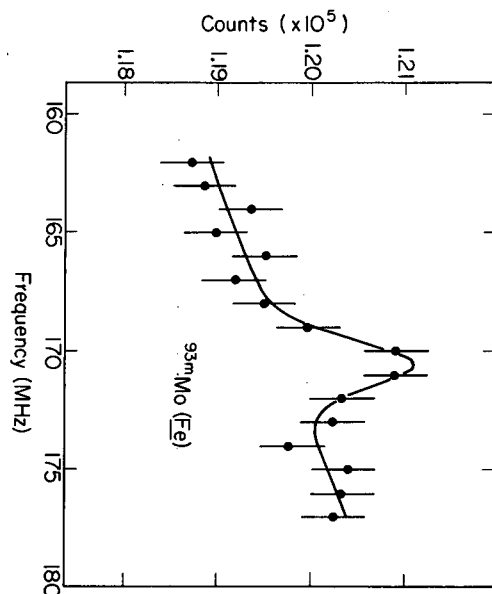


Fig. 2. Frequency dependence of the anisotropy of the sum of the 263-, 1477-, and 685-keV gamma rays, observed in direction of the polarizing field $H_{\text{ext}} = 1$ kOe. The time span between neighboring points was 2 minutes. (XBL 728-3689)

small, since the temperature of the sample was only $1/T \approx 50^\circ \text{K}^{-1}$ at the time the resonance curve was recorded. From a least-squares fit of a Gaussian line with linear background to the data a resonance frequency of

$$\nu_{\text{res}} = 170.5 \pm 0.4 \text{ MHz}$$

was obtained.

With the previously assigned value for the

spin of the isomeric state, $I = 21/2$, this result agrees well with that of the NO experiment. Taking into account the different external polarizing fields, as well as the hyperfine field of Mo in iron at 4.2°K, $H_{hf} = -256 \pm 5$ kOe,⁵ we obtain for the ratio $(\gamma H_{hf})_{NO}/(\gamma H_{hf})_{NMR}$ a value of 1.03 ± 0.02 for a spin of $21/2$, while spins of $19/2$ and $23/2$ would result in values of 1.14 ± 0.02 , respectively. Thus the spin assignment of Ref. 1 is confirmed in a direct way by the present results. The same method had previously been used to determine the spins of isomeric states in ^{195}Pt (ref. 6) and ^{200}Au .⁷

With $I = 21/2$ and $H_{hf} = -256.5$ kOe, a value of

$$\mu(21/2) = 9.21 \pm 0.20 \text{ n. m.}$$

is obtained for the magnetic moment of the isomeric state. This value supports the interpretation of the 6.9-hr isomeric state as a three-particle state with shell-model configuration $[\pi(g_{9/2} - g_{7/2}); \nu d_{5/2}] 21/2$.[†]

Footnotes and References

*Present address: Physik-Department E15,

Technische Universität München, D-8046 Garching, Germany.

†Present address: Department of Chemistry, Morehouse College, Atlanta, Georgia 30314.

1. S. I. H. Naqvi, I. F. Bubb, and J. L. Wolfson, Phys. Rev. C 3, 412 (1971), and references therein.
2. F. Bacon (thesis), Lawrence Berkeley Laboratory (1972).
3. D. C. Camp and A. L. Van Lehn, Nucl. Instr. Meth. 76, 192 (1969).
4. E. Matthias and R. J. Holliday, Phys. Rev. Letters 17, 897 (1966).
5. M. Kontani and J. Itoh, J. Phys. Soc. Japan 22, 345 (1967).
6. F. Bacon, G. Kaindl, H. -E. Mahnke, and D. A. Shirley, Phys. Rev. Letters 28, 720 (1972).
7. F. Bacon, G. Kaindl, H. -E. Mahnke, and D. A. Shirley, Phys. Rev. C, in press.

NUCLEAR QUADRUPOLE ALIGNMENT OF ^{180m}Hf AND ^{175}Hf IN HAFNIUM METAL

G. Kaindl,* F. Bacon,† A. J. Soinski, and D. A. Shirley

Thermal equilibrium nuclear orientation in ferromagnetic host metals has been applied extensively in the past to the study of magnetic hyperfine interactions.¹ The degree of nuclear orientation is usually determined from the anisotropy of nuclear radiations, especially of gamma rays. On the other hand, until now nuclear quadrupole alignment has been observed via nuclear radiations only in paramagnetic salts.^{2,3} We report the first radiative detection of nuclear quadrupole alignment in the electric field gradient (EFG) of a hexagonal metal.

^{175}Hf and ^{180m}Hf nuclei were oriented in a single crystal of hafnium metal at temperatures down to 3 mK. From the temperature dependence of gamma-ray anisotropies, values for the electric quadrupole interaction (EQI) energies were obtained. For magnetic hyperfine (hf) interactions only the magnitude of the hf interaction energies can be obtained; however, for electric hf interactions the sign of the interaction energies can also be obtained

if the signs of the angular distribution parameters of the relevant nuclear radiations are known to within a sign.

In each experiment a single-crystal disk of hafnium metal was contact-cooled by the adiabatic demagnetization of cerium magnesium nitrate. These disks were produced from a single crystal of 99.99% Hf metal by spark cutting perpendicular to the [0001] direction and electropolishing to various thicknesses down to 180 micron. The ^{175}Hf ($t_{1/2} = 70$ d) and ^{180m}Hf ($t_{1/2} = 5.5$ hr) activities were produced by irradiating these disks with fast neutrons which were generated by 45-MeV deuterons from the LBL 88-inch cyclotron on a beryllium target. Only the two desired activities were appreciably produced.

The Hf metal disk and a hexagonal $^{60}\text{CoCo}$ single crystal which served as a thermometer were soft soldered to the Cu fin of an adiabatic demagnetization apparatus. A high-resolution coaxial Ge(Li) diode at 0° with respect to the

common [0001] direction of both crystals was used to record spectra continuously over 15-minute intervals during the warming up of the samples following adiabatic demagnetization.

The results of the analysis for the temperature dependence of gamma ray anisotropies are presented in Fig. 1 for the 343-keV gamma ray of ^{175}Hf and in Fig. 2 for the 443-keV gamma ray of $^{180\text{m}}\text{Hf}$. The data points are

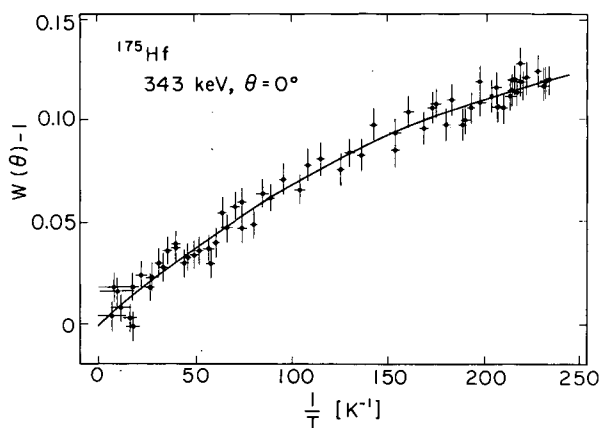


Fig. 1. Temperature dependence of the anisotropy of the 343-keV gamma rays of ^{175}Hf emitted from a single crystal of hafnium metal parallel to the hexagonal C-axis. (XBL 728-3733)

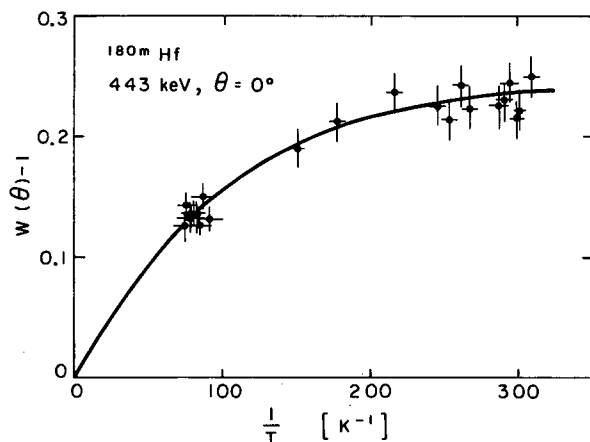


Fig. 2. Temperature dependence of the anisotropy of the 443-keV gamma rays of $^{180\text{m}}\text{Hf}$ emitted from a hafnium metal single crystal parallel to the [0001] direction. (XBL 728-3732)

the results of two independent experiments with separate Hf single crystals with different thicknesses ($180\ \mu$ and $560\ \mu$) and different strong activities. Also two different soldering techniques were used, one using regular soldering with Bi/Cd eutectic alloy of a Ni-plated Hf disk, and the other using ultrasonic soldering with In metal of an unplated Hf disk. The fact that the results of the different runs agree justifies the assumption that the temperature measured by the $^{60}\text{CoCo}$ single crystal was identical to the lattice temperature of the Hf sample.

The solid curves in the figures are the results of a least-squares fit of the data with the anisotropy function

$$W(\theta) = 1 + \sum_{k=2,4} B_k U_k F_k Q_k P_k(\cos \theta),$$

using suitable solid angle correction factors Q_k .⁴ Only in the $^{180\text{m}}\text{Hf}$ case, however, is the decay scheme⁵ known well enough to permit an unambiguous calculation of the reorientation parameters U_k and the angular distribution parameters F_k .

From a least-squares fit of the anisotropy curve of the 443-keV gamma ray of $^{180\text{m}}\text{Hf}$ a value of

$$e^2 q Q(8^-) = + (6.61 \pm 0.42) \times 10^{-18} \text{ erg}$$

results for the EQI of the 8^- isomeric state. Using $e q = + (9.5 \pm 0.4) \times 10^{17} \text{ V/cm}^2$ (Ref. 6) for the EFG in hafnium metal, we derive

$$Q(8^-) = + 4.3(5) \text{ barns}$$

for the electric quadrupole moment of the 8^- two-quasiparticle state. This corresponds to an intrinsic quadrupole moment of $Q_0 = 6.2(7) \text{ b}$.

The 343-keV level of ^{175}Lu is populated both directly by the beta decay of ^{175}Hf and by an 89-keV mixed transition from the 433-keV level. Although the relative sizes of the various β -decay matrix elements of the two relevant first-forbidden decays from ^{175}Hf to ^{175}Lu are unknown, the smallness of the log ft values⁷ indicates that the $\Delta J = 2$ components are small and were therefore neglected in calculating U_2 and U_4 . The uncertainties in our derived values reflect the fact that both Gamov-Teller and Fermi electron capture decay are permitted to the 343-keV level of ^{175}Lu . The magnitude of the mixing ratio for the 343-keV transition is known to be 0.26(3).⁸ Our data require that this mixing ratio and the quadrupole moment of ^{175}Hf have opposite signs; assuming that the quadrupole moment is positive,

we report $\delta_{343} = -0.27(3)$. For the EQI energy of the ^{175}Hf ground state we obtain $e^2qQ(5/2) = (4.05 \pm 0.50) \times 10^{-18}$ erg, from which we derive $Q(5/2) = 2.66(35)b$ or $Q_0 = 7.45(97)b$ for the intrinsic quadrupole moment.

Footnotes and References

*Present address: Physik-Department E15, Technische Universität München, D-8046 Garching, Germany.

†Present address: Department of Chemistry, Morehouse College, Atlanta, Georgia 30314.

1. N. J. Stone, in Hyperfine Interactions in Excited Nuclei, edited by G. Goldring and R. Kalish (Gordon and Breach, New York, 1971), p. 237.

2. J. Blok and D. A. Shirley, Phys. Rev. **143**, 911 (1966).

3. L. Nielson and W. J. Huiscamp, Physica **50**, 259 (1970).

4. D. C. Camp and A. L. Van Lehn, Nucl. Instr. Meth. **76**, 192 (1969).

5. K. S. Krane, C. E. Olsen, J. R. Sites, and W. A. Steyert, Phys. Rev. Letters **26**, 1579 (1971).

6. P. Boolchand, B. L. Robinson, and S. Jha, Phys. Rev. **187**, 475 (1969).

7. A. Jasinski and C. J. Herrlander, Ark. Fys. **37**, 585 (1968).

8. P. G. Hansen, P. Hornshøj, and K. H. Johansen, Nucl. Phys. **A126**, 464 (1969).

NUCLEAR MAGNETIC RESONANCE ON ORIENTED ^{101m}Rh

G. Kaindl,* F. Bacon,† H.-E. Mahnke,‡ and D. A. Shirley

This paper reports on thermal equilibrium nuclear orientation (NO) of the 4.5 d isomer of ^{101}Rh in ferromagnetic nickel. As a result, spin and magnetic moment of the isomeric state, as well as the mixing ratios of the 306.7- and 544.5-keV gamma transitions of ^{101}Ru , following the EC decay of the isomeric state, were obtained.

The ^{101m}Rh activity was synthesized by the $\text{Ru}(d, 2n)^{101m}\text{Rh}$ reaction with 25-MeV deuterons on a natural ruthenium metal target (99.999% pure), and subsequent chemical separation, using the standard ruthenium-rhodium separation method¹ with only minor modifications. Dilute alloys were prepared by electroplating the carrier-free activity on a high-purity nickel foil (99.999%) and subsequent melting in hydrogen atmosphere. From these in ingots thin foils ($\sim 10\,000$ Å thick) were produced by cold-rolling and annealing. For the purpose of cooling into the millidegree region they were attached with Bi/Cd solder to the copper fin of an adiabatic demagnetization apparatus,² using CMN as a cooling salt. The experimental technique for the NO and NMR-ON experiments was the same as described in the preceding contributions.³

The temperature dependences of the anisotropies of the 306.7-keV and the weak 544.5-keV gamma rays were measured for ^{101m}Rh in nickel at temperatures down to $1/T = 270^0 \text{ K}^{-1}$. The results, presented in Figs. 1 and 2, show

that both gamma rays exhibit large positive anisotropies. The data were fitted with the

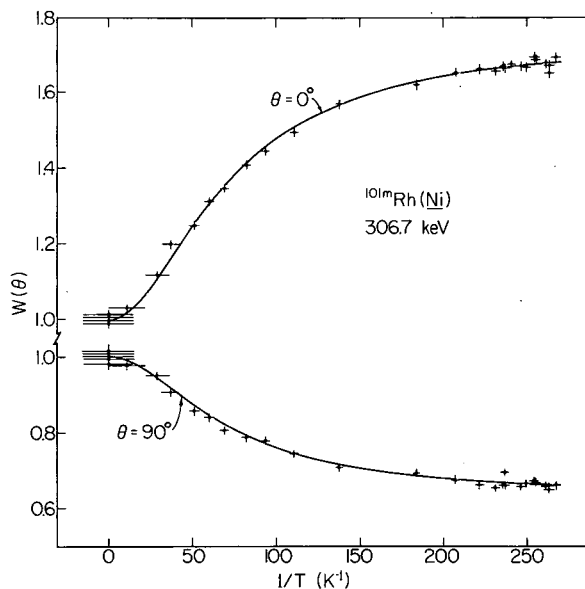


Fig. 1. Temperature dependence of the anisotropies of the 306.7-keV gamma rays emitted from a source of $^{101m}\text{Rh}(\text{Ni})$ parallel ($\theta = 0^\circ$) and perpendicular ($\theta = 90^\circ$) to the direction of the external polarizing field, $H_{\text{ext}} = 4 \text{ kOe}$. (XBL 725-3087)

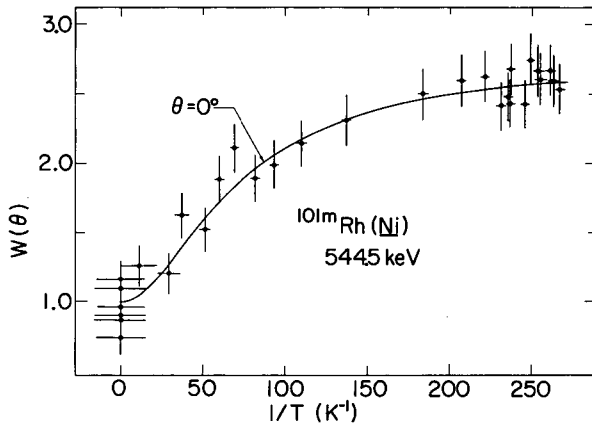


Fig. 2. Anisotropy curve for the 544.5-keV gamma rays, emitted from a source of $^{101}\text{Rh}(\text{Ni})$ at $\theta = 0^\circ$ ($H_{\text{ext}} = 4$ kOe). (XBL 728-3686)

theoretical anisotropy function, assuming $I = 9/2$ for the spin of the isomeric state and $I = 7/2$ for the spins of both the 544.5-keV and the 306.7-keV levels of ^{101}Ru . Only the magnetic hyperfine interaction of the isomeric state, $\mu(9/2) \cdot H_{\text{eff}}$, and the E2/M1 mixing ratios of the two gamma transitions were used as adaptable parameters.

In addition NMR was observed on the isomeric state in ferromagnetic nickel at a temperature of ~ 5 mK via the effects of an externally applied rf field on the anisotropy of the 306.7-keV gamma rays, emitted at an angle of 0° relative to the external polarizing field. Figure 3 shows the results of two individual runs with different modulation bandwidths of the rf field. As expected, the experimental line width of the resonance curve decreases with decreasing bandwidth. From a least-squares fit of the data with a Gaussian curve with linear background, the resonance frequency was obtained as

$$\nu_{\text{res}} = 206.2 \pm 0.4 \text{ MHz.}$$

Table I summarizes the results for the magnetic hyperfine interaction. The quoted values are the weighted means of the individual results. Both measurements can be brought into agreement only if the spin of the isomeric state is equal to $9/2$, in agreement with the assignment of Ref. 4. In the present case this method of spin determination is quite sensitive, due to the small value of the spin.⁵ For $I = 9/2$ we obtain for the ratio $(\gamma H_{\text{hf}})_{\text{NO}} / (\gamma H_{\text{hf}})_{\text{NMR}}$ a value of 1.02 ± 0.03 .

For a derivation of a value of the magnetic moment of ^{101}mRh a value for the hyperfine field at rhodium impurities in nickel at

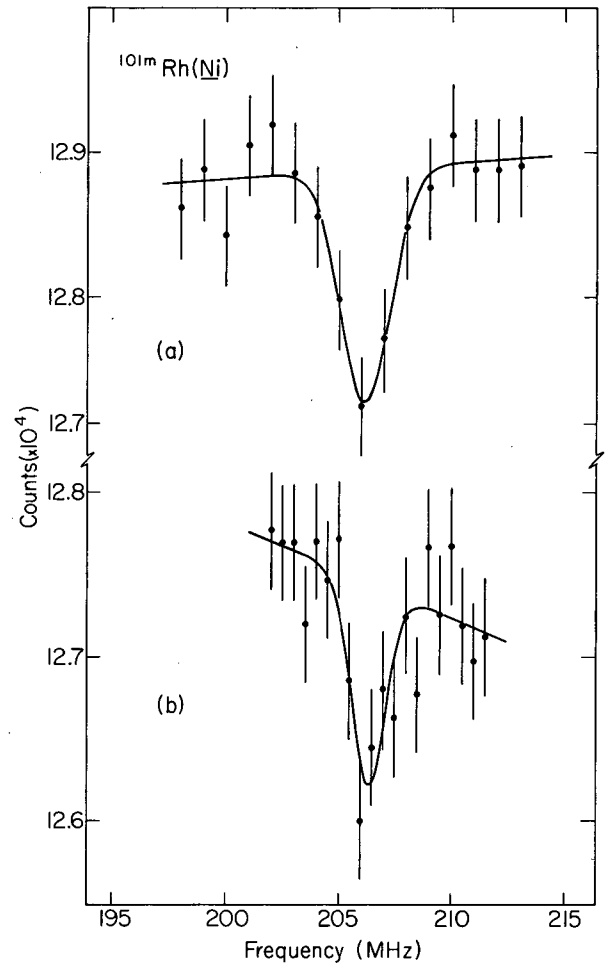


Fig. 3. NMR-ON spectrum of the 306.7-keV gamma rays, emitted from a $^{101}\text{mRh}(\text{Ni})$ source at $\theta = 0^\circ$ relative to the external polarizing field of 1 kOe. The rf frequency was changed in steps of 1 MHz (0.5 MNz) and modulated over a bandwidth of 2 MHz (1 MHz) in spectrum a (b). (XBL 725-3088)

Table I. Summary of experimental results for the magnetic hyperfine interaction of ^{101}mRh in nickel.

Host	Method	$1H_{\text{eff}}$ (10^{-18} erg)	Resonance frequency (MHz)
Nickel	NO	6.2 \pm 0.2	--
Nickel	NMR-ON	(6.147 \pm 0.012)	206.2 \pm 0.4

$T < 1 \text{ K}^0$ is needed. This field has been measured until now only at 77°K and higher temperatures,⁶⁻⁸ and it was found that the temperature dependence of the reduced field follows closely that of the reduced bulk magnetization of nickel.⁸ Since the bulk magnetization changes less than 1% between 77°K and $T \rightarrow 0$, we can safely use the value at 77°K , $H_{\text{hf}} = 222 \pm 3 \text{ kOe}$.⁸ This results in

$$\mu(9/2^+) = (+) 5.51 \pm 0.09 \text{ n. m. ,}$$

corresponding to a g-factor of $g(9/2^+) = 1.22 \pm 0.02$ for the $\pi: g9/2$ state of ^{101}Rh .

We may compare now the present result with the known g-factors of $\pi: g9/2$ states of neighboring nuclei; this has been above in Table II. It is evident that the absolute size of $g(g/2)$ decreases with an increasing number of protons in the $1 g9/2$ proton shell.

Table II. The g-factors of proton states of the $1 g9/2$ shell.

Nuclear	State	$g(9/2^+)$	Reference
$^{93}_{41}\text{Nb}$	ground state	1.3707 ± 0.0001	9
$^{99}_{43}\text{Tc}$	ground state	1.2625 ± 0.0001	9
$^{101}_{45}\text{Rh}$	157 keV	1.22 ± 0.02	This work
$^{103}_{45}\text{Rh}$	93 keV	1.38 ± 0.20	8

The large positive anisotropy observed for the 544.5-keV gamma rays confirms the spin assignment $I = 7/2$ for the 544.5-keV level¹¹ and rules out a spin of $I = 5/2$.¹² From least-squares fits of the anisotropy curves values for the E2/M1 mixing ratios δ of the two gamma transitions were obtained¹³

$$\delta(544.5 \text{ keV}) = -0.98 \pm 0.10,$$

$$\delta(306.7 \text{ keV}) = -0.10 \pm 0.01.$$

These values for the mixing ratios may be compared with $B(E2 \uparrow)$ values as derived from Coulomb excitation experiments on ^{101}Ru .¹² In qualitative agreement with the present results the $B(E2 \uparrow)$ value for the 544.5-keV level was found to be 0.140 ± 0.010 , while that of the 306.7-keV state was only 0.007 ± 0.002 , both in units of $e^2 \times 10^{-48} \text{ cm}^4$.¹²

The authors would like to thank Mrs. Winifred Heppler for performing the chemical separations.

Footnotes and References

* Present address: Physik-Department E15, Technische Universität München, D-8046 Garching, Germany.

† Present address: Department of Chemistry, Morehouse College, Atlanta, Georgia 30314.

‡ Present address: Hahn-Meitner Institut für Kernforschung, Abt. Kernphysik, D-1000 Berlin, Germany.

1. G. R. Choppin, Nuclear Science Series NAS-NS 3008, p. 26 (1960).

2. F. Bacon, G. Kaindl, H. -E. Mahnke, and D. A. Shirley, Phys. Rev. C, in press.

3. G. Kaindl, F. Bacon, H. -E. Mahnke, and D. A. Shirley, preceding contribution.

4. M. E. Phelps and D. G. Sarantites, Nucl. Phys. A159, 113 (1970).

5. Compare with the preceding paper on ^{93}mMo , and references therein.

6. S. Koicki, T. A. Koster, R. Pollak, D. Quitmann, and D. A. Shirley, Phys. Letters 32B, 351 (1970).

7. M. Kontani and J. Itoh, J. Phys. Soc. Japan 22, 345 (1967).

8. R. C. R. Reno (thesis), Brandeis University, Waltham, Massachusetts (1970).

9. C. V. K. Baba, S. K. Battacherjee, and H. C. Jain, in Hyperfine Interactions in Excited Nuclei, edited by G. Goldring and R. Kalish (Gordan and Breach, New York 1971), p. 1173.

10. I. Lindgren, Arkiv Fysik 29, 553 (1965).

11. C. M. Ledere, J. M. Jacklevic, and J. M. Hollander, Nucl. Phys. A169, 489 (1971).

12. O. C. Kistner and A. Schwarzschild, Phys. Rev. 154, 1182 (1967).

13. We used the definition of K. S. Krane and R. M. Steffen, Phys. Rev. C 2, 724 (1970).

MAGNETIC MOMENTS OF THE 12^- STATES IN $^{196}, ^{198}, ^{200}\text{Au}$ F. Bacon,* G. Kaindl,[†] H.-E. Mahnke,[‡] and D. A. Shirley

The magnetic moment of the $h_{9/2}$ proton outside the ^{208}Pb core is quite well known from ^{209}Bi and ^{210}Po . The large deviation from the single-particle value could only partially be explained by spin polarization, while the remainder was attributed to an anomalous orbital magnetism Δg_ℓ .¹ In this context, it seemed desirable to determine the magnetic moment of the spin orbit partner $h_{11/2}$ proton (hole).

The nuclei closest to ^{208}Pb with $h_{11/2}$ components are the Au isotopes; in the even-mass Au isotopes the coupling of an $h_{11/2}$ proton hole to an $i_{13/2}$ neutron hole leads to low-lying isomeric states with $I = 12$.

Using thermal equilibrium nuclear orientation techniques, we have measured the magnetic moment of the 12^- states in ^{196}Au (Ref. 2) and ^{200}Au . With NMR on oriented $^{200m}\text{Au}(\text{Ni})$ a more precise value of the g-factor could be obtained.³ In ^{198}Au we have found a new isomer which is very likely the corresponding 12^- state to the neighboring ^{196}Au and ^{200}Au .

Since the ^{196}Au and ^{200m}Au results have already been published, experimental data will be presented here only for ^{198m}Au . The ^{198}Au activity was produced by the $^{196}\text{Pt}(\alpha, \text{pn})^{198}\text{Au}$ and $^{198}\text{Pt}(\alpha, 2n)^{198m}\text{Au}$ reactions, using 35-MeV α particles and 18-MeV deuterons, respectively. In the gamma ray spectrum three new gamma lines at energies of 181, 203, and 214 keV could be attributed to the decay of ^{198m}Au , with a half-life of $T_{1/2} = 49 \pm 2$ hours.

In the nuclear orientation experiments the temperature dependence of the anisotropy of the 203- and 214-keV gamma lines was measured for sources of $^{198m}\text{Au}(\text{Fe})$ and $^{198m}\text{Au}(\text{Ni})$, using the activity produced by the (α, pn) reaction. After the gold activity had been separated carrier-free from the platinum target by the standard ethyl-acetate separation procedure and electroplated on iron and nickel foils, respectively, the usual experimental technique described previously was applied.⁴

Figure 1 shows the results for the temperature dependence of the anisotropy of the 214-keV gamma rays of $^{198m}\text{Au}(\text{Fe})$. From a simultaneous least-squares fit of these anisotropy curves with the theoretical anisotropy

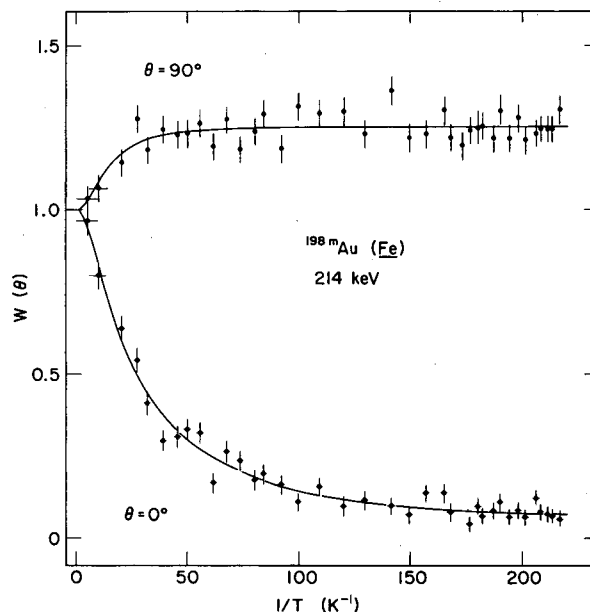


Fig. 1. Temperature dependence of the anisotropy of the 214-keV gamma rays of $^{198m}\text{Au}(\text{Fe})$, emitted parallel ($\theta = 0^\circ$) and perpendicular ($\theta = 90^\circ$) to the external polarizing field of 4 kOe. (XBL 722-2485)

function, a value of

$$\mu \cdot H_{\text{eff}} = (29.2 \pm 1.6) \times 10^{-18} \text{ erg}$$

was obtained for the magnetic hyperfine interaction of ^{198m}Au in iron. From it a value for the magnetic moment was derived, using the hyperfine field determined for the 2^- ground state of ^{198}Au . As in the cases of ^{196m}Au and ^{200m}Au a 2.5% correction for hyperfine anomaly was applied.^{2, 3}

Table I summarizes the magnetic moments for the isomeric states of the three isotopes. From the measured moment of ^{200m}Au , where the experimental error can be neglected in comparison with the estimated error for the applied correction, we can deduce the proton contribution. Taking the neutron part as $\mu(i_{13/2}) = -0.8 \pm 0.2$ n.m. (from ^{195}Pt and $^{193}, ^{195}, ^{197}, ^{199}\text{Hg}$), we obtain $\mu(h_{11/2}) = 6.9 \pm 0.3$ n.m., i.e. $g(h_{11/2}) = 1.25 \pm 0.06$, which is in good agreement with $\mu(h_{11/2})_{\text{core}} = 6.7$ n.m. calculated with the spin-polarization procedure of Arima and Horie.

Table I. Magnetic moments of the 12^- isomeric states in even-mass gold isotopes. The values corrected for hyperfine anomaly, μ_{corr} , are listed in the last column.

A	$T_{1/2}$ [h]	Method	μ (n. m.)	μ_{corr} (n. m.)
196	9.7	NO	5.24 ± 0.20	5.35 ± 0.20
198	49	NO	5.40 ± 0.34	5.55 ± 0.34
200	18.7	NMR/ON	5.90 ± 0.04	6.10 ± 0.20

The authors would like to thank Mrs. Winifred Heppler for performing the chemical separations.

Footnotes and References

*Present address: Department of Chemistry, Morehouse College, Atlanta, Georgia 30314.

†Miller-Fellow 1969-1971. Present address: Physik-Department E15, Technische Universität München, D-8046 Garching, Germany.

‡Present address: Hahn-Meitner Institut für Kernforschung, Abt. Kernphysik, D-1000 Berlin, Germany.

1. S. Nagamiya and T. Yamazaki, Phys. Rev. C 4, 1961 (1971).

2. F. Bacon, G. Kaindl, H. -E. Mahnke, and D. A. Shirley, Phys. Letters 37B, 181 (1971).

3. F. Bacon, G. Kaindl, H. -E. Mahnke, and D. A. Shirley, Bull. Am. Phys. Soc. 17, 658 (1972); Nuclear Chemistry Division Annual Report for 1971, LBL-666, p. 209; submitted to Phys. Rev. C.

4. See previous contributions on $^{93\text{m}}\text{Mo}$ and $^{101\text{m}}\text{Rh}$.

NUCLEAR QUADRUPOLE INTERACTION STUDIES BY PERTURBED ANGULAR CORRECTIONS*

H. Haas and D. A. Shirley

A comprehensive study was made of the applicability of gamma-ray angular correlations to the determination of quadrupole interactions in metals and insulating solids. Dynamic effects were studied in solutions and gases. A total of 14 gamma-ray cascades were employed. Several nuclear spins were confirmed (Fig. 1), and the quadrupole moments of ten excited nuclear states were determined or estimated from the data (Table I). Quadrupole coupling constants were determined for excited states of the following nuclei in metallic host lattices of the same element: ^{44}Sc , ^{99}Ru , ^{111}Cd , ^{117}Cd , ^{117}In , ^{187}Re , ^{199}Hg . Coupling constants were also measured for the following isotope (lattice) combinations: $^{99}\text{Ru}(\text{Zn}, \text{Cd}, \text{Sn}, \text{Sb})$, $^{100}\text{Rh}(\text{Zn}, \text{Ru}, \text{Cu}_5\text{Zn}_8, \text{Pd}_2\text{Al}, \text{PdPb}_2)$, $^{111}\text{Cd}(\text{In}, \text{Hg}, \text{Tl}, \text{CdSb}, \text{Cd}_3\text{Ag}, \text{Zn}, \text{Ga}, \text{In}, \text{Sn}, \text{Sb}, \text{Bi}, \text{AuIn}, \text{InBi}, \text{In}_2\text{Bi})$, $^{115}\text{In}(\text{Cd})$, $^{117}\text{In}(\text{Cd}, \text{Sn})$, $^{131}\text{I}(\text{Te})$, $^{181}\text{Ta}(\text{HfB}_2, \text{HfSi}_2)$, $^{204}\text{Pb}(\text{Cd}, \text{In}, \text{Sn}, \text{As}, \text{Sb}, \text{Bi}, \text{Hg}, \text{Tl}, \text{PdPb}_2)$. Systematic variations of e^2qQ with host-lattice structure was observed (Fig. 2), and host and solute properties were found to be separable to some extent for non-transition metals.

The nuclei ^{111}Cd , ^{115}In , ^{117}In , ^{199}Hg ,

and ^{204}Pb were used to determine a total of 50 quadrupole coupling constants in insulators, including 20 with nonzero asymmetry parameters, which give oscillatory but aperiodic correlation functions. It was strikingly (and exhaustively) demonstrated that good determinations of quadrupole coupling constants could be made following isomeric transitions (with no elemental transmutation) and beta decay (with elemental transmutation). However, in no case was it possible to derive a coupling constant from a gamma-ray cascade preceded directly by electron-capture decay, presumably because the sudden creation of a K-hole and the Auger and "shake-off" events that follow destroy the chemical integrity of the species under study. Figure 3 shows typical time-spectra for the three cases.

Relaxation times were determined for a number of liquid samples. Studies of dimethyl- $^{111\text{m}}\text{Cd}$ in various buffer gases showed that the spin memory was lost in one collision with heavy molecules, but that light molecules required several collisions, as shown in Fig. 4.

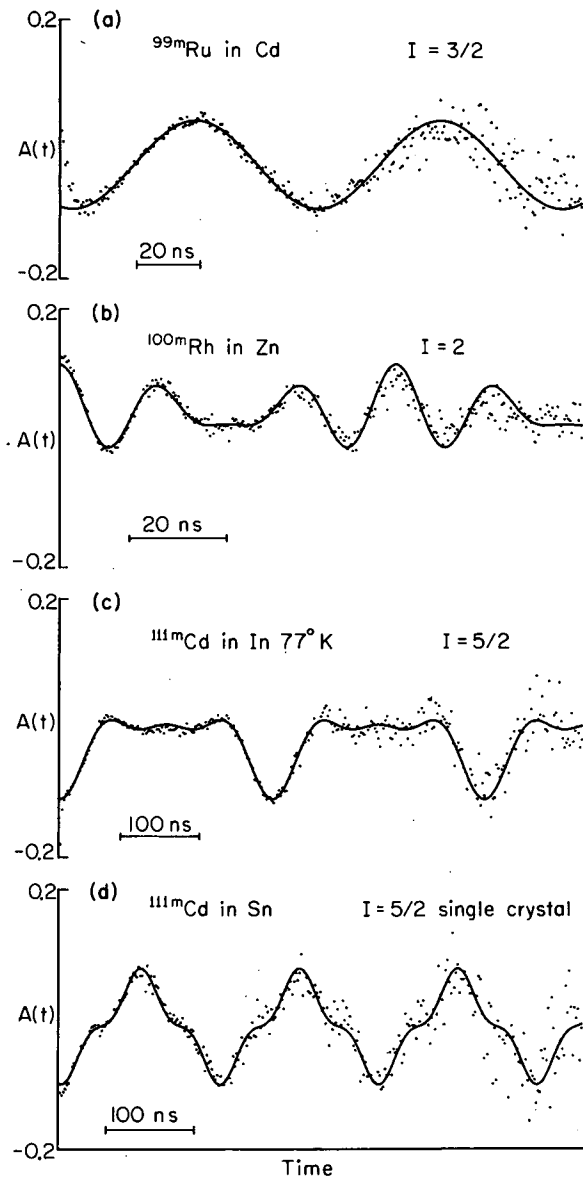


Fig. 1. Spin dependence of the perturbation function with axially symmetric field gradient. Data and theoretical curves are shown for each case. (XBL 726-3150)

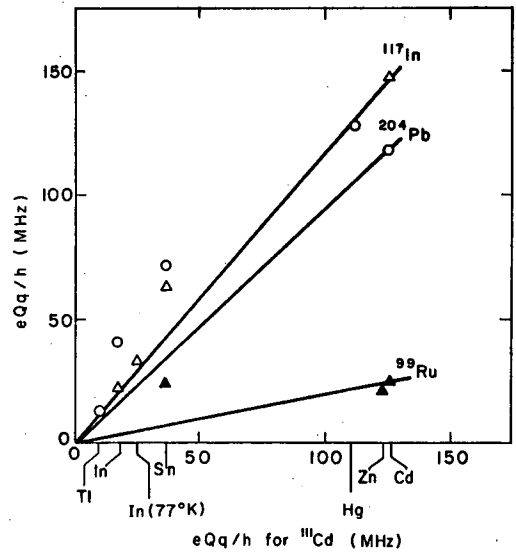


Fig. 2. Quadrupole coupling constants for ^{111}Cd (247 keV) in several non-cubic metals compared to those of some other nuclei. (XBL 7210-4223)

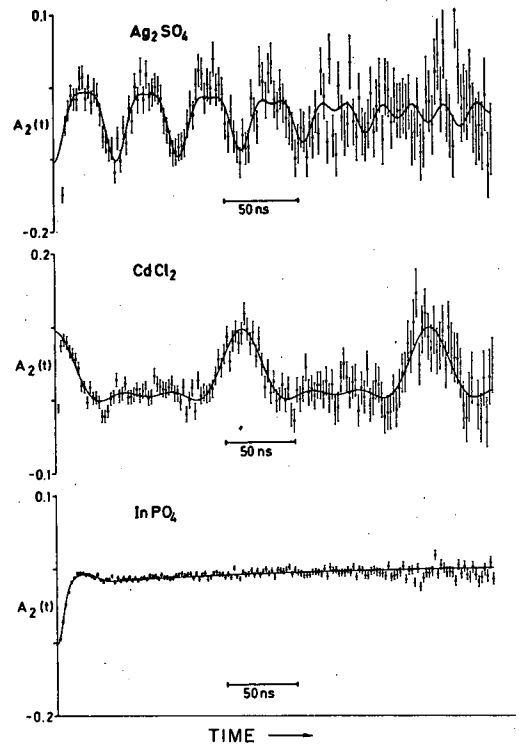


Fig. 3. Typical perturbations observed in insulators for isomeric state decay, β -decay, and EC decay. (XBL 724-747)

Table I. Quadrupole Moments from PAC Studies.

Lattice	Nucleus	eQq(MHz)	Reference	eQq(MHz)	Q-Ratio	Ref.-Q(b)	Q (b)
^{44}Ti <u>Sc</u>	^{44}Sc (68 keV)	1.90±0.10	^{45}Sc (g.s.)	2.02±0.03	0.94±0.05	0.22±0.01	0.21±0.02
^{99}Rh <u>Cd</u>	^{99}Ru (90 keV)	25.4±0.6	^{117}In (659 keV)	143±3	[0.18]	0.58±0.06	[0.10]
^{100}Pd <u>Zn</u>	^{100}Rh (75 keV)	11.4±0.2	^{111}Cd (247 keV)	123±2	[0.093]	[0.50]	[0.05]
^{111}In <u>Cd</u>	^{111}Cd (247 keV)	125±2	^{117}In (659 keV)	143±3	[0.87]	0.58±0.06	[0.50]
^{115}Cd	^{115}In (829 keV)	149±6	^{117}In (659 keV)	143±3	1.04±0.05	0.58±0.06	0.60±0.08
^{117}Cd <u>In</u>	^{117}In (659 keV)	21.0±0.5	^{115}In (g.s.)	30.0±0.1	0.70±0.02	0.83±0.06	0.58±0.06
^{131}Te	^{131}I (1797 keV)	409±30	^{129}I (28 keV)	373±6($\eta=0.8$)	1.10±0.10	0.68±0.05	0.74±0.08
^{187}W <u>Re</u>	^{187}Re (206 keV)	376±5(300°K)	^{187}Re (g.s.)	256.2±1.0(4.2°K)	1.47±0.02	2.24±0.50	3.3±0.7
$^{199\text{m}}\text{HgCl}_2$	^{199}Hg (158 keV)	1290±80	^{201}Hg (g.s.)	708±2	1.82±0.12	0.50±0.05	0.91±0.12
$^{204\text{m}}\text{Pb}$ <u>Hg</u>	^{204}Pb (1274 keV)	129	^{199}Hg (158 keV)	210±20	[0.61]	0.91±0.12	[0.56]

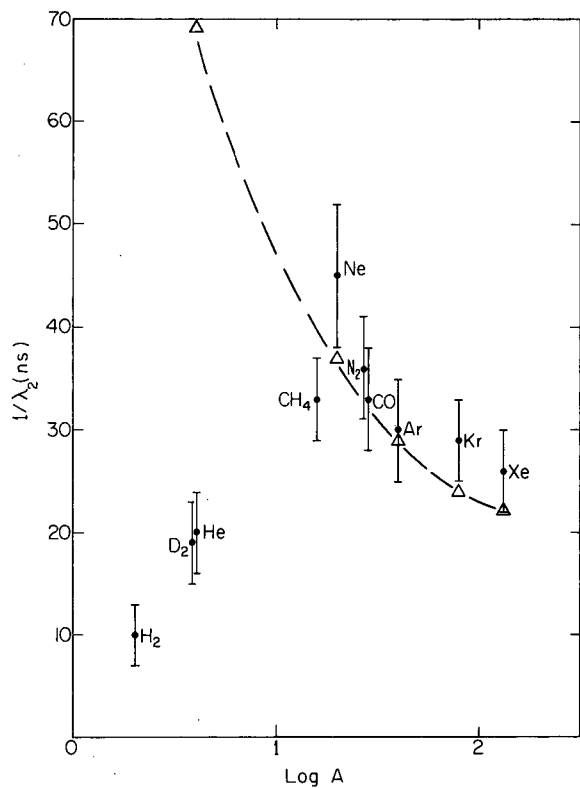


Fig. 4. Effect of different gases on the relaxation time in $\text{Cd}(\text{CH}_3)_2$. The theoretical curve is for the case of strong collisions.
(XBL 726-3148)

Footnote

* Condensed from LBL-1284. To be published, Journal of Chemical Physics. See also the review article by D. A. Shirley and H. Haas, Ann. Rev. Phys. Chem. 23, 385 (1972).

PROPERTIES OF 2- AND 3-PHOTON DECAY

R. W. Schmieder

There exist certain metastable atomic states from which all single-photon and all even-parity multiphoton (e. g., 2E1) decay modes are forbidden. Such states can decay only by odd parity multiphoton modes like E1M1 and 3E1. These processes may be of interest in connection with stellar or interstellar environments where collisional de-excitation would be sufficiently low to permit the spontaneous decay. We have analytically examined the symmetry properties of the relevant matrix elements in order

to determine the general properties of these modes. For instance, it was found that for a $J = 0 \rightarrow J = 0$ transition the 3E1 transition probability is zero whenever any two photons have the same energy, thus determining roughly the emission spectrum. In the absence of other Z-dependent effects such as spin-orbit mixing, the 3E1 rate scales with atomic number as Z^8 . In most atoms, the 3E1 and E1M1 modes compete, and a detailed numerical calculation may be necessary to determine whether one mode is dominant.

ALIGNMENT OF SOME TRIPLET AND SINGLET D STATES OF HELIUM

J. Yellin, T. Hadeishi, and M. C. Michel

The beam-foil interaction process is known to lead to an alignment of excited atomic states.¹ Alignment has been reported for a number of atomic as well as ionic² states; however, there appears to be as yet no systematic study of the dependence of alignment on principle quantum number, angular momentum state, and spin state. Such a study is of interest both for an understanding of the beam-foil interaction process and for the performance of experiments based on alignment, e. g., level-crossing and radiofrequency spectroscopy. The present investigation was undertaken as part of a program to utilize the alignment induced in the beam-foil scattering process for the measurement of atomic constants.³ We report here on the alignment of the $n^3D_{1,2,3}$ and n^1D_2 states of ^4He for principle quantum numbers $n = 3, 4, 5$, and 6. These measurements were done for incident energies of 40 kV. Carbon foils of 6.0 and 6.7 $\mu\text{g}/\text{cm}^2$ density were used.

The polarization is defined by Eq. (1):

$$\pi = \frac{I_{\perp} - I_{\parallel}}{I_{\perp} + I_{\parallel}}, \quad (1)$$

where I_{\perp} is the intensity of light with polarization vector perpendicular to the beam axis and I_{\parallel} is the intensity of light with polarization vector parallel to the beam axis. A direct measurement of the polarization fraction is susceptible to serious error resulting from reflection polarization in the detector optical system, and it is for this reason that we chose to make the measurements by observing the "quantum-beat" and zero-field level-crossing signal (Hanle effect).

The intensity fluctuation or quantum beat for an aligned singlet D state is given by

$$I(\omega, t) \propto e^{-\gamma t} [1 + A \cos 2(\omega t - \theta)], \quad (2)$$

where $\omega = g \mu_0 H / \hbar$, θ is the angle which the polarizer makes with the beam axis, and A is the alignment, and γ is the reciprocal lifetime in radians/sec of the 1D_2 state. In Eq. (2), t is the time following excitation in the foil at which the observation is made and hence $t = l/v$, where l is the foil-detector separation and v the beam velocity. The detector is assumed to view a short region of the beam path, Δl , such that $\Delta l/v \ll 1/\gamma$. Thus by observing the intensity fluctuation the polarization fraction can be determined. If the detector slit width is finite or, what is equivalent, if observation is made for many overlapping detector-foil separations, then the signal is

$$S(\omega) = \int_{t_1}^{t_2} I(\omega, t) dt \propto \frac{1}{\gamma} \left(e^{-\gamma t_2} - e^{-\gamma t_1} \right) + \frac{A\gamma/4}{\left(\frac{\gamma}{2}\right)^2 + \omega^2} \left\{ e^{-\gamma t_2} \left[\frac{2\omega}{\gamma} \sin 2(\omega t_2 - \theta) - \cos 2(\omega t_2 - \theta) \right] - e^{-\gamma t_1} \left[\frac{2\omega}{\gamma} \sin 2(\omega t_1 - \theta) - \cos 2(\omega t_1 - \theta) \right] \right\}, \quad (3)$$

where $t_1 = \ell_{\min}/v$ and $t_2 = \ell_{\max}/v$. If the limits are carried from 0 to ∞ we have,

$$S(\omega) \propto \frac{1}{Y} + \frac{Ay/4}{\left(\frac{Y}{2}\right)^2 + \omega^2} \left(\frac{2\omega}{Y} \sin 2\theta + \cos 2\theta \right).$$

Thus, if observation is made of the polarization parallel to the beam axis ($\theta = 0^\circ$) or perpendicular to the beam axis ($\theta = 90^\circ$) we see that $A = \pm[s(0) - s(\infty)]/s(\infty)$, respectively. In other words the relative amplitude of the Hanle or zero-field level-crossing signal gives the polarization fraction. This result is independent of the observation limits, t_1, t_2 . For the $^3S_{1,2,3}$ state additional modulation terms occur, corresponding to the fact that there

are three gJ factors and, in addition, modulations due to mixing of fine structure and Zeeman frequencies occur, but the latter do not contribute to the zero-field level-crossing signals. The interpretation of the 3D signals is otherwise the same as for the 1D states. In beam-foil experiments it is not usually practical to extend the limits of observation to many lifetimes, but this does not affect the results. Considerations of magnetic field uniformity impose a severe limit on the maximum detector-foil separation, which in the present experiment was 7 cm, corresponding to an upper limit of 59 nsec. Curve-fitting was used to determine the polarization fraction when inspection did not suffice. The measurements reported here also yield lifetime information for the states studied;⁴ however, we are presently concerned only with the alignment.

Details of the experimental technique have been described elsewhere.⁴ A schematic of the apparatus is shown in Fig. 1.

Table I summarizes the polarization fraction measurements, and in Fig. 2 we show a typical beat and Hanle signal for the $5^3D_{1,2,3}$ state. Counting errors in all cases contributed an uncertainty of $\approx 1/2\%$ to the polarization fraction. The polarization fraction varied by $\sim 1.5\%$ from foil to foil and from day to day, and this is reflected in the errors. This variation we believe to be due to the condition of the foil. We have observed structural variations between some foil batches and this plus contamination of the foil in preparation, handling, or in the vacuum system of the apparatus may be responsible for the variations.

Table I. Measured percentage polarization for the singlet and triplet D states. λ is the wavelength of the transition observed; $n^3D_{1,2,3} - 2^3P_{2,1,0}$ and $n^1D_2 - 2^1P_1$.

n	1D	$\lambda(\text{\AA})$	3D	$\lambda(\text{\AA})$
3			3.6 ± 2^a	5876
4	12.0 ± 2	4922	2.9 ± 2	4473
5	9.4 ± 1.4	4388	4.0 ± 2	4026
6	4.3 ± 2^a	4144	5.0 ± 2	3820

^aThese values were based on the quantum beat signal only.

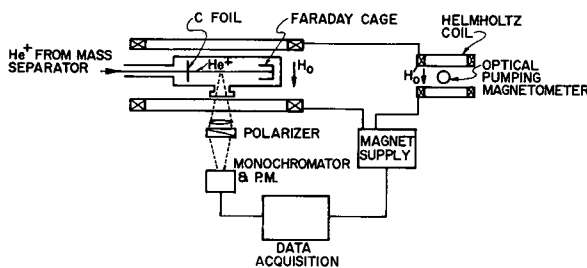


Fig. 1. Experimental apparatus. (XBL 729-1917)

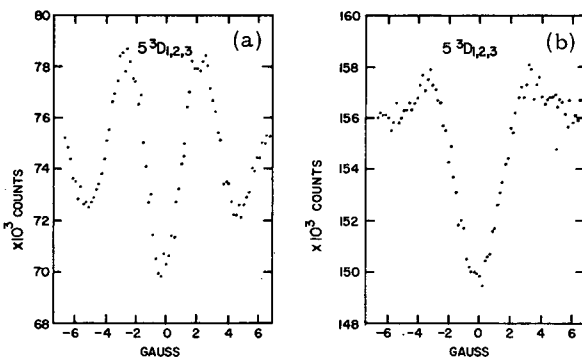


Fig. 2. Alignment signal for the $5^3D_{1,2,3}$ state of ^4He . (a) "quantum beat" signal. The detector viewed a 7 mm portion of the beam 7 cm downstream from the foil. Thus this is not a pure beat signal but really a delayed Hanle signal with the observation time extending from 51.2 to 56.6 nsec. (b) Zero-field level-crossing (Hanle) signal. The observation extended from zero foil-detector separation to 7 cm foil-detector separation, corresponding to about one lifetime of observation. Note the modulations in the wings. The polarizer axis was perpendicular to the beam axis, hence the inverted signal.

(XBL 7212-7484)

References

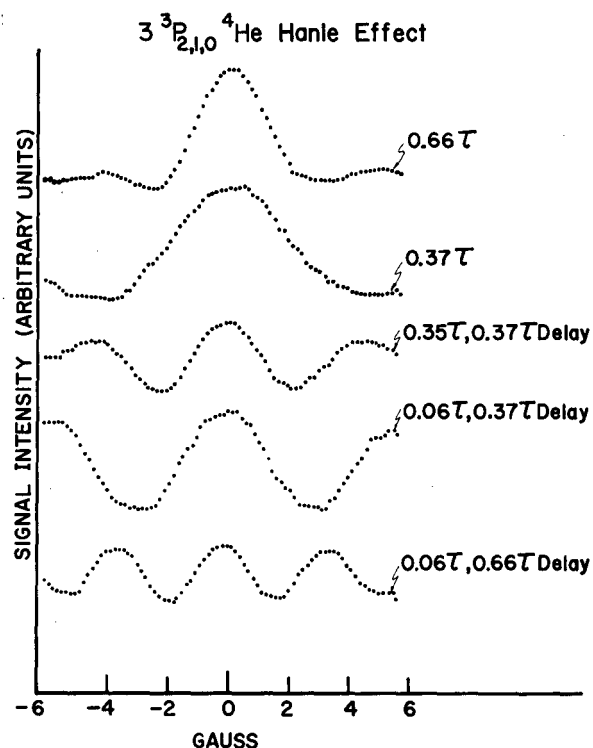
1. S. Bashkin, W. S. Bickel, D. Fink, and R. K. Wangness, *Phys. Rev. Letters* **15**, 284 (1965); T. Hadeishi, *Phys. Rev. Letters* **21**, 957 (1968).
2. W. S. Bickel and S. Bashkin, *Phys. Rev.* **162**, 12 (1967); see also Proceedings of the 2nd Intl. Conf. on Beam-Foil Spectroscopy, Nucl. Instr. Methods (1970) for additional references.
3. T. Hadeishi, M. C. Michel, J. Yellin, and E. Geneux, in the Proceedings of the 3rd Intl. Conf. on Beam-Foil Spectroscopy (to be published).
4. J. Yellin, T. Hadeishi, and M. C. Michel, LBL-1608 (January 1973), to be published.

TIME RESOLVED HANLE EFFECT IN THE $3^3P_{2,1,0}$ STATE OF ^4He

J. Yellin, T. Hadeishi, and M. C. Michel

We have observed the Hanle effect in the 3^3P state of ^4He by the beam-foil method. 40-kV $^4\text{He}^+$ ion beams from the Berkeley mass separator were incident on a thin carbon foil and polarization of the 3889 Å line emitted by neutral He atoms emerging from the foil was studied as a function of the intensity of a magnetic field perpendicular to the beam axis. A polarization of ~15% was observed in the 3^3P state. The Hanle effect was studied by integrating piecewise the light emitted from small segments of the He beam downstream from the foil. Time delays were introduced into the observation, and the phenomenon of line-narrowing¹ resulting from delayed observation was demonstrated experimentally. The lifetime of the 3^3P state was determined to be 87 ± 5 nsec, in excellent agreement with previous measurements.² The results are shown in Fig. 1.

Fig. 1. Hanle effect in the $3^3P_{2,1,0}$ state of ^4He . The upper two curves are without delay. Delay is introduced into the lower three curves by beginning the observation downstream from the foil. (XBL 7211-7429)



References

1. G. Copley, B. P. Kibble, and G. W. Series, *J. Phys. B*, **724** (1968).
2. Michelle Manjean and M. Jean-Pierre Descoubes, *C. R. Acad. Sc. Paris* **264B**, 1653 (1967); I. Martinson et al. *J. Opt. Soc. Am.* **60**, 352 (1970).

LIFETIME AND ALIGNMENT OF THE 5^1D_2 STATE OF ^4He BY BEAM-FOIL LEVEL CROSSING

J. Yellin, T. Hadeishi, and M. C. Michel

The beam-foil method has the useful property that the atoms (ions) are excited at a

precisely known position. This fact has been exploited to measure atomic (ionic) lifetimes

by observing the exponential decay of excited states.¹⁻⁵ The method suffers from a serious drawback in that the measurements are sensitive to cascading from highly excited states that feed the state under observation. In the experiment reported here we have used another useful property of the beam-foil interaction process to measure the lifetime of the 5^1D_2 of ^4He . The atoms emerge from the foil in a partially aligned state so that application of a magnetic field perpendicular to the beam axis results in the creation of a coherent superposition of states with magnetic quantum numbers $+m_J$, $-m_J$. This leads to the quantum beat phenomenon which has been exploited in the measurement of g factors and alignment⁶ and to the Hanle effect which has been used to measure lifetimes.⁷ In the present investigation we have used the zero-field level-crossing method (Hanle effect) to measure both the lifetime and alignment of the 5^1D_2 state of ^4He . Previously, alignment was determined from quantum beat experiments, while lifetimes were determined from the Hanle effect. The purpose of the present measurement is to compare the lifetime as determined by the technique reported here with lifetimes based on conventional beam-foil and level-crossing methods. The lifetime of the 5^1D_2 state was previously measured by both the conventional beam-foil⁸ and level-crossing

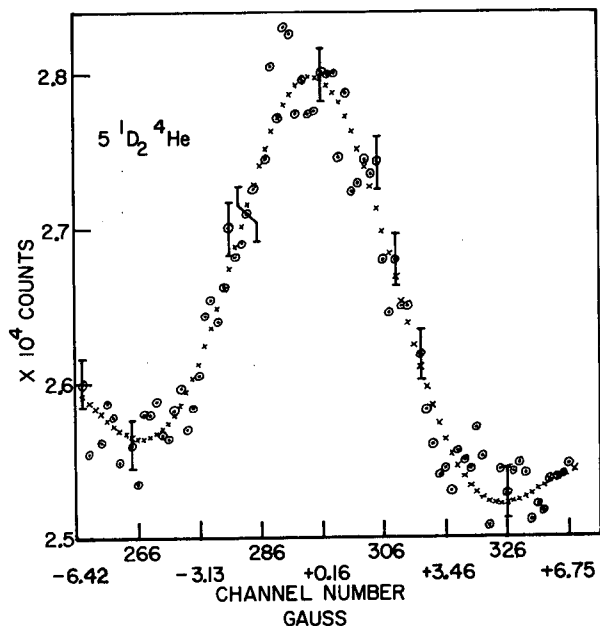


Fig. 1. Zero-field level-crossing signal for the 5^1D_2 state of He. The circles are experimental points and the x's are the calculated points from a least-squares fit. The slope of the curve is due to foil aging and was corrected for in the curve fit.

(XBL 731-2)

methods.⁹ It is of interest to compare these measurements since level crossing is inherently less sensitive to cascading.

The intensity of the $5^1D_2-2^1P_1$ (4388-Å) transition when the observation is made through a linear polarizer whose axis is parallel to the beam axis is given by

$$I(\omega, t) = Ae^{-\gamma t} (1 + B/A \cos 2\omega t), \quad (1)$$

where γ is the reciprocal lifetime in rad/sec, B/A is the alignment, and $\omega = g\mu_0 H/\hbar$. H is the magnetic field intensity and t is the time following excitation at which the observation is made. This relation holds for an infinitesimal detector slit width. When a finite segment of the beam is viewed, the signal observed is

$$S(\omega) = \int_{l_{\min}/v}^{l_{\max}/v} I(\omega, l/v) d(l/v), \quad (2)$$

where $l_{\max} - l_{\min}$ is the segment of beam intercepted by the solid angle of the detector, v is the beam velocity, and $t = l/v$ is the time following excitation. In our experiment $l_{\max} - l_{\min} = 7$ mm, but by changing the foil-detector separation and summing up contributions from many overlapping 7 mm segments, the integration path was effectively increased to 7 cm, corresponding to 59 nsec of observation time or about one lifetime. Details of the experiment have been described elsewhere.^{11,12}

The result is shown in Fig. 1 along with a least-squares fit of the data to Eq. (2). The lifetime is summarized in Table I along with previous measurements and is seen to be in better agreement with conventional level crossing than with the conventional beam-foil determination. A source of uncertainty in the type of experiment reported here is the velocity of the atoms, since the foil thickness is known to at best 5% and, furthermore, there is an uncertainty in the calculated energy loss.

Table I. Comparison of the lifetime of the 5^1D_2 state of He as determined by conventional beam foil (BF), level crossing (LC), and level crossing combined with beam foil (BF-LC).

Lifetime (nsec) of 5^1D_2 state of He		
BF	LC	BF-LC
66±4	49±5	52±6

Initially we used the theoretical velocity $v = 1.30 \times 10^8$ cm/sec calculated from the energy loss, and then adjusted the velocity to obtain the best fit. The best fit was obtained for a velocity 1% lower than that calculated. In addition to the lifetime we also determined the polarization of the 5^1D_2 state resulting from the beam-foil interaction at 40 kV. The polarization was found to be 12%.

In conclusion the beam-foil level-crossing method combines the best features of the beam-foil and level-crossing technique. On the one hand, beam foil offers a universal means of producing coherently excited states, bypassing the technical difficulties of electron excitation in magnetic fields; on the other hand, level crossing in inherently more accurate for lifetime determinations. Furthermore, the polarization induced in the beam-foil interaction process can be determined simultaneously with the lifetimes. The method is being extended to high-field level crossing.¹²

Footnote and References

1. W. S. Bickel and S. Bashkin, Phys. Letters 20, 488 (1966).

2. A. S. Goodman and D. J. Donahue, Phys. Rev. 141, 1 (1966).

3. S. Bashkin, ed., Beam-Foil Spectroscopy, Proceedings of the 1st Intl. Beam-Foil Conf. (Gordon and Breach, New York, 1968).

4. Proceedings of the 2nd Intl. Conf. on Beam-Foil Spectroscopy, Nucl. Instr. Methods 90 (1970).

5. Proceedings of the 3rd Intl. Conf. on Beam-Foil Spectroscopy, to be published in Nucl. Instr. Methods.

6. C. H. Liu, S. Bashkin, W. S. Bickel, and T. Hadeishi, Phys. Rev. Letters 26, 222 (1971).

7. D. A. Church, M. Druetta, and C. H. Liu, Phys. Rev. Letters 27, 1763 (1971).

8. I. Martinson et al., J. Opt. Soc. Am. 60, 352 (1970).

9. M. Maujean and M. Jean-Pierre Descoubes, C. R. Acad. Se. Paris 264B, 1653 (1967).

10. The foils were obtained from the Arizona Carbon Foil Co.

11. J. Yellin, T. Hadeishi, and M. C. Michel, LBL-1602 (December 1972), to be published.

12. T. Hadeishi, M. C. Michel, J. Yellin, and E. Genaux in Ref. 5.

ENERGY LEVELS OF Es I AND II

J. G. Conway and E. F. Worden*

Table I. Levels of Es I.

Configuration	Designation	Level	
		Observed cm^{-1}	Predicted cm^{-1}
$5f^{11}7s^2$	$4^1_{15/2}$	0.00	0.0
	$4^1_{13/2}$	8759.25	
$5f^{11}7s7p$	$6^1_{15/2}$	17802.89	19000±2000
	$6^1_{17/2}$	19209.15	
$5f^{10}6d7s^2$	$6^1_{17/2}$	19367.93	19000±2000
	-	28418.71	
$f^{10}_{ds^2}$	-	28372.83	
f^{11}_{sp}	13/2	28446.74	
$f^{10}_{ds^2}$	-	28578.71	
-	-	28689.61	
-	-	29159.28	
f^{11}_{sp}	-	29204.70	
$f^{10}_{ds^2}$	-	31886.18	

New observation of the spectrum of einsteinium has resulted in a more extended line list. We now have a list of 290 lines in the wavelength region of 2600 to 6900 Å. Ten lines have been assigned as transitions into the $5f^{11}7s^24^1_{15/2}$ ground state of Es I on the basis of line reversal and hyperfine structure. The next odd level is $4^1_{13/2}$ at 8759.25 cm^{-1} . The lowest even level is the $6^1_{15/2}$ of the $5f^{11}7s7p$ configuration at 17802.89 cm^{-1} . The lowest level of the $5f^{10}6d7s^2$ configuration is $6^1_{17/2}$ at 19367.93 cm^{-1} . A total of 15 lines are classified as transitions between Es I spectrum levels. Twenty-three lines are assigned as transitions to the two know lowest levels of Es II. Table I contains the energy levels of Es I and Table II the energy levels of Es II.

*Lawrence Livermore Laboratory.

Table II Known levels of Es II.

Configuration	Designation	J	Level
$5f^{11}7s$	$5I^0$	8	0.00
		7	938.66
		7	27 751.12
		8	28 178.80
			32 632.50
			32 897.77
		8	34 452.20
		7	34 641.82
		7	36 090.35
		8	36 692.15
		7	36 807.69
		9	36 907.71
		8	38 042.68
			38 321.25

SPECTRUM AND ENERGY LEVELS OF DOUBLY IONIZED SCANDIUM (Sc III)*

C. H. H. Van Deurzen,[†] J. G. Conway, and S. P. Davis[‡]

The Sc²⁺ ion has a ground state [Ar]3d²D_{3/2} and is isoelectronic with K I. The analysis of the lower levels by Gibbs and White,¹ as revised by Smith,² and the prediction of seven new levels by Russell and Lang³ (RL) has been confirmed and extended. Several lines observed by others have also been confirmed.^{4,5}

To excite and separate the spectra of Sc I, II, and III, a vacuum sliding spark was used similar to the one in use at the National Bureau of Standards and the Johns Hopkins University.⁶⁻⁹ It consists essentially of two 6 mm diameter by 25 mm cylindrical electrodes of 99.7% pure scandium metal, separated 6 mm by a hollow (3-mm inside diameter) quartz spacer through which the spark passes. The electrodes are water cooled and the source is operated in a vacuum of about 5×10^{-6} mm of Hg. Separation of the spectra

was achieved by varying the circuit parameters L and R, which varied the peak current from 10 A (L and R maximum, Sc I predominates) to 500 A (L and R minimum, Sc III predominates). Lines belonging to a given stage of ionization were identified by observing their common intensity behavior with current. Excellent separation of the Sc I, II, and III spectra was achieved by careful control of the excitation circuit parameters. The spectrum of Sc III has been measured by using the vacuum sliding spark at 250 A peak current. In all, 93 lines in the region 550 to 9400 Å are listed, which give rise to 23 new levels. The ionization energy of Sc III is revised to 199677.37 ± 0.1 cm⁻¹, based on the ng series, and series formulae were used to predict some of the newly found levels to within 0.25 cm⁻¹. Figure 1 is the energy level diagram of Sc III.

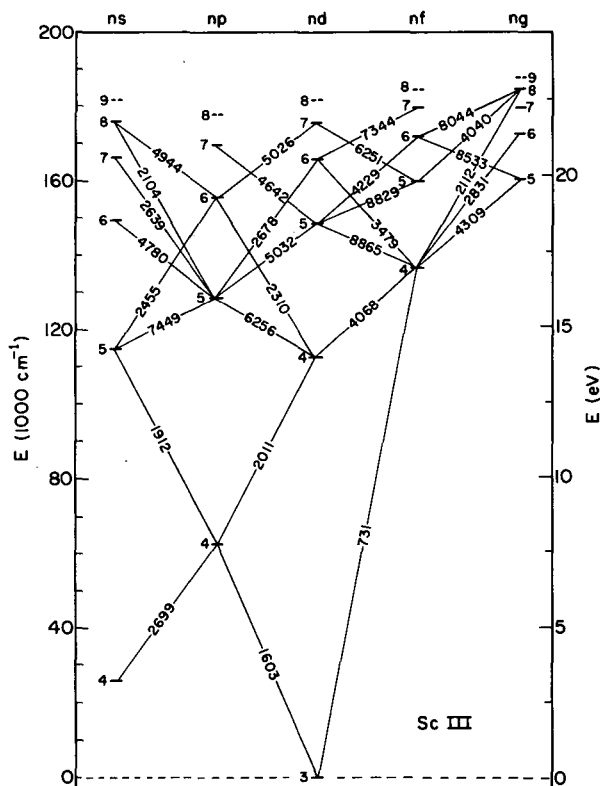


Fig. 1. Energy-level diagram for Sc III. The figures give the approximate wavelength of the leading line in each multiplet. The dotted lines are the next predicted levels. (XBL 728-3756)

Footnotes and References

* Condensed from LBL-1217. A preliminary report of this work was given at the 1972

Spring meeting of the Optical Society of America [J. Opt. Soc. Am. 62, 714 (1972)]. The final version accepted for Publication in the J. Opt. Soc. Am. 63, 158 (1973); also as LBL-1217.

† Department of Physics and Lawrence Berkeley Laboratory, University of California, Berkeley.

‡ Department of Physics, University of California, Berkeley.

1. R. C. Gibbs and H. E. White, Proc. Nat. Acad. Sci. 12, 599 (1926).
2. Stanley Smith, Proc. Nat. Acad. Sci. 13, 66 (1927).
3. H. N. Russell and R. J. Lang, Astroph. J. 66, 19 (1927).
4. A. Beckman, *Bidrag till kännedomen om skandiums specktrum i yttersta ultraviolett* (Almqvist and Wiksell, Uppsala, 1937).
5. R. Buchta, L. J. Curtis, I. Martinson, and J. Brzozowski, Physica Scripta 4, 55 (1971).
6. G. H. Dieke, H. M. Crosswhite, and B. Dunn, J. Opt. Soc. Am. 51, 820 (1961).
7. Wm. R. Callahan, J. Opt. Soc. Am. 53, 695 (1963).
8. Jack Sugar, J. Opt. Soc. Am. 53, 831 (1963).
9. Joseph Reader, Gabriel L. Epstein, and Jan Olof Ekberg, J. Opt. Soc. Am. 62, 273 (1972).

SPECTRUM OF THORIUM IV

J. G. Conway, G. V. Shalimoff, and C. H. H. Van Deurzen

Very pronounced separation of ionization states of thorium has been obtained with an improved sliding-spark source. Lines believed to be Th IV have been observed in addition to the known classified Th IV lines.

The spectrum of ionized thorium was photographed in the 3000 to 8000 Å region with a 3-meter Jarrell-Ash spectrograph. Excitation was made at intervals from 50 to 600 Å

peak current. The Th IV spectrum lines are quite pronounced at 300 Å peak current and are easily detected from thorium spectra obtained at lower currents. The Th IV lines were measured and a line list compiled for this wavelength region.

Similar spectra will be photographed in the vacuum ultraviolet region with a McPherson 3-meter vacuum spectrograph.

ZERO-FIELD SPLITTINGS OF Gd^{3+} and Cm^{3+} IN CeO_2 AND ThO_2 [†]

W. Kolbe, N. Edelstein, C. B. Finch,* M. M. Abraham*

In previous investigations of Gd^{3+} cubic EPR spectra in the fluorite-type crystals CeO_3 and ThO_2 ,¹ it was pointed out that although the cubic crystal field in CeO_2 ($a = 5.4 \text{ \AA}$) was expected to be larger on the basis of a simple point charge model, the actual splitting observed for Gd^{3+} in CeO_2 was smaller than that observed for the more expanded ThO_2 lattice ($a = 5.6 \text{ \AA}$). The various mechanisms by which the eightfold degeneracy of the S ground state for this $4f^7$ ion ($^8S_{7/2}$) is lowered are not understood. Hence, it is not certain why the splitting of the Gd^{3+} ground state in CeO_2 is smaller than in ThO_2 . In this investigation, we report the

$\Gamma_8 - \Gamma_6$ splitting of Cm^{3+} (the $5f^7$ actinide analog of Gd^{3+}) in CeO_2 , and by comparison with earlier data on Cm^{3+} and Gd^{3+} in other fluorite-type hosts, point out that the cubic splittings of the $5f^7$ ion, unlike the $4f^7$ case, do follow qualitatively the predictions of the point charge model.

The EPR spectra of Cm^{3+} in both CeO_2 and ThO_2 were observed previously at X-band frequencies ($\sim 10 \text{ GHz}$), establishing the ground doublet as a Γ_6 doublet in a cubic crystal field.² In both crystals, a single line was observed whose position did not vary with crystal orientation. Observation of this reso-

Table I. $\Gamma_8 - \Gamma_6$ splitting of S-state ions in cubic crystal field at 4.2° K.

	Lattice constant (\AA)	Gd^{3+} (cm^{-1})	Cm^{3+} (cm^{-1})
CeO_2	5.41	0.0653 ± 0.0004^a	17.8 ± 0.3^b
ThO_2	5.60	0.06645 ± 0.00008^c	15.5 ± 0.3^d
CaF_2	5.46	0.0578 ± 0.0001^e	13.4 ± 0.5^f
SrF_2	5.80	0.0501 ± 0.0002^g	11.2 ± 0.4^d
BaF_2	6.20	0.0448 ± 0.0002^h	-
$SrCl_2$	6.98	0.01979 ± 0.00004^i	5.13 ± 0.05^d

^aM. M. Abraham, L. A. Boatner, C. B. Finch, E. J. Lee, and R. A. Weeks, *J. Phys. Chem. Solids* **28**, 81 (1967).

^bThis work.

^cM. M. Abraham, E. J. Lee, and R. A. Weeks, *J. Phys. Chem. Solids* **26**, 1249 (1965).

^dW. Kolbe, N. Edelstein, C. B. Finch, and M. M. Abraham, *J. Chem. Phys.* **56**, 5432 (1972).

^eM. M. Abraham, L. A. Boatner, E. J. Lee, and R. A. Weeks, in *Proc. of the Sixth Rare Earth Conference*, 89 (1967), Gatlinburg, Tennessee.

^fN. Edelstein and W. Easley, *J. Chem. Phys.* **48**, 2110 (1968).

^gL. A. Boatner and M. M. Abraham, unpublished.

^hL. A. Boatner, R. W. Reynolds, and M. M. Abraham, *J. Chem. Phys.* **52**, 1248 (1970).

ⁱM. M. Abraham, L. A. Boatner, E. J. Lee, *Phys. Letters* **25A**, 230 (1967).

nance at a high frequency (and thus a higher magnetic field) enables the $\Gamma_8 - \Gamma_6$ zero-field splitting to be determined from measurements of the g-value anisotropy of the Γ_6 ground state caused by Zeeman mixing of the Γ_8 excited state. Such splittings have been reported previously³ for several fluorite-type crystals, including ThO_2 , using K_a -band frequencies (~ 35 GHz). Utilizing the same techniques as before,³ we have determined the $\Gamma_8 - \Gamma_6$ splitting of $\text{CeO}_2: \text{Cm}^{3+}$ to be $17.8 \pm 0.3 \text{ cm}^{-1}$ at 4.2°K .

We have observed that for the non-S-state ions, Pu^{3+} and Am^{4+} ($5f^5$), the crystal field of CeO_2 is indeed larger than ThO_2 .^{4,5} In fact, the interpretation of the experimental g values for Pu^{3+} indicate that the entire series of fluorite-type crystals can be arranged as CeO_2 , ThO_2 , CaF_2 , SrF_2 , BaF_2 , and SrCl_2 in descending order of cubic crystal field strengths.⁴⁻⁶

In Table I, the $\Gamma_8 - \Gamma_6$ splittings are compiled for Gd^{3+} and Cm^{3+} in these fluorite-type lattices. On the basis of the point charge model, the magnitude of the crystalline electric field should depend upon the distance of the neighboring charges from the impurity ion. In particular, decreasing the distance of the nearest neighbors should increase the magnitude of the field. It can be seen from Table I that as the lattice constant decreases from 7 \AA for SrCl_2 to 5.46 \AA in CaF_2 , the splittings for both Cm^{3+} and Gd^{3+} increase. Changing the nearest neighbor from the monovalent halogen to the divalent oxygen increases the crystal field further, and the splittings observed for both Gd^{3+} and Cm^{3+} are correspondingly larger. However, the analogy between Gd^{3+} and Cm^{3+} breaks down in the oxide crystals. The ground state of Gd^{3+} is approximately 97% pure S state while that of Cm^{3+} is only 79%,⁷ and the mechanisms proposed for S-state crystal-field splittings all depend to some extent upon the non-S-state admixtures from excited levels into the ground state. The Cm^{3+} splitting is dominated by intermediate coupling effects because of the large spin-orbit coupling constant.

For the $4f^7$ ions, no particular contribution to the splitting is dominant, so the dependence upon the crystal field strength does not necessarily follow the qualitative predictions of the point charge model.

Footnotes and References

[†]Published in Journal of Chemical Physics 58, 820 (1973).

*Solid State Division, Oak Ridge National Laboratory, Oak Ridge, Tennessee 37830.

1. M. M. Abraham, L. A. Boatner, C. B. Finch, E. J. Lee, and R. A. Weeks, J. Phys. Chem. Solids 28, 81 (1967); M. M. Abraham, E. J. Lee, and R. A. Weeks, J. Phys. Chem. Solids 26, 1249 (1965).
2. M. M. Abraham, C. B. Finch, and G. W. Clark, Phys. Rev. 168, 933 (1968).
3. W. Kolbe, N. Edelstein, C. B. Finch, and M. M. Abraham, J. Chem. Phys. 56, 5432 (1972); M. M. Abraham, L. A. Boatner, C. B. Finch, R. W. Reynolds, and H. Zeldes, Phys. Rev. B 1, 3555 (1970); N. Edelstein and W. Easley, J. Chem. Phys. 48, 2110 (1968).
4. W. Kolbe, N. Edelstein, C. B. Finch, and M. M. Abraham, to be published.
5. M. M. Abraham, L. A. Boatner, C. B. Finch, and R. W. Reynolds, Phys. Rev. B 3, 2864 (1971).
6. N. Edelstein, H. F. Mollet, W. C. Easley, and R. J. Mehlhorn, J. Chem. Phys. 51, 3281 (1969).
7. W. T. Carnall and B. G. Wybourne, J. Chem. Phys. 40, 3428 (1964); B. G. Wybourne, Spectroscopic Properties of Rare Earths (Interscience, New York, 1965), p. 204.

ELECTRONIC STRUCTURE OF SIMPLE INORGANIC MOLECULES

H. F. Schaefer III

Perhaps the most important aspect of the work of the Berkeley electronic structure group during the year 1972 involved the extension of *ab initio* methods to molecules containing very heavy atoms. An extensive series of calculations on xenon fluorides is

under way, and simpler calculations have been completed for lead monoxide. For the sake of completeness, we note that three related papers¹⁻³ discussed in the Nuclear Chemistry Annual Report for 1971 have now been published.

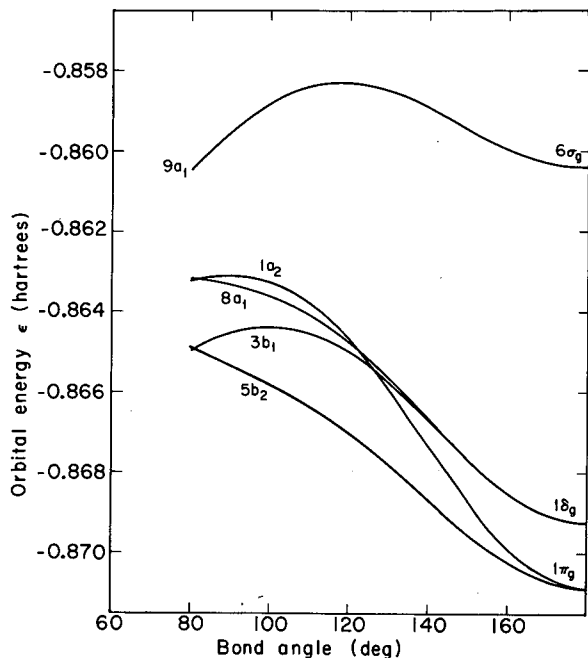


Fig. 1. Orbital energies as a function of bond angle for ZnF_2 . The molecular orbitals shown correspond fairly closely to Zn 3d atomic orbitals. (XBL 723-2623)

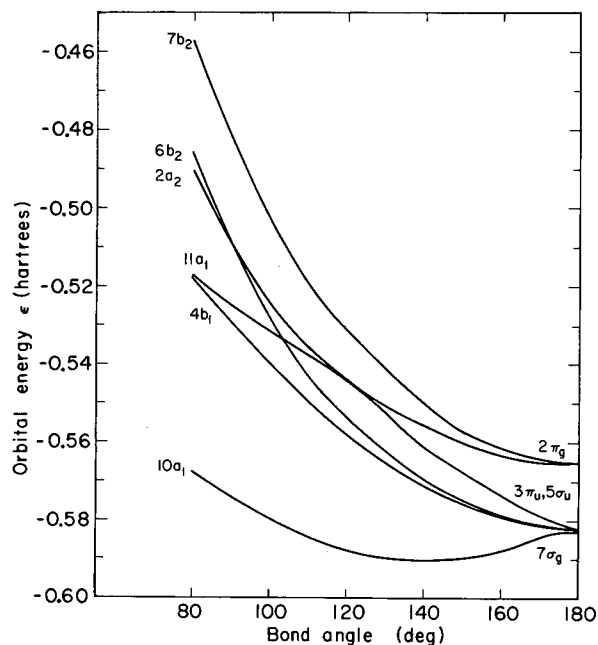


Fig. 2. Six highest orbital energies of ZnF_2 as a function of bond angle. In the simplest picture, these orbitals correspond to the orbitals of the two F^- ions. (XBL 723-2624)

Walsh Diagram for Zinc Difluoride⁴

An *ab initio* self-consistent-field study of the electronic structure of ZnF_2 has been carried out using an extended basis set. The resulting Walsh diagram (Figs. 1 and 2) and molecular orbitals are discussed, and several calculated molecular properties reported.

Linear Symmetric H_4 (Ref. 5)

Nonempirical calculations have been carried out for the lowest $^1\Sigma_g^+$ state of H_4 . A contracted Gaussian basis set of two s and one p functions centered on each atom was used. Self-consistent field (SCF), SCF plus all singly and doubly excited configurations, and full configuration interaction (2172 configurations) calculations were carried out. The results may be pertinent both to the H_2+D_2 reaction and the problem of the linear antiferromagnetic chain. It is predicted that two H_2 molecules may approach to within 1.6 bohr with an energy only 43 kcal above that of the separated molecules. A van der Waals attraction of 22°K is predicted at H_2 - H_2 center-of-mass separation 7.1 bohr. Equidistant H_4 is predicted to have lowest energy at 1.67 bohr, lying 7.1 eV below the exact energy of four H atoms but 44 kcal above two H_2 molecules. The electronic structure of linear equidistant H_4 is

discussed as a function of H-H separation and no evidence of a Mott transition is found.

The Long-Range Intermolecular Potential of H_2 - H_2 (Ref. 6)

In an analysis of forces between two interacting molecules one considers various contributions to the intermolecular potential: (1) electrostatic interaction between the permanent multipoles of the molecules; (2) induction energy due to a permanent multipole on one molecule and the polarizability of the other; (3) dispersion attraction due to the polarizabilities of the molecules; and (4) "overlap energy," which includes charge cloud repulsion and charge transfer interactions. The H_2 - H_2 system is the simplest (neutral) intermolecular complex where each of these terms contributes to the energy.

The majority of theoretical analyses of intermolecular potentials use a classical or semiclassical approach to calculate contributions (1), (2), and (3) and quantum-mechanical methods to compute the contribution of (4) to the potential. Reasonable success has been achieved in predicting the short-range potential (4) for small systems. No one, however, has compared terms (1) and (2) calculated quantum mechanically with values pre-

dicted from the classical multipole model at separations where the short-range repulsion should vanish. We have analyzed accurate SCF-MO calculations for the H₂-H₂ interaction at large internuclear separations for a variety of geometrical configurations.

We conclude that the classical point quadrupole model is an excellent representation of the non-dispersion part of the intermolecular potential at distances greater than 10 a. u. Perturbation theory has justified the use of classical forms for the electrostatic and induction energies at large R, and the numerical results presented here support these arguments.

⁷Σ⁺ and ⁷Π States of Manganese Hydride⁷

Ab initio self-consistent-field calculations have been carried out close to the Hartree-Fock limit for the high-spin ⁷Σ⁺ and ⁷Π electronic states of MnH. Five different hydrogen-centered basis sets of Slater functions are

tested for H⁻ and MnH. Predicted spectroscopic constants (with experimental values in parentheses) for the ⁷Σ⁺ ground state are D_e = 1.57 eV (2.4 ± 0.3), ω_e = 1549 cm⁻¹ (1548), r_e = 1.789 Å (1.722), and B_e = 5.32 cm⁻¹ (5.68). And for the ⁷Π state, T_e = 21 870 cm⁻¹ (17 700), ω_e = 1708 cm⁻¹, r_e = 1.703 Å, and B_e = 5.88 cm⁻¹ (6.43). The electronic structure of the two states is discussed with respect to the contributions of the different molecular orbitals to the electric dipole moment and population analysis (see Table I). Although the population analysis predicts the ⁷Σ⁺ state to be more ionic than the ⁷Π state, the dipole moments are computed to be 1.6 and 4.1 debyes, both +MnH⁻. The small dipole moment of the ⁷Σ⁺ state is seen to be due to a large -MnH⁺ contribution from the nonbonding 8σ orbital (which is replaced by 4π in the ⁷Π state). The manganese atom 3d⁵ configuration survives essentially unchanged in both states of MnH, and it is suggested that the electronic structure of other transition metal hydrides may be quite similar, involving a single ionic bonding σ orbital.

Table I. Mulliken population analyses for the valence SCF orbitals of manganese hydride.

	s	p	d	f	s	p
<u>⁷Σ⁺ State</u>						
(R = 3.35 bohrs)						
6σ	0.023	0.009	0.958	0.000	0.010	0.000
7σ	0.315	0.156	0.068	0.002	1.444	0.016
8σ	0.598	0.378	0.002	0.000	0.021	0.002
3π	--	0.001	1.998	0.000	--	0.001
1δ	--	--	2.000	0.000	--	--
<u>⁷Π State</u>						
(R = 3.25 bohrs)						
6σ	0.048	0.005	0.937	0.000	0.009	0.000
7σ	0.509	0.113	0.096	0.002	1.267	0.014
3π	--	0.001	1.998	0.000	--	0.001
4π	--	1.007	0.001	0.000	--	-0.007
1δ	--	--	2.000	0.000	--	--

tion interaction. These results are seen in Fig. 3. The principal inelastic process in low-energy collisions of ground state He and O^+ is seen to be the $4S \rightarrow 2D$ excitation of O^+ , the transition arising from a spin-orbit interaction at a crossing of the lowest 4Σ and 2Π states of HeO^+ . Much more accurate calculations were thus carried out for these two states, as well as a semiclassical calculation of the cross section for $He + O^+(4S) \rightarrow He + O^+(2D)$. The cross section has no activation energy other than its energetic threshold (3.3 eV) and rises to a maximum of $\sim 8.6 \times 10^{-3} \text{ \AA}^2$ at ~ 6 eV. There is a residual oscillatory structure in the energy dependence of the cross section, and it is shown how experimental observation of this could be used to obtain precise information concerning the relevant potential curves.

Use of Nonrelativistic Wave Functions for the Prediction of Properties of Molecules Containing Atoms of High Z: PbO as a Test Case. (Ref. 10)

Using a minimum basis set of Slater functions, nonrelativistic self-consistent-field calculations have been carried out for the lead monoxide molecule. The purpose of the calculations was to provide an indirect test of the importance of relativistic effects in molecules containing atoms with atomic number as high as 82. The predicted spectroscopic constants (see Table II) of PbO are in about as good agreement with experiment as were the results from comparable calculations on the obviously nonrelativistic molecule CO. The electronic structures of the two molecules are briefly compared in terms of Mulliken population analyses.

ELECTRONIC STRUCTURE OF SIMPLE ORGANIC MOLECULES

H. F. Schaefer III

Although a priori electronic structure calculations have been feasible for organic molecules for several years,¹ 1972 can be considered a banner year, in that many organic chemists became convinced for the first time of the relevance of theory to many of their own problems. One manifestation of this new relationship was a meeting between theoreticians and organic chemists in Paris entitled "Computation of Reaction Paths and Reaction Mechanisms." Having attended this meeting

Acknowledgments

We thank D. R. Yarkony, C. F. Bender, P. A. Kollman, P. S. Bagus, S. Rothenberg, S. D. Augustin, W. H. Miller, P. K. Pearson, G. M. Schwenzer, D. H. Liskow, B. Liu, A. D. McLean, and M. Yoshimine for their contributions to the work reported herein.

References

1. P. S. Bagus and H. F. Schaefer, *J. Chem. Phys.* **56**, 224 (1972).
2. V. Bondybey, P. K. Pearson, and H. F. Schaefer, *J. Chem. Phys.* **57**, 1123 (1972); also LBL-258.
3. P. S. Bagus, B. Liu, and H. F. Schaefer, *J. Am. Chem. Soc.* **94**, 6635 (1972).
4. D. R. Yarkony and H. F. Schaefer, *Chem. Phys. Letters* **15**, 514 (1972).
5. C. F. Bender and H. F. Schaefer, *J. Chem. Phys.* **57**, 217 (1972).
6. C. F. Bender, H. F. Schaefer, and P. A. Kollman, *Mol. Phys.* **24**, 235 (1972).
7. P. S. Bagus and H. F. Schaefer, *J. Chem. Phys.* **58**, 1844 (1973).
8. S. Rothenberg and H. F. Schaefer, *J. Am. Chem. Soc.* **95**, 0000 (1973).
9. S. D. Augustin, W. H. Miller, P. K. Pearson, and H. F. Schaefer, *J. Chem. Phys.* **58**, 0000 (1973); also LBL-1187.
10. G. M. Schwenzer, D. H. Liskow, H. F. Schaefer, P. S. Bagus, B. Liu, A. D. McLean, and M. Yoshimine, *J. Chem. Phys.* **58**, 0000 (1972).

and presented an invited paper, I was surprised to find how rapidly the gulf between organic and theoretical chemistry is disappearing. The present article reviews the 1972 work of the Berkeley electronic structure group on simple organic molecules. Note that our paper, discussed in last year's Nuclear Chemistry Annual Report, on the geometry of methylene was only recently published.²

Bending Frequency of the C₃ Molecule³

Ab initio calculations have been carried out to determine a potential curve for the bending motion of C₃. The work was in part motivated by the disagreement between theoretical and experimental values of the entropy of C₃. Three basis sets were used, with (4s2p), (4s2p1d), and (4s3p1d) centered on each carbon atom. Both self-consistent-field (SCF) and configuration interaction (CI) (656 configurations) calculations were carried out with the smallest basis. The CI wave functions were obtained by a method which may be viewed as an extension of the pseudonatural orbital technique of Edmiston and Krauss. Using the smallest basis, both SCF and CI calculations yield "normal" bending frequencies, ~ 320 cm⁻¹. It is concluded that electron correlation has little effect on the bending frequency. The larger (4s2p1d) and (4s3p1d) basis SCF calculations yield much smaller bending frequencies, the latter being 69 cm⁻¹, in good agreement with the unusually low experimental value of Gausset, Herzberg, Lagerqvist, and Rosen. The bending potential is predicted to be quite anharmonic, as may be seen in Fig. 1. These results are discussed qualitatively in terms of a Walsh diagram and the importance of d orbitals by symmetry considerations.

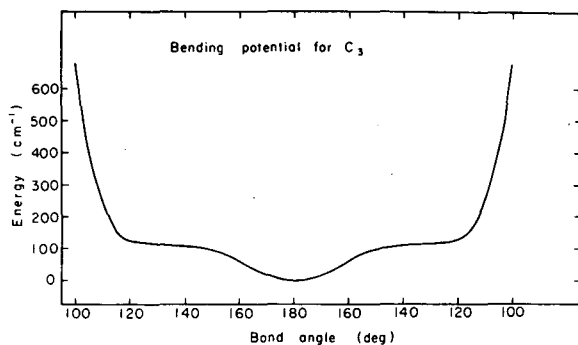


Fig. 1. Minimum energy path for the bending motion of C₃. The figure is a result of the (4s3p1d) SCF calculations. (XBL 712-2001)

Multiconfiguration Wave Functions for the Lowest ($\pi\pi^*$) Excited States of Ethylene⁴

Rigorous quantum mechanical calculations have been carried out for the T(³B_{1u}) and V(¹B_{1u}) states of ethylene in a planar nuclear configuration. A "double zeta" gaussian basis, augmented by diffuse functions, was used. A wide variety of configuration interaction wave functions (including as many as

1605 configurations), optimized by the iterative natural orbital method, were computed. The calculations are summarized in Table I and predict the ¹B_{1u} state to lie 3.8-4.1 eV above the ³B_{1u} state. The spatial extent of the triplet state is that of a normal valence state with $\langle x^2 \rangle \approx 12$ bohr.² The singlet state, on the other hand, is found to be quite diffuse or Rydberg-like, $\langle x^2 \rangle \approx 35$ bohr²; electron correlation was found to decrease $\langle x^2 \rangle$ by 30% from the Hartree-Fock value (52 bohr²). This result is not consistent with simple notions concerning π -electron theory.

Sign of the Dipole Moment and Other Properties of Methylsilane⁵

Nonempirical electronic structure calculations have been carried out on CH₃SiH₃ in its staggered form. A flexible basis set of contracted Gaussian functions was used. The present self-consistent-field calculations predict the electric dipole moment to be 0.58 D, +C Si-. This result is in good agreement with the experimental magnitude, 0.73 D, but disagrees with simple electronegativity arguments concerning the polarity of carbon-silicon bonds. However, Shoemaker and Flygare have recently argued on the basis of molecular Zeeman experiments that the sign of the dipole moment should be +C Si-. The predicted sign of the molecular quadrupole moment agrees with experiment, but the quantitative agreement in magnitude is poor. The *ab initio* sign of the dipole moment is not consistent with atomic charges obtained from a Mulliken population analysis of the wave function. The electronic structure of CH₃SiH₃ is discussed and several other molecular properties are reported. Table II summarizes the results.

Singlet-Triplet Energy Separation, Walsh-Mulliken Diagrams, and Singlet d-Polarization Effects in Methylene⁶

The singlet-triplet (¹A₁ ↔ ³B₁) energy separation in methylene has been computed by correlated *ab initio* wave functions of the highest accuracy yet reported. The type of configuration interaction wave function used is indicated in Table III. Results from these wave functions plus additional small corrections lead to a prediction of 11.0 ± 2 kcal/mol for the singlet-triplet energy difference. Other independent theoretical estimates also lend support to a value in this range. This relatively small separation arises primarily from the differential lowering effect produced by basis functions of d symmetry. Walsh-Mulliken (orbital energy vs bond angle) diagrams are constructed and shown to be qualitatively valid representations for this molecule. Their topology is also the same for both the ¹A₁ and ³B₁ states. Interpretation of these diagrams

Table I. Summary of *ab initio* calculations on the $T(^3B_{1u})$ and $V(^1B_{1u})$ states of ethylene. Ground state (planar) geometry.

Orbitals correlated	$T(^3B_{1u})$		Second moments (bohr ²)		
	Number of configurations	Energy (hartrees)	$\langle x^2 \rangle$	$\langle y^2 \rangle$	$\langle z^2 \rangle$
None	1	-77.8847	11.9	9.2	10.7
$1b_{3u}1b_{2g}$	36	-77.8919	11.8	9.0	10.7
$3a_g^2 1b_{3u}1b_{2g}$	663	-77.9020	12.0	9.2	10.8
$1b_{2u}^2 3a_g^2 1b_{3g}^2 1b_{3u}1b_{2g}$	1605	-77.9600	12.2	9.3	10.9
$2a_g^2 2b_{1u}^2 1b_{2u}^2 3a_g^2 1b_{3g}^2 1b_{3u}1b_{2g}$	1050	-78.0181	12.1	9.3	10.8

Orbitals correlated	$V(^1B_{1u})$		Singlet-triplet splitting E(V)-E(T) (eV)	Second moments (bohr ²)		
	Number of configurations	Energy (hartrees)		$\langle x^2 \rangle$	$\langle y^2 \rangle$	$\langle z^2 \rangle$
None	1	-77.7363	4.04	51.8	21.0	48.9
$1b_{3u}1b_{2g}$	36	-77.7422	4.06	49.1	19.9	46.4
	40	-77.7424	- -	48.2	19.6	45.5
$3a_g^2 1b_{3u}1b_{2g}$	492	-77.7610	3.84	41.1	17.4	38.2
$1b_{2u}^2 3a_g^2 1b_{3g}^2 1b_{3u}1b_{2g}$	1394	-77.8182	3.86	35.4	15.8	32.8
$2a_g^2 2b_{1u}^2 1b_{2u}^2 3a_g^2 1b_{3g}^2 1b_{3u}1b_{2g}$	1018	-77.8716	3.98	38.3	16.8	35.7

 Table II. Some SCF Properties of CH_3SiH_3 as a function of basis set.

Property	Basis set		
	1 C(4s, 2p) Si(7s, 4p) H(2s)	2 C(4s, 2p, 1d) Si(7s, 4p, 1d) H(2s)	3 C(4s, 2p, 1d) Si(7s, 4p, 1d) H(2s, 1p)
Total energy (hartrees)	-330.22769	-330.28191	-330.29929
Dipole moment, D, +C Si-	0.50	0.56	0.58 (0.73)
Quadrupole moment, 10^{-26} esu-cm ²	-0.68	-0.63	-0.62(-6.31±0.46) or 11.74±0.46)
Atomic populations			
H(bonded to C)	0.811	0.820	0.881
C	6.847	6.781	6.607
Si	13.249	13.286	13.138
H(bonded to Si)	1.156	1.158	1.204

Table III. Configurations included in the approximate "first-order" wave functions for 1A_1 CH₂^a.

Excitation		No. of 1A_1 eigenfunctions per orbital occupancy	Excitation		No. of 1A_1 eigenfunctions per orbital occupancy
1st	$1a_1^2 2a_1^2 1b_2^2 3a_1^2$	1	2d	$1a_1^2 2a_1^2 1b_2^2 1b_1^2$	1
ref-	$2a_1 \rightarrow 4a_1$	1	ref-	$2a_1 \rightarrow 4a_1$	1
con-	$1b_2 \rightarrow 2b_2$	1	con-	$1b_2 \rightarrow 2b_2$	1
figu-	$3a_1 \rightarrow 4a_1$	1	figu-	$2a_1 \rightarrow 3a_1 4a_1, 4a_1^2, 2b_2^2$	1
ration	$2a_1^2 \rightarrow 1b_1^2, 4a_1^2, 2b_2^2$	2	ration	$2a_2 1b_2 \rightarrow 3a_1 2b_2, 4a_1 2b_2$	2
	$2a_1 1b_2 \rightarrow 4a_1 2b_2$	1		$1b_2^2 \rightarrow 3a_1 4a_1, 4a_1^2, 2b_2^2$	1
	$2a_1 3a_1 \rightarrow 1b_1^2, 4a_1^2, 2b_2^2$	1		$2a_1^2 \rightarrow 3a_1 ma_1, 4a_1, ma_1$	1
	$1b_2^2 \rightarrow 1b_1^2, 4a_1^2, 2b_2^2$	2		$2a_1 \rightarrow 2b_2 mb_2$	1
	$1b_2 3a_1 \rightarrow 4a_1 2b_2$	1		$2a_1 1b_2 \rightarrow 3a_1 mb_2, 4a_1 mb_2$	2
	$3a_1^2 \rightarrow 4a_1^2, 2b_2^2$	1		$2a_1 1b_2 \rightarrow 2b_2 ma_1$	2
	$2a_1 \rightarrow ma_1$	1		$2a_1 1b_1 \rightarrow 4a_1 mb_1$	2
	$1b_2 \rightarrow mb_2$	1		$2a_1 1b_1 \rightarrow 2b_2 ma_2$	2
	$3a_1 \rightarrow ma_1$	1		$1b_2^2 \rightarrow 3a_1 ma_1, 4a_1 ma_1$	1
	$2a_1^2 \rightarrow 1b_1 mb_1$	1		$1b_2 \rightarrow 2b_2 mb_2$	1
	$2a_1^2 \rightarrow 4a_1 ma_1$	1		$1b_2 1b_1 \rightarrow 4a_1 ma_2$	2
	$2a_1^2 \rightarrow 2b_2 mb_2$	2		$1b_2 1b_1 \rightarrow 2b_2 mb_1$	2
	$2a_1 1b_2 \rightarrow 1b_1 ma_2$	2			
	$2a_1 1b_2 \rightarrow 4a_1 mb_2$	2			
	$2a_1 1b_2 \rightarrow 2b_2 ma_1$	2			
	$2a_1 3a_1 \rightarrow 1b_1 mb_1$	2			
	$2a_1 3a_1 \rightarrow 4a_1 ma_1$	2			
	$2a_1 3a_1 \rightarrow 2b_2 mb_2$	1			
	$1b_2^2 \rightarrow 1b_1 mb_1$	1			
	$1b_2^2 \rightarrow 4a_1 ma_1$	1			
	$1b_2^2 \rightarrow 2b_2 mb_2$	2			
	$1b_2 3a_1 \rightarrow 1b_1 ma_2$	2			
	$1b_2 3a_1 \rightarrow 4a_1 mb_2$	2			
	$1b_2 3a_1 \rightarrow 2b_2 ma_1$	2			
	$3a_1^2 \rightarrow 1b_1 mb_1$	2			
	$3a_1^2 \rightarrow 4a_1 ma_1$	2			
	$3a_1^2 \rightarrow 2b_2 mb_2$	2			

^a ma_1 includes $5a_1-16a_1$, ma_2 includes $1a_2-2a_2$, mb_1 includes $2b_1-5b_1$, and mb_2 includes $3b_2-9b_2$.

leads to a simple physical picture of the orbital distortions in the 1A_1 state generated by the d-polarization functions. It is demonstrated that methylene insertion and addition reactions are facilitated by d polarization. An argument as to why methylene insertion is not observed in carbon-carbon single bonds is also given.

Acknowledgments

Thanks are due to D. H. Liskow, C. F. Bender, T. H. Dunning, W. A. Goddard, W. J. Hunt, D. R. Franceschetti, and L. C. Allen for their contributions to the work reported herein.

References

1. H. F. Schaefer, The Electronic Structure of Atoms and Molecules: A Survey of

Rigorous Quantum Mechanical Results (Addison-Wesley, Reading, Massachusetts, 1972).

2. D. R. McLaughlin, C. F. Bender, and H. F. Schaefer, *Theoretica Chimica Acta* **25**, 352 (1972).
3. D. H. Liskow, C. F. Bender, and H. F. Schaefer, *J. Chem. Phys.* **56**, 5075 (1972); also LBL-291.
4. C. F. Bender, T. H. Dunning, H. F. Schaefer, W. A. Goddard, and W. J. Hunt, *Chem. Phys. Letters* **15**, 171 (1972).
5. D. H. Liskow and H. F. Schaefer, *J. Am. Chem. Soc.* **94**, 6641 (1972); also LBL-629.
6. C. F. Bender, H. F. Schaefer, D. R. Franceschetti, and L. C. Allen, *J. Am. Chem. Soc.* **94**, 6888 (1972).

POTENTIAL ENERGY SURFACES FOR SIMPLE CHEMICAL REACTIONS

C. F. Bender,* D. H. Liskow, S. V. O'Neil, P. K. Pearson,
H. F. Schaefer III, and D. R. Yarkony

The purpose of this article is to summarize theoretical work carried out at Berkeley during the past year on potential energy surfaces for simple chemical reactions. For an introduction to the study of electronic structure by *ab initio* methods, the reader is referred elsewhere.¹ The year 1972 was a particularly exciting one for us, as we were able to obtain, from quantum mechanical first principles only, a potential surface of "chemical accuracy" for the $F + H_2 \rightarrow HF + H$ reaction. Prior to this work, the H_3 system was the largest for which comparable results had been obtained.

Refined Potential Energy Surface for $F + H_2 \rightarrow HF + F^2$

Our first calculations on FH_2 employed a double zeta basis set, 4s 2p on fluorine and 2s on each hydrogen. For general geometry (C_s symmetry), the first-order wave function included 214 configurations, and orbitals were optimized by the iterative natural orbital procedure. The barrier height was calculated to be 34.3 kcal (SCF) and 5.7 kcal (CI), both greater than the experimental activation energy, 1.7 kcal/mol. Similarly the exothermicity was predicted to be -0.6 kcal (SCF) and 20.4 kcal (CI), both less than experiment, 31.8 kcal. It was possible to conclude that,

within the double zeta basis, the SCF approximation gives a very poor description of the surface, while the CI surface is at best qualitatively reasonable. A large number of calculations were performed for nonlinear FH_2 to examine the anisotropy of the surface. The simplest conclusion drawn was that, in agreement with the London-Eyring-Polanyi-Sato (LEPS) model, the minimum energy path occurs for collinear geometry.

Since a more accurate surface was clearly needed, our second step was to add polarization functions (d functions on F, p functions on H) to the basis. This enlargement of the basis has the effect of roughly doubling the number of configurations in the first-order wave function. The most important characteristics of the potential surface obtained in this way are seen in Table I, and a contour map of the collinear surface is given in Fig. 1. Table I suggests that the potential surface obtained may approach quantitative accuracy.

One point which is not susceptible to experimental verification is the saddle point geometry. In this regard, note the surprisingly large difference between the SCF and CI saddle point geometries. In general, of course, one expects SCF geometries to be quite adequate. Here, however, the inclusion

Table I. Characteristics of the refined potential energy surface for $F + H_2 \rightarrow HF + H$.

	SCF	CI	Experiment
Barrier height (kcal/mol)	29.3	1.66	1.7 ^a
Exothermicity (kcal/mol)	13.2	34.4	31.8
Saddle point geometry (Å)			
F-H	1.18	1.54	--
H-H	0.836	0.767	--

^aExperimental activation energy.

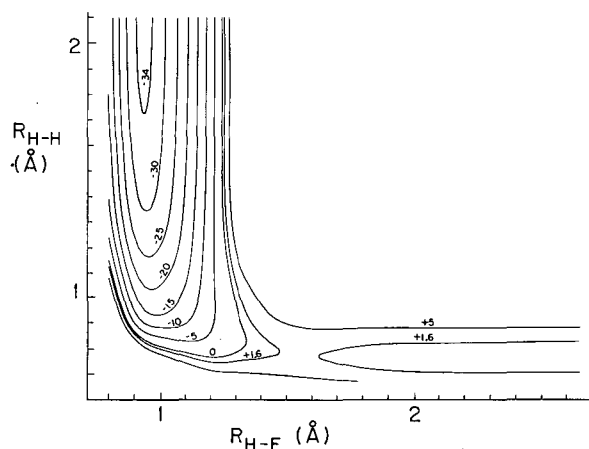


Fig. 1. Ab Initio contour map for the collinear $F + H_2$ potential energy surface. (XBL 723-2656)

of correlation effects alters the surface so radically (the SCF surface has a very large barrier, the CI surface almost no barrier at all) that the saddle point is shifted far into the entry channel. After completion of the calculations, we learned of some related work by James Muckerman of Brookhaven on the $F + H_2$ dynamics. By carrying out classical trajectories on five different semiempirical surfaces and comparing with Polanyi's infrared chemiluminescence results, Muckerman attempted to deduce some of the characteristics of the true potential surface. Interestingly enough, Muckerman's "best" empirical surface places the saddle point in uncanny (to within 0.005 Å) agreement with our ab initio prediction.

It is worth pointing out two other uses which have been made of our surface. Don Truhlar of Minnesota has compared our ab initio minimum energy path with that obtained by

Johnston's Bond-Energy-Bond-Order (BEBO) method. The two reaction coordinates agree to within 0.02 Å, suggesting the BEBO method may be more reliable than could have been anticipated. Finally, Hofhacker at Munich has used the curvature of our surface to obtain good agreement with experiment for certain features of the dynamics of $F + H_2$.

Theoretical Reaction Coordinate for the Methyl Isocyanide Isomerization³

Ab initio self-consistent-field calculations have been carried out to approximately determine the minimum energy path for the $CH_3NC \rightarrow CH_3CN$ reaction. The coordinate system used is seen in Fig. 2. A set of four s and two p functions on C and N and two s functions on H was used. The predicted

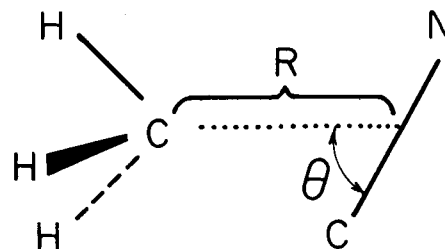


Fig. 2. Coordinate system used to describe the methyl isocyanide isomerization. (XBL 727-3556)

exothermicity was 17.4 kcal/mol, in reasonable agreement with Benson's empirical estimate of 15 kcal. The calculated barrier height was 58.8 kcal compared to Rabinovitch's experimental value of 38.4 kcal. The difference is ascribed to an expectation that electron correlation will be greater for the transition state than for either CH_3NC or CH_3CN . The calculations differ from the extended Hückel treatment of Van Dine and Hoffmann in that we predict the CH_3 group to remain pyramidal ($H-C-H$ angle 106°) at the saddle point. The planar CH_3 structure lies 14 kcal higher in energy. The question of changes in "charge" on the methyl carbon is investigated in detail. Mulliken atomic populations suggest that the charge on the methyl carbon at the transition state is intermediate between CH_3NC and CH_3CN . This is completely consistent with the conclusions of Casanova, Werner, and Schuster. However, it is suggested that several other properties (including the potential at each nucleus, the 1s electron binding energies, and the electric field gradients) give a more reliable picture of the changes in electronic structure. These properties suggest

that at the transition state there is somewhat more charge on the methyl carbon than in either the product or reactant. The unfavored transition state, in which the CH₃ group is forced to be planar, has a large amount of charge on the methyl carbon, resulting in an electronic structure approaching [CH₃⁺][CN⁻].

Additional Features of the CH₃NC → CH₃CN Surface⁴

We have examined an additional 75 points on the potential surface for the CH₃NC → CH₃CN isomerization. Due to interest in the possible non-RRKM behavior of CH₃NC, the magnitude of the barrier to rotation of the methyl group is examined as a function of the reaction coordinate. The transition state or saddle point geometry is determined by minimizing the potential energy with respect to five geometrical parameters and maximizing the respect to a sixth. The geometries of CH₃NC and CH₃CN are also predicted (see Table II) and found to agree closely with experiment. Finally, it is established that, contrary to semiempirical results, the present theoretical approach does not predict the existence of a relative minimum in the reaction coordinate.

Relation between Electronic Structure and the Chemiluminescence Arising from Collisions between Alkaline Earth Atoms and Halogen Molecules⁵

The chemiluminescence ascribed by Jonah and Zare to radiative association of Ba and Cl₂ has been examined in light of the electronic

structure of the ground and excited states of alkaline earth dihalides. A simple discussion is first given in terms of the possible curve crossings and avoided crossings. (See Fig. 3) In addition ab initio self-consistent-field calculations are reported for CaF₂, using an extended basis set. The ¹B₂ excited state, from which the molecule may radiate to the ground state, is predicted to have an equilibrium bond angle of 54° and bond distance of 4.06 bohrs. The vertical excitation energy to the ¹B₂ equilibrium geometry is 1.3 eV. These results appear consistent with the model proposed by Jonah and Zare. In addition, a variety of properties (dipole moments, field gradients, etc.) of CaF₂ are reported.

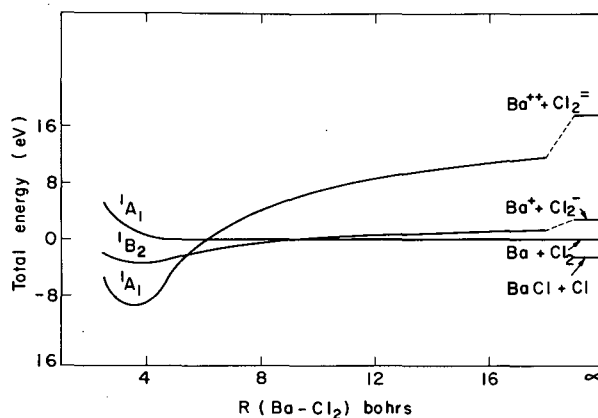


Fig. 3. Empirical potential curves for the perpendicular approach of a Ba atom to a Cl₂ molecule. The state symmetries indicated refer to C_{2v} geometry. (XBL 726-3153)

Table II. Geometries and energies of three points on the minimum-energy path for CH₃ → CH₃CN.

Parameter	CH ₃ NC	Saddle point	CH ₃ CN
θ	180° (180°)	100.8°	0° (0°)
φ	--	0°	--
H CX angle	110.0° (109.1)	106.2°	110.0° (109.5°)
R(CH)	1.081 Å (1.101)	1.074 Å	1.082 Å (1.102)
R(CX)	1.967 Å (1.962)	1.822 Å	2.086 Å (2.081)
R(CN)	1.167 Å (1.166)	1.198 Å	1.146 Å (1.157)
E(hartrees)	-131.85166	-131.75546	-131.87927
E(kcal/mol)	0.0	60.4 (38.4)	-17.3 (14.7-16.8)

The $H + F_2 \rightarrow HF + F$ Reaction.
 An Ab Initio Potential Energy Surface⁶

Rigorous quantum mechanical calculations have been carried out to predict the

Table III. Natural orbital occupation numbers for three points on the $H + F_2 \rightarrow HF + F$ potential energy surface.

	Reactants H + F ₂	Saddle point H-F-F	Products HF + F
1a'	2.0000	2.0000	2.0000
2a'	2.0000	2.0000	2.0000
3a'	2.0000	2.0000	1.9999
4a'	2.0000	2.0000	1.9996
5a'	1.9977	1.9977	1.9995
6a'	1.9905	1.9905	1.9945
7a'	1.8358	1.8358	1.9752
8a'	1.0000	1.0000	1.0002
9a'	0.1730	0.1730	0.0253
10a'	0.0052	0.0052	0.0051
11a'	0.0019	0.0019	0.0004
12a'	0.0004	0.0004	0.0003
13a'	a	a	0.0002
14a'	a	a	a
15a'	a	a	a
16a'	a	a	a
17a'	a	a	a
18a'	a	a	a
1a''	1.9977	1.9977	1.9995
2a''	1.9905	1.9905	1.9946
3a''	0.0052	0.0052	0.0051
4a''	0.0019	0.0019	0.0003

^aOccupation number less than 5×10^{-5} .

$H + F_2 \rightarrow HF + F$ potential energy surface. A double zeta basis set was used and open-shell self-consistent-field (SCF) calculations were carried out. In addition, electron correlation was explicitly treated using first-order wave functions, made up of 553 ²A' configurations. Orbitals were optimized by the iterative natural orbital method. From the SCF calculations the barrier height and exothermicity are predicted to be 12.2 and 132.4 kcal/mol, respectively. The configuration interaction (CI) values are 1.0 and 88.3 kcal, in much better agreement with the experimental values, 1.2 and 102.5 kcal. The saddle point is predicted from the CI calculations to occur for a linear geometry, $R(H-F) = 2.05 \text{ \AA}$. This corresponds to an H-F separation more than twice as great as in the HF molecule but an F-F separation is only slightly (0.03 \AA) longer than in the isolated F₂ molecule. A substantial number of calculations were carried out for nonlinear HF₂ to determine the anisotropy of the surface. Finally, a brief description is given of electronic structure changes during the reaction. (See Table III).

Footnotes and References

*Present address: Lawrence Livermore Laboratory, Livermore, California 94550.

1. H. F. Schaefer, The Electronic Structure of Atoms and Molecules: A Survey of Rigorous Quantum Mechanical Results (Addison-Wesley,

2. C. F. Bender, S. V. O'Neil, P. K. Pearson, and H. F. Schaefer, *Science* **176**, 1412 (1972); also LBL-250.

3. D. H. Liskow, C. F. Bender, and H. F. Schaefer, *J. Am. Chem. Soc.* **94**, 5178 (1972); also LBL-290.

4. D. H. Liskow, C. F. Bender, and H. F. Schaefer, *J. Chem. Phys.* **57**, 4509 (1972); also LBL-696.

5. D. R. Yarkony, W. J. Hunt, and H. F. Schaefer, to be published; also LBL-681.

6. S. V. O'Neil, P. K. Pearson, H. F. Schaefer, and C. F. Bender, *J. Chem. Phys.* **58**, 1126 (1973); also LBL-1200.

III. Physical, Inorganic, and Analytical Chemistry

X-Ray Crystallography

Radiation Chemistry

Physical and Inorganic Chemistry

Applications of Activation Analysis Methods

THE CRYSTAL STRUCTURE OF $\text{Xe}_2\text{F}_{11}^+\text{AuF}_6^-$ †

K. Leary,* A. Zalkin and N. Bartlett*

Recently we reported¹ the novel oxidation state (+5) of gold. We have now solved the crystal structure of the $\text{Xe}_2\text{F}_{11}^+\text{AuF}_6^-$ salt: $\text{F}_{17}\text{AuXe}_2$, $M = 782.5$, orthorhombic, $a = 9.115(6)$, $b = 8.542(25)$, $c = 15.726(20)$ Å, $V = 1224$ Å³, $z = 4$, $D_c = 4.24$ g cm⁻³, space group Pnma . Structural analysis employing three-dimensional Mo K α - x ray data from four different crystals has proceeded routinely to a final conventional R factor of 0.035 for 862 independent reflections for which $I \geq 3\sigma(I)$.

The anion is essentially octahedral. This is in keeping with the t_{2g}^6 configuration of Au(V) and is as anticipated from the vibrational spectroscopic¹ and Mössbauer studies.²

The cation consists of two approximately square-based pyramidal XeF_5 groups linked by a common fluorine atom (F7). This bridging F atom subtends approximately the same angle ($\sim 146^\circ$) to each of the axial XeF bonds, as do the F atoms which make close approach to the XeF_5^+ ion in its salts. Furthermore, the approach of the angle $\text{Xe}(1)\text{-F}(7)\text{-Xe}(2)$ [$169.2(2)^\circ$] to linearity, indicates that the canonical form $\text{XeF}_5^+\text{F}^-\text{XeF}_5^+$ is a major one in the resonance hybrid description of the cation.

Although each XeF_5 group in the complex cation departs significantly from the ideal C_{4v} symmetry of the XeF_5^+ cation,³ each is still characterized by $F_{\text{axial}}\text{-Xe-F}_{\text{equatorial}}$ angles of $\sim 80^\circ$.

Footnotes and References

† Condensed from LBL-1189; accepted for publication in Chemical Communication, January 1973.

* Department of Chemistry, University of California, Berkeley.

1. K. Leary, and N. Bartlett, Chem. Comm. 903 (1972).

2. G. Kaindl, K. Leary, and N. Bartlett, to be published. (The Au 197 Mössbauer spectra spectra of $\text{Xe}_2\text{F}_{11}^+\text{AuF}_6^-$ exhibits a sharp single line shifted 2.28 mm per sec relative to gold metal. The singularity is in accord with the octahedral symmetry of the anion and the shift with the +5 oxidation state.)

3. N. Bartlett, K. Leary, D. Templeton, and A. Zalkin, "The Crystal Structure of $(\text{XeF}_5^+)_2\text{PdF}_6^{2-}$," to be published.

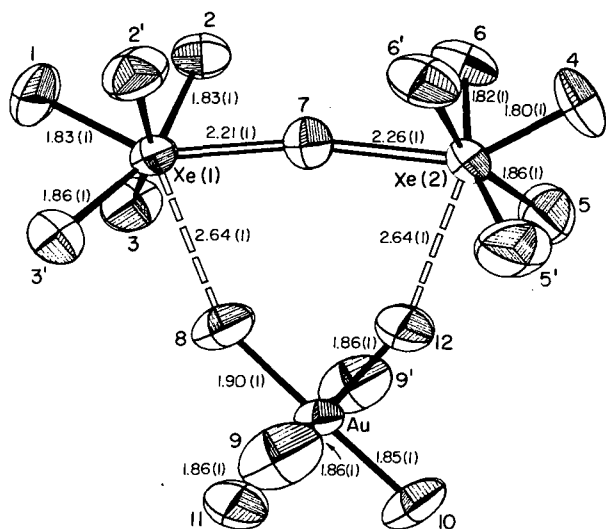


Fig. 1. $\text{Xe}_2\text{F}_{11}^+\text{AuF}_6^-$ cluster.
(XBL 7210-7119)

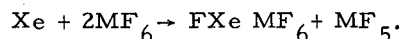
THE CRYSTAL STRUCTURES OF $[\text{XeF}]^+ [\text{RuF}_6]^-$
AND $[\text{XeF}_5]^+ [\text{RuF}_6]^-$

N. Bartlett,* M. Gennis,* D. D. Gibler, B. K. Morrell* and A. Zalkin

An investigation of the products of the interaction of xenon and fluorine with platinum pentafluoride, undertaken by Bartlett and Stewart¹ to help clarify the earlier studies, by Bartlett and Jha,² of the Xe/PtF₆ and Xe/RhF₆ systems, revealed that xenon(II) and xenon(VI) fluoride complexes with PtF₅ could be prepared. Curiously, Xe(IV) complexes were not observed. In a subsequent investigation,³ Bartlett and Sladky confirmed that XeF₄ does not form complexes with the known noble-metal pentafluorides, and they were able to exploit their finding to provide a chemical purification of xenon tetrafluoride.

Since x-ray crystallographic studies⁴ had shown the 1:1 XeF₆ complex with PtF₅ to be the salt $[\text{XeF}_5]^+ [\text{PtF}_6]^-$, the absence of a salt $[\text{XeF}_3]^+ [\text{PtF}_6]^-$ implied that XeF₆ is a superior fluoride ion donor to XeF₄. On the other hand, the vibrational spectroscopic studies⁵ of the XeF₂·MF₅ complexes indicated that they were, at least approximately, the salts $[\text{FXe}]^+ [\text{MF}_6]^-$. On this basis, XeF₄ was seen to be inferior as a fluoride ion donor to both XeF₂ and XeF₆.

Crystal structure support for the $[\text{FXe}]^+ [\text{MF}_6]^-$ salt formulation was clearly desirable to confirm this peculiar fluoride-ion donor behavior of the binary xenon fluorides. However, the $[\text{FXeMF}_6]$ compounds were also of interest to us because the compounds $[\text{FXePtF}_6]$ and $[\text{FXeRhF}_6]$ are formed when xenon interacts with the appropriate hexafluoride in excess:^{2, 5}



The ruthenium compound, $[\text{FXeRuF}_6]^+$ was chosen as the representative of the $[\text{FXeMF}_6]^+$ class, since the x-ray scattering factor for Ru is less dominant than the Ir or Pt factors and the RuF₅ complex is more readily prepared and handled than its RhF₅ relative. To provide for a direct comparison of the $[\text{XeF}]^+$ and $[\text{XeF}_5]^+$ species, the crystal structure of $[\text{XeF}_5]^+ [\text{RuF}_6]^-$ was also carried out. A secondary purpose of the latter study was to improve the description of the $[\text{XeF}_5]^+$ ion, since the precision of the $[\text{XeF}_5]^+ [\text{PtF}_6]^-$ structure determination⁴ was rather low.

The 1:1 XeF₂-RuF₅ complex was made by fusion, at 120°, of the components, which were prepared as previously described.⁵ Crystals of the compound were grown by slow solidification of minute quantities of the fused material

contained in closed quartz x-ray capillaries. An electrically heated tube, with a smooth temperature gradient from 100 to 120° along its length, provided for the crystal development. The 1:1 XeF₆-RuF₅ complex was prepared by fluorinating a sample of the 1:1 XeF₂-RuF₅ complex with excess gaseous fluorine (460 Torr) at 350° overnight. The material melts at 152°. Crystals were grown in quartz x-ray capillaries by sublimation under reduced pressure.

XeRuF₇ (mol wt 365.36) is monoclinic with $a = 7.991$, $b = 11.086$, $c = 7.250$, (all ± 0.006) Å, $\beta = 90.68 \pm 0.05^\circ$, $V = 642.2 \text{ \AA}^3$, $z = 4$, and $d_c = 3.78 \text{ g cm}^{-3}$. Single-crystal precession photographs indicated the space group to be $P2_1/n$.

XeRuF₁₁ is orthorhombic with $a = 16.771$, $b = 8.206$, $c = 5.617$ (all ± 0.010) Å, $V = 773.03 \text{ \AA}^3$, $z = 4$, $d_c = 3.79 \text{ g cm}^{-3}$. Single-crystal precession and Weissenberg photographs indicated space groups $Pnma$ or $Pn2_1a$. The structure was successfully refined in $Pnma$.

A Picker automatic four-circle diffractometer, equipped with a fine-focus Mo anode tube, was used for data collection. Intensities were measured using the θ - 2θ scan technique. The x-ray were monochromatized with a graphite crystal.

XeRuF₇. The crystal used was an irregularly shaped oval tablet, $\sim 0.3 \times 0.2 \times 0.1$ mm. Two unique data sets, the $-h, k, l$ and the h, k, l , were collected for $2\theta \leq 60^\circ$. A total of 4137 intensity data were recorded which were averaged to yield a data set of 1887 independent reflections. No absorption correction was made.

XeRuF₁₁. A tablet of dimensions $0.15 \times 0.10 \times 0.06$ mm was selected for the data collection. Intensity data were collected for the sets of reflections: $-h, k, l$ and $h, -k, l$, for $2\theta \leq 55^\circ$. No decomposition was noted during the period of data collection. A total of 2948 intensity data were recorded, which were averaged to give a set of 960 independent reflections. No absorption correction was made.

XeRuF₇. The positions of the heavy atoms were determined from a three-dimensional Patterson synthesis. A difference Fourier phased by the heavy atom revealed the fluorine atoms. A full matrix refinement with all atoms

anisotropic gave $R = 0.09$. The poorest agreement occurred with the low-angle high-intensity reflections, and since absorption and extinction corrections could not be reliably made, the lower-angle data ($\sin \theta / \lambda \leq 0.20$) was given zero weight in the final least-squares refinements. This resulted in $R = 0.07$, $R_2 = 0.08$ and a standard deviation for an observation of unit weight of 1.28. The number of non-zero-weighted data in this refinement was 1044.

XeRuF₁₁. Since x-ray powder patterns and Raman spectra indicated $F_{11}XeRu$ to be isostructural with the platinum compound, initial atomic parameters were taken from the platinum structure.⁴ The full-matrix refinement with all atoms anisotropic gave a conventional R factor of 0.062. At this point limiting the refinement to the 556 reflections where $I \geq 3\sigma(I)$, reduced R to 0.042, $R_2 = 0.078$ and a standard deviation for an observation of unit weight = 1.08.

XeRuF₇. The crystal structure consists of an ordered arrangement of discrete $FXeRuF_5$ units, Fig. 1, the closest contact between units being 2.90(27) Å, which is a contact between fluorine atoms F(7) and F(1) bound to ruthenium and xenon respectively. The closest contacts between a xenon of one formula unit and fluorine atoms in neighboring units exceed 3.1 Å. The arrangement of the structural units in the lattice is illustrated in Fig. 2.

XeRuF₁₁. The structural analysis shows each xenon atom to be close coordinated by five fluorine atoms in an approximately square pyramidal arrangement. Each ruthenium atom is surrounded by six fluorine atoms in a distinct, approximately octahedral, RuF_6 group. The important interatomic distances and the group

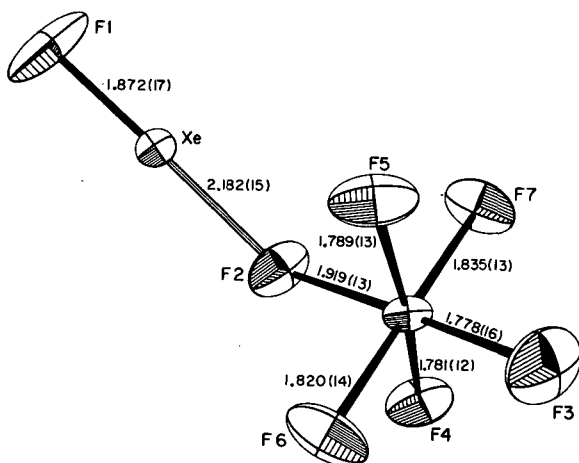


Fig. 1. The $XeF_5^+RuF_6^-$ structural unit (distances in Ångströms and standard deviations in parentheses). (XBL 725-3040)

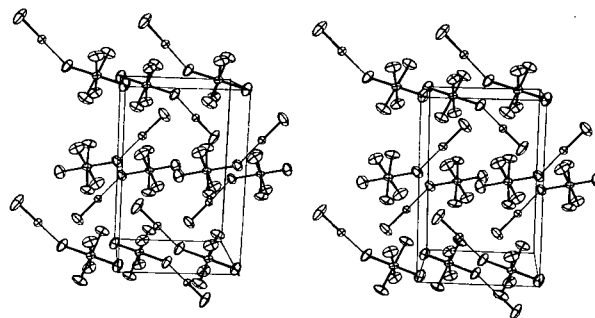


Fig. 2. Stereoscopic view to show packing of the $XeFRuF_6$ units in the crystal lattice. (XBL 725-6298)

geometries and dispositions are illustrated in Fig. 3, and the group arrangements in the crystal lattice may be seen from the stereoscopic view given in Fig. 4.

Comparison of the two structures reveals that the RuF_6 group is more distorted in $XeRuF_7$ than in $XeRuF_{11}$. The average $Ru-F$ distance in the former is 1.81 Å, and the longest bond (1.91 Å) is associated with the fluorine atom, F(2), which makes a close approach (2.19 Å) to the xenon atom. The shortest bond [$Ru-F(3)$] is trans to $RuF(2)$. It appears that the RuF_6 distortion in $XeRuF_7$ is due primarily to the interaction of that group with the $Xe-F$ group. In the $XeRuF_{11}$ case, the average $Ru-F$ distances in the RuF_6 group is 1.85 Å and the greatest deviations from this value are only ± 0.03 Å. The

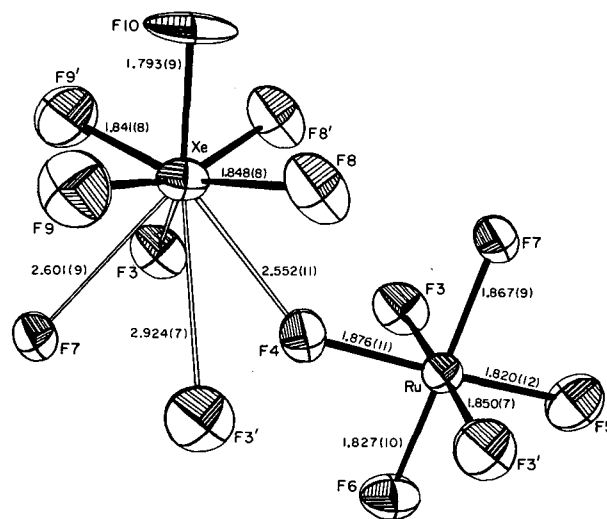


Fig. 3. The XeF_5^+ and RuF_6^- structural units and the coordination of XeF_5^+ (distances in Ångströms and standard deviations in parentheses). (XBL 725-3039)

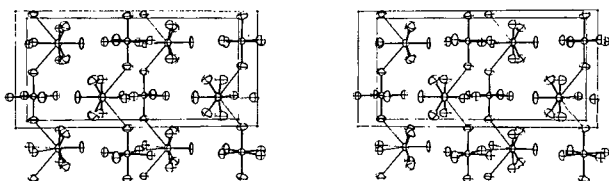


Fig. 4. Stereoscopic view showing the arrangement of XeF_5^+ and RuF_6^- units in the crystal lattice. (XBL 725-6299)

separation of a RuF_6 group from a xenon atom in the XeRuF_{11} case [closest contact $\text{Xe} \cdots \text{F}(4) = 2.55 \text{ \AA}$].

The structure of XeRuF_{11} should be formulated as $[\text{XeF}_5]^+[\text{RuF}_6]^-$. Such a formulation is compatible with the bond lengths in the RuF_6 group. The close similarity in shape of the XeF_5 species with that of IF_5 and TeF_5^- , supports its formulation as a cation. The angle $\text{F}(\text{axial})-\text{Xe}-\text{F}(\text{equatorial})$ is $\sim 80^\circ$ for all three isoelectronic species. The bond length shortening in the sequence TeF_5^- , IF_5 , XeF_5^+ may be attributed to the increase in the nuclear charge $\text{Te} \rightarrow \text{Xe}$. The XeF_5^+ species also occurs in the salts $[\text{XeF}_5]^+[\text{AsF}_6]^-$ and $[\text{XeF}_5]_2^+[\text{PdF}_6]^{2-}$. Crystalline XeF_6 may be formulated as $[\text{XeF}_5]^+\text{F}^-$.⁶ It should be noted that the XeF_5^+ species occurring in those structures are similar in shape to that seen in $[\text{XeF}_5]^+[\text{RuF}_6]^-$, but the coordination of the cation is often different.

Although the rather short cation-anion contacts in $[\text{XeF}_5]^+[\text{RuF}_6]^-$ and in $[\text{XeF}_5]^+[\text{RuF}_6]^-$ could be interpreted as evidence of some covalency, we believe that the ionic formulations, with due allowance for the polarizing influence and symmetry of the cation, provide simple and sufficient explanations.

Footnotes and References

[†] Condensed from LBL-850; submitted to *Inorg. Chem.*

* Chemistry Department, University of California, Berkeley.

1. N. Bartlett, F. Einstein, D. F. Stewart, and J. Trotter, *Chem. Commun.* 550 (1966).
2. N. Bartlett and N. K. Jha, in *Noble Gas Compounds*, edited by H. H. Hyman (University of Chicago Press, Chicago and London, 1963), pp. 23-30.
3. N. Bartlett and F. O. Sladky, *J. Amer. Chem. Soc.* **90**, 5317 (1968).
4. N. Bartlett, F. Einstein, D. F. Stewart, and J. Trotter, *J. Chem. Soc. A*, 1190 (1967).
5. F. O. Sladky, P. A. Bulliner, and N. Bartlett, *J. Chem. Soc. A*, 2179 (1969).
6. R. D. Burbank and G. R. Jones, *Science* **168**, 248 (1970) and **161**, 485 (1971).

THE CRYSTAL STRUCTURE OF RHODIUM PENTAFLUORIDE[†]

B. K. Morrell,* A. Zalkin, A. Tressaud,* and N. Bartlett*

Of the Group VIII transition metals, the pentafluorides of Ru, Os, Rh, Ir, and Pt have been made. Attempts to prepare PdF_5 have failed so far. Only the crystal structures of RuF_5 and OsF_5 have been reported, and x-ray powder photography has shown all of the platinum-metal pentafluorides to be isomorphous. Evidently these pentafluorides constituted a class which is structurally distinct from the pentafluorides of Tc and Re on the one hand and those of Nb, Mo, Ta, and W on the other hand. Although the close resemblance of the x-ray powder photographs of the pentafluorides of Rh, Ir, and Pt suggested close structural similarities, the isostructural relationship to those of Ru and Os remained to be proved. Furthermore, neither the RuF_5 nor the OsF_5 structure has been determined with high precision. Although more difficult to handle than IrF_5 and PtF_5 , RhF_5

offered the possibility of highest precision as a consequence of its lower absorption coefficient and the lower ratio of the metal to fluorine scattering factors.

Crystals were grown by vacuum sublimation in a quartz tube, the parent sample being at $\sim 100^\circ$. A ruby-red crystal grown in this way, approximately $0.130 \times 0.11 \times 0.07 \text{ mm}$ was wedged in a 0.3-mm-diameter quartz x-ray capillary, which was sealed under dry nitrogen. RhF_5 is monoclinic with $a = 12.3376(13)$, $b = 9.9173(8)$, $c = 5.5173(6) \text{ \AA}$, and $\beta = 100.42(2)^\circ$, $V = 663.85 \text{ \AA}^3$, $z = 8$, $d_c = 3.95 \text{ g cm}^{-3}$. As usual with dense reactive fluorides, the number of fluorine atoms in the unit cell was estimated by applying Zachariason's criterion[†] of $\sim 18 \text{ \AA}^3$ per F atom. This indicated $z = 8$. Single-crystal precession photographs indicated the systematic absences

characteristics of space group $P2_1/a$. A Picker automatic four-circle diffractometer, equipped with a fine-focus Mo anode tube, was used for data collection. Data were collected by the θ - 2θ scan technique. Three standard reflections were monitored and showed no decay in intensity during the course of data collection. All reflections of the form $\pm h k l$ were measured out to a 2θ angle of 60° . A total of 2124 intensity data were collected and averaged to yield a data set of 1945 unique reflections, of which 1775 were greater than background. An omega scan of the crystal showed a peak width at half height of $\sim 0.1^\circ$. The absorption coefficient is $\mu = 50.02$, and $\mu r \approx 0.5$. No absorption correction was made.

A three-dimensional Patterson synthesis was used to locate the two rhodium atoms of the asymmetric unit. A Fourier synthesis, phased by the Rh positions, revealed ten more peaks which were assigned as F atoms. With isotropic thermal parameters the structure refined to a conventional R of 0.067. Refining all atoms anisotropically, limiting the refinement to the 1207 for which $I > 3\sigma(I)$ reduced the R to 0.033, and applying an extinction correction to correct for discrepancies of high-intensity reflections in a final R value of 0.029; R was 0.054 for all 1945 data. The standard deviation of an observation of unit weight was 1.09. The final weighted R_2 was 0.037.

Crystals of rhodium pentafluoride consist of close-packed tetrameric units. The tetramer is illustrated in Figs. 1 and 2. The packing of

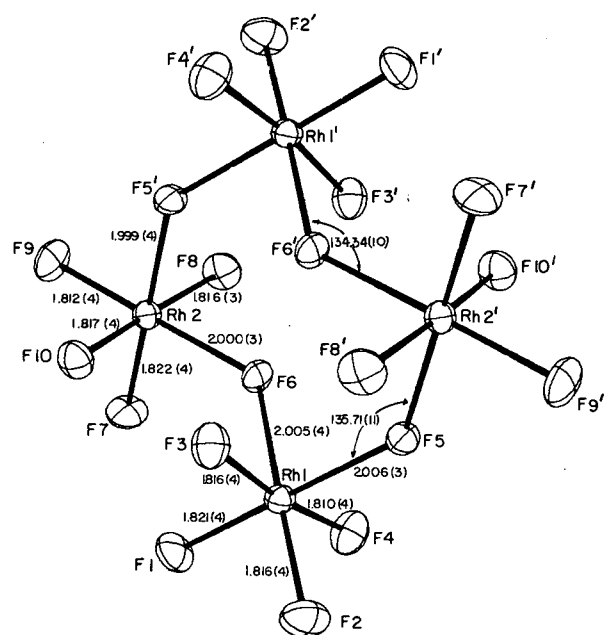


Fig. 1. The RhF_5 tetramer. (XBL 728-6758)

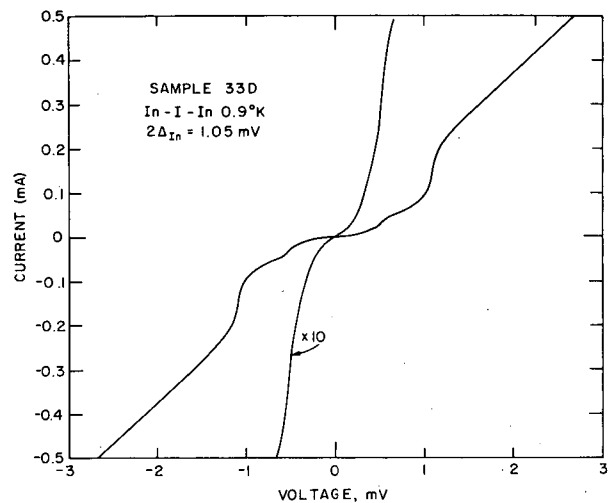


Fig. 2. Stereoscopic view of the RhF_5 tetramer. (XBL 728-6789)

the tetramers is shown in Fig. 3. The F atom arrangement in the structure approximates to a hexagonal close-packed arrangement as described² by Mitchell and Holloway for OsF_5 and RuF_5 . The closest interatomic distances between tetramers are consistent with van der Waals interactions. The crystal structure of RhF_5 establishes that it is isostructural with RuF_5 ³ and OsF_5 ². Unfortunately, the RuF_5 and OsF_5 structures are not of high precision and the clear differentiation of the non-bridging M-F interatomic distances from the bridging seen in RhF_5 is not apparent in the OsF_5 and RuF_5 results. The shapes of the tetrameric units of RuF_5 and OsF_5 are, however, essentially the same as found for RhF_5 , and the same bond length and bond angle pattern seen in $[\text{RhF}_5]_4$ probably pertains in them too.

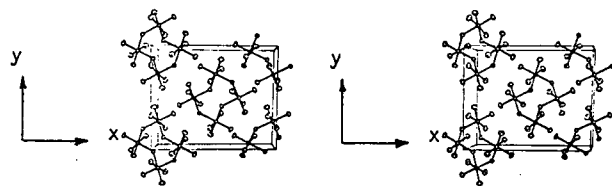


Fig. 3. The packing of RhF_5 tetramers and the unit cell. (XBL 734-448)

Although single crystals of IrF_5 have been obtained by us, none was of suitable size and shape to yield an accurate structure, and when it became clear that the structure would be no more precise than that reported for RuF_5 , the

analysis was abandoned. Nevertheless, the precession and Weissenberg photographic data have established the space group $\overline{P}2_1/a$ and indicate a close structural relationship to the other platinum-metal pentafluorides. We, therefore, believe that these pentafluorides will all show essentially the same tetrameric unit as detailed for RhF_5 in Fig. 1.

It remains to be seen whether AuF_5 , PdF_5 , and MnF_5 can be obtained as crystalline solids. There is no certainty that these pentafluorides would be fluorine-bridged polymers and not monomers (like AsF_5 and PF_5), but if bridging does occur, the RhF_5 type structure appears to be the most likely one to be adopted.

STRUCTURAL STUDIES OF TRIFLUOROSULFUR (IV)-YL, $[\text{SF}_3]^+$, SALTS INCLUDING THE CRYSTAL STRUCTURE OF $[\text{SF}_3]^+[\text{BF}_4]^-$

D. D. Gibley,* C. J. Adams,* M. Fischer,* A. Zalkin, and N. Bartlett

Many of the non-metal fluorides interact with strong fluoride ion acceptors, such as BF_3 and the metal pentafluorides, to form adducts. Work in these laboratories has indicated that adducts of the xenon and iodine fluorides may be adequately formulated as salts, e.g., $[\text{XeF}]^+[\text{RuF}_6]^-$, $[\text{Xe}_2\text{F}_3]^+[\text{AsF}_6]^-$, $[\text{XeF}_5]^+[\text{RuF}_6]^-$, $[\text{IF}_4]^+[\text{SbF}_6]^-$, $[\text{IF}_6]^+[\text{AsF}_6]^-$. A simple example, which appeared to belong to this class, was the 1:1 $\text{SF}_4 \cdot \text{BF}_3$ adduct, first reported (along with other SF_4 , SeF_4 , and TeF_4 adducts) by Bartlett and Robinson.¹ Bartlett and Robinson had initially proposed that the compound might be a Lewis adduct, but their later finding,² that the $\text{SF}_4 \cdot \text{SbF}_5$ adduct possesses a primitive cubic lattice, led them to favor a salt formulation, involving the SF_3^+ ion, for all of the SF_4 adducts. Muetterties and his co-workers,³ while admitting the validity of an ionic formulation, also allowed, on the basis of solution-nmr studies, that the $\text{SF}_4 \cdot \text{BF}_3$ adduct could be a fluorine-bridged dimer or polymer. More recently from vibrational spectroscopic studies, Gillespie and his co-workers concluded that the SF_4 adducts with BF_3 , AsF_5 , and SbF_5 were essentially SF_3^+ salts; however, they interpreted deviations of the observed spectra from the idealized behavior in terms of fluorine bridging between the oppositely charged species. Fluorine bridging between the oppositely charged ions is indicated in the structures of the SeF_4 adducts $\text{SeF}_4 \cdot \text{NbF}_5$ and $\text{SeF}_4 \cdot 2\text{NbF}_5$ reported by Edwards and his co-workers.⁵ Although the structures are suggestive of salt formulations ($[\text{SeF}_3]^+[\text{NbF}_6]^-$ and $[\text{SeF}_3]^+[\text{Nb}_2\text{F}_{11}]^-$ respectively), each cation has three

Footnotes and References

† Condensed from LBL-1154; submitted to *Inorganic Chemistry*.

* Department of Chemistry, University of California, Berkeley.

1. W. H. Zachariason, *J. Amer. Chem. Soc.* **70**, 2147 (1948).

2. S. J. Mitchell and J. H. Holloway, *J. Chem. Soc. (A)* 2789 (1971).

3. J. H. Holloway, R. D. Peacock, and R. W. H. Small, *J. Chem. Soc.* 644 (1964).

anion contacts at $< 2.5\text{\AA}$. These short fluorine-bridge contacts may indicate some covalency (multicenter bonding), as Edwards and his co-workers have suggested. Indeed, Bartlett and Robinson had argued² that fluorine bridging might be more important in the SeF_4 adducts than in those of SF_4 , since SeF_4 is superior to SF_4 as a fluoride ion acceptor; also, the higher fusion temperatures of the SF_4 compared with their SeF_4 relatives suggested greater ionicity in the SF_4 compounds. Calvert and his co-workers⁶ from single-crystal studies of $\text{SF}_4 \cdot \text{BF}_3$, suggested that the $\text{SF}_4 \cdot \text{BF}_3$ structure might be the anti NH_4IO_3 structure although they did not undertake a complete analysis.

The adduct $\text{SF}_4 \cdot \text{BF}_3$ was prepared by condensation of SF_4 (excess) and BF_3 in a monel can provided with a teflon-gasketed lid. Crystals were grown by sublimation, by establishing small temperature gradients in the capillaries at $\sim 60^\circ$. Most of the crystals grown by this technique proved to be twinned when examined under the polarizing microscope. Even crystals which appeared to be satisfactory under microscopic examination showed poor mosaic quality when examined on the x-ray diffractometer. The crystal was roughly rectilinear with dimensions $0.4 \times 0.2 \times 0.2$ mm.

The $\text{SF}_4 \cdot \text{AsF}_5$ adduct was also investigated and was prepared by co-condensing SF_4 (excess) and AsF_5 , in a monel can fitted with a teflon-gasketed lid, warming to ambient temperature and removing excess SF_4 under vacuum. Single

crystals were grown by sublimation in quartz capillaries. Two crystals were indexed and a complete set of intensity data was gathered on each. No obvious systematic discrepancies were observed between the two data sets.

$\text{SF}_4 \cdot \text{BF}_3$ is orthorhombic with $a = 9.599(3)$, $b = 5.755(3)$, $c = 8.974(3) \text{ \AA}$, $V = 495.8 \text{ \AA}^3$, $z = 4$, $d_c = 2.34 \text{ g cm}^{-3}$; the space group is Pnma. The unit cell volume satisfies Zachariason's criterion for close-packed fluoride lattices, since the effective volume per fluorine atom is 17.7 \AA^3 .⁷

$\text{SF}_4 \cdot \text{AsF}_5$ is orthorhombic with $a = 20.375(3)$, $b = 8.508(3)$, $c = 11.224(3) \text{ \AA}$, $V = 1945.7 \text{ \AA}^3$, $z = 12$, $d_c = 2.84 \text{ g cm}^{-3}$. The effective volume per fluoride ion is 18 \AA^3 . Single-crystal precession photographs were obtained from which systematic absences were observed to be consistent with the space groups $\text{Cmc}2_1$, $\text{C}2\text{cm}$, and Cmcm .

Diffraction data were collected on a Picker automatic four-circle diffractometer equipped with a fine-focus Mo anode tube. Intensity data were collected by the θ - 2θ scan technique with radiation monochromatized by a graphite crystal. A complete set of $-hkl$ reflections was collected to a 2θ of 65° as well as a portion of the $h-k-l$ set. An averaged set of 980 unique reflections was obtained from 1240 intensity measurements; of these, 700 were used in the least-squares refinement.

A combination of Patterson and "direct" methods were used to determine the structure. Isotropic refinement gave $R = 0.10$ and incorporation of anisotropic temperature factors reduced R to 0.043 for the non-zero weighted data, and 0.063 for all the data.

Although we were unsuccessful in determining a complete structure of the $\text{SF}_3 \text{ As F}_6$ salt we were able to get some information about the structure. The data from $\text{SF}_3 \text{ As F}_6$ were averaged to give 1530 unique reflections, of which 487 were greater than 3σ . The paucity and poor quality of the data may be responsible for our failure to solve this structure. Evidence for twinning and disorder also exists. The Patterson synthesis indicated that the space groups $\text{C}2\text{cm}$ and Cmcm were unlikely. Space group $\text{Cmc}2_1$ were assumed. The sulfur and arsenic atoms, derived from a solution of the Patterson map, refined by least squares to yield a conventional R factor of 0.37. This arrangement is essentially that of a nickel arsenic lattice. Each sulfur atom is approximately at the center of a trigonal prismatic arrangement of arsenic atoms, and each arsenic atom is approximately at the center of an octahedron of sulfur atoms. Although subsequent Fourier and least-squares calculations, in which fluorine atoms were also included, yielded a small conventional R factor,

the resulting structure was chemically unreasonable. The trigonal prismatic arrangement of the $[\text{AsF}_6]^-$ ions about the $[\text{SF}_3]^+$ species suggests a disordering of the cation equivalent to inversion along the threefold axis.

Raman spectra of the powdered adducts of $\text{SF}_4 \cdot \text{BF}_3$ and $\text{SF}_4 \cdot \text{AsF}_5$ were excited at 4880 \AA , using a 100 mw C. R. L. argon-ion laser and were recorded with a Cary 83 spectrometer. The Raman spectrum of indene was used for calibration, and the accuracy of the reported frequencies is $\pm 3 \text{ cm}^{-1}$. The Raman spectra which we obtained for solid $\text{SF}_4 \cdot \text{BF}_3$ and $\text{SF}_4 \cdot \text{AsF}_5$ and our assignments of the lines contained therein Fig. 1 are in essential agreement with those reported by earlier workers,⁴ except that we observe an additional weak feature at 711 cm^{-1} in the spectrum of $\text{SF}_4 \cdot \text{AsF}_5$. This new feature is attributable to a fundamental transition in the formally Raman-inactive mode $\nu_3(t_{1u})$ of the AsF_6^- anion. Using a simple valence force field and the geometry established in this work, the fundamentals of SF_3^+ in $\text{SF}_4 \cdot \text{BF}_3$ [$\nu_1(a_1)$, 938 cm^{-1} ; $\nu_2(a_1)$, 530 cm^{-1} ; $\nu_3(e)$, 914 cm^{-1} ; $\nu_4(e)$, 411 cm^{-1}] were analyzed to yield the following force constants: f_r , $5.67 \text{ mdyn \AA}^{-1}$; f_{r_1} , $0.19 \text{ mdyn \AA}^{-1}$; f_a/r^2 , $0.85 \text{ mdyn \AA}^{-1}$; $f_{a'}/r^2$, $0.12 \text{ mdyn \AA}^{-1}$.

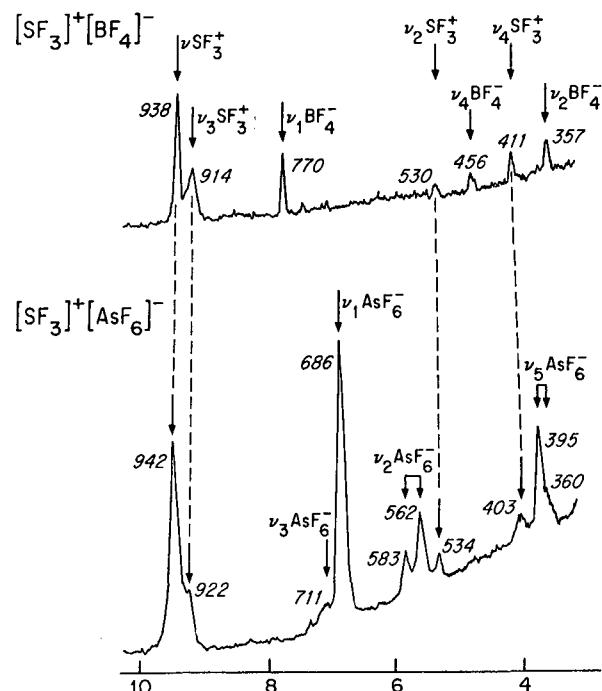


Fig. 1. The Raman spectra of $[\text{SF}_3]^+[\text{BF}_4]^-$ and $[\text{SF}_3]^+[\text{AsF}_6]^-$. (XBL 734-444)

The atomic arrangement in $[\text{SF}_3]^+[\text{BF}_4]^-$ is illustrated in Fig. 2. The sulfur atoms and the boron atoms lie in mirror planes. Each sulfur atom has three close neighbor fluorine atoms which define an SF_3 group with C_{3v} symmetry (see Fig. 3). The BF_4 group is approximately tetrahedral. Each sulfur atom is approximately equidistant from three fluorine atoms of three different BF_4 species, distances, of 2.624(2) (twice) and 2.593(3) Å. The entire arrangement appears to be simply dictated by the closest packing of SF_3 and BF_4 species, with slight angle distortions in the latter being a consequence of close packing with the SF_3 group. It should be noted that this structure is not the anti type of the reported $\text{NH}_4^+\text{IO}_3^-$, as had been supposed by Calvert *et al.*⁶

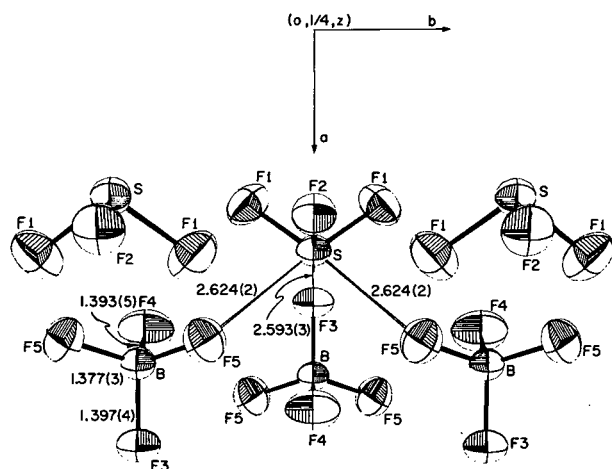


Fig. 2. The atomic arrangement in $[\text{SF}_3]^+[\text{BF}_4]^-$. (XBL 7110-4512)

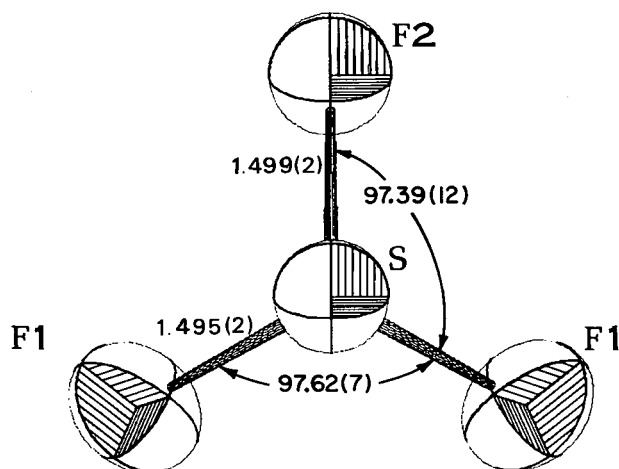


Fig. 3. The shape of the $[\text{SF}_3]^+$ ion in $[\text{SF}_3]^+[\text{BF}_4]^-$. (XBL 7110-4597)

On chemical grounds we can formulate the sulfur species as SF_3^+ and the boron species as BF_4^- . The sulfur atom of the SF_3 group is the effective center of positive charge. Since fluorine atoms are highly electron attracting, they should be neutral if not slightly negative in net charge, even in the SF_3^+ ion. On the F atom side of the SF_3^+ ion it is therefore reasonable to suppose that the positive charge would be more effectively screened than on the sulfur side. However, the non-bonding valence electron pair of sulfur will provide appreciable screening on the threefold axis, if it occupies a spatially directed orbital (e.g., and $s p^3$ hybrid). Such steric activity of the "non-bonding pair" suits the arrangement observed in this structure, since the F ligands of the BF_4^- make their close approach, to the sulfur atom, well off the C_3 axis. The fluorine atom arrangement about each sulfur atom is therefore that of a trigonally distorted octahedron, in which three are bound and three are electrostatically attracted. In BF_4^- the B-F interatomic distances are not significantly different within the set, and are in excellent agreement with the mean values found in NaBF_4 , KBF_4 , and NH_4BF_4 . The SF_3^+ species is similar in shape to its isoelectronic relative PF_3 .⁸ The higher nuclear charge of the sulfur atom is responsible for the S-F interatomic distance being 0.07 Å shorter than the P-F distance.

The full refinement of the crystal structure of $[\text{SF}_3]^+[\text{BF}_4]^-$ and the partial solution of the structure of $[\text{SF}_3]^+[\text{AsF}_6]^-$ each show the anion occupying a lattice site of symmetry lower than T_d and O_h , respectively. The anionic vibrational frequencies of these two compounds lie close to those found for the anions in other salts or in solution, but the spectra clearly show "site effects," viz., the splitting of degenerate fundamentals [$\nu_2(\text{e}_g)$ of AsF_6^-] and the breakdown of gross selection rules so that $\nu_3(\text{t}_{1u})$ of AsF_6^- is observed in the Raman spectrum of $[\text{SF}_3]^+[\text{AsF}_6]^-$, as are $\nu_1(\text{a}_1)$ and $\nu_2(\text{e})$ of BF_4^- in the infrared spectrum of $[\text{SF}_3]^+$.¹¹ These effects are small, and certainly originate in unit-cell dynamics and in the slight deviation of the ions from structural regularity rather than in extensive interionic fluorine-bridging interactions, as proposed by Gillespie;⁴ we note that comparable "site effects" are seen in the spectra of the alkali metal tetrafluoroborate.⁹ Neither our crystallographic nor spectroscopic studies of the SF_4 adducts reveal the signally deformed anions evident in adducts of BrF_3 ¹⁰ with fluoride-acceptors, which are possibly caused by fluoride bridging to the strongly polarizing BrF_2^+ cation. The S-F stretching-force constant for SF_3^+ we find to be 5.67 m dyn Å⁻¹ for the S-F equatorial stretching force constant of SF_4 and approximately twice the value of 2.8 m dyn Å⁻¹ derived for the axial bonds in that molecule.

Footnotes and References

† Condensed from LBL-469; published in *Inorg. Chem.* **11**, 2325 (1972).

* Department of Chemistry, University of California, Berkeley.

1. N. Bartlett and P. L. Robinson, *Chem. and Indus. (London)* 1351 (1956).

2. N. Bartlett and P. L. Robinson, *J. Chem. Soc. A.* 3417 (1961).

3. A. L. Oppeguard, W. L. Smith, E. L. Muetterties, and V. A. Engelhard, *J. Am. Chem. Soc.* **82**, 3835 (1960).

4. M. Azeem, M. Brownstein, and R. J. Gillespie, *Can. J. Chem.* **47**, 4159 (1969).

5. A. J. Edwards and G. R. Jones, *J. Chem. Soc. A.* 1491 (1970).

6. L. D. Calvert and J. R. Norton, *Acta Cryst.* **17**, 617 (1964).

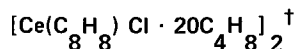
7. W. H. Zachariason, *Acta Cryst.* **2**, 388 (1949).

8. Yonezo Morino, Kozo Kuchitsu, and Kohei Moritani, *Inorg. Chem.* **8**, 867 (1969).

9. J. Groubeau, and W. Bues, *Z. anorg. u allgm. Chem.* **268**, 221 (1952); N. N. Greenwood, *J. Chem. Soc.* 3811 (1959).

10. K. O. Christie and C. J. Schack, *Inorg. Chem.* **9**, 2296 (1970); A. J. Edwards and G. R. Jones, *Chem. Comm.* 1304 (1967); *J. Chem. Soc. A.* 1467 (1969).

A DIMERIC π -CYCLOOCTATETRAENE DIANION COMPLEX OF
CERIUM(III). THE CRYSTAL AND MOLECULAR STRUCTURE OF



K. O. Hodgson* and K. N. Raymond*

Although the chemistry of the π -carbocyclic anion complexes is now extensive, there is a distinct absence of the structural data necessary to form a solid foundation for explaining their bonding properties and spectra. Our interest in the structures of f transition series organometallic compounds has extended from the initial structural studies of the uranium cyclooctatetraene dianion complex, $\text{U}(\text{C}_8\text{H}_8)_2$,¹ and its thorium analog² to the recently reported cyclooctatetraene dianion (COT^{2-}) complexes of the lanthanides.^{3,4}

Recent attempts by Mares, Hodgson, and Streitwieser to prepare a neutral complex containing COT^{2-} and cyclononatetraene anion resulted in a new series of lanthanide complexes containing the cyclooctatetraene dianion.⁴ This series was difficult to characterize due to facile loss of THF. A single-crystal x-ray diffraction analysis was begun on the cerium member of this series and the structure determination and subsequent full elemental analysis showed that the true composition is $[\text{Ce}(\text{C}_8\text{H}_8)\text{Cl} \cdot 2\text{THF}]_2$.

Crystals suitable for x-ray studies were obtained by controlled evaporation of a saturated THF solution of the complex under argon atmosphere at room temperature. The air- and

water-sensitive crystals were mounted in thin-walled quartz capillaries with Kel-F fluorocarbon grease under an argon atmosphere. The crystals conform to space group $P2_1/c$ with $a = 11.869(6)$, $b = 12.621(5)$, $c = 13.497(7)\text{\AA}$, and $\beta = 122.91(3)^\circ$. The calculated density for two dimeric molecules per cell is 1.66 g/cm^3 and that observed by flotation is 1.69.

A total of 2626 reflections were measured with $F^2 > 3\sigma(F^2)$. These were corrected for absorption and used in the final refinement. The structure was solved by standard Patterson and difference Fourier techniques and refined by full-matrix least-squares minimization to an agreement factor on F of 3.6%.

A packing diagram of the crystal is shown in Fig. 1. The molecular geometry is shown in Fig. 2. Figures 3 and 4 give detailed views of the cyclooctatetraene dianion ring and the THF molecules, respectively.

The crystal structure consists of discrete dimers which show no unusually short intermolecular non-bonded distances. There are two cerium atoms in the dimeric unit which are bridged asymmetrically by the two chloride ions with Ce-Cl bond lengths of $2.855(2)$

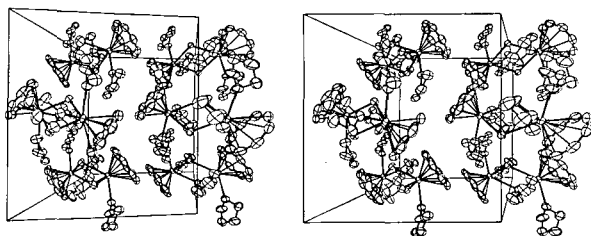


Fig. 1. A stereoscopic packing diagram of $[\text{Ce}(\text{C}_8\text{H}_8)\text{Cl} \cdot 2(\text{OC}_4\text{H}_8)]_2$ viewed normal to the x - y plane. One unit cell is outlined. The origin is at the back lower left, the horizontal axis is a , and the vertical axis is b . The dimeric units at $0\ 0\ 1$, $0\ 1\ 0$, $0\ 1\ 1$, and $1\ 1\ 1$ have been omitted. (XBL 734-540)

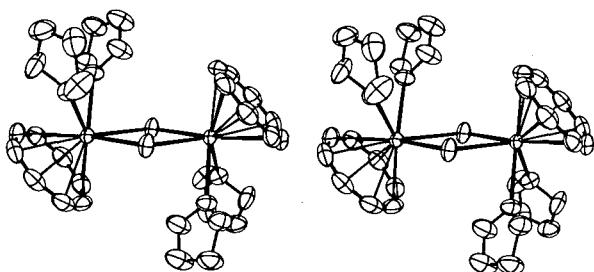


Fig. 2. A stereoscopic diagram of the $[\text{Ce}(\text{C}_8\text{H}_8)\text{Cl} \cdot 2(\text{OC}_4\text{H}_8)]_2$ complex. Thermal ellipsoids are drawn at the 40% probability contour. The numbering sequence in the COT ring on the right is counterclockwise, such that C_8 is uppermost and C_1 is in front of C_8 . The THF ring #1 is in the right foreground. Carbon atom numbering for both THF rings is clockwise and sequential, and begins at the oxygen atom. (XBL 734-449)

and $2.935(2)\text{\AA}$. The cyclooctatetraene dianion ring is planar with eightfold molecular symmetry and an average C-C bond length of $1.394(4)\text{\AA}$. It is symmetrically bonded to the cerium atom with an average Ce-C distance of $2.710(2)\text{\AA}$. The Ce-O distances are equal and average $2.583(2)\text{\AA}$. The two tetrahydrofuran (THF) oxygens and the five-membered THF rings differ in conformation; the first is in a skew or twist form (C_2 symmetry) and the second has the envelope conformation (C_8 symmetry).

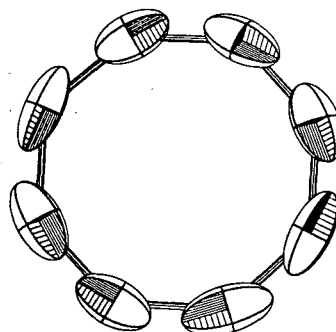
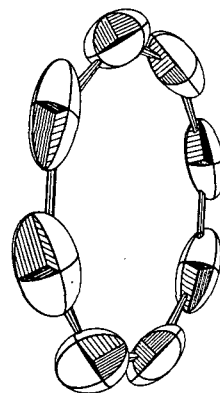


Fig. 3. The cyclooctatetraene dianion ring carbons viewed perpendicular to the plane of the ring are shown in the lower view. In the upper view the plane is rotated 65° . The numbering sequence increases sequentially in a clockwise direction from the upper right carbon atom, C_1 , in both rings. (XBL 734-446)

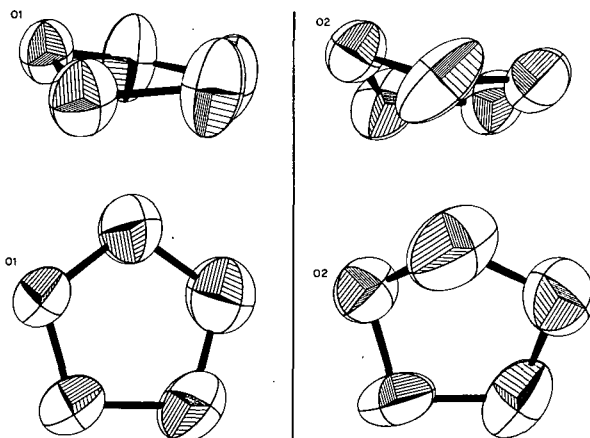


Fig. 4. Perspective drawings of the two tetrahydrofuran molecules. The THF ring carbon atoms are numbered sequentially, begin with C_{11} or C_{12} and proceed in a counterclockwise direction from the oxygen atom. (XBL 734-451)

Footnotes and References

† Condensed from a report published in *Inorg. Chem.* **11**, 171 (1972).

* Department of Chemistry, University of California, Berkeley.

1. A. Zalkin and K. N. Raymond, *J. Am. Chem. Soc.* **91**, 5667 (1969).

2. A. Avdeef, K. N. Raymond, K. O. Hodgson, and A. Zalkin, *Inorg. Chem.* **11**, 1083 (1972).

3. F. Mares, K. Hodgson, and A. Streitwieser, Jr., *J. Organometal Chem.* **24**, C68 (1970).

4. F. Mares, K. Hodgson, and A. Streitwieser, *ibid.* **25**, C24 (1971).

ROTOMERIC CONFIGURATIONS OF A METHYL-SUBSTITUTED
CYCLOOCTATETRAENE DIANION COMPLEX OF URANIUM(IV).
THE CRYSTAL AND MOLECULAR STRUCTURE OF $U[C_8H_4(CH_3)_4]_2^{\dagger}$

K. O. Hodgson* and K. N. Raymond*

Following the initial synthesis^{1,2} and single-crystal structure determination^{3,4} of bis-(cyclooctatetraenyl)uranium(IV), "uranocene," there has been interest in the extent to which there is contribution to the bonding from the uranium 5f orbitals. Contact shift proton magnetic resonance is one technique which can be used to study the electronic interactions in these complexes, if the molecular structure of the complexes is well enough known so that the geometrically dependent contributions to the chemical shift can be evaluated. The original nmr study of $U(C_8H_8)_2$ by Edelstein, La Mar, Mares, and Streitwieser⁵ was interpreted using the molecular parameters of the single-crystal structure and indicated a large positive net contact shift that suggested some form of covalency. However, in the absence of data which would indicate the type of ligand molecular orbital (σ or π) containing the delocalized spin, no attempt could be made to evaluate the possible role of f orbitals in such covalency. Methyl substitution on the π -carbocyclic ring provides a useful technique for characterizing the mechanism of spin delocalization in these ligands. For spin in the π orbitals it is well known that an attached ring proton and methyl group proton exhibit hyperfine coupling constants of comparable magnitude but of opposite sign; for spin in σ orbitals the coupling constants are of the same sign with the ring methyl shift attenuated 3-5 times the ring proton shift. In order to utilize this approach in the interpretation of the $U(C_8H_8)_2$ spectrum, Streitwieser and co-workers prepared and studied the nmr spectrum of bis(1,3,5,7-tetramethylcyclooctatetraenyl)uranium(IV).⁶ The derived contact shifts were of opposite signs for the methyl and ring protons and the result has been interpreted as being consistent with f-orbital participation in the bonding of these complexes.

There were three main reasons for interest in the structure of $U(C_8H_4(CH_3)_4)_2$. The first reason was to compare the geometry with $U(C_8H_8)_2$,^{3,4} and $Th(C_8H_8)_2$.⁴ The second reason was to determine which of the possible rotomeric conformations involving the relative orientations of the methyl groups and the dianion rings exist in the solid state, the object being to determine indirectly the ease of rotation of one ring with respect to another around the molecular symmetry axis. The third reason for interest was the opportunity to measure the relative planarity of the tetramethylcyclooctatetraenyl ligand. Any concave or convex distortion of the unsubstituted cyclooctatetraenyl dianion ring cannot be determined by x-ray diffraction studies because the substituent hydrogen atoms are not located with sufficient accuracy. Replacement of the ring substituent hydrogen atoms by a methyl group makes this measurement possible.

Single crystals of the complex suitable for x-ray structural studies were prepared by slow sublimation under a definite temperature gradient and argon pressure in a sealed tube. Pure $U(TMCOT)_2$ (50 mg) obtained from a previous sublimation was placed in a small copper crucible in a glass sublimation tube. The air- and moisture-sensitive crystals were mounted with Corning high-vacuum silicon grease in thin-walled quartz capillaries under argon atmosphere. The large, burgundy-red plates have the following crystal data: monoclinic space group, $P2_1/c$, cell constants $a = 20.224(5)$, $b = 12.066(3)$, $c = 17.467(6)$ Å, and $\beta = 101.57(2)$. For eight formula units per cell the calculated density is 1.74 g/cm^3 . The structure was refined with full-matrix least-squares methods using 4341 independent reflections for which $F^2 > 3\sigma(F^2)$ to a standard unweighted R factor of 3.68%. There are two crystallographically

independent π -carbocyclic sandwich molecules per unit cell. In both cases the uranium atom is symmetrically bonded to two planar, methyl-substituted cyclooctatetraenyl dianion rings. The packing of these two types of molecules in the crystal is diagrammed in Fig. 1. The individual molecules are diagrammed in Fig. 2. The U-C bond lengths are equal and average 2.658(6) Å. The U-C bond lengths within the four aromatic rings are also equal and average 1.409(7) Å. The two rings in both molecules, when viewed down the molecular symmetry axis, are rotated 14° from a conformation in which the ring carbon atoms are eclipsed. However, the two molecules differ in the relation of the substituent methyl groups. On molecule A the methyl groups are approximately eclipsed, and in molecule B the methyl groups are approximately staggered. All sixteen independent methyl groups are bent inward an average of 4.1° from the planes of the dianion ring carbons toward the uranium atom.

The general similarity of the crystal environment of types A and B leads immediately to the question of why two distinct rotomeric conformers should exist. We believe the answer lies in a detailed consideration of the intermolecular methyl-methyl interactions in the crystal. The van der Waals contact distance for methyl groups is approximately 4.00 Å.⁷ There are many interactions of methyl groups in this structure near, or much less, than this value. In many cases there is a kind of "interlocking gear" arrangement for adjacent molecules in the crystal in which the teeth of the gears are the methyl groups. This links the orientations of the rings through a complex three-dimensional network. However, one feature does stand out: There are more, and stronger, one molecular methyl-methyl contacts for type A than for type B. The intramolecular contacts for type A are much more severe than for type B. The distances between the eclipsed methyl groups range from 3.73 to 3.80 Å and average 3.86 Å. For the corresponding distances in the nearly staggered

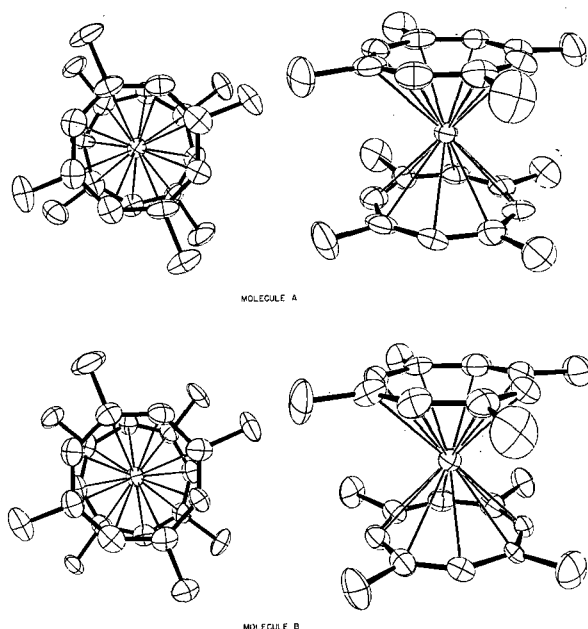


Fig. 2. The two crystallographically independent molecules, A and B, in the crystal structure of $U(C_8H_4(CH_3)_4)_2$.

(XBL 734-455)

conformation of type B the range is from 3.91 to 4.20 Å and the average is 4.04 Å. Thus in type B the methyl groups for the two rings of the molecule are just at the contact distance while in type A they are nearly 0.3 Å less than this value, and in type A must be strongly repelling one another. Apparently the greater intramolecular methyl-methyl contacts of molecule A are sufficient to force it into what must be a higher energy conformation. Any rotation away from the observed conformation relieves some intramolecular strain but at too great an

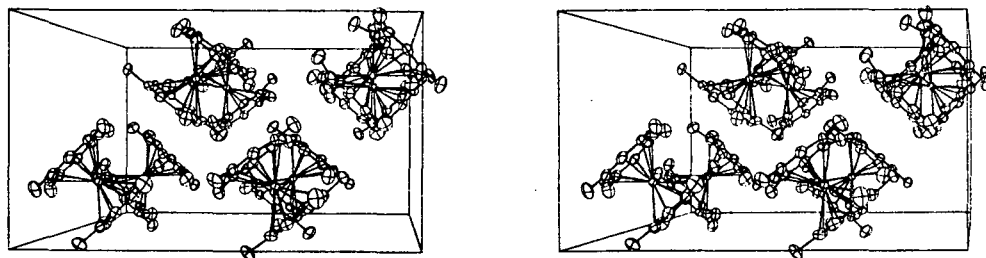


Fig. 1. A stereoscopic packing diagram of $U(C_8H_4(CH_3)_4)_2$ viewed normal to the x-y plane. The origin is at the lower back left corner, the horizontal axis is a and the vertical is b.

(XBL 734-445)

-expense in decreased intermolecular methyl-methyl distances and resultant increase in energy.

One very recent structure analysis shows the same type of concave ring distortion as observed in $U(C_8H_4(CH_3)_4)_2$. In the low-temperature neutron diffraction study of $Cr(h^6-C_6H_6)(CO)_3$ Rees and Coppens have found that the benzene ring exhibits a convex distortion with the hydrogen atoms bent in an average of 1.7° toward the chromium atom.⁸ Although substantially smaller than the distortion observed in $U(C_8H_4(CH_3)_4)_2$, it appears that a convex distortion of carbocyclic rings in sandwich structures may be a general phenomenon. It is particularly interesting that the same effect should be observed in both a 3d and a 5f transition metal compound.

In $U(C_8H_4(CH_3)_4)_2$ there is no question that in the case of both molecules A and B all of the methyl groups bend in toward the metal. Van der Waals' attraction cannot account for this convex bending in both types of molecules. In fact, molecule A has intramolecular methyl-methyl contact 0.3 \AA shorter than the sum of the Van der Waals' radii of two methyl groups. In spite of this short contact distance the methyl groups on molecule A are on an average bent inward toward the uranium atom as much as those in molecule B. There are also no intermolecular effects which would force all of the methyl groups to bend inward.

Both intermolecular packing effects and intramolecular Van der Waals' attraction thus unambiguously can be ruled out as explanations for the inward bending of the methyl groups in molecules A and B, and explanations of this phenomenon must be found in the electronic structure of the molecules. One possible explanation would involve the overlap of the p- π orbitals on the cyclooctatetraene dianion ring with the uranium metal orbitals. Overlap of the metal 5f orbitals with the ligand molecular orbitals of cyclooctatetraene dianion has been shown to be of significance in these types of actinide organometallic complexes.^{2, 5, 6} The inward bending of the methyl substituents makes each carbon slightly pyramidal with the π -orbital of the $C_8H_8^{2-}$ ring bent inwards toward the uranium atom. This change provides greater directionality for overlap between the π -orbitals and the metal orbitals. This slight bending would result in only a small loss in the conjugation energy of the aromatic system.

A second explanation can be based on stereochemical effects of the π electron density. In an uncoordinated $C_8H_8^{2-}$ ring, the π -cloud of electrons above and below the plane would be symmetrical. The approach and coordination of the highly charged metal ion would result in

two effects: 1) slight polarization of the ligand electron density toward the metal and, more important, 2) the contraction in volume (but not in total electron charge) of the electron density on the side of the ring adjacent to the metal ion. In the same way that non-bonded electron pairs in the Gillespie-Nyholm model are stereochemically more active than bonding electron pairs,⁹ the electron density on the side of the dianion ring away from the metal atom would repel the methyl groups more than the electron density on the adjacent side of the ring, since the density on the side of the ring away from the metal electron density occupies a relatively larger volume of space. The result for the structure would be the observed inward bend of the methyl groups as a result of the non-bonded interactions of these groups with the higher electron density in the π -system on the side opposite the metal ion. The effect would be expected to be more important for the more highly charged actinide cations than for the +2 cations of the transition metals, and this is in agreement with the observations in substituted ferrocenes and, more important, with the $Cr(h^6-C_6H_6)(CO)_3$ structure.

Footnotes and References

† Condensed from a report which has been accepted for publication in *Inorganic Chemistry*. A preliminary report appeared in *Chem. Comm.* **1971**, 1592.

* Department of Chemistry, University of California, Berkeley.

1. A. Streitwieser, Jr., and U. Muller-Westerhoff, *J. Am. Chem. Soc.* **90**, 7364 (1968).
2. A. Streitwieser, Jr., U. Muller-Westerhoff, G. Sonnichsen, F. Mares, K. O. Hodgson, C. Harmon, and D. G. Morrell, submitted to *J. Am. Chem. Soc.*
3. A. Zalkin and K. N. Raymond, *J. Am. Chem. Soc.* **91**, 5667 (1969).
4. A. Avdeef, K. N. Raymond, K. O. Hodgson, and A. Zalkin, *Inorg. Chem.* **11**, 1083 (1972).
5. N. Edelstein, G. N. La Mar, F. Mares, and A. Streitwieser, Jr., *Chem. Phys. Letters* **8**, 399 (1971).
6. A. Streitwieser, Jr., D. Dempf, G. N. La Mar, D. G. Karraker, and N. Edelstein, *J. Am. Chem. Soc.* **93**, 7343 (1971).
7. L. Pauling, *The Nature of the Chemical Bond*, 3rd ed. (Cornell University Press, Ithaca, New York, 1960), p. 260.

8. B. Rees and P. Coppens, paper submitted for publication. We thank Professor Coppens for providing us with a manuscript of this paper

prior to publication.

9. R. J. Gillespie, J. Chem. Soc. 4679 (1963).

AN ION PAIR COMPLEX FORMED BETWEEN
BIS(CYCLOOCTATETRAENYL) CERIUM(III) ANION AND
 AN ETHER-COORDINATED POTASSIUM CATION. THE
 CRYSTAL AND MOLECULAR STRUCTURE OF
 $[K(CH_3OCH_2CH_2)_2O][Ce(C_8H_8)_2]^{\dagger}$

K. O. Hodgson* and K. N. Raymond*

Streitwieser and co-workers have characterized two homologous series of lanthanide(III) complexes with cyclooctatetraene dianion:¹⁻³ $[Ln(C_8H_8)Cl \cdot 2C_4H_8O]_2$ and $K[Ln(C_8H_8)_2]$. The crystal and molecular structure determination of the cerium member of the monocyclooctatetraenyl chloride series established the chemical composition as well as the structure of this π -carbocyclic complex.⁴ The structural result also allowed an assignment of structure

for the other, homologous members of the series of complexes, containing two cyclooctatetraene dianion ligands per metal, were suspected to be isostructural with $U(C_8H_8)_2$ ⁵ based on striking similarities in the ir spectra of the uranium as compared to the lanthanide complexes.^{1, 3} To determine the molecular geometry of the $[Ln(C_8H_8)_2]^-$ anion we have completed the single-crystal structure analysis of the cerium member of the bis-cyclooctatetraenyl series.

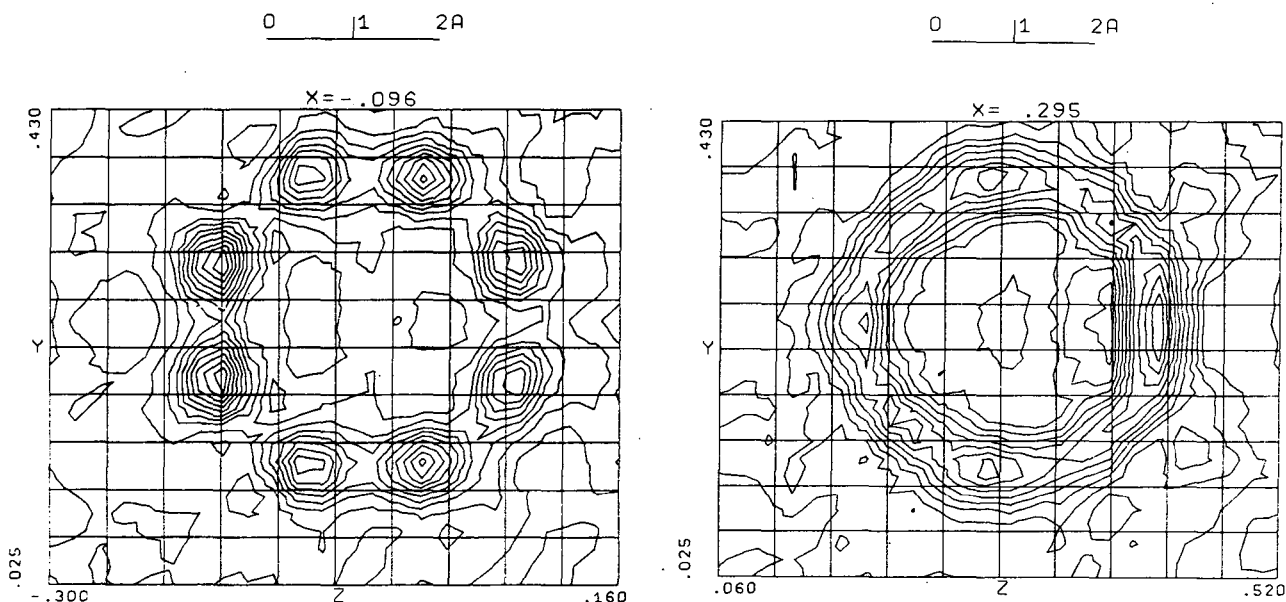


Fig. 1. Sections from the electron density map (calculated with values of F_{obs} and phases of F_{calcd}) for cyclooctatetraene dianion rings. These sections are in the planes of the cyclooctatetraene rings. Slight deviations in the contour maps from the crystallographic mirror symmetry are an artifact of the computation procedure. Ring #1 is shown on the left and ring #2 is shown on the right. The mirror plane in both cases is horizontal at $y=1/4$ and relates the top and bottom halves of the sections.
 (XBL 734-447)

Crystals were obtained from slow evaporation of a saturated tetrahydrofuran (THF) solution of the complex under argon atmosphere at room temperature. As soon as the crystals were removed from the mother liquor, however, they rapidly decolorized on the surface and became an amorphous powder. Since the crystals were probably losing coordinated solvent we chose to recrystallize the complex

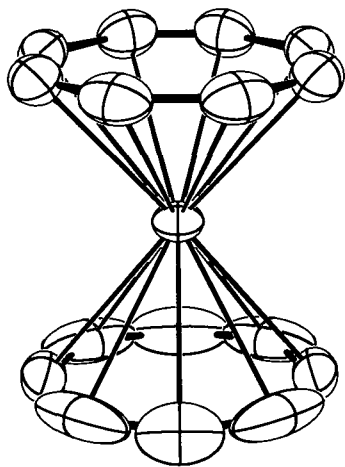


Fig. 2. A perspective view of the contact ion pair, $[K(\text{diglyme})][\text{Ce}(\text{C}_8\text{H}_8)_2]$. Thermal ellipsoids are drawn at the 50% probability contour scale. (XBL 734-454)

from the higher boiling coordinating ether solvent, diglyme, $\text{CH}_3\text{OCH}_2\text{CH}_2\text{OCH}_2\text{CH}_2\text{OCH}_3$. If a saturated solution of the complex in diglyme was prepared at the boiling point of the solvent (162°) under argon atmosphere and then allowed to cool, beautifully formed large green single crystals were obtained in sizes up to $1\text{ mm} \times 0.5\text{ mm} \times 0.5\text{ mm}$. Several of the air- and moisture sensitive crystals were mounted in thin-walled quartz capillaries with Kel-F fluorocarbon grease under an argon atmosphere. The bright green plates have the following crystal data: orthorhombic space group Pnma , cell constants: $a = 16.897(4)$, $b = 14.014(5)$, $c = 9.358(2)\text{ \AA}$, $Z = 4$, $\rho_{\text{calcd}} = 1.56\text{ g/cm}^3$.

X-ray diffraction intensity data were collected by counter methods. A total of 2789 reflections with $F^2 > 3\sigma(F^2)$ was used in the final refinements. The structure was solved by Patterson and Fourier techniques. Final refinement was by full-matrix least-squares minimization to an agreement factor of 5.9%. In the refinement process it was found that one of the $\text{C}_8\text{H}_8^{2-}$ rings is well ordered with relatively low thermal motion, while the second shows librational thermal motion about an axis normal to the plane of the ring. This is diagrammed in Fig. 1.

The molecular structure consists of a discrete $[\text{Ce}(\text{C}_8\text{H}_8)_2]^-$ anion combined in a contact ion pair with the $[\text{K}(\text{CH}_3\text{OCH}_2\text{CH}_2)_2\text{O}]^+$ solvated cation. One side of the cation is coordinated by the complexing ether, diglyme. The opposite side is coordinated by one of the two cyclooctatetraenyl dianion rings in the structure. The Ce and K ions lie on a crystallographic mirror plane such that the entire complex has crystallographically imposed mirror symmetry. The average Ce-C bond length is $2.742(8)\text{ \AA}$. The cyclooctatetraene dianion rings are planar with equal aromatic C-C bond distances. In one case the ring is bisected by the mirror plane through two C-C bonds, and in the other through two C atoms. The molecular symmetry of the $[\text{Ce}(\text{C}_8\text{H}_8)_2]^-$ anion is

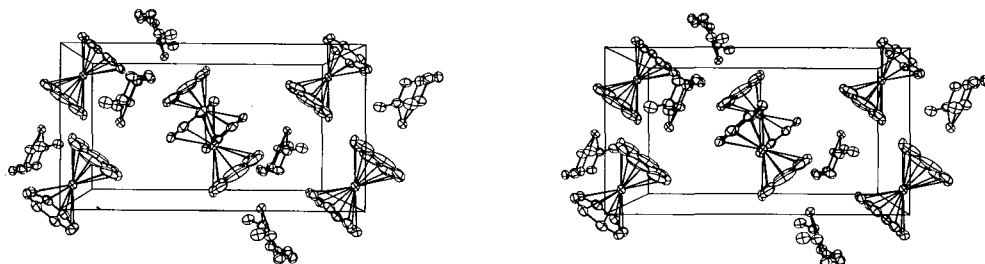
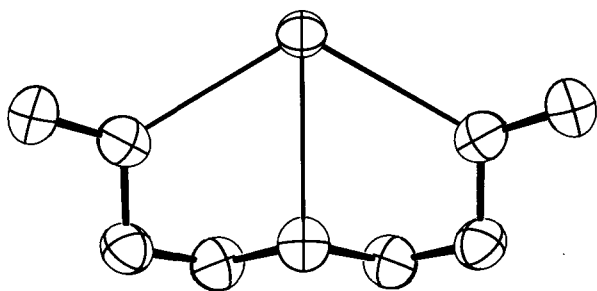


Fig. 3. A stereoscopic packing diagram of $[K(\text{diglyme})][\text{Ce}(\text{C}_8\text{H}_8)_2]$. The entire unit cell is shown. The horizontal axis is \underline{a} and the vertical is \underline{c} . The origin of the cell is the lower left front corner. (XBL 734-452)

D_{8d}. The five independent K-C bond lengths between the K⁺ ion and the C₈H₈²⁻ ring averages 3.16(3)Å, and the two independent K-O distances from the diglyme oxygens in the ether complexed cation are 2.792(5) and 2.741(4)Å.

Footnotes and References

† Condensed from a report published in *Inorg. Chem.* **11**, 3030 (1972).

* Chemistry Department, University of California, Berkeley.

1. F. Mares, K. Hodgson, and A. Streitwieser, Jr., *J. Organometal. Chem.* **24**, C68 (1970).

2. F. Mares, K. Hodgson, and A. Streitwieser, Jr., *ibid.* **25**, C24 (1971).

3. K. O. Hodgson, F. Mares, D. F. Starks, and A. Streitwieser, Jr., submitted for publication.

4. K. O. Hodgson and K. N. Raymond, *Inorg. Chem.* **11**, 171 (1972).

5. (a) A. Zalkin and K. N. Raymond, *J. Am. Chem. Soc.* **91**, 5667 (1969).

(b) A. Avdeef, K. N. Raymond, K. O. Hodgson, and A. Zalkin, *Inorg. Chem.* **11**, 1083 (1972).

THE PREPARATION AND STRUCTURAL CHARACTERIZATION OF TRIS(BENSYL CYCLOPENTADIENIDE)CHLOROURANIUM(IV), $U(C_5H_4CH_2C_6H_5)_3Cl$ †

J. Leong,* K. O. Hodgson,* and K. N. Raymond*

Of the few lanthanide and actinide organometallic compounds which have been characterized structurally the majority have been the recently prepared complexes of cyclooctatetraene dianion.¹⁻⁷ A complex of U(III) with benzene, $U(C_6H_6)(AlCl_4)_3$, is known in which the benzene is symmetrically π -bound to the uranium ion.⁸ The remaining lanthanide or actinide π -sandwich compounds which have been the subjects of structural studies are complexes of cyclopentadiene anion, or the related indenide anion.

The structures of two lanthanide(III) complexes with cyclopentadienide anion, tris(indenide)samarium⁹ and the disordered tris(cyclopentadienide)samarium¹⁰ have been reported. The structure determination of tris(cyclopentadienide)chlorouranium(IV), $U(C_5H_5)_3Cl$, was the first of an actinide(IV) π -sandwich complex. However, very little information can be derived from this structure since the carbon atom positions were not well determined. More recently the structure of tris(indenide)chlorouranium(IV), $U(C_9H_7)_3Cl$ has been reported and a substantial difference was found in the C-C bond lengths for individual carbon atoms in the five-membered ring of the indenyl anion.¹² Since it was not clear to what extent this asymmetry was due to the electronic structure of the indenyl anion as opposed to bonding effects in

the uranium coordination, we have determined the crystal and molecular structure of a cyclopentadienide complex, $U(C_5H_4CH_2C_6H_5)_3Cl$.

In order to insure a well-ordered crystal, a substituted cyclopentadiene was chosen as a ligand. To minimize perturbation of the electronic structure of the cyclopentadienyl anion a saturated carbon substituent was desired, but one for which the side chain would promote ordered crystallization. The benzyl group was chosen for this purpose because of the crystallization energy usually released by the π stacking forces between aromatic rings.

The compound was prepared in a manner similar to related materials. Characterization was by elemental analysis, nmr spectra, mass spectra, and the final structure analysis. Crystals suitable for x-ray studies were obtained by controlled evaporation of a saturated cyclohexane-toluene solution of the complex under argon atmosphere at room temperature. The apparently oxygen-stable, but water-sensitive, crystals were mounted in thin-walled quartz capillaries with Kel-F fluorocarbon grease under an argon atmosphere. Deep red trapezoidal prisms of $U(C_5H_4CH_2C_6H_5)_3Cl$ have the following crystal data: monoclinic space group $P2_1/n$, cell constants $a = 11.133(2)$, $b = 16.275(3)$, $c = 16.367(3)$ Å, $\beta = 100.45(2)^\circ$, $z = 4$,

$\rho_{\text{obs}} = 1.68$, and $\rho_{\text{calc}} = 1.68 \text{ g/cm}^3$. The structure has been refined by full-matrix least-squares methods using 2964 independent reflections with $F^2 > 3\sigma(F^2)$ and a model which includes anisotropic thermal motion with fixed hydrogen positions to a standard unweighted R factor of 3.13%.

The crystal structure consists of four discrete molecules of $\text{U}(\text{C}_5\text{H}_4\text{CH}_2\text{C}_6\text{H}_5)_3\text{Cl}$ per unit cell. A stereoscopic view of the unit cell is shown in Fig. 1. There are no unusually short intermolecular non-bonded distances (less than 4.1\AA). In particular, there is no evidence of stacking of the phenyl rings. This surprising result counters the reason for preparing this derivative and is apparently due to the fan configuration of these rings imposed by the coordination geometry.

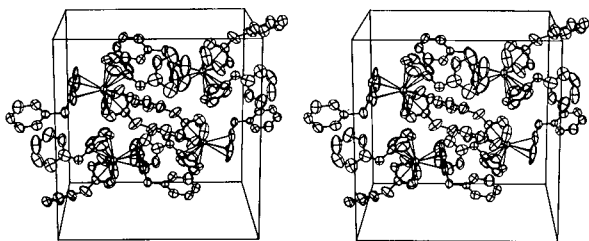


Fig. 1. A stereoscopic packing diagram of $\text{U}(\text{C}_5\text{H}_4\text{CH}_2\text{C}_6\text{H}_5)_3\text{Cl}$ viewed normal to the y-z plane. The entire unit cell is shown. The horizontal axis is *a* and the vertical is *c*. The origin of the cell is the lower left rear corner. (XBL 734-453)

A stereoscopic drawing of the molecule viewed approximately parallel to the uranium-chlorine bond is shown in Fig. 2. A perspective drawing of the molecule viewed perpendicular to the uranium-chlorine bond is shown in Fig. 3.

The molecular structure consists of a uranium atom symmetrically bonded to the carbon atoms of three planar aromatic cyclopentadienyl anions at an average distance of $2.733(1)\text{\AA}$ and to one chloride ion at $2.627(2)\text{\AA}$ in a distorted tetrahedral geometry with approximately C_{3v} coordination symmetry. The uranium atom is located 0.428\AA above the plane defined by the centers of the three cyclopentadienyl anions, in contrast to a distance of 0.824\AA expected for tetrahedral geometry. The average bond length in the three planar cyclopentadienyl anions is $1.374(2)\text{\AA}$. The average bond distance for the three planar benzene rings is $1.359(5)\text{\AA}$. The average C-C-C bond angle about the methylene carbon

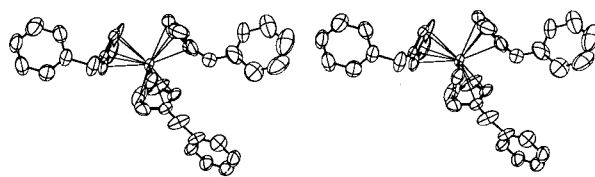


Fig. 2. A stereoscopic diagram of $\text{U}(\text{C}_5\text{H}_4\text{CH}_2\text{C}_6\text{H}_5)_3\text{Cl}$ viewed approximately parallel to the uranium-chlorine bond. Thermal ellipsoids are drawn at the 40% probability contour scale. An isotropic temperature factor of $5.0 \text{ e}/\text{\AA}^3$ has been assigned to methylene carbon atom, C_{b30} (located in lower left corner), since its anisotropic temperature factors are unusually large. (XBL 734-456)

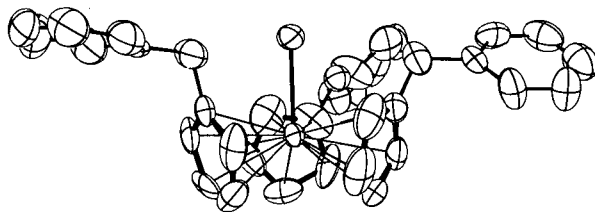


Fig. 3. The $\text{U}(\text{C}_5\text{H}_4\text{CH}_2\text{C}_6\text{H}_5)_3\text{Cl}$ molecule viewed perpendicular to the uranium-chlorine bond. Thermal ellipsoids are drawn at the 40% probability contour scale. Isotropic methylene carbon, C_{b30} , is located to the right of the chlorine atom. (XBL 734-457)

atoms of $118.2(40)^\circ$ is an appreciable deviation from tetrahedral geometry.

This structure provides the first proof of the symmetrical pentahapto bonding in cyclopentadienyl complexes of the actinides. Presumably the lanthanide complexes also show this geometry. The complicated bridging structure reported for $\text{Sm}(\text{C}_5\text{H}_5)_3^{11}$ would appear to be anomalous, but the severe experimental difficulties associated with that structure analysis leaves the issue open.

Footnotes and References

† Condensed from a report accepted for publication in *Inorganic Chemistry*.

* Department of Chemistry, University of California, Berkeley.

1. Three relatively recent reviews of the chemistry of the organo-actinides and -lanthanides are:

(a) R. G. Hayes and J. L. Thomas, *Organometal. Chem. Rev. A.*, **7**, 1 (1971).

- (b) H. Gysling and M. Tsutsui, *Adv. in Organometal. Chem.* 9, 361 (1970).
- (c) F. Calderazzo, *Organometal. Chem. Rev. B.*, 9, 131 (1972).
2. A. Zalkin and K. N. Raymond, *J. Am. Chem. Soc.* 91, 5667 (1969).
 3. A. Avdeef, K. N. Raymond, K. O. Hodgson, and A. Zalkin, *Inorg. Chem.* 11, 1083 (1972).
 4. K. O. Hodgson, D. Dempf, and K. N. Raymond, *Chem. Comm.* 1971, 1592.
 5. K. O. Hodgson and K. N. Raymond, *Inorg. Chem.*, in press.
 6. K. O. Hodgson and K. N. Raymond, *Inorg. Chem.* 11, 171 (1972).
 7. K. O. Hodgson and K. N. Raymond, *Inorg. Chem.* 11, 3030 (1972).
 8. M. Cesari, U. Pedretti, A. Zaggatta, G. Lugli, and W. Marconi, *Inorg. Chim. Acta* 5, 439 (1971).
 9. J. L. Atwood, J. H. Burns, and P. G. Laubereau, Abstract J10, American Crystallographic Society, Winter Meeting, January 1971.
 10. C. H. Wong, T. Y. Lee, and Y. T. Lee, *Acta Cryst. Sect. B*, 25, 2580 (1969).
 11. C. H. Wong, Y. M. Yen, and T. Y. Lee, *Acta Cryst. Sect. B*, 18 340 (1965).
 12. J. H. Burns and P. G. Laubereau, *Inorg. Chem.* 10, 2789 (1971).

THE CRYSTAL STRUCTURE OF
 ℓ -FERROUS-TRIS(1, 10-PHENANTHROLINE)
 BIS(ANTIMONOUS \underline{d} - TARTRATE) OCTAHYDRATE[†]

A. Zalkin, D. H. Templeton, and T. Ueki*

Ferrous ion and 1, 10-phenanthroline make octahedral complexes which exist in enantiomers that can be resolved by precipitation of the ℓ -isomer with antimony \underline{d} -tartrate. Professor R. E. Powell of this University provided us crystals of this precipitate and suggested that we determine the structure and absolute configuration by x-ray diffraction to permit a check of methods of configuration determination by theoretical analysis of the optical properties. We show that the $(-)-[\text{Fe phen}_3]^{2+}$ which precipitates with \underline{d} -tartrate is in the conformation of a left-handed propeller, in agreement with the assignment of McCaffery, Mason, and Norman¹ on the basis of analysis of circular dichroism, thus providing a confirmation of the validity of that method.

Another result of this study is that the antimony tartrate, which has been formulated classically in tartar emetic and similar salts as "antimonyl tartrate," $\text{SbO}(\text{C}_4\text{H}_4\text{O}_6)^-$, or sometimes as $\text{H}_2\text{O Sb}(\text{C}_4\text{H}_2\text{O}_6)^-$, exists in this crystal as a cyclic dimer of composition $((\text{C}_4\text{H}_2\text{O}_6)\text{Sb})_2^{2-}$. In this complex Sb(III) has displaced hydrogen from the alcohol groups as well as the carboxyl groups and is complexed only by tartrate. The same complex anion has been found by Kiosse, Golovastikov,

and Belov² in \underline{d} , ℓ - $(\text{NH}_4)_2\text{Sb}_2(\text{C}_4\text{H}_2\text{O}_6)_2 \cdot 4\text{H}_2\text{O}$, by Kiosse, Golvastikov, Ablov, and Belov³ in \underline{d} - $(\text{NH}_4)_2\text{Sb}_2(\text{C}_4\text{H}_2\text{O}_6)_2 \cdot 3\text{H}_2\text{O}$, and by Kamenar, Grdenic, and Prout⁴ in \underline{d} , ℓ - $\text{K}_2\text{Sb}_2(\text{C}_4\text{H}_2\text{O}_6)_2 \cdot 3\text{H}_2\text{O}$.

The sample of ℓ -ferrous tris(1, 10-phenanthroline) bis(antimonous \underline{d} -tartrate) octahydrate consisted of crystals of small deep-red needles. A fragment ~0.1 mm in diameter and ~0.3 mm long was glued to a pyrex fiber in air. Cell dimensions and intensities were measured with a manual quarter-circle Eulerian-cradle goniostat, using a scintillation counter and Zr filtered Mo K α x-rays. Counts for 10 sec each were made of 1748 independent reflections, using a stationary-counter stationary-crystal technique; these include all the reflections whose indices are positive and whose Bragg angles are less than 22.5°. Background was plotted as a function of 2θ . Eighty reflections were observed to be equal to or below background, and an additional 64 had intensities less than an estimated standard deviation; in the least-squares refinements these data were assigned zero weights. No correction was made for absorption or extinction.

In the course of some experiments using

CuK α radiation, the cell dimensions were observed to be very much affected by relative humidity. When the relative humidity, as read from a simple Abbeon Relative Humidity Indicator, read 30% the trigonal cell dimensions were calculated to be $a = 18.55$ and $c = 12.00$ Å; at 46% they swelled to 18.61 and 12.04 Å. This behavior is somewhat similar to that we observed in collecting data for ferrichrome-A.⁵ Had we had fluctuations to the limits of the two extremes in humidity reported above, the error in the 2θ angle at 45° with Mo x-rays is about 0.15; this does not produce a serious setting error, and in fact no problem was noticed during the manual collection of the data. With copper radiation, setting errors are serious, for at a comparable $\sin\theta/\lambda$ value the error amounts to about 0.6° .

The cell dimensions are $a = 18.58 \pm 0.02$ and $c = 12.04 \pm 0.02$ Å at $\sim 24^\circ$; the accuracy is limited by the humidity effect and these reported values are estimated to have been measured when the relative humidity was between 35 and 40%. The observed Laue symmetry of the reflections is $\bar{3}ml$. The observed setting of the symmetry $I(hkl) = I(kh\bar{l})$, the known asymmetry of the molecules, and the observed absences where $00l \neq 3n$ indicate the enantiomorphic pair of space groups $P3_121$ and $P3_221$ as the sole choices; anomalous dispersion effects established the space group to be $P3_221$, (D_3^2). Allowing for three formula units per unit cell, the calculated x-ray density is 1.77 g/cc.

The positions of the iron and antimony atoms were readily determined from a three-dimensional Patterson map. The rest of the structure was determined by Fourier and least-squares methods. Hydrogen atoms did not show up very well on the difference Fourier maps, and eventually the parameters of all but the water hydrogens were included but constrained to their estimated positions with a fixed isotropic thermal parameter of 5.0 \AA^2 . From the humidity effect it is evident that water is loosely bound in this crystal and most probably occurs in its sites with partial occupancy. This conclusion is supported by the large temperature parameters of the water oxygen atoms. Since there is no clear-cut ordered hydrogen bond pattern in the water substructure, we could not estimate the hydrogen positions of the water molecules. The refinement was arbitrarily started in space group $P3_121$, but this was changed to $P3_221$ in order that the configuration of the *d*-tartrate would be the same as that reported by Bommel and Bijvoet.⁶ The final *R* factor on 1600 non-zero weighted data is 0.048; the weighted *R*₂ factor is 0.056; the standard deviation of an observation of unit weight is 1.07; and the *R* factor for all 1748 data, including the zero-weighted ones, is 0.057. A difference function based on the final set of parameters was calculated. The maximum peak height on this map was $0.8 e/\text{\AA}^3$. The largest peaks appear near the antimony atom. From the size of these peaks and their locations, it is evident that there is no anti-mononyl type oxygen in this compound.

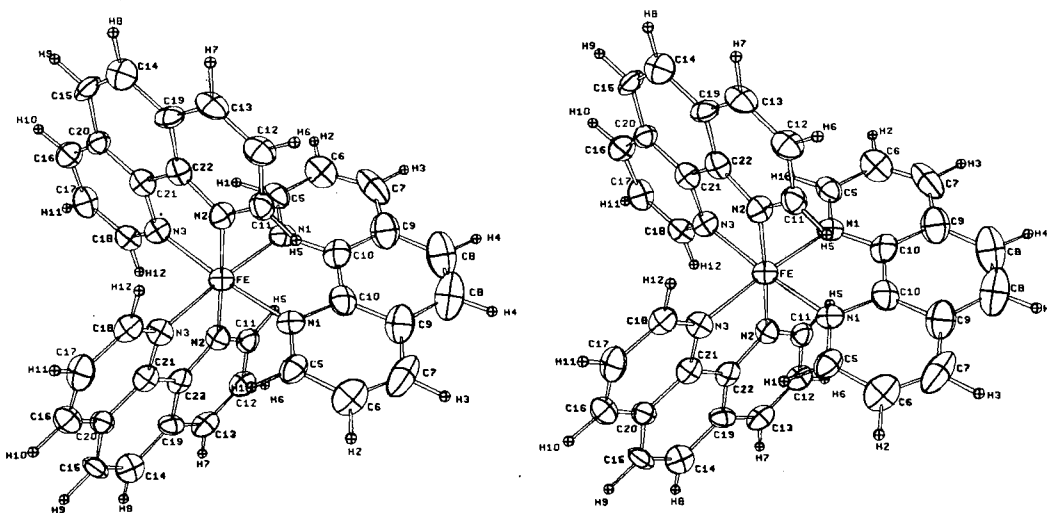


Fig. 1. Stereoscopic view of the (−)₅₈₉Fe phen₃²⁺ ion. (XBL 713-582)

A series of refinements made with the anomalous dispersion reversed resulted in R increasing from 0.048 to 0.052, and R_2 went from 0.056 to 0.062. This is in agreement with the configuration for the *d*-tartrate determined by Bommel and Bijvoet.⁶ An additional confirmation of the absolute configuration came from 528 data CuK α representing about 120 independent reflections measured with CuK α radiation. The Fe and Sb were refined anisotropically; carbon, oxygen, and nitrogen were included with isotropic thermal parameters but were not refined; hydrogen atoms were omitted. The set of 120 reflections refined to $R = 0.06$ with the correct configuration; when the anomalous dispersion effect was reversed the R factor went to 0.10.

The cation consists of an iron atom complexed by three planar phenanthroline ligands to form a left-handed propeller-type structure; see Fig. 1. In keeping with recent nomenclature proposals⁷ this ion would be described as $\Lambda(-)589\text{Fe phen}_3^{2+}$, phenanthroline. The ion itself lies on a crystallographic twofold axis, but its molecular symmetry is also very nearly threefold. The iron atom is coordinated to all six nitrogen atoms of the three phenanthroline groups at an average distance of $1.97 \pm 0.01 \text{ \AA}$.

The anion consists of a dimer of antimony tartrate on a crystallographic two-fold axis. Figure 2 shows a stereoscopic view of this ion. Each antimony is coordinated to four oxygen atoms from the tartrate ligands, and there is no evidence in this study of any further coordination to the antimony, i.e., an antimonyl oxygen. The same complex has been reported with very similar shape in the studies cited above.²⁻⁴

The anion and cation pack in a way which is not simple to describe. A stereographic view

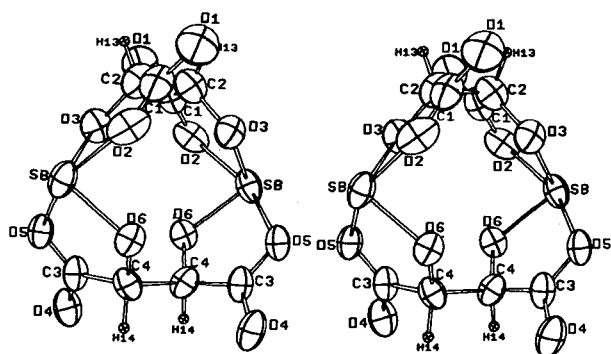


Fig. 2. Stereoscopic view of the bis(antimony *d*-tartrate)²⁻ ion. (XBL 711-581)

of the structure looking down the three-fold axis is shown in Fig 3.

The water structure in this crystal is indicated in Fig. 3; in this figure all contact distances less than 3.04 \AA are indicated with a connection. The temperature factors of the water molecules are large, which probably represents incomplete occupancy and disorder. The observation that the cell dimensions change reversibly and radically with humidity is indicative that water can readily enter and leave the crystal, and that these sites were partially occupied under the conditions of the experiment.

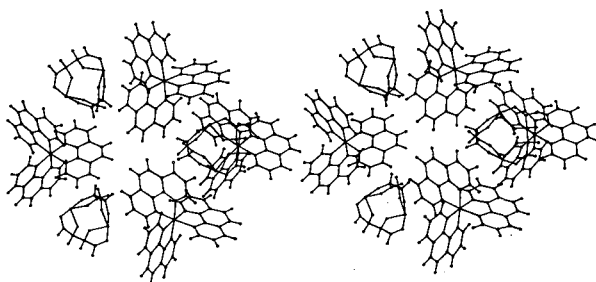


Fig. 3. Stereoscopic packing diagram as viewed down the c axis. (XBL 718-1267)

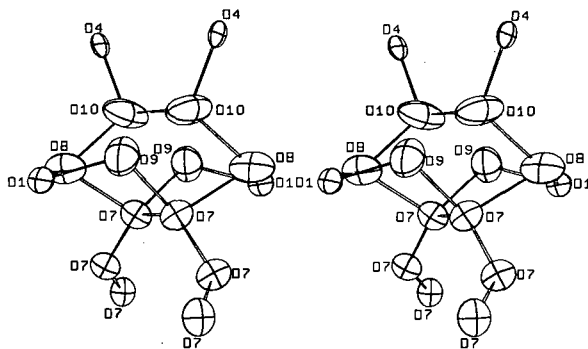


Fig. 4. Stereoscopic view showing the water oxygen structure. Atoms O(7) through O(10) represent water oxygen atoms; O(1) and O(4) represent tartrate oxygen atoms. (XBL 718-1268)

Disorder in the water structure is evident in the close approach across twofold axes of O(7) to another O(7) and similarly O(10) to O(10); for if the close approaches are due to hydrogen bonding one must invoke disorder to describe the hydrogen atom positions.

Footnotes and References

† Condensed from LBL-1265; submitted to *Inorganic Chemistry*.

* Present address: University of Osaka, Osaka, Japan.

1. A. J. McCaffery, S. F. Mason, and B. J. Norman, *J. Chem. Soc. (A)*, 1969, 1428.

2. G. A. Kiosse, N. I. Golovastikov, and N. V. Belov, *Dokl. Akad. Nauk SSSR* **155**, 545 (1964).

3. G. A. Kiosse, N. I. Golovastikov, A. V. Ablov, and N. V. Belov, *Dokl. Akad. Nauk*

SSSR **177**, 329 (1967).

4. B. Kamenar, D. Grdenic, and C. K. Prout, *Acta Crystallogr. Sect. B*, **26**, 181 (1970).

5. A. Zalkin, J. D. Forrester, and D. H. Templeton, *J. Am. Chem. Soc.* **88**, 1810 (1966).

6. A. J. van Bommel and J. M. Bijvoet, *Acta Cryst.* **11**, 61 (1958).

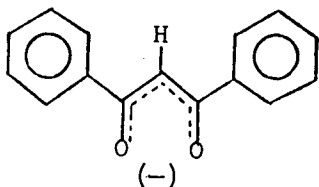
7. Tentative Proposals for Nomenclature of Absolute Configurations Concerned with Six-Coordinated Complexes Based on the Octahedron, *Inorg. Chem.* **9**, 1 (1970).

INVESTIGATIONS OF ALKALINE-EARTH β -DIKETONE COMPLEXES.

I. THE CRYSTAL AND MOLECULAR STRUCTURE OF BIS(DIMETHYLFORMAMIDO)BIS(1,3-DIPHENYL-1,3-PROPANEDIONATO)MAGNESIUM[†]

F. J. Hollander,* D. H. Templeton, and A. Zalkin

Alkaline-earth ions are known to make complexes with various diketones, but few crystal structures of the compounds have been reported. We became interested in these substances and have investigated several complexes of 1,3-diphenyl-1,3-propanedione anion (DPP):



With Mg, Ca, and Sr as cations we obtained suitable crystals only when certain solvent molecules were involved in the coordination.

The compound was synthesized by combining an aqueous solution of magnesium acetate and an ethanolic solution of 1,3-diphenyl-1,3-propanedione (HDPP) in a strong $\text{NH}_3/\text{NH}_4\text{Cl}$, pH 10, buffer. A pale yellow precipitate formed

immediately, and after several hours was filtered and dried in air. Evaporation of dimethylformamide (DMF) solutions of the compound yielded very good crystals. Weissenberg and precession photographs indicated a monoclinic unit cell with absences consistent with space groups Cc or $C2/c$. Solution of the structure confirmed $C2/c$ as the space group. The cell parameters and their standard deviations are $a = 16.893(3) \text{ \AA}$, $b = 12.853(2) \text{ \AA}$, $c = 16.927(3) \text{ \AA}$, $\beta = 117.085(5)^\circ$, at 23°C . The density, $Z = 4$, is $d_c = 1.10 \text{ g/cm}^3$. Intensity data were collected with a Picker/Nuclear four-circle diffractometer, using graphite monochromatized $\text{Cu K}\alpha$ radiation and a θ - 2θ scan technique. A total of 2433 unique reflections were measured; 614 reflections were smaller than their standard deviation.

The structure was solved by "direct methods" followed by a series of Fourier and least-squares calculations. Hydrogen atoms were located and refined with isotropic thermal parameters; all of the other atoms were given anisotropic thermal parameters. The final R_1 was 0.067 for 1817 reflections. The final weighted R_2 was 0.065 and the standard deviation of an observation of unit weight was 1.30.

The structure is separated into well-defined complex groups with composition $\text{Mg}(\text{DPP})_2(\text{DMF})_2$, Fig. 1. The six oxygen atoms coordinating the magnesium lie on the corners of a

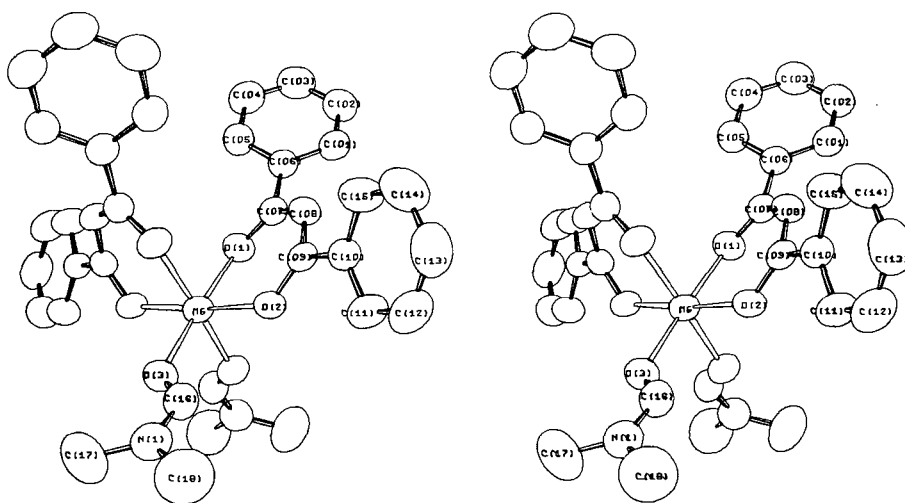


Fig. 1. Stereoscopic view of the complex, showing configuration and labeling. The two-fold crystallographic axis runs vertically in the plane of the drawing. Hydrogens have been omitted for clarity. Thermal ellipsoids are scaled to include 50% probability. (XBL 722-136)

slightly distorted octahedron. The distances from the magnesium to the oxygens in the DPP ligand are identical to within a standard deviation, at 2.055(2) Å and 2.057(3) Å, while the Mg-O distance to the DMF is slightly, but significantly, longer at 2.095(3) Å. Both of these distances fall well within the range for typical Mg-O distances in the literature (2.0-2.15 Å), with the Mg-O(DPP) distance being shorter than the Mg-O(DMF), as expected from electrostatic interactions.

The complexes themselves are packed in an interlocking manner shown in Fig. 2. The shortest inter-complex contacts between non-hydrogen atoms is 3.39 Å.

The octahedral coordination of Mg in $\text{Mg}(\text{DPP})_2(\text{DMF})_2$ is similar to that exhibited by other β -diketone complexes of divalent metals, e.g., diaquobis(acetylacetonato)-magnesium, $\text{Mg}(\text{AA})_2(\text{H}_2\text{O})_2$ (Morqsin, 1967),¹ $\text{Co}(\text{AA})_2(\text{H}_2\text{O})_2$ (Bullen, 1959),² and $\text{Ni}(\text{AA})_2(\text{H}_2\text{O})_2$ (Montgomery and Lingafelter, 1963).³ In each case the divalent metal cation is octahedrally coordinated by two β -diketone ligands and two solvent molecules in a monomeric unit. The $\text{Mg}(\text{DPP})_2$ complex differs from the other octahedral complexes in that the solvent molecules are *cis* to one another on the coordination octahedron (Fig. 1).

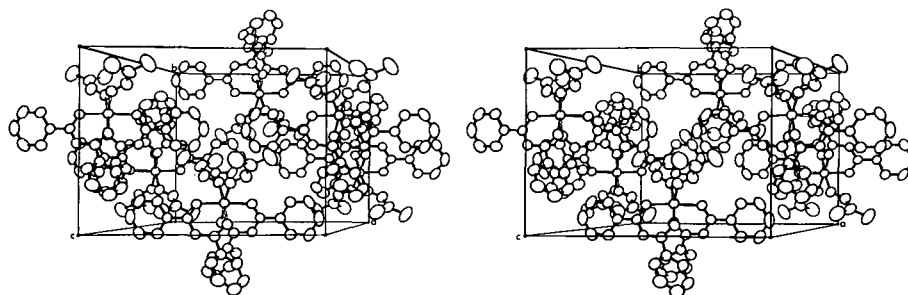


Fig. 2. Stereoscopic view of the unit cell, showing packing of complexes. Labeled axes are positive from the origin. Hydrogens have been omitted for clarity. (XBL 722-280)

Footnotes and References

† Condensed from LBL-1266; submitted to Acta Crystallographica.

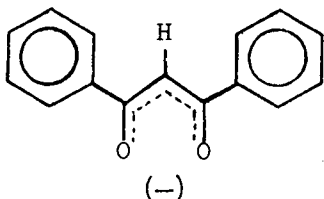
* Present address: Chemistry Department, University of Iowa, Iowa City, Iowa.

1. B. Morosin, Acta Cryst. 22, 316 (1967).
2. G. J. Bullen, Acta Cryst. 12, 703 (1959).
3. H. Montgomery and E. C. Lingafelter, Acta Cryst. 17, 1481 (1963).

INVESTIGATIONS OF ALKALINE-EARTH β -DIKETONE COMPLEXES.
 II. THE CRYSTAL AND MOLECULAR STRUCTURE OF
 BIS(1,3-DIPHENYL-1,3-PROPANEDIONATO)CALCIUM
 HEMIETHANOLATE[†]

F. J. Hollander,* D. H. Templeton, and A. Zalkin

Alkaline-earth metal cations form complexes with the anion of 1,3-diphenyl-1,3-propanedione:



We succeeded in crystallizing the calcium complex only when ethanol was present.

The complex was synthesized by mixing a solution of calcium acetate in aqueous ethanol with an ethanolic solution of 1,3-diphenyl-1,3-propanedione (HDPP) and adding concentrated $\text{NH}_3/\text{NH}_4\text{Cl}$, pH 10, buffer. A lemon yellow precipitate appeared immediately upon addition of the buffer solution. The mixture was refluxed for one hour to allow the reaction to go to completion. The precipitate dissolved on heating but reappeared as the mixture was cooled. It was filtered and dried in air and stored in a desiccator over Drierite. Attempts to recrystallize the complex generally yielded a viscous orange oil. However, well-formed clear yellow crystals were obtained by slow evaporation of a warm chloroform solution. The oil dissolved in many organic solvents, but formed a cloudy solid on addition of ethanol. The crystals were triclinic with cell dimensions $\underline{a} = 15.247(1) \text{ \AA}$, $\underline{b} = 13.555(1) \text{ \AA}$,

$\underline{c} = 14.097(3) \text{ \AA}$, $\alpha = 74.64(1)^\circ$, $\beta = 95.97(1)^\circ$, $\gamma = 113.59(1)^\circ$. For $Z=4$, the density is 1.32 g/cm^3 . A crystal approximately 0.12 mm in radius was used for data collection, using monochromatized Cu K α radiation and a θ - 2θ scan technique. In the entire experiment 5824 reflections were measured, including remeasurements in connection with the decay correction. The standards showed a decrease of about 10%. The data were corrected accordingly and processed to give 5294 unique reflections of which 4504 were observed greater than their standard deviations. No correction was made for absorption ($\mu = 23 \text{ cm}^{-1}$).

The structure was solved using "direct methods."

The assumption of the centric space group $\text{P}\bar{1}$ is confirmed by the successful refinement of the structure. Anisotropic refinement of the non-hydrogen atoms and isotropic refinement of the hydrogens proceeded by least-squares with three blocks to an \underline{R}_1 of 0.048. Availability of a larger computer allowed further refinement in two blocks, the first containing the two "inner" DPP molecules and the second containing the two "outer" DPP molecules and the ethanol. The final \underline{R}_1 was 0.040 for 4503 reflections, and the weighted \underline{R}_2 was 0.043. The standard deviation of an observation of unit weight was 1.14.

The complex consists of clusters of composition $(\text{Ca}_2(\text{DPP})_4(\text{C}_2\text{H}_5\text{OH}))_2$ around the symmetry at 0, $1/2$, $1/2$. There is only one such cluster per unit cell, and its neighbors are related to it by unit cell translations. There are no contact distances of less than 3.50 \AA between non-hydrogen atoms in different clusters. The two independent calcium atoms Ca(1) and Ca(2) are respectively six- and

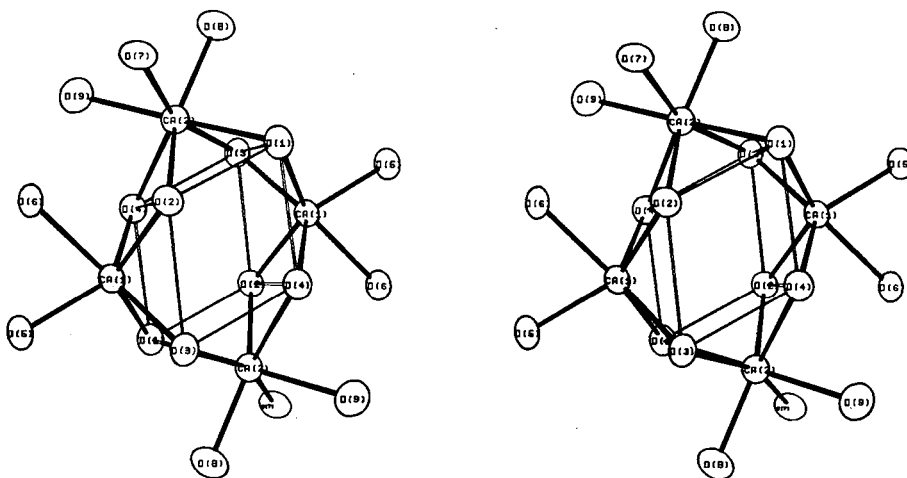


Fig. 1. Stereoscopic view of the coordination around the Ca atoms. The center of symmetry at 0, 1/2, 1/2 is in the center of the cluster. Thermal ellipsoids have been scaled to include 50% probability. (XBL 723-543)

seven-fold coordinated by the oxygens of the DPP ligands and the ethanol (Fig.1). Each calcium shares two oxygens with each of two neighboring calcium atoms of the other kind so that four of them are linked around the center of symmetry. The bridging oxygens, O(1) and O(2) of DPP(1), O(3) and O(4) of DPP(2), form a slightly distorted parallelepiped. Ca atoms cap each of four nearly rectangular faces, and DPP ligands project into the area above the two non-rectangular faces (Fig.2). The Ca-O

distances average 2.367 \AA with a standard deviation of 0.026 \AA calculated from the scatter of the measurements. The average compares well to the sum of the crystal radii (Pauling, 1960),¹ 2.39 \AA .

The bond distances and angles in the ligands are normal for complexed DPP molecules.²⁻⁴ The diketone ring is spread, with O-C-C and C-C-C bond angles $\sim 125^\circ$, to give the ligand a bigger "bite," and the interior

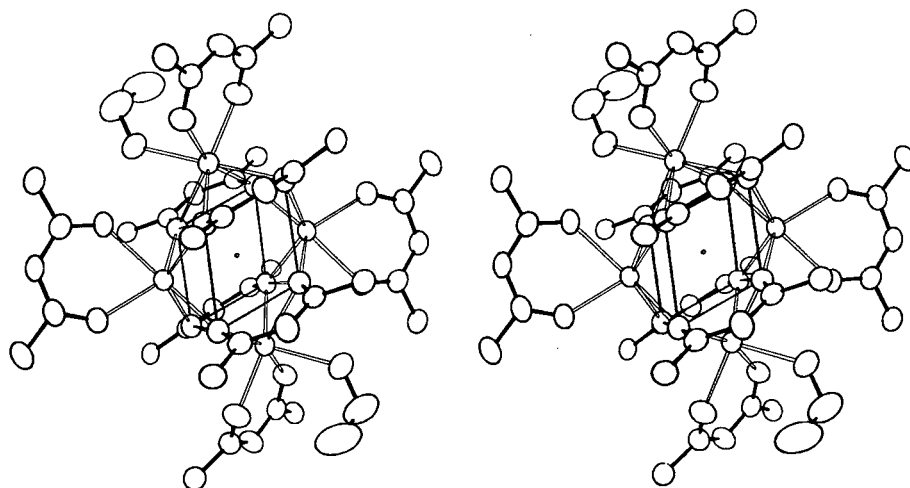


Fig. 2. Stereoscopic view of the complex cluster. Phenyl carbons not attached directly to the diketone and hydrogen atoms have been omitted for clarity. View direction and scaling of the thermal ellipsoids are the same as in Fig. 1. (XBL 724-663)

angle in the phenyl ring at the juncture to the diketone is reduced from 120° to $\sim 118^\circ$.

Footnotes and References

† Condensed from LBL-1267; submitted to *Acta Crystallographica*.

* Present address: Chemistry Department, University of Iowa, Iowa City, Iowa.

1. L. Pauling, *The Nature of the Chemical Bond*, 3rd ed. (Cornell University Press, Ithaca, New York, 1960).

2. F. J. Hollander, D. T. Templeton, and A. Zalkin, (1973a); in press (Mg(DPP)₂).

3. F. J. Hollander, D. T. Templeton, and A. Zalkin, (1973b); in press (Sr(DPP)₂).

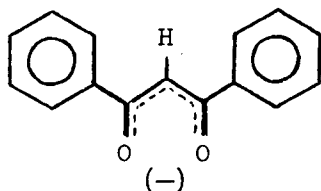
4. A. Zalkin, D. T. Templeton, and D. G. Karraker, *Inorg. Chem.* **8**(12), 2680 (1969).

INVESTIGATIONS OF ALKALINE-EARTH β -DIKETONE COMPLEXES.

III. THE CRYSTAL AND MOLECULAR STRUCTURE OF BIS(1,3-DIPHENYL-1,3-PROPANEDIONATO)STRONTIUM HEMIACETONATE†

F. J. Hollander,* D. H. Templeton, and A. Zalkin

Alkaline-earth metal cations form complexes with the anion of 1,3-diphenyl-1,3-propanedione:



This paper reports the structure of Sr(DPP)₂ hemiacetate. The complex forms tetrameric polymers of the same general configuration as those found for the DPP complex of calcium. However, the solvent molecule included in the Sr complex is acetone, rather than the ethanol of the Ca complex and there are differences in the details of the polymer shape. Thus, despite the fact that the general form of the complexes are similar and the space group ($P1$) the same, the structures are not isomorphous and the unit cells cannot be brought into congruence.

The complex was synthesized by using a modification of the method of Hammond, Nonhebel, and Wu (1963). Strontium nitrate was dissolved in a small amount of water, and

ethanol added until precipitation was just observed. This solution was added to an ethanolic solution of 1,3-diphenyl-1,3-propanedione (HDPP), and a strong aqueous NH₃/NH₄Cl, pH 10, buffer was added to the mixture. A whitish precipitate [probably either Sr(NO₃)₂ or HDPP] immediately formed, and the mixture was refluxed for an hour with constant stirring. The precipitate dissolved, and upon cooling a very pale yellow crystalline precipitate appeared which was filtered and dried in air. Attempts to recrystallize the compound generally yielded a viscous oil, but finally a few crystals were obtained by very slow evaporation of an ethanol solution with a very small amount of acetone added to it. Of these few, only one was good enough for crystallographic study. This crystal, a thin plate of approximate dimensions 0.03 × 0.17 × 0.32 mm was fixed to a glass fiber. Precession photographs indicated a triclinic unit cell. The cell parameters are: $a = 13.759(10) \text{ \AA}$, $b = 14.182(9) \text{ \AA}$, $c = 16.034(9) \text{ \AA}$, $\alpha = 107.57(3)^\circ$, $\beta = 90.36(3)^\circ$, $\gamma = 113.07(3)^\circ$ at 23°C, where the standard deviations are those estimated by least squares; these parameters were used throughout the structure analysis. We estimate respectively 0.05 Å, 0.01 Å, 0.02 Å, 0.03°, 0.2°, and 0.2° as standard deviations which reflect the variation of parameters during the experiment. The calculated density for $Z = 4$ is 1.38 g/cm³. Data were collected by using a θ - 2θ scan technique and graphite-monochromatized MoK α radiation. All reflections in the hemisphere of reciprocal space were collected for $2\theta < 30^\circ$; no reflection beyond this region were strong enough to be observed. Two reflections were

monitored every 100 data. A degradation of these intensities of ~16% was recorded and was adjusted accordingly. A total of 2371 reflections were measured; of these, 260 were measured with zero intensity; 684 were smaller than their standard deviation. An absorption correction was applied to the intensities, $\mu = 21.2 \text{ cm}^{-1}$. The correction factors ranged from 1.07 to 1.41.

Two independent Sr atoms were located by the three-dimensional Patterson function and gave $R_1 = 0.36$. Alternate difference Fourier and least-squares refinement revealed most of the non-hydrogen atoms of the complex. With only the Sr atoms given anisotropic thermal parameters, R_1 was 0.094. A difference Fourier showed a large triangular area of electron density with a peak at each corner and high density in the center, and attempts to refine this residual density as a disordered ethanol were unsuccessful. We then realized that the triangular region of electron density could also be fitted by an acetone molecule, and doing so resulted in a final R_1 of 0.088, R_2 of 0.072; standard deviation of observation of unit weights was 1.47. The thermal parameters of all of the acetone atoms were in keeping with those of the rest of the structure. No attempt was made to refine hydrogen atoms.

The complex consists of clusters of composition $\text{Sr}_2(\text{DPP})_4(\text{CH}_3)_2\text{CO}_2$ around the center of symmetry at the origin. The clusters are related only by unit cell translations, and the only inter-cluster contact of less than 3.50 \AA is 3.42 \AA between two phenyl carbon atoms across the center of symmetry at $0, 1/2, 0$. The Sr(1) and Sr(2) atoms are respectively

seven- and six-coordinated by the oxygens of the DPP ligands and the acetone (Fig. 1). Each Sr atom shares two oxygen atoms with each of two neighboring Sr atoms, forming a cluster around the center of symmetry. The bridging oxygens, O(1) and O(2) of DPP(1) and O(3) and O(4) of DPP(2), occupy the corners of a slightly distorted parallelepiped, with four rectangular faces capped by Sr atoms and the two nonrectangular faces occupied by the DPP ligands (Fig. 2). The distances from Sr to the bridging oxygens average 2.55 \AA with no significant difference between the two differently coordinated Sr atoms. The distances from the Sr atoms to the unshared oxygens average to 2.44 \AA indicating the expected tighter bonding to the unshared ligands, and the Sr(1) to O(9) distance is 2.60 \AA , in keeping with the fact that the acetone is uncharged and thus not as tightly bound as the negative DPP ligands.

The primary difference between the Sr and Ca molecular conformation is the degree of distortion of the central parallelepiped of O atoms (Fig. 1). The acute angle between the rectangular faces is 69° for the Ca and 83° for the Sr complex. The planes that make up the central parallelepiped are closer together in the Ca compound than they are in the Sr complex. These effects can be explained by the differences between the Ca-O and Sr-O bond lengths, which are compatible with the difference in ionic radius between Ca and Sr ($\text{Ca-O}_{\text{ave}} = 2.37 \text{ \AA}$, $\text{Sr-O}_{\text{ave}} = 2.55 \text{ \AA}$; $r_{\text{Ca}} = 0.99 \text{ \AA}$, $r_{\text{Sr}} = 1.13 \text{ \AA}$).

These results suggest that a combination of the bulk of the ligand and the length of the

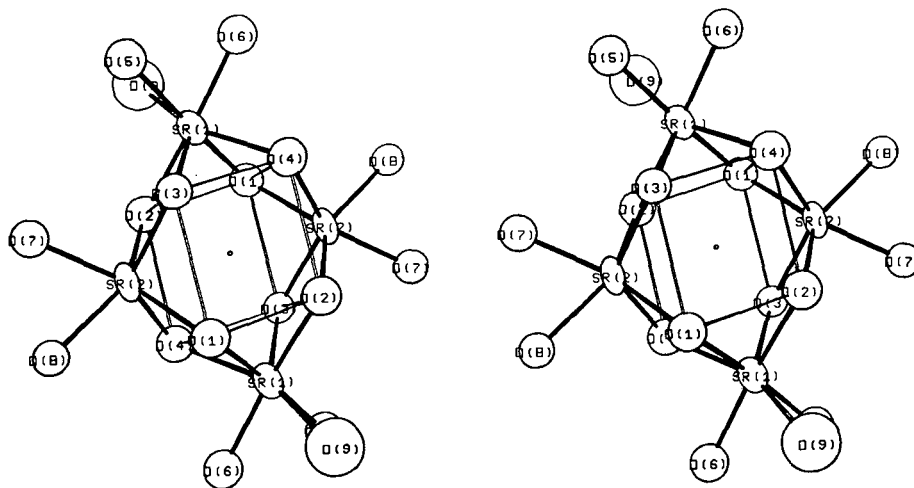


Fig. 1. Stereoscopic view of the coordination around the Sr atoms. The center of symmetry at $0, 0, 0$ is indicated. Thermal ellipsoids have been scaled to include 50% probability. (XBL 724-793)

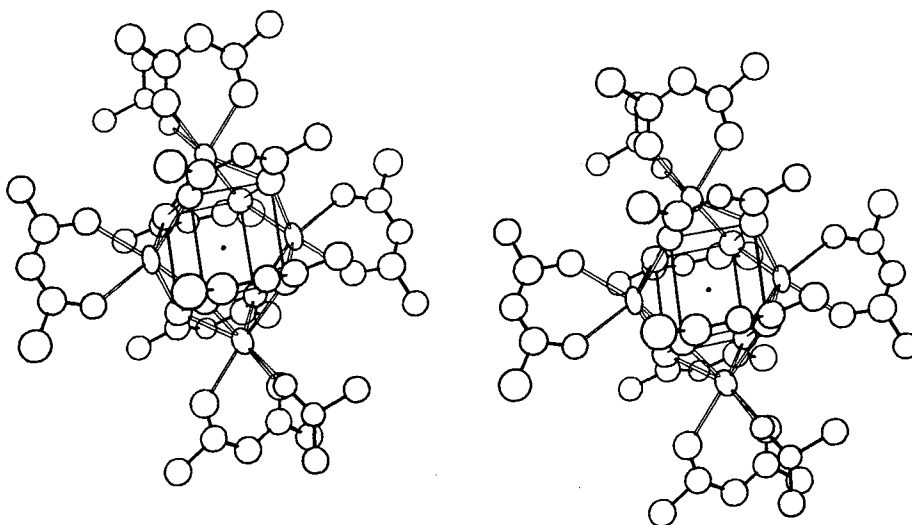


Fig. 2. Stereoscopic view of the complex cluster. Phenyl carbons except for those attached directly to the diketone have been omitted, and the acetone atoms have been given artificial thermal parameters for clarity. View direction and scaling of the thermal ellipsoids are the same as in Fig. 1. (XBL 724-792)

M-O bond is the criterion for whether or not polymerization is favorable. With a short M-O bond length, as with Mg or the divalent first-row transition metals, ligands with side groups as bulky as *t*-butyl (DPM) or phenyl (DPP) are forced too close to one another in the configurations necessary for polymerization. When the M-O distance increases, as for Ca, Sr, or Pr(III), then neighboring ligands need not be so close together, and the advantage of sharing ligands to get greater

coordination from the negative ions can be realized.

Footnotes

† Condensed from LBL-1268; submitted to Acta Crystallographica.

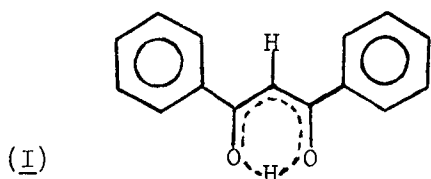
* Present address: Chemistry Department, University of Iowa, Iowa City, Iowa.

THE CRYSTAL AND MOLECULAR STRUCTURE OF 1, 3-DIPHENYL-1, 3-PROPANEDIONE ENOL[†]

F. J. Hollander,* D. H. Templeton, and A. Zalkin

The crystal structure of 1, 3-diphenyl-1, 3-propanedione (HDPP), **I**, was solved as part of a study of complexes of its anion with alkaline-earth metals¹ before we learned of another

determination of the structure.² We report our results for comparison with the earlier work as an example of two accurate determinations of the same structure.



The HDPP was recrystallized from aqueous ethanol. The crystals are orthorhombic, space group *Pbca*. The cell dimensions are $a = 10.853(1) \text{ \AA}$, $b = 24.441(1) \text{ \AA}$, and $c = 8.755(1) \text{ \AA}$ at 23° C as determined by least squares on twelve well-centered reflections in good agreement with the previous work [$a = 10.857(2)$, $b = 24.446(5)$, and $c = 8.756(2) \text{ \AA}$]. Intensity

data were collected on a crystal of dimensions $0.19 \times 0.23 \times 0.12$ mm, using monochromatized Cu K α radiation and a θ - 2θ scan technique on a Picker automatic diffractometer. 1724 unique data were collected, of which 1070 had $F > \sigma(F)$ and were included in least squares.

The structure was solved by direct methods. The structure was refined by least squares to a final R value of 0.027, with isotropic thermal parameters for hydrogen and anisotropic parameters for the other atoms. Details are given elsewhere.¹

Our results are similar but not identical to those of Williams.² We used individual thermal parameters for hydrogen atoms, which Williams did not, and reduced R_1 to 0.027, compared with Williams' $R_1 = 0.059$. Consideration of the distances and angles reveals no differences between the two structures that are much greater than the sum of the standard deviations for each. The hydrogen atom in the hydrogen bond, H(29), is found more nearly

equidistant from the two oxygen atoms than in the earlier determination, and shifts of slightly less than one standard deviation in its coordinates would make it exactly equidistant. The differences in the O(16)-C(13)-C(14)-C(15)-O(17) distances indicate a slight preference for the tautomer with H(29) on O(17) as in the earlier study.

Footnotes and References

† Condensed from LBL-1273; submitted to Acta Crystallographica.

* Present address: Chemistry Department, University of Iowa, Iowa City, Iowa.

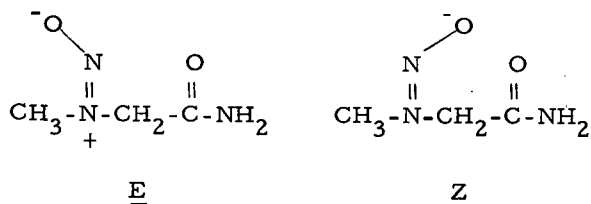
1. F. J. Hollander (Ph.D. thesis), LBL-670 (1972).

2. D. E. Williams, Acta Cryst. 21, 340 (1966).

THE CRYSTAL AND MOLECULAR STRUCTURE OF 2-(N-NITROSOMETHYLAMINO) ACETAMIDE†

L. K. Templeton, D. H. Templeton, and A. Zalkin

Kenyon and Rowley¹ found 2-(N-nitrosomethylamino) acetamide as the hydrolysis product of a secondary N-nitrosoamine. It crystallized as a mixture of needles and plates. On the basis of nmr spectra they concluded that the needles contained a mixture of the E and Z isomers:²



We report a crystal structure determination which confirms this result. We found a 50:50 mixture of the isomers with conformation as shown in Fig. 1.

Colorless, needlelike crystals, synthesized by the reaction of sarcosinamide with nitrous acid,¹ were provided by Professor Kenyon of the University of California, Berkeley. A crystal of dimensions $0.066 \times 0.042 \times 0.111$ mm was glued to the tip of a glass fiber in air.

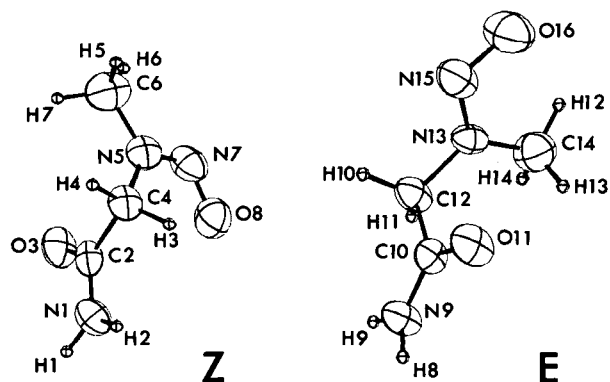


Fig. 1. Perspective drawing of the E and Z isomers. Thermal boundaries are at the 50% probability level. For this drawing the hydrogen atoms were given artificial thermal parameters of $B = 0.5$. (XBL 719-1339)

Preliminary x-ray diffraction data were obtained from oscillation and Weissenberg photographs taken with copper radiation. Accurate unit cell dimensions were determined from

measurement of $h\ 0\ 0$; $0\ k\ 0, 0\ 0\ l$ reflections, using a Picker automatic diffractometer equipped with a full circle goniostat, graphite monochromator. Intensity data were collected with the same instrument by a θ - 2θ scan technique. From monitoring three reflections it was found that there was a 30% decay in the intensities during the experiment, and the intensities were adjusted on the assumption that all reflections decreased at the same rate. No correction for absorption was made; it is estimated to affect the intensities no more than 7%. All reflections in the hemisphere $\pm h, k, \pm l$ were measured. Excluding systematic space group absences, there were 2444 data which represent 1417 unique reflections, of which 1184 are greater than one standard deviation.

The crystals are monoclinic with unit cell dimensions measured at room temperature ($\sim 24^\circ\text{C}$): $a = 16.681 \pm 0.030$, $b = 4.774 \pm 0.005$, $c = 14.318 \pm 0.015\ \text{\AA}$, $\beta = 92.95 \pm 0.2^\circ$. There are eight molecules of $\text{C}_3\text{H}_7\text{N}_3\text{O}_2$ (four of each isomer) in the unit cell. The calculated density $\rho = 1.367\ \text{g/cc}$ agrees well with the observed density $\rho = 1.36 \pm 0.02\ \text{g/cc}$ measured by flotation in solutions of chloroform and hexane. The extinction rules are characteristic of space group $\text{P}2_1/\text{n}$.

The structure was solved from statistics. The phases of normalized structure factors E were calculated for 16 possible combinations

of signs of four reflections. One combination of signs was better than the rest, with a consistency index of 0.80, compared with the next best value of 0.77. The Fourier synthesis of this best E set showed both the \underline{E} and \underline{Z} isomers and yielded the coordinates of the 16 non-hydrogen atoms (carbon, nitrogen, and oxygen) in the asymmetric unit.

With anisotropic thermal parameters (for the 16 atoms) the full-matrix least-squares refinement reduced R_1 to 0.089 for 1184 non-zero reflections. All 14 hydrogens except for one in the methyl group of the \underline{E} isomer showed well-defined peaks in a difference Fourier. With the addition of three positional parameters and an isotropic thermal temperature factor for each of the 14 hydrogens, refinement gave $R_1 = 0.044$.

Corresponding bond distances in the two isomers (Fig. 1) are equal within the experimental accuracy except perhaps the N-N and N-O distances; the latter differ respectively by three and two times the sum of the standard deviation. The dimensions of the amide groups (corrected for thermal motion) are in excellent agreement with the corresponding bond lengths C-N = 1.338(7) and C-O = 1.258(6) \AA reported by Denne and Small³ for acetamide, and C-N = 1.334(4) and C-O = 1.254(4) \AA reported by Chieh, Subramanian, and Trotter.⁴ For the amide-methylene bond (uncorrected for thermal motion) our values C-C = 1.513(4),

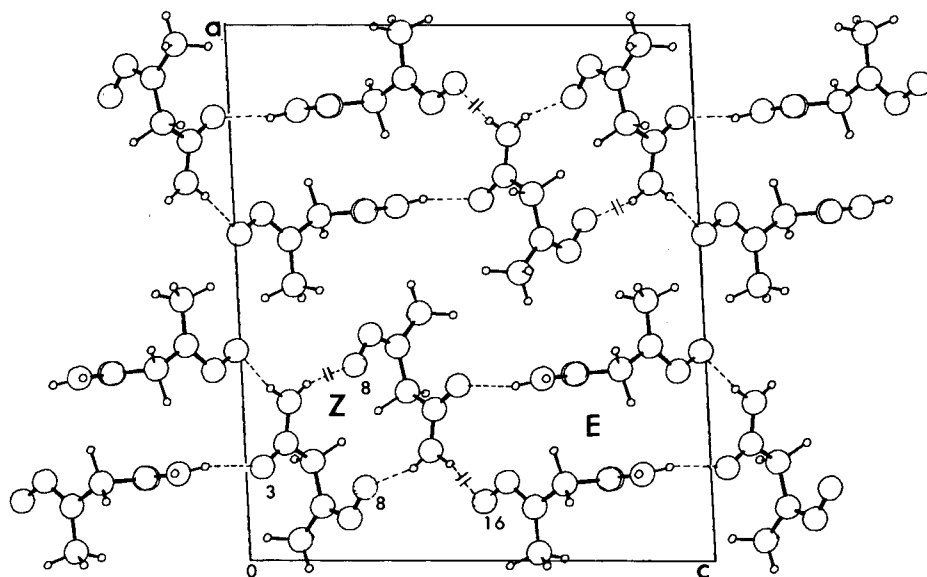


Fig. 2. Projection of the unit cell looking down the b axis. Hydrogens are represented by the small circles. The dotted lines are hydrogen bonds. When the line is broken the bond is to the molecule above or below. The numbers identify the different oxygen atoms.

(XBL 724-778A)

1.5184) Å are close to C-C = 1.507(4) in malonamide.⁴ The C-N bond lengths exhibit the partial double-bond character typical of amides. The bond lengths in the vicinity of the nitroso groups agree within 0.03 Å or better with corresponding bonds in gaseous nitrosodimethylamine as determined by electron diffraction:⁵ N-O = 1.235(2), N-N = 1.344(2), and N-C = 1.461(2) Å. We have failed to find reports of accurate determinations in the solid phase of structures of strictly analogous molecules.

Each amide hydrogen atom is pointed toward an oxygen atom at a reasonable distance for an N-H...O hydrogen bond. These bonds, as shown in Fig. 2, connect the amide of the *Z* molecule to nitroso oxygen atoms of each kind of molecule. The amide of the *E* molecule is connected to carbonyl oxygen atoms of each kind of molecule. These bonds connect the molecules in infinite layers parallel to *b* and *c*.

(±)4*a*, 8*a*, 14β-TRIMETHYL-18-NOR-5*a*, 13β-ANDROST-9(11)-en-3, 17-DIONE, A SYNTHETIC PRECURSOR TO FUSIDIC ACID[†]

D. L. Ward, D. H. Templeton, and A. Zalkin

Fusidic acid has been shown to be effective in combating infections caused by staphylococci. The total synthesis of the tetracyclic nucleus of fusidic acid has been accomplished by Dauben, *et al.*¹ yielding a (±) material whose NMR spectrum is essentially identical with that of the (+) material obtained from fusidic acid. The crystal and molecular structure determination of the synthetic (±) material, 4*a*, 8*a*, 14β-trimethyl-18-nor-5*a*, 13β-androst-9(11)-en-3, 17-dione, C₂₁H₃₀O₂, was undertaken to establish its structure and stereochemistry. The structural formula is shown in Fig. 1.

A crystal of approximate dimensions 0.30×0.16×0.13 mm ($\mu_{\text{Mo K}\alpha} = 0.81 \text{ cm}^{-1}$) was used. Weissenberg photographs revealed the diffraction conditions to be compatible with space groups C2/c and Cc. Diffraction data were measured at 24°C with an automatic diffractometer using graphite monochromatized Mo K α radiation: Monoclinic, C2/c, *a* = 19.562(6) Å, *b* = 11.915(4) Å, *c* = 15.623(4) Å, β = 107.84(4)°, 24°C, C₂₁H₃₀O₂, *M* = 314.47, *Z* = 8, *D_x* = 1.208 g·cm⁻³. Intensities for the hemisphere with *k* positive were collected for 2θ < 40° using the θ-2θ scan method. Assuming 2/*m* symmetry, equivalent reflections were averaged to give 1622 unique reflections of which 495, with *I* < 3σ(*I*), were given zero weight.

Footnote and References

[†] Condensed from LBL-669; Acta Cryst. B29, 50 (1973).

1. G. L. Kenyon and G. L. Rowley, J. Amer. Chem. Soc. 93, 5552 (1971).
2. Designated as *entgegen* and *zusammen*, IUPAC; J. Org. Chem. 35, 2849 (1970).
3. W. A. Denne and R. W. H. Small, Acta Cryst. B27, 1094 (1971).
4. P. C. Chieh, E. Subramanian, and J. Trotter, J. Chem. Soc. (A), 179 (1970).
5. P. Rademacher, R. Stølevik, and W. Lüttke, Angew. Chem. 80, 842 (1968).

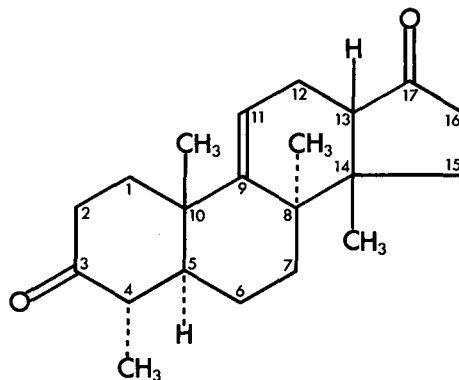


Fig. 1. Structural Formula
(XBL 7212-7483)

The crystal structure was solved using the program MULTAN.² It was refined by full-matrix least-squares to *R*₁ = 0.0336 and *R*₂ = 0.0412; *R*₁ = 0.0539 including zero-weighted data. Three additional cycles of full-matrix least-squares refinement using the polar complex hydrogen scattering factors as described by Templeton, Olson, Zalkin and Templeton³ led to *R*₁ = 0.338, *R*₂ = 0.0409, *R*₁ (including zero-weighted data) = 0.0538.

The structure is closely related to that of fusidic acid reported as the methyl ester 3-p-bromobenzoate by Cooper and Hodgkin.⁴ A major difference between the stereochemistry of the tetracyclic nucleus in the two structures is the 13β -hydrogen in the present compound leading to a *cis* C/D junction; this is apparently of no consequence in establishing a chemical relationship between the two compounds as the configuration at C(13) can be inverted by the enol-keto equilibrium at C(17) during the anticipated synthesis of fusidic acid from the present compound. The observed bond lengths do not appear to differ significantly

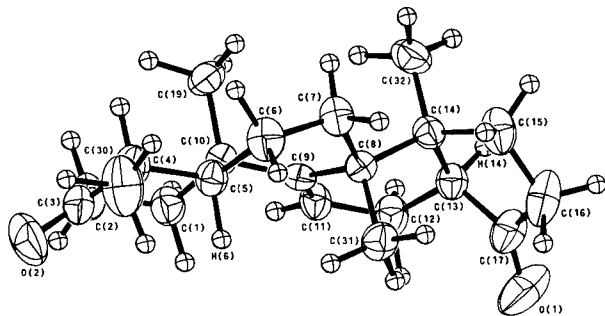


Fig. 2. Molecular Structure. The thermal ellipsoids were drawn at the 50% probability level and the hydrogens were given arbitrary temperature factors of 1.0 \AA^2 .
(XBL 7212-7482)

from the typical values for steroid structures. Angle distortion in the 5-member D ring appears to be a real effect of strains in the molecule resulting from the $>C=O$ entity at C(17), the $9(11) >C=C<$ bond, the *cis* C/D ring junction, and the methyl groups substituted at C(8) and C(14). Similar effects were reported for fusidic acid.⁴

A drawing of the molecule is shown in Fig. 2. This particular view of the molecule emphasizes the distortion of the tetracyclic nucleus from the relatively planar form found when there are all *trans* ring junctions and when there is no unsaturation in or adjacent to the rings.

Footnote and References

† Condensed from LBL-1609.

1. W. G. Dauben, G. Ahlgren, T.J. Leitereg, W. C. Schwarzel, and M. Yoshioka, submitted *J. Am. Chem. Soc.* **94**, 8593-8594 (1972).
2. G. Germain, P. Main, and M. M. Woolfson, *Acta Cryst.* **A27**, 368-376 (1971).
3. D. H. Templeton, A.J. Olson, A. Zalkin, and L. K. Templeton, Collected Abstracts of the Ninth International Congress of the I. U. Cr., Kyoto, Japan; abstract XVV-2 (1972).
4. A. Cooper and D. C. Hodgkin, *Tetrahedron* **24**, 909-922 (1968).

SCAVENGER EFFECTS IN THE RECOIL TRITIUM REACTIONS OF CYCLOHEXENE*

D. C. Fee and S. S. Markowitz

Many recoil tritium experiments have used scavengers to remove thermalized tritium atoms and radical intermediates from the system before such species can yield products which might be confused with high-energy tritium reactions.¹ The yield of products formed solely by high-energy (hot) reactions will remain unchanged over a wide range of scavenger concentrations. The yield of products formed by both thermal and hot processes will decrease rapidly with the addition of scavenger until a plateau is reached where the yield becomes relatively insensitive to scavenger concentration. In this region all thermal reactions, except with the scavenger, have presumably been suppressed and the yield is due entirely to hot reactions.²

The comparative efficiency of sulfur dioxide and oxygen as radical scavengers has recently been determined in the T+cyclohexene gas phase system.³ Ethylene-t and butadiene are primarily high-energy products from the unimolecular decomposition of excited cyclohexene-t formed by direct substitution.⁴ The ethylene-t yield exhibited identical scavenger plateaus with sulfur dioxide and oxygen scavenging. The butadiene-t yield was unaffected by sulfur dioxide scavenging but increased by nearly 50% with oxygen scavenging. This anom-

alous increase in the butadiene-t yield with oxygen scavenging is similar to an anomalous increase in the ethylene-t yield with O₂ scavenging that was reported by Urch and Welch in the T+ethane system.⁵

The anomalous ethylene-t increase in the T+ethane system was explained by Baker and Wolfgang.⁶ Apparently, in the absence of O₂, radiation-produced H atoms were being scavenged by the ethylene-t formed by hot tritium reactions. This reduced the ethylene-t yield in unscavenged systems. When O₂ is added, the radiation-produced H atoms were being scavenged by more efficient O₂ and the ethylene-t yield increased from essentially zero to its "hot" value.

We decided to determine how the butadiene-t yield from T+cyclohexene reactions varied with scavenging by butadiene-d₆ and by hydrogen sulfide. The pertinent rate constants are shown in Tables I and II. We use methyl radicals as representative of all alkyl radicals; the rate constants of other alkyl radicals are not known for all potential scavengers. Abstraction is the reaction whose product is H₂ and CH₄ when hydrogen atoms and methyl radicals are respectively one of the reactants. Addition is the reaction which removes H-atoms or methyl radicals

Table I. Hydrogen atom reaction rate constants at 25° C.

Reactant	Addition		Abstraction	
	[10 ⁹ cm ³ mol ⁻¹ sec ⁻¹]		[10 ⁹ cm ³ mol ⁻¹ sec ⁻¹]	
butadiene	1500	Ref. (7)	22	(7)
cyclohexene	600	(8)	n. d. ^a	
O ₂	300	(9)	-- ^b	
ethylene	200	(7)	13	(7)
trans-2-butene	180	(7)	24	(10)
H ₂ S	--		160	(7)
SO ₂	6	(11)	--	
n-butane	--		0.6	(12)

^aNot determined.

^bNot applicable.

Table II. Methyl radical reaction rate constants at 25° C.

Reactant	Addition		Abstraction	
	[10 ⁶ cm ³ mol ⁻¹ sec ⁻¹]		[10 ⁶ cm ³ mol ⁻¹ sec ⁻¹]	
O ₂	15 000 Ref. (13, 14)		-- ^b	
SO ₂	5 000	(13)	--	
H ₂ S	--		3 000	(15)
butadiene	160	(16)	n. d. ^a	
ethylene	1.2	(16)	0.02	(16)
trans-2-butene	0.3	(16)	0.2	(16)
cyclohexene	n. d.		n. d.	
n-butane	--		0.004	(17)

^aNot determined.

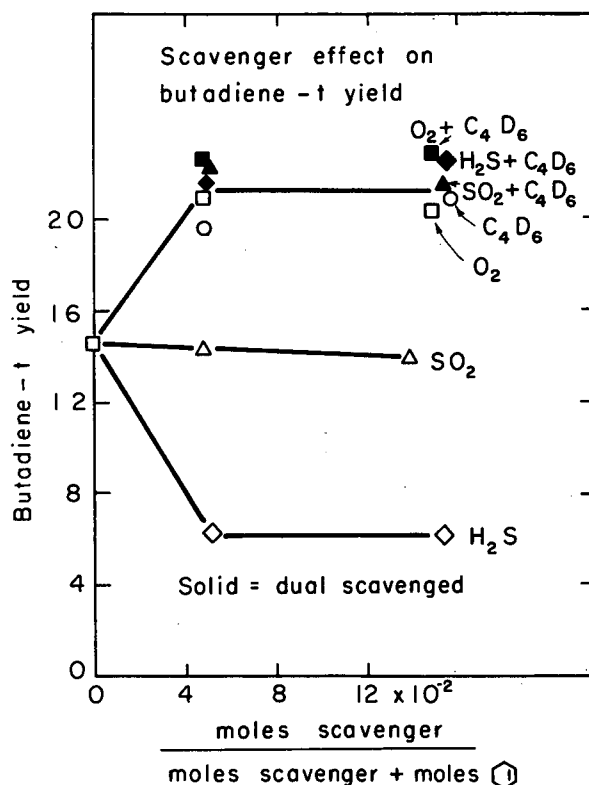
^bNot applicable.

from the system by forming a new radical (via radical addition to the double bond of the scavenger) or by forming a stable molecule such as CH₃SO₂. From these tables, two things are clear: 1) Butadiene-t is the most reactive hydrocarbon in the T+ cyclohexene system. It could be selectively depleted not only by hydrogen atoms but by also by radiolysis-produced radicals. However, a "radical contribution" to the anomalous increase in the butadiene-t yield in the oxygen-scavenged T+cyclohexene system can safely be neglected. Both O₂ and SO₂ are orders of magnitude more reactive with radicals than butadiene-t. 2) Butadiene-d₆ is the most efficient of the four scavengers (O₂, SO₂, H₂S, C₄D₆) for removing H atoms. The effect of butadiene-d₆ scavenging on the butadiene-t yield should be unambiguous.

Figure 1 shows that the butadiene-t yield increases with butadiene-d₆ scavenging. The

Fig. 1. The effects of O₂, SO₂, H₂S, C₄D₆ and C₄D₆ plus O₂, C₄D₆ plus SO₂, C₄D₆ plus H₂S on the butadiene-t yield from T+cyclohexene reactions. Product yields are listed relative to the cyclohexene-t yield as 100. The O₂ and SO₂ single scavenger points are from Ref. 3. The solid data points represent C₄D₆ plus another scavenger used jointly. The abscissa in this case does not include the moles of C₄D₆. The zero scavenger data point and the 5 mole % scavenger data point have been connected with line for clarity. We do not imply that the variation of yield with added scavenger is linear in this region. (XBL 726-3104)

scavenger plateau is identical to that obtained with O₂ scavenging. This supports the hypothesis that the butadiene-t yield is selectively depleted by radiolysis-produced H atoms in the absence of O₂. The butadiene-t yield de-



creases with H₂S scavenging. H₂S is a source of H atoms through radiolysis.¹⁸ Table I shows that H₂S is inefficient as an H atom scavenger. The increase in H atom concentration with no increase in the ability to scavenge H atoms (relative to butadiene-t) would further reduce the butadiene-t yield.

The hypothesis that butadiene-t is selectively depleted by reactions with H atoms from the radiolysis of H₂S and/or cyclohexene is supported by the dual scavenger data in Fig. 1. The solid data points show the effect on the butadiene-t yield when two scavengers are used simultaneously. All samples were scavenged by butadiene-d₆. The butadiene-d₆/(cyclohexene + butadiene-d₆) ratio was constant at 0.15. Varying amounts of H₂S, O₂, or SO₂ were added as indicated. The butadiene-t yield is the same for each of the combinations of scavengers and is slightly higher than for O₂ or butadiene-d₆ used solely.

Therefore we conclude that the "hot" butadiene-t value from T + cyclohexene reactions can only be determined with O₂ or butadiene-d₆ scavenging.

Footnote and References

* Condensed from LBL-668. Accepted by J. Inorg. and Nucl. Chem. 35, (1973).

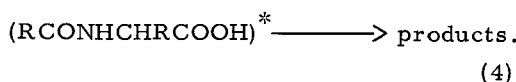
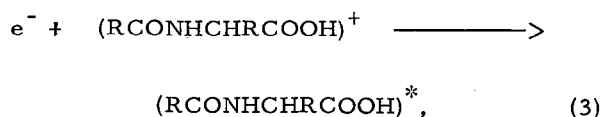
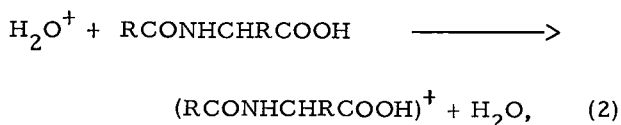
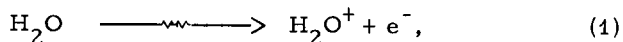
1. R. L. Wolfgang, Progress in Reaction Kinetics, III, edited by G. Porter (Pergamon, Oxford, 1965).
2. J. Hawke and R. L. Wolfgang, Radiochimica Acta **14**, 116 (1970).
3. D. C. Fee, S. S. Markowitz, and J. K. Garland, Radiochimica Acta **17**, 135 (1972).
4. R. W. Weeks and J. K. Garland, J. Phys. Chem. **73**, 2508 (1969); R. W. Weeks and J. K. Garland, J. Am. Chem. Soc. **93**, 2380 (1971).
5. D. S. Urch and M. J. Welch, Trans. Faraday Soc. **62**, 388 (1966).
6. R. T. K. Baker and R. L. Wolfgang, Trans. Faraday Soc. **65**, 1842 (1969).
7. G. R. Wolley and R. J. Cvetanovic, J. Chem. Phys. **50**, 4697 (1969); R. J. Cvetanovic and L. C. Doyle, J. Chem. Phys. **50**, 4705 (1969).
8. H. W. Melville and J. C. Robb, Proc. Roy. Soc. A **202**, 181 (1950).
9. R. W. Getzinger and G. L. Schott, J. Chem. Phys. **43**, 3237 (1965); P. Riesz and E. J. Hart, J. Phys. Chem. **63**, 858 (1959).
10. K. R. Jennings and R. J. Cvetanovic, J. Chem. Phys. **35**, 1233 (1961).
11. R. W. Fair and B. A. Thrush, Trans. Faraday Soc. **65**, 1550 (1969).
12. H. A. Kazmi and D. J. LeRoy, Can. J. Chem. **42**, 1145 (1964).
13. A. Good and J. C. J. Thynne, Trans. Faraday Soc. **63**, 2708 (1967).
14. M. I. Christie, Proc. Roy. Soc. A **244**, 411 (1958).
15. N. Imai and O. Toyama, Bull. Chem. Soc. Japan **33**, 652 (1960).
16. R. H. Cvetanovic and R. S. Irwin, J. Chem. Phys. **46**, 1694 (1967).
17. W. M. Jackson, J. R. McNesby, and B. de B. Darwent, J. Chem. Phys. **37**, 1610 (1962).
18. G. Meissner and A. Henglein, Z. Naturforsch. **20b**, 1005 (1965).

PHOTOLYSIS OF AQUEOUS N-ACETYLALANINE AT 2288Å

M. E. Jayko, H. A. Sokol, and W. M. Garrison

Our studies of the γ -radiolysis of simple peptides such as the N-acylamino acids in concentrated aqueous solution have provided evidence that excited-molecule reactions are involved in the observed radiolytic degradation of the peptide main-chain.¹ Recent informa-

tion suggests that excited states of solute species in concentrated aqueous systems are produced through a charge transfer mechanism.² In the case of the N-acylamino acids such reaction would be of the form



These considerations suggest that peptide main-chain chemistry may also be induced photochemically. Accordingly we have examined the photo-induced reactions of the simple peptide N-acetylalanine in oxygen-free solution, using the cadmium 2288 Å line. Observed reaction products and quantum yields, Φ , are summarized in Table I. The major findings can be interpreted in terms of the stoichiometries

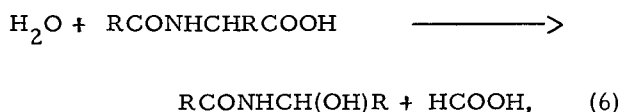
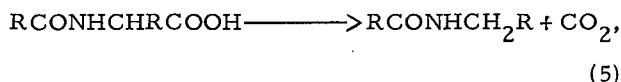
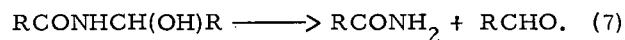


Table I. Photolysis of N-acetylalanine (0.3 M) at 2288 Å.

Product	Quantum yield (Φ)
carbon dioxide	0.15
ammonia (amide)	0.08
acetaldehyde	0.06
formic acid	0.05
pyruvic acid	<0.001
propionic acid	<0.001

The decarboxylation reaction (5) which occurs with $\Phi = 0.15$ is characteristic of compounds containing the C-COOH linkage and does not involve specific peptide chemistry. On the other hand, reaction (6) which is observed with $\Phi = 0.06$ yields the dehydropeptide, RCONHCH(OH)R. This species is labile and decomposes to the corresponding amide and aldehyde products



In accord with the formulation given in Eqs. (6) and (7), we find $\Phi \text{HCOOH} \approx \Phi \text{RCHO}$ as shown in Table I. More extensive studies of the role of dehydropeptide production in the photolysis of simple peptides in aqueous systems are in progress.

References

1. W. M. Garrison, M. E. Jayko, and M. A. J. Rogers, *Adv. Chem. Ser.* **81**, 384 (1968).
2. W. H. Hamill, *J. Phys. Chem.* **73**, 1341 (1969).

RADIATION-INDUCED REACTIONS OF AMINO ACIDS AND PEPTIDES*

W. M. Garrison

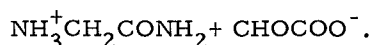
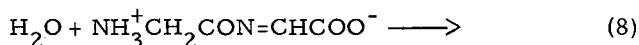
During the past few years there has been a very marked increase in the amount of work being done on the radiation chemistry of bioorganic compounds both in aqueous solution and in the solid state. Our work in this area has been confined to those simpler compounds that represent well-defined physico-chemical systems. In the present paper we review the specific role of ionic, free-radical, and excited-molecule reactions involved in the γ -

radiolysis of the simpler α -amino acids, N-acylamino acids, and oligopeptide derivatives in dilute solution, in concentrated solution, and in the solid state.

Footnote

* Condensed from UCRL-20440; published in *Radiation Res. Rev.* **3**, 305 (1972).

ated solution. The disproportionation reaction (7) leads to formation of the dehydropeptide $\text{NH}_4^+\text{CH}_2\text{CON}=\text{CHCOO}^-$, which species is labile and yields amide and glyoxylic acid on mild hydrolysis:



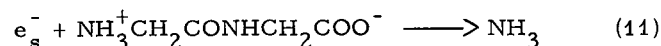
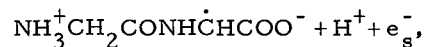
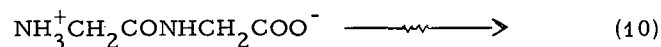
The data for 0.05 M glycylglycine are in quantitative accord with the above mechanism and the reported yields for the γ -ray-induced step (1).

On increasing the glycylglycine concentration from 0.05 M to 1 M, we find that the yield of free ammonia increases from 2.8 to 3.8. This increase is accompanied by a corresponding increase in the combined yields of acetylglutamine and aspartic acid, which products are derived from the $\dot{\text{C}}\text{H}_2\text{CONHCH}_2\text{COO}^-$ radical. The evidence is that the yield of the reductive deamination reaction (2) increases with increasing glycylglycine concentration in qualitative accord with the spur-diffusion model.⁵

We note also that the relative yields of final products derived from the $\dot{\text{C}}\text{H}_2\text{CONHCH}_2\text{COO}^-$ radical, i. e., acetylglutamine and aspartic acid, are markedly dependent on glycylglycine concentration. For example, in 0.05 M solutions, the acetylglutamine and aspartic acid are produced in essentially equal yield. However, in the 1 M solution, the acetylglutamine yield is almost an order of magnitude greater than the aspartic yield. This is consistent with the formulations of reactions (4) and (5) as written. At the higher solute concentrations the radical-molecule reaction (4) is favored over the radical-radical reaction (5).

As shown in Table I, we find that acetylglutamine and ammonia are also formed as major products in the radiolysis of glycylglycine in the solid state. In fact, the specific yields of these products from solid glycylglycine and from the concentrated glycylglycine solution are remarkably similar. We have pointed out elsewhere^{1,2} that such a result would be expected if electrons formed in the polar glycylglycine solid escape the positive charge and subse-

quently react through reductive deamination via the analog of reaction(2); i. e.,



The peptide radicals of the type formed in reaction (10) correspond to the long-lived radical species observed in irradiated glycylglycine at room temperature.⁶ The $\dot{\text{C}}\text{H}_2\text{CONHCH}_2\text{COO}^-$ radicals formed in reaction (11) are removed through the equivalent of the hydrogen-abstraction reaction (4) to yield acetylglutamine and additional peptide radicals. On dissolution of the irradiated solid in oxygen-free water, the long-lived peptide radicals formed in steps (10) and (4) are removed, primarily through dimerization via step (6) to yield the diaminosuccinic acid derivative.

The stoichiometry of reactions (10), (11), and (4) provide a basis for estimating the yield for ion-pair production in solid glycylglycine; i. e., $G(\text{I. P.}) \approx G(\text{NH}_3)_f \approx G(\text{CH}_3\text{CONHCH}_2\text{COOH}) \approx 3.5$.

Footnote and References

* Condensed from LBL-1269, December 1972; to appear in *Radiation Res.* (1973).

1. W. M. Garrison, *Current Topics in Radiation Research*, Vol. IV (North-Holland, Amsterdam, 1968).
2. W. M. Garrison, *Radiation Res. Rev.* **3**, 305 (1972).
3. H. A. Makada and W. M. Garrison, *Radiation Res.* **50**, 48 (1972).
4. I. Draganic, *Radiation Chemistry of Water* (Academic Press, New York, 1971).
5. H. A. Schwarz, *J. Phys. Chem.* **73**, 1928 (1969).
6. H. C. Box, H. G. Freund, and K. Lilga, *Free Radicals in Biological Systems* (Academic Press, New York, 1961).

FURTHER STUDIES ON THE METASTABLE DISSOCIATION OF THE
 CH^+ ION PRODUCED BY ELECTRON IMPACT*

A. S. Newton and A. F. Sciamanna

Basic studies on the formation and dissociation characteristics of the metastable states of the CH^+ and CD^+ ions respectively were described in the 1971 LBL Nuclear Chemistry Annual Report.¹ Owing to questions by the referee of this paper, further work has been done to clarify the appearance potential, A.P., of the unimolecular dissociating states of CH^+ or CD^+ as contrasted to the A.P. for the unimolecular process combined with a small amount of collision-induced dissociation in previous determinations.

CH^+ ions are formed by electron impact on acetylene. Any molecule containing the CH group can be used, but acetylene gives the highest yields of CH^+ ions in the metastable state. In order to eliminate collision-induced dissociations of CH^+ ions from the ionization efficiency curve for the appearance of the products of the metastable dissociation,



the curve must be determined at zero pressure of gas in the mass spectrometer. Since this is

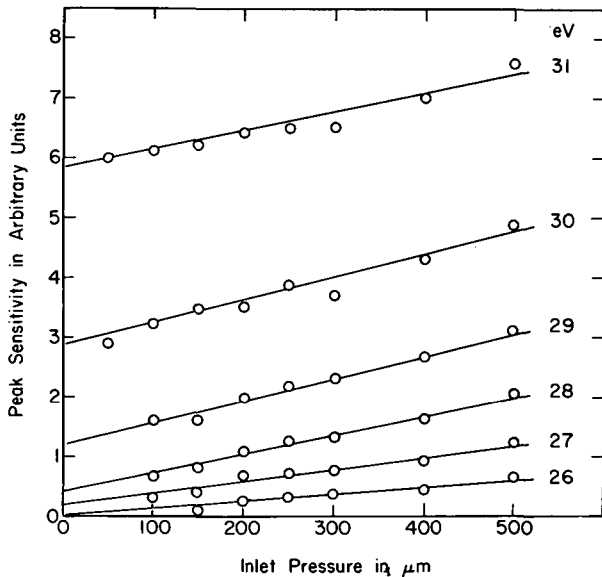


Fig. 1. Peak sensitivity vs pressure of $(M/q)^* = 10.286$ in the mass spectrum of C_2D_2 at various ionizing electron energies. Energy standard: $^{22}\text{Ne}^+$ appearance potential. (XBL 724-656)

impossible, an extrapolation procedure was used. At each electron energy, the peak sensitivity (intensity/pressure) of the metastable ion peak from C_2D_2 was determined as a function of pressure. The curve for each electron energy was then extrapolated to the zero pressure intercept. Plotting the intercepts against electron energy then yields an ionization efficiency curve at zero pressure. This curve is characteristic of the unimolecular dissociation process only.

The sensitivity vs pressure curves at various electron energies are shown in Fig. 1. At an electron energy of 26 eV, the curve extrapolates to zero sensitivity at zero pressure, but at 27 eV and above, positive intercepts characteristic of the unimolecular process are observed. In Fig. 2 the ionization efficiency curve is plotted. The

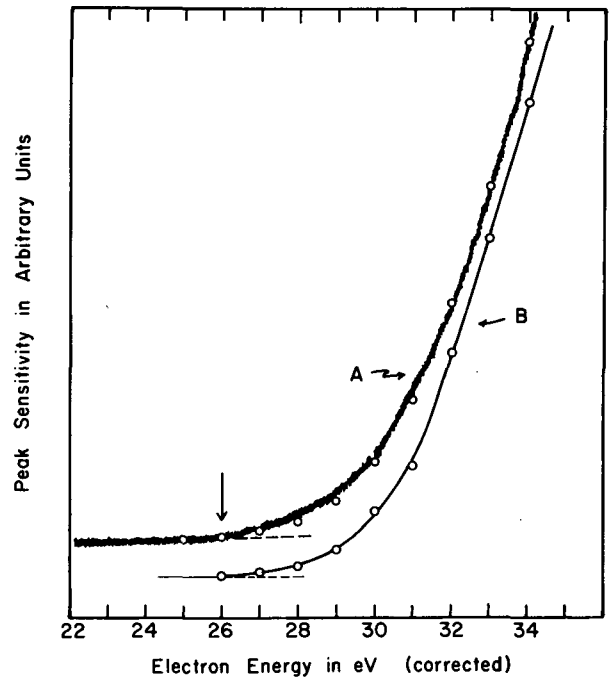


Fig. 2. Ionization-efficiency curve for production of $(M/q)^* = 10.286$ in the mass spectrum of C_2D_2 . Curve A: An X-Y recording of ion intensity vs electron energy at an inlet pressure of 150 μm . Points are from peak sensitivity vs pressure curves (Fig. 1) at an inlet pressure of 150 μm . Curve B: Zero pressure intercepts of peak sensitivity-pressure plots from Fig. 1. (XBL 724-655)

present results at zero pressure (curve A) are compared to previous results at 150 μm inlet system pressure ($\sim 1.4 \times 10^{-4}$ μm ion source pressure and $\sim 1.4 \times 10^{-6}$ μm analyzer tube pressure), curve B, solid curve. Also plotted on curve B (open circles) are the normalized 150 μm intercepts from Fig. 1. The agreement is satisfactory and it is evident that the A.P. of $\text{CD}^+(\text{m})$ from C_2D_2 is 26.0 ± 0.5 eV. These curves show the excitation cross section to increase slowly for the first few volts above the A.P. and rise faster above 29 eV. The dissociation of $\text{CD}^+(\text{m})$ was found to be accompanied by the release of 1.4 ± 0.4 eV of kinetic energy. The dissociation limit of C_2D_2 to $\text{C}^+(^2\text{P}_{1/2}) + \text{H}(^2\text{S}) + \text{CD}(^2\Pi, \nu=0)$ is 24.78 eV, assuming no kinetic energy release in the initial fast dissociation of C_2D_2 . The 1.4 eV of kinetic energy in the dissociation of $\text{CD}^+(\text{m})$ gives a calculated A.P. of the metastable ion of 26.2 eV, in good agreement with the observed value.

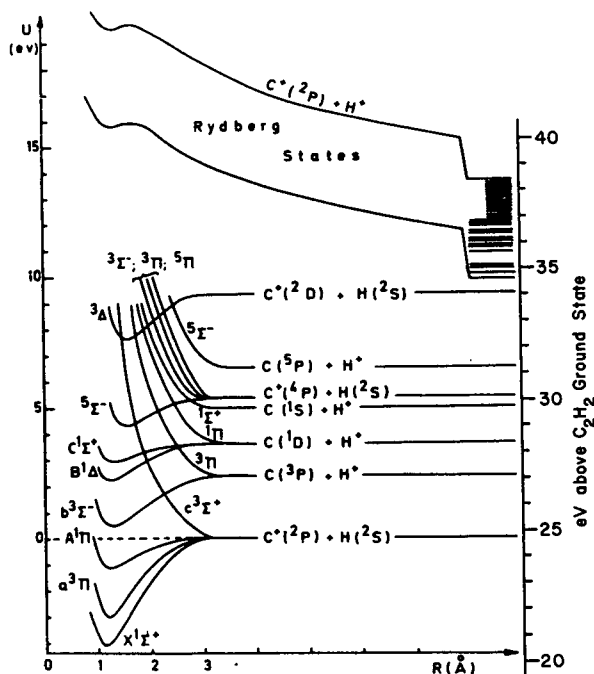


Fig. 3. Potential energy curves of the CH^+ ion as calculated by Lorquet et al. (Ref. 2). The energy scale on the right refers to the energy above the ground state of C_2H_2 with CH fragment formed in $\nu = 0$ of the $\text{X } ^2\Pi$ ground state and with no release of initial kinetic energy. (XBL 723-563)

In Fig. 3 are shown the calculated potential energy curves of states in the CH^+ system.^{2,3} The A.P. and kinetic energy release for the metastable CH^+ (or CD^+) ion are consistent with the metastability arising from predissociation of the $b^3\Sigma^-$ state of CH^+ with the repulsive $c^3\Sigma^+$ state. The crossing is forbidden by the selection rule $\Sigma^- \not\leftrightarrow \Sigma^+$. The $b^3\Sigma^-$ state can radiate to the $a^3\Pi$ state by an allowed transition, and two bands of this system have been observed.⁴ No radiative lifetime data are available, but correlation of many $^3\Sigma \leftrightarrow ^3\Pi$ transitions corrected to this energy range indicate that a radiative lifetime of 0.4 to 1.0 μsec is not unreasonable. Therefore the 0.4- μsec half-life for the metastable dissociation observed may be the partial half-life determined by competition of dissociative and radiative processes.

Because the initial excitation with electrons is the excitation of C_2H_2^+ , no conclusions regarding higher states of CH^+ which may be metastable (as has been postulated to be the case by Lorquet, et al.³) is possible. The formation of possible excited states of the CH fragment, possible kinetic energy release in the fast fragmentation of C_2H_2^+ , and a lack of knowledge of higher excited states of C_2H_2^+ and their fragmentation patterns make questionable any conclusions derived from the shape of the excitation curve for the metastable ion.

Footnote and References

* Abstracted from the paper "On the Metastable Dissociation of the CH^+ Ion Produced by Electron Impact," LBL-295, Sept. 1972. Accepted for publication in *J. Chem. Phys.*; publication date: Feb. 15, 1973.

1. A. S. Newton and A. F. Sciamanna, LBL-666, May 1972. p. 182.
2. A. J. Lorquet, J. C. Lorquet, J. Momigny, and H. Wankenne, *J. Chim. Phys. Supplement* (20th Meeting Soc. Chim. Phys. Paris, May 1969) pp. 64-68 (1970).
3. A. J. Lorquet, J. C. Lorquet, J. Momigny, H. Wankenne and H. Lefebvre-Brion, *J. Chem. Phys.* **55**, 4053 (1971).
4. M. Carre, *Physica* **41**, 63 (1969).

GROUP SEPARATIONS FOR SUPERHEAVY ELEMENTS

J. V. Kratz,* J. O. Liljenzin,† R. J. Silva,‡ and G. T. Seaborg

Many calculations¹ have been performed on the ground state electron configurations of gaseous atoms of the Superheavy Elements (SHE), their oxidation potentials, and other properties. However, there is only a loose connection between those properties and the chemistry of a given element in aqueous solutions. This is due to the fact that in solution important processes such as solvation and complex formation take place, properties that have not been predicted on the basis of calculations at the present time.

A survey of the chemistry of the lighter homologs of the SHEs 107 through 116 in aqueous solutions shows a strong tendency of these elements towards complex formation with halide ions: The stability constants^{2,3} of halide complexes increase within a given column of the periodic system with increasing element number, and the ligand dependence is $F^- \ll Cl^- < Br^- < I^-$. According to Ahrlund⁴ this sequence is typical for the so-called "soft" acceptor ions whereas "hard" acceptors, such as lanthanide and actinide ions, form stronger fluoride complexes than chloride, bromide, or iodide complexes ($F^- \gg Cl^- > Br^- > I^-$). In Fig. 1 the stability constants for the first halide complexes in subgroup IIa are plotted versus element number. Similar tendencies hold for the complex stabilities in groups VIIa, VIIIa, Ia, and for the heavy homologs in groups III, IV, V, and VI; thus we would expect extremely strong bromide or iodide complexes for the SHEs (see Table I). For practical reasons the use of hydriodic acid solutions is disadvantageous because noble metal ions may be reduced by iodide. Therefore we expect hydrobromic acid to be the best medium for a conversion of SHE ions into anionic complexes and to keep hard metal ions, e. g., trivalent transplutonium element ions, uncomplexed.

Separations of anionic species from cations can be achieved by i) cation exchange, ii) solvent extraction by aliphatic amines (as suggested by E. P. Horwitz⁵), or iii) by anion exchange. We have investigated these three systems, using radioactive tracers of Zn, Ru, Ag, Cd, In, Sn, Sb, Os, Ir, Pt, Au, Hg, Tl, Pb, Bi, Po. In addition ²³⁸U was used in amounts up to 60 mg to study the decontamination from large amounts of target material, and ¹⁵⁴Eu served as a tracer for lanthanide and actinide elements.

i) Cation exchange separation. Columns of Dowex 50X8 (~400 mesh) (3X140 mm) were transferred to the hydrogen-form with

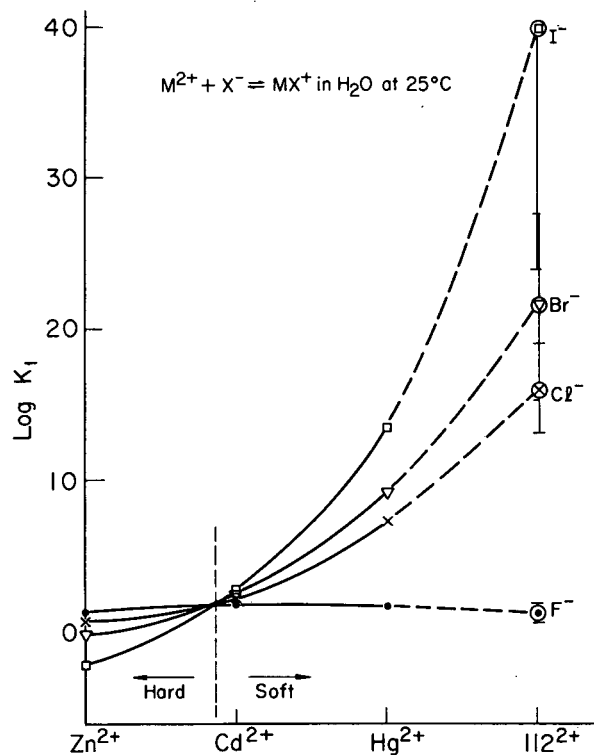


Fig. 1. Stability constants for the first halide complex MX^+ for elements of subgroups IIa and extrapolation to element 112. Data are taken from Refs. 2 and 3. (XBL 734-2716)

Table I. Predicted $\log K_1$ values for halide complexes of elements 111 through 114.

Ligand	111 ^{III}	112 ^{II}	113 ^{III}	114 ^{II}
F ⁻	~ -3	1.2±0.5	3.5±0.5	-1±1
Cl ⁻	~ 18 ^a	16±3	13±2	~1.1
Br ⁻	~ 20 ^a	22±6	24±6	~2
I ⁻	~ 24 ^a	40±16	34±10 ^b	~3

^aMixed constants: $M(OH)_4^- + H^+ + X^- \rightleftharpoons M(OH)_3X^- + H_2O$.

^bMay be unstable against reduction to 113^I.

dilute hydrobromic acid, containing a small amount of bromine. Os, Ir, Pt, Au, Hg, Tl, Bi, and Po are eluted by 4 column volumes of 0.1 M HBr/Br₂, whereas UO₂²⁺ and Eu³⁺ are

strongly absorbed on the resin. About 30% of NpO_2^+ and 95% of Mo are eluted by this solution. To elute Pb together with the remaining parts of Np and Mo it is necessary to wash with 6 column volumes of 0.65 M HBr. A 1/2-mil-thick U-foil (24.1 mg/cm^2) of 1/2-inch diameter (30.5 mg of U) uses about 1/7 of the capacity of such a column. The first detectable amount of U is not eluted before 8 column volumes of 0.65 M HBr. The separation is illustrated in Fig. 2. This separation has been tested by processing a U-target irradiated with ^{40}Ar ions.

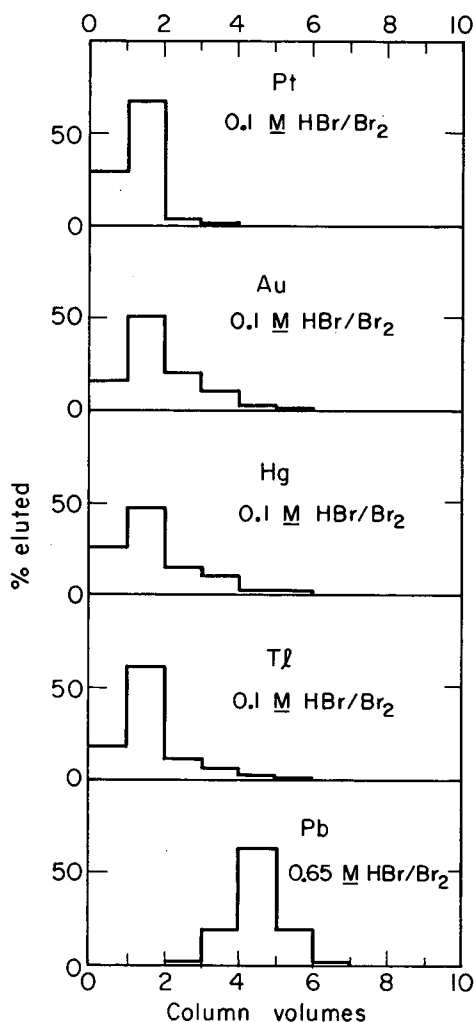


Fig. 2. Some examples of the elution of homologs of the SHEs with 0.1 M HBr/Br₂ or 0.65 M HBr/Br₂ from a Dowex 50×8 column. Elution rate one drop per 5 seconds, 70 °C. (XBL 734-2717)

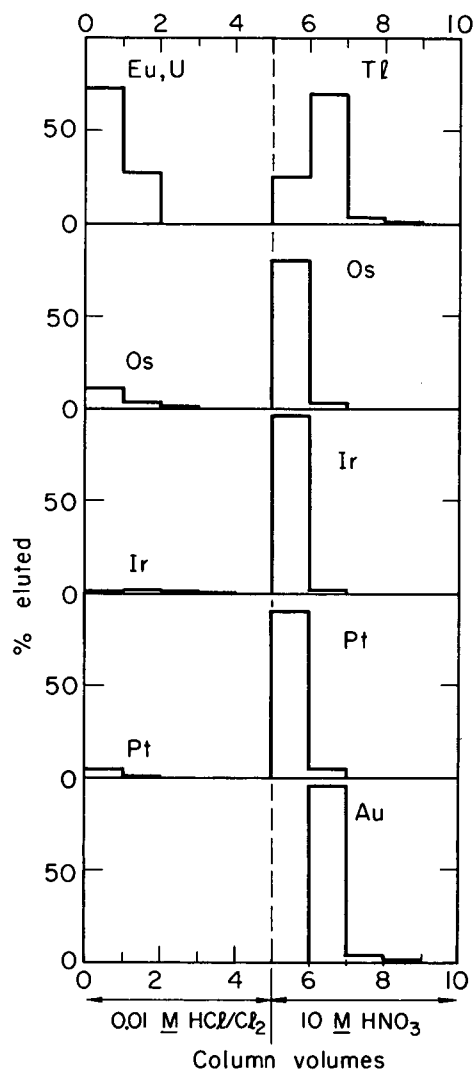


Fig. 3. Examples for the behavior of homologs of the SHEs in the group separation, using a 3×50 mm column of 1 wt% Aliquot 336 (TCMA·Cl) on Zipax (24 μ). Elution rate one drop per 5 seconds, 70 °C. This column was kindly supplied by E. P. Horwitz, ANL. (XLB 734-2718)

ii) Solvent extraction. Various aliphatic amines have been tested in extraction chromatographic columns by using hydrophobic Bioglass, Celite, or Zipax as the inert support. Sufficiently strong absorption of the Os through Po complexes (except Pb^{2+}) on the column is achieved with tertiary amines or quaternary ammonium salts such as Tri-isooctylamine (TiOA) or Tri-caprylyl-methylammonium chloride (TCMA·Cl), respectively. As some elements, e.g., Au and Tl are difficult to back-extract into the aqueous phase, the amines have to be applied in rather low

concentrations (typical 0.05 M solution in aromatic diluent), and feeding of the column should be performed in dilute hydrochloric acid rather than in hydrobromic acid solutions. UO_2^{2+} and Eu^{3+} are not extracted under these conditions. After feeding the column in 0.01 M HCl/Cl_2 and washing with 5 column volumes of the same solution to ensure complete elution of the uranium, the elements Os through Po are stripped quantitatively within 4 column volumes of 10 M HNO_3 , as shown in Fig. 3. The losses of Os, Ir, and Pt in the feeding and washing cycle are caused by reduction of these elements by the organic phase.

iii) Anion exchange. Strong basic anion exchange resins such as Dowex 1 show extremely high K_D values ($\sim 10^6$)⁶ for some of the noble metal complexes. Desorption of all the elements from these resins by one single solution was found to be impossible. For example, Au which cannot be desorbed by any aqueous solution, is eluted with 1 M HI in acetone; Pt must be eluted with large amounts of strong perchloric acid, while other elements (Tl, Hg, Bi, Po) must be eluted with nitric acid solutions. Thus, anion exchange resins were judged to be less suitable for group separations of SHEs than the above-mentioned materials.

Footnotes and References

* On leave from Institut für Anorganische Chemie und Kernchemie der Universität Mainz, with a fellowship from Gesellschaft für Schwerionenforschung GSI, Darmstadt, Germany.

† Department of Nuclear Chemistry, Chalmers University of Technology, Gothenburg, Sweden.

‡ Oak Ridge National Laboratory.

1. G. T. Seaborg, *Am. Rev. Nucl. Sci.* **18**, 53 (1968); B. Fricke and J. T. Waber, *Actinide Reviews* **1**, 433 (1971); *Proceedings of the Robert A. Welch Foundation Conferences on Chemical Research, XIII. The Transplutonium Elements—The Mendeleev Centennial*, Houston, Texas, November 17-19, 1969.
2. L. G. Sillén and A. E. Martell, *Stability Constants of Metal-Ion Complexes*, Special Publications No. 17 and 25 (The Chemical Society, London, 1964 and 1972).
3. E. Högföldt and L. G. Sillén, *Tentative Equilibrium Constants for 25°C on Infinite Dilution Scale*, UCSD 1966.
4. S. Ahrland, in C. K. Jørgensen et al., *Structure and Bonding*, Chap. 5 (Springer, Berlin, 1968).
5. E. P. Horwitz, private communication.
6. O. Samuelson, *Ion Exchange Separations in Analytical Chemistry* (Wiley, New York, 1963).

ANION EXCHANGE RESIN SELECTIVITY AS A FUNCTION OF RESIN COMPOSITION, REVISITED*

J. Bucher, R. M. Diamond, and B. Chu

It has long been known that the selectivity coefficient or equilibrium quotient

$$K_{B/A} = \frac{[\bar{B}][A]}{[\bar{A}][B]}$$

for the (univalent) ion exchange reaction



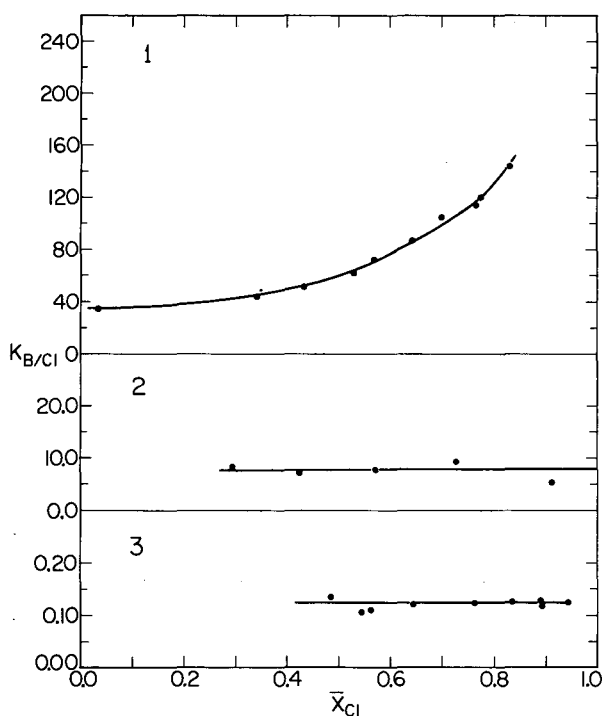
(where the superscript bar denotes the resin phase) generally depends upon the resin composition. The data available are mostly for cation exchange, and they show that with moderate to high cross-linked resins the value of $K_{B/A}$ usually remains constant or decreases slightly as \bar{X}_B , the mole fraction of B in the

resin phase, increases.¹⁻⁵ The decrease usually is more marked, the higher the cross linking.

There are a number of exceptions to this general behavior, one of the most dramatic sets being three univalent anion-exchange systems studied by Gregor et al.⁶ using a strong-base resin, Dowex 2-X8. With perchlorate, thiocyanate, and trichloroacetate ions vs. chloride, they found a steep increase in $K_{B/Cl}$ with \bar{X}_B , of the order of a factor of 10^2 . Other anions, such as I^- , Br^- , NO_3^- , IO_3^- , CH_3CO_2^- , and F^- , showed the usual pattern of a slight decrease. To explain the behavior of ClO_4^- , SCN^- , and Cl_3CO_2^- , the authors postulated that 1) selectivity was

due to ion-pair formation between the resin group and the counter ion, and 2) these particular anions caused an enhancement of the likelihood of another ion pair occurring in the vicinity of one already formed, a clustering of the ion pairs. Since we did not think that electrostatic ion pairing occurs to any significant extent between the large trimethylbenzylammonium cations of the resin and the ClO_4^- , SCN^- and Cl_3CO_2^- counter ions,⁷ and since if it did occur we might expect the resulting decrease in local charge density to cause the opposite effect, namely a hindrance to nearby ion pairing, we decided to repeat these measurements.

In Fig. 1 are plotted the values of $K_{\text{B}/\text{Cl}}$ vs. \bar{X}_{Cl} found in the present study for ReO_4^- - Cl^- , Cl_3CO_2^- - Cl^- , and CH_3CO_2^- - Cl^- exchanges. In all three systems the values of $K_{\text{B}/\text{Cl}}$ remain constant or increase slightly with \bar{X}_{Cl} . This agrees with what was found for the CH_3CO_2^- - Cl^- system in Ref. 6, but disagrees completely with the 100-fold decrease for ClO_4^- and Cl_3CO_2^- found there. We do not know the reason for the disagreement, but our ReO_4^- - Cl^- data are in agreement with a detailed study of the similar ClO_4^- - Cl^- system published by Freeman.⁸ We believe these results are correct, and so interpretable without recourse to a new type of clustered ion pairing.



Indeed, there have been a number of explanations for the usual type of behavior; 1, 5, 9-12 most have in common the idea that some form of resin heterogeneity is the ultimate origin. That is, micro-regions in the resin phase differ from each other for one or more of a number of physical or chemical reasons.^{13,14} For example, in the original polymerization of the styrenedivinylbenzene mixture, it is likely that micro-regions in the resulting beads differ in their cross linking and pore-size distribution, as well as the degree of entanglement of the matrix. The reactions used to create the ionic exchange groups can further alter the microstructure in a non-uniform way by the addition of methylene bridges and by the number and placement of the resin-ion sites on the polymer matrix. As a result, the charge density and water content may vary in the resin on a micro-scale. So there are a variety of ways in which micro-regions in the resin may differ, and there is evidence of varying degrees of confidence that all these ways do occur. As a result, the different micro-regions may have differing selectivities for ions (this does not require ion pairing in the resin, but is more likely related to the availability of water in these regions to hydrate the ions and to reduce the electrostatic free energy of the charged resin matrix). Naturally, those sites that most favor the favored ion, say B, will be occupied first by it, and only as \bar{X}_{B} increases will the other less favorable sites be exchanged. Thus, the value of $K_{\text{B}/\text{A}}$ will gradually fall to an average over all sites as $\bar{X}_{\text{B}} \rightarrow 1$.

More specific explanations are possible, and we would like to mention one which is compatible with the idea of resin heterogeneity. Since we believe selectivity is determined mostly by the differences in hydration of the two ions in the two phases,⁷ we must consider how the availability of water for ion hydration changes with a change in resin composition. As the resin equivalent fraction of the ion least in need of hydration increases, the amount of water in the resin phase decreases, but the availability of water for hydrating ions increases. As a result, the resin phase becomes slightly more favorable to that ion most in need of hydration, and so the latter ion's distribution into the resin may increase, causing $K_{\text{B}/\text{A}}$ to fall with increasing \bar{X}_{B} .

Fig. 1. Plot of the equilibrium quotient, $K_{\text{B}/\text{Cl}}$, vs. resin mole fraction, \bar{X}_{Cl} , for 1) Dowex 1-X10 ReO_4^- - Cl^- ; 2) Dowex 1-X8 Cl_3CO_2^- - Cl^- , 3) Dowex 1-X10 CH_3CO_2^- - Cl^- systems. (XBL 7211-4365)

Footnotes and References

* Condensed from LBL-631.

1. D. Reichenberg and D. J. McCauley, *J. Chem. Soc.* 2741 (1955).
2. O. D. Bonner, *J. Phys. Chem.* 59, 719 (1955); O. D. Bonner and L. L. Smith, *ibid.* 61, 326 (1957).
3. H. P. Gregor and J. I. Bregman, *J. Colloid Sci.* 6, 323 (1951); H. P. Gregor, M. J. Hamilton, R. J. Oza, and F. Bernstein, *J. Phys. Chem.* 66, 263 (1956).
4. G. E. Myers and G. E. Boyd, *J. Phys. Chem.* 60, 521 (1956); S. Lindenbaum and G. E. Boyd, *J. Phys. Chem.* 69, 2374 (1965).
5. J. R. Millar, D. G. Smith, W. E. Marr, and T. R. E. Kressman, *J. Chem. Soc.* 2740 (1964).
6. H. P. Gregor, J. Belle, and R. A. Marcus, *J. Am. Chem. Soc.* 77, 2713 (1955).
7. B. Chu, D. C. Whitney, and R. M. Diamond, *J. Inorg. Nucl. Chem.* 24, 1405 (1962); R. M. Diamond and D. C. Whitney, *Ion Exchange*, Vol. 1, edited by J. Marinsky (M. Dekker, New York, 1966), Chap. 8.
8. D. H. Freeman, *J. Chem. Phys.* 35, 189 (1961).
9. I. H. Spinner, J. Ciric, and W. F. Graydon, *Can. J. Chem.* 32, 143 (1954).
10. E. H. Cruickshank and P. Meares, *Trans. Faraday Soc.* 54, 174 (1958).
11. E. Högfeldt, *Arkiv. Kemi* 13, 491 (1959).
12. E. Glueckauf and R. E. Watts, *Proc. Roy. Soc. (London)* A268, 339 (1962); E. Glueckauf, *Proc. Roy. Soc. (London)* A268, 350 (1962).
13. L. Goldring, *Ion Exchange*, Vol. 1, edited by J. Marinsky (M. Dekker, New York, 1966), Chap. 6.
14. D. Reichenberg, *ibid.*, Chap. 7.

ANION STABILIZATION IN THE EXTRACTION OF HAuCl_4 , HReO_4 , HClO_4 ,
 HI and HBr BY TRIBUTYL PHOSPHATE IN CCl_4 AND BENZENE

J. J. Bucher and R. M. Diamond

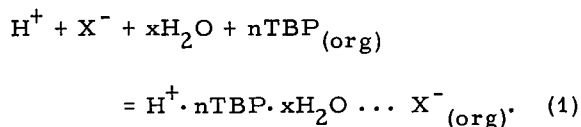
In a previous two-part study¹ of HReO_4 , HClO_4 extraction by dilute solutions of tributyl phosphate (TBP) in various diluents, stepwise complexing, namely a 2TBP·acid and a 3TBP·acid complex, was found. This behavior, within the range of TBP concentrations employed, was particularly evident in iso-octane (a relatively inert hydrocarbon) and in CCl_4 (a halogenated diluent capable of moderate dispersion force interactions). CCl_4 was better able to stabilize the 2:1 complex than could iso-octane. In each diluent system the TBP and additional waters were thought to be bonded to the three positive sites of the H_3O^+ ion.

In another diluent, 1,2-dichloroethane (a high-dielectric-constant solvent) which permitted dissociation of the extracted ions, only a 3 TBP complex was observed. In this diluent, interaction with the anion is lost and so the hydronium (or more likely, the partially hydrated hydronium) cation is required to obtain its solvation more completely from the TBP.

In the present study the extraction of a stronger acid, HAuCl_4 , and of weaker acids,

HBr and HI , by TBP in some of the previously studied diluents is presented. It is expected that for the HAuCl_4 -TBP-diluent systems, a greater range of 3:1 TBP:acid complex should be realized since the anion, AuCl_4^- , is even less basic than either ReO_4^- or ClO_4^- . Conversely, with the somewhat more basic anions, I^- and Br^- , it is expected, if anion stabilization is a contributing factor, that a greater range of 2:1 TBP:acid complex would be realized.

The extraction of HX by TBP solutions in low-dielectric-constant media where the extracted species are ion-paired is written:



If the assumption is made that the ratio of activity coefficients $y_{\text{HX}}/y_{\text{TBP}}$ is a constant in the dilute organic-phase solutions employed, (previously demonstrated to be reasonable) then

$$K_n^a = \frac{[H^+ \cdot nTBP \cdot xH_2O \cdots X^-]_{org}}{[TBP]_{org}^n (H_2O)^x (H^+X^-)} \quad (2)$$

where K_n^a is the mixed equilibrium quotient and brackets indicate concentrations. Since in each of the diluents considered herein the TBP-HReO₄ and TBP-HClO₄ species showed only ion-pair formation, it is only of interest to determine the value of n , the TBP coordination number. As indicated by Eq. (2), the slopes of log-log plots of extracted acid ($[HX]_o$) vs. TBP concentration at a constant aHX yield directly the value of n . Such plots are shown in Figs. 1 and 2 for TBP-CCl₄ and TBP-benzene systems. Also included in these plots are the previously determined data for HReO₄, HClO₄, as reference.

Part II of Fig. 1 illustrates the stepwise complexing for TBP-HReO₄-CCl₄, with the dashed lines indicating resolution of the raw data into components having either slope two ($n = 2$) or three ($n = 3$). In part I of this same figure, lines a and c show the extraction for TBP-HAuCl₄-CCl₄ and a line of slope three ($n = 3$) holds even down at TBP concentration where the HReO₄ system shows a slope of 2. For TBP-HI-CCl₄ (line b, Fig. 1) only a slope two ($n = 2$) line is observed. Similarly, for the HBr data shown in Part III, all lines are drawn with a slope two ($n = 2$).

The TBP-HAuCl₄, HReO₄, HClO₄-benzene systems are shown in Fig. 2. Lines a and b are for HClO₄ and HReO₄ and are drawn with slopes two ($n = 2$). Curve c is for HAuCl₄, and can be resolved into components with $n = 2$ and $n = 3$. Since benzene is a somewhat better solvating diluent than CCl₄ the order observed is reasonable. Benzene molecules can help stabilize the extracted (partially hydrated) hydronium cation

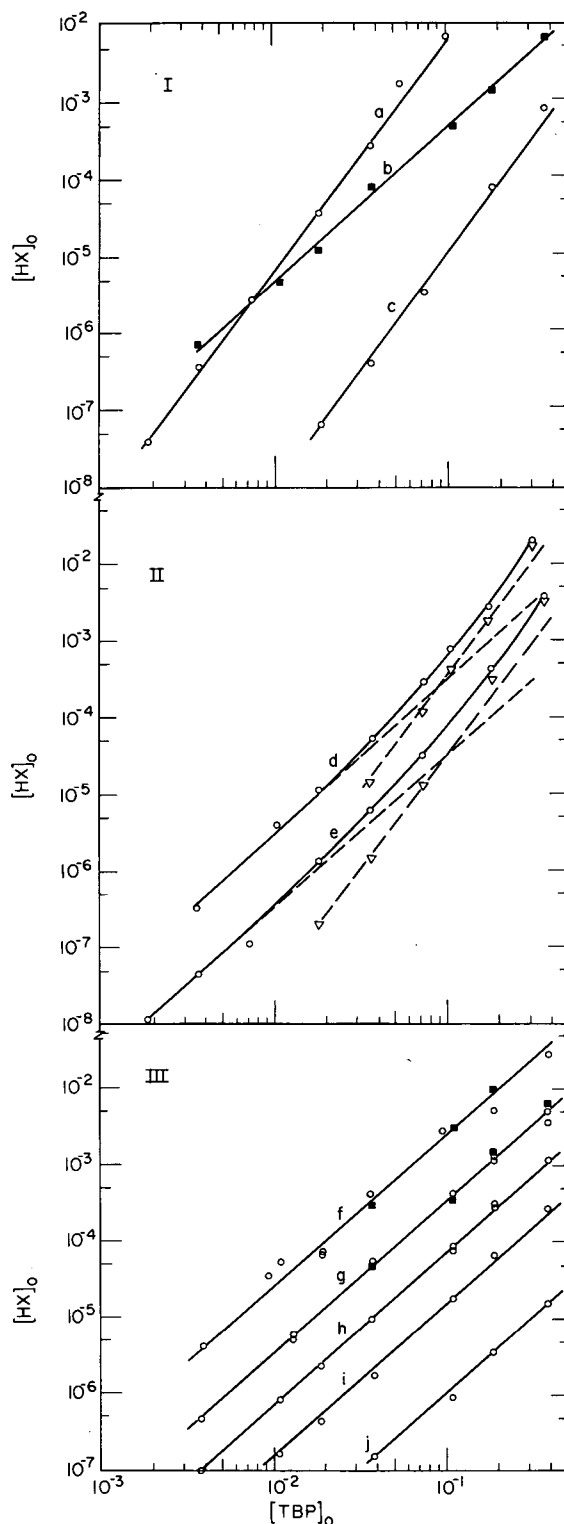


Fig. 1. Variation of acid content of the organic phase with TBP concentration in CCl₄ for aqueous HX. Part I: aqueous HAuCl₄ in 1.0 M HCl: line a, HAuCl₄ = 0.50 M; line c, HAuCl₄ = 0.0010 M. Line b, ■, is for aqueous HI = 2.04 M. Part II: aqueous HReO₄ concentrations of 2.91 M (curve d) and 1.60 M (curve e). Part III: aqueous HBr concentrations of 6.4 M (line f), 5.0 M (line g), 3.9 M (line h), 3.2 M (line i), and 0.97 M (line j). The slope of lines a and c in Part I is three, while line b is drawn with slope two. In Part II, the dashed lines are drawn with either slope two or three (∇). All lines in Part III are drawn with slope two and, ■ denotes titrated points, with all other circled points being measured by tracer Br⁻. (XBL 734-2719)

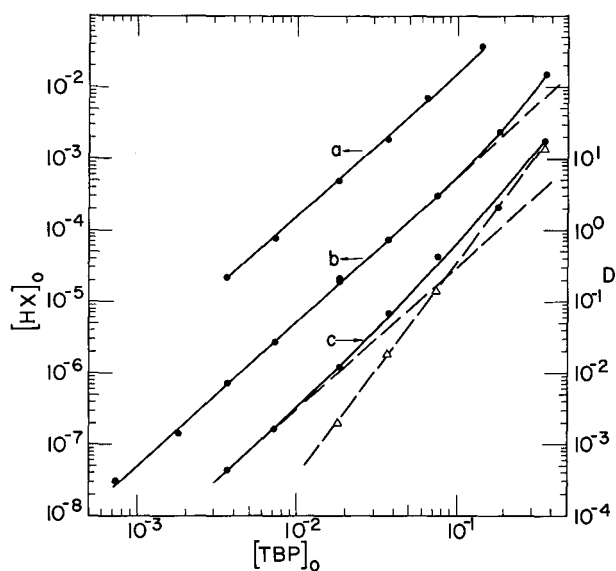


Fig. 2. Variation of acid content of the organic phase with TBP concentration for aqueous HClO_4 concentration of 4.07 M (line a) and for 1.60 M HClO_4 (line b), and variation of distribution ratio, D , with TBP in benzene for 1.2×10^{-3} HAuCl_4 in 3.00 M HCl (curve c). Lines 1 and 2 are drawn with slope two, while the dashed lines of curve 3 are drawn with either slope two or three (∇).

(XBL 734-2720)

via their π -electrons and for HReO_4 , HClO_4 only two molecules of TBP need be coordinated, along with the associated ReO_4^- or ClO_4^- anion. For the HAuCl_4 -benzene system, presumably the same degree of diluent stabilization is present, but the less basic anion, AuCl_4^- , is less effective than ReO_4^- or ClO_4^- in furnishing some of the solvation needs of the hydronium cation. As a consequence, a third TBP is coordinated at the higher TBP concentrations.

CCl_4 is less able than benzene to stabilize the extraction complexes. Instead of observing stepwise complexing in the HAuCl_4 - CCl_4 system, only the 3:1 complex is observed and only with the more basic ReO_4^- anion are the two components observed in the CCl_4 system. The additional stabilization afforded by the still more basic I^- and Br^- anions produces only 2:1 TBP:acid complexes for these acids in the available TBP concentration range.

We conclude that anion stabilization of the extracted hydronium-TBP complex is a contributing factor in the extraction of acids by TBP, but that this influence is dependent upon the diluent and anion employed in a reasonably understandable manner.

References

1. J. J. Bucher and R. M. Diamond, J. Phys. Chem. 73, 675 (1969); *ibid.* 73, 1494 (1969).

MULTICOLUMN RADIO-GAS-CHROMATOGRAPHIC ANALYSIS OF RECOIL TRITIUM REACTION PRODUCTS*

D. C. Fee and S. S. Markowitz

Gas chromatography has been widely applied in the separation and analysis of multicomponent systems. If the components are radioactive, the effluent from a chromatographic column may be mixed with a counting gas and the radioactivity measured as the mixture flows through an internal proportional counter.¹ This immediate radioassay is called radio-gas-chromatography. The radio-gas-chromatographic analysis of tritium-labeled hydrocarbons is of particular interest to us. We are studying the reactions of recoil tritium atoms.^{1,2}

There were several *a priori* considerations for the design of a general radio-gas-chromatographic analysis system for the products of recoil tritium reactions: 1) The components of the hydrocarbon mixture differ

widely in boiling point and physico-chemical properties¹⁻³ 2) The sample injection volume is large; namely, the whole sample.⁴ 3) The flow rate through the detector is constant.⁵ 4) All peaks are monitored with the same detector (beta proportional counter).³ This system uses four columns in series and has the capability for 1) stop flow,⁶ 2) recycle,⁷ 3) center cut,⁸ 4) stepwise pressure programming,⁹ and 5) stepwise temperature programming applications.¹⁰

Pressure regulation of the helium carrier gas began at the commercially available tank with a standard two-stage regulator. This regulator maintained a pressure of 100 psi in the ballast tank. The ballast tank was a common input to five single-stage regulators used for pressure programming. These

single-stage regulators each exhausted through a check valve (on/off) into a common manifold. The preset pressure maintained a helium flow rate through the counter of 30 cc/min. This manifold was the beginning of the arrangement of columns and 4-way valves shown in Fig. 1

The flow downstream from the manifold was through 1/16-in. -o.d. stainless steel tubing. The stainless steel tubing and 4-way valves were operated at 25°C. Following the buffer the helium flow stream was mixed with propane in a standard 1/4-inch Swagelock Tee. The combined helium and propane flow passed through the counter, through a soap bubble flow meter, and was then exhausted into a hood. The combined flow rate was maintained at 83 cc/min, giving the desired 1.8/1.0 propane-to-helium mixture.⁵ The propane pressure was not changed during an analysis.

A typical analysis of the products of recoil tritium reactions with methylcyclohexene is shown in Fig. 2. The sequence of operations used to obtain this radio-chromatogram

is given in Table I. Table I also lists the column abbreviations. The techniques used in the analysis shown in Fig. 2 in the order of their appearance are:

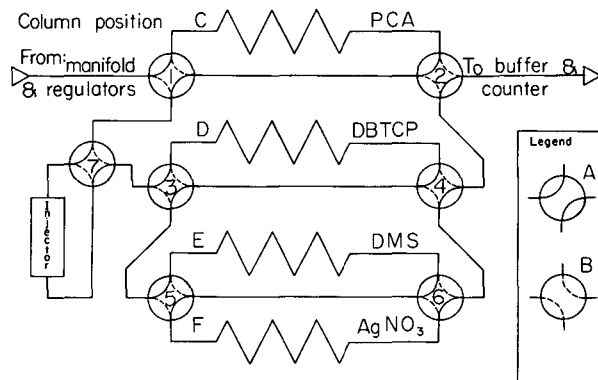


Fig. 1. Schematic diagram of the chromatographic flow stream. See Table I for definition of columns. (XBL 729-4074)

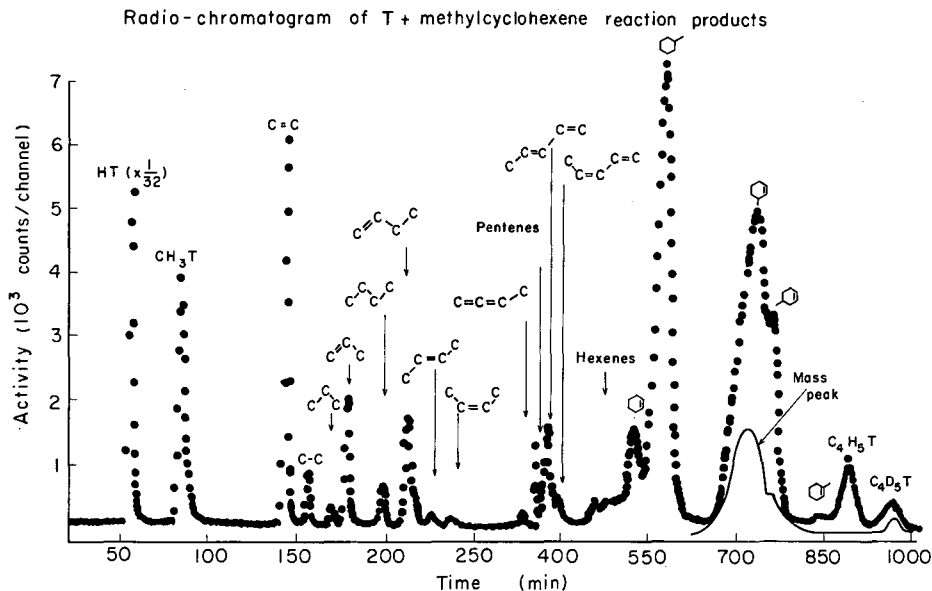


Fig. 2. Typical radio-gas chromatogram of the products or recoil tritium reactions with methylcyclohexene. The sample was a 1720 Pyrex capsule (14 nl internal volume) to which 8.5 cm Hg 3-methylcyclohexene, 2.6 cm of 4-methylcyclohexene, 1.5 cm butadiene-d₆, and 30 cm of ³He had been added (pressure corrected to 135°C). The irradiation was for 24 hr at a temperature of 135°C at a flux of $3.9 \times 10^8 \text{ n cm}^{-2} \text{ sec}^{-1}$ in the Hohlraum of the Berkeley Campus Nuclear Reactor. (XBL 731-2146)

(1) Stop flow. At 30 min, C₅ product peaks are just about to emerge from the DBTCP column. C₄ and lighter product peaks have already emerged and are in the DMS and PCA columns. At 30 min, the C₅ to C₇ product peaks are "stored" in the DBTCP column for future analysis when flow in the DBTCP column is stopped. At 38 min, C₃ product peaks are just about to emerge from the DMS column. C₂ and lighter product peaks have already emerged and are in the PCA column. At 38 min, the C₃ to C₄ product peaks are "stored" in the DMS column for future analysis.

At 165 min, flow is restarted in the DMS column. Storage for a little over two hours has affected the peak shape. For example, the FWHM (full width half maximum) of a trans-2-butene mass peak increased by 10% because of peak storage. At 380 min, flow is similarly restarted in the DBTCP column. The FWHM of a cyclohexene mass peak increased by 15% because of peak storage in the DBTCP column for nearly six hours.

(2) Stepwise pressure programming. A constant helium flow rate through the detector was maintained when the DBTCP column

Table I. Sequence of operations.

Time (min)	Manifold pressure (psi)	Arrangement of valves ^a			Column order in flow stream ^b	Comment
		123	456	7		
-1	34.4	BBA	AAB	B	DBTCP, DMS, PCA-78	Break capsule (injector at 135°C)
0		BBA	AAB	A		Inject sample; timing interval: 0.5 min/channel
10		BBA	AAB	A		Injector bypassed
30	34.2	BBB	AAB	B	DMS, PCA-78	DBTCP bypassed
38	28.0	ABB	AAB	B	PCA-78	DMS bypassed
90						Flow check: 83 cc/min
98	32.0				PCA-8	Temp. change -78 to 8°C for PCA
160						Flow check: 83 cc/min
162					PCA-78	Temp. change -8 to -78°C for PCA
165	34.2	AAB	AAB	B	PCA-78, DMS	Flow restarted in DMS
250						Change timing interval to 1.5 min/channel, flow check: 83 cc/min
265	36.2	AAB	AAA	B	PCA-78, DMS, AgNO ₃	AgNO ₃ center cut of butadienes
300		AAB	ABB	B	PCA-78, AgNO ₃ , DMS	End center cut
370						Flow check: 83 cc/min
375		AAB	AAA	B	PCA-78, DMS, AgNO ₃	Order switched
380		AAB	BAA	B	PCA-78, DMS, AgNO ₃ , DBTCP	Flow restarted in DBTCP
400						Flow check: 83 cc/min

^aSee Fig. 1.

^bPCA = 50-ft column of 10% propylene carbonate on 60/70 mesh activated alumina.
DMS = 50-ft column of 25% 2,4-dimethyl sulfolane on 30/60 mesh Chromosorb P;
operated at 25°C.

DBTCP = 4.5-ft column of 22% di-n-butyltetrachlorophthalate of 30/60 mesh Chromosorb P;
operated at 25°C.

AgNO₃ = 25-ft column of saturated silver nitrate/ethylene glycol on 30/60 mesh Chromosorb P;
operated at 25°C.

Buffer = 25-ft column of 60/80 mesh glass beads; operated at 25°C; used to minimize flow perturbations due to column-switching and temperature-programming.

and the DMS column were removed from the flow stream by decreasing the manifold pressure at 30 and 38 min, respectively. Similar use of the pressure "presettings" is made at later times in the analysis when columns are added to or removed from the flow stream.

(3) Stepwise temperature programming.

At 98 min, the operating temperature of the PCA column is changed from -78 to -8°C. This shortens the elution time of the ethylene-t peak by 400 min.

(4) Center cut. It is known from calibration data that the unresolved butadiene-t and butadiene-d₅t peaks would have emerged from the DMS column and been counted at 275 to 290 min. The center cut of these peaks is made by placing the AgNO₃ column downstream from the DMS column during that interval.

(5) Recycle. The inherent recycle capability of this system is displayed in the permutations of the column order at 265, 300, and 375 min. A careful analysis of Fig. 1 will reveal a nested series of recycle loops. The recycle capability is used here to allow separation of the butadiene-t and butadiene-d₅t peaks to proceed simultaneously with the counting of peaks emerging from the DMS and DBTCP columns. The recycling of the butadiene-t and butadiene-d₅t peaks through the DBTCP column is unnecessary for the sake of resolution. However, this recycling is advantageous because after 380 min the analysis is automatic.

In summary, we have developed a multi-column gas-chromatographic analytical system that has general applicability beyond the presently demonstrated recoil tritium determinations.

GAS CHROMATOGRAPHY IN ENVIRONMENTAL STUDIES

A. S. Newton, A. F. Sciamanna, and M. Evett

Gas Chromatography of Halogenated Compounds

Some of the most insidious environmental pollutants are halogenated compounds which are not readily biodegraded. Examples are the chlorinated pesticides, DDT, Lindane, Chlordane, heptachlor, dieldrin, etc., and the polychlorinated biphenyls (PCB's) which have been used in electrical transformers, as plasticizers in various plastics, and miscellaneous uses where high-boiling inert compounds are useful. In order to be able to

Footnote and References

* Condensed from LBL-1249; accepted by Anal. Chem.

1. D. C. Fee, S. S. Markowitz, and J. K. Garland; *Radiochimica Acta* **17**, 135 (1972).
2. D. C. Fee and S. S. Markowitz, J. *Inorg. Nucl. Chem.* **35**, (1973).
3. D. S. Urch, *MTP Intern. Rev. of Sci., Inorg. Chem. Ser.* **8**, 149 (1972).
4. J. W. Root and F. S. Rowland, *Radiochimica Acta* **10**, 104 (1968).
5. J. K. Lee, E. K. C. Lee, B. Musgrave, Y-N. Tang, J. W. Root, and F. S. Rowland, *Anal. Chem.* **34**, 741 (1962).
6. H. Borfitz, *Anal. Chem.* **33**, 1632 (1961).
7. J. W. Root, E. K. C. Lee, and F. S. Rowland, *Science* **143**, 676 (1964).
8. R. L. Burnett, *Anal. Chem.* **41**, 606 (1969).
9. L. S. Ettore, L. Mazor, and J. Takacs, *Adv. in Chromatography* **8**, 271 (1969).
10. L. Mikkelsen, *Adv. in Chromatography* **2**, 337 (1966).

study such compounds, an electron capture detector was fabricated and added to the Loenco Model 70 gas chromatograph. By multiple stream-splitting, this instrument can simultaneously record peaks on flame ionization, thermal conductivity, and electron capture detectors. The electron capture detector was fabricated with 10 mCi of ⁶³Ni.

In order to operate all three detectors simultaneously, the column, a 2-meter glass column, 6-mm o.d. packed with 3% OV-1 on 80-100 mesh H. P. Chromosorb W A/W,

HMDS treated, was operated with helium carrier gas at a flow rate of 60 ml/min. A 10% split of the effluent was passed through the electron capture detector where it was diluted with 40 ml/min of dry N₂ gas. After optimization of the operating parameters, a sensitivity of ~ 120 divisions/ng DDE [1,1-dichloro-2,2-bis(p-chlorophenyl)ethylene] was achieved. With injection of 5 μ l samples, the detectable limit is 0.001 ppm. Levels of 0.01 ppm were measured with better than 5% reproducibility. The linearity of response of this detector, as is true with all E. C. detectors, is approximately a factor of 100, i.e., from 0.005 to 0.5 ng injected. This is illustrated in Fig. 1. This detector was used to check the DDE and PCB content of mussels collected from a contaminated area (San Pedro) and a clean area (Bodega) of the California coast. The San Pedro mussels were high in DDE.

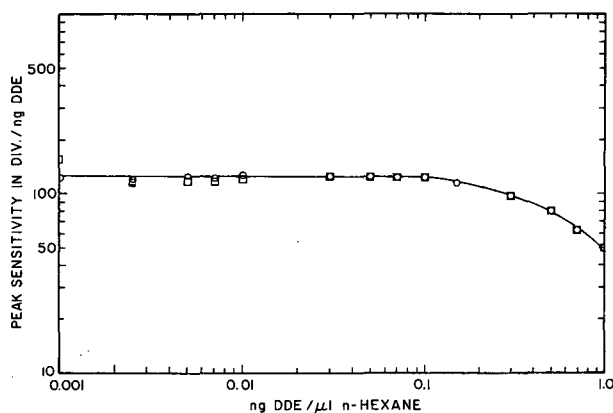


Fig. 1. Linearity with concentration of peak intensity for DDE. ⁶³Ni electron capture detector. 5- μ l sample of each concentration injected onto a 2-meter 3% OV-1 on Chromosorb W, AW, HMDS glass column. Temp. = 170°C, He carrier gas.

(XBL 734-459)

Gas Chromatography of Mercury Compounds

In the identification and measurement of specific mercury compounds in environmental studies, gas chromatography of benzene extracts of the sample are analyzed. (Westö's method¹ or some modification is usually used for extraction.) The usual detector is an electron capture detector, but this suffers from poisoning by mercury.² Backe and Lisk³ describe a method utilizing excitation of the mercury compound in a helium plasma to excite the emission of 2537-Å light, isolation

of this line with a monochromator, and measurement of the light intensity with a photomultiplier.

A GLC system for studying mercury compounds has been set up. It consists of an isothermally operated column with the outlet leading to a quartz tube. Argon carrier gas is used. This is excited with a Burdick-Model MW200 Microwave Diathermy source. This unit gives approximately 100 watts full power output at the excitation cavity. The light emitted is focused onto the slit of a Bausch and Lomb Model 33-86-25 Monochromator with a uv grating first-order blazed at 250 nm. Entrance and exit slit-widths of 0.28 and 0.16 mm respectively were used, giving ~ 56% light transmission with a 1-nm bandwidth. The light output is measured with a Kiethley Model 410 microammeter. The input of this amplifier was modified with a bucking circuit to zero the light from the argon plasma (argon exhibits a continuum in the region of 2537 Å) which is transmitted by the monochromator. This light is referred to as the plasma current. A 10-mV recorder is used to record the signal from the excitation of mercury compounds. A bypass system in which the argon can be passed over a gold foil contaminated with a trace of mercury and directly into the quartz tube in the excitation chamber is used to align the optics and maximize the signal due to mercury.

Lisk³ used He carrier gas but this suffers from the necessity of operating the column exit at low pressures in order to maintain the plasma. This modification was tried but discarded when it was found that the sensitivity for mercury compounds was only half that with an argon plasma operated at atmospheric pressure. Similarly it was reported by D' Silva and Fassel⁴ that with x-ray excitation of mercury, a mixture of 1% N₂ in argon gave increased sensitivity. With microwave excitation the addition of 1% N₂ decreased the sensitivity for CH₃HgCl detection by 42%.

Lisk³ observed that the maximum sensitivity using argon is obtained by using a 1.5 mm quartz tube for excitation. This was confirmed as shown in Table I.

The plasma current (light from the argon continuum) is about 4×10^{-7} A, with a noise level of approximately 8×10^{-10} A. The dark current of the photoelectron multiplier is approximately 1×10^{-10} A. The 2537-Å signal from CH₃HgCl is $\sim 1.2 \times 10^{-7}$ A/ng. At the 1 ng level, the signal to noise ratio is ~ 125 . A detection limit for mercury is ~ 0.01 ng of CH₃HgCl.

Table I. Effect of ID of quartz tube on sensitivity.

Tube	i. d. (mm)	Plasma current ($\times 10^{-7}$ A)	Hg sensitivity (div/ng Hg as CH_3HgCl)
A	1.5	5.0	61.3
B	1.5	4.6	64.4
C	1.5	5.0	58.6
D	1.9	5.8	50.4
E	1.0	4.4	42.6

Several columns have been tried for separation of CH_3HgCl . The best results have been with a 2-meter glass column (6 mm o. d.) packed with a mixture of 3% Carbowax 20M-TPA and 3% PMPE (6 ring) on 60-70 mesh Gas Chrom Q, AW, DMCS. With this column at 173°C and an argon flow rate of 60 ml/min, the emergence time for CH_3HgCl is 6.8 min with a half width of ~ 0.5 min. As the column aged the half width increased. The useful life of the column is at least 2 months at this temperature. The injection septum must be changed daily.

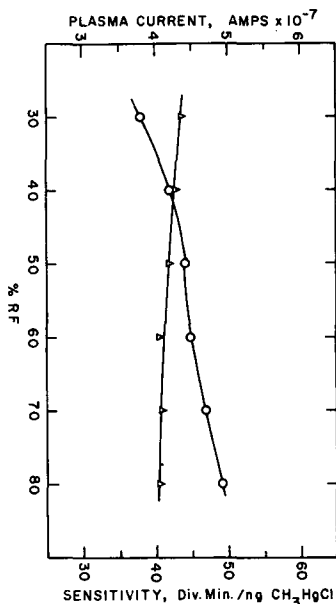


Fig. 2. Effect of rf power applied to discharge on the plasma current from argon and the peak sensitivity of CH_3HgCl . 1-mm-diameter quartz discharge tube. (XBL-734-458)

O - plasma current
 Δ - peak sensitivity response of CH_3HgCl .

The sensitivity for mercury is not a strong function of the microwave power. As shown in Fig. 2, the sensitivity for mercury decreases $\sim 10\%$ with increasing microwave power from 30 to 80%, while the plasma current increases by 30% with this increase in power. Operation at 40 or 50% power gives reproducible results with a stable plasma. The operation is not sensitive to the solvent. Solutions in isooctane, benzene, or ethanol give good results and the solvent peak (which extinguishes the discharge) is well separated from the methyl mercury peak. With water solutions, tailing of the water peak makes the system less reproducible, and sometimes the methyl mercury peak appears as a double peak. This is not understood, but the effect is corrected by changing the injection septum. The same anomaly has appeared in the analysis of water solutions of dimethyl mercury, using a Porapak P column and with either the argon plasma detection system or with a thermal conductivity detector (with more concentrated samples). The anomaly does not appear when dimethyl mercury is dissolved in alcohol or a low-boiling hydrocarbon solvent.

References

1. G. Westöf, *Acta Chemica Scand.* **20**, 2131 (1966); **21**, 1790 (1967); **22**, 2277 (1968).
2. J. O'G. Tatton and P. J. Wagstatte, *J. Chromatogr.* **44**, 289 (1969).
3. C. A. Bache and D. J. Lisk, *Anal. Chem.* **43**, 950 (1971).
4. A. P. D'Silva and V. A. Fassel, *Anal. Chem.* **44**, 2115 (1972).

DETERMINATION OF METHYL MERCURY WITH ANODIC STRIPPING

R. G. Clem

A paper published over 20 years ago described the polarographic behavior of organomercuric compounds.¹ It was determined that methyl mercury was reduced in two one-electron steps at the DME (dropping mercury electrode) and that it was possible to differentiate between organic and inorganic mercury ions. Inorganic mercury is reduced near 0.0 vs. SCE (saturated calomel electrode) a potential in excess of -1.0 V is required to reduce methyl mercury to the metal. On the basis of this information it seemed reasonable that the anodic stripping technique could also be made discriminate between organic and inorganic mercury through the proper selection of the potential employing a paraffin-impregnated graphite electrode.²

Preliminary work has indicated the feasibility of developing a stripping method for methyl mercury over the range of from 0.2 to ≥ 100 ppb in a pH 4.7 acetate buffer. A potential of -1.3 V vs. SCE is employed to accumulate the methyl-mercuric-related mercury over a period of 7-10 min after which an anodic-going potential ramp is effected. The stripping peak is located at +0.150 V vs. SCE. If it is desired to determine the inorganic mercury ion content of the sample, an accumulation potential of -0.40 V vs. SCE is employed. The stripping peak for this component is, of course, also located at +0.150 V vs. SCE.

The addition of copper to the sample seems to be an essential feature. At -1.3 V vs. SCE,

copper is coreduced with the methyl mercury. Its presence appears to very strongly catalyze the reduction of the methyl mercury, for in its absence the sensitivity attainable is less by more than a factor of 10.

The original workers suggested that the methyl mercury was reduced first to dimethyl dimercury on the first reduction step and that this compound was responsible for the second one-electron step, which might involve free radicals. What role copper plays in the reduction of the methyl mercury is not clear, but its presence is definitely required to obtain high sensitivities.

The original data also points to the feasibility of developing a controlled-potential coulometric method for methyl-mercuric ions. Analytical methods for this substance are indirect and usually require the measurement of the anion portion of the salt such as chloride ion. Since the methyl-mercuric ion is electrochemically active, and the potential for the first one-electron step is not prohibitively negative, development of a direct method for this ion should not be difficult.

References

1. R. and R. Benesch, *J. Am. Chem. Soc.* **73**, 3391 (1951).
2. W. R. Matson, D. K. Roe, and D. E. Carritt, *Anal. Chem.* **37**, 1594 (1965).

COMPUTER RESOLUTION OF POLAROGRAPHIC BACKGROUND CURRENTS

R. G. Clem and G. Litton

An intrinsic problem has always existed in the measurement of polarographic diffusion current heights. The graphical method commonly used consists of making a linear extrapolation through the background preceding the wave and through the diffusion current plateau. The diffusion current height is then measured through the $E_{1/2}$ potential as the difference between the two extrapolated current levels. This approach works well when dealing with fairly large diffusion currents; however, this measurement method becomes ever less attractive as the diffusion height becomes ever smaller. This difficulty arises because, when examined in detail, neither

the diffusion current plateau nor the background current preceding it is truly a linear function. Such a problem is readily solved by use of computer-generated curves and least-squares minimization routines.

The routines developed to deal with polarographic data are in a large user-interactive program, called POLAR, written for the CDC 6600 and require the use of a teletype and a VISTA console. The number of data points employed before and after the wave can be changed and the polynomial degree varied as needed. The input to these routines may be an input tape containing raw data or from

the MSS (mass storage system). The data produced as a result of the processing—diffusion current heights—are plotted against concentration to generate a calibration curve. Any number of analyses of "unknowns" can then be processed. Alternatively, the routines may be used to analyze an unknown sample by the method of standard additions.

The utility and desirability of this new program is illustrated by the data given in Table I. The deviation of the results from that added is generally less than 0.04 $\mu\text{g/mliter}$ for Cd and Pb. Ni is reduced at fairly negative potentials and its presence on the mercury drop substantially lowers the hydrogen overvoltage characteristics of mercury. Even so, the deviation of the results from the amount added is usually less than 0.1 $\mu\text{g/mliter}$.

This effort permits the accurate analysis of electroactive substances at levels above that directly amenable to anodic stripping and at levels below those easily reached with coulometry.

Table I.

Element	Added ($\mu\text{g/mliter}$)	Found ($\mu\text{g/mliter}$)	Deviation ($\mu\text{g/mliter}$)
Ni	2.706	2.703	-0.00
	5.413	5.357	-0.06
	8.120	8.253	+0.13
	10.830	10.750	-0.08
Cd	0.6687	0.6947	+0.03
	1.337	1.298	-0.04
	2.006	2.009	+0.00
	2.675	2.684	+0.01
Pb	0.6907	0.6820	-0.01
	1.373	1.369	-0.00
	2.045	2.083	-0.04
	2.709	2.684	-0.03

SOME PRELIMINARY STUDIES ON THE CHEMISTRY OF DILUTE SOLUTIONS OF DIMETHYL MERCURY

A. S. Newton and A. F. Sciamanna

The Solubility of Dimethyl Mercury in Water

The only datum found for the solubility of dimethyl mercury in water was one measurement by Barbara Hardin Beck.¹ She found the solubility at 45°C to be 0.0087 M in distilled water and 0.0054 M in 1.25 M KBr solution.

Measurements of the solubility at 25 and 0°C showed that the rate of solution is quite slow. Three days was required to reach saturation. Analyses were made of the water solution by gas chromatography, using a Porapak P column operated at 189°C with a thermal conductivity detector. The solubility at 0°C was $0.0140 \pm 0.0002 \text{ M}$ and at 25°C was $0.0123 \pm 0.0002 \text{ M}$. The compound has a negative solubility coefficient, as expected for a volatile compound.

The Rate of Evaporation of Dimethyl Mercury from Water Solutions

One of the postulates made to explain the occurrence of mercury in unpolluted lakes and waters of Sweden is due to Jensen and Jernelöv.² It is suggested that in contaminated waters, biological action produces both methyl and dimethyl mercury. The dimethyl mercury

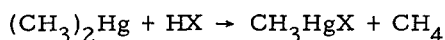
evaporates from neutral or alkaline waters. Either methyl mercury or dimethyl mercury is postulated to be brought down in otherwise uncontaminated areas by rain. Central to this postulate is the necessity for dimethyl mercury to preferentially evaporate from water solution.

A solution of dimethyl mercury in water in an open flat container was exposed to a draft of air across the surface. The air velocity was 75 lineal feet/minute (a 0.85 MPH wind velocity). After an initial period of about 1.5 hr during which the dimethyl mercury concentration decreased with a half period of ~ 1.6 hr, an exponential decrease was observed and the dimethyl mercury was removed from solution with a half period of 1 hr. In 3 hr 70% of the dimethyl mercury was lost with the loss of less than 7% of the water. It is concluded that if dimethyl mercury is formed by biological action in lakes and streams, it will be rapidly lost to the atmosphere, as has been postulated.

The Reaction of Dimethyl Mercury with Acids

Many studies of the reaction of dimethyl mercury with acids have been made both for

I) as a preparative method of methyl mercury salts,³



and II) as a medium for studying the mechanism of the reaction.^{2,4,5} The later studies have been made at higher temperatures, 40 to 60°C, while preparative methods were at high acid concentrations and high temperatures.

As a first check, the production of CH_4 by hydrolysis of $(\text{CH}_3)_2\text{Hg}$ at low concentrations (initial conc. = 0.013 M) was confirmed. The solution was reacted with 2 M HCl. The gas evolved as measured by mass spectrometric measurements was pure methane, and the stoichiometry of the reaction was confirmed. One molecule of $(\text{CH}_3)_2\text{Hg}$ yielded one molecule of CH_4 within the experimental error of $\pm 1\%$.

Preliminary measurements have been made of the rate of reaction in dilute solution [$\sim 1 \times 10^{-4}$ M $(\text{CH}_3)_2\text{Hg}$]. In 10^{-3} M HCl, the hydrolysis rate was extremely slow and an initial apparent first-order half-life of ~ 1800 hr was observed. In 0.1 M HCl, the rate is much faster and an initial apparent first-order half-life of ~ 10 hr was observed. In 1 M HCl the initial reaction was too fast to measure.

These results indicate that the postulate of the translocation of mercury by hydrolysis of dimethyl mercury in lakes and streams is probably incorrect in this regard, since even at pH = 3 (and few waters reach this acidity) the reaction is much too slow. A more plausible suggestion⁶ is the reaction on acidic particulates in air, e. g., H_2SO_4 or SO_2 absorbed on particulate matter in air. The methyl mercury produced can then be washed from the air by rain. This suggested mechanism has not been confirmed.

The Reaction of Mercuric Salts with Dimethyl Mercury

The reaction $\text{HgX}_2 + (\text{CH}_3)_2\text{Hg} \rightarrow 2 \text{CH}_3\text{HgX}$ has been used as a preparative method for alkyl mercuric salts.³ No measurements are available on the rate or the equilibrium constant for the reaction.

A few experiments have been made at low concentrations of dimethyl mercury. A solution 7.8×10^{-5} M in $(\text{CH}_3)_2\text{Hg}$ and 1.2×10^{-4} M in HgCl_2 was made by mixing solutions at 25°C. Within 15 min no dimethyl mercury was detectable and a quantitative amount of methyl mercuric chloride was formed. It is apparent that the reaction is fast and that the equilibrium is strongly in favor of methyl mercuric chloride. It is also apparent that measurement of the rate constant for the reaction will require the development of special techniques.

The rapid rate of this reaction also brings into question those results (6,7) in which dimethyl mercury is stated to be a product of the methylation of mercuric salts. If dimethyl mercury is formed, it should be rapidly converted to methyl mercury in the presence of excess mercuric salt.

References

1. Barbara Hardin Beck, "The Acid Cleavage of Dialkyl Mercury Compounds" (dissertation), University of California, Department of Chemistry, September 8, 1967.
2. S. Jenson and A. Jernelöv, *Nature* **223**, 753 (1968).
3. F. C. Whitmore, "Organic Compounds of Mercury," Chemical Catalog Co., Inc., N. Y., 1921, pp. 26-29.
4. C. K. Ingold, *Helv. Chim. Acta* **47**, 1191 (1964).
5. F. R. Jensen and R. J. Ouellette, *J. Am. Chem. Soc.* **83**, 4477 (1961).
6. A. Jernelöv, *Nordisk Hygienisk Tidskrift* **50**, 174 (1969).
7. J. M. Wood as reported in *Chem. and Eng. News*, July 5, 1971, p. 22.

A SURVEY OF METHYL MERCURY IN FOOD FISH OF THE SAN FRANCISCO BAY AREA

M. Evett, A. F. Sciamanna, and A. S. Newton

The disastrous results (e.g., 52 deaths) of human poisoning by methyl mercury from sea food at Minamata and Niigata, Japan, have

caused concern about man's intake of this deadly toxin.¹ Although similar incidents have not occurred outside of Japan, high levels of

mercury have been detected in fish in Sweden, Canada, and the United States. Sweden has set a limit of 1.0 parts per million (ppm) mercury in commercially marketed fish, while the United States and Canada have set a limit of 0.5 ppm. Apparently, common foods other than fish and shellfish make only a small contribution to the mercury intake of Americans.²

It has been estimated that a 70-kg man would need to eat about 4 kg/week of fish containing 0.5 ppm methyl mercury to maintain a blood level which would cause toxic symptoms (0.2 ppm). Although the average fish consumption in the United States is only about 120 g/person/week, the margin is not large since the long-term effects of subtoxic levels of methyl mercury are not known.¹

Although fish are the important source of methyl mercury in our diet, little has published on the levels of mercury in American food fish. Large-mouth bass in a Mississippi reservoir were found to contain about 0.2 ppm mercury.³ Lake trout from Lake Cayuga, Ithaca, New York, contained 0.2 to 0.6 ppm mercury, and the mercury content increased with age.⁴ Various fish from the Saskatchewan River system, which is polluted by municipal and industrial sources (including a chlor-alkali plant), contain 0.2 to 8.9 ppm mercury, while fish from lakes in the area without known sources of pollution contain 0.1 to 1.1 ppm.⁵

Four species of benthopelagic fish from the Atlantic contained 0.3 to 0.8 ppm mercury, while another species contained about a tenth of that; benthopelagic fish are not used for human consumption.⁶ Although the Food and Drug Administration's regulations are resulting in large amounts of data for the mercury in tuna, none of this information has been published. However, a few specimens of fresh and canned tuna contained 0.1 to 0.5 ppm mercury, and fresh swordfish had 0.2 to 1.3 ppm.⁷

In order to estimate the human intake of methyl mercury from fish other than tuna and swordfish, we have measured the methyl mercury content of the dorsal muscle of several fish of commercial importance. Most of the specimens were obtained the day after they were caught by a trawler operating about 40 miles off San Francisco. In addition, we obtained a crab caught commercially in the gulf off San Francisco and mackerel caught off Mexico; striped bass (a noncommercial species) and king salmon were obtained from sport fishermen.

Because it is the dominant form of mercury in fish and because it presents a greater hazard to humans than inorganic mercury, we chose to analyze specifically for methyl mer-

cury. In our early determinations we used a slightly modified version of the Westöo method to extract the methyl mercury from the fish.⁸ However, most of the results reported here were obtained by using a method which is based upon that developed by Tony Cortez of the National Cannery Association. Briefly, this method begins with two extractions with acetone to remove water and lipids from the ground tissue, followed by acidification with hydrochloric acid to free the methyl mercury from the protein. Benzene is then added to extract methyl mercuric chloride.

The benzene extracts were analyzed in the gas chromatograph with a plasma discharge detector which we have described in another section of this annual report. The methyl mercuric chloride content of the benzene extracts was calculated from the recorder traces by comparison with the traces of standard solutions of methyl mercuric chloride.

The results are listed in Table I. Because we have attempted to examine a large number of species (few of the important West Coast species have been emitted), no species has been examined in detail. For the most part the intraspecific variations were as large as the interspecific variations.

A few of the species which we have examined have been analyzed for mercury by neutron activation at Battelle Northwest Laboratory.⁹ Five specimens of rex sole contained 0.02 to 0.07 ppm mercury, while a sixth had 0.25 ppm. Five English ("lemon") sole had 0.03 to 0.19 ppm, and two Dungeness crabs contained 0.10 ppm. In general their specimens were smaller and contained less mercury than those which we have analyzed.

We conclude that although the food fish which we have examined contain somewhat less methyl mercury than tuna and swordfish, these species will be a major source of this toxin for those who eat them regularly.

In order to corroborate the validity of our methods, we have analyzed a swordfish sample by our version of the Westöo method, by the Cortez method, and by the Zeeman effect atomic absorption method of R. D. McLaughlin and T. Hadeishi of this laboratory. We have also compared the Cortez method with the x-ray fluorescence measurements of R. D. Giaque of this laboratory on three fish samples which have been distributed to ninety laboratories by the Environmental Protection Agency. The results are given in Table II.

We have used our methods to examine the methyl mercury content of the livers of sea lions which whelp on the Channel Islands in the Los Angeles Basin. These samples were

Table I. Methyl mercury in the muscle of some Pacific Coast fishes.

	Standard length (cm)	Hg as CH ₃ HgCl (ppm wet weight)
<u>Rockfishes</u>		
Channel (Sebastolobus alascanus)	40 34.6	0.49 0.18
Bocaccio (Sebastes paucispinis)	42	0.11
Chillipepper (S. goodei)	36.2	0.38
Big-eyed (S. zacentrus)	36	0.29
<u>Sole</u>		
Dover (Microstomus pacificus)	32.5	0.10
Rex (Glyptocephalus zachirus)	29.2 24	0.12 0.052
English (Parophrys vetulus)	27.7 30	0.088 0.051
Petrale (Eopsetta jordani)	35 28.5	0.096 0.074
<u>Others</u>		
Dungeness crab (Cancer magister)	16	0.096
Sablefish (Anoplopoma fimbria)	49.2	0.048
Pacific mackerel (Pneumatophorus diego)	35	0.11
Monterey Spanish mackerel (Scomberomorus concolor)	23	0.019
King salmon (Oncorhynchus tshawytscha)	46.5	0.027
Striped bass (Morone saxatilis)	63.5* 49	0.46 0.16

* Total length.

Table II. Intercalibration of methods. Ppm mercury in standard fish samples.

Sample	Method			
	Modified Westöc	Cortez	X-ray fluorescence	Zeeman effect atomic absorption
LBL Swordfish	0.84 ± 0.02	0.87 ± 0.03	-	0.80 ± 0.11
EPA Round robin fish	72C1222	2.16 ± 0.02	2.4 ± 0.6	-
	72C1223	5.76 ± 0.02	7.3 ± 0.7	-
	72C1224	7.27 ± 0.21	7.6 ± 0.7	-

obtained from R. L. DeLong and W. Gilmartin of the Naval Undersea Research and Development Center, who are trying to determine the cause of a high incidence of premature births. Methyl mercury is one of many suspects in this problem because a land-locked seal in

Finland contained more than 100 ppm methyl mercury in its liver. The results of our analyses are given in Table III. These specimens contained much less methyl mercury than that from Finland.

Table III. Methyl mercury content as ppm mercury in the livers of sea lion mother-pup pairs.

Mother	Premature pup	Mother	Normal term pup
0.58	0.076	2.50	1.52
1.26	0.18	1.28	0.87
0.98	0.11	3.81	1.37
0.82	0.42	1.30	1.05
0.90	0.05	1.58	0.78

References

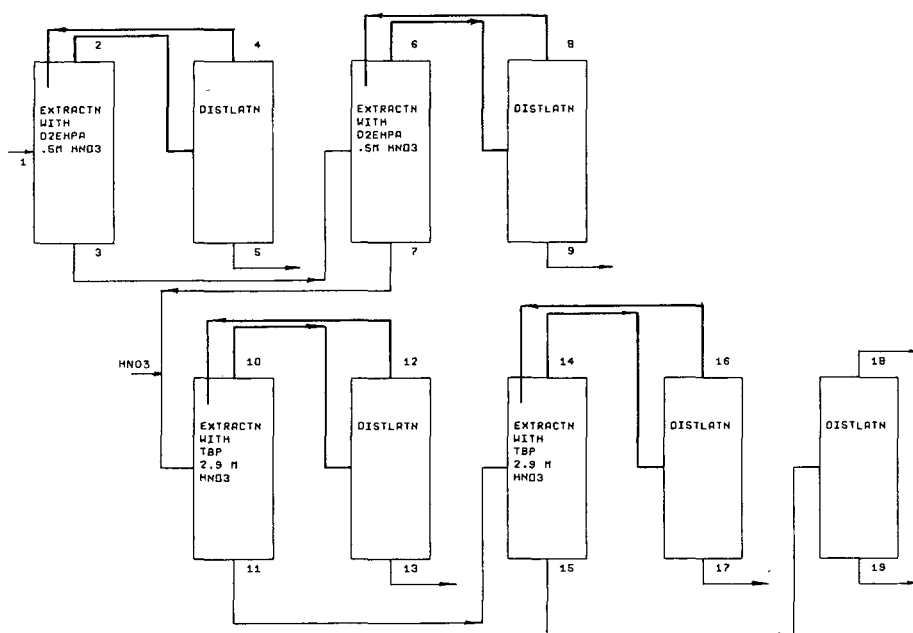
1. Study Group on Mercury Hazards, Department of Health, Education, and Welfare, *Environmental Research* 4, 1 (1971).
2. J. T. Tanner, M. H. Friedman, and D. N. Lincoln, *Science* 177, 1102 (1972).
3. L. A. Knight and J. Herring, *Pesticides Monitoring Journal* 6, 103 (1972).
4. C. A. Bache, W. H. Gutenmann, and D. J. Lisk, *Science* 172, 951 (1971).
5. A. K. Sumner, J. G. Saha, and Y. W. Lee, *Pesticide Monitoring Journal* 6, 122 (1972).
6. R. T. Barber, A. Vijayakuma, and F. A. Cross, *Science* 178, 636 (1972).
7. G. E. Miller, P. M. Grant, R. Kishore, F. J. Steinkruger, F. S. Rowland, and V. P. Guinn, *Science* 175, 1121 (1972).
8. G. Westöo, *Acta Chemica Scandinavica* 22, 2277 (1968).
9. D. E. Robertson, L. A. Rancitelli, J. C. Langford, and R. W. Perkins, in "Baseline Studies of Pollutants in the Marine Environment," background papers for a workshop at Brookhaven National Laboratory, May 1972.

LOGICAL APPROACHES TO THE SELECTION OF SEPARATION PROCESSES

R. W. Thompson* and C. J. King

This project has developed and tested logical methods for the selection and sequencing of separation processes for splitting multi-component feed mixtures into a number of specified products. The synthesis of separation sequences is carried out by using the digital computer, with relatively detailed simulations of sizing and cost factors for the various candidate separation processes. Algorithmic and heuristic procedures have both been used. Several real separation problems have been used as test examples. The project was completed in 1972 and is reported in two publications. ^{1, 2}

As an example of the sort of problem considered, Fig. 1 shows a process synthesized for the separation of a mixture of rare earths by solvent extraction. The table in the figure gives the sequence of units in the process, light and heavy key components in each separator, the type of separator, and costs associated with the individual units. Table I shows the feed mixture postulated and the various solvents (mass separating agents) considered. Table II is a list of separators considered as candidates for the process, and Table III shows the distribution coefficients for different solute-solvent systems. Table



STRM	CHPONT	PRODUCT	SEP	NXT	MSA	LST	COST	PRODUCTS IN STREAM							
NUMB	LK	HK	HK	LK	NLM	STR	RCL	STR	1	2	3	4	5	6	
1	8	7	3	4	5	2	4	0	16170	1	2	3	4	5	6
2	14	9	4	10	1	4	0	1	-8	4	10				
3	6	5	2	3	5	6	8	1	127176	1	2	3	5	6	
4	0	0	0	0	0	0	0	2	0	10					
5	0	0	0	0	0	0	0	2	0	4					
6	14	6	3	10	1	8	0	3	36	3	10				
7	4	3	1	2	3	16	12	3	68967	1	2	5	6		
8	0	0	0	0	0	0	0	6	0	10					
9	0	0	0	0	0	0	0	6	0	3					
10	12	5	2	8	1	12	0	7	259	2	8				
11	2	1	5	1	3	14	16	7	107886	1	5	6			
12	0	0	0	0	0	0	0	10	0	8					
13	0	0	0	0	0	0	0	10	0	2					
14	12	3	1	8	1	16	0	11	2551	1	8				
15	10	1	5	6	1	18	0	11	7293	5	6				
16	0	0	0	0	0	0	0	14	0	8					
17	0	0	0	0	0	0	0	14	0	1					
18	0	0	0	0	0	0	0	15	0	6					
19	0	0	0	0	0	0	0	15	0	5					
TOTAL \$							330336								

Fig. 1. Example solvent extraction process for the separation of rare earths.

(XBL 726-1180)

IV shows the specifications for which components should be in which product.

The number of possible combinations of different separators which may be used to carry out the specified separation is extremely large, and the chief thrust of the research has been to identify and develop efficient logic which will lead rapidly to one of the most desirable process configurations. The components of the final logic program are shown in Fig. 2.

There is a considerable saving in search requirements if infeasible and/or quite unattractive sequences can be identified at an early point in the logic. The initial step in

the logic is to identify a feasible product set for meeting the specifications; this may require splitting and recombining one or more of the specified products. Candidate separators at various points are now stored in the form of a product separability matrix. A Check routine is implemented to perform an early identification of separators which will involve extreme flow ratios of solvents or which will involve miscible solvent phases and thereby not be feasible. The Product Separability Matrix is updated accordingly.

A heuristic, or rule-of-thumb, is then used to generate a process sequence, starting with the feed mixture and introducing separators until the specified products have been

Table I. Component numbering.

Component	Symbol	No.	Feed mol fraction
<u>Feed:</u>			
Lanthanum	La	1	0.00614
Cerium	Ce	2	0.01175
Praseodymium	Pr	3	0.0015
Neodymium	Nd	4	0.00488
Samarium	Sm	5	0.00053
Europium	Eu	6	0.000025
Gadolinium	Gd	7	0.000125
Terbium	Tb	8	0.000025
Dysprosium	Dy	9	0.000025
Water		10	0.975
<u>Mass-separating agents:</u>			
TBP vs. 0.266 M HNO ₃		11	
TBP vs. 2.9 M HNO ₃		12	
TBP vs. 12.5 M HNO ₃		13	
D2EHPA (0.75 M in toluene) vs. 0.5 M HNO ₃		14	
0.266 M HNO ₃ vs. TBP		15	
2.9 M HNO ₃ vs. TBP		16	
12.5 M HNO ₃ vs. TBP		17	
0.5 M HNO ₃ vs. D2EHPA		18	

Table II. Potential separators.

No.	Separator	Feed phase	Second phase
1	Distillation		
2	Solvent extraction	0.266 M HNO ₃	TBP
3	Solvent extraction	2.9 M HNO ₃	TBP
4	Solvent extraction	12.5 M HNO ₃	TBP
5	Solvent extraction	0.5 M HNO ₃	0.75 M D2EHPA in toluene
6	Solvent extraction	TBP	0.266 M HNO ₃
7	Solvent extraction	TBP	2.9 M HNO ₃
8	Solvent extraction	TBP	12.5 M HNO ₃
9	Solvent extraction	0.75 M D2EHPA in toluene	0.5 M HNO ₃

achieved. A successful heuristic in many instances has been that of picking as the next separator that one from among the candidates which has the lowest predicted cost. This heuristic does fail upon occasion though, such as when quite large flows can build up at the later stages of solvent extraction processes, such as that in Fig. 1.

Sizing and costing are performed on the process generated, and the estimated costs of the various candidate separators are updated on the basis of the information gained

(a learning procedure). The logic then recycles and generates another sequence, continuing until the synthesis procedure stabilizes upon some one cheapest-indicated process.

Test cases considered have included solvent extraction schemes using a variety of solvents giving different component orderings (see Table III), and hydrocarbon separations involving distillation, extractive distillation, absorption, stripping, and solvent extraction.

Table III. Distribution coefficients of rare earths.

Rare earth	Into tributyl phosphate (TBP)			Into D2EHPA
	0.226 M HNO ₃	2.9 M HNO ₃	12.5 M HNO ₃	0.5 M HCl
	D _c	D _c	D _c	D _c
La	0.02	0.15	0.092	0.0001
Ce	0.023	0.24	0.184	0.0025
Pr	0.026	0.29	0.291	0.0056
Nd	0.03	0.35	0.36	0.01
Pm	0.033	0.40	0.622	0.32
Sm	0.036	0.45	1.22	0.063
Eu	0.04	0.51	2.01	0.16
Gd	0.039	0.52	2.84	0.316
Td	0.024	0.50	6.21	1.41
Dy	0.018	0.45	8.99	3.16

$D_c = \frac{\text{concentration in solvent}}{\text{concentration in water}}$

Table IV. Multicomponent product set—example No. 4.

Index	Components
1	= 1 2
2	= 3 4
3	= 6 7
4	= 5
5	= 8
6	= 9
7	= 10
8	= 11
9	= 12
10	= 13
11	= 14
12	= 15
13	= 16
14	= 17
15	= 18

Footnote and References

* Present address: Unit 1500, Upjohn Corp., Kalamazoo, Michigan 49001.

1. R. W. Thompson and C. J. King, Systematic Synthesis of Separation Schemes, LBL-607, January 1972. Paper presented at Symposium on Computer-Aided Process Synthesis, Amer. Inst. Chem. Engrs. Natl. Mtg., Dallas, Texas, February 21, 1972. A. I. Ch. E. Journal 18, 941 (1972).

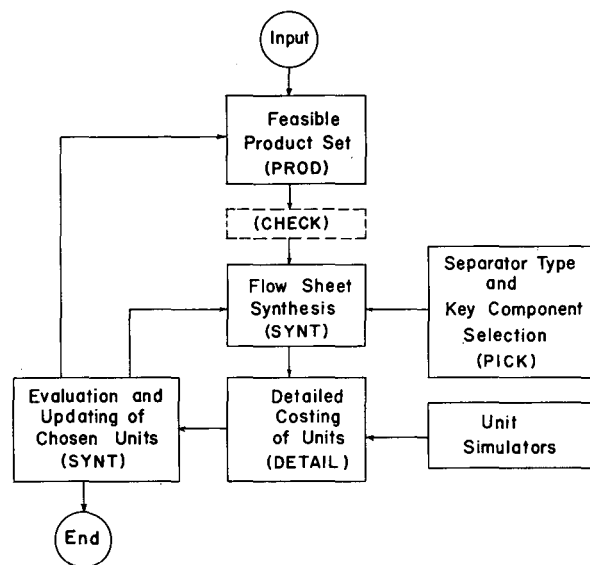


Fig. 2. General strategy. (XBL 724-718)

2. R. W. Thompson and C. J. King, Synthesis of Separation Schemes, LBL-614, July 1972.

MASS AND HEAT TRANSFER BETWEEN PHASES; INFLUENCES OF INTERFACIAL INSTABILITY AND HIGH RATES OF MASS TRANSFER

I. F. Davenport* and C. J. King

This project is examining factors which complicate and augment interphase mass and heat transfer processes, with particular reference to extractors, absorbers, direct fluid-fluid contact heat exchangers, and enclosed vessels of fluid undergoing heat exchange with the environment through natural convection. Previous work has successfully predicted and analyzed high-flux effects and has demonstrated the importance of interfacial convection generated by gradients in density and/or surface tension.

Measurements of the surface tension of solutions of sulfur dioxide in water were made to elucidate previous experiments which appeared to indicate a strong effect of surface rigidity or surface contamination upon the initiation of convection. These measurements indicated that the effect was most likely one of adverse surface tension gradient forces resisting density-driven convection rather than a result of rigidity.¹

In a broad study, carefully constructed devices were used to observe the onset of convection in a one-dimensional heat flow situation, involving either cooling from above by a thermoelectric cooler or a spray cooler, or heating from below with an electrical heater. The results of these studies are extensive and are presented elsewhere.^{2,3} Experiments were carried out to ascertain the effects of changing from fixed to free surfaces, of Prandtl number, of fluid depth, of fluid width, of external vibration level, and of the shape of the surface temperature history. The results were used to test various predictions of existing theories—the quasi-steady-state (QSA) theory and the amplification theory. Both theories were found lacking, and an improved mechanistic explanation was therefore conceived and confirmed qualitatively with the data. Significant conclusions will be outlined here.

1) The effects of different surface-temperature histories and different fluid depths are satisfactorily correlated by a unique value of Ra_l , a Rayleigh group based upon the effective thermal boundary layer depth. Figure 1 shows the depth effect for a fixed surface, contrasted with the predictions of Currie from QSA theory.

2) External vibration promotes instability, in directional accord with the prediction of both previous theories.

3) For a low-vibration situation, decreasing the Prandtl number of the fluid increases the

Rayleigh number for instability. The asymptotic Ra - Pr functionalities, as shown in Fig. 2 for the fixed-surface case, are in agreement with amplification theory, but correspond to very different amplification factors required for observable convection. QSA theory predicts independence of Prandtl number.

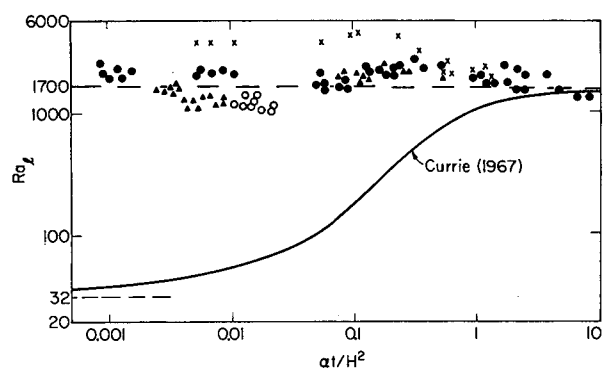


Fig. 1. Experimental values of Ra_l as a function of the depth factor ($\alpha t/H^2$) for the fixed-surface case, with linear decay of surface temperature.

● n-Butanol, $Pr = 43$,
 ▲ Silicone oil 50 cs, $Pr = 465$,
 ○ Silicone oil 1000 cs, $Pr = 8500$,
 × Methanol, $Pr = 7.6$. (XBL 726-3166)

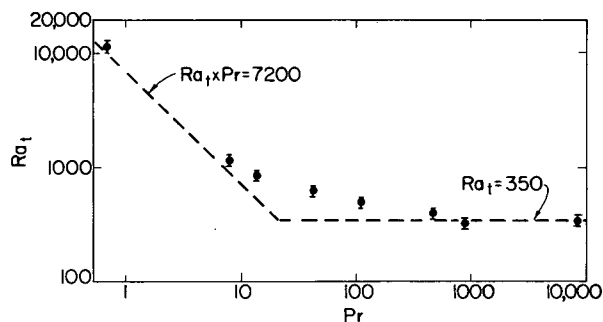


Fig. 2. Experimental values of Ra_l for a linear surface temperature decay at a fixed surface as a function of Pr showing the two experimentally fitted asymptotes.

(XBL 726-3165)

4) In the absence of surface waves and external vibration the conditions for instability in deep pools are the same for fixed and free surfaces, as illustrated in Fig. 3. This result is in conflict with both QSA and amplification theories and strongly suggests that the point of incipient convection is at the bulk-fluid edge of the thermal boundary layer.

5) In the absence of surface waves, meniscuses, and gradients in surface temperature or composition, there is no surface-tension influence upon free-surface convection initiation in deep and shallow pools, even for Marangoni numbers more than three orders of magnitude above those predicted for instability by the QSA analysis. This relates to the absence of any effect of surface rigidity, and again indicates that the point of instability does not initially interact with the surface. Previous reported instances of surface-tension-driven instability in deep-pool situations may be attributed to surface waves and/or meniscuses.

6) Conclusions 4) and 5) differ from the reported observations of time-independent convection studies where destabilizing surface tension forces and free surface shear conditions have affected the conditions for density-driven convection initiation. The explanation for this should lie in the manner by which the destabilizing effect interacts with the unstable field in the fluid.

In another phase of this study² the knowledge obtained from the studies of convection initiation was used to interpret the transitions which occur in natural convection heat-transfer coefficients at higher Rayleigh numbers. A successful interpretation is made in terms of the frequency of generation of thermals at the inner-fluid edge of the thermal boundary layer.

Footnote and References

* Present address: Assistant Professor of Chemical Engineering, Massachusetts Institute of Technology, Cambridge, Massachusetts 02139.

1. I. F. Davenport and C. J. King, Marangoni Stabilization of Density-Driven Convection, LBL-608, January 1972.

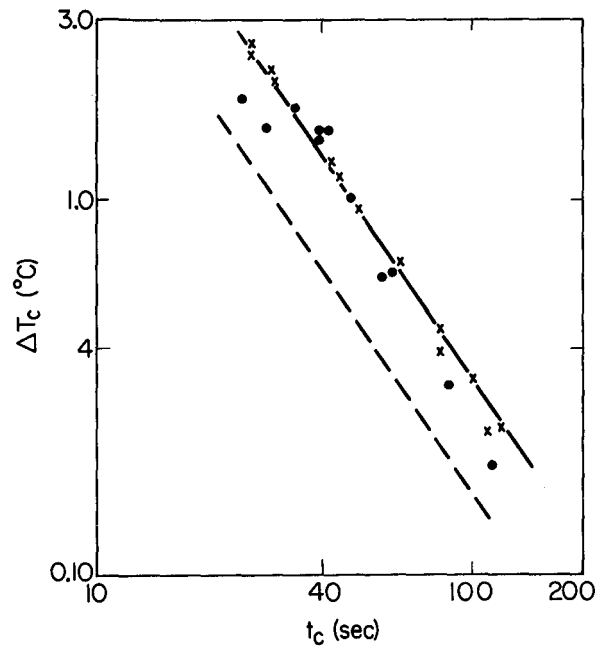


Fig. 3. Experimental conditions of onset of convection in n-decane ($Pr = 13$) for a linear surface-temperature decay in a deep pool, using the thermoelectric cooler.

× Fixed-surface data,

● Free-surface data,

-- Free-surface predictions of Mahler (1970) assuming same amplification factor as for fixed-surface results.

(XBL 726-3178)

2. I. F. Davenport and C. J. King, The Initiation of Natural Convection Caused by Time-Dependent Profiles, LBL-660, June 1972.

3. I. F. Davenport and C. J. King, An Experimental Study of Convection Initiation in Deep Pools, LBL-1252, September 1972.

QUANTITATIVE NEUTRON ACTIVATION ANALYSIS
OF HUMAN TISSUES

T. Budinger, B. Moyer, H. V. Michel, F. Asaro, and I. Periman

The present study was a trial program to determine the experimental conditions, the range of elements and chemical compositions which could be measured, with precision in a large-scale program using neutron activation analysis techniques. Budinger et al. have already presented¹ the qualitative study of the elements which can be detected by this technique.

In this study we have quantitatively analyzed for 20 elements and set upper limits for an additional 27 elements in human liver, kidney, spleen, heart, and lung tissue.

Sample Preparation, Irradiation, and
Gamma Analysis

The tissues were frozen in liquid nitrogen and lyophilized overnight. The wet samples lost about 80% of their weight in this process. Each sample of dried tissue (~100 mg) was weighed and pressed into a 1-cm diameter × 1.5-mm pill. Using techniques similar to those developed for pottery analysis, five pills were heat-sealed in polyethylene and radially placed in a high-density polyethylene capsule along with a standard-pottery² pill, an Al foil, and CaCO₃ and KCl standards. The capsule

Table I. Elemental abundances in human tissues based on lyophilized weight.^a

Element	Liver	Kidney	Spleen	Heart	Lung
	(in ppm or % of lyophilized tissue)				
Potassium(%) ^b	1.10±.10	.98±.13	1.41±.13	1.37±.12	.49±.10
Phosphorous(%) ^c	.91	.68	.96	.77	.48
Chlorine(%) ^b	.69±.01	1.13±.04	1.02±.04	.65±.03	.98±.04
Sodium(%) ^b	.424±.005	1.01±.01	.493±.007	.459±.007	.677±.008
Iron(%)	.262±.007	.062±.006	.250±.009	.038±.004	.130±.010
Zinc	348±8	198±8	78±8	112±8	83±8
Bromine	143±2	77±2	182±2	107±2	187±2
Rubidium	32±4	7±5	32±4	26±5	27±10
Cadmium ^c	7.3±2.2	255±4	1.8±2.6	4.6±2.3	12.0±214
Molybdenum	2.5±.5	.6±.6	.8±.6	.7±.5	1.0±.5
Selenium ^c	2.4±.5	7.3±1.1	.7±.7	1.6±.6	7.1±.9
Cobalt	.23±.02	.10±.02	---	---	---
Cesium	.18±.04	.21±.06	.33±.04	.18±.05	.36±.09
Thorium	.01±.03	.05±.03	.09±.03	.03±.03	.47±.05
Scandium	.065±.006	.084±.008	.093±.006	.062±.006	.143±.013
Tantalum	.130±.002	.016±.002	.425±.004	.296±.004	.073±.004
Mercury ^c	.05±.09	3.0±.1	.24±.10	-.01±.09	-.03±.09
Antimony	.037±.018	.025±.040	.007±.014	-.04±.02	.88±.10
Samarium	.004±.004	.025±.004	.034±.004	.022±.004	.065±.004
Hafnium	.00±.04	.03±.06	.04±.05	.01±.05	.54±.11

^aTo obtain abundances based on wet weight, divide all abundances and errors by 5.

^bThese values are more precise because of a special higher flux irradiation.

^cThese elements have poor calibration standards. These abundances are tentative, and P was determined from bremsstrahlung radiation. Some Hg may be lost in the preparation and irradiation procedures.

was irradiated while being rotated in the TRIGA reactor of the Department of Nuclear Engineering, University of California, Berkeley, for 20 min at 11 kW power ($\sim 4 \times 10^{11}$ n/cm²/sec). Within 8-10 min after the end of the bombardment the first sample was placed on the detector and each was analyzed for 1 min. This spectrum was used to determine the Al, Mg, Ca, V, and Cl. After approximately 2 hr of decay these samples were again analyzed for 10 min each to determine the Na, Mn, Dy, Ba, Sr, Ga, and In. New samples were made for the long irradiation. It was necessary to mix 100 mg of pure powdered Si to 100 mg of tissue in order to main-

tain the sample integrity during the 8-hr irradiation at 1000 kW ($\sim 3 \times 10^{13}$ n/cm²/sec). These pills were pressed as before, wrapped in pure Al foil, and placed radially in an Al capsule along with standard pottery. After 5-6 days cooling, the samples were analyzed on a high-resolution detector (0.077 keV/channel). The samples were allowed to cool for another 3 weeks before analyzing for the longer-lived isotopes with gamma energies up to ~ 1.7 MeV (~ 1 keV/channel). Finally the samples were again analyzed on the high-resolution detector to obtain better values for some of the longer-lived isotopes.

Table II. Limits on elemental abundances in selected human tissues based on lyophilized weight.^a

Element	Liver	Kidney	Spleen	Heart	Lung
(in ppm or % of lyophilized tissue)					
Mg(%)	.21 ^b	1.9	.6	.6	.95
Ca(%)	.13 ^b	.9	.9	.5	.8
Al(%)	.014 ^b	.16	.24	.46	.79
Sr	158 ^b	397	142	201	113
Ti	139	365	266	224	350
Ba	40	43	77	40	63
Sn	16	36	18	18	40
Ga	12	40	17	18	26
Ni	7 ^b	18	9	9	23
V	5.1 ^b	26	9	18	14
Cr	4.9	9.7	---	---	---
Nd	4.5	3.0	4.9	1.4	1.7
Mn	4 ^e				
As	2.6	2.6	4.5	2.7	3.6
La	1.6	.9	1.3	1.2	1.6
In	1.6	4.2	2.0	3.9	.6
Ce	1.1	1.3	.8	.6	2.0
W	.8	1.0	.8	1.0	1.2
Ag	.4	.6	.5	.4	.5
Dy	.22 ^b	.3	.3	.2	.3
Yb	.19	.26	.39	.27	.25
U	.06	.06	.06	.08	.05
Au	.031	.014	.035	.035	.14 ^c
Lu	.03	.06	.06	.05	.07
Tb	.024	.039	.023	.008	.003
Eu	.011	.017	.031	.022	.059
Ir ^d	.0025	.0035	.0027	.0029	.003

^aTo obtain limits based on wet weight, divide all values by 5.

^bThese values are more precise because of a special higher flux irradiation.

^cMay be due to contamination.

^dIridium had no calibration standard; values are only approximate.

^eLimit due to ⁵⁶Fe (n, p) ⁵⁶Mn reaction.

Results

Table I lists the values for 20 elements seen in the five tissues. The values for Co and Cr in spleen, heart, and lung are not shown because of possible sample contamination.

Upper limits for 27 additional elements are shown in Table II, the limit being the value plus 2σ .

Separate analyses were made on three samples of the liver tissue. The average values for 13 elements are shown in Table III. The average counting error and the root-mean-square error of the three measurements are shown. The errors in the K, Na, Rb, and Ta values are mainly due to counting statistics, whereas the rms errors for Br, Cs, Cl, Fe, Sc, and Zn values are 2-5 times

larger and indicate the variations in the sample preparation techniques or within the liver itself. Further measurements on representative selected portions of the liver would be necessary to distinguish between these effects.

Conclusion

It is feasible to make large-scale precise neutron activation elemental abundance measurements on human tissues. Initial experiments should probably be concentrated on determination of the variation of composition within particular organs. This could be followed by large-scale analysis on many subjects and a selected number of organs to cast some additional light on the etiological relationship between elemental abundances and human health.

Table III.

Element (% or ppm)	Average	Average error	rms error
Potassium(%)	1.02	± 0.11	± 0.12
Chlorine(%)	0.70	± 0.02	± 0.05
Sodium(%)	0.431	± 0.010	± 0.012
Iron(%)	0.262	± 0.008	± 0.015
Zinc	348	± 4	± 7
Bromine	135	± 2	± 11
Rubidium	32	± 6	± 4
Cadmium	8.4	± 2.2	± 1.5
Selenium	1.8	± 0.6	± 0.6
Cesium	0.18	± 0.04	± 0.08
Tantalum	0.13	± 0.03	± 0.01
Scandium	0.065	± 0.006	± 0.018
Samarium	0.014	± 0.015	± 0.014

References

1. T. Budinger, J. R. Farwell, A. R. Smith, and H. Bichsel, UCRL-20236 (1970).
2. I. Perlman and F. Asaro, Pottery analysis by neutron activation analysis, *Archaeometry* 11, 21 (1969).
3. T. F. Budinger, J. R. Farwell, A. R. Smith, and H. Bichsel, Human Tissue Trace Element Detection by Neutron Activation Without Chemical Separation, *International Journal of Applied Radiation and Isotopes*, Vol. 23, 49 (1972).

ARCHAEOLOGICAL IMPLICATIONS OF COMPOSITION VARIATIONS IN OBSIDIAN SOURCES*

H. R. Bowman, F. Asaro, and I. Perlman

The chemical compositions of obsidian artifacts have been used by a number of investigators to "fingerprint" them and thereby locate the sources of some of man's early im-

plements.¹⁻³ Although obsidian artifacts are found widely, the possible sources of volcanic glass are comparatively few. The evidence is good that obsidian was an article of commerce,

and there is some incentive in establishing specific trade patterns or to deduce what other circumstances resulted in the appearance of artifacts away from obsidian sources.

It is implicit in this chemical approach to provenience studies that one determines the composition of obsidian from specific sources. A group of samples from one place will, of course, show some dispersion introduced by error of measurement even if the obsidian flow is very homogeneous. Beyond this, the source material may be intrinsically inhomogeneous. In such a case, provenience of artifacts can still be established if differences in composition between different sources are sufficiently great.

The present communication is based largely upon a geochemical study published elsewhere⁴ and stresses two points which are pertinent to archaeological problems: (1) An obsidian flow or source can show considerable variation in composition. (2) In the case studied, the coherence in variation of the elements is extraordinary, so much so that the judgment of provenience is just as definitive as it would be if the flow were extremely homogeneous.

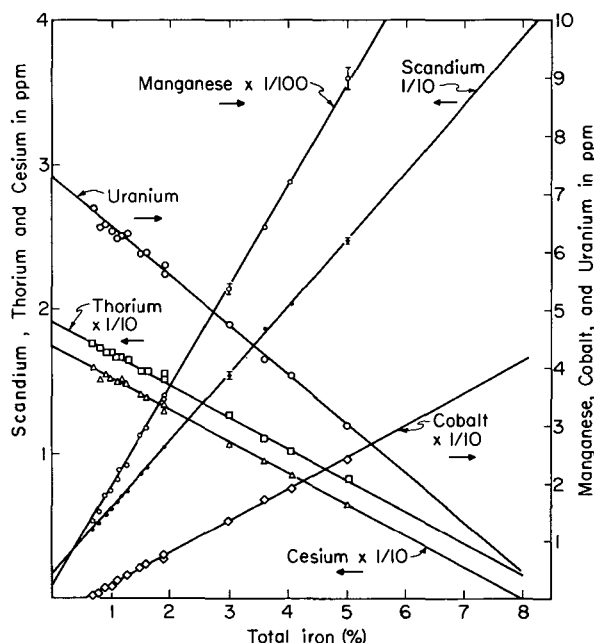


FIGURE CAPTIONS

Fig. 1. The chemical variation diagrams for scandium, manganese, cobalt, uranium, cesium, and thorium plotted against total iron content for obsidian and dacite from the Borax Lake source area. (XBL 725-2856)

Analytical data presented here pertain to a small volcanic flow at Borax Lake in Lake County, Northern California. It has been described⁵ as a thin layer of dacite (15-25 ft) overlain by a thicker layer of obsidian (40-50 ft). The procedure employed was neutron activation analysis as described in some detail in an earlier publication.⁶ This system of analysis emphasizes the trace elements and, in all, some 40 elements are determined, including a considerable number for which the precision is high.

Figure 1 shows the variation of six of the trace elements relative to iron and embraces the whole range of obsidians and dacites.

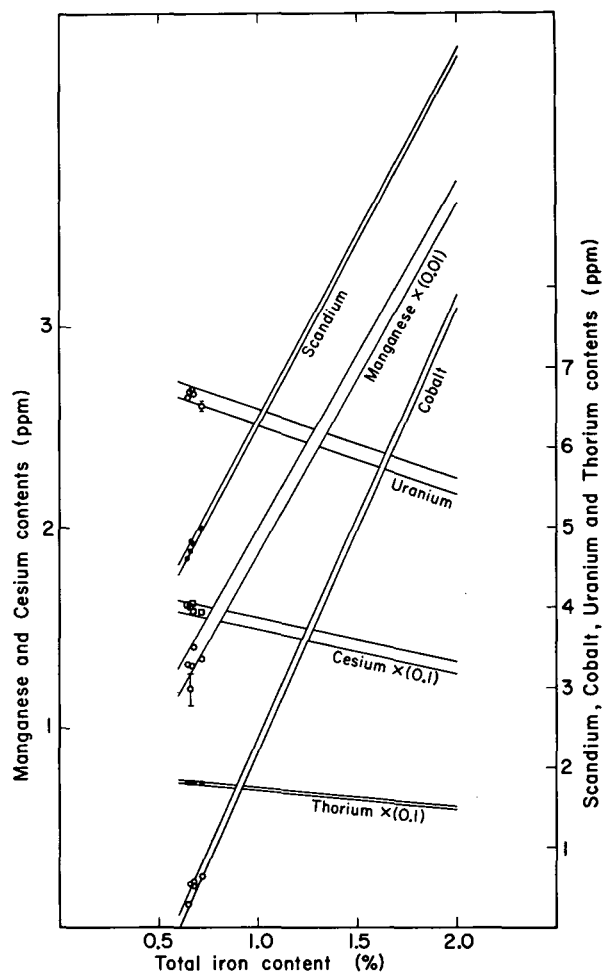


Fig. 2. The comparison of the elemental composition of obsidian implements (excavated at Borax Lake, Calif.) with the chemically variable obsidian from the same area. The two lines for each element are the rms deviations obtained from the analysis of obsidian and dacite samples from the source area. (XBL 724-2854)

The data of Fig. 1 are displayed in Fig. 2 with some modifications in format. The range is confined to those specimens which can be classed as obsidian and the zones, each defined by a pair of lines, represent ± 0 to the least-squares-fit line (not shown). Statistically, two out of three data points would lie within the zone shown. If one wishes to know whether an artifact was made from Borax Lake obsidian one simply enters the data points on this diagram. Selecting, say, 21 elements chosen to display a variety of chemical behavior, about 14 of these should lie within the zones. This analysis provides extremely fine discrimination between different flows even where there is a large range in composition, provided it is proved that the variations are coherent as found here.

The data points displayed in Fig. 2 were obtained from the analysis of five obsidian artifacts found at Borax Lake.⁷ Considering that these were found at a site with a ready source of obsidian, there was hardly any question of their provenience, consequently our interest in these was of a more microscopic nature. It is seen from Fig. 2 that all five have compositions near one extreme of the range, corresponding to the most silicic material, but artifacts made from any local material should fit as well. In terms of sampling locus, obsidian of this composition was obtained at one end of the flow locally termed "the gravel pit" in deference to alluvial deposits of small rocks in this area.

There is some evidence that inhabitants of this site used obsidian covering a wider range of compositions than that encountered in the five specimens analyzed by us. Stevenson, Stross, and Heizer² analyzed a considerable number of artifacts from Borax Lake, using the x-ray fluorescence technique and found a variation in composition. We shall only be concerned with their iron and manganese data, because only with these do we have possible intercomparisons. They presented their data in arbitrary units so that comparisons cannot be made directly. However, they also analyzed obsidian from another flow (Mt. Konocti) found by us to be sufficiently uniform in composition that conversion of their arbitrary units to absolute numbers was possible. In our measurements of 37 randomly-selected pieces of obsidian from Mt. Konocti the rms deviations for iron and manganese were respectively 5% and 6% of the mean values.

One group of seven Borax Lake artifacts² proved to have an iron content of $0.65 \pm 0.05\%$, which agrees well with the five artifacts analyzed by us (see Fig. 2). Another group showed $Fe = 1.04 \pm 0.07\%$. The corresponding manganese values for these two groups are

118 ± 15 and 186 ± 24 ppm respectively. These two groups are significantly different from each other and both will be found to fit well on the Mn vs Fe plot in Fig. 2.

Of interest to the archaeologist is the question of whether the Borax Lake compositional picture is singular or should one expect to encounter this situation elsewhere and commonly. There can be no unequivocal answer at this point, but we are inclined to the view that this picture may be common but will vary in degree. A sampling from a fairly large flow in Napa County, California, showed the obsidian to be fantastically homogeneous; at Mt. Konocti (like Borax Lake, in Lake County) a variational pattern was seen, but of lower order than that from Borax Lake. Where the variation in composition is small, all artifacts from that source will show essentially the same composition; where variations are severe, artifacts from the same source could prove difficult to interpret unless the pattern of source obsidians has been determined. Finally, it is possible that one area may have different flows which have different geochemical histories. We have some fragmentary experimental evidence from the Medicine Lake region in the far north-east of California that we are confronted with just such a situation. The geological complexity of this region of volcanism is well known⁸ and, even without our experimental results, should serve as a warning of what might be encountered in provenience studies.

Finally, some further identification might be provided for the particular artifacts from Borax Lake that were analyzed. All of these were fluted points typologically attributed to an early culture dating back some 10,000 years.⁷ Results from hydration-layer dating⁹ were not unequivocal but were nevertheless consistent with this date, and even earlier, for occupation at Borax Lake.

Footnote and References

* Condensed from LBL-657.

1. J. R. Cann and C. Renfrew, Proc. Pre-historic Soc. 30, 110 (1964).
2. D. P. Stevenson, F. S. Stross, and R. F. Heizer, Archaeometry 13, Part 1, 17 (1971).
3. J. B. Griffin, A. A. Gordus, and G. A. Wright, Amer. Antiquity 34, No. 1 (1969).
4. H. R. Bowman, F. Asaro, and I. Perlman, Jour. of Geol. May 1973 issue.
5. C. A. Anderson, Bull. Geol. Soc. Am. 47, 629 (1936).

6. I. Perlman and F. Asaro, *Archaeometry* 11, 21 (1969).

7. M. R. Harrington, Southwest Museum (Los Angeles) Paper No. 16 (1948).

8. C. A. Anderson, *Univ. Calif. Publ. in Geol. Sci.* 25, 347 (1941).

THE ORIGIN OF THE "PALESTINIAN" BICHROME WARE*

M. Artzy, F. Asaro, and I. Perlman

Introduction

During the decade bridging the year 1930, a repertory of bichrome pottery appeared from excavations in Palestine,¹ Cyprus² and coastal Syria.³ The Bichrome Ware, as the pottery was called, was dated to the Late Bronze I Period, but may have appeared earlier. Major notice was called to this ware in the publication by Petrie in 1931 of his excavations at Tell el-'Ajjul, and since then they have been the object of detailed study. The complex arguments concerning their evolutionary associations will be summarized elsewhere but, for the moment, we only point out that the pottery has been considered indigenous to Palestine or Syria.

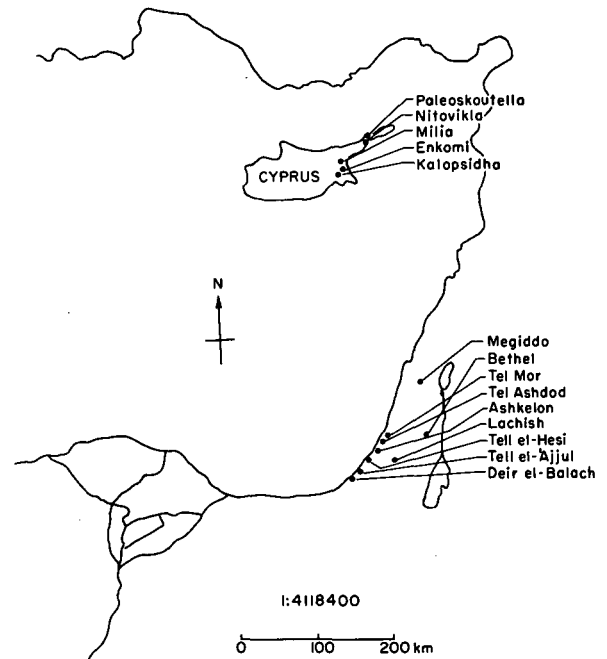
The detailed studies of the Bichrome Style by William Heurtley⁴ and by Claire Epstein⁵ both emphasize a complex pattern of stylistic influence which includes major elements of typical Cypriote wares. The two authors disagree in important aspects of interpretation, but each finds reasons to fit these wares into a Syro-Palestinian setting. The appearance of Cypriote shapes and decorations in Bichrome pottery is simply taken as an instance of strong external influence.

We turn to an issue which has beclouded the consideration of this repertory as part of a local Cypriote sequence. The Bichrome Ware is wheel-made and it is commonly accepted that the potter's wheel was not used in Cyprus as early as the Late Bronze Age. This premise has led to difficulties in interpreting other pottery styles excavated in Cyprus as well. Some major Cypriote styles of this period such as White Slip and Base Ring, do indeed seem to be almost exclusively hand-made, but others are represented by both techniques of pottery making. There are copious references for the appearance of wheel-made Cypriote styles such as Whited Painted, Plain White, Black Slip, Black Lustrous, Red Slip, and Plain Ware in the same context with hand-made forms (see, for example, Tomb 10 in Enkomi.⁶ Sometimes, in the comments on the two types, attention is called to

distinctions in "workmanship" which give added reason to label the wheel-made varieties as "imports". We have not examined extensive collections of parallel varieties in juxtaposition but, from what we have seen, the differences seem no greater than one would expect from different techniques employed by different potters.

Origins of the Bichrome Ware

In presenting the results which follow, we are faced with multidimensional comparisons: comparisons between pottery of the same style from different sites, different styles from the same site, and ancillary evidence from sites not directly associated with the Bichrome Ware. This will have to be done sequentially and not entirely in the order suggested in the previous discussion of an "ideal" provenience investigation. A substantial fraction of the analytical data obtained in this study will not be presented in this report. Some of the omit-



ted results provide useful embellishment to points which will be made and other pertain to intriguing side issues for further investigation. These will have a proper place in a lengthier report which will go beyond the few simple points we set out to make here.

Tell el-'Ajjul and Milia Main Groups. The two largest assemblages of Bichrome Ware analyzed came from two sites: 54 pieces from 'Ajjul in Palestine and 39 from Milia, Cyprus. (See map.) From the 'Ajjul Bichrome, a single chemical group was made up of 36 pieces; and from Milia, 27 pieces were placed in a single

group. Discussion of the pieces which are not included in these two groups will be presented in later sections.

In Table I are presented the statistical data on 18 elements showing the mean values and standard deviations for a group as indicated. Attention is called to the first two columns for the moment. It would appear that the Bichrome Ware groups from 'Ajjul and Milia are indistinguishable within the statistical dispersions (and this is the case) although for statistical clarity one should compare each sherd individually with a group rather than group with group.

Table I. Comparison of Bichrome Ware from Tell el-'Ajjul and Milia, and other wares from these sites.

	Aju. Bichr. (36 pieces) M±σ	Mla. Bichr. (27 pieces) M±σ	Aju. Plain (5 pieces) M±σ	Mla. Handmade (8 pieces) M±σ
Fe(%)	5.54±0.23	5.87±0.21	4.31±0.27	5.00±0.50
Ta	0.691±0.034	0.734±0.025	1.355±0.127	0.658±0.066
Sc	22.08±0.92	23.50±0.65	13.95±0.71	20.83±2.56
Co	30.54±1.78	31.33±3.19	17.21±1.09	27.13±2.94
Cs	4.70±0.50	4.71±0.43	1.13±0.49	3.59±0.63
Cr	351±68	346±31	116±14	346±62
Hf	2.95±0.21	3.23±0.17	9.74±1.02	2.97±0.29
Th	7.05±0.46	7.34±0.54	8.27±0.88	6.81±0.78
Ni	251±21	276±21	48±11	229±19
Rb	95±25	84±17	34±10	63±16
La	21.2±1.2	20.3±2.1	33.2±1.2	20.7±1.9
Lu	0.319±0.019	0.325±0.025	0.433±0.040	0.320±0.019
U	2.56±0.92	1.82±0.17	2.38±0.71	2.48±0.77
Ti(%)	0.420±0.034	0.457±0.033	0.577±0.037	0.454±0.031
Mn	973±99	984±172	855±26	1076±94
Na(%)	1.076±0.187	1.116±0.177	0.648±0.100	1.202±0.213
Al(%)	6.85±0.39	7.08±0.31	5.34±0.24	—*
Ca(%)	9.8±1.7	6.2±1.7	6.9±0.7	9.9±2.6

The numbers for the respective elements are group mean values (M) and the standard deviations (±σ). All are in units of parts-per-million unless designated "(%)".

'Aju. Plain' is a group of typical MB/LB Plain Ware from Tell el-'Ajjul.

'Mla. Handmade' is a group of hand-made White Painted and Plain Wares from Milia.

* At the time these wares from Milia were analyzed, aluminum was not measured.

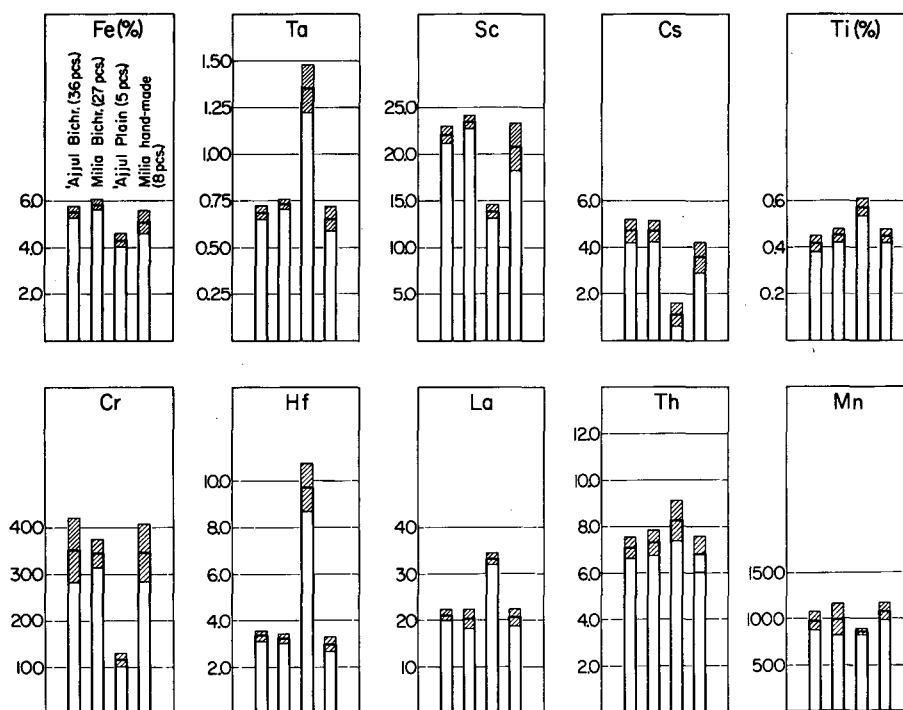


Fig. 1. The bars represent mean values for the indicated pottery groups; the hatched zone on each is \pm the standard deviation for the group. The value for each element is in units of parts-per-million unless designated "%."

'Ajjul Bichr: A group of 39 pieces of Bichrome Ware excavated at Tell el-'Ajjul; 'Ajjul Plain: A group of 5 pieces of MB/LB typical local ware.

Milia Bichr: A group of 27 pieces of Bichrome Ware excavated at Milia; Milia Hand-made: A group of 8 pieces of hand-made Cypriote wares typical of the period.

(XBL 7211-4387)

For ease in visualization, some of the data of Table I are displayed in bar-graph form in Fig. 1 where the top of each bar relates to the mean value, and the hatched zone is the extent of the dispersion in standard-deviation form. At this point we only conclude that the Bichrome Ware groups from 'Ajjul and Milia are so much alike in chemical composition that they very likely have the same provenience.

The other two columns of Table I and bars of Fig. 1 pertain to two small groups of "local wares" from 'Ajjul and Milia, respectively. It is seen that the group from Milia agrees rather well in composition with the Milia and 'Ajjul Bichrome Ware, whereas the group of plain ware from 'Ajjul is vastly different. These added considerations expand the conclusions: (1) All of the Bichrome Ware thus far

discussed came from the same place. (2) If we must choose between Milia and 'Ajjul, the place is clearly Milia, Cyprus.

When we analyzed pottery from sites on the eastern plain of Cyprus such as Milia, Enkomi and Kalopsidha, we did not find single chemical groups which embraced all of the specimens from the respective sites. Instead, a considerable number of groups appeared which are chemically quite similar to each other but readily discernible by our system of analysis. Because of the number and similarity of such groups we are inclined to believe that this region has a considerable number of places from which the ancient potters drew their clays, and that these sources share a similar geochemical history. In short, the Bichrome Ware thus far mentioned is chemically similar to a

Table II. Comparison of Tell el-'Ajjul Bichrome and Plain Wares from Table I with pottery groups from Deir el-Balach, Tel Ashkelon and Tel Ashdod.

	Aju. Bichr. (36 pieces) M±σ	Aju. Plain (5 pieces) M±σ	Balach (8 pieces) M±σ	Ashkelon (20 pieces) M±σ	Ashdod (110 pieces) M±σ
Fe(%)	5.54±0.23	4.31±0.27	4.26±0.25	3.97±0.17	3.75±0.22
Ta	0.691±0.034	1.355±0.127	1.258±0.064	1.280±0.056	1.340±0.064
Sc	22.08±0.92	13.95±0.71	13.32±0.80	13.09±0.52	12.47±0.65
Co	30.54±1.78	17.21±1.09	18.21±1.27	17.39±1.14	16.77±0.99
Cs	4.70±0.50	1.13±0.49	1.6±0.3	1.8±0.2	1.7±0.2
Cr	351±68	116±14	102±11	113±7	121±7
Hf	2.95±0.21	9.74±1.02	9.03±1.05	11.92±0.97	14.16±1.17
Th	7.05±0.46	8.27±0.88	7.56±0.53	7.66±0.38	8.03±0.45
Ni	251±21	48±11	46±11	57±14	42±14
Rb	95±25	34±10	52±14	56±10	57±7
La	21.2±1.2	33.2±1.2	30.2±2.0	30.1±1.4	30.1±1.5
Lu	0.319±0.019	0.433±0.040	0.397±0.024	0.434±0.018	0.463±0.027
U	2.56±0.92	2.38±0.71	1.62±0.18	1.89±0.22	1.94±0.12
Ti(%)	0.420±0.034	0.577±0.037	0.557±0.031	0.629±0.032	0.691±0.038
Mn	973±99	855±26	891±58	754±40	776±46
Na(%)	1.076±0.187	0.648±0.100	0.624±0.116	0.688±0.096	0.666±0.035
Al(%)	6.85±0.39	7.08±0.31	5.66±0.41	5.43±0.24	5.25±0.30
Ca(%)	9.8±1.7	6.9±0.7	6.4±1.2	7.7±1.2	6.3±0.7

The numbers in this table are defined in Table I.

'Balach' refers to a group of 8 Plain Ware vessels from Deir el-Balach.

'Ashkelon' refers to a group of 20 Philistine sherds from Tel Ashkelon.

'Ashdod' refers to a group of 110 sherds from Tel Ashdod, mostly Philistine.

number of pottery groups from the eastern plain of Cyprus, and matches very closely with this particular group of eight sherds from Milia. We shall compare some of these other groups presently.

Pottery of southern coastal Israel. As already mentioned, we are somewhat dissatisfied with the use of only five 'Ajjul plain ware sherds to represent local materials. Consequently, we shall compare the 'Ajjul plain wares with pottery drawn from three other sites in the region: Deir el-Balach which lies 6 km south of 'Ajjul, Tel Ashkelon which is about 25 km to the north and Tel Ashdod 15 km still further north. (See map.)

The data on these four sites are shown in Table II along with the 'Ajjul Bichrome group from Table I for comparison. The data for a

selected group of elements are also shown in Fig. 2 in bar-graph form. It is seen, first of all, that the four sites from southern coastal Israel have much in common although there are differences between them. These distinctions should be compared with the gross differences which all have from the 'Ajjul Bichrome group which we take to come from eastern Cyprus. Note for example, the elements Ta, Sc, Cs, Cr, and Hf, among others.

The fact that typical local potteries from three sites to the north and south of 'Ajjul all look similar to the small collection of local 'Ajjul wares gives one added confidence that these do indeed represent local manufacture. It should be emphasized that the evidence presented in Table II only shows that it is highly unlikely that the 'Ajjul Bichrome Ware was made locally. The crucial point concerning

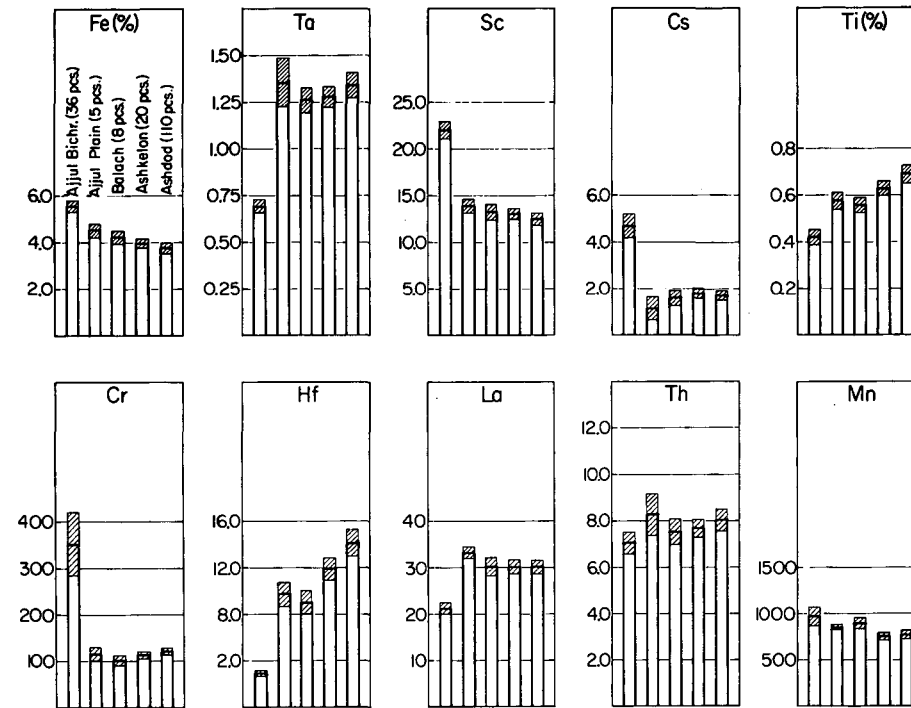


Fig. 2. The bars and hatching have the same meaning as in Fig. 1. The bars designated 'Ajjul Bichr' and 'Ajjul Plain' are repeated from Fig. 1.

Balach: refers to a group of 8 Plain Ware vessels from Deirel-Balach.

Ashkelon: 20 Philistine sherds from Tel Ashkelon.

Ashdod: 110 sherds from Tel Ashdod, mostly Philistine. (XBL 7211-4388)

their provenience is that they do agree with pottery from eastern Cyprus.

'Ajjul locally-made Bichrome. The six Bichrome pieces which we term 'locally-made' cannot specifically be assigned to 'Ajjul partly because we do not have adequate numbers of local wares with which to compare them (see Tables I and II). One piece of Bichrome does fit very well with the reference group of five pieces of plain ware from 'Ajjul; the others are somewhat different.

After finding that six Bichrome sherds were of Palestinian (if not specifically 'Ajjul) origin, we consulted our description notes and photographs to see if anything distinguished them visually. A summary for the six pieces fol-

lows: one of is a biconical jar, another a flat plate decorated with an unusual pigment and with no known parallel in Bichrome repertory, a krater sherd with unique bird head (duck-like rather than the graceful ibis), two sherds with a very soft clay, and one for which we have no photograph or notes.

It would be rash, perhaps, to assert that all of these specimens are atypical of the Bichrome repertory and on this basis to class them as imitations. Arguments of this kind are sometimes unsatisfactory in that they presuppose fixed boundaries of style, workmanship, and firing conditions, beyond which a vessel is excluded. What can be said about these six pieces is that a couple of them are singular among everything yet seen and that others are atypical in one respect or another.

Bichrome Ware from other Palestinian sites. Attention has been focused on 'Ajjul because from here came the largest number of pieces which we analyzed. It turned out that the assemblage presented a concise picture of provenience in which all specimens but a few could be clearly traced to Cypriot origin. More subjectively, the assemblage was also characterized by stylistic homogeneity in the sense that there is little doubt that the vast majority of the pieces fit clearly within the pottery repertory with which we are concerned.

Samples thus far taken from other sites are relatively few in number. The results will be presented in abbreviated form, in part because they do not constitute a reasonable sampling, but also because a broad issue has arisen about which concise answers cannot be given at present. This issue has to do with the relation between Bichrome Ware and decorated LB Palestinian pottery some of which is painted in two colors. The question has already been dealt with by Rith Amiran⁷ in considering which among these may be taken as styles derived from the Bichrome and which should be properly placed within that repertory. Indeed, Heurtley⁴ divided the Megiddo two-color pottery into two classes which he ascribed to an "early" and "late" phase of the Bichrome style. Although his chronology was shown by Epstein⁵ to be faulty, it does not follow that there are no distinctions which might be correlated temporally. For the present, we believe that there are still questions of typology and chronology which cannot be answered satisfactorily.

Beth-El. Six pieces from this site were analyzed, all of which appeared to be good examples of Bichrome Ware. Five of these had compositions indistinguishable from the large groups from Milia and 'Ajjul and are classed by us as imports from eastern Cyprus. One piece was grossly different and is clearly unlike any of the large numbers of specimens analyzed from Cyprus. It is also vastly different from the compositions we associate with southern coastal Israel.

Lachish and Tell el-Hesi. Only three samples of Bichrome Ware from Lachish and one from Tell Hesi were analyzed and all were of eastern Cypriote composition.

Tel Mor. This site, on the sea coast a short distance north west of Tel Ashdod, was a seaport settlement and is characterized by large numbers of imported wares among the pottery finds.⁸ The sherds that were sampled were small and much effaced through weathering, consequently the identification as Bichrome Ware was quite uncertain for a number of them.

Two or three fragments which could conceivably be two-colored, hence Bichrome, are probably not of Cypriote origin, but the provenience is not yet known. Nine others, for which the identification varied from "certain" to "uncertain," could be fitted among the three reference groups from Cyprus already mentioned.

Megiddo. This is an important site for the problem at hand if for no other reason than that it figured prominently in the early studies of Bichrome Ware by Heurtley and by Epstein. Here we encounter in full force the problem previously discussed, that is, what boundaries to place on the Bichrome repertory.

Among the pieces analyzed from Megiddo were found a substantial number which are as clearly of Cypriote origin as those from 'Ajjul and the other sites. There were also a number of pieces with two-color decoration which are not of Cypriote composition and agree in composition with other decorated and undecorated vessels from Megiddo. These are likely to be of local manufacture although this issue has not yet been settled on the basis of the analyses so far made. In the light of these analytical results on the two-color wares it will be necessary to re-examine typological features to see if there are any added reasons to consider these as a group apart.

Summary

The data presented here, both chemical and typological, point to eastern Cyprus as the source of the "Palestinian" Bichrome Ware. Probably, it would be incorrect to assert that every piece of pottery which is reasonably classified as Bichrome Ware was made in Cyprus; nevertheless, the vast majority of those analyzed can be traced to Cyprus and of these the preponderance came from the region around Milia.

A stylistic antecedents of the Bichrome Ware are readily at hand within the long tradition of Cypriote painted wares. Although the Bichrome repertory contains some innovative features, most of the vessel shapes and design motifs bear a striking resemblance to those of the White Painted sequence of the Middle Cypriote Period.

In view of the virtual certainty that the wheel-made Bichrome Ware was made on Cyprus, it seems no longer necessary to classify other pottery of the period as imports to Cyprus solely because they were made on the potter's wheel. Consequently, deductions which have been based upon wheel-made wares of White Painted, Black Slip, Plain Ware and other styles should be re-examined.

The acceptance of Cypriote provenience for the Bichrome Ware also brings into focus some issues concerning the typological extent of the repertory and the chronology associated with any stylistic divisions which can be made. The possibility now exists for distinguishing between Bichrome Ware and Late Bronze Palestinian Painted Ware which is sometimes termed "Bichrome" because it may be painted with two colors. In the southern sites which were destroyed by Ahmosis, Bichrome Ware appeared before the destruction, and this also points to an earlier date than that at which we believe the LB Painted Ware belongs. Obviously, these tentative conclusions call for a careful re-examination of stratigraphic information and for chemical analyses of a larger array of pottery of these periods.

Footnote and References

* Condensed from LBL-1286.

1. Sir Flinders Petrie, Ancient Gaza II (London, 1932).

2. A. Westholm, "Some Late Bronze Tombs at Milia," Quarterly of the Department of Antiquities in Palestine, VIII (1939), pp. 1-20.

3. C. Schaeffer, Missions en Chypre 1932-1935 (Paris, 1936), 1. 49.

4. W. A. Heurtley, "A Palestinian Vase Painter of the Sixteenth Century B.C.," Quarterly of the Department of Antiquities in Palestine, VIII (1939), pp. 21-34.

5. Claire Epstein, Palestinian Bichrome Ware Leiden, 1966).

6. P. Dikaios, Enkomi Excavations 1948-1958 I (Mainz am Rhein, 1969-1971) p. 389.

7. Ruth Amiran, Ancient Pottery of the Holy Land (Jerusalem, 1969) p. 124.

8. Moshe Dothan, "Tel Mor," Entziklopedia le-Khak Archiologiyot be-Eretz-Yisrael II (Massada, 1970), p. 586.

ORIGIN OF THE COLOSSI OF MEMNON

R. F. Heizer,[†] F. S. Stross,[†] R. F. Hester,[†] A. D. Albee,[†]
H. R. Bowman, I. Perlman, and F. Asaro

The two colossal statues of the Egyptian pharaoh Amenhotep III (called "Colossi of Memnon" since Roman times) have been tentatively traced to the ancient quarries near Cairo by modern nuclear-chemical techniques. These statues, which stand about 20 yards apart, were moved as monoliths to their present location in the western plain of Thebes near modern Luxor in Egypt around 1400 B. C.

Their enormous weight, some 720 metric tons, and size (46.9 feet high), have caused considerable controversy about the origin of the statues and the method of transportation. The statues were each cut from a single block of quartzite, although an earthquake in 27 B.C. toppled the upper half of the northern colossus and it was reconstructed with quartzite by the Roman, Septimus Severus, around 200 A.D.

The present work describes principally the nuclear chemical techniques used in determining the origin of these artifacts, and we shall first discuss the general applicability of the method.

Neutron activation analysis has been used most successfully in the determination of the provenience (place of origin) of pottery and some other materials when the chemical com-

positions of the artifacts from a particular area form a rather homogeneous group or groups. Provenience determination can be rather unambiguous also when chemical compositions vary considerably if there is a high degree of coherence between the elements (Bowman, Asaro, Perlman, 1973).¹ When chemical compositions vary greatly within single monoliths as we found for the Colossi of Memnon and also vary greatly among the samples of quartzite from a single quarry, the determination of provenience becomes much more difficult.

In an ideal situation, one would find that a considerable number of elements had distinctive abundances for each quarry of possible interest. Then, the levels of these elements in a statue would match one of these patterns and none of the others.

Where the material in a quarry is very ununiform chemically, the abundances of the various elements cover a broad range and it may be impossible to find many, or any, elements for which there is no overlap. It is still possible to make meaningful provenience deductions. Let us suppose that a good sampling of a statue produces a range of levels for each

element which coincides neatly with the ranges for a particular quarry which has been adequately sampled. Even with such overlap between quarries the pattern fitting could be distinctive. Furthermore, this would show that the ununiformity in the statue is probably reflected throughout the quarry. If the composition of the statue varied less than the quarry as a whole, one might be able to find from which particular part of quarry it came by finding localized quarry samples which showed this smaller spread.

The ideal situations certainly do not exist in the present instance. We have analyzed over 110 samples from 7 quarries and 9 artifacts. We had 23 quarry samples from Cairo and 37 from three locations near Aswan. These samples had been selected by a geologist and their origin is certain. A few samples were also available from quarries between Luxor and Aswan, but their origin is less certain and their numbers are too small to give a good perspective of the chemical-composition variations possible in these quarries. The sampling was perforce limited and was particularly difficult because of entry restrictions at certain quarry locations, and had to be done through intermediaries.

On the basis of the samples analyzed we can show that the Cairo quarry some 420 miles downstream on the Nile is far more likely the source of the Colossi of Memnon than the quarries at Aswan which are upstream at a distance of only about 130 miles. Nevertheless, the full composition range encountered in a single statue monolith was not encompassed by the "grab samples" from the Cairo quarry. This fact leaves us somewhat unsatisfied as one must assume that either (1) the quarry sampling was inadequate, or (2) the rock with the exact composition range as that of the statues has been removed through the ages.

The chemical composition of the samples were measured by neutron activation analysis (Perlman and Asaro, 1969, 1970).² In this technique the abundances of some 40 elements are measured with a precision approaching 1% in the most favorable cases. Most of these elements are in the part-per-million range. The quartzite samples were broken open, and ~2 grams of chips from the center were crushed to a powder with a ceramic mortar and pestle. Powder samples of 100 mg were pressed into pills, using cellulose as binder, and irradiated along with pottery standards of known composition in the University of California Research Reactor. Comparison of the abundances of the gamma rays emitted by the samples and standards leads to the absolute abundances of the various elements in the samples.

Table I identifies the various quarries and artifacts sampled, the general area in which the artifacts or quarries are located, the number of samples from each location and the approximate distance from the Colossi of Memnon. A complete listing of the analytical data will be presented in a later publication. Except at "Kom Ombo, 8 Km S. of Edfu," the major elements aluminum, magnesium, calcium, and titanium were below 1%, sodium and potassium were below 0.18% and iron was highly variable. Silica, the most massive constituent, was not measured. The quarries will be considered individually along with their distinguishing features.

Kom Ombo, 8Km South of Edfu—The provenience of the quarry samples bearing this designation is uncertain because there is a Kom Ombo listed in the Times Atlas of the World which is closer to 70 kilometers south of Edfu rather than the 8 listed for the samples. The four samples from this quarry were very distinctive in their chemical compositions for many elements and were fairly homogeneous. For example, the manganese (~0.4%) and calcium (~15%) contents were a factor of 10 higher than found for any other samples. The Colossi of Memnon and the other samples studies are certainly not related to this material. A wide sampling of this quarry is desirable to see if these distinctions are pervasive.

Silsila—Only one sample was available from Silsila and it also was very distinctive in its composition. The barium content, for example, was 1.0%, over one order of magnitude higher than any of the other samples. It is not like any of the statue samples, but is closest to the "Kom Ombo, 8Km South of Edfu" composition. As with the other quarry discussed, a much wider sampling is needed to determine if the distinctiveness from the statue samples persist throughout the quarry.

8 and 9 kilometers North of Edfu—There are no quarries just north of Edfu as far as one of the authors (F. S.) could determine from the literature. These quarries are presumably in the immediate vicinity of Edfu. Only two samples were available, and these could not be distinguished from the quarry samples from the Aswan area. A wider sampling of the quarries might permit such a distinction.

Aswan quarries (Gebel Osman, Osman Valley, Gebel Simeon)—34 samples were run from these three quarries. Although further sampling might permit distinguishing between them, it is not possible now.

Table I

Quarry Samples	General Area	No. of Samples	Approximate Distance from the Colossi of Memnon (kilometers)
Gebel Ahmar	Cairo	22	676 North
9 kilometers North of EDFU?	EDFU	1	97? South
8 kilometers North of EDFU?	EDFU	1	98? South
8 kilometers South of EDFU?	EDFU	4	114? South
Silsila	Silsila	1	148 South
Gebel Osman	Aswan	14	214 South
Osman Valley	Aswan	9	214 South
Gebel Simeon	Aswan	11	214 South
<u>Artifact Samples</u>			
Statue of Ramses II in Memphis Storage yard	Cairo	1	650 North
North Statue of Memnon	Luxor	13	
Reconstructed Portion		3	
Pedestal, loose block		1	
South Statue of Memnon		8	
Pedestal, Main block		3	
Statue Samples	General Area	No. of Samples	Approximate Distance from the Colossi of Memnon (kilometers)
Rear block		1	
Loose blocks		3	
Ruined Colossus		1	
Sculpture of a Mortuary Temple of Amenhotep III		1	
Great Stela of Mortuary Temple of Amenhotep III		3	
South Statue in front of 10th Pylon at Karnak		5	
Pedestal of North Statue in front of 10th Pylon at Karnak		1	
Sarcophagus of Thoutmoses IV		1	

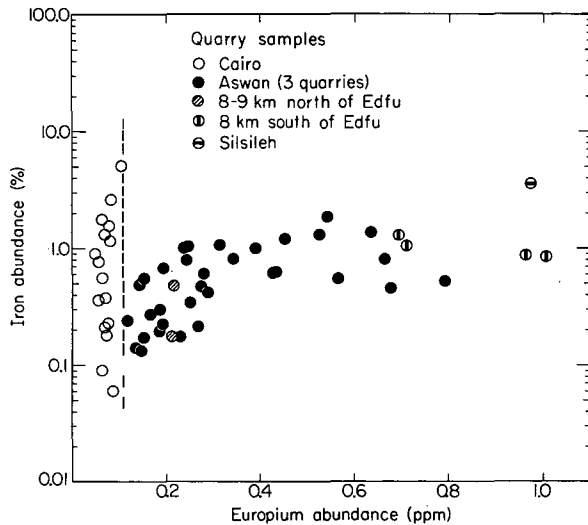


Fig. 1. Abundance of iron versus europium in the quarry samples. The dashed line separating the quarry samples is somewhat arbitrarily placed at 0.11 ppm europium.
(XBL 732-2242)

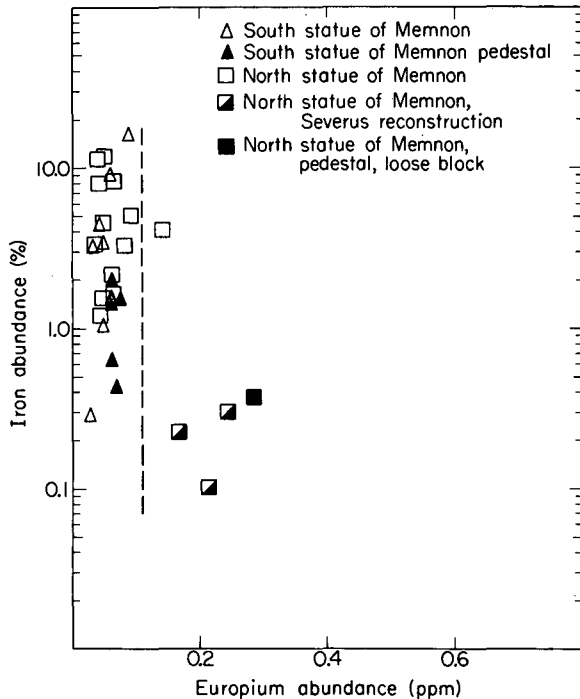


Fig. 2. Abundances of iron versus europium in the colossi samples. The dashed line is at 0.11 ppm europium as in Fig. 1.
(XBL 732-2244)

Cairo quarry (Gebel Ahmar)—22 samples from the Cairo quarry were measured. Samples from all the quarries mentioned above can be distinguished from the Cairo samples by the abundances of the light rare earths, especially Eu.

Figure 1 shows the abundance of Eu plotted against Fe for the various quarries. The Cairo samples have Eu abundances in the 0.05-0.1 part-per-million (ppm) region, while the other quarries have a much wider range of Eu values which do not go below 0.1 ppm.

Colossi of Memnon

Eu content: Fig. 2 shows the Eu content of the samples from the Colossi of Memnon, their pedestals, and the reconstructed portion of the North Colossus. In general, the Eu abundances were below 0.1 ppm, which is consistent with the Cairo quarry but with none of the others sampled. The samples from the reconstructed portion of the North Colossus and a loose block on the pedestal match more closely the Aswan and Edfu compositions.

Fe content: The iron content in the Colossi ranges up to 15%, much higher than found in any of the quarries sampled. The highest iron contents are found, however, in the Cairo material. This may just reflect that if these Colossi came from the Cairo quarry they came from an area or from material which we have not sampled. In this respect, a quartzite statue of Ramses II found in Memphis near Cairo and presumed to have come from the Cairo quarry had a high Fe abundance (4%) as well as a Eu content below 0.1 ppm.

Co content: Because there is a coherence between the abundance of iron and some of the other elements, it seemed desirable to distinguish between the Aswan and Cairo quarries using only those samples of low iron content in a range common to both areas and the Colossi.

In Fig. 3 is plotted the Co abundance as a function of the iron content for the Aswan and Cairo quarries and the Colossi samples. It is seen that the Cairo and Aswan samples have distinctively different patterns and that the North and South Colossi samples and the samples from the pedestal of the South Colossus are much nearer to the Cairo than the Aswan pattern. The samples from the quarries "8-9 Km North of Edfu" fall in with the Aswan material and those from the quarry "8 Km South of Edfu" fall in with the Cairo material.

The samples from the reconstructed portion of the North Colossus do not match the Cairo pattern, but are consistent with both

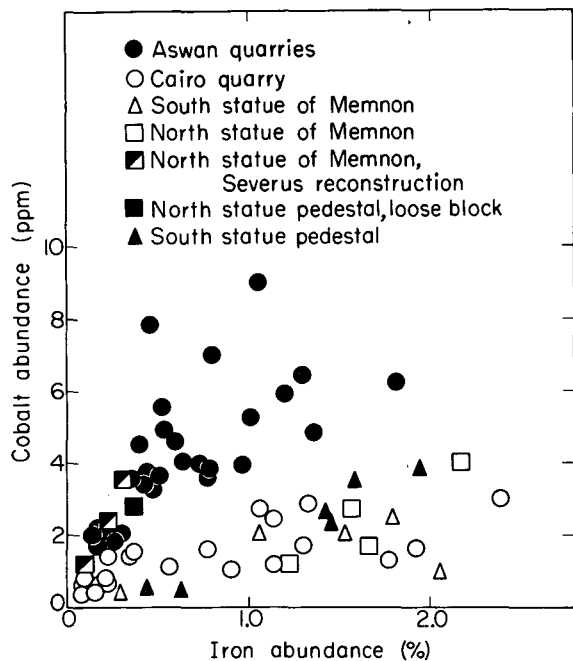


Fig. 3. Abundance of cobalt versus iron in colossi samples, and the Aswan and Cairo quarry samples. (XBL 732-2243)

the Aswan and "8-9 Km N of Edfu" quarry samples. A loose block on the North Colossus pedestal behaves similarly.

In conclusion, the abundance of Eu, Fe, and Co in the various samples indicate that the Colossi of Memnon and the pedestal of the South Colossus came from Cairo rather than Aswan if our sampling was representative. If this is true, then these massive monoliths were transported some 420 miles upstream rather than about 130 miles downstream as had been previously thought by other scholars.

Analysis of other artifacts shown in Table I indicate they also came from Cairo rather than Aswan, if those quarries are the only choices and our sampling was representative of the quarries.

Footnotes and References

* Condensed from LBL-1624.

† Department of Anthropology, University of California, Berkeley.

1. H. R. Bowman, F. Asaro, I. Perlman, Composition Variations in Obsidian Sources and Archaeological Implications, *Archaeometry* (in press).

2. I. Perlman and F. Asaro, Pottery Analysis by Neutron Activation, *Archaeometry* 11, 21 (1969); Pottery Analysis by Neutron Activation, published in *Science and Archaeology*, edited by Robert H. Brill (MIT Press, Cambridge, Massachusetts, and London, 1971). pp. 182-195.

^3He ACTIVATION ANALYSIS FOR S, Cl, K, and Ca[†]

D. M. Lee and S. S. Markowitz

Three easily-detected radionuclides, ^{38}Cl , $^{34\text{m}}\text{Cl}$, and ^{38}K , produced from the interactions of sulfur, chlorine, potassium, and calcium, were used as "signals" for the determination of the latter elements by ^3He activation analysis. A number of samples were analyzed non-destructively by using differing nuclear reactions to examine the accuracy of the method and the extent of interferences. Absolute excitation functions for the ^3He reactions are given.

The unique advantages that the ^3He ion offers as an incident particle for activation analysis were first suggested by Markowitz and Mahony.¹ Since then considerable efforts have been devoted to developing the practicality of this system for solving various analytical problems.²⁻⁷ Although ^3He activation analyses of oxygen, carbon, and fluorine have been investigated extensively in recent years,⁸⁻¹²

there is much less information available about the ^3He reactions with sulfur, chlorine, potassium, and calcium. Activation of S, Cl, K, and Ca by thermal neutrons, fast neutrons, protons, deuterons, and alpha particles has been reported;¹³⁻¹⁹ most of these analyses were applied to a specific matrix with various degrees of success. The use of ^3He ions provides alternative methods for the determination of the above elements with high sensitivity, and is a more convenient one in some cases, particularly at low energy.

In order to utilize the charged-particle activation technique to its optimum, a measurement of activation cross sections for a specific nuclear reaction is essential. This knowledge of excitation functions is also valuable for the production of radionuclides and for studies of nuclear reaction mechanisms.

Target Preparation and Assembly

For the measurements of the excitation functions the targets used were prepared by vacuum-depositing CaF_2 , KI, PbCl_2 and pure sulfur onto tantalum backing-foils. Sulfur targets were protected by depositing a thin film of aluminum over the sulfur to promote heat transfer during the irradiations. The thickness of the targets was determined by weighing; they ranged from 1.5 to 4.5 mg/cm^2 . For the subsequent analyses, samples were synthesized as thin targets or as thick ones. Thin targets were prepared either by vacuum evaporation or by settling the finely-ground powder onto a tantalum backing-foil from an ether suspension; the powder was fixed to the foil with a drop of dilute polystyrene in dichloroethylene. The thick targets were prepared by homogenizing a known small amount of material to be analyzed, with pure lead powder (approx. 200 mg/cm^2) and then pressing the mixture into a 1-inch (2.54-cm) diameter thin disk. Targets were mounted on an aluminum ring and were covered with thin gold or aluminum foils to form one target assembly. This target assembly was constructed to facilitate the handling of a fragile target, to promote heat transfer, to avoid recoil loss, and to obtain a proper reproducible geometry.

Irradiation

Irradiations were performed at the Berkeley 88-inch cyclotron. Aluminum foils were

placed in front of the sample assembly to degrade the beam from an initial energy of 30-MeV ^3He to an appropriate energy for each irradiation. The length of bombardment varied between 8 to 15 minutes. The average beam currents were about 0.1 to 0.4 μA of ^3He ($++$). Thin targets were irradiated simultaneously at different energies by stacked-foil technique; thick targets were irradiated one-at-a-time with a thin standard in the same stack, or with a thick standard from two successive irradiation. The total charge received from the Faraday cup was measured by a calibrated integrating electrometer.

Radioactivity Measurements and Data Acquisition

After irradiation, samples were analyzed by gamma-ray spectrometry using Ge(Li) detectors, coupled to a 1024-channel analyzer with a magnetic tape recording unit.

Two Ge(Li) detectors, having active volumes of 16 cm^3 and 30 cm^3 , manufactured by the nuclear detector group at LBL, were used for this work. The gamma-ray photo-peak efficiencies were calibrated by using a set of eight absolute gamma-ray standards, obtained from the International Atomic Energy Authority, Vienna.

Half-lives and gamma rays used for the measurements are given in Table I.

TABLE I. Nuclear data, Q value for the reactions investigated in the present work.

Nuclear Reaction	$T_{1/2}$ of Product Nuclide(min)	Gamma-ray Energies (% Intensity)	Gamma-rays Used for Measurement (MeV)	Q Value (MeV)
$^{32}_{\text{S}}(^3\text{He}, p)^{34\text{m}}\text{Cl}$	32.5	0.145(45%), 0.511(100%), 1.17(12%), 2.12(38%), 3.30(12%)	2.12	+6.08
$^{35}_{\text{Cl}}(^3\text{He}, \alpha)^{34\text{m}}\text{Cl}$	32.5	"	"	+7.94
$^{39}_{\text{K}}(^3\text{He}, 2\alpha)^{34\text{m}}\text{Cl}$	32.5	"	"	-5.70
$^{37}_{\text{Cl}}(^3\text{He}, 2p)^{38}\text{Cl}$	37.1	1.60(38%), 2.17(47%)	2.17	-1.61
$^{37}_{\text{Cl}}(^3\text{He}, 2n)^{38}\text{K}$	7.7	0.511(200%), 2.170(100%)	"	-4.19
$^{39}_{\text{K}}(^3\text{He}, \alpha)^{38}\text{K}$	"	"	"	+7.49
$^{40}_{\text{Ca}}(^3\text{He}, \alpha p)^{38}\text{K}$	"	"	"	+0.84

TABLE II. Cross sections (in mb) for ^3He nuclear reactions on S, Cl, K, and Ca.

Average Beam Energy (MeV)	Energy Interval (MeV)	^{32}S	^{35}Cl	^{37}Cl	^{37}Cl	^{39}K	^{39}K	^{40}Ca
		($^3\text{He}, p$) ^{34}S	($^3\text{He}, \alpha$) ^{34}Cl	($^3\text{He}, 2p$) ^{38}Cl	($^3\text{He}, 2n$) ^{38}Cl	($^3\text{He}, \alpha$) ^{38}K	($^3\text{He}, 2\alpha$) ^{34}Cl	($^3\text{He}, \alpha p$) ^{38}Ca
4.2	4.6-3.8	0.25						
4.6	5.0-4.3	1.1						
5.2	5.6-4.9	3.1						
6.3	6.6-6.1	11.1						
7.5	7.8-7.3	28.4	7.9	0	0.5	6.4		
8.2	8.4-8.1			0.1	3.8	8.2		0.36
8.7	9.0-8.4	35.2				9.8	0	
8.9	9.2-8.6		10.3	2.8				
10.1	10.3-9.4	34.2			9.1	10.2		5.9
10.6	10.9-10.4		12.1	13.4	9.3	9.9		
11.2	11.5-11.0		11.6	21.8	12.9			
11.9	12.1-11.6	31.0						
12.4	12.6-12.3				18.3	7.7	0	22.4
13.8	14.0-13.6	23.1	9.5	48.0	22.8			39.1
14.8	15.0-14.7		8.5	53.1	23.0	6.9	0.5	50.5
15.4	15.6-15.3	16.2	7.4	60.5				
15.9	16.0-15.7		7.8	62.2	22.6			
16.2	16.4-16.0					6.3	3.6	62.6
17.1	17.3-17.0	12.4	7.7	70.0				
18.0	18.1-17.8	10.3	6.7	75.0	20.1	6.1	7.1	72.1
18.8	19.0-18.6	9.7						
20.0	20.2-19.9	7.2	8.1	77.7	17.2	5.8	8.2	76.6
22.0	22.1-21.8	6.7						

Excitation Functions

Absolute cross sections were calculated based on the assumption that the reactions in Table I were attributed entirely to a single reaction of a specific target nuclide. A summary of experimental cross-section data obtained in this work is presented in Table II; the excitation functions for each element are shown in LBL-682. Each of the cross sections shown in Table II represents an average value of 2-3 replicates; the precision (average deviation) was about 5%. Additional uncertainties include: (1) the determination of total beam current, (2) the half-lives of nuclides, (3) the determination of disintegration rates, (4) the uniformity of thickness of targets, (5) possibility of recoil gas losses during irradiation. With all the above considerations, the estimated absolute errors in the cross sections are 10% for S data, 10-15% for Cl, 20% for K, and 10% for Ca.

Interferences

Interferences are discussed in detail in LBL-682.

Sensitivity of the Method

Applying Currie's²⁰ "working expression" for the interference-free determinations of S, Cl, K, and Ca by activation with ^3He at the energy of the maximum cross section, using 1- μA current for one half-life irradiation, starting counting immediately after irradiation for one half-life, and employing a photo-peak counting efficiency of only about 0.5%, we estimate the determination limits to be 0.025 μg for S, 0.05 μg for Cl, 0.2 μg for K, and 0.025 μg for Ca, in a 1-gram sample.

Samples Analyses

Samples containing compounds with known amounts of S, Cl, K and Ca were analyzed non-destructively. The A_0 values (activity at the end of bombardment) were determined by following the gamma-ray photo-peaks for 5 to 6 half-lives; the intensity of the photo-peaks was analyzed by computer code SAMPO,²¹ and the A_0 values were obtained by decay-curve analysis using CLSQ²² code. The amount of elements present was calculated by comparing the ratio of the A_0 values of the samples to the

TABLE III. Results of ^3He activation analyses.

Sample	Element Sought	^3He Beam (MeV)	Nuclide Used	Element, mg/cm ²		Dev. from Known (%)
				Present	Found ^a	
S-1	S	10	$^{34\text{m}}\text{Cl}$	0.21	0.20	-4.7
S-2	S	10	$^{34\text{m}}\text{Cl}$	0.54	0.52	-3.7
S-3	S	10	$^{34\text{m}}\text{Cl}$	1.09	1.14	+4.5
S-4+Pb	S	15	$^{34\text{m}}\text{Cl}$	0.56	0.61	+8.9
S-5+Pb	S	15	$^{34\text{m}}\text{Cl}$	1.12	1.20	+7.0
Saran-1	Cl	15	^{38}Cl	1.20	1.13	-5.8
Saran-2	Cl	15	^{38}K	0.99	0.95	-4.0
AgCl-1	Cl	10	$^{34\text{m}}\text{Cl}$	0.75	0.80	+6.6
AgCl-2	Cl	15	^{38}K	0.75	0.78	+4.0
NaCl-1	Cl	15	^{38}Cl	0.21	0.20	-4.7
NaCl-2	Cl	15	^{38}K	1.08	1.06	-1.8
PbCl ₂ +Pb	Cl	15	^{38}Cl	0.10	0.09	-10
PbCl ₂ +Pb	Cl	15	^{38}K	0.10	0.09	-10
KCl-1	Cl	15	^{38}Cl	1.35	1.31	-2.9
KCl-1	K	8	^{38}K	1.48	1.41	-4.7
Mica-1	K	10	^{38}K	0.09	0.08	-11
Mica-2	K	10	^{38}K	0.07	0.06	-14
Mica-3	K	20	^{38}K	0.18	0.16	-11
CaF ₂ -1	Ca	20	^{38}K	0.54	0.55	+1.8
CaF ₂ -2	Ca	20	^{38}K	0.26	0.27	+3.8
CaF ₂ -3	Ca	20	^{38}K	0.13	0.14	+7.7
^a Average of 2 measurements.						Av. Dev. 6%

appropriate standards. The standards used for this work were pure S, PbCl₂, KI, and CaF₂, having thicknesses similar to the samples. The results of these sample analyses are shown in Table III; the average deviation from the known concentrations of all samples is about 6%.

Footnote and References

[†]Condensed from LBL-682, June 1972; J. Radioanal. Chem. 12, (1973), in press. Presented at Reunions Internationales Sur L'Analyse Par Activation, Saclay, France; October 2-6, 1972; Am. Chem. Soc., Division of Nuclear Chem. Mtg. Newport Beach, Calif. Jan. 28-Feb. 1, 1973.

1. S. S. Markowitz and J. D. Mahony, Anal. Chem. **34**, 329 (1962).
2. Enzo Ricci and R. L. Hahn, Anal. Chem. **37**, 742 (1965).
3. *Ibid.* **39**, 795 (1967).
4. J. D. Mahony (Ph.D. thesis), Lawrence Radiation Laboratory Report UCRL-11780 (1965).
5. J. F. Lamb, D. M. Lee, and S. S. Markowitz, Anal. Chem. **42**, 212 (1970).
6. *Ibid.* **42**, 212 (1970).
7. J. F. Lamb (Ph.D. thesis), Lawrence

Radiation Laboratory Report UCRL-18981 (1969).

8. A. C. Demildt, *Anal. Chem.* **35**, 1228 (1963).

9. S. S. Markowitz and J. D. Mahony, in *Radiochemical Methods of Analysis*, Vol. I (IAEA, Vienna, 1965), p. 419.

10. J. F. Lamb, D. M. Lee, and S. S. Markowitz, in *Proc. 2nd Conf. on Practical Aspects of Activation Analysis with Charged Particles*, Liege, 1967, Vol. I (Euratom, Brussels, 1968), p. 225.

11. D. M. Lee, C. V. Stauffacher, and S. S. Markowitz, *Anal. Chem.* **42**, 994 (1970).

12. D. M. Lee, J. F. Lamb, and S. S. Markowitz, *Anal. Chem.* **43**, 542 (1971).

13. C. Persiani and J. F. Cosgrove, *Radiochem. Radioanal. Letters* **4**, 203 (1970).

14. M. Peisach and R. Pretorius, *Anal. Chem.* **38**, 956 (1966).

15. R. Pretorius and E. A. Schweikert, *Radioanal. Chem.* **7**, 319 (1971).

16. R. B. Heslop, *Anal. Chim. Acta* **47**, 183 (1969).

17. D. Gibbons and H. Simpson, "Radioisotopes in the Physical Sciences and Industry, Vol. II IAEA, Vienna (1962), p. 269.

18. J. L. Debrun and P. Albert, *Bull. Soc. Chim. Fr.* **3**, 1017-1020 (1969).

19. S. May and G. Pinte, *J. Radioanal. Chem.* **3**, 329 (1969).

20. L. A. Currie, *Anal. Chem.* **40**, 586 (1968).

21. J. T. Routti and S. G. Prussin, *Nucl. Instr. Methods* **72**, 125 (1969).

22. J. B. Cumming, "Applications of Computers to Nuclear and Radiochemistry," edited by G. D. O'Kelly, Nat. Acad. Sci-Nat. Res Council, Nucl. Sci. Ser. NAS-NS 3107, 25 (1963).

QUANTITATIVE ANALYSIS FOR THE MAJOR ELEMENTS IN ROCKS AND MINERALS BY NONDISPERSIVE SOFT X-RAY FLUORESCENCE

A. J. Hebert and K. Street, Jr.

A lithium-drifted silicon detector¹ and multichannel analyzer system has been combined with a multiple-target soft-x-ray generator and a high-vacuum sample-handling system to provide an x-ray fluorescence unit for quantitative analyses of the elements from oxygen to iron. A cross-sectional sketch of the unit is shown in Fig. 1.

For mineral or rock analyses, the powdered sample is fused in a 10:1 LiBO₂ mix and the resultant glass cast on a polished vitreous carbon plate into an open metal ring. The vitreous carbon surface provides a relatively smooth and contamination-free homogeneous glass sample surface for analysis. The procedure requires less than 10 minutes per sample when starting with a 200-mesh powder.

Major element absorption corrections are calculated from experimental cross sections tabulated by McMaster et al.²

Fig. 1. Cross-sectional sketch of the soft x-ray fluorescence spectrometer.

(XBL 734-2754)

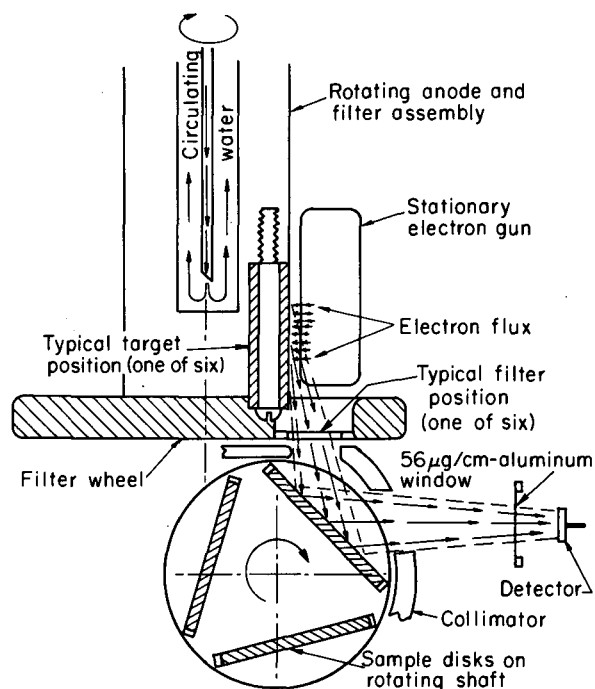


Table I. A Comparison of XRF and Conventional Chemical Values³ for the Major Elements in Six USGS Standard Rocks as Percent Oxide.

Sample	Source	Na ₂ O	MgO	Al ₂ O ₃	SiO ₂	K ₂ O	CaO	TiO ₂	FeO
G-2	XRF	4.17	0.77	15.26	69.21	4.50	1.98	0.51	2.40
	Ref. 3	4.15	0.77	15.31	69.29	4.51	2.00	0.48	2.38
GSP-1	XRF	2.84	0.99	15.02	67.08	5.54	2.08	0.67	3.81
	Ref. 3	2.86	0.95	14.92	67.32	5.52	2.06	0.66	3.82
AGV-1	XRF	4.36	1.51	16.90	59.60	2.93	4.97	1.03	6.03
	Ref. 3	4.32	1.53	16.92	59.10	2.92	4.98	1.05	6.04
PCC-1	XRF	0.02	43.42	0.67	41.21	0.007	0.54	0.010	7.42
	Ref. 3	0.0077	43.26	0.72	41.84	0.0031	0.54	0.01	7.34
DTS-1	XRF	0.007	49.68	0.41	40.15	0.009	0.117	0.013	7.73
	Ref. 3	0.0084	49.83	0.30	40.48	0.0015	0.03	0.01	7.79
BCR-1	XRF	3.30	3.52	13.42	55.01	1.68	7.02	2.20	12.06
	Ref. 3	3.32	3.46	13.44	54.22	1.70	7.00	2.22	12.08

Analyses of three separately prepared sets of six different USGS standard rock powders indicate reproducibility and accuracy of the order of 1 to 2% for the eight elements from sodium to iron when calibrated against published wet chemical results.³ A comparison of values is shown in Table I. The observed values were obtained with a 5-minute average analysis time per element, or 40 minutes per sample. One- to four-percent analyses can be obtained with total run times of 10 minutes per sample. The sensitivity in a 5-minute analysis at 10:1 dilution varies from 0.09% for Na to 0.01% for Fe.

Up to six samples can be simultaneously introduced to the high-vacuum analysis chamber. The samples are positioned and ready to analyze at a pressure of less than 10^{-6} mmHg within a total loading and pump-down time of less than 3 minutes. Subsequent sample and x-ray anode target changes require less than 10 seconds each.

The present multiple-target x-ray anode and filter system provides adequate and easily monitored fluxes of magnesium, aluminum, silicon, silver, titanium, and nickel x-rays with electron energies of 7 to 10 kV and an anode current of 150 μ A.

The electron gun features hidden thorium-oxide-coated filaments (one spare) and a control grid which is capable of modulating or diminishing the x-ray flux by a factor of 10^4 in 1 μ sec with a +9 to -5 volt signal and roughly 300 μ A of grid current.

Preliminary experiments indicate that the apparatus is also suitable for the analysis of other types of samples. The sensitivity for biological samples such as pressed protein powder or freeze dried blood varies from 0.8% for oxygen to 0.001% for iron in a 5-minute analysis. It also appears that 1 to 2% oxygen analyses may be obtainable on rock or mineral powder.

References

1. J. M. Jaklevic and F. S. Goulding, I. E. E. E. Trans. Nucl. Sci. NS-18, #1, 187 (1971).
2. W. H. McMaster et al., Compilation of X-Ray Cross Sections, Sec. II, Rev. 1, UCRL-50174, May 1969.
3. I. S. E. Carmichael, J. Hampel, and R. N. Jack, Chem. 3, 59 (1968).

IV. Instrumentation

DOPPLER-TUNED BEAM-FOIL X-RAY SPECTROMETER

R. W. Schmieder and R. Marrus

A new type of x-ray spectrometer for use with fast beams has been devised and tested. The spectrometer operates by matching the Doppler shifted emission from the beam to a known absorption feature (such as a K edge) in a thin filter in front of the detector. Tuning is accomplished by varying the angle between the detector and the beam. Knowledge of the angle, beam velocity, and absorption profile of the filter is sufficient to determine the emission spectrum of the beam source. Due to the extreme sharpness of x-ray edges, the device

has resolving power $10^3 - 10^5$, thus competing with ordinary crystal spectrometers. A prototype device has been constructed and operated at the Berkeley Hilac. In the initial experiments, the Lyman α lines of hydrogen-like Ar, produced by passing a 412-MeV Ar beam through a C foil, was resonated with the L_{III} absorption edge of Ag near 3.36 keV. The principle of this spectrometer can be extended to other spectral ranges, and it should be useful for both survey scan and high precision measurements.

IMPROVED RESOLUTION METHODS FOR BEAM-FOIL SPECTROSCOPY*

T. Hadeishi, M. C. Michel, J. Yellin and E. Geneux†

The ability to perform high resolution experiments with conventional beam-foil spectroscopy is limited by the effects of cascading, beam divergence, and beam velocity uncertainty and spread. There is a class of experiments which does not depend upon these properties, being the direct extension of radio-frequency spectroscopy and allied resonance methods to beam-foil work. Examples are radio-frequency spectroscopy,¹ nonzero field level crossing,² light beats,³ and antilevel crossing.⁴ These various effects have in common the need for alignment of the ions or atoms to be studied. It has been shown that the beam-foil interaction leads rather generally to alignment of all states characterized by $L \geq 1$, J and $F > 1/2$.⁵

We are at present conducting a systematic study to attempt to apply these higher resolution techniques to beam-foil spectroscopy. The ability to excite many states of an atom at the same time and in a period of about 10^{-14} sec, while aligning a significant number of the excited atoms or ions leads to some interesting possibilities, one of which we propose to exploit for increased resolution in level-crossing special properties of the foil excitation, it should be possible by means of time-delayed observations, partially to remove the limitation of the natural line width of the state in determining a resonance position.

Considering the uncertainty principle relation, $\Delta\nu\Delta t \sim 1$, for a resonance experiment, Δt is the lifetime of the state, and $h\nu$ is the transition energy, while the observed times can extend from a fraction of a lifetime to several lifetimes. Thus, the precision with

which $\Delta\nu (\sim 1/\Delta t)$ can be measured, depends on the experimental conditions. For any system, it should be generally possible to choose conditions such that $\Delta\nu$ is below the natural line width. As a practical matter this can be done most conveniently with the beam-foil system.

If we limit the discussion to rf resonance and level crossing, conventional techniques integrate the observations over a time long compared with the mean lives of the states of interest, since the atoms or ions involved remain in the interaction region for a time long compared with the mean life. However, the work of Ma et al.⁶ for an rf resonance, and of Copley, Kible and Series⁷ for a level crossing, show that the technique of delayed observation is sound. We feel that this method is particularly suited to the beam-foil system.

Figure 1 shows the basic fine structure and Zeeman level system for the $3^3P_{1,2}$ states of ^4He . The $\Delta m_j = 2$ crossings are marked and are the level crossings of interest in this work. If we denote as $S(\omega)$ the signal (changing part of the photon intensity) observed from these states of the ^4He atoms at time t after excitation and with polarization vector in the appropriate plane, then

$$S(\omega) = \int_{t_1}^{t_2} B e^{-\gamma t} \cos [(\omega' - 2\omega)t - 2\theta] dt + \int_{t_1}^{t_2} C e^{-\gamma t} \cos [(\omega'' - 2\omega)t - 2\theta] dt,$$

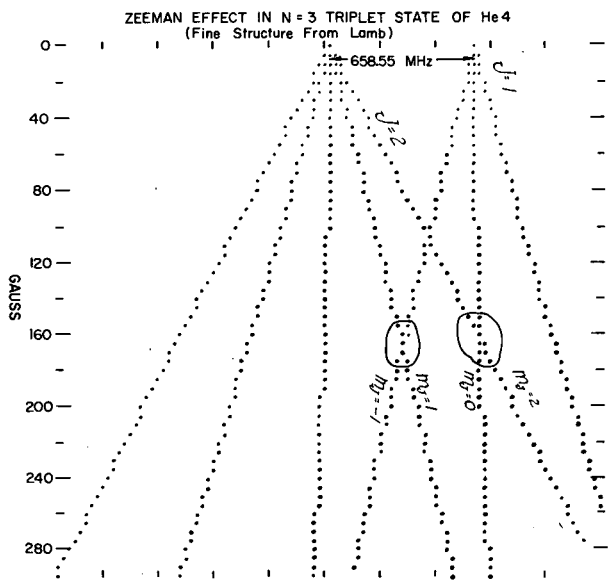


Fig. 1. Level system for $3^3P_{1,2}$ levels in ^4He . (XBL 7212-7476)

where $\omega = g_j \mu_0 H / \hbar$ and t_1 and t_2 are the times corresponding to the beginning and end of observation along the light path. ($t_1 = l_1 / v$ and $t_2 = l_2 / v$, where l_1 and l_2 are the distances behind the foil and v is the particle velocity.)

The result of integrating from $t_1 = 0$ to $t_2 = 10$ lifetimes is essentially the full level crossing signal and is shown in Fig. 2. Figure 3 gives the result of the integration for a delayed observation where $t_1 = 1$ lifetime and $t_2 = 2$ lifetimes. The two level crossings are even sharper than the natural width and easily distinguished from the undulations in the wings of the signal that are the result of the incomplete integration. These undulations increase in amplitude and shift in position with different delay, but they do not affect the position of the real level crossing signals.

The experimental arrangement is shown in Fig. 4. To meet the requirement for delayed integration we have merely used a relatively wide slit, accepting about 7 mm of the light path. The magnetic field is swept by approximately 30 gauss centered on the level crossing region, with a multiscaler synchronized with the field sweep storing the photon counts as a function of applied field. After storing an appropriate number of sweeps of the field, the foil is moved farther away from the detector and the same number of field sweeps added to the previously stored data. By successive, slightly overlapping additions of data from new

foil positions, the signal is integrated and the initial and final foil positions determine the delay and the length of integration. By choosing the closer position to be one-half lifetime or more, we obtain the results shown in Fig 5. The line widths are still greater than the natural width but agree with theory and should decrease as the delay increases. The undulations predicted by the theory are quite prominent.

We believe that our experimental observations of the time-delayed level crossings on ^4He show conclusively the power of the beam-foil method for high precision measurements. In addition to the narrow signal width, collisional effects common to conventional techniques such as rf spectroscopy are absent, and high-field Stark effect experiments could also be performed without voltage breakdown problems.

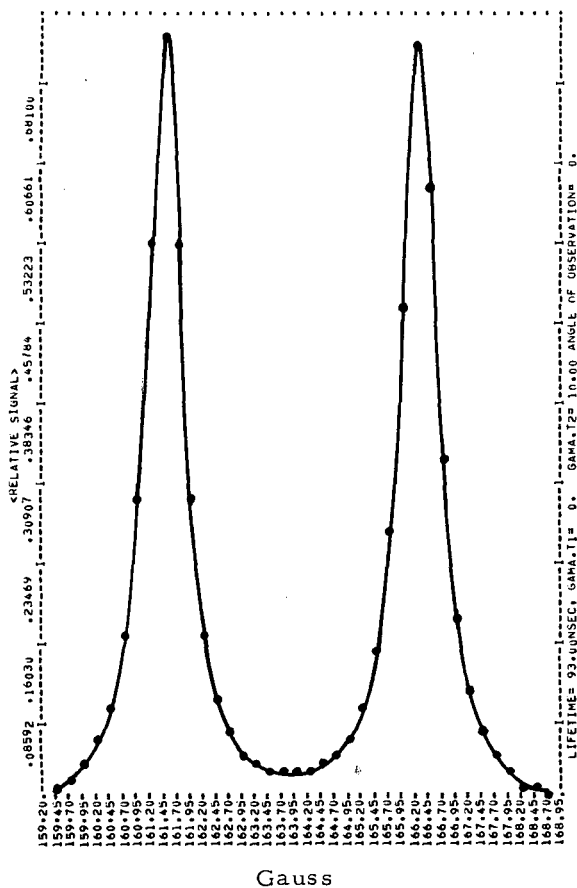


Fig. 2. Level crossing in ^4He for integration from $t = 0$ to $t = 10$ lifetimes. (Left half of XBL 729-1883)

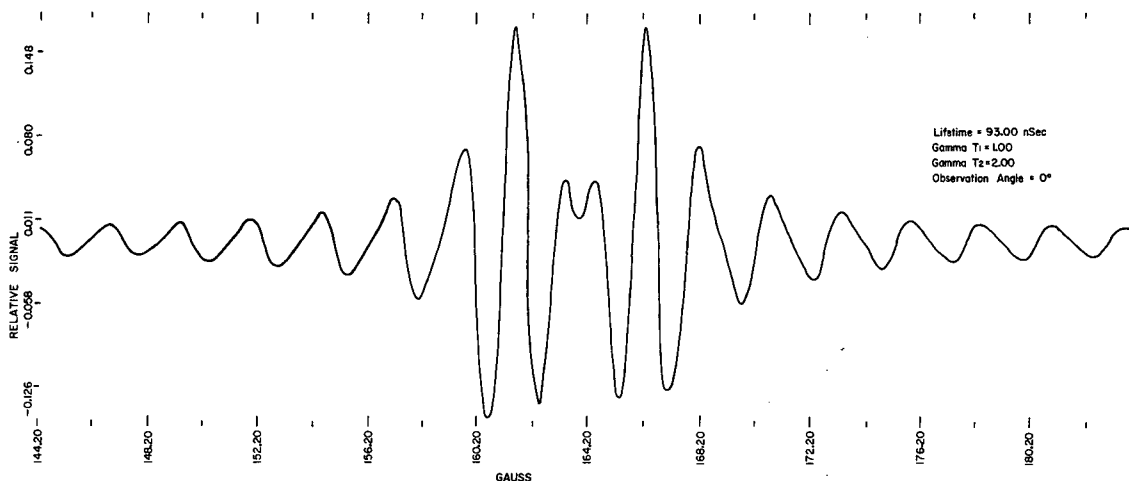


Fig. 3. Delayed level crossing in ^4He for integration from $t = 1$ lifetime to $t = 2$ lifetimes. (XBL 7212-7477)

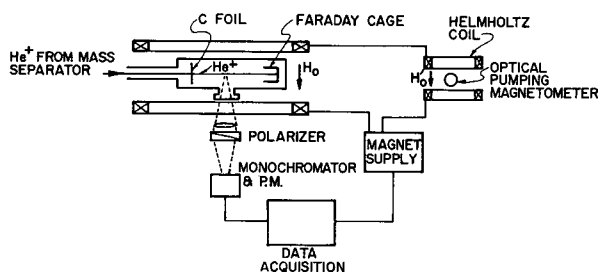


Fig. 4. Experimental arrangement for delayed level crossing measurement. (XBL 729-1917)

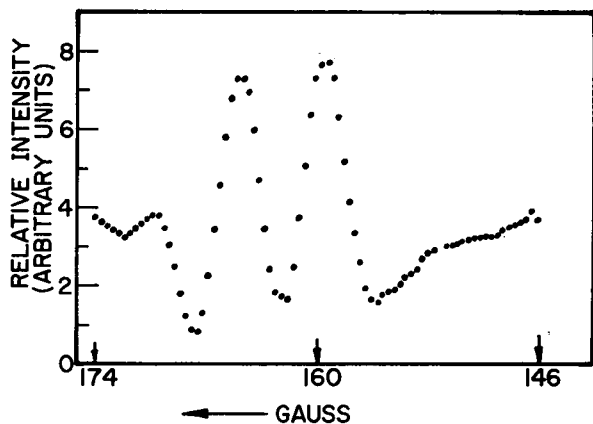


Fig. 5. Observed delayed level crossing signal in ^4He ($3^3P_{1,2}$ states). (XBL 729-1949)

Footnotes and References

* This work supported in part by the Office of Naval Research.

† Present address: Institut d'Optique Physique Lausanne, Switzerland.

1. J. Brossel and F. Bitter, *Phys. Rev.* **86**, 308 (1952).
2. P. A. Franken, *Phys. Rev.* **121**, 508 (1961).
3. J. N. Dodd and G. W. Series, *Proc. Roy. Soc. (London)* **A273**, 41 (1963).
4. H. Wieden and T. G. Eck, *Phys. Rev.* **153**, 103 (1967).
5. C. H. Liu, S. Bashkin, W. S. Bickel, and T. Hadeishi, *Phys. Rev. Letters* **26**, 222 (1971); T. Hadeishi, R. D. McLaughlin, and M. C. Michel, *J. Opt. Soc. Am.* **61**, 653 (1971).
6. I. J. Ma, G. zu Putlitz, and G. Schütte, *Physica* **33**, 282 (1965). I. J. Ma, J. Mertens, G. zu Putlitz, and G. Schütte, *Z. Physik* **208**, 352 (1968).
7. G. Copley, B. P. Kibble, and G. W. Series, *J. Phys. B. (Proc. Phys. Soc.) Ser. 2*, Vol. **1**, 724 (1968).

DEVELOPMENTS IN ZEEMAN ATOMIC ABSORPTION SPECTROSCOPY*

T. Hadeishi, R. D. McLaughlin, D. A. Church, B. Chang,† and M. Nakamura

A method has been described of automatically correcting for interferences in atomic absorption spectroscopy by monitoring the relative intensities of Zeeman components of the source radiation while the sample is being vaporized into the optical path.^{1,2} This technique is referred to as Zeeman Atomic Absorption (ZAA). Developments in ZAA which have been achieved during the past year can be divided into three categories:

- improvement of technique
- application to specific environmental problems
- application to elements other than Hg.

Three separate improvements of technique have been accomplished. An integral part of ZAA equipment is a quarter wave retardation plate which is made to rotate at a selected frequency. Mechanical rotation of commercially available quarter wave plates was found to be inefficient. A highly effective but simple solution to this problem was devised; see Fig. 1. The retardation was accomplished by applying pressure to a quartz plate which was sandwiched between two laminated C-magnets. These magnets could be activated by passing current through coils wound about the magnet cores.

In order to measure the quantity of trace-element regardless of original form of host material (water, food, rock, vegetable, wood, etc.), it was necessary to find a way to operate the furnace such that the measurement would be matrix-independent. A theoretical description of the operation of furnace-absorption tube combination was completed and this theoretical prediction was tested experimentally. The development of this description allows operating parameters to be chosen such that the resulting signal does not depend upon the sample matrix.

To better control the combustion process, a high-current low-voltage heating system was constructed, which uses the furnace shell as the heating element. The furnace temperature is controlled using SCR (silicon controlled rectifier) and line synchronization logic to cause a transformer to supply the required high current without core saturation.

Three applications of ZAA to environmental problems are in progress. Because of the greater toxicity of alkyl Hg compounds compared to inorganic Hg compounds, there is a need for analysis of biological samples for

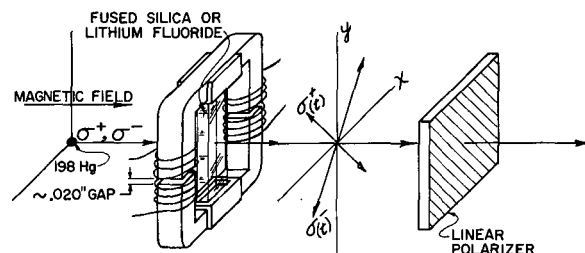


Fig. 1. Device for producing retardation plate by applying stress to a quartz plate.

(XBL 733-245)

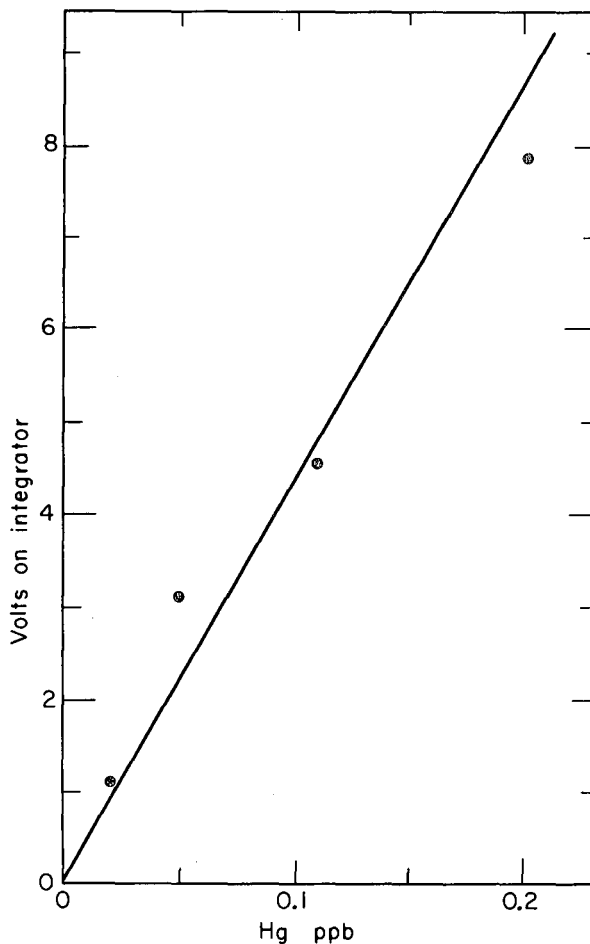


Fig. 2. Calibration curve using sea water to which known amounts of Hg had been added. After sitting for three days, a background of 0.8 V (or 0.02 ppb of Hg) was found in the sea water.

(XBL 733-2373)

organic Hg. In collaboration with scientists from the National Canner's Association in Berkeley, California, we are devising a method to determine both organic and total Hg, in various fish samples. These samples will be run using both ZAA and conventional methods.

The concentration of background Hg in sea water is extremely small (~ 0.02 parts per billion). In order to determine the effects of waste disposal into rivers and bays it is necessary to develop highly sensitive detection methods. We have found that by reducing Hg in water to elemental form and collecting this Hg upon a Au foil, we can determine Hg at levels less than 0.02 ppb. Figure 2 displays a calibration curve obtained by adding known amounts of mercury to water obtained from the San Francisco Bay.

A graduate student in Department of Public Health at the University of California at Berkeley is working under our supervision financially supported by DNET (Division of Nuclear Education Training). He plans to study the relative importance of HgCl_2 and methyl mercury uptake and retention from water and food by planktonic species. The ZAA detector is the only instrument that can handle this type of problem since the sample size is small and the mercury content is less than one ppm. Commercial equipment is simply inadequate to analyze such small amounts of sample at such low levels.

The work to apply ZAA to other elements is concentrating upon Cd and Pb. Construction of lamps of these elements is no trivial task. Operation temperatures, the kind of buffer gas and its pressure, as well as the lamp envelope profile must be chosen in order to minimize self-reversal and maximize lamp life time. A technique was developed which allows the line profile to be determined more easily

and very likely more accurately than can be accomplished using classical high resolution spectrometry. The technique we developed is the inverse of Bitter's magnetic scanning method and also the inverse of our ZAA technique. To obtain the spectral line profile, a Cd-vapor absorption cell in vacuum was placed in the magnetic field. By changing the magnetic field on the Cd vapor and monitoring the transmitted light as a function of magnetic field, the line profile of the Cd lamp can be measured quite simply and extremely accurately.

So far, the Cd, Pb, and Hg detectors we are developing are primarily useful for trace-element detection in food and water. It would be valuable to adapt these detectors for air pollution monitoring. Also, it would be quite useful to extend our ZAA detector to many elements in the periodic table in the future. However, when new techniques become feasible, they should also be developed. With this in mind, some of our effort is directed to using a combined Zeeman-Faraday effect to detect air pollution resulting from Hg, Cd, and Pb. This involves use of the Faraday effect in a long optical path amounting to several meters.

Footnotes and References

* Research funded by RANN contract No. W-7405-ENG-48.

† Present address: California State University at Los Angeles, 5151 State University Drive, Los Angeles, California 90032.

1. T. Hadeishi, and R. D. McLaughlin, *Sci.* **174**, 404 (1971).
2. J. Hadeishi, *Appl. Phys. Letters* **21**, 438 (1972).

SEARCH FOR NEW ISOTOPES WITH THE He-JET TECHNIQUE AT THE BEVATRON

J. D. Bowman, A. M. Poskanzer, R. E. Eppley, and E. K. Hyde

In previous work,¹ a study was made using the He-jet transport technique of the alpha emitting products of the interaction of 5-GeV protons with heavy nuclei. The work has been extended by improving the speed and efficiency of the transport system, and a search was made for new isotopes. It was thought that high-energy reactions would be appropriate for a search for new isotopes, because such reactions typically produce a broad distribution of products with appreciable yields of nuclei

far from stability. A selection of targets was used so that all parts of the chart of the nuclides accessible by high-energy reactions were explored. The modes of decay searched for were delayed fission, alpha decay, and delayed proton emission.

The He-jet system transported the activity from the target cell (1.25-in. diameter by 0.6 in. thick) through 15 feet of 0.125-in. inside diameter tubing to an evacuated counting

chamber outside the Bevatron shielding. The gas in the target cell was at a pressure of four atmospheres and expanded through a 0.01-in. diameter pinhole at the exit of the cell. The transport time profile measured by the build-up of ^8Li activity at the detector exhibited a delay after a short beam burst of 0.25 sec, followed by an additional 0.25 sec for accumulation of half of the activity. An important factor in increasing the transport speed was the small size of the target cell. The transport efficiency was determined by measurements of the alpha activity of ^{149}Tb produced from gold targets. The activity at the detector was compared to that simultaneously collected on a catcher foil adjacent to a second gold target just upstream in vacuum. A typical transport efficiency was about 5%. Important factors in obtaining this efficiency were the size of the pinhole, the saturation of the He stream with water, and the addition of 10% by volume of air to the He stream. In the searches to be described, the targets were thick compared to the range of the recoils. The beam spill was 0.5 sec long, coming every 6 sec, and for the typical experiment the total incident flux was 5×10^{15} protons. The data were recorded as a function of time after the start of the beam, but, because of the higher background during the beam, most of the data presented here represent the counting interval between beam bursts.

The search for delayed fission was carried out using a surface barrier detector with a 15% counting geometry. For both gold and uranium targets, less than three counts were observed in the fission fragment region.

The search for new alpha activities was seriously hampered by the presence of ^8Li and ^8B produced in high yield from all targets. These isotopes decay by two alpha particle break-up producing a continuous alpha spectrum peaking at 1.5 MeV, but with a tail extending up to about 8 MeV. In the final arrangement the activity from the He-jet was deposited on a 0.6 mg/cm^2 Ni foil and viewed through the foil by an alpha detector with 6% counting geometry and a total resolution of 100 keV. Because of the 180° correlation of the two alpha particles following the decay of ^8Li and ^8B , their counting rate could be greatly reduced by an anticoincidence arrangement. Thus, a large-area anticoincidence counter was placed opposite the first detector, and viewed all the activity exposed to it. This

reduced the $^8\text{Li} - ^8\text{B}$ counting rate, by a factor of 400, to 5 counts/100 keV at 3 MeV and 0.2 counts/100 keV at 5 MeV. For the targets Al, Ni, Mo, and Pr, no peaks were observed above this background. For the Tm target small amounts of ^{149}Tb and ^{150}Dy were seen with about 10^{-3} of the yield seen in previous work¹ with Ta and Au targets.

The search for high-energy alpha activities and delayed proton activities was conducted using a telescope consisting of a 28μ ΔE transmission detector followed by a 270μ E detector. The activity was deposited on a 0.6 mg/cm^2 Ni foil located in front of the ΔE detector; the telescope efficiency was 5%. It was found that $^8\text{Li} - ^8\text{B}$ decaying between the two elements of the telescope simulated protons. Thus, it was necessary to enclose the telescope to exclude the He gas from the detector system. The proton energy range covered was 1.8 to 6 MeV. For the Al, Ni, Mo, Pr, Tm, and Ta targets, about 5 counts in peaks and 50 counts in a continuum were observed. The peaks could be accounted for by the well-known, 0.1 sec, light element, delayed proton emitters. The continuum which had a half-life of about one second could be accounted for by beta-alpha coincidences from $^8\text{Li} - ^8\text{B}$ simulating a proton identification. In addition, from the Au and U targets a few counts of a longer lived unidentified proton activity were observed. For alpha particles, the telescope was sensitive from 6.5 to 18 MeV. A small tail from $^8\text{Li} - ^8\text{B}$ was observed, but above 9.25 MeV there were zero counts from the Al, Ni, Mo, Pr, Tm, and Ta targets. From the U target, 20 events were observed at 11.7 MeV from ^{212}mPo . In addition, there was one unidentified alpha event at 9.5 MeV from U and one at 10.2 MeV from Au.

In summary, no new isotopes with charged particle decay modes were observed, which indicates that no such isotopes are produced with appreciable cross sections in high-energy reactions. However, the He-jet technique as applied here has an inherent limitation in sensitivity because the useful target thickness is restricted to the effective recoil range of the products, and this is small for spallation products from high-energy reactions.

Reference

1. Nuclear Chemistry Division Annual Report for 1971, LBL-666, pp. 18, 324, 325.

DESIGN OF, AND SKIMMER TESTS WITH, A He-JET TRANSPORT SYSTEM

R. A. Gough, R. G. Sextro, and J. Cerny

The study of nuclei far removed from β -stability provides information essential for testing many theories and models in nuclear physics. Such information can be acquired from studying the charged-particle decays of neutron-deficient nuclei. This report describes an on-line He-jet system^{1,2} which has been used,^{2,3,4} in conjunction with the 88-inch cyclotron, to investigate β^+ -delayed-proton emitters in the light elements. This system, coupled with solid state detector telescopes and a Goulding-Landis particle identifier⁵ has provided the low-background and good energy-resolution capabilities essential to present-day delayed-proton studies.

There has been considerable recent interest in separating activity from the He carrier gas once the recoils have been transported to a low-background region, remote from the bombardment area. The nozzle-skimmer separation method⁶ has now been demonstrated both here and at other laboratories.^{7,8,9} This leads to the attractive possibility of on-line mass separation^{7,10} of activities produced in a nuclear reaction, and a wealth of new information which would result from the study of high-isospin nuclei inaccessible with presently available techniques.

The essential feature of any He-jet system is the rapid transport of activity to a region free of unwanted background radiation. In the case of accelerator-produced activity, a natural separation from the target is afforded by the linear momentum transferred to the recoils. These recoils thermalize in He gas, which is then conducted, by differential pumping, through a suitable length of capillary tube leading to a separate, low-background chamber. The recoils are swept along with the He and can adhere to a collector surface positioned in this chamber a few millimeters from the exit of the capillary. The sticking probability for He atoms (as well as for reaction products which are gases at the temperature of the collector) is nearly zero and they are therefore pumped away. Decays from the activity that sticks to the collector can then be registered by nearby detectors and associated electronics.

A schematic view of the present He-jet system is shown in Fig. 1. The beam (~ 5 mm diam.) enters the target area through an 8-mm-diam., water-cooled entrance foil (typically 2-6 μ m Ni), and leaves through a similar, 17-mm-diam. exit foil. The beam is then refocused with a quadrupole magnet

into a Faraday cup 1.8 m downstream. Targets are mounted on a six-position, externally-controlled selector wheel. An identical wheel (on which targets could also be mounted) is located 2 cm upstream; this wheel is used for mounting foils to degrade the energy of heavy ion beams. The entire volume between the vacuum isolation foils is filled with He. (Optimum efficiency for our system has been achieved using a He pressure of 1.5 to 1.7 atm.) Reaction products recoiling from the target are thermalized by the He inside a 25-mm-long cylinder with a 16 mm inside diameter (i. d.). This cylinder defines the He flow lines and is presumed to be the principal

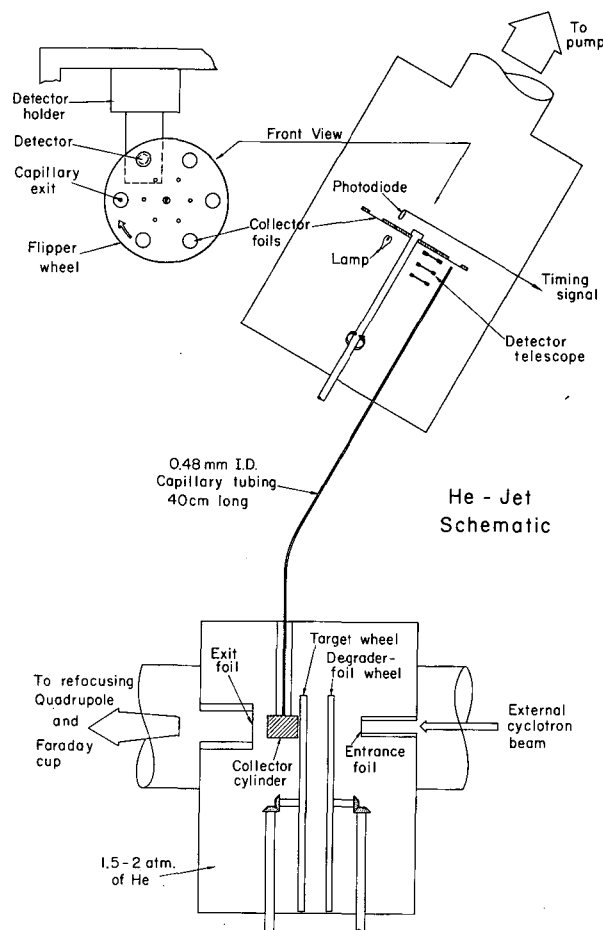


Fig. 1. A schematic view of the He-jet system used for β^+ delayed-proton studies.

(XBL 724-2755)

factor in determining the average collection time. The He flows at a rate of 15-20 Torr-liters/sec through the stainless steel capillary tube which, for most experiments, has a 0.48 mm i. d. and is 40 cm long.

A high capacity (500 liters/sec of He) roots-blower maintains a residual pressure of 50-100 μ in the collector-counting chamber at the exit end of the capillary. In the setup shown in Fig. 1, six collection foils (usually Al or Ni) are symmetrically mounted on a light, aluminum flipper wheel. Continuous target bombardment and He sweeping result in a deposition of activity on the collector foil, which is positioned 3 mm from the capillary exit. At suitable intervals (typically three half-lives), a solenoidal stepping motor is used to rotate the flipper wheel 60°. Thus the activity is quickly (\sim 20 msec) repositioned in front of the counter telescope while a fresh foil is brought into the collection position. The mechanism can be reliably activated up to ten times per second. Since the detectors can be placed arbitrarily close to the small (\sim 2 mm diam.) activity spot, ΔE -E telescope geometries of 0.25 sr. are easily achieved. The absolute efficiency has been measured for the $^{24}\text{Mg}(p,\alpha)^{20}\text{Na}$, $^{24}\text{Mg}(p,2n)^{23}\text{Al}$ and $^{40}\text{Ca}(^3\text{He},2n)^{41}\text{Ti}$ reactions, and was found to be \sim 10% in each case.

The flipper wheel also provides a timing signal which can be used to initiate each counting sequence. Small holes in the wheel are located on the same radial axes as are the collector foils. A dc light source shines through one of the holes onto a photodiode. The optical circuit is interrupted when the wheel is stepped; the light beam reestablishes the "on" signal when the wheel stops moving. This circuitry provides both a timing signal for half-life sequencing and an assurance that the mechanism is functioning properly throughout the experiment.

Two types of gas targets have been successfully employed. For less expensive gases, the He can be mixed with the target gas and the resulting mixture then serves as both carrier and target. For example, in our ^{24}Mg studies, a ^{20}Ne target was supplied from a bottle of spark chamber gas: 90% Ne and 10% He. A special gas handling system has been built for more expensive separated-isotope gas targets, and has been used in our ^{37}Ca work. The gas is transferred into a 3-cm³ cylindrical cell having a 1.9-cm diameter. The cell, mounted on the target wheel (see Fig. 1), is fed by a small bore, flexible gas line so its positioning in or out of the beam can be externally controlled. Nickel foils have been used on the cell to separate the target gas from the He. The downstream foil must be very thin to per-

mit the recoils to escape into the He. For our $^{36}\text{Ar}(^3\text{He},\alpha n)^{37}\text{Ca}$ bombardments at 40 MeV, a 200 $\mu\text{g}/\text{cm}^2$ Ni foil was utilized for this purpose. The gas handling system enabled us to monitor the pressure differential across this foil and to keep it from exceeding \sim 5 Torr at all times, which was necessary to prevent the foil from breaking.

In addition, some preliminary studies have been successfully completed using the nozzle-skimmer method⁶ to separate ^{20}Na activity from the He carrier gas. As the He expands into the vacuum at the capillary exit, the heavier components (carried by the gas) expand into a less divergent cone⁶ than the He. If, as previously suggested⁷ the recoil is loosely attached to a massive (10^6 - 10^8 amu) molecular cluster, it has a high probability of leaving the capillary at a very small angle to the axis of the capillary-skimmer system. In these circumstances, a very efficient separation might be expected as the He is skimmed off and pumped away, while the heavier, radioactive nuclides are transmitted through the skimmer.

For these tests, 1-3 μA of 40 MeV protons were utilized to produce the 446 msec¹¹ β^+ -delayed alpha emitter ^{20}Na via the reaction $^{24}\text{Mg}(p,\alpha)$. The target chamber described in Fig. 1 was used at the optimum He pressure of 1.5 atm; however, for these studies, a 6 m length of 1 mm i. d. capillary was employed in conjunction with the skimmer-counter chamber shown in Fig. 2. The capillary tube was made of stainless steel, though both Teflon and polyethylene tubing were found to be equally satisfactory. Several tube diameters

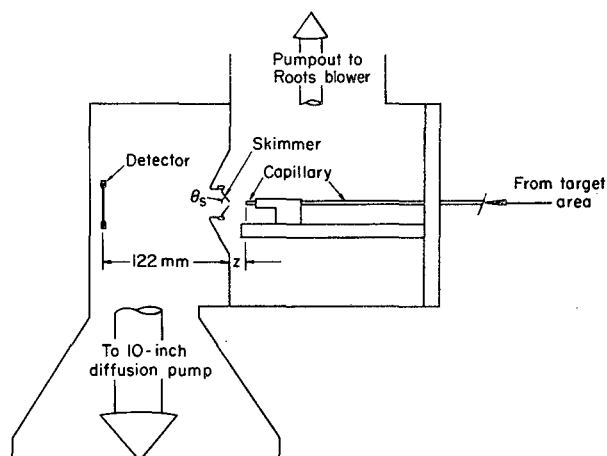


Fig. 2. A schematic representation of the skimmer used to separate the activity from the He carrier gas. (XBL 733-2372)

were tested (with the skimmer removed) ranging from 0.6 to 1.5 mm i. d., the 1 mm i. d. tube resulted in the highest yield. In this arrangement the activity was collected on the front surface of a 15-mm-diam. detector. While the position of the detector and skimmer was fixed, the capillary tube could be moved independently along three mutually orthogonal axes. Two of these were used to align the capillary with the skimmer, while the third was used to vary the distance (z) between them. The capillary chamber was maintained at a pressure of $40\ \mu$ by the roots blower; the pressure in the detector chamber was reduced to 10^{-4} to 10^{-6} Torr by a 10-in. diffusion pump.

In one experiment, with the skimmer again removed, the yield was found to remain constant as the capillary-detector distance was varied from 10 to 170 mm. Beyond 170 mm, the yield gradually decreased until, at 280 mm, the yield had been reduced by a factor of two. If we attribute this loss in yield to activity falling outside the detector diameter, these data then define an opening angle of $\sim 3^\circ$ associated with the cone of activity expanding from the capillary exit.

Skimmers with 1-mm orifices and angles (see Fig. 2) $\theta_s = 30^\circ$, 60° and 90° (flat plate) were tested and the yield was marginally higher with the 60° skimmer at all values of z . Figure 3(a) illustrates how the yield decrease with increasing z for both 1 mm and 1.5 mm skimmers. These results are normalized at $z = 0$ to the no-skimmer yield. Unlike the similar work (using ^8Li) of Jungclas et al,⁷ these results showed no indication of a substantial yield loss at $z = 0$ associated with the presence of a skimmer of the same diameter as the capillary tube. This, and other dissimilarities with work of the Texas A & M group,⁷ are thought to arise from subtle differences between the He-jet techniques employed and the differing roles played by large molecular clusters. (Reagent grade He was used in this work and no attempt was made to control or deliberately add impurities.)

The ambient background pressure in the detector chamber during the above skimmer tests was a sensitive function of z ; this dependence is shown in Fig. 3(b) for both the 1.0- and 1.5-mm skimmers. These pressure curves show that, having demonstrated a capability for transporting activity over large distances and directing it with reasonable efficiency through the skimmer, we can maintain a residual pressure within the operating range of common ion sources.¹²

Work currently in progress is directed toward expanding the present system into an operational on-line mass separator to be used

to further our studies of exotic nuclei in the light elements.

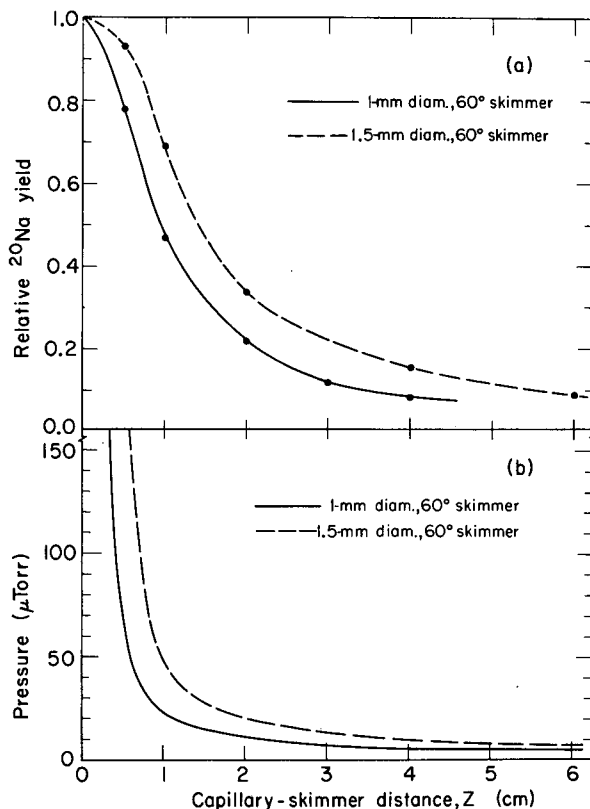


Fig. 3(a). The yield of ^{20}Na , relative to the same yield without a skimmer, is shown as a function of the capillary-skimmer distance (z) for both a 1.0 mm and a 1.5 mm diameter skimmer.

Fig. 3(b). The residual pressure (after skimming) in the detector area is shown versus z for comparison with the relative yield illustrated in Fig. 3(a) above.

(XBL 733-2371)

References

1. R. D. Macfarlane, R. A. Gough, N. S. Oakey, and D. F. Torgerson, Nucl. Instr. Methods **73**, 285 (1969).
2. R. G. Sextro, R. A. Gough, and J. Cerny, submitted to Phys. Rev. C.
3. R. A. Gough, R. G. Sextro, and J. Cerny, Phys. Rev. Letters **28**, 510 (1972).
4. R. A. Gough, R. G. Sextro, and J. Cerny, Phys. Letters **43B**, 33 (1973).

5. F. S. Goulding, D. A. Landis, J. Cerny, and R. H. Pehl, *Nucl. Instr. Methods* 31, 1 (1964).
6. J. B. Anderson, R. P. Andres, and J. B. Fenn, *Advan. Chem. Phys.* 10, 275 (1966), and references therein.
7. H. Jungclas, R. D. Macfarlane and Y. Fares, *Radiochim. Acta* 16, 141 (1971).
8. Martine Sarda Gugliermi (Ph. D. Thesis), Université Paris-Sud, 1972.
9. W. -D. Schmidt-Ott, R. L. Mlekodaj and C. R. Bingham, to be submitted to *Nucl. Instr. Methods*.
10. J. M. Nitschke, in Proceedings of the International Conference on the Properties of Nuclei far from the Region of Beta-stability, Leysin, Switzerland, 1970 (CERN, Geneva, 1970), Vol. 1, p. 153 (1970).
11. D. H. Wilkinson, D. E. Alburger, D. R. Goosman, K. W. Jones, E. K. Warburton, G. T. Garvey, and R. L. Williams, *Nucl. Phys.* A166, 661 (1971).
12. G. Sidenious, First International Conference on Ion Sources, Saclay, France, p. 401 (1969).

EFFICIENCY OF DETECTING A ^8Be WITH A ΔE -E COUNTER TELESCOPE*

G. J. Wozniak and H. L. Harney†

The question of whether quartet configurations play an important role in nuclear structure has prompted a great deal of experimental work on alpha-transfer reactions.¹ During the last year there has been much interest in the new alpha-particle transfer reaction (^{12}C , ^8Be). A ^8Be event can be confused with a ^7Li (see Ref. 2) if the two alpha particles from the decay of a ^8Be in flight simultaneously traverse a counter telescope.

Since ^8Be is particle unstable, the probability of detecting a ^8Be event is less than one because the "effective solid angle" for detection of the two breakup alphas is always smaller than the geometric solid angle of the counter telescope. This can be seen by observing that for a ^8Be whose center-of-mass velocity falls within the solid angle subtended by the detector, there is usually a portion of the breakup cone which extends beyond the collimator limits. Thus there is an appreciable probability that one or both of the breakup alpha-particles will fall outside the counter telescope, causing the event to be lost.

To determine the relative population of states by the (^{12}C , ^8Be) reaction and their absolute cross sections, one must calculate the ^8Be -detection efficiency of a counter telescope. A report has been written³ that derives the necessary formalism and presents a computer program that calculates the "effective solid angle" for a detector telescope with rectangular collimators.

A very simple formula for the ^8Be detection efficiency (ϵ) is derived using an approximation

which is valid in the limit of "small"⁴ geometric solid angles,

$$\epsilon = \frac{\Omega E_8}{8\pi Q}$$

where Ω is the geometric solid angle, E_8 is the lab energy of the ^8Be in MeV, and Q is the ^8Be breakup Q -value in MeV. For the case of "large" solid angles ($\Omega > 5 \times 10^{-4}$ sr) the resulting expression for ϵ is much more complicated requiring numerical integration to evaluate ϵ . The FORTRAN program EFFI is described and was used to evaluate ϵ for the case of "large" solid angles. The case of a gas target is also treated.

Footnotes and References

* Abstracted from LBL-1214.

† Present address: Max Planck Institut für Kernphysik, Heidelberg, W. Germany.

1. K. Bethge, *Annual Review of Nuclear Science* 20, 255 (1970).

2. G. J. Wozniak, H. L. Harney, K. H. Wilcox, and J. Cerny, *Phys. Rev. Letters* 28, 1278 (1972) and LBL-635.

3. H. L. Harvey and G. J. Wozniak, LBL-1214, 1972.

4. For $\Omega \leq 5 \times 10^{-4}$ sr, the simple expression for ϵ holds to 2% or better.

A PROTON POLARIMETER OF HIGH EFFICIENCY AND GOOD ENERGY RESOLUTION

J. Birchall, W. Dahme,* J. Arvieux,† R. M. Larimer and H. E. Conzett

Measurement of spin dependent effects in elastic and inelastic scattering yields a large amount of information not available from cross-section measurements alone. A polarimeter has been designed to measure the polarization of protons arising from a scattering or a nuclear reaction. The polarimeter has high detection efficiency and good energy resolution and is compact enough to be mounted on a counter arm inside a scattering chamber, facilitating the measurement of angular distributions of polarization. The properties of the device make it especially suitable for polarization transfer and depolarization measurements, as well as for experiments of the type (d, \hat{p}) , $(^3\text{He}, \hat{p})$, $(^4\text{He}, \hat{p})$ etc.,¹ where the flux of polarized protons is necessarily small. Particular emphasis is being placed here on the development of a polarimeter for depolarization measurements where, as indicated by Sherif and Hussein,² much information can be gathered on the spin-spin interaction, and where little has yet been done.

The usefulness of silicon as a polarization analyzer for protons was pointed out by Miller³ and a number of polarimeters using a silicon analyzer have been built.^{4,5} The present polarimeter, as those of references 4 and 5, uses a silicon solid-state detector as analyzer. It is shown schematically in Fig 1. Polarized protons are incident on the analyzer detector. Those protons which are scattered to the left and right at an angle θ are detected by the left and right detectors respectively. Addition of the analyzer signal to the left or right detector signal gives the energy of the proton incident on the analyzer. Thus, energy resolution is not lost by straggling in the analyzer, and good energy resolution (limited by the noise level of the detectors used) can be preserved, even while using a thick analyzer. The random coincidence rate between the analyzer and side detectors is reduced by placing an anticoincidence detector after the analyzer to veto those analyzer pulses which correspond to protons passing through the analyzer with no, or with little, scattering.

Spectra obtained in a preliminary run are shown in Fig. 2a and 2b. Figure 2a shows the total energy spectrum of the analyzer and the left detector; Fig. 2b is of the analyzer plus the right detector. A 1-mm-thick analyzer was used ($\Delta E = 4.4$ MeV). The spectra correspond to unpolarized $p - ^{12}\text{C}$ scattering at 25 MeV at a laboratory angle of 33° . The elastic scattering peak, at channel 75, has a width of

approximately 300 keV FWHM, attributable almost entirely to analyzer detector noise. The peak at channel 60 in the right spectrum corresponds to scattering to the first excited state of carbon ($Q = -4.43$ MeV). We hope to reduce the relatively high random coincidence level without loss of resolution by use of wider side detector collimators and reduction of beam current and by improved shielding.

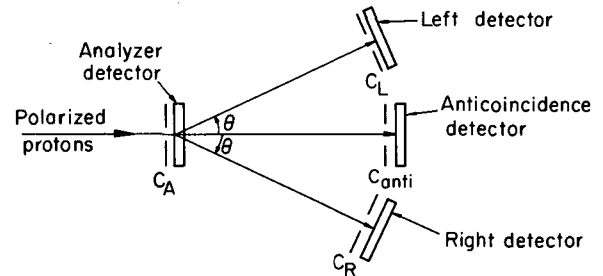


Fig. 1. Schematic diagram of the polarimeter. C_A , C_L , C_R and C_{ANTI} are collimators. (XBL 733-2368)

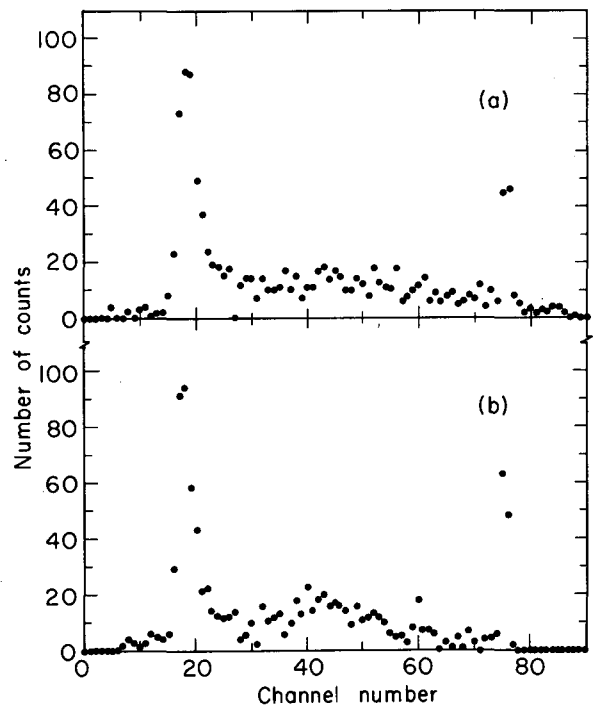


Fig. 2. Total energy spectra of protons scattered a) to the left and, b) to the right from the analyzer detector. (XBL 733-2370)

Footnotes and References

* DAAD exchange student from University of Munich, West Germany.

† Permanent address: Institut des Sciences Nucléaires, Grenoble, France.

1. H. E. Conzett, B. Frois, R. Lamontagne, Ch. Leemann, R. J. Slobodrian, Nuclear Chemistry Division Annual Report 1971, LBL-666 p. 63.

2. H. S. Sherif, A. H. Hussein, Phys. Letters 41B, 465 (1972).

3. D. W. Miller, in Proc. of the Second International Symposium on Polarization Phenomena of Nucleons (Birkhauser, Basel, 1966).

4. B. Frois, J. Birchall, R. Lamontagne, R. Roy, and R. J. Slobodrian, Nucl. Instr. Methods 96, 431 (1971).

5. J. P. Martin and R. J. A. Lévesque, Nucl. Instr. Methods 84, 211 (1970).

PARTICLE-IDENTIFYING FOCAL PLANE DETECTOR

B. G. Harvey, H. Homeyer, J. Mahoney, and G. Gabor

The spectrometer focal plane detector system used for heavy ion experiments at the 88-inch cyclotron was described in the 1971 Annual Report.¹ Briefly, it consists of a Borkowski-Kopp resistive wire proportional counter^{2,3} which measures simultaneously the position of a particle along the focal surface and its energy loss dE/dx in the counter gas. A plastic scintillator, light guide, and photomultiplier behind the proportional counter measure the time of arrival of the particle with respect, in the system previously described, to the cyclotron rf. During the past year of very satisfactory operation, attempts have been made to improve both the resolution in dE/dx (which determines the atomic number

resolving power) and the timing resolution (which determines the particle mass resolving power).

The dE/dx resolution was found to be influenced mainly by the energy-loss statistics: it improves as the counter gas pressure and therefore the energy-loss increase. Table I shows some dE/dx resolutions calculated from energy-loss straggling⁴ and the measured values. Approximately, the calculated width $W_c(\%)$ is related to the experimental width $W_e(\%)$ by:

$$W_e^2 = W_c^2 + 25.$$

Table I. Comparison of calculated energy loss straggling and measured dE/dx resolution.

Particle	Energy (MeV)	Gas pressure (atm)	Energy loss (MeV)	dE/dx resolution (%)	
				Calc. ^a	Expt.
¹⁶ O	60	0.2	1.35 ^a	6.8	9.0
¹⁶ O	104	0.2	0.9 ^a	10.2	11.6
¹⁶ O	104	0.4	1.8 ^a	7.1	8.5
¹⁶ O	140	0.4	1.5 ^a	9.2	10.5
²⁰ Ne	150	0.4	~2.2	—	9.0
⁴ He	25	0.2	~0.057 ^a	40.0	~30.0

Note: ^aCalculated, ref. 4.

There is a practical upper limit to the gas pressure (about 0.7 atm) imposed by the difficulty of making a strong enough Mylar window. Furthermore, the maximum gas multiplication giving a linear response is lower at higher gas pressure.

Therefore, a smaller pulse output must be accepted, and while this is satisfactory for the dE/dx measurement ($W_e \sim 7-12\%$), the position resolution ($W \approx 0.16\%$ of the counter length) is compromised by the lower signal/noise ratio.

Since the timing resolution was limited to 5-6 nsec by the time-duration of the cyclotron beam pulses, two alternative methods were tried. In both of them, particles are detected in "time-zero" counters before they enter the spectrometer.

- A) Secondary electrons from a thin carbon foil were detected by an open photomultiplier (PM).⁵
- B) Scintillations in thin foils of NE 111 were detected by one or two PM's.⁶

Method A gave satisfactory results (time resolution ~ 2 nsec with efficiencies $\sim 66\%$) with very small carbon foils, but the large foils required for the normal aperture of the spectrometer caused severe focusing problems of the secondary electrons into the PM so that this method was not further studied. The use of large-area channel plates could perhaps improve the results.

For method B, the two systems shown in Fig. 1a,b were used. System 1 consists of a Lucite frame as a foil holder which is attached with optical grease to the PM and surrounded by a mirror. In system 2 a solid Lucite light guide is connected to phototubes on top and bottom. The foil, on a Lucite frame, is easily mounted into the light guide with optical grease to provide good optical contact. The size of the foil is $1/2 \times 2$ in. RCA 8850 PM's are used. The timing signal was obtained from ORTEC constant fraction discriminators following the anode signal. An electrostatic electron suppressor at the exit of the scattering chamber was necessary to reduce the high background produced by electrons from the target.

Both systems gave satisfactory results with respect to the time resolution — 2.3 nsec for 104-MeV ^{16}O at a solid angle of 1 msr which corresponds to a $\Delta t/t = 1.2\%$ and is approximately the dispersion in flight paths through the spectrometer at this solid angle. With a solid angle of 0.3 msr, the time resolution was 1.3 nsec, corresponding to $\Delta t/t$ of 0.7%.

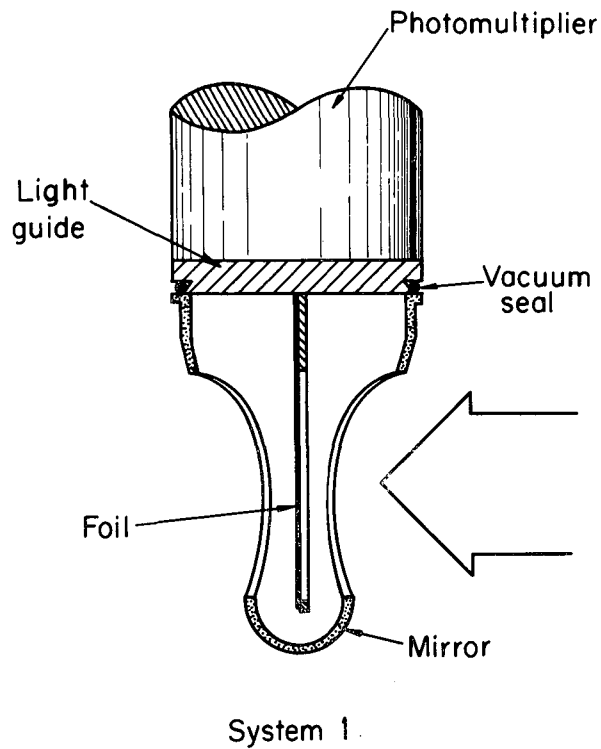


Fig. 1(a) (XBL 733-2367)

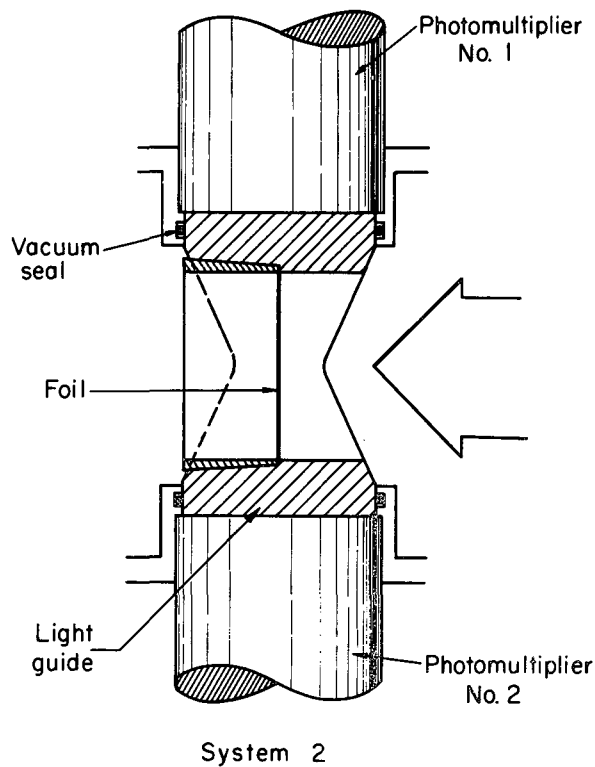


Fig. 1(b) (XBL 733-2366)

The foil thickness was $80 \mu\text{g}/\text{cm}^2$ and the efficiency 98%. Homogeneous foils of this thickness did not affect the energy resolution of $\sim 120 \text{ keV}$ of the scattered particles.

In order to investigate the lowest limit of foil thickness for ^{16}O ions of 104 MeV, the light output for foils of different thickness ($30\text{-}250 \mu\text{g}/\text{cm}^2$) was measured with system 1 in which it is easier to change foils. It was found that the light output is linear with foil thickness. The thinnest foil which gave efficiency $> 90\%$ was $80 \mu\text{g}$. In this case the photoelectron (PE) production is approximately 7 at an energy loss of $\sim 320 \text{ keV}$ which corresponds to $(40\text{-}50) \text{ keV}/\text{PE}$. As the light collection is more efficient with the two tubes of system 2 (probably by a factor of 2) the use of $(40\text{-}50) \mu\text{g}/\text{cm}^2$ foils should be possible.

HEAVY-ION ACCELERATION AT THE BERKELEY 88-INCH CYCLOTRON

D. J. Clark, J. Steyaert,* J. Bowen, A. Carneiro, D. Morris

The intensity of heavy ions from an ion source is strongly dependent on the arc power. The original ion source for the cyclotron used a hot filament and a $1/8$ -inch diam. arc-defining hole. The maximum arc power was 500-800 W. The heavy ion output was about a microamp external beam of nitrogen and oxygen at 5-10 MeV/nucleon. External beams of N^{5+} were a few nanoamps. Since the PIG (Penning Ion Gauge) type source with arc-heated cathode buttons is known to give much higher heavy-ion current,¹ we built an internal PIG source which started operation in Sept. 1971.² The external PIG source² has been tested on lithium beam injection. It has given external cyclotron beams of 50- to 80-MeV Li^{2+} at intensities up to 50 nanamps, without bunching, but the lithium feed system needs improvement. Since the internal PIG source is giving good beams of all required ions, including lithium, very little effort has been put on the external source recently.

The internal PIG source was designed to fit on the standard 2-1/4-in. diam. shaft which is inserted through the lower pole of the cyclotron. It is shown in cross section in Fig. 1. The anode and cathode holder are made of water-cooled copper. The cathode holder makes the electrical connection between cathodes, eliminating the need for an external connection to the top cathode. The cathodes are now usually made with a shoulder and dropped into the holders so set screws are not required. A loose fit gives lower operating voltage, resulting in longer cathode life. The alumina

References

1. Nuclear Chemistry Division Annual Report for 1971, LBL-666, p. 322.
2. C. J. Borkowski and M. K. Kopp, IEEE Trans. Nucl. Sci. NS17, No. 3, 340 (1970).
3. B. G. Harvey et al., Nucl. Instr. Methods 104, 21 (1972).
4. C. C. Maples, unpublished.
5. W. F. W. Schneider, B. Kohlmeyer, and R. Berk, Nucl. Instr. Methods 87, 297 (1970).
6. C. K. Gelbke, K. D. Hildenbrand, and R. Bock, Nucl. Instr. Methods 95, 397 (1971); M. L. Muga, Nucl. Instr. Methods 95, 349 1971.

base insulator forms a vacuum seal and makes insulated water connections to the anode and cathode circuits from two water lines coming through the source shaft. A drop-in boron nitride cover insulator protects the alumina, and is easily removable for cleaning. The electron dump provides a component of electric field, E , parallel to the magnetic field, B , causing electrons circulating around the cathode holder in an ExB mode to be dumped on the outer tantalum cover. Photos of the

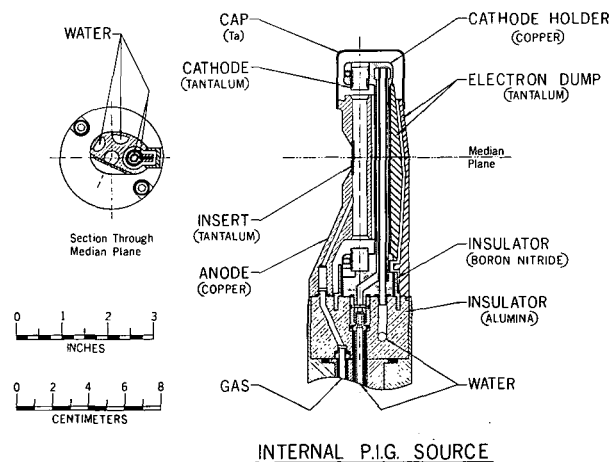


Fig. 1. Internal PIG ion source.

(XBL 7110-1536)

assembled and partly disassembled source are shown in Figs. 2 and 3. The top and side covers slide off, and the anode is removed by loosening 2 screws.

To start the arc, the voltage is raised to 3 kV and the gas flow increased. When the arc strikes, the current increases to 2-4 A and the voltage drops to 400-800 V. The gas is then reduced for maximum stable beam. The arc power is thus 2-3 kW, compared to 500-800 W of the old filament source. Since the high charge state heavy ion output increases

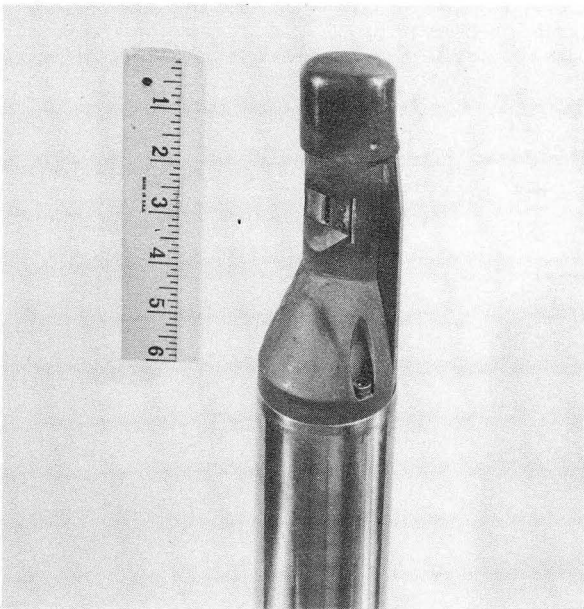


Fig. 2. Internal PIG source assembled on shaft. Scale is in inches. (CBB 7110-4844)

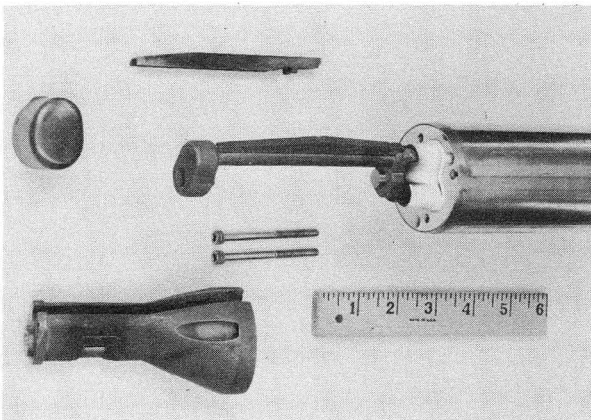


Fig. 3. Internal PIG source disassembled for cathode change. (CBB 7110-4836)

exponentially as the second or third power of the arc power, the output of heavy ions is greatly increased over that of the filament source. For example, the N^{4+} and O^{4+} beams are 3-10 times more intense, and the N^{5+} output is 200 times larger than that of the filament source.

To obtain a beam of lithium, a solid material containing lithium had to be used in the source, since no gas containing lithium was available. Other laboratories have used solid material in the cathodes or in the anode.¹ Trials were made using 10-20% lithium fluoride or oxide mixed with tungsten powder and pressed into a cylinder for use as a cathode. Some ${}^7\text{Li}^{2+}$ beam was obtained. Later LiF was melted into a tantalum insert placed in the arc hole. This produced more lithium vapor near the beam exit slit and gave external beam intensities of about $1\ \mu\text{A}$ of 60-80 MeV Li^{2+} over periods of several hours between cathode changes. N_2 or CO_2 support gas is used as needed. There are still some problems in obtaining consistent good intensity with this system, and development is continuing.

The range of particles and energies which can be accelerated in the cyclotron is shown in the resonance chart, Fig. 4. The higher energy heavy ions use first harmonic acceleration and the lower energies use third or occasionally fifth harmonic. The maximum energy for ions heavier than α -particles is $E = 140 Q^2/A$ MeV where Q and A are ion charge and mass in proton units. This is set by the maximum magnetic field of 17 kG.

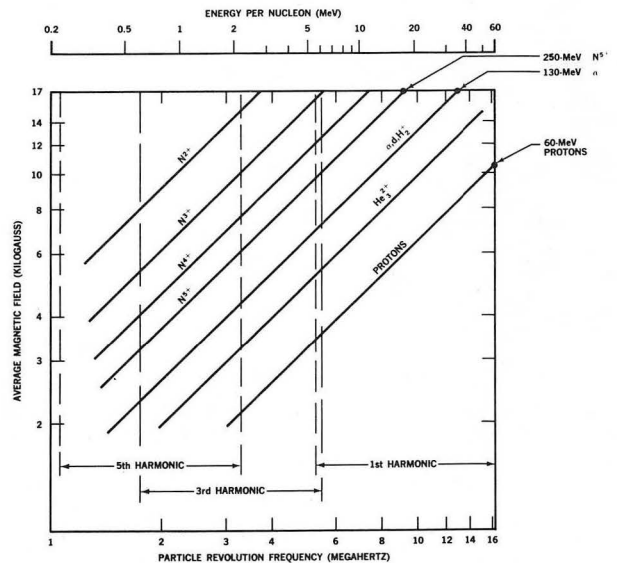


Fig. 4. Resonance chart for 88-Inch Cyclotron. (XBL 678-4701)

The narrow gap of the center-region inserts³ reduces the gap transit time. This is especially useful for the higher energy third harmonic beams. Operation with the inserts gives a beam intensity twice that produced without the inserts for 60-MeV O^{3+} , for example. The sliding edge on the dummy dee insert installed in 1969³ caused numerous operational problems and was replaced by a fixed edge with an open area for ion source motion. The center region settings used for heavy ions are similar to those of light ions with the same number of turns. Because of the charge-exchange beam loss during acceleration, of a factor of 2-3, high dee voltages of 60-70 kV are used to minimize the number of turns. Trim coil solutions are calculated with the computer code CYDE.⁴ Tuning has to be done more carefully with heavy ions since beams of lower charge states on higher harmonics can be accelerated simultaneously with the required beam through a number of turns, and can spiral out along a hill-valley boundary and

appear on an external beam probe without going through the deflector. Tuning is sometimes done after the first external switching magnet to eliminate these spurious beams. A useful technique for the very high charge, low intensity beams is to start the tuning with a lower mass ion with the same charge/mass ratio, and then change frequency slightly to get the required ion. If the charge-to-mass ratio is different by more than about 1%, the scaling method of Ref. 2 can be used.

Most of the heavy ion beams which have been accelerated and extracted from the cyclotron with the internal source are listed in Table I. The PIG ion source is now always used for heavy ions. But previously, the old filament source gave the surprisingly high charge states of Kr^{11+} and Kr^{12+} at very low intensities. The beam currents are listed as electrical μA or particles/sec. The lower number is a typical good beam and the higher number is the highest value recorded.

Table I. Heavy-ion beams.

Ion	Energy (MeV)	Harmonic	Source	External beam
${}^7Li^{2+}$	60-80	1	PIG	1-3 μA
${}^{12}C^{3+}$	65-105	3,1	PIG	5-14 μA
${}^{14}N^{4+}$	100-160	1	PIG	5-10 μA
${}^{14}N^{5+}$	250	1	PIG	1-7 μA
${}^{14}N^{6+}$	360	1	PIG	10^3 part./sec
${}^{16}O^{3+}$	50-75	3	PIG	5-18 μA
${}^{16}O^{4+}$	105-140	1	PIG	5-44 μA
${}^{20}Ne^{5+}$	130-150	1	PIG	0.5 μA
${}^{56}Fe^{9+}$	175	3	PIG	10 part./sec
${}^{56}Fe^{10+}$	220	3	PIG	1 part./sec
${}^{84}Kr^{11+}$	174	3	Filament	1 part./sec
${}^{84}Kr^{12+}$	207	3	Filament	1 part./sec

Footnotes and References

*On leave of absence from University of Louvain and IISN, Belgium-NATO Fellowship.

1. J. R. J. Bennett, IEEE Trans. Nucl. Sci., NS19, 2, 48 (1972).

2. D. J. Clark et al., IEEE Trans. Nucl. Sci., NS19, 2, 114 (1972).

3. D. J. Clark et al., in Fifth International Cyclotron Conference (Butterworths, London, 1971), p. 610.

4. Computer code CYDE available from J. Colonias, Lawrence Berkeley Laboratory.

CYCLOTRON INJECTION SYSTEMS

D. J. Clark

The early work on developing injection systems for cyclotrons was directed toward injecting polarized beams from the polarized ion sources which were first developed about 1960. These sources were much larger than the space available in the cyclotron center region. Development work was started by Keller at CERN. The first injection of unpolarized beam into a full size cyclotron was the axial system reported by Powell at Birmingham in 1962. In 1963 Thirion at Saclay injected a polarized neutral deuteron beam, which was ionized at the center of the cyclotron and accelerated without loss of polarization. Many other groups developed radial and axial injection systems in the following years. The progress in this field has been reviewed previously by Powell in 1965 at the Karlsruhe Conference,¹ again by Powell in 1966 at the

Gatlinburg Conference,² and by Clark in 1969 at the Oxford Conference.³ The various systems are briefly described with emphasis on the developments during the past 3 years.

The various injection systems for cyclotrons which are now in operation are shown in Table I. The neutral systems have the advantage of simplicity, but the ion systems give better transmission. Radial and axial ion systems are comparable in performance when they are carefully designed. The rebuilt injection line at Birmingham looks quite good on first tests, giving 12% transmission from source to external beam. The construction of the new separated sector machines such as at Zurich and Indiana makes higher energy injection easy. This would be especially useful for two-stage heavy ion designs.

Table I. External injection systems in operation.

	Cyclotron energy (MeV)	Type	Source Energy	Injected current	Focusing	Transport		Cyclotron beam ^a		Transmission source to:		Comments	
						Buncher	Inflector	Accel.	External	Accel. ^b (%)	Ext. ^b (%)		
Radial neutral beam													
Lyon, France	28 d	Pol.	Thermal	0.1 mA	None		Ionizer		0.01 nA			FM Cycl.	
Rez, Czech.	13 d	rf/Pol.	40 keV	4.5/0.3 μ A	Elec. grad.	Yes	Foil		6/0.075 nA		0.14/0.03	Classical Cycl.	
Radial ion													
Dubna	7 MeV/A Xe	Cyclotron	0.9 MeV/A	1 μ A Xe ⁹⁺	Quads		Cycl.	Foil	100 nA Xe ³⁰⁺		3		Classical Cycl.
Indiana Inj.	15 p,...	Duo.	700 keV		Quads			Channel					Testing 1964
Lebedev	0.15 p, 0.3 d	Penning	15-30 keV	5 μ A	Sect. grad.	No		Channel	1 μ A		20		
Orsay	5 MeV/A Kr	Linac	1 MeV/A	3 μ A Kr ⁸⁺	Mag. quads			Foil	20 nA Kr ²³⁺	4 nA Kr ²³⁺	0.2	0.05	80 nA Ar ¹²⁺ ext.
Saclay	27 p,...	Pol.	5 keV p	5 μ A	Einzel	Yes				100 nA			
Axial ion													
Berkeley	65 d,...	Pol.	10 keV p	2 μ A	Elec. quads	Yes	Mirror	400 nA	150 nA		20	7	
Birmingham	12 d,...	Pol.	11 keV d	100 nA	Elec. quads	Yes	Mirror	35 nA	12 nA		35	12	New ionizer, transp.
Cycl. Corp.	30 H ⁺	Ehlers	15 keV	2.5 mA	Elec. quads	Yes	Mirror	120 μ A	40 μ A		5	1.5	For A. N. U. Cyclograaff
Duke	15 H ⁺	Ehlers	16 keV p	1 mA	Elec. quads	Yes	Mirror	90 μ A	25 μ A		9	2.5	
Grenoble	60 p,...	Duo./Pol	10 keV d	100/3 μ A	Mag. quads	Yes	Channel	10/0.3 μ A	5/0.12 μ A		10	5/4	
Harwell	50 p,...	PIG	16 keV/q	240 μ A C ²⁺	Mag. quads	No	Mirror	40 μ A			16		1969 Test
Karlsruhe	55 d	Duo.	10 keV d	7 μ A	Elec. quads + einzel	No	Channel	0.7 μ A			10		Plan Pol., PIG source Cyclograaff
Livermore	15 H ⁺	Ehlers	15 keV		Similar to Duke								
Oak Ridge	65 p,...	Pol.	12 keV p	3 μ A	Elec. quad + Sol.	Yes	Mirror	50 nA	30 nA		1.7	1	
Phillips	14 p	PIG	7.5 keV d	800 μ A	Elec. quads	No	Mirror	30 μ A	10 μ A		3.7	1.2	
UCLA	50 p	Ehlers	15 keV H ⁺	2-0.1 mA	Elec. quads		Mirror	5 μ A					

^aElectrical current^bParticle transmission

References

1. W. B. Powell, Proc. Second International Symposium on Polarization Phenomena of Nucleons (Birkhauser, Basel, 1966), p. 47.

2. W. B. Powell, IEEE Trans. Nucl. Sci., NS13, 4, 147 (1966).

3. D. J. Clark, Fifth International Cyclotron Conference (Butterworths, London, 1971), p. 583.

88-INCH CYCLOTRON OPERATION AND DEVELOPMENT

J. Bowen, D. J. Clark, P. Frazier, and D. Morris

During 1972, the cyclotron was scheduled for 20 eight-hour shifts per week for experiments in nuclear chemistry, physics, biomedical studies, isotope production and beam development. One shift per week was used for

maintenance. The time distribution is shown in Table I. Ions heavier than helium occupied 51% of the operating time. The particle distribution is shown in Table II; their history in Fig. 1.

Table I. 1972 Time distribution

Tune-up	8%	
Beam optics	4%	
Experiments	53%	
Beam development	<u>12%</u>	
Operating time		77% (6096 hr)
Planned maintenance	12%	
Unplanned maintenance	<u>11%</u>	
Total maintenance		<u>23%</u> (1863 hr)
Total work time		<u>100%</u> (7959 hr)

Table II. 1972 Particle distribution

Internal ion source:		
Protons	5%	
Deuterons	3%	
Helium 3	10%	
Helium 4	18%	
Lithium	11%	
Carbon	8%	
Nitrogen	9%	
Oxygen	19%	
Neon	<u>4%</u>	
Total		87%
External ion source:		
Polarized protons and deuterons	12%	
Heavy ion source	<u>1%</u>	
Total		<u>13%</u>
Total operating time		<u>100%</u> (6096 hr)

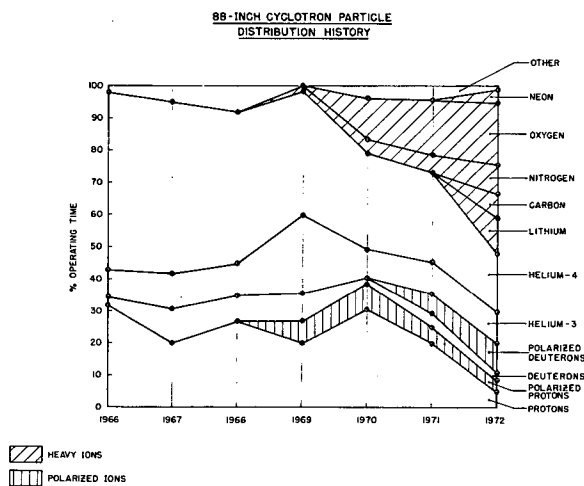


Fig. 1 (XBL 733-244)

Using the new internal PIG source, more heavy ion beams were developed. In addition to the nitrogen and oxygen beams of the previous year, beams of carbon and neon were run at energies of about 7 MeV/nucleon. Beams of lithium of 60-80 MeV were developed with the internal PIG source, using LiF in the source arc chamber and cathode regions. This is a simpler method and gives more intensity than using the external PIG source. A low intensity beam of iron (Fe^{9+}) of 175 MeV of a few particles/sec was used to bombard plastics and minerals for cosmic ray track calibration. The beam was formed by putting an iron sleeve in the internal PIG source anode.

In May the original rf oscillator system feeding the dee was removed, and the new master-oscillator power-amplifier system was installed. The new wide-band system uses a distributed amplifier, and only the master oscillator and dee resonator panels have to be changed when the frequency is changed. This wide-band system has thus far shown improvement over the old system in dee voltage regulation and quick resetting under heavy ion source loading as well as its expected high degree of frequency stability.

Several small improvements were made on the cyclotron. A sublimation pump was in-

stalled at the south wall of the dee tank. The modification of the ion source bases was completed, so that the PIG, filament, and inflector shafts are all usable on the elevator, and utilize the automatic plug-in of water and power when the sources are raised to operating position. The dee insert for the internal source was split into upper and lower halves to eliminate the connecting post, which was periodically melted by heavy ion beams. A spare puller tray was built. Multi-turn collimators for beam clipping at 10 to 15-in. radius were tested. Beam read-out fingers were installed at the ends of the deflector elements to provide useful information for deflector positioning. The new third section deflector electrodes, containing electric quadrupole radial focusing, were installed. They give the predicted radial focusing, and good transmission for high resolution transport to the magnetic spectrometer. A biased internal ion source was completed and is under test. A filament-heated PIG source is also under test. A new external PIG source was built, based on the successful internal PIG source geometry. A velocity filter was added to the polarized-source injection line to separate the polarized protons or deuterons from the air beam for better tuning of the polarized beam.

During September beam heating of the lower edge of the dee and dummy dee center region inserts was observed. Foil burn studies showed that the beam was low at 3- to 14-in. radius by as much as $3/8$ inch. Removing the center region inserts, half-turn and multi-turn collimators, and dummy dee had no effect on this beam droop. It was finally decided in October that the radial shape of the median plane error matched that which would result from a vertical drop of one of the 8-in.-diam. center pole plugs. The droop was corrected by raising the upper 8-in. plug by 0.030 in. It was difficult to understand how the upper plug could have dropped, so it is possible that the lower plug had dropped. Careful measurements were made of the plug heights in the center of the cyclotron so that any further similar problems could be quickly diagnosed. The axial injection quadrupole line was cleaned during this period, since most of it had to be removed for work on the upper plug.

ACCELERATORS FOR NUCLEAR PHYSICS

D. J. Clark

This article describes the principle charged-particle accelerators being used today for research in nuclear physics in the energy range up to about 1000 MeV. The accel-

ators include Van de Graaffs, sector cyclotrons and linear accelerators for both positive ions and electrons. For each type of accelerator a brief treatment is given of the recent his-

Table I. Principal operating accelerators for nuclear physics, 0-1000 MeV.

Accelerator	Maximum energy (MeV)	Variable energy	External Beam		Emit-tance (mm-mr)	Best analyzed beam		Macro D. F. (%)	Micro D. F. (%)	Shortest Pulse	Polarized p, d (nA)	Heavy Ions largest A at 5 MeV/A
			(μ A)	ΔE		(μ A)	$\frac{\Delta E}{E}$ (%)					
<u>D. C. Accelerators</u>												
Single-ended	0.1-9p 0.1-9 α	Yes	1-15,000	0.25-5keV at 2 MeV	10-15	10-30	0.01%	100	100	0.8ns	15	¹ H
Tandem	8-30p 8-32 α	Yes	1-100	1-5 keV	1-10	1-10	0.01%	100	100	0.7ns	50-200	¹⁶ O
<u>Cyclotrons</u>												
Classical	5-22p 20-45 α	Usually No	10-300	1-3%				100	1		0.03-0.07	⁶⁴ Zn
F. M.	50-730p 50-900 α	No	0.01-0.1	0.1-5%				1-80	10-100	2ns	0.002-0.03	⁴ He
Sector	3-100p 20-160 α	Usually Yes	1-200	0.02-0.5%	5-50	0.5	0.01%	100	5	0.2ns	50-200	⁴⁰ Ar
Dubna 2 stage	7/A	Yes	10 ⁹ /sec					100				¹³⁶ Xe
<u>Linacs</u>												
Heavy Ion	10/A	Limited	1-50	2-4%				0.1-3	10			⁴⁰ Ar
Electron	20-20,000	Yes	1-1000	0.2-30%	10-0.1			0.01-6	1	2ns		
<u>2 Stage Hybrid</u>												
Cyclograaff	27-30	Yes	2	15-50 keV				100	5			
Orsay	5/A	Yes	10 ⁸ /sec	0.8%				30	5			⁸⁴ Kr

Table II. New types of accelerators under construction for nuclear physics 0-1000 MeV.

- EXTERNAL BEAM -									
	Location	Estimated completion	Max. energy (MeV)	Variable energy	Intensity (μ A)	Macro. D. F. (%)	$\frac{\Delta E}{E}$ (%)	Comments	
<u>D. C. Machines</u>									
	A. N. U.	Australia	1972	28p Other ions	Yes	5-10	100	0.01	Tandem Pelletron
	HILAB	U. S. A.	Indef.	$\geq 7/A$ $A \leq 200$	Yes	0.1-10	100	0.03	TU+MP tandems, heavy ions
<u>Cyclotrons</u>									
<u>F. M.</u>									
	CERN	Switz.	1972	600p	No	10-20	≤ 80	0.1-0.5	Conversion: New rf, center region
	Columbia	U. S. A.	1972	550p	No	10-40	≤ 50		Conversion: 3 sectors, new rf and center region
<u>Sector</u>									
	Indiana	U. S. A.	1973	200p Other ions	Yes	10	100	0.01-0.2	D. C. injector+2 cyclotrons, sep. sector
	Vancouver	Canada	1973	500p	Yes	100	100	0.05-0.2	H ⁻ accel., multiple external beams
	Zurich	Switz.	1974	585p	No	100	100	0.3	2 cyclotrons, sep. sector final stage
<u>Linacs</u>									
<u>Ion</u>									
	Los Alamos	U. S. A.	1972	800p	Yes	1000	6-12	1	Alvarez + side coupled, simul. H ⁺ and H ⁻ beams
	Super-Hilac	U. S. A.	1972	8.5/A All A	Yes	0.1-100	30-80	0.6	Alvarez, 2.5 MV inj., heavy ions
	UNILAC	Germany	1974	$\geq 7/A$ All A	Yes	0.1-100	> 25	0.02-10	Wideröe+Alvarez+cavities, heavy ions
<u>Electron</u>									
	M. I. T.	U. S. A.	1972	400e	Yes	300	2-6	0.4	High D. F., similar to Saclay
	Stanford	U. S. A.	1974	2000e	Yes	100	100	0.01	First superconducting, 100% D. F.

tory, operating principles, some special techniques, a typical facility, and some examples of experimental data from that type of accelerator. Descriptions are also given of new types of machines under construction, such as Pelletrons, frequency-modulated sector cyclotrons, separated sector cyclotrons, and superconducting linear accelerators. New ideas for the future are mentioned, including multi-stage tandem-cyclotrons, and the electron ring accelerator. The reader is assumed to have no experience in accelerators or nuclear physics.

Figure 1 shows the number of each type of accelerator operating during the last 30 years. Table I gives typical beam characteristics for each type. Table II gives the specifications of new types of accelerators now under construction or just coming into operation. The paper contains 63 figures and 167 references.

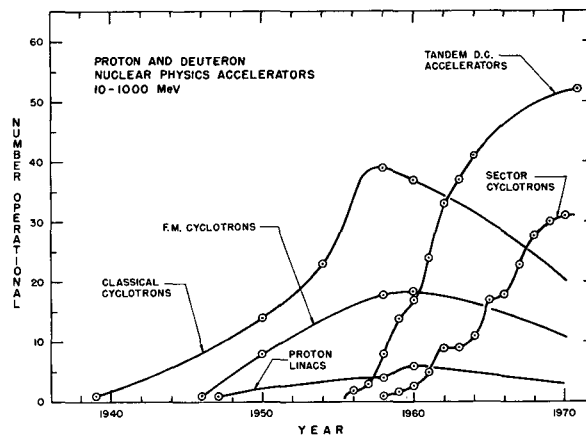


Fig. 1. Number of operating proton and deuteron accelerators for nuclear physics during the past 30 years, 10-1000 MeV, world-wide. (XBL 722-332)

DESIGN OF A HIGH-TEMPERATURE NEUTRON IRRADIATION CONTAINER*

D. C. Fee and S. S. Markowitz

The temperature of the sample during irradiation is an important parameter in radiation chemistry¹ and hot-atom chemistry.² The primary and secondary processes being studied may be temperature dependent. In addition, the phase (gas, liquid or solid) of the sample during irradiation is obviously temperature dependent. Temperature control during irradiation may be advantageous in activation analysis.³ Numerous low temperature irradiation devices have been reported.⁴⁻⁹ High-temperature neutron irradiations have also been made by controlling the rate of loss of the heat that was generated in the sample by neutron absorption. The sample was essentially self-heated.^{10, 11}

We are interested in hot-atom chemistry in general and recoil tritium reactions in particular. In hot-atom chemistry it is often desirable to irradiate many samples simultaneously. This ensures that all the samples in a series are irradiated under the same experimental conditions. The important experimental parameters during irradiation are temperature (as discussed) and total neutron dose. Intersample comparisons of absolute product yields can only be made if each sample receives the same neutron dose.^{2, 12} Furthermore, it is advantageous if these temperature and dose-controlled irradiations could be made in the most commonly available neutron irradiation facility, a pool-type nuclear reactor. Dose-controlled hot-atom studies are easily made at pool temperatures using the

"Lazy Susan" facility.¹³ Previously mentioned low-temperature irradiation techniques are readily adapted to allow low temperature, dose-controlled hot-atom studies.¹⁴ The high-temperature irradiation techniques mentioned earlier cannot be adapted to hot-atom studies because little heat is generated in the hot-atom sample by neutron bombardment.

Our design concept is simple. The samples are irradiated in a temperature-controlled oil bath placed in the Hohlraum of the reactor. The samples are rotated so that each sample receives the same neutron dose. The rotation is achieved by directly coupling a motor to the sample rack. Neutron shielding is required to protect the motor.

Figure 1 is a cut-away side view of the apparatus. All materials are 1100F aluminum (greater than 99% pure) unless otherwise stated. Constructing the irradiation container chiefly from 1100F aluminum minimizes the potential radiation hazard. The

²⁷Al(n, γ)²⁸Al reaction during irradiation gives ²⁸Al with a 2.8-minute half-life. After allowing the short-lived ²⁸Al to decay away, the sample capsules can be removed from the irradiation container. The 1/2-in. -thick neutron shielding, A in Fig. 1, is "Composition 254" from Reactor Experiments, Inc. This thickness of shielding reduces the flux at the motor by a factor of 10⁻¹⁰. This shielding protects the steel alloy Bodine motor which

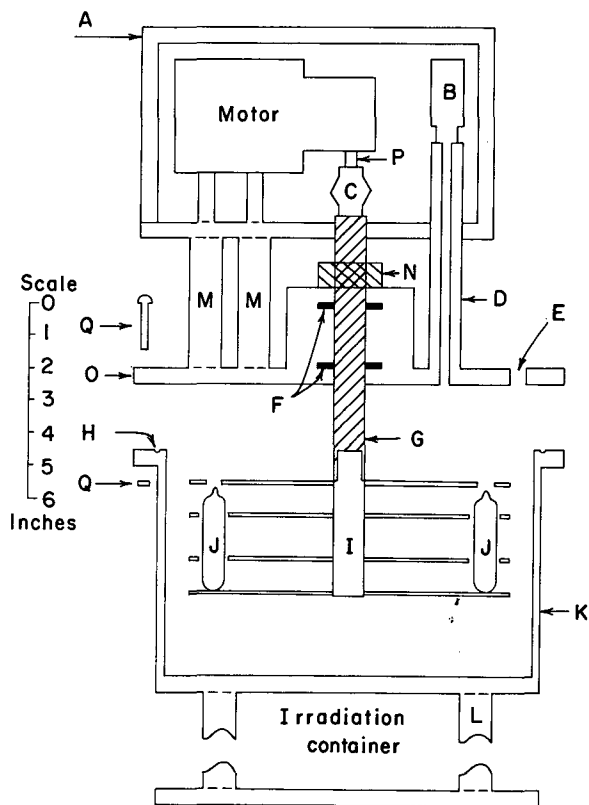


Fig. 1. Irradiation container. The lid has been raised for purposes of illustration. Legend: A, neutron shield; B, brass pressure relief valve; C, flexible rubber coupling; D, pipe to pressure relief valve; E, hole for thermocouple lead plug; F, Teflon gaskets; G, nylon shaft; H, O-ring groove; I, sample rack; J, sample capsule; K, oil bath container; L, 13-in. support leg; M, motor support leg; N, nylon collar; O, lid; P, motor shaft; Q, nylon bolt and nut.

(XBL 7210-4143)

operates at 6 rpm. The motor is connected through a flexible rubber coupling (C) and nylon shaft (G) to the sample rack (I). The sample rack is a right cylinder which rotates on the same axis as the nylon shaft. A top view of the sample rack would show 24 slots for the standard¹³ 1720 Pyrex glass sample capsules (J). The sample slots are evenly spaced on a circle near the perimeter of the sample rack. If the period of irradiation is long compared to the period of rotation of the sample rack, each sample in the rack will receive the same neutron dose. A slotted lid, shown in Fig. 1 as the uppermost part of the sample rack, keeps the sample capsules from floating out of the slots when the rack is immersed in the oil bath. The oil used is heavy mineral oil (B. P. 360 to 390°C). This oil is

housed in a cylindrical container (K), which is supported on legs 13-in. long (L) that raise the level of the samples to the center line of the Hohlraum. This puts the samples in the highest flux possible. The container is heated by three silicone-coated heating tapes (1 in. X 8 ft.) wound around the sides of the cylinder. A fourth heating tape is looped back and forth on the bottom of the oil bath. Temperature control is maintained by operating three of these heating tapes via a rheostat at all times during the irradiation. The rheostat is adjusted so that the three tapes would maintain the temperature of the oil bath at 5 to 10°C less than the desired temperature. The fourth heating tape ("controller tape") is turned on and off by a temperature controller to maintain the desired temperature. The proportional temperature controller is remote from the Hohlraum. The temperature probe used with the temperature controller is an iron-constantan thermocouple placed in the oil bath.

Excellent temperature control ($\pm 0.5^\circ\text{C}$) has been achieved at all temperatures in the 25 to 200°C range in tests outside the reactor. Irradiations have been made for sixteen hours at the Berkeley Campus Nuclear Reactor. Excellent temperature control was obtained at $135 \pm 0.5^\circ\text{C}$. The irradiation container was removed from the Hohlraum 40 hours after the end of bombardment. The observed radiation was primarily from the heating tapes; two inches from the irradiation container and heating tapes (at the level of the sample capsules) it was only 130 mr/hr on the side that was nearest the core and 70 mr/hr on the side that was farthest from the core. The flux at the sample level (in units of $10^8 \text{n cm}^{-2} \text{sec}^{-1}$) was 34.5 on the side of the container nearest the core, 10.3 on the side farthest from the core, and 3.90 in the sample position. The flux was monitored with cobalt foils. Na(I) counters were used to monitor the ^{60}Co from the $^{59}\text{Co}(n, \gamma)^{60}\text{Co}$ reaction.

Footnotes and References

* Condensed from LBL-1264. Submitted to Nucl. Instr. Methods (1973).

1. G. R. Freeman, Radiation Res. Rev. 1, 1 (1968).
2. R. Wolfgang, Progress in Reaction Kinetics 3, 97 (1965).
3. D. Brune, Anal. Chim. Acta 44, 15 (1969).
4. G. Glanz, N. Dutescu, and A. Georgescu, Rev. Romaine Phys. 9, 137 (1964).

5. A. C. Klank, T. H. Blewitt, J. J. Minarik, and T. L. Scott, *Bull. Instr. Intern. Froid, Annexe* 5, 373 (1966).
6. W. Decker, J. Diehl, K. Hain, H. Katheder, and C. Leitz, *Kerntechnik* 8, 257 (1966).
7. N. Berglund, D. Brune, and B. Schüberg, *Nucl. Instr. Methods* 75, 103 (1969).
8. J. Ahlf and G. A. Melkonian, *Atomkernenergie* 10, 459 (1965).
9. J. H. O'Donnell, *Chem. Ind. (London)* 15, 481 (1968).
10. J. Ahlf, D. Anders, and R. Benefeld, *Kerntechnik* 8, 173 (1966).
11. T. Hayashi and M. Kudoh, *J. Nucl. Sci. Technol.* 6, 390 (1969).
12. A. H. Rosenberg and R. Wolfgang, *J. Chem. Phys.* 41, 2159 (1964).
13. D. C. Fee and S. S. Markowitz, *J. Inorg. Nucl. Chem.*, 35, (1973).
14. A. Hosaka and F. S. Rowland, *J. Phys. Chem.* 75, 378 (1971).

A 100 PSEC PULSE-WIDTH DISCRIMINATOR

J. D. Bowman, A. M. Poskanzer, and D. Landis

A program to search for very neutron-rich light isotopes produced in high-energy nuclear reactions using telescopes of semi-conductor detectors has been in progress at the Bevatron.¹ The isotopes are identified by measuring their rate of energy loss, total energy, and time of flight. An important limitation to the sensitivity of the search has been background produced by random coincidences. The pulse-width discriminator described here has eliminated this background.

A pulse-width discriminator measures the width of an amplified and shaped detector signal and produces an output which reflects

changes in the time profile of charge deposition and collection. A block diagram of the apparatus and wave forms illustrating its operation is given in Fig. 1. The time-to-amplitude converter measures the time difference between the leading edge of the output of a unipolar shaping amplifier and the crossover of a bipolar signal. If charge collected from the detector results from a single heavy ion, the wave forms labeled G are produced. In the case of two particles striking the detector at different times, the wave forms labeled B are produced and the time difference from leading edge to crossover is larger than in the former case. A pulse-width discriminator is sensitive to random coincidences occurring within times shorter than the pulse width and it may be supplemented by a pile-up rejector sensitive to times longer than the pulse width, if necessary.

A pair of instruments were constructed and used in an experiment at the Bevatron designed to search for ¹⁷B and other neutron-rich isotopes. Each heavy ion passed through an 18 μ Si(P) ΔE detector and stopped in an 80 μ Si(P) E detector. The flight time over the 25-cm distance separating the two detectors was recorded, as well as the ΔE and E amplitude signals and signals from the pulse-width discriminators connected to each detector. One million events were observed.

Because the rise time of the preamplifiers was 3 nsec the walk with energy of the pulse-width discriminators was large compared to their intrinsic resolution and was removed by their intrinsic resolution and was removed by off-line analysis. The walk results from shift of the time at which the leading edge dis-

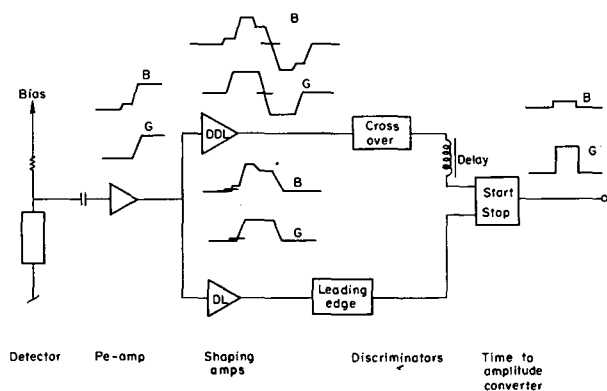


Fig. 1. Block diagram illustrating the operation of the pulse-width discriminator. Discriminator levels are represented by horizontal lines on wave forms. The labels G and B indicate wave forms typical of unperturbed events and accidental coincidence events, respectively. (XBL 733-2439)

criminator fires as a function of amplitude. For a pulse which rises as t^p , the leading edge trigger time shifts as $A^{-1/p}$ where A is the amplitude of the signal. We fit the experimentally observed graphs of pulse-width discriminator output signal (PWD) vs E or ΔE amplitude to an equation of the form, $PWD = \alpha + \beta A^{-1/3}$ where p was chosen to be 3, and α and β were adjustable parameters. A walk-corrected pulse-width discriminator signal was calculated for each event as $PWD - (\alpha + \beta A^{-1/3})$. The FWHM of the walk-corrected ΔE and E pulse-width discriminator signals were 110 and 65 psec, respectively. The energy ranges were 5 to 30 MeV in ΔE and 13 to 50 MeV in E .

For each event mass and charge were calculated as in Ref. 1. Figure 2 shows mass yield plots obtained previously¹ and in the work described here. In the present work the data were edited by application of windows to the walk-corrected ΔE and E pulse-width discriminator signals of widths 135 and 100 psec, respectively, which included ~90% of the events. The background has been reduced by more than a factor of 20.

In conclusion, we have built and used a pulse-width discriminator which is capable of detecting accidental coincidences on a time scale small compared to the preamplifier rise time and have eliminated our background. Analysis shows that the pulse-width discriminator described here is very effective in protecting a crossover timing signal from perturbations caused by a small amplitude accidental pulse coming early. Further analysis shows that this instrument could be improved to protect the crossover timing signal from small pulses coming early or late by using leading edge to trailing edge timing on single clipped pulses.

A HILAC DATA COLLECTION PROGRAM

J. B. Hunter, R. C. Jared and S. G. Thompson

A data acquisition system has been developed for a PDP-15 computer (Digital Equipment Corporation) at the Heavy Ion Linear Accelerator (HILAC). This system is presently being used to process data obtained in some reactions with heavy ions.¹ The input data is obtained from a particle telescope composed of four detectors designated as follows: ΔE_1 , ΔE_2 , E , and E_{reject} .

The signals meeting proper coincidence requirements from the detectors are stored in an analog multiplexer. These signals are

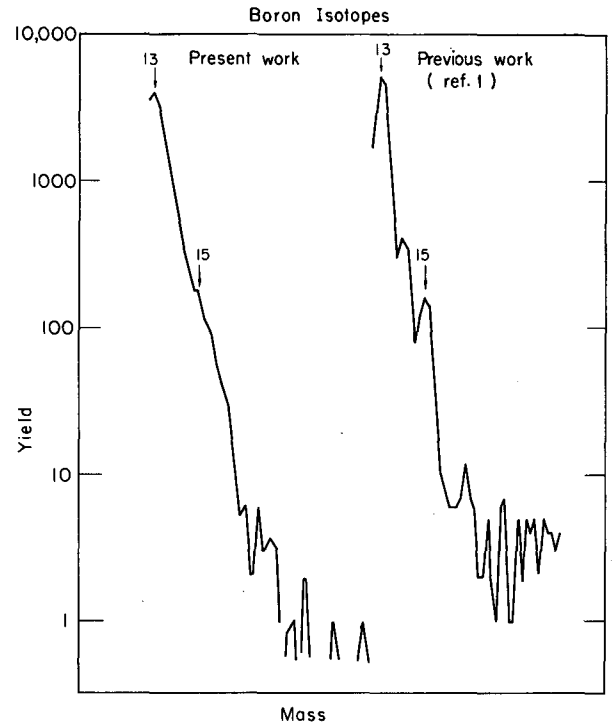


Fig. 2. Mass yield plots for heavy boron isotopes from this work and previous work. The background in the high-mass region, mass greater than 17, which has been reduced by a factor of 20 or more. (XBL 733-2440)

References

1. G. W. Butler, A. M. Poskanzer, and D. A. Landis, Nucl. Instr. Methods, **89**, 189 (1970).

then digitized by means of an analog-to-digital converter (ADC) which is connected to the analog multiplexer. The information from the ADC is transferred via a Camac data channel to the input buffer at the computer. The data are then packed on magnetic tape with proper identification. The program is also used to give four single parameter energy distributions, which are used for monitoring the experiment. Access to these distributions is controlled by teletype commands. This program is being modified to include the option of making particle identifier (PI) cal-

culations on-line in order to monitor the PI resolution during the experiments. The data on the magnetic tapes are analyzed using other computers at LBL in terms of the well-known power law, $PI = (E + \Delta E)^P - E^P$, or by a similar modified form of this law in order to identify particles passing through the detector telescope. The energy spectra associ-

ated with each type of particle are also obtained.

References

1. S. G. Thompson, L. G. Moretto, R. C. Jared, D. Huenemann, R. C. Gatti, Fragment production in ^{40}Ar -induced reactions on a Cu target (elsewhere in this report).

REAL TIME FORTRAN FOR A PDP-9 COMPUTER

R. C. Jared, J. B. Hunter, and S. G. Thompson

Experience has shown that times of the order of one year are often required to write a data acquisition program of moderate complexity for small computers. Thus, large programming efforts have been necessary to generate systems for a PDP-9 computer when the latter is used for a research program which is even moderately complicated. One way to circumvent this difficulty would be to develop a program that can take a variety of input data and reproduce its image on an output magnetic tape; however, this operation does not require a computer. A relatively inexpensive multidimensional pulse-height analyzer would serve just as well. The advantage of the computer comes only in its ability to perform on-line calculations on the input data and produce reduced data promptly at an output device.

We have been able to make a large reduction in our programming effort and still use the full capability of our computer by adding to the Digital Equipment Corporation Fortran 4 system a set of subroutines that enable the experimentalist to have real-time control of input and output devices. Real-time Fortran as defined here provides a means of commanding an input or output device to perform a certain function and then to continue in the program executing the subsequent statement while the device is carrying out its func-

tion. It is, of course, necessary that the programmer test the input or output device to see that it has performed the necessary function before a new command is issued to that device.

The basic functions that have been added to the PDP-9 Fortran package are: magnetic tape control, display control, CalComp control, analog-to-digital converter control, and control of an external 4096 word memory. The above minimum set of functions has proven to be adequate for data acquisition. However, more commands will be added to obtain real-time control of the disk memory and decapex devices. This will give the experimentalist a much more flexible system.

The above mentioned expanded system has been used for several experiments. In some cases persons without previous experience with a PDP-9 computer have written an operational multidimensional data acquisition program in a time of about one week. Typically these programs have been used to collect data on magnetic tape and to perform partial data analysis. As one example: particle identifier spectra have been produced in which the energy spectra for each type of particle was obtained. The reduced output data are plotted by a CalComp plotter and are also printed using a line printer.

HIGH RATE X-RAY FLUORESCENCE ANALYSIS BY PULSED EXCITATION†

J. M. Jaklevic, F. S. Goulding and D. A. Landis

We describe a pulsed excitation method which demonstrates significant improvements in count-rate performance relative to conventional x-ray fluorescence techniques. When applied to X-ray fluorescence analysis, measurement times are reduced by at least a factor of four.

Description of Method

The effect of pile-up rejection at high rates is illustrated in Fig. 1 where we have plotted the calculated output versus input counting rate for the case of a continuous, random excitation source. We assume that each input

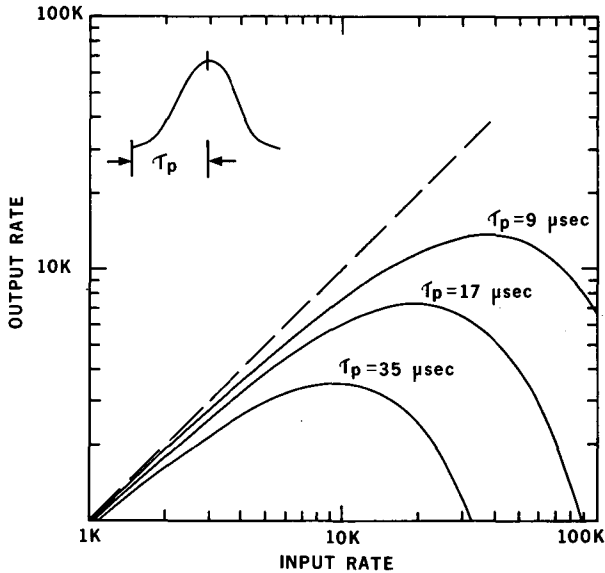


Fig. 1. Output versus input counting rate for continuous excitation with pile-up rejection. (XBL 722-204)

pulse generates a dead-time during which any additional event is rejected. Each of the curves represents a different peaking time τ_p of the Gaussian shaped amplifier output pulse. We assume a dead time $\tau_d = 3\tau_p$ corresponding to that used in the pile-up rejector described in Ref. 1. It is apparent from the curves that there is a maximum output rate for each τ_p corresponding to less than 40% of the input rate. This decrease of output rate arises from fundamental statistical considerations and cannot be remedied except by somehow modifying the time distribution of input pulses.

The basis of the pulsed excitation method is the elimination of the necessity for pile-up rejection by ensuring that no additional pulses will reach the detector in the time interval required to process an event. As shown in Fig. 2, a transmission x-ray tube² with grid control supplies the excitation for the sample. Detection of an event by the system triggers a fast turn-off of the electron beam for a specified dead time determined by the amplifier time constant, thus eliminating the possibility of any signals interfering with the original pulse. Although this description emphasizes the use of x-ray tubes, the pulsed method could be adapted to other excitation modes (such as electron probes or heavy charged particles from accelerators).

Considering the operation of the system in detail, we note several features:

- a) The system output rate is equal to the

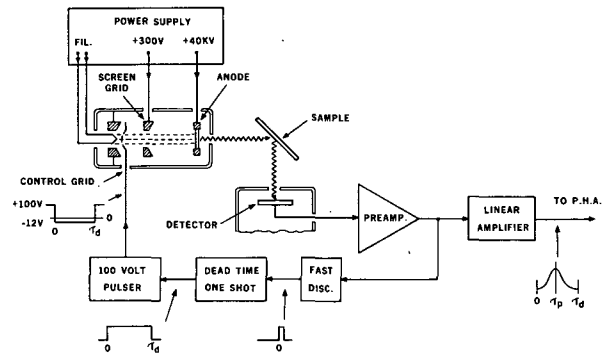


Fig. 2. Schematic of pulsed x-ray system. (XBL 722-203)

input rate. This is obvious since the tube is on only when the amplifier system is able to accept a pulse for processing.

b) At very high rates the arrival of events becomes essentially periodic. As the x-ray intensity is increased, there is a large probability of detection of an event in a time interval short with respect to the amplifier time constants; the tube is on for only a small part of the total cycle time and the events appear periodic.

c) The maximum count-rate $\frac{1}{\tau_d}$ where τ_d is the dead time per pulse--this is a corollary to (b).

d) If we continue to increase the x-ray intensity after reaching this limit, no apparent increase in output will result, but multiple events will become more common during the time required to shut off the tube following the detection of an event. Thus, although the output rate remains the same, an increasing fraction constitutes pile-up.

Results

With these preliminary ideas in mind it becomes possible to understand the input-output characteristics illustrated in Fig. 3. These data were obtained by allowing the Mo x-ray from the pulsed tube to strike an Fe target. The curves shown were taken with $\tau_d = 23, 41,$ and $79 \mu\text{sec}$ corresponding to amplifier peaking times of $\tau_p = 9, 17$ and $35 \mu\text{sec}$ respectively. The measured output rate is restricted to only these pulses which did not undergo pile-up at the high rates--this choice of representation was selected because the non-pile-up output is a more valid measure of the capability of the system. Furthermore, the data for total output versus input counting rate are far less interesting,

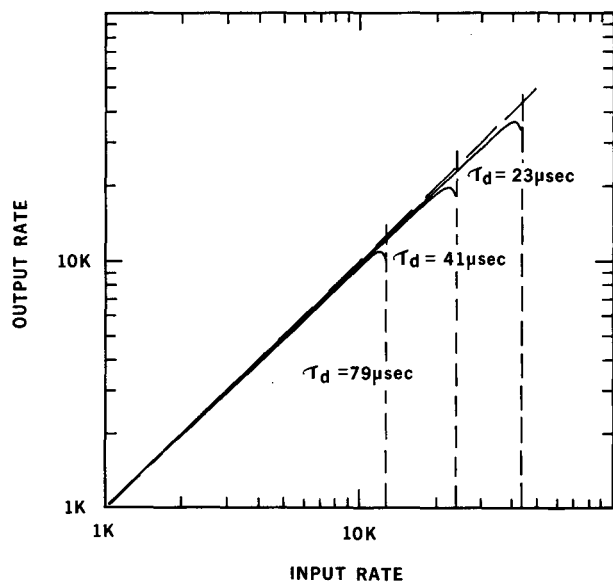


Fig. 3. Output versus input counting rate for pulsed system. Output rate is limited to non-pile-up events. Vertical dashed lines correspond to $(\tau_d)^{-1}$. (XBL 722-207)

since the rates are equal to within 2% over the total range for all time constants. The $\frac{1}{\tau_d}$ input rate limits are indicated by the vertical lines. The periodic behavior of the out-

put data at these limits can be observed on an oscilloscope.

The pile-up probability at high rates is evidenced by the decrease in output rate near the $\frac{1}{\tau_d}$ input counting rate limits in Fig. 3.

Although the losses are minimal for the system shown, they could be reduced still further by designing an x-ray tube with faster turn-off characteristics.

References

† Condensed from IEEE Trans. on Nucl. Sci., NS-19, No. 3, 392 (1972).

1. D. A. Landis, F. S. Goulding, R. H. Pehl and J. T. Walton, IEEE Trans. Nucl. Sci. Vol. NS-18, No. 1, 115 (1971).

2. J. M. Jaklevic, R. D. Giauque, D. F. Malone, and W. L. Searles, Small x-ray tubes for energy dispersive analysis using semiconductor spectrometers, presented at the 20th Annual Denver x-ray Conference, Aug. 11-13, 1971, Denver, Colorado. Lawrence Berkeley Laboratory Report Number LBL-10.

TRACE ELEMENT ANALYSIS WITH SEMICONDUCTOR DETECTOR X-RAY SPECTROMETERS†

R. D. Giauque, F. S. Goulding, J. M. Jaklevic, and R. H. Pehl

The analytical technique of x-ray emission spectroscopy depends upon the ability to excite and accurately measure characteristic K and L x-rays emanating from the specimen. The main conditions that limit x-ray fluorescence sensitivities are the x-ray peak intensities and their ratios to the background. Some of the principal factors affecting sensitivities are the selection of the exciting radiation, the geometry employed, and the form of the specimen.

A method of obtaining high sensitivity and accuracy in x-ray-fluorescence analysis using semiconductor detector spectrometers is discussed. Monoenergetic exciting radiation is employed to generate characteristic x-rays from trace elements in thin, uniform specimens. Specimens are prepared thinner than the critical thicknesses for the x-ray energies

of interest and corrections for matrix absorption effects are determined experimentally. Corrections for matrix enhancement effects are omitted as they are negligible for many thin specimens. A single element thin-film standard is used to calibrate for the x-ray geometry, and theoretical cross sections and fluorescent yield data are employed to calculate the x-ray yields for a wide range of elements to the thin-film standard. Table I lists a comparison of calculated and experimental values of relative excitation and detection efficiencies, K_j , for the system employed, for seven x-ray lines normalized to the $\text{CuK}\alpha$ values. For our experiments a guard-ring detector with pulsed light feedback electronics was used. Excitation was provided by a molybdenum transmission x-ray tube. An angle near 90° between the exciting and detected radiation is maintained to yield the

Table I. Relative excitation and detection efficiencies (K_j)

Line	Calculated	Determined
CrK α	0.381	0.370 \pm 0.011
MnK α	0.450	0.435 \pm 0.003
FeK α	0.587	0.559 \pm 0.003
NiK α	0.884	0.882 \pm 0.007
CuK α	1.000	1.000 \pm 0.015
AsK α	1.653	1.660 \pm 0.083
SeK α	1.776	1.753 \pm 0.057
PbL α	0.804	0.774 \pm 0.019

highest peak-to-background ratios. X-ray spectral backgrounds are determined from the intensities of the coherent and incoherent scattered radiation.

Using a single excitation energy, the concentration of more than fifteen trace elements may be simultaneously determined during a 15-minute interval for concentrations of 1 ppm or less. This corresponds to less than 10 ng/cm² on air particulate filters. The x-ray intensities and elemental concentrations may be expressed as:

$$I = I_0 G K_j m_j \frac{-(\mu_1 \csc \phi_1 + \mu_2 \csc \phi_2) m}{(1 - e^{-(\mu_1 \csc \phi_1 + \mu_2 \csc \phi_2) m})}$$

Table II shows the results of the analyses of standard NBS SRM 1571 orchard leaves. Table III illustrates a comparison of the results obtained by x-ray fluorescence and LBL neutron activation on standard pottery. Figure 1 shows a spectrum obtained from a standard pottery specimen of mass 5 mg/cm². The concentrations of many elements present in air collection specimens on filter papers are simply determined by measuring the intensities of the characteristic x-rays. Figure 2 shows the spectrum and results obtained on an air pollution filter of mass 5 mg/cm². The concentrations are listed in ng/cm².

Theoretical limits of detection for the equipment used are shown in Table IV for three types of specimens. The minimum detectable amount is defined as that concentration on

Table II. Analysis of NBS SRM 1571 orchard leaves

	X-ray fluorescence	NBS
Cr	2.5ppm \pm 1.6	2.3ppm
Mn	88.6ppm \pm 2.2	91ppm \pm 4
Fe	276ppm \pm 8	300ppm \pm 20
Ni	1.3ppm \pm 0.4	1.3ppm \pm 0.2
Cu	12.6ppm \pm 0.6	12ppm \pm 1
Zn	23.7ppm \pm 0.8	25ppm \pm 3
As	10.6ppm \pm 0.8	14ppm \pm 2
Br	9.3ppm \pm 0.6	10ppm
Rb	11.0ppm \pm 0.8	12ppm \pm 1
Sr	36.6ppm \pm 1.2	37ppm
Pb	45.4ppm \pm 2.0	45ppm \pm 3

quantity which gives a line intensity above background equal to three times the square root of the background for counting times not to exceed 1000 sec. Higher sensitivity for these elements may be obtained by employing other x-ray tubes and a double guard-ring detector.

The use of monoenergetic exciting radiation and a semiconductor detector, and the preparation of thin uniform specimens per-

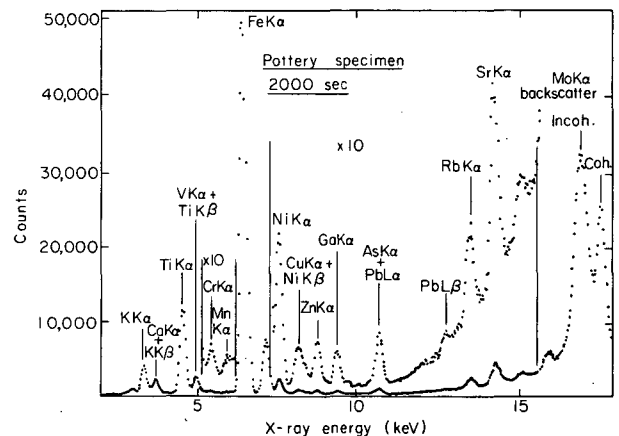


Fig. 1. Spectrum from pottery specimen of mass 5 mg/cm². (XBL 725-2934)

Table III. Analysis of pottery specimen

K	0.95% ± 0.02	1.35% ± 0.04
Ca	0.28% ± 0.01	<1.0%
Ti	0.77% ± 0.1	0.78% ± 0.3
V	176ppm ± 16	176ppm ± 16
Cr	107ppm ± 5	115ppm ± 4
Mn	31ppm ± 4	40.9ppm ± 0.5
Fe	1.05% ± 0.01	1.017% ± 0.012
Ni	277ppm ± 4	279ppm ± 20
Cu	56ppm ± 2	59ppm ± 8
Zn	61ppm ± 1	59ppm ± 8
Ga	46ppm ± 1	44ppm ± 5
As	32ppm ± 1	30.8ppm ± 2.2
Se	<2ppm	—
Br	<3ppm	2.3ppm ± 0.9
Rb	70ppm ± 2	70.0ppm ± 6.3
Sr	145ppm ± 2	145ppm ± 22
Pb	35ppm ± 3	—

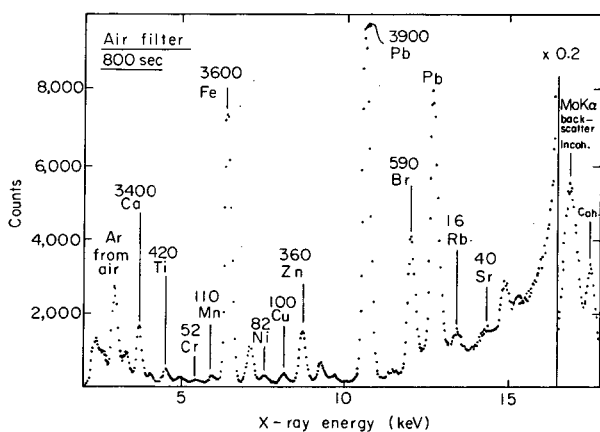


Fig. 2. Spectrum from air filter of mass 5 mg/cm². Concentrations listed in ng/cm². (XBL 725-2933)

Table IV

Specimen	Theoretical limits of detection		
	Biological	SiO ₂ on filter of mass 5 mg/cm ²	Air particulate on filter of mass 5 mg/cm ²
Mass (mg/cm ²)	30	5	—
Tube current (μ amps)	250	400	400
Area analyzed (cm ²)	3	2	3
Element and spectral line			
TiKα	3 ppm	10 ppm	15 ng/cm ²
CrKα	1	4	9
FeKα	0.6	3	5
CuKα	0.3	1	3
HgLα	0.4	2	5
PbLα	0.4	2	5
BrKα	0.3	1	3
RbKα	0.4	2	6

mits many trace element analyses to be performed with relative ease, in shorter time intervals, and often with higher sensitivity than other analytical techniques such as neutron activation and atomic absorption. The ability to use a single element thin-film standard to accurately calibrate for the analyses of many elements is unique for instrumental methods of analysis.

Footnotes

† Condensed from LBL-647. Presented at 11th Natl. Meeting Soc. Appl. Spectroscopy, Dallas, Texas, Sept. 10-15, 1972. To be published in Anal. Chem.

INSTRUMENTATION FOR ENVIRONMENTAL MONITORING: AIR

C. D. Hollowell, G. Y. Gee, R. D. McLaughlin

Understanding the environmental pollution problem begins with the ability to accurately monitor its presence. As better monitoring systems are established, one will be able to identify build-up areas for pollutants, identify flow and dispersment patterns, and eventually learn to predict serious health episodes. It is essential to make good measurements of the environmental pollutants, but in many cases the present state of the art is far from satisfactory, with old, inadequate and cumbersome techniques still in wide use. Because of this, much research and development is going on now to develop new instrumentation. The field is moving so rapidly, in fact, that there are many gaps in information about what instrumentation is available for a particular need, how good it is, how expensive it is, etc. It is vital that modern instrumental techniques find their way rapidly into this important field, and that encouragement be given to further development of instrumentation for environmental quality monitoring. In order to fill these information gaps, the Laboratory has undertaken a three-year, in-depth survey of instrumentation in the environmental field.

In June 1971 the Environmental Instrumentation Group of the Energy and Environment Programs received an NSF-RANN (National Science Foundation-Research Applied to National Needs) grant to conduct a survey of instrumentation for environmental monitoring, including monitors of air quality, water quality, radiation, and biomedicine. Consideration is given to instruments and techniques presently in use and to those developed for other purposes but having possible applications to this work. The results of the survey include descriptions of the physical and operating characteristics of available instruments, critical comparisons among instrumentation methods and recommendations for the development of new instruments, and of promising methodology. The survey material is compiled in four loose-leaf volumes that will be periodically updated.

Instrumentation for Environmental Monitoring: Air, Lawrence Berkeley Laboratory Report LBL-1, Volume 1, is now available from the Technical Information Division, Lawrence Berkeley Laboratory, University of California, Berkeley, CA 94720, at a cost of \$7.00 per volume, postage paid. Volume 1 as initially issued covers sulfur dioxide and mercury-in-air monitoring instrumentation; additional sections on oxides of nitrogen, photochemical oxidants, carbon

monoxide, hydrocarbons, hydrogen sulfide, lead, beryllium, and asbestos are in progress and will be issued before June 1973.

The Sulfur Dioxide section² contains descriptive literature for over sixty commercially available instruments. These monitors are classified into thirteen different principles of operation. The strengths and weaknesses of these principles of operation are discussed. Information concerning instrument calibration, sampling, emissions standards, techniques for controlling sources and effects of sulfur dioxide is also included. Contents for the SO₂ monitoring instrumentation section are shown in Fig. 1.

INSTRUMENTATION FOR ENVIRONMENTAL MONITORING	AIR-SO ₂ Contents Mar. 1972
CONTENTS FOR SO ₂ MONITORING INSTRUMENTATION	
	<u>Mnemonic</u>
A. <u>Introduction</u>	AIR-SO ₂ Introduction
1. Characteristics	
2. Sources	
3. Effects	
4. Techniques of Controlling Sulfur Oxide Emissions	
5. National SO ₂ Air Quality and Emission Standards	
B. <u>SO₂ Monitoring Systems</u>	AIR-SO ₂ Systems
1. Systems Concept	
2. Sampling	
3. Calibration	
4. Data Acquisition and Reduction	
5. Units	
C. <u>SO₂ Instrumentation</u>	AIR-SO ₂ Instrumentation
1. Static Samplers	
2. Mechanical Samplers	
3. Continuous Analyzers	
3.1 Conductimetric Analyzers	
3.2 Colorimetric Analyzers	
3.3 Coulometric (Amperometric) Analyzers	
3.4 Electrochemical Transducer Analyzers	
3.5 Analyzers Using Flame Photometry or Gas Chromatography-Flame Photometry	
3.6 Thermal Conductivity Analyzers	
3.7 Nondispersive Absorption Spectrometers	
3.8 Dispersive Absorption Spectrometers	
3.9 Correlation Spectrometers	
3.10 Second Derivative Spectrometers	
3.11 Condensation Nuclei Formation Analyzers	
3.12 New Developments in Air Monitoring Instrumentation	
D. <u>Appendices</u>	AIR-SO ₂ Appendices
E. <u>SO₂ Instrument Notes</u>	
1. Glossary	AIR-SO ₂ Glossary
2. Table of SO ₂ Instruments	AIR-SO ₂ Table
3. Ambient Air Monitors	AIR-SO ₂ Ambient
4. Stationary Source Monitors	AIR-SO ₂ Source

Fig. 1

The Mercury-In-Air section contains descriptive literature for twenty commercially available instruments. Eight different

CONTENTS
FOR
MERCURY-IN-AIR
MONITORING INSTRUMENTATION
A. Introduction

1. Characteristics
2. Forms of Mercury in Air
3. Sources
4. Toxicology
5. Control of Airborne-Mercury Emissions
6. Health Standards for Airborne Mercury
7. National Emission Standards for Mercury

 Mnemonic
AIR-HG
Introduction
B. Mercury-in-Air Monitoring Systems

1. Systems Concept
2. Sampling
3. Calibration
4. Data Acquisition and Reduction
5. Units

 AIR-HG
Systems
C. Mercury-in-Air Instrumentation

1. Mechanical Samplers and Analytical Methods
 - 1.1 Colorimetry
 - 1.2 Atomic Absorption Photometry
 - 1.3 Neutron Activation Analysis
 - 1.4 X-Ray Fluorescence
 - 1.5 Emission Spectroscopy
 - 1.6 Anodic Stripping Voltammetry
 - 1.7 Other
2. Automatic Analyzers
 - 2.1 Colorimetry
 - 2.2 Atomic Absorption Photometry
 - 2.3 Condensation Nuclei Formation
 - 2.4 Other Automatic Needs
3. Outlook and Needs

 AIR-HG
Instrumentation
D. Appendix: National Emission Standards for Mercury
 AIR-HG
Appendix
E. Mercury-in-Air Instrument Notes

1. Glossary
2. Table of Mercury-in-Air Instruments
3. Ambient Air Monitors
4. Stationary Source Monitors

 AIR-HG
Instrument Notes

 AIR-HG
Glossary

 AIR-HG
Table

 AIR-HG
Ambient

 AIR-HG
Source

approaches to mercury monitoring are discussed. Also included is information on sources, toxicology, national emission standards, sampling, and calibration procedures. Contents for the Mercury-In-Air monitoring instrumentation section are shown in Fig. 2.

References

1. Environmental Instrumentation Group, Instrumentation for Environmental Monitoring: Air, LBL-1, Volume 1.

2. C. D. Hollowell, G. Y. Gee, and R. D. McLaughlin, "Current instrumentation for continuous monitoring for SO₂," *Anal. Chem.* **5**, 63A (1973). (Preprint LBL-955.)

Fig. 2

A TWO-LEVEL SPEED CONTROLLER FOR THE ROTATED MERCURY COULOMETER CELL

R. G. Clem and F. Vogelsberg

The rotated mercury cell for controlled-potential coulometry provided electrolysis rate constants comparable with the fastest conventional cells then available.¹ There was no doubt that the solution phase was being stirred very efficiently with the stationary co-axial salt-bridge; however, direct observation of the mercury under stroboscopic light revealed that no, or at best very little, stirring was taking place in the mercury phase. The current-time trace presented in the previous paper also confirmed this. See Fig. 1.

A partially successful attempt was made to stir the mercury phase, but further engineer support would be required to place this new technique on a practical basis. The previous rotated mercury cell was modified. Shallow protrusions were made in the wall of the cylindrical cell. In operation these pro-

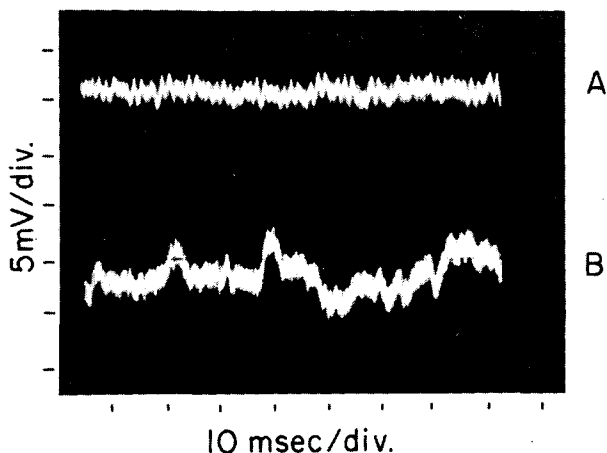


Fig. 1. Current-time trace of the cell noise.

 A. Cell current noise; 1 mV = 1 μ A.

B. Variations in the control potential;

1 mV = 1 mV. (XBB 711-147)

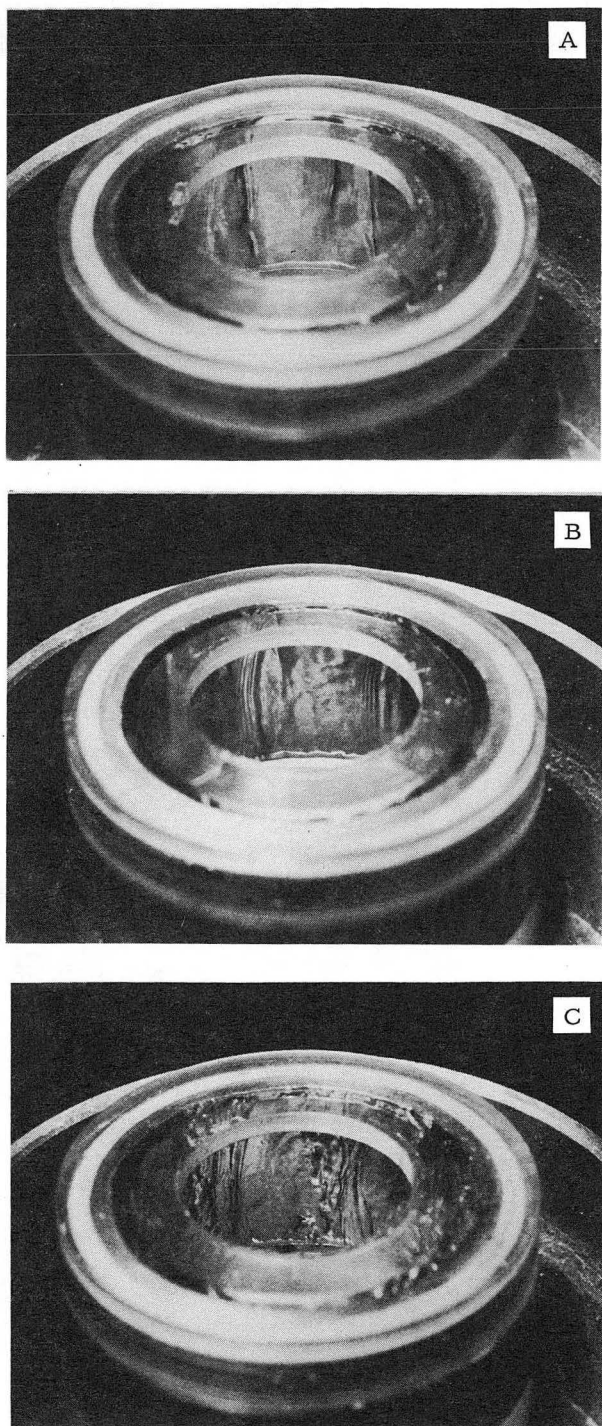


Fig. 2. Effect of step rotating the mercury cell.

A, B, C is a photosequence showing the beginning of the step rotation, the gathering turbulence, and the most violent stage of the stirring. Note the cavitation pockets in photo C.

trusions or vanes are covered with the mercury. Presenting two frequencies alternately to the synchronous cell motor causes the cell to alternately speed up, then slow down. Since the rotating mercury has high inertia, very efficient stirring of this phase occurs as a result of the mercury slipping over the protrusions. Figure 2a, b, and c shows the effect this stirring action has on the mercury phase. At the instant of motor speed transition, the sheer imported to the solution by the wrinkling mercury phase is so great that vacuum or cavitation pockets appear. The electrolysis rate constants obtained are more than 3 times greater than those obtained with even the best designed conventional cell.

Despite this great advantage, the technique is not yet practically applicable. No provisions were made in this initial effort to synchronize the stirring with the data acquisition cycle. This results in the superimposition of beats or nodes on the data. The problem could be solved if it were possible to channel advance only at the end of a preselected number of stirring cycles.

Electronically, the stirring action is effected by shifting the rate of rotation of the motor between preselected limits. The dwell periods, t_1 and t_2 , at the lower and upper frequencies are determined using tandem monostable multivibrators. The suitably biased output of the multivibrators alter the resistive frequency components of a modified Wien bridge oscillator. The variable resistance characteristics of junction FET's operated at very small drain currents are used to control the oscillator in two ways. Q_1 and Q_2 vary the resistive arms of the bridge in response to gate voltage changes, shifting the output frequency. Q_3 , in the negative feedback path, controls amplitude and oscillator

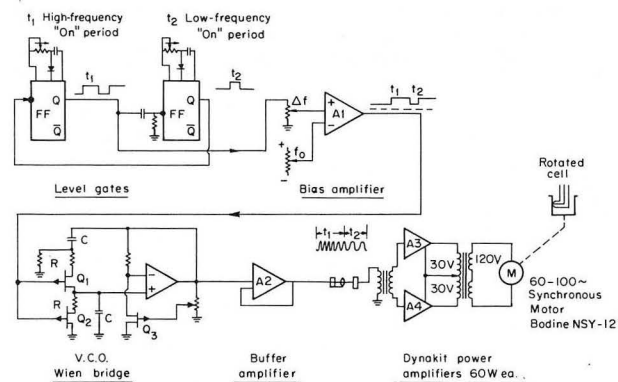


Fig. 3. Block diagram of the rotated cell drive circuit. (XBL 733-2396)

stability. Over moderate ranges, these effects are linear. Frequency shifts of from 60 to 100 Hz with dwell time ranges of from 0.2 to 1 sec have been used. Figure 3 is a block diagram of the electronics drive circuitry.

Reference

1. R. G. Clem, F. Jakob, D. H. Anderberg, and L. D. Ornelas, *Anal. Chem.*, **43**, 1398 (1971).

EFFECT OF WAX CRYSTALLINITY ON THE PERFORMANCE OF ANODIC STRIPPING ELECTRODES†

R. G. Clem

The paraffin impregnated, mercury plated, graphite electrode used in our anodic stripping efforts evolved from less suitable but similar electrode systems.

One of the first electrodes used was a hanging mercury drop.^{1,2} This electrode was not entirely satisfactory for analytical work because the rather large mercury volume employed resulted in the need for prolonged amalgam accumulation times necessitating the use of large sample volumes. Since a finite time is necessary for the amalgamated metal ions to diffuse to the mercury drop/solution interface to be available for stripping, rather low scan rates were employed. The stripping peak height, hence sensitivity, is directly related to the scan rate. To reduce the mercury volume employed and thus allow the use of faster scan rates, several thin mercury film-type electrodes were offered.³⁻⁶ These electrodes differed only in the metal substrates used. As expected, the sensitivity attainable with these electrodes was much improved, however, in some cases the amalgam appeared to react with the metal substrates of these film electrodes. This resulted in poor reproducibility.

In an attempt to overcome problems associated with substrates, Matson and co-workers developed a mercury plated, paraffin impregnated, graphite electrode,^{7,8} which is, in our opinion, the best electrode ever offered for stripping analysis. We differ with them, however, on several experimental and methodological points.

The previous workers recommended using a "good grade of paraffin". We can state unequivocally that no casual relation exists between the paraffin used and the results obtained. Electrode stability critically depends upon the degree of crystallinity of the wax. Electrodes impregnated with an essentially 100% crystalline wax such as Chevron micro-crystalline wax 154/156 AMP, fail within a few hours after impregnation owing to the cracking and separating of the wax from the

graphite substrate. Similar results are obtained using polyethylene as the impregnation substance.⁸ Sonneborn Multiwax 180M which contains 40% noncrystalline hydrocarbons was used to prepare electrodes exhibiting stability for about one month. Failure of these electrodes results when the exposed graphite particles suddenly and unexplainably detach from the active electrode surface. Figure 1 is a photograph of such a surface and Fig. 2 shows a stripping polarogram taken with the electrode at failure.

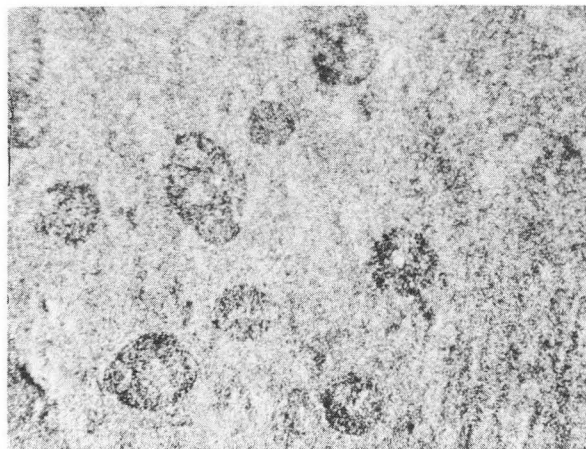


Fig. 1. Photomicrograph (230X) of the electrode used to obtain the upper trace in Fig. 2. Note: The surface is almost devoid of graphite sites. (XBB 7212-6307)

Unrefined ceresin wax is more crystalline than is the Sonneborn wax and, as expected, the electrodes fashioned employing this wax fail within one to two weeks. Failure occurs when a cathodic indentation appears near the copper stripping peak. (See Fig. 3.) Continued use of such an electrode results in a progressive deepening of the cathodic indenta-

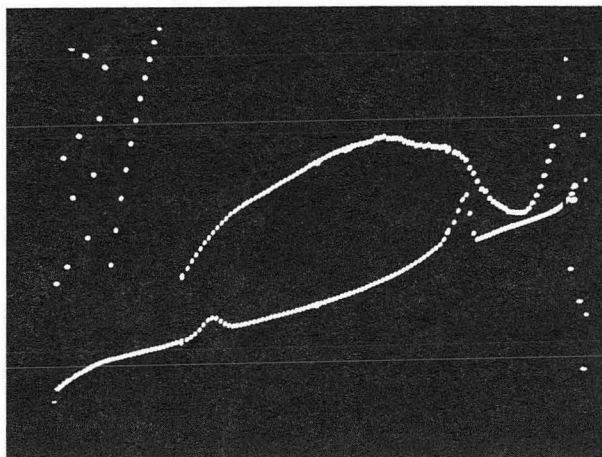


Fig. 2. The Sonneborn wax electrode behavior at failure and after repolishing. Upper trace: anodic stripping polarogram taken at the point of failure; lower trace: a scan of the same solution with the failed electrode after buffing. Normal behavior is restored. (XBB 7212-6308)

tion and in increasingly poor sensitivity for elements giving peaks at potentials more negative than the indentation.

Attempts are now being made to find a substance more suitable than the recommended Sonneborn wax. Waxes with known crystallinity prepared by mixing the Chevron wax with mineral oil are being tried and, in the future, impregnation with methyl-methacrylate will be tried.

References

† Abstracted in part from LBL-679 Rev.

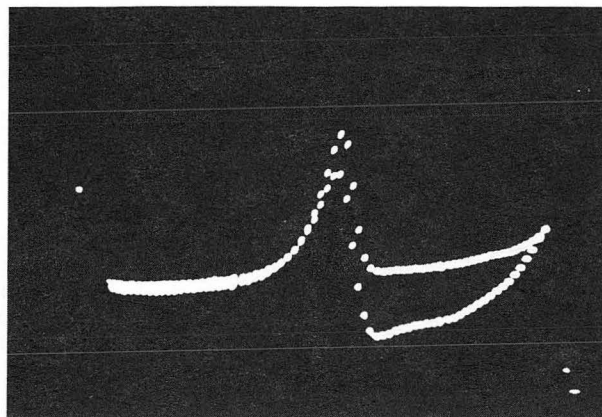


Fig. 3. The cathodic indentation. (XBB 726-3240)

1. R. J. Joyce and C. C. Westcott, Symposium on Trace Char., NBS (1966).
2. H. Gerischer, *Z. Physik. Chem.* 202, 302 (1953).
3. D. K. Roe and J. E. A. Toni, *Anal. Chem.*, 37, 1503 (1965).
4. T. L. Marple and L. B. Rogers, *Anal. Chim. Acta*, 11, 574 (1954).
5. R. Neeb, *Z. Anal. Chem.*, 180, 161 (1961).
6. P. J. Elving and D. L. Smith, *Anal. Chem.*, 32, 1849 (1960).
7. W. R. Matson, D. K. Roe, and D. E. Carritt, *Ibid.*, 37, 1594 (1965).
8. W. R. Matson, Ph. D. Thesis, MIT, 1968.

V. Thesis Abstracts

Thesis Abstracts

NUCLEAR ORIENTATION STUDIES ON SOME HIGH SPIN ISOMERS IN
FERROMAGNETIC AND NON-FERROMAGNETIC LATTICES

Fredrick Bacon

(LBL-1271)

The methods of nuclear orientation and magnetic resonance on oriented nuclei have been applied to study the magnetic hyperfine interactions of some spin isomers in the $g_{9/2}$, $h_{11/2}$, and $i_{13/2}$ shell closure regions. It is demonstrated that from a nuclear orientation experiment alone only the magnetic hyperfine interaction constant can be determined unambiguously and that from the combined data of an orientation experiment and a magnetic resonance experiment on oriented nuclei the spin of the parent level can be determined. The nuclear magnetic dipole moments of the 12^- levels of ^{196}Au , ^{198}Au , and ^{200}Au were determined. From a magnetic resonance experiment on the oriented ground states of ^{196}Au and ^{198}Au the induced hyperfine fields in nickel for these nuclei were determined. The hyperfine anomalies between $^{196,198}\text{Au}$ and ^{197}Au were derived. A comparison of these derived anomalies and the one measured by the spin echo method is made and from this comparison a discussion of the non-contact contribution to the induced nickel field is presented. The spins, nuclear magnetic dipole moments and magnetic resonance frequencies were determined for ^{200m}Au , ^{195m}Pt , and ^{93m}Mo and E2/M1 mixing ratio for the 99 keV gamma of ^{195m}Pt was measured. A brute force polarization of ^{93m}Mo in niobium was demonstrated and the possibility of obtaining the single level hyperfine anomaly from a combined brute force and ferromagnetic polarization experiment is discussed. The magnetic hyperfine interaction constants for ^{101m}Rh in nickel and iron were determined and the magnetic resonance frequency for this isotope in nickel was observed.

THE INITIATION OF NATURAL CONVECTION CAUSED BY
TIME-DEPENDENT PROFILES

Ian Frank Davenport

(LBL-660)

This experimental study is concerned with the initiation of convection in deep pools (penetration depth is small compared with the fluid depth) and shallow pools (penetration depth is comparable to the fluid depth). Fluids covering a wide range of Prandtl number, Pr , were either cooled from above through a gas-liquid surface where both surface tension and density forces were expected to contribute to the convection, or heated from below where only the density forces were present. The study of these two systems simultaneously allowed identification and separation of density and surface tension effects. The results were then used to evaluate current models of convection initiation driven by either density forces, surface tension forces or a combination of both over a wide range of experimental conditions.

The onset of convection in deep pools driven by density forces was observed to be described by high Prandtl number and low Prandtl number phenomenon. The high Prandtl number phenomenon was observed to behave similar to the onset of convection from a linear density gradient across the fluid (shallow pool). However, the striking dissimilarity between the deep pool and shallow pool phenomena was that the critical Rayleigh number in the deep pool case was independent of the rigidity of the heating or cooling boundary, which is opposite to that found in the shallow pool case. The understanding of the low Prandtl number, deep pool phenomenon has yet to be developed.

Convection initiation driven by surface tension forces was observed not to occur in fluids with planar surfaces, and one dimension temperature gradients. However, some important conditions for surface-tension motion at a gas-liquid interface were identified, including surface deformation, i. e. waves, meniscus, and point source surface-tension sinks.

Prediction of steady state convection heat transfer coefficients, using Howard's (1966) model of density boundary layer growth and destruction and convection initiation data, appears limited when the predicted values are compared with experimental values.

GLASS BEADS IN AFRICAN ARCHAEOLOGY: RESULTS OF NEUTRON ACTIVATION ANALYSIS, SUPPLEMENTED BY RESULTS OF X-RAY FLUORESCENCE ANALYSIS

Claire C. Davison

(LBL-1240)

Glass beads from archaeological sites of sub-Saharan Africa were analyzed by neutron activation and by X-ray fluorescence, and the results interpreted archaeologically. The glass beads from Igbo Ukwu (Nigeria), dated approximately to the ninth century A. D., were mostly soda-lime glasses, but a few potassium glasses were found. The glass artifacts from Ife (Nigeria), dated to approximately the tenth to twelfth centuries A. D., were mostly potassium glasses, with some soda-lime glasses. Some close resemblances were found between the glasses of the two sites. Evidence for glassworking which exists at Ife is interpreted as evidence of reworking, rather than manufacture from raw materials. A European provenience is suggested for the potassium glasses, but the provenience of the soda-lime glasses is unclear.

Blue-green glass beads from Bambandyanalo (Republic of South Africa), dated approximately to the eleventh century A. D., chemically match large beads known as garden roller beads found at Bambandyanalo and other sites. The hypothesis, known in the literature, that the garden roller beads were made at Bambandyanalo by reworking the blue-green beads is supported by this chemical match. Certain other glass beads found at Bambandyanalo, but not typical there, were found chemically to match glass beads from the nearby site of Mapungubwe.

Samples from a large series of glass beads known as trade wind beads were found to be chemically alike. These beads occur in archaeological sites of southern and eastern Africa, and in the Philippine Islands, and are dated archaeologically from c. the eleventh century A. D. at Bambandyanalo to c. the end of the seventeenth and early eighteenth centuries A. D. at Dambarare, Dhlo Dhlo, and related sites (Rhodesia), with a possible archaeological occurrence in the nineteenth century at Kilwa (Tanzania), and with a twentieth-century occurrence as heirlooms among the Lovedu and probably other groups at the Transvaal (Republic of South Africa). The long time span of archaeological dating of this group is difficult to reconcile with the chemical similarity of the beads. If the archaeological dating is correct, the long time span of the group indicates that chemical groups of glass may not always be sensitive indicators of relative date. The hypothesis, known in the literature, of Indian manufacture of these beads was tested despite its questionable nature, and the available evidence was found inconclusive.

The beads found in archaeological sites of eastern and southern Africa are all soda-lime glasses. The origins of all beads of soda-lime glass found in African archaeological sites are unclear. Soda-lime compositions are undiagnostic and could be consistent with European or Near Eastern origins. Suggestions of provenience hinge on the dating of the samples rather than on links to factory sites, and even so are only conjectural. It is noted that data from glass factory sites are needed, and it is suggested that future research turn in this direction.

SOME PROPERTIES OF PROTACTINIUM METAL AND ITS COMPOUNDS

Raymond Lloyd Dod

(LBL-659)

A modification of the usual metallothermic method of metal production is described, utilizing a molten salt crucible which substantially reduces the probability of contaminating the protactinium metal with crucible material. The method may have general applicability to the preparation of small quantities of high melting point metals.

A redetermination of the magnetic susceptibility of protactinium metal was made, resulting in a substantial change in value although not in temperature dependence from that previously reported. The new value is $(190 \pm 5) \times 10^{-6}$ cgs units/mole and is independent of temperature from $\sim 7^\circ$ K to 300° K. This value holds for both the normal tetragonal form of the metal and also the f. c. c. high temperature modification. The magnetic susceptibility of PaF_4 is also reported. The observed behavior can be interpreted to follow the Curie-Weiss law with an effective moment of 1.81 Bohr magnetons and a Weiss constant of 22.5° .

The reactions of protactinium metal with several common gases at temperatures up to 700° are described. Standard x-ray powder diffraction techniques were used to analyze the results. New compounds reported include two nitrides prepared by reaction of the metal with nitrogen and with ammonia. Both exhibited a cubic fluorite type lattice. The observed lattice parameters were $a_0 = 5.436 \pm 6 \text{ \AA}$ and $a_0 = 5.395 \pm 3 \text{ \AA}$. A new hydride structure for PaH_3 was observed, isomorphous with α -uranium hydride with $a_0 = 4.152 \pm 2 \text{ \AA}$. Additionally, an unidentified phase was observed in reaction of hydrogen with Pa metal at 400° C, which was presumed to be a hydride since thermal decomposition regenerated the metal. The hydride previously reported for protactinium was not observed, nor was any evidence for the existence of the reported monoxide, PaO , seen in any reaction, including those with air, oxygen and water.

The melting point and thermal expansion coefficients for a high purity sample of the metal have shown that the previous values, derived from samples of dubious quality, were more accurate than had been thought.

CRYSTAL STRUCTURES OF DIKETONE COMPLEXES OF ALKALINE EARTH METALS AND OTHER COMPOUNDS

Frederick John Hollander

(LBL-670)

The structures of six compounds were determined by means of x-ray crystallographic techniques applied to single crystals of $((\text{C}_6\text{H}_5)_3\text{PCH}_3)^+((\text{B}_6\text{C}_2\text{H}_8)\text{Mn}(\text{CO})_3)^-$, $\text{XeF}_5^+\text{AsF}_6^-$, 1,3-diphenyl-1,3-propanedione enol (HDPP), $\text{Mg}(\text{DPP})_2$ (dimethylformamide) $_2$, $\text{Ca}(\text{DPP})_2 \cdot (\text{C}_2\text{H}_5\text{OH})_{1/2}$, and $\text{Sr}(\text{DPP})_2 \cdot (\text{CH}_3)_2\text{CO}_{1/2}$.

$((\text{C}_6\text{H}_5)_3\text{PCH}_3)^+((\text{B}_6\text{C}_2\text{H}_8)\text{Mn}(\text{CO})_3)^-$ crystallizes in the triclinic space group $\overline{\text{P}}1$ with cell dimensions $\underline{a} = 11.216(5) \text{ \AA}$, $\underline{b} = 11.285(4) \text{ \AA}$, $\underline{c} = 11.464(5) \text{ \AA}$, $\alpha = 105.79(1)^\circ$, $\beta = 104.46(1)^\circ$, $\gamma = 98.04(1)^\circ$. The observed density is 1.25 gm/cm^3 , compared to 1.29 gm/cm^3 , compared to 1.29 gm/cm^3 calculated for one molecule in the asymmetric unit. The structure was solved by Patterson methods and refined to an R value of 0.041 for 2862 reflections. The cation has a propeller shape as expected. The anion has a non-crystallographic mirror plane and confirms

the structure expected on the basis of spectroscopic work. Comparisons are made to some other dicarbollide fragments.

$\text{XeF}_5^+\text{AsF}_6^-$ crystallizes in the monoclinic space group $\underline{P}2_1/\underline{c}$ with cell dimensions $\underline{a} = 5.886(3) \text{ \AA}$, $\underline{b} = 16.054(10) \text{ \AA}$, $\underline{c} = 9.051(4) \text{ \AA}$, $\beta = 91.564(35)^\circ$. Volume criteria were used to determine that there were four formula units per unit cell. The structure was solved by Patterson methods and refined to an R value of 0.116 for 925 reflections. The salt forms dimer rings containing two cations and two anions connected by bridging fluorines around a center of symmetry. The forms of the cation and anion are respectively square pyramidal and octahedral. Deviations from ideal forms for both the cation and the anion are discussed and compared to results for other structures.

HDPP crystallizes in the orthorhombic space group \underline{Pbca} with cell dimensions $\underline{a} = 10.853(1) \text{ \AA}$, $\underline{b} = 24.441(1) \text{ \AA}$, $\underline{c} = 8.755(1) \text{ \AA}$. The measured density of 1.22 gm/cm^3 compares to the calculated density of 1.28 gm/cm^3 for eight molecules in the unit cell. The structure was solved by direct methods and refinement proceeded to an R value of 0.027 for 1070 reflections. HDPP exists entirely in the enolic form and there is a strong internal hydrogen bond involving the enolic hydrogen. The structure is described and compared to the results of a previous study.

$\text{Mg}(\text{DPP})_2(\text{DMF})_2$ crystallizes in a monoclinic unit cell with dimensions $\underline{a} = 16.893(3) \text{ \AA}$, $\underline{b} = 12.853(2) \text{ \AA}$, $\underline{c} = 16.927(3) \text{ \AA}$, $\beta = 117.085(5)^\circ$. The centric space group $\underline{C}2/\underline{c}$ was chosen over the non-centric group $\underline{C}c$ on the basis of refinement in the former. The structure was determined by direct methods and refined to an R value of 0.067 on 1817 reflections. The coordination of the Mg atom is octahedral, with the Mg on a crystallographic two-fold axis. The two DMF molecules are cis to one another on the coordination octahedron.

$\text{Ca}(\text{DPP})_2(\text{C}_2\text{H}_5\text{OH})_{1/2}$ crystallizes in the triclinic space group $\underline{P}\bar{1}$ with cell dimensions $\underline{a} = 15.247(1) \text{ \AA}$, $\underline{b} = 13.555(1) \text{ \AA}$, $\underline{c} = 14.097(1) \text{ \AA}$, $\alpha = 74.64(1)^\circ$, $\beta = 95.97(1)^\circ$, $\gamma = 113.59(1)^\circ$. The density calculated with four formula units in the cell is $d_c = 1.32 \text{ gm/cm}^3$. The structure was solved by direct methods and refined to an R value of 0.040 for 4503 reflections. The complex forms novel polymeric clusters around a center of symmetry. There are two Ca atom environments, one six- and one seven-fold coordinated. The form of the polymer is described in detail.

$\text{Sr}(\text{DPP})_2((\text{CH}_3)_2\text{CO})_{1/2}$ crystallizes in the triclinic space group $\underline{P}\bar{1}$ with cell dimensions $\underline{a} = 13.759(10) \text{ \AA}$, $\underline{b} = 14.182(9) \text{ \AA}$, $\underline{c} = 16.031(9) \text{ \AA}$, $\alpha = 107.57(3)^\circ$, $\beta = 90.36(3)^\circ$, $\gamma = 113.07(3)^\circ$. The data crystal was poor, with data out only to an effective limit of $2\theta = 25$ in molybdenum radiation. The structure was solved by Patterson methods and refined to an R value of 0.088 on 1561 reflections. The hydrogen atoms were not located. The structure shows similar novel polymerization to the Ca complex, though differences between the two structures are enough to make them non-isomorphic. The polymerization is described in detail.

Comparison is made between the DPP complexes studied in this thesis and other β -diketone complexes. The $\text{Mg}(\text{DPP})_2(\text{DMF})_2$ structure is compared with other octahedral β -diketone complex structures, and the Sr and Ca complexes are compared with polymeric acetylacetonates and with each other. Some notes are made on the structure of the DPP^- ligand.

BETA ASYMMETRY FROM ORIENTED MANGANESE 52

Sammy Tung-Chuen Hung

(LBL-1256)

The nuclear orientation technique has been used to investigate the mixed allowed beta transition of ^{52}Mn . Nuclei of ^{52}Mn were polarized in an iron lattice utilizing the adiabatic demagnetization method to achieve low temperatures. The positrons emitted were detected with

a high-purity germanium detector situated at the 1° K liquid helium bath. The angular distribution fits the correlation function

$$W(\theta) = 1 + (v/c) A \langle m_z \rangle / I \cos \theta$$

and the asymmetry parameter A was determined. The Fermi to Gamow-Teller mixing ratio can be calculated from the experimental value of A if time-reversal invariance is assumed. The value of the mixing ratio was found to be -14.5%. This value represents the largest negative interference term to date on the ^{52}Mn mixed transition, although a comparable but positive interference term has been reported on the same nuclide. A large interference term implies that ^{52}Mn is a favorable candidate for further investigation on the time-reversal invariance property. However, many other serious experimental difficulties should be taken into consideration, and they are discussed in this report. To further test the accuracy of the system, the beta asymmetry of ^{60}Co was also measured. The value of A was found to be -0.971, which agrees well with the theoretical prediction of -1.00.

A SELF-CONSISTENT TREATMENT OF PHONONS AND QUASIPARTICLES IN FINITE FERMI SYSTEMS AND APPLICATIONS TO RARE EARTH NUCLEI

John David Immele

(LBL-675)

Using a Green's function formalism, the quasiparticle self-energy in a finite Fermi system is described in terms of the coupling of even- and odd-mass nuclear eigenmodes. The self-energy includes the usual QPC core polarization diagram, a "backwards" exchange diagram with ground state correlations, and higher order diagrams which correct for exclusion principle violations in the propagation of the quasiparticle and the microscopic phonon. Intermediate lines in the self-energy are described self-consistently, thereby including multiple-phonon core excitations. It is shown that the generalized Dyson's equation for the self-energy may be solved by matrix diagonalization rather than the usual dispersion relation. Renormalized phonons are calculated by taking into account splitting of the quasiparticle strength by QPC in the solution of the Bethe-Salpater equation. The quasiparticle self-energy and the phonon are calculated self-consistently.

The theory is used to calculate energy levels, transition probabilities, and one-nucleon transfer cross-sections for even- and odd-mass isotopes in the rare earth region. An "intruder" state is predicted in the Eu and Tb isotopes. The splitting of the $K_0 \pm 2$ states in ^{165}Ho and ^{167}Er is derived from higher order contributions to the self-energy. The interference of pairing and quadrupole correlations in the ground state is discussed.

This dissertation includes an introduction to the applications of Green's function techniques in nuclear theory and an extensive review of the literature, in which the various theoretical attempts to describe low-energy properties of even- or odd-mass nuclei from the perspective of phonon and quasiparticle correlations are collated.

THE APPLICATION OF ^3He -INDUCED NUCLEAR REACTIONS FOR SENSITIVE CHEMICAL ANALYSIS OF SULFUR, CHLORINE, POTASSIUM, AND CALCIUM

Diana M. Lee

(LBL-1291)

Three easily-detected radionuclides, ^{38}Cl , $^{34\text{m}}\text{Cl}$, and ^{38}K , produced from ^3He reactions on sulfur, chlorine, potassium, and calcium, were used as "signals" for the determination of the latter elements. This method of activation analysis is capable of determining the above elements individually at the microgram level or submicrogram level in some cases. A number of samples were analyzed non-destructively by using differing nuclear reactions to examine the accuracy of the method and the extent of interferences.

Experimentally determined absolute excitation functions have been measured in the ^3He energy range from 3 to 22 MeV for the following nuclear reactions: $^{32}\text{S}(^3\text{He}, \text{p})^{34\text{m}}\text{Cl}$, $^{35}\text{Cl}(^3\text{He}, \alpha)^{34\text{m}}\text{Cl}$, $^{39}\text{K}(^3\text{He}, 2\alpha)^{34\text{m}}\text{Cl}$, $^{37}\text{Cl}(^3\text{He}, 2\text{p})^{38}\text{Cl}$, $^{37}\text{Cl}(^3\text{He}, 2\text{n})^{38}\text{K}$, $^{39}\text{K}(^3\text{He}, \alpha)^{38}\text{K}$, and $^{40}\text{Ca}(^3\text{He}, \alpha)^{38}\text{K}$.

PRODUCTION OF L-ASPARAGINASE BY CULTURES OF ERWINIA AROIDEAE

Thomas F. Murphy

(LBL-1283)

Since 1967, L-asparaginase from E. coli has been used successfully in the treatment of certain human leukemias. Although more than half the patients treated in early stages undergo one remission, treatments for subsequent relapses often fail because patients develop immunity to the E. coli enzyme. Erwinia aroideae and other microorganisms produce L-asparaginases which are immunologically distinct from E. coli L-asparaginases and could be used successfully with patients immune to E. coli L-asparaginase. The production of L-asparaginase by cultures of Erwinia aroideae was studied to provide basic background information for large scale fermentation of the organism for use as an alternate source of L-asparaginase.

Five liter stirred jar batch and continuous cultures were used to analyze the effects of medium composition, temperature, pH, dissolved oxygen concentration, and growth rate on production of L-asparaginase by submerged fermentations of Erwinia aroideae. Experimental work was directed toward maximizing specific L-asparaginase activity. Maximum specific activity leads to minimum recovery and purification costs. These costs are probably primary in determining the cost of L-asparaginase produced for medical use.

Survey of complex and chemically defined media showed that L-asparaginase is inducible in Erwinia aroideae and that high specific activities are obtained when L-asparagine is the sole carbon and nitrogen source. In this case, production of L-asparaginase is growth associated and specific activity, growth rate, and cell mass yield are all maximized by the same set of fermentation conditions. The optimum temperature is 29° C and the optimum pH is 7.0. Operation with pH control is essential for optimum L-asparaginase production. Submerged cultures must be vigorously aerated for best L-asparaginase production, although dissolved oxygen tensions above atmospheric are not beneficial. Growth of Erwinia aroideae in L-asparagine limited continuous culture is characterized by specific L-asparaginase activity independent of growth rate and cell mass yield which decreases with increasing growth rate.

Two areas of further investigation are indicated by this study. First, two stage cultures, batch or continuous, may be advantageous in increasing the efficiency of L-asparagine use for L-asparaginase induction. Second, other more readily available substances may also be

effective L-asparaginase inducers. In the event production of L-asparaginase from Erwinia aroidae becomes a reality, these areas should be investigated.

ELECTRONIC DENSITIES OF STATES OF SOLIDS FROM X-RAY PHOTOEMISSION SPECTROSCOPY

Roger Alan Pollak

(LBL-1299)

High-resolution, monochromatic x-ray photoemission valence-band spectra for a variety of solids are presented, related to ground state eigenvalue spectra, and compared with existing theory. Valence-band spectra of C (diamond), Al, Si, Ga, Ge, As, Pd, Ag, Cd, In, Sn, Sb, Te, Ir, Pt, Au, Tl, Pb, Bi, GaAs, ZnSe, PbS, PbSe, PbTe, NiO, CoO, Tl₂O, GaP, GaSb, ZnO, ZnS, ZnTe, CdS, CdSe, CdTe, InSb, HgTe, NaI, NaBr, NaCl, NaF, KI, KBr, KCl, and KF are reported.

With increasing atomic number in the 4d5s5p elements Pd through Te the 4d structure evolves from d bands to spin-orbit split atomic-like core levels. Band-structure broadening was detectable in Cd, for which the 4d doublet is 11 eV below the Fermi energy. Structure was observed in the 5s5p bands for the first time by this method.

Structural features in the valence-band XPS spectra vary from Ir to Au as expected on the basis of 5d6s band filling. Spin-orbit splitting of the 6p band is manifest in the XPS spectra of Pb and Bi. Lowered energies of the 6s band indicate the presence of the mass-velocity and Darwin terms.

The total valence bands of crystalline and amorphous silicon and germanium are reported. For the crystals, the XPS spectra yield results that are strikingly similar to current theoretical calculations of the electron density of states, $\rho(E)$. Amorphous Si and Ge exhibit definite band structures that are similar to one another but markedly different from the crystalline results.

The XPS valence-band spectra for the isoelectronic series Ge, GaAs, and ZnSe are compared with theoretical valence-band density-of-states calculations using the empirical pseudopotential method. The agreement between the experimental and theoretical results is quite good, particularly for Ge and GaAs. For ZnSe the x-ray photoemission spectrum shows the Zn 3d-states to be higher in energy than the lowest valence-band s-states. In order to obtain this ordering of states in the theoretical calculation, a pseudopotential with an explicit energy dependence is required.

The high-resolution XPS valence-band spectrum from a cleaved natural diamond single crystal is reported. The absence of extrinsic structure allows a reliable comparison with band theory. The XPS molecular-orbital spectra of methane, silane, and germane are also given. The modulation of photoelectric cross section in the valence bands of diamond, Si, and Ge are discussed and compared with atomic XPS cross sections derived from the spectra of CH₄, SiH₄, and GeH₄.

XPS spectra of the valence bands of As, Sb, and Bi show a splitting, ΔE , of the "s-like" peak for the crystalline phase that disappears in the amorphous phase. This similarity to tetrahedrally coordinated semiconductors is explained by describing the semimetals as layers of distorted covalently bonded hexagonal rings. This generalizes the "even-odd" ring effect to the A7 lattice. The relation of ΔE to interatomic distance is described by a universal curve.

XPS valence-band spectra of PbS, PbSe, and PbTe are compared with available band theory results. Relativistic OPW results exhibit the best overall agreement with experiment. EPM results show similar agreement for all but the most tightly bound valence bands.

The charging behavior of 26 semiconductors and insulators is reported and discussed. Charging is found to be correlated with the energy band gap between the valence and conduction bands.

The XPS characteristic energy loss structure of Ag through Te is reported. It can be almost entirely accounted for by excitations similar to those observed in electron reflection experiments. Most of the structure can be assigned to bulk and surface plasmon excitations.

The XPS valence-band spectra of CoO and NiO are presented and discussed in terms of our current understanding of their electronic structure. A 3.5 eV wide structure with two components whose separation appears related to the exchange splitting Δ_{ex} is assigned to the 3d electrons.

Preliminary results from studies of the oxidation of Tl and Ni demonstrate the ability of XPS to monitor the chemistry of surfaces. Preliminary ultrahigh vacuum XPS spectra of the valence-band and 2s level of aluminum are reported. The valence band exhibits the expected free electron structure.

LARGE SEPARATIONS VIA CYCLING ZONE ADSORPTION

Ross Dale Rieke

(LBL-1255)

A theoretical and experimental study is presented of "Cycling Zone Adsorption", a wave-propagating adsorption process which produces alternating high- and low-concentration product streams from a packed bed, the temperature of which is cycled. Although the separations are small for a single zone of such a process, large changes in composition can be obtained by adding stages in series, by feed-back of product streams to the feed, and by arranging groups of stages into cascades.

Liquid mixtures of n-heptane and toluene were separated using silica gel adsorbent particles. Optimum operating conditions of a single-cycling zone adsorber were investigated with the main emphasis upon optimum bed temperature switching frequency as a function of liquid concentration and bed length. Failure to achieve square-wave changes in solid-particle temperatures, owing to resistance to heat transfer, caused a reduction in performance which was minimized by correct allowance for mass transfer. Use of a square-wave feed concentration, either from product feed-back or from recycling output portions of a previous cycling stage in a cascade, led to increased separations but was limited by longitudinal diffusion in the interstitial fluid as it passed through the packing.

A theoretical development allowed calculation of effluent stream concentration profiles for a single stage experiencing a square-wave temperature response, with either a square-wave feed concentration input or a constant feed concentration input. The theoretical calculations have accounted for the limiting effect of longitudinal diffusion.

Study of several variations in the arrangement of stages in a cascade led to the conclusion that large separations can be obtained in a well-designed plant. The energy requirements of such a system are estimated to be attractive in comparison with a conventional separation process.

MÖSSBAUER SPECTROSCOPY OF THE 6.2 keV γ RAY TRANSITION OF ^{181}Ta

Dan Ben Jacov Salomon

(LBL-1276)

Recoilless nuclear resonance absorption of the 6.2 keV γ rays of ^{181}Ta , was used for the hyperfine interactions of dilute ^{181}Ta impurities in the 5d, 4d, and 3d transition metals (Hf, Ta, W, Re, Os, Ir, Pt, Nb, Mo, Ru, Rh, Pd, V, and Ni) and the Ta compounds LiTaO_3 , NaTaO_3 , KTaO_3 , and TaC . Ratios of the nuclear parameters of the 6.2 keV excited state ($I = 9/2$) to the ground state ($I = 7/2$) were derived from completely resolved magnetic and electric-quadrupole split spectra:

$$g(9/2)/g(7/2) = 1.77 \pm 0.02$$

$$Q(9/2)/Q(7/2) = 1.133 \pm 0.010$$

and estimates for the change of the mean-square nuclear charge radius were obtained:

$$\Delta \langle r^2 \rangle \left\{ \begin{array}{l} \sim -1.6 \text{ fm}^2 \\ \sim -4.5 \text{ fm}^2 \end{array} \right.$$

The measured isomer shifts covered a range of 110 mm/s, corresponding to 17,000 times the natural line-width or more than 1,600 times the best experimental line-width of the 6.2 keV transition. In addition, both the sign and the magnitude of the electric field gradient were measured in the hexagonal transition metals Hf, Re, Os, and Ru, and in the tantalum compounds LiTaO_3 and NaTaO_3 . Temperature studies of the isomer shifts in the transition metals, Ta, W, Ir, Pt, Mo, Pd, and Ni, were carried out, showing shifts of the isomer-shifts much larger than the second order Doppler shift.

Mössbauer-NMR is reviewed in connection with the ^{181}Ta resonance.

THE QUESTION OF EQUILIBRIUM AT A PHASE BOUNDARY DURING CRYSTAL GROWTH

Tsung-Shen Thomas Shih

(LBL-1226)

The rates of crystal growth from undercooled binary organic melts were studied using a simple eutectic system of salol and thymol.

A temperature-gradient microinterferometric method was used to determine the interfacial liquid and solid concentrations and temperatures as well as the liquid concentration gradients near the growing faces of the crystals.

The experimental results indicated that considerable departure of the interfacial compositions and temperatures from equilibrium can occur, depending on the growth rate and the interface conditions. It was found that, even at small crystal growth rates, equilibrium at the phase boundary did not exist at all.

Both the absolute rate theory and the liquid inclusion theory were discussed and compared with the experimental data. It was found that the Eyring-type of kinetic rate expression predicted the growth rate of crystallization for pure substances within an order of magnitude.

No liquid inclusions were observed in this system. The criterion for breakdown of planar interfaces was found not to be valid in the eutectic organic system used. The presence of a stabilizing temperature gradient applied to the interfacial liquid had no effect on the concentration of impurity in the crystal but did affect interfacial shape and stability.

SYNTHESIS OF SEPARATION SCHEMES

Roger W. Thompson

(LBL-614)

The ability of the computer to synthesize complex separation schemes has been investigated and demonstrated. Several new concepts were generated as a result of the evolving programming study. The hierarchical ordering of executive routines in a synthesis system allows great flexibility in adding or modifying detailed simulation routines for separator units. Products rather than components are being separated; this concept is important when there are multicomponent products. A Product Separability Matrix was created to identify the candidate separations and to eliminate those which are infeasible as early as possible in the selection process. Incorporation of heuristics into the programming was done where no algorithmic procedure could be ascertained or where the use of heuristic procedures would save time without a major loss of generality. A number of heuristics were designed and evaluated.

A new general heuristic which should be of value to the design engineer, whether or not he is using the computer, is that the next separator to be incorporated into the separator sequence at any point is the one that is cheapest. This rule-of-thumb is useful when the candidate feasible separator sequences have been identified previously, as with the Product Separability Matrix. This heuristic rule has been explored in some depth, and factors leading to exceptions from the rule have been identified.

A number of illustrative examples are included.

MASS TRANSFER TO NEWTONIAN AND NON-NEWTONIAN SYSTEMS IN STIRRED TANK GAS-LIQUID CONTACTORS

William C. Wernau

(LBL-680)

An experimental method for the simultaneous determination of the interfacial areas and mass transfer coefficients in gas-liquid stirred tank contactors, such as those used for aerobic fermentation, was used to determine the effects of power input and the presence of Newtonian and non-Newtonian solid additives on these parameters. Measurements of the gas holdup in these systems were coupled with the interfacial area measurements to yield the values of the average bubble diameters in a 12" diameter stirred tank contactor.

The results of these experiments indicate that the power range common to industrial operations corresponds to the transition region between "large" and "small" bubbles in this scale equipment. A significant decrease in mass transfer coefficient and bubble diameter with increasing power input was shown to take place in this power region. The Newtonian additive was shown to affect this transition region drastically, resulting in a larger bubble diameter at

any power input and a decreased mass transfer coefficient at any bubble diameter. A logarithmic dependence of mass transfer coefficient on bubble diameter was found for both the Newtonian and the non-Newtonian systems in the transition region.

The overall volumetric mass transfer coefficients ($K_{L,a}$ or $K_{L,a}^R$) were determined using both the sodium sulphite oxidation system and the dissolved oxygen probe transient response method. The sodium sulphite method used a copper sulphate catalyst and systems investigated by this method were found to be in the "small" bubble regime because of the high ionic strength of the solutions. A definite effect of ionic strength on $K_{L,a}$ was determined with the dissolved oxygen probe.

In those systems in which interfacial areas were determined, the $K_{L,a}$ values were found using the dissolved oxygen probe response to a step change in oxygen feed composition. Simultaneously, the interfacial areas per unit volume (a) were determined by the steady state absorption of CO_2 into dilute alkali-salt solutions in the pseudo-first order reaction regime. Weak alkali-salt mixtures of 0.1M ionic strength, with and without the addition of additives, were investigated.

In addition, $K_{L,a}$ determinations were made with the dissolved oxygen probe in distilled water with and without additives, and in sodium sulphate solution. The latter measurements determined the enhancement effect of chemical reaction on the sodium sulphite $K_{L,a}^R$ values. The effects of gas flow on $K_{L,a}$ and $K_{L,a}^R$ were also determined for several of the systems investigated.

The application of these results for scale-up and design is discussed and recommendations for future rational investigation of mass transfer in these systems are presented. Several innovations in technique and analysis are also reported.

TRANSFER REACTIONS IN THE Zr-Mo REGION INDUCED BY α PARTICLES AND HEAVY IONS

Michael Steven Zisman

(LBL-1247)

The (α, d) and (α, t) reactions on targets of $^{90}, ^{91}, ^{92}, ^{94}Zr$ and ^{92}Mo have been investigated with 50 and 65 MeV α -particle beams from the Berkeley 88-inch cyclotron. High-spin proton states observed in the (α, t) reaction, based on comparisons with ($^3He, d$) data on the same targets, include: ^{91}Nb [2.39, 2.53, 2.61, 2.77, 2.90, 3.01, 4.18, 4.77, 4.89, and (5.14) MeV], ^{93}Tc [0.68, (3.58), 3.91, 4.37, (4.47), (4.67), 4.77, 4.90, 6.01 (multiplet), 6.17, and 6.44 MeV], ^{92}Nb [≈ 5 MeV multiplet], ^{93}Nb [1.08, 1.29, and ≈ 4.5 MeV], and ^{95}Nb [1.27, 1.65, (2.10), and ≈ 4.5 MeV]. A difference in Q-values for the $^{90}Zr(\alpha, t)^{91}Nb$ and $^{91}Zr(\alpha, t)^{92}Nb$ reactions of 680 ± 25 keV yields a new Q-value, -14.643 ± 0.027 MeV, for the $^{90}Zr(\alpha, t)$ reaction. This corresponds to a change in the ^{91}Nb mass excess of +98 keV, in agreement with other recent determinations of this quantity.

Two groups of strongly excited states appear in the (α, d) data. Members of the lower group [^{92}Nb (g. s.), ^{94}Nb (0.08 MeV), and ^{96}Nb (0.23 MeV)] have been previously identified as $(\pi g_{9/2}, \nu d_{5/2})_7^+$ states. From the $^{92}Mo(\alpha, d)^{94}Tc$ results, the ^{94}Tc ground state can also be assigned $J^\pi = 7^+$. The higher levels [^{92}Nb (2.58 MeV), ^{94}Nb (2.42 MeV), ^{96}Nb (2.38 MeV), and ^{94}Tc (2.68 MeV)] are believed to be either $(\pi g_{9/2}, \nu h_{11/2})_{10}^-$ or $(\pi g_{9/2}, \nu g_{7/2})_8^+$ states, based on the results of shell model matrix element calculations and the (α, d) structure factors of Glendenning. As an example of the systematics of the (α, d) reaction, results from the $^{14}N(\alpha, d)^{16}O$ reaction at 40 MeV are also included here. Accurate excitation energies and widths for the previously observed [^{14}N (1^+) + $(d_{5/2})_5^+$] triplet in ^{16}O have been determined to be: 14.40 ± 0.03 MeV ($\Gamma_{c.m.} = 30 \pm 30$ keV), 14.82 ± 0.03 MeV ($\Gamma_{c.m.} = 69 \pm 30$ keV), and 16.24 ± 0.04 MeV ($\Gamma_{c.m.} = 125 \pm 50$ keV).

The $(^{16}\text{O}, ^{15}\text{N})$ and $(^{16}\text{O}, ^{15}\text{O})$ reactions on targets of $^{90}, ^{91}, ^{94}\text{Zr}$, ^{92}Mo , and ^{93}Nb were also investigated with a 104 MeV ^{16}O (4+) beam from the Berkeley 88-inch cyclotron. Outgoing heavy ions were detected in the focal plane of a magnetic spectrometer with a Borkowski-Kopp type position sensitive proportional counter backed by a plastic scintillator and phototube. The $(^{16}\text{O}, ^{15}\text{N})$ and $(^{16}\text{O}, ^{15}\text{O})$ data indicate a preference for high angular momentum transfer similar to (but less pronounced than) that shown by the (α, t) and $(\alpha, ^3\text{He})$ reactions on the same targets. Contrary to a suggestion by Nickles et al., no strong evidence for a multi-step excitation of core-excited states is apparent from the present data.

VI. 1972 Publications

1972 Publications

PAPERS PUBLISHED AND LBL REPORTS ISSUED, 1972

- ABRAHAM, M. M., (See Kolbe, W., LBL-286)
- ALONSO, C. T., (See Rezanka, I., LBL-1223)
- ALONSO, J. R., (See Rezanka, I., LBL-1223)
- AMANN, J. F., (See Diener, E. M., LBL-602)
- ARTZY, M., F. Asaro, and I. Perlman
The origin of the "Palestinian" bichrome ware
LBL-1286, October 1972
J. Am. Oriental Soc.
- ASARO, F., (See Bowman, H. R., UCRL-20403)
- ASARO, F., (See Karageorghis, V., LBL-625)
- ASARO, F., (See Bowman, H. R., LBL-657)
- ASARO, F., (See Bowman, H. R., LBL-661)
- ASARO, F., (See Perlman, I., LBL-674)
- ASARO, F., (See Artzy, M., LBL-1286)
- ASCUITTO, R. J., and N. K. Glendenning
Quantum mechanical treatment of particle transfer between heavy ions near the coulomb
barrier in the presence of coulomb excitation
LBL-233, September 1971
Nucl. Phys. A188, 185 (1972)
- ASCUITTO, R. J., N. K. Glendenning, and B. Sørensen
The importance of indirect transitions on (p, t) reactions on deformed nuclei
LBL-248, October 1971
Nucl. Phys. A183, 60 (1972)
- BACHER, A. D., E. A. McClatchie, M. S. Zisman, T. A. Weaver, and T. A. Tombrello
Observation of the 14 MeV resonance in $^{12}\text{C}(p, p)^{12}\text{C}$ with molecular ion beams
UCRL-20903, June 1971
Nucl. Phys. A181, 453 (1972)
- BACHER, A. D., (See de Swiniarski, R., LBL-201)
- BACHER, A. D., (See Plattner, G. R., LBL-269)
- BACHER, A. D., G. R. Plattner, H. E. Conzett, D. J. Clark, H. Grunder, and W. F. Tivol
Polarization and cross-section measurements for p- ^4He elastic scattering between 20 and
45 MeV
LBL-280, November 1971
Phys. Rev. C 5, 1147 (1972)

- BACHER, A. D., F. G. Resmini, H. E. Conzett, R. de Swiniarski, H. Meiner, and J. Ernst
Observation of high-lying levels in ^8Be from alpha-alpha elastic scattering
LBL-1228, August 1972
Phys. Rev. Letters
- BACHER, A. D., (See Bruge, G., LBL-1238)
- BACON, F., J. A. Barclay, W. D. Brewer, D. A. Shirley, and J. E. Templeton
A temperature-independent spin-lattice relaxation time in metals at low temperature
UCRL-20465, March 1971
Phys. Rev. B 5, 2397 (1972)
- BACON, F., G. Kaindl, H. -E. Mahnke, and D. A. Shirley
Nuclear magnetic resonance on oriented platinum-195m in iron
LBL-297, January 1972
Phys. Rev. Letters 28, 720 (1972)
- BACON, F., H. Haas, G. Kaindl, and H. -E. Mahnke
Magnetic hyperfine fields at bismuth in iron and nickel
LBL-603, December 1971
Phys. Letters 38A, 401 (1972)
- BACON, F.
Nuclear orientation studies on some high spin isomers in ferromagnetic and non-ferromagnetic
lattices
LBL-1271, September 1972
Ph. D. Thesis
- BACON, F., G. Kaindl, H. -E. Mahnke, and D. A. Shirley
Nuclear magnetic resonance on oriented gold-196, 198, and 200 m
LBL-1289, November 1972
Phys. Rev.
- BAER, H. W., (See Vergados, J. D., LBL-690)
- BARCLAY, J. A., (See Bacon, F., UCRL-20465)
- BASSICHIS, W. H., A. K. Kerman, C. F. Tsang, D. R. Tuerpe, and L. Wilets
A study of deformation energy surfaces obtained from single particle energies
UCRL-73044, January 1971
Magic Without Magic: John A. Wheeler, ed. by John R. Klauder (W. H. Freeman and Co.,
San Francisco, 1972)
- BASSICHIS, W. H., C. F. Tsang, D. R. Tuerpe, and L. Wilets
A consistent test of the Strutinsky-Nilsson method
UCRL-74225, September 1972
Phys. Rev. Letters
- BECCHETTI, F. D., D. G. Kovar, B. G. Harvey, J. Mahoney, B. Mayer, and F. G. Pühlhofer
Inelastic scattering of ^{16}O from ^{208}Pb
LBL-695, July 1972
Phys. Rev. Letters
- BECCHETTI, F. D., (See Kovar, D. G., LBL-1201)

- BECCHETTI, F. D.
Experimental situation on nucleon transfer between heavy ions, elastic and inelastic scattering of heavy ions
LBL-1208, July 1972
Talk presented at the ORNL Heavy-Ion Summer Study, Oak Ridge, Tennessee, June 12-23, 1972
- BECCHETTI, F. D.
Elastic and inelastic scattering of ^{16}O and ^{12}C from nuclei $40 \leq A \leq 96$
LBL-1258, September 1972
Nucl. Phys.
- BECCHETTI, F. D., (See Siemens, P. J., LBL-1274)
- BENDER, C. F., P. K. Pearson, S. V. O'Neil, and H. F. Schaefer III
Potential energy surface including electron correlation for the chemical $\text{F} + \text{H}_2 \rightarrow \text{FH} + \text{H}$
I. Preliminary surface
LBL-250, October 1971
J. Chem. Phys. 56, 4626 (1972)
- BENDER, C. F., (See Liskow, D. H., LBL-290)
- BENDER, C. F., (See Liskow, D. H., LBL-291)
- BENDER, C. F., S. V. O'Neil, P. K. Pearson, and H. F. Schaefer III
Potential energy surface including electron correlation for $\text{F} + \text{H}_2 \rightarrow \text{FH} + \text{H}$: refined linear surface
LBL-630, March 1972
Science 176, 1412 (1972)
- BENDER, C. F., (See Liskow, D. H., LBL-696)
- BENDER, C. F., (See O'Neil, S. V., LBL-1200)
- BENNETT-CORNIEA, W., (See Garrison, W., LBL-1269)
- BENSON, D., C. M. Lederer, and E. Cheifetz
Search for γ transitions emitted in the formation of a fission isomer
LBL-1216, August 1972
Nucl. Phys.
- BENSON, D. Jr., (See Stephens, F. S., LBL-1282)
- BERNAS, M., (See Stock, R., Phys. Rev. C 6, 1226 (1972))
- BERNTHAL, F. M., (See Rezanka, I., LBL-1223)
- BONDYBEY, V., P. K. Pearson, and H. F. Schaefer III
Ground and excited electronic states of neon hydride
LBL-258, November 1971
J. Chem. Phys. 57, 1123 (1972)
- BOWEN, J., (See Clark, D. J., LBL-644)
- BOWMAN, H. R., J. G. Conway, and F. Asaro
Atmospheric lead and bromine concentration in Berkeley, Calif. (1963-1970)
UCRL-20403, April 1971
Environmental Sci. and Tech. 6, 558 (1972)

- BOWMAN, H. R., (See Wilhelmy, J. B., LBL-256)
- BOWMAN, H. R., F. Asaro, and I. Perlman
Composition variations in obsidian sources and the archaeological implications
LBL-657, September 1972
Archaeometry 15, 123 (1973)
- BOWMAN, H. R., F. Asaro, and I. Perlman
On the uniformity of composition in obsidians and evidence for magmatic mixing
LBL-661, April 1972
J. Geol.
- BOWMAN, H. R., (See Goda, L., LBL-1235)
- BOWMAN, J. D., (See Eppley, R. E., LBL-643)
- BREWER, W. D., (See Bacon, F., UCRL-20465)
- BROWN, S., (See Kenjo, T., LBL-249)
- BRUGE, G., M. S. Zisman, A. D. Bacher, and R. Schaeffer
The $^{38}\text{Ar}(^3\text{He}, t)^{38}\text{K}$ reaction at 40 MeV and the effective force for $(^3\text{He}, t)$ reactions
LBL-1238, September 1972
Phys. Letters
- BUCHER, J., (See Jensen, C. H., LBL-225)
- BUCHER, J. J., and R. M. Diamond
Extraction of HauCl_4 and HClO_4 by trioctylphosphine oxide in CCl_4 , isooctane and cyclohexane
LBL-609, January 1972
J. Inorg. Nucl. Chem. 34, 3531 (1972)
- BUCHER, J., R. M. Diamond, and B. Chu
Selectivity in heterovalent anion exchange. Ion pairing vs ion hydration
LBL-611, January 1972
J. Phys. Chem. 76, 2459 (1972)
- BUCHER, J., (See Chu, B., LBL-631)
- CALVIN, M., (See Fischer, M. S., LBL-646)
- CARNEIRO, A., (See Clark, D. J., LBL-644)
- CARROLL, J. C., (See Igo, G., Nucl. Phys. A195, 33 (1972))
- CAVELL, R. G., S. Kowalczyk, L. Ley, R. Pollak, B. Mills, D. A. Shirley, and W. Perry
X-ray photoemission cross-section modulation in diamond, silicon, germanium, methane, silane, and germane
LBL-1213, November 1972
Phys. Rev. Letters
- CERNY, J.
Masses of light nuclei far from stability
LBL-234, September 1971
Invited paper, Fourth International Conference on Atomic Masses and Fundamental Constants,
The National Physical Laboratory, Teddington, England, September 6-10, 1971, appeared
in Atomic Masses and Fundamental Constants 4, ed. by J. H. Saunders and A. H. Wapstra
(Plenum Press, 1972) pp. 26-37.

- CERNY, J., (See Maples, C., LBL-288)
- CERNY, J., (See Gough, R. A., LBL-296)
- CERNY, J., R. A. Gough, R. G. Sextro, and J. E. Esterl
Further results on the proton radioactivity of $^{53}\text{Co}^m$
LBL-626, February 1972
Nucl. Phys. A188, 666 (1972)
- CERNY, J., (See Wozniak, G. J., LBL-635)
- CERNY, J., (See Gough, R. A., LBL-1292)
- CHADI, D. J., (See Pollak, R. A., LBL-1204)
- CHEIFETZ, E., (See Wilhelmy, J. B., LBL-256)
- CHEIFETZ, E., R. C. Jared, E. R. Giusti, and S. G. Thompson
Search for superheavy elements in nature
LBL-613, January 1972
Phys. Rev. C 6, 1348 (1972)
- CHEIFETZ, E., (See Benson, D., LBL-1216)
- CHU, B., (See Bucher, J., LBL-611)
- CHU, B., J. Bucher, and R. M. Diamond
Anion exchange resin selectivity as a function of resin composition revisited
LBL-631, March 1972
J. Phys. Chem.
- CLARK, D. J., (See Bacher, A. D., LBL-280)
- CLARK, D. J., J. Steyaert, J. Bowen, A. Carneiro, and D. Morris
Heavy ion acceleration at the Berkeley 88-inch cyclotron
LBL-644, June 1972
Sixth International Cyclotron Conference, University of British Columbia, Vancouver, B. C.,
Canada, July 18-21, 1972
- CLARK, D. J.
Accelerators for nuclear physics
LBL-645, April 1972
Rept. Progr. Phys. 35, 1007 (1972)
- CLARK, D. J.
Cyclotron injection systems
LBL-654, July 1972
Sixth International Cyclotron Conference, University of British Columbia, Vancouver, B. C.,
Canada, July 18-21, 1972
- CLARK, D. J., (See Fuchs, G., IEEE Trans. Nucl. Sci., NS-19 (1972) p. 84)
- CLEM, R. G., (See Goldsworthy, W. W., LBL-282)
- CLEM, R. G., G. Litton, and L. D. Ornelas
A new cell for rapid anodic stripping analysis. A user-interactive computer program for the
analysis of anodic stripping data
LBL-679, June 1972, Anal. Chem.

- CLEM, R. G.
What happened to polarography
LBL-1295, November 1972
Industrial Research
- COHEN, M. L., (See Pollak, R. A., LBL-1204)
- CONWAY, J. G., (See Bowman, H. R., UCRL-20403)
- CONWAY, J., (See Stacy, J. J., LBL-698)
- CONWAY, J. G., (See Van Deurzen, C. H., LBL-1217)
- CONWAY, J. G., (See Goda, L., LBL-1235)
- CONZETT, H. E., (See Plattner, G. R., LBL-269)
- CONZETT, H. E., (See Bacher, A. D., LBL-280)
- CONZETT, H. E., (See Bacher, A. D., LBL-1228)
- CONZETT, H. E., (See McKee, J. S. C., LBL-1270)
- COSPER, S. W., (See Harvey, B. G., LBL-651)
- CUNNINGHAM, B. B., (See Marei, S. A., LBL-200)
- DAVENPORT, I. F., and C. J. King
Marangoni stabilization of density-driven convection
LBL-608, January 1972
Chem. Eng. Science
- DAVENPORT, I. F., and C. J. King
The initiation of natural convection caused by time-dependent profiles
LBL-660, June 1972
Ph. D. Thesis
- DAVENPORT, I. F., and C. J. King
An experimental study of convection initiation in deep pools
LBL-1252, September 1972
J. Fluid Mech.
- DAVIS, D. W., D. A. Shirley, and T. D. Thomas
X-ray photoelectron spectroscopy of fluorinated benzenes
LBL-270, November 1971
J. Am. Chem. Soc. 94, 6565 (1972)
- DAVIS, D. W., and D. A. Shirley
A relaxation correction to core-level binding-energy shifts in small molecules
LBL-633, March 1972
Chem. Phys. Letters 15, 185 (1972)
- DAVIS, S. P., (See Van Deurzen, C. H., LBL-1217)

DAVISON, C. C.

Glass beads in African archaeology: results of neutron activation analysis, supplemented by results of x-ray fluorescence analysis

LBL-1240, September 1972

Ph. D. Thesis

de SWINIARSKI, R., A. D. Bacher, F. G. Resmini, G. R. Plattner, D. L. Hendrie, and J. Raynal

Determination of deformation parameters of ^{20}Ne and ^{22}Ne by inelastic scattering of polarized protons

LBL-201, July 1971

Phys. Rev. Letters 28, 1139 (1972)

de SWINIARSKI, R., (See Bacher, A. D., LBL-1228)

DIAMOND, R. M., (See Maier, K. H., UCRL-19593)

DIAMOND, R. M., G. D. Symons, J. L. Quebert, K. H. Maier, J. R. Leigh, and F. S. Stephens

Lifetimes of ground-band states in ^{154}Sm

UCRL-20463, March 1971

Nucl. Phys. A184, 481 (1972)

DIAMOND, R. M., (See Jensen, C. H., LBL-225)

DIAMOND, R. M., (See Maier, K. H., LBL-243)

DIAMOND, R. M., (See Kenjo, T., LBL-249)

DIAMOND, R. M., (See Pühlhofer, F., LBL-604)

DIAMOND, R. M., (See Bucher, J. J., LBL-609)

DIAMOND, R. M., (See Bucher, J., LBL-611)

DIAMOND, R. M., (See Chu, B., LBL-631)

DIAMOND, R. M., (See Stephens, F. S., LBL-652)

DIAMOND, R. M.

E2 static moments and E2, E4 transition moments by coulomb excitation

LBL-1225, August 1972

International Conference on Nuclear Moments and Nuclear Structure, Osaka, Japan, September 4-8, 1972

DIAMOND, R. M., (See Newton, J. O., LBL-1227)

DIAMOND, R. M., (See Stephens, F. S., LBL-1282)

DIENER, E. M., J. F. Amann, P. Paul, and J. D. Vergados

Isospin effects in the giant dipole resonance of ^{42}Ca

LBL-602, January 1972

Phys. Rev.

DOD, R. L.

Some properties of protactinium metal and its compounds

LBL-659, May 1972

Ph. D. Thesis

- ECKART, G., and M. Weigel
Electromagnetic transitions in the renormalized random-phase-approximation
LBL-639, April 1972
Phys. Rev. (Addenda)
- EDELSTEIN, N., (See Kolbe, W., LBL-286)
- EDELSTEIN, N., (See Stacy, J. J., LBL-638)
- EDELSTEIN, N., and R. G. Hayes
An elementary molecular orbital calculation on $U(C_8H_8)_2$ and its application to the electronic structures of $U(C_8H_8)_2$ and $Pu(C_8H_8)_2$
LBL-650, April 1972
Am. Chem. Soc.
- EDELSTEIN, N., (See Stacy, J. J., LBL-698)
- EDELSTEIN, N., (See Rajnak, K., LBL-1218)
- ELLIS, L. A., (See Leigh, J. R., UCRL-20494)
- EMMOTT, M. J., (See Leigh, J. R., UCRL-20494)
- EPPLEY, R. E., J. D. Bowman, and E. K. Hyde
Alpha-emitting products of the interaction of 4.5 GeV protons with U, Th, Au, and Ta
LBL-643, April 1972
Phys. Rev.
- ERNST, J., (See Bacher, A. D., LBL-1228)
- ESKOLA, K.
A study of 66-sec isomeric state of ^{222}Ac
LBL-232-Rev., September 1971
Phys. Rev. C 5, 942 (1972)
- ESKOLA, P.
Studies of Mendeleevium isotopes with mass numbers 248 through 252
UCRL-20441-Rev., May 1972
Phys. Rev. C 7, 280 (1973)
- ESTERL, J. E., (See Cerny, J., LBL-626)
- EVANS, M. C., (See Leigh, J. R., UCRL-20494)
- FADLEY, C. S., R. N. Healey, J. M. Hollander, and C. E. Miner
Design of a high-resolution, high-efficiency, magnetic spectrometer for electron spectroscopy
UCRL-20478, June 1971
J. Appl. Phys. 43, 1085 (1972)
- FAIVRE, J. C., (See Harvey, B. G., LBL-651)
- FAIVRE, J. -C., (See Hendrie, D. L., LBL-656)
- FEE, D. C., and S. S. Markowitz
Sulfur dioxide as a radical scavenger in alkene systems
UCRL-20470, April 1971
Radiochim. Acta 17, 135 (1972)

- FEE, D. C., and S. S. Markowitz
Scavenger effects in the recoil tritium reactions of cyclohexene
LBL-668, March 1972
J. Inorg. Nucl. Chem.
- FEE, D. C., and S. S. Markowitz
Multicolumn radio-gas-chromatography analysis of recoil tritium reaction products
LBL-1249, September 1972
Anal. Chem.
- FEE, D. C., and S. S. Markowitz
Design of a high temperature neutron irradiation container
LBL-1264, October 1972
Nucl. Instr. Methods
- FINCH, C. B., (See Kolbe, W., LBL-286)
- FISCHER, M. S., D. H. Templeton, A. Zalkin, and M. Calvin
Crystal and molecular structure of methyl pheophorbide with applications to the chlorophyll
arrangement in photosynthetic lamellae
LBL-646, November 1971
J. Am. Chem. Soc. 94, 3613 (1972)
- FONG, J. C., (See Igo, G., Nucl. Phys. A195, 33 (1972))
- FUCHS, G., J. Steyaert, and D. J. Clark
Electron cyclotron resonance in a penning ion source
IEEE Trans. Nucl. Sci. NS-19 (1972) p. 84, Proc. Int'l. Conf. Multiply-Charged Ion Sources
and Accel. Systems, October 1971
- GARRISON, W. M.
Radiation-induced reactions of amino acids and peptides
UCRL-20440, March 1971
Radiation Res. Rev. 3, 305 (1972)
- GARRISON, W. M., (See Makada, H. A., LBL-242)
- GARRISON, W., H. A. Sokol, and W. Bennett-Corniea
Radiation chemistry of glycyglycine in oxygen-free systems
LBL-1269, October 1972
Radiation Res.
- GATTI, R. C., (See Moretto, L. G., LBL-294)
- GAUL, G., (See Stock, R., Phys. Rev. C 6, 1226 (1972))
- GAVIN, B. F.
Performance characteristics of a compact self heated cathode source and analyzer and the
Berkeley 3-MV superhilac injector
LBL-1219, September 1972
Second International Conference on Ion Sources, Vienna, Austria, September 11-16, 1972
- GHIORSO, A., K. Eskola, P. Eskola, and M. Nurmi
Isomeric states discovered in ^{250}Fm and ^{254}No
LBL-1277, October 1972
Phys. Rev.

- GIAUQUE, R. D., and J. Jaklevic
Rapid quantitative analysis by x-ray spectrometry
LBL-204, July 1971
Advances in X-Ray Analysis, ed. by K. F. Heinrich, C. S. Barrett, J. B. Newkirk, and
C. O. Ruud (Plenum Publ. Co., New York), Vol. 15, 164 (1972)
- GIAUQUE, R. D., F. S. Goulding, J. M. Jaklevic, and R. H. Pehl
Trace element analysis with semiconductor detector x-ray spectrometers
LBL-647, June 1972
Anal. Chem.
- GIUSTI, E. R., (See Cheifetz, E., LBL-613)
- GLASHAUSSER, C., (See Moss, J. M., Nucl. Phys. A194, 12 (1972))
- GLENDENNING, N. K., (See Ascutto, R. J., LBL-233)
- GLENDENNING, N. K., (See Ascutto, R. J., LBL-248)
- GLENDENNING, N. K., (See Schaeffer, R., LBL-689)
- GO, M. K., and S. S. Markowitz
Test of independence postulate in Bohr theory of compound nucleus decay: ^{50}Cr system
LBL-1230, August 1972
Phys. Rev.
- GODA, L., J. G. Conway, and H. R. Bowman
Further studies on the atmospheric lead and bromine concentrations in the San Francisco
east bay region
LBL-1235, August 1972
NFP
- GOITEIN, M., (See Igo, G., Nucl. Phys. A195, 33 (1972))
- GOLDSWORTHY, W. W., and R. G. Clem
A bipolar digipotentiogrator for electroanalytical uses. Direct conversion of charge to a
digital number
LBL-282, December 1971
Anal. Chem. 44, 1360 (1972)
- GORMAN, D. J., A. Rytz, and H. V. Michel
Absolute energy measurement of the alpha particles emitted by ^{232}U
LBL-622, February 1972
Comptes rendus
- GOUGH, R. A., R. G. Sextro, and J. Cerny
The beta-delayed proton emission of ^{23}Al
LBL-296, January 1972
Phys. Rev. Letters 28, 510 (1972)
- GOUGH, R. A., (See Cerny, J., LBL-626)
- GOUGH, R. A., R. G. Sextro, and J. Cerny
On the lowest $T = 3/2$ state in ^{41}Sc
LBL-1292, November 1972
Phys. Letters

- GOULDING, F. S., (See Giauque, R. D., LBL-647)
- GOULDING, F. S., (See Harvey, B. G., LBL-651)
- GRUNDER, H., (See Bacher, A. D., LBL-280)
- HAAS, H., (See Bacon, F., LBL-603)
- HAAS, H., (See Shirley, D. A., LBL-667)
- HAAS, H., and D. A. Shirley
Nuclear quadrupole interaction studies by perturbed angular correlations
LBL-1284, October 1972
J. Chem. Phys.
- HALBACH, K.
Field correction windings for iron magnets
UCRL-18969, November 1970
Nucl. Instr. Methods
- HALBACH, K.
Some eddy current effects in solid core magnets
LBL-1242, September 1972
Nucl. Instr. Methods
- HARNEY, H. L., (See Wozniak, G. J., LBL-635)
- HARNEY, H. L., and G. J. Wozniak
Efficiency of detecting a ^8He with a ΔE -E counter telescope
LBL-1214, August 1972
NFP
- HARTE, J., (See Hollander, J. M., "Elements of a National Energy Policy")
- HARVEY, B. G., (See Zisman, M. S., LBL-226)
- HARVEY, B. G., (See Sherman, J. D., LBL-227)
- HARVEY, B. G., J. Mahoney, F. G. Pühlhofer, F. S. Goulding, D. A. Landis, J. C. Faivre,
D. G. Kovar, M. S. Zisman, J. R. Meriwether, S. W. Cospers, and D. L. Hendrie
A spectrometer focal plane detector for heavy ions
LBL-651, April 1972
Nucl. Instr. Methods 104, 21 (1972)
- HARVEY, B. G., (See Hendrie, D. L., LBL-656)
- HARVEY, B. G., (See Becchetti, F. D., LBL-695)
- HARVEY, B. G., (See Kovar, D. G., LBL-1201)
- HARVEY, B., (See Stock, R., Phys. Rev. C 6, 1226 (1972))
- HASHMALL, J. A., B. E. Mills, D. A. Shirley, and A. Streitwieser Jr.
A comparison of valence shell and core ionization potentials of alkyl iodides
LBL-211, July 1971
J. Am. Chem. Soc. 94, 4445 (1972)
- HAYES, R. G., (See Edelstein, N., LBL-650)

HEALEY, R. N., (See Fadley, C. S., UCRL-20478)

HELD, E., (See Kenjo, T., LBL-249)

HENDRIE, D. L., (See de Swiniarski, R., LBL-201)

HENDRIE, D. L., (See Sherman, J. D., LBL-227)

HENDRIE, D. L., (See Harvey, B. G., LBL-651)

HENDRIE, D. L., B. G. Harvey, J. R. Meriwether, J. Mahoney, J.-C. Faivre, and D. G. Kovar

Multiple deformation of ^{238}U

LBL-656, April 1972

Phys. Rev. Letters

HENDRIE, D. L., (See Moss, J. M., Nucl. Phys. A194, 12 (1972))

HENDRIE, D. L., (See Igo, G., Nucl. Phys. A195, 33 (1972))

HENDRIE, D., (See Stock, R., Phys. Rev. C 6, 1226 (1972))

HOLLANDER, F. J.

Crystal structures of diketone complexes of alkaline earth metals and other compounds

LBL-670, May 1972

Ph. D. Thesis

HOLLANDER, F. J., D. H. Templeton, and A. Zalkin

Investigations of alkaline-earth β -diketone complexes. I. The crystal and molecular structure of bis(dimethylformamido)bis(1, 3-diphenyl-1, 3-propanedionato)magnesium

LBL-1266, September 1972

Acta Cryst.

HOLLANDER, F. J., D. H. Templeton, and A. Zalkin

Investigations of alkaline-earth β -diketone complexes. II. The crystal and molecular structure of bis(1, 3-diphenyl-1, 3-propanedionato)calcium hemimethanolate

LBL-1267, September 1972

Acta Cryst.

HOLLANDER, F. J., D. H. Templeton, and A. Zalkin

Investigations of alkaline-earth β -diketone complexes. III. The crystal and molecular structure of bis(1, 3-diphenyl-1, 3-propanedionato)strontium hemiacetate

LBL-1268, September 1972

Acta Cryst.

HOLLANDER, F. J., D. H. Templeton, and A. Zalkin

The crystal and molecular structure of 1, 3-diphenyl-1, 3-propanedione enol

LBL-1273, October 1972

Acta Cryst.

HOLLANDER, J. M., (See Fadley, C. S., UCRL-20478)

HOLLANDER, J. M., (See Jardine, L. J., LBL-278)

- HOLLANDER, J. M.
Scientists and the Environment: New Responsibilities
AMBIO 1, 116 (1972)
- HOLLANDER, J. M., and J. Harte
Elements of a national energy policy
Unpublished, August 1972
- HOLZWARTH, G., (See Kleber, M., LBL-1293)
- HUIZENGA, J. R., and L. G. Moretto
Nuclear level densities
LBL-662, April 1972
Ann. Rev. Nucl. Sci.
- HUNT, W. P., (See Yarkony, D. R., LBL-681)
- HULTBERG, S., (See Rezanka, I., LBL-1223)
- HUNG, S. T. -C.
Beta asymmetry from oriented manganese 52
LBL-1256, September 1972
Ph. D. Thesis
- HYDE, E. K., (See Eppley, R. E., LBL-643)
- HYDE, E. K., (See Korteling, R. G., LBL-663)
- IGO, G., J. C. Fong, S. L. Verbeck, M. Goiten, D. L. Hendrie, J. C. Carroll, B. McDonald, A. Stetz, and M. C. Makino
Large angle elastic scattering of deuterons from hydrogen: $T_K = 433, 362, \text{ and } 291 \text{ MeV}$
Nucl. Phys. A195, 33 (1972)
- IMMELE, J. D., and G. L. Struble
Gamma and octupole vibrations in deformed nuclei
LBL-238, September 1971
Nucl. Phys. A187, 459 (1972)
- IMMELE, J. D.
A self-consistent treatment of phonons and quasiparticles in finite fermi systems and applications to rare earth nuclei
LBL-675, August 1972
Ph. D. Thesis
- JAKLEVIC, J., (See Giaque, R. D., LBL-204)
- JAKLEVIC, J. M., (See Giaque, R. D., LBL-647)
- JARDINE, L. J., S. G. Prussin, and J. M. Hollander
Decay of ^{210}At to levels in ^{210}Po
LBL-278, November 1971
Nucl. Phys. A190, 261 (1972)
- JARED, R. C., (See Wilhelmy, J. B., LBL-256)
- JARED, R. C., (See Cheifetz, E., LBL-613)

- JENSEN, C. H., A. Partridge, T. Kenjo, J. Bucher, and R. M. Diamond
Anion exchange in aqueous-organic solvent mixtures, II
LBL-225, August 1971
J. Phys. Chem. 76, 1040 (1972)
- JOANNOPOULOS, J. D., (See Pollak, R. A., LBL-1204)
- KAINDL, G., D. Salomon, and G. Wortmann
Quadrupole splitting of the 6.2-keV gamma rays of ^{181}Ta in rhenium metal
LBL-279, November 1971
Phys. Rev. Letters 28, 952 (1972)
- KAINDL, G., (See Bacon, F., LBL-297)
- KAINDL, G., (See Bacon, F., LBL-603)
- KAINDL, G., and D. Salomon
Electronic quadrupole interaction of Ta-181 in hexagonal transition metals
LBL-641, March 1972
Phys. Letters
- KAINDL, G., and D. Salomon
High-resolution Mössbauer spectroscopy with tantalum-181
LBL-1210, July 1972
International Conference on Applications of the Mössbauer Effect, Israel, August 27-31, 1972
- KAINDL, G., and D. Salomon
Hyperfine interaction of ^{181}Ta in nickel
LBL-1288, November 1972
Phys. Letters
- KAINDL, G., and D. Salomon
Effects of temperature on the energy of the 6.2-keV Mössbauer gamma rays of ^{181}Ta
LBL-1604, November 1972
Phys. Rev. Letters
- KAMMURI, T., (See Stephens, F. S., LBL-652)
- KARAGEORGHIS, V., F. Asaro, and I. Perlman
Concerning two mycenaean pictorial sherds from Kouklia (Palaepaphos), Cyprus
LBL-625, February 1972
Arch. Anzeiger
- KENJO, T., (See Jensen, C. H., LBL-225)
- KENJO, T., S. Brown, E. Held, and R. M. Diamond
Coordination of fluoride and chloride anions with alcohol and phenol
LBL-249, October 1971
J. Phys. Chem. 76, 1775 (1972)
- KERMAN, A. K., (See Bassichis, W. H., UCRL-73044)
- KIENLE, P.
Summary talk - experimental
LBL-1296, November 1972
International Conference on Nuclear Moments and Nuclear Structure, Osaka, Japan,
September 4-8, 1972

- KING, C. J., (See Thompson, R. W., LBL-607)
- KING, C. J., (See Davenport, I. F., LBL-608)
- KING, C. J., (See Thompson, R. W., LBL-614)
- KING, C. J., (See Davenport, I. F., LBL-660)
- KING, C. J., (See Davenport, I. F., LBL-1252)
- KLEBER, M., and Holzwarth, G.
Neutron transfer between BCS nuclei
LBL-1293, November 1972
Nucl. Phys.
- KOLBE, W., N. Edelstein, C. B. Finch, and M. M. Abraham
Zero-field splittings of Cm^{3+} and Am^{2+} in fluorite type crystals
LBL-286, December 1971
J. Chem. Phys. 56, 5432 (1972)
- KORTELING, R. G., D. Toren, and E. K. Hyde
Characteristics of fragments ejected from silver and uranium bombarded with 4.8 GeV
protons
LBL-663, May 1972
Phys. Rev.
- KOVAR, D. G., (See Harvey, B. G., LBL-651)
- KOVAR, D. G., (See Hendrie, D. L., LBL-656)
- KOVAR, D. G., (See Becchetti, F. D., LBL-695)
- KOVAR, D. G., F. D. Becchetti, B. G. Harvey, F. Pühlhofer, J. Mahoney, D. W. Miller, and
M. S. Zisman
j dependence of heavy-ion-induced reactions
LBL-1201, July 1972
Phys. Rev. Letters 29, 1023 (1972)
- KOWALCZYK, S., (See Pollak, R. A., LBL-664)
- KOWALCZYK, S., (See Ley, L., LBL-688)
- KOWALCZYK, S., L. Ley, R. Pollak, and D. A. Shirley
High-resolution XPS spectra of Ir, Pt, and Au valence bands
LBL-691, July 1972
Phys. Letters
- KOWALCZYK, S., (See Ley, L., LBL-1203)
- KOWALCZYK, S., (See Pollak, R. A., LBL-1204)
- KOWALCZYK, S., (See Cavell, R. G., LBL-1213)
- KOWALCZYK, S., (See McFeely, R., LBL-1253)

- KOWALCZYK, S., L. Ley, R. A. Pollak, F. R. McFeely, and D. A. Shirley
New multiplet structure in photoemission from MnF_2
LBL-1275, October 1972
Phys. Rev. Letters
- KOWALCZYK, S. P., (See Ley, L., LBL-1278)
- LANDIS, D. A., (See Harvey, B. G., LBL-651)
- LARIMER, R. M., (See McKee, J. S. C., LBL-1270)
- LEDERER, C. M.
Computer analysis of spectra
UCRL-18948, September 1969
Radioactivity in Nuclear Spectroscopy (Gordon and Breach, 1972), Vol. 1, p. 73
- LEDERER, C. M., (See Benson, D., LBL-1216)
- LEE, D. M., and S. S. Markowitz
 He^3 activation analysis for S, Cl, K, and Ca
LBL-682, June 1972
J. Radioanal. Chem.
- LEE, D. M.
The application of ^3He -induced nuclear reactions for sensitive chemical analysis of sulfur, chlorine, potassium, and calcium
LBL-1291, November 1972
M.S. Thesis
- LEEMANN, Ch., (See McKee, J. S. C., LBL-1270)
- LEIGH, J. R., (See Maier, K. H., UCRL-19593)
- LEIGH, J. R., (See Diamond, R. M., UCRL-20463)
- LEIGH, J. R., J. O. Newton, L. A. Ellis, M. C. Evans, and M. J. Emmott
A study of the odd-A rhenium isotopes: ^{179}Re and ^{177}Re
UCRL-20494, June 1971
Nucl. Phys. A183, 177 (1972)
- LEIGH, J. R., (See Maier, K. H., LBL-243)
- LEIGH, J. R., (See Stephens, F. S., LBL-652)
- LEY, L., (See Pollak, R. A., LBL-664)
- LEY, L., S. Kowalczyk, R. Pollak, and D. A. Shirley
X-ray photoemission spectra of crystalline and amorphous Si and Ge valence bands
LBL-688, July 1972
Phys. Rev. Letters
- LEY, L., (See Kowalczyk, S., LBL-691)
- LEY, L., R. Pollak, S. Kowalczyk, and D. A. Shirley
The onset of relativistic effects in the density of states of the 6s6p elements Tl, Pb, and Bi
LBL-1203, July 1972
Phys. Letters

- LEY, L., (See Pollak, R. A., LBL-1204)
- LEY, L., (See Cavell, R. G., LBL-1213)
- LEY, L., (See McFeely, R., LBL-1253)
- LEY, L., (See Kowalczyk, S., LBL-1275)
- LEY, L., R. A. Pollak, S. P. Kowalczyk, R. McFeely, and D. A. Shirley
Evidence for covalent bonding in crystalline and amorphous As, Sb, and Bi from valence
band photoelectron spectra
LBL-1278, October 1972
Phys. Rev. Letters
- LISKOW, D. H., C. F. Bender, and H. F. Schaefer III
Theoretical reaction coordinate for the methyl isocyanide isomerization
LBL-290, December 1971
J. Am. Chem. Soc. 94, 5178 (1972)
- LISKOW, D. H., C. F. Bender, and H. F. Schaefer III
Bending frequency of the C₃ molecule
LBL-291, December 1971
J. Chem. Phys. 56, 5075 (1972)
- LISKOW, D. H., and H. F. Schaefer III
Sign of the dipole moment and other properties of methylsilane
LBL-629, March 1972
J. Am. Chem. Soc. 94, 6641 (1972)
- LISKOW, D. H., C. F. Bender, and H. F. Schaefer III
Some features of the CH₃NC → CH₃CN potential surface
LBL-696, July 1972
J. Chem. Phys.
- LITTON, G., (See Clem, R. G., LBL-679)
- MAHNKE, H. -E., (See Bacon, F., LBL-297)
- MAHNKE, H. -E., (See Bacon, F., LBL-603)
- MAHONEY, J., (See Harvey, B. G., LBL-651)
- MAHONEY, J., (See Hendrie, D. L., LBL-656)
- MAHONEY, J., (See Becchetti, F. D., LBL-695)
- MAHONEY, J., (See Kovar, D. G., LBL-1201)
- MAHONEY, J., (See Stock, R., Phys. Rev. C 6, 1226 (1972))
- MAIER, K. H., K. Nakai, J. R. Leigh, R. M. Diamond, and F. S. Stephens
Effective single-particle magnetic moments around ²⁰⁸Pb
UCRL-19593, October 1970
Nucl. Phys. A183, 289 (1972)
- MAIER, K. H., (See Diamond, R. M., UCRL-20463)

- MAIER, K. H., K. Nakai, J. R. Leigh, R. M. Diamond, and F. S. Stephens
Stroboscopic measurement of the g-factors of the 7^- isomer in ^{206}Pb and the $21/2^+$ isomer
in ^{207}Bi
LBL-243, October 1971
Nucl. Phys. A186, 97 (1972)
- MAIER, M. R., (See Stephens, F. S., LBL-1282)
- MAIN, R. M., and R. Yourd
Edge cooled tape magnet coils for high current density applications
LBL-1222, October 1972
Fourth International Conference on Magnetic Technology, Upton, Long Island, New York,
September 19-22, 1972
- MAIN, R. M.
Alignment of drift tube quadrupole lenses using a pulsed wire
LBL-1224, September 1972
Fourth International Conference on Magnetic Technology, Upton, Long Island, New York,
September 19-22, 1972
- MAKADA, H. A., and W. M. Garrison
Radiolytic oxidation of peptide derivatives of glycine in aqueous solution
LBL-242, October 1971
Radiation Res. 50, 48 (1972)
- MAKINO, M. C., (See Igo, G., Nucl. Phys. A195, 33 (1972))
- MAPLES, C., and J. Cerny
High-spin assignments in the lp-shell obtained with the J-dependent (p, α) reaction
LBL-288, December 1971
Phys. Letters 38B, 504 (1972)
- MAREI, S. A., and B. B. Cunningham
Magnetic measurements of curium metal, CmF_3 , and CmOCl
LBL-200, July 1971
J. Inorg. Nucl. Chem. 34, 1203 (1972)
- MARGARITIS, A., and C. R. Wilke
Engineering analysis of the rotorfermentor
LBL-222, August 1971
Developments in Industrial Microbiology 13, 159 (1972)
- MARKOWITZ, S. S., (See Fee, D. C., UCRL-20470)
- MARKOWITZ, S. S., (See Fee, D. C., LBL-668)
- MARKOWITZ, S. S., (See Lee, D. M., LBL-682)
- MARKOWITZ, S. S., (See Go, M. K., LBL-1230)
- MARKOWITZ, S. S., (See Fee, D. C., LBL-1249)
- MARKOWITZ, S. S., (See Fee, D. C., LBL-1264)
- MARRUS, R., and R. W. Schmieder
Forbidden decays of hydrogenlike and heliumlike argon
UCRL-20823, June 1971
Phys. Rev. A 5, 1160 (1972)

- MAYER, B., (See Becchetti, F. D., LBL-695)
- McCLATCHIE, E. A., (See Bacher, A. D., UCRL-20903)
- McDONALD, B., (See Igo, G., Nucl. Phys. A195, 33 (1972))
- McFEELY, R., S. Kowalczyk, L. Ley, R. A. Pollak, and D. A. Shirley
High-resolution XPS spectra of PbS, PbSe, and PbTe valence bands
LBL-1253, September 1972
Phys. Rev.
- McFEELY, F. R., (See Kowalczyk, S., LBL-1275)
- McFEELY, R., (See Ley, L., LBL-1278)
- McKEE, J. S. C., H. E. Conzett, R. M. Larimer, and Ch. Leemann
Further evidence for the dominance of nucleon-nucleon p-wave forces in vector polarizations
in N-d scattering below 15 MeV
LBL-1270, October 1972
Phys. Rev. Letters 29, 1613 (1972)
- McLAUGHLIN, R. D., (See Stacy, J. J., LBL-638)
- McLAUGHLIN, R. D., (See Stacy, J. J., LBL-698)
- MEHLHORN, R., (See Rajnak, K., LBL-1218)
- MEINER, H., (See Bacher, A. D., LBL-1228)
- MERIWETHER, J. R., (See Harvey, B. G., LBL-651)
- MERIWETHER, J. R., (See Hendrie, D. L., LBL-656)
- MICHEL, H. V., (See Gorman, D. J., LBL-622)
- MICHEL, H. V., (See Perlman, I., LBL-674)
- MILLER, D. W., (See Kovar, D. G., LBL-1201)
- MILLS, B. E., (See Hashmall, J. A. LBL-211)
- MINER, C. E., (See Fadley, C. S., UCRL-20478)
- MITRA, G., and C. R. Wilke
Ultrafiltration of trichoderma viride cellulase
LBL-1250, September 1972
J. Ferment. Technol. 50, 914 (1972)
- MORETTO, L. G.
Shell model calculations of fission decay widths and probabilities in superheavy nuclei
LBL-206, July 1971
Nucl. Phys. A180, 337 (1972)
- MORETTO, L. G.
Statistical description of a paired nucleus with the inclusion of angular momentum
LBL-219, August 1971
Nucl. Phys. A185, 145 (1972)

- MORETTO, L. G.
 Statistical description of deformation in excited nuclei and disappearance of shell effects
 with excitation energy
 LBL-228, August 1971
 Nucl. Phys. A182, 641 (1972)
- MORETTO, L. G.
 Note on the shell effects disappearance with excitation energy and its relation with the
 Strutinski smoothing procedure
 LBL-287, December 1971
 Phys. Letters 38B, 393 (1972)
- MORETTO, L. G., S. G. Thompson, J. Routti, and R. C. Gatti
 Influence of shells and pairing on the fission probabilities of nuclei below radium
 LBL-294, January 1972
 Phys. Letters 38B, 471 (1972)
- MORETTO, L. G.
 Novel approach to the evaporation of complex fragments
 LBL-634, March 1972
 Phys. Letters 40B, 185 (1972)
- MORETTO, L. G.
 Pairing fluctuations in excited nuclei and the absence of a second order phase transition
 LBL-648, April 1972
 Phys. Letters 40B, 1 (1972)
- MORETTO, L. G., (See Huizenga, J. R., LBL-662)
- MORETTO, L. G., (See Nardi, E., LBL-1263)
- MORRIS, D., (See Clark, D. J., LBL-644)
- MOSS, J. M., D. L. Hendrie, C. Glashauser, and J. Thirion
 The spectroscopy of ^{54}Fe via the reaction $^{54}\text{Fe}(p, p'\gamma)^{54}\text{Fe}$ at 10 MeV
 Nucl. Phys. A194, 12 (1972)
- MURPHY, T. F., and C. R. Wilke
 Production of L-asparaginase by cultures of erwinia aroideae
 LBL-1283, October 1972
 M. S. Thesis
- MYERS, W. D.
 The droplet model
 LBL-209, July 1971
Proceedings of the Mont Tremblant International Summer School on "The Dynamic Structure
 of Nuclear States", Mont Tremblant, Canada, August 1-14, 1971, ed. by D. J. Rowe, L.
 E. H. Trainor, S. S. M. Wong, and T. W. Donnelly (University of Toronto Press, 1972)
- MYERS, W. D.
 Geometric properties of leptodermous distributions with applications to nuclei
 LBL-1259, October 1972
 Nucl. Phys.

NAGARAJAN, M. A.

Comments on a three body model of stripping
LBL-640, March 1972
Phys. Letters 40B, 65 (1972)

NAGARAJAN, M. A.

The effect of recoil on single nucleon transfer in heavy ion reactions
LBL-697, July 1972
Nucl. Phys.

NAKAI, K., (See Maier, K. H., UCRL-19593)

NAKAI, K., (See Maier, K. H., LBL-243)

NAKAI, K., (See Stephens, F. S., LBL-652)

NARDI, E., L. G. Moretto, and S. G. Thompson

Calculations of neutron evaporation from ^{252}Cf fission fragments based on the shell model
LBL-1263, October 1972
Phys. Letters

NEWTON, A. S., and A. F. Sciamanna

On the metastable dissociation of the CH^+ ion produced by electron impact
LBL-295, January 1972
J. Chem. Phys.

NEWTON, J. O., (See Leigh, J. R., UCRL-20494)

NEWTON, J. O., F. S. Stephens, and R. M. Diamond

Feeding times in $(\text{HI}, \text{x}\gamma)$ reactions
LBL-1227, December 1972
Nucl. Phys.

O'NEIL, S. V., (See Pearson, P. K., LBL-214)

O'NEIL, S. V., (See Bender, C. F., LBL-250)

O'NEIL, S. V., (See Bender, C. F., LBL-630)

O'NEIL, S. V., P. K. Pearson, H. F. Schaefer III, and C. F. Bender

The $\text{H} + \text{F}_2 \rightarrow \text{HF} + \text{F}$ reaction. An ab initio potential energy surface
LBL-1200, July 1972
J. Chem. Phys.

ORNELAS, D., (See Clem, R. G., LBL-679)

OWAIS, M., (See Scott, A., LBL-672)

PARTRIDGE, A., (See Jensen, C. H., LBL-225)

PAUL, P., (See Diener, E. M., LBL-602)

PEARSON, P. K., S. V. O'Neil, and H. F. Schaefer III

Role of electron correlation in a priori predictions of the electronic ground state of BeO
LBL-214, August 1971
J. Chem. Phys. 56, 3938 (1972)

- PEARSON, P. K., (See Bender, C. F., LBL-250)
- PEARSON, P. K., (See Bondybey, V., LBL-258)
- PEARSON, P. K., (See Bender, C. F., LBL-630)
- PEARSON, P. K., (See O'Neil, S. V., LBL-1200)
- PEHL, R. H., (See Giauque, R. D., LBL-647)
- PERLMAN, I., (See Karageorghis, V., LBL-625)
- PERLMAN, I., (See Bowman, H. R., LBL-657)
- PERLMAN, I., (See Bowman, H. R., LBL-661)
- PERLMAN, I., F. Asaro, and H. V. Michel
Nuclear applications in art and archaeology
LBL-674, May 1972
Ann. Rev. Nucl. Sci.
- PERLMAN, I., (See Artzy, M., LBL-1286)
- PETROVICH, F.
Effective moment operator for magnetic moments and M1 transitions in the Pb region
LBL-649, August 1972
Nucl. Phys.
- PETROVICH, F., (See Scott, A., LBL-672)
- PIGFORD, R. L., (See Rieke, R. D., LBL-1255)
- PLATTNER, G. R., (See de Swiniarski, R., LBL-201)
- PLATTNER, G. R., A. D. Bacher, and H. E. Conzett
Phase shifts for p - ^4He elastic scattering between 20 and 40 MeV
LBL-269, December 1971
Phys. Rev. C 5, 1158 (1972)
- PLATTNER, G. R., (See Bacher, A. D., LBL-280)
- POLLAK, R. A., S. Kowalczyk, L. Ley, and D. A. Shirley
Evolution of core states from energy bands in the 4d5s5p region from Pd to Xe
LBL-664, May 1972
Phys. Rev. Letters 29, 274 (1972)
- POLLAK, R., (See Ley, L., LBL-688)
- POLLAK, R., (See Kowalczyk, S., LBL-691)
- POLLAK, R., (See Ley, L., LBL-1203)
- POLLAK, R. A., L. Ley, S. Kowalczyk, D. A. Shirley, J. D. Joannopoulos, D. J. Chadi, and M. L. Cohen
X-ray photoemission valence band spectra and theoretical valence band density of states for Ge, GaAs, and ZnSe
LBL-1204, July 1972
Phys. Rev. Letters

- POLLAK, R. A., (See Cavell, R. G., LBL-1213)
- POLLAK, R. A., (See McFeely, R., LBL-1253)
- POLLAK, R. A., (See Kowalczyk, S., LBL-1275)
- POLLAK, R. A., (See Ley, L., LBL-1278)
- POLLAK, R. A.
Electronic densities of states of solids from x-ray photoemission spectroscopy
LBL-1299, December 1972
Ph. D. Thesis
- PRUSSIN, S. G., (See Jardine, L. J., LBL-278)
- PÜHLHOFER, F., and R. M. Diamond
Enhancement of direct processes in heavy-ion reactions at high angular momenta
LBL-604, January 1972
Nucl. Phys. A191, 561 (1972)
- PÜHLHOFER, F. G., (See Harvey, B. G., LBL-651)
- PÜHLHOFER, F. G., (See Becchetti, F. D., LBL-695)
- PÜHLHOFER, F., (See Kovar, D. G., LBL-1201)
- QUEBERT, J. L., (See Diamond, R. M., UCRL-20463)
- RAJNAK, K., R. Mehlhorn, and N. Edelstein
Calculation of the crystal field splittings of Sm^{3+} levels in LaCl_3 with inclusion of J-mixing
LBL-1218, August 1972
J. Chem. Phys. 58, 609 (1973)
- RASMUSSEN, J. O., (See Wilhelmy, J. B., LBL-256)
- RASMUSSEN, J. O., (See Rezanka, I., LBL-1223)
- RAYNAL, J., (See de Swiniarski, R., LBL-201)
- RESMINI, F. G., (See de Swiniarski, R., LBL-201)
- RESMINI, F. G., (See Bacher, A. D., LBL-1228)
- REZANKA, I., J. O. Rasmussen, F. M. Bernthal, C. T. Alonso, J. R. Alonso, S. Hultberg,
and H. Ryde
Rotational states in ^{171}Hf
LBL-1223, August 1972
Nucl. Phys. A197, 430 (1972)
- RIEKE, R. D., and R. L. Pigford
Large separations via cycling zone adsorption
LBL-1255, September 1972
Ph. D. Thesis
- ROUTTI, J., (See Moretto, L. G., LBL-294)
- RYDE, H., (See Rezanka, I., LBL-1223)

- RYTZ, A., (See Gorman, D. J., LBL-622)
- SALOMON, D., (See Kaindl, G., LBL-279)
- SALOMON, D., (See Kaindl, G., LBL-641)
- SALOMON, D., (See Kaindl, G., LBL-1210)
- SALOMON, D.
Mössbauer spectroscopy of the 6.2 keV γ ray transition of ^{181}Ta
LBL-1276, September 1972
Ph. D. Thesis
- SALOMON, D., (See Kaindl, G., LBL-1288)
- SALOMON, D., (See Kaindl, G., LBL-1604)
- SANTO, R., (See Stock, R., Phys. Rev. C 6, 1226 (1972))
- SCHAEFER III, H. F., (See Pearson, P. K., LBL-214)
- SCHAEFER III, H. F., (See Bender, C. F., LBL-250)
- SCHAEFER III, H. F., (See Bondybey, V., LBL-258)
- SCHAEFER III, H. F., (See Liskow, D. H., LBL-290)
- SCHAEFER III, H. F., (See Liskow, D. H., LBL-291)
- SCHAEFER III, H. F., (See Liskow, D. H., LBL-629)
- SCHAEFER III, H. F., (See Bender, C. F., LBL-630)
- SCHAEFER III, H. F., (See Yarkony, D. R., LBL-681)
- SCHAEFER III, H. F., (See Liskow, D. H., LBL-696)
- SCHAEFER III, H. F., (See O'Neil, S. V., LBL-1200)
- SCHAEFFER, R., and N. K. Glendenning
Second order effects in the (h, t) reaction
LBL-689, July 1972
Nucl. Phys.
- SCHAEFFER, R., (See Bruge, G., LBL-1238)
- SCHMIEDER, R. W.
Matrix elements of the quadratic stark effect on hyperfine structure
UCRL-19560, February 1970
Am. J. Phys. 40, 297 (1972)
- SCHMIEDER, R. W., (See Marrus, R., UCRL-20823)
- SCHMIEDER, R. W.
Interference effects in laser modulated electron beams
LBL-220, August 1971
Appl. Phys. Letters 20, 516 (1972)

- SCHMIEDER, R. W.
Large diameter rotating lid vacuum chamber
LBL-628, February 1972
Nucl. Instr. Methods 102, 313 (1972)
- SCHMIEDER, R. W.
Radiative decay of metastable 3P_0 atomic states
LBL-1257, September 1972
Phys. Rev. Letters
- SCIAMANNA, A. F., (See Newton, A. S., LBL-295)
- SCOTT, A., M. Owais, and F. Petrovich
Inelastic proton scattering from ^{209}Bi at 61 MeV
LBL-672, May 1972
Nucl. Phys.
- SEXTRO, R. G., (See Gough, R. A., LBL-296)
- SEXTRO, R. G., (See Cerny, J., LBL-626)
- SEXTRO, R. G., (See Gough, R. A., LBL-1292)
- SHERMAN, J. D., B. G. Harvey, D. L. Hendrie, M. S. Zisman, and B. Sørensen
Strong and weak 0^+ excitations in the $^{142}\text{Ce}(p, t)^{140}\text{Ce}$ and $^{140}\text{Ce}(p, t)^{138}\text{Ce}$ reactions
LBL-227, September 1971
Phys. Rev. C 6, 1082 (1972)
- SHERMAN, J., (See Stock, R., Phys. Rev. C 6, 1226 (1972))
- SHIH, T. S.
The question of equilibrium at a phase boundary during crystal growth
LBL-1226, September 1972
M. S. Thesis
- SHIRLEY, D. A.
Mössbauer spectroscopy
UCRL-20447, February 1971
Magnet. Res. Rev. 1, 143 (1972)
- SHIRLEY, D. A., (See Bacon, F., UCRL-20465)
- SHIRLEY, D. A., (See Hashmall, J. A., LBL-211)
- SHIRLEY, D. A., (See Davis, D. W., LBL-270)
- SHIRLEY, D. A.
High-resolution x-ray photoemission spectrum of the valence bands of gold
LBL-277, November 1971
Phys. Rev. B 5, 4709 (1972)
- SHIRLEY, D. A., (See Bacon, F., LBL-297)
- SHIRLEY, D. A.
ESCA
LBL-610, January 1972
Advan. Chem. Phys.

SHIRLEY, D. A., (See Davis, D. W., LBL-633)

SHIRLEY, D. A.

Near equivalence of the quantum mechanical potential model and the thermochemical model of ESCA shifts

LBL-653, April 1972

Chem. Phys. Letters 15, 325 (1972)

SHIRLEY, D. A., (See Pollak, R. A., LBL-664)

SHIRLEY, D. A., and H. Haas

Perturbed angular correlation of gamma rays

LBL-667, February 1972

Ann. Rev. Phys. Chem.

SHIRLEY, D. A.

The effect of atomic and extra-atomic relaxation on atomic binding energies

LBL-678, June 1972

Chem. Phys. Letters

SHIRLEY, D. A., (See Ley, L., LBL-688)

SHIRLEY, D. A., (See Kowalczyk, S., LBL-691)

SHIRLEY, D. A., (See Ley, L., LBL-1203)

SHIRLEY, D. A., (See Pollak, R. A., LBL-1204)

SHIRLEY, D. A.

Relaxation effects on auger energies

LBL-1207, July 1972

Chem. Phys. Letters 17, 312 (1972)

SHIRLEY, D. A., (See Cavell, R. G., LBL-1213)

SHIRLEY, D. A., (See McFeely, R., LBL-1253)

SHIRLEY, D. A., (See Kowalczyk, S., LBL-1275)

SHIRLEY, D. A., (See Ley, L., LBL-1278)

SHIRLEY, D. A., (See Haas, H., LBL-1284)

SHIRLEY, D. A., (See Bacon, F., LBL-1289)

SHIRLEY, D. A.

Static orientation methods and experiments with oriented radioactive targets

Proceedings of the IInd Int'l. Conf. on Polarized Targets, August 30 - September 2, 1971,

ed. by G. Shapiro, Nat'l. Tech. Info. Service, U. S. Dept. of Commerce, p. 223 (1972)

SIEMENS, P. J., and F. D. Becchetti

Particle-wave ambiguities in the interpretation of heavy-ion reactions

LBL-1274, October 1972

Phys. Letters 42B, 389 (1972)

SIMON, R. S., (See Stephens, F. S., LBL-273)

- SOKOL, H. A., (See Garrison, W., LBL-1269)
- SØRENSEN, B., (See Sherman, J. D., LBL-227)
- SØRENSEN, B., (See Ascutto, R. J., LBL-248)
- STACY, J. J., N. Edelstein, and R. D. McLaughlin
Effects of gamma-irradiation on actinide ions in calcium fluoride
LBL-638, March 1972
J. Chem. Phys.
- STACY, J. J., N. Edelstein, R. D. McLaughlin, and J. Conway
Optical Zeeman spectra of Am^{3+} , Cm^{3+} , and Nd^{3+} in CaF_2
LBL-698, July 1972
J. Chem. Phys. 58, 807 (1973)
- St. CLAIR, D., A. Zalkin, and D. H. Templeton
The crystal structure of tetraethylammonium 2, 2'-commo-bis(nonahydrodicarba-2-cobalta-closo-decaborate), a salt of the cobalt derivative of the nonahydrodicarbanonaborate (2-) ligand
UCRL-18901, April 1969
Inorg. Chem. 11, 377 (1972)
- STEPHENS, F. S., (See Maier, K. H., UCRL-19593)
- STEPHENS, F. S., (See Diamond, R. M., UCRL-20463)
- STEPHENS, F. S., (See Maier, K. H., LBL-243)
- STEPHENS, F. S., and R. S. Simon
Coriolis effects in the yrast states
LBL-273, November 1971
Nucl. Phys. A183, 257 (1972)
- STEPHENS, F. S., R. M. Diamond, J. R. Leigh, T. Kammuri, and K. Nakai
Decoupled yrast states in odd-mass nuclei
LBL-652, April 1972
Phys. Rev. Letters 29, 438 (1972)
- STEPHENS, F. S., (See Newton, J. O., LBL-1227)
- STEPHENS, F. S.
Coriolis effects in nuclei
LBL-1251, August 1972
Lectures presented at the 5th Nuclear Physics Summer School held at Rudziska, Poland, September 1972
- STEPHENS, F. S., R. M. Diamond, D. Benson Jr., and M. R. Maier
Rotation of moderately-deformed odd-A nuclei
LBL-1282, October 1972
Phys. Rev. Letters
- STETZ, A., (See Igo, G., Nucl. Phys. A195, 33 (1972))
- STEYAERT, J., (See Clark, D. J., LBL-644)
- STEYAERT, J., (See Stock, R., Phys. Rev. C 6, 1226 (1972))

- STEYAERT, J., (See Fuchs, G., IEEE Trans. Nucl. Sci. NS-19 (1972), p. 84)
- STOCK, R., G. Gaul, R. Santo, M. Bernas, B. Harvey, D. Hendrie, J. Mahoney, J. Sherman, J. Steyaert, and M. Zisman
Anomalous backward α scattering
Phys. Rev. C 6, 1226 (1972)
- STREITWIESER Jr., A., (See Hashmall, J. A., LBL-211)
- STRUBLE, G. L., (See Immele, J. D., LBL-238)
- SYMONS, G. D., (See Diamond, R. M., UCRL-20463)
- TEMPLETON, D. H., (See St. Clair, D., UCRL-18901)
- TEMPLETON, J. E., (See Bacon, F., UCRL-20465)
- TEMPLETON, D. H., (See Fischer, M. S., LBL-646)
- TEMPLETON, D. H., (See Templeton, L. K., LBL-669)
- TEMPLETON, D. H., (See Zalkin, A., LBL-1265)
- TEMPLETON, D. H., (See Hollander, F. J., LBL-1266)
- TEMPLETON, D. H., (See Hollander, F. J., LBL-1267)
- TEMPLETON, D. H., (See Hollander, F. J., LBL-1268)
- TEMPLETON, D. H., (See Hollander, F. J., LBL-1273)
- TEMPLETON, L. K., D. H. Templeton, and A. Zalkin
The crystal and molecular structure of 2-(N-nitrosomethylamino)acetamide
LBL-669, May 1972
Acta Cryst.
- THIRION, J., (See Moss, J. M., Nucl. Phys. A194, 12 (1972))
- THOMAS, T. D., (See Davis, D. W., LBL-270)
- THOMPSON, R. W., and C. J. King
Systematic synthesis of separation schemes
LBL-607, January 1972
A. I. Ch. E. J. 18, 941 (1972)
- THOMPSON, R. W., and C. J. King
Synthesis of separation schemes
LBL-614, July 1972
Ph. D. Thesis
- THOMPSON, S. G., (See Wilhelmy, J. B., LBL-256)
- THOMPSON, S. G., (See Moretto, L. G., LBL-294)
- THOMPSON, S. G., (See Cheifetz, E., LBL-613)

- THOMPSON, S. G., and C. F. Tsang
Superheavy elements
LBL-665, May 1972
Science 178, 1047 (1972)
- THOMPSON, S. G., (See Nardi, E., LBL-1263)
- TIVOL, W. F., (See Bacher, A. D., LBL-280)
- TOMBRELLO, T. A., (See Bacher, A. D., UCRL-20903)
- TOREN, D., (See Korteling, R. G., LBL-663)
- TSANG, C. F., and J. B. Wilhelmy
Interpretation of mass asymmetry in fission based on deformation energy surfaces
LBL-254, November 1971
Nucl. Phys. A184, 417 (1972)
- TSANG, C. F., (See Thompson, S. G., LBL-665)
- TSANG, C. F., (See Bassichis, W. H., UCRL-73044)
- TSANG, C. F., (See Bassichis, W. H., UCRL-74225)
- TUERPE, D. R., (See Bassichis, W. H., UCRL-73044)
- TUERPE, D. R., (See Bassichis, W. H., UCRL-74225)
- UEKI, T., (See Zalkin, A., LBL-1265)
- VAN DEURZEN, C. H. H., J. G. Conway, and S. P. Davis
The spectrum and energy levels of doubly ionized scandium (Sc III)
LBL-1217, August 1972
J. Opt. Soc. Am.
- VERBECK, S. L., (See Igo, G., Nucl. Phys. A195, 33 (1972))
- VERGADOS, J. D., (See Diener, E. M., LBL-602)
- VERGADOS, J. D., and H. W. Baer
Importance of momentum dependent terms in radiative pion capture
LBL-690, July 1972
Phys. Letters
- WEAVER, T. A., (See Bacher, A. D., UCRL-20903)
- WEIGEL, M., (See Eckart, G., LBL-639)
- WERNAU, W. C., and C. R. Wilke
Mass transfer to newtonian and non-newtonian systems in stirred tank gas-liquid contactors
LBL-680, August 1972
Ph. D. Thesis
- WERNAU, C. W., and C. R. Wilke
New method for evaluation of dissolved oxygen probe response for K_L determination
LBL-1209, July 1972
Bioeng. and Biotech.

- WILCOX, K. H., (See Wozniak, G. J., LBL-635)
- WILETS, L., (See Bassichis, W. H., UCRL-73044)
- WILETS, L., (See Bassichis, W. H., UCRL-74225)
- WILHELMY, J. B., (See Tsang, C. F., LBL-254)
- WILHELMY, J. B., E. Cheifetz, R. C. Jared, S. G. Thompson, H. R. Bowman, and J. O. Rasmussen
Angular momentum of primary products formed in the spontaneous fission of ^{252}Cf
LBL-256, November 1971
Phys. Rev. C 5, 2041 (1972)
- WILKE, C. R., (See Margaritis, A., LBL-222)
- WILKE, C. R., (See Wernau, W. C., LBL-680)
- WILKE, C. R., (See Wernau, W. C., LBL-1209)
- WILKE, C. R., (See Mitra, G., LBL-1250)
- WILKE, C. R., (See Murphy, T. F., LBL-1283)
- WORTMANN, G., (See Kaindl, G., LBL-279)
- WOZNIAK, G. J., H. L. Harney, K. H. Wilcox, and J. Cerny
Alpha-particle transfer via the (^{12}C , ^8Be) reaction: application to studies of ^{16}O and ^{20}Ne
LBL-635, March 1972
Phys. Rev. Letters 28, 1278 (1972)
- WOZNIAK, G. J., (See Harney, H. L., LBL-1214)
- YARKONY, D. R., W. P. Hunt, and H. F. Schaefer III
Relation between electronic structure and the chemiluminescence arising from collisions
between alkaline earth atoms and halogen molecules
LBL-681, June 1972
J. Chem. Phys.
- YOURD, R., (See Main, R. M., LBL-1222)
- ZALKIN, A., (See St. Clair, D., UCRL-18901)
- ZALKIN, A., (See Fischer, M. S., LBL-646)
- ZALKIN, A., (See Templeton, L. K., LBL-669)
- ZALKIN, A., D. H. Templeton, and T. Ueki
The crystal structure of ℓ -ferrous-tris(1,10-phenanthroline)bis(antimonous d-tartrate)
octahydrate
LBL-1265, September 1972
Inorg. Chem.
- ZALKIN, A., (See Hollander, F. J., LBL-1266)
- ZALKIN, A., (See Hollander, F. J., LBL-1267)

ZALKIN, A., (See Hollander, F. J., LBL-1268)

ZALKIN, A., (See Hollander, F. J., LBL-1273)

ZISMAN, M. S., (See Bacher, A. D., UCRL-20903)

ZISMAN, M. S., and B. G. Harvey

High-spin levels of $^{92, 93, 94, 95, 96}\text{Nb}$ and ^{94}Tc populated with (α, d) and (α, t) reactions at
50 MeV

LBL-226, August 1971

Phys. Rev. C 5, 1031 (1972)

ZISMAN, M. S., (See Sherman, J. D., LBL-227)

ZISMAN, M. S., (See Harvey, B. G., LBL-651)

ZISMAN, M. S., (See Kovar, D. G., LBL-1201)

ZISMAN, M. S., (See Bruge, G., LBL-1238)

ZISMAN, M. S.

Transfer reactions in the Zr-Mo region induced by α particles and heavy ions

LBL-1247, August 1972

Ph. D. Thesis

ZISMAN, M., (See Stock, R., Phys. Rev. C 6, 1226 (1972))

VII. Author Index

Author Index

Contributors to This Report

- Abraham, M. M., 253
 Adams, C. J., 274
 Albee, A. D., 342
 Alonso, C. T., 134, 158
 Alonso, J., 124, 163
 Artzy, M., 336
 Arvieux, J., 57, 70, 365
 Asaro, F., 8, 331, 333, 336, 342
 Ascutto, R. J., 113
 Bacher, A. D., 50, 67
 Bacon, F., 234, 236, 238, 241, 393
 Bartlett, N., 226, 269, 270, 272, 274
 Bassichis, W. H., 142
 Becchetti, F., 85, 87, 90, 93, 95, 115
 Bender, C. F., 262
 Bennett-Corniea, W., 304
 Benson Jr., D., 15
 Birchall, J., 57, 365
 Bonner, B. E., 58
 Bowen, J., 368, 372
 Bowman, H. R., 333, 342
 Bowman, J. D., 4, 359, 378
 Broste, W. D., 58
 Browne, E., 3
 Bucher, J., 310, 312
 Budinger, T., 321
 Camplan, J., 112
 Carneiro, A., 368
 Cavell, R. G., 184
 Cerny, J., 67, 70, 71, 74, 76, 77, 81, 361
 Chadi, D. J., 181
 Chang, B., 358
 Cheifetz, E., 44
 Chu, B., 310
 Church, D. A., 258
 Clark, D. J., 368, 371, 372, 373
 Clem, R. G., 320, 386, 388
 Clements, T., 149
 Cohen, M. L., 181
 Conway, J. G., 250, 251, 252
 Conzett, H. E., 50, 52, 55, 57, 58, 59, 61, 63, 365
 Dahme, W., 55, 57, 58, 59, 61, 365
 Dairiki, J., 3
 Davenport, I. F., 329, 393
 Davis, D. W., 171, 197
 Davis, S. P., 251
 Davison, C. C., 394
 de Swiniarski, R., 50, 63
 Diamond, R. M., 12, 15, 17, 19, 310, 312
 Dod, R. L., 395
 Doebler, R., 3
 Drury, J. S., 44
 Edelstein, N., 253
 Eppley, R. E., 4, 359
 Erdal, B. R., 112
 Ernst, J., 50
 Evett, M., 317, 322
 Fee, D. C., 300, 314, 376
 Finch, C. B., 253
 Fischer, M. S., 274
 Frazier, P., 372
 Frois, B., 63
 Gabor, G., 366
 Garrison, W. M., 302, 303, 304
 Gatti, R. C., 25, 41
 Gee, G. Y., 385
 Geneux, E., 355
 Gennis, M., 270
 Giaunque, R. D., 382
 Gibler, D. D., 270, 274
 Giorni, A., 119
 Giusti, E. R., 44
 Glendenning, N. K., 113, 136
 Go, M. K., 100
 Gorman, D. J., 6
 Gough, R. A., 77, 81, 361
 Goulding, F. S., 380, 382
 Gunnink, R., 10

- Haas, H., 242
 Hadeishi, T., 246, 248, 355, 358
 Halperin, J., 44
 Hanna, S. S., 232
 Hansen, P. G., 112
 Harney, H. L., 67, 71, 74, 364
 Harvey, B. G., 85, 87, 90, 93, 95, 366
 Hebert, A. J., 350
 Heizer, R. F., 342
 Hendrie, D. L., 93, 95, 97, 119, 136
 Hester, T. R., 342
 Heunemann, D., 37, 41
 Hodgson, K. O., 277, 279, 282, 284
 Hollander, F. J., 289, 291, 293, 295, 395
 Hollander, J. M., 3, 9
 Hollowell, C. D., 385
 Homeyer, H., 93, 95, 366
 Huizenga, J., 25
 Hunter, J. B., 379, 380
 Hung, S. T.-C., 396
 Hyde, E. K., 4, 359

 Immele, J. D., 146, 147, 397

 Jacob Jr., N. P., 106
 Jaklevic, J. M., 380, 382
 Jardine, L. J., 3, 9
 Jared, R. C., 37, 41, 43, 44, 379, 380
 Jayko, M. E., 302
 Jolley, N. A., 70, 71, 74
 Joannopoulos, J. D., 181

 Kaindl, G., 213, 215, 220, 223, 225, 226,
 228, 232, 234, 236, 238, 241
 Kataria, S. K., 33, 37, 153
 King, C. J., 325, 329
 King, N. S. P., 58
 Klapisch, R., 108, 109, 112
 Kleber, M., 117
 Kolbe, W., 253
 Kovar, D. G., 61, 85, 87, 90, 93, 95
 Kowalczyk, S., 177, 180, 181, 184, 187,
 189, 192, 202, 208
 Krappe, H. J., 132
 Kratz, J. V., 308
 Kugler, E., 112

 Lamontagne, R., 63
 Landis, D. A., 378, 380
 Larimer, R. M., 52, 57, 59, 61, 365
 Leary, K., 226, 269
 Lederer, C. M., 3, 10
 Lee, D. M., 346, 398
 Leemann, Ch., 52, 55, 58, 59, 61
 Leigh, J. R., 12
 Leong, J., 284
 Ley, L., 177, 180, 181, 184, 187, 189, 192,
 202, 208
 Liljenzin, J. O., 308
 Liskow, D. H., 262
 Litton, G., 320
 Loiseaux, J. M., 76

 Ma, C. W., 160, 167
 Macdonald, J. A., 55, 67
 Mahnke, H.-E., 238, 241
 Mahoney, J., 85, 87, 90, 93, 95, 366
 Maier, K. H., 12
 Maier, M. R., 15
 Maples, C., 3
 Markowitz, S. S., 100, 106, 300, 314, 346,
 376
 Marrus, R., 355
 Mayer, B., 61, 85, 87
 McFeely, F. R., 187, 189, 192
 McKee, J. S. C., 52, 59
 McLaughlin, R. D., 358, 385
 Meiner, H., 50
 Mendelson Jr., R. A., 76
 Meulders, J. P., 55
 Meunier, R., 112
 Meyer, R. A., 10
 Michel, H. V., 6, 8, 331
 Michel, M. C., 246, 248, 355
 Miller, D. W., 87
 Mills, B., 184
 Möller, P., 126, 140
 Moretto, L. G., 22, 25, 28, 31, 37, 41,
 149, 153, 155
 Morrell, B. K., 270, 272
 Morris, D., 368, 372
 Moyer, B., 331
 Murphy, T. F., 398
 Myers, W. D., 128, 140

- Nagarajan, M. A., 90, 114, 115
 Nakai, K., 12
 Nakamura, M., 358
 Nardi, E., 22, 31, 33
 Needham, R., 163
 Newton, A. S., 306, 317, 321, 322
 Newton, J. O., 19
 Nifenecker, H., 35, 43
 Nilsson, S. G., 17, 140
 Nix, J. R., 132, 140
 O'Neil, S. V., 262
 Pearson, P. K., 262
 Pehl, R. H., 382
 Perlman, I., 331, 333, 336, 342
 Perry, W., 184
 Petrovich, F., 121, 122, 144
 Prieels, R., 108, 109
 Pollak, R. A., 177, 180, 181, 184, 187, 189, 192, 202, 208, 399
 Poskanzer, A. M., 108, 109, 112, 359, 378
 Prussin, S. G., 9
 Pühlhofer, F., 12, 85, 87
 Randrup, J., 126, 140
 Rasmussen, J. O., 158, 160, 163
 Raymond, K. N., 277, 279, 282, 284
 Resmini, F. G., 50
 Rezanka, I., 163
 Ribbe, W., 163
 Rieke, R. D., 400
 Rigaud, C., 108, 109
 Roeckl, E., 108, 109
 Russell, P. B., 228, 232
 Rytz, A., 6
 Sagle, A., 58
 Salomon, D., 213, 215, 220, 223, 225, 401
 Schaefer III, H. F., 254, 258, 262
 Schmieder, R. W., 246, 355
 Sciamanna, A. F., 306, 317, 321, 322
 Seaborg, G. T., 308
 Sextro, R. G., 77, 81, 361
 Shalimoff, G. V., 252
 Sherman, J. D., 85, 93, 97, 119
 Shih, T.-S. T., 401
 Shihab-Eldin, A., 3
 Shirley, D. A., 3, 171, 177, 180, 181, 184, 187, 189, 192, 195, 197, 202, 204, 208, 210, 234, 236, 238, 241, 242
 Siemens, P. J., 115
 Silva, R. J., 44, 308
 Sletten, G., 112
 Slobodrian, R. J., 63
 Soinski, A. J., 236
 Sokol, H. A., 302, 304
 Stephan, C., 112
 Stephens, F. S., 12, 15, 17, 19
 Steyaert, J., 368
 Stoughton, R. W., 44
 Street Jr., K., 350
 Stross, F. S., 342
 Struble, G. L., 146, 147
 Sundell, S., 112
 Swiatecki, W. J., 140
 Templeton, D. H., 286, 289, 291, 293, 295, 296, 298
 Templeton, L. K., 296
 Thibault, C., 108, 109
 Thomas, T. D., 171
 Thompson, R. W., 325, 402
 Thompson, S. G., 22, 25, 31, 33, 37, 41, 43, 44, 46, 379, 380
 Tressaud, A., 272
 Tsang, C. F., 46, 140, 142, 167
 Tuerpe, D. R., 142
 Tys, J., 112
 Ueki, T., 286
 Van Deurzen, C. H. H., 251, 252
 Vautherin, D., 136
 Veneroni, M., 136
 Vogelsberg, F., 386
 von Groote, H., 131, 140
 von Oertzen, W., 93, 95
 Ward, D. L., 298
 Weisenmiller, R. B., 70, 71, 74
 Wernau, W. C., 402
 Westgaard, L., 112

Wilcox, K. H., 70, 74

Wilets, L., 142

Worden, E. F., 250

Wortmann, G., 215

Wozniak, G. J., 70, 71, 74, 76, 364

Yarkony, D. R., 262

Yellin, J., 246, 248, 355

Zalkin, A., 269, 270, 272, 274, 286, 289,
291, 293, 295, 296, 298

Zisman, M. S., 85, 87, 93, 403

in

Numerical

order

12/3/98

LEGAL NOTICE

This report was prepared as an account of work sponsored by the United States Government. Neither the United States nor the United States Atomic Energy Commission, nor any of their employees, nor any of their contractors, subcontractors, or their employees, makes any warranty, express or implied, or assumes any legal liability or responsibility for the accuracy, completeness or usefulness of any information, apparatus, product or process disclosed, or represents that its use would not infringe privately owned rights.